COLLECTED REPRINTS OF THE WAVE PROPAGATION LABORATORY

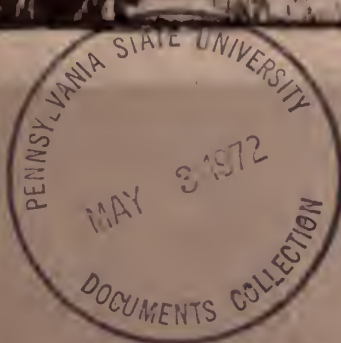**U.S. DEPARTMENT OF COMMERCE**
National Oceanic and Atmospheric Administration
Environmental Research Laboratories
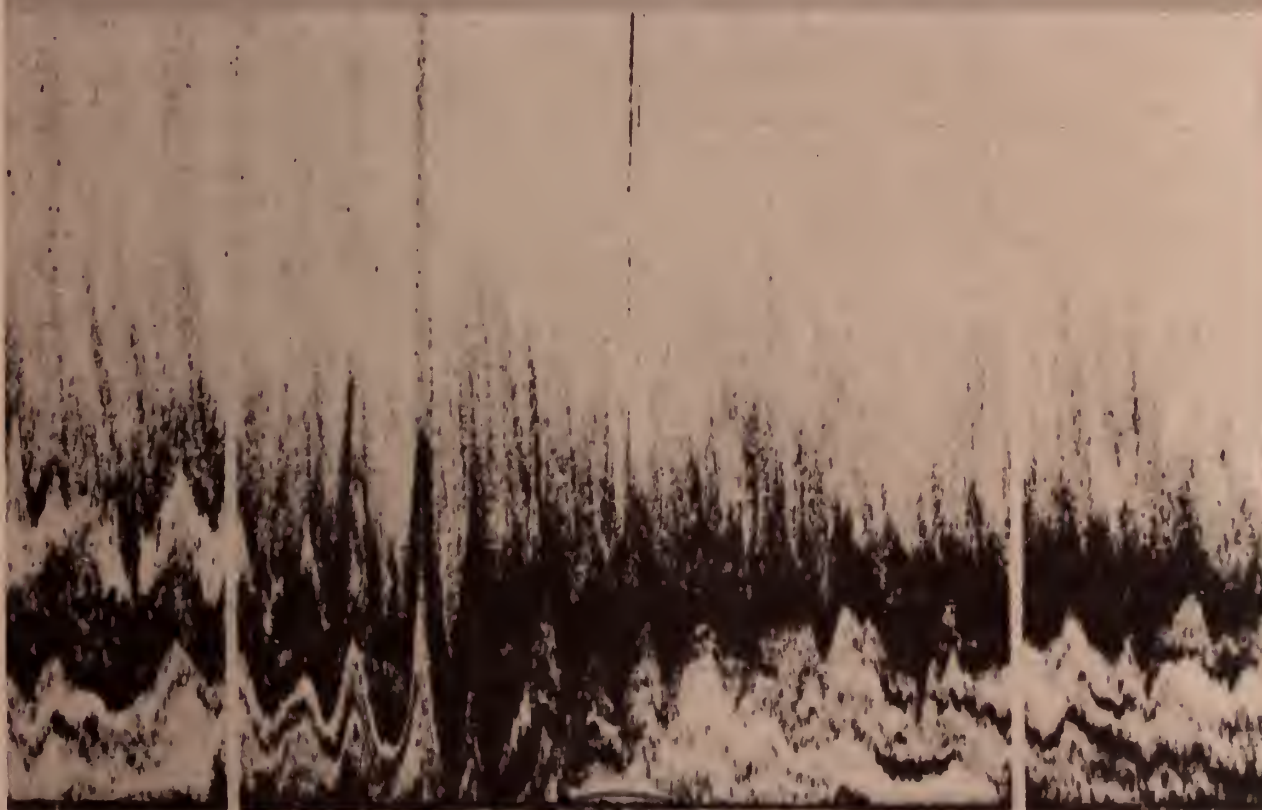
BOULDER, COLO.
NOVEMBER 1971

U.S. DEPARTMENT OF COMMERCE
Maurice H. Stans, Secretary

NATIONAL OCEANIC AND ATMOSPHERIC ADMINISTRATION
Robert M. White, Administrator

ENVIRONMENTAL RESEARCH LABORATORIES
Wilmot N. Hess, Director

COLLECTED REPRINTS

OF THE

WAVE PROPAGATION LABORATORY

(May 1967 Through December 31, 1969)

TABLE OF CONTENTS

9.   Earnshaw, K. B., and J. C. Owens, 1967, A dual wavelength optical distance measuring instrument which corrects for air density, IEEE Journal of Quantum Electronics QE-3, No. 11, 544-550.

10. Kleen, R. H., and N. L. Abshire, 1968, Atmospheric scattering from a 1.15-micron laser beam and its off-axis detectable range, ESSA Technical Report ERL 90-WPL 5, February.

11. Lawrence, R. S., J. C. Owens, and K. B. Earnshaw, 1967, The practicality of using light beams to distribute local oscillator signals over large antenna array, Proceedings of AGARD/EPC Symposium, No. 33, Ankara, Turkey, October 9-12, 1967.

12. Ochs, G. R., 1969, Measurement of 0.63 μm laser-beam scintillation in strong atmospheric turbulence, ESSA Technical Report, ERL 154-WPL 10, December.

13. Ochs, G. R., and R. S. Lawrence, 1969, Measurements of laser beam spread and curvature over near-horizontal atmospheric paths, ESSA Technical Report, ERL 106-WPL 6, February.

14. Ochs, G. R., R. R. Bergman, and J. R. Snyder, 1969, Laser-beam scintillation over horizontal paths from 5.5 to 145 kilometers, Letters to the Editor, Journal of Optical Society of America 59, No. 2, 231-234.

15. Ochs, G. R., and R. S. Lawrence, 1969, Saturation of laser-beam scintillation under conditions of strong atmospheric turbulence, Journal of Optical Society of America 59, No. 2, 226-227.

16. Owens, J. C., 1968, The use of atmospheric dispersion in optical distance measurement, presented at the Fourteenth General Assembly, International Union of Geodesy and Geophysics, September 25-October 7, 1967, Lucerne, Switzerland, Bulletin Geodesique, September.

17. Thayer, G. D., and B. R. Bean, 1969, A comparison of radar and radio interferometer refraction errors, IEEE Transactions on AES, AES-5, No. 2, March, 346-350.

SECTION 3
Remote Sensing of Atmospheric Properties

18. Bean, B. R., and Q. L. Florey, 1968, A field study of the effectiveness of fatty alcohol mixtures as evaporation reducing monomolecular films, Water Resources Research 4, No. 1, February, 206-208.

19. Bean, B. R., 1967, Our battle for water, ESSA World 2, No. 4, October, 12-13.

20. Bean, B. R., R. E. McGavin, C. B. Emmanuel, and R. W. Krinks, 1969, Radio-physical studies of evaporation at Lake Hefner, 1966 and 1967, ESSA Technical Report, ERL 115-WPL 7, June.

21. Bean, B. R., and B. D. Warner, 1967, Some radio-physical considerations in studies of the fine scale structure of the atmosphere, Proceedings of the International Colloquium, Moscow, June 15-22, 1965, ed. A. M. Yaglom and V. I. Tatarsky, Nauka.

22. Bowman, H. S., 1968, 'Subsonic' waves and severe weather phenomena, Proceedings of ESSA/ARPA Acoustic-Gravity Wave Symposium, July 15-17, 1968, October, 215-222.

23. Emmanuel, C. B., 1968, Radiative equilibrium temperature distribution of the atmosphere of Mars, Journal of Geophysical Research 73, No. 10, May 15, 3213-3218.

24. Grossman, R. L., B. R. Bean, and W. E. Marlatt, 1969, Airborne infrared radiometer investigation of water surface temperature with and without an evaporation-retarding monomolecular layer, Journal of Geophysical Research 74, No. 10, May 15, 2471-2476.

25. Krause, F., V. E. Derr, N. L. Abshire, and R. G. Strauch, 1969, Remote probing of wind and turbulence through crosscorrelation of passive signals, Proceedings of Sixth International Symposium on Remote Sensing of the Environment, University of Michigan, October 13-16, 1969, 327-358.

26. Lawrence, R. S., 1969, Remote atmospheric probing by ground-to-ground line of sight optical methods, Atmospheric Exploration by Remote Probes, RAPP Report, NAS-NRC, Committee on Atmospheric Science 2, 91-110.

27. Lhermitte, R. M., 1969, Atmospheric probing by Doppler
     Radar, RAPP Report, NAS-NRC, Committee on Atmospheric
     Science 2, 253-285.

28. Lhermitte, R. M., 1969, Doppler Radar observation of a
     convective storm, Proceedings of Sixth Conference on
     Severe Storms, American Meteorological Society, Chicago,
     Illinois, April 8-10, 1969, 139-145.

29. Lhermitte, R. M., 1969, Note on the observation of
     small-scale atmospheric turbulence by Doppler Radar
     techniques, Radio Science 4, No. 12, 1241-1246.

30. Lhermitte, R. M., 1969, Turbulent air motion as observed
     by Doppler Radar, Proceedings of the Wind Measurement
     Session, Thirteenth Radar Meteorology Conference, Pro-
     ceedings of American Meteorological Society, August,
     498-503.

31. Little, C. G., 1969, Acoustic methods for the remote
     probing of the lower atmosphere, Proceedings of the IEEE
     57, No. 4, 571-578.

32. Little, C. G., 1968, Monitoring the earth environment,
     AIAA Seminar, July 19-20, 1968, Colorado State
     University, Fort Collins, Colorado.

33. Owens, J. C., 1969, Optical Doppler measurement of
     micro-scale wind velocity, Proceedings of the IEEE 57,
     No. 4, 530-536.

34. Westwater, E. R., and O. N. Strand, 1968, Statistical
     information content of radiation measurements used in
     indirect sensing, Journal of the Atmospheric Sciences
     25, No. 5, September, 750-758.

S E C T I O N   4

Development of Instruments and Techniques

35. Bean, B. R., and R. O. Gilmer, 1969, Comparison of
     barium fluoride humidity element with the microwave
     refractometer for studies of rapid fluctuations of
     atmospheric humidity, Radio Science 4, No. 12, 1155-1157.

36. Dougherty, H. T., 1969, An expansion of the Helmholtz
     integral and its evaluation, Radio Science 4, No. 11,
     991-995.

37. Dougherty, H. T., 1969, Radio wave propagation for ir-
     regular boundaries, Radio Science 4, No. 11, 997-1004.
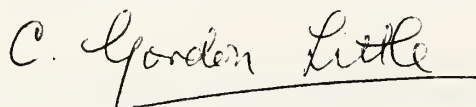
38. Lhermitte, R. M., 1968, New developments in Doppler Radar methods, Proceedings of the Thirteenth Radar Conference, August, 14-17.

39. McNice, G. T., and V. E. Derr, 1969, Analysis of the cylindrical confocal laser resonator having a single circular coupling aperture, Journal of Quantum Electronics QE-5, No. 12, 569-575.

40. Ochs, G. R., 1968, A circuit for the measurement of normalized crosscorrelations, ESSA Technical Report, ERL 63-WPL 2, March.

41. Ochs, G. R., 1967, A resistance thermometer for measurement of rapid air temperature fluctuations, ESSA Technical Report, IER 47-ITSA 46, October.

42. Schwiesow, R. L., 1969, Optimum illumination geometry for laser raman spectroscopy, Journal of Optical Society of America 59, No. 10, 1285-1287.

43. Strauch, R. G., D. A. Stephenson, and V. E. Derr, 1969, Refractive index of D_2O at the HCN laser frequency, Infrared Physics 9, Letters, Pergamon Press, October, 137-138.

44. Strauch, R. G., 1969, Technique for measurement of HCN-laser linewidth, Electronic Letters 5, No. 11, May 29.

45. Strand, O. N., and E. R. Westwater, 1968, Minimum-RMS estimation of the numerical solution of a Fredholm integral equation of the first kind, SIAM Journal on Numerical Analysis 5, No. 2, 287-295.

46. Strand, O. N., and E. R. Westwater, 1968, Statistical estimation of the numerical solution of a Fredholm integral of the first kind, Association for Computing Machinery, Inc., Journal of the Association for Computing Machinery 15, No. 1, 100-114.

Cover: Representation of traces of acoustic echo sounding of the atmosphere, taken at the Table Mountain Field Site, on March 3, 1971.

FOREWORD

The Wave Propagation Laboratory was created on May 7, 1967 to
focus initiative and resources within NOAA (then ESSA) on the problem
of developing <u>new</u> or improved methods for the remote measurement of
geophysical parameters. A comprehensive program of atmospheric remote
probing has evolved from an initial nucleus of electromagnetic wave
propagation projects previously located in the Institute for Telecommuni-
cation Sciences and Aeronomy. During the time period covered by this
volume of reprinted scientific papers, new projects, staff members
and resources were added to achieve a broadened research capability
which now includes basic and applied research on both the theoretical
and experimental aspects of electromagnetic and acoustic wave propa-
gation.

This first volume of Collected Reprints of the Wave Propagation
Laboratory comprises work published from the origin of the Laboratory
in May 1967, through December 31, 1969. The papers and reports con-
tained in this volume have been selected to minimize inclusion of
duplicate or extraneous material. Many of these papers were originally
published in relatively obscure media, and others take on added
significance by being presented with complementary or supplementary
reports. It is hoped that this and subsequent volumes will provide
the reader with a valuable source of information on recent progress
in the study of the interaction of EM and acoustic waves with the
atmosphere. Although this first volume only hints of results which
have already been obtained, and which will presumably be available
in the next volume, the discerning reader will recognize that remote
probing is not merely an extension of standard atmospheric in situ
measurements but produces significant new insights and information
about the atmosphere previously unattainable by other methods.

C. Gordon Little

C. Gordon Little

1

Spectral interdependence of the radio refractivity and water vapor in the atmosphere

B. R. Bean and C. B. Emmanuel

Wave Propagation Laboratory
ESSA Research Laboratories, Boulder, Colorado 80302

Continuous measurements of temperature, water vapor, and radio refractivity were taken over several days at a height of 11 meters above ground over the high plains of Colorado. A spectral analysis indicates that temperature fluctuations contribute little to radio refractivity fluctuations, which are primarily caused by variations in water vapor density over a wide range of spectral frequencies.

INTRODUCTION

The expression for radio refractivity N is normally written [*Bean and Dutton*, 1966]

$$N = K_1(P/T) + K_2(\rho_w/T) \quad (1)$$

where P is the atmospheric pressure in mb, T is the temperature in °K, ρ_w is the water vapor density in g/m³, and K_1 and K_2 represent constants whose values are well known. If for the particular period of analysis we assume a constant pressure, P_0, and let the temperature have a mean value plus a fluctuation about the mean, i.e.,

$$T = T_0 + t \quad (2)$$

then (1) may be written

$$N = \frac{K_1}{T_0} \frac{P}{(1 + t/T_0)} + \frac{K_2}{T_0} \frac{\rho_w}{(1 + t/T_0)} \quad (3)$$

Noting that $t/T_0 \sim 0.02$, we may expand (3) to

$$N = K_1 \frac{P_0}{T_0}\left(1 - \frac{t}{T_0}\right) + K_2 \frac{\rho_w}{T_0}\left(1 - \frac{t}{T_0}\right) \quad (4)$$

For standard atmospheric conditions,

$$D_0 \equiv K_1(P_0/T_0) \sim 200$$

and

$$W_0 \equiv K_2(\rho_{w_0}/T_0) \sim 20$$

Then neglecting t/T_0 leads to errors of $\sim 4N$ and $\sim 0.4N$ units in D_0 and W_0, respectively. We therefore write

$$N = K_1(P_0/T_0)[1 - (t/T_0)] + K_2(\rho_w/T_0) \quad (5)$$

from which results

$$\rho_w = (NT_0/K_2) - (K_1/K_2)P_0 + (K_1/K_2)(P_0/T_0)t \quad (6)$$

We will indicate ρ_w as determined from (6) as $\rho_w(N, t)$.

We may now take $S[\rho_w(N, t)]$, the spectral density of ρ_w, as the sum of the spectral densities of N and t [*Davenport and Root*, 1958]

$$S[\rho_w(N, t)] = \left(\frac{T_0}{K_2}\right)^2 S(N) + \left(\frac{K_1 P_0}{K_2 T_0}\right)^2 S(t)$$

$$+ 2\frac{K_1 P_0}{K_2^2} C(N, t) \quad (7)$$

where $C(N, t)$ represents the cross spectrum between N and t. Again, for average experimental conditions, we find that

$$S[\rho_w(N, t)] = (2.29 \times 10^{-2})S(N)$$

$$+ (1.7 \times 10^{-4})S(t) + (4.45 \times 10^{-3})C(N, t) \quad (8)$$

Figures 1 and 2 show the spectral density of T, ρ_w, and N for several wavelengths of approximately 30 to 3000 meters at 11 meters above ground during experiments on July 25, 1963, and August 15, 16, 1963, at the Gunbarrel Hill site in Colorado. Details of these experiments have been discussed previously by *Bean et al.* [1967]. Each point represents a 45-minute average centered about the time indicated. As was shown by *Bean and Warner* [1967], the spectral variation of N and ρ_w for slightly stable conditions (0645–0730, $Ri = +0.5$) and for unstable conditions (1300–1345, $Ri = -0.18$) yields values of (coherence)$^{1/2} \geq 0.6$ for all wavelengths greater than about 100 meters (Figure 3). A third

Fig. 1.   Spectral density per unit bandwidth of temperature, water vapor, and refractivity at several wavelengths measured 11 meters above ground on July 25, 1963 (MST), at Gunbarrel Hill, Colorado.
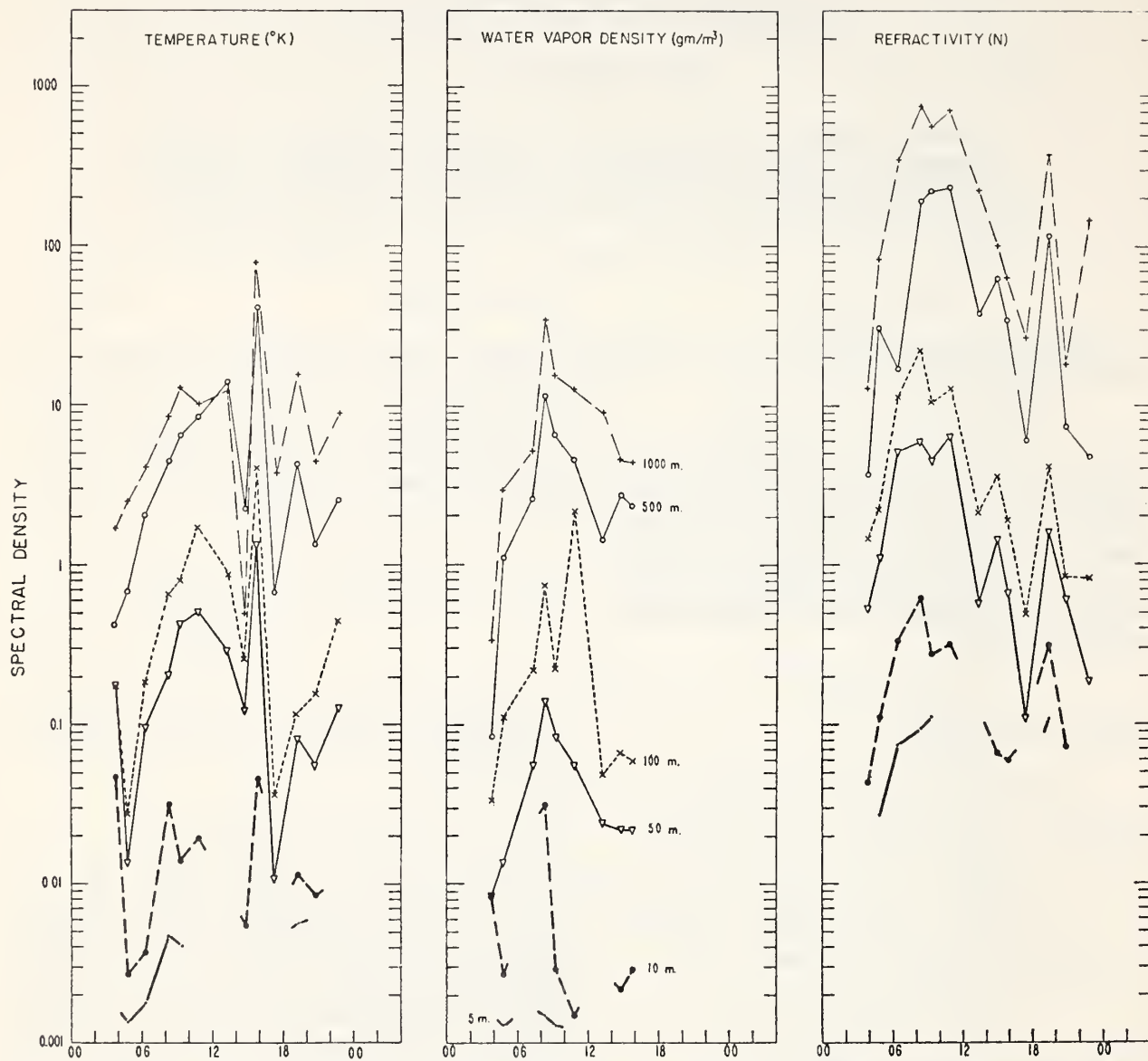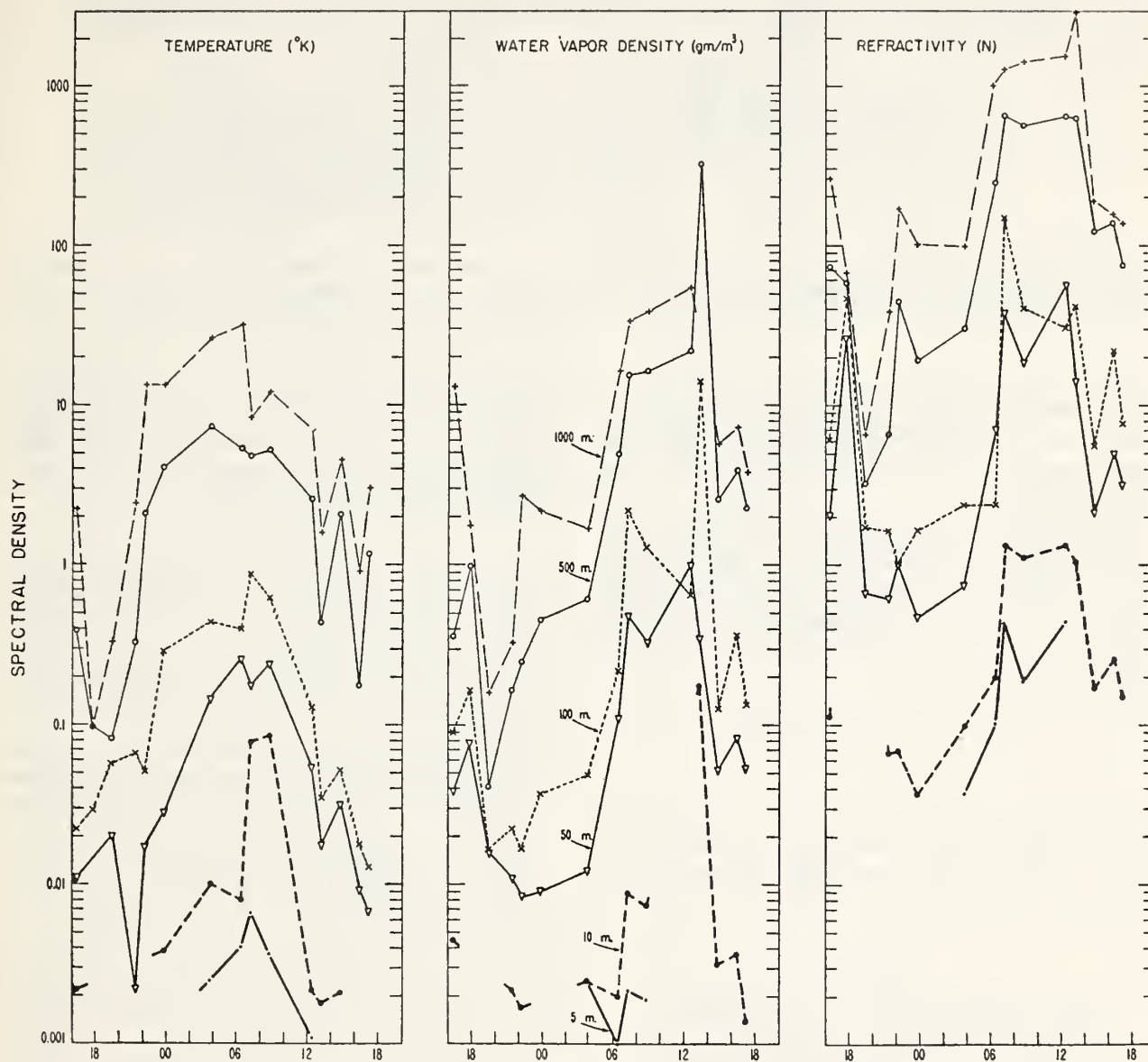
Fig. 2.   Spectral density per unit bandwidth of temperature, water vapor, and refractivity at several wavelengths measured 11 meters above ground on August 15 and 16, 1963 (MST), at Gunbarrel Hill, Colorado.
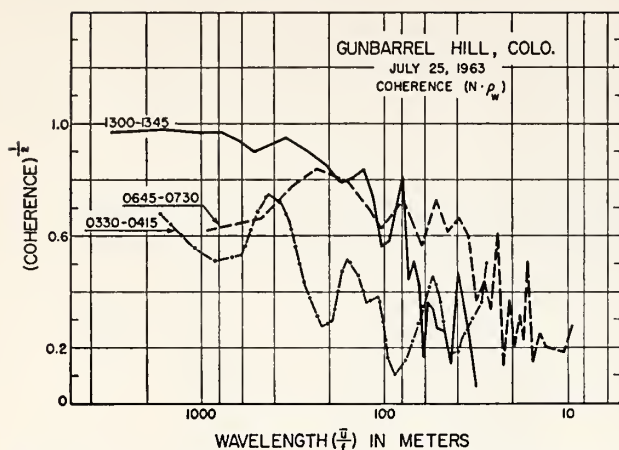
Fig. 3. Coherence of N and ρ_w for stable (0330–0415 and 0645–0730 MST) and unstable (1300–1345 MST) conditions, Gunbarrel Hill, Colorado, July 25, 1963.

Fig. 4. Percentage of spectral density of ρ_w contributed by temperature when ρ_w is calculated as a function of N and temperature.

coherence curve is given for a very stable case (0330–0415), in which the spectral variations of N and ρ_w are small compared with the other two cases and the coherence remains low throughout the range of observation.

In our experiments, N was found to vary 10 to 20 units compared with t, indicating that variations of t would contribute 5 to 10% of the observed variation in $\rho_w(N, t)$. Thus, one can evaluate the percentage contribution of t to $\rho_w(N, t)$ for any particular frequency as

$$\frac{(1.7 \times 10^{-4})S(t) + (4.45 \times 10^{-3})C(N, t)}{S(\rho_w)} \times 100$$

This quantity was evaluated for the data of August 16, 1963; the results for various frequencies are shown in Figure 4. We can see that the contribution of t to $\rho_w(N, t)$ is greatest at night and at the lowest

frequencies, but it never exceeds 7%. This indicates that variations of $\rho_w(N, t)$ are well correlated with variations of N for the conditions of this experiment, and they would probably be even more closely correlated for more humid climates.

REFERENCES

Bean, B. R., and E. J. Dutton (1966), *Radio Meteorology, NBS Monograph 92*, 1–21, U. S. Government Printing Office, Washington, D. C.

Bean, B. R., C. B. Emmanuel, and R. W. Krinks (1967), Some spectral characteristics of the radio refractivity in the surface layer of the atmosphere, *Radio Sci., 2(5)*, 503–510.

Bean, B. R., and B. D. Warner (1967), Some radio-physical considerations in studies of the fine scale structure of the atmosphere, in *Atmospheric Turbulence and Radio Wave Propagation*, 215–224, Nauka, Moscow, USSR.

Davenport, W. B., Jr., and W. L. Root (1958), *An Introduction to the Theory of Random Signals and Noise*, McGraw-Hill, New York.

Some Spectral Characteristics of the Radio Refractivity in the Surface Layer of the Atmosphere

B. R. Bean, C. B. Emmanuel, and R. W. Krinks

Institute for Telecommunication Sciences and Aeronomy, ESSA, Boulder, Colo. 80302, U.S.A.

Experimental data suggest that the spectral density of the radio refractivity, N, exhibits a strong dependence on stability (Richardson's number, R_i) at the low frequency range and a weak dependence on stability at the high frequency range. Furthermore, the average spectral decay of N was found to be in reasonably good agreement with the "$-5/3$" law; however, significant departures from this law were observed depending upon the frequency range considered. In fact, systematically smaller spectral decays were observed at low frequencies and larger decays at high frequencies.

1. Introduction

The last decade has seen ever increasing use of radio waves propagated through the troposphere. Although radio physicists have many conflicting views on the precise manner in which these waves are propagated, all agree that the radio refractive index, n, plays a central role in such propagation. (For a recent review of present theories, see Du Castel, 1965.) For example, the gradient of n determines the refraction of radio waves while the scintillation of radio signals is attributed to the rapid temporal and spatial variation of n. For this reason, there have been many studies of the n structure of the troposphere. Straiton (1964) has given a recent review of the state of the art of radio refractometry, comparative accuracy of different techniques, and typical experimental arrangement of instruments.

The present study differs from previous ones in that it utilizes refractometer cavities spaced vertically on a tower that is also equipped with sufficient auxiliary meteorological sensors to determine atmospheric stability. This, then, allows comparison of the spectral variation of n with that found in the more classical literature of turbulence.

2. Data and Analysis

The experimental data were obtained at the Gunbarrel Hill field site of the National Bureau of Standards, located approximately 9 miles NE of Boulder, Colorado. The general features of the terrain along the direction of the prevailing wind are shown on figure 1. The observing tower is of the open-mast type and approximately 150 ft in height. The instruments were all mounted 6 ft away from the tower so that the prevailing wind would impinge on them before the tower, thus reducing tower interference. General information concerning the meteorological

instruments used in this study is given in table 1. The measurements for this study were as follows:

(i) 25 ft — wet and dry bulb temperature, relative and absolute refractive index, wind speed and direction;
(ii) 36 ft — same as (i), also vertical wind via angle of attack of total wind;
(iii) 62 ft — relative refractive index;
(iv) 150 ft — same as (i).

Calibrations of temperature, humidity, refractive index, and pressure sensors were maintained by Assman psychrometer and Paulin barometer readings taken at each of the recording levels at approximately half-hour intervals. All data, except the wind, were recorded on magnetic tape and subsequently digitized at a rate of 25 samples per second. These latter data were then averaged over 1 sec periods. The wind speed and direction were recorded on paper charts, subsequently transferred onto magnetic tape, and then analyzed in a fashion similar to the other data.
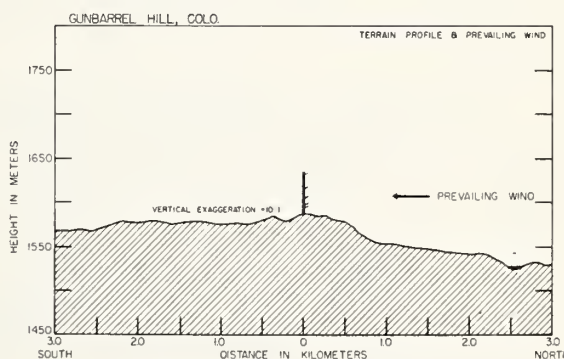

FIGURE 1. *Terrain variation in the direction of the prevailing wind.*

TABLE 1.   *Recording Instrumentation—Gunbarrel Hill—Summer, 1963.*

Parameter to be measured	Type of sensor	Signal conditioning equipment	Frequence response of system	System accuracy*	Comments
Precipitation..........	Weighing rain gauge	None...............	....	± .01" rain (a).........	Remote recording
	Tipping bucket rain gauge	None...............		± .01" rain (a).........	Remote recording
Temperature..........	Thermocouples 5 mil copper constantan	D.C. amplifiers........	Dry bulb 4 Hz. Wet bulb 0.5 Hz (limited by sensor)	± 0.25 °C(a)	Calibrated with mercury thermometers, in reference baths
		Reference oven			
Wind speed..............	Cup anemometers ...	None...................	Distance constant = 4.6 ft	± 1 mph a..............	Accuracy very poor below 3 mph
Direction (horizontal)	Plastic vane (sine-cosine potentiometer)	None...................	Reaches 100% of swing with gust length of 5 ft but overshoots 300% with repeated gusts of 10 ft in length. Settles down to 110% for gust length of 25 ft	....	Accuracy good if repeated gusts of around 10 ft in length are not encountered
Vertical..................	Bivane...................	None...................	Reaches 90% with < 15 ft gust length	± 0.5°...................	Overshoot 12% at 20 ft gust length
Refractivity.............	Absolute ref. (vetter absolute)	None...................	1 Hz (limited by servo in system)	≅ 1.0N(a)** 0.01N(r)**	See footnote A
	Relative ref.............	None...................	10 Hz (limited by cavity, distance constant 2')†	± 0.01N(r)**	
Time....................	Motor driven timer ...	Relays.............	....	0.25 sec (a) 0.1 sec (r)	Calibrated daily with WWV

*Absolute accuracy.
**(a) Exclusive of cavity errors.
(r) For periods of the order of 1 hr.
†Gilmer, et al. (1964).
A. (a) Absolute accuracy: i.e., can be calibrated within these limits.
   (r) Resolution: i.e., can distinguish changes of 0.01 N.
Comments: Drift in electronics over reasonably long periods, e.g., 1 hr is no greater than 0.1 N.
          Drift due to thermal characteristics of the cavity is slow and can be compensated by frequent calibration. Overall absolute accuracy is approximately 1.5 N.

The data available for the present analyses were taken on July 25–26 and August 14–16, 1963. Examples of the refractivity, N, as defined by $N = (n-1) 10^6$, and temperature data are given on figure 2 for the night of July 25, 1963. Of interest here are the large and rapid fluctuations of N that occurred between 2300 on the 25th and 0100 on the 26th. During this time rain was observed to fall on the tower; the wet bulb at 25 ft remained relatively constant while the dry bulb followed very closely the refractive index fluctuations.

The recorded data were sampled and digitized at the rate of 25 samples per second in 45-min blocks. The digitized samples were averaged in nonoverlapping sets of 25 samples to obtain a sample rate of 1 per sec. The averaged data were prewhitened, spectrally analyzed, and the spectral densities corrected for the effects of averaging and prewhitening as described by Blackman and Tukey (1958).

An examination of a few selected samples will bring forth the pertinent points of the more extensive analysis that follows. These samples, all taken from the July 25, 1963, data are:

Case I (0330–0415): Calm, stable, temperature inversion.
Case II (0645–0730): Temperature inversion partially destroyed by solar heating.
Case III (1115–1200): Fully developed convection.
Case IV (2115–2200): Developing nocturnal radiation inversion.
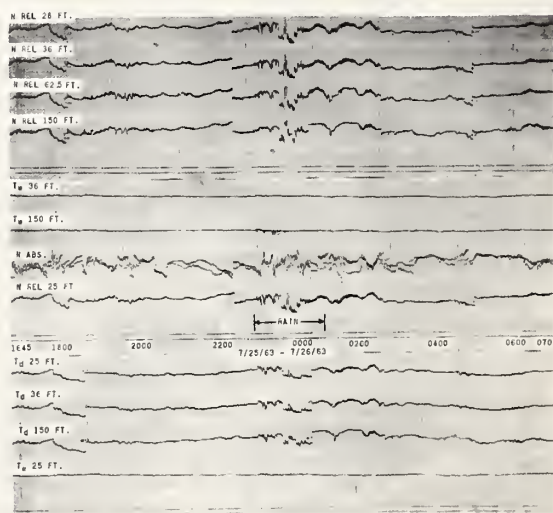
FIGURE 2. *Example of* N, *dry and wet bulb temperature recordings on July 25–26, 1963; Gunbarrel Hill, Colorado.*
(Note: These data are presented to show relative variations. Scale relations are: all N_{rel}, 4.2 N/large division; N_{abs}, 2.5 N/large division; all T, 1.8 °C/large division.)

These four cases are plotted in figures 3 and 4.

One should view these data as indicative of the large variation of spectral estimates of N with atmospheric stability. Further, considering the errors
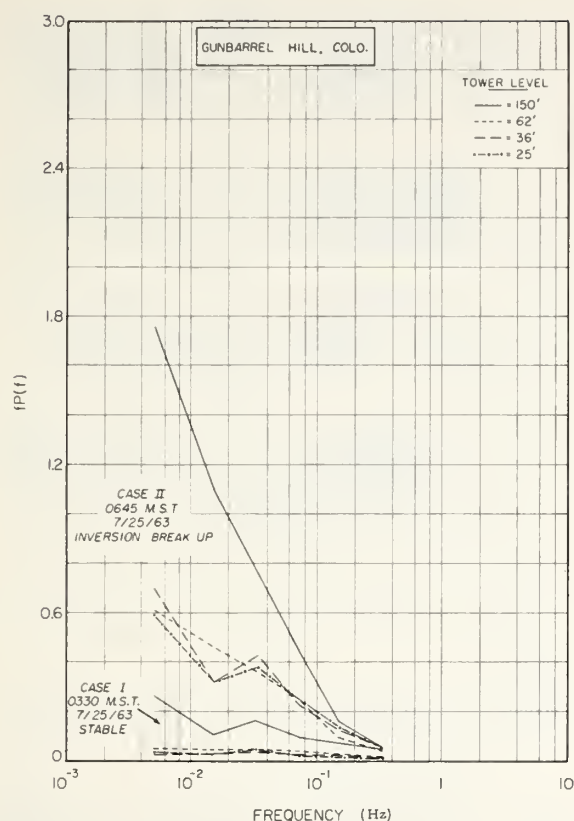
FIGURE 3. *Spectral density of* N *for stable and slightly un-stable conditions at Gunbarrel Hill, Colorado, July 25, 1963.*
(Note: Spectral density of *N* has the units of Hz⁻¹ so that *f*P(*f*) is dimension-less).

FIGURE 4. *Spectral density of* N *for fully developed convection and developing inversion at Gunbarrel Hill, Colorado, July 25, 1963.*

of spectral estimates, one would not expect that varia-tions of spectral density of, say, 10 percent to be necessarily due to real processes in the atmosphere. The most striking feature of these data is the sensi-tivity of the low frequencies to stability. For ex-ample, compare Case I (stable) with Case II, where the nocturnal radiation inversion was partially de-stroyed by solar heating. All frequencies in Case II display greater spectral density, especially the lowest, arising from the mixing of moist dense air from near the surface with that at greater heights. The humidity contrast appears to be greatest at 150 ft where the low frequency spectral density is nearly three times greater than at 25 and 62 ft. By late morning, Case III, the lowest frequencies, shows a greater increase in spectral density, due perhaps to the presence of very long scales associated with convective mixing. Case IV represents conditions associated with a developing radiation inversion. Again, one notes that the entire spectrum is depressed compared to the unstable Case III.

This general trend as indicated by the four cases discussed is further illustrated by the isopleths of

spectral density versus height and time in figures 5 and 6. The data for July 25–26, 1963, follow rather closely the pattern described by the four cases men-tioned above, with one notable exception: the area of high spectral density about midnight on July 26, 1963, corresponds to the time of passage of a thundershower (see fig. 2). One notes that the increased spectral variation at the low frequencies originates at the ground and builds upwards with time. This is assumed to be associated with evaporation of the observer-reported trace of rain from the ground and subsequent upward turbulent mixing. Similarly, the data for August 15–16, 1963, follow the previously mentioned pattern even more closely, with the largest spectral densities being associated with the breakup of noc-turnal radiation inversions and convective activity during the late morning and afternoon hours.

A somewhat more quantitative analysis of these data was performed by dividing the spectral data into 6 frequency intervals (approximately logarithmic): 1.65×10^{-3} to 8.31×10^{-3} Hz, 10^{-2} to 2×10^{-2} Hz, 2.19×10^{-2} to 4.47×10^{-2} Hz, 4.68×10^{-2} to 9.78×10^{-2} Hz, 10^{-1} to 2.14×10^{-1} Hz, 2.19×10^{-1} to 4.70×10^{-1}
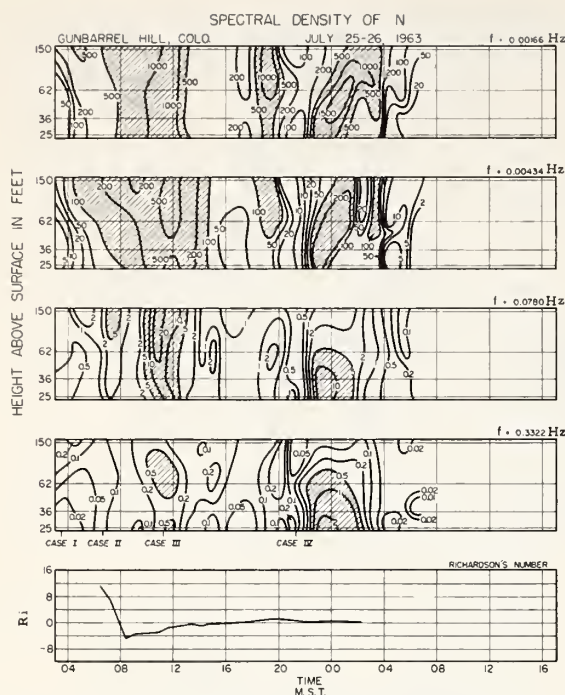
FIGURE 5. *Spectral density of* N *over the 150-ft tower at Gunbarrel Hill, Colorado during July 25–26, 1963.*
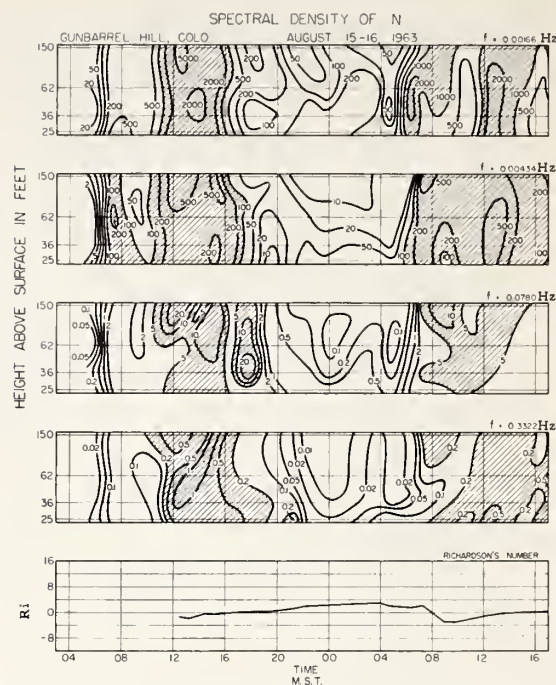

FIGURE 6. *Spectral density of* N *over the 150-ft tower at Gunbarrel Hill, Colorado during August 15–16, 1963.*

Hz. The data for each frequency range were then, via the method of least-squares, fitted to a function of the form $P(f) = P(f)_0 f^k$; then the average spectral density was determined for each frequency interval as well as the spectral slope, k.

The *average* spectral densities at all four tower heights so obtained are plotted on figure 7 for the lowest and highest frequency range, as well as all four tower heights versus Richardson's number, R_i. Richardson's number given by

$$R_i = \frac{g}{\overline{T}} \frac{\frac{\partial \overline{T}}{\partial z} + \Gamma}{\left(\frac{\partial \overline{u}}{\partial z} \right)^2},$$

where g is the acceleration due to gravity (m/s^2), $\overline{T}$ is the average temperature (°K), $\overline{u}$ is the average wind velocity (m/s), and Γ is the adiabatic lapse rate (°C/m), was obtained between the 25- and 150-ft tower heights for each 45-min interval. The values so obtained are accurate to within ±0.05. The data from each frequency range were in general agreement with the previous conclusions of the dependence of spectral density upon height and stability, but differed in important details. One would like to be guided by theory in the mathematical description of these details, but as Lumley and Panofsky (1964) warn in their recent

review of the structure of atmospheric turbulence, all expressions suggested to date have been essentially empirical interpolation formulae. Accordingly, the data were further divided into increments of one-half unit of R_i, a median determined, and an empirical estimate of the variation of average spectral density versus R_i drawn. The results of such an analysis for the 25- and 150-ft levels are given for comparison with the data points on figure 7 for the lowest and highest frequency intervals. This process was performed by several people as a consistency check. Cross-plotting and contouring was also performed for each height with frequency range as a parameter. The results of these checks indicate that the given contours are consistent to about 10 percent. A similar analysis was performed for the intermediate frequency intervals, but the results are not shown here.

A study of the results in figure 7 indicate two regions of high spectral density: one at slightly unstable conditions $(-2 < R_i < 0)$, and a second maximum during stable conditions at $R_i \approx +6$. This secondary maximum is particularly noticeable at the 150-ft level and at the lowest frequency ranges. However, one must be cautious with any conclusions drawn from this secondary maximum since it is based on a single observation. The maximum observed at $R_i \approx -1$ is well defined by many observations, and appears to be associated with convective mixing arising from
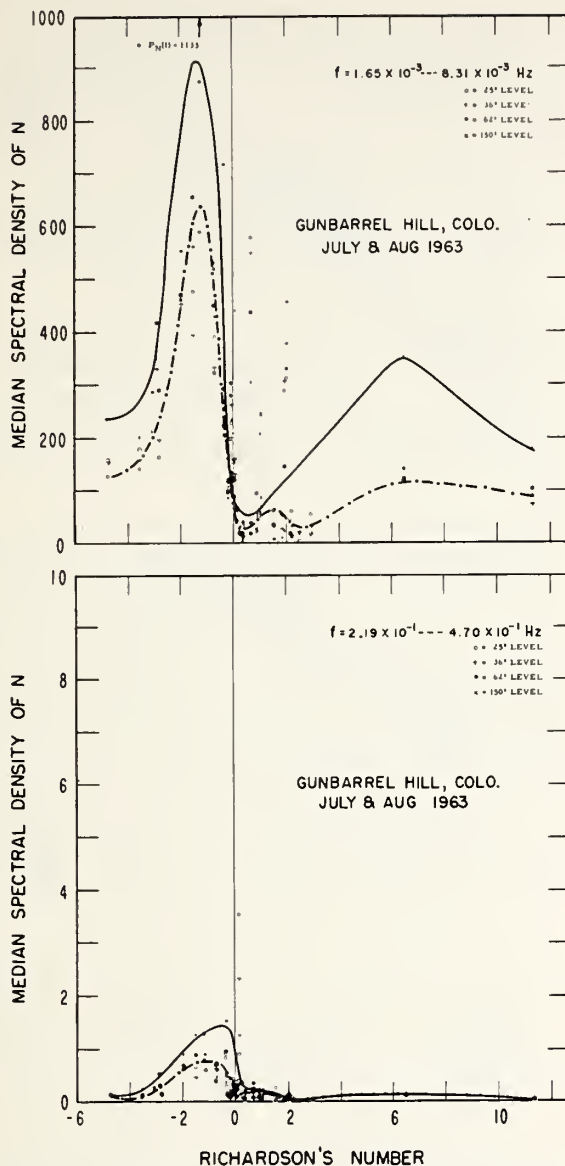
FIGURE 7.   *Spectral density of N versus Richardson's number for the frequency range shown.*

the destruction of the nocturnal radiation inversion by solar heating of the ground.   The low values of spectral density at $R_i \simeq 0$ are in agreement with what one would expect for a well-mixed atmosphere.   Under these conditions a passive parameter, such as N, will be distributed according to its adiabatic height distribution.   Although there might be a great deal of vertical motion, air parcels arriving at the observing point would have traveled along isentropic trajectories and thus display no variation in magnitude of N.

The relatively smaller spectral density at $R_i \simeq -5$ also corresponds to well-mixed conditions in that

the observed temperature gradient of -34.8 °C/km exceeds that necessary for autoconvection.

The ratio of median spectral density at 150 ft to that at 25 ft is given in figure 8.   It is apparent from this figure that a height dependence does exist, but that it depends entirely upon the frequency and stability range one is considering.   For example, the lower frequency range displays a ratio for 150 to 25 ft of ~ 1.5 for $R_i < -1$, increases rapidly to 6 for $R_i = +3$, then decreases to 2 for $R_i = +11$.   On the other hand, the highest frequency range, after a peak of 3 at $R_i = -4$ and 3.8 at $R_i = 0$ rapidly decreases to 1 for all $R_i > +2$, which is a completely different distribution than that for the low frequency range.   One observes, then, that the simple linear increase of spectral density with height which is often observed for the vertical wind is *not* evident in these data.
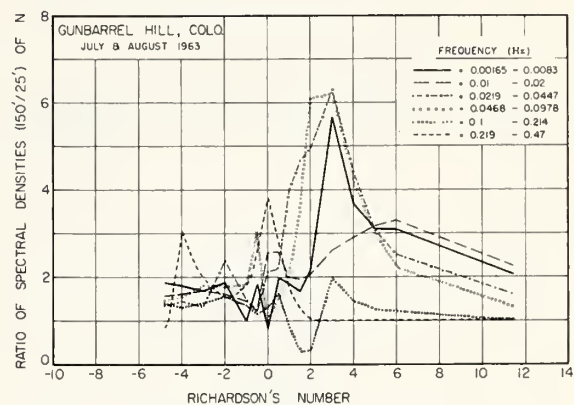
FIGURE 8.   *Ratio of spectral density of N at 150 ft to that at 25 ft versus Richardson's number.*

The spectral slopes, k, as determined from the power law least-square fits to the data, are plotted versus Richardson's number for the lowest and highest frequency range on figures 9 and 10.   It appears from these data that k does not display any marked height dependence.   The data were divided into small ranges of R_i, mean values determined for k by pooling data for all heights, and free-hand estimates drawn for each frequency interval.   The results of this procedure are shown on figure 11, where, for reference, the $-5/3$ slope is also drawn.   Although the overall average slope as a function of stability is dependent upon the frequency band of concern, one notes that there is a general trend for k to be greater than $-5/3$ at the lowest frequencies.   This is what one might expect if spectral energy was inserted at the lower frequencies and dissipated at the higher frequencies.   Further analysis of the data was accomplished by returning to the 1/25 sec data and determining the spectral slope in the frequency range 0.1 to 3 Hz.   Typical results of this analysis are shown
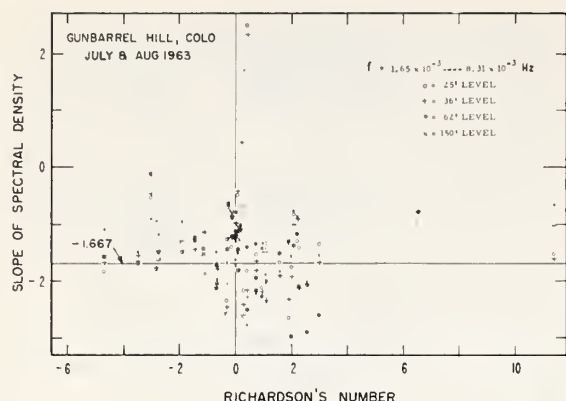
FIGURE 9. *Slope of spectral density of* N *for the frequency range* $1.65 \times 10^{-3} < f < 8.31 \times 10^{-3}$ Hz.

FIGURE 11. *Height and stability dependence of spectral slope of* N.

FIGURE 10. *Slope of spectral density of* N *for the frequency range* $2.19 \times 10^{-1} < f < 4.70 \times 10^{-1}$ Hz.

on figure 12, where the spectra of N are given for 25 and 150 ft for stable and unstable conditions (0330 and 1030 MST, July 25, 1963, respectively). Thus it is evident, that the assumed power law model of $P(f) \propto f^k$ is in good accord with observation. It is equally evident that the spectral decay tends to be greater than $-5/3$. However, this increased slope could also indicate that the "$-5/3$" law is inadequate for the refractivity, N, an eventuality given some weight by the recent discussion of Calder (1966) to the effect that the classical form of the similarity theory cannot be applied legitimately to the variances of the horizontal components of the wind velocity fluctuations.

The results of analyzing all available data for spectral decay are shown on figure 13 for the frequency range 0.1 to 3 Hz. Although the spectral decay varies from 0 to -3, the median values are shown on table 2 along with their estimated standard deviation.

The above treatment of the decrease of spectral decay with height was done by ordering the observations and then preparing the cumulative probability

FIGURE 12. *Spectral density of* N *for* $0.1 < f < 3$ *Hz at 25 and 150 ft for stable (0330 MST) and unstable (1030 MST) conditions.*

(Units: Hz^{-1}).
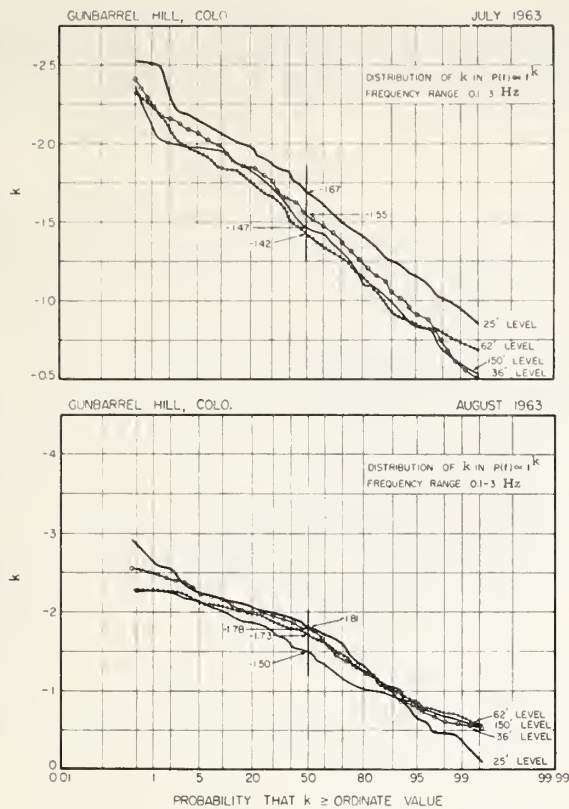
FIGURE 13. *Cumulative probability distribution of* k *in* P(f) ∝ f^k *for the frequency range 0.1 to 3Hz for July and August, 1963.*

TABLE 2. *Spectral decay of the refractivity,* N

Height (ft)	July	August
25	-1.67 ± 0.04	-1.81 ± 0.03
36	-1.55 ± 0.06	-1.78 ± 0.02
62	-1.42 ± 0.06	-1.73 ± 0.04
150	-1.47 ± 0.05	-1.50 ± 0.11

distributions. One may, however, proceed in another way, namely, preparing cumulative distributions of the *ratio* of the spectral exponent at the two heights. This is done on figure 14 where it is seen that the median ratio is 0.91 for July and 0.88 for August, comparing favorably with the 0.88 and 0.83 that one obtains from figure 13. Figure 15 summarizes the distributions of spectral decay of *N* reported in the literature with those of the present experiment. The two curves for CRPL are those for the 150-ft level, chosen so as to compare with the 56-m data of the Heinrich Hertz Institute. The 150-ft CRPL data appear to be consistently below the other data. Nearly complete agreement could have been obtained, however, had the distributions for a lower height been used (see fig. 13). It is perhaps coincidental that the average
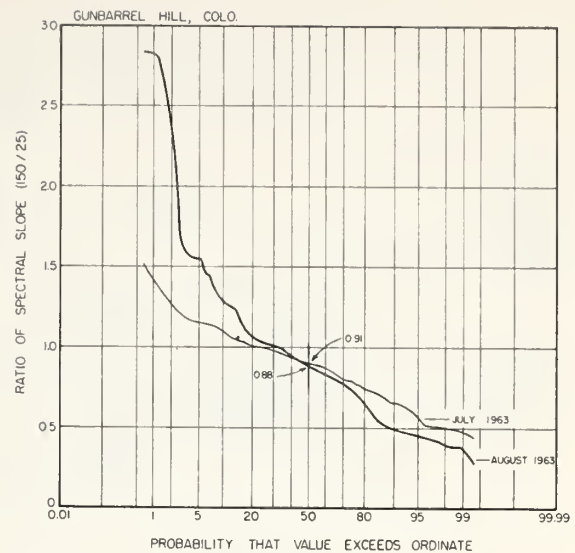
FIGURE 14. *Cumulative probability distribution of the ratio of spectral decay at 150 and 25 ft for July and August, 1963.*
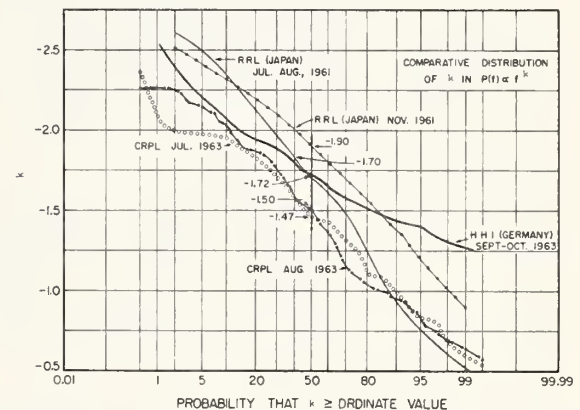
FIGURE 15. *Cumulative probability distributions of* k *in* P(f) ∝ f^k *from CRPL, RRL (Japan), and HHI (Germany) over the range*
CRPL: $0.1 < f < 3$ Hz
HHI: $0.04 < f < 2$ Hz
The RRL data is given in wave number, $k(m^{-1})$ with $5 \times 10^{-3} < k < 8m^{-1}$.

of the medians on this figure is 1.66. A more detailed comparison is given in table 3, where it is seen that the present results are somewhat low compared to the others, but in reasonable agreement with the "−5/3" law. The experimental results summarized in table 3 were obtained by a variety of techniques such as towers, balloons, and aircraft under a variety of meteorological conditions, and thus suggest that the spectral decay of *N*, both near the earth's surface and at significant altitudes, is an extremely variable quantity.

TABLE 3. *Comparison of spectral decay of N*

Reference	Number of spectra—comments	Average spectral decay
Birnbaum & Bussey, 1955	18	−1.6
Norton, 1959	10	−3.0
Thompson, Janes & Kirkpatrick, 1960	16 (Hawaii)	−2.2
	9 (Colorado)	−1.6
Gossard, 1960	28	−2.01
Edmonds, 1960	15	−1.55
Straiton, Deam & Walker, 1962	50	−1.82
Fukushima, Iriye & Akita, 1962	Examples drawn from wet and dry thermistor measurements July–Aug.	−1.7
	November	−1.9
Fukushima, Iriye & Akita, 1964	Three examples of refractometer measurements	~ −5/3
Bull, 1966	164	−1.68
Wickerts, 1966	Airborne refractometer measurements at different heights up to 3 km	~ −5/3
Bean, Emmanual & Krinks (present study)	~ 125 at 4 heights for 2 recording periods of 2 days	
	7-63	−1.53
	8-63	−1.70
	Average	−1.62

3. Conclusion

The objective of this paper was to study the turbulent characteristics of the radio refractive index. It has been found that the spectral density of N tends to increase with height and the lowest frequencies studied are strongly dependent upon stability. The largest spectral densities are observed at $R_i \approx -1$. The high frequency end of the spectrum *tends* to be less sensitive to stability than the low frequency end of the spectrum. However, the present data do not indicate that the high frequency end is totally independent of stability.

Conditions of neutral stability ($R_i = 0$) appear to represent times of thorough mixing of N by the rapidly varying vertical wind. Under these conditions, the air and N are being rapidly mixed with a resultant decrease in spectral variation. One may speculate that the transition from stable layering to turbulent mixing is quite rapid since the spectral density as observed at $R_i = 0$ is so low.

The average spectral decay of N is in reasonably good agreement with the "−5/3" law, but significant departures from this law may be observed depending upon the frequency range considered; systematically smaller spectral decays are observed at low frequencies and greater decays at high frequencies.

4. References

Birnbaum, G., and H. E. Bussey (1955), Amplitude, scale, and spectrum of refractive index inhomogeneities in the first 125 meters of the atmosphere, Proc. IRE **43**, No. 10, 1412–1418.

Blackman, R. B., and J. W. Tukey (1958), The measurement of power spectra from the point of view of communications engineering, Bell Syst. Tech. J. **37**, No. 1, 185–282; No. 2, 485–569.

Bull, G. (1966), Power spectra of atmospheric refractive index from microwave refractometer measurements, J. Atmospheric Terrest. Phys. **28**, No. 5, 513–519.

Calder, K. L. (1966), Concerning the similarity theory of A. S. Monin and A. M. Obukhov for the turbulent structure of the thermally stratified surface layer of the atmosphere, Quart. J. Roy. Meteorol. Soc. **92**, No. 391, 141–146.

DuCastel, F. (1965), Influences climatiques en propagation tropospherique, Progress in Radio Science 1960–63, **II**, Radio and Troposphere (Elsevier Publishing Company, London).

Edmonds, F. N. (1960), An analysis of airborne measurements of tropospheric index of refraction fluctuations, Statistical Methods in Radio Wave Propagation (Proc. Symp., Univ. of Calif., 1958), ed. W. C. Hoffmann, 197–211 (Pergamon Press, Inc., New York, N. Y.).

Fukushima, M., H. Iriye, and K. Akita (1962), Spatial distribution characteristics of atmospheric refractive index from helicopter and kytoon observations, J. Radio Res. Lab. (Tokyo), **9**, 369–383.

Fukushima, M., H. Iriye, and K. Akita (1964), Preliminary study of spatial distribution of atmospheric refractive index from aircraft observation, J. Radio Res. Lab. (Tokyo), **11**, 75–87.

Gilmer, R. R., R. E. McGavin, and B. R. Bean (1964), The response of microwave refractometer cavities to atmospheric variations, World Conf. on Radio Meteorol. Boulder, Colo. September, 1964. (Sponsored by URSI and UGGI).

Gossard, E. E. (1960), Power spectra of temperature, humidity and refractive index from aircraft and tethered balloon measurements. IRE Trans. **AP-8**, No. 2, 186–201.

Lumley, J. L., and H. A. Panofsky (1964), The Structure of Atmospheric Turbulence (Interscience Publishers, New York, N.Y.).

Norton, K. A. (1959), Recent experimental evidence favouring the $\rho K_1(\rho)$ correlation function for describing the turbulence of refractivity in the troposphere and stratosphere, J. Atmospheric and Terrest. Physics **15**, 206–227.

Straiton, A. W. (1964), Measurement of the radio refractive index of the atmosphere, Advances in Radio Research, **I**, (Academic Press, New York, N. Y.).

Straiton, A. W., A. P. Deam, and G. B. Walker (1962), Spectra of radio refractive index between ground level and 5000 feet above ground, IRE Trans. **AP-10**, No. 6, 732–737.

Thompson, M. C. Jr., H. B. Janes, and A. W. Kirkpatrick (1960). An analysis of time variations in tropospheric refractive index and apparent radio path length, J. Geophys. Res. **65**, No. 1, 193–201.

Wickerts, S. (1966), On the fine structure of the refractive index field (in Swedish), Rept. No. FOA 3, A 660, Electronics Dept., Research Institute of National Defense, Stockholm, Sweden.

(Paper 2–5–218)

METEOROLOGICAL FACTORS AFFECTING THE FINE-SCALE

STRUCTURE OF THE RADIO AND OPTICAL REFRACTIVE INDEX*

B. R. Bean

Summary

The radio and optical refractive index are both known functions of atmospheric pressure, temperature and humidity. Although refractive index profile and short-term fluctuations have long been studied, it is only recently that attempts have been made to relate these fluctuations to the hydrodynamically important wind shear and thermal stability. Data taken on a 150-foot tower on the high plains of Colorado with vertically spaced microwave refractometer cavities have been spectrally analysed and examined for systematic variation as a function of wind shear and thermal stability. Experimental data on temperature, radio refractive index and optical propagation characteristics are all found to be consistent with the theoretical conclusion that wind-induced mixing may greatly reduce their variation.

METEOROLOGICAL FACTORS AFFECTING THE FINE-SCALE
STRUCTURE OF THE RADIO AND OPTICAL REFRACTIVE INDEX

B. R. Bean

The atmospheric and radio scientist sometimes find when they discuss turbulent scattering of radio energy to beyond-the horizon, or distortion of optical or radio wavefronts by atmospheric inhomogeneities, that their concepts of "turbulence" are very different. The atmospheric scientist is apt to consider "turbulence" as any motion that transports any property across its average flow pattern whilst the radio scientist may call the fluctuations recorded by his tower or airborne refractometer "turbulence." The discussion that follows is aimed at consolidating these views. The discussion will start with some consequences of the assumptions of modern statistical theories of turbulence as regards small-scale fluctuations in wind, temperature, and the radio and optical refractive index. Several examples will then be presented to illustrate and emphasize these differences.

Theory   The Kolmogorov statistical theory of turbulence hypothesizes the presence of an inertial sub-range of small eddies in which average properties of the flow are determined solely by the average rate of dissipation of energy per unit mass of the fluid (ϵ). A consequence of this hypothesis is that the structure function, $D_u(r)$, for wind, u, measured at a distance r from the origin but referenced to r_0,

$$D_u(r) = [u(r_0) - u(r_0+r)]^2 \quad ,$$

must, by dimensional arguments, take the form

$$D_u(r) = a^2 \epsilon^{2/3} r^{3/2} \quad ,$$

where a is a constant. Similar arguments lead to the conclusion that the structure functions for temperature, T, and radio refractivity, N, are of the form

$$D_T(r) = a^2 \epsilon^{-1/3} G_T r^{3/2}$$

$$D_N(r) = a^2 \epsilon^{-1/3} G_N r^{3/2} \quad ,$$

G_T and G_N are, respectively, the average rate of dissipation of temperature and refractive index fluctuations per unit mass. The presence of these additional dissipation terms in $D_T(r)$ and $D_N(r)$ accounts for a fundamental difference in their spectral behavior compared to $D_u(r)$. We, therefore, now examine expressions for ϵ, G_T, and G_N in terms of mean winds, gradients, etc.

B. R. Bean is with the Wave Propagation Laboratory, ESSA Research Laboratories, Boulder, Colorado.

Writing the equation for the time rate of change of kinetic energy per unit mass, E, Lumley and Panofsky (1964) obtain:

$$\frac{d\overline{E}}{dt} = -\overline{u'w'}\frac{\partial \overline{u}}{\partial z} + \frac{\overline{w'T'}}{T} - \frac{\partial \overline{w'E}}{\partial z} - \epsilon \quad , \qquad (1)$$

where t is time, u is the wind in the direction of flow and w that in the vertical direction, z. The primes denote departure from the average as denoted by an overbar, i.e., u'=u-$\overline{u}$. Gravity is denoted by g. $\frac{d\overline{E}}{dt}$ is usually small. The first term on the right hand side of (1) is a measure of mechanical generation of kinetic energy. Since $\overline{u'w'}$ has the opposite sign to the gradient the total term is positive. The flux divergence is normally assumed small (as were the other divergence terms in the deri-vation of (1)). Further, if we restrict our attention to those conditions where buoyance effects, $\overline{gw'T'/T}$, are small compared to the mechanical ones, then

$$\epsilon \approx \overline{u'w'}\frac{\partial \overline{u}}{\partial z} \quad . \qquad (2)$$

One may obtain similar expressions for temperature,

$$\frac{1}{2}\frac{d\overline{(T')^2}}{dt} = -\overline{w'T'}\frac{\partial \overline{\theta}}{\partial z} - \frac{1}{2}\frac{\partial \overline{w'(T')^2}}{\partial z} - G_T$$

and refractivity,

$$\frac{1}{2}\frac{d\overline{(N')^2}}{dt} = -\overline{N'w'}\frac{\partial \overline{N}}{\partial z_*} - \frac{1}{2}\frac{\partial \overline{w'(N')^2}}{\partial z} - G_N \quad .$$

Utilizing similar arguments to those used to derive (2) one may obtain

$$G_T \approx \overline{w'T'}\frac{\partial \overline{\theta}}{\partial z}$$

$$G_N \approx \overline{w'N'}\frac{\partial N}{\partial z_*} \quad , \qquad (3)$$

where one notes that the potential temperature, θ, and potential refractivity, N_*, enter. Remembering that

$$\frac{\partial \theta}{\partial z} = \frac{\partial T}{\partial z} + \Gamma \quad ,$$

where Γ is the adiabatic lapse of temperature ($\Gamma \approx -10^{\circ}C/km$) one notes that it is entirely possible for $\partial \theta/\partial z \to 0$ and thus $G_T \to 0$ with the result that $D_T(r) \to 0$. The same is true for the gradient of potential refractivity with similar implications for $D_N(r)$. This is due to θ and N_* being assumed dynamically passive parameters in the generation of mechanical turbulence. The physical interpretation is that the mechan-ical turbulence will mix temperature and refractive index inhomogeneities until each assumes the appropriate adiabatic height distribution. Thus, although there might be active vertical mixing, the fluctuations of temperature and refractivity T' and N', have been effectively smoothed out. Several specific examples of this effect will now be examined.

Experimental Examples   The first example is that of the fluctuations of temperature and wind measured at 50 feet above ground at Gunbarrel Hill, Colorado. The instrumentation (Bean, Emmanuel and Krinks, 1967) has adequate bandwidth to delineate fluctuations over the frequency range of Figure 1. P(f) is the spectral density at a given frequency f. The coordinates f P(f) versus log f are used to maintain equal area - equal spectral contribution over the wide frequency range of meteorological fluctuations observed. Two hours were selected for study: 0650-0750 and 1300-1400 on November 24, 1964. The early morning, run 1, was characterized by stable conditions with temperature increasing with height, a light wind of 2.84 mps, practically no fluctuations of vertical wind but relatively large fluctuations of temperature at low frequency (f≈0.002 cps). The temperature fluctuations of Figure 1, run 1, are perhaps associated with the "undulance" observed under stable conditions (Lumley and Panofsky, 1964). By 1300, run 2, a cold front had passed the observing tower with a resultant increase of wind to 15.6 mps and Richardson's number near zero. The observed temperature gradient was within measurement error of the adiabatic lapse of T. The rapid fluctuations of the vertical wind experienced by an observer on the tower left no doubt that the atmosphere was in a condition of strong mechanical turbulence. Note, however, that temperature fluctuations are low at all frequencies as one would expect from (3). This, then, is one illustration of conditions where $D_u(r) \neq 0$ whilst $D_T(r) \to 0$.

The second example chosen is that of the variability of spectral density of the radio refractive index with changes in atmospheric stability. The radio refractive index is strongly affected by humidity and, to a less extent, by temperature fluctuations. The data presented in Figure 2 were taken during July and August of 1963 with a multi-cavity microwave refractometer sampled at several levels on a 150-foot tower. Details of the experiment are given by Bean, Emmanuel and Krinks (1967). Although there is a wide spread in the experimental data, it is again observed that regions of relatively low spectral density occur where $\partial\theta/\partial z \to 0$ and thus $R_i \to 0$.

The third example is drawn from the observations of propagation characteristics of optical beams made by the author's colleague, G. R. Ochs (Ochs and Little, 1968). The particular meteorological condition for the observations of Figure 3 is that of the chinook or Föhn wind which is a warm, dry wind on the lee side of a mountain range, the warmth and dryness of the air being due to the adiabatic compression upon descending the mountain slopes (Glossary of Meteorology, 1959). On this particular day the chinook started about 0500 when the wind increased from a few miles per hour to over 30 mph. The optical beam width, which is strongly affected by temperature inhomogeneities along the propagation path (15 km in length with a vertical rise of 80 meters) decreased from about 125 to 25 μradians. This decrease in beam width is consistent with what one would expect under chinook conditions, i. e., $\partial\theta/\partial z \to 0$ and $D_T(r) \to 0$. Quite consistent with decrease in beam width is the increase in vertical beam wander, or change in apparent elevation angle. Recalling that the optical refractive index is proportional to air density, then the increase in temperature lapse from say, the normal -6°C/km to the adiabatic lapse of -10°C/km would tend to

lessen the normal density gradient and thus produce less bending and a rise in the beam position (the "auto-convective" or constant density lapse rate of -34.3°C/km would produce straight rays). The change in total bending under these assumed conditions would lessen atmospheric bending by some 80 μradians, a number not inconsistent with that observed. The vertical beam wander remains high and the beam width low through 1600 hours, indicating that the air along the path remains well mixed even though the wind, which is recorded only at the lower terminal, decreases.

Conclusions Theoretical and experimental evidence indicates that wind-induced mixing near the ground may so thoroughly mix parameters such as the radio and optical refractive index that their normal short-term variability effectively vanishes. It is evident, from both the many assumptions of the theoretical development and the lack of supporting meteorological observations during the optical experiments, that simultaneous combined radio, optical and meteorological measurements are required to further explore these preliminary conclusions.

Acknowledgment The author thanks Mr. G. R. Ochs for the use of the data of Figure 3 prior to his own publication of his complete experimental results.

References

Bean, B. R., C. B. Emmanuel and R. W. Krinks (May, 1967), Some spectral characteristics of the radio refractivity in the surface layer of the atmosphere, Radio Science 2, No. 5, 503-510.

Glossary of Meteorology (1959), American Meteorological Society, Boston, Massachusetts.

Lumley, J. L. and H. A. Panofsky (1964), The Strucutre of Atmospheric Turbulence, John Wiley and Sons, New York.

Ochs, G. R. and C. G. Little (1968), Studies of atmospheric propagation of laser beams on 5.5, 15, 45 and 145 km paths, To be presented at the Conference on "Tropospheric Wave Propagation," London, England.

4

SUBSONIC ATMOSPHERIC OSCILLATIONS

Richard K. Cook

Environmental Science Services Administration
Geoacoustics Group
Rockville, Maryland 20852

Some long-period oscillations, 300 seconds and greater, of sound
pressure in the atmosphere travel at subsonic phase velocities,
30 m/s and greater, over the earth's surface. The subsonic waves
are evidently generated by the jet stream. The distributions of
sound pressures and atmospheric motions are obtained at various
altitudes.

Introduction

The passage of a jet stream in the atmosphere over the eastern (Atlantic) seaboard of the United States is occasionally accompanied by large oscillations in barometric pressure at infrasonic frequencies. The periods of oscillation are usually greater than five minutes, and the pressure fluctuations at the earth's surface are of the order of 100 dynes/cm^2.

The jet stream is a thin layer of fairly high-speed wind. The location of the layer in the atmosphere is in the neighborhood of the tropopause, at an altitude of about 10 km. The thickness of the stream is about three kilometers. The wind speed along the axis is at least 30 meters/sec, and sometimes as great as 80 meters/sec. The wind blows towards a direction between northeast and southeast, and the width of the stream (in a direction transverse to the direction of flow) is generally at least 100 km.

The oscillations in barometric pressure, hereinafter referred to as "sound pressure," are measured by means of line-microphones located on the ground. The Washington station of our laboratory has an array of four such microphones located at ground level and spaced about 5 - 10 km apart. Each line microphone produces frequency-modulated voltages proportional to the sound pressure in the atmosphere. The voltages are transmitted by telephone wires to a recording location. Here they are demodulated, amplified and filtered, and recorded in analog form both as ink-on-translucent-paper traces, and on magnetic tape. An important feature of the recordings is the provision of accurate timing schemes. More complete technical details of the electroacoustical equipment are given in Reference (1).

The microphone array at the station is currently designed for the measurement of four principal characteristics of infrasonic waves. These are (1) the amplitude and waveform of the incident sound pressure, (2) the direction of propagation of the wave, (3) the horizontal phase velocity, and (4) the dominant period (or periods) of oscillation.

The results of observations made at our station in Washington, D. C. show that almost all sound waves coming from subsonic oscillations of the jet stream have wavefront surfaces of constant phase which are almost plane. The sound pressure has the following features when the jet stream is blowing. (1) The direction of propagation of lines of constant-phase sound pressure across the Washington area is very close to the direction of the jet stream over Washington. (2) The horizontal phase velocity c_o = 30 to 100 m/sec is about the same as the speed of the jet. (3) The sound pressures are mainly in the range 50 - 400 dynes/cm^2. (4) Periods of oscillation T = 300 to 1000 seconds.

A brief summary of a few observations made in Washington is given in Figure 1. The data show the correlation between the features of the sound pressure, and the characteristics of the jet stream causing the sound pressure. A detailed study of the waves observed at the Washington station has been made by Mary W. Hodge and her associates, see Reference (2). Further data on the Washington waves have been summarized by A. J. Bedard in Reference (3). Sound pressures caused by the jet stream have been observed elsewhere; a comprehensive report on waves in the Boston, Massachusetts area has been prepared by Elizabeth A. Flauraud and her associates, Reference (4).

The sound pressure probably has its origin in flow instability of the jet stream. The mechanism of the instability is not known. We can conjecture that it arises from a combination of viscous shear between the jet stream and the surrounding atmosphere, and unstable temperature gradients. We assume that the jet stream oscillations force the atmosphere into oscillation. The purpose of the investigation is determination of the

WIND VEL-TEMP. PROFILE (DULLES AIRPORT)

PRESSURE WAVES EXIST (WASH., D. C.)

			C_o, m/s	DIR.,	T, secs.	MAX. AMP., d/cm²
• ○	JAN. 1, 1964, 0000 UT		48	225°	650	62
+ *	" 7, " 1200 UT		54	232°	425	35
△ □	" 24, " 1800 UT		36	258°	725	45
x x	TEMP.					
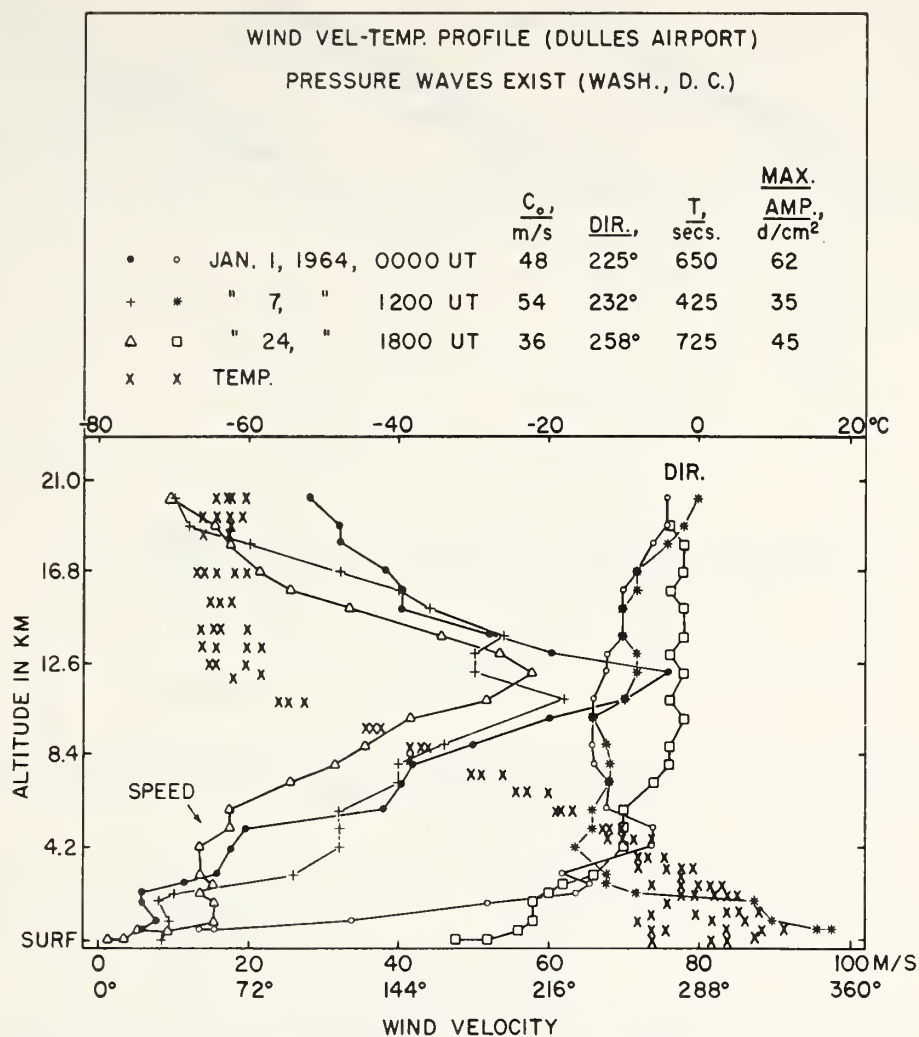
Figure 1. Observations on jet stream oscillations

relationship between the measured sound pressure and the oscillatory displacement of the jet.

Equations of Atmospheric Motion

The well-known equations of motion for sound waves in a wind-free atmosphere, see for example Reference (5), are presented here subject to the following conditions: (1) The atmosphere is isothermal and wind-free. (2) The waves are sinusoidal in time, and all quantities vary like $\exp(i\omega t)$. (3) All motions are in the x-z plane, and so the particle velocity, with components u, v, w, has its y-component $v \equiv 0$, see Figure 2. (4) The traces of the straight lines of constant-phase sound pressure on the x-y plane have a phase velocity $c_o = \omega/k_o$, and so all quantities vary like $\exp(-ik_o x)$; the waves are advancing in the (+x) direction. The equations of motion reduce to

$$\frac{\partial}{\partial x}\left(\frac{\partial u}{\partial x}+\frac{\partial w}{\partial z}\right) + k^2 u - (g/c^2)\frac{\partial w}{\partial x} = 0$$

$$\frac{\partial}{\partial z}\left(\frac{\partial u}{\partial x}+\frac{\partial w}{\partial z}\right) + k^2 w - (g/c^2)\frac{\partial w}{\partial z} - (\gamma-1)(g/c^2)\left(\frac{\partial u}{\partial x}+\frac{\partial w}{\partial z}\right) = 0$$

(1)
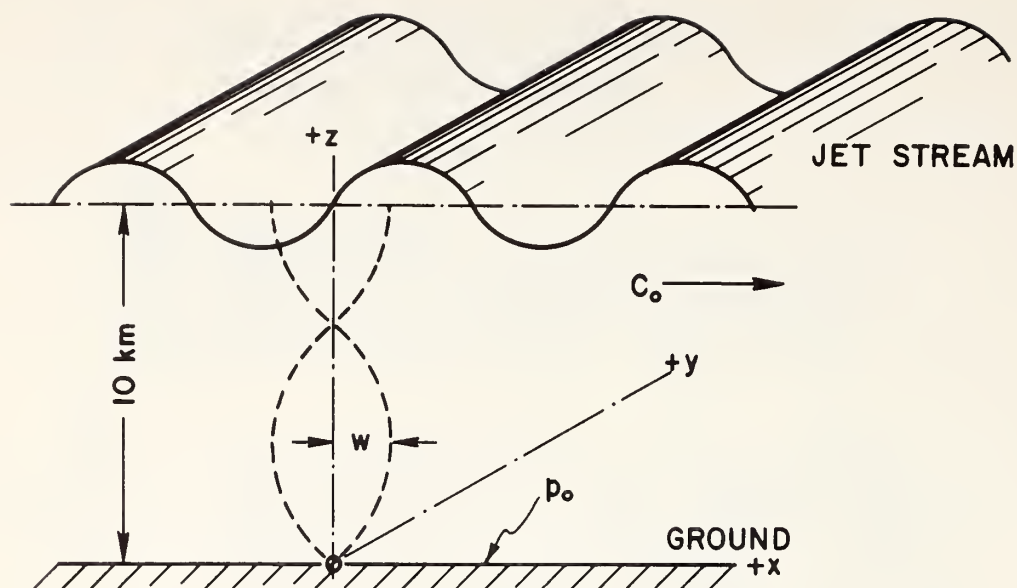
Figure 2. Radiation of sound pressure by jet stream oscillations

with the boundary condition $w = 0$ at the xy-plane. $\gamma = 1.40$ for the atmosphere, c = velocity of sound = ω/k, and g = the acceleration of gravity. The components of particle velocity, $\underline{u}$ and $\underline{w}$, vary with $\underline{x}$ like $\exp(-ik_o x)$, and with $\underline{z}$ like $\exp(Kz)$.

$$u = u_o \exp(-ik_o x + Kz)$$

$$w = w_o \exp(-ik_o x + Kz) \tag{2}$$

Introduction of these expressions into the equations of motion leads to a quadratic equation in $\underline{K}$, from which the allowed values of $\underline{K}$ are given by

$$HK = \frac{1}{2} \pm i \sqrt{\frac{\gamma-1}{\gamma^2} \cdot \frac{k_o^2}{k^2} - H^2(k_o^2-k^2) - \frac{1}{4}} \tag{3}$$

$$= \frac{1}{2} \pm i\beta$$

where H = scale height of the atmosphere = $c^2/\gamma g$ = 8.1 km for an isothermal atmosphere with c = 333 m/sec.

β is a real number for a typical subsonic oscillation. By "subsonic" we mean that the phase velocity is less than the high-frequency limit for the speed of sound in an isothermal atmosphere. Between the jet stream and the ground, the atmosphere is traversed by both upward-going and downward-going plane waves, combined so as to have $w = 0$ at the ground. The phase velocities are indicated in Figure 3 for two angles of incidence (and reflection), $\alpha = 45°$ and $90°$. The curves are computed from Eq.(3).

The final expression for $\underline{w}$ is

$$w = w_o \sin(\beta z/H) \exp(z/2H - ik_o x) \tag{4}$$

From this we see that the oscillatory amplitude of $\underline{w}$ increases exponentially with altitude. The increase is inversely as the square root of the ambient atmosphere pressure.

The coefficient $\underline{w}_o$ can be computed from the measured sound pressure at the ground level, $z = 0$. The sound pressure is

$$P_o = \frac{-\gamma \beta}{i\omega} \left(\frac{\partial u}{\partial x} + \frac{\partial w}{\partial z} \right) \text{ , at } z = 0. \tag{5}$$

-211-
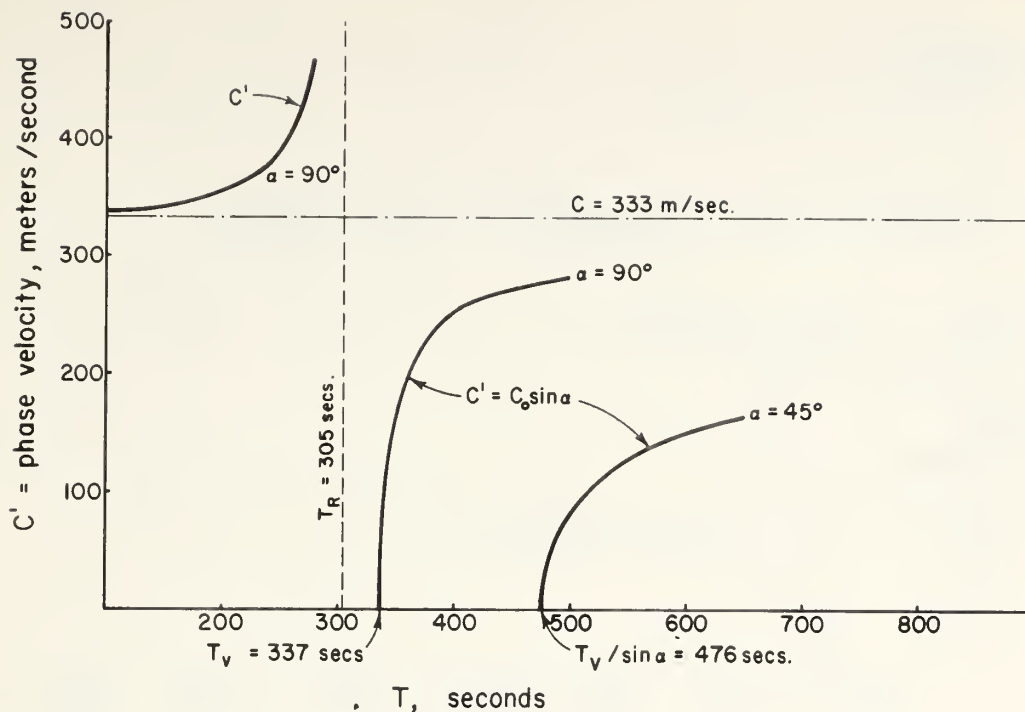
Figure 3. Phase velocities for sound waves in the atmosphere at very low frequencies

Combination of the expressions for $\underline{w}$ and $\underline{p}_o$ with the equation of motion gives the following expression for the amplitude of the vertical component of particle displacement at the altitude $z = 10$ km of the jet stream

$$\Delta z = 2H(k_o^2 - k^2)|p_o|/\beta \gamma B k^2 \tag{6}$$

As an example, consider a wave with $T = 500$ secs, $c_o = 33$ m/sec $(\approx c/10)$, and $|p_o| = 200$ dynes/cm^2. We find $\Delta z = 60$ meters, which must be the jet stream's vertical oscillatory displacement at an altitude of 10 km necessary to produce the measured sound pressure at the ground.

Standing-wave Hypothesis

The mechanism of the oscillation is not known, and there is no obvious limitation on the vertical component β/H of the wave-number vectors. We examine the conjecture that the vertical component $\underline{w}$ of the particle velocity has a maximum at the jet stream's nominal altitude of 10 km, see Figure 1. From Eq.(4), this occurs approximately when

$$\beta z/H = \frac{\pi}{2}, \frac{3\pi}{2}, \frac{5\pi}{2}, \dots \tag{7}$$

Introduction of these values into Eq.(3) for β leads to a series of curves showing how the horizontal trace velocity $\underline{c}_o$ varies with the period of oscillation $\underline{T}$. Two of the curves are shown in Figure 4. The curves all start with $c_o = 0$ at $T_v = 337$ secs., this being the Väisälä period for the isothermal atmosphere ($c = 333$ m/sec.) under consideration. Also plotted are some observed values of jet-stream horizontal phase velocities corresponding to well-defined periods of oscillation for the jet stream over Washington during January 1964. The data do not seem to confirm the hypothesis of Eq.(7). But evidently gravitational forces play a substantial role in the generation mechanism, since most of the observed oscillations occur at periods greater than the Väisälä $\underline{T}_v$.

-212-
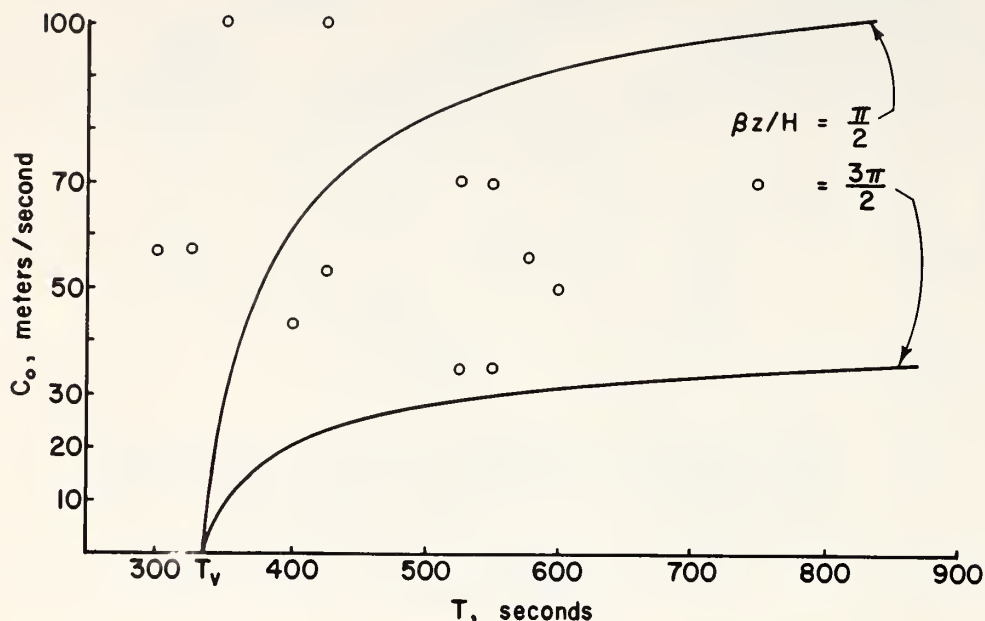
Figure 4. Horizontal phase velocities at various oscillation periods
0 = observed velocities

Propagation to the Ionosphere

The displacement and velocity amplitudes in the jet stream, see Eqs.(6) and (4), can be expected to serve as sources for radiation of subsonic waves upward into the ionosphere. Eq.(4) shows that the amplitude of the vertical component $\underline{w}$ of the particle velocity increases exponentially with altitude.

$$|w| = w_j \exp[(z-10)/2H] \tag{8}$$

where $\underline{w}_j = (2\pi/T)\Delta z$ = the amplitude at $z = 10$ km. For the example given above, $T = 300$ secs. etc., we find that at an altitude of $z = 100$ km, $|w| \approx 100$ m/sec., and $\Delta z \approx 9$ km. This estimate for $|w|$ is much greater than the phase velocity of the wave (≈ 30 m/sec.). It appears that subsonic waves traveling upward will probably undergo substantial waveform changes, e.g., taking on a shock-wave configuration, well before reaching the ionosphere.

References

(1) Richard K. Cook, "Strange sounds in the atmosphere" (Part I), Sound, Vol. 1, No. 2, pp. 12-16 (March 1962)
(2) Mary W. Hodge & David T. Volz, "Possible relations of mesoscale surface pressure waves to the jet stream region and to clear air turbulence", Third National Conference on Aerospace Meteorology, pp 557-563 (New Orleans, Louisiana, May 6-9, 1968)
(3) A. J. Bedard, Jr., "Some observations of traveling atmospheric pressure disturbances", National Bureau of Standards Report No. 9364 (July 1966)
(4) E. A. Flauraud, A. H. Mears, F. A. Crowley, Jr., and A. P. Crary, "Investigation of microbarometric oscillations in Eastern Massachusetts", Geophysical Research Papers No. 27 of the Air Force Cambridge Research Center (May 1954)
(5) H. Lamb, "Hydrodynamics", Dover Publications, New York (1945)

5

Chapter **24**

Weather Effects on Radar

BRADFORD R. BEAN
E. J. DUTTON
and
B. D. WARNER

Environmental Science Services Administration

24.1 INTRODUCTION

Weather effects on radar may be categorized as (1) refraction of the radar beam by the troposphere, (2) attenuation by atmospheric gases, (3) attenuation and scattering by both particulate matter and hydrometeors, and (4) returns from the clear atmosphere. All these effects must be considered at some phase of the design of a radar system.

Refraction effects are frequency-independent at frequencies below 100 GHz, thus affecting the performance of most operational radar systems. However, refraction effects are relatively unimportant to short-range airborne radar systems such as weapon-control radars, side-looking terrain-mapping radars, and weather-avoidance radars. Conversely, refraction effects are of utmost importance to long-range surveillance radars where target-height determination at low elevation angles is one of the primary objectives.

Attenuation by atmospheric gases begins to affect the performance of radars operating at frequencies above 10 GHz. Radars operating at these frequencies are generally intended for short-range applications and the problem is not very severe, unless the frequency is near an oxygen or water-vapor absorption line.

Particulate scattering and attenuation effects begin to appear at 10-cm and shorter wavelengths. Although particulate attenuation is usually negligible at 10 cm, it may produce significant attenuation at 3 cm. The WSR-57 radars used by the ESSA (Environmental Science Services Administration) Weather Bureau operate at 10 cm. In general, this radar is capable of measuring rainfall rates from backscatter while being relatively unaffected by the attenuation. The 10-cm wavelength is sensitive to precipitating moisture droplets but is relatively insensitive to nonprecipitating droplets. Thus a 10-cm radar is able to detect rain showers, thunderstorms, tornadoes, and hurricanes without being confused by "fair weather" clouds.

Detection of backscatter from the clear atmosphere requires very sensitive radar systems. Although the signal levels are not large enough to be detrimental to most radar applications, they are of significant interest to the atmospheric scientist. In contrast, these signals can create a clutter problem for the prospective designer of a high-power radar operating at centimeter wavelengths.

In this chapter, the meteorological effects discussed above are considered in more detail.

24.2 RADIO REFRACTIVE INDEX OF AIR

The atmosphere normally causes a downward curvature of horizontally launched radar beams that is about one-quarter of the curvature of the earth. This downward curvature results from the normal decrease of the refractive index of air with height.

The velocity of an electromagnetic wave, v, in a medium of refractive index n is related to the velocity of light $in \ vacuo$, c, by $v = c/n$. By Dale and Gladstone's law, the refractive index for light may be determined from

$$n = 1 + k\rho \tag{1}$$

where ρ = density of medium
  k = constant for that medium

The second term on the right side of Eq. (1) is about 300×10^{-6} for the atmosphere. It is customary in practice to speak, therefore, of the refractivity N:

$$N = (n - 1)10^6$$

The equation for N for light must be modified for radio applications to account for the polarizability of water vapor:[1]

$$N = K_1 \frac{P}{T} + K_2 \frac{e}{T^2} \tag{2}$$

where T = temperature, °K

P = total atmospheric pressure, millibars

e = partial pressure of water vapor, millibars

A survey of the various determinations of K_1 and K_2 by the world's metrology laboratories led Smith and Weintraub[2] to recommend the use of

$$K_1 = 77.6°K/\text{millibar}$$

and

$$K_2 = 3.73 \times 10^5 (°K)^2/\text{millibar}$$

to determine N with a standard error of 0.5 percent for frequencies up to 30 GHz and normally encountered ranges of pressure, temperature, and humidity. A subsequent laboratory test by Boudouris[3] confirmed the Smith-Weintraub constants. Details of the derivation of Eq. (2) may be found in several reviews.[3-5] Boudouris[3] is especially useful to those interested in the experimental determination of K_1 and K_2.

A high degree of accuracy of temperature, pressure, and water-vapor pressure measurements is necessary for precise determinations of the refractive index from Eq. (2). If one assumes that the formula for N is exact, a relation between small changes in N and small changes in temperature, pressure, and vapor pressure may be evaluated from

$$dN = \frac{\partial N}{\partial T} dT + \frac{\partial N}{\partial e} de + \frac{\partial N}{\partial P} dP$$

The partial derivatives may be evaluated by reference to some standard atmosphere to yield the approximate expression

$$\Delta N = a\Delta T + b\Delta e + c\Delta P$$

The root-mean-square (rms) error is then

$$\Delta N = [(a\Delta T)^2 + (b\Delta e)^2 + (c\Delta P)^2]^{1/2}$$

if it is assumed that the errors in P, T, and e are unrelated. Typical values of the constants a, b, and c, based upon the International Civil Aviation Organization (ICAO) standard atmosphere and with the assumption of 60 percent relative humidity, are given in Table 1 for various altitudes. For example, by assuming errors of $\pm$ 2

TABLE 1 Values of the Constants a, b, and c in the Expression $\Delta N = a\Delta T + b\Delta e + c\Delta P$ for the ICAO Standard Atmosphere and 60 Percent Relative Humidity

Altitude, km	N	T, °C	P, millibars	e, millibars	a, °K^{-1}	b, (millibars)$^{-1}$	c, (millibars)$^{-1}$
0	319	15.0	1,013	10.2	−1.27	4.50	0.27
1	277	8.2	893	6.5	−1.09	4.72	0.28
3	216	−4.5	701	2.6	−0.86	5.17	0.29
10	92	−50.3	262	0.04	−0.50	7.52	0.30
20	20	−56.5	55	0	−0.09	7.96	0.35
50	0.2	9.5	0.8	0	−0.0008	4.67	0.27

millibars in P, $\pm 1°C$ in T, and ± 5 percent in relative humidity common in radiosonde observations, we may obtain an rms error of $4.1N$ units for sea-level conditions compared with an error of $1.6N$ units arising from uncertainties of the constants in N. Currently one must use radiosonde data for the determination of N gradients, with the result that the overall accuracy is determined more by the errors in the meteorological sensors than by the errors in the constants in the equation for N. Until such time as better measurement methods for T and e are developed, there appears to be little or no need for more accurate determination of the constants in Eq. (2).

24.3 TROPOSPHERIC REFRACTION EFFECTS ON RADAR

If a radio ray is propagated in free space, where there is no atmosphere, the path followed by the ray is a straight line. However, a ray that is propagated through the earth's atmosphere encounters variations in atmospheric refractive index along its trajectory that cause the ray path to become curved. The geometry of this situation is shown in Fig. 1, which defines the variables of interest. The total angular refraction of the ray path between two points is designated by the Greek letter τ and is commonly called the *bending* of the ray. The atmospheric radio refractive index n always has values slightly greater than unity near the earth's surface (e.g., 1.0003) and approaches unity with increasing height. Thus ray paths usually have a curvature that is concave

Fig. 1 Geometry of the refraction of radio waves.

downward, as shown in Fig. 1. For this reason, downward bending is usually defined as being positive.

If it is assumed that the refractive index is a function only of height above the surface of a smooth, spherical earth (i.e., it is assumed that the refractive-index structure is horizontally homogeneous), the path of a radio ray will obey Snell's law for polar coordinates:

$$n_2 r_2 \cos \theta_2 = n_1 r_1 \cos \theta_1 \qquad (3)$$

In Eq. (3), the two infinitesimal layers of refractive index n_1 and n_2 are assumed concentric with the earth's surface and of radii r_1 and r_2 and they have been consecutively penetrated by the radar ray in such a manner that the respective angles between the ray and the layers are θ_1 and θ_2. The geometry used with this equation is shown in Fig. 1. With this assumption, τ may be obtained from the following integral,

$$\tau_{1,2} = -\int_{n_1}^{n_2} \cot \theta \, \frac{dn}{n} \qquad (4)$$

The derivation of the above equation can be found in the text by Smart.[6]

The elevation angle error ϵ is an important quantity to the radar engineer since it is a measure of the difference between the apparent elevation angle θ_0 to a target, as indicated by radar, and the true elevation angle. Under the same assumptions made previously, ϵ is given as a function of τ, n, and θ by

$$\epsilon = \arctan \frac{\cos \tau - \sin \tau (\tan \theta) - n/n_s}{(n/n_s) \tan \theta_0 - \sin \tau - \cos \tau \tan \theta}$$

The apparent range to a target, R_e, as indicated by a radar, is defined as an integrated function of n along the ray path:

$$R_e = \int_0^R n \, dR = \int_0^h \frac{n \, dh}{\sin \theta} \qquad (5)$$

However, the maximum range error (R_e minus the true range) likely to be encountered is only about 200 m; hence the evaluation of Eq. (5) is not of great importance unless one is dealing with an interferometer or phase-measuring system.

The integral for τ [Eq. (4)] cannot be evaluated directly without a knowledge of the behavior of n as a function of height. Consequently, the approach of the many
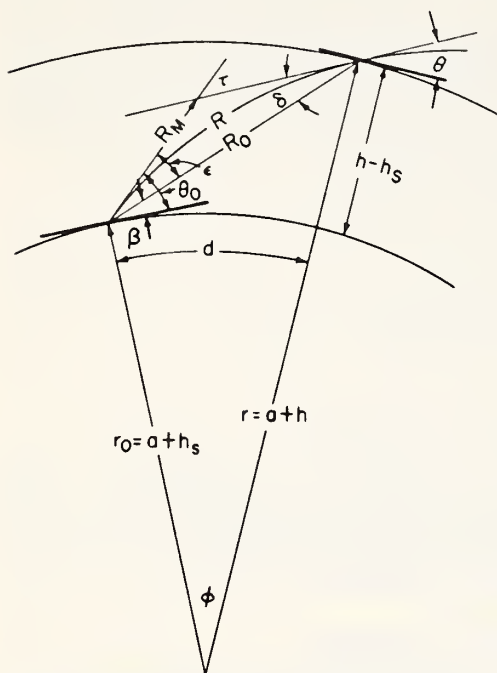
workers in this field has been along two distinct lines: the use of numerical-integration techniques and approximation methods to evaluate τ without full knowledge of n as a function of height, and the construction of model n-atmospheres in order to evaluate average atmospheric refraction. The following sections are devoted to a discussion of these methods.

The reader should keep in mind that the equations given above are subject to the following restrictions of ray tracing:

1. The refractive index should not change appreciably in a wavelength.

2. The fractional change in the spacing between neighboring rays (initially parallel) must be small in a wavelength.

Condition 1 will be violated if there is a discontinuity in the refractive index (which will not occur in nature) or if the gradient of refractive index, dn/dr, is very large, in which case condition 2 will also be violated. Condition 1 should be satisfied if

$$\frac{(dn/dh) \text{ per km}}{N} < 0.002 f_{\text{kHz}}$$

where refractivity N is defined as $N = (n - 1) \times 10^6$ and f_{kHz} is the carrier frequency in kilohertz.[7] Condition 2 is a basic requirement resulting from Fermat's principle for geometrical optics. An atmospheric condition for which both conditions 1 and 2 are violated is known as *trapping* of a ray, and it can occur whenever a layer exists with a vertical decrease of N greater than 157 N units per kilometer. A layer of this type is called a *duct*, and the mode of propagation through such a layer is similar to that of a waveguide.[8] When refractive-index gradients are taken into account, a cutoff frequency may be derived for waveguidelike propagation through a ducting layer.[9]

In addition to the above limitations, it should be remembered that the postulate of horizontal homogeneity, made in order to use Eq. (3), is not realized under actual atmospheric conditions; some degree of horizontal inhomogeneity is always present.

A method may be derived for determining ray bending from a knowledge only of n at the endpoints of the ray path, if it is assumed that the initial elevation angle is large. Equation (4) in terms of refractivity N is equal to

$$\tau_{1.2} = -\int_{N_1}^{N_2} \cot \theta \, dN \times 10^{-6}$$

with the assumption of $n \cong 1$ in the denominator. Integration by parts yields

$$\tau_{1.2} = -\int_{N_1}^{N_2} \cot \theta \, dN \times 10^{-6}$$
$$= -\left[N \cot \theta \times 10^{-6} \right]_{N_1}^{N_2} - \int_{\theta_1}^{\theta_2} \frac{N}{\sin^2 \theta} \, d\theta \times 10^{-6} \quad (6)$$

Note that the ratio $N/\sin^2 \theta$ becomes smaller with increasing θ for values of θ between 0 and 90°. If point 1 is taken at the surface, then $\theta_1 = \theta_0$ and $N_1 = N_s$. Then for $\theta_0 = 10°$, $N_2 = 0$, and $\theta_2 = \pi/2$, the last term of Eq. (6) amounts to only 3.5 percent of the entire equation, and for the same values of N_2 and θ_2, but with $\theta_0 = 87$ mrad ($\sim 5°$), the second term of Eq. (6) is still relatively small (~ 10 percent). Thus it would seem reasonable to assume that for

$$\theta_0 \geq 87 \text{ mrad } (\sim 5°)$$

the bending $\tau_{1.2}$ between the surface and any point r is given sufficiently well by

$$\tau_{1.2} = -\left[N \cot \theta \times 10^{-6} \right]_{N_s}^{N_r}$$

or

$$\tau_{1.2} = N_s \cot \theta_0 \times 10^{-6} - N_r \cot \theta_r \times 10^{-6} \quad (7)$$

The term $-N_r \cot \theta_r \times 10^{-6}$ is practically constant and small with respect to the first term, for a given value of θ_0 and r, in the range $\theta_0 \geq 87$ mrad. Thus $\tau_{1.2}$ is seen to be essentially a linear function of N_s in the range $\theta_0 \geq 87$ mrad. For bending

through the entire atmosphere (to a point where $N_r = 0$), and for $\theta_0 < 87$ mrad, Eq. (7) reduces to

$$\tau = N_s \cot \theta_0 \times 10^{-6}$$

For initial elevation angles less than about 5°, the errors inherent in this method exceed 10 percent (except near the surface) and rise rather rapidly with decreasing θ_0. There are several other methods of computing refraction, many of which are discussed by Bean and Dutton,[5] who also give numerical examples.

24.4 LINEAR OR EFFECTIVE-EARTH'S-RADIUS MODEL

The classical method of accounting for the effects of atmospheric refraction of radio waves is to assume an effective earth's radius, $a_e = ka$, where a is the true radius of the earth and k is the effective-earth's-radius factor. This method, advanced by Schelleng, Burrows, and Ferrell,[10] assumes an earth suitably larger than the actual earth so that the curvature of the radio ray may be absorbed in the curvature of the effective earth and the relative curvature of the two remains the same. Thus radio rays can be drawn as straight lines over this earth rather than as curved rays over the true earth. This method of accounting for atmospheric refraction permits a tremendous simplification in the many practical problems of radio propagation engineering although the height distribution of refractive index implied by this method is not a very realistic representation of the average refractive-index structure of the atmosphere. This section will consider the refractive-index structure assumed by the effective-earth's-radius model and how this differs from the observed refractive-index structure of the atmosphere. Further, the limits of applicability of the effective-earth's-radius approach will be explored and a physically more realistic model, the exponential, will be described for those conditions where the effective-earth's-radius model is most in error.

Fig. 2 Differential geometry used in the derivation of the effective-earth's-radius-model atmosphere.

It is instructive to give a derivation of the expression relating the curvature of radio rays to the gradient of refractive index. In Fig. 2 a wavefront moves from AB to $A'B'$ along the ray path. If the phase velocity along AA' is v and $v + dv$ along BB', then, from consideration of the angular velocity,

$$\frac{v}{\rho} = \frac{v + dv}{\rho + d\rho}$$

or

$$\frac{dv}{v} = \frac{d\rho}{\rho} \tag{8}$$

where ρ is the radius of curvature of the arc AA'. Now, since the phase velocity v is

$$v = \frac{c}{n}$$

where c is the velocity of light *in vacuo*, one obtains

$$\frac{dv}{v} = -\frac{dn}{n} \tag{9}$$

By combining (8) and (9), the familiar equation

$$\frac{1}{\rho} = -\frac{1}{n}\frac{dn}{d\rho}$$

is obtained.   If the ray path makes an angle θ with the surface of constant refractive index,

$$dr = d\rho \cos \theta$$

and

$$\frac{1}{\rho} = -\frac{1}{n}\frac{dn}{dr}\cos \theta$$

If the curvature of the effective earth is defined as

$$\frac{1}{a_e} = \frac{1}{a} - \frac{1}{\rho}$$

then

$$a_e = ka = \frac{1}{1/a - 1/\rho}$$

and

$$k = \frac{1}{1 + (a/n)(dn/dh)\cos \theta}$$

For the small values of θ normally used in tropospheric propagation, $\cos \theta$ may be set equal to unity.   Further, by setting

$$\frac{dn}{dh} \equiv -\frac{1}{4a}$$

one obtains the familiar value of $k = \frac{4}{3}$ for the effective-earth's-radius factor.   By assuming that the gradient of n is constant, a linear model of N versus height has been adopted.

For this model, the bending

$$\tau_{1,2} = -\int_{n_1}^{n_2} \cot \theta \, dn$$

is written

$$\tau_{1,2} = \int_{h_1}^{h_2} \frac{\cot \theta}{4a} \, dh \tag{10}$$

since

$$N = N_0 - \frac{h}{4a} 10^6$$

and

$$dn = dN \times 10^{-6} = -\frac{dh}{4a}$$

Further, for the case $h_1 = h_0 = 0$, and

$$0 \leq \theta_0 \leq 10°$$

where θ_0 is the initial elevation angle of a ray, Eq. (10) may be approximated by

$$\tau_{0,h} = -\int_0^h \frac{dh}{4a\theta} \tag{11}$$

The angle θ may be determined from ($\theta_h = \theta$)

$$\theta_h = \left[\theta_0^2 + 2(N - N_0) + \frac{2}{a}(h - h_0) \times 10^6 \right]^{\frac{1}{2}}$$

$$= \left(\theta_0^2 + \frac{3}{2}\frac{h}{a} \right)^{\frac{1}{2}} \tag{12}$$

For the case when $\theta_0 = 0$, Eq. (11) becomes

$$\tau_{0,h} = \frac{1}{2\sqrt{6a}} \int_0^h \frac{dh}{\sqrt{h}} = \frac{1}{\sqrt{6}} \sqrt{\frac{h}{a}} \Big]_0^h$$

$$\tau_{0,h} = \frac{1}{\sqrt{6}} \sqrt{\frac{h}{a}} \tag{13}$$

Now, from the geometrical relationship,

$$\tau_{0,h} = \frac{d_{0,h}}{a} + (\theta_0 - \theta_h)$$

one finds, for $\theta_0 = 0$,

$$d_{0,h} = a(\tau_{0,h} + \theta_h)$$

which upon substitution from Eqs. (12) and (13) gives

$$d_{0,h} = \sqrt{2h(4/3)\,a}$$

or, more familiarly,

$$d_{0,h} = \sqrt{2kah} \tag{14}$$

A very convenient working formula is derived from Eq. (14) by $k = 4/3$, $a = 3,960$ statute miles, and by using units of statute miles for the ground distance to the radio horizon, $d_{0,h}$, and feet for the antenna height h:

$$d_{0,h} = \sqrt{2h} \qquad \text{statute miles}$$

This is the familiar expression often used in radio-propagation engineering for the distance to the radio horizon.

Extensive tables, graphs, and maps of gradients of N that permit worldwide estimation of the seasonal range of k and thus the radio-horizon distance are available.[11]

24.5 MODIFIED EFFECTIVE-EARTH'S-RADIUS MODEL

The effective-earth's-radius model, although very useful for engineering practice, is not a very good representation of actual atmospheric N structure. For example, the data in Fig. 3 represent the average of individual radiosonde observations over a 5-year period at several locations chosen to represent the extremes of refractive-index profile conditions within the United States. The Miami, Fla., profile is typical of warm, humid sea-level stations that tend to have maximum refraction effects whereas the Portland, Me., profile is associated with nearly minimum sea-level refraction conditions. Although Ely, Nev., has a much smaller surface N value than either Miami or Portland, it is significant that, when its N profile is plotted in terms of altitude above sea level, it falls within the limits of the maximum and minimum sea-level profiles. It is to take advantage of this simplification that altitude above sea level, h_s, rather than height above ground is frequently used throughout this chapter. The N distribution for the 4/3 earth atmosphere is also shown in Fig. 3. It is evident that the 4/3 earth distribution has about the correct slope in the first kilometer above the earth's surface but decreases much too rapidly above that height. It is also seen, by noting that Fig. 3 is plotted on semilogarithmic paper, that the observed refractivity distribution is more nearly an exponential function of height than a linear function of height as assumed by the 4/3 earth atmosphere. One might expect the refractivity to decrease exponentially with height since the first term of the refractivity Eq. (2) involving P/T comprises at least 70 percent of the total and is proportional to air density, a well-known exponential function of height.

One might wonder, in the light of the data of Fig. 3, why the effective-earth's-radius approach has served so well for so many years. It appears that this success is due to the 4/3 earth model being in essential agreement with the average N structure near the earth's surface, which largely controls the refraction of radio rays at the small values of θ_0 common in long-range surface radar.

It would seem that the deficiency of the effective-earth's-radius approach could be lessened by modifying that theory in the light of the average N structure of the atmosphere. An indication of the average N structure was obtained by examining a variety of N profiles which were carefully selected from 39 station-years of individual radiosonde observations to represent the range of N-profile conditions during summer and winter at 13 climatically diverse locations. It was noted that the range of N values
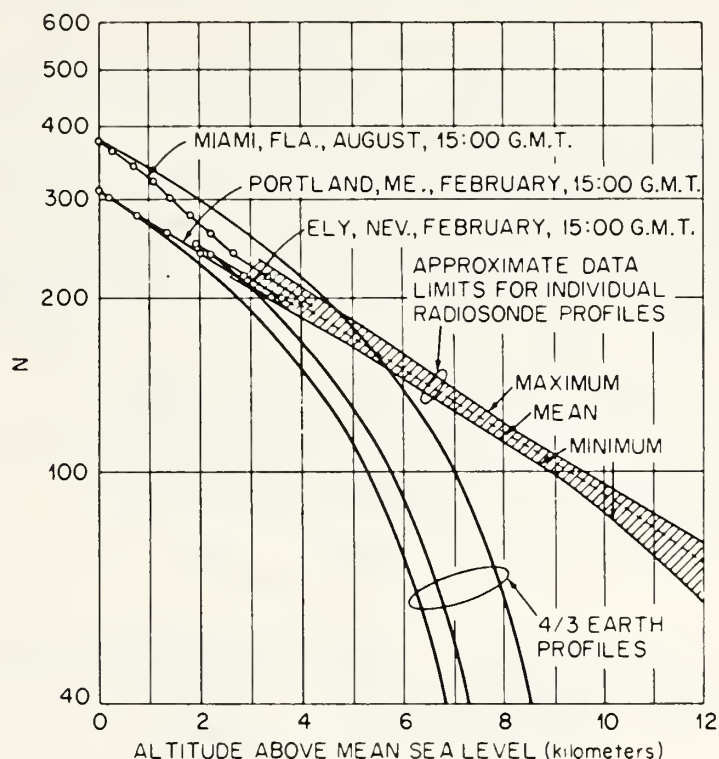
Fig. 3 Typical N-versus-height distributions.

had a minimum at 8 to 9 km above sea level but was systematically greater above and below that altitude. The average value of 104.8 at 9 km corresponds to a similar value reported by Stickland[12] as typical of the United Kingdom. Further, the altitude of 8 km corresponds to the altitude reported by Humphreys[13] where the atmospheric density is nearly constant regardless of season or geographical location. Since the first term in the expression for refractivity is proportional to air density, and the water-vapor term is negligible at an altitude of 9 km, the refractivity also tends to be constant at this altitude. It seems reasonable, then, to adopt a constant value of $N = 105$ for 9 km, thus further facilitating the specification of model atmospheres. Further, when values of N are plotted such as in Fig. 3 it is seen that the data strongly suggest that N may be represented by an exponential function of height of the form

$$N(h) = N_0 e^{-bh}$$

in the altitude range of 1 to 9 km above sea level.

When dealing with low-altitude radar propagation problems where the ray paths involved do not exceed 1, or at most 2, km above the earth's surface one can use the effective-earth's-radius method to solve the associated refraction problems. The

reader should refer to the tables of Bean and Dutton[5] where effective-earth's-radius factors are tabulated along with other refractivity variables. When the effective-earth's-radius treatment is used, height is calculated as a function of distance, for a ray with $\theta_0 = 0$, with the equation $h = d^2/2ka$, where d is the distance, k is the effective-earth's-radius factor, and a is the true radius of the earth ($\sim$6,373 km). The errors likely to be incurred when using this equation, if one assumes as a true atmosphere an exponential $N(h)$ profile as given in the following section, will not exceed 5 percent for heights of 1 km or less.

A logical sequence of models (or assumptions) to describe the effects of atmospheric refraction might be as follows:

1. Assume an invariant model that is near to the actual average conditions and facilitates the calculation of radio field strengths. This has been done by the 4/3 earth model.

2. Assume a variable effective-earth's-radius factor for the calculation of radio field strengths in various climatic regions. This approach has been followed by Norton, Rice, and Vogler.[14] When it has become apparent that the effective-earth's-radius approach is inadequate, one might proceed by step 3.

3. Correct the effective-earth's-radius model by assuming a more realistic N structure in the region where that model is most in error. This "modified-effective-earth's-radius" model (described in the remainder of this section) would then maintain, for some applications, the advantages of the original model.

4. Assume an entirely new model of N structure guided by the average N structure of the atmosphere. (This is described in Sec. 24.6.) It is assumed that models 3 and 4 would allow for seasonal and climatic changes of the average refractive-index structure of the atmosphere.

The modified effective-earth's-radius model of atmospheric refractivity that will be considered is based upon the effective-earth's-radius concept in the first kilometer. In this atmosphere N is assumed to decay linearly with height from the surface h_s to 1 km above the surface, $h_s + 1$. This linear decay is given by

$$N(h) = N_s + (h - h_s)\,\Delta N \qquad h_s \leq h \leq h_s + 1$$

where
$$-\Delta N = 7.32 e^{0.005577 N_s} \tag{15a}$$

This last relationship comes from the observed relationship between 6- to 8-year averages of daily observations of N_s and ΔN, the difference between N_s and the value of N at 1 km above the earth's surface:

$$-\Delta N = N_s - N(1\text{ km})$$

It may be further assumed that N decreases exponentially from $h_s + 1$ to a constant value of 105 at 9 km above sea level. In this altitude range N is defined by

$$N = N_1 e^{-c(h - h_s - 1)} \qquad h_s + 1 \leq h \leq 9\text{ km} \tag{15b}$$

where
$$c = \frac{1}{8 - h_s} \ln \frac{N_1}{105}$$

and N_1 is the value of N at 1 km above the surface.

Above the altitude of 9 km, where less than 10 percent of the total bending occurs, a single exponential decrease of N may be assumed. The coefficients in the exponential expression

$$N = 105 e^{-0.1424(h - 9)} \qquad h \geq 9\text{ km} \tag{15c}$$

were determined by a least-squares analysis of The Rocket Panel data.[63] This expression is also in agreement with the ARDC (Air Research and Development Command) Model Atmosphere 1956[64] and Dubin's[65] conclusion that a standard density distribution may be used to determine the refractivity distribution at altitudes in excess of 20,000 ft.

The three-part model of the atmosphere expressed by Eqs. (15a) to (15c) has the advantage of the effective-earth's-radius approach plus being in reasonably good agreement with the average N structure of the atmosphere.

24.6 EXPONENTIAL MODEL

This model of the atmosphere may be specified by assuming a single exponential distribution of N:

$$N = N_s e^{-c_e(h-h_s)} \qquad (16a)$$

where h_s, as defined in Fig. 1, is the surface height and

$$c_e = \ln \frac{N_s}{N(1 \text{ km})} = \ln \frac{N_s}{N_s + \Delta N} \qquad (16b)$$

These equations are used to determine N at all heights. This model of atmospheric refractivity is a close representation of the average refractivity structure within the first 3 km. Further, the single-exponential model has the advantage of being an entire function and therefore is easily used in theoretical studies. This model of the atmosphere has been adopted for use within the National Bureau of Standards with specific values of the constants in Eqs. (16a) and (16b). These constants are given in Table 2 and specify the CRPL Exponential Reference Atmosphere—1958.

TABLE 2 Table of the Constant c_e for the CRPL Exponential Radio Refractivity Atmospheres

$$N = N_s e^{-c_e(h-h_s)}$$

ΔN	N_s	c_e (per km)
0	0	0
22.3318	200.0	0.118400
29.5124	250.0	0.125625
30.0000	252.9	0.126255
39.2320	301.0	0.139632
41.9388	313.0	0.143859
50.0000	344.5	0.156805
51.5530	350.0	0.159336
60.0000	377.2	0.173233
68.1295	400.0	0.186720
70.0000	404.9	0.189829
90.0406	450.0	0.223256

Figure 4 compares the N structure of the above exponential model, the modified effective-earth's-radius model of Sec. 24.5 [denoted the reference refractivity atmosphere and described by Eqs. (15a) to (15c)], and the 4/3 earth model. It can be seen that the 4/3 earth assumption agrees with the reference atmosphere in the first kilometer, which is to be expected since $N_s = 301$ is the value required to yield the 4/3 gradient from Fig. 4. Figure 4 illustrates the essential agreement of the CRPL reference refractivity atmosphere with the Rocket Panel[63] and ARDC data.[64] The exponential reference atmosphere is also shown in Fig. 4 for $N_s = 313$, the average value for the United States. The exponential reference atmosphere appears to be a reasonable single-line representation of N throughout the height interval shown.

The total angular refraction of the ray path, or bending, in the 4/3 earth atmosphere is compared with that in the exponential reference atmosphere in Fig. 5. The bending
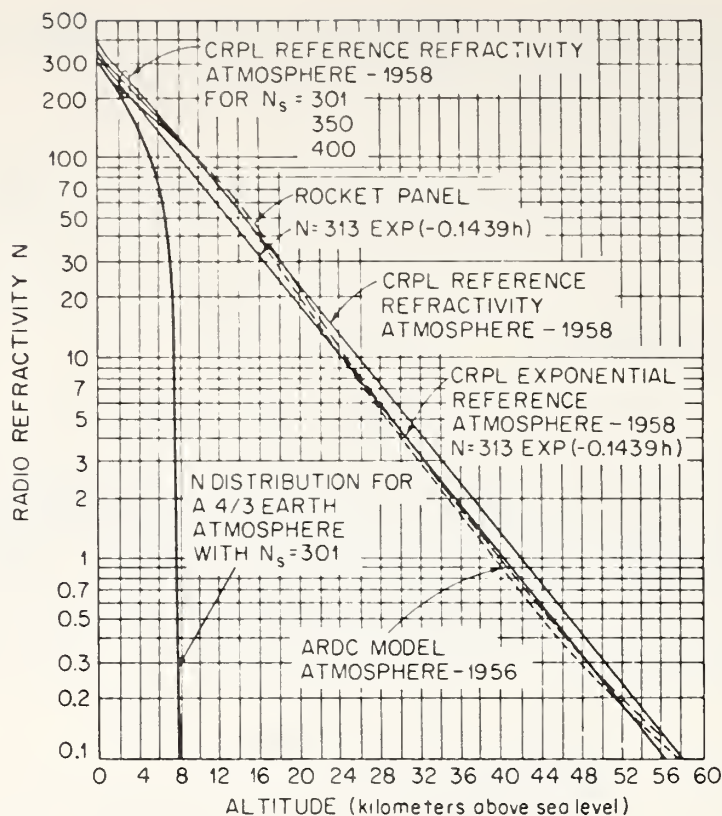
Fig. 4 Comparison of radio refractivity profiles for three models: ⅘ earth, the modified effective-earth's-radius model (called the CRPL reference refractivity atmosphere), and the CRPL exponential reference model. Also shown for comparison are data of the Rocket Panel and the ARDC Model Atmosphere—1956.
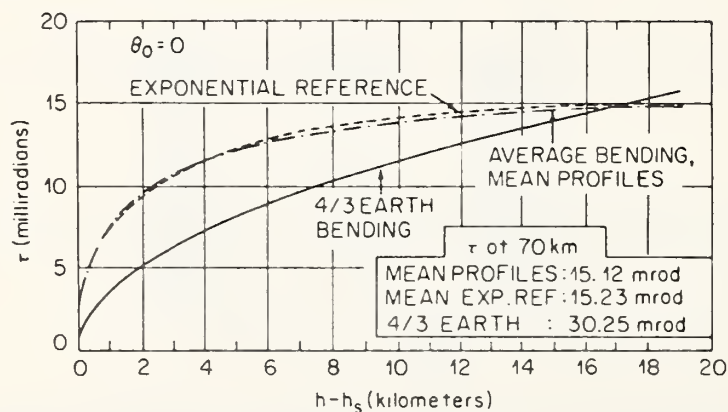
Fig. 5 Bending vs. height.

in an "average" atmosphere is also given. This average atmosphere is a composite of the 5-year mean profiles for both summer and winter at 11 United States radiosonde stations and was used as a readily available measure of average conditions.

24.7 ATTENUATION

Gaseous absorption and scattering and attenuation by precipitation and clouds affect the power requirements of a radar system and so need consideration. They also have an important application in the field of meteorology, particularly in cloud and precipitation physics, although other applications (such as to clear-air turbulence) are

also important. The study of radar meteorology is summarized excellently else-where,[15],[16] and it is not the purpose of this section to undertake a detailed exam-ination of this subject. Rather, this section will deal with the fundamentals and characteristics of scattering and absorption, with particular emphasis on absorption.

The attenuation experienced by radar is the result of two effects: (1) absorption and (2) scattering. At wavelengths greater than a few centimeters, absorption by atmospheric gases is generally thought to be negligibly small except where very long distances are concerned. However, cloud and rain attenuation should be considered at wavelengths less than 10 cm; it is particularly pronounced in the vicinity of 1 and 3 cm, or shorter.

24.8 ATTENUATION BY ATMOSPHERIC GASES

The major atmospheric gases that need to be considered as absorbers in the frequency range of 100 to 50,000 MHz are water vapor and oxygen. For these frequencies the gaseous absorption arises principally in the 1.35-cm line (22,235 MHz) of water vapor and the series of lines centered around 0.5 cm (60,000 MHz) of oxygen.[17] The variations of these absorptions with pressure, fre-quency, temperature, and humidity are described by the Van Vleck[17],[18] theory of absorption. The frequency dependence of these absorptions is shown in Fig. 6.[17]

In Fig. 6 the water-vapor absorption values have been adjusted to correspond to the mean absolute humidity ρ (grams of water vapor per cubic meter) for Washing-ton, D.C., 7.75 g/m³. The reason for this adjustment is that water-vapor absorption is directly proportional to the absolute humidity[19] and thus variations in signal intensity due to water-vapor absorption may be specified directly in terms of the varia-tions in the absolute humidity of the atmosphere.

It can be seen from Fig. 6 that the water-vapor absorption exceeds the oxygen absorp-tion in the frequency range 13,000 to 32,000 MHz, indicating that in this frequency range the total absorption is the most sensitive to changes in the water-vapor content of the air, whereas outside this frequency range the absorption is more sensitive to changes in oxygen density. Only around the resonant frequency corres-

Fig. 6 Atmospheric absorption by the 1.35-cm line of water vapor and the 0.5-cm line of oxygen.

ponding to $\lambda = 1.35$ cm is the water-vapor absorption greater than the oxygen absorption. The absorption equations and the conditions under which they are applicable have been discussed by Van Vleck[17] and Bean and Abbott.[20]

The Van Vleck theory describes these absorptions from 100 to 50,000 MHz in the following manner. The oxygen absorption at $T = 293°K$ and standard atmospheric pressure in decibels per kilometer, γ_1, is given by the expression

$$\gamma_1 = \frac{0.34}{\lambda^2} \left[\frac{\Delta\nu_1}{1/\lambda^2 + \Delta\nu_1^2} + \frac{\Delta\nu_2}{(2 + 1/\lambda)^2 + \Delta\nu_2^2} + \frac{\Delta\nu_2}{(2 - 1/\lambda)^2 + \Delta\nu_2^2} \right] \quad (17)$$

where λ is the wavelength for which the absorption is to be determined and $\Delta\nu_1$ and $\Delta\nu_2$ are line-width factors with dimensions of reciprocal centimeters. This formula is based on the approximations of collision broadening theory.

The water-vapor absorption at 293°K arising from the 1.35-cm line, γ_2, is given by

$$\frac{\gamma_2}{\rho} = \frac{3.5 \times 10^{-3}}{\lambda^2} \left[\frac{\Delta\nu_3}{(1/\lambda - 1/1.35)^2 + \Delta\nu_3{}^2} + \frac{\Delta\nu_3}{(1/\lambda + 1/1.35)^2 + \Delta\nu_3{}^2} \right] \quad (18)$$

where ρ is the absolute humidity and $\Delta\nu_3$ is the line-width factor of the 1.35-cm water-vapor absorption line. The additional absorption arising from absorption bands above the 1.35-cm line, γ_3, is described by

$$\frac{\gamma_3}{\rho} = \frac{0.05\Delta\nu_4}{\lambda^2}$$

where $\Delta\nu_4$ is the effective line width of the absorption bands above the 1.35-cm line. The nonresonant term has been increased by a factor of 4 over the original Van Vleck formula in order better to satisfy experimental results.[21]

Although Van Vleck gives estimates of the various line widths, more recent experimental determinations were used whenever possible, as summarized in Table 3.

TABLE 3   Line-width Factors Used to Determine Atmospheric Absorption

Line width	Temperature, °K	Value, cm⁻¹ atm⁻¹	Sources
$\Delta\nu_1$	293	0.018	Birnbaum and Maryott[22]
$\Delta\nu_2$	300	0.049	Artman and Gordon[23]
$\Delta\nu_3$	318	0.087	Becker and Autler[21]
$\Delta\nu_4$	318	0.087	Becker and Autler[21]

The preceding expressions for gaseous absorption are given as they appear in the literature and do not reflect the pressure and temperature sensitivity of either the multiplying factor in the expressions for γ_1, γ_2/ρ, and γ_3/ρ, or the line widths.

The pressure (millibars) and temperature (degrees Kelvin) dependence of the multiplying factors and line widths are given in Table 4.   Table 5 shows attenuation

TABLE 4   Values Used in the Calculation of Atmospheric Absorption

Absorption, db/km	Multiplying factor	Line width, cm⁻¹
γ_1	$\dfrac{0.34}{\lambda^2} \dfrac{P}{1013.25} \left(\dfrac{293}{T}\right)^2$	$\Delta\nu_1 \dfrac{P}{1013.25} \left(\dfrac{293}{T}\right)^{3/4}$ and $\Delta\nu_2 \dfrac{P}{1013.25} \left(\dfrac{300}{T}\right)^{3/4}$
$\dfrac{\gamma_2}{\rho}$†	$\dfrac{0.0318}{\lambda_2} \left(\dfrac{293}{T}\right)^{5/2} e^{-644/T}$	$\Delta\nu_3 \dfrac{P}{1013.25} \left(\dfrac{318}{T}\right)^{1/2} (1 + 0.0046\rho)$
$\dfrac{\gamma_3}{\rho}$†	$\dfrac{0.05}{\lambda^2} \left(\dfrac{293}{T}\right)$	$\Delta\nu_4 \dfrac{P}{1013.25} \left(\dfrac{318}{T}\right)^{1/2} (1 + 0.0046\rho)$

† ρ is water-vapor density in grams per cubic meter.

by water vapor at various temperatures and wavelengths. As the temperature decreases, oxygen absorption increases gradually between 0.7- and 10-cm wavelengths. Table 6 shows some correction factors.

TABLE 5† Water-vapor Attenuation (One Way) In Decibels per Kilometer

P = pressure, in atmospheres; W = water-vapor content, in grams per cubic meter

T (°C)	λ (cm) 10	5.7	3.2	1.8	1.24	0.9
20	$0.07 \times 10^{-3}\,PW$	$0.24 \times 10^{-3}\,PW$	$0.7 \times 10^{-3}\,PW$	$4.3 \times 10^{-3}\,PW$‡	$22.0 \times 10^{-3}\,PW$‡	$9.5 \times 10^{-3}\,PW$
0	$0.08 \times 10^{-3}\,PW$	$0.27 \times 10^{-3}\,PW$	$0.8 \times 10^{-3}\,PW$	$4.8 \times 10^{-3}\,PW$‡	$23.3 \times 10^{-3}\,PW$‡	$10.4 \times 10^{-3}\,PW$
−20	$0.09 \times 10^{-3}\,PW$	$0.30 \times 10^{-3}\,PW$	$0.9 \times 10^{-3}\,PW$	$5.0 \times 10^{-3}\,PW$‡	$24.6 \times 10^{-3}\,PW$‡	$11.4 \times 10^{-3}\,PW$
−40	$0.10 \times 10^{-3}\,PW$	$0.34 \times 10^{-3}\,PW$	$1.0 \times 10^{-3}\,PW$	$5.4 \times 10^{-3}\,PW$‡	$26.1 \times 10^{-3}\,PW$‡	$12.6 \times 10^{-3}\,PW$

† After Gunn and East.[34]
‡ The pressure dependencies shown are only approximate.   Near the 1.35-cm water-vapor absorption line (between 1.0 and 2.0 cm) no simple power dependency of P and W is accurate.

TABLE 6† Pressure and Temperature Correction for Oxygen Attenuation for Wavelengths between 0.7 and 10 cm

T, °C	Factor (P is pressure, in atmospheres)
20	$1.00\ P^2$
0	$1.19\ P^2$
−20	$1.45\ P^2$
−40	$1.78\ P^2$

† After Gunn and East.[34]

24.9 ESTIMATES OF THE RANGE OF GASEOUS ABSORPTION

The range in gaseous absorption can be seen by considering the data for the months of February and August at Bismarck, N.Dak., and Washington, D.C., two stations with very different climates. The values of total gaseous absorption (defined as the sum of γ_1, γ_2, and γ_3, where γ_1 = oxygen absorption in decibels per kilometer, γ_2 = water-vapor absorption arising from the 1.35-cm line, and γ_3 = additional absorption arising from absorption lines whose frequencies are considerably higher than that corresponding to the 1.35 line) at each station and elevation up to 75,000 ft are shown in Figs. 7 and 8 for each of the four station-months for the frequency range of 100 to 50,000 MHz. Above 75,000 ft the absorption values for all four station-months are identical and are given for each frequency in Fig. 9. The absolute humidity was calculated by using the upper-air monthly average values of temperature, pressure, and humidity as reported by Ratner.[24] Readings for the relative humidity are not generally given in this report for altitudes greater than about 15 km because of the inability of the radiosonde to measure the small amount of humidity present at these altitudes. It is believed that the climates represented by these station-months encompass the range of those of the majority of the continental United States radio propagation paths.

An interesting property of the annual range of absorption as a function of the frequency may be seen in Figs. 7 and 8. For the first 5,000 ft above the surface, in the frequency range of 10 to 32.5 GHz the summer values are greater than the winter values because of increased humidity of the summer months. Outside this frequency range, however, the winter values of absorption are greater because of the increased oxygen density.

In the frequency range 6 to 45 GHz atmospheric absorption γ_ν at a frequency ν arises primarily from oxygen absorption $\gamma_{d\nu}$ and water-vapor absorption $\gamma_{w\nu}$; that is,

$$\gamma_\nu = \gamma_{d\nu} + \gamma_{w\nu}$$

Zhevankin and Troitskii[25] have indicated that $\gamma_{d\nu}$ and $\gamma_{w\nu}$ can be represented as exponential functions of height, Z, above the earth's surface,

$$\gamma_{d\nu} = \gamma_{d\nu 0}e^{-Z/H_{d\nu}} \qquad \gamma_{w\nu} = \gamma_{w\nu 0}e^{-Z/H_{w\nu}}$$

where $\gamma_{d\nu 0}$ and $\gamma_{w\nu 0}$ are the values of $\gamma_{d\nu}$ and $\gamma_{w\nu}$, respectively, at the earth's surface, and $H_{d\nu}$ and $H_{w\nu}$ are called the *scale heights* of $\gamma_{d\nu}$ and $\gamma_{w\nu}$. This model is known as the *biexponential* model of absorption, and $\gamma_{d\nu}$ and $\gamma_{w\nu}$ are often called the "dry" and "wet" terms of γ_ν. The scale height for the dry term in the frequency range 6 to 45 GHz can be written as[26]

$$H_{d\nu}\ \text{(in km)} \cong \frac{T_0}{c + b\alpha} \tag{19}$$

$$c = 68.6°\text{K/km} \qquad b = -2.75$$
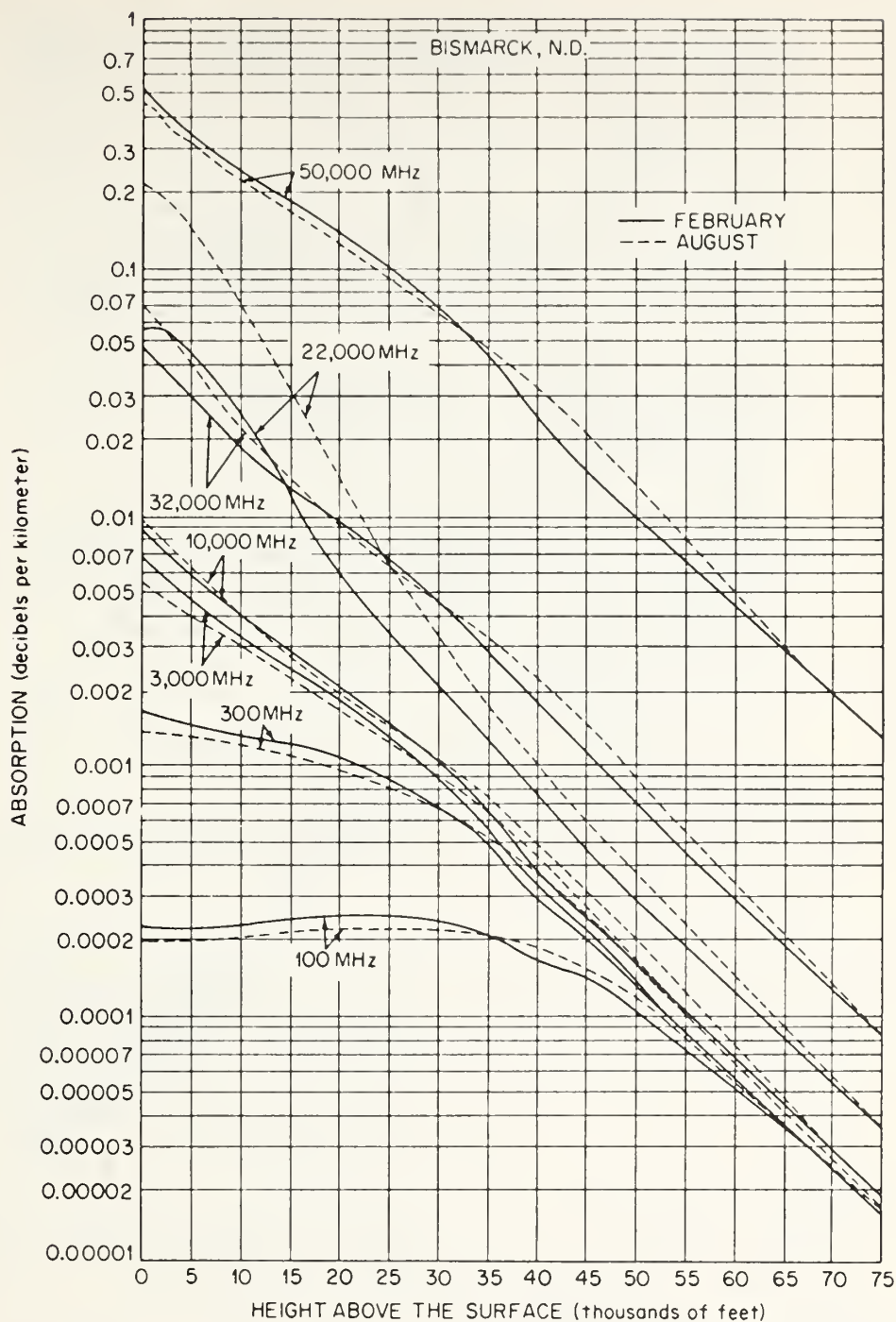
Fig. 7 Gaseous atmospheric absorption from the surface to 75,000 ft: Bismarck, N.Dak.

where T_0 is the surface temperature in degrees Kelvin, α is the temperature-lapse rate with height in degrees Kelvin per kilometer, and b, c are constants determined from thermodynamic considerations. Because of the hump in the $H_{w\nu}$ curves as opposed to the flat $H_{d\nu}$ curve in Fig. 10, such a handy expression as Eq. (19) for $H_{w\nu}$ is not possible in the 6- to 45-GHz frequency range (Fig. 10 was determined from actual radiosonde data at Verkhoyansk, U.S.S.R.).
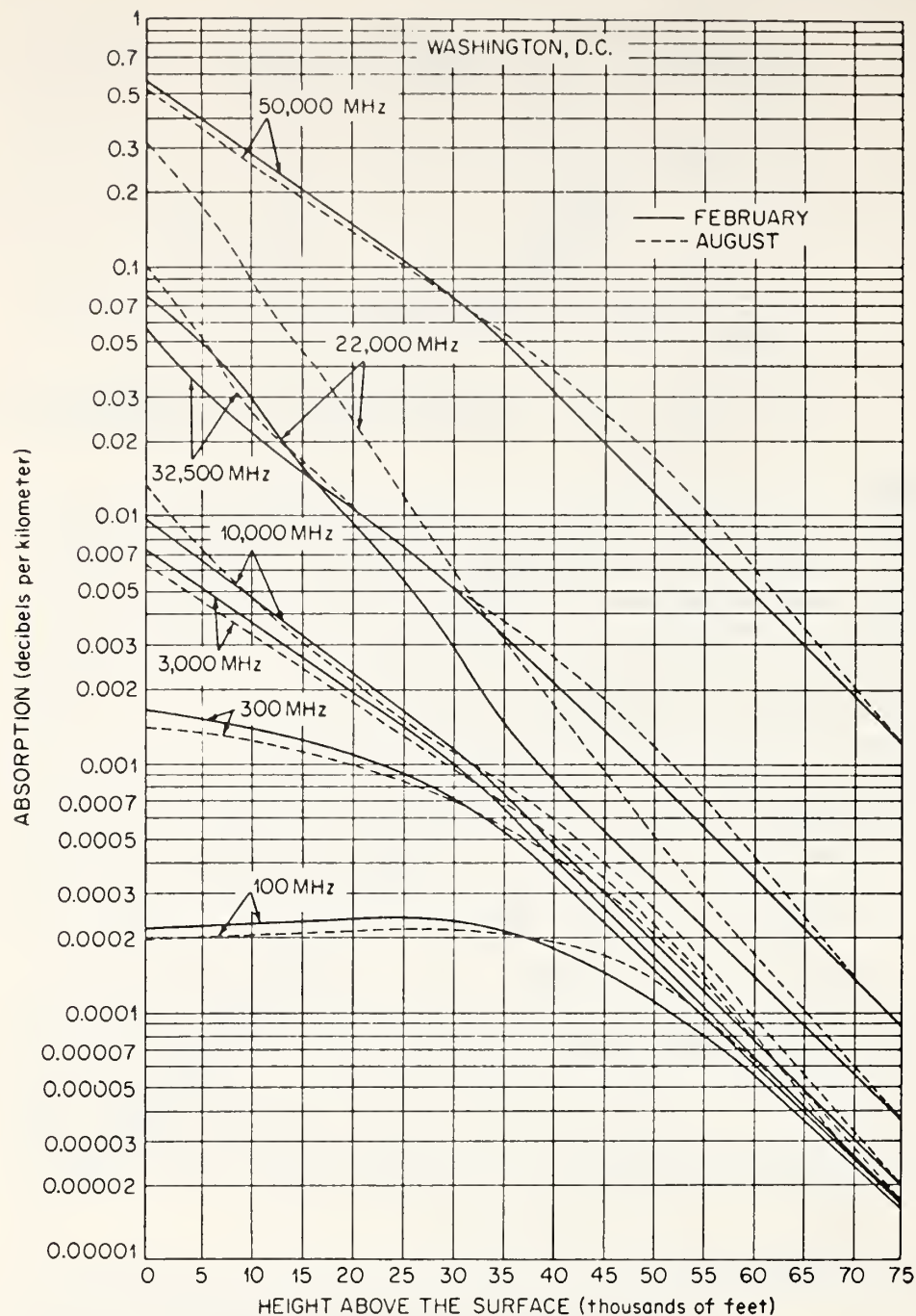
Fig. 8 Gaseous atmospheric absorption from the surface to 75,000 ft: Washington, D.C.

24.10 TOTAL RADIO-PATH ABSORPTION

The total path absorption is determined by calculating the various absorption coefficients as functions of the heights along the ray path and then numerically integrating the values along the entire path, using standard ray-tracing techniques outlined earlier. The values of total path integration over a 300-mile path thus obtained are presented in Fig. 11 for Bismarck, N.Dak., and Washington, D.C. The difference between the two climates is evident principally at the higher frequencies, where the
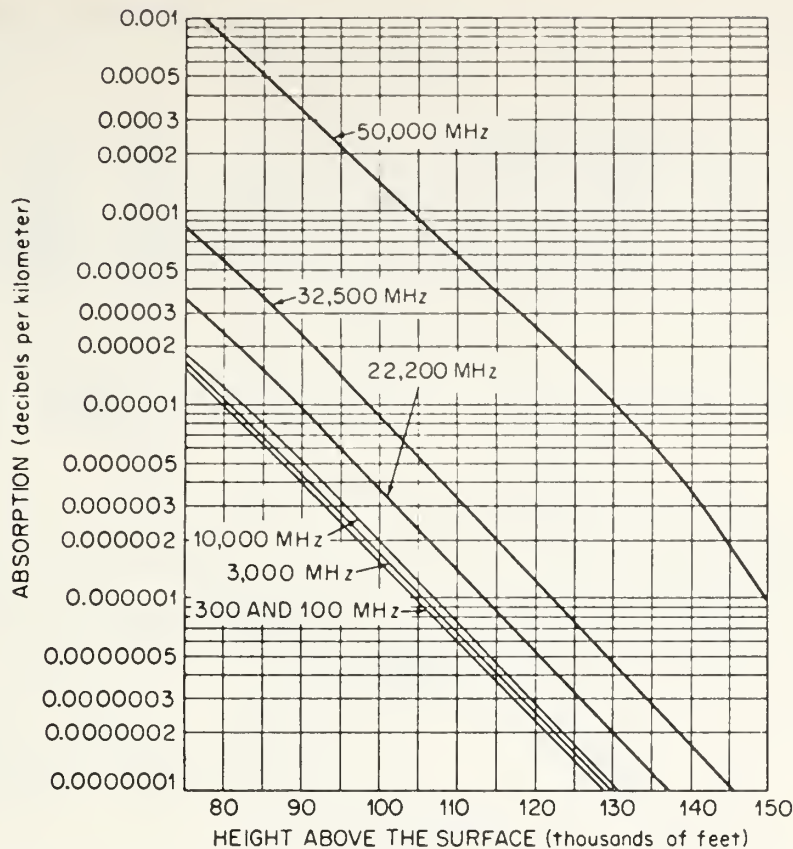
Fig. 9 Common values of total gaseous atmospheric absorption for elevations greater tnan 75,000 ft.

Washington absorptions are consistently above the Bismarck values. This is apparently due to a combination of generally greater humidities and greater refractive effects. These two effects are related. The increased humidity at Washington enhances the water-vapor absorption and increases the refraction, causing the radio ray to travel consistently through lower levels of the atmosphere with consequent increase in total path absorption.

The values of total path absorption given above are for two specific locations. A means for arriving at estimates of geographic and annual variations of total path absorption for various surface distances and frequencies is given by Bean and Dutton.[5]
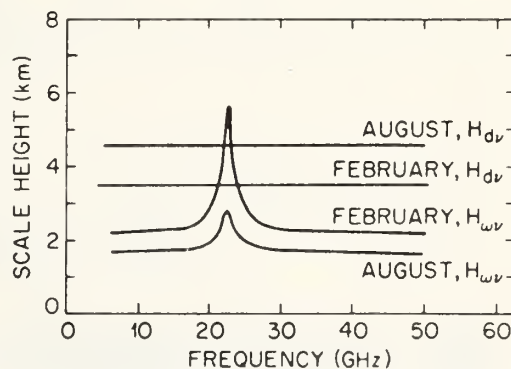
Fig. 10 Variations with frequency of the scale heights of the biexponential absorption model at Verkhoyansk, U.S.S.R.

24.11 ATTENUATION AND SCATTERING BY SINGLE SPHERICAL PARTICLES

In this section, dust, smog, and smoke particles will be ignored because their dielectric constants are so small, relative to water droplets, that they have a negligible effect on radar propagation. As electromagnetic propagation impinges on a single suspended particle, some fraction q_s of the incident energy E_i is scattered in an amount E_o in all directions. Some other fraction q_a of E_i is absorbed by the
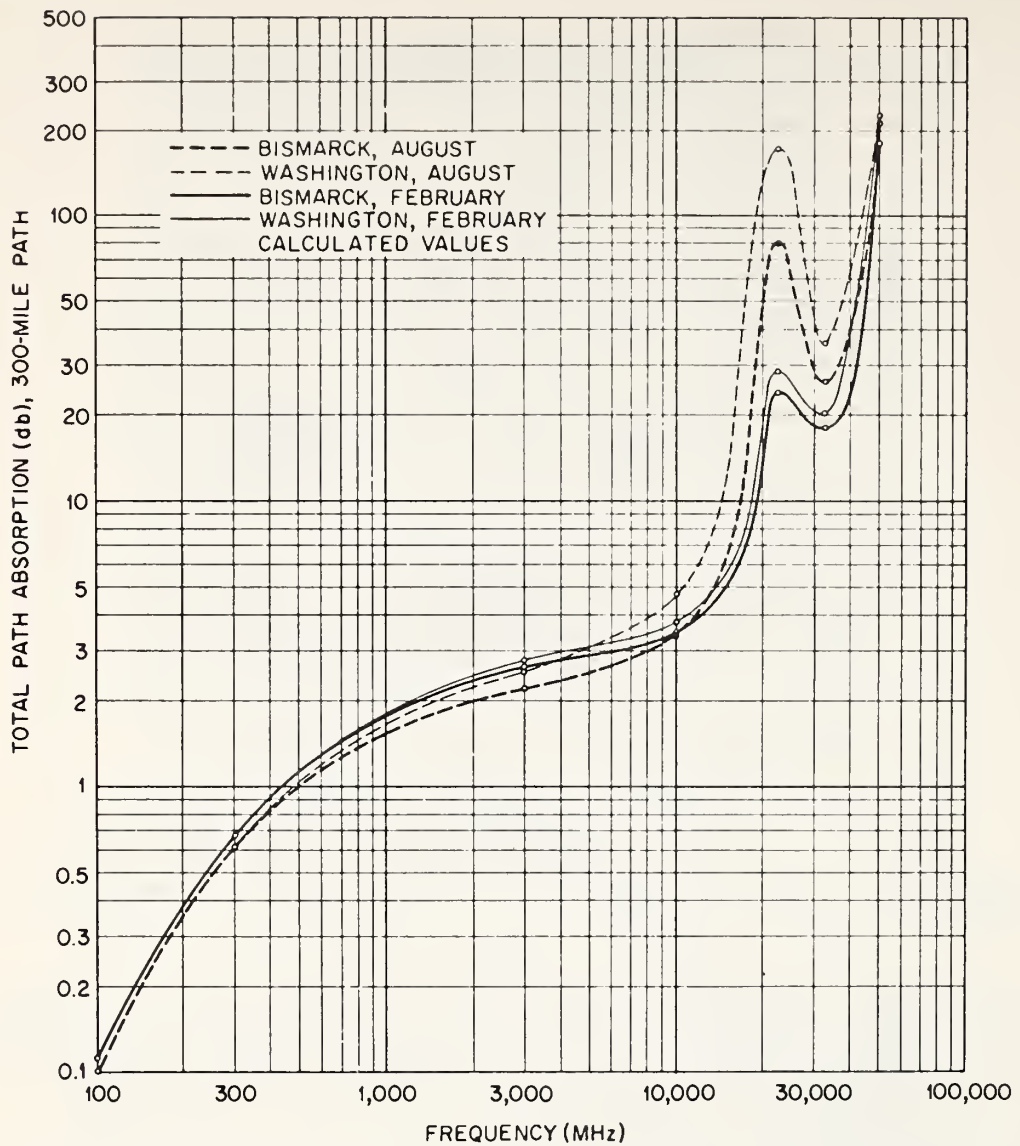
Fig. 11   Total path absorption over a low-initial-elevation-angle, 300-mile propagation path.

particle in an amount E_{0a}.   Hence,

$$\frac{E_{0s}}{E_i} = q_s \qquad \text{and} \qquad \frac{E_{0a}}{E_i} = q_a$$

The total energy thus removed from the radar beam, as it progresses forward, is clearly the sum of the scattered and absorbed energy.   Thus the total fraction q_T of energy removed from the radar beam is

$$q_T = \frac{E_{0s} + E_{0a}}{E_i} = q_s + q_a \tag{20}$$

The symbols q_T, q_s, and q_a are called the total attenuation, scattering, and absorption cross sections of the particle, respectively.

For water droplets, Mie[27] assumed each to be a sphere of radius r and showed that

$$q_T = -\frac{\lambda^2}{2\pi} A(r,\lambda,m) \tag{21}$$

where λ is the wavelength of the electromagnetic energy incident on the droplet. In Eq. (21), m is the complex index of refraction of water, studied in some detail at radar frequencies by Saxton and Lane[29] and Saxton.[66] A is a very cumbersome expression which is covered in great detail elsewhere.[30-33] For the centimeter and millimeter wavelengths of interest in radar the so-called Rayleigh approximation[15] yields

$$q_s = \frac{2\lambda^2}{3\pi} \beta^6 \left| \frac{m^2 - 1}{m^2 + 2} \right|^2 \tag{22}$$

where $\beta = 2\pi r/\lambda$ and r is the droplet radius. Furthermore, it can be shown from Ref. 34, by using Eqs. (20) to (22) in the $\beta \ll 1$ region, that

$$q_a = \frac{\lambda^2}{\pi} \beta^3 \text{Im} \left(-\frac{m^2 - 1}{m^2 + 2} \right) \tag{23}$$

where Im ( ) is the imaginary part of ( ). The symbol K is often used† instead of $(m^2 - 1)/(m^2 + 2)$.

If scattering were isotropic, Eq. (22) would represent the scattering cross section in every direction. However, the radiation pattern of a particular droplet is unknown, and probably the second simplest assumption to that of isotropicity is that a droplet sufficiently small compared with wavelength ($\beta \ll 1$) will behave as a dipole when a plane wave is incident upon it.[31,35] In this case the droplet back-scattering cross section σ is given by

$$\sigma = \frac{\lambda^2}{4\pi} B(r,\lambda,m) \tag{24}$$

where, again, B is a rather complicated expression obtainable from many of the literature references mentioned heretofore. However, for $\beta \ll 1$, Eq. (24) reduces to

$$\sigma = \frac{\lambda^2}{\pi} \beta^6 |K|^2 \tag{25}$$

24.12 VOLUME SCATTERING

What is of interest in the radar equation [Eq. (32) of Sec. 24.18] is the combined backscattering effects of a unit volume

$$\eta = \sum_{i=1}^{N} \sigma_i \tag{26}$$

where N is the number of scatterers per unit volume and σ_i is the backscatter cross section of the ith scatterer. The symbol η is called the *radar reflectivity* and has units of reciprocal length. From Eq. (25), Eq. (26) can be written

$$\eta = \frac{\lambda^2}{\pi} |K|^2 \sum_{i=1}^{N} \beta_i^6 = \frac{\pi^5}{\lambda^4} |K|^2 \sum_{i=1}^{N} D_i^6 \tag{27}$$

where D_i is the diameter of a droplet. The reflectivity factor Z is defined as

$$Z = \sum_{i=1}^{N} D_i^6 \tag{28}$$

† Not to be confused with K used later for attenuation coefficients.

and thus Eq. (27) becomes

$$\eta = \frac{\pi^5}{\lambda^4} |K|^2 Z$$

24.13 ATTENUATION IN CLOUDS

Cloud droplets are regarded here as those water or ice particles having radii smaller than 100 microns, or 0.01 cm. For wavelengths of incident radiation well in excess of 0.5 cm, the attenuation becomes independent of the drop-size distribution. The generally accepted equations for attenuation by clouds usually show the moisture component of the equations in the form of the liquid-water content (grams per cubic meter). Observations indicate that the liquid-water concentration in clouds generally ranges from[36] 1 to 2.5 g/m^3, although Weickmann and aufm Kampe[37] have reported isolated instances of cumulus congestus clouds with a reading of 4.0 g/m^3 in the upper levels. In ice clouds, it rarely exceeds 0.5 and is often less than 0.1 g/m^3. The attenuation of cloud drops may be written

$$K = K_1 M$$

where K = attenuation, db/km
$\quad K_1$ = attenuation coefficient, db/km/g/m^3
$\quad M$ = liquid-water content, g/m^3
From Eq. (23) and

$$M = \frac{4\pi\rho}{3} \sum_{i=1}^{N} r_i^3$$

where N is the number of drops per unit volume and ρ is the density of water (= 1 g/cm^3), then

$$K_1 = 0.4343 \frac{6\pi}{\lambda} \,\mathrm{Im}\left(-\frac{m^2-1}{m^2+2}\right)$$

Values of K_1 for ice and water clouds are given for various wavelengths and temperatures by Gunn and East in Table 7.

TABLE 7† **One-way Attenuation Coefficient K_1 in Clouds in db/km/g/m^3**

Temperature, °C		Wavelength, cm			
		0.9	1.24	1.8	3.2
Water cloud	20	0.647	0.311	0.128	0.0483
	10	0.681	0.406	0.179	0.0630
	0	0.99	0.532	0.267	0.0858
	−8	1.25	0.684	0.34 (extrapolated)	0.112 (extrapolated)
Ice cloud	0	8.74×10^{-3}	6.35×10^{-3}	4.36×10^{-3}	2.46×10^{-3}
	−10	2.93×10^{-3}	2.11×10^{-3}	1.46×10^{-3}	8.19×10^{-4}
	−20	2.0×10^{-3}	1.45×10^{-3}	1.0×10^{-3}	5.63×10^{-4}

† After Gunn and East.[34]

Several important facts are demonstrated by Table 7. The decrease in attenuation with increasing wavelength is clearly shown. The values change by about an order of magnitude for a change of λ from 1 to 3 cm. The data presented here also show that attenuation increases with decreasing temperature. Ice clouds give attenuations

about two orders of magnitude smaller than water clouds of the same water content. The attenuation of microwaves by ice clouds can be neglected for all practical purposes.[16] The comprehensive works of Gunn and East[34] and Battan[15] on attenuation offer excellent sources of detailed information on this subject.

24.14 ATTENUATION BY RAIN

Ryde and Ryde[30] calculated the effects of rain on microwave propagation and showed that absorption and scattering effects of raindrops become more pronounced at the higher microwave frequencies where the wavelength and the raindrop diameters are more nearly comparable. In the 10-cm band and at shorter wavelengths the effects are appreciable, but at wavelengths in excess of 10 cm the effects are greatly decreased.

It is also known that suspended water droplets and rain have an absorption rate in excess of that of the combined oxygen and water-vapor absorption.[20]

In practice it has been convenient to express rain attenuation as a function of the precipitation rate R, which depends on both the liquid-water content and the fall velocity of the drops, the latter in turn depending on the size of the drops.

Laws and Parsons[38] observed the distribution of drop sizes for various rates of fall on a horizontal surface. The higher the rainfall rate, the larger are the drops, and also the greater the range in size of the drops. However, in order to derive the size distributions occurring while the drops are falling in the air, each rainfall rate must be divided by the particular velocity of fall appropriate to the corresponding drop diameter.

Ryde studied the attenuation of microwaves by rain and deduced by using Laws and Parsons' distributions that this attenuation in decibels per kilometer can be approximated by

Fig. 12 Theoretical rain attenuation vs. rainfall rate.

$$K_R = K \int_0^r [R(r)]^\alpha \, dr \tag{29}$$

where K_R = total attenuation, db

K = function of frequency[15]

$R(r)$ = rainfall rate along path r

r = length of propagation path, km

α = function of frequency[15]

Medhurst[33] shows that $\alpha = 1$ is probably a sufficiently good assumption based on data taken to date.

The excess path loss per mile, according to Ryde, for the three carrier frequency bands of 4, 6, and 11 GHz is shown in Fig. 12.

The greatest uncertainty in predictions of attenuation because of rainfall, when theoretical formulas are used as a basis for calculation, is the extremely limited knowledge of drop-size distribution in rains of varying rates of fall under differing climatic and weather conditions. There is little evidence that a rain with a known rate of fall has a unique drop-size distribution, although studies on this problem seem to indicate that a certain most probable drop-size distribution can be attached to a rain of given rate of fall.[35] Results of this study are shown in Table 8, which gives the percentage of total volume of rainfall occupied by raindrops of different diameters (centimeters) and varying rainfall rates (millimeters per hour). On the basis of these
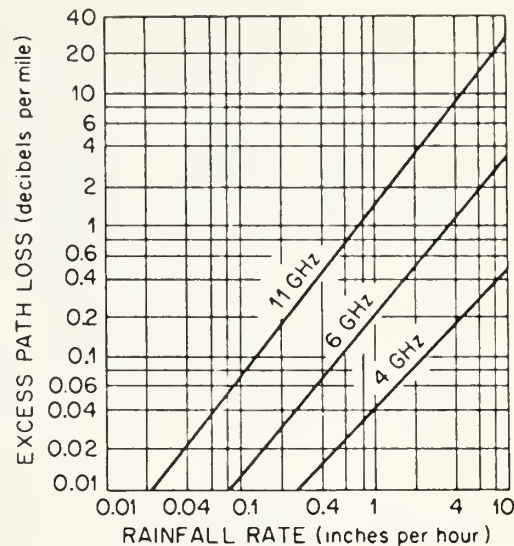
results, the absorption cross section of raindrops of different sizes has been computed for use in Table 9. This table gives the decibel attenuation per kilometer in rains of different rates of fall and radio wavelengths between 0.3 and 10 cm. In Table 10, similar to Table 9, an additional set of results is contained for rains of measured drop-size distribution. All these data refer to raindrops at 18°C.

TABLE 8†   Drop-size Distribution

Drop diameter D, cm	Precipitation rate p, mm/hr							
	0.25	1.25	2.5	12.5	25	50	100	150
	Percentage of a given volume containing drops of diameter D							
0.05	28.0	10.9	7.3	2.6	1.7	1.2	1.0	1.0
0.10	50.1	37.1	27.8	11.5	7.6	5.4	4.6	4.1
0.15	18.2	31.3	32.8	24.5	18.4	12.5	8.8	7.6
0.20	3.0	13.5	19.0	25.4	23.9	19.9	13.9	11.7
0.25	0.7	4.9	7.9	17.3	19.9	20.9	17.1	13.9
0.30	....	1.5	3.3	10.1	12.8	15.6	18.4	17.7
0.35	....	0.6	1.1	4.3	8.2	10.9	15.0	16.1
0.40	....	0.2	0.6	2.3	3.5	6.7	9.0	11.9
0.45	....	....	0.2	1.2	2.1	3.3	5.8	7.7
0.50	....	....	....	0.6	1.1	1.8	3.0	3.6
0.55	....	....	....	0.2	0.5	1.1	1.7	2.2
0.60	....	....	....	....	0.2	0.5	1.0	1.2
0.65	....	....	....	....	....	0.2	0.7	1.0
0.70	....	....	....	....	....	....	....	0.3

† From Burrows and Attwood.[39]

TABLE 9†   Attenuation in Decibels per Kilometer for Different Rates of Rain Precipitation at Temperature 18°C

Precipitation rate p, mm/hr	Wavelength λ, cm								
	λ = 0.3	λ = 0.4	λ = 0.5	λ = 0.6	λ = 1.0	λ = 1.25	λ = 3.0	λ = 3.2	λ = 10
0.25	0.305	0.230	0.160	0.106	0.037	0.0215	0.00224	0.0019	0.0000997
1.25	1.15	0.929	0.720	0.549	0.228	0.136	0.0161	0.0117	0.000416
2.5	1.98	1.66	1.34	1.08	0.492	0.298	0.0388	0.0317	0.000785
12.5	6.72	6.04	5.36	4.72	2.73	1.77	0.285	0.238	0.00364
25.0	11.3	10.4	9.49	8.59	5.47	3.72	0.656	0.555	0.00728
50	19.2	17.9	16.6	15.3	10.7	7.67	1.46	1.26	0.0149
100	33.3	31.1	29.0	27.0	20.0	15.3	3.24	2.80	0.0311
150	46.0	43.7	40.5	37.9	28.8	22.8	4.97	4.39	0.0481

† From Burrows and Attwood.[39]

Since the total attenuation cross section[27] depends on the temperature (because of its effects on the dielectric properties of water), it is important to evaluate the attenuation of rains whose drops are at different temperatures from those in the preceding tables. Table 11 contains the necessary data relative to the change of attenuation with temperature and is to be used with Table 9. For example, in Table 9, with a precipitation rate of $p = 0.25$ mm/hr, temperature of 18°C, $\lambda = 1.25$ cm, the attenuation is 0.0215 db/km. With the correction factors obtained from Table 11, for the

same general conditions of precipitation and wavelength, for a temperature reading of 0°C, the attenuation reads 0.02043 db/km; for a value of 30°C an attenuation of 0.019350 db/km is noted; and for a temperature of 40°C the attenuation is 0.01742 db/km.

To determine total attenuation caused by rainfall through a particular storm, something must be known about the nature of the storm itself and, consequently, about

TABLE 10† Attenuation in Rains of Known Drop-size Distribution and Rate of Fall (Decibels per Kilometer)

Precipitation rate p, mm/hr	Wavelength λ, cm											
	1.25		3		5		8		10		15	
2.46	1.93	10^{-1}	4.92	10^{-2}	4.24	10^{-3}	1.23	10^{-3}	7.34	10^{-4}	2.80	10^{-4}
4.0	3.18	10^{-1}	8.63	10^{-2}	7.11	10^{-3}	2.04	10^{-3}	1.19	10^{-3}	4.69	10^{-4}
6.0	6.15	10^{-1}	1.92	10^{-1}	1.25	10^{-2}	3.02	10^{-3}	1.67	10^{-3}	5.84	10^{-4}
15.2	2.12		6.13	10^{-1}	5.91	10^{-2}	1.17	10^{-2}	5.68	10^{-3}	1.69	10^{-3}
18.7	2.37		8.01	10^{-1}	5.13	10^{-2}	1.10	10^{-2}	6.46	10^{-3}	1.85	10^{-3}
22.6	2.40		7.28	10^{-1}	5.29	10^{-2}	1.21	10^{-2}	6.96	10^{-3}	2.27	10^{-3}
34.3	4.51		1.28		1.12	10^{-1}	2.32	10^{-2}	1.17	10^{-2}	3.64	10^{-3}
43.1	6.17		1.64		1.65	10^{-1}	3.33	10^{-2}	1.62	10^{-2}	4.96	10^{-3}

† From Burrows and Attwood.[39]

TABLE 11† Correction Factor (Multiplicative) for Rainfall Attenuation

Precipitation rate p, mm/hr	λ, cm	0°C	10°C	18°C	30°C	40°C
0.25	0.5	0.85	0.95	1.0	1.02	0.99
	1.25	0.95	1.00	1.0	0.90	0.81
	3.2	1.21	1.10	1.0	0.79	0.55
	10.0	2.01	1.40	1.0	0.70	0.59
2.5	0.5	0.87	0.95	1.0	1.03	1.01
	1.25	0.85	0.99	1.0	0.92	0.80
	3.2	0.82	1.01	1.0	0.82	0.64
	10.0	2.02	1.40	1.0	0.70	0.59
12.5	0.5	0.90	0.96	1.0	1.02	1.00
	1.25	0.83	0.96	1.0	0.93	0.81
	3.2	0.64	0.88	1.0	0.90	0.70
	10.0	2.03	1.40	1.0	0.70	0.59
50.0	0.5	0.94	0.98	1.0	1.01	1.00
	1.25	0.84	0.95	1.0	0.95	0.83
	3.2	0.62	0.87	1.0	0.99	0.81
	10.0	2.01	1.40	1.0	0.70	0.58
150	0.5	0.96	0.98	1.0	1.01	1.00
	1.25	0.86	0.96	1.0	0.97	0.87
	3.2	0.66	0.88	1.0	1.03	0.89
	10.0	2.00	1.40	1.0	0.70	0.58

† From Burrows and Attwood.[39]

how its rainfall rates and drop sizes are distributed. Medhurst's[33] data indicate clearly that verification of Eq. (29) has been made only for *surface* paths and *surface* rainfall rates. Another problem is that Eq. (29) implies an instantaneous point rainfall rate. Bussey[40] was among the first to consider the comparison of time- and space-averaged rainfall rates with instantaneous point rates; he found reasonably good comparisons. Hogg[41] considers the problem of point vs. space-averaged rainfall rates

also and finds a close comparison for a 3-km path, thus tending to confirm Bussey's results. How well Eq. (29) applies above the earth's surface is not entirely known. If Eq. (29) is assumed to apply for nonsurface attenuation, it becomes imperative to determine the three-dimensional distribution of rainfall rate R in the particular storm system of interest. A systematic vertical variation of R, decaying with height above a measured surface value, seems to be appropriate in rainfall of a widespread (continuous) nature.[42] Widespread rainfall is usually triggered by a relatively large-scale mechanism, such as a frontal or monsoon situation. A vertical variation of R of the form

$$R = R_0 e^{-ch^2} \tag{30}$$

can be assumed to be appropriate under continuous rainfall conditions.[42,43] In Eq. (30), R_0 is the surface rainfall rate, h is the height above the earth's surface, and c is a constant, equal to about 0.2.
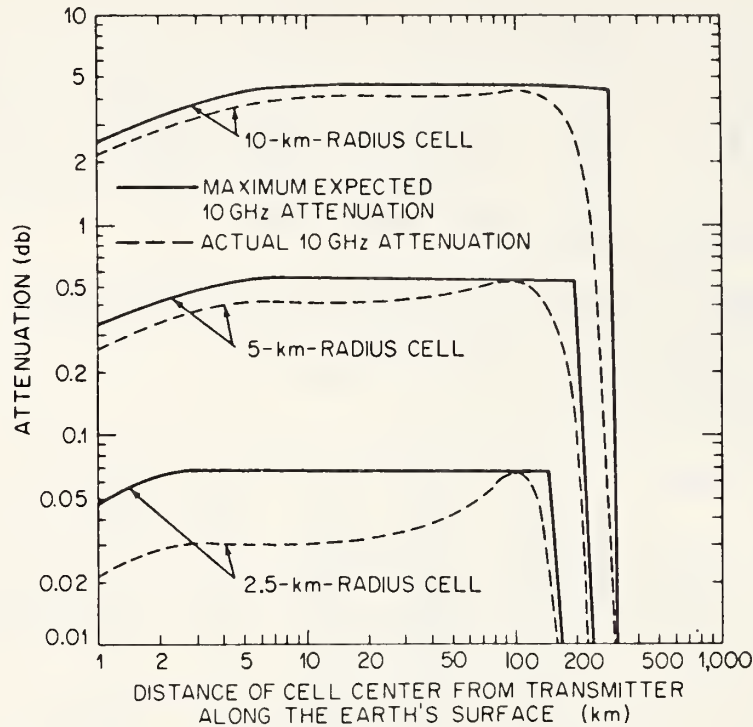

Fig. 13 Distance variation of attenuation caused by a single convective cell on an initially horizontal ray path at 10 GHz.

Convective-type precipitation, however, seems to show a quite different nature. The presence of the *virga* (precipitation aloft) associated with so many shower-type clouds indicates that Eq. (30) is not especially representative of shower rainfall. This is because Eq. (30) implies R decays with height from its surface value (which for the virga case is equal to zero). Dennis[44] has done considerable work in examining rainfall determinations in shower-type activity. His observations show that the reflectivity factor Z (mm^6/m^3) of an element of a vertical slice taken through a spherical shower cell is well represented by a regression line in the form

$$Z = c_1(r_0 - r)^{c_2} \tag{31}$$

In Eq. (31), r is the distance† from the center of the cell of radius r_0, and c_1 and c_2 are positive constants. Earlier observations by Hartel, Clark, and Moyer[45] provide further justification for the use of Eq. (31).

† Not to be confused with the r used previously for droplet radius.

Equation (31) suggests that the reflectivity in a shower cell, for both light showers and heavier thunderstorms, could be approximated by a spherical distribution model. If such a relation is indeed true, it is necessary to know the position of the cell with respect to the transmission path and to determine precipitation rates from Z to calculate total path attenuations. Figure 13 shows a plot of 10 GHz attenuation and its maximum expected value (one of the few special frequencies where both can be obtained) along an initially horizontal radio ray. These values are obtained from Dutton[28] for an individual shower cell (a thunderstorm being composed of one or more such cells) centered 1 km above the earth's surface and placed at several different distances from the transmitter along the earth's surface. The cell's center and the ray path are assumed to be in the same vertical plane. An effective-earth's-radius factor of 4/3 is assumed. Figure 13 shows the attenuation for three cells, each with different radii. One should note two things about this Figure. First, after a traverse of about 300 km, the ray is clear of even the largest storms; second, the large reduction in attenuation as the cell's radius is made smaller is an especially salient feature.
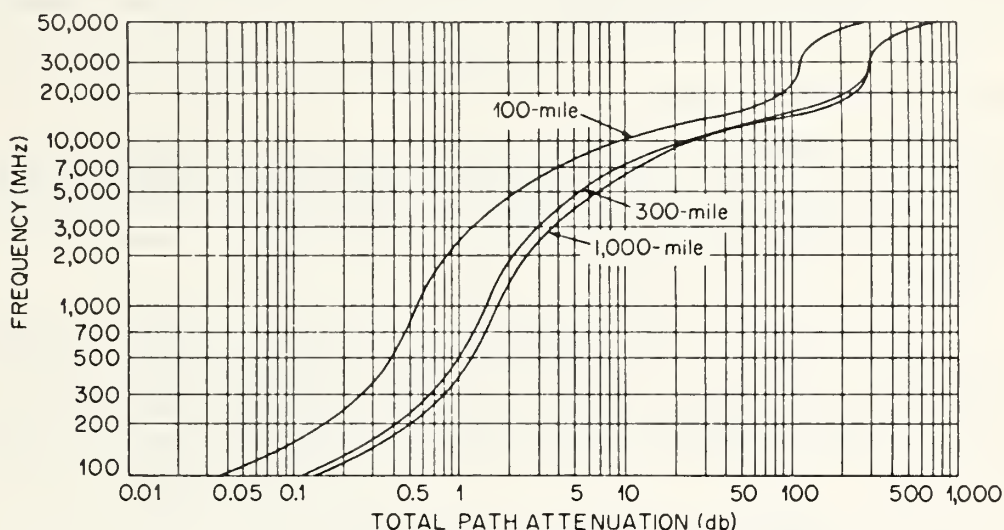

Fig. 14 Combined rain and gaseous absorption to be exceeded 1 percent of the time.

The above paragraphs have been concerned with a descriptive presentation of the theoretical and technical background of the problem of power loss caused by attenuation by rain and atmospheric gases. In an attempt to circumvent the difficulties of the above methods of attenuation prediction, it was considered important to try a climatological approach to this problem. The results of such a study can be disappointing because problems of a systematic climatological estimation of rainfall attenuation are many and varied. Answers are needed for some questions: How often do various rainfall rates and drop sizes occur in geographical areas, and over how large an area do these rates and drop-size statistics apply? Furthermore, to what height in the atmosphere do these data apply? In view of these questions, only engineering estimates of the combined gaseous and rain absorption are provided.

In this regard, Bussey[40] has shown that the absorption due to rainfall exceeds that of gaseous constituents about 5 percent of the time for frequencies around 6 GHz. The 5 percent figure was obtained by a study of the rainfall-rate distribution for various locations in the United States. Figure 14 shows the combined rain and gaseous absorption to be exceeded 1 percent of the time.

24.15 ATTENUATION BY HAIL

Ryde concluded that the attenuation caused by hail is one-hundredth that caused by rain, that ice-crystal clouds cause no sensible attenuations, and that snow produces

very small attenuation even at the excessive rate of fall of 5 in. an hour. However, the scattering by spheres surrounded by a concentric film of different dielectric constant does not give the same effect that Ryde's results for dry particles would indicate.[46,47] For example, when one-tenth of the radius of an ice sphere of radius 0.2 cm melts, the scattering of 10-cm radiation is approximately 90 percent of the value that would be scattered by an all-water drop.

At wavelengths of 1 and 3 cm with $\gamma = 0.126$ ($\gamma = 2a/\lambda$; a = radius of drop) Kerker, Langleben, and Gunn[47] found that particles attained total attenuation cross sections corresponding to all-melted particles when less than 10 percent of the ice particles were melted. When the melted mass reached about 10 to 20 percent, the attenuation was about twice that of a completely melted particle. These calculations show that the attenuation in the melting of ice immediately under the 0°C[48] isotherm can be substantially larger than in the snow region just above and, under some circumstances, greater than in the rain below the melting level. Further melting cannot lead to much further enhancement, apparently, and may lead to a lessening of the reflectivity of the particle by bringing it to sphericity or by breaking up the particle. This effect, combined with the fact that hail has greater terminal velocities than rain, gives rise to the so-called "bright band" near the 0° isotherm.

24.16 ATTENUATION BY FOG

The characteristic feature of a fog is the reduction in visibility. Visibility is defined as the greatest distance in a given direction at which it is just possible to see and identify with the unaided eye (1) in the daytime, a prominent dark object against the sky at the horizon and (2) at night, a known, preferably unfocused moderately intense light source.[49]

Although the visibility depends upon both drop size and number of drops and not entirely upon the liquid-water content, yet, in practice, the visibility is an approximation of the liquid-water content and therefore may be used to estimate radio-wave attenuation.[48] On the basis of Ryde's work, Saxton and Hopkins[50] give the figures in Table 12 for the attenuation in a fog or clouds at 0°C temperature. The attenuation varies with the temperature because the dielectric constant of water varies with temperature; therefore, at 15 and 25°C the figure in Table 12 should be multiplied by

TABLE 12† Attenuation Caused by Clouds or Fog
Temperature = 0°C

Visibility, m	Attenuation, db/km		
	$\lambda = 1.25$ cm	$\lambda = 3.2$ cm	$\lambda = 10$ cm
30	1.25	0.20	0.02
90	0.25	0.04	0.004
300	0.045	0.007	0.001

† From Saxton and Hopkins.[50]

0.6 and 0.4, respectively. It is immediately noted that cloud or fog attenuation is an order of magnitude greater at 3.2 cm than at 10 cm. Nearly another order of magnitude increase occurs between 3.2 cm and 1.25 cm.

24.17 METEOROLOGICAL RADAR ECHOES

Atlas[51] cites the birth of radar meteorology as a science as occurring on Feb. 20, 1941, when a rain shower was tracked a distance of 7 miles by a 10-cm radar located on the English coast. Since the early 1940s a great deal of study and effort has been applied

to the field of radar meteorology. The history of radar meteorology can be roughly divided into two periods. The first period, extending from the mid-1940s to the late 1950s, was primarily a descriptive period in which meteorological echoes were observed, classified, and related to synoptic weather conditions. Since 1960, the scientific effort has shifted to a phase of quantitative interpretation of radar echoes to relate such parameters as rainfall rate and drop-size distribution, particulate velocities to turbulence intensities, etc.

Much controversy exists over the accuracy of quantitative radar measurements of meteorological echo intensities. Most of this controversy is a result of the basic fact that the laboratory for radar meteorology studies lies in the troposphere and "laboratory conditions" are beyond scientific control.

The brief remarks above are intended to caution the prospective user of the information contained in this chapter. Accurate meteorological radar measurements are extremely difficult to obtain. If meteorological radar measurements are contemplated where the accuracy demands an error no greater than ± 3 db, the experimentalist is advised to review the results of the latest available radar meteorology experiments.

24.18 RADAR EQUATION FOR PARTICULATE SCATTERING

The most fundamental form of the radar equation describing the echo from incoherent scatterers distributed over a large volume is[52]

$$\bar{P}_r(d) = \frac{e^{-2\alpha}G_0{}^2\lambda^2}{(4\pi)^3} \int_0^\infty \frac{P_t(d - 2R/c)}{R^2} dR \int_{4\pi} f^4(\theta,\phi) \, d\Omega \int_0^\infty n(\sigma)\sigma \, d\sigma \qquad (32)$$

where d = radar delay time

$\bar{P}_r$ = time average of many return echoes

P_t = peak transmitted power

λ = radar wavelength

R = range corresponding to delay time d

c = velocity of propagation

σ = radar cross section

The antenna gain G_0 is the gain along the beam axis with $f^2(\theta,\phi) \leq 1$ describing the angular pattern of antenna gain. The density function $n(\sigma) \, d\sigma$ gives the number of scatterers per unit volume with cross sections between σ and $\sigma + d\sigma$. The parameter $e^{-2\alpha}$ is used to denote the two-way attenuation with

$$\alpha = \int_0^R (\gamma_g + \gamma_c + \gamma_p) \, dR$$

where the subscripts g, c, and p represent the one-way attenuation by gases, clouds, and precipitation, respectively.

Equation (32) indicates some of the difficulties encountered in making precision precipitation-backscatter measurements. At first inspection the three integrals appear to be independent; however, a close examination of the problem will disclose the scattering integral is also a function of the range R and solid angle Ω. If the mean scattering cross section does not change significantly in a distance equivalent to one-half the radar pulse length, the scattering integral may be assumed to be independent of range. Also, for narrow-beam antennas, the scattering cross section per unit volume is usually assumed to fill the beam.

The transmitted pulse is usually approximated by a rectangular pulse resulting in a value of $P_t\tau c/2$ for the first integral, with τ representing the half-power duration of the transmitted pulse. The integral of the antenna pattern is usually approximated by $\pi\theta_0\phi_0/4$, where θ_0 and ϕ_0 now represent the half-power beamwidth of the antenna. The last integral yields the value $N\bar{\sigma}$, where $\bar{\sigma}$ is the average scattering cross section and N is the number of scatterers per unit volume. The product $N\bar{\sigma}$ is often defined as the reflectivity η.

By combining the approximations discussed above, Eq. (32) may be written

$$\bar{P}_r = \frac{e^{-2a}P_tG^2\lambda^2\theta_0\phi_0c\tau\eta}{512\pi^2R^2} \tag{33}$$

In many radar-rainfall experiments the attenuation for $\lambda \geq 3$ cm may be set equal to zero in all but the heaviest rainfall. This is a result of conducting rainfall measurements at relatively short radar ranges over a fixed surface rain-gage network, which is usually of somewhat limited extent. Operational rainfall measurements may require several decibels of correction for attenuation through an extended range of rainfall echoes. Equation (33) may be further simplified with the relations $G \approx 4\pi/\theta_0\phi_0$ and $G = 4\pi A_e/\lambda^2$. Thus the most frequently found radar equation for volume particulate scatter is

$$\bar{P}_r = \frac{P_tA_ec\tau\eta}{32R^2} \tag{34}$$

The meteorological equation for radar echoes was rederived by Probert-Jones.[53] Particular attention was given to the relationships of antenna gain, effective area, and beamwidths. It was shown that radar equations using the half-power beamwidths as volume scatter boundaries overestimate the received power by a factor of $2 \ln 2$, and the gain is overestimated by a factor of $16/\pi^2$. Although the arguments of Probert-Jones appear to be built upon a solid foundation, papers published in the Proceedings of the Twelfth Conference on Radar Meteorology[54] give little consideration to these antenna correction factors. There are additional factors involved (e.g., in rainfall measurements) which tend to obscure the correction factors derived by Probert-Jones.

A single spherical particle of radius a_i has a backscattering cross section

$$\sigma_i = 64\,\frac{\pi^5}{\lambda^4}\,|K|^2a_i^6 \tag{35}$$

where $|K|^2 = |(\epsilon_c - 1)/(\epsilon_c + 1)|^2$

ϵ_c = complex dielectric constant of spheroid

The value of $|K|^2$ for water is 0.9313 at a temperature of 10°C and a wavelength of 10 cm. For ice, $|K|^2 = 0.197$ for all temperatures and centimeter wavelengths.[15,34] Equation (35) may be applied to spheroids whose circumference is small compared with a wavelength, that is, $2\pi a_i \ll \lambda$.

With the relationships $\eta = N\bar{\sigma} = \sum_i \sigma_i$, Eq. (34) becomes

$$\bar{P}_r = \frac{2\pi^5P_tA_ec\tau|K|^2Z}{\lambda^4R^2}\sum_i a_i^6 \tag{36}$$

Equation (36) is the basic form of the radar equation describing the power received from hydrometeors. There are several variations of this equation, one of the most common being obtained by replacing A_e with $2A_p/3$, where A_p is the physical area of the antenna.[15] If the definition of Eq. (28) is used for the reflectivity factor Z, Eq. (36) becomes

$$\bar{P}_r = \frac{\pi^5P_tA_ec\tau|K|^2Z}{32\lambda^4R^2} \tag{37}$$

With the exception of Z and R, the remainder of the parameters are determined by the radar system. Once these parameters are known, they are usually combined to yield a constant C and

$$\bar{P}_r = \frac{CZ}{R^2} \tag{38}$$

Equation (38) is the operational form of the radar equation for volume scatter echoes.

24.19 CLOUD AND FOG DETECTION

Radar has been shown to be a useful tool in the study of cloud physics.[15] As most cloud droplets are about 100 microns or less in diameter, Rayleigh scatter theory is applicable and the results of the preceding section may be fully utilized. However, before a quantitative number is obtained for the liquid-water content of clouds, some relationship must be established between the reflectivity factor Z and the liquid-water content M. Battan[15] quotes a Z-M relationship of

$$Z = 4.8 \times 10^{-8} M^{2.0}$$

where Z has dimensions of millimeters to the sixth power per cubic meter and those of M are milligrams per cubic meter.

The relationship above was obtained by empirical studies. It has been established that the backscatter from clouds and fog is some 8 db lower than that expected from the conventional $Z = \Sigma M_i D_i^6$ relationship. Naito and Atlas[55] and Raemer[56] theorize on the reasons for the discrepancy. They conclude that multiple-wavelength studies of cloud echoes are desirable for determining a $\bar{P}_r$-versus-λ relationship. Preliminary results[56] indicate the wavelength dependence of cloud echoes is of the order of $\lambda^{-0.3}$ to $\lambda^{-1.2}$. This would be in large contrast to the λ^{-4} relationship predicted by Rayleigh scatter theory. It is worthy of note that prima facie evidence indicates most clouds detectable by conventional weather radars probably contain precipitable particles that are large ice crystals.[55]

24.20 RAINFALL DETECTION

Radar's ability to detect rainfall has proved extremely valuable to the field of meteorology and, in particular, real-time storm observation. All intense storm systems eventually develop large condensation particles which are easily detected with 10-cm radars. Observation of such storms over a period of a few hours allows the trained observer to make reasonably reliable predictions of the future position and intensity of the storm.

Quantitative measurements of the rainfall reflectivity factor may be obtained over extremely large areas. The rainfall rate r is empirically related to the reflectivity factor Z by

$$Z = ar^b$$

The literature[15,51] generally lists a large number of values for the constants a and b. The constants appear to be a function of the type of storm and the duration of observation. The constants that are considered to be most representative of rainfall rates yield

$$Z = 200r^{1.6} \tag{39}$$

Atlas[51] discusses a 24-hr observation of rainfall from which the average radar rainfall calculated from Eq. (39) was low by less than 2 percent. He attributes this accuracy to the space and time fluctuations of the drop-size distribution which were thoroughly averaged out over the 24-hr observation period.

Shorter observations tend to show more variability in the constants a and b. A good portion of this variability is probably caused by the wind field within the storm system. As the radar antenna is pointed to an elevation that minimizes ground clutter, the radar examines the elevated portion of the storm, and the radar rainfall may be in considerable disagreement with the rainfall collected by a surface rain-gage network.

The Rayleigh scatter theory applies to the heaviest rainfalls at 10- and 5-cm wavelengths. At 3-cm wavelength the transition from Rayleigh to Mie scatter begins to take place, and rainfall data should be corrected accordingly.[15]

24.21 DETECTION OF HAIL

Radars are able to discriminate precipitation regions containing hail from regions containing liquid water. The equivalent reflectivity factor for hail appears to have a 10-cm threshold value[51] of $Z_e = 3 \times 10^5$. This is equivalent to a thunderstorm rainfall rate of 120 mm/hr.

Quantitative radar measurements of hailstorms are difficult to obtain because of the nature of the process: dry particles, water-coated particles, and melted particles. In addition, the shape of hailstones is known to be very irregular.

24.22 DETECTION OF SNOW

Radar backscatter from snow is less intense than backscatter from water for two reasons: (1) The value of $|K|^2$ for ice is 0.197, and (2) snowfall rates are generally less than rainfall rates. A satisfactory Z-r relationship for snow has been determined from empirical studies as

$$Z = 1{,}000r^{1.6}$$

where r is in millimeters per hour of water measured when the snow is melted.[57] Five of nine snowstorms were major storms with rates ranging from 4 to 30 mm/hr. Three of the storms were light snowfall (0.5 to 4 mm/hr), and the radar precipitation rates were underestimated.

TABLE 13 Characteristics of Angel Echoes

Type of echo	Characteristics	Most probable cause
Tropospheric layers.......	Continuous or semicontinuous echoes over long periods of time (hr).	Definitely associated with meteorological conditions: subsidence and radiation inversions, weather fronts.
Wind-carried scatterers...	Short-duration coherent echoes (sec).	Particulate matter, most probably insects or possibly birds.
Associated with clouds....	1. Large, wind-carried echo at boundary of cloud structure. 2. Precursor lines.	1. Refractive-index inhomogeneities in boundary region. 2. Either gravity waves† or from the region of intersection of cold and warm fronts.
Wind-independent scatterers	Small echoes possibly appearing in a swarm; velocities less than 50 knots; semiregular movements; PPI tracks are smooth gentle curves.	Particulate matter, most probably birds and insects; also convective bubbles scattering energy forward to ground which is then backscattered to radar by the reciprocal path.
Ring angels.............	Rings or expanding rings on PPI display; possibly periodic in appearance.	Point-source gravity wave; warm dry air over cool moist air; cross section of rising thermals; birds leaving roosting area.
Lightning echoes and spherics	PPI display shows lightning; spherics are spikes unsynchronized with radar.	Lightning discharge and ionization of path; spherics are probably RF energy radiated by lightning discharge.

† Gravity waves are wave disturbances in which buoyancy acts as the restoring force on atmospheric parcels displaced from hydrostatic equilibrium.

24.23 ANGEL ECHOES

The class of "meteorological" radar echoes that are described as angel echoes has puzzled researchers for a number of years. The frequency of observation of angel echoes has increased with the expanded operational use of radar, better receivers, larger antennas, and higher-powered transmitters. Some of the echoes are readily associated with meteorological conditions, birds, or insects. Other angel echoes have been more difficult to explain.

Some of the confusion of interpreting angel echoes may have been brought on by the variety of radar displays used to acquire data. Four basic types of radar displays have been used to obtain angel echoes: PPI, RHI (range-height-indicator),
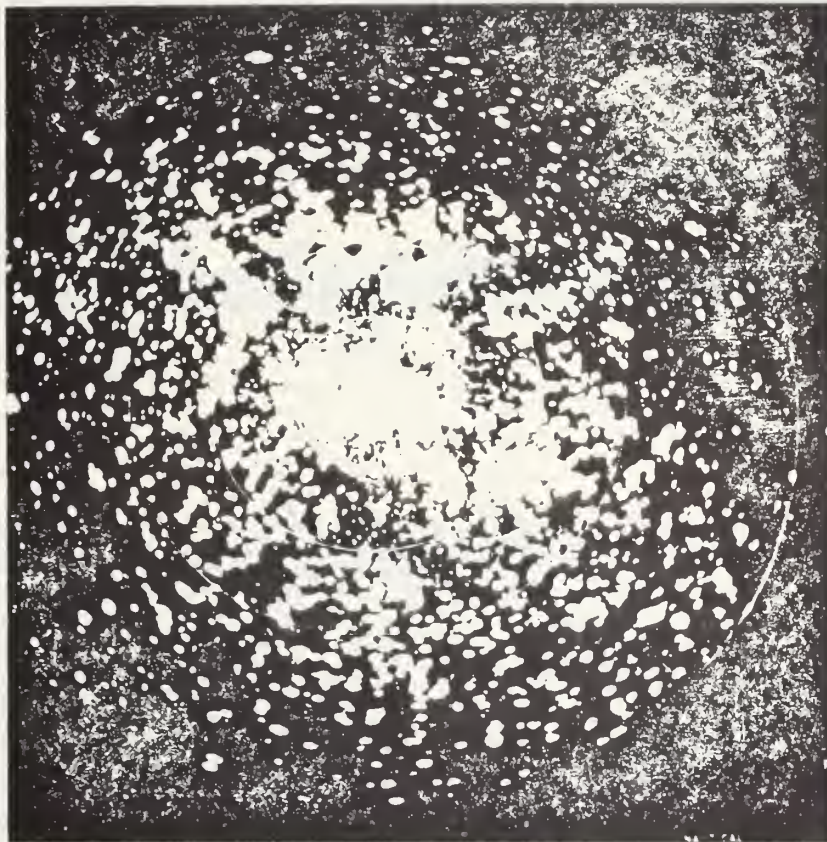

Fig. 15 MTI (moving target indication) video PPI display of echoes received from birds near Oklahoma City with the *L*-band ARSR-1A. The display radius is 25 nmi. (*Courtesy of W. W. Shrader, Raytheon Co.*)

A-scope, and height-time. The height-time display is frequently used with a stationary vertically pointing antenna. The oscilloscope coordinate system displays radar height as a vertical deflection, real time as a horizontal deflection, and echoes as intensity modulation. The radar system incorporating both PPI and RHI displays is the exception rather than the rule. Thus, for example, the appearance of a given type of echo on a PPI display might be very different from the same type of echo on a height-time display where the spatial resolution is considerably better.

The various angel echoes can be roughly characterized as shown in Table 13. An excellent discussion of angel echoes, their probable causes, and typical photographs of the radar display are given by Plank.[58]

When the vast amount of angel-echo material has been examined, it is apparent this type of echo most severely affects the performance of surveillance radars with PPI

displays. In contrast, the PPI and RHI displays are probably the best type of displays for presenting angel echoes, and the tracking radar with a range gate is best for obtaining quantitative measurements of angel echoes.[59,60] PPI photographs of bird and insect echoes are shown in Figs. 15 and 16. RHI and PPI photographs of echoes from atmospheric boundaries are shown in Figs. 17 and 18.

Of interest to the radar designer are typical values of reflectivity and scattering cross sections of angel echoes. The comparison of the two types of echoes from volume and point sources is difficult; however, some reasonably comparative data have been given by Hardy, Atlas, and Glover.[61] At a wavelength of 10 cm the volume reflectivity of the atmosphere is of the order of 10^{-15} cm^{-1}, and the equivalent volume

Fig. 16 MTI video PPI display of echoes received from insects near Oklahoma City with the *L*-band ARSR-1A. The display radius is 25 nmi. The shadow line at 7 o'clock on the display is cast by a nearby water tower. (*Courtesy of W. W. Shrader, Raytheon Co.*)

reflectivity of several discrete targets is of the order of 5×10^{-14} cm^{-1}. At a wavelength of 50 cm the volume reflectivity of the two types of targets is comparable and of the order of 5×10^{-16} cm^{-1}. Note the small amount of wavelength dependence for atmospheric reflectivity; in contrast, the volume reflectivity of discrete targets is of the order of λ^{-4} (Rayleigh scatterers).

The data of Hardy et al.[61] indicate that extremely sensitive radars are required to observe atmospheric echoes at moderate ranges of 20 to 40 km. Thus echoes from atmospheric boundaries are not an extreme problem in the design of many radar systems. However, echoes from birds and insects are readily detected at wavelengths of 20 cm or less and can pose a problem in the optimum operation of a surveillance radar. These echoes may be reduced by utilizing moving-target-indication and sensitivity-time-control techniques.
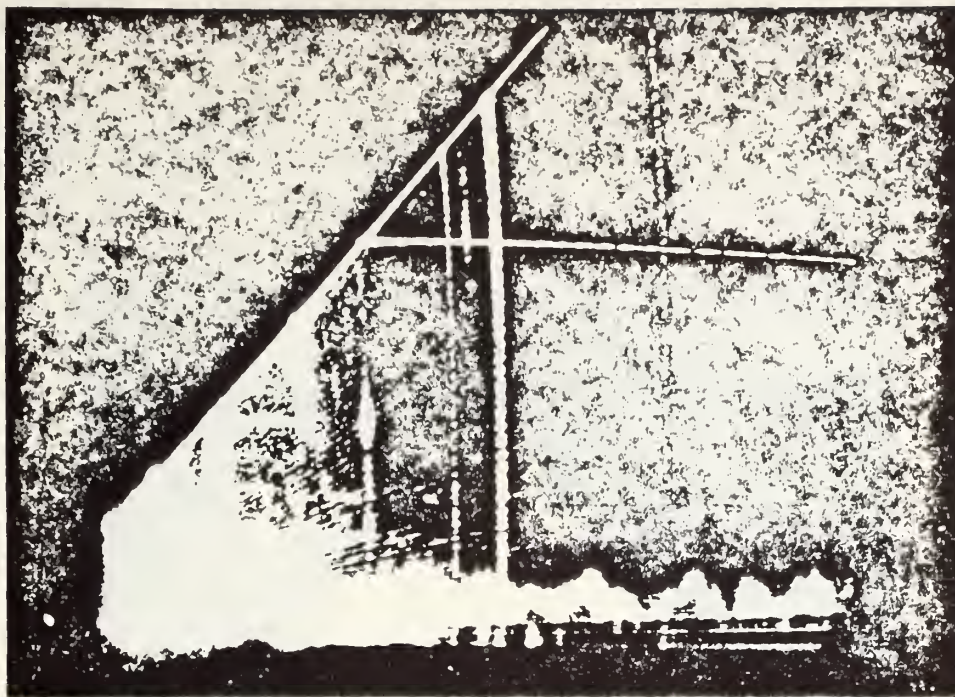
Fig. 17   RHI display at 10.7-cm wavelength, azimuth 0°, afternoon of May 13, 1966, Wallops Island, Va.   The range marks are at 5-nmi intervals, and the height mark appears at 20,000 ft.   A test signal appears at 11 nmi.   The wavelike perturbations in the lower 3,000 ft are the boundaries of convective cells seen in Fig. 18.   (*Courtesy of K. R. Hardy, Air Force Cambridge Research Laboratory.*)

Fig. 18   Sector PPI display at 2° elevation angle which cuts through the convective cells seen in Fig. 17.   The range marks are at 10-nmi intervals, and the azimuth limits are from 334 to 60°.   (*Courtesy of K. R. Hardy, Air Force Cambridge Research Laboratory.*)

24.24 WEATHER AND RADAR DESIGN CONSIDERATIONS

Consideration of weather effects on the performance of a radar system should be one of the primary studies for any newly proposed radar system.   As an example, precision tracking radars that are expected to track targets at long ranges and elevation angles below 5° are seriously affected by refraction.   There may be a requirement for an absolute maximum tracking error which would drastically increase the cost of the antenna and tracking servomechanism.   In addition, refraction effects may cause an absolute tracking error greater than the specified maximum error.   Some of the refraction effects possibly could be removed by a computer at an additional cost.

Fig. 19 PPI display of a large storm system detected by the *L*-band ARSR-1A radar near Washington, D.C., using linear polarization.   Display radius is 40 nmi.   (*Courtesy of W. W. Shrader, Raytheon Co.*)

Thus the specified maximum tracking error must be weighed against the cost of achieving the specification.   The reason for specifying the maximum tolerable tracking error must also be considered; a human-life factor may prevent relaxing the tracking-error specification.

Major storm systems may seriously impair the optimum performance expected from an aircraft-surveillance radar.   The backscatter from precipitable particles saturates larger areas of a PPI display and completely obscures aircraft echoes. This is graphically illustrated by Fig. 19.   The precipitation clutter may be reduced by transmission and reception of circularly polarized waves, as shown by Fig. 20.

Theory shows that the backscattering cross section of a smooth target is zero for circularly polarized radiation.[67] In practice, meteorological echoes show a cancellation ratio of the order of 15 db for wet snowflakes and 30 db for dense rainfall. A representative figure for improvement of the target signal to precipitation signal is then about 15 to 20 db.[52]

The considerations that dictate specifications for a new radar system are far too numerous and varied to be discussed here. The examples discussed above are intended to point out how weather considerations may play an important part in radar design. In contrast, weather effects may be of secondary importance in the
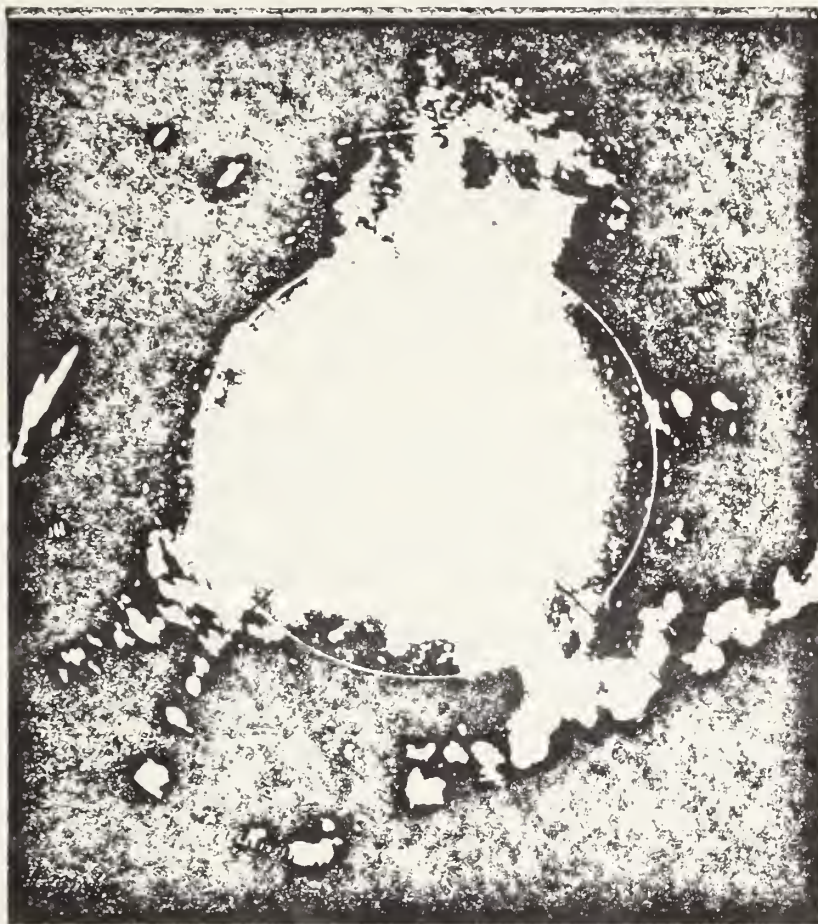

Fig. 20 PPI display of the same storm as in Fig. 19 detected with circular polarization. Note that, although the storm is considerably reduced, the echoes from the mountains at 9 o'clock are essentially unaffected by the circular polarization. A few aircraft can be seen on the display as three consecutive returns, because the camera shutter was left open for three antenna revolutions. (*Courtesy of W. W. Shrader, Raytheon Co.*)

design of a UHF radar system. Each radar system is generally designed to optimize the realization of a specific set of measurements or observations. Once this design criterion has been achieved, it is difficult to utilize the radar system for other purposes without extensive modification.

REFERENCES

1. Debye, P.: "Polar Molecules," pp. 89–90, Dover Publications, Inc., New York, 1957.
2. Smith, E. K., and S. Weintraub: The Constants in the Equation for Atmospheric Refractive Index at Radio Frequencies, *Proc. IRE*, vol. 41, pp. 1035–1037, August, 1953.

3. Boudouris, G.: On the Index of Refraction of Air, the Absorption and Dispersion of Centimeter Waves by Gases, *J. Res. Natl. Bur. Std.*, vol. 67D (Radio Propagation), no. 6, pp. 631–684, 1963.

4. Straiton, A. W.: Measurement of the Radio Refractive Index of Air, in J. A. Saxton (ed.), "Advances in Radio Research," pp. 1–52, Academic Press Inc., New York, 1964.

5. Bean, B. R., and E. J. Dutton: Radio Meteorology, *Natl. Bur. Std. (U.S.), Monograph* 92, 1966.

6. Smart, W. M.: "Spherical Astronomy," chap. 3, Cambridge University Press, New York, 1931.

7. Bean, B. R., and G. D. Thayer: On Models of the Atmospheric Refractive Index, *Proc. IRE*, vol. 47, pp. 740–755, May, 1959.

8. Booker, H. G., and W. Walkinshaw: The Mode Theory of Tropospheric Refraction and Its Relation to Wave Guides and Diffraction, "Meteorological Factors in Radiowave Propagation," pp. 80–127, The Physical Society, London, 1947.

9. Freehafer, John E.: Tropospheric Refraction, in D. E. Kerr (ed.), "Propagation of Short Radio Waves," MIT Radiation Laboratory Series, vol. 13, pp. 9–22, McGraw-Hill Book Company, New York, 1951.

10. Schelleng, J. C., C. R. Burrows, and E. B. Ferrell: Ultra-short-wave Propagation, *Proc. IRE*, vol. 21, pp. 427–463, March, 1933.

11. Bean, B. R., B. A. Cahoon, C. A. Samson, and G. D. Thayer: A World Atlas of Atmospheric Radio Refractivity, *ESSA Monograph* 1, 1966.

12. Stickland, A. C.: Refraction in the Lower Atmosphere and Its Application to the Propagation of Radio Waves, "Meteorological Factors in Radio-wave Propagation," pp. 253–267, The Physical Society, London, 1947.

13. Humphreys, W. J.: "Physics of the Air," p. 82, McGraw-Hill Book Company, New York, 1940.

14. Norton, K. A., P. L. Rice, and L. E. Vogler: Use of Angular Distance in Estimating Transmission Loss and Fading Range for Propagation Through a Turbulent Atmosphere over Irregular Terrain, *Proc. IRE*, vol. 43, pp. 1488–1526, October, 1955.

15. Battan, L. J.: "Radar Meteorology," The University of Chicago Press, Chicago, 1959.

16. Harrold, T. W.: Estimation of Rainfall Using Radar—a Critical Review, *Meteorol. Off. Sci. Paper* 21, H. M. Stationery Office, London, 1965.

17. Van Vleck, J. H.: The Absorption of Microwaves by Oxygen, *Phys. Rev.*, vol. 71, pp. 413–424, April, 1947.

18. Van Vleck, J. H.: The Absorption of Microwaves by Uncondensed Water Vapor, *Phys. Rev.*, vol. 71, pp. 425–433, April, 1947.

19. Van Vleck, J. H.: Theory of Absorption by Uncondensed Gases, in D. E. Kerr (ed.), "Propagation of Short Radio Waves," MIT Radiation Laboratory Series, vol. 13, pp. 646–664, McGraw-Hill Book Company, New York, 1951.

20. Bean, B. R., and R. Abbott: Oxygen and Water Vapor Absorption of Radio Waves in the Atmosphere, *Geofis. Pura Appl.*, vol. 37, pp. 127–144, May–August, 1957.

21. Becker, G. B., and S. H. Autler: Water Vapor Absorption of Electromagnetic Radiation in the Centimeter Wavelength Range, *Phys. Rev.*, vol. 70, pp. 300–307, Sept. 1 and 15, 1946.

22. Birnbaum, G., and A. A. Maryott: Microwave Absorption in Compressed Oxygen, *Phys. Rev.*, vol. 99, p. 1886, Sept. 15, 1955.

23. Artman, J. O., and J. P. Gordon: Absorption of Microwaves by Oxygen in the Millimeter Wavelength Region, *Phys. Rev.*, vol. 96, pp. 1237–1245, December, 1954.

24. Ratner, B.: Upper Air Average Values of Temperature, Pressure, and Relative Humidity Over the United States and Alaska, U.S. Weather Bureau, 1945.

25. Zhevankin, S. A., and V. S. Troitskii: Absorption of Centimetre Waves in the Atmosphere, *Radiotekh. i Elektron.*, vol. 4, pp. 21–27, 1959.

26. Dutton, E. J., and B. R. Bean: The Biexponential Nature of Tropospheric Gaseous Absorption of Radio Waves, *Radio Sci., J. Res. Natl. Bur. Std.*, vol. 69D, pp. 885–892, June, 1965.

27. Mie, G.: Beitrage zur Optik trüber Medien, speziell Kolloidaler Metaläsungen, *Ann. Physik*, vol. 25, p. 377, 1908.

28. Dutton, E. J.: Estimation of Radio Ray Attenuation in Convective Rainfalls, *J. Appl. Meteorol.*, vol. 6, pp. 662–668, 1967.

29. Saxton, J. A., and J. A. Lane: The Anomalous Dispersion of Water at Very High Radio Frequencies. 1: Experimental Determinations of the Dielectric Properties of Water in the Temperature Range 0°C to 40°C for Wavelengths of 1.24 cm and 1.58 cm, "Meteorological Factors in Radio Wave Propagation," pp. 278–292, The Physical Society and Royal Meteorological Society, London, 1946.

30. Ryde, J. W., and D. Ryde: Attenuation of Centimeter Waves by Rain, Hail, Fog, and Clouds, General Electric Co., Wembly, England, 1945.

31. Stratton, J. A.: The Effect of Rain and Fog on the Propagation of Very Short Radio Waves, *Proc. IRE*, vol. 18, pp. 1064–1074, June, 1930.

32. Goldstein, H.: Attenuation by Condensed Water, in D. E. Kerr (ed.), "Propagation of Short Radio Waves," MIT Radiation Laboratory Series, vol. 13, pp. 671–692, McGraw-Hill Book Company, New York, 1951.

33. Medhurst, R. G.: Rainfall Attenuation of Centimeter Waves: Comparison of Theory and Measurement, *IEEE Trans.*, vol. AP-13, pp. 550–564, July, 1965.

34. Gunn, K. L. S., and T. W. R. East: The Microwave Properties of Precipitation Particles, *Quart. J. Roy. Meteorol. Soc.*, vol. 80, pp. 522–545, October–December, 1954.

35. Goldstein, L.: Absorption and Scattering of Microwaves by the Atmosphere, *Columbia Univ., Div. War Res., Wave Prop. Group, Rept.* WOG-11, 1945.

36. Donaldson, Ralph J., Jr.: The Measurement of Cloud Liquid-water Content by Radar, *J. Meteorol.*, vol. 12, pp. 238–244, June, 1955.

37. Weickmann, H. K., and H. J. aufm Kampe: Physical Properties of Cumulus Clouds, *J. Meteorol.*, vol. 10, pp. 204–221, June, 1953.

38. Laws, J. O., and D. A. Parsons: The Relationship of Raindrop Size to Intensity, *Trans. Am. Geophys. Union*, 24th Annual Meeting, pp. 452–460, April, 1943.

39. Burrows, C. R., and S. S. Attwood: "Radio Wave Propagation, Consolidated Summary Technical Report of the Committee on Propagation, NDRC," p. 219, Academic Press Inc., New York, 1949.

40. Bussey, H. E.: Microwave Attenuation Statistics Estimated from Rainfall and Water Vapor, *Proc. IRE*, vol. 38, p. 781, August, 1950.

41. Hogg, D. C.: Path Diversity in Propagation of Millimeter Waves Through Rain, *IEEE Trans.*, vol. AP-15, pp. 410–415, May, 1967.

42. Atlas, D., and E. Kessler III: A Model Atmosphere for Widespread Precipitation, *Aeron. Eng. Rev.*, vol. 16, pp. 69–75, February, 1957.

43. Rice, P. L., A. G. Longley, K. A. Norton, and A. P. Barsis: Transmission Loss Predictions for Tropospheric Communication Circuits, *Natl. Bur. Std. (U.S.) Tech. Note* 101, vol. I, 1965.

44. Dennis, A. S.: Rainfall Determinations by Meteorological Satellite Radar, *Stanford Res. Inst., SRI Rept.* 4080, 1963.

45. Hartel, H. W., R. A. Clark, and V. E. Moyer: Investigation of Space and Time Variations of Convective Precipitation as Revealed by Radar Reflectivity Measurements, *Proc. Ninth Weather Radar Conf.*, pp. 83–89, 1961.

46. Ryde, J. W.: The Attenuation and Radar Echoes Produced at Centimetre Wavelengths by Various Meteorological Phenomena, "Meteorological Factors in Radio Wave Propagation," pp. 169–188, The Physical Society, London, 1946.

47. Kerker, M., M. P. Langleben, and K. L. S. Gunn: Scattering of Microwaves by a Melting Spherical Ice Particle, *J. Meteorol.*, vol. 8, p. 424, December, 1951.

48. Best, A. C.: "Physics in Meteorology," Sir Isaac Pitman & Sons, Ltd., London, 1957.

49. "Glossary of Meteorology," vol. 3, p. 613, American Meteorological Society, Boston, 1959.

50. Saxton, J. A., and H. G. Hopkins: Some Adverse Influences of Meteorological Factors on Marine Navigational Radar, *Proc. IEE (London)*, vol. 98, pt. III, p. 26, January–February, 1951.

51. Atlas, D.: Advances in Radar Meteorology, in H. E. Landsberg and J. Van Mieghem (eds.), "Advances in Geophysics," vol. 10, pp. 318–468, Academic Press Inc., New York, 1964.

52. Kerr, D. E.: Application of the Lorentz Reciprocity Theorem to Scattering, in D. E. Kerr (ed.), "Propagation of Short Radio Waves," MIT Radiation Laboratory Series, vol. 13, p. 693, McGraw-Hill Book Company, New York, 1951.

53. Probert-Jones, J. R.: The Radar Equation in Meteorology, *Quart. J. Roy. Meteorol. Soc.*, vol. 88, pp. 485–495, 1962.

54. Proceedings of Twelfth Conference on Radar Meteorology, Norman, Oklahoma, Oct. 17–20, 1966, American Meteorological Society, Boston.

55. Naito, K., and D. Atlas: On Microwave Scatter by Partially Coherent Clouds, *Proc. 12th Conf. Radar Meteorol.*, pp. 7–12, 1966.

56. Raemer, H. R.: Some Observations Pertinent to the Theory of Radar Scattering by Clouds, *Proc. 12th Conf. Radar Meteorol.*, pp. 13–16, 1966.

57. Austin, P. M.: Radar Measurements of the Distribution of Precipitation in New England Storms, *Proc. 10th Weather Radar Conf.*, pp. 247–254, 1963.

58. Plank, V. G.: Radar Echoes from the Atmosphere, in D. Levine, "Radargrammetry," pp. 222–243, McGraw-Hill Book Company, New York, 1960.

59. Atlas, D., K. R. Hardy, and T. G. Konrad: Radar Detection of the Tropopause and Clear Air Turbulence, *Proc. 12th Conf. Radar Meteorol.*, pp. 279–284, 1966.

60. Konrad, T. G., and D. Randall: Simultaneous Probing of the Atmosphere by Radar and Meteorological Sensors, *Proc. 12th Conf. Radar Meteorol.*, pp. 300–305, 1966.
61. Hardy, K. R., D. Atlas, and K. M. Glover: Multiwavelength Backscatter from the Clear Atmosphere, *J. Geophys. Res.*, vol. 71, pp. 1537–1552, 1966.
62. Bean, B. R., and R. M. Gallet: Applications of the Molecular Refractivity in Radio Meteorology, *J. Geophys. Res.*, vol. 64, pp. 1439–1444, October, 1959.
63. The Rocket Panel: Pressures, Densities, and Temperatures in the Upper Atmosphere, *Phys. Rev.*, vol. 88, pp. 1027–1032, 1952.
64. Handbook of Geophysics for Air Force Designers, USAF, ARDC, Air Force Cambridge Research Center, Geophysics Research Directorate, 1957.
65. Dubin, M.: Index of Refraction Above 20,000 Feet, *J. Geophys. Res.*, vol. 59, pp. 339–344, September, 1954.
66. Saxton, J. A.: The Anomalous Dispersion of Water at Very High Radio Frequencies. II: Relation of Experimental Observations to Theory, "Meteorological Factors in Radio Wave Propagation," pp. 292–306, The Physical Society and Royal Meteorological Society, London, 1946.
67. Goldstein, H., D. E. Kerr, and A. E. Bent: Meteorological Echoes, Origin of the Echo, in D. E. Kerr (ed.), "Propagation of Short Radio Waves," MIT Radiation Laboratory Series, vol. 13, p. 588, McGraw-Hill Book Company, New York, 1951.

Anomalous Dispersion Calculated for Atmospheric Water Vapor

Robert F. Calfee

ESSA Research Laboratories, Boulder, Colorado 80302.
Received 4 March 1968.

The normal atmospheric dispersion due to changes in the average refractive index varies slowly with frequency in the ir region of the electromagnetic spectrum. Goody[1] shows that for dry air at a temperature $\theta = 15°C$ and pressure $P = 760$ torr, the expression for the refractive index $n(\theta; P)$ is

$$[n(15; 760) - 1] \, 10^6 = 64.328 + 29498.1 \, (146 - \nu^2)^{-1} + 225.4 \, (41 - \nu^2)^{-1}, \quad (1)$$

where ν is the reciprocal of the wavelength. For this expression, the units of ν are microns^{-1}. The dependance upon pressure P (torr) and temperature θ (°C) is given by

$$[n(\theta; P) - 1] = [n(15; 760) - 1] \, \frac{P[1 + P(1.049 - 0.0157\theta) \, 10^{-6}]}{720.883(1 + 0.003661\theta)}. \quad (2)$$

An additional correction to the dry air expression is necessary to compensate for the presence of water vapor with pressure e (torr). The quantity $(n-1) \, 10^6$ for dry air must be reduced by an amount

$$\Delta(n - 1) \, 10^6 = \frac{0.0624 - 0.000680\nu^2}{1 + 0.003661\theta} \, e. \quad (3)$$

Although the normal refractive index for the atmosphere, Eq. (1), varies slowly with frequency and is only slightly affected by the presence of water vapor, Eq. (3), there are variations that take place about the normal value that are much larger near the resonance frequencies of absorption lines due to absorbing gases in the atmosphere. These large variations that become evident under high resolution produce what is known as an anomalous dispersion. Water vapor and carbon dioxide are the principal atmospheric constituents that absorb ir radiation and produce an anomalous dispersion. The calculation of these anomalous effects for atmospheric water vapor that occur under high resolution is considered here.

High resolution experimental work on the refraction of gases in the ir has been done to determine line intensities and line halfwidths in the spectral regions where there are isolated lines.[2,3]

In the near and intermediate ir regions $(1-50 \mu)$ of the spectrum, the Van Vleck-Weisskopf line shape can be replaced by the less complicated Lorentzian shape when the line broadening is predominantly due to intermolecular collisions. Under these conditions, the monochromatic absorption coefficient $k_i(\nu)$ as a function of frequency depends upon the intensity S_i of a line at frequency ν_i and the halfwidth α_i as follows:

$$\mathcal{K}_i(\nu) = S_i \alpha_i / \pi [(\nu - \nu_i)^2 + \alpha_i^2]^{-1}. \quad (4)$$

The corresponding variation in refractive index is

$$n_i(\nu) = n_0(\nu) + \frac{S_i}{4\pi^2\nu_i} \left[\frac{(\nu_i - \nu)}{(\nu - \nu_i)^2 + \alpha_i^2} \right], \quad (5)$$

where $n_0(\nu)$ is the refractive index of the nonabsorbing gas.

The anomalous dispersion may be written as

$$\Delta n(\nu) = n_i(\nu) - n_0(\nu) = \frac{S_i}{4\pi^2\nu_i} \left[\frac{(\nu_i - \nu)}{(\nu - \nu_i)^2 + \alpha_i^2} \right]. \quad (6)$$

As used here, the frequency will be expressed in cm^{-1}, the intensity in cm^{-1}/(atm cm), and the halfwidth in cm^{-1}/atm. If S_0 and α_0 are the values of intensity and halfwidth at a set of reference conditions of pressure P_0 (in atmospheres) and temperature T_0 (in degrees kelvin), the values at other pressures and temperatures are found from:

$$S(T, p) = S_0 p (T_0/T)^a \exp\{(-E''/k)[(T_0 - T)/(T_0 T)]\} \quad (7)$$

and

$$\alpha(T,P) = \alpha_0 P_e (T_0/T)^b. \quad (8)$$

The exponential factor arises from the assumption of a Boltzmann distribution of the population of molecules, E'' being the energy of the molecule in the lower state of the transition responsible for the spectral line, and k is Boltzmann's constant. The pressure p in Eq. (7) is the partial pressure of the absorbing gas. The pressure P_e in Eq. (8) is the effective pressure which makes allowance for the difference between foreign broadening and self-broadening[4]:

$$P_e = P + (B - 1)p, \quad (9)$$

where P is the total pressure and B is the self-broadening factor that depends upon the absorbing gas. The value quoted for water vapor is $B = 5$. The exponents a and b depend on the absorbing gas; for water vapor, $a = 1.5$ and $b = 0.62$.

Equations (4) and (5) apply for a single line, but in the case of water vapor at atmospheric pressures, the lines are not isolated enough to be treated in this manner. One must consider the accumulative effect of many lines on either side of the spectral point under consideration. This requires the summing of the individual contributions and can be written as

$$\mathcal{K}(\nu) = \sum_i \mathcal{K}_i(\nu) = \frac{1}{\pi} \sum S_i \alpha_i [(\nu - \nu_i)^2 + \alpha_i^2]^{-1}, \quad (10)$$

$$\Delta n(\nu) = \sum_i \Delta n_i(\nu) = \frac{1}{4\pi^2} \sum \frac{S_i}{\nu_i} \frac{(\nu_i - \nu)}{(\nu - \nu_i)^2 + \alpha_i^2}, \quad (11)$$

where the individual intensities S_i and halfwidths α_i have been corrected for pressure and temperature using Eqs. (7) and (8).

With the aid of a large computer, it is possible to perform the computation of Eqs. (10) and (11). A computer program for computing the absorption coefficient $\mathcal{K}(\nu)$ has been described by Deutschman and Calfee.[5] A very similar process can be used to get the corresponding values for the anomalous dispersion $\Delta n(\nu)$. Such computations have been made for selected ir spectral intervals and are displayed in Fig. 1. These intervals include the
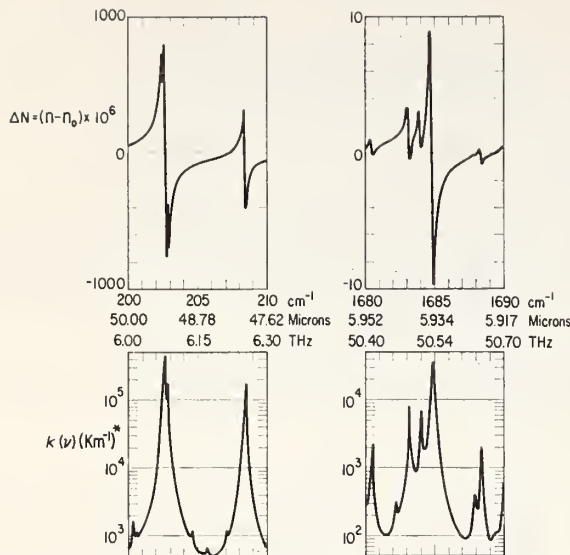
Fig. 1. The anomalous dispersion and absorption coefficients of water vapor as a function of frequency under atmospheric conditions of 50% relative humidity and temperature of 296 K over a 1-km path at sea level.

strongest lines in the fundamental vibrational and the rotational bands of water vapor. Calculations made by this method in other regions of the ir spectrum where comparisons with experimental measurements were possible have shown good agreement to within 2–5%.[6] For purposes of presentation, atmospheric conditions were selected that are representative of actual conditions; namely, a relative humidity of 50% and a temperature of 296 K over a path of 1 km at a pressure of 1 atm. The amount of water vapor under these conditions is equal to approximately 1 precipitable centimeter or 1245 atm cm.

Both the absorption coefficient and the anomalous dispersion increase with the intensity of the lines. The greatest change in the refractive index occurs in the region where the absorption is also high. For some satellite measurements, the use of a strongly absorbing infrared line is necessary to measure small quantities of water vapor by sensing changes in the intensity of solar radiation transmitted by the atmosphere. Difficulties may occur because of the differences in the anomalous dispersion of visible and ir light. If, as is usually the case, visible light is used as a means of sun tracking to keep the source focused on the detecting system, the ir radiation being received will not have come from exactly the same location as the visible light used for control. For example, an anomalous dispersion Δn of the order of 10^{-4} may produce an angular deviation in a light beam of the order of 1°. This phenomenon should be considered in the use of other tracking and pointing systems employing high resolution ir detection devices.

Similar effects can be calculated for other atmospheric constituents that are infrared absorbing.

References

1. R. M. Goody, *Atmospheric Radiation* (Clarendon Press, Ltd., Oxford, 1964), Vol. 1, p. 389.
2. J. H. Jaffe, in *Advances in Spectroscopy*, H. W. Thompson, Ed. (Interscience Publishers, Ltd., London, 1961), Vol. 2, pp. 263–291.
3. J. H. Jaffe and W. S. Benedict, J. Quant. Spectrosc. Radiat. Transfer **3**, 87 (1963).
4. D. E. Burch, E. B. Singleton, and D. Williams, Appl. Opt. **1**, 359 (1962).
5. E. M. Deutschman and R. F. Calfee, "Two Computer Programs to Produce Theoretical Absorption Spectra of Water Vapor and Carbon Dioxide," ESSA Tech. Rep. IER 31–ITSA 31 (April, 1967).
6. R. F. Calfee, J. Quant. Spectrosc. Radiat. Transfer **6**, 221 (1966).

ATMOSPHERIC SOUND PROPAGATION

Richard K. Cook

Geoacoustics Group, Research Laboratories
Environmental Science Services Administration
Rockville, Maryland 20852

ABSTRACT

The propagation of sound waves at infrasonic
frequencies (oscillation periods 1.0 - 1000
seconds) in the atmosphere is being studied
by a network of seven stations separated
geographically by distances of the order of
thousands of kilometers. One of the typical
stations, in Washington, D. C., has an array
of five microphones separated by distances
of about 7 kilometers. Each microphone is
at ground level and is connected to the
central station by means of a leased tele-
phone line. In effect the array is "steered"
to look for sound waves in a programmed se-
quence of search directions. The station
measures the following characteristics of
infrasonic waves passing through Washington:
(1) the amplitude and waveform of the inci-
dent sound pressure, (2) the direction of
propagation of the wave, (3) the horizontal
phase velocity, and (4) the distribution of
sound wave energy at various frequencies of
oscillation. Some infrasonic sources which
have been identified and studied include the
aurora borealis, tornadoes, volcanos, gravity
waves on the oceans, earthquakes, and atmo-
spheric instability waves caused by winds at
the tropopause. Waves of unknown origin
seem to radiate from several geographical
locations, including one in the Argentine.

1. INTRODUCTION

Sound waves have two principal uses to which acoustical researches have been directed intensively during the last fifty years. The first use, a very ancient one, is in the art of communication between men and the handling of everyday affairs, by hearing and speech. Audio-frequency waves, those audible to man in the frequency range from 15 to 17000 Hz, are necessary for this purpose. They are propagated through the atmosphere for relatively short distances. But unwanted sounds — noise — of the same frequencies interfere with communication and indeed with other aspects of man's activity. The importance of audible sound to man has led to an extensive technology for the quantitative measurement, analysis, and display of such sound waves. Researchers have developed equipment and methods for producing controlled amounts of sound and vibration, and for reducing noise.

A more recent use for sound waves is for researches into the structure and properties of matter — solids, liquids, and gases. Generally speaking, high-frequency sound (at ultrasonic frequencies) is used for studying solids and liquids. Industry has found ultrasonic waves valuable for location of flaws in thick pieces of metal, by measurement and display of the scattered sound from the flaws. Sound waves offer the only practical method for exploring the contours of the sea bottoms, and for locating underwater objects such as submarines at distances more than a few feet away. But for researches on gases, including the atmosphere, sound waves have been found useful over a wide range of frequencies. The microstructure of gases is studied in the laboratory with ultrasound. Waves at audible and infrasonic frequencies, some as low as 10^{-4} Hz, are studied in the free atmosphere. When the details of propagation through a medium are known, then properties of the source itself can be deduced from the sound it radiates, measured at distant points.

Researches on the two principal uses for sound are dependent upon, and unified by, (a) modern electroacoustics which makes the controlled generation of sound waves and accurate measurements of them possible, and (b) the theory of sound propagation and its mathematical-physical formulation.

We are considering in particular propagation through the atmosphere. Some studies aim at measuring the influence of unwanted sound, e.g., aircraft noise on man. Others look towards measurement of atmospheric properties by probing — remote sensing — with sound waves. Still others seek to determine the properties of distant sources of sound. But all researches on atmospheric

sound must depend on theoretical analysis of sound propagation, coupled with measurements of sound at only a relatively few available locations, to arrive at useful results.

We concentrate our attention on infrasound in the atmosphere — sound waves whose frequencies of oscillation are less than the lowest frequency, about 15 Hz, that can be heard. Of particular interest are those waves whose oscillation periods lie in the range of 1.0 to 1000 sec, because such waves propagate for distances of thousands of kilometers without substantial loss of energy. Sounds at these frequencies are almost always present at measurable intensities. Those of natural origin have many causes, including tornadoes, volcanic explosions, earthquakes, the aurora borealis, waves on the seas, and large meteorites. Man-made sources include powerful explosions and the shock waves from vehicles moving through the atmosphere at supersonic speeds, at altitudes below about 125 km.

2. PRINCIPAL FEATURES OF SOUND PROPAGATION

    2.1 Sound Pressure

        The passage of an infrasonic wave causes <u>pressure oscillations</u> as it traverses the atmosphere. For infrasound of natural origin, the amplitude p of the sound pressure is often in the range of 0.1 to 100 dyn/cm^2, and infrasonic microphones are usually designed to respond to such pressures. The atmospheric pressure $B \approx 10^6$ dyn/cm^2.

A microphone converts the sound pressure at a particular point into electric current variations having the same waveform. The passage of a sound wave is also accompanied by small vibratory displacements and small variations in temperature of the atmosphere. Microphones have been designed which respond to one or the other of these parameters of the sound wave. For example, the hot-wire microphone responds to the vibratory particle velocity of the air. But any microphone must be located in principle out-of-doors, and it therefore responds to the variable pressure effects of the turbulent eddies associated with the wind, in addition to the effects of the sound wave. An examination of the generation of noise pressure variations caused by turbulent flow shows that the ratio of the desired acoustical signal to unwanted flow noise is greater (by at least an order of magnitude) for the sound pressure than is the ratio for the particle velocity. Therefore measurements of atmospheric sound are always made with pressure microphones.

2.2 Speed of Sound

The square of the phase velocity c^2 for sound in a gas at a uniform temperature is the ratio of the gas's modulus of elasticity to its density: $c^2 = \gamma B/\rho$ where B (see above) is the atmospheric pressure in dynes per square centimeter, and ρ is the density in grams per cubic centimeter. For air, the adiabatic gas constant $\gamma = 1.402$ (dimensionless). γB is the adiabatic modulus of elasticity for the atmosphere. But the equation of state for air is $B = \rho RK$, where K is the absolute temperature and R is a constant. Therefore $c^2 = \gamma B/\rho = \gamma \rho RK/\rho = \gamma RK$, and so finally

$$c = \text{constant} \times \sqrt{K} \tag{1}$$

Equation (1) shows that the speed of sound is independent of the density of the atmosphere, but directly proportional to the square root of the absolute temperature. For air at a temperature of 20 °C = 293 °K, the speed c is about 344 m/sec. From this, the sound velocity can be found at other temperatures by means of Eq. (1). The formula is applicable for all sound waves from the low infrasonic frequency of f = 0.01 Hz (wavelength λ = 34 km) through audible frequencies, $f \approx 1000$ Hz, to ultrasonic frequencies, $f > 20,000$ Hz.

Although the sound speed c is an important parameter, the propagation of sound waves through the atmosphere cannot be characterized by a single unique speed. It is useful to distinguish between four velocities of sound. The phase velocity c (see above) is the speed at which a surface of constant phase travels through the atmosphere for a sinusoidal oscillation having $\omega = 2\pi f$ (f is the frequency). The local phase velocity of sound is fixed only by the temperature of the atmosphere in the vicinity of the region of interest. For long waves extending vertically in the atmosphere with its substantial differences in temperature, the phase velocity is a function of the entire temperature distribution (see the next sub-section 2.3). In such cases, the phase velocity depends upon the wavelength λ, and hence upon $k = 2\pi/\lambda$. The group velocity is defined in acoustics as $c_g = d\omega/dk$. The signal velocity is defined by $c_s = D/T$, where D is the distance from the source of sound to the microphone, and T is the time between the radiation from the source and the emergence (at the microphone) of the signal from noise. In general, the signal velocity differs from both the phase velocity and the group velocity; the relationships between them depend on the structure of the entire atmospheric path, including winds.

The fourth velocity is directly measured at an infrasonic station. In-frasonic microphones are usually on the earth's surface and therefore approx-imately in the same plane. The speed of a line of constant phase for a sound wave traveling over the earth's surface can be determined from the output of the several microphones. This speed c_h is usually called the <u>horizontal trace velocity</u>. It depends on the elevation above the horizon of the ray direction for incident plane waves. When the angle of incidence is θ (eleva-tion angle $= \pi/2 - \theta$), then $c_h = c/\sin\theta$.

2.3 Effect of Temperature Distribution

The atmosphere is never in an isothermal state, but is approximately horizontally stratified with the variation in temperature being a function principally of altitude above the surface. In fact the first evidence for a region of warm air at an altitude of about 50 km, at the same or a slightly higher temperature than that at ground level, came from early observations on the anomalous audibility of sounds from large explosions heard at dis-tances greater than about 100 km from the explosive source. The audible waves were in effect used to remotely sense the temperature at the 50 km altitude of the mesosphere.

The phase velocity therefore varies with altitude since the temperature does, see Eq. (1). This variation is a gross feature of the atmosphere and substantially affects the propagation to great distances. The data on the atmosphere obtained from sound propagation measurements, and from instru-mented rockets and satellites, show that the temperature, and hence the local phase velocity, depend on location on the earth's surface as well as on altitude, and also vary with time. The average properties have been incor-porated into various "standard atmospheres." The distribution of tempera-ture and sound speed with altitude for the 1962 U. S. Standard Atmosphere is shown in Figure 1. The curves should be regarded as averages over all seasons of the year for northern temperate latitudes. The standard atmo-sphere is useful for analytical investigations into sound propagation.

A detailed mathematical analysis for the propagation of sound shows that the speed minimum in the stratosphere results in waves emitted at low altitudes being "channeled" between the ground and the layer of relatively high sound speed at 50 km altitude. Loosely speaking, the layer serves as a reflector, albeit a poor one. For the shorter waves, $T < 15$ sec (approx-imately), sound-ray trajectories are useful for studying propagation.
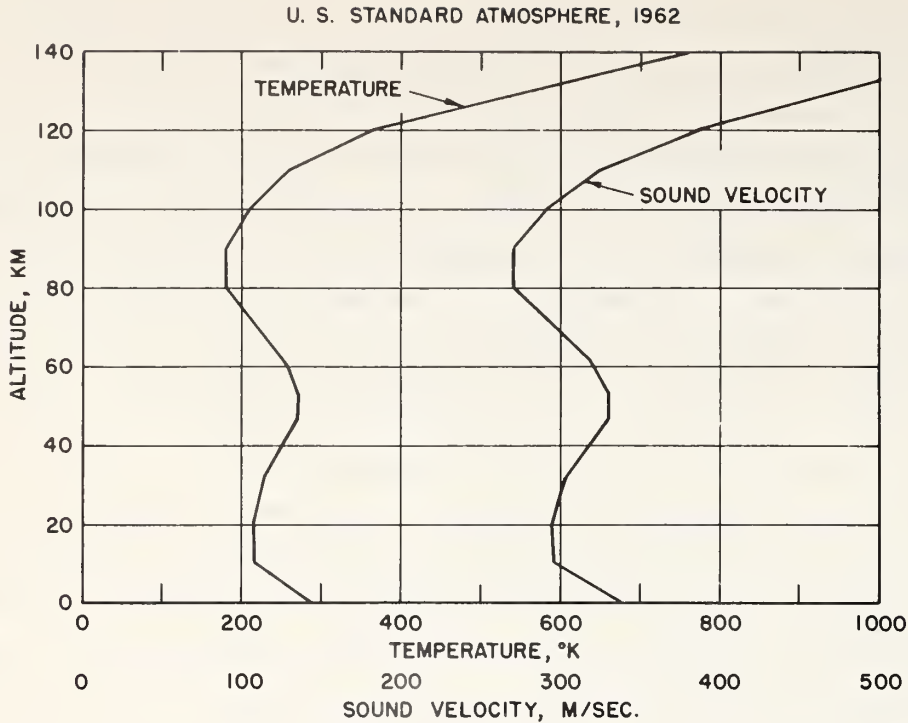
U. S. STANDARD ATMOSPHERE, 1962

Figure 1.   Temperature and sound velocity in the 1962 U. S. Standard Atmosphere.   Details of the real atmosphere vary with location on the earth's surface and with the seasons.

In general, the rays emitted at low elevation angles θ from a source at ground level are alternately reflected between the layer at 50 km altitude and the surface of the ground.

2.4   Influence of Gravity

Since the atmosphere is in the gravitational field of the earth, its density decreases approximately exponentially with altitude z above the surface.   For an isothermal atmosphere with a sound velocity c = 333 m/sec, the density will decrease as exp $(-z/H)$, where H = scale height of the atmosphere $\approx$ 8.1 km.   The sound pressure for a plane wave of sound sent vertically upward will decrease as exp $(-z/2H)$, but the particle velocity will increase as exp $(+z/2H)$, so that the sound intensity would remain constant. If the frequency of oscillation is decreased until $T_R = 4\pi c/\gamma g$ = 305 sec, (γ = 1.40, g = 9.8 m/sec^2), then the phase velocity of the upward traveling wave becomes infinite.   But for waves of period shorter than about 100 sec (frequencies greater than about 10^{-2} Hz), gravity effects on sound speed
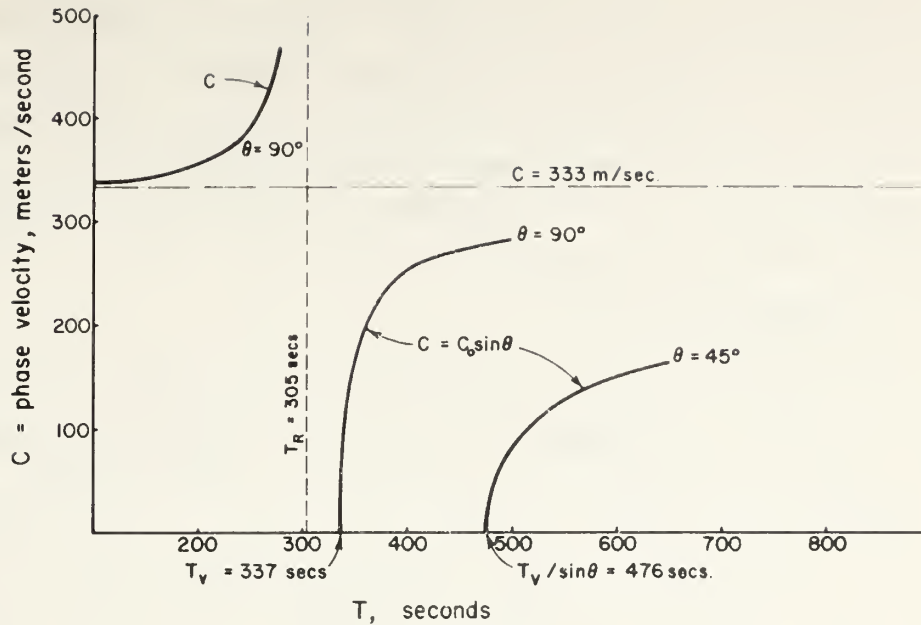
638

Figure 2. Phase velocities for sound waves in the atmosphere at very low
frequencies. θ = angle of incidence for plane waves.

are not significant.

T_R is the resonant period for vertical oscillations of the atmosphere.
Another important resonant period is the Väisälä period T_V = 337 sec, for
the isothermal atmosphere (c = 333 m/sec) under consideration. T_V is the
natural period of oscillation for a small parcel of air which is displaced
adiabatically in a vertical direction, in an isothermal atmosphere horizon-
tally stratified by gravity. Plane sinusoidal waves of periods T > 337 sec
are usually called "acoustic-gravity" waves, although the atmospheric mo-
tions satisfy the same equations of motion as do the sound waves of shorter
period T < T_R. Because the phase velocity is substantially less than the
high-frequency velocity c = 333 m/sec, the waves might be called subsonic
oscillations. The phase velocity is furthermore, for a particular period T,
a function of the angle θ between the direction of propagation and the hori-
zontal plane. See Figure 2 for curves showing how the speeds of plane acous-
tic-gravity waves vary with frequency and angle θ.

In general the speeds are low enough so that wind and temperature gra-
dients can have a strong effect on the propagation. In fact, it appears
that acoustic-gravity waves have never been detected with certainty more
than a hundred kilometers or so away from the source. For example, vertical

oscillations of the jet stream at an altitude of about 10 km produce strong
subsonic pressure oscillations, at periods $T > 300$ sec, at ground level over
a large area of the eastern seaboard of the United States. But these occur
only when the jet stream is vertically overhead. Acoustic-gravity waves are
probably scattered and absorbed strongly by wind and temperature gradients
in the atmosphere, and so are not propagated with measurable intensities
over global distances away from the source area.

2.5 Atmospheric Absorption

The absorption of infrasound in the atmosphere, due to viscosity
and heat conduction, is considerably less than the absorption for audible
sounds because of the low frequency of oscillation. The absorption coeffi-
cient $\underline{\alpha}$, defined by the spatial variation of $\underline{p}$, $|p(x)| = p_o \exp(-\alpha x)$, is
about $1.6 \times 10^{-4}/T^2 B$ decibels (dB)/m. $\underline{B}$ is the barometric pressure in dyn/cm^2.
For a plane wave of sound in the lower atmosphere at $T = 10$ sec, the absorp-
tion is, therefore, less than 2×10^{-9} dB/km. Hence the loss due to this
absorption mechanism is totally insignificant, even for propagation over
distances of thousands of kilometers. The absorption in the upper atmosphere
is substantially greater because of the lower barometric pressure. At an al-
titude of 90 km, where the barometric pressure ≈ 1 dyn/cm^2, the absorption
$\approx 2 \times 10^{-3}$ dB/km for waves of 10-sec periods.

Up to altitudes of about 10 km in the troposphere, the absorption due
to water vapor should be considered. The exact variation of this absorption
with barometric pressure is not accurately known for infrasonic frequencies.
We estimate that at sea level (altitude = 0 km) the absorption coefficient
might be as large as $5 \times 10^{-9}/T^2$ dB/m, which is about 30 times greater than
the absorption for viscosity and heat conduction, as indicated previously.
But the absorption due to water vapor is still insignificant for infrasound
at $T = 10$ sec, being only 5×10^{-8} dB/km. This corresponds to an energy
loss of less than one percent after propagation half-way around the earth,
a distance of 20,000 km.

At very low frequencies, there is an absorption due to relaxation of
the thermal energy stored in vibrations of the diatomic molecules in air.
We estimate the absorption coefficient to be almost 1000 times greater than
that of the viscosity-heat-conduction loss. Therefore, waves in the lower
atmosphere at $T = 10$ sec have $\alpha \approx 10^{-6}$ dB/km. Again, this is an insignifi-
cant loss.

The atmosphere has inhomogeneities in temperature and density arising, for example, from solar heating of the ground. Inhomogeneities in density and motion are associated with turbulence in the wind as it passes over trees, buildings, hills, etc. Furthermore, sound waves are scattered by such obstacles as well as by the atmospheric inhomogeneities. All of these effects cause attenuation of sound-wave energy. But, the attenuation is estimated to be quite small when the wavelength is greater than about 1 km.

The net result is that the total attenuation for infrasound in the atmosphere is small enough so that propagation can occur over thousands of kilometers without substantial loss of energy. An example of this is the sound from the tremendous explosion of the volcano Krakatoa in the East Indies in 1883. The absorption of infrasound from the explosion was low enough so that the waves were still detectable after having traveled around the earth several times. Even though electroacoustic equipment suitable for measurement of infrasound did not then exist, the inaudible sound waves from this disturbance had sound pressures so great that readable deflections were produced on barographs all over the world.

2.6 Influence of Winds

The wind speed $\underline{w}$ near the surface of the earth is rarely a substantial fraction of the speed of sound $\underline{c}$. The wind Mach number $\beta = w/c$ is usually less than 0.05. But when the jet stream blows at the tropopause at an altitude of about 12 km, then β is at least 0.1 and sometimes as great as 0.25.

Winds near the stratopause at an altitude of 50 km can be even stronger, and $\beta = 0.35$ occasionally. At the stratopause the phase velocity of sound has a maximum, since there is a temperature maximum at that level (see Figure 1). Therefore the wind speed and its direction with respect to the direction of sound propagation have important influences on the channeled propagation of sound between the surface of the earth and the stratopause.

In temperate latitudes in the northern hemisphere, there are strong westerly winds for a long regime (about five months) during the winter. There is a shorter regime of strong easterlies during the summer, about two and one-half months. The following is a short table of winds at the stratopause over the continental United States.

Table 1

East-West (Zonal) Winds at Several Geometric Altitudes

Altitude km	Mean values of wind speed in m/sec. (+) = towards east, (-) = towards west			
	16 Oct. to 31 March	1 April to 31 May	1 June to 15 Aug.	16 Aug. to 15 Oct.
50	+52	+2	-42	0
55	+58	-5	-47	+2
60	+61	-8	-51	+5

The mean north-south (meridional) wind components are less than 10 m/sec at any time of the year, and have an annual average speed of 6 m/sec toward the north. Fuller details on the winds at various altitudes have been published by the Air Force Cambridge Research Laboratories (1965).

We see that the effective speed of sound at the stratopause for propagation to the east during the winter is 330 + 57 = 387 m/sec (see Figure 1 and Table 1), whereas at the surface the speed is much less, c = 335 m/sec. But for propagation to the west, the effective speed at the stratopause is 330 - 57 = 273 m/sec, and the speed at the surface is substantially greater. In brief, the conclusion is that over the continental United States the 50-km thick atmospheric layer between the stratopause and the surface of the earth serves as a waveguide for eastward propagation of sound energy during the winter, but not for westward propagation. In summer the opposite is true; the waveguide effect is only for westward propagation.

For sound waves generated by a source near the earth's surface, the signal velocity c_s for propagation eastward will generally differ from that westward. The amount of the difference will of course vary with the seasons, because of the seasonal changes in the stratopause winds. In addition because of the difference in waveguide properties, the attenuation of infrasonic waves for eastward propagation will differ from westward propagation. For example, the westward attenuation in winter will be much greater.

Analytical expressions for the effect of stratopause winds on infrasonic signal velocity and attenuation need to be developed. We suggest that such expressions, applied properly to data on propagation of infrasound, could be used to remotely sense winds at the stratopause.

3.   MEASUREMENTS OF INFRASOUND

    3.1 Measurement System

        The electroacoustic system used at each of the infrasonic stations
in the ESSA network consists of an array of at least four microphones, asso-
ciated electronic filter-amplifiers, and recorders.   The system is designed
for determining four characteristics of infrasonic waves passing through the
station area: (1) the amplitude and waveform of the incident sound pressure,
(2) the direction of propagation of the wave, (3) the horizontal phase veloc-
ity, and (4) the distribution of sound wave energy at various frequencies of
oscillation.

    The microphones are located at ground level, approximately in the same
plane, and about 7 km apart.   See Figure 3 for the station at Washington,
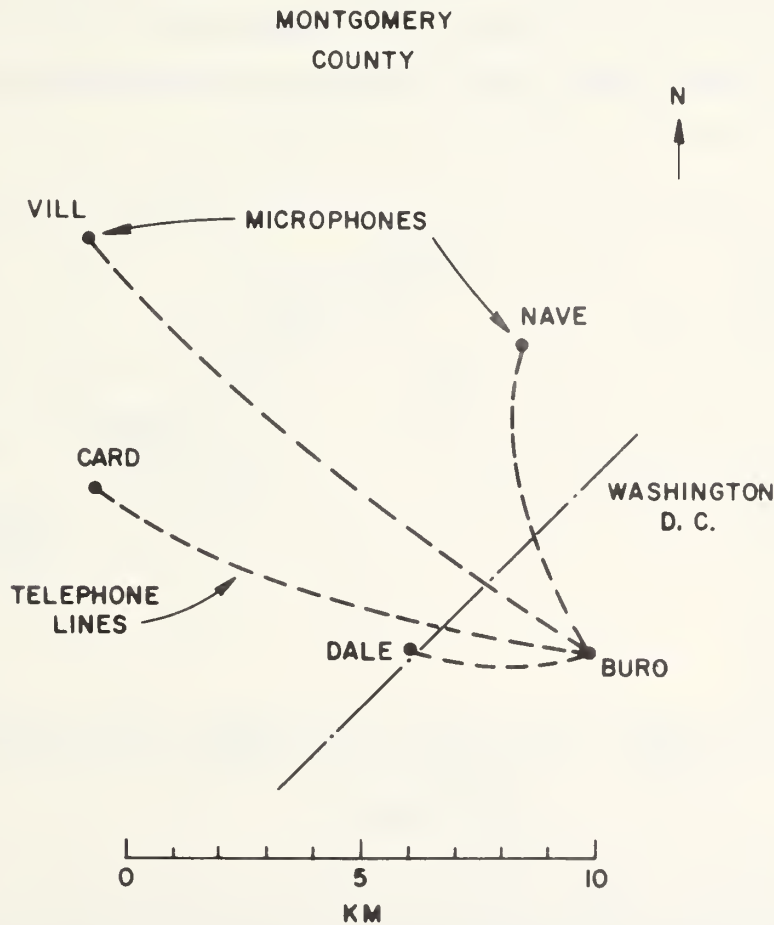D. C.   Effects on each microphone of pressure fluctuations caused by local

Figure 3.   Location of line-microphones at the infrasonics station in Wash-
            ington, D.C.   Recordings are made at the Buro site.

turbulent wind eddies are minimized by noise-reducing lines of pipe which are about 300 m long, have capillary inlets, and are connected to the inlet to the microphone. The theory of this noise-reducing line has been described by Daniels (1959). For sound waves of wavelength greater than about 3 km, the line microphone is essentially nondirectional and does not attenuate the sound pressure appreciably. However, noise due to random pressure fluctuations in the period range of 1.0 to 30 sec, such as that caused by wind turbulence, is reduced considerably.

The microphones are of the electrostatic condenser type, and produce frequency-modulated voltages, on a carrier frequency of about 1500 Hz, proportional to the incident sound pressure. These voltages are transmitted by telephone wires to a central location where they are demodulated, amplified, and recorded by several means that will be described below. Band-pass filters are introduced into the amplifiers when a higher signal-to-noise ratio is desired for the sound under study. Earthquake waves, for example, are best studied with a band-pass filter passing sounds having periods of oscillation between 0.4 and 20 sec, as in Figure 4.
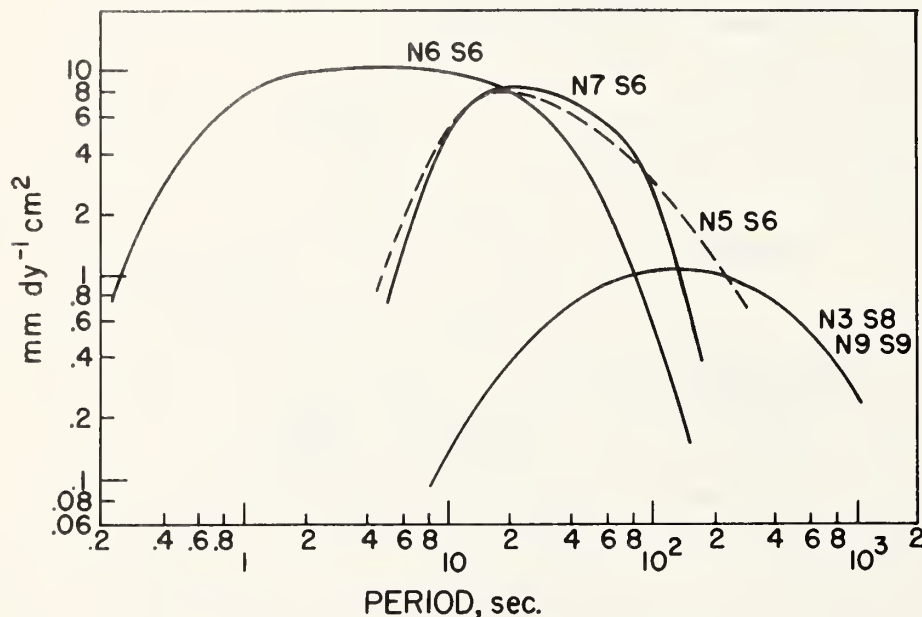

Figure 4. Response curves of some filters used with an infrasonic microphone system. The ordinate scale applies to ink-on-translucent-paper chart recordings.

644

Calibration of each microphone is done by connecting its inlet through a short hose to a calibrating barrel with a volume of about 0.19 m^3. An oscillating piston on top of the barrel produces accurately known sinusoidal sound pressures within it at various low frequencies.

3.2 Recording on Paper Charts

A convenient recording scheme has been in use for many years. It is in analog form, in real time, as ink-on-translucent-paper traces. Each line-microphone is recorded on its own paper chart. The waveform of each recording is that of the sound pressure as modified by the gain, as a function of frequency, of the microphone and electronic filter combination. An important feature of the scheme is the accurate timing trace for each recording.

The four characteristics of the sound wave (see the preceding subsection 3.1) are obtained from the ink-on-paper traces by a procedure based on visual congruence (correlation) between pairs of recordings, which are matched by superposition on a transparent table top illuminated from below, for example. At "best correlation," time differences are obtained for arrival of the same sound waveform at the several pairs of microphones. The direction of propagation and the horizontal phase velocity are found from these differences by a simple geometrical procedure described by Matheson (1966). The sound pressure amplitude is obtained from a calibration of the microphone-recording system with an oscillating piston source, and the dominant periods are found by inspection of the recorded waveform. The success of the correlation scheme depends on the fact that almost all sound waves coming from distant sources have approximately plane wavefront surfaces of constant phase.

3.3 Magnetic Tape Recording

With the magnetic tape scheme, sound pressures at the several line-microphones are recorded in analog form on parallel channels (tracks) on the tape along with time. When a sound wave is present, its direction of propagation and horizontal phase velocity are obtained from the magnetic tape recording by means of an automatic multichannel correlator. This is essentially an analog computing instrument which receives the magnetic tape recording and produces an output trace (on paper tape) proportional to the average of the cross-correlations between pairs of microphone voltages.

Variable time delays are mechanically introduced into each microphone channel, with the delays corresponding to a systematic search for correlation at all azimuths and over a range of horizontal phase velocities between c = the speed of sound and $c \sqrt{2}$. Details on the automatic correlator have been given by Brown (1963). The direction of propagation and the horizontal phase velocity are read from the output trace of the correlator.

4.   RESULTS OF OBSERVATIONS ON INFRASONIC WAVES

We proceed to describe infrasound caused by the following geophysical disturbances: volcanic explosions, the aurora borealis, earthquakes, microbaroms due to ocean waves, subsonic oscillations of the jet stream, and shock waves from the entry of meteorites and satellites into the atmosphere.

There are other natural sources of infrasound not yet fully studied. In particular severe storms such as tornadoes (Cook and Young, 1962), and the passage of winds over certain mountainous areas, give rise to infrasonic waves in the atmosphere. Two areas of "mountain" waves seem to be the Pacific coast of North America between north latitudes 40° and 60°, and the region of Argentina east of the Andes Mountains between south latitudes 25° and 35°.

4.1   Volcanic Explosions

Sufficiently strong volcanic explosions occur frequently enough to provide many useful data on the propagation of infrasound over global distances through the atmosphere. We mentioned earlier the tremendous explosion of Krakatoa in the East Indies in 1883, whose infrasonic waves were still detectable after having traveled around the earth several times. Following are a few of the volcanos whose explosions radiated substantial amount of infrasound: Bezymyanny in eastern Siberia in 1956, reported by Passechnik (1959); Mt. Agung on the island of Bali in 1963, reported by Goerke et al (1965); Mt. Redoubt in southern Alaska in 1966, reported by Wilson (1966); the caldera on Isla Fernandina in the Galapagos Islands in the spring of 1968, still under study.

The sound waves from Mt. Agung were observed at three infrasonic stations in the continental U.S.A. The essential features of the data are shown in Table 2 and Figure 5.

Table 2

Sound Waves from the Explosion of Mt. Agung

8.3° south lat., 115.5° east long.,

at 0855 h, May 16, 1963 (UT).

	Infrasonic Stations		
	Boulder, Colo.	Boston, Mass.	Washington, D.C.
Location	40.1°N 105.2°W	42.5°N 71.2°W	39.0°N 77.1°W
Short great-circle distance from Mt. Agung, km	14,700 25,300*	16,200	16,300
Observed infrasonic arrival, UT	2301 h, May 16 0757 h,* May 17	0028 h, May 17	0150 h, May 17
Signal velocity m/sec	288 305*	289	268 ┼
Maximum amplitude, dyn/cm²	>6.6 2.4*	10.6	9.0
Measured azimuth of sound wave arrival	304° 111° *	350°	347° ‡
Azimuth of great- -circle to Mt. Agung	300.5° 120.5° *	348.3°	336.4°

* Via great-circle path through antipode

┼ Uncertain because start of received signal was obscured by noise.

‡ Observed about 2 1/2 hr. after start of signal.

The sound pressure at each station emerged slowly from noise, and so the measured transit times might be somewhat greater than the "true" (least) time. In particular, the rather low signal velocity deduced from the Washington data is due to masking of the early part of the infrasound by wind noise. The low signal velocity of 288 m/sec deduced from the Boulder and Boston data (short great-circle paths) might be due in part to easterly winds at the stratopause over the Pacific Ocean and the continental United
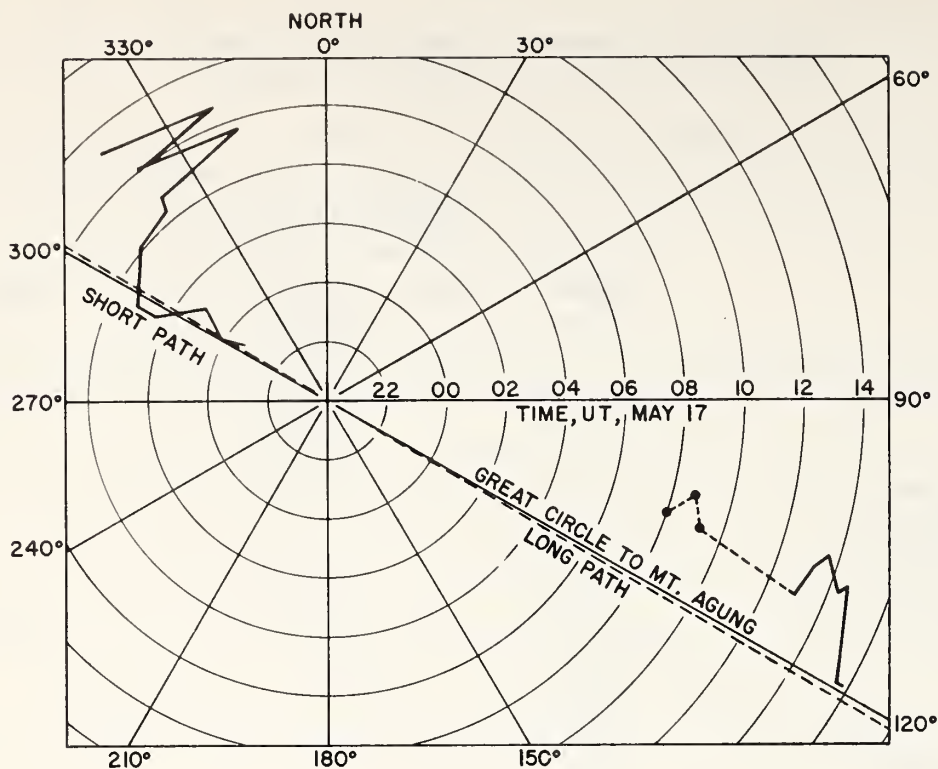
Figure 5. Variations of azimuth for arrival of infrasound from Mt. Agung in
Boulder on May 16 - 17, 1963. The three points are for sporadic
appearances of sound waves in noise at about 0800 - 0900 h.

States, (see Table 1).

About two-thirds of the antipodal (long) great-circle path to Boulder is
in the southern hemisphere, where much less is known of the upper atmosphere
winds. The infrasonic signal velocity of 305 m/sec is a little higher than
the average of 300 m/sec for the wind-free atmosphere. We therefore estimate
that the stratopause winds at the 50 km altitude in the southern hemisphere,
during the infrasound transit in May, must have been mainly toward the west,
at an average speed no greater than − 10 m/sec.

But this conclusion is at variance with the deduction from Webb's (1964)
hypothesis that the southern hemisphere winds can be deduced by symmetry from
the northern hemisphere data. The hypothesis would lead to strong winds, at
the southern hemisphere stratopause, toward the east at + 50 m/sec over about
half of the infrasonic propagation path. Furthermore, such strong adverse
winds, if present, would have reduced the antipodal sound intensity by a
much greater amount than was actually observed.

The reader should note that the wind data published by the AFCRL (1965) for the stratopause are based on measurements made with vertically ascending rockets at a number of geographical locations. In other words, the wind measurements were made at isolated points on the earth's surface, separated by thousands of kilometers. Measurements of sound propagation offer the potentiality (not yet realized in full) of obtaining average winds over long paths in the atmosphere. These propagation data should be useful supplements to the rocket data.

4.2 Auroral Infrasonic Waves

Two types of infrasonic waves caused by the auroral borealis are found in the atmosphere of the northern hemisphere at temperate and high latitudes. The first type is found at mid-latitudes during sufficiently strong magnetic storms even in the absence of a visible aurora at the geographical location of the infrasonic station. The second type of infrasonic wave, found near the auroral oval at high latitudes when visible sharply-defined auroral forms travel overhead across the station location at supersonic speeds, has directions of propagation and horizontal trace velocities very nearly the same as those of the visible auroral form. Before discussing these two types of waves, we digress to present a short description of a magnetic storm and related phenomena.

With the advent of a solar flare or a sun storm, electromagnetic radiation reaches the earth almost immediately. An ionized-gas cloud sometimes arrives one or two days later. This plasma cloud perturbs the magnetic field of the earth. Mid-latitude observatories see a rise in the horizontal component of the magnetic field, followed by a larger decrease and a recovery lasting several days. The strong and erratic variations that result are known as magnetic storms, magnetic activity, or disturbance variations. A measure of this solar-particle radiation effect is furnished by the planetary magnetic index K_p which is derived from data from a number of participating magnetic observatories. One of a series of numbers from 0 to 9 is given to each three-hour interval of each day, a larger number indicating a greater departure from undisturbed conditions. During large magnetic storms, magnetic fluctuations with periods from a few seconds to several minutes occur, radio communications are disturbed, x-rays are observed with instruments carried in balloons, and the aurora is observed in mid-latitudes.

Waves recorded during the magnetic storm of February 11, 1958, at

Washington, exhibited a more-or-less typical behavior pattern. The storm began on February 11 at 0126 UT. It was accompanied by an intense red aurora visible in Washington. The first distinguishable sound waves arrived about 0642 UT from a north-northwest direction and had a trace velocity of 775 m/sec. Measurements at 0905 UT indicated a direction slightly more from the west and a trace velocity of 750 m/sec. The sound waves decreased in amplitude and disappeared between 1100 and 1200 UT. Comparison of the large trace velocity, usually greater than 400 m/sec at the mid-latitudes of Washington and Boulder, with the local speed of sound is often enough to distinguish these waves from other infrasound. There are variations with time in the apparent direction and trace velocity of the waves. There is an apparent short-period cutoff near T = 15 sec.
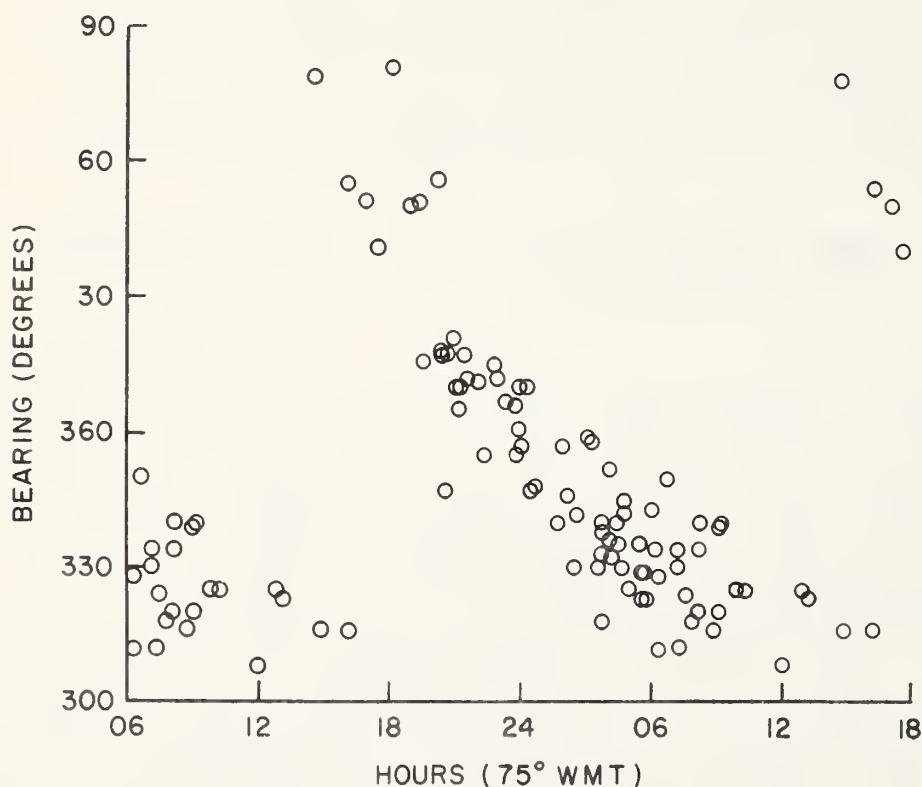

Figure 6. Azimuth of auroral infrasound arriving during magnetic storms, as a function of local time in Washington, D.C. Bearing (= azimuth) = angle, in degrees east of north, to the direction from which the sound comes. The open circles are measured azimuths during 1956 - 1962.

The remarkably consistent changes in direction of arrival with time of day are shown in Figure 6. Direction changes from the northeast in the evening, through north about midnight, then northwest in the morning, and to the northeast again somewhat suddenly after local noon. The data in this figure were restricted to signals with trace velocities above 390 m/sec to help prevent possible confusion with sound from other sources.

Sound waves usually arrive at Washington, D. C., within 5 or 6 hr of rise of K_p to a value of 5 or higher. Predominant periods range from 20 to several hundred seconds. The pressure amplitude is usually less than 3 dyn/cm^2, but is sometimes 7 or greater. Durations range from 1 or 2 hr to more than 24 hr, with a mean of about 6 hr. During the active solar years 1960 and 1961, auroral infrasonic waves were observed for more than 200 hr each year at Washington, D. C. Additional details are given by Chrzanowski et al (1961, 1962).

A very simple hypothesis may serve to explain qualitatively the experimental observations on these sound waves at mid-latitudes. Imagine a somewhat diffuse source in the lower ionosphere and fixed in geomagnetic latitude on the side of the earth opposite the sun. Let the magnetic latitude of the center of the source be that of the auroral zone, or about 66°. Waves from the source spread out through the ionospheric plasma at supersonic speeds. Sound waves leak out from the lower surface of the plasma and therefore have the supersonic horizontal trace velocities observed at mid-latitudes. The earth will turn underneath the source once each day. This qualitatively explains the diurnal change of direction of infrasound observed at Washington, D. C. The relative absence of short periods and the large trace velocity suggest a high-altitude source where the mean free path of the molecules is long and the modes excited in the atmospheric wave guide have wave normals with a vertical component. This picture is, of course, oversimplified. Since the aurora moves south with increasing geomagnetic activity, it is possible that the sound source may vary in geomagnetic latitude with strength of the disturbance. Fluctuations in longitude of the source may also occur.

On the basis of the above hypothesis and the observations of duration and amplitude at Washington, D. C., it seems reasonable to assume that perhaps one quarter of the earth's surface is simultaneously bathed in acoustic radiation with an average pressure of about 1 dyn/cm^2. This suggests an acoustic source of roughly 10^9 W during a typical magnetic storm.

The other type of infrasonic waves, caused by visible aurorae, has been observed by C. R. Wilson and his colleagues (1967a, 1967b) at the infrasonic station at College, Alaska. The basic observations are: (a) the horizontal trace velocity is supersonic, $c_h > 450$ m/sec; (b) the transient pulses of sound have about the same direction of propagation and velocity as fast-moving auroral arcs overhead at Alaska, measured with an all-sky camera; (c) the dominant period of oscillation is about 20 sec; (d) peak sound pressure is typically 5 dyn/cm^2; and (e) each pulse is of only a few minutes duration.
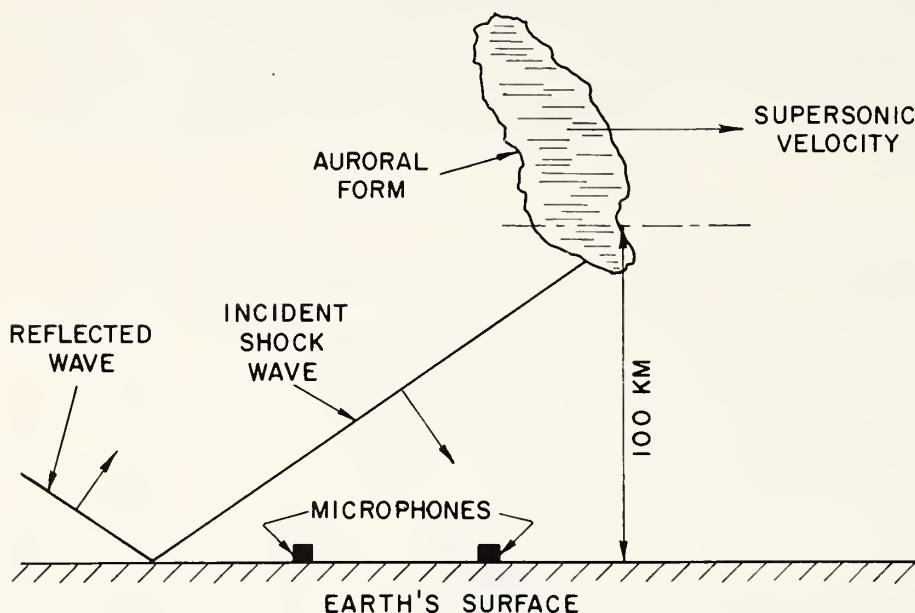
Figure 7. Acoustical shock wave caused by supersonic motion of the leading edge of an auroral form.

The observations can be very well explained by means of Wilson's shock wave model, in which the supersonic motion of the leading edge of an auroral wave gives rise to an acoustical shock wave (see Figure 7). The lower edge of the aurora serves as a line source (perpendicular to the plane of the paper). A particular pulse arrived at the ground station microphones 420 sec after an auroral arc passed overhead. The 420-sec delay corresponds to a source altitude of 140 km for an assumed average $c = 300$ m/sec and measured $c_h = 680$ m/sec. This altitude is to be compared with the known heights of visible auroral arcs, which in most instances have streamers extending from 110-km to 145-km altitudes.

Auroral infrasound is apparently not propagated into the equatorial zone. The infrasonic stations at Huancayo, Peru (12° S lat.) and La Paz, Bolivia (17° S lat.) have not yet detected infrasound from either the aurora borealis or the aurora australis. The station at Tel Aviv, Israel (32° N lat.) has observed auroral infrasound on only two or three occasions. These observations are consistent with the leakage of acoustic waves from an ionospheric disturbance originating in the auroral zone.

4.3 Earthquakes

After a strong earthquake, traveling waves spread from it over the earth's surface and radiate sound into the atmosphere as well. The vertical component of the earth's surface motions gives rise to the sound radiation. There are several different types of earthquake waves, and they all travel with speeds much greater than the velocity of sound in air. As a consequence, the sound radiations are propagated upward in a direction almost perpendicular to the earth's surface. The strongest surface motions at locations away from the epicenter of the earthquake are those caused by Rayleigh waves. These travel entirely on the surface of the earth and have periods of oscillation T between about 10 and 50 sec. The phase velocities c_o of these waves when traveling over continental surfaces are about 3.5 km/sec. The sound from Rayleigh waves is occasionally strong enough to reach the ionosphere and cause substantial motions there.

The sound radiated by strong earthquakes can be measured at infrasonic stations. Usually the detected sound is that locally radiated by earthquake waves passing through the geographical area of the station. But from a very strong earthquake, sound radiated directly from the epicentral area into the atmosphere can be measured at an infrasonic station several thousand kilometers away. This occurred at the time of the great Alaskan earthquake in 1964, whose epicentral sound was readily measured at the Washington, D. C. infrasonic station.

Let us look into the characteristics of a few of the waves which spread out from the focus of an earthquake. The focus is the location on or near the surface at which the earthquake occurs (Figure 8). The epicenter is the point on the surface where a radius vector terminates on passing from the center of the earth through the focus. There are three waves of principal interest to our discussion. The first wave to arrive at a distant location is a longitudinal wave which has passed through the body of the earth; this
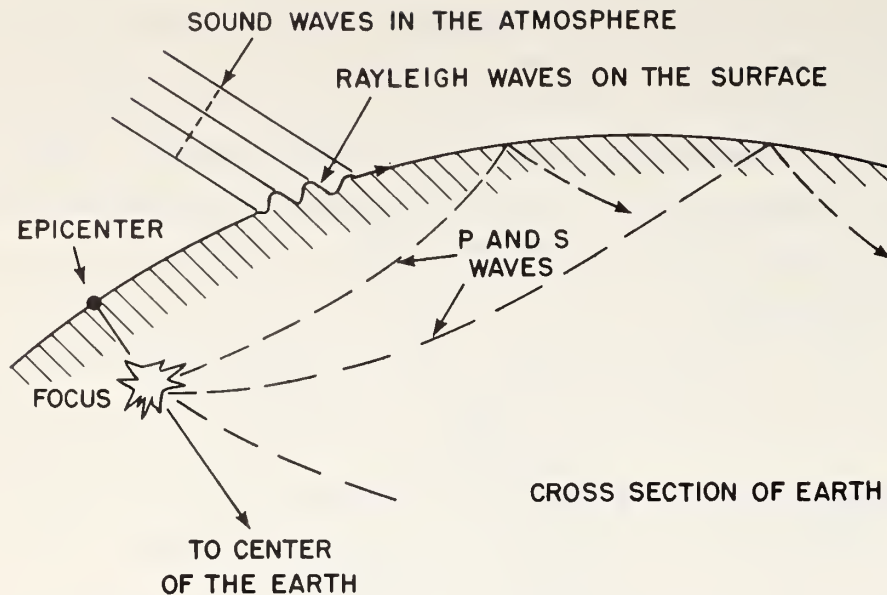
Figure 8. Seismic waves from the focus of an earthquake, and sound radiated into the atmosphere by the seismic waves.

is called a P_ wave. The second to arrive is a transverse or shear wave traveling more slowly and designated as an S_ wave.   The third wave, which travels entirely on the surface, is the Rayleigh wave. These three are accompanied by many others, for example, by P_ and S_ waves reflected from the boundary between the mantle and core 2900 km below the surface. From measurements of arrival times of the waves received at several seismological stations, the epicenter and focal depth of an earthquake can be determined very accurately.

Montana Earthquake

The great earthquake in Montana at 0637.27 UT on August 18, 1959, produced seismic waves strong enough in the Washington, D. C. area to cause easily measured infrasonic waves in the atmosphere. The epicenter in Montana was 2860 km away from the Washington infrasonic station on a great-circle bearing 66° west of north.

The sound radiated by the P_ wave arrival was obscured by wind noise and microbaroms and could not be distinguished with certainty. The arrival of the S_ waves (shear waves) produced measurable infrasound, from which it was deduced that the shear waves came from 44° west of north with a period of oscillation of 11 sec and a horizontal trace velocity of 6.0 km/sec. The

arrival was from a direction 22° north of the great-circle bearing. The earth's displacement in Washington, deduced from a peak-to-peak sound pressure of 0.8 dyn/cm^2, was 0.34 mm.

The very strong Rayleigh waves had periods initially of about 15 sec, which shortened to about 8 sec after a minute or so. This change came about because the group velocity of the 8-sec waves was less than for the 15-sec waves, and so it took longer for the 8-sec waves to travel across the country to Washington. The earth's displacement, calculated from the large peak-to-peak sound pressure of 5 dyn/cm^2, was 3.0 mm. The average trace velocity of the Rayleigh waves was 3.8 km/sec. They came mainly from the great-circle direction of the epicenter, with the later waves coming from a slightly more northerly direction.

We can only conjecture about the reason for the arrival of the seismic waves from directions mostly north of the great-circle bearing. Refraction on passing from the Appalachian Mountains onto the Piedmont Plateau might have been the cause.

Acoustical Radiation Zones

An interesting feature of the sound radiated into the atmosphere by Rayleigh waves is that the sound pressure at any point on the surface is due to the integrated effect of an extensive area of the traveling waves. This is in contrast to a seismometer, which measures the earth's displacement only at the spot where the instrument is located.

We present the results of an analysis showing how much of the traveling wave motion is effective in producing sound pressure at a point just above the surface. For a long train of sinusoidal surface waves of wavelength λ_o, the waves in a circular area of radius $4 \lambda_o$ contribute at least 70 percent to the amplitude of the sound pressure at the center of the circle. We call this circular area the "radiation zone" for the sound pressure produced by the surface waves. If the Rayleigh waves have a period T = 25 sec, then λ_o = 88 km, and so R = $4 \lambda_o \approx 350$ km; this is the radius of the radiation zone for such long waves. Fuller details have been given by Cook (1965).

Ionospheric Motions

At the time of the Alaskan earthquake on March 28, 1964, Rayleigh waves of considerable amplitude passed across the United States. The sound waves which they produced at infrasonic frequencies were propagated upward and

caused substantial motions of the ionosphere.

We examine first the equation for propagation of a sound wave into the less dense regions of the upper atmosphere. We recall that the sound wave travels almost vertically upward in a direction arcsin $(c/c_o) \approx 6°$ from the vertical. The main features of the propagation can therefore be seen from a consideration of plane waves of sound traveling vertically upward parallel to the z - axis in an approximately isothermal atmosphere. The differential equation for the particle velocity v in the waves is

$$\frac{\partial^2 v}{\partial z^2} - \frac{\gamma g}{c^2} \frac{\partial v}{\partial z} = \frac{1}{c^2} \frac{\partial^2 v}{\partial t^2} \qquad (2)$$

In this $c^2/\gamma g = H$ = the scale height of the atmosphere ≈ 8.4 km (in the lower atmosphere), for $\gamma = 1.40$, and $g = 9.8$ m/sec^2, $c = 340$ m/sec. The density ρ of the atmosphere as a function of altitude z is given by $\rho = \rho_o \exp(-z/H)$. The particle velocity v, obtained from equation (2) for sinusoidal waves $(\omega = 2\pi/T)$ is

$$v = |v_o| \exp (z/2H) \cos \left[\omega t - z \sqrt{k^2 - (1/2H)^2}\right] , \qquad (3)$$

where $|v_o|$ = amplitude of vibration at ground level (z=o). From this we see that for vertically traveling sound waves in the atmosphere, the amplitude of vibration varies inversely as the square root of the atmospheric density.

Let us see how this applies to the Rayleigh waves from the Alaskan earthquake. The infrasonic stations at Boulder and Washington measured sound pressures of about 20 dyn/cm^2, the period T of the waves being of the order of 25 sec. These very substantial sound pressures correspond to vertical surface motions $|v_o| \approx 0.5$ cm/sec. A wave that starts out with an amplitude of 0.5 cm/sec will increase to an amplitude of about 10^4 cm/sec at an altitude of 160 kilometers.

A little before it reaches this altitude the sound wave becomes a discontinuous shock wave. From the analysis that follows we can estimate the altitude Z at which this occurs. In a real gas the pressure-crests in a sound wave continually gain on the troughs, since the crests have the excess velocity $|v|$ computed above. The atmospheric waves start out sinusoidal, and the time T' at which the crests overtake the troughs and discontinuity begins is given by

$$\frac{\lambda}{2\pi} = \int_0^{T'} |v| dt = \int_0^{T'} |v_o| \exp(ct/2H) \, dt = 2(H|v_o|/c) \left[\exp(cT'/2H) - 1\right]. \qquad (4)$$

The foregoing is based on Lord Rayleigh's (1945) analysis. Continuing, we find that the altitude z is approximately

$$Z = cT' = 2H \log \lfloor 1 + c\lambda/4\pi |v_o| H \rfloor \approx 138 \text{ km.} \tag{5}$$

From the foregoing analysis we estimate that the oscillatory vertical motions of the atmosphere at higher altitudes, caused by the Rayleigh waves, are of the order of hundreds of meters per second.

We consider next the results of observations on ionospheric motions near Boulder, Colorado. These observations were made by Mr. Donald M. Baker of ESSA's Boulder Laboratories. He sent radio waves almost vertically upward and observed the waves reflected from the ionosphere back down to a receiving station on the ground. At the time the Rayleigh waves passed through the Boulder area, Doppler shifts of more than 3 Hz occurred for the radio waves at 4 MHz. Such shifts correspond to a vertical motion of the ionosphere, at the 4 MHz reflection height of about 240 kilometers, of more than 200 meters per second. Similar Doppler shifts occurred in the 10-MHz radio wave propagated from the standard-frequency station WWV in Hawaii and received in Boulder, but it is difficult to estimate the geographical area of the ionosphere from which reflections might have occurred.

The Doppler shifts started about 9 min after the Rayleigh waves arrived at Boulder. The sound waves travel vertically upward with an average velocity c of about 1/3 km/sec up to an altitude of 140 km. At higher altitudes the velocity c is about 700 m/sec. The computed transit time to the ionosphere at an altitude of 240 km is therefore less than 10 min, which is confirmed by the observed transit time of 9 min.

We conclude from the foregoing that the Rayleigh waves traveling across the continental United States from the Alaskan earthquake produced sound waves which, on propagation upward through the atmosphere, caused substantial motions of the ionosphere.

The absorption and dissipation into heat energy of the sound waves takes place in the ionosphere. This can be seen from the results of the measurements. These show that the intensity on entering the ionosphere is at least of the same order of magnitude as the computed intensity, the latter being based on no absorption in the lower atmosphere. We can estimate the total energy dissipated. The intensity of the sound waves traveling upward was about 10 erg/(cm^{2}sec) for about 300 sec. Therefore the total sound energy carried up into the ionosphere, and there dissipated as heat, was roughly

6×10^{20} ergs for the area of North America (about 20,000,000 km^2). This surprisingly large energy is to be compared with the total estimated seismic energy released by the Alaskan earthquake, which was about 10^{24} ergs.

4.4 Microbaroms

Natural sounds in the atmosphere having dominant periods of oscillation between 4 and 7 sec seem to be particularly widespread and are commonly called microbaroms. They are characterized by their persistence at a given geographic location for many hours, by a rather constant period of oscillation, and by an amplitude which seldom exceeds 3 or 4 dyn/cm^2 in the area of Washington, D. C. Microbaroms of 4-sec periods were observed by Gutenberg and Benioff (1941) at Pasadena in southern California. They found the microbaroms to be sound waves traveling approximately parallel to the earth's surface and coming from a direction southwest of Pasadena. Saxer (1945, 1953-54) and Dessauer et al (1951) observed microbaroms at Fribourg in Switzerland. They found the waves traveling parallel to the earth's surface to come from a direction northwest of Fribourg, with periods ≈ 5 sec, and sound pressures $\approx 0.5 - 1$ dyn/cm^2. Furthermore, the sound pressures seemed to be correlated with the heights of water waves in the north Atlantic Ocean due to storms and with the strength of microseisms in the earth observed at Strasbourg (about 200 km north of Fribourg). Observations on microbaroms in the Washington area will be discussed later.

What causes microbaroms? Similarities between them and microseisms on the earth's surface suggest that one causes the other. But it can be easily shown that, on the one hand, the sound waves radiated into the atmosphere by microseisms are much weaker than microbaroms. On the other hand, sound pressure of the latter on the earth's surface is not strong enough to produce observable microseisms (Cook and Young, 1962).

It had long been conjectured (e.g., Daniels, 1962) that the gravity waves created by storms on the surfaces of the seas radiate sound into the atmosphere. In the analysis that follows we shall introduce quantitative expressions showing that long trains of such waves cannot radiate sound power, because their phase velocities are less than the phase velocity $\underline{c}$ of sound in the atmosphere. On the other hand sound power radiation can occur (a) when the waves come to an abrupt stop as, for example, on the beach, and (b) when waves traveling in different directions have an interference pattern which causes periodic oscillations in the potential energy of the atmosphere over the waves.
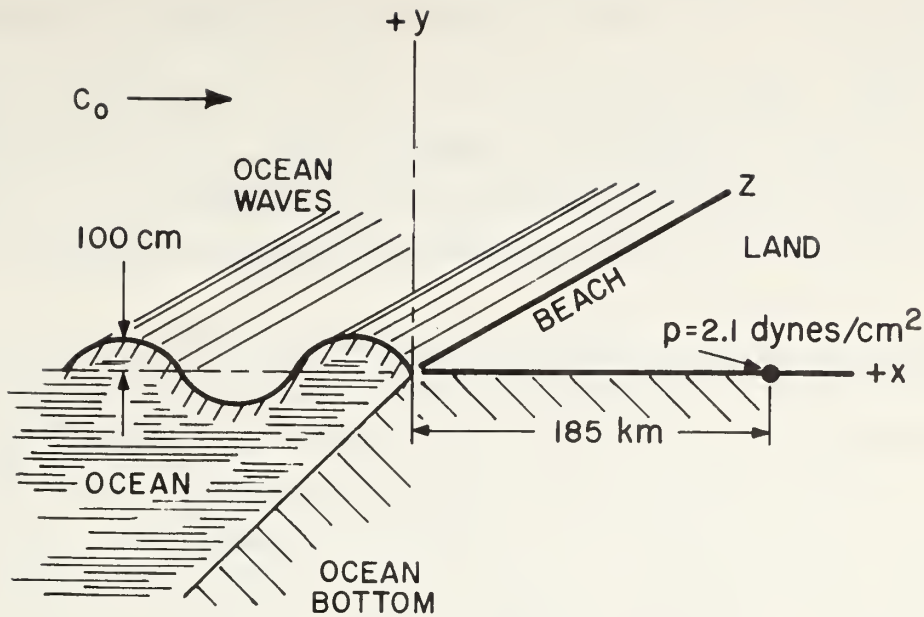
Figure 9. Radiation of infrasound by a semi-infinite wave train on a water surface.

Radiation by an infinite train of surface waves on water

We consider first a sinusoidal gravity wave on water, of amplitude A and period T, the wave fronts being straight lines parallel to the z-axis. (See Figure 9). We suppose the depth to be substantially greater than $\frac{1}{k_o} = \lambda_o/2\pi$ (λ_o = wavelength), and so the deep-water wave speed is $c_o = gT/2\pi = g/\omega$, where g = acceleration of gravity. Therefore the surface displacement can be represented by

$$y_o = A \exp i(\omega t - k_o x) \qquad (6)$$

for all x.

In the atmosphere above the water a distribution of sound pressure and particle motions is caused by the surface wave. The velocity potential for this distribution must satisfy the sound wave equation and the boundary condition at the water surface. The final result is that the sound pressure in the atmosphere above the water is

$$p = \frac{\rho c \, \omega A}{\sqrt{\beta^2 - 1}} \exp\left[-\sqrt{k_o^2 - k^2} \; y \div i(\omega t - k_o x) \right] \qquad (7)$$

where ρ = density of the atmosphere, c = speed of sound, $\beta = c/c_o$, and k = ω/c.

Note that the sound pressure at the water surface is in phase with the displacement. Hence no net work is done and no sound power is radiated into the atmosphere.

For water waves of period T = 2π = 6.28 sec, ω = 1.0/sec, c_o = 9.80 m/sec, and λ_o = 61 meters. Suppose the displacement amplitude A = 100 cm. Then the sound pressure at the water surface is $|p| \approx 120$ dyn/cm^2. But at a height of 100 m above the surface the sound pressure is reduced by a factor of $e^{-10} \approx$ 1/22000 to less than 10^{-2} dyn/cm.

Radiation by a semi-infinite wave train

We consider next a sinusoidal gravity wave on water coming from $-\infty$ and stopping abruptly at x = 0, the wavefronts again being straight lines parallel to the z-axis (see Figure 9). The surface displacement $\underline{y_o}$ is the same as in Eq. (6) for $-\infty < x < 0$, and y_o = 0 for x > 0. We imagine the line x = 0 in the xz-plane to be the beach, and the region x > 0 to be the landward side.

The velocity potential ψ for the total wave field at y = 0 is readily found by superposition of the hemicylindrical waves generated by each line element, parallel to the z-axis and of width $\underline{du}$, of the surface waves.

$$\psi = -\frac{\omega A e^{i\omega t}}{2} \int_{-\infty}^{0} [J_o(kx - ku) - i\, Y_o(kx - ku)] e^{-ik_o u} \, du \tag{8}$$

for x > 0.

A good approximation to this integral is found as follows. We first replace the Bessel functions J_o and Y_o by the first terms of their asymptotic expansions. This leads to a Fresnel integral expression for $\underline{\psi}$, whose asymptotic form for large $\underline{x}$ yields

$$\psi \sim \frac{cA}{\sqrt{2\pi}\,(\beta-1)} \frac{(-i e^{\pi i/4}\, e^{i(\omega t - kx)}}{\sqrt{kx}} . \tag{9}$$

From this we find the sound pressure on the landward side (x >> 0) to be

$$|p| = \frac{\rho cA}{(\beta-1)T} \sqrt{\frac{\lambda}{x}} , \tag{10}$$

where λ = wavelength of the atmospheric sound. As before we suppose the water waves to have a period T = 2π sec and A = 100 cm. Then β = 35 and λ = 2130 m. At a distance x = 185 km from the beach, the sound pressure will be 2.1 dyn/cm^2.

Suppose the wave starts abruptly at the beach x = 0 and travels towards x = $-\infty$. We find the sound pressure on the landward side to be almost the same as before; for such a wave the factor β - 1 in Eq. (10) above is replaced

by $\beta + 1$. Therefore a standing wave caused by reflection of an incoming wave by a beach will also give rise to a radiated sound field.

Since an infinite wave train radiates no sound power, whereas there is radiation by a semi-infinite train stopping abruptly at x = 0, we can imagine that the radiated power is due to a line source on the beach. The assumption is not strictly correct, but we can use it to estimate the power by means of Eq. (10). For the water waves of the period $\underline{T}$ and amplitude $\underline{A}$ considered above, we find the radiated sound power to be about 30 kW per kilometer of beach.

Radiation by a standing wave

A theory, analogous to the Longuet-Higgins analysis for the generation of microseisms, explains the generation of microbaroms by standing water waves associated with marine storms. The theory is based on the vertical oscillations of the center of gravity of the atmosphere immediately above the standing waves, which might be near a beach as well as out at sea. The frequency of oscillation of the atmosphere's gravitational potential energy is twice that of the ocean waves. The varying potential energy has a radiated sound field ossociated with it, with sound waves at twice the ocean wave frequency. Full details of the analysis have been given by Posmentier (1967) and by Brekhovskikh (1968).

Comparison with observed microbaroms

The foregoing (for waves on a beach) analysis is for the idealized case of straight-line wavefronts of infinite length, the waves being perpendicularly incident on a straight-line beach. But natural beaches are not very straight; the waves arriving at one point might not be coherent with those arriving at a point on the beach a few kilometers away; the strength of the wave can be affected by reflection from the upper atmosphere; etc. The mathematically derived sound field of Eq. (10) can therefore be expected to yield only order-of-magnitude estimates for sound pressures at a large distance from a beach.

Microbaroms have been observed in the Washington area with the infrasonic system described in Section 3. The Atlantic Ocean beach is 185 km east-south-east of the infrasonic station. Generally speaking, the microbarom sound waves come from the east and travel parallel to the earth's surface. They appear at almost all times of the year, and occasionally have sound pressures as great as 6 dyn/cm^2. For a typical recording made on March 11, 1961, $T \approx 5.5$ sec and $p \approx 1$ dyn/cm^2. On the basis of the analysis given above, microbaroms

at Washington could be caused by waves on the Atlantic Ocean beaches ranging in amplitude from about 20 cm to 100 cm.

Fribourg (Switzerland) is about 650 km from the Atlantic Ocean beach on the west coast of France. Microbaroms observed at Fribourg often had daily average sound pressures ≈ 0.4 dyn/cm^2. From the above analysis the expected pressure at Fribourg due to ocean waves of A = 100 cm would be 1.0 dyn/cm^2. But the sound waves were reported as arriving from a northwest direction. The Atlantic Ocean is about 1500 km away in this direction, beyond north Ireland and Scotland. It seems that the standing-wave hypothesis can account for the microbaroms observed at Fribourg by Saxer and Dessauer.

4.5 Subsonic Oscillations

The passage of a jet stream in the atmosphere over the eastern (Atlantic) seaboard of the United States is occasionally accompanied by large oscillations in barometric pressure at infrasonic frequencies. The jet stream is a thin layer of fairly high speed wind. The location of the layer in the atmosphere is in the neighborhood of the tropopause, at an altitude of about 10 km. The thickness of the stream is about three kilometers. The wind speed along the axis is at least 30 m/sec, and sometimes as great as 80 m/sec. The wind blows towards a direction between northeast and southeast, and the width of the stream (in a direction transverse to the direction of flow) is generally at least 100 km.

An important characteristic is that the periods of oscillation are usually greater than the resonant period $T_R \approx 300$ sec of the atmosphere (see Section 2.4). Since, as we recall, the phase velocities for plane waves of such long periods are substantially less than the high-frequency sound velocity, the waves may be called subsonic oscillations.

The results of observations made at our station in Washington show that almost all sound waves coming from subsonic oscillations of the jet stream have wavefront surfaces of constant phase which are almost plane. The sound pressure has the following features when the jet stream is blowing. (1) The direction of propagation of lines of constant-phase sound pressure across the Washington area is very close to the direction of the jet stream over Washington. (2) The horizontal phase velocity c_o = 30 to 100 m/sec is about the same as the speed of the jet. (3) The sound pressures are mainly in the range 50 - 400 dyn/cm^2. (4) Periods of oscillation T = 300 to 1000 sec.
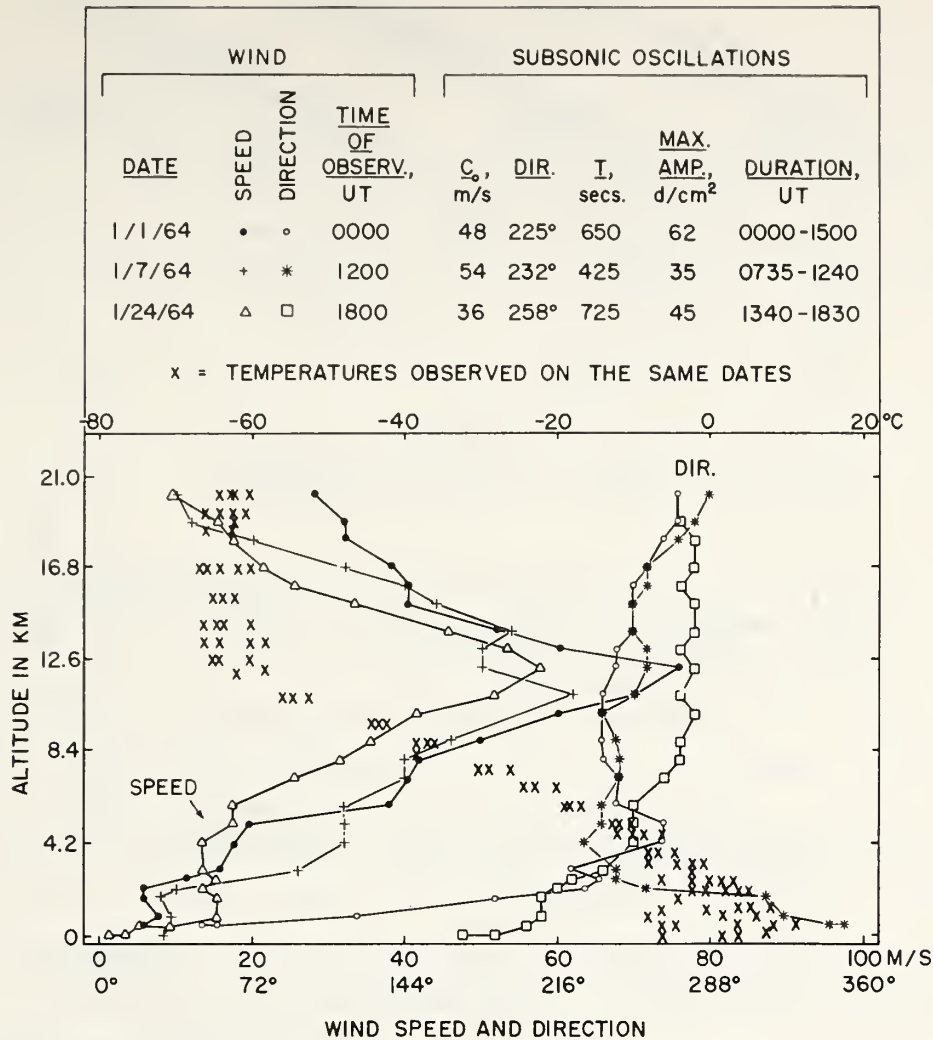
Figure 10.   Observations on jet stream oscillations.

A brief summary of a few observations made in Washington is given in Figure 10.   The data show the correlations between the features of the sound pressure, and the characteristics of the jet stream causing the sound pressure. The waves observed at the Washington station have been studied in detail by Mary W. Hodge and her associates (1968).   Further data on the Washington waves have been summarized by A. J. Bedard, Jr. (1966).   Sound pressures caused by the jet stream have been also observed elsewhere; a comprehensive report on waves in the Boston, Massachusetts, area has been prepared by Elizabeth A. Flauraud and her associates (1954).

The sound pressure probably has its origin in flow instability of the jet stream.   The mechanism of the instability is not known.   We can conjecture
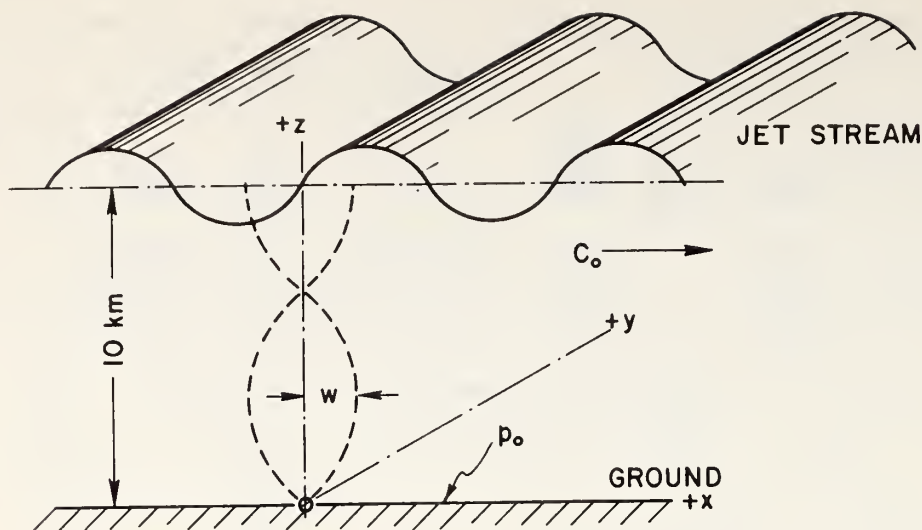
Figure 11.   Radiation of sound pressure by jet stream oscillations. w = ver-
tical component of the atmospheric particle velocity at altitude
z. P_o = pressure at ground level.

that it arises from a combination of viscous shear between the jet stream and
the surrounding atmosphere, and unstable temperature gradients. We assume
that the jet stream oscillations force the atmosphere into oscillation. The
well-known equations of motion for sound waves in a wind-free atmosphere (see
Lamb, 1945) can be used to determine the relationship between the sound pres-
sure measured at the ground and the assumed oscillatory displacement of the
jet. The basic idea is that the atmosphere between the oscillating jet stream
and the surface of the ground is filled with downward-traveling plane waves,
and reflected upward-traveling waves, with both waves having a forward compo-
nent of phase velocity the same as the speed of the jet stream. Figure 11 is
a schematic drawing for the mathematical analysis that has been carried out in
detail by Cook (1968), under the following physical assumptions. (1) The at-
mosphere is isothermal and wind-free. (2) The waves are sinusoidal in time,
and all quantities vary like $\exp(i\omega t)$. (3) All motions are in the x-z plane,
and so the particle velocity, with components u, v, w, has its y-component
$v \equiv 0$. (4) The traces of the straight lines of constant-phase sound pressure
on the x-y plane have a phase velocity $c_o = \omega/k_o$, and so all quantities vary
as $\exp(-ik_o x)$; the waves are advancing in the (+x) direction. The equations
of motion finally yield the following expression for the amplitude of the
vertical component of particle displacement at the altitude z = 10 km of the
jet stream:

$$\Delta z = 2H(k_o^2 - k^2) \, |P_o| / \beta \gamma B k^2 \qquad (11)$$

where H = scale height of the atmosphere = $c^2/\gamma g$ = 8.1 km for an isothermal atmosphere with c = 333 m/sec. Also c = ω/k, γ = 1.40, and $\underline{\beta}$ is a real number for a typical subsonic oscillation. As an example, consider a wave with T = 500 sec, c_o = 33 m/sec ($\approx$ c/10), and $|P_o|$ = 200 dyn/cm^2. We find Δz = 60 m, which must be the jet stream's vertical oscillatory displacement at an altitude of 10 km necessary to produce the measured sound pressure at the ground.
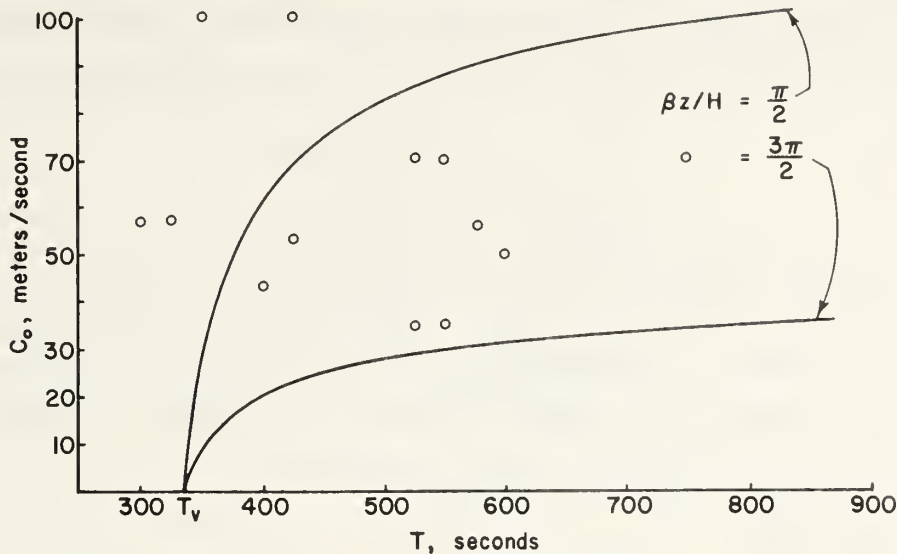
Figure 12. Horizontal phase velocities at various oscillation periods. Solid lines = theoretical velocities. 0 = observed velocities.

Standing-Wave Hypothesis

The mechanism of the oscillation is not known, and there is no obvious limitation on the vertical component β/H of the wave-number vectors. We examine the conjecture that the vertical component $\underline{w}$ of the particle velocity (which is zero at the ground) has a maximum at the jet stream's nominal altitude of 10 km (see Figure 11). The analysis shows that this occurs approximately when

$$\beta z/H = \pi/2, \ 3\pi/2, \ 5\pi/2, \ \ldots \ \ldots \qquad (12)$$

Use of these values for $\underline{\beta}$ leads to a series of curves showing how the horizontal trace velocity c_o varies with the period of oscillation $\underline{T}$. Two of the curves are shown in Figure 12. The curves all start with c_o = 0 at T_v = 337 sec, this being the Väisälä period of stability oscillations for the isothermal atmosphere (c = 333 m/sec) under consideration. Also plotted are some

observed values of horizontal phase velocities corresponding to well-defined periods of oscillation for the jet stream over Washington during January 1964. The data do not seem to confirm the hypothesis of Eq. (12). But gravitational forces evidently play a substantial role in the generation mechanism, since most of the observed oscillations occur at periods greater than the Väisälä T_v.

Propagation to the Ionosphere

The displacement and velocity amplitudes in the jet-stream oscillation can be expected to serve as sources for radiation of subsonic wave power upward into the ionosphere. The equations of motion show that the amplitude of the vertical component $\underline{w}$ of the particle velocity increases exponentially with altitude.

$$|w| = w_j \exp[(z-10)/2H] , \tag{13}$$

where $w_j = (2\pi/T) \Delta z$ = the amplitude at $z = 10$ km. For the example given above, $T = 500$ sec, etc., we find that at an altitude of $z = 100$ km, $|w| \approx 100$ m/sec and $\Delta z \approx 9$ km. This estimate for $|\underline{w}|$ is greater than the phase velocity of the wave (≈ 30 m/sec). It appears that subsonic waves traveling upward will probably undergo substantial waveform changes, e.g., taking on a shock-wave configuration, well before reaching the ionosphere.

4.6 Shock Waves from Satellite Entry

The entry of a meteorite, artificial satellite, or other solid object into the upper atmosphere at supersonic speeds will generally produce an acoustical shock wave. Sometimes the shock wave strength is great enough so that it can be measured at an infrasonic station. For example, the entry of the Cosmos 213 rocket body into the atmosphere on April 19, 1968, was accompanied by a Mach cone whose shock wave was observed and measured at ESSA's infrasonic station in Boulder, Colorado. The paper-chart recordings of the shock wave's sound pressure at ground level resembled a single sine wave — a pseudo N-waveform — with a peak-to-peak sound pressure of 1.2 dyn/cm^2 and a duration of about 2.5 sec. The rocket body passed overhead through the ionosphere near Boulder at an elevation of 112 km, on a path almost parallel to the earth's surface.

The measurement system used at Boulder was the same as that described earlier (see Section 3.1). The band-pass filter was N6 S6 (see Figure 4). But an N-waveform of duration 2.5 sec has a Fourier transform with a substantial spectral density at higher frequencies, outside the N6 S6 "window." In short, the paper-chart recording was that of the N-waveform sound pressure

appreciably modified by the filter.

If an N-waveform is recorded and measured accurately, it can be used to deduce some information about the object producing the wave. For example, one can obtain the altitude of an artificial satellite during atmospheric entry, even if its large Mach number ≈ 25 is not accurately known. This is because the shock strength and duration in the so-called far field, at a miss-distance $\underline{h}$ (= altitude) moderately large relative to the greatest linear dimension ℓ of the object, is determined essentially by the following factors: (1) The geometrical size and shape of the object. (2) The ambient atmospheric pressure $\underline{B}$ at the altitude of the object. (3) The Mach number $\underline{M}$ of its supersonic speed. (4) The miss-distance $\underline{h}$. The pressure jump at the head of the N-waveform is given by

$$\Delta p = B(M^2 - 1)^{1/8} \times (\ell/h)^{3/4} \times (K_s D/\ell) \quad , \tag{14}$$

where D = an equivalent maximum diameter for the object, and K_s = its aerodynamic shape factor for supersonic speeds. The pressure jump Δp observed will be increased, because of the approximately exponential increase in ambient pressure, by a factor of about $e^{h/2H}$ when the shock wave propagates down to the ground. It will be increased also by a factor of 2 because of reflection at the ground surface.

REFERENCES

Air Force Cambridge Research Laboratories staff, 1965: Handbook of geophysics and space environments. Published by AFCRL of the U.S. Air Force.

Bedard, A. J., Jr., 1966: Some observations of traveling atmospheric pressure disturbances. National Bureau of Standards Report No. 9364.

Brekhovskikh, L. M., 1968: Radiation of infrasound into the atmosphere by ocean waves. Izvestiya Akademii Nauk SSSR, Fizika Atmosfery i Okeana, 4, 444-450.

Brown, R. F. Jr., 1963: An automatic multichannel correlator. National Bureau of Standards J. Research, 67C, 33-38.

Chrzanowski, P., G. Greene, K. T. Lemmon, J. M. Young, 1961: Traveling pressure waves associated with geomagnetic activity. J. Geophys. Res., 66, 3727-3733.

Chrzanowski, P., J. M. Young, G. Greene, K. T. Lemmon, 1962: Infrasonic pressure waves associated with magnetic storms. J. Phys. Soc. of Japan, 17, Suppl. A-2, 9-13.

Cook, R. K., 1965: Radiation of sound by earthquakes. Reports of the 5e Congrès International d'Acoustique, Liège, Belgium, Report No. K 19.

Cook, R. K., J. M. Young, 1962: Strange sounds in the atmosphere. Part 2. Sound, 1, No. 3, 25 - 33.

Cook, R. K., 1968: Subsonic atmospheric oscillations. Reports of the 6th International Congress on Acoustics, Tokyo, Japan, Report No. H-5-17.

Daniels, F. B., 1959: Noise-reducing line microphone for frequencies below 1 cps. J. Acoust. Soc. Am., 31, 529 - 531.

Daniels, F. B., 1962: Generation of infrasound by ocean waves. J. Acoust. Soc. Am., 34, 352 - 353.

Dessauer, F., W. Graffunder, J. Schaffhauser, 1951: On atmospheric pulsations. Archiv. Meteorol.Geophys. u.Bioklimatol. Series A 3, 453.

Flauraud, E. A., A. H. Mears, F. A. Crowley, Jr., A. P. Crary, 1954: Investigation of microbarometric oscillations in Eastern Massachusetts. Geophysical Research Papers No. V 27 of the Air Force Cambridge Research Center.

Goerke, V. H., J. M. Young, R. K. Cook, 1965: Infrasonic observations of the May 16, 1963, volcanic explosion on the Island of Bali. J. Geophy. Res., 70, 6017-6022.

Gutenberg, B. H., H. Benioff, 1941: Atmospheric pressure waves near Pasadena. Trans. Am. Geophys. Union, 22, 424-426.

Hodge, M. W., D. T. Volz, 1968: Possible relation of mesoscale surface pressure waves to the jet stream region and to clear air turbulence. Third Nat. Conf. on Aerospace Meteor., 557-563.

Lamb, H., Hydrodynamics. Dover Publications, New York (1945)

Matheson, H., 1966: A nomogram for determining azimuth and horizontal trace velocity from tripartite measurements. Earthquake Notes, 37, 33-37.

Passechnik, I. P., 1959: Seismic and airwaves which arose during an eruption of the volcano Bezymyanny, on March 30, 1956. Bull. Acad. Sci. USSR, Geophys. Ser., (English trans.) No. 9, 650-653.

Posmentier, E. S., 1967: A theory of microbaroms. Geophys. J. Roy. Astr. Soc., 13, 487-501.

Rayleigh, 1945: Theory of Sound, Vol. II, page 36. Dover Publications, New York.

Saxer, L., 1945: Electrical measurement of small atmospheric pressure oscillations. Helv. Phys. Acta., 18, 527.

Saxer, L., 1953-1954:   <u>Archiv</u>. <u>Meteorol</u>. <u>Geophys</u>. <u>u</u>. <u>Bioklimatol</u>.   <u>Series</u> <u>A</u> <u>6</u>, 451-463.

<u>U. S. Standard Atmosphere, 1962</u>.   Published by NASA, U. S. Air Force, and U. S. Weather Bureau.

Webb, W. L., 1964:   Stratospheric solar response.   <u>J</u>. <u>Atmospheric</u> <u>Sci</u>., <u>21</u>.

Wilson, C. R., S. Nichparenko, R. B. Forbes, 1966:   Evidence of two sound channels in the polar atmosphere from infrasonic observations of the eruption of an Alaskan volcano.   <u>Nature</u>, <u>211</u>, 163-165.

Wilson, C. R., S. Nichparenko, 1967a: Infrasonic waves and auroral activity. <u>Nature</u>, <u>214</u>, 1299-1302.

Wilson, C. R., 1967b: Infrasonic pressure waves from the aurora: a shock wave model.   <u>Nature</u>, <u>216</u>, 131-133.

Estimation of Radio Ray Attenuation in Convective Rainfalls

E. J. Dutton

Institute for Telecommunication Sciences and Aeronomy,[1] ESSA, Boulder, Colo.

(Manuscript received 19 January 1967, in revised form 9 March 1967)

ABSTRACT

A model is developed for use in estimating rainfall attenuation at frequencies above 3 GHz in showers and other types of sporadic rainfall, usually associated with atmospheric convective activity. The model assumes a spherical distribution of rainfall rate in an individual shower. The approximate rainfall attenuation and its maximum expected value are calculated at 10 GHz through a severe thunderstorm, and through some shower patterns. The variation of attenuation as individual cells move along a ray path is also given. It is concluded that this method of attenuation estimation could be particularly useful in analyzing radar data to determine the attenuation effects of convective activity.

1. Introduction and background

Rainfall attenuation of radio propagation plays an important role in point-to-point ground communication, although estimation of its variation is made difficult by the complexity and variability of storm systems. An effort is made here to distinguish local, convective rainstorms from more widespread storms and to examine their particular influence on radio attenuation.

The attenuation per unit length in the direction of propagation of a radio wave is referred to as the attenuation coefficient of the radio wave. A frequent assumption (Ryde and Ryde, 1945; Battan, 1959; Medhurst, 1965) for this attenuation coefficient K_p is

$$K_p = k_2 R^\gamma \qquad (1)$$

in the frequency region 3 to 30 GHz, where R is the precipitation rate. The parameters k_2 and γ are frequency dependent, and can be determined by graphical interpolation between the known data points, given in Battan (1959).

Three-dimensional distributions of R along a given transmission path are thus vital to the appropriate determination of total rainfall attenuation along that path. A systematic vertical variation of R, decaying with height above a measured surface value, seems to be appropriate in rainfall of a widespread (continuous) nature (Atlas and Kessler, 1957). Widespread rainfall is usually triggered by a relatively large-scale mechanism, such as a frontal or monsoon situation. A vertical variation of R of the form

$$R = R_0 \exp(-ch^2) \qquad (2)$$

can be assumed to be appropriate under continuous rainfall conditions (Rice *et al.*, 1965; Atlas and Kessler, 1957). In (2), R_0 is the surface rainfall rate, h the height above the earth's surface, and c a constant.

Convective-type precipitation, however, seems to show a quite different nature. The presence of virga (precipitation aloft) associated with so many shower-type clouds indicates that (2) is not especially representative of shower rainfall. This is because (2) implies R decays with height from its surface value (which for the virga case is equal to zero). Dennis (1963) has done considerable work in examining rainfall determinations in shower-type activity. His observations show that the reflectivity factor Z (mm⁶ m⁻³) of an element of a vertical slice taken through a spherical shower cell is well represented by a regression line of the form

$$Z = c_1(r_0 - r)^{c_2}. \qquad (3)$$

In (3), r is the distance from the center of the cell of radius r_0, and c_1 and c_2 are positive constants.[2] Earlier observations by Hartel *et al.* (1961) provide further justification for the use of (3).

More recently, data from a report by Culnan *et al.*[3] working at gigahertz frequencies and some data from the National Severe Storms Laboratory, ESSA, Norman, Okla., show distributions of reflectivities tending to confirm (3). Fig. 1 shows a sample of the Culnan *et al.*, data recorded at 9.1 GHz. The contours describe radar reflectivity η(m⁻¹) values and are plotted in decibels relative to 1 m⁻¹. The radar reflectivity is proportional to Z, and, if the frequency is known, Z can be recovered from η (Battan, 1959). Fig. 2 shows

---

[2] In the computations of Section 3, c_1 is taken as 560 and $c_2 = 2.5$, for r and r_0 in nautical miles (Dennis, 1963).

[3] Culnan, D. E., F. O. Guiraud and R. E. Skerjanec, 1965: Radio scattering cross sections of thunderstorms (unpublished report).

a redrafted composite of photos of the PPI scope displaying the NSSL data taken near Oklahoma City. The contours here are Z in decibels with respect to 1 mm^6 m^{-3}. There is a slight distortion introduced into Fig. 2 because a portion of the polar coordinate representation has been transformed into rectangular coordinates in the figure.[4] Both Figs. 1 and 2 show a concentric tendency of the contour lines.

There are many empirical relations (Battan, 1959; Harrold, 1965) for the determination of R from Z. One of the most common is

$$Z = 200R^{1.6} \qquad (4)$$

for rain. In (4), Z is expressed in mm^6 m^{-3} and R is expressed in mm hr^{-1}. Much heavy convective activity contains hail. Formulas for Z, such as those given by Douglas (1964) for hail, may be acting in combination with formulas like (4) for rain, although in the present discussion they have not been considered.

In the vicinity of the 0C isotherm height, the so-called "bright band" occurs. Byers and Braham (1949) indicate that most convective activity does not show well-defined bright bands. Therefore, it has been assumed that only rainfall in the form of (4) will be a significant contributor to (3), and that (3) represents a *three*-dimensional spherical distribution of Z.

2. Theory

All of the above would suggest that the reflectivity in a shower cell, for both light showers and heavier thunderstorms, could be approximated by a spherical distribution model such as (3). If such a relation is

FIG. 1. Vertical radio cross section (η contours in db relative to 1 m^{-1}) of a thunderstorm, 1531 MST 27 July 1964, 9.1 GHz, near Akron, Colo.

[4] It should be pointed out that in the case of the Culnan *et al.* (1965), and the NSSL data, no regressions were run confirming (3). The conclusions are strictly "eyeball." Also, all the data of this paper are taken in areas with a high degree of continentality. The c_1 and c_2, or even the form of (3), might well be modified over water or in the presence of additional orographic effects.

FIG. 2. Horizontal WSR-57 radar cross section (Z contours in db relative to 1 mm^6 m^{-3}) of a thunderstorm, 1959–2000 CST 18 April 1963, near Norman, Okla.

indeed true, then it is necessary to know the position of the cell with respect to the transmission path, and to determine precipitation rates from Z in order to calculate total path attenuations.

With some knowledge of the distribution of the number, size and location of shower cells in an area of interest, one needs first to consider the attenuating characteristics of an individual cell. Then, as is done for some sample paths in the next section, one can sum all the individual cells affecting the path of interest. By employing (3) and (4), we obtain as a model for the rainfall rate,

$$R^\gamma = M(r_0 - r)^k, \qquad (5)$$

where $M = (c_1/200)^{\gamma/1.6}$, $k = c_2\gamma/1.6$, and $\gamma > 0$. The total integrated rainfall attenuation τ using (1) and (5), is given by

$$\tau = \int_{s_1}^{s_2} K_p ds = \int_{s_1}^{s_2} k_2 R^\gamma ds = \int_{s_1}^{s_2} k_2 M(r_0 - r)^k ds, \qquad (6)$$

where ds is an element of the ray path length, $s_2 - s_1$, in a shower cell. In order to integrate (6), it is necessary to establish a relationship between r and s.

Consider the cross section of the cell model of radius r_0 shown in Fig. 3. This cell is assumed to be centered at the lifting condensation level (LCL) which is approximately the height of maximum reflectivity in convective precipitation.[5] It is convenient to use the LCL because its height can be computed from surface meteorological measurements (Hewson and Longley, 1944). Fig. 3 makes the assumption that the path is a straight line through the cell. This assumption is probably valid in that there is very little bending in a cell;

[5] Although this assumption is made throughout this paper, it has been shown (Donaldson, 1961; Holtz and Marshall, 1966) that the height of maximum precipitation is variable and can be found as high as 10 km.
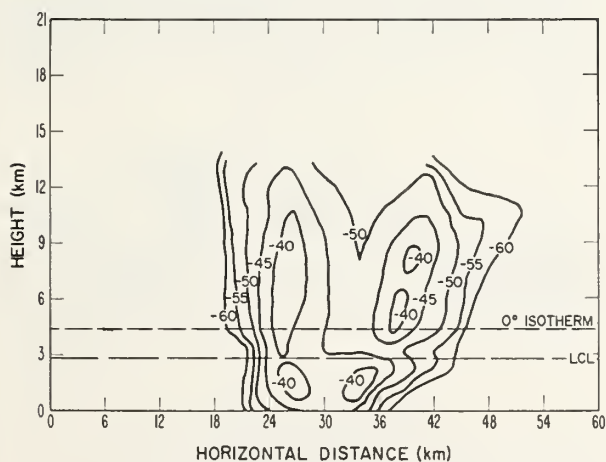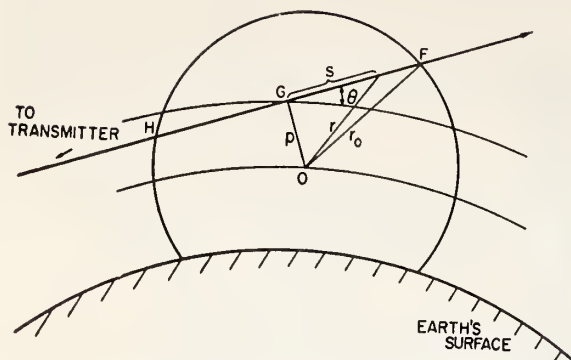
FIG. 3. Geometry used in calculating the attenuation in a spherical convective precipitation cell.

the smaller the cell, the less the bending. Also, in what follows, the "tilt" of the ray is determined at the height directly above, on, or below the center of the storm, which makes the tilt (elevation) angle an average of all the elevation angles that the ray assumes in the storm.

For the arbitrary ray path in Fig. 3,

$$r = \sqrt{s^2 + p^2}, \qquad (7)$$

where p is the perpendicular distance from the cell's center to the ray path. Using (7) and spherical symmetry, the total rainfall attenuation τ_i along the portion of the ray path, HF, passing through the cell centered at O (Fig. 3), is

$$\tau_i = 2k_2 M \int_{GF} (r_0 - r)^k ds$$

$$= 2k_2 M \int_0^{s_1} [r_0 - (p^2 + s^2)^{\frac{1}{2}}]^k ds, \quad (8)$$

assuming the origin of s at G and $s = s_1$ at F.

The evaluation of (8) can be approached by numerical integration methods. Also, for some *special* values of k, (8) can be integrated in closed form. In what follows, (6) and the geometry of Fig. 3 are used to evaluate an upper bound of (8).

Since

$$s \leq r, \qquad (9)$$

the inequality

$$r_0 - r \leq r_0 - s, \qquad (10)$$

results. Furthermore, since $r_0 - s$, $r_0 - r$ and k are all positive, another inequality

$$(r_0 - r)^k \leq (r_0 - s)^k, \qquad (11)$$

also results. Integration of (11) between 0 and s_1, along s, yields

$$\int_0^{s_1} (r_0 - r)^k ds \leq \int_0^{s_1} (r_0 - s)^k ds, \qquad (12)$$

whereupon, from (6)

$$\tau_i \leq 2k_2 M \int_0^{s_1} (r_0 - s)^k ds,$$

or

$$\tau_i \leq \frac{2k_2 M}{k+1} [r_0^{k+1} - (r_0 - s_1)^{k+1}]. \qquad (13)$$

The total rainfall attenuation τ is

$$\tau = \sum_i \tau_i,$$

for many cells affecting a ray path. An estimate of the maximum τ is thus obtained by summing the right hand side of the inequality (13) over all cells affecting a ray path. The same result as (13) can be obtained by assuming that the largest possible attenuation in a cell will occur when a ray path passes through the cell's center. In other words, $ds = dr$, and (6) can be integrated directly between 0 and s_1.

The remaining problem is that of obtaining s_1 and p from knowledge of only surface meteorological measurements. Since beams on ground based point-to-point paths are frequently transmitted with an initial elevation angle of $0°$, the low-angle refraction techniques of Schulkin (1952) can be employed in a method for obtaining p and s_1, assuming again from Fig. 3 that the ray path HF is a straight line.

Fig. 4 shows a ray leaving a transmitter at an initial elevation angle of θ_0. The ray intercepts a storm cell which is centered (in this case in the same vertical plane as the ray) at a great-circle distance d from the storm. In an atmosphere where the refractive index n is spherically stratified and horizontally homogeneous, the "tilt" or elevation angle θ of the ray at the distance
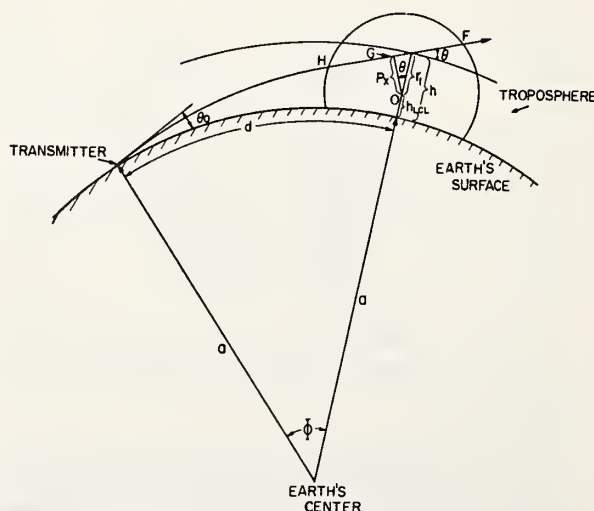

FIG. 4. Spherical convective precipitation cell geometry relative to earth's geometry in a vertical cross section.

d and height h is

$$\theta^2 = \theta_0^2 + \frac{2h}{a} - 2\Delta n, \tag{14}$$

where a is the earth's radius and Δn is the difference between surface n and n at the height h. Also, the angular bending of the ray Ψ is

$$\Psi = \Phi - (\theta - \theta_0) \cong \frac{2\Delta n}{\theta_0 + \theta}, \tag{15}$$

or

$$\Phi \cong \frac{2\Delta n}{\theta_0 + \theta} + \theta - \theta_0, \tag{16}$$

where Φ is the angle subtended by great circle distance d at the earth's center. Thus, after manipulation,

$$\theta^2 - \theta_0^2 + 2\Delta n = \Phi(\theta + \theta_0), \tag{17}$$

but also from (14)

$$\frac{2h}{a} = \Phi(\theta + \theta_0), \tag{18}$$

or

$$\theta = \frac{2h}{\Phi a} - \theta_0. \tag{19}$$

It can be shown that,[6] for the case of $\theta_0 = 0$,

$$h \cong \frac{d^2}{2ka}, \tag{20}$$

where k, called the effective earth's radius factor, is given by

$$k \cong \frac{1}{1 + a\dfrac{dn}{dh}}. \tag{21}$$

Values of k are given by Bean and Thayer (1959) for the normally expected exponential decay of n with h. However, in the following sections, dn/dh is assumed to be linear and equal to $-1/4a$ (Schelleng et al., 1933).[7] This makes $k = \frac{4}{3}$.

---

[6] Otherwise,

$$h = \frac{ka\left[\cos\theta_0 - \cos\left(\theta_0 + \dfrac{d}{ka}\right)\right]}{\cos\left(\theta_0 + \dfrac{d}{ka}\right)} \cong \theta_0 d + \frac{d^2}{2ka},$$

for small θ_0.

[7] The assumption that dn/dh is linear is reasonable over a sufficiently short interval in the lower atmosphere when well mixed convective-type conditions prevail (Bean et al., 1963). If, for example, the use of a linear dn/dh is restricted between 0 and 2 km in the troposphere, the use of typical values in the expected exponential character of dn/dh (Bean et al., 1962) indicates that the relative error incurred by using a linear dn/dh is only 4%.

Again for $\theta_0 = 0$, and defining

$$r_1 = h - h_{\mathrm{LCL}}, \tag{22}$$

where h_{LCL} is the height of the LCL, then from the geometry of Fig. 4 and (19)

$$\theta = \frac{2h}{d}, \tag{23}$$

$$p_x = r_1 \cos\theta. \tag{24}$$

If a storm center is a distance p_y from the vertical plane of the ray or beam axis, then

$$p = (p_x^2 + p_y^2)^{\frac{1}{2}}, \tag{25}$$

and

$$s_1 = (r_0^2 - p^2)^{\frac{1}{2}}. \tag{26}$$

3. Results and computations

The following computations were made for a frequency of 10 GHz, which causes the exponent k in (8) to come out equal to about 2.04. If it is assumed that $k = 2$, (8) can be integrated exactly to yield

$$\tau_i = 2k_2 M\left[p^2 s_1 + \frac{s_1^3}{3} - p^2 r_0 \ln\left(\frac{s_1 + r_0}{p}\right) \right]. \tag{27}$$

Eq. (27) then can be used to provide a comparison with the maximum attenuations obtained from (13) for 10-GHz computations. This has been done in the computations that follow.

Schleusener and Henderson (1962), working in eastern Colorado in the summers of 1961 and 1962, made a survey of the sizes of thunderstorms and hailstorms. Their results indicate that the largest cells were
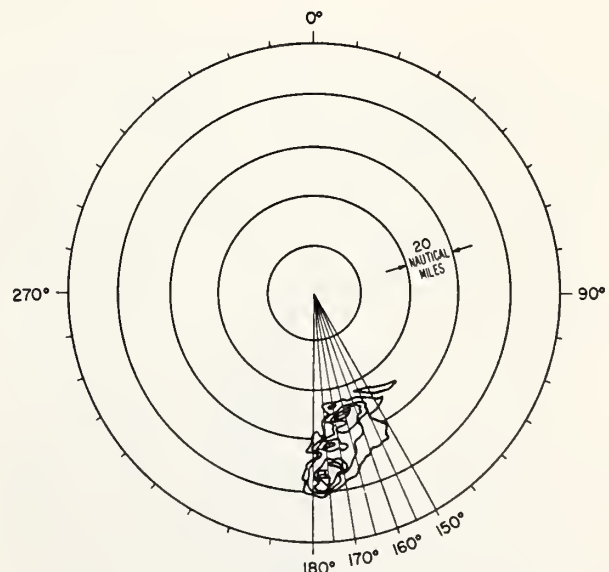

Fig. 5. Composite PPI scope picture of a large area of convective precipitation (Fig. 2 data).

about 6 km in radius, with some overlapping onto other cells when "bands" of showers were formed. These conditions do not appear to be typical of the central plains states of the United States, however. The NSSL data of Fig. 5 show that a cell of about 10–15 km radius can be expected in a severe storm.

A sample calculation of attenuations and their maximum values have been run for ray paths passing through the storm of Fig. 5. The paths were assumed to pass through the storm at azimuths between 150° and 180° (as marked on Fig. 5) at 5° intervals (except for a path at 167.5°). The initial elevation angle of the path was assumed to be 0° and the frequency of propagation was taken as 10 GHz. It was, of course, necessary to represent the storm in terms of spheres, so that their radii could be employed in evaluating (13), (26) and (27). The spherical representation (on a cross-section basis) is shown in Fig. 6. The choice of these particular radii is based entirely on the curvature of the contours in Fig. 5 and their intensities.

The results of the computation are shown in Fig. 7, where the points representing the actual calculations have been joined by straight line segments. Two sets of points denote attenuations calculated assuming the Z-R relationship of (4). However, Harrold (1965) notes that in thunderstorms the coefficient of $R^{1.6}$ can be as high as 350. Under the assumption, then, that

$$Z = 350R^{1.6}, \qquad (28)$$

the other two sets of points (joined by line segments) have been plotted on Fig. 7.

Fig. 8 shows another shower development as displayed on a PPI scope. These data are taken from Dennis (1963) and represent the development of small, isolated showers at Urbana, Ill., at 1440 CST 20 May
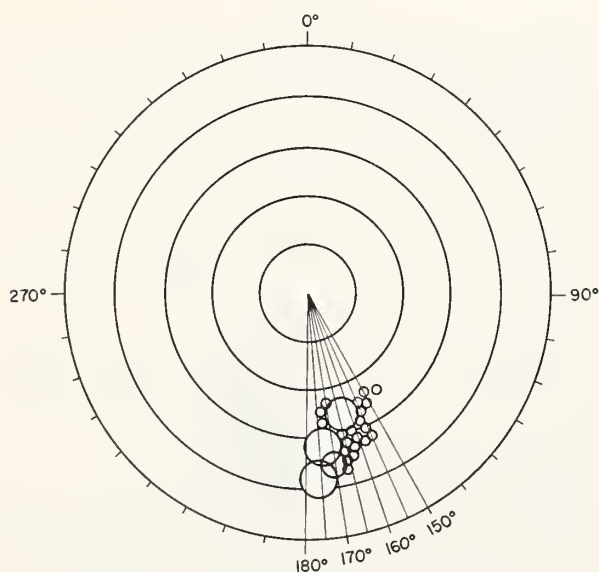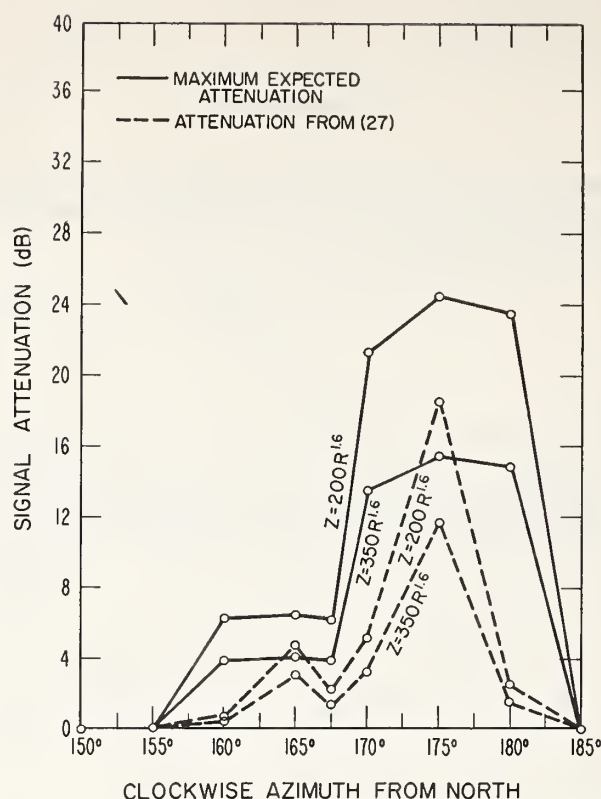

FIG. 7. Total 10-GHz attenuation along horizontal ray paths emanating at the radar site and passing through the cell arrangement of Fig. 6.

1960. The contributions to rainfall attenuation of cells lying along three ray paths (as labeled on Fig. 8) were computed[8] using (4), (13), and (27). These attenuations are shown in Table 1. The attenuations and their maximum values are much smaller as compared to some of these in Fig. 7, but this would be expected in a weak, showery, rainfall pattern.

Knowing the attenuations and their greatest values in individual cells, one can then arrange these individual cells along a ray path in any sort of three-dimensional pattern desired, and hence obtain an idea of total attenuation. A plot of attenuation of an individual cell placed at different locations along a given path is useful in seeing what an individual cell would contribute to the total attenuation in any given three-dimensional

FIG. 6. Replacement of storm in Fig. 5 with spherical precipitation cells.

TABLE 1. Rainfall attenuation for various paths in Urbana, Ill., shower situation.

Path (Fig. 8)	Maximum expected attenuation (db)	Attenuation from Eq. (27) (db)
No. 1	0.788	0.192
No. 2	0.288	0.061
No. 3	1.60	0.607

[8] In the computations involving Figs. 5 and 8, the difference in radii of cells as indicated on the PPI scope and the same cells centered at the LCL was negligible.

pattern along this path. Fig. 9 shows a plot of the 10-GHz attenuation and its maximum value along an initially horizontal radio ray. These values are obtained from (12) and (27) for an individual shower cell centered 1 km above the earth's surface and placed at several different distances from the transmitter along the earth's surface. The cell's center and the ray path are assumed to be in the same vertical plane. An effective earth's radius factor of $\frac{4}{3}$ is assumed. Fig. 9 shows the attenuation for three cells, each with different radii. One should note two things about Fig. 9. First, after a traverse of about 300 km, the ray is clear of even the
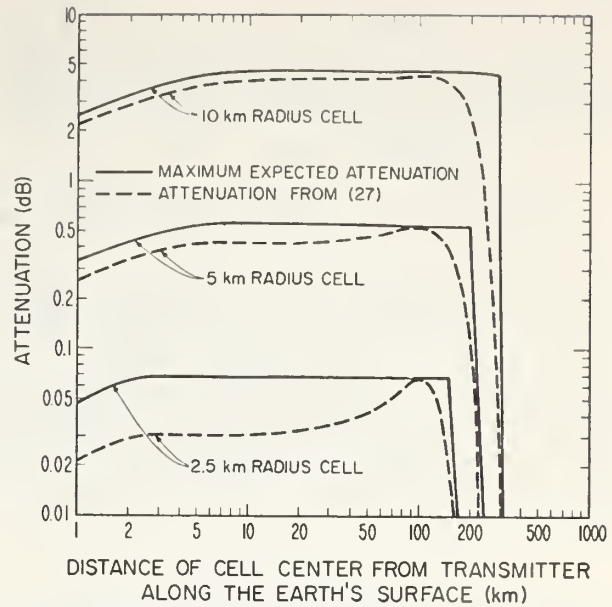
FIG. 9. Distance variation of attenuation caused by a single convective precipitation cell on a horizontal ray path at 10 GHz.

largest storms; second, the large reduction in attenuation as the cell's radius is made smaller is an especially salient feature.

Eq. (3) is a statistical result, and hence, more properly, should include the standard error of estimate, S.E. When this result is carried through to (13) and (27), a variation in the coefficient M can be obtained that corresponds to the S.E. of (3). However, in this paper the S.E. has not been considered because in the integration to obtain (13) and (27), it is assumed that, from the mean value theorem for integrals, the S.E. associated with (3) will effectively cancel out.

4. Conclusions

Based on many observations of signals reflected from convective storms, a spherical distribution has been applied to a particular storm cell in order to obtain values of cumulative maximum signal attenuation caused by several of these storm cells. In addition, there has been included an exact integration (27) to obtain attenuation. Other exact integrations can be obtained for certain other *special* values of k in (8), and one may prefer to approximate k by these special values. Whatever the case, since there is precious little data on rainfall rate and rainfall attenuation, about all that can be said regarding experimental verification of the results presented here is that they do not appear to be unreasonable for the storms analyzed. A most interesting result is that the attenuation difference between isolated shower cell cases and bands of showers or thunderstorms appears to be quite sharp.

An advantage of the spherical cell method of calculating attenuation and/or its maximum value is that
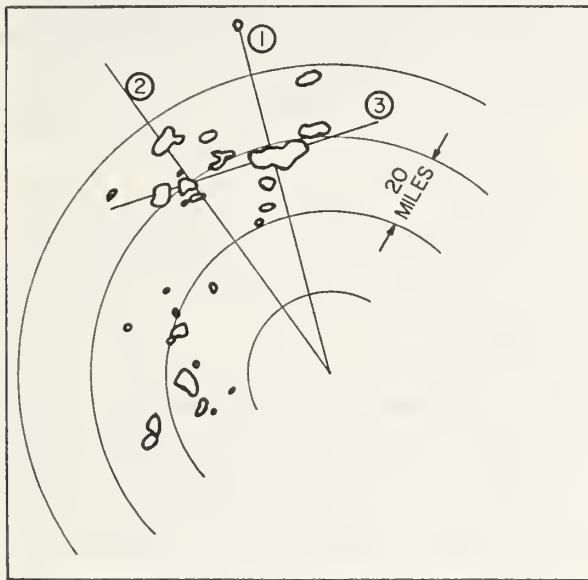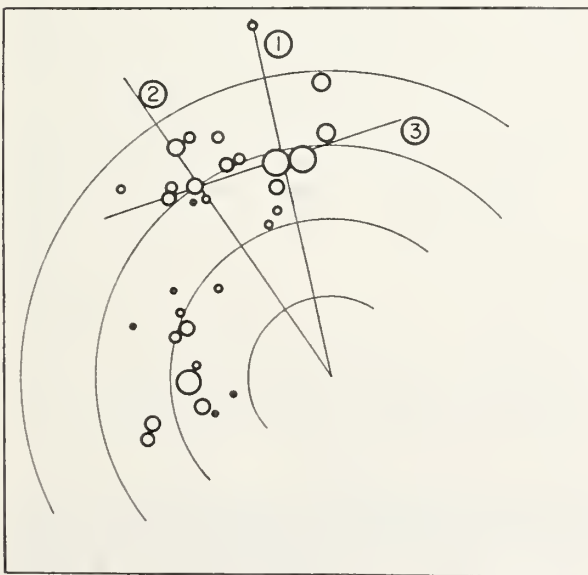
FIG. 8. Weak showers as seen on a PPI scope, a., and their replacement with spherical precipitation cells, b.

relatively quick observations on the character of rainfall can be made from radar or other reflection methods. The method can be useful in statistical attenuation studies if a preponderance of data is taken in conjunction with weather radar.

REFERENCES

Atlas, David, and Edwin Kessler, III, 1957: A model atmosphere for widespread precipitation. *Aero. Eng. Rev.*, **17**, No. 2, 69–75.

Battan, L. J., 1959: *Radar Meteorology.* Chicago, University of Chicago Press, 161 pp.

Bean, B. R., and G. D. Thayer, 1959: CRPL exponential reference atmosphere. *NBS Monograph*, No. 4, 67 pp.

——, E. J. Dutton, J. A. Lane and W. B. Sweezy, 1963: A radiometeorological study, Part III. A new turbulence parameter. *J. Res. NBS*, **67D**, 605–608.

——, J. D. Horn and L. P. Riggs, 1962: Synoptic radio meteorology. National Bureau of Standards Tech. Note 98, 87 pp.

Byers, H. R., and R. R. Braham, Jr., 1949: *The Thunderstorm.* Report of the Thunderstorm Project, U. S. Government Printing Office, 278 pp.

Dennis, A. S., 1963: Rainfall determinations by meteorological satellite radar. SRI Rept. No. 4080, Stanford Research Institute, Menlo Park, Calif., 105 pp.

Donaldson, Ralph J., Jr., 1961: Radar reflectivity profiles in thunderstorms. *J. Meteor.*, **18**, 292–305.

Douglas, R. H., 1964: Hail size distributions. *Proc. World Conf. Radio Meteor. Incorporating 11th Wea. Rad. Conf.*, Boston, Amer. Meteor. Soc., 146–149.

Harrold, T. W., 1965: Estimation of rainfall using radar—a critical review. *Meteorological Office Scientific Paper*, No. 21. London, England, Her Majesty's Stationary Office, 53 pp.

Hartel, H. W., R. A. Clark and V. E. Moyer, 1961: Investigation of space and time variations of convective precipitation as revealed by radar reflectivity measurements. *Proc. 9th Wea. Rad. Conf.*, Boston, Amer. Meteor. Soc., 83–89.

Hewson, E. W., and R. W. Longley, 1944: *Meteorology, Theoretical and Applied.* New York, John Wiley & Sons, 352 pp.

Holtz, C. D., and J. S. Marshall, 1966: Total precipitation aloft in a summer storm. *Proc. 12th Conf. Rad. Meteor.*, Boston, Amer. Meteor. Soc., 479–482.

Medhurst, Richard G., 1965: Rainfall attenuation of centimeter waves: comparison of theory and measurement. *IEEE Trans.* **AP-13**, 550–564.

Rice, P. L., A. G. Longley, K. A. Norton and A. P. Barsis, 1965: Transmission loss predictions for tropospheric communication circuits. Vol. I, National Bureau of Standards, Tech. Note No. 101, 3–4.

Ryde, J. W., and D. Ryde, 1945: Attenuation of centimeter waves by rain, hail, fog, and clouds. Wembly, England, General Electric, 39 pp.

Schelleng, J. D., C. R. Burrows and E. B. Ferrell, 1933: Ultrashortwave propagation. *Proc. IRE*, **21**, 429–463.

Schleusener, Richard A., and Thomas J. Henderson, 1962: Radar climatology of hailstorms in and near northeastern Colorado, 15 May–31 July 1962 with comparative data for 1961. CER62RAS79, Civil Engineering Section, Colorado State University, Fort Collins, Colo., 31 pp.

Schulkin, M., 1952: Average radio-ray refraction in the lower atmosphere. *Proc. IRE*, **40**, 554–561.

9.6—A Dual Wavelength Optical Distance Measuring Instrument Which Corrects for Air Density

K. B. EARNSHAW AND J. C. OWENS, MEMBER, IEEE

Abstract—An instrument has been constructed which simultaneously measures optical path length at two wavelengths and so permits determination of average refractive index over the common path and hence distance to 1×10^{-6} or better without extensive meteorological observations. Using a He–Ne laser (6328 Å) and a filtered high-pressure mercury arc lamp (3681 Å), the instrument is expected to measure distances to 15 kilometers with accuracies as high as a few parts in ten million. Preliminary measurements over a 5.3-km path give a standard deviation of 0.15 cm, or better than 3×10^{-7}.

I. INTRODUCTION

THE most convenient technique for making geodetic distance measurements involves measurement of the transit time of electromagnetic waves over the path.[1] The measured transit time, when multiplied by the velocity of light in air, gives the geometrical distance. Because the time required for light to travel 10 km is about 33 μs, the time measurement must be accurate to about 3 ps in order to obtain a distance measurement having a precision of 1×10^{-6}. Because pulse techniques do not presently provide the required precision, and direct optical interferometry is precluded by atmospheric turbulence, the transit time is most conveniently found by measuring the phase delay that a radio or microwave signal undergoes in traversing the distance. This signal may be either propagated directly, in which case the propagation velocity involves the phase refractive index of air, or used to modulate a light beam, in which case the propagation velocity depends on the group index of refraction for the optical carrier wavelength. Accurate distance measurements, therefore, require accurate knowledge of both transit time and propagation velocity. Transit-time measurements depend on the accuracy to which phase can be measured, and for a given precision of phase measurement the transit time can be measured more accurately at higher frequencies. Although it appears that the optimum frequencies for precise distance measurement are in the microwave range, the use of microwaves propagating directly through the atmosphere suffers from several drawbacks. First, the microwave index of refraction depends strongly on the amount of water vapor in the atmosphere,[2] so that precise measurements of average temperature, pressure, and humidity over the path are necessary. Second, the well-collimated microwave beams which would be required to eliminate multipath propagation effects necessitate the use of inconveniently large antennas. Because of these difficulties, microwave distance measurements precise to one part in a million require averaging times of several hours[3] and can be made only over uniform terrain which permits the use of several meteorological sensors along the path.

Many of the disadvantages of direct microwave propagation can be overcome by using a light beam which is modulated at a microwave frequency.[4] Here the beam divergence can be small, and the group velocity is only slightly dependent on atmospheric water vapor. However, the meteorological conditions must still be very well known in order to make distance measurements to 1×10^{-6}, and averaging times of several hours are still required. The index of refraction desired is the instantaneous index integrated throughout the volume of the measuring beam, and meteorological measurements can be made at only a few points within this volume with averaging times of several seconds. A good measurement requires that the air move past the meteorological sensors for a sufficient period of time so that short-period fluctuations tend to cancel. When an accurate distance measurement is desired over irregular terrain, such as between mountain peaks or over a valley, meteorological measurements can be made only at the two end points, and a precision of a part in a million can be obtained, if at all, only by averaging for very long periods of time (days or even weeks).

The purpose of this paper is to describe an optical instrument which measures not only transit time but also the instantaneous group index of refraction integrated throughout the volume of the light beam, hence permitting determination of the true geometrical path length. The theory of operation of the instrument, which has previously been presented,[5],[6] may be qualitatively understood as follows: the optical refractive index n of the lower atmosphere is dispersive, so different colors of light traveling over the same path will have slightly different velocities. Because the refractivity $(n-1)$ at a given wavelength is proportional to air density, the difference in refractivity, and hence the difference in transit time for the two colors, will be proportional to the average air density over the path. A measurement of the difference in transit times, therefore, can be used to give

the average density over the path. From this quantity the average refractive index for either color may be calculated, providing the desired correction for the distance measurement. The atmosphere increases the transit time by about 300×10^{-6} at sea level and the difference in transit time for 6328 Å and 3681 Å is about 30×10^{-6}, corresponding to a difference in apparent path length of about 40 cm for a 15-km path. Hence measuring the difference in transit time to 1 part in 300 allows the average atmospheric density to be determined to approximately the same fractional precision and the length to about 1×10^{-6}. By thus providing rapid spatial averaging of refractive index, the use of this dispersion method should significantly reduce the present limitations to the accuracy of long-range distance measurement. The most serious noninstrumental source of error is due to variations in humidity, which change the dispersion parameters. It can be shown[7] that an error of 8 mbar in the average partial pressure of water vapor (corresponding to a relative humidity of about 50 percent at 15°C) leads to an error of 1×10^{-6} in the ultimate length determination, and so a rough estimate of the average humidity will be required for high accuracy or under conditions of high absolute humidity.

The two-color system is designed to operate at a high modulation frequency (3 GHz) to provide high precision and accuracy with a simple method of phase measurement. In addition, servo-control of the modulation frequency is provided so that path length changes are properly tracked and automatic readout is possible. A common optical system for both transmitted and received light permits a compact design, reduces the chance of systematic errors, and simplifies the calibration of the instrument.

II. Instrument Design

A. Measuring Technique

The basic measuring technique involves a round-trip path to a distant reflector and modulation that is analogous to using a rotating toothed wheel which chops the light into short pulses, causing the average received intensity to depend on transit time. Polarization, rather than amplitude, modulation is used to give a larger net microwave-frequency modulation. A vertically polarized light beam is passed through a KH_2PO_4 electrooptic modulator[8] which varies its polarization between right- and left-hand elliptical during one modulation period, is transmitted by a 20-cm Cassegrainian telescope along the path to be measured, and is returned by a cat's-eye retroreflector directly back to the telescope and back through the same modulator. Returning light, upon passing through the modulator, undergoes a second modulation which doubles or cancels the first modulation when the modulation phase of the returning light is correspondingly in- or out-of-phase with the modulator excitation. For this reason the returning light, after making its

second pass through the modulator, will have an average polarization which depends on the distance to the retroreflector. Maximum intensity of the received horizontally polarized light is observed when the transit time is an integral number of modulation periods. When two colors of light are modulated simultaneously the modulation wavelengths are unequal (in air) so that maxima or minima of light will generally not occur for the same path length. Thus, if the reflector is allowed to move away from the modulator at a constant speed, the detectors of the two colors of light will observe maxima and minima with periodicities which constantly shift in phase with respect to each other. The amount of relative phase shift depends on the atmospheric density. By introducing a measured additional path length in the red beam to remove the relative phase shift the effect of the average density of the atmosphere over the measured path can be determined and can then be used to correct the apparent path length for either color and so obtain the true distance.

B. Light Sources

Because a practical modulator requires light beams which diverge less than about $\frac{1}{2}°$ and which are less than 3 or 4 mm in diameter, it is important to use light sources of high spectral radiance. A He–Ne CW laser operating at 6328 Å performs very well as the red light source, and a 100-watt high-pressure mercury arc lamp which emits a broad, strongly self-reversed line near 3650 Å having two peaks 150 to 200 Å wide is adequate as a violet source. Light from the lamp is passed through an interference filter of 70-Å bandwidth centered at 3681 Å, near the center of the longer-wavelength peak. Although a laser would be preferable as the violet light source, no satisfactory laser operating in the 3500- to 4000-Å range is yet available. The use of a gas laser is, of course, very convenient because of its narrow linewidth, high useful intensity, excellent collimation, and high degree of polarization. If eventually an ultraviolet laser or a laser emitting both spectral lines becomes available the range of the instrument will be greatly extended.

C. Optical System

The two light beams must be joined in a common vertically polarized beam and passed through the modulator. After returning from the distant retroreflector and back through the modulator, the beam must be analyzed for horizontally polarized light, separated into the two colors, and detected by photomultiplier tubes. Fig. 1 shows a layout of the optical system as well as a block diagram of the electronic system. Fig. 2 is a photograph of the optical system. It was found that a relatively simple optical system could be used in which just one optical element (a 12° Wollaston prism) performs the combined functions of polarizing and analyzing the light,

as well as joining and separating the two colors. Thus vertically polarized fractions of the two colored beams are joined by the Wollaston when the correct angle of incidence is used for each color. To make the system more compact the red beam is folded by reflecting it from a mirror placed close to the violet beam. Horizontally polarized light from the two light sources is deflected out of the transmitted beam and not used.

The two-color beam passes through the modulator to a dichroic mirror which reflects red light into a "beam stretcher" in order to introduce an additional path length for red light but which allows violet light to pass through. After reflection from two right-angle prisms, the red light rejoins the violet light and proceeds to a simple double convex quartz lens which serves as a telescope eyepiece. Because the slight divergence of the violet light just compensates the chromatic aberration of the lens, both colors are brought to a sharp focus at the focal point of a Cassegrainian telescope to produce a 20-cm collimated beam. The 20-cm beam is transmitted to the cat's-eye retroreflector (a 20-cm telescope with a plane mirror at its focal point) where it is reflected back through the optical system to emerge from the modulator. On returning through the Wollaston prism, the light is resolved .

into horizontally and vertically polarized components. The vertical components, which are maximum when the modulation cancels, return to their respective sources. The horizontal components, which are maximum when the modulation adds, become separated in color and are directed, respectively, to the photomultiplier detectors for red and blue light.

Since polarization modulation is used, care must be exercised to prevent polarization effects on reflection at any optical component. All reflection angles (except total internal reflections) should be less than 15°. Thus the dichroic mirror is set within $6\frac{1}{2}°$ of normal incidence, and the mirrors in the two telescopes are of relatively long focal lengths (one meter or greater). Reflections from the two prisms in the red beam stretcher present only phase shifts between the vertical and horizontal components of polarization, because the reflections are total internal reflections in which all light is reflected with virtually the same efficiency. The beam-stretcher phase shift may be compensated by placing a correcting waveplate in the red light beam. Phase compensation of the beam stretcher is not necessary when the net phase shift (in one direction) between vertical and horizontal polarizations is close to an integral number of quarter wavelengths, but, in general, ignoring phase compensation will reduce the contrast between maxima and minima, resulting in reduced sensitivity in the distance measurement.

Because a common optical system is used for both transmitted and received light beams it is important that reflections from the various optical elements not return to the photomultiplier tubes. Although coated optics are used throughout some reflections still occur, and these can be large compared to light returning from the distant reflector. Therefore, each optical component is angled slightly.

D. Microwave System

The microwave system provides the light modulator with a stable, accurately measured frequency and enough power to produce a desirable modulation index. Since the
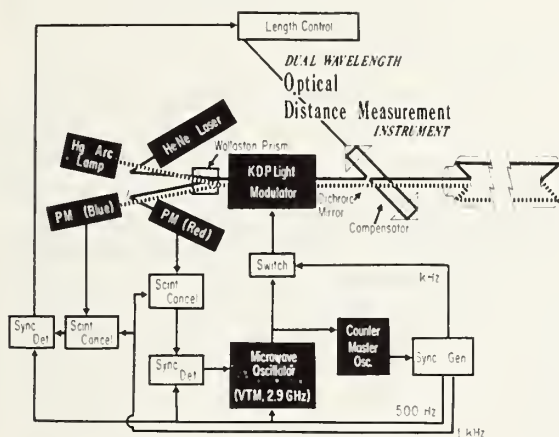

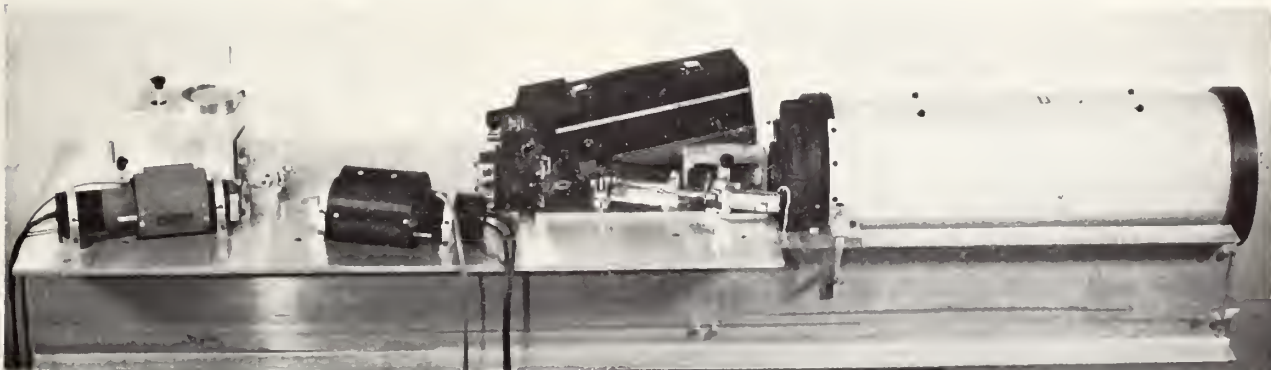Fig. 1. Diagram of the instrument.

Fig. 2. The optical system. Overall length of the system is about 2.5 meters. The 20-cm-diameter, 1-meter focal length telescope used as a retroreflector is not shown.
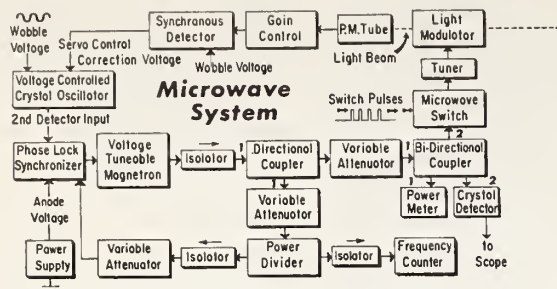
Fig. 3. Block diagram of the microwave system.

modulator gives a peak retardation of only 0.1 radian at its maximum average power rating of 1 watt, it is desirable to use higher-power pulses at a low duty cycle to obtain a reasonably large percentage of modulation. The modulation pulses must be long compared to the time required for light to travel over the measurement path, and the pulse repetition rate must be high compared to the fluctuations in atmospheric density. Atmospheric fluctuations have a power spectrum extending from very low frequencies up to about 500 Hz. The system is therefore designed to deliver 10 watts at a 10-percent duty cycle at repetition frequencies of 1000 Hz (for distances up to 8 km) and 500 Hz (for distances up to 16 km). In order to simplify further discussion, it will be assumed that the pulse repetition rate is always 1000 Hz.

In order to have a stable frequency which can be measured accurately, the microwave power source is operated continuously. The source, a voltage tunable magnetron, is frequency-stabilized with a commercial phase-lock synchronizer, and the power to the modulator is supplied through a microwave switch which is driven at the pulse repetition rate. Small microwave signals are supplied through isolators and variable attenuators to the phase-lock synchronizer and to the frequency counter. A sample of the signal pulse reflected back from the light modulator is used to tune the modulator cavity on resonance. The microwave system is diagrammed in Fig. 3.

In order to track the fluctuations in optical path, a servo-control circuit is used that locks the microwave modulation frequency to the optical path length so that the path always remains an integral number of modulation wavelengths. This is done by modulating the frequency of the microwave oscillator by a small amount at 500 Hz, causing the returning light signal to be amplitude-modulated at 500 Hz unless the average transit time is an integral number of modulation half periods. The output of the photomultiplier detecting the violet light is synchronously demodulated at 500 Hz, thus generating an error signal if the average refractive index over the path changes, and the center frequency of the microwave oscillator is shifted accordingly. The necessary averaging of path length fluctuations is performed

by a counter which determines the average modulation frequency during each counting period, normally one or ten seconds. Thus the instrument is self-balancing, a convenience when the optical path is systematically changing.

A second servo loop, operating from the detected red light, controls the length of the red beam stretcher so that the red optical path length also remains an integral number of modulation wavelengths. The length of the beam stretcher provides the correction for atmospheric density which allows an accurate distance measurement to be made. A potentiometer is connected to the beam stretcher so that a voltage proportional to beam stretcher movement can be recorded.

The effects of atmospheric scintillation are largely cancelled by automatic normalizing circuits between the photomultipliers and the synchronous detectors. Rather than using beamsplitters to pick off a portion of the returning light, light intensity leaking through the modulator between signal pulses is monitored and used to control the gain of the normalizing amplifiers. In this way, optimum amplification can be maintained in the servo systems without overloading during bursts of high light intensity.

III. Instrument Operation

A. Ambiguity Resolution

The first step in making a distance measurement is to determine the number of modulation wavelengths along the measurement path. This requires determining the apparent distance to within a quarter of a modulation wavelength, and is done by measuring frequency at several lock-in positions. These ambiguity-resolving measurements must be done at a time when the atmospheric density is not changing rapidly because it must be assumed that the index of refraction is either constant during the time of measurement or changing at a known rate.

For the red light beam, the number of modulation wavelengths along the measurement path is related to the frequency by

$$N = (n_R^a L_R + k_R) \frac{2f}{c} \tag{1}$$

and, hence, we have

$$\frac{\Delta N}{\Delta f} = \frac{2}{c} (n_R^a L_R + k_R), \tag{2}$$

where

N is the integral number of modulation wavelengths over the two-way path,

n_R^a is the group index of refraction for red light,

L_R is the total one-way geometrical path length between the modulator and the retroreflector mirror (including the beam stretcher),

k_R is the apparent increase in one-way path length due to the optical components, and

f/c is the reciprocal of the vacuum wavelength at the microwave frequency.

The right-hand side of (2), and hence N, can be determined by measuring $\Delta N/\Delta f$. This is done by manually sweeping the frequency between two lock-in positions which are several wavelengths apart. In practice, this is quite simple because as the frequency is increased the detected light signal goes through one cycle of amplitude change each time one additional wavelength is included in the path. Once a value of $\Delta N/\Delta f$ has been determined by sweeping the frequency over several wavelengths, successively more accurate values can be obtained by sweeping the frequency over wider ranges. Since ΔN may be several hundred or more for long paths and the maximum frequency change allowed by the modulator, it is convenient to note that the number of wavelengths need not be counted during successive sweeps but can be determined from the approximate value of $\Delta N/\Delta f$ obtained in each preceding one. This procedure is continued until the uncertainty in N due to uncertainty in the frequency measurement is less than 1. To find the corresponding number of modulation wavelengths for the violet light, it is necessary to know the apparent distance only within approximately 0.5 km, since one extra violet wavelength is added to the number of red wavelengths every 1.9 km of one-way distance at sea level.

B. Distance Measurement

Once the number of wavelengths over the path is known, a distance measurement is made by servo-controlling the frequency and the red beam stretcher so that an integral number of modulation wavelengths are maintained for both violet and red light. Frequency and red beam-stretcher length are monitored continuously while temperature, humidity, and pressure are monitored periodically at one end point (once every hour is normally sufficient). The measured quantities are substituted in the following relations to obtain the apparent distances for red and violet light.

Red apparent length:

$$n_R^G L = \frac{N_R \lambda_0}{2} - k_R - B \tag{3}$$

violet apparent length:

$$n_V^G L = \frac{N_V \lambda_0}{2} - k_V \tag{4}$$

where

n_R^G, n_V^G are the group indices of refraction for red and violet light,

N_R, N_V are the number of modulation wavelengths along the path for red and violet light,

λ_0 is the modulation wavelength in vacuum,

B is the air path length added by the beam stretcher, and

k_R, k_V are the corrections for optical components in the red and violet light beams.

The latter two quantities are determined by measuring carefully the thickness of each optical element in the optical paths, multiplying each thickness by the appropriate group index of refraction, and adding the individual apparent lengths for red and violet light to obtain the total apparent lengths caused by the optical components.

The geometrical distance is calculated by using the difference in apparent path lengths to correct either the red or violet apparent length for the apparent extra length caused by the atmosphere. The corrected length is thus given by

$$L = n_V^G L - A_V(n_V^G L - n_R^G L) \tag{5}$$

or

$$L = n_R^G L - A_R(n_V^G L - n_R^G L) \tag{6}$$

where

$$A_R = \frac{n_R^G - 1}{n_V^G - n_R^G} \tag{7}$$

and

$$A_V = \frac{n_V^G - 1}{n_V^G - n_R^G} = A_R + 1. \tag{8}$$

In a dry atmosphere of standard composition the correction factors A_V or A_R depend only on the two optical wavelengths and are known to high accuracy. However, water vapor changes the composition of the atmosphere and therefore changes the values of A necessary for the true correction of distances. Fortunately, the dependence of A on water vapor pressure is small so that very accurate values of relative humidity and temperature are not needed. For example, when measured temperatures and relative humidity are in error by 5°C and 10 percent, respectively, the error in calculated distance will be less than 5×10^{-7}.

C. Results of Field Testing

The instrument was tested during August, 1966, over a 1.6-km path across Lake Hefner, near Oklahoma City, Okla. Although the path was quite short and too uniform to illustrate clearly the advantages of the dispersion method over conventional methods, it was chosen because accurate meteorological data at three points along the path were available for comparison. Unfortunately, technical difficulties prevented simultaneous distance measurement at the two wavelengths from being made and it was necessary to lock the modulation frequency alternately onto the red and violet pathlengths. Variations in atmospheric density during the switching and

measurement period (about one or two minutes) introduced random errors which reduced the precision of the corrected distance below the levels expected.

The Lake Hefner results[9] showed the precision of the instrument in detecting optical path length changes for either wavelength to be about 3×10^{-8} with an averaging time of 10 seconds. This was checked by physically moving the retroreflector through small distances; a motion of about 5×10^{-3} cm could be detected. Using 177 measurements of corrected distance over a period of four days, the standard deviation was found to be 1.55 mm, slightly better than 1×10^{-6}. For comparison, the standard deviation of optical path length, which would be the error of a one-wavelength distance measurement if no meteorological information were used for correction and there were no other sources of error, was 2.2×10^{-6}, and the standard deviation of length corrected using meteorological data from both end points and the center of the path was 0.8×10^{-6}. Although the precision of the dispersion-corrected measurements is slightly lower, it is better than had been expected for sequential measurements over such a short path and is highly encouraging, for we expect that the precision of the dispersion correction relative to the meteorological correction will increase with longer paths and simultaneous measurements. Finally, uncorrected and meteorologically corrected measurements of microwave distance taken over the some path using a new 9.6-GHz instrument[10] and the same meteorological data gave standard deviations of 10.5×10^{-6} and 1.6×10^{-6}, respectively.

Tests over a 5.3-km path between two hills north of Boulder, Colo., were begun in May, 1967, using an instrument which had been rebuilt to include a satisfactory line stretcher, coated optics, more sensitive photomultiplier tubes, and a narrower filter for the violet light. Only a limited number of measurements have been made, but these have given results closer to those expected. The recent measurements have demonstrated a precision in detecting optical path length changes of about 3×10^{-9} with averaging times of ten seconds, and a measurement of corrected length using 14 measurements over a period of two hours gave a standard deviation of 0.15 cm, better than 3×10^{-7}. As an indication of the importance of simultaneous measurements, 18 determinations of corrected length using alternate measurements for red and violet over a period of seven hours gave a standard deviation of 0.49 cm, about 1×10^{-6}.

D. Sources of Error

The absolute accuracy of the corrected length measurements cannot be ascertained from the existing data. The most direct and accurate calibration could be made by taking measurements through a long (1 km or more) pipe which could be evacuated. Since the position of the effective modulation point (the "zero error") and the modulation frequency can be known with sufficient accuracy; measurements through such a pipe at various air densities could be used to determine the absolute accuracy of the correction method, within the small remaining uncertainty due to variations in air composition. Alternatively, measurements through the atmosphere under widely varying conditions plus theoretical limits placed on the various known sources of systematic error could be used to determine the absolute accuracy, although a longer time would be required and the calibration would probably be less precise. The most serious sources of error are 1) uncertainties in the mean wavelength of the violet light, giving a length error of 3×10^{-7}/Å, and 2) uncertainty in the dispersion parameter A due to inexact knowledge of the water vapor partial pressure, giving 1×10^{-7}/mbar. The error due to water vapor can be reduced by using meteorological measurements at one or more points along the path or, for very high accuracy, by including a third distance measurement over the same path at a microwave or millimeter-wave frequency.

IV. CONCLUSIONS

The practical value of lasers as convenient, monochromatic, and optically efficient light sources and the utility of such techniques as microwave-frequency light modulation in geodetic distance measurement are clear. The results of field tests of a new instrument using a simple and reasonably compact optical system over a 5.3-km path have demonstrated a precision better than 1×10^{-8} in detecting changes in optical path length with averaging times of ten seconds, and a precision of 3×10^{-7} in corrected length. The determination and correction of systematic errors is in progress, and the instrument is expected to give an absolute accuracy of at least 1×10^{-6} without long-term averaging. Although it has not yet been actually proven, the use of the two-wavelength optical dispersion method is expected to permit the measurement under average atmospheric conditions of true geometrical distance over paths several tens of kilometers long to an accuracy of a few parts in ten million with averaging times less than a minute.

REFERENCES

[1] P. L. Bender, "Laser measurements of long distances," *Proc. IEEE*, vol. 55, pp. 1039–1045, June 1967.
[2] B. R. Bean and E. J. Dutton, "The radio refractive index of

air," in *Radio Meteorology*, NBS Monograph. Washington, D. C.: U. S. Government Printing Office.

[3] M. C. Thompson, Jr., "The effects of propagation on measurements of distance, angle-of-arrival, and Doppler effect in ground-to-ground systems," presented at XV General Assembly of URSI, Munich, September 1966; in *Progress in Radio Science, 1963–1966* (to be published).

[4] K. D. Froome and R. H. Bradsell, "Distance measurement by means of a light ray modulated at a microwave frequency," *J. Sci. Instrum.*, vol. 38, pp. 458–462, 1961.

[5] M. T. Prilepin, "Light-modulating method for determining the average index of refraction of air along a line," *Trans. Institute of Geodesy, Aeronomy, and Cartography* (USSR), no. 114, pp. 127–130, 1957.

[6] P. L. Bender and J. C. Owens, "Correction of optical distance measurements for the fluctuating atmospheric index of refraction," *J. Geophys. Research*, vol. 70, pp. 2461–2562, 1965.

[7] J. C. Owens, "Optical refractive index of air: dependence on pressure, temperature and composition," *Appl. Optics*, vol. 6, pp. 51–59, 1967.

[8] I. P. Kaminow and E. H. Turner, "Electrooptic light modulators," *Appl. Optics*, vol. 5, pp. 1612–1628, 1966.

[9] Further details may be found in J. C. Owens, "Recent progress in optical distance measurement: Lasers and atmospheric dispersion," *Proc. Internat'l Assn. Geodesy Symp on Figure of the Earth and Refraction*, Vienna, March 14–17, 1967 (to be published).

[10] R. O. Gilmer and D. M. Waters, "A solid-state system for measurement of integrated refractive index," U. S. Government Printing Office, Tech. Rept. IER-40/ITSA-40, 1967 (to be published).

10

U. S. DEPARTMENT OF COMMERCE
C. R. Smith, Secretary

ENVIRONMENTAL SCIENCE SERVICES ADMINISTRATION
Robert M. White, Administrator

ESSA RESEARCH LABORATORIES
George S. Benton, Director

ESSA TECHNICAL REPORT ERL 90-WPL 5

Atmospheric Scattering From a 1.15-Micron Laser Beam and Its Off-Axis Detectable Range

ROGER H. KLEEN

NORMAN L. ABSHIRE

TABLE OF CONTENTS

ATMOSPHERIC SCATTERING FROM A 1.15-MICRON LASER BEAM AND ITS OFF-AXIS DETECTABLE RANGE

Roger H. Kleen

and

Norman L. Abshire

The detectability of a laser beam through a fog can be predicted fairly accurately for various detector and collecting optical systems if temperature, relative humidity, and fog extinction coefficient are known. Smoke is much more variable and can not be characterized by only its extinction coefficient. Fog and smoke angular scattering patterns determined experimentally are presented.

Key Words: Fog-scattering, infrared, laser, smoke-scattering

1. INTRODUCTION

In an infrared communications link it is important to know how much energy is scattered out of the main beam and how far that energy could be detected. Figure 1 shows a typical arrangement when a laser is used for such a link.
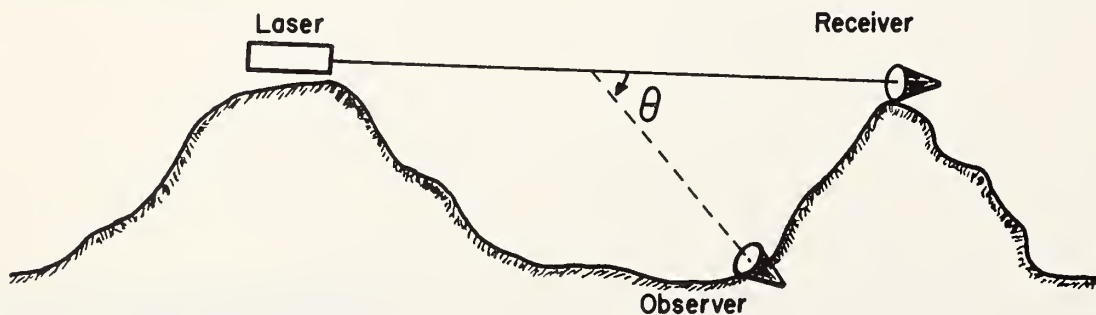

Figure 1. Communication link with observer.

The atmospheric conditions in the receiving and observing paths are of paramount importance. There was no detectable scattering under clear air, dusty (a very heavy dust storm was not investigated), heavy rain, and heavy snow conditions, but in fog and smoke appreciable scattering could be observed because of the much higher particle densities. This scattering is the subject of this report.

The detectable range in a fog can be predicted fairly accurately if the following specifications are known:

(1) Collector area and focal length.

(2) Detector detectivity and area.

(3) System bandwidth.

(4) Temperature and relative humidity over the paths.

(5) Direction and distance from the beam.

(6) Extinction coefficient for the particular fog or smoke in the path.

In the next two sections of this report the problem of determining the off-axis detectable range of a 1.15-μ laser beam is outlined and some pertinent examples are given of how this range is calculated. Section 4 describes the experiment from which the angular scattering functions in figures 11 and 13 were determined.

2. BACKGROUND

There are three possible sources of loss in the main beam: water vapor absorption; absorption by the particles themselves; and scattering out of the beam.

Water vapor absorption

There is always water vapor in a path. It may vary considerably depending on the temperature and humidity. Under foggy conditions, the relative humidity is 100 percent.

The usual exponential law holds for attenuation due to water vapor:

$$I = I_0 \exp(-k_\nu \, w) \quad ,$$

where I is the power at the receiver, I_0 is the transmitter power, k_ν is the absorption coefficient at the transmitter frequency, and w is the total water in the path in precipitable centimeters. Path length, temperature, and humidity are needed to determine w.

For determining k_ν, Deutschman and Calfee (1967) have developed computer programs to which absorption line parameters as well as temperature and pressure serve as input. If the transmitter bandwidth is smaller than the line widths, the program "Spectrum" should be run, but if the bandwidth covers several lines, the "Degrade" should be used. Absorption line parameters have been calculated for many of the water vapor and carbon dioxide absorption regions below 20 μ, and new regions are being calculated (for the latest information, contact R. F. Calfee of the Wave Propagation Laboratory, ESSA).

The laser line at 1.152276 μ (seven significant figures are necessary to specify the position on the water vapor spectrum) falls in a region of moderate absorption. Figure 2 (Long, 1966) shows that this laser is operating on the edge of a strong absorption line.

In a 1-km path, the transmission is 95 percent at 0 $^\circ$F and 10-percent relative humidity, but only 2×10^{-7} percent (87 dB/km) at 100 $^\circ$F and 100-percent relative humidity. This large range in water vapor attenuation means that the temperature and humidity must be fairly well known for any range calculations.

For other lasers in the infrared region, the absorption due to water vapor is far less, which would make range calculations less complex. Comparative absorption coefficients are given in table 1.
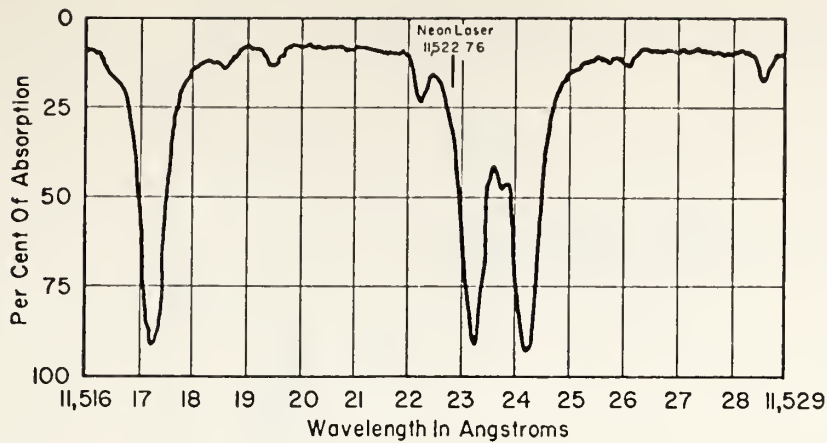
3

Figure 2. Atmospheric absorption near the 11523 Å neon laser wavelength

Table 1. Water Vapor Absorption Coefficients

λ microns	ν_0 cm^{-1}	k_ν precipitable cm^{-1}
1.1522	8676.1	4.40
1.0648	9391.0	6.95×10^{-5}
2.10	4760.6	2.5×10^{-4}
3.39	2998.6	5.57×10^{-3}
3.50	2851.3	3.8×10^{-5}

Particulate absorption--fog

In addition to water vapor absorption, absorption in the droplets themselves is possible. This absorption can be calculated from Mie theory if the complex index of refraction and particle size are known.

The absorption coefficient of liquid water, as given by the International Critical Tables (1930), is $\gamma = 1$ cm^{-1} for a 1.15-μ wavelength. The complex index of refraction is $m = n - in'$, the loss term is

$$\tan \beta = \frac{n'}{1 - n} \quad ,$$

4

and the absorption coefficient (particle) is

$$\gamma = \frac{4\pi n'}{\lambda} \quad .$$

If $\gamma = 1 \text{ cm}^{-1}$, $n' = 9.1 \times 10^{-5}$, then

$$m = 1.33 - 9.1 \times 10^{-5} i$$

$$\beta \approx 0.1^{\circ} \quad .$$

Since this is a very small loss term, there is no appreciable absorption in the particle itself. Van de Hust (1957) defines efficiency factors as

$$Q_{ext} = Q_{abs} + Q_{sca} \quad ,$$

where Q_{ext} is the extinction cross section divided by the projected particle area, Q_{abs} is the absorption (in the particle) efficiency factor, and Q_{sca} is the scattering efficiency factor. Since $Q_{abs} \approx 0$, $Q_{ext} = Q_{sca}$, this is not the total extinction as it does not include the water vapor absorption. When visible scattering is considered, the water vapor absorption can be negelected. Consistent with the bulk of the literature, the word extinction in this report does not include water vapor absorption.

As shown by figures 3 and 4, fog and cloud drops have a peak radius distribution at about 3 or 4 μ. Figure 3 gives the distribution for haze and two fogs (Arnulf et al., 1957). For obtaining the true distribution, it is necessary to divide by a "capture coefficient", which is itself proportional to the radius. The peak at 3 μ then becomes even more accentuated.

Carrier et al. (1967) conducted an extensive lierture search on the properties of various cloud types. This compilation (see fig. 4)
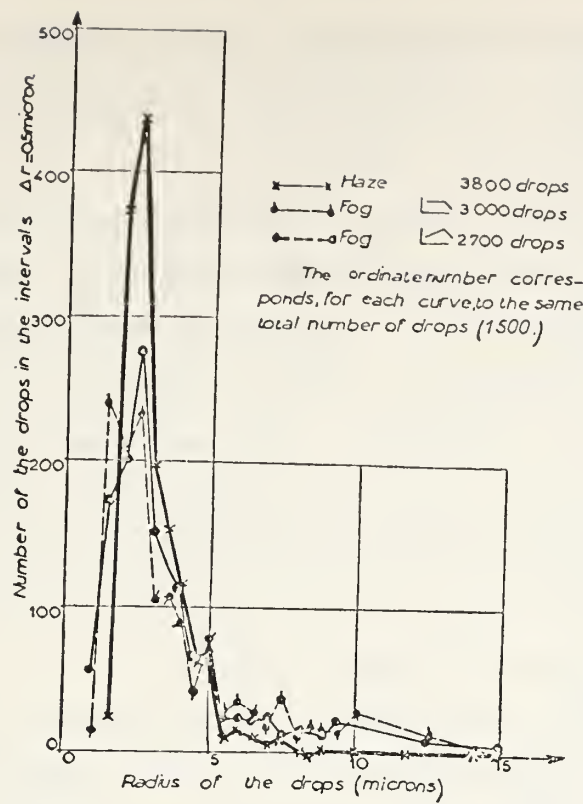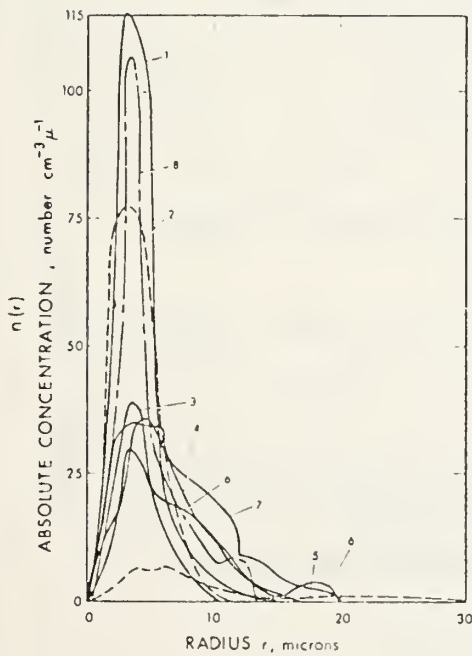
Figure 3. Distribution of the radius of drops.

Figure 4. Model cloud drop
spectra (1) stratus I, (2) strato-
cumulus, (3) fair-weather cumulus,
(4) stratus II, (5) cumulonimbus,
(6) cumulus congestus, (7) nimbo-
stratus, and (8) altostratus.

shows the peaks for most cloud types between a radius of 3 and 4 μ, but cumulus congestus and nimbostratus do, however, have a significant fraction of particles above a radius of 10 μ.

Penndorf (1963) has calculated scattering patterns for water drops from Mie theory. His results for 2.5-μ and 2.0-μ radii are shown in figures 5 and 6, respectively. In both, the general pattern is marked by considerable oscillations; a change of only 0.5 μ in the radius produces a large shift in these oscillations. Such oscillations will not be observed with the range of particle sizes in fog, since there will be an overall smoothing. A main beam that is not monochromatic would have the same effect, but the general shape would be preserved, and this shape was, indeed, the one we observed experimentally.

The theoretical curves contain two components, i_1 and i_2, that represent the two possible polarizations of the incident beam in relation to the plane of observation. We studied both conditions experimentally and detected no difference; evidently the range of particle sizes also averages out polarization effects. Any small variations would not be detectable because of fog variability from one run to the next.

Spencer (1960) has published a very important set of curves (fig. 7) for fog scattering in the visible. Both real and artificial, as well as dense and light, fogs were normalized at the 20° scattering point. He found that all curves had the same characteristic shape for angles greater than 20°.

Figure 8 shows the work of Reisman et al. (1967), who established a straight-line relationship between the scattered intensity and the extinction coefficient at 6328 Å. Data obtained by these authors on experimental angular scattering for two different fog densities are given in figure 9, which also indicates that the curve shape is the same past the 20° scattering angle.
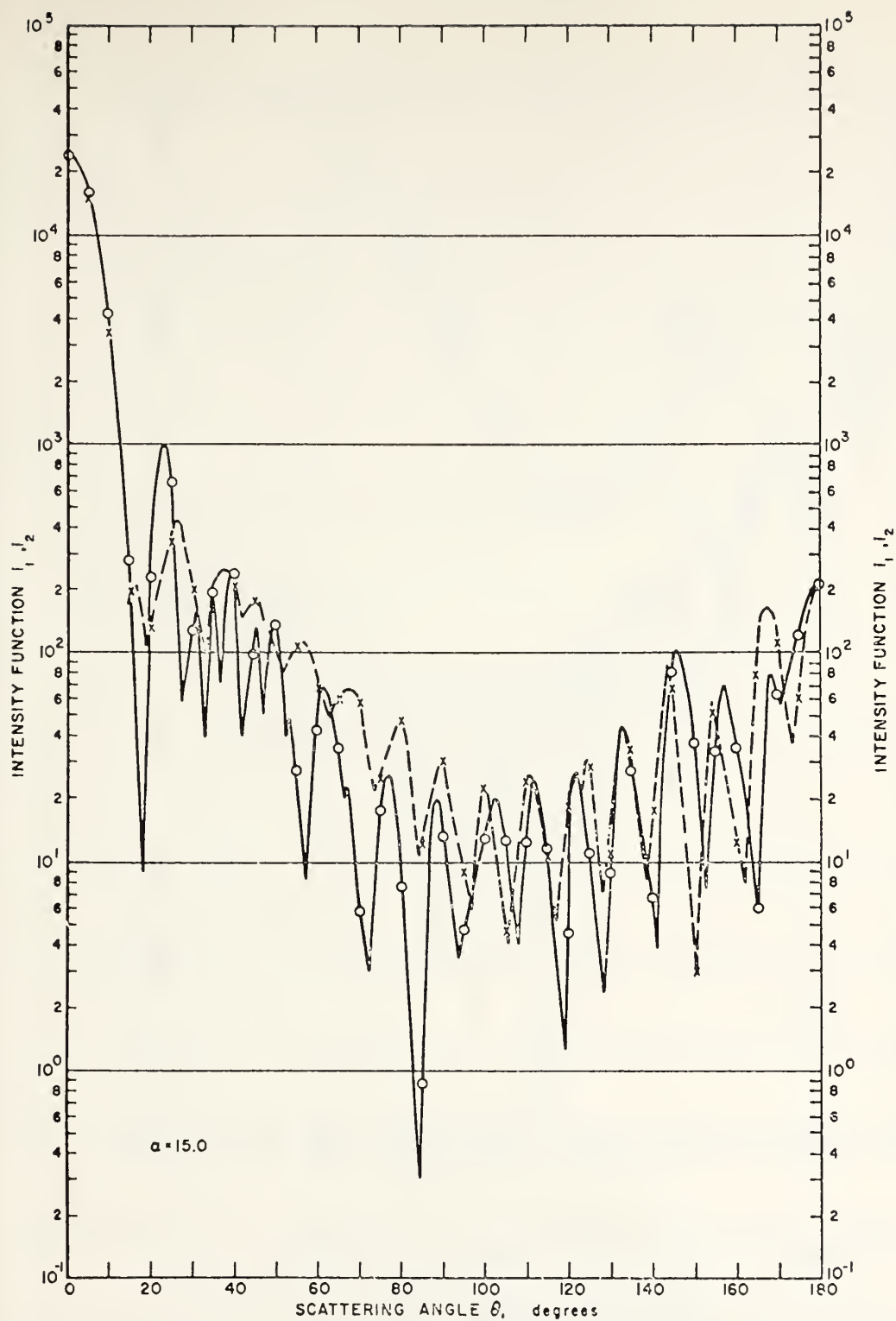
Figure 5. Theoretical scattering patterns;
m = 1.33 - oi, λ = 1 μ;
radius of spheres = 2.5 μ.

8
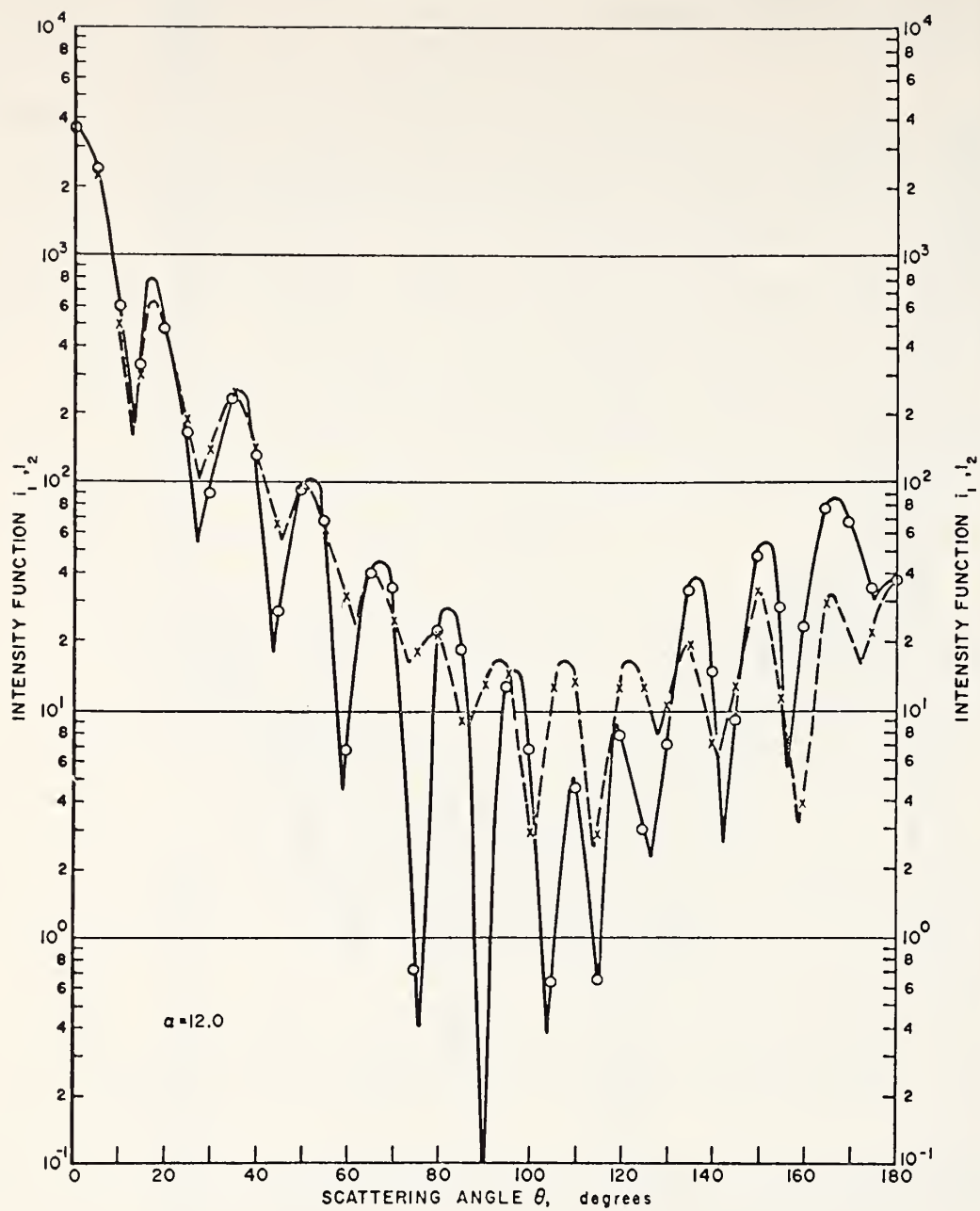
Figure 6. Theoretical scattering patterns;
m = 1.33 - oi, λ = 1 μ;
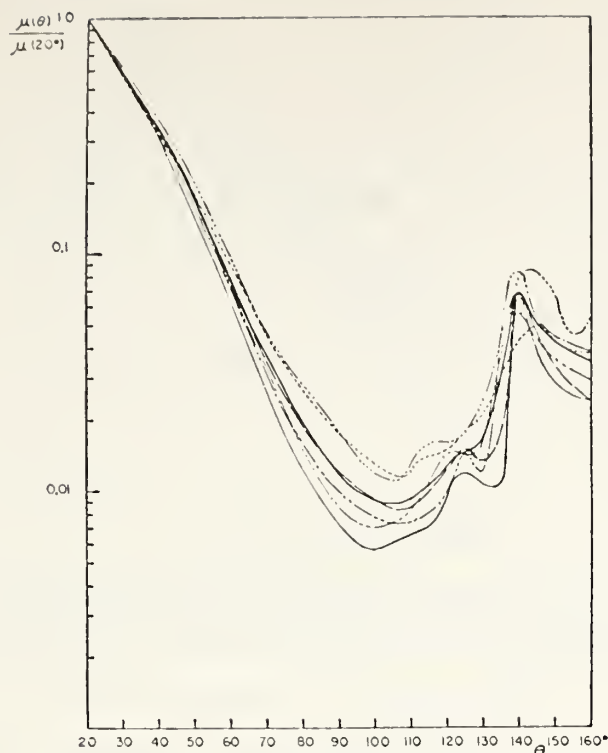radius of spheres = 2.0 μ.

9

Figure 7.   Experimental data   on the scattering coefficient.

- - - - — Test No. 1, artificial fog, University of Michigan, July 3, 1956,
     $\alpha = 1.820 \times 10^{-1} m^{-1}$.

-- —— Test No. 2, natural fog, University of Michigan, July 21, 1956,
     $\alpha = 1.56 \times 10^{-1} m^{-1}$.

- - - - - Test No. 3, artificial fog, Pennsylvania State University,
     August 31, 1956, $\alpha = 2.44 \, m^{-1}$.

- —— Test No. 4, natural fog, Asbury Park, New Jersey, September 1,
     1956, $\alpha = 8.76 \times 10^{-3} m^{-1}$.

—— Test No. 5, natural fog, University of Michigan, November 2,
     1956, $\alpha = 3.42 \times 10^{-2} m^{-1}$.

— — Test No. 6, natural fog, University of Michigan, February 26,
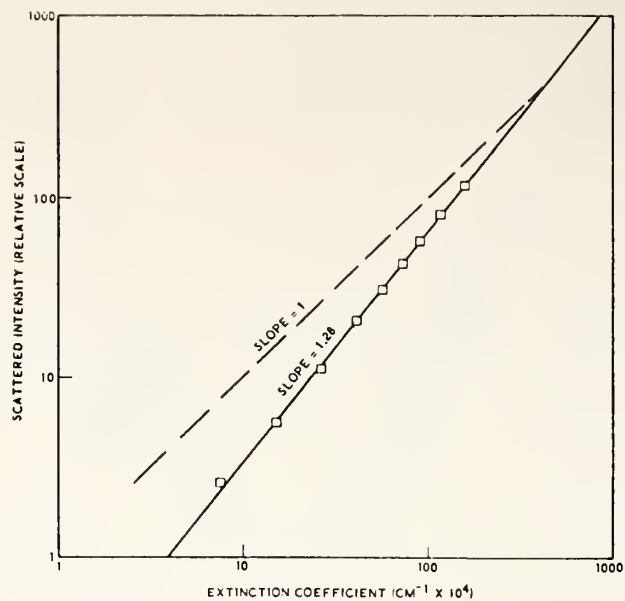   1957, $\alpha = 5.30 \times 10^{-3} m^{-1}$.

10

Figure 8. Scattered intensity vs. extinction coefficient. Perpendicular polarization. □Incoherent light, $\theta = 90^{\circ}$.
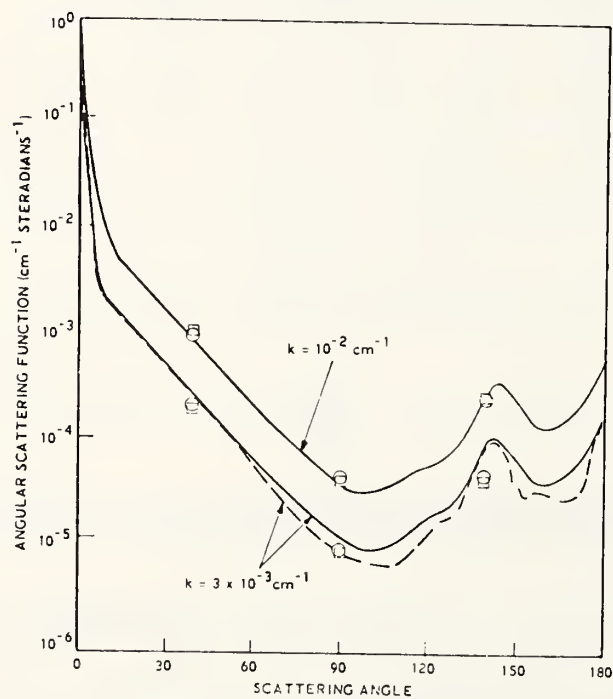

Figure 9. Angular scattering function vs. scattering angle. Perpendicular polarization. — 2-μ analytical data, -- 4-μ analytical data, O laser light, □incoherent light.

11

In our study, we assumed that these effects also hold at 1-μ wavelength, but they were difficult to actually measure because the noise equivalent power of lead sulphide is about 10^4 less than that of a visible photomultiplier. When the fog was made less dense, the signal to noise at 100° scattering angle was not adequate for detection.

Conner and Hodkinson (1967) show (see fig. 10) that the scattering is on a flat portion of the curve for droplet size variations at 1-μ and 0.5-μ wavelengths. If the laser were at 10-μ wavelength, however, any particle size variations in one fog versus another could make a large difference in the amount scattered.

In view of the above, it seems that Spencer's result can be extended to 1-μ wavelength, but a 10-μ wavelength would be open to question. Any variation in fog droplet sizes would make an appreciable difference in both the extinction and scattering at a wavelength of 10 μ. This assumption is reflected in figure 11, where the curve with $k = 4.1 \times 10^{-3}$ cm^{-1} is the experimental curve and the rest of the curves have the same shape. If the extinction coefficient in a fog is known or can be measured, the angular scattering pattern can be predicted and the detectable range calculated.

Particulate absorption--smoke

In smoke, water vapor will still be present and its absorption must be accounted for but, in contrast to fog, the relative humidity generally will not be 100 percent. Again, however, the extinction does not include water vapor absorption.

According to van de Hulst (1957), the complex index of refraction for carbon particles at 1-μ wavelength is m = 1.59 - 0.66 i. The loss factor is tan β = 1.1, and thus β = 48°. This loss factor is much larger than for liquid water and there will be considerable absorption in the particles themselves.
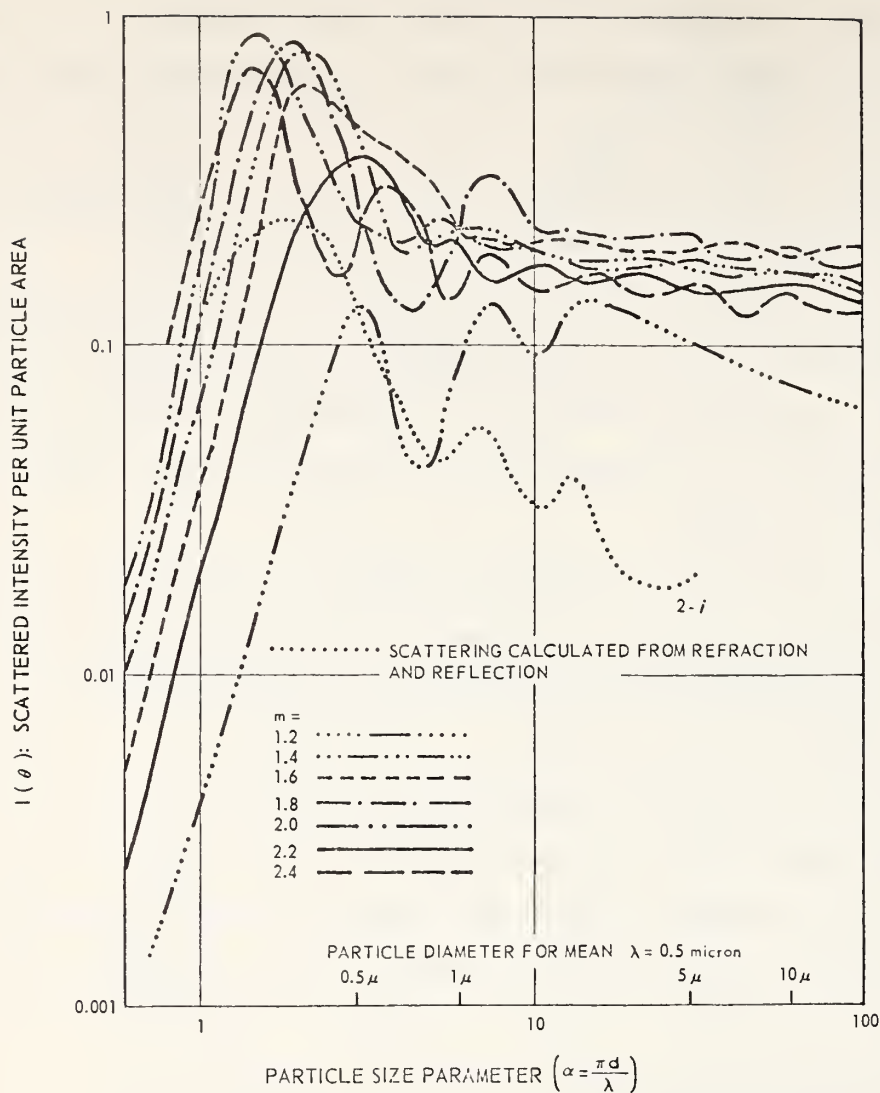
Figure 10. Scattering at 45° by transparent spheres, calculated from Mie theory.

To calculate the efficiency factor for this absorption, the particle size must be known. Conner and Hodkinson (1967) put the mean particle radius at 0. 2 μ for white oil smoke and at 0. 1 μ for black oil smoke. There is reason to believe that the range of sizes is larger than for the case of fog droplets.

13
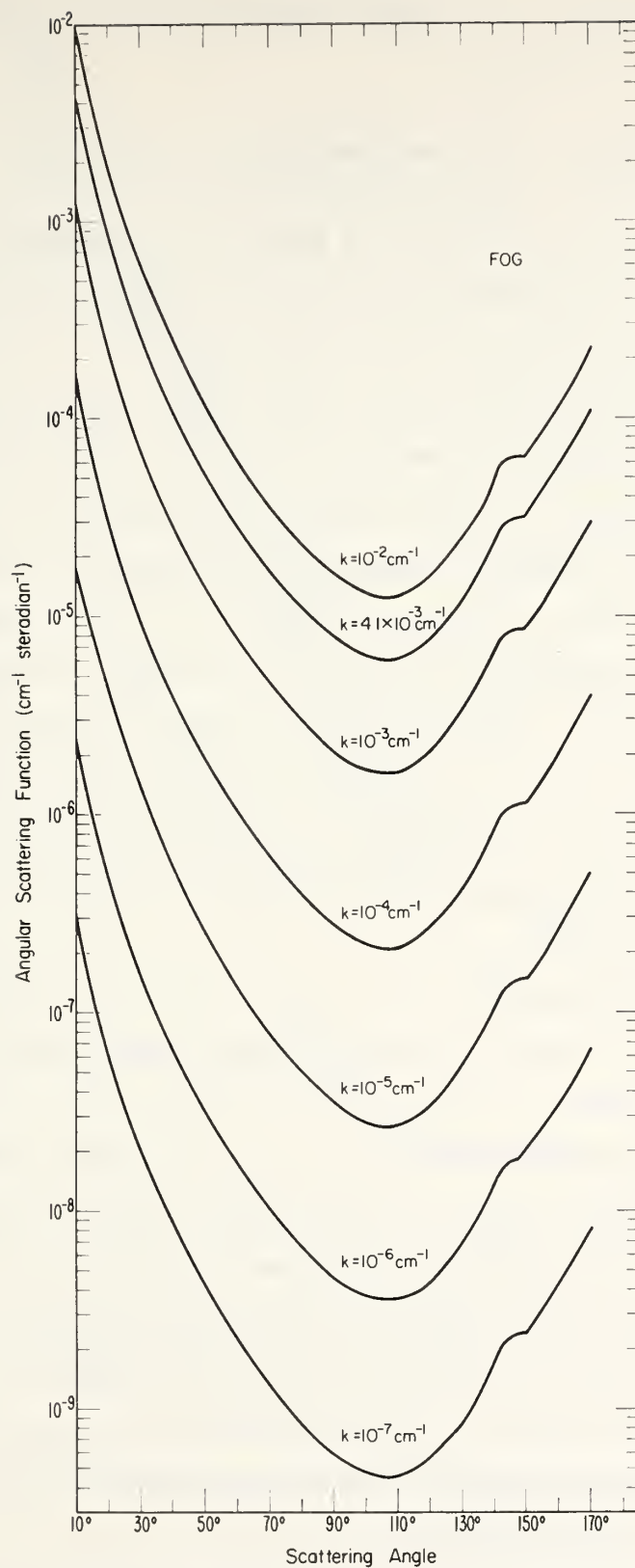
Figure 11. Angular scattering functions. Experimental curve
curve $k = 4.1 \times 10^{-3}$ cm^{-1}.

14

For white oil smoke (.2 μ radius), the equations and tables given by van de Hulst (1957, ch. 11) yield

$$Q_{ext} = 1.39, \ Q_{abs} = 0.78, \ \text{and, therefore,} \ Q_{sca} = .61.$$

Hence, 56 percent of the incident beam intensity is absorbed by the particles themselves. For black oil smoke (0.1-μ particles) the calculations yield 69 percent absorption by the particles.

These small particles place the consideration on the steep slope (Rayleigh region) of figure 10, and, hence, any variations in particle size can change the extinction and scattering considerably. Conner and Hodkinson (1967) studied the visible scattering from various smoke plumes, and their results are shown in figure 12. There the curves are not similar in shape, although a particular smoke has the same family of curves as in figure 11. Therefore, the assumption that the smoke is the same because it comes out of the same generator and uses the same fuel is not valid. Conner and Hodkinson (1967) observed that denser smoke had larger particle sizes even though it came from the same source as less dense smoke.

As a basis for some representative calculations presented in the sections that follow, a family of curves similar to the one for fog was constructed for oil smoke (see fig. 13). For this curve to be valid, the particle size and composition must stay the same as the smoke becomes more dense. One curve is experimental and has the value of $k = 4.1 \times 10^{-3} \ cm^{-1}$.

The oil smoke curves in figure 13 give 57 percent less scattered intensity than the fog curves of figure 11 for the same extinction coefficient. The previous theoretical calculation of Q_{sca} gave a value of 44 percent, a good agreement since the exact particle size was not known, and even this difference could be explained if the smoke particles in the experiment were a little larger than 0.2 μ.

15
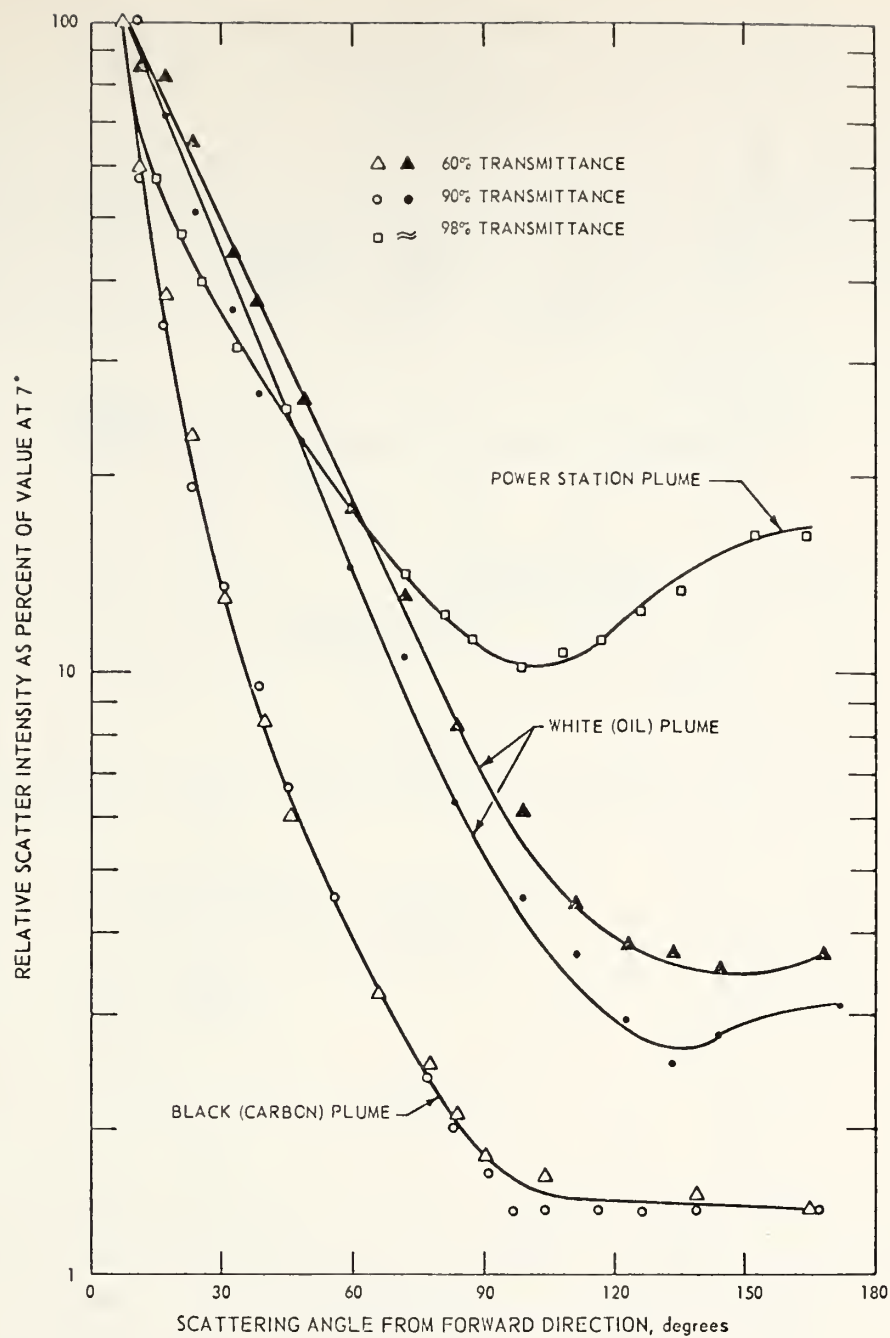
Figure 12. Angular scattering measurements of smoke plumes.
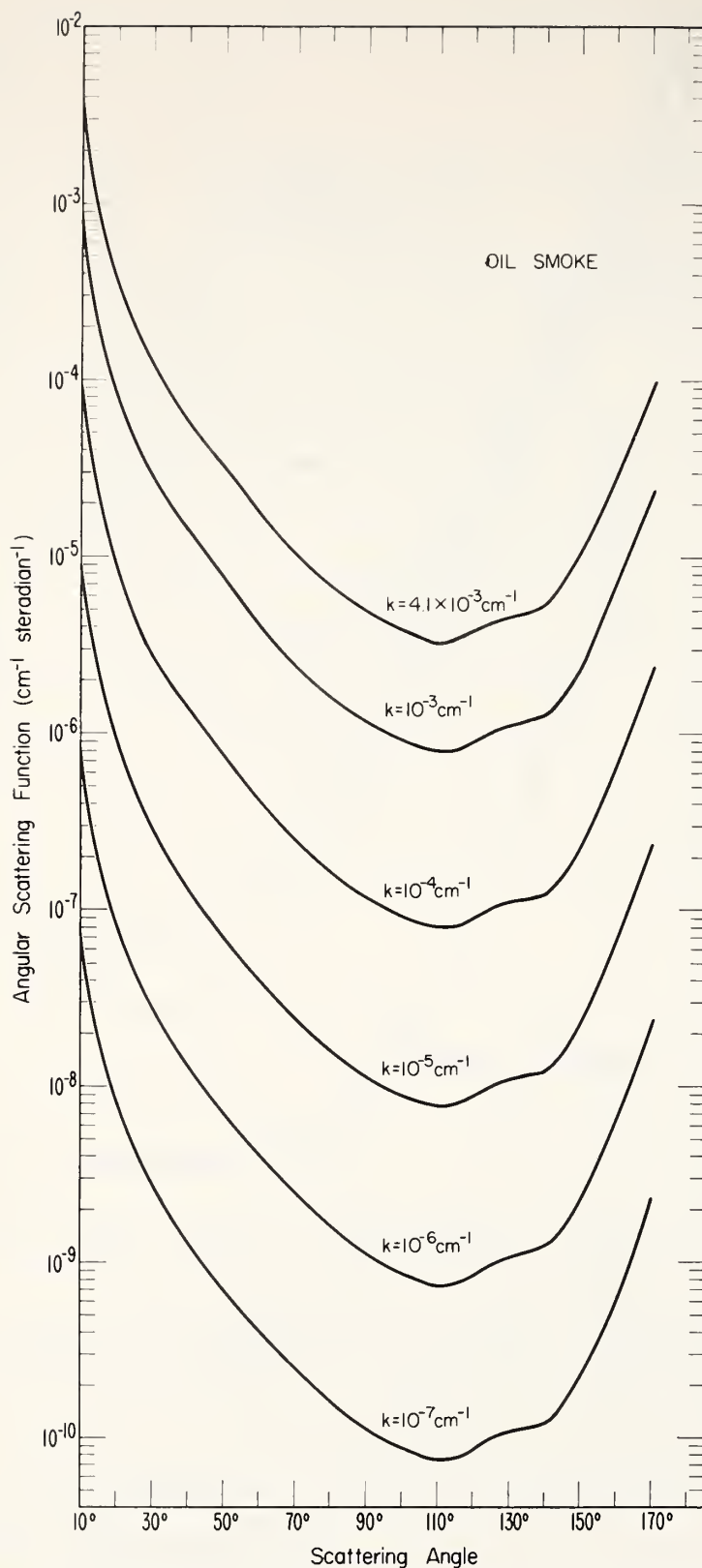
Figure 13. Angular scattering functions. Experimental curve $k = 4.1 \times 10^{-3} \text{cm}^{-1}$.

3. RESULTS

To demonstrate the type of calculations that can be made from figure 11 or 13, some sample calculations will be given. Figure 14 shows the optical arrangement under consideration.
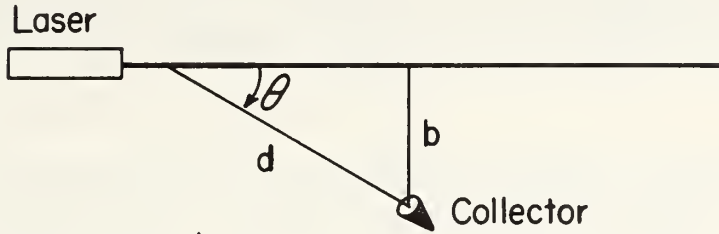
Figure 14. Range Calculation Diagram

The power incident on the detector is given by

$$P = P_L \eta S \ell \Omega e^{-(k+k_m)d}$$

$$\ell = \frac{(d)(\ell')}{f}$$

$$\Omega = \frac{A}{d^2} \quad ,$$

where P is the power at the detector, P_L is the laser power, η is the efficiency of the collector optics, S is the scattering function from figures 11 and 13, ℓ is the length of beam the collector sees, Ω is the solid angle the collector accepts, k is the extinction coefficient in figures 11 and 13, k_m is the molecular water vapor absorption expressed in distance and not precipitable cm, d is the distance from the beam, ℓ' is the detector length, f is the collector focal length, and A is the collector area.

The conditions used for the following calculations are:

Collector: Area = 1 m^2, focal length = 1 m, efficiency = .9

Detector: 10 mm by 1 mm, noise equivalent power in 1-Hz
             bandwidth = 10^{-11} W

Laser: 10^{-1} W at 1.152276 μ

Atmospheric Conditions: 26° C, 100 percent RH, 1 atm, therefore
$k_m = 1.06 \times 10^{-4} cm^{-1}$ (expressed in distance and not precipitable cm).

Fog

Table 2 gives the power at the detector for fog of various density.
Any values below 10^{-11} W would not be detectable with uncooled lead
sulphide.

Table 2.   Power at the Detector for Fog (W)

$k(cm^{-1})$	$\theta = 90°$ d = 10 m	$\theta = 90°$ d = 100 m	$\theta = 45°$ d = 140 m b = 100 m	$\theta = 10°$ d = 575 m b = 100 m
10^{-2}	6.0×10^{-12}			
10^{-3}	6.7×10^{-9}	8.1×10^{-14}		
10^{-4}	2.2×10^{-9}	3.6×10^{-11}	1.1×10^{-10}	1.5×10^{-13}
10^{-5}	3.2×10^{-10}	1.3×10^{-11}		
10^{-6}	4.0×10^{-11}	1.6×10^{-12}		

At 10 m, fog corresponding to k = 10^{-3} gives the most power, but at
100 m less dense fog (k=10^{-4}) gives the most power, because the absorption
in the path is more than the decreased scattering. At an angle of 45°, the
signal is greater than at either 90° or 10° when the observer is 100 m from
the closest point on the beam.

19

Smoke

As pointed out before, the variability of smoke makes it impossible to categorize smoke by its extinction coefficient and to determine its scattering. The scattering function for the particular smoke studied has the same shape as, but half the intensity of the water vapor scattering function. The values of detector power are half those in table 2, as the other half of the energy is absorbed by the particles themselves. Unfortunately, one cannot assume that all, or even most, smoke will exhibit the properties of table 2.

One aspect of smoke scattering is particularly interesting. If the main laser beam strikes a column of smoke on a clear cold day, the scattering would be observable up to 8 km. The conditions are as follows: the same collector and detector as specified earlier, $-20\,^{\circ}C$, 10 percent relative humidity, d = 8 km and b = 1.4 km.

4. EXPERIMENT

Figure 15 shows the setup for the experiment discussed below. To make the equipment suitable for field use, many advanced techniques (such as cooling detectors) were avoided.

Laser Power and Wavelength

Several lasers in the near infrared are available. The helium neon laser at $1.152276\ \mu$ was chosen because it has moderate water vapor absorption, which made it possible to study both scattering and absorption. The laser has a power output of 30 mW CW and consists of a narrow band of closely spaced frequencies. The amplitude changes less than 3 percent when the ambient temperature is held reasonably constant. The laser's length (75 in.) and height (11 in.) made it rather difficult to handle, but the high output power and excellent dependability were more important.
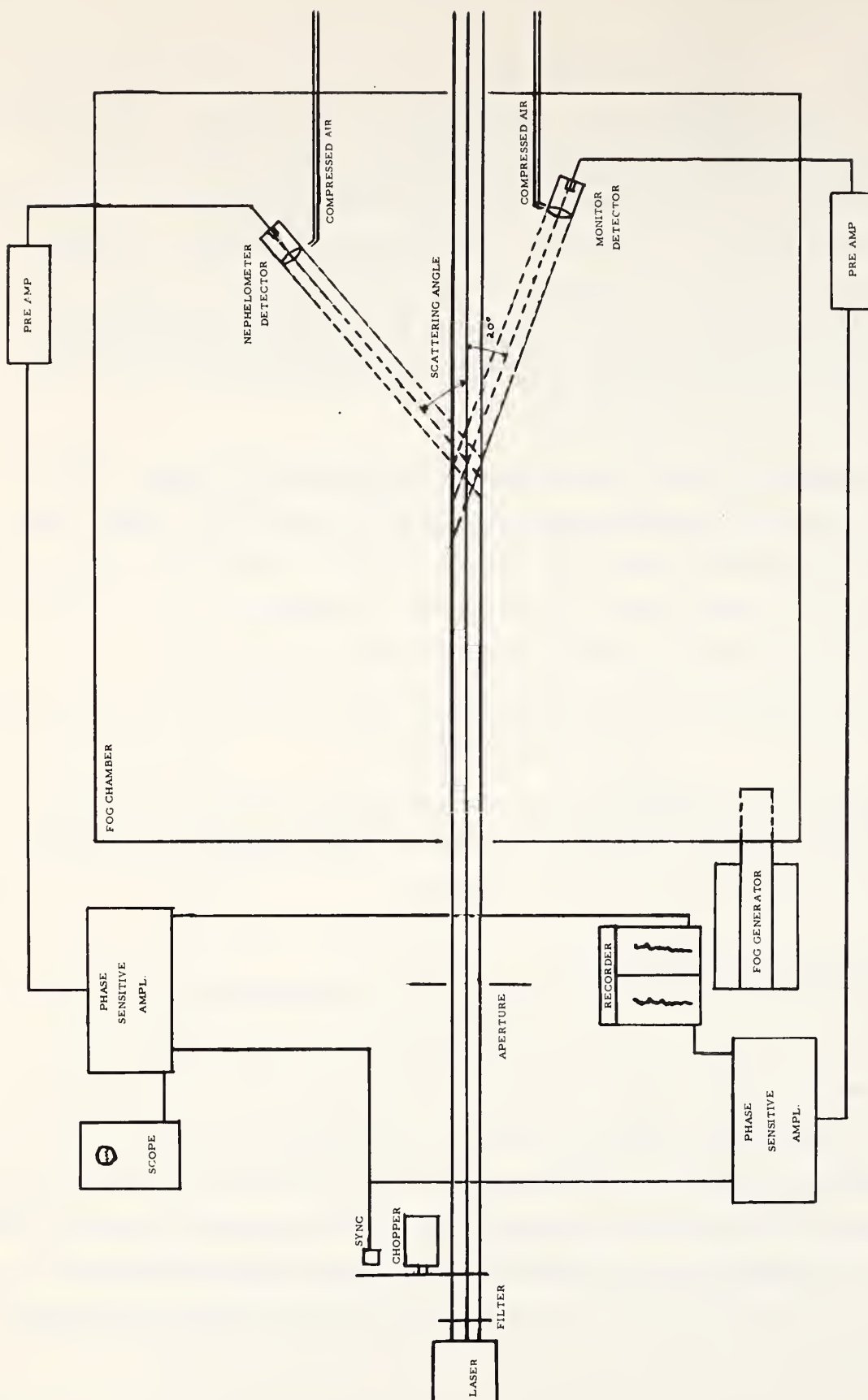
Figure 15. Experimental setup

21

Detector

The criteria for selecting the detector were high sensitivity and simplicity. Two types of detectors were tried: silicon p-n and uncooled lead sulphide. The silicon detector was tried in the hope of eliminating the sensitivity change with temperature that occurs in lead sulphide. Its sensitivity at 1.15-μ wavelength proved to be insufficient for detecting the scattered signal. Therefore, two identical uncooled lead sulphide detectors were used. Both were placed in the same temperature environment, and the ratio of their two outputs was used to generate the data. This canceled any temperature effects.

The noise equivalent power(NEP) for lead sulphide is determined by the equation

$$NEP = \frac{\sqrt{A \Delta f}}{D^*} \quad ,$$

where A is the area, Δf is the frequency bandwidth in hertz, and D^* is the detectivity of the detector. The detectors used in this experiment had a manufacture-quoted D^* of $5 \times 10^{10} \frac{cm-sec^{1/2}}{W}$ at 1.15μ and an area of 0.25 cm^2. For a bandwidth of one hertz, the NEP was 5×10^{-11} W. The laser beam was chopped at lead sulphide's optimum chopping frequency of 900 Hz. Two lock-in amplifiers were used with the lead sulphide detectors. The signals were recorded on a dual channel recorder.

Collecting Optics

The optics consisted of a zoom lens 1 cm in diameter, held at a radius of 40 cm from the scattering volume by the use of a nephelometer. The solid angle (Ω) collected was 4.9×10^{-3} steradians. About 12 cm of the beam length was in the field of view at 90°; this length increases as the cosecant of the scattering angle for other angles.

The nepholometer was constructed to hold the collecting optics and detector at any given position on a sphere with a radius of 40 cm. The detector and lens were aligned to look at the center of the sphere. The scattering pattern could then be established. An aperture (larger than the laser beam diameter) was set up about 1 m in front of laser to cut out side diffraction and stray radiation from the laser.

Scattering Patterns

Preliminary laboratory studies with a small fog chamber showed that the scattering was measurable, but, due to diffraction from the chamber entrance apertures and reflections from around the room, the data were invalid. The equipment was then moved outside the building, where the air varied from clear to moderately dusty. There was no detectable scattering.

The equipment was subsequently moved to an ESSA laboratory on Fritz Peak about 20 mi west of Boulder at an elevation of 9000 ft. This site was chosen because it has more ground fog than Boulder and is less populated. The laser was put in a room with good temperature control and pointed toward the Continental Divide. By the time the equipment had been set up, optics aligned, and a method devised to blow compressed air across the optics to keep condensation off, no fog could be expected for the rest of the summer. Therefore, a large fog chamber about 6 x 6 x 2 ft was constructed out of canvas stretched over a frame. The nepholometer was placed in the chamber and holes cut so that the laser beam would not touch the chamber walls. The beam was carefully aligned to pass through the center of the nepholometer sphere. A second detector and optical system was attached to the nepholometer bench and set at $\theta = 20°$ in order to monitor the scattering volume. Taking the ratio between the signal from the movable detector and the stationary one made it possible to correct the detector both for responsivity drifts caused

by temperature changes and for changes in the density of the scattering volume.

The fog was generated by an insecticide fogger in which water was used in place of insecticide. For the smoke tests, oil heated on a hot plate was used. The fog runs had to be done in the evening or early morning when it was sufficiently cool for creating a consistent fog. The fogger generated a fog for about 30 min, limiting the number of points that could be measured during each run. Therefore, the scattering was only measured every 10°.

Several runs were made for each polarization and then averaged. No appreciable difference between the two polarizations was observed. Both were averaged to give the experimental curves in fog (fig. 11) and smoke (fig. 13).

The measurements were started at $\theta = 10^O$ and terminated at $\theta = 170^O$ so that the collecting optics would not be in the main beam. The laser power was measured before and after each angular measurement sequence by letting the movable detector look straight down the beam after a filter of known attenuation had been placed in the beam. Runs with a significant change in laser power were discarded. Fogs were made as dense as possible for the measurements and had a transmission of 50 percent over the 1-m path. Smoke could be made so dense that no scattering or transmission were detectable, and the density, therefore, was adjusted for a maximum signal on the reference detector. This was a fairly critical adjustment and the wind had to be calm outside the chamber before satisfactory runs could be made. The attenuation under this condition was again 50 percent.

Transmission Measurements

Experimental data on the absorption of water at $1.15\ \mu$ are given by Long (1966). In view of the discrepancy between his results and absorption calculated by the Deutschman and Calfee (1967) program (using

24

the latest line parameters), the laser used in this experiment was taken to Oklahoma City, and an attempt was made to measure the absorption in a 1.5-km path across Lake Hefner. An evaporation study was being conducted by B. R. Bean of the Wave Propagation Laboratory in conjunction with the U. S. Bureau of Reclamation. The lake was instrumented with numerous meteorological devices so that the total amount of water in the path of the laser beam could be determined.

The beam spreads according to the relation $\theta = 1.22 \lambda / d$, where θ is the half cone angle, λ the wavelength of radiation, and d the diameter of the initial aperture. With a 2-mm laser aperture, the diameter of the laser spot would be 2.1 m at 1.5 km. Because this is too large to collect on a reasonably sized mirror, a beam expander was constructed out of simple lenses to increase the beam diameter at the laser. The beam diameter across the lake would then be about 10 cm. This 10-cm spot could not be located with an infrared phosphor card on the other side of the lake. If the laser had operated in the visible, it would have been relatively simple. The time preparation had been very short, and the necessary modifications could not be made in the field.

By overfilling the collecting optics on the other side of the lake with a laser having a 2-mm aperture the signal could be found. It was hoped that recording these data would indicate changes in water vapor in the path. The data obtained, however, showed that the background sunlight changes were greater than the fluctuations caused by water vapor changes. This experiment could be done with a good pointing system and collimator.

5. CONCLUSIONS

The detectable range of a laser beam through a fog can be predicted fairly accurately for various detectors and collecting optical systems if the temperature, relative humidity, and fog extinction coefficient are

known. Some idea of the extinction coefficient in a particular fog may be gained from its visibility.

If the transmission is less than 80 percent over the path in question, multiple scattering can become important. This is a complicated effect that needs further study; the exponential extinction law will give less intensity than will actually be seen over long paths.

Smoke presents many problems unless the particle size distribution and composition are known. Each case needs to be studied individually, but the task is not impossible. Such studies of different types of smokes and their scattering patterns would allow one to fix maximum and minimum bounds for smoke. The particular smoke studied showed that very long detectable ranges could be expected under certain smoke conditions.

6. ACKNOWLEDGEMENTS

7. REFERENCES

Arnulf, A. , J. Bricard, E. Cure, and C. Veret (1957), "Transmission by haze and fog in the sprectal region 0.35 to 10 microns," J. Opt. Soc. Am. 47, 491.

Carrier, L. , G. Cato, and K. von Essen (1967), "The backscattering and extinction of visible and infrared radiation by selected major cloud models," Appl. Opt. 6, 1209.

Conner, W.D. , and J. R. Hodkinson (1967), "Optical properties and visual effects of smoke-stack plumes," Public Health Service Publication No. 999-AP-30 (U.S. Govt. Printing Office).

Johnson, D.R. , and D. E. Burch (1967), "Attenuation by artificial fogs in the visible, near infrared, and far infrared," Appl. Opt. 6, 1497.

Long, R. K. (1966), "Atmospheric absorption and laser radiation," Eng. Exp. Station Bull. No. 199, Ohio State Univ. , Columbus, Ohio.

National Academy of Sciences-National Research Council (1930), "International Critical Tables of Numerical Data Physics," Editor in chief, Edward W. Washburn, Chemistry and Technology 7, 13 (McGraw-Hill, New York, N.Y.).

Penndorf, R. (1963), "Research on aerosol scattering in the infrared," Tech. Rept. RAD-TR-63-26, Contract AF 19(604) - 5743, Prepared for Air Force Cambridge Research Labs. , Bedford, Mass. by Avco Corp, Wilmington, Mass.

Reisman, E. , G. Cumming, and C. Bartky (1967), "Comparison of fog scattered laser and monochromatic incoherent light," Appl. Opt. 6, 1969.

Spencer, D. (1960), "Scattering function for fogs," J. Opt. Soc. Am. 50, 584.

Van de Hulst, H. C. (1957), "Light Scattering by Small Particles" (John Wiley and Sons, New York, N. Y.).

27

57

Practicality of Using Light Beams to Distribute Local-Oscillator Signals over Large Antenna Arrays

R.S. LAWRENCE, K.B. EARNSHAW, J.C. OWENS
Environmental Science Services Administration Research
Laboratories, Boulder, Colorado, U.S.A.

Summary

Maintenance of phase uniformity in the distribution of local-oscillator signals is one
of the major problems facing the designer of microwave antenna arrays that extend
for many kilometers. Although satisfactory round-trip systems involving cables
can be designed, a desire for economy and flexibility is an incentive to examine
direct radiating systems such as modulated light beams.

The irregular atmosphere limits the performance of optical systems through the in-
troduction of variable optical path length. We present measurements of the mag-
nitude of this effect and discuss its importance to a proposed optical distribution
system. The system involves the use of two colors of light and is a one-way rather
than a round-trip system. An effective path-length stability of 3×10^{-8} is predict-
ed.

Background

Antenna arrays now being considered for use in radio astronomy will extend for tens
of kilometers. The ultimate limitation to the performance of such phased arrays
placed on the earth's surface will be the irregular phase fluctuations imposed upon
the down-coming wave by the atmosphere. Before that limitation prevails, one of
the major problems facing the designers of such large radio telescopes is the main-
tenance of phase coherence among the waves received from various parts of the
array as they are carried to a central receiver or processing unit. If, as is usually
the case, the incoming waves are converted to a lower frequency before transmiss-
ion to the central point, the problem is unchanged, because it then becomes necess-
ary to distribute over the array a local oscillator signal with suitable phase stability.
Direct radio transmission of the signal through the open atmosphere is clearly un-
desirable because, as soon as the size of the array exceeds the effective height of
the atmosphere, several kilometers, the phase fluctuations introduced in trans-
mission to the central point will exceed those introduced by the vertical passage
through the atmosphere.

Although the problem and the remarks we shall make concerning possible solutions
apply to any large array, we shall, for the purpose of numerical example, direct
our attention to the stability requirements stated by the astronomers at the U.S.
National Radio Astronomy Observatory in their recent proposal for a very large
array (VLA) (1). The VLA is to include individual antennas separated by as much
as 36 km, and the local oscillator will have a frequency of 2695 MHz. The des-
igners suggest that the difference in phase of the local oscillator signals received at
any two points of the array must remain constant over an 8-hour period to within an
rms error of 2°. This stringent requirement is several times better than the re-
lative phase stability of the down-coming signals from the sky and, if it can be met,

will insure that local oscillator phase noise will not be a limitation to performance of the telescope.

Over the 18-km distance to the center of the array, this stability requirement corresponds to changes in phase path length of only 0.6 mm, or 3 parts in 10^8. The corresponding requirement for stability of the average refractivity of the air to 0.03 N unit is sufficiently unrealistic that we may dismiss consideration of direct open-air transmission of the microwave signal. Even the direct use of an optical carrier that would be only 1/100 as sensitive to the variable water-vapor content of the air is impractical because the average temperature of the air along the path would have to be known to 0.03°K. Cables, with their temperature coefficient of phase velocity some 20 times larger than that of air, would have to be maintained at a temperature constant to 0.0017°K.

Round-trip phase-correcting systems have been devised to solve these problems. These systems permit the phase errors to be measured after the signal has made a round trip and then, with the assumption that equal errors have accumulated in each direction, to be used to make an appropriate correction. This simple description of the principle of round-trip systems might be thought to imply that each antenna element in the array would require a separate loop of transmission line. This is true for the open-air microwave systems that have been proposed, but the designers of the VLA propose to use a clever system attributed to Dr. John Granlund of ITT Federal Laboratories. In the Granlund scheme, the signals travelling in the two directions on the loop are each one-half the desired local oscillator frequency and are arranged to have, at any distance from the center of the array, equal and opposite phase errors. Mixing of the two provides, at any point, the required phase-stable signal.

The Granlund system can certainly be made to work well enough to satisfy the requirements of the VLA. The principal practical difficulty is that, because directional couplers are not perfect, it is necessary to isolate the forward and backward signals by separating their frequency. This means that the opposite phase errors will not, in fact, be exactly equal. The difference in the phase errors must be kept within acceptable bounds by such cumbersome means as the use of coaxial cables buried a meter in the ground so that their differential temperature variations will not exceed about 0.2°C.

The various practical problems associated with even the Granlund system force the estimated cost of the local-oscillator distribution system for the VLA to well over a million dollars. Thus it seems relevant to examine in more detail the possible use of a refinement of the optical system that we discarded summarily a moment ago.

Before examining the possibilities of optical systems, let us consider to what extent separate, independent oscillators at the various antennas will meet the requirements. A phase fluctuation of 2° at 2695 MHz corresponds to a fluctuation of 6.5 x 10^{-5} rad at 5 MHz. Oscillators operating at 5 MHz are readily available which will drift less than this amount over a period of 0.1 sec. Thus, in principle at least, it would be possible to meet the VLA requirements with a phase correcting system having a time constant as long as 0.1 sec.

More stable independent oscillators, even if they should prove to be economically feasible, would still be inadequate. For example, two good cesium-beam standard oscillators can be expected to drift apart by 6 x 10^{-5} rad (at 5 MHz) in less than a second, and even two hydrogen masers will not maintain this degree of phase synchronism for more than a few tens of seconds (2).

Optical Systems

Measurements have recently been made of the fluctuations in phase of microwave modulation impressed upon a laser beam and transmitted over a round-trip path through the open atmosphere to a retroreflector several kilometers away. The experimental apparatus was constructed to investigate the suggestion by Bender and Owens (3) that a measurement of the dispersion caused by the atmosphere would permit optical distance meaasurements to be corrected for atmospheric retardation. The apparatus has been described in detail by Earnshaw and Owens (4). Briefly, it contains sources of red and blue light, a 3-GHz modulator, an 8-inch transmitting telescope and a distant retroreflector. The modulated beam is reflected back through the telescope and the modulator so that its intensity drops to a minimum when the distance from the modulator to the reflector is an odd number of half-wavelengths. The distance-measuring application requires a 'beam stretcher' in the red light path so that both the red and blue intensities can be minimized simultaneously. We speak of the measured path length as 'phase path length', thinking in terms of the microwave signal in which we are interested. It depends of course on the group velocity of the modulated optical wave. We summarize below the results of those measurements that are relevant to our present problem.

On a round-trip path of 10.6 km, the usual rms fluctuation of 1-sec averages of phase path relative to the 30-sec moving average is found to be 3×10^{-9} of the total path. The diurnal drift of many parts in 10^6, principally caused by the many-degree change in temperature, causes a steady change in the average phase path in addition to these rapid fluctuations. A typical recording is shown in figure 57-1. Figure 57-2 shows an extremely noisy example observed after a heavy rain.

In dry air, the difference in observed phase-path length using red (6328Å) and blue (3683Å) light is accurately proportional to and approximately 9 percent of the phase-path delay introduced into the red beam by the atmosphere. Thus, when red and blue phase paths are measured simultaneously, each with an accuracy of 3×10^{-9}, it is possible to correct either for long-term drift to an accuracy of 3×10^{-8}. In this calculation we assume that the phase-path fluctuations of the red and blue beams are well correlated. Although presently available apparatus has not permitted an explicit demonstration of this correlation, it can be inferred from the observed excellent agreement of intensity fluctuations shown in figure 57-3. Even if the rapid phase fluctuations on the two colors are uncorrelated, the accuracy would suffer only by an additional factor of $\sqrt{2}$. Excepting a constant zero-point error that is of no concern to our present discussion, a corrected distance measurement with a precision of 3×10^{-7} has already been demonstrated over the 10.6 km path using 10-sec averages. The additional loss of a factor of 10 in this measurement relative to the accuracy predicted above has been identified with instrumental effects in the present distance-measuring apparatus rather than to atmospheric limitations.

With these observations in mind, we suggest that a different apparatus using the dispersion technique could provide an economical and useful means of distributing local-oscillator signals through the open air. This two-colour optical system is a one-way system, so the desired signal is available simultaneously at an arbitrary number of receiving locations along the beam. One such receiver is shown in figure 57-4. The coincident red and blue beams, which have been modulated with the master-oscillator frequency at the center of the array, arrive at the receiving station with a phase difference $\phi_B - \phi_R$. Here the beams pass through a second modulator excited at frequency $\omega_1 < \omega_0$. The two colors are separated and detected, the resulting frequency $\omega_0 - \omega_1$ being in the vicinity of 100 kHz. The difference frequencies derived from the red and blue beams still possess the phase difference $\phi_B - \phi_R$. The difference frequency from the red detector is compared in a discriminator with the difference frequency from the highly stable local oscillator ω_0'. The difference is used to tune that local oscillator slightly so that it

agrees with the master oscillator frequency ω_0. This local oscillator must be sufficiently stable so that it will not drift beyond the acceptable 2° within the time constant of the servo loop, say 0.1 second.

To keep $\omega_0{}'$ at a constant phase relationship with the master oscillator ω_0, the effect of the atmosphere must be determined by measuring the phase difference $\phi_B - \phi_R$ between red and blue signals. This difference is measured with the phase meter, and the resulting voltage is multiplied in a simple analog computer by a factor of approximately 11. This factor is necessary because the red-blue dispersion of the atmosphere is about 1/11 the total atmospheric phase retardation of the red light. The exact value of the factor depends slightly upon the relative humidity of the air (5) and must be controlled slowly in response to the outputs of appropriate meteorological sensors. The phase correction voltage from the computer drives a phase shifter to produce the desired constant-phase local-oscillator signal. Alternatively, if the radio telescope is a correlator array involving a central computer, the phase correction could be applied by that computer.

An accuracy of 0.3 mb in the average partial pressure of water vapor, which can reasonably be expected over uniform ground in dry climates, would be required for the specified phase accuracy. The optical refractive index obtained by the dispersion method, however, can be shown to be only 1/40 as sensitive to water vapor as is the microwave refractive index. Hence a parcel of moist air drifting through the optical path and in front of one of the radio antennas will cause only 1/40 as much phase error in the local-oscillator signal as in the down-coming microwave signal. Allowing for the difference between 18 km and the effective thickness of water vapor in the atmosphere, we find that the optical signal is only about 1/10 as sensitive to water vapor fluctuations as the radio signal. Therefore the humidity-caused variations in phase of the down-coming wave, rather than the errors in local-oscillator phase, will be the dominant limitation of the radio telescope.

Let us reiterate what performance we might expect from this two-color optical system. We have already seen that the rapid fluctuations of the red beam are about 3×10^{-9} and that it is possible with an existing instrument to obtain corrected distance to within 3 parts in 10^7 with 10-sec averaging. The use of two lasers, rather than a laser and a mercury arc lamp, and of a one-way rather than a round-trip path would significantly improve the signal-to-noise ratio and precision of the instrument, and the relative reduction of instrumental noise that should accompany longer paths would also improve its performance. Assuming adequate water vapor information, we may confidently estimate that the two-color system would permit a stability of about 3×10^{-8} to be achieved. This estimate seems sufficiently promising to warrant the construction of a prototype device to evaluate the method.

Conclusion

Observations of the atmospheric effects upon optical path-length measurements indicate the possibility of using a two-color optical system to provide adequate phase stability for the distribution of local-oscillator signals over the large antenna arrays being proposed for radio astronomy.

References

1.   'A proposal for a very large array radio telescope', Nat. Radio Astronomy Observatory Rep., Jan. 1967.

2.   McCoubrey, A.O., Proc. IEEE 55, 805, 1967.
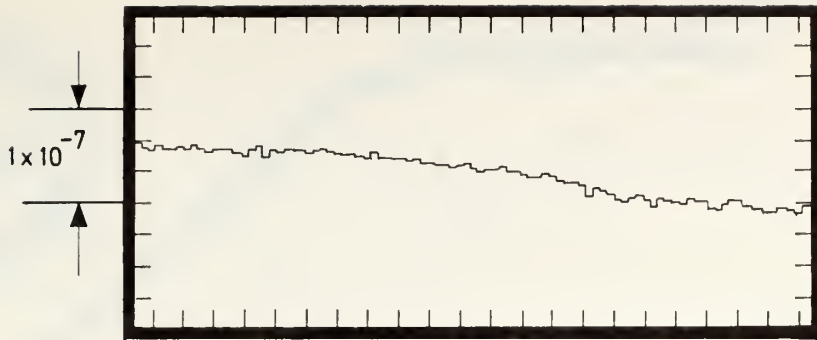
Fig. 57-1   Path-length observations with an optical beam traversing
a round-trip path of 10.6 km under normal conditions.
The rms fluctuation of these 1-sec averages relative to
a smooth average is 3×10^{-9} of the total path
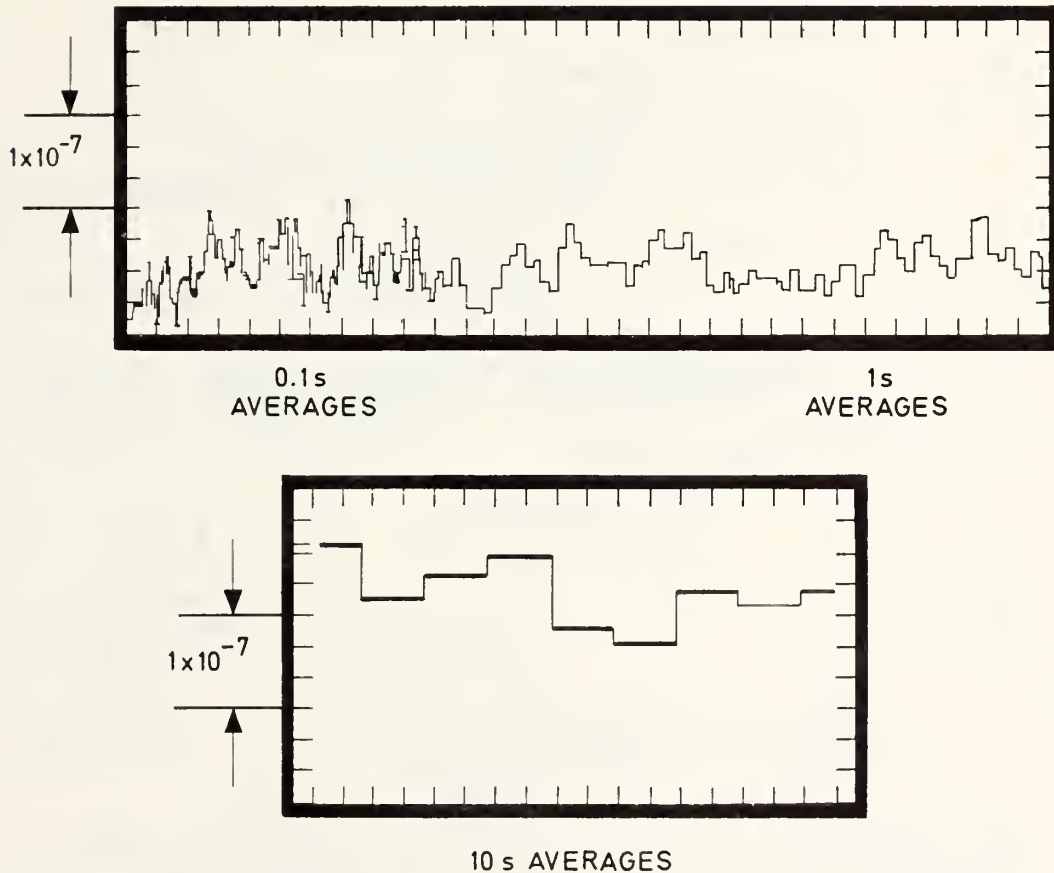
Fig. 57-2   Examples of path-length fluctuations with an optical beam
traversing a round-trip path of 10.6 km under unusually
noisy conditions.   The rms fluctuation is about 3×10^{-8},
nearly independent of averaging time between 0.1 sec and
10 sec

CORRELATION COEFFICIENT
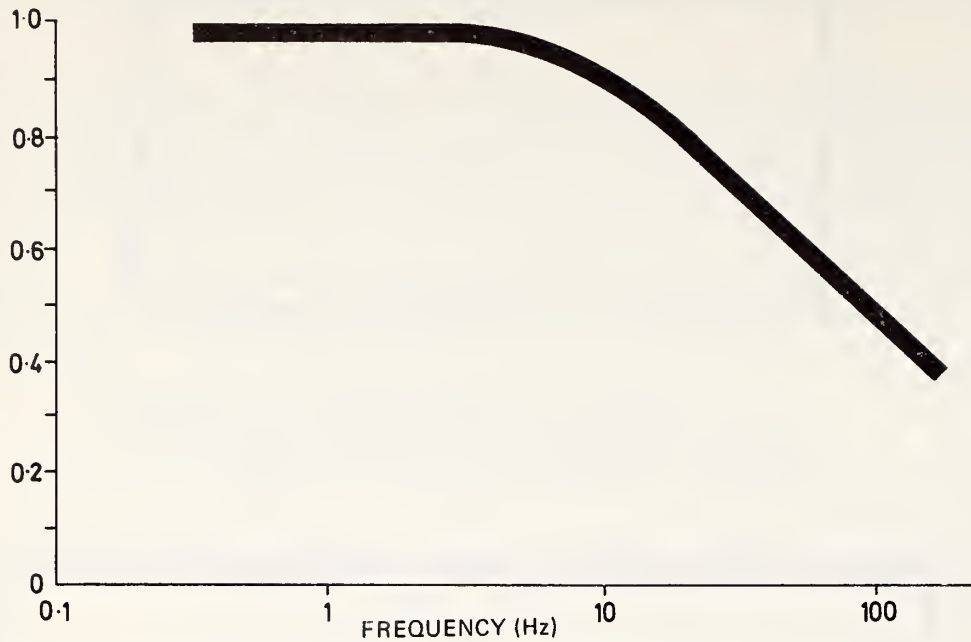
Fig. 57-3 Correlation of the intensity fluctuations of red and blue light. Beam diameter, 20 cm; round-trip path, 10.6 km
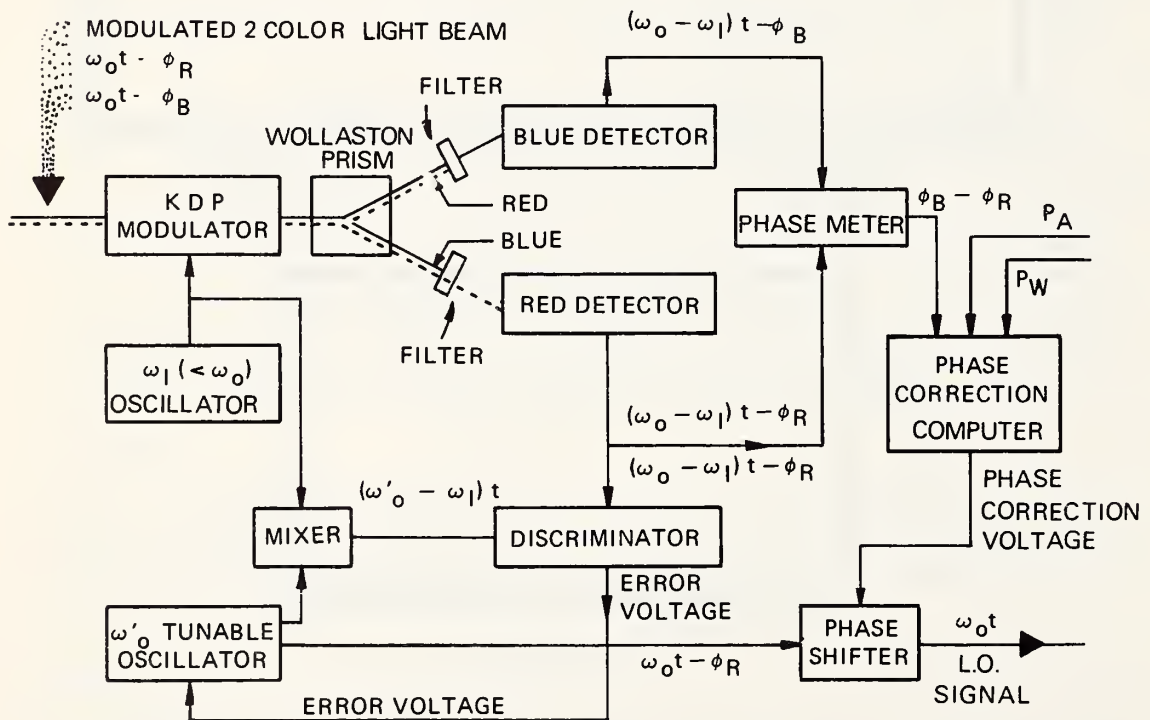
Fig. 57-4 Block diagram of one of the receiving locations for a one-way, two-color local-oscillator frequency distribution system

ESSA TECHNICAL REPORT ERL 154-WPL 10

Measurements of 0.63 μm Laser-Beam Scintillation in Strong Atmospheric Turbulence

G. R. OCHS

TABLE OF CONTENTS

MEASUREMENTS OF 0.63 μm LASER-BEAM SCINTILLATION IN STRONG ATMOSPHERIC TURBULENCE

G. R. Ochs

Log-amplitude variance and covariance of the scintillation of a diverging optical beam have been measured over a 48-hr period at a wavelength of 0.63 μm, on 490 and 1000 m optical paths 2 m above the surface of a flat mesa near Boulder, Colorado. Simultaneous measurements of the refractive-index structure of the atmosphere have been obtained from temperature-structure-function measurements at spacings of 1, 3, and 10 cm. A saturation of scintillation occurs for values of log-amplitude variance between 0.5 and 1. After reaching a peak, the log-amplitude variance then decreases with both increasing range and increasing refractive-index turbulence. The spatial covariance of the fluctuations tends to increase in the saturation region. In the unsaturated region, the log-amplitude variance is approximately that predicted by the spherical-wave propagation theory of Tatarski.

I. INTRODUCTION

In the presence of strong atmospheric refractive-index turbulence, the magnitude of scintillation of an optical beam appears to reach a limit that it very seldom exceeds, regardless of the strength of the atmospheric refractive-index fluctuations. For visual light, this phenomenon, known as saturation, is likely to occur, for example, in the daytime on optical paths a few meters or less above ground and more than 0.5 km long. Saturation was originally observed by Gracheva and Gurvich (1965) and has since been reported by Gracheva (1967), Deitz and Wright (1968), Ochs and Lawrence (1969), Mevers et al. (1968), and Johnson (1969). The original propagation theory of Tatarski did not predict saturation. Later, Tatarski (1967) and de Wolf (1968) advanced theories to explain the experimental observations. It is now generally agreed that a saturation of

scintillation occurs, but there is less agreement about the cause. Additional observations reported here were made to better understand the saturation process.

The measure of scintillation that has been used is log-amplitude variance, $C_\ell(0)$, defined as

$$C_\ell(0) = \overline{(\ln v - \overline{\ln v})^2} \, , \tag{1}$$

where v is the light amplitude (square root of irradiance) received in a 1 mm diameter aperture as a function of time. Additional statistical information about the nature of the fluctuating light pattern has been obtained by measuring the normalized log-amplitude covariance, $C_\ell^s(\rho)/C_\ell(0)$, where ρ is the aperture separation. Generally these results will be compared with the spherical wave propagation theory of Fried (1967), developed from Tatarski's earlier work, which does not predict a saturation of scintillation. According to this theory,

$$C_\ell(0) = 0.124 \left(\frac{2\pi}{\lambda}\right)^{7/6} Z^{11/6} C_n^2 \, ,$$

where λ is the wavelength of the light, Z is path length, and C_n^2 is refractive-index structure parameter; C_n^2 was measured independently, using small, high-speed, platinum resistance thermometers. The method is described in Ochs et al. (1969).

2. EXPERIMENTAL PROCEDURE

All measurements were made on an east-west optical path 2 m above the grass-covered surface of Table Mountain, a very flat mesa approximately 12 km north of Boulder, Colorado. A continuous-wave HeNe

2

laser with 3-mW single-mode output at 0.6328-μm wavelength, used in conjunction with a beam-expanding telescope, provided a beam of essentially Gaussian irradiance cross section. The transmitter was directed toward three photomultiplier receivers, one 490 m and the other two 1000 m down-range. The receivers were slightly displaced from the center of the beam, so that they could be used simultaneously. They had 1-mm diameter apertures, a 1-mrad field of view, and 10 Å filters. The received band-width was restricted to the range 0-3 kHz. The receivers 1000 m down-range were separated vertically for covariance measurements.

Temperature structure function measurements were made at three vertical spacings, 1, 3, and 10 cm, with high-speed thermometers placed near the center of the 1000 m path. Wind velocity measurements were also made near this location.

In order to record several days of data, analog preprocessing was used, and the mean values of the quantities of interest were digitally recorded once each minute, for later computer processing. The analog methods of computation are described by Ochs et al. (1969). These techniques for the measuring of log-amplitude variance might lack sufficient dynamic range for values of $C_\ell(0)$ such as encountered in the saturation region; hence, in addition to the precautions mentioned in Ochs et al. (1969), an occasional check, consisting of an amplitude distribution analysis was made when the optical signal was in saturation. From the portion of the amplitude plot having the best signal-to-noise, $C_\ell(0)$ was then determined and this value used as a calibration point for the analog equipment. The analog computation of $C_\ell(0)$ is independent of the amplitude distribution of the signal fluctuations. When using a portion of the amplitude distribution function to derive $C_\ell(0)$, one must assume that the entire distribution is log normal. The distribution is usually very close to log-normal but, especially at short ranges, there are occasional deviations.

Though it is difficult to say exactly how accurate the log-amplitude variance measurement is in the saturation region, the error limits certainly lie between -10% and +20%.

3. RESULTS

In figures 1 and 2, $C_\ell(0)$ is recorded as a function of time of day, midnight to midnight, for the 490-m and 1000-m optical paths. The data are averaged with a 100-sec time constant. On September 7 (fig. 1), cumulus clouds caused alternate sunlight and shadow along the path from approximately 1030 through the remaining daylight hours. The extreme dips in scintillation intensity occur at the shaded times. The following day (fig. 2) was clear until approximately 1630, with alternate sunlight and shade from cumulus clouds for the remainder of the daylight hours. According to the scintillation-distance relationship expressed in equation (2), $C_\ell(0)$ at 1000 m should be 3.7 times that at 490 m. It is obvious that the actual relationship is very different during much of the time. In figure 1, from approximately 0800 to 1000 there is an almost linear increase in $C_\ell(0)$ at 490 m, but then it clearly begins to saturate below a value of 0.6. Somewhat after 1000, the sun went behind a cloud and a very sharp decrease occurred in both. The 490 m path immediately started to decrease while the 1000 m path remained in saturation until the refractive index fluctuation approximately reached the point where the saturation occurred originally.

In figure 2, a similar phenomenon is seen from 0800 to 1000. After 1000, the day remained clear and the turbulence continued to increase. Another phenomenon occurred at that time; $C_\ell(0)$ at 1000 m began to decrease, while $C_\ell(0)$ at 490 m continued to increase, resulting in higher scintillation at 490 m than at 1000 m during the middle of the day. During this period, $C_\ell(0)$ predicted from the temperature fluctuation measurements and equation (2) for the 1000-m path remained well above the level of

4

scintillation actually observed. Thus, it appears that after a certain level of scintillation is reached, further increases in either the refractive-index turbulence level or the path length cause a reduction in the scintillation level.

Data in figure 1 have been compared at 1-min intervals as a function of scintillation predicted from equation (2). Figure 3 is an example of the resulting scatter plots, each point representing 100-sec averages of the scintillation observed and the predicted log-amplitude variances at 1000 m for all of September 7. Although there is a great deal of scatter, two characteristics are apparent: (1) the pronounced saturation of the scintillation and (2) the rough agreement of the observed scintillation below the saturation region with that predicted from spherical-wave propagation theory. There also appears to be two levels in the saturation region. In figure 4, the same data are separated for day and night, showing that the higher level of saturation occurred at night. Three, more or less, distinct groupings appear at night in the unsaturated region, while the daytime observations below saturation show a better agreement between theory and experiment.

The September 7 data were also sorted by wind velocity, with the result shown in figure 5. There appears to be a relation between saturation level and wind velocity; the level decreases with increasing wind velocity. There is also an unusual amount of spread in the unsaturated data when the wind velocity is less than 2 m/sec, presumably indicating that the turbulence is far from homogeneous and affects the point temperature sensors differently from the optical beam.

The same type of analysis has also been applied to figure 6, which shows data taken at 490 m. Here there is no evidence of saturation. As shown in figures 7 through 11, there is less spread of the data during the day than during the night, and calm wind conditions enhance the scatter. Additionally, the predicted scintillation tends to be less than that actually

5

observed. The reason for this discrepancy may lie in the shape of spectrum of turbulence. C_n^2 was derived from temperature probes vertically spaced 1, 3, and 10 cm, so that the form of the spectrum could be observed. C_n^2 derived from the 3 and 10-cm spacings was nearly the same when averaged over the 24-hour period; however, C_n^2 derived from the 1-cm spacing was consistently higher than the other two. A comparison of 1 and 3-cm data is shown in figure 12. Now, all of the predicted scintillation shown in the scatter diagrams has been obtained from C_n^2 based on the 10-cm spacing, as these data had somewhat less scatter from minute to minute. But, especially over the 490 m path, irregularities of 1 cm or less are primarily responsible for the observed scintillation. If C_n^2 derived from the 1-cm spacing had been used, the average prediction would have been more in agreement with the theory.

Another property of the scintillating wavefront is the distribution of the pattern sizes of the bright and dark places in the light pattern. The statistical measure used is the normalized log-amplitude covariance of the signal as a function of spacing normal to the direction of propagation of the light. Apertures 1 mm in diameter were used with varying vertical spacing to make the measurement, with results as shown in figure 13. The solid curves are taken from Fried (1967) and are the theoretical prediction for horizontal propagation of a spherical wave. The circles are the experimental measurements, taken in sequence from large to small spacings, then repeated from small to large spacings. Each point is a 30-sec average. The scintillation was strongly saturated at 1220. It was less so at 0930 and 1650, but still in saturation. Conditions were close to the saturation point at 2120. The departure from the predicted function is greater at the larger separations, indicating that in the saturation region there is a relative increase in the larger sizes of the fluctuating light pattern or, what is equivalent, the small-scale structure in the pattern is "washed out" by the saturation phenomenon.

6

4. ACKNOWLEDGEMENTS

5. REFERENCES

Deitz, Paul H. and N. J. Wright (1968), Saturation of scintillation magnitude in near-earth optical propagation, Mem. Report No. 1941, Ballistic Research Laboratory, Aberdeen Proving Ground, Maryland.

deWolf, D. A. (1968), Saturation of irradiance fluctuations due to turbulent atmosphere, J. Opt. Soc. Am. 58, 461.

Fried, D. L. (1967), Propagation of a spherical wave in a turbulent medium, J. Opt. Soc. Am. 57, 175.

Gracheva, M. E. and A. S. Gurvich (1965), On strong fluctuations of the intensity of light when propagating in the lower layer of the atmosphere, Izv. Vuz. Radiofiz., 8, 717.

Gracheva, M. E. (1967), Research into the statistical properties of the strong fluctuations of light when propagated in the lower layer of the atmosphere, Izv. Vuz. Radiofiz., 10, 775.

Johnson, W. B. (1969), Turbulence-induced "supersaturation" of laser scintillation observed over a 3.5-kilometer horizontal range, presented at AGU 50th Annual Meeting, April 2-24, 1969.

Mevers, G. E., M. P. Keister, Jr., and D. L. Fried (1969), Saturation of scintillation, presented at Spring Meeting, Opt. Soc. Am., March 11-14, 1969.

Ochs, G. R., R. R. Bergman, and J. R. Snyder (1969), Laser-beam scintillation over horizontal paths from 5.5 to 145 kilometers, J. Opt. Soc. Am. 59, 231.

Ochs, G. R. and R. S. Lawrence (1969), Saturation of laser-beam scintillation under conditions of strong atmospheric turbulence, J. Opt. Soc. Am. 59, 226.

Tatarski, V. I. (1967), On strong amplitude fluctuations of a wave propagating in a medium with weak random inhomogeneities, Radiofiz., 10, 1.
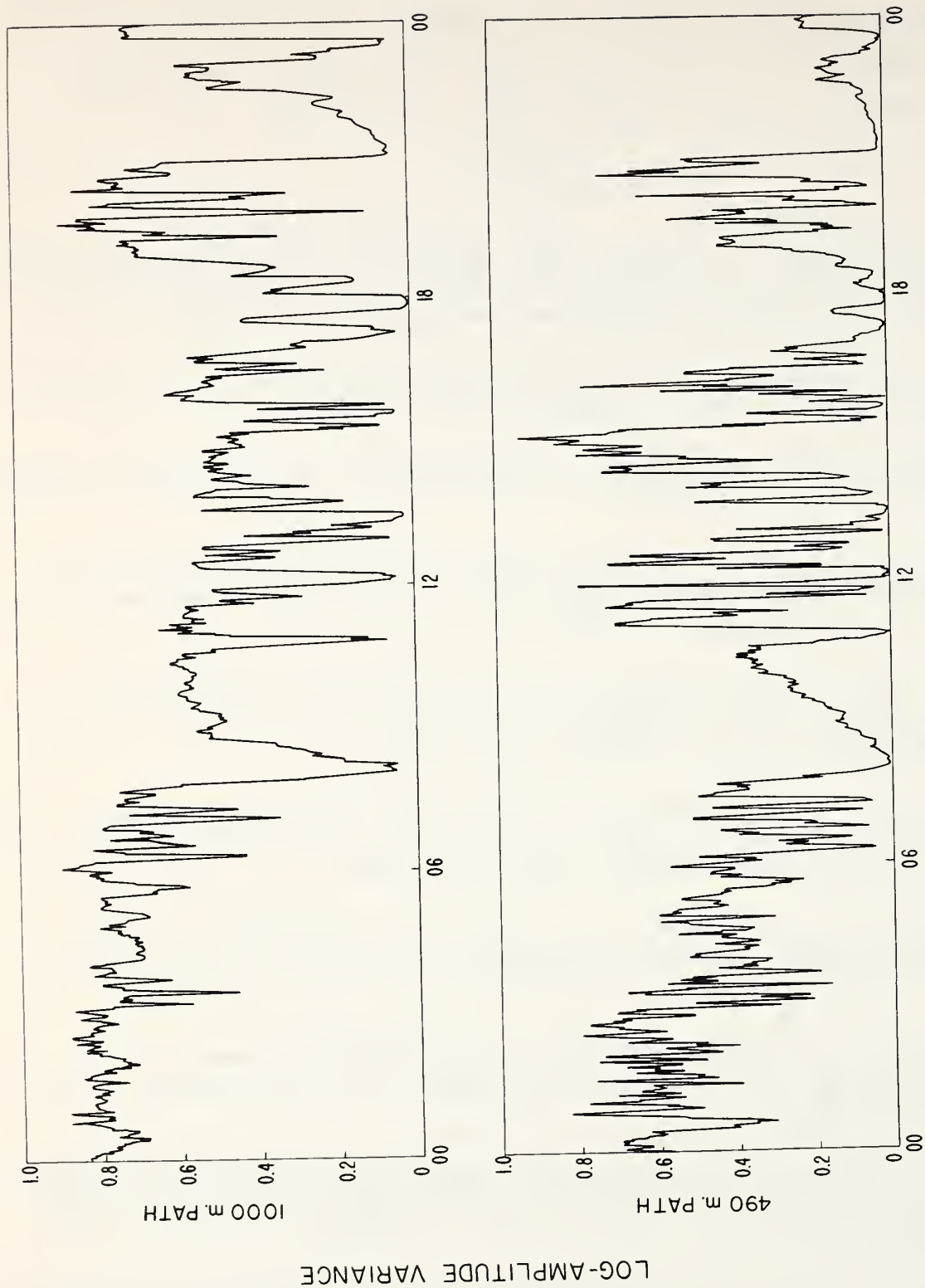
Figure 1. Log-amplitude variance versus time of day. The 490 and 1000 m paths are along nearly the same line of sight. Cumulus clouds caused alternate sunlight and shadow along the path from approximately 1030 through the remaining daylight hours.
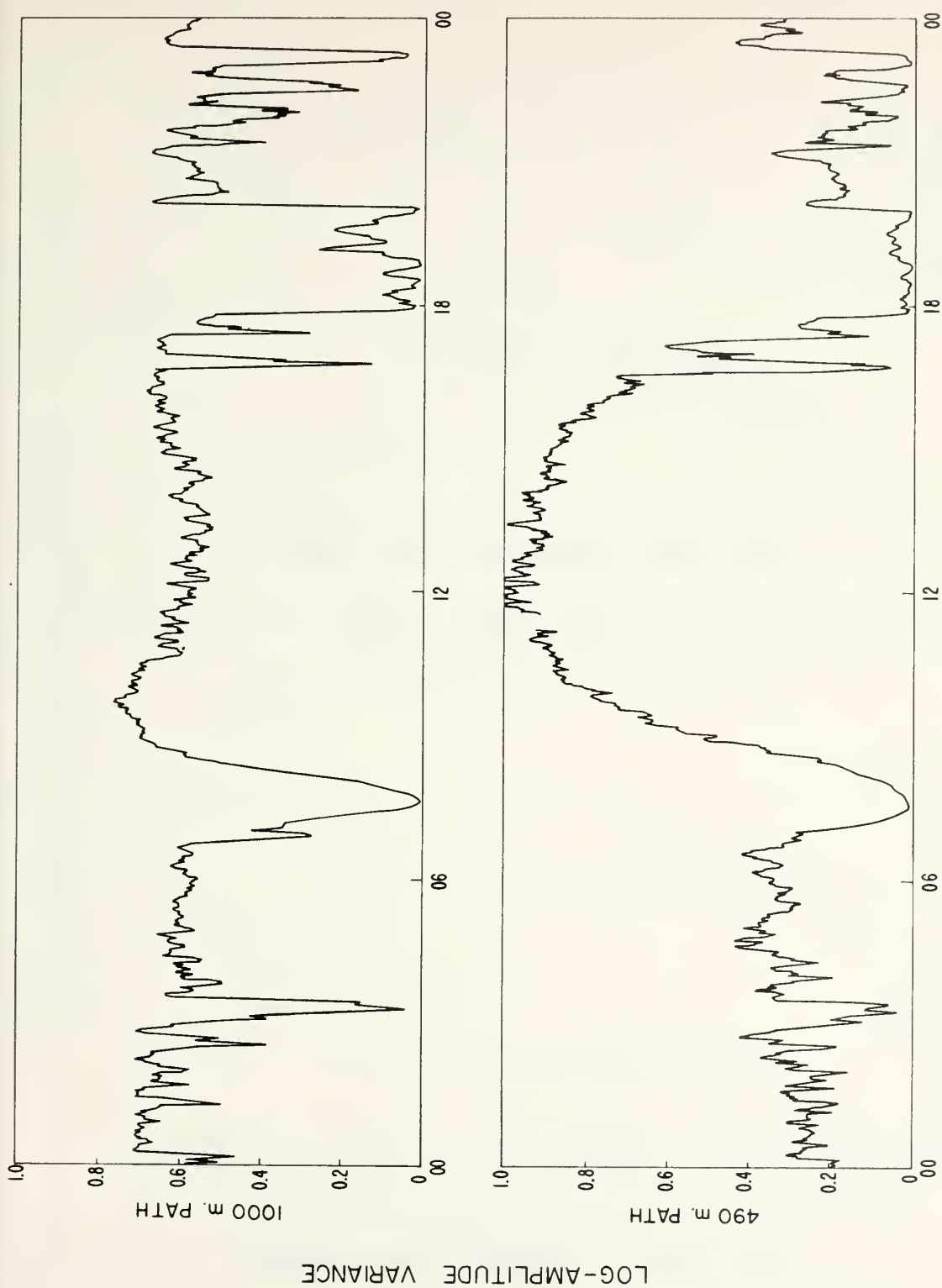
8

Figure 2. Log-amplitude variance versus time of day. The 490 and 1000 m paths are along nearly the same line of sight and were measured simultaneously. The day was clear until approximately 1630, with alternate sunlight and shade from cumulus clouds for the remainder of the daylight hours.

9
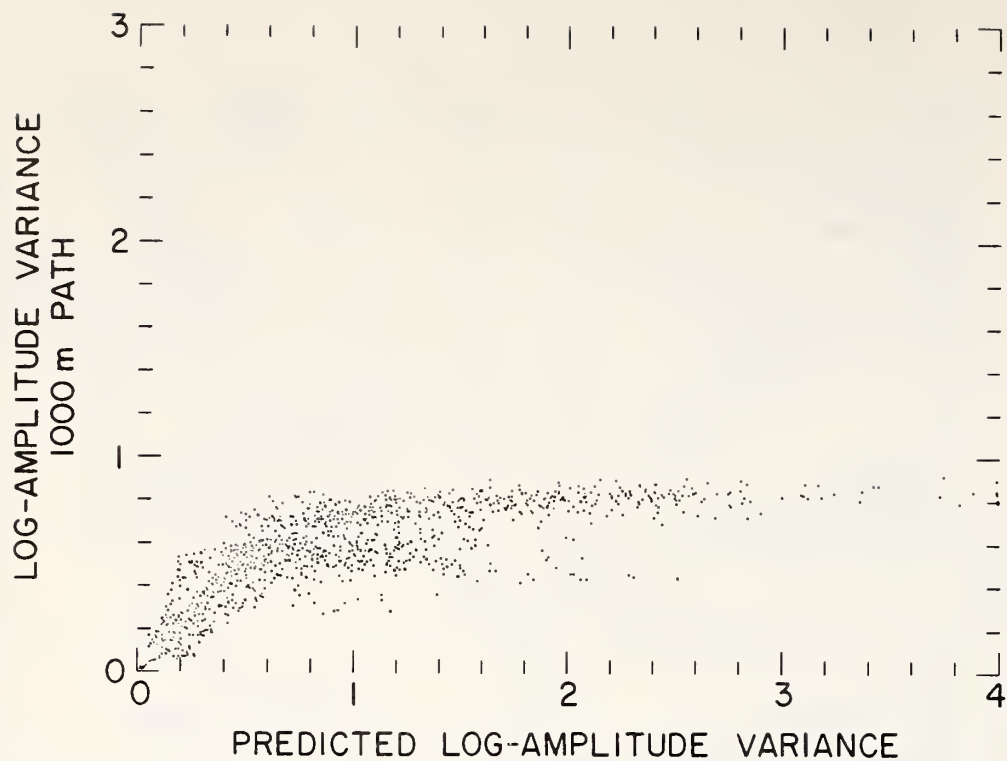
Figure 3. Scatter plot of log-amplitude variance at 1000 m versus log-amplitude variance predicted·
from temperature-structure-function measurements.
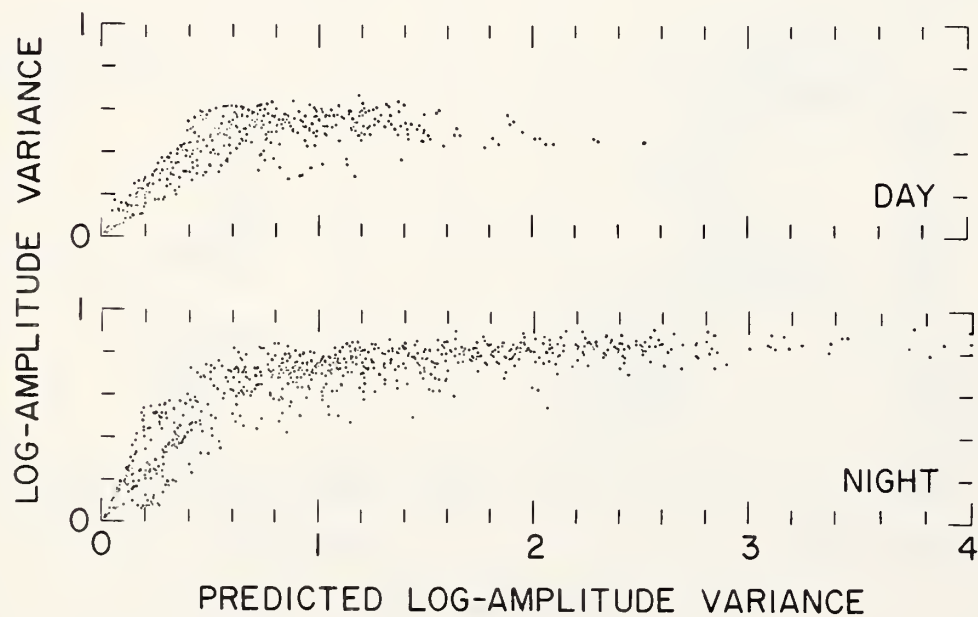
Figure 4. The data of figure 3 separated by day and night.
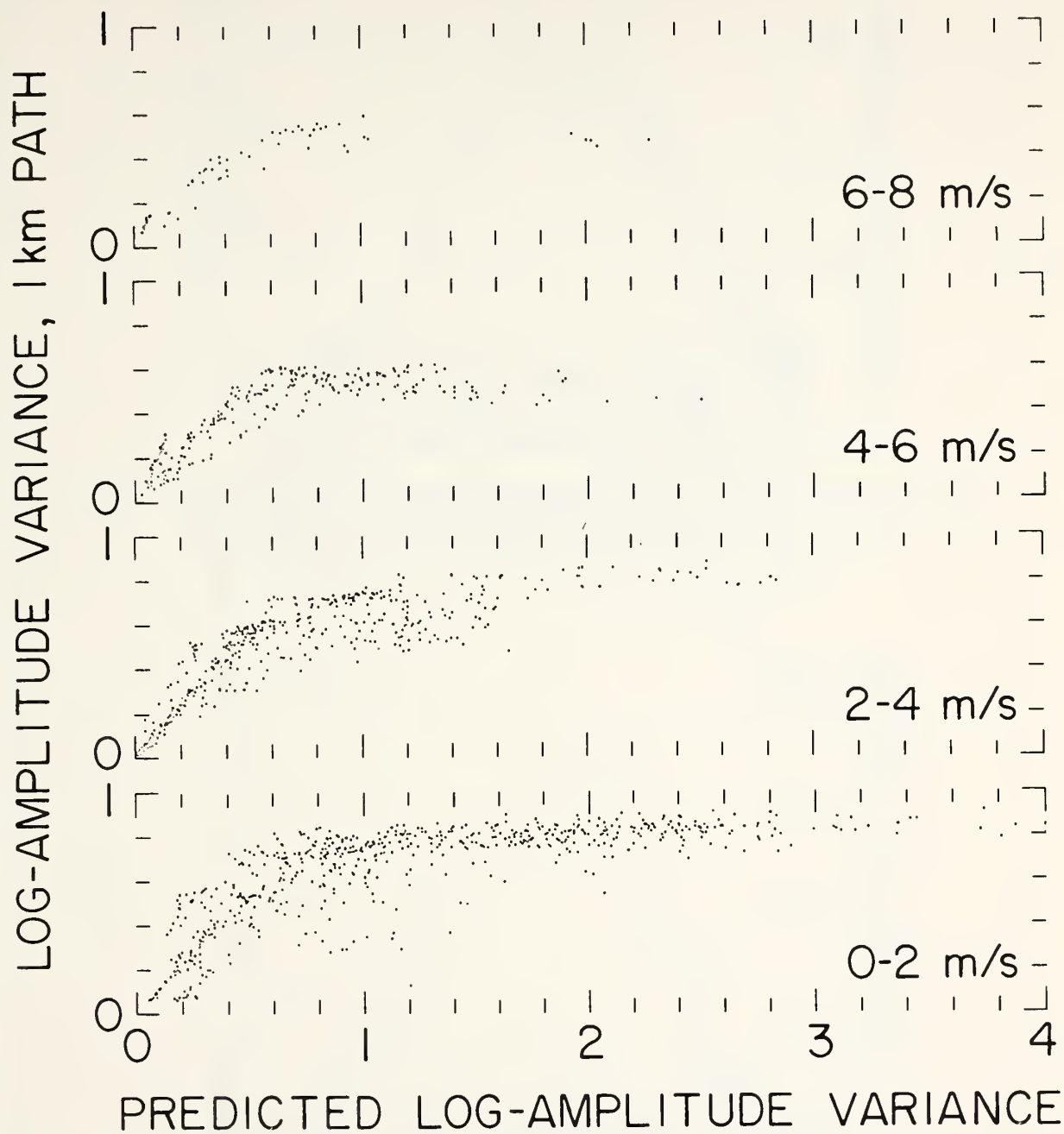
Figure 5.   The data of figure 3 separated by wind velocity.

11
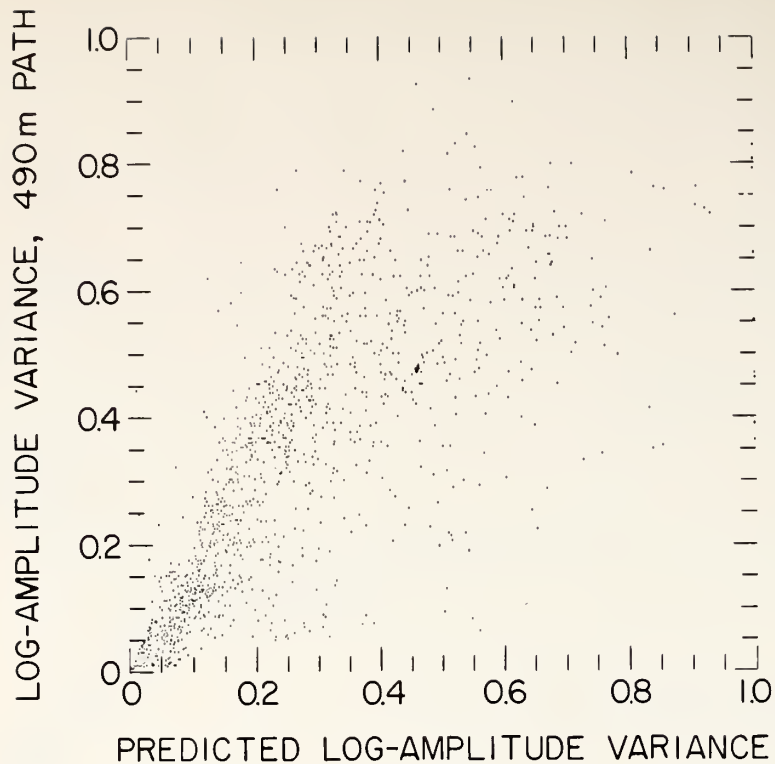
Figure 6. Scatter plot of log-amplitude variance at 490 m versus log-amplitude variance from temperature-structure-function measurements.
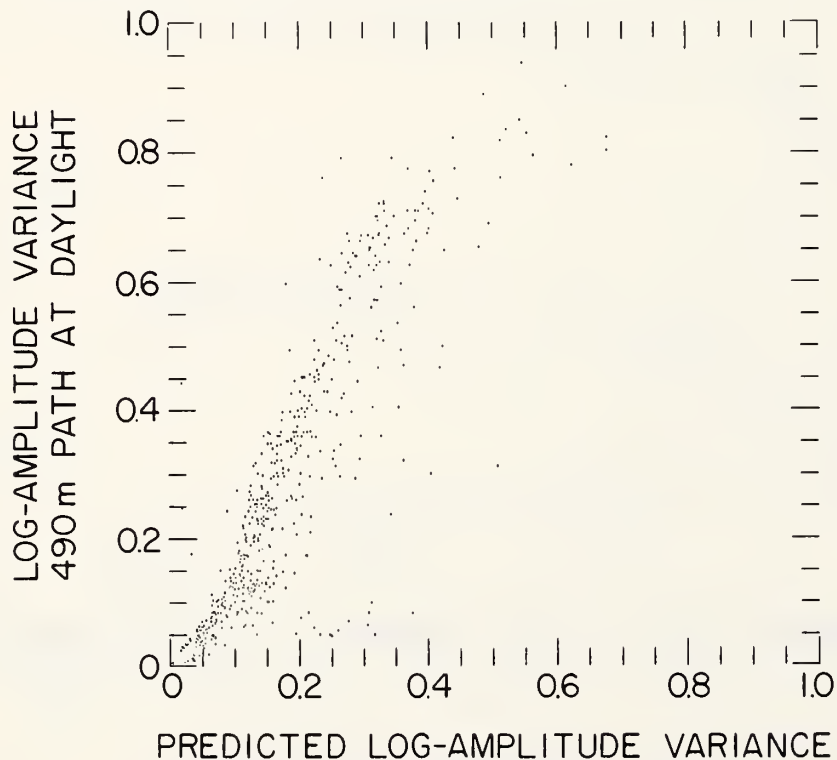
Figure 7. Scatter plot of log-amplitude variance at 490 m versus log-amplitude variance predicted from temperature-structure-function measurements, containing only that portion of the data of figure 4 taken in the daytime.

12
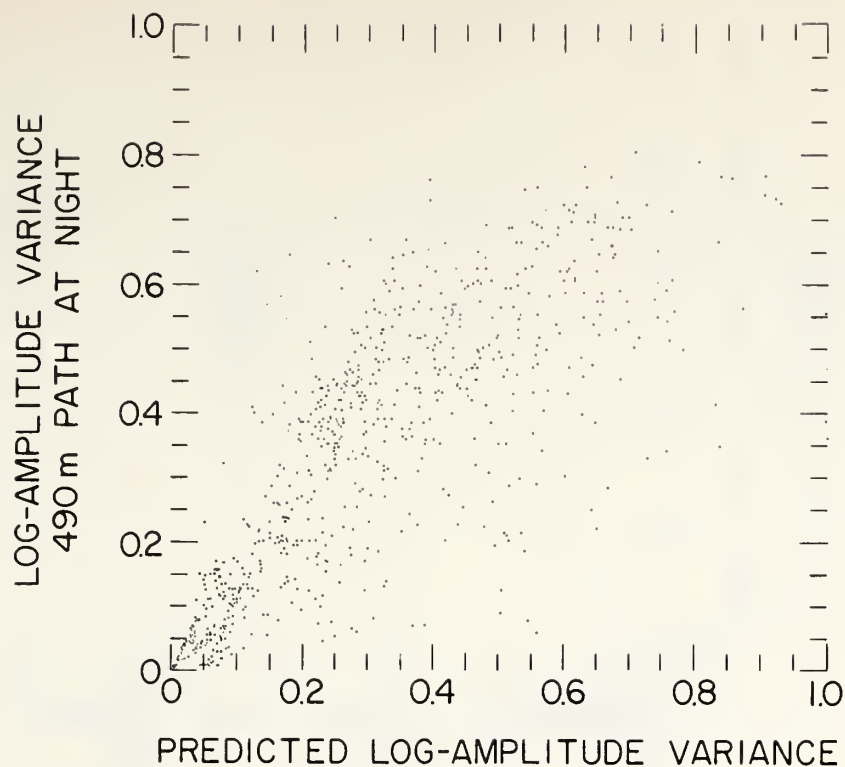
Figure 8. Scatter plot of log-amplitude variance at 490 m versus log-amplitude variance predicted from temperature-structure-function measurements, containing only that portion of·the data of·figure 4 taken at night.
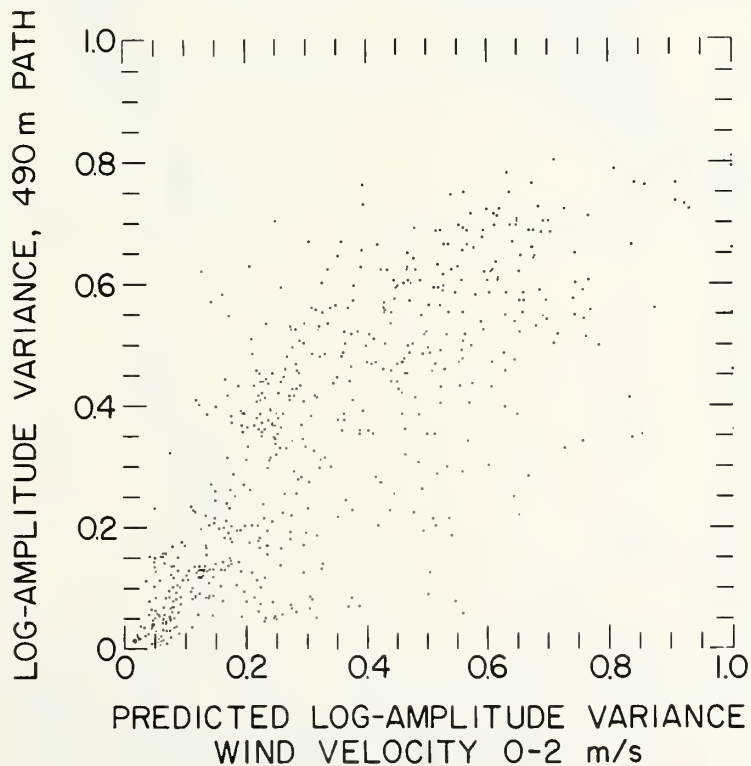
Figure 9. Scatter plots of log-amplitude variance at 490 m versus log-amplitude variance predicted from temperature-structure-function measurements, containing only that portion of the data taken in wind velocity ranges 0-2 m/s.
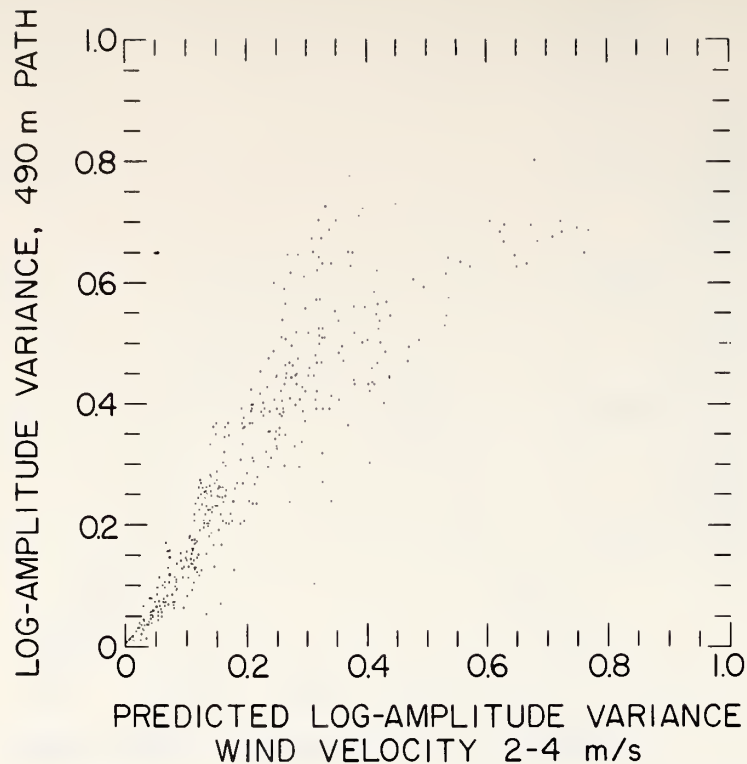
Figure 10. Scatter plots of log-amplitude variance at 490 m versus log-amplitude variance predicted from temperature-structure-function measurements, containing only that portion of the data taken in wind velocity ranges 2-4 m/s.
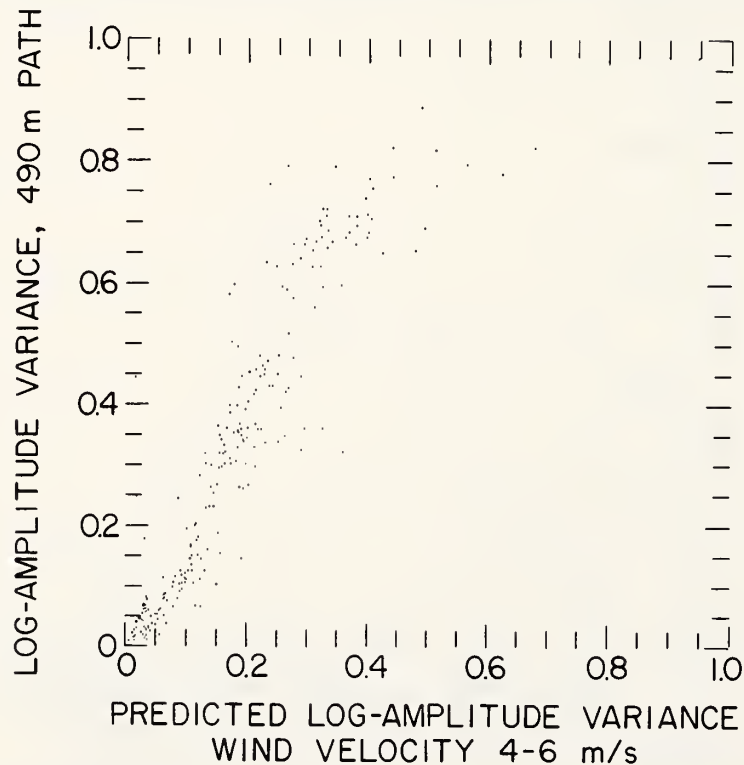
Figure 11. Scatter plots of log-amplitude variance at 490 m versus log-amplitude variance predicted from temperature-structure-function measurements, containing only that portion of the data taken in wind velocity ranges 4-6 m/s.
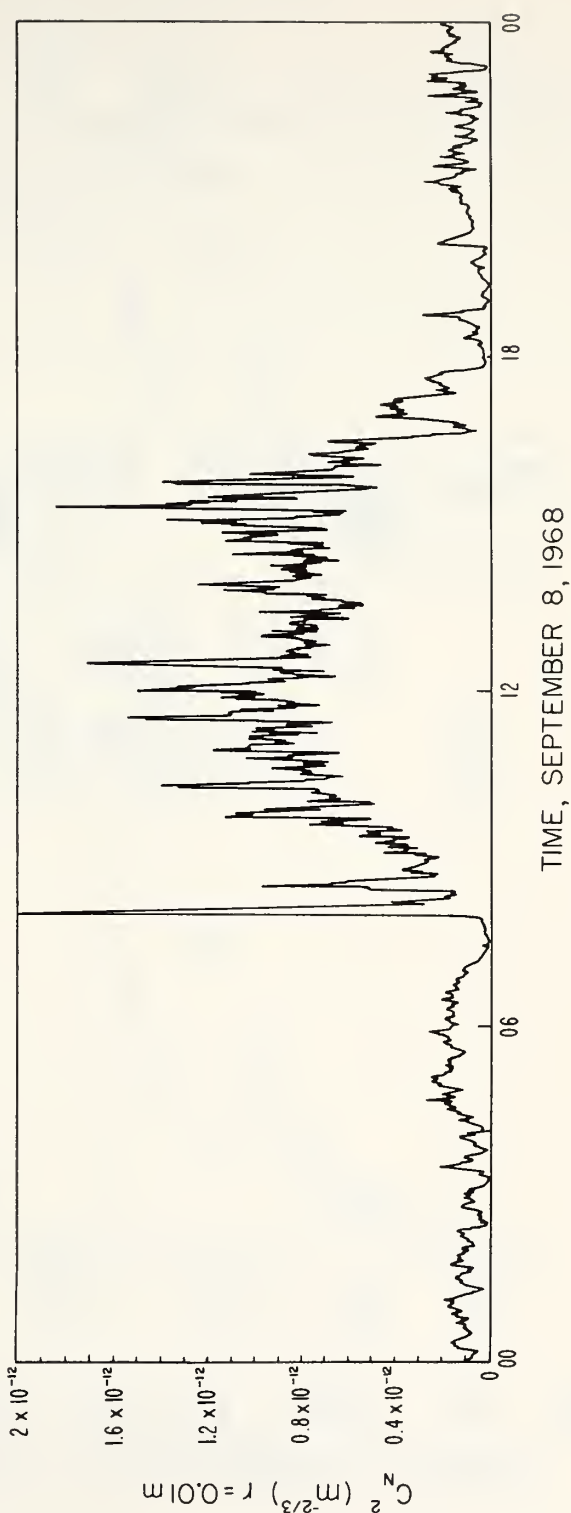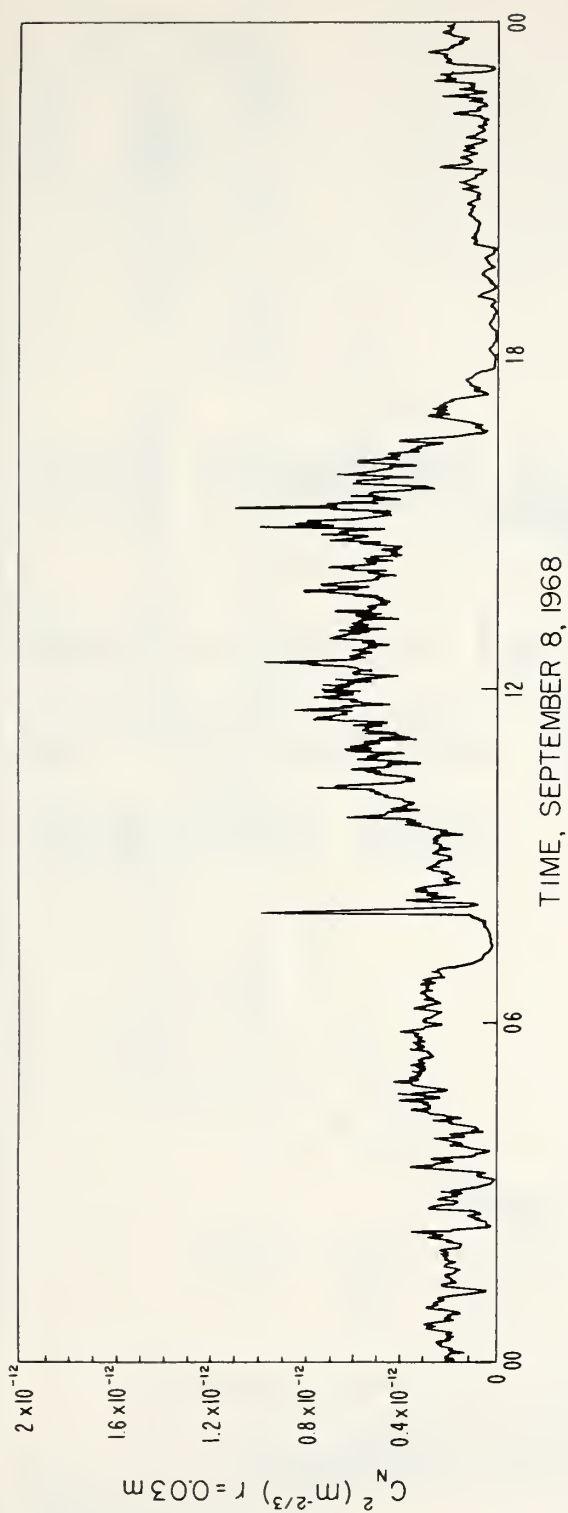
Figure 12. Refractive-index structure constant versus time of day. The measurements were derived from temperature-structure-function measurements made with vertical spacings of 0.01 and 0.03 m.

15
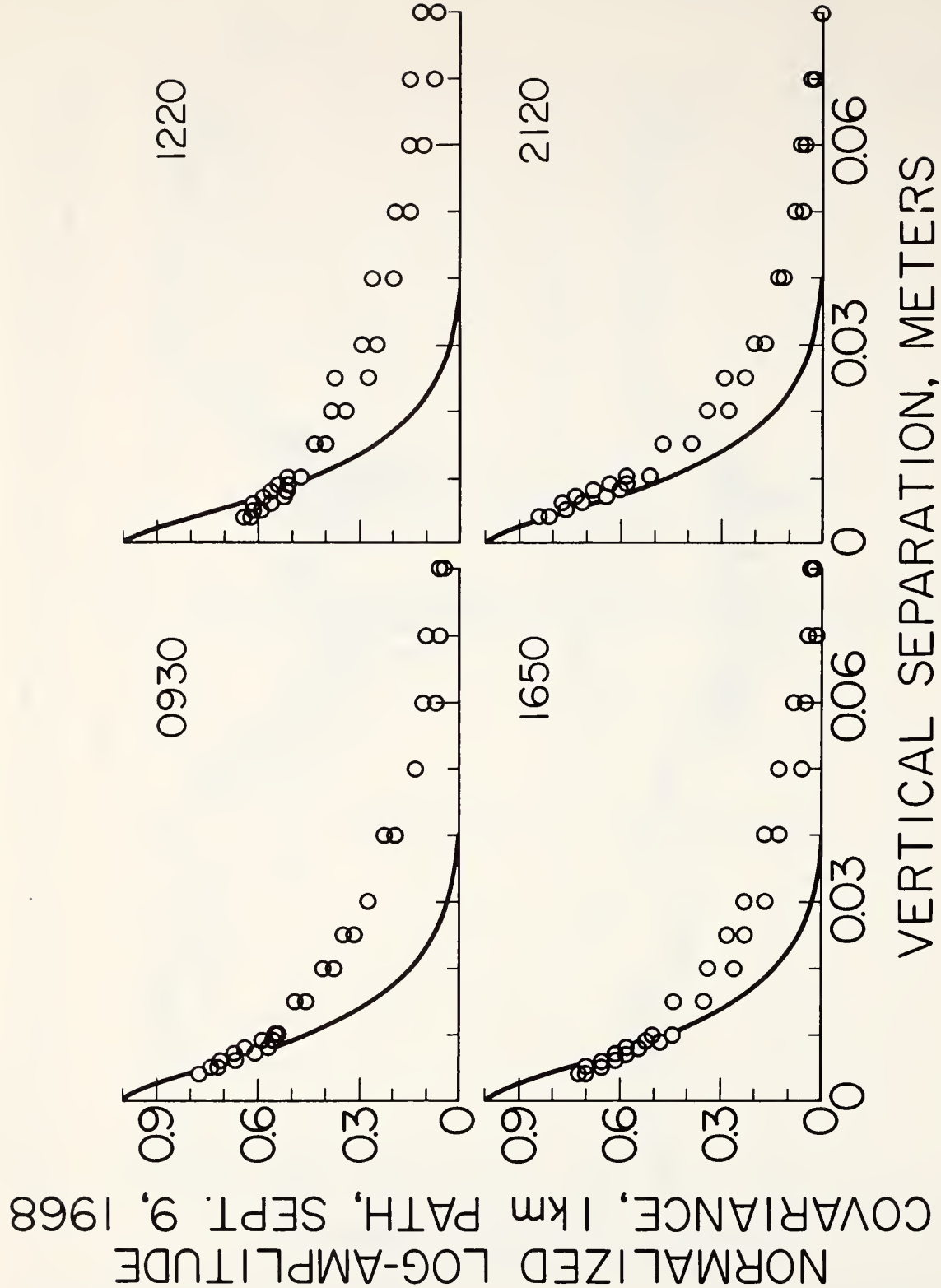
Figure 13. Normalized log-amplitude covariance functions taken at 1 km range. The solid curves are taken from Fried (1967) for horizontal propagation of a spherical wavefront.

16

U. S. DEPARTMENT OF COMMERCE
Maurice H. Stans, Secretary

ENVIRONMENTAL SCIENCE SERVICES ADMINISTRATION
Robert M. White, Administrator
RESEARCH LABORATORIES
George S. Benton, Director

ESSA TECHNICAL REPORT ERL 106-WPL 6

Measurements of Laser Beam Spread and Curvature Over Near-Horizontal Atmospheric Paths

G. R. OCHS

R. S. LAWRENCE

TABLE OF CONTENTS

Page

MEASUREMENTS OF LASER BEAM SPREAD AND CURVATURE OVER NEAR-HORIZONTAL ATMOSPHERIC PATHS

G. R. Ochs and R. S. Lawrence

Beam curvature and beam spread have been measured with a 0.63-μm wavelength beam over paths 5.5, 15, 45, and 145 km long along the eastern foothills of the Rocky Mountains. The paths vary from a nearly uniform 50 m above ground for the shortest path to a slant height above ground increasing from 50 to 1700 m for the longest path. Except for the 145-km path, measurements were made continuously over several days or more. The measured beamwidth referred to the transmitter varies from as small as 5 μrad (the theoretical half-intensity beamwidth) to 150 μrad, varying more with time of day than length of path. Beam curvature is less than 0.4 μrad/100 m in the horizontal direction but varies diurnally in the vertical by as much as 4 μrad/100 m.

1. INTRODUCTION

With the advent of the laser, many new applications take advantage of the ability of this intense coherent source to form beams of very small divergence. Radiators of modest dimensions can produce beams of narrower angle than is permitted by the refractive index fluctuations in the atmosphere.

This paper discusses in greater detail some of the material presented by Ochs and Little (1968). We have measured two aspects of beam distortion caused by the atmosphere and rather loosely define them as beam curvature and beam spreading. Beam curvature is a change in direction of the entire beam, while beam spreading is a general enlargement of the beam. Any such description is of course an arbitrary division, which in this paper has been defined by the technique of measurement.

2. EXPERIMENTAL TECHNIQUE

In the transmitting system a He-Ne laser of 2-mW average power is directed through a beam-expanding telescope of 15-cm aperture. The intensity distribution across the aperture is essentially Gaussian so that,

in clear atmosphere without turbulence, both the received focussed pattern and the beam intensity distribution at any point along the path are Gaussian. The focussed received pattern subtends an angle referred to the transmitter,

$$\omega_o = \frac{\lambda}{\pi \alpha} \quad (\alpha \ll 1), \tag{1}$$

where λ is the light wavelength, α is the tangent of the half-apex angle of the cone of converging light, and ω_o is the angular radius of the spot size where the amplitude has fallen to $1/e$ (Yariv and Gordon, 1963). We have found it more convenient to rewrite this relationship as

$$\beta = \frac{2\lambda \ln 2}{\pi D}, \tag{2}$$

where D is the diameter of the half-irradiance contour on the radiator, and β is the angular divergence of the diameter of the half-irradiance contour of the received pattern, as seen from the transmitter. For our system, $D = 5.2$ cm, resulting in $\beta = 5.3\,\mu\text{rad}$. The transmitter aperture distribution is truncated by the 14-cm diameter of the objective lens, but this has a negligible effect upon the focussed Gaussian pattern.

The receiving system consists of an array of two pairs of photo-multiplier units arranged on the horizontal and vertical diagonals of a square. Each pair has an angular separation of 40 μrad, as seen from the laser. These units have apertures 2 cm in diameter, a 10-mrad field of view, and 50-$\overset{\circ}{\text{A}}$ interference filters. In operation, the outputs of the vertically and horizontally spaced photomultipliers are compared, and radio signals are sent to the laser transmitter to change its azimuth or elevation as necessary to keep the beam pointed at the center of the square array. To further discriminate against the effects of stray light, the laser

is modulated at 10 kHz and phase detected at this frequency. A block diagram of the system is presented in figure 1.

Azimuth and elevation of the transmitter mount are monitored continuously and the most intense portion of the beam is tracked at 7.5 μrad/s. Every 15 min the beam is unlocked from the servo system for 2.5 min, and a slow (1.9 μrad/s) sweep is initiated past a fifth photomultiplier placed above the servo array to provide beam-spread information. This sweep information is averaged with a 0.5-s time constant, and the logarithm of the signal is recorded. The beam spread is obtained by measuring the angular width subtended between half-irradiance points of the beam when it is swept past the receiver. Each beamsweep requires 3 to 80 s. The sweep rate of 1.9 μrad/s is about as rapid as is practical with the sweep method. With a more rapid rate, the sampling time is too short and there is great variance between sweeps. Figure 2 is a sample of the type of recording used to measure beam spread. The time scale is discontinuous as the recorder runs only about 2.5 min each 1/4 hour. This particular record shows a decrease in beam spread occurring in the afternoon.

Figure 3 shows the profiles of the four optical paths used. All are in a southerly direction along the eastern foothills of the Rocky Mountains; the laser is located at the edge of Table Mountain, approximately 12 km north of Boulder, Colorado. The 5.5-km path is reasonably uniform, and the foreground of both the transmitter and receiver drops off rather rapidly. The 15-km path is less uniform in height above ground, and near the receiving end it passes over the city of Boulder. Generally these two paths lie below the marked temperature inversion that often occurs over the Boulder area in winter. This is not true for the 45-km and 145-km paths, however. These paths, to the top of Lookout Mountain west of Golden, Colorado, and to the top of Pikes Peak, respectively, frequently graze the inversion layer when it exists over the Boulder valley.

3. RESULTS

Three days of observations on the 15-km path are shown in figure 4, where curvature is plotted in the sense that upward movement of the received beam (if the transmitter were stationary) corresponds to an increase in the ordinate. If we assume a temperature gradient normal to the optical path and uniform along it, the beam curvature is a sensitive measure of temperature gradient changes. A laser servo system such as the one used for these measurements is particularly convenient for measuring optical refraction.

The curvature C of the optical path and the vertical temperature gradient are related as follows. From Bean and Dutton (1966)

$$C = - \frac{1}{n} \frac{dn}{dh} \cos \theta \; , \tag{3}$$

where $\frac{dn}{dh}$ is the local refractivity gradient and θ is the local elevation angle of the ray. For n and $\cos \theta \simeq 1$,

$$C \simeq \frac{dn}{dh} \; . \tag{4}$$

Now, at a wavelength of 0.63 μm, Bean (1966) gives the approximate refractive index n of air as

$$(n-1)10^6 = \frac{79P}{T} \; , \tag{5}$$

where P is the pressure in millibars, and T is the temperature in Kelvin. Differentiating (5) with respect to h and substituting in (4), we obtain

4

$$C = \left(\frac{79}{T} \frac{\partial P}{\partial h} - \frac{79P}{T^2} \frac{\partial T}{\partial h} \right) \cdot 10^{-6} \qquad (6)$$

Inserting in (6) the approximate atmospheric conditions at Boulder during the tests, we have

$$C = 2.8 - 0.75 \frac{\partial T}{\partial h} , \qquad (7)$$

where C is the curvature in μrad/100 m (concave downward is positive) and $\frac{\partial T}{\partial h}$ is in Kelvin per 100 m. If we make the assumption that minimum refractive index turbulence (and hence minimum beamwidth) exists when $\frac{\partial T}{\partial h}$ is equal to the adiabatic lapse rate (- 1 K/100 m), an approximate scale of curvature may be assigned, as has been done for the upper graph in figure 4. Note that while the change in beam curvature is calibrated, the degree of curvature itself has only been estimated by the above technique. The lower graph in figure 4 is a plot of the central intensity of the beam. This intensity should be inversely proportional to the square of the beam spread if its variation is caused by changes in beam size alone, but there is often an additional decrease during the day because of extinction due to haze.

Actual vertical beam-curvature records taken over the 5.5- and 45-km paths are compared in figure 5. Since the ordinates are proportional to the angular deviation referred to the transmitter, the curvature scales are inversely proportional to the path length. Very severe inversion conditions existed over the Boulder area in January when the 45-km path record was made, resulting in large and rapid vertical beam motions. As a matter of fact, during some of the tests, the servo correction rate

was far too slow to track the beam. Visual observations at night indicated that the beam was moving several hundred microradians in a few seconds. Under these conditions, measurements of beam spread by the slow sweep technique do not give meaningful results. The beam curvature observed on three different path lengths during sunny summer days is shown in figure 6. Here the plots are all to the same curvature scale.

During high winds, the beam changes its curvature very little, and the beam is very narrow. Figure 7 illustrates this condition when a rather strong dry westerly wind of the Föhn or chinook type was blowing across the 15-km optical path. The relationship between beam spread and curvature under these conditions has been discussed by Bean (1968). In general, the high wind increases the negative vertical temperature gradient and, at the same time, reduces the temperature fluctuations. Since pressure variations propagate with the speed of sound, the temperature fluctuations are almost entirely responsible for the refractive index fluctuations affecting the laser beam.

Figure 8 is a comparison of beam spread measurements made over the 5.5-km path with temperature fluctuation measurements at both ends. The temperature sensors, platinum wires 2.5 μm in diameter and 1.5 mm long, have a thermal response time to air temperature changes of 0.3 to 0.9 ms, depending on wind velocity. The three records correspond in general, but not in detail. The temperature measurements were made 2 m above the ground, although the average height of the optical path above ground is 50 m. Nevertheless, since the temperature fluctuations in the optical path near the laser transmitter have the greatest effect upon the beam spread, there should be reasonably good correlation between temperature fluctuations and beamwidth.

6

Figure 9 compares average beam spread on the 5.5- and 15-km paths and includes some data for the 145-km path to the top of Pikes Peak. The average height of the optical paths increases with increasing path length, as shown in figure 3, but the ground profile below the beginning of both the 5.5- and 15-km paths is rather similar. Since the beam spread is caused primarily by refractive index fluctuations near the transmitter, a comparison of the beam spread on the 5.5- and 15-km paths gives a reasonable indication of the variation of beam spread with distance. In fact, calculations based on Hufnagel's (1966) model for the height dependence of turbulence show that the weighted mean height for beam spreading of these two paths differs by only 3 percent. There appears to be little difference in the beam spreads during the evening hours but the daytime increase is about 1.6 times as great for the 15-km path. The beam spread results are in the same range as the predictions by Davis (1966), if we assume that moderate turbulence conditions existed during the nighttime measurements.

4. ACKNOWLEDGEMENTS

5. REFERENCES

Bean, B. R., and E. J. Dutton (1966), Radio Meteorology, NBS Monograph 92 (U. S. Government Printing Office, Washington, D. C.).

Bean, B. R. (1968), "Meteorological factors affecting the fine-scale structure of the radio and optical refractive index," IEEE Conf. on Tropospheric Wave Prop., London, Sept. 30-Oct. 2, 1968.

Davis, J. I. (1966), "Consideration of atmospheric turbulence in laser systems design," Appl. Opt. 5, 139, 1966.

Hufnagel, R. E. (1966), "An improved model turbulent atmosphere,"
    Woods Hole Summer Study, NAS 2 .

Ochs, G. R., and C. G. Little.(1968), "Studies of atmospheric propagation
    of laser beams on 5.5, 15, 45 and 145 km paths," IEEE Conf. on
    Tropospheric Wave Prop., London Sept. 30-Oct. 2, 1968.

Yariv, A., and J. P. Gordon (1963), "The laser," Proc. IEEE 51, 4-29.
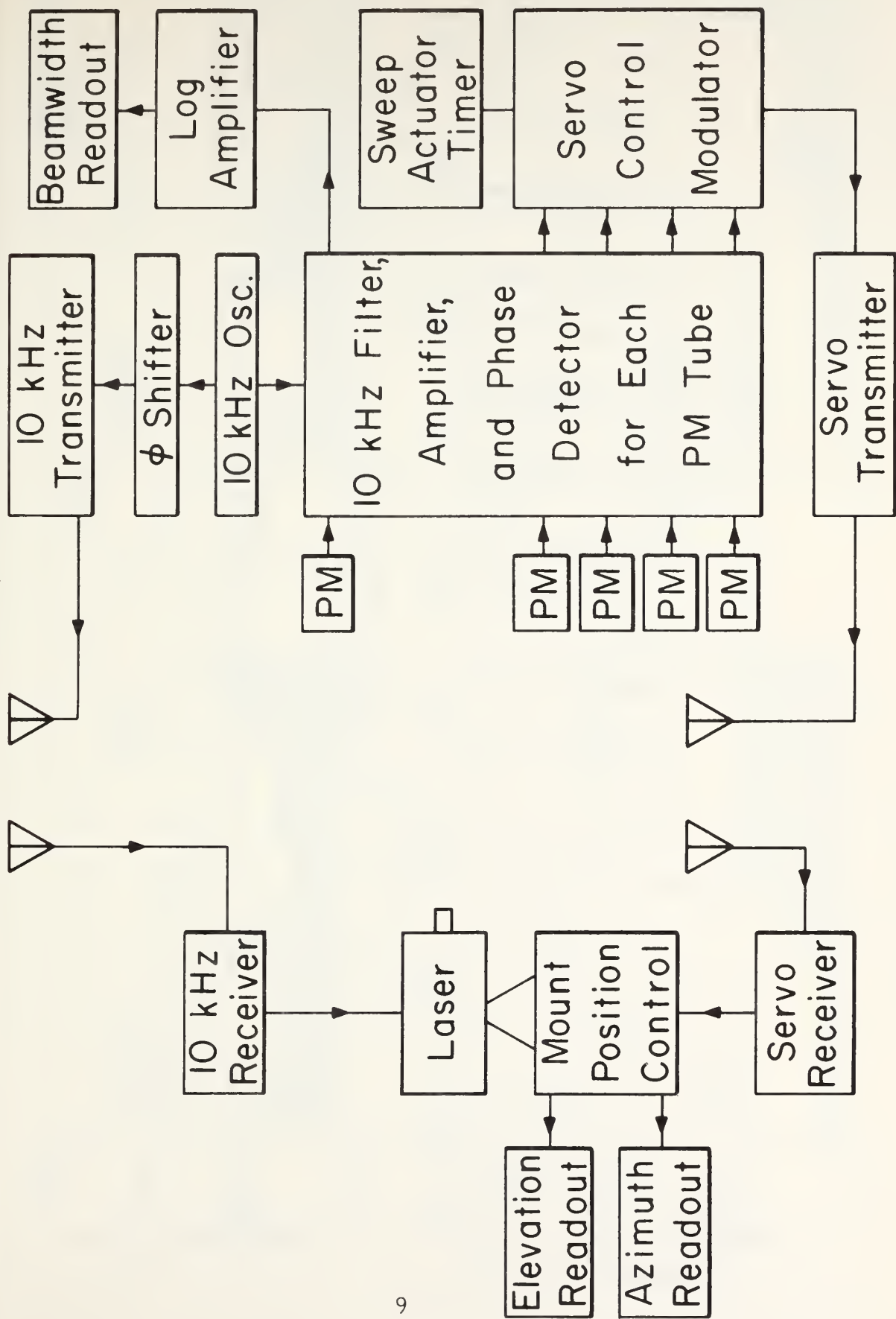
Figure 1. Block diagram of the system used to measure beam spread and beam curvature.

9
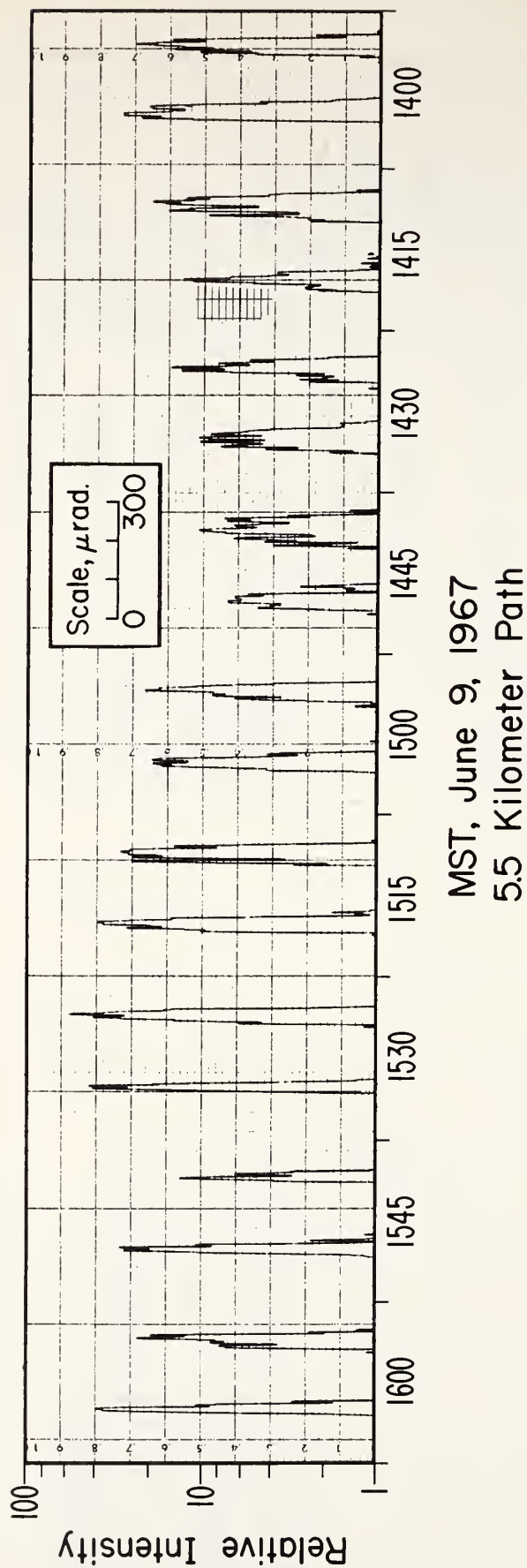
Figure 2. Sample of beam spread record. The sweep rate is 1.9 µrad/s and 2.5 min are required for each up and down sweep. The recorder runs only during the measurement, resulting in a discontinuous time scale.

10
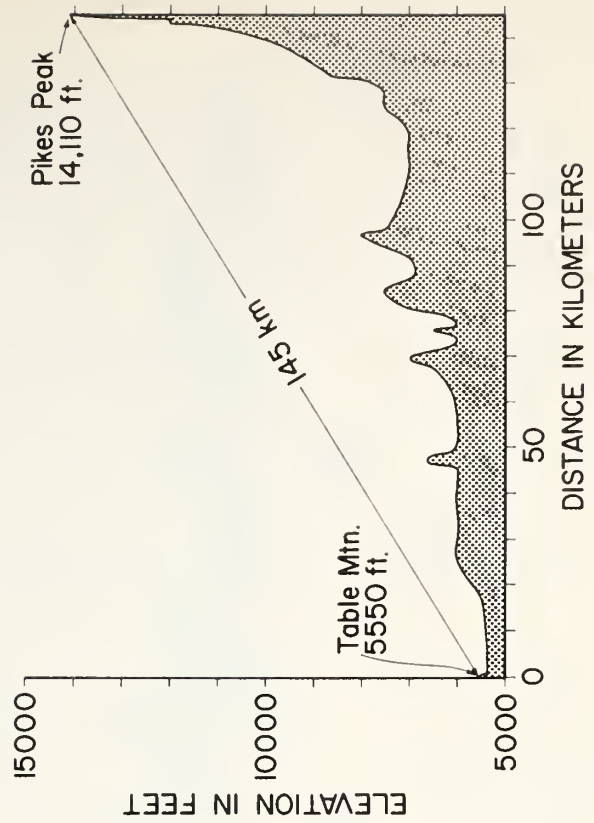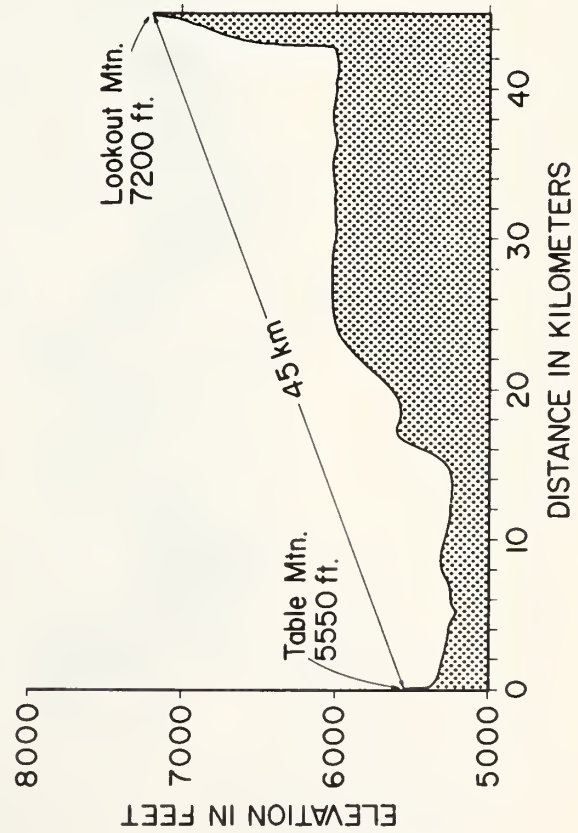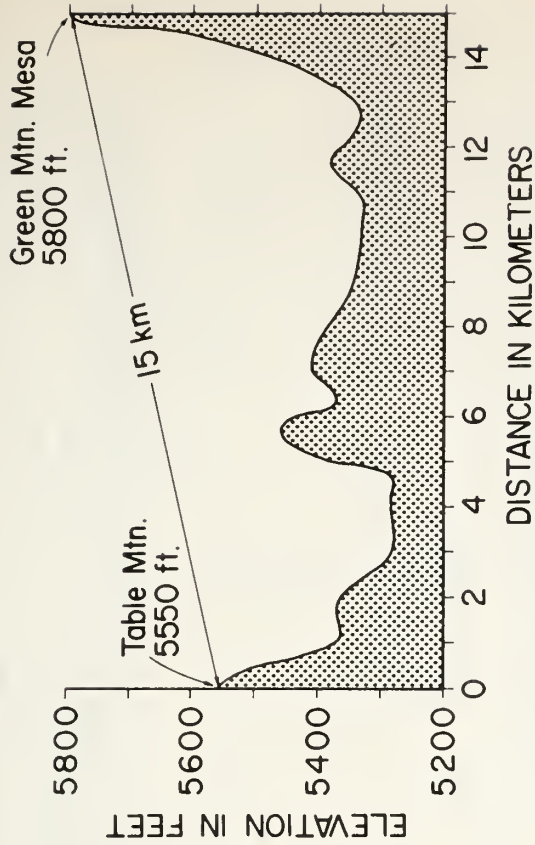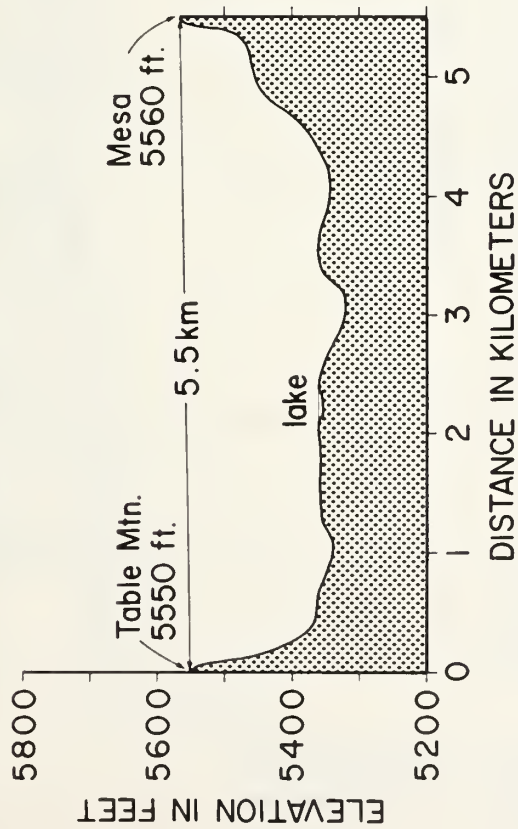
Figure. 3. Elevation profiles of the optical paths.

11

Figure 4. Beam curvature, spread, and intensity variations observed every 15 min for 3 days over the 15 km path. The undistorted beamwidth is 5.3 μrad. Horizontal curvature, not shown here, is less than 50 μrad. Note that while the beam curvature change is calibrated, the degree of curvature itself is only estimated (see text).

12
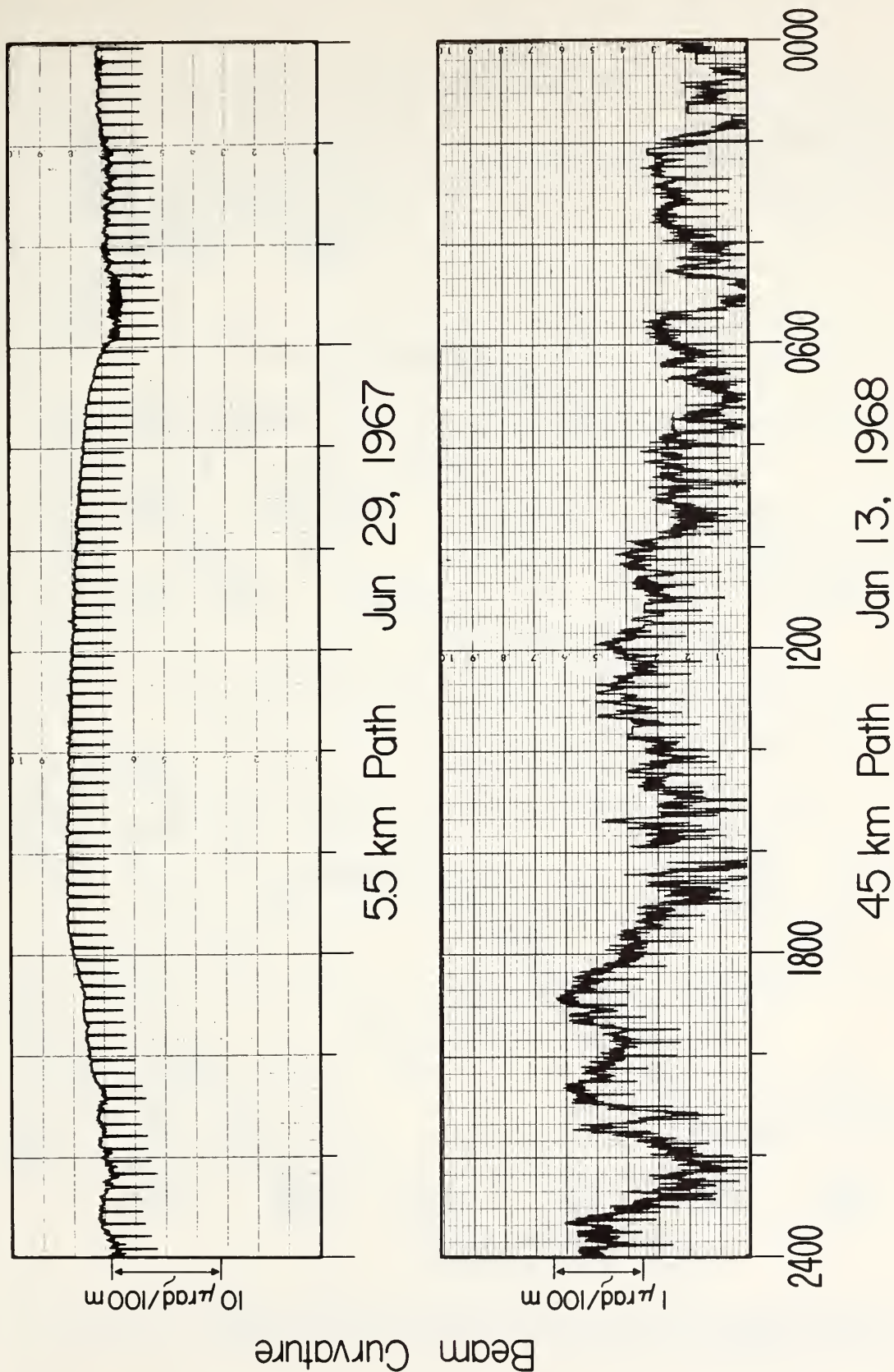
Figure 5. Beam curvature on the 5.5 km path compared with beam curvature on the 45-km path when the beam was grazing an inversion layer over Boulder, Colorado. Note that the ordinate scale for the 45 km path has almost 10 times the sensitivity of the 5.5-km record. The regular downward spikes every 15 min result from the beam spread measurement.

13
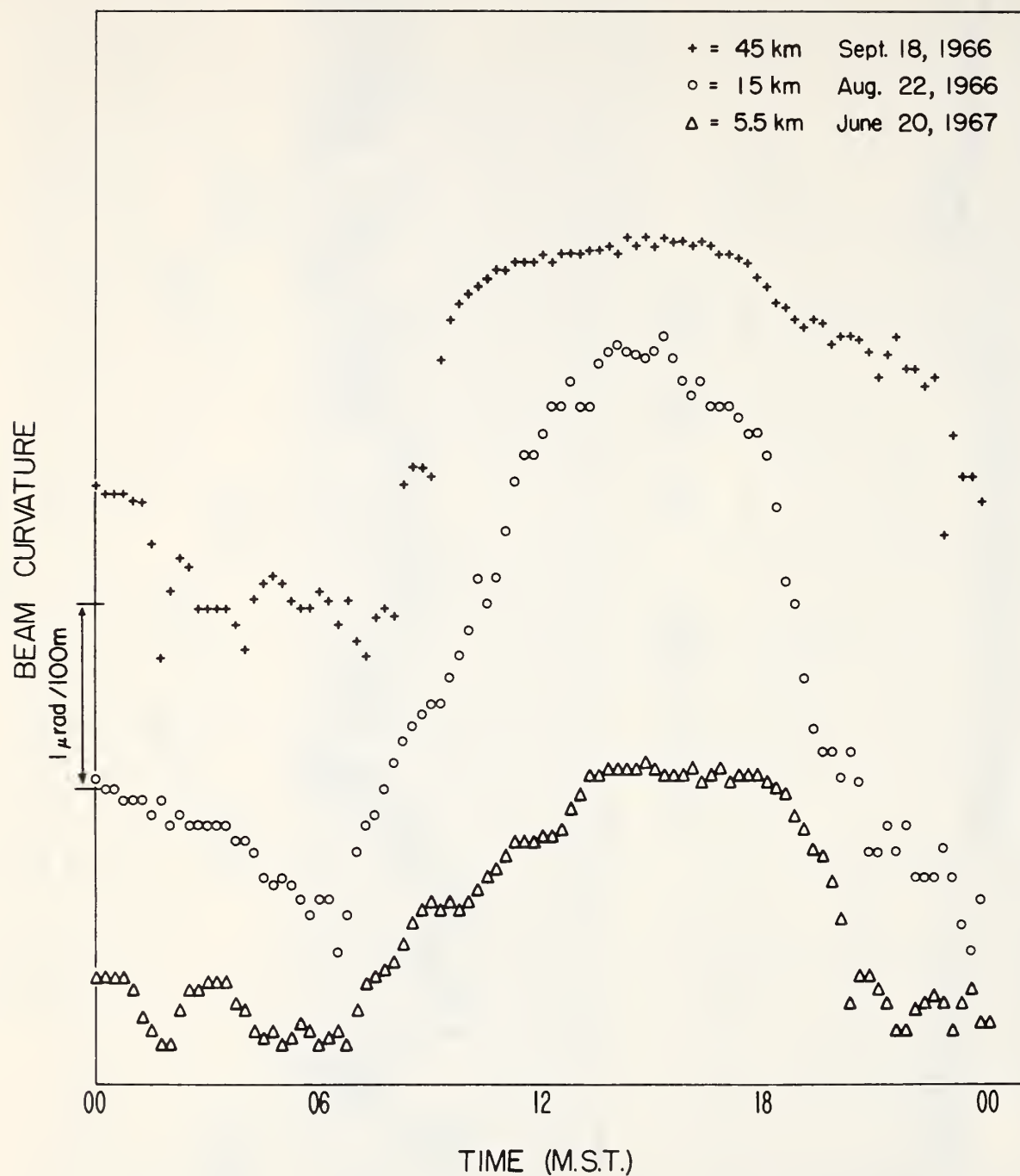
Figure 6. Vertical beam curvature versus time of day for the 5.5-, 15-, and 45-km paths.

14
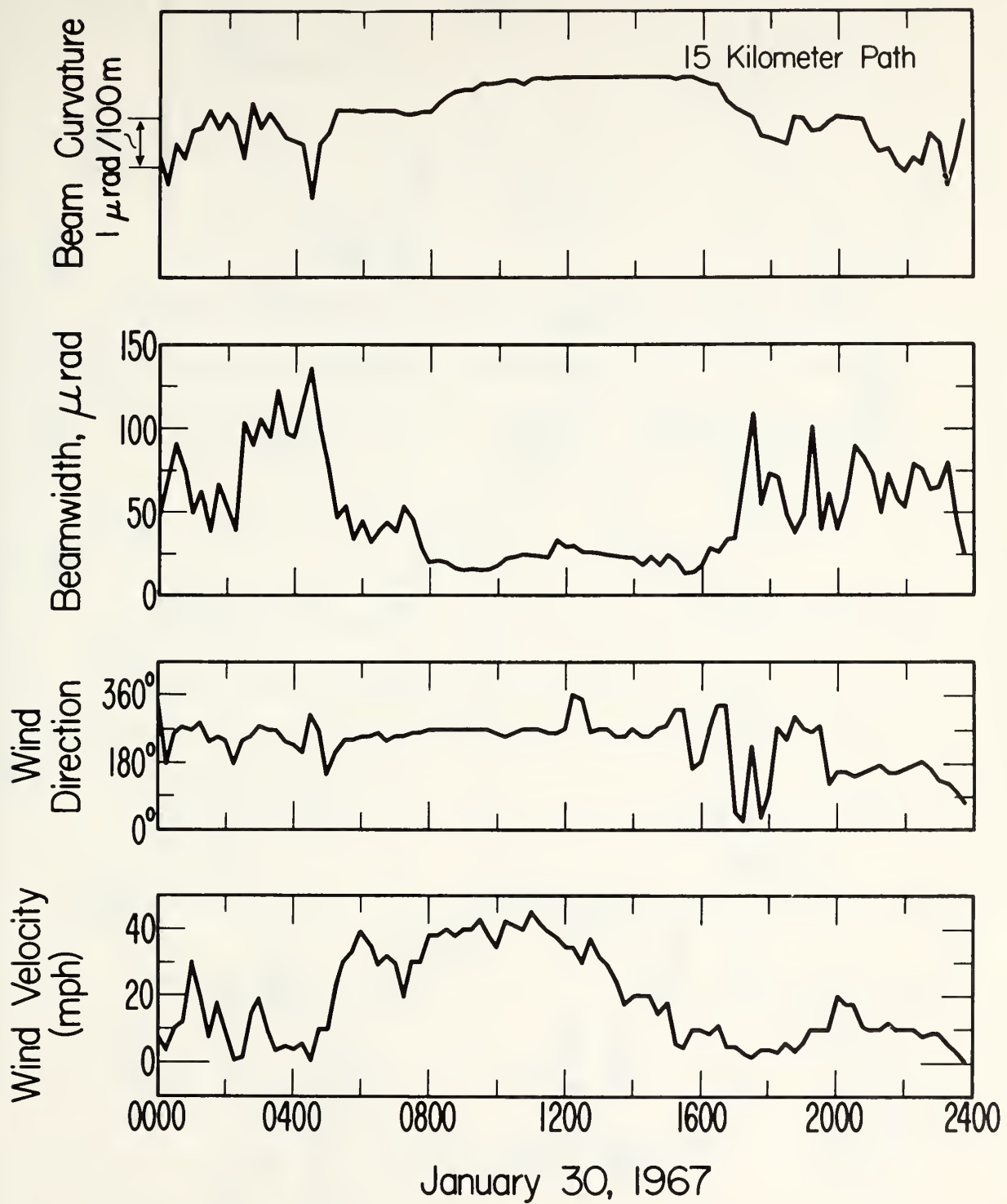
Figure 7. Beam curvature and beamwidth during high-wind conditions.

15
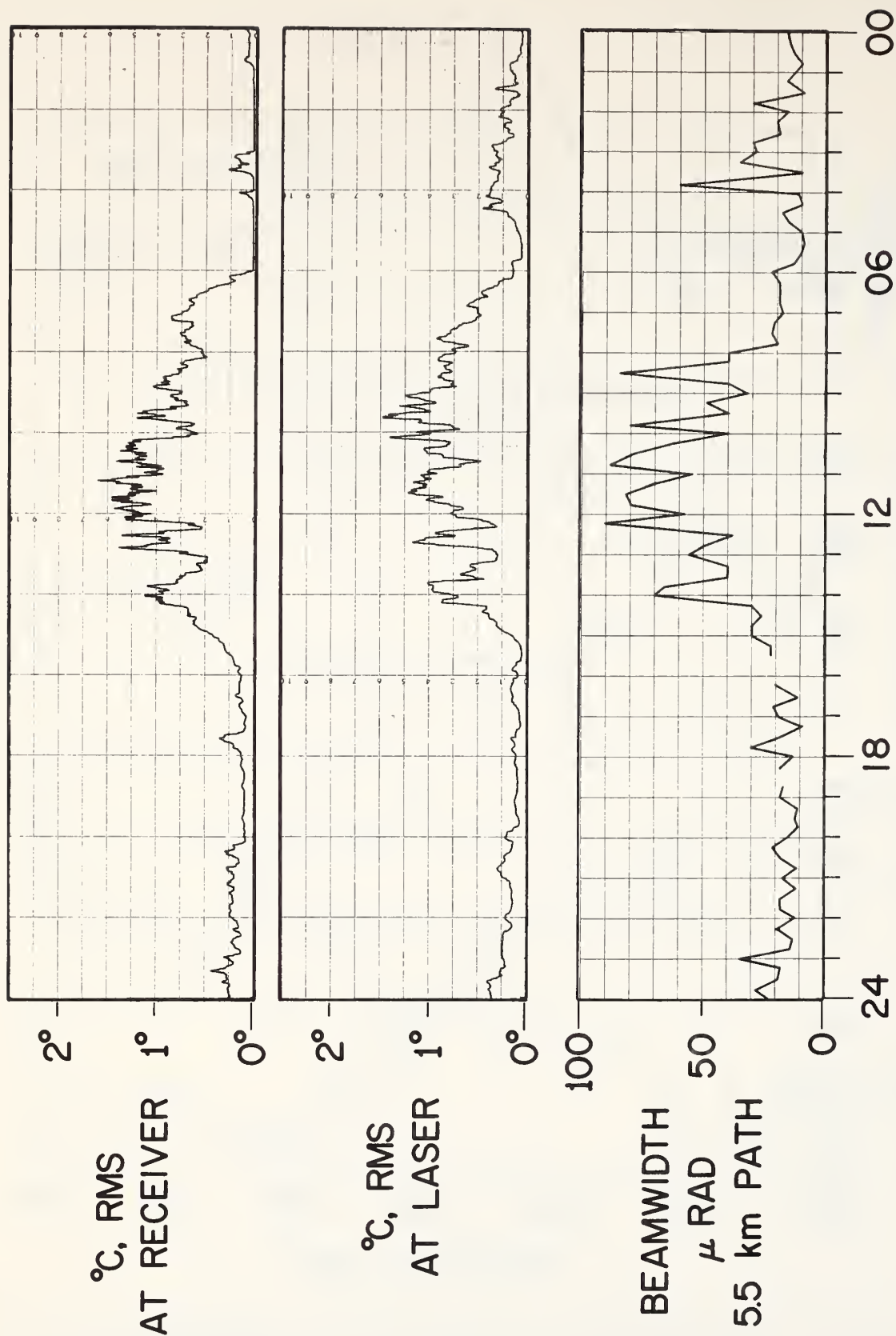
Figure 8. Comparison of beamwidth and rms temperature fluctuations at the ends of the 5.5-km path.
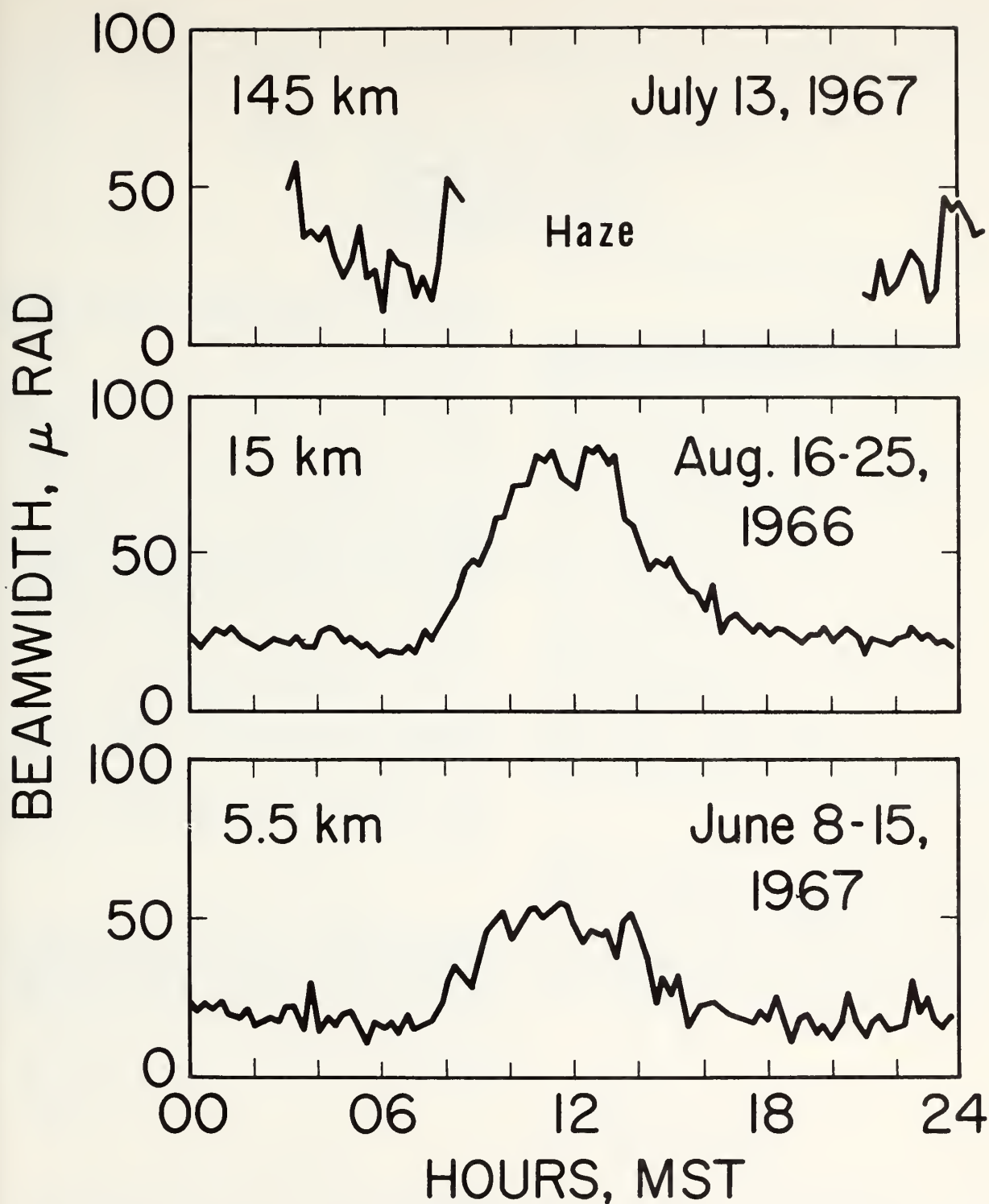
Figure 9. Beamwidth versus time of day for the 5.5-, 15-, and 145-km paths.

17

14

Laser-Beam Scintillation over Horizontal Paths from 5.5 to 145 Kilometers

G. R. Ochs, R. R. Bergman, and J. R. Snyder

ESSA Research Laboratories, Boulder, Colorado 80302

SOME observations of laser-beam scintillation at night over long atmospheric paths along the eastern foothills of the Rocky Mountains show that the measured log-amplitude covariance is in agreement with the theoretical predictions of Fried[1] for 5.5- and 15-km paths. However, at a range of 45 km, the covariance is much less at close spacings and somewhat greater at larger spacings. The effect seems to be due to the nonuniformity of the 45-km path. The amplitude distribution of light fluctuations in a small aperture is log-normally distributed for ranges from 5.5 to 145-km at night. Measurements of log-amplitude variance made at night are as high as 0.3 on a 15-km path, but do not exceed 0.7 on a 5.5-km path in the daytime. Values of the refractive-index structure constant, C_n, derived from both temperature fluctuations and log-amplitude variance measurements agree well with Hufnagel's[2] estimates of C_n vs altitude above ground.

A He–Ne laser operating cw with approximately 4-mW output, single mode at 6328 Å with a beam-expanding telescope provides a beam with an essentially gaussian irradiance distribution. The beam leaving the telescope has a half-irradiance beamwidth of 5.2 cm. For the measurements discussed here, the telescope is defocused so that the angular divergence is at least 300 μrad, when measured at the receiver under low scintillation conditions. Changing the divergence does not seem to affect the results as long as the divergence is sufficient to prevent contributions from beam wandering.

One and 2.5-mm-diam receiving apertures were used together with a 10-Å interference filter. No difference in test results was observed between the two aperture sizes. The paths were all in a southerly direction, along the eastern foothills of the Rocky Mountains, with the stationary laser mount located on the southern edge of Table Mountain, approximately 8 miles north of Boulder, Colorado. The path foreground drops abruptly so that the optical path essentially begins 50 m above the ground. The 5.5-km path is reasonably uniform; the 15-km path somewhat less so, as it passes over the city of Boulder, near the receiving end. The

45-km path grazed the top of an inversion layer over Boulder during most of the tests, with the result that the beam wandered in the vertical direction several hundred microradians in a few seconds, something that was not seen on the other paths or at other times of the year on this path.

The over-all dynamic range of the equipment was greater than 30 dB, as measured with a laser source and calibrated neutral-density filters. The received bandwidth has been restricted to 0 to 2 kHz. For the highest winds encountered, the spectral power at 2 kHz was at least 25 dB below the peak power in the optical signal. The principal method of checking for sufficient signal-to-noise ratio consisted of reducing laser power by 10 dB. For all ranges except the 145-km path, this produced no apparent change of the log-amplitude variance or covariance as measured with the on-line equipment. For the 45-km measurements, we also checked the covariance by placing a neon bulb, modulated at 100 Hz, in front of the interference-filter and photomultiplier-tube assemblies, and adjusted it to give about the same output as the laser beam. The measured correlation coefficient of this signal in the presence of background noise was 0.99. These results indicated that background noise levels were not significantly altering the results.

Atmospheric temperature fluctuations were monitored at the laser transmitter by means of high-speed platinum resistance thermometers. Platinum filaments, 2.5 μ in diameter and 1.5 mm long, having thermal response times to air-temperature changes of 0.3 to 0.9 msec, depending on wind velocity, were used. Two sensors were separated vertically a distance r (4 to 10 cm), and mounted approximately 2 m above ground. The temperature difference, (T_2-T_1), at these two locations defines the temperature structure constant, C_T, as

$$C_T{}^2 = \langle T_2 - T_1 \rangle^2{}_{\mathrm{av}} / r^{2/3} \qquad (1)$$

where the mean denoted by the sharp brackets corresponds to a time constant of 100 sec; C_n is similarly defined for refractive-index fluctuations. It is well known that the refractive-index fluctuations at optical wavelengths are almost entirely due to temperature fluctuations. Thus in the range where the Kolmogorov–Obukov similarity laws apply, the two are linearly related. Using the
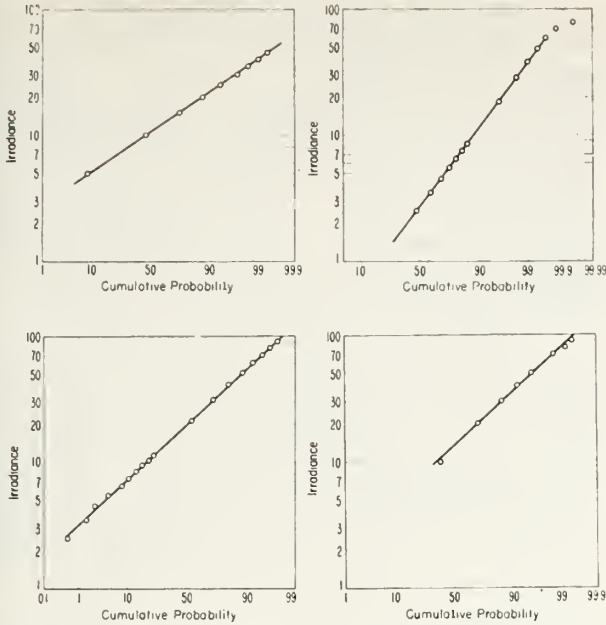
FIG. 1. Evening observations of irradiance probability distributions for scintillation. Reading from upper left to lower right, these graphs correspond to observations taken over path lengths of 5.5, 15, 45, and 145 km. Log-amplitude variances for the respective paths are 0.081, 0.32, 0.15, and 0.13. Apertures 2.5 mm in diameter were used for the 45- and 145-km while 1-mm apertures were used for the shorter paths.

expression[3]

$$n = \frac{77.6P}{T}\left[1 + \frac{0.00753}{\lambda^2}\right] \times 10^{-6}, \tag{2}$$

where n = refractive index, P = pressure (mb), T = temperature (°K) and λ = radiation wavelength (μ), we differentiate with respect to T, obtaining

$$\frac{\partial n}{\partial T} = \frac{-77.6P}{T^2}\left[1 + \frac{0.00753}{\lambda^2}\right] \times 10^{-6}. \tag{3}$$

Remembering the definitions of C_n and C_T, we may then write

$$C_n = \frac{77.6P}{T^2}\left[1 + \frac{0.00753}{\lambda^2}\right] \times 10^{-6}C_T. \tag{4}$$

For the amplitude-distribution analysis, the photomultiplier tube signal is tape recorded, and the fraction of time the signal is below a given threshold is measured for different thresholds with the aid of a level-discriminating circuit which gates a 10-kHz square-wave signal to a counter. Zero level is ascertained from the tape-recorded signal obtained when the laser beam is turned off. In each case, 2 min of data are analyzed. The irradiance vs the percentage of time the signal is below this level was plotted on gaussian-probability paper. The results for four ranges are shown in Fig. 1.

The log-amplitude variance, $C_l(0)$, is defined as

$$C_l(0) = \langle (\ln v - \langle \ln v \rangle_{av})^2 \rangle_{av}, \tag{5}$$

where v is received light amplitude (square root of irradiance) as a function of time. Thus $C_l(0)$ may be computed from the slopes of the lines in Fig. 1, with due allowance for the fact that irradiance rather than amplitude is plotted and that the logarithmic ordinates are to the base 10 rather then the base e.

The irradiance-probability measurements were taken at night on relatively high paths so they are well below the possible saturation region discussed by Strohbehn.[4] Thus it appears that at least in the region of $C_l(0) \lesssim 0.3$, the irradiance distribution (and hence the amplitude distribution) is log normal in 2-min intervals, within the accuracy of the measurements. For the 145-km path,
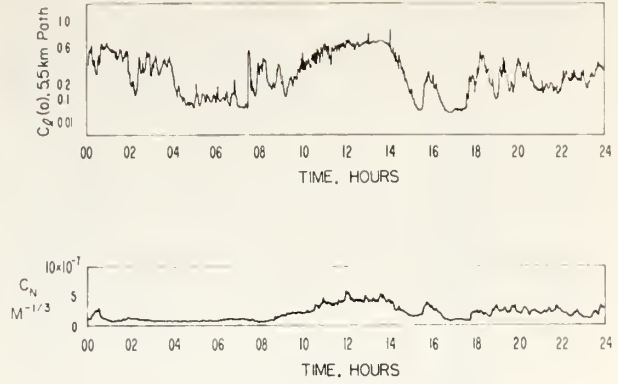
FIG. 2. Diurnal change of log-amplitude variance on the 5.5-km path with a weighted average height of 60 m. C_n, as derived from spaced high-speed temperature probes 2 m above the ground, is also plotted. Mountain standard time, 8 February 1968, is shown on the abscissa.
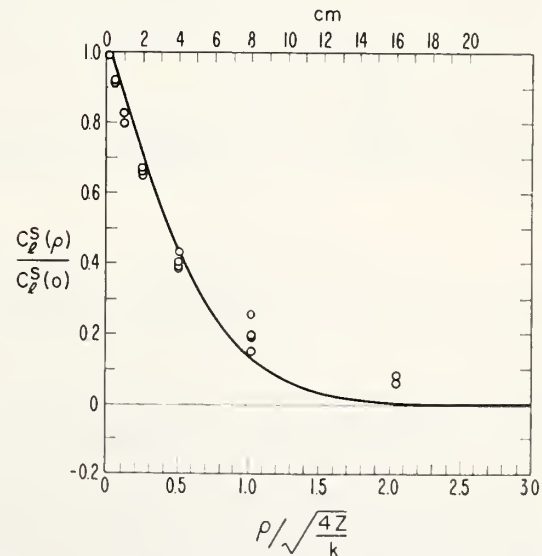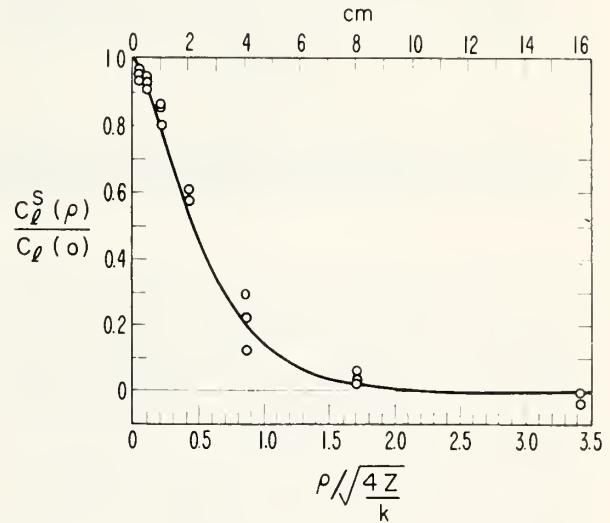
FIG. 3. Normalized log-amplitude covariance functions at 5.5 km (top graph) and 15 km. The solid curve is taken from Fried[1] for horizontal propagation of a spherical wave of wave number k over a distance z. The measurements were made in the evening with apertures 1 mm in diameter.
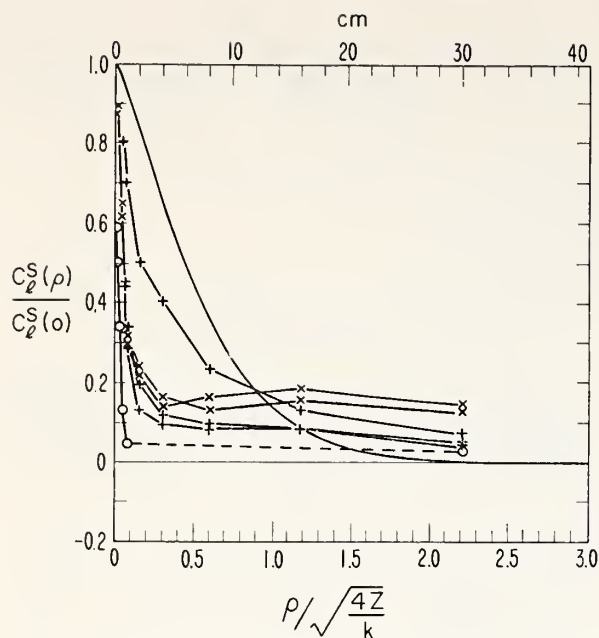
FIG. 4. Normalized log-amplitude covariance function at 45 m. The solid curve is taken from Fried[1] for horizontal propagation of a spherical wave of wave number k over a distance z. The measurements were made on the evenings of 24 November (+ data), 30 November (× data), and 7 December 1967 (0 data).

the data points lie in a slight curve but we believe this results from the less favorable signal-to-noise ratio at this distance. The two upper points, which deviate from a straight line on the 15-km plot, are thought to be the result of the analysis technique. Over the longer paths, C_n is not constant but this apparently does not affect the log normal distribution within the measured range.

In all cases, a separate analog method of calculating $C_l(0)$ was also employed. The photomultiplier output was first fed to a logarithmic amplifier and then to a capacitively coupled true-root-mean-square voltmeter having a low-frequency cutoff of 2 Hz. Thus the variance of the logarithm of the signal may be obtained by calibrating this reading. The analog system was used on-line during the tape recording of the data presented in Fig. 1, and the values of $C_l(0)$ thus obtained agreed within 5% of those obtained by the amplitude-distribution analysis.

The analog method is calibrated by inserting a square-wave signal, biased so that it is negative at all times, in place of the photomultiplier output. If the ratio of the high and low amplitudes of the square wave is k, then one can show by insertion into Eq. (5) that

$$C_l(0) = \tfrac{1}{4}(\ln k/2)^2. \qquad (6)$$

The $\tfrac{1}{4}$ factor arises because the photomultiplier measures irradiance rather than amplitude. No correction for noise background is made as zero signal is taken to be zero current into the logarithmic converter.

Continuous observations of $C_l(0)$ were made over the 5.5-km path by the analog method. A day's record is shown in Fig. 2. A laser-beam divergence of 1 mrad was used. On this record, $C_l(0)$ does not exceed 0.7, indicating that the scintillation may have saturated at this value. However the calibration of $C_l(0)$ becomes uncertain in this region due to the wide dynamic range required. An amplitude-distribution analysis was not available for this value of $C_l(0)$. Shown immediately below this curve is a plot of C_n derived from temperature fluctuations measured 2 m above the ground near the laser transmitter. The center of the path would have been a better location for the temperature measurement but it was inaccessible.

To obtain the normalized log-amplitude covariance (Figs. 3 and 4), two apertures were used, with adjustable spacing in the vertical direction. One minute of data was obtained for each data point appearing on the covariance plots. Thus it required a little over 6 min to obtain one set of points at all spacings. This process was repeated several times, and the degree of repeatability may be judged by the point spread at each spacing. An analog on-line computation of normalized log-amplitude covariance was made by taking the logarithms of the photomultiplier signals and applying them to the inputs of a one-bit correlator. This device subtracts the means and measures, the normalized crosscorrelation of two signals having jointly normal amplitude distributions,[5] which is true for the logarithms of the signal irradiance fluctuations.

We compared our scintillation results with those predicted by spherical-wave theory. The laser transmitter only approximates this condition because the beam does not originate from a point source, but starts through the atmosphere as the small end of a truncated cone 5 cm in diameter. This probably has little effect since the refractive-index fluctuations near the center of the path have the greatest influence on the observed irradiance fluctuations. Another approximation is the limited solid angle of the laser beam. At 5.5 km, we found experimentally that the test results are unaffected as long as the beam divergence is greater than the divergence caused by the atmosphere at the time of the test. Beam divergences greater than this were used in all cases.

The covariance at 45 km (Fig. 4), shows a pronounced departure from the function predicted by Fried, after rather good agreement at both 5.5 and 15 km. The irradiance distribution as shown in Fig. 1 for 45 km is representative of conditions during the evening of December 7. There was little variation of $C_l(0)$ over the period when the variance and covariance measurements were made. Pronounced inversion conditions were present on 7 December, as evidenced by a layer of haze over Boulder; the geometry of this path is such that the laser beam just grazed the top of this layer. Conditions were somewhat similar, but less pronounced, on 30 November, but on 24 November there were much higher winds near the center of the path, as measured by an anemometer of the National Center for Atmospheric Research. The results were much the same, however, with the exception of the last run of the evening, which was made under a heavy overcast.

It is interesting to compare our results with the curves of C_n vs height obtained by Hufnagel.[2] Since $C_l(0)$ is sufficiently small so
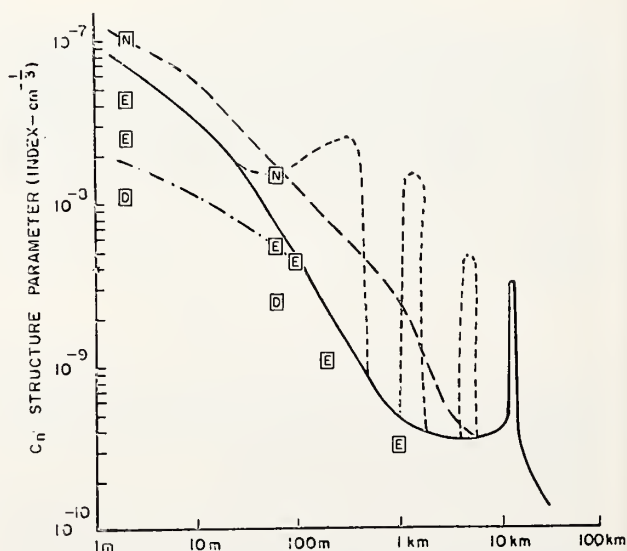
FIG. 5. C_n as a function of altitude above ground from Hufnagel.[2] The circled letters indicate experimental determinations of C_n. Those at an altitude of 2 m are derived from spaced high-speed temperature probes. All other points are from optical measurements.

TABLE I. Refractive-index structure constants derived from optical and temperature measurements.

Path length, (km)	Time of day	C_{n_0} (m$^{-1/3}$)	Effective height of C_{n_0} (meters)	C_{n_t} (m$^{-1/3}$)	Height of C_{n_t} (meters)
5.5	noon	7.0×10^{-8}	60	50×10^{-8}	2
5.5	dusk	1.2	60	6	2
5.5	evening	2.5	60	12	2
15	evening	2.0	95	...	...
45	evening	0.49	190	21	2
145	evening	0.16	970	...	...

that it should not be in the region where saturation[4] may occur, we derive C_{n_0} from optical-beam data from the relation

$$C_l{}^s(0) = 0.124 k^{7/6} z^{11/6} C_{n_0}{}^2 \qquad (7)$$

for horizontal propagation of a spherical wave of wave number k over a distance z^1. C_{n_0} is a weighted average of the refractive-index fluctuations all along the path, with the central portion contributing most effectively and the ends contributing not at all. Thus the effective height of an optical path of nonuniform height above the ground may be different from the average height. We have used a parabolic weighting function to obtain the effective height, but the height so obtained differs less than 10% from the average heights of the optical paths above ground.

The results are summarized in Table I and (after conversion of ordinates to cm$^{-1/3}$) are plotted in Fig. 5 on Hufnagel's[2] curves of C_n vs altitude above local ground. In four cases, the refractive index structure constant C_{n_t} obtained from temperature-fluctuation measurements made 2 m above the ground at the laser transmitter are also available. The results and Hufnagel's curves appear to be in reasonably close agreement, especially since most of the evening observations were made during somewhat overcast conditions, so that C_n quite likely would be less than that expected for a clear night.

We gratefully acknowledge the helpful discussions with Robert S. Lawrence on all phases of these measurements.

[1] D. L. Fried, J. Opt. Soc. Am. **57**, 175 (1967).
[2] R. E. Hufnagel (private communication).
[3] *Handbook of Geophysics and Space Environments*, Shea L. Valley, Ed. (McGraw–Hill Book Co., New York, 1965).
[4] J. W. Strohbehn, J. Opt. Soc. Am. **58**, 139 (1968).
[5] G. R. Ochs, "A Circuit for the Measurement of Normalized Cross-correlations," ESSA Tech. Report ERL 63-WPL 2 (U. S. Gov't Printing Office, Washington, D. C., 1968).

15

Saturation of Laser-Beam Scintillation under Conditions of Strong Atmospheric Turbulence*

G. R. Ochs and R. S. Lawrence

ESSA Research Laboratories, Boulder, Colorado 80302
(Received 29 June 1968)

THERE has been considerable recent interest in the characteristics of optical scintillation under conditions of strong atmospheric turbulence. Experimental results of Gracheva and Gurvich and theoretical predictions of Tatarski, as reported by Strohbehn,[1] indicate that the magnitude of scintillation, measured by the variance of the logarithm of the amplitude of the light wave, tends to saturate. DeWolf[2] has also derived a theoretical expression for saturation; a comparison of experimental and theoretical results appears in Figs. 3 and 4 of his paper. In the saturation region, Tatarski postulates a log-normal distribution. We find that the magnitude of scintillation does saturate and even tends to decrease with increasing turbulence after saturation, while the distribution amplitude remains log-normal.

A continuous-wave He–Ne laser with 3-mW single-mode output at 6328 Å in conjunction with a beam-expanding telescope was used to provide a beam of essentially gaussian irradiance cross section. The angular divergence between the half-irradiance points was 2 mrad, which was sufficient to prevent the beam from wandering off the detector. The transmitter was directed toward a photomultiplier receiver 990 m away, having a 1-mm-diam aperture, a 1-mrad field of view, and a 10-Å interference filter. The received bandwidth was restricted to the range 0–3 kHz. The

Fig. 2. Log-amplitude variance of light fluctuations received from 2100 MDT, 14 May, to 0555 MDT, 16 May 1968 in a 1-mm aperture at the end of a 990-m optical path 2 m above the ground. Observed log-amplitude variance $C_l(0)$ is plotted vs log-amplitude variance $C_{l^s}(0)$ predicted from spherical wave propagation theory. $C_{l^s}(0)$ is determined from a temperature structure-function measurement made near the center of the path.

path is 2 ± 0.3 m above the grass-covered surface of a very flat mesa approximately 12 km north of Boulder, Colorado.

Using methods described by Ochs et al.,[3] we have measured the magnitude of the irradiance fluctuations, expressed as the variance $C_l(0)$ of the natural logarithm of the received light amplitude, and the distribution function of the fluctuating irradiance. The refractive-index structure constant C_n^2 was derived from measurements of the temperature structure function made with high-speed platinum resistance thermometers. As described later, C_n^2 is used to compute a predicted log-amplitude variance $C_{l^s}(0)$ proportional to C_n^2.

Typical summer-time diurnal variations of the observed log-amplitude variance $C_l(0)$ and the spherical-wave log-amplitude variance $C_{l^s}(0)$ predicted from temperature fluctuations appear in Fig. 1. $C_{l^s}(0)$ was computed from an average of three temperature structure-function measurements made 250, 500, and 750 m along the light path from the receiver. Both $C_l(0)$ and $C_{l^s}(0)$ are smoothed with a 100-sec time constant. In Fig. 2, $C_l(0)$ is plotted as a function of $C_{l^s}(0)$, using 31 h of consecutive data, including the data illustrated in Fig. 1.

Fig. 1. Log-amplitude variance as a function of Mountain Daylight Time 15 May 1968. $C_l(0)$ is measured every 5 min from light received in a 1-mm aperture at the end of a 990-m optical path 2 m above the ground. $C_{l^s}(0)$ is determined from the average of three temperature structure-function measurements made along the path 250, 500, and 750 m from the receiver. Wind velocity is measured at the receiver.

FIG. 3. Irradiance probability distributions of light fluctuations received in a 1-mm aperture over a path length of 990 m during periods of high refractive-index fluctuations. The irradiance level is plotted vs the percentage of time the signal is below this level. Upper curve: 1236–1238 MDT, 3 June 1968, $C_l(0) = 0.69$; lower curve: 1224–1226 MDT, 11 June 1968, $C_l(0) = 0.66$.

The saturation of scintillation above $C_l(0) \approx 0.6$ is evident during the midmorning and afternoon hours. In fact, there appears to be a decrease of $C_l(0)$ when $C_l{}^s(0)$ becomes large. Below a value of 0.6 there is rough agreement between $C_l(0)$ and $C_l{}^s(0)$. The pronounced anomaly that occurred around 2000 MDT was apparently associated with calm wind conditions and may have arisen because the situation was not that described by the isotropic Kolmogorov theory. During the remainder of the run, the wind was along the path, averaging about 4 m/sec; temperature varied from 5°C at night to 15°C at midday.

It is difficult to calibrate accurately an analog measurement for the higher values of $C_l(0)$, due to the large dynamic range involved. An alternative technique, useful as a check, is to measure the irradiance distribution of the received light and to obtain $C_l(0)$ from the slope of the noise-free portion of the curve. Irradiance probability distributions of the received light measured during a 2-min interval near noon on 3 and 11 June 1968 are shown in Fig. 3. The irradiance that exceeds the ordinate for various percentages of the time is plotted on gaussian-probability paper. The $2\frac{1}{2}$ decades of dynamic range were achieved by tape-recording the logarithm of the photomultiplier output current and analyzing the distribution of these logarithmic values of irradiance.

Values of $C_n{}^2$, measured at the same time, near the center of the light path provide the predicted log-amplitude variance $C_l{}^s(0)$ according to Fried's relationship,[4]

$$C_l{}^s(0) = 0.124(2\pi/\lambda)^{7/6}Z^{11/6}C_n{}^2. \tag{1}$$

Here λ is the wavelength of the light and Z is the path length. Comparing the values of $C_l(0)$ determined from the slope of the lines in Fig. 3 with the predicted values of log-amplitude variance $C_l{}^s(0)$ from Eq. (1), we have

Date	$C_l(0)$	$C_l{}^s(0)$
3 June	0.69	1.4
11 June	0.66	2.0.

It is apparent that the fluctuations of irradiance (and therefore of amplitude) are log-normally distributed over more than two decades, even though scintillation saturates. The departure from linearity at very low signal irradiances is caused by photomultiplier noise.

In summary, our observations agree with the experimental results of Gracheva and Gurvich. In addition, we find that log-amplitude variance not only saturates but, for even stronger turbulence, appears to decrease. The distribution of irradiance remains log-normal well into the saturation region, showing no tendency to approach the Rayleigh distribution.

[1] J. W. Strohbehn, J. Opt. Soc. Am. 58, 139 (1968).
[2] D. A. deWolf, J. Opt. Soc. Am. 58, 461 (1968).
[3] G. R. Ochs, R. R. Bergman, and J. R. Snyder, J. Opt. Soc. Am. 59, 231 (1969).
[4] D. L. Fried, J. Opt. Soc. Am. 57, 175 (1967).

16

The Use of Atmospheric Dispersion in Optical Distance Measurement

James C. Owens
Institutes for Environmental Research
Environmental Science Services Administration
Boulder, Colorado

The Use of Atmospheric Dispersion in Optical Distance Measurement

James C. Owens
Institutes for Environmental Research
Environmental Science Services Administration
Boulder, Colorado

ABSTRACT

The development of lasers, new electro-optic light modulation methods, and improved electronic techniques have made possible significant improvements in the range and accuracy of optical distance measurements, thus providing not only improved geodetic tools but also useful techniques for the study of other geophysical, meteorological, and astronomical problems. One of the main limitations, at present, to the accuracy of geodetic measurements is the uncertainty in the average propagation velocity of the radiation due to inhomogeneity of the atmosphere. Accuracies of a few parts in ten million or even better now appear feasible, however, through the use of the dispersion method, in which simultaneous measurements of optical path length at two widely separated wavelengths are used to determine the average refractive index over the path and hence the true geodetic distance. The design of a new instrument based on this method, which utilizes wavelengths of 6328 Å and 3681 Å and 3 GHz polarization modulation of the light, is summarized. Preliminary measurements over a 5.3 km path with this instrument have demonstrated a sensitivity of 3×10^{-9} in detecting changes in optical path length for either wavelength using 1-second averaging, and a standard deviation of 3×10^{-7} in corrected length. The principal remaining sources of error are summarized, as is progress in other laboratories using the dispersion method or other approaches to the problem of refractivity correction.

The Use of Atmospheric Dispersion in Optical Distance Measurement

James C. Owens
Institutes for Environmental Research
Environmental Science Services Administration
Boulder, Colorado

I.   INTRODUCTION

The application of lasers and modern electronic techniques has
resulted in significant improvements within the last few years in the
measurement of long distances. Both a thorough general reference on
electromagentic distance measurement[1] and an excellent survey of the
applications of lasers to geodetic, geophysical, and astronomical
problems[2] have recently become available. A brief general summary of
progress during the last few years in radio and optical distance measure-
ment is also being presented at this Assembly.[3] The present paper gives
a more detailed exposition of the most promising of the new methods, the
dispersion method, including a summary of the optical and radio-optical
work progressing in several laboratories. Recent developments in micro-
wave distance measurement will be mentioned only for comparison but not
generally reviewed.

The most convenient technique for making geodetic distance measure-
ments involves the measurement of the transit time of electromagnetic
waves over the path, multiplication of this transit time by the propagation
velocity of the radiation in vacuum, and application of an appropriate
correction for the refractive index of the atmosphere along the path.
Because pulse techniques do not provide the requisite precision at present
and direct optical interferometry is precluded by atmospheric turbulence,
the transit time is normally found through measurements of the phase of
a radio-frequency signal. To provide directivity, this information signal

is transmitted as modulation on a microwave carrier, in which case the refractive index correction involves the low-frequency phase refractive index of air, or on a light beam, in which case the correction requires the use of the group refractive index for the optical carrier frequency.

The modern optical method was first developed by Bergstrand,[4] whose instrument utilized amplitude modulation of the light at 8.3 MHz and a photomultiplier tube for demodulation. Subsequent development has been sufficiently successful that although their maximum range is typically less than half of that achievable with microwave methods, the Geodimeter and related instruments are now routinely used in a large fraction of first-order surveys. Under good conditions, when sufficiently accurate meteorological information along the path can be obtained, these instruments are capable of an accuracy of about one part per million over paths of a few kilometers or, at night, a few tens of kilometers.[5] Replacement of the conventional tungsten or arc lamp by a gas laser, however, and utilization of recently developed modulation techniques[6,7] can result in significant improvements in range and precision. By replacing the light source with a helium-neon laser, replacing the Kerr cell with a KH_2PO_4 electro-optic crystal modulator, and using an improved photomultiplier tube, the operating range of an otherwise conventional Geodimeter has been doubled with no loss of precision.[5,8] Even better performance could be achieved by further modifications, such as the use of modern phase measuring techniques, or by designing a completely new instrument.

II.   ESTIMATION OF AVERAGE REFRACTIVE INDEX
A. Sampling

The principal limitation to the accuracy of both microwave and optical measurements is the uncertainty in the average refractive index over the path due to inhomogeneity and turbulence in the lower atmosphere, which

sets a limit to useful instrumental precision. At present, the average refractive index is usually estimated from measurements of pressure, temperature, and humidity made at one or more points along the path. Higher accuracy in the point measurements could be achieved by using optical or microwave cavity refractometers instead of meteorological sensors, but the fundamental problem of averaging over the path would still remain. Very good results can be obtained under favorable circumstances, that is, when the path is horizontal and at a constant distance above the ground, meteorological conditions are relatively uniform along the path and slowly varying in time, several sets of sensors are used, and averaging times are sufficiently long so that short period fluctuations tend to cancel. An example of the precision attainable is given by a set of microwave measurements over a 17.1 km path along the coast of Florida using refractive index measurements at both end points,[9] for which the standard deviation of the mean was found to be less than 1×10^{-6} for averaging times longer than 12 hours. Under unfavorable circumstances, however, as in measuring the distance between mountain peaks where meteorological conditions are less uniform and sensors can be placed only at the ends of the path, accuracies much less than one part per million would normally be expected. Microwave measurements over a 25.9 km path in Hawaii between the peak of Mt. Haleakala and sea level, corrected using refractivity measurements at the end points, have shown[10] that a 1 hour averaging time results in a standard deviation in path length of 9×10^{-6}, while increasing the averaging time to 8 hours decreases the standard deviation only to 7×10^{-6}. Moreover, even if meteorological conditions and path geometry permit the correct spatial average of refractive index to be found by this technique, drifts and rapid fluctuations in transit time due to atmospheric turbulence provide a background noise which can, under unfavorable conditions, severely limit the precision of existing instruments and can even preclude their use.

Although these limitations apply to both optical and microwave systems, the much smaller effect of water vapor in the optical region, only about 1% as large as the effect on the microwave refractive index, should permit the corrections to be made with somewhat higher accuracy for optical than for microwave measurements. In addition, the better collimation possible with optical beams eliminates the troublesome complication of multipath propagation effects. Nevertheless, even using optical techniques, rapid measurements or measurements of the highest accuracy will require a direct measurement of the average refractive index over the path rather than an approximation obtained by sampling.

B. Infrared Absorption

One method of obtaining the average dry air and water vapor densities and hence the average refractive index which is being investigated[11] utilizes measurements of differential infrared absorption over the path. Three wavelengths are used: 1.26 microns, coincident with an oxygen absorption line, 1.37 microns, at a water vapor line, and 1.21 microns, in an atmospheric window having low absorption. The measured absorption at the first wavelength is essentially proportional to the total mass of oxygen per unit area integrated over the path, and hence to the average dry air density, while the absorption at the second wavelength similarly gives the average water vapor density. The absorption at the third wavelength is used to normalize the first two observations, correcting for geometrical and other effects. It is expected that this technique will permit the correction of optical distance measurements to give an accuracy of 1 or 2×10^{-6}, and that microwave distance measurements could be corrected equally well if a fourth transmissometer operating at 22 GHz were added to the three infrared channels.[12] The 3-channel system is now being set up on a 3-mile path, and a 4-channel system is under construction.

C. Dispersion

A more direct optical method of determining the desired average refractive index which appears capable of higher accuracy was proposed by Prilepin in 1957,[13] although the technical feasibility of the method was unclear.[14] The same idea has recently been put forward independently[15] along with suggestions for its experimental realization through modifications to existing instruments[16] or the construction of new instruments.[17] The method is based on the fact that the refractive index $\underline{n}$ of the lower atmosphere is dispersive in the visible spectral region, and hence two light signals traversing the same path but having different wavelengths will travel at slightly different velocities. Because $(\underline{n}-1)$ at a given wavelength is proportional to air density for dry air, the difference in refractive index and hence the difference in transit time for the two signals will be proportional to the average air density over the path. A measurement of the difference in transit times, therefore, can be used to give the average density over the path. From this quantity the average refractive index for either wavelength may be calculated, providing the desired correction for the distance measurement. Because the refractivity of air increases sharply as the wavelength is reduced, in order to have large dispersion it is desirable to choose the longer wavelength in the red or near infrared and the shorter in the violet or near ultraviolet spectral regions. The atmosphere increases the transit time for all wavelengths by about 300×10^{-6} at sea level over the time which would be required in vacuum. The difference in transit time for 6328 Å and 3681 Å, a suitable pair, is about 30×10^{-6}, corresponding to a difference in apparent path length of about 40 cm for a 15 km path. Hence measuring the difference in transit time to 1 part in 300 (measuring the 40 cm to 1.3 mm) allows the average atmospheric density to be determined to approximately the same fractional precision, and the length to about 1×10^{-6}. This precision has already

been significantly exceeded by the instrument to be described. By thus providing rapid and convenient spatial averaging of refractive index, the dispersion method should significantly reduce the present limitations to the accuracy of long-range distance measurement.

Three types of errors must be considered in analyzing the ultimate limits of the method: (1) instrumental, (2) dispersion, and (3) geometrical. The first type consists of such errors as uncertainties in the optical wavelengths, the modulation frequency, and the effective modulation point. Although they may be troublesome (the first error mentioned has been a particular problem), these can be made negligible by suitable calibration of sufficiently stable and precise apparatus. The second type consists of errors due to inadequate knowledge of the dispersion parameters which are needed to calculate the average refractive index from the measured dispersion. A thorough discussion of this problem has been given.[18] The most serious source of this error is variation in humidity. It can be shown that an error of 8 mb in the average partial pressure of water vapor assumed (corresponding to a relative humidity of about 50% at 15°C.) leads to an error of 1×10^{-6} in the ultimate length determination. For most purposes, therefore, a rough estimate of the average humidity will suffice, but for high accuracy or under conditions of high humidity more careful measurements of humidity are required. Some recent results[19] comparing fluctuations in measured radio ranges over fixed paths of 15 to 17 km with estimates of the mean humidity over the path as obtained from meteorological measurements at both ends of the path indicate that the average relative humidity over a path of this length can be estimated to within about 5%, more or less independent of temperature. At 15°C., the residual error in distance due to this 5% error in humidity is 1×10^{-7}.

The third type of error, which we call "geometrical," is due to refraction and the resultant curvature of the propagation paths. Because the refractive indices differ for the different wavelengths, the curvatures

6

of the rays also differ, and each of the ray paths will be of a different length. In addition, since the ray paths are not in general coincident, the atmospheric structure will differ slightly between the paths. An excellent and thorough analysis of these geometrical effects, corrections, and limitations has been given by Thayer,[20] who analyzed both the ground-to-ground and, using ray tracing through a standard set of refractivity profiles on a large computer, the ground-to-air case. For the ground-to-ground case, he found that the strictly geometrical effects such as difference in length of the ray paths were small except for very long paths and unusual conditions, and could be made negligible by assuming a standard refractive index gradient. For a 25 km path and a typical gradient of optical refractive index, -30 ppm/km, the entire correction is only 3×10^{-8}. The second effect, non-coincidence of the ray paths and the resultant loss of correlation in the fluctuations of path length for the two wavelengths, is also small. For 15 km, the maximum separation of beam centers for 6328 Å and 3660 Å is only 2.7 cm. For ground-to-ground paths, none of the geometrical effects are as important as the 5% uncertainty in humidity previously discussed. Thayer concluded that the dual wavelength optical method could provide an accuracy of about 1×10^{-7} except for paths more than 25 km long or in tropical weather conditions (humid, and with temperature over 25°C.). The method appears sufficiently promising, especially under favorable conditions, that its use has been suggested for quite demanding applications.[21,22]

In the same report, Thayer also considers a three-wavelength system using distance measurements at 3 cm wavelength as well as 6328 Å and 3660 Å. Although the geometrical corrections for the microwave channel are larger than those for the optical wavelengths, the microwave-optical dispersion measurement provided in addition to the optical-optical would give an accurate measurement of the average water vapor density over the path. Such a three-wavelength system should be capable of accuracies of

2 to 3 x 10^{-8} for distances up to 50 km and temperatures up to 30°C. under reasonably normal refractive conditions. Microwave-optical measurements of this type for the determination of average humidity have already been reported,[19] and further experiments are planned with apparatus now under construction.[23]

III. NEW INSTRUMENTS AND RESULTS

A. The ESSA Instrument: Construction

A block diagram of the dual wavelength, microwave modulation frequency instrument under development at the ESSA Institute for Telecommunication Sciences and Aeronomy in Boulder, Colorado, is shown in Figure 1. Details of instrumental design and operation are available elsewhere.[24] The basic principles of the instrument are quite straightforward and are known to anyone familiar with conventional optical measurements of the velocity of light. For light of either wavelength passing out and back through the modulator, the intensity at the appropriate detector, averaged over a time long in comparison with the modulation period, will be a maximum if the round-trip transit time is an integral multiple of the modulation period. Hence observation of this intensity permits measurement of the transit time in terms of the modulation period. Measurements at different modulation frequencies permit the resolution of path length ambiguity. A high modulation frequency (3 GHz) was chosen because, for a given precision of phase measurement, the transit time can be measured more accurately at higher frequencies. Although most existing instruments use information frequencies of the order of 10 MHz, it appears that the optimum frequencies for precise distance measurement may in fact lie in the UHF or microwave range (300-3000 MHz).

A photograph of the optical system is shown in Figure 2. Two separate light sources are simultaneously used, a helium-neon gas laser and a high pressure mercury arc lamp filtered to emit a narrow spectral band centered at 3681 Å, because at present there is no satisfactory laser which operates in the 3500 - 4000 Å range. The light from the two sources is collimated and superimposed, passed through a KDP electro-optic light modulator[25]

8

operating at a frequency of 3 GHz, and transmitted by an 8'' Cassegrainian telescope. The light traverses the path to be measured and is returned by an 8'' cat's-eye retroreflector, passes through the modulator a second time, and is detected by one of a pair of photomultiplier tubes. Because the polarization, rather than the amplitude, of the light is modulated, a Wollaston prism may be used instead of a beamsplitter to separate the outgoing and returning beams. This prism also polarizes the light, combines the beams for transmission and separates them upon reception, and separates the modulated from the unmodulated component of the returning light. Thus one prism replaces an array of beamsplitters, polarizers, and dichroic mirrors. This instrument, having a modulation wavelength of 10 cm, will measure the one-way distance to a precision of 1.5 mm if the modulation phase can be determined to 10°.

The arrangement for measuring the difference in optical path ΔS is very simple. The blue light is transmitted directly from the modulator to the telescope, but the red light is diverted by a dichroic mirror and two prism reflectors around an adjustable supplementary path. A polarization compensator corrects for the effects of the prisms. By adjusting the position of one of the reflectors to give simultaneous intensity minima for both colors, the optical paths for red and blue are made equal (aside from an integral number of modulation wavelengths) and the difference in atmospheric optical path may be read out simply in terms of the distance the prism is moved from a reference position.

In order to track the fluctuations in optical path caused by changes in refractive index, a servo-control circuit locks the microwave modulation frequency to the optical path length in such a way that the path always remains an integral number of modulation wavelengths. This is done by modulating the frequency of the microwave oscillator by a small amount at 500 Hz, causing the returning light signal to be amplitude modulated at 500 Hz unless the transit time is an integral number of modulation

9

half-periods. The output of the photomultiplier detecting the red light is synchronously demodulated at 500 Hz, thus generating an error signal if the average refractive index over the path changes and hence the transit time no longer satisfies the half-integral condition. This error signal is applied to the microwave oscillator and shifts its frequency until the error is minimized. The necessary averaging over the frequency fluctuations is then performed by a counter which continuously monitors the microwave frequency. A second servo loop controlling the length of the "line stretcher" for red light tracks the changes in dispersion. These servo systems make the instrument self-balancing, a convenience when the optical path length is systematically changing, as at sunrise and sunset.

Finally, the effects of scintillation are largely cancelled by automatic normalizing circuits between the photomultipliers and the synchronous detectors. Rather than using beamsplitters to pick off reference signals, the microwave power is applied to the modulator in 100-μsec pulses with a pulse repetition rate of 1 kHz. The light intensity leaking through the modulator between signal pulses is monitored and used to control the gain of the normalizing amplifiers. In this way, optimum amplification can be maintained in the servo systems without overloading during periods of high light intensity.

B. The ESSA Instrument: Results of Field Testing

The instrument was tested during August, 1966, over a 1.6 km path across Lake Hefner, near Oklahoma City, Oklahoma. Although the path was quite short and too uniform to illustrate clearly the advantages of the dispersion method over conventional methods, it was chosen because accurate meteorological data at three points along the path were available for comparison. Unfortunately, technical difficulties prevented simultaneous distance measurements at the two wavelengths from being made and

it was necessary to lock the modulation frequency alternately onto the red and violet path lengths. Variations in atmospheric density during the switching and measurement period (about 1 or 2 minutes) introduced random errors which reduced the precision of the corrected distance below the levels expected.

The Lake Hefner results[26] showed the precision of the instrument in detecting optical path length changes for either wavelength to be about 3×10^{-8} with an averaging time of 10 seconds. This was checked by physically moving the retroreflector through small distances; a motion of about 5×10^{-3} cm could be detected. Using 177 measurements of corrected distance over a period of 4 days, the standard deviation was found to be 1.55 mm, slightly better than 1×10^{-6}. For comparison, the standard deviation of optical path length, which would be the error of a one-wavelength distance measurement if no meteorological information were used for correction and there were no other sources of error, was 2.2×10^{-6}, and the standard deviation of length corrected using meteorological data from both end points and the center of the path was 0.8×10^{-6}. Although the precision of the dispersion-corrected measurements is slightly lower, it is better than had been expected for sequential measurements over such a short path and is highly encouraging, for we expect that the precision of the dispersion correction relative to the meteorological correction will increase with longer paths and simultaneous measurements. Finally, uncorrected and meteorologically corrected measurements of microwave distance taken over the same path using a new 9.6 GHz instrument[27] and the same meteorological data gave standard deviations of 10.5×10^{-6} and 1.6×10^{-6}, respectively.

Tests over a 5.3 km path between two hills north of Boulder, Colorado, were begun in May, 1967, using an instrument which had been rebuilt to include a satisfactory line stretcher, coated optics, more sensitive photomultiplier tubes, and a narrower filter for the violet light. The usual rms fluctuations of one-second averages of apparent distance relative to the 30-

11

second moving average are found to be 3×10^{-9} of the total path. The diurnal drift of many parts in 10^6 causes a steady change in the average path length in addition to these rapid fluctuations. A typical recording is shown in Figure 3. Figure 4 shows an extremely noisy example observed after a heavy rain. A corrected distance measurement over this path with a precision of 3×10^{-7} has already been demonstrated, using 14 measurements over a period of 2 hours.

The absolute accuracy of the corrected length measurements cannot be ascertained from the existing data. The most direct and accurate calibration could be made by taking measurements through a long (1 km or more) pipe which could be evacuated. Since the position of the effective modulation point (the "zero error") and the modulation frequency can be known with sufficient accuracy, measurements through such a pipe at various air densities could be used to determine the absolute accuracy of the correction method, within the small remaining uncertainty due to variations in air composition. Alternatively, measurements through the atmosphere under widely varying conditions plus theoretical limits placed on the various known sources of systematic error could be used to determine the absolute accuracy, although a longer time would be required and the calibration would probably be less precise.

C.   Other Dispersion Measurements

Fowler and Castellano[28] have measured the dispersion between 6328 Å and 1.15 microns over a 35 km round-trip distance, finding that the corrected distance could be obtained with a precision of about 3×10^{-6}, limited by inadequate signal power at 1.15 microns and by the precision of their phase measurement. They are now building a new instrument using lasers at 6328 Å and 4880 Å and a much improved phase meter, and hope to have it in operation this year.[29]

Thompson and Wood have used a modified Geodimeter to measure the dispersion using four spectral lines of mercury between 4048 Å and 5790 Å and path lengths of 7.5 and 15 km,[16] and are at present carrying out radio-optical dispersion measurements over paths up to 65 km long in Hawaii.[30]

Finally, Sullivan[31,32] has used measurements of dispersion in the microwave region to determine average water vapor and dry air densities for refraction correction. By using measurements at 15.6 and 31.2 GHz, on either side of the 22 GHz water vapor line, and at 45 and 90 GHz, bracketing the several oxygen lines near 60 GHz, he was able to reduce the rms fluctuation of distance measurements made with a 10 GHz instrument over a 23 km path from 13×10^{-6} to about 2×10^{-6}. At the time this work ended the water vapor measurements were apparently satisfactory, although the stability of the oxygen equipment was still inadequate.

IV.   CONCLUSIONS

The importance of the multiple wavelength dispersion technique in geodetic distance measurement, and the practical value of lasers and modern light modulation and electronic methods which make the dispersion technique feasible, are clear. Field tests of a new instrument over a 5.3 km path have already demonstrated a precision of 3×10^{-9} in detecting changes in optical path length with a 1-sec averaging time, and a precision of 3×10^{-7} in corrected length. The determination and correction of systematic errors is in progress, as is the development of other instruments in other laboratories. Although it has not yet been actually demonstrated, it is expected on the basis of present results and a careful theoretical analysis that the dispersion method will permit absolute accuracies of a few parts in ten million to be achieved in measurements of paths several tens of kilometers long.

ACKNOWLEDGEMENTS

REFERENCES

1). Jordan/Eggert/Kneissl, <u>Handbuch der Vermessungskunde, Band VI:</u>
   <u>Die Entfernungsmessung mit Elektro-Magnetischen Wellen und</u>
   <u>ihre Geodätische Anwendung</u>, K. Rinner and F. Benz, Eds.
   (J. B. Metzlersche Verlagsbuchhandlung, Stuttgart, 1966).

2). P. L. Bender, "Laser measurements of long distances," Proc. IEEE
   <u>55</u>, 1039-1045 (1967).

3). M. C. Thompson, Jr., "A summary of progress in problems related
   to terrestrial electronic distance measuring in the United
   States since 1963," paper presented at the XIV General
   Assembly of the IUGG, Lucerne, Switzerland, 25 Sept. - 7 Oct.
   1967.

4). E. Bergstrand, "A determination of the velocity of light," Arkiv
   Fysik <u>2</u>, 119-151 (1950).

5). B. K. Meade, "High-precision geodimeter traverse surveys in the
   United States," paper presented at the XIV General Assembly
   of the IUGG, Lucerne, Switzerland, 25 Sept. - 7 Oct. 1967.

6). K. D. Froome and R. H. Bradsell, "Distance measurement by means
   of a light ray modulated at a microwave frequency," J. Sci.
   Instr. <u>38</u>, 458-462 (1961).

7). I. P. Kaminow, "Microwave modulation of the electro-optic effect
   in KH_2PO_4," Phys. Rev. Letters <u>6</u>, 528-530 (1961).

8). S. E. Smathers, G. B. Lesley, R. Tomlinson, and H. S. Boyne,
   "Preliminary measurements with a laser geodimeter" (to be
   published).

9). M. C. Thompson, Jr., "The effects of propagation on measurements
   of distance, angle-of-arrival, and Doppler effect in ground-to-
   ground systems," presented at XV General Assembly of URSI,
   Munich, Germany, Sept. 1966; to be published in Progress in
   Radio Science, 1963-1966.

10). M. C. Thompson, Jr., H. B. Janes, and F. E. Freethey,
   "Atmospheric limitations on electronic distance-measuring
   equipment," J. Geophys. Res. <u>65</u>, 389-393 (1960).

11). W. G. Tank, W. T. Kreiss, J. J. Rowley, and T. Y. Palmer, "Improved sampling techniques," Technical Report RADC-TR-66-407 (The Boeing Co., Aug. 1966).

12). W. G. Tank, private communication.

13). M. T. Prilepin, "Light-modulating method for determining the average index of refraction of air along a line," Trudi Tsentral'nogo Nauchno-Issledovetel'skogo Instituta Geodezii, Aeros'emki i Kartografii, No. 114, pp. 127-130 (1957).

14). E. Bergstrand, "The geodimeter system: a short discussion of its principal function and future development," J. Geophys. Res. 65, 404-409 (1960).

15). P. L. Bender and J. C. Owens, "Correction of optical distance measurements for the fluctuating atmospheric index of refraction," J. Geophys. Res. 70, 2461-2562 (1965).

16). M. C. Thompson, Jr. and L. E. Wood, "The use of atmospheric dispersion for refraction correction of optical distance measurements," Proc. International Association of Geodesy Symposium on Electromagnetic Distance Measurement, Oxford, England, 6-10 Sept. 196⁵, pp. 165-171.

17). J. C. Owens and P. L. Bender, "Multiple wavelength optical distance measurements," Proc. International Association of Geodesy Symposium on Electromagnetic Distance Measurement, Oxford, England, 6-10 Sept. 1965, pp. 159-164.

18). J. C. Owens, "Optical refractive index of air: dependence on pressure, temperature, and composition," Appl. Opt. 6, 51-59 (1967).

19). B. R. Bean and C. B. Emmanuel, "Application of radio and optical path length measurements to studies of low level turbulence," Proc. Joint Technical Exchange Conference, Monterey, Calif., April 1967.

20). G. D. Thayer, "Atmospheric effects on multiple-frequency range measurements," IER/ITSA Tech. Rept. (U.S. Government Printing Office) (to be published).

21). J. C. Owens and K. B. Earnshaw, "Long-distance optical strain-meters for fault zone instrumentation," Proc. ESSA Symposium on Earthquake Prediction (United States Government Printing Office, 1966), pp. 85-92.

22). R. S. Lawrence, K. B. Earnshaw, and J. C. Owens, "The practicality of using light beams to distribute local oscillator signals over large antenna arrays," Proc. AGARD-EPC Symposium on Phase and Frequency Instability in Electromagnetic Wave Propagation, Ankara, Turkey, 9-12 Oct. 1967 (to be published).

23). B. R. Bean and R. E. McGavin, "Electromagnetic phase variability as a measure of water vapor and temperature variations over extended paths," Proc. AGARD-EPC Symposium on Phase and Frequency Instability in Electromagnetic Wave Propagation, Ankara, Turkey, 9-12 Oct. 1967 (to be published).

24). K. B. Earnshaw and J. C. Owens, "A dual wavelength optical distance measuring instrument which corrects for air density," IEEE J. Quantum Electronics (to be published, November, 1967).

25). I. P. Kaminow and E. H. Turner, "Electrooptic light modulators," Appl. Opt. 5, 1612-1628 (1966).

26) Further details may be found in J. C. Owens, "Recent progress in optical distance measurement: lasers and atmospheric dispersion," Proc . International Association of Geodesy Symposium on Figure of the Earth and Refraction, Vienna, Austria, 14-17 March 1967 (to be published).

27). R. O. Gilmer and D. M. Waters, "A solid-state system for measurement of integrated refractive index," Tech. Rept. IER-4C/ITSA-40 (U. S. Government Printing Office, 1967) (to be published).

28). R. A. Fowler and V. Castellano, "Geodetic laser survey system (GLASS) - an application to earthquake prediction," Trans. Am. Geophys. Union 47, 166-167 (1966).

29). R. A. Fowler, private communication.

30). M. C. Thompson, Jr., private communication.

31). "Final report on line integral refractometer," Rept. MTP-19 (Mitre Corp., Dec. 1965).

32). J. F. Sullivan, private communication.
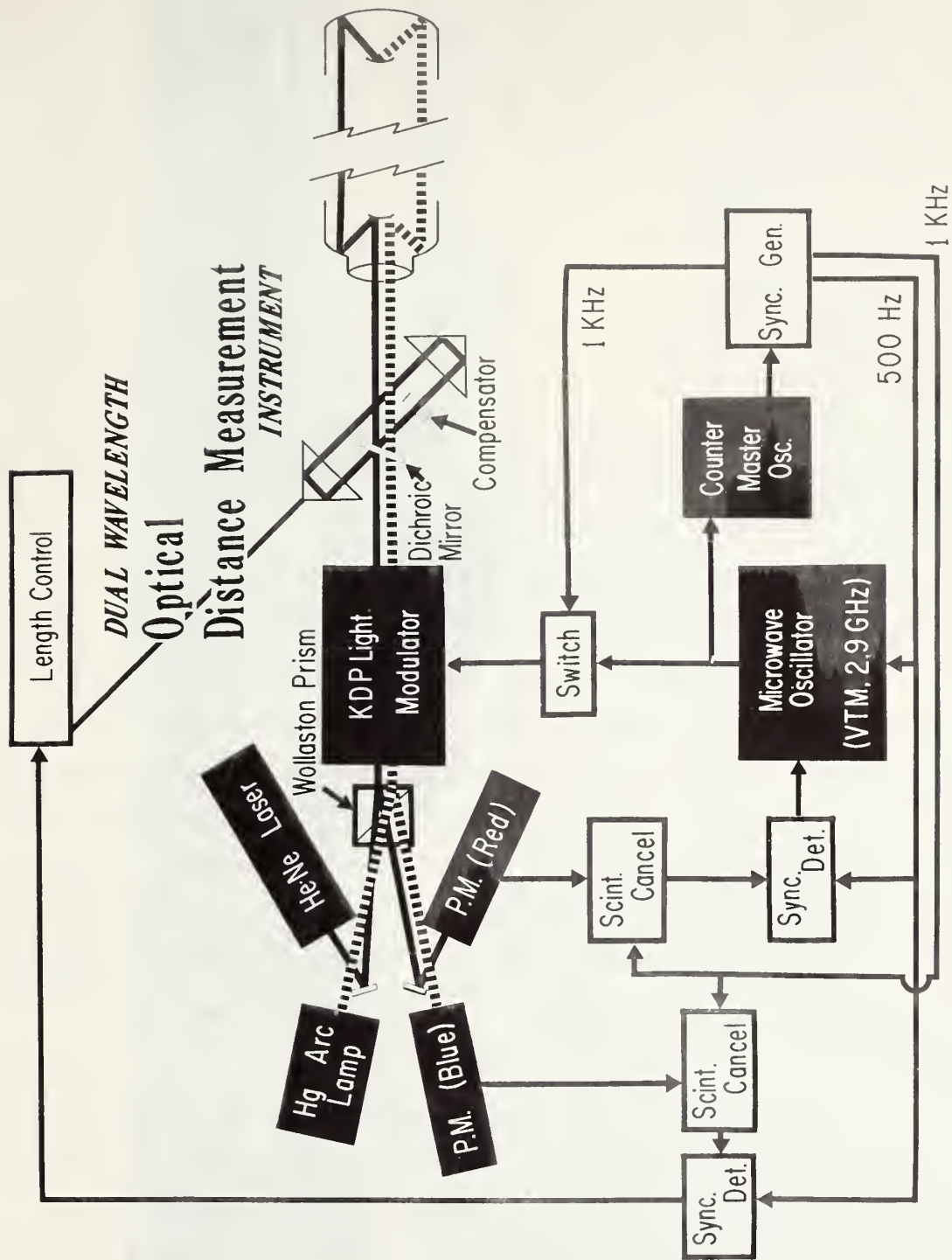
Figure 1. Block diagram of the ESSA instrument.
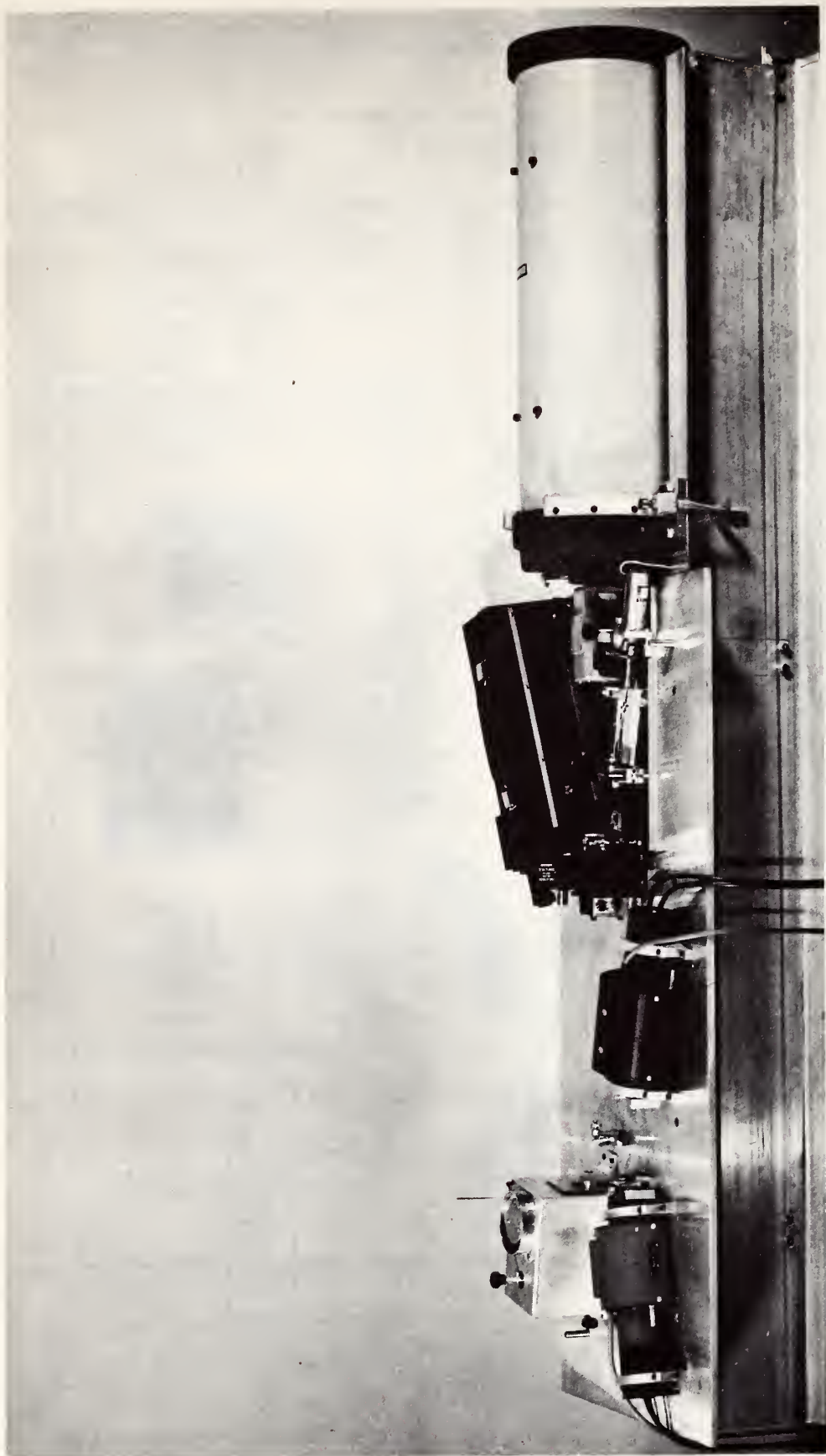
Figure 2. Photograph of the optical system. Overall length of the system is about 2.5 meters. The 20 cm diameter, 1 m focal length telescope used as a retroreflector is not shown.
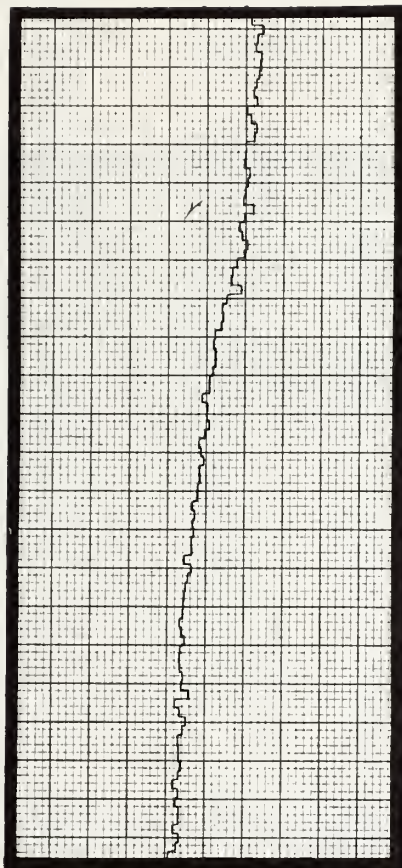
Figure 3. Path-length observations with an optical beam traversing a round-trip path of 10.6 km under normal conditions. The rms fluctuation of these one-second averages relative to a smooth average is 3×10^{-9} of the total path.
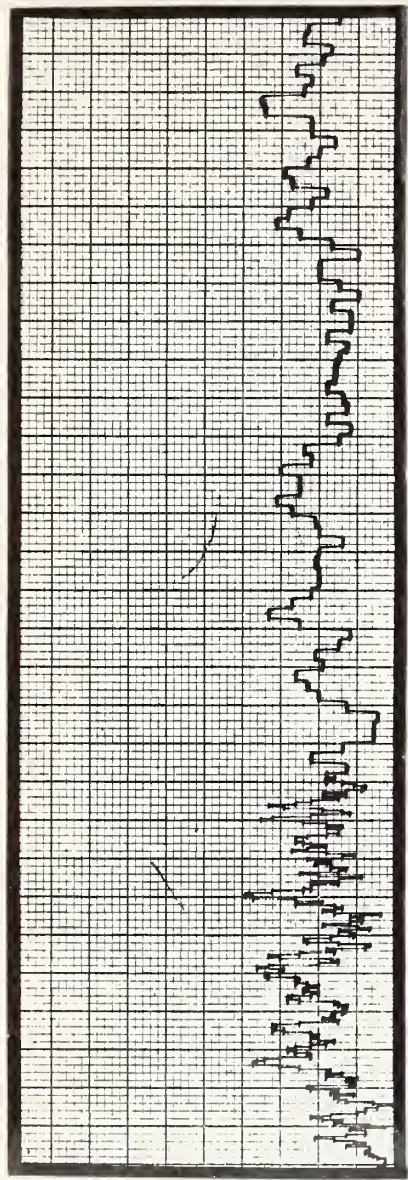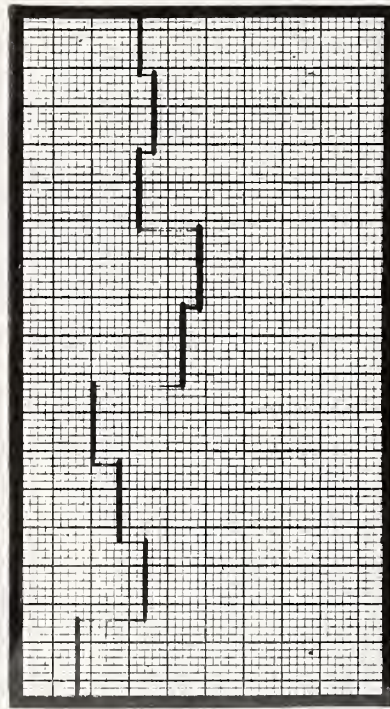
Figure 4. Examples of path-length fluctuations with an optical beam traversing a round-trip path of 10.6 km under unusually noisy conditions. The rms fluctuation is 3×10^{-8}, nearly independent of averaging time between 0.1 sec and 10 sec.

Reprinted from IEEE Transactions on AES, AES-5, No. 2, March 1969, 346-350.

17

A Comparison of Radar and Radio Interferometer Refraction Errors

Abstract

The refraction error ϵ' in measurements made with the simple interferometer is found to be similar in nature to the refraction error ϵ in the conventional radar measurement. For elevation angles $\theta > 10°$, $\epsilon' - \epsilon > 0.05$ mrad, when ϵ' is computed after correcting for refraction along the interferometer extra-path S_3.

The purpose of this correspondence is to demonstrate the nature of the effects of atmospheric refraction on the simple two-element interferometer. A comparison of the interferometer refraction error with the elevation angle error in a conventional radar provides a meaningful approach to the problem. The need for clarification of these effects has become apparent since the publication of an incorrect analysis by the National Bureau of Standards (NBS) [1] whose results have been quoted in a National Academy of Sciences report [2]. The same basic approach as that of the NBS authors will be used, because it leads to a simple formulation and solution of the problem and pinpoints the errors in the NBS analysis.

Fig. 1 shows the complete geometry of the problem. We shall impose the following conditions.

1) The ratio of slant range to baseline length is restricted to $r/B > 100$.
2) The elevation angle is confined to the range $10° < \theta < 90°$.
3) The atmosphere is spherically stratified.

A phase difference is measured with the simple interferometer. The phase difference is proportional to a radio range difference

$$\Delta_0 = r_{0_1} - r_{0_2}, \qquad (1)$$

which is used to compute an angle. The relationships between this angle, the elevation angle θ, and the ray angle θ_0 are our central concern. The angle we determine obviously depends on how we choose to involve Δ_0 in a computation. Bean and Thayer [1] of the NBS choose to compute an angle

$$\beta^* = \cos^{-1} \Delta_0 / B. \qquad (2)$$

The radio range to the target P from the ith antenna is given by geometrical optics as

$$r_{0.} = \int_0^{S_i} n(s) ds, \qquad (3)$$

where

S_i = length of the ith ray path,
s = the displacement along the arc S_i, and
$n(s)$ = the refractive index of the atmosphere.

We define the average index of refraction along S_i as

$$\bar{n}_i \triangleq \frac{1}{S_i} \int_0^{S_i} n(s) ds, \qquad (4)$$

from which we see that

$$r_{0.} = \bar{n}_i S_i. \qquad (5)$$

Also, the radio range may be expressed as

$$r_{0.} = r_i + \Delta r_0 \qquad (6)$$

where

r_i = the ith slant range, and
$\Delta r_{0.}$ = the component of r_{0_i} due to atmospheric refraction.

Now we rewrite (1) as

$$\Delta_0 = \Delta + \delta, \qquad (7)$$

in which

$$\Delta \triangleq r_1 - r_2, \qquad (8)$$

and

$$\delta \triangleq \Delta r_{0_1} - \Delta r_{0_2}. \qquad (9)$$

Putting (5), (6), and (8) into (9) gives

$$\delta = \bar{n}_1 S_1 - \bar{n}_2 S_2 - \Delta. \qquad (10)$$

It can be shown that $(\bar{n}_1 - \bar{n}_2)/\bar{n} < 1$ ppm under the conditions assumed if $n(s)$ is taken to be the CRPL exponential atmosphere [3] and $\bar{n}$ is the average refractive index along S. For these same conditions, the fractional bending error $\delta r_i / S_i \triangleq (S_i - r_i)/S_i < 1$ ppm. Thus, we neglect ray bending in (10), set $\bar{n}_1$, $\bar{n}_2 = \bar{n}$, and write

$$\delta / \Delta \simeq (\bar{n} - 1). \qquad (11)$$

Substituting (7) into (2), we find

$$\beta^* = \cos^{-1} \frac{\Delta}{B} \left(1 + \frac{\delta}{\Delta} \right). \qquad (12)$$

The formula

$$\cos^{-1} x(1 + y)$$
$$= \cos^{-1} x - \frac{x}{(1 - x^2)^{1/2}} y$$

Fig. 1. Refraction geometry for the simple interferometer with antennas A_1 and A_2.
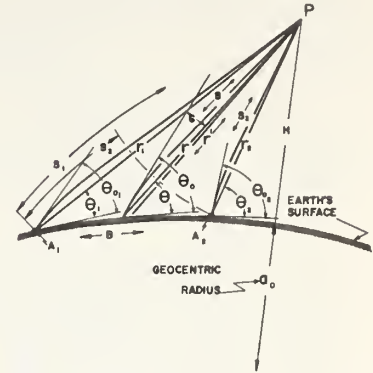
Fig. 2. Comparison of refraction error of radar with refraction error $\Delta\theta$ of radio interferometer when no correction is made for refraction along path S_3 (see Fig. 1).

$\Delta\theta = (\bar{n}-1) \cot \theta$
ϵ = RADAR ERROR
H = TARGET HEIGHT

$H = 1$ km
$H = 10$ km
$H = 50$ km
$H = 90$ km

$10°$

Fig. 3. Comparison of refraction error of radar with refraction error ϵ' of radio interferometer when correction is made for refraction along path S_3 (see Fig. 1).

$\epsilon' = (1 - \bar{n}/n_a) \cot \theta$
ϵ = RADAR ERROR
TARGET HEIGHT H (km)

90
50
10
$10°$
1
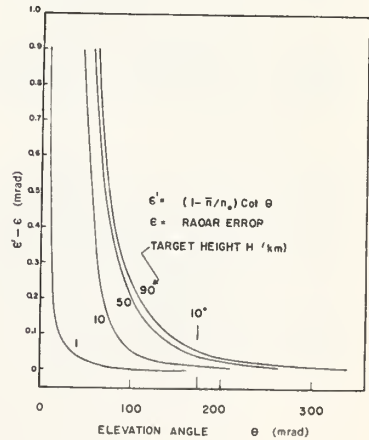
$$- \frac{x^3}{2!(1 - x^2)^{3/2}} y^2$$

$$- \frac{x^3(1 + 2x^2)}{3!(1 - x^2)^{5/2}} y^3 + \cdots \quad (13)$$

given by Simmons [4], allows (12) to be written

$$\Delta\theta = \beta^* - \theta \simeq (\bar{n} - 1) \cot \theta. \quad (14)$$

In (14), we have dropped second-order and higher terms, eliminated δ/Δ using (11), and introduced

$$\theta \simeq \cos^{-1}(\Delta/B), \quad (15)$$

an approximation justified on the original assumptions. It has been shown [5] that $\bar{n}$ is essentially independent of elevation angle for a constant target height H. Thus, (14) has the cot θ character of the conventional radar refraction error ϵ. Had not the analysis of Bean and Thayer gone astray,[1] they would have obtained this same result. Fig. 2 is a comparison of $\Delta\theta$ and ϵ for values of $H=1$, 10, 50, and 90 km. For $\theta > 10°$, the curves show that the errors are similar in character but quantitatively different. The values $\bar{n}$, θ, and ϵ were taken from NBS tables [3] for an exponential atmosphere.

Rather than use (2), we now compute the interferometer angle from the expression

$$\theta_0' = \cos^{-1} S_3/B, \quad (16)$$

where S_3 is the extra arc traversed by the ray reaching antenna A_1 as compared with the arc traversed by the ray arriving simultaneously at $A_2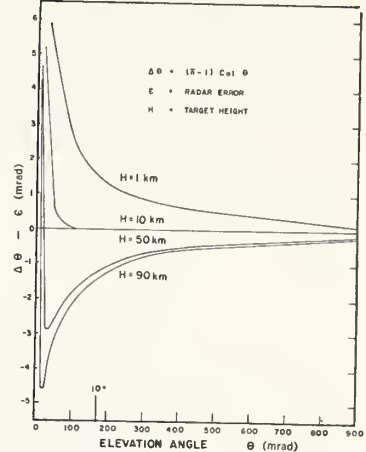$. We will show that θ_0' is a good approximation to the angle of arrival θ_0. From geometrical optics, S_3 is related to the range difference measurement by

$$S_3 = \Delta_0/\bar{n}_3 \quad (17)$$

in which $\bar{n}_3$ is the average index of refraction along S_3. Approximating $\bar{n}_3$ with the surface value of refractive index

---

[1] The authors made an error in approximating $\Delta\theta_0 = \theta_{0_1} - \theta_{0_2}$, as well as an error in expanding $1/[\sin (\theta_{0_1} + \Delta\theta_0)]$. The correct value, $\Delta\theta_0 \simeq (B/r) \sin \theta$, substituted into the proper expansion would have led Bean and Thayer to the result $\Delta\theta \simeq [(10^{-6}/H)\int_0^H N(h)dh] \cot \theta$. This is equivalent to (14) since the bracketed term is equal to $\bar{n}-1$ to the same order of approximation used by Bean and Thayer.

n_0 and putting (17) in (16), we have

$$\theta_0' \simeq \cos^{-1} \frac{\Delta}{n_0 B} \left[1 + \frac{\delta}{\Delta} \right]. \quad (18)$$

Using (11) in (18), expanding according to (13), and making use of (15), we have

$$\epsilon' \triangleq \theta_0' - \theta \simeq (1 - \bar{n}/n_0) \cot \theta. \quad (19)$$

Equation (19) also has the character of the conventional radar error. Moreover, in Fig. 3, ϵ' and ϵ are seen to be essentially the same quantity for $\theta > 10°$. Fig. 3 was also prepared with data taken from NBS tables in which $n_0 = 1.000313$.

From the foregoing discussion, it is seen that the basic difference between the radar and the interferometer is that the aperture of the interferometer is not tilted to null out the phase difference between the arriving rays. This introduces an atmospheric path S_3, which is not encountered in the conventional radar measurement. Dividing the range difference (phase) measurement from the interferometer by the surface value of the refractive index very nearly compensates for the extra-path refraction along S_3. This does not correct for the refraction along S_2 and the part of S_1 that excludes S_3. The uncorrected effects simply cause the interferometer to indicate angle of arrival θ_0 rather than true elevation angle θ (the same phenomena experienced with a conventional radar).

ROBERT H. PAUL
White Sands Missile Range
N. Mex.

REFERENCES

[1] G. D. Thayer and B. R. Bean, "An analysis of atmospheric refraction errors of phase measuring radio tracking systems," NBS Rept. 7254, pt. 1, June 5, 1962.
[2] "Report of the ad hoc panel on electromagnetic propagation," Advisory Committee to AF Systems Command, Nat'l Academy of Sciences. Nat'l Research Council, ASTIA AD 296845, pp. 6–13, February 1963.
[3] B. R. Bean and G. D. Thayer, "CRPL exponential reference atmosphere," NBS, Central Radio Propagation Lab., Boulder, Col., Mono. 4, 1959.
[4] G. A. Simmons, "A study of the error involved in the near use of a radio interferometer," Sandia Corp., Tech. Memo. SCTM122-59-(52), p. 9, April 4, 1959.
[5] P. Milnarich, Jr., and R. H. Paul, "Simultaneous estimation of target position and atmospheric refractivity from radio range data," Proc. 1963 Nat'l Winter Conv. on Military Electronics, pp. 6–33.

Authors' Reply[2]

Abstract

Apparent discrepancies between two methods of estimating the direction angle error of radio "interferometers" are analyzed. The analysis shows that both yield correct results, but they have mutually exclusive domains of applicability. Paul's result is correct under conditions of short baselines and target positions where flat-earth geometry is permissible; the authors' previous result is correct for conditions of curved-earth geometry and deep-space tracking where the incoming radio wavefront is nearly planar. A more general result is given here, which is valid under either set of conditions.

The apparent discrepancies between Paul's equation and the Thayer and Bean equation for estimating the direction angle error of radio interferometers have been analyzed; the results, which are summarized below, show that both equations are essentially correct, but that they have mutually exclusive domains of applicability. Paul's result is correct for short baselines and target positions such that flat-earth geometry is permissible; the authors' result is correct for curved-earth geometry and deep-space tracking conditions such that the incoming radio wavefront is nearly planar. A more general error equation, combining both of the earlier results and applicable over both domains, is given.

The error in direction angle of a simple two-element interferometer or baseline system depends upon the range errors of the radio rays received at the two antennas. The radio range error in turn depends on the refractive index profile assumed and the initial elevation angle of the radio ray. If the distance to the target (the range r) is large compared with the baseline B, then a good approximation to the direction angle error is [6]

$$\Delta\beta \cong \frac{\Delta r_1 - \Delta r_2}{B} \csc \beta, \quad (20)$$

where β is the direction angle to the target and Δr is the radio range error, which is given by [(3) is equivalent]

$$\Delta r \cong \int_0^r [n(z, s) - 1] \csc \{\theta(z)\} dz, \quad (21)$$

where $n(z, s)$ is the radio refractive index at height z along the ray path s, $\theta(z)$ is the elevation angle of the ray, and z is

---

[2] Manuscript received October 21, 1968.
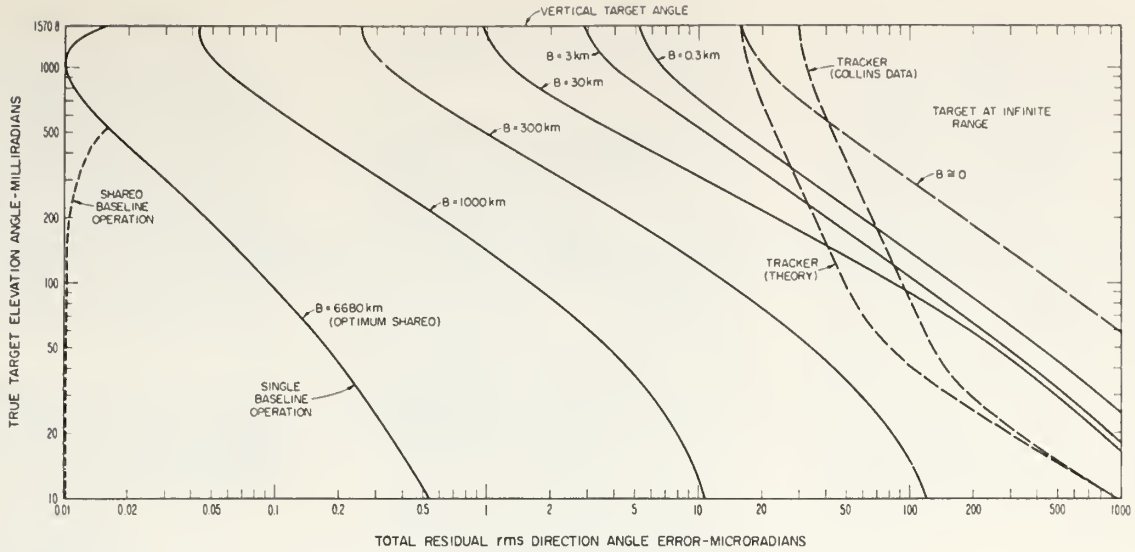
Fig. 4. Residual direction angle errors of baseline tracking systems after refraction correction.

the height above the earth's surface. It is obvious from (21) that if a homogeneous atmosphere is assumed, so that n is a function only of z, then Δr_1 and Δr_2 in (20) will differ only if θ is different for the two rays, i.e., if the initial elevation angles are different.

For initial elevation angles θ in excess of about 10° and a homogeneous atmosphere, (21) may be well approximated by

$$\Delta r \cong \csc \theta \int_0^h [n(z) - 1]dz, \quad (22)$$

where h is the target height. If (22) is substituted into (20), we have

$$\Delta \beta \cong \frac{I(h) \csc \beta}{B} [\csc \theta_1 - \csc \theta_2], \quad (23)$$

where $I(h)$ represents the integral in (22). If we assume a fairly small baseline ($B < 30$ km), then $\beta = \theta_1$ (same as Paul's θ_1). If we write $\Delta \theta \equiv \theta_2 - \theta_1$ and expand the term inside the brackets of (23), assuming further that $\cos \Delta \theta = 1$, $\sin \Delta \theta = \Delta \theta$, and $\Delta \theta \cot \theta_1 \ll 1$, we obtain the approximate expression

$$\Delta \beta \cong \frac{I(h)}{B} \Delta \theta \csc^2 \beta \cot \beta. \quad (24)$$

The evaluation of $\Delta \theta$ in (24) depends a great deal upon the assumptions made.

Paul assumes that a flat-earth model may be used; this is equivalent to the restriction $r \ll a_0 \sin \theta_1$, where a_0 is the radius of the earth (~ 6373 km). If $r \gg B$ is also assumed (as Paul does), then a good approximation to $\Delta \theta$ may be easily shown to be

$$\Delta \theta \cong \frac{B}{r_1} \sin \theta_1. \quad (25)$$

Substituting (25) into (24), we have

$$\Delta \beta \cong \frac{I(h)}{r_1 \sin \beta} \cot \beta$$
$$\cong \frac{I(h)}{h} \cot \beta \quad (26)$$
$$\cong (\bar{n} - 1) \cot \beta.$$

This is Paul's result (14). Combining the restrictions on r and B, and assuming the double inequality to be equivalent to a factor of 100, we find that this result is valid only for baselines less than about 640 meters at $\beta = 90°$, and only for B less than about 100 meters at $\beta = 10°$:

$$B < 10^{-4} a_0 \sin \beta. \quad (27)$$

On the other hand, in the NBS report, the authors assumed that "the target is far enough away so that the rays from A_1 and A_2 (the antennas) are sensibly parallel." For a flat-earth model, this assumption results in essentially no error in β, since the elevation angles of the two rays are the same. Any difference between Δr_1 and Δr_2 that exists under this restriction is due to the curvature of the earth. Ignoring refraction per se, it may be easily shown that the difference $\Delta \theta$ for a curved earth and parallel rays is equal to the angle subtended at the earth's center by the baseline B:

$$\Delta \theta \cong \Delta \phi = \frac{B}{a_0}. \quad (28)$$

Substituting (28) into (24), we obtain

$$\Delta \beta \cong \frac{I(h)}{a_0} \csc^2 \beta \cot \beta$$
$$\cong \frac{I(h)}{a_0} \csc^3 \beta \cos \beta. \quad (29)$$

This result is the same as that arrived at in the Thayer–Bean NBS report, with the exception of the factor $\cos \beta$. Since the sponsor of the work covered in the report was interested in elevation angles mostly between 10° and 30°, and only an estimate of the error $\Delta \beta$ was being derived in the section of the report in question, the factor $\cos \beta$ was left out for simplicity. Unfortunately, the restriction $\beta < 30°$ was inadvertently omitted from some of the equations. The restriction $r \gg B$ is inadequate to ensure parallel rays. The NBS report was, of course, preliminary, and later published material [7] goes into more detail, specifically considering the effects of atmospheric inhomogeneities on baseline tracking systems. Horizontal refractive index gradients and refractive index turbulence are, in general, more important in baseline systems than the systematic refraction produced by a homogeneous atmosphere. Fig. 4, taken from [7], shows the results of a more complete analysis of baseline system refraction errors.

A more general error equation for homogeneous refraction effects on baseline systems has been derived. A simple form of this equation, with a relative error of less than 10^{-1} for $B < 30$ km and $r > 100$ B, is

$$\Delta \beta \cong - I(h) \csc^2 \beta \cot \beta$$
$$\cdot \left[\frac{\sin \beta}{r} + \frac{1}{a_0} \right] \quad (30)$$

which may be rewritten as

$$\Delta \beta \cong - \left[\frac{I(h)}{r} \csc \beta \cot \beta \right.$$
$$\left. + \frac{I(h)}{a_0} \csc^2 \beta \cot \beta \right]. \quad (31)$$

For flat-earth conditions, i.e., when $r \sin \beta = h$, the first term in the brackets of (31) reduces to Paul's expression; the second term inside the brackets represents the Thayer-Bean expression. Therefore, the effects of target "nearness" and earth curvature are separable and additive, i.e., there is no significant interaction between the two effects. The general expression (30) should be used to evaluate baseline system error for most applications. Only when the two terms inside the brackets of (30) are markedly different may either the Paul or Thayer-Bean expression be used alone. This criterion reduces easily to $a_0 \sin \beta \gg r$, or vice versa, as may be seen by inspection; these are the same criteria as used earlier for deriving the separate expressions.

In conclusion, we may state the following.

1) Under the conditions $\beta > 10°$, $r \ll a_0 \sin \beta$, and $r \gg B$, and hence only for baselines of a few hundred meters or less, Paul's analysis is correct.

2) Under the conditions $\beta > 10°$, $r \gg a_0 \sin \beta$, and $B < 50$ km, the Thayer-

Bean analysis is correct (subject to the inclusion of the factor $\cos \beta$ as pointed out).

3) The sum of the two expressions (after modifying Paul's for accuracy, where $r \sin \beta \neq h$) forms a general error expression valid for $B > 10°$, $B < 50$ km, and $r \gg B$, where the ratio $r/a_0 \sin \beta$ may assume any value.

4) The two expressions for $\Delta\beta$, Paul's and Thayer-Bean's, cannot be directly compared because they apply to mutually exclusive portions of the $r/a_0 \sin \beta$ domain. The confusion evidently arose from the use of different notation; Paul uses r and r_0 for range to the target, while Thayer and Bean used r and r_0 for the radius vector from the center of the earth. Thus, Paul's footnote to the discussion of (14) is correct for flat-earth conditions if $r = $ range, whereas for deep-space tracking conditions and $r = $ radius vector, as in the NBS report, the Thayer-Bean result is correct.

Finally, we wish to bring attention to the following disclaimer appearing on the inside cover page of the NBS report referred to by Paul.

Authors wishing to reference material in an NBS Report, ESSA Technical Memorandum, or the equivalent, are usually requested to list the reference as a private communication.

Gordon D. Thayer
Bradford R. Bean
U. S. Dept. of Commerce
ESSA Research Labs.
Boulder, Col. 80302

REFERENCES

[6] D. L. Hagen, "Radar refraction errors in an interferometer missile guidance tracking system," G.E. Defense Systems Develop. Rept. ASER-6-1959.
[7] G. D. Thayer and B. R. Bean, "Systematic atmospheric refraction errors of baseline-type radio tracking systems and methods for their correction," *Proc. 1964 1st Space Congress* (Cocoa Beach, Fla., April 1964).

A Field Study of the Effectiveness of Fatty Alcohol Mixtures as Evaporation Reducing Monomolecular Films

B. R. BEAN

Environmental Science Services Administration
Boulder, Colorado

Q. L. FLOREY

U. S. Bureau of Reclamation
Denver, Colorado

Abstract. A field study of the effectiveness of fatty alcohol mixtures as evaporation reducing monomolecular films was carried out at Lake Hefner, Oklahoma. Evaporation, as determined by the eddy flux method, was reduced, on the average, by 58%. (Key words: Evaporation; water balance; water resources.)

Our study of evaporation from Lake Hefner, Oklahoma, is focused in particular upon the reduction of this evaporation by monomolecular films of mixtures of hexadecanol and octadecanol. Figure 1 gives a plan view of the experiment. A water sprinkler system serves as a vehicle for introducing the film onto the lake. The prevailing summertime southerly wind is relied upon to spread the film across the lake. A tower is installed at the 'raft-site,' and measurements are made of the evaporation as the film spreads under the measuring instruments placed at 2 meters elevation.

The evaporation reported here was determined by the eddy-correlation technique [*Swinbank*, 1951; *Dyer*, 1961]. In this technique the evaporation E[gm cm⁻² sec⁻¹] is determined from

$$E = \overline{m'w'} \qquad (1)$$

where m is the water vapor density [gm cm⁻³], and w is the vertical wind [cm sec⁻¹]. The quantities m' and w' are defined as $m' = (m - \bar{m})$ and $w' = (w - \bar{w})$, where the overbar denotes a 10-minute average of observations taken every second. (The one-second observations are *the average* of 30 observations per second.) The average of the product, $m'w'$ is similarly determined for 10 minutes.

The vertical wind was measured with an anemometer-bivane. The humidity was measured with an experimental barium fluoride humidity element capable of resolving fluctuations of several cycles per second [*Jones and Wexler*, 1960].

The effect of a 40% hexadecanol-60% octadecanol mixture on humidity fluctuations is illustrated by Figure 2. One can see that the presence of the film affects both the amplitude and frequency of the humidity variations. One would expect the film to have two effects upon the water vapor density observed at the tower: 1. to reduce the water vapor density by reducing evaporation upwind; and 2. to warm the ambient air by reducing evaporative cooling and thus lowering the relative humidity.

Effect 2 is clearly not observed in this case, as the relative humidity behaves in the opposite fashion, owing to the nearly constant air temperature during this period. The variation of relative humidity thus reflects effect 1 in the water vapor density varied 0.1 to 0.6 gm/m³ in the proper direction with changes from film to no-film. The main effect of the film is to suppress the amplitude of the short-term variations of humidity and thus to affect the magnitude of w' in equation 1. Interestingly, this change in short-term variations is 'anticipated' by the humidity element before a change in film to no-film conditions. The short-term fluctuations change from film to no-film conditions some 20 to 30 minutes before the film either comes under or leaves the water under the
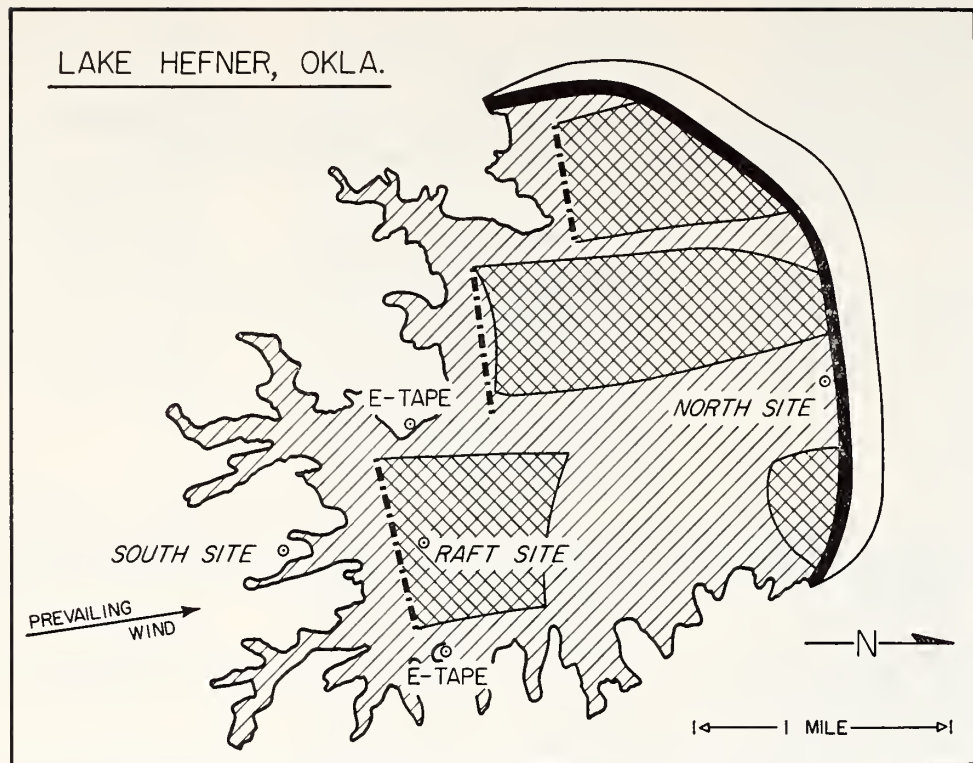
Fig. 1. Plan view of the Lake Hefner Experiment. The sprinkler systems for applying film-forming materials are indicated by ——. ——. Center tower is located at the 'raft site.'
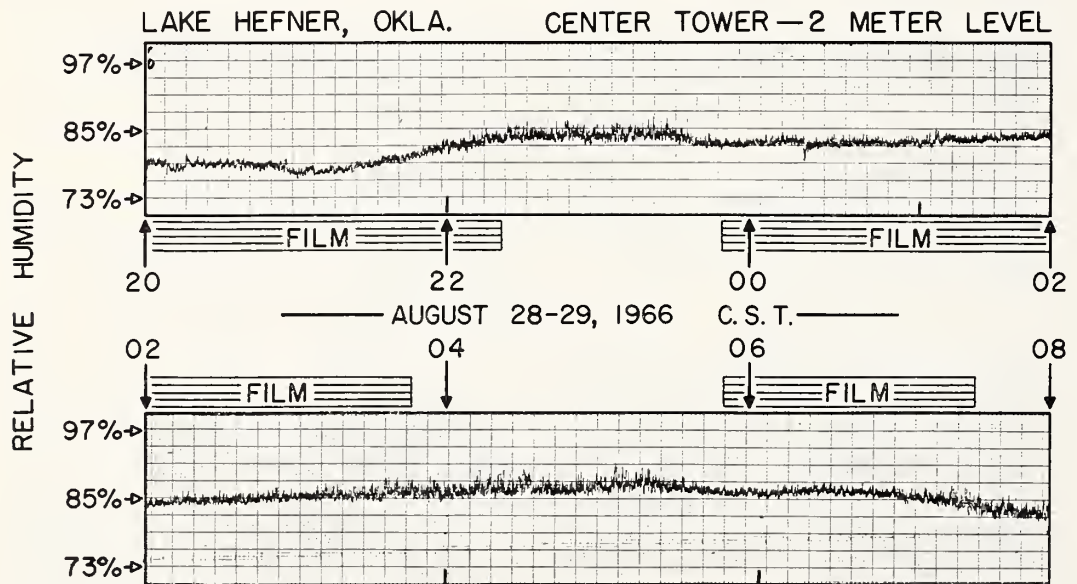
Fig. 2. Fluctuations in relative humidity as the evaporation-reducing film passes under the observing tower. Note that the presence of the film tends to lower the relative humidity and to change the character of the short-term fluctuations.

LAKE HEFNER, OKLA.   CENTER TOWER—2 METER LEVEL
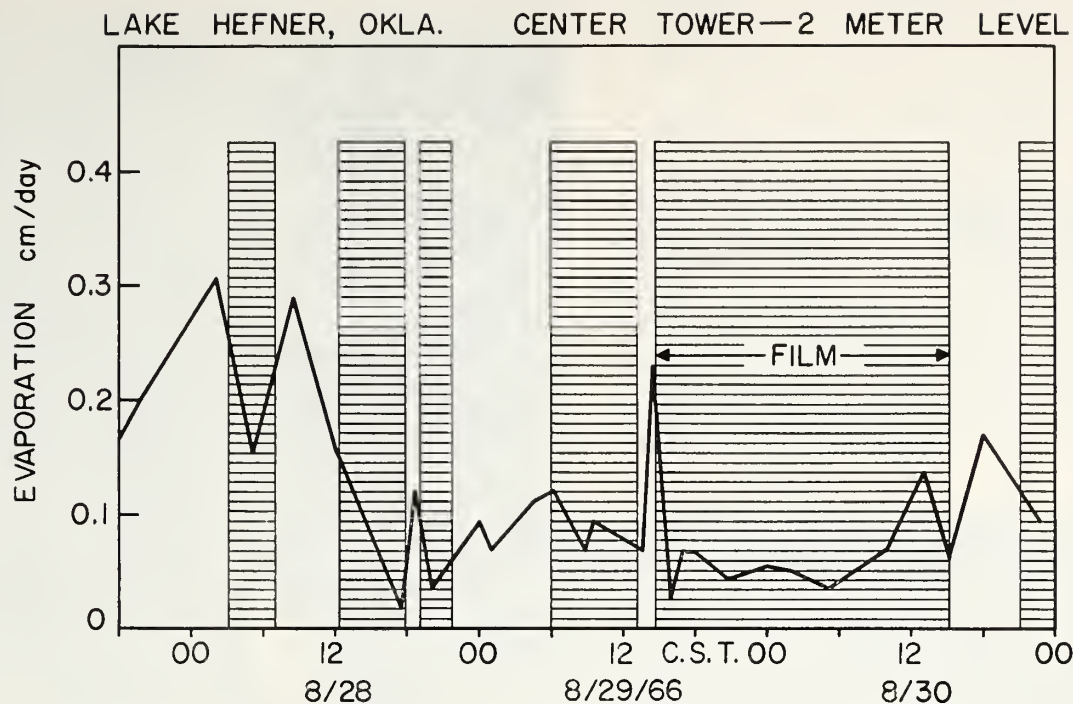
Fig. 3. Evaporation as determined by the eddy correlation method with and without the film under the observing tower. Here E has been converted to equivalent centimeters of liquid water per day.

humidity sensor, reflecting the amount of up-wind water covered with the film.

Figure 3 shows the variation of E with time and the presence of the monomolecular film under the sensing elements as indicated by cross-hatching. The period chosen for evaluation of E by equation 1 was selected to emphasize the effect of the film on E. The values of E so determined were then simply connected by straight lines. For this quantitative evaluation the period 2345 on the 28th to 0330 on the 29th was considered as no-film, since the film was actually observed to be in spotty patches upwind from the tower. The cross-hatching thus represents cases of solid coverage between the observing tower and the sprinkler system. The film clearly reduces evaporation. This effect may be expressed quantitatively by obtaining the average ratio γ of successive measurements with and without film

$$\gamma = \langle E \text{ (with film)}/E \text{ (without film)} \rangle \qquad (2)$$

where $< >$ indicates an average over the available data. The value of γ so obtained was 0.42, indicating an average reduction in evapora-

tion of 58% (i.e., $1 - \gamma$). This same value of evaporation reduction may be obtained by integrating under the curve of Figure 3 and normalizing to evaporation per unit time.

The 58% reduction in evaporation effected by the monolayer during the 3-day test period described is seen to be in excellent agreement with values of 54 and 56% obtained in screening tests of the film-forming material. The screening tests were made under field conditions in standard 4-foot-diameter evaporation pans during a period of 1 month.

REFERENCES

Dyer, A. J., Measurements of evaporation and heat transfer in the lower atmosphere by an automatic eddy-correlation technique, *Quart. J. Roy. Meteorol. Soc., 87,* 401–412, 1961.

Jones, F. E., and A. Wexler, A barium fluoride film hygrometer element, *J. Geophys. Res., 65,* 2087–2095, 1960.

Swinbank, W. C., The measurement of vertical transfer of heat and water vapor by eddies in the lower atmosphere, *J. Meteorol., 8,* 135–145, 1951.

There is no shortage of water in the world. Water, man's most plentiful resource, covers 71 per cent of the earth. The trouble is that usable water often appears in the wrong place, at the wrong time, in the wrong amount for human convenience.

Along with other water control problems, the Bureau of Reclamation has been attacking water scarcity through conservation for more than a half century, particularly in the 17 western states officially declared arid and semi-arid. These states cover 60 per cent of the land area of the contiguous United States, yet possess just 25 per cent of the fresh water supply. As a consequence, the region is unable to take advantage of the potential productivity of its arable land.

During the past two years the Bureau of Reclamation, assisted by scientists from ESSA's Boulder research headquarters, has been performing conservation experiments at Lake Hefner, part of Oklahoma City's water supply system.

Lake Hefner is hydrologically famous because of its suitability for such experiments. The size of the lake—two by three miles in diameter—is convenient for evaporation experiments. The bottom is of Hennessey shale, almost impervious to water seepage. No streams flow into or out of the lake. The lake is filled from a canal where inflow is easily metered. The experiments have dealt primarily with evaporation retardation by spreading a monomolecular film on the surface.

ESSA scientists measured evaporation in the presence and absence of the film, at various time intervals during day and night, under differing conditions.

Previous measurement methods required seven to ten days; when it rained the experiment had to be rerun. These previous techniques required measurement of water balance, temperature, and wind as well as solar radiation.

ESSA's scientists cut down the measurement time from days to minutes. They used temperature sensors, humidity sensors, solar radiation sensors, infrared and optical lasers, wind and sound meters, and radio wave meters. With these instruments they analyzed the complex relationships of humidity, temperature, wind velocity, and similar related factors to discover the amount of water evaporating from the lake.

As an example of measurement technique, the Boulder scientists sent infrared laser beams across Lake Hefner. The amount of energy received was measured against the amount of energy sent. The difference indicated the energy absorbed and scattered by the water vapor and enabled the scientists to compute the percentage of humidity in the air over the lake.

Optical laser and radio beams were also sent across the lake. In these experiments time, rather than energy absorption, was the determining factor. Water molecules reduce the speed of laser and radio beams; thus, the more water vapor, the longer the trip time.

To determine wind velocity, ESSA scientists used a regular anemometer. A sonic anemometer was used to determine vertical wind. Sound, traveling upward with the moving air, was measured along a 20 centimeter path vertically from the lake's surface. At the same time, a downward traveling sound moving against the air flow and traveling the same distance was measured. The difference in travel time of the two sounds (a few microseconds) established the speed of the updraft carrying moisture.

ESSA experiments on an Oklahoma lake help in

Our Battle for

BY
DR. BRADFORD R. BEAN
Institutes for
Environmental Research

Another instrument the ESSA men used to measure humidity was a barium fluoride element whose electrical resistance goes down when the humidity goes up.

Measurement data fed into a computer revealed that evaporation on a typical summer day drew off enough water from Lake Hefner to fulfill the needs of a city of 25,000.

When the monomolecular film was applied, ESSA tests showed it to be 60 per cent effective: monomolecular films on the surface of the lake could save enough water under ideal conditions to provide for 15,000 persons on the average summer day.

These conclusions established the importance of pursuing a solution of the evaporation problem.

There are still questions to be answered in the use of evaporation retardants. How can their efficiency be increased? How can the chemical film on the water's surface be maintained? Waves break up the film. Winds over 15 miles per hour tear it; and it tends to pile up on the shore away from the wind. Nevertheless, chemical retardants show real promise as weapons in the water conservation war.

The Lake Hefner experiments marked a new approach by ESSA scientists to the measurement problem. Instead of using the cumbersome and indirect inflow-outflow method or the energy balance method to determine the amount of water lost into the air, the Boulder men measured evaporation itself. The techniques represent a considerable advance in the efficiency of water vapor measurements with consequent time savings.

ESSA scientists at Lake Hefner represented the program areas of radio meteorology, infrared propagation, and optical propagation from the Institutes for Environmental Research in Boulder. Chief scientist for the experiment was the author, assisted by Raymond E. McGavin, radio meteorology; Norman Abshire, infrared; and Dr. James Owens, optics.

Many other groups were affiliated directly or indirectly with this scientific effort. Included were Cornell Aeronautical Laboratory, Oklahoma State University, Colorado State University, North Texas State University, the Advanced Research Projects Agency, the National Bureau of Standards, and ESSA's Sea-Air Interaction Laboratory. □

(Left) Tower near center of Lake Hefner has highly sophisticated instruments for measuring humidity, temperature, atmospheric pressure, wind velocity and the refractive index of air over water.

(Below) Raymond E. McGavin, assistant chief, Radio Meteorology, calibrates a three-dimensional bivane wind sensor used in the turbulence and evaporation studies at Lake Hefner.

Water

Aerial view of Lake Hefner and part of Oklahoma City. Lake Hefner is famous world-wide for hydrology experiments. The lighter streaks on the water are caused by the experimental monomolecular film on the surface estimated to be 60% effective in preventing evaporation.

(Left) The scientific equipment on the north intake tower of the Oklahoma City Water System demonstrates the inter-facility activities at Lake Hefner this summer. Represented are ESSA, the Bureau of Reclamation, Colorado State University, Cornell University and Oklahoma State University.

13

20

U. S. DEPARTMENT OF COMMERCE
Maurice H. Stans, Secretary

ENVIRONMENTAL SCIENCE SERVICES ADMINISTRATION
Robert M. White, Administrator
RESEARCH LABORATORIES
George S. Benton, Director

ESSA TECHNICAL REPORT ERL 115-WPL 7

Radio-Physical Studies of Evaporation at Lake Hefner, 1966 and 1967

B. R. BEAN
R. E. McGAVIN
C. B. EMMANUEL
R. W. KRINKS

WAVE PROPAGATION LABORATORY
BOULDER, COLORADO
June 1969

TABLE OF CONTENTS

RADIO-PHYSICAL STUDIES OF EVAPORATION
AT LAKE HEFNER, 1966 AND 1967

B. R. Bean, R. E. McGavin, C. B. Emmanuel,
and R. W. Krinks

Experimental methods developed for the study
of the radio refractivity in the lower atmosphere are
modified to study the evaporation suppressing qualities
of monomolecular films applied to the water surface.
The eddy correlation method and an ESSA designed
instrument, the "microwave evapotron", were used
to measure evaporation in field studies conducted at
Lake Hefner, Oklahoma, during the summers of 1966
and 1967. The results obtained in these field studies
indicate that the evaporation suppressing effective-
ness of the films is approximately 55 percent.

Key Words: Evaporation, eddy correlation method,
water balance, evaporation control,
monomolecular films.

1. INTRODUCTION

Study and control of evaporation have been examined in recent

years by the Bureau of Reclamation. Monomolecular films have been

utilized that, when spread on a water surface, tend to suppress evapo-

ration. The Environmental Science Services Administration (ESSA), on

the other hand, has been concerned with the study of the characteristics

of water vapor turbulence and has developed techniques of measuring

evaporation in a direct manner. This paper reports ESSA's results in

a joint effort with the Bureau of Reclamation in the study of evaporation.

ESSA has utilized new experimental techniques based on the eddy corre-

lation method for evaluating the efficiency of these evaporation inhi-

biting films. The physical processes pertinent to evaporation have

attracted the attention of many people; consequently much work has

already been done. Most experimental work, however, has been carried out with small tanks and under well controlled conditions. Evaporation from large bodies of water and its suppression by the application of chemical films on the water surface has received increasing attention in recent years.

Heretofore the process of evaporation has been studied by various methods, including the water budget, energy balance, and bulk-aerodynamic methods (Webb, 1960). The water budget method is heavily dependent upon metering water flow into and out of the lake or reservoir, and the quantities measured require long-term averages, with the result that they yield evaporation estimates for periods of about a week. The bulk-aerodynamic method must rely on the assumption of an empirical relationship concerning the wind and humidity profiles over the water surface. Frenkiel (1963) concluded that for the combined energy budget and bulk-aerodynamic method there is no firm basis for regarding any evaporation reduction of less than 20 percent as falling outside the range of random experimental errors, even under the most favorable assumptions.

Measurement of evaporation over short periods of time would be very desirable, for then the diurnal cycle of evaporation and the evaporation suppressing characteristics of chemical films could be more easily studied. The eddy correlation method (Swinbank, 1951) used in the Lake Hefner, Oklahoma, experiments shows great promise for such studies. As shown in appendix A, the eddy flux of water vapor is expressed as

$$E = \overline{\rho_w' \, w'} \quad (g/m^2 \text{ sec}), \tag{1}$$

where E is the evaporation, ρ_w is the water vapor density, and w is the vertical component of the wind velocity. The primes indicate departures from the mean values. The overbar denotes a time average,

2

normally of the order of a few minutes, rather than the many hours or days required by other techniques. The eddy correlation method is inherently more accurate and versatile than any of the methods discussed previously (see app. A). The eddy correlation method has been used by Dyer (1961) and Maher (1965) to measure evaporation over level surfaces with conventional sensing devices.

2. BACKGROUND FOR RADIO TECHNIQUES

The relative velocity of a radio wave characterized by the radio refractive index is influenced by temperature, pressure, and humidity. It can be shown (Bean and Dutton, 1966) that

$$N = (n - 1)10^6 = 77.6 \frac{P}{T} + 1.72 \times 10^3 \frac{\rho_w}{T},$$

where N = refractivity,

n = radio refractive index,

P = atmospheric pressure in mb,

T = temperature in $^\circ$K,

ρ_w = water vapor density in g/m^3 .

Because of the above relationship, researchers in radio wave propagation have long taken an interest in the physical processes affecting the water vapor characteristics of the atmosphere. Their investigations have resulted in equipment that can be adapted for the continuous monitoring of evaporation.

2.1. Point Measurements of Humidity

Variations in water vapor density cause the short-term fluctuations in the radio refractive index. The determination of the radio refractive index had been a very difficult task, since it was accomplished from measurements of temperature, pressure, and humidity measured by conventional means. Difficulty in measuring the water vapor density

3

to the required degree of accuracy led to the development of the micro-
wave refractometer, which is capable of measuring the radio refractive
index directly.

Accuracies of 1 part per million (ppm) in refractive index be-
came common with resolutions of a part in one hundred million. With
extensive use of the refractometer, the high correlation between fluc-
tuations in refractive index and fluctuations in humidity was confirmed
(Bean and McGavin, 1965). It then became reasonable to invert the
process and utilize the refractometer to reflect humidity perturbations.
A microwave hygrometer was developed (McGavin and Vetter, 1965)
that yielded the absolute humidity to within 0.2 g/m^3 with a resolution
of 0.02 g/m^3 (equivalent to a 2 percent maximum error at standard sea
level conditions). This microwave hygrometer is described in detail in
appendix C.

Spectral characteristics of water vapor variability can be meas-
ured by the fast response of the refractometer. Comparison with con-
ventional means of measuring humidity indicated that the microwave
hygrometer yields mean values comparable to those obtained with con-
ventional methods but that it also produced the finer scale spectra of the
variations and was virtually free of the adverse temperature effects of
most humidity sensors.

2.2. Integrated Measurements of Humidity

The velocity of propagation of a radio wave is determined by the
refractive index of the medium through which it passes. The radio path
appears to be longer than the geometric path, an important considera-
tion in radio geodesy. The radio path length L is related to the geo-
metric path length S by

$$L = \int_0^S n\,dS, \tag{2}$$

4

where n is the radio refractive index. This can be expressed as

$$L = <n>S,\tag{3}$$

where $<n>$ is the path integrated radio refractive index. L is normally measured in degrees of phase over the path, i.e.,

$$\phi = \frac{360 f}{c} n S,\tag{4}$$

where f is the frequency, and c is the velocity of light in vacuo. As the refractive index along the path changes, the phase of the signal changes. Appendix D contains details on the microwave phase system.

The short-term variability of the refractive index reflects, primarily, humidity variations. As with point measurements, the mean of the changes in phase are highly correlated with the average of humidity point measurements taken along the path.

Additional accuracy can be achieved when we correct the microwave phase output for variations in temperature. In appendix E, we consider the expected accuracy in determining integrated humidity from the microwave system alone, as well as accuracy expected when, in addition, an optical phase system (modulated laser) is used to correct for temperature.

3. APPLICATION OF RADIO TECHNIQUES TO THE STUDY OF EVAPORATION

3.1. Point Measurements

The microwave hygrometer yields accuracies and resolutions that are not available by conventional means. To apply this instrument to the measurement of evaporation requires only the addition of a vertical wind sensor to acquire the product

$$\overline{\rho_w' \, w'},$$

5

which is equal to the vertical transport of water vapor, i.e., the evaporation.

Both Dyer (1961) and Maher (1965) used versions of hot wire anemometers to measure the vertical wind, w. In the Hefner experiment in 1966 and 1967, both bivanes and a sonic anemometer were used to determine w.

The bivane is an instrument that measures the vector wind, the azimuth and the elevation angle; these are easily converted to u, v, and w, the three components of the wind. The vertical component of the wind is thus available from this instrument. The product $\overline{\rho'_w w'}$ can then be obtained either by electronic multiplication directly in the field or by use of a computer at a later time. The latter method was used with remarkable success at Lake Hefner in 1966. The computer output was conditioned so that the evaporation was expressed in centimeters per day.

A sonic anemometer (app. B) was designed to overcome the inertia effects of the bivane that caused overshoot and high frequency filtering and was used for vertical wind measurements in the 1967 Lake Hefner experiments. The output of the modified refractometer was combined with the sonic anemometer in such a way that a measure of the evaporation in centimeters per day was immediately available as an output. Details on this "microwave evapotron" are given in appendix C.

3.2. Integrated Measurements

The microwave phase system does not measure evaporation directly, since it is not sensitive to the vertical transport of water vapor but is sensitive to the amount of water vapor within the radio beams. A microwave beam sent across a body of water is influenced by the water content of the air. If the water content is reduced, the radio path length shortens; if it is increased, the path appears longer. Over an evaporating surface, changes in evaporation can be detected as changes in the radio

6

path length. These must be viewed as short-term measurements, since we must assume that the air flowing from the land is of constant humidity. Any sizeable increase in humidity in the air mass before it passes over the lake would be seen as an increase of evaporation--an obvious error. Also, it must be remembered that the phase system integrates over the entire path.

4. THE EXPERIMENT

Lake Hefner, Oklahoma, was selected because its characteristics were known. In 1952 extensive work was done on the water budget, mass transport, and energy balance (Water Loss Investigations, Vol. 1, Lake Hefner Studies, 1952). It is an off stream lake fed by a metered canal and drained through a metered filter plant. Bank storage, seepage, and sources are well known from earlier studies. The prevailing wind in late summer is southerly, which permits installation of meterological sensors in line with the prevailing wind and thus in line with the evaporation process itself.

The evaporation experiment described herein represents a first attempt of using radio techniques to study the process of evaporation. Both point and integrated measurements were used and were compared with conventional measurements. Application of evaporation suppressing films on the water surface permitted evaluation over a large range of humidity and evaporation conditions.

The experiment was carried out at Lake Hefner during the summer months of 1966 and 1967. Although the lake is only about 3 km in diameter, enough water evaporates from it to supply the needs of approximately one-third of Oklahoma City's 365, 000 inhabitants.

After a preliminary study in the summer of 1965, five sites were fully instrumented in the summer of 1966 (fig. 1). One site was at the south side of the lake (fig. 2) and a second at about one-fifth the distance

across the lake on a north-south line (fig. 3). A third site (fig. 4) was instrumented on the north end of the lake at the intake tower, approximately in line with the south and lake sites. Sensors were mounted at preselected heights to measure the pertinent atmospheric parameters. Standard Weather Bureau type instruments recorded large scale changes in temperature, pressure, and relative humidity. Signals from all sensors were preconditioned, and the information was recorded on magnetic tape by an analog FM method. Means were provided for complete system calibration whenever desired.

The south site (fig. 2) consisted of a single mast tower with three recording levels:

(1) Surface-level measurements of temperature and pressure.

(2) Two-meter-level measurements of the temperature difference, ΔT, between the 2-m and the 8-m levels, relative humidity, and vector wind.

(3) Eight-meter-level measurements of temperature, relative humidity, and vector wind.

The lake site consisted of a rectangular tower extending 16 m above the lake surface as seen in figure 3. At this site, five recording levels were instrumented:

(1) Lake-surface measurements of the temperature difference, ΔT, between the 8-m level and the surface.

(2) Two-meter-level measurements of the temperature difference, ΔT, between the 8-m and the 2-m levels, relative humidity, and vector wind.

8
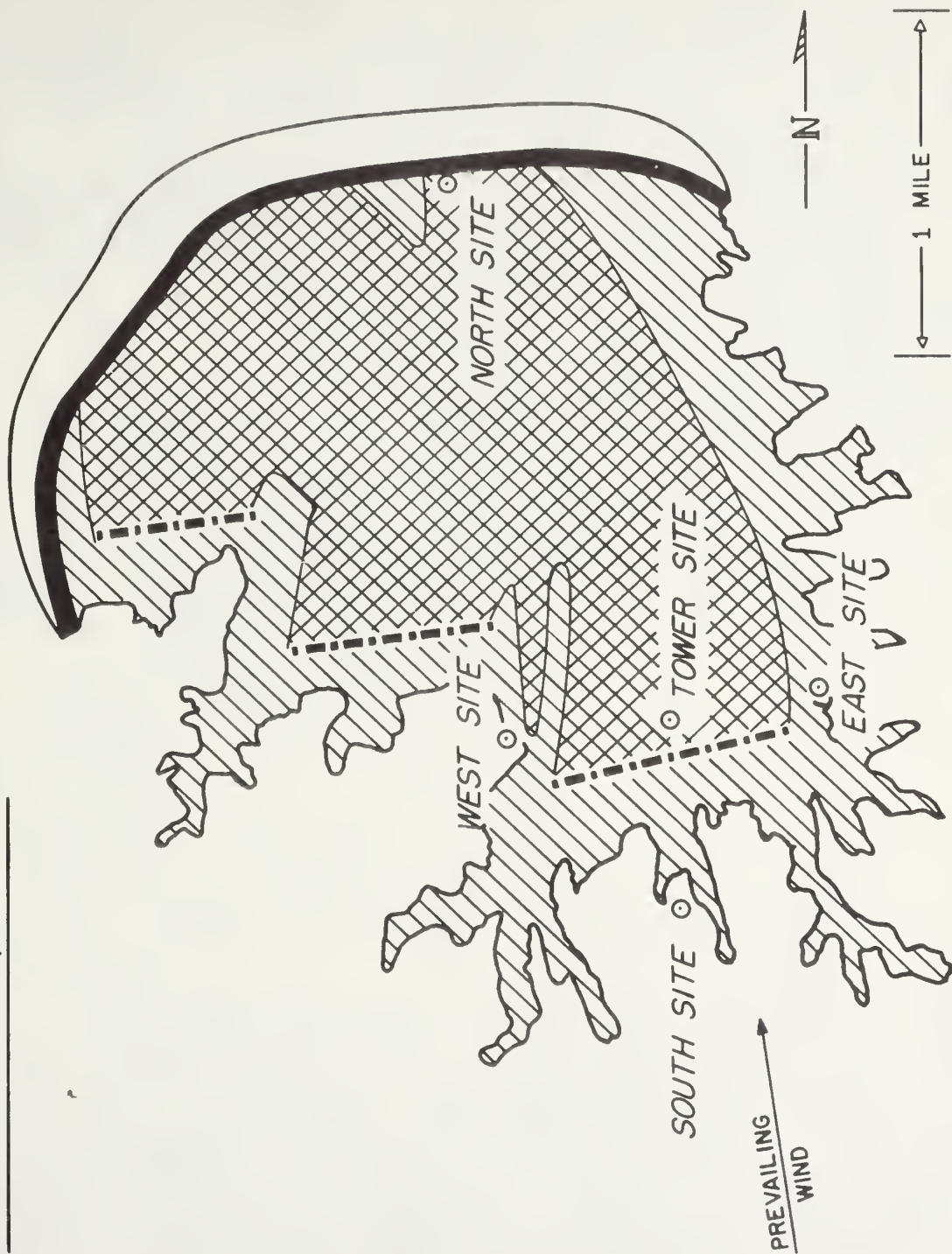
Figure 1. Plan view of the Lake Hefner Experiment. The sprinkler systems for applying film-forming materials are indicated by ·——·——·.

9

Figure 2. The south site, Lake Hefner experiment.

10
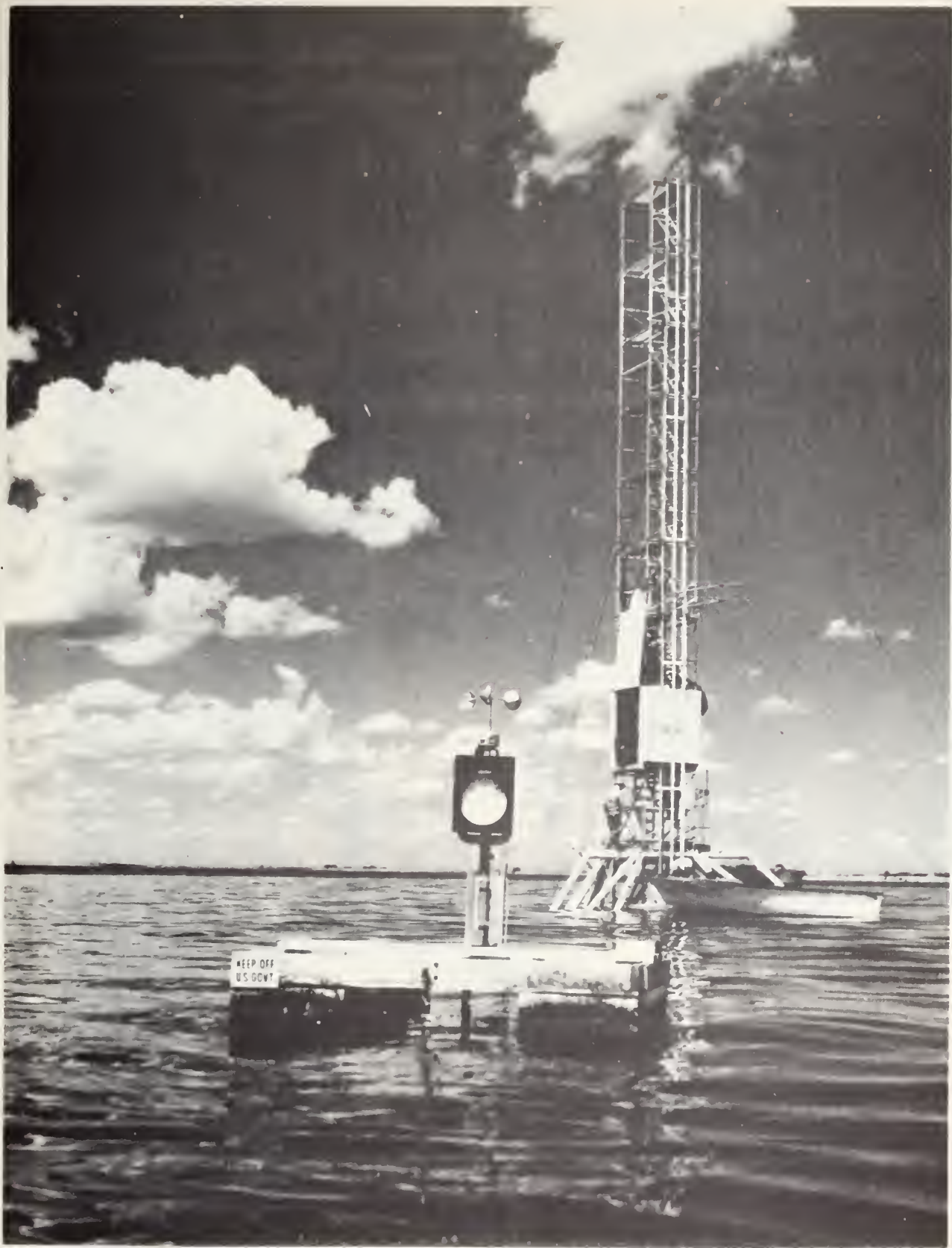
Figure 3.   The tower site, Lake Hefner experiment.

11
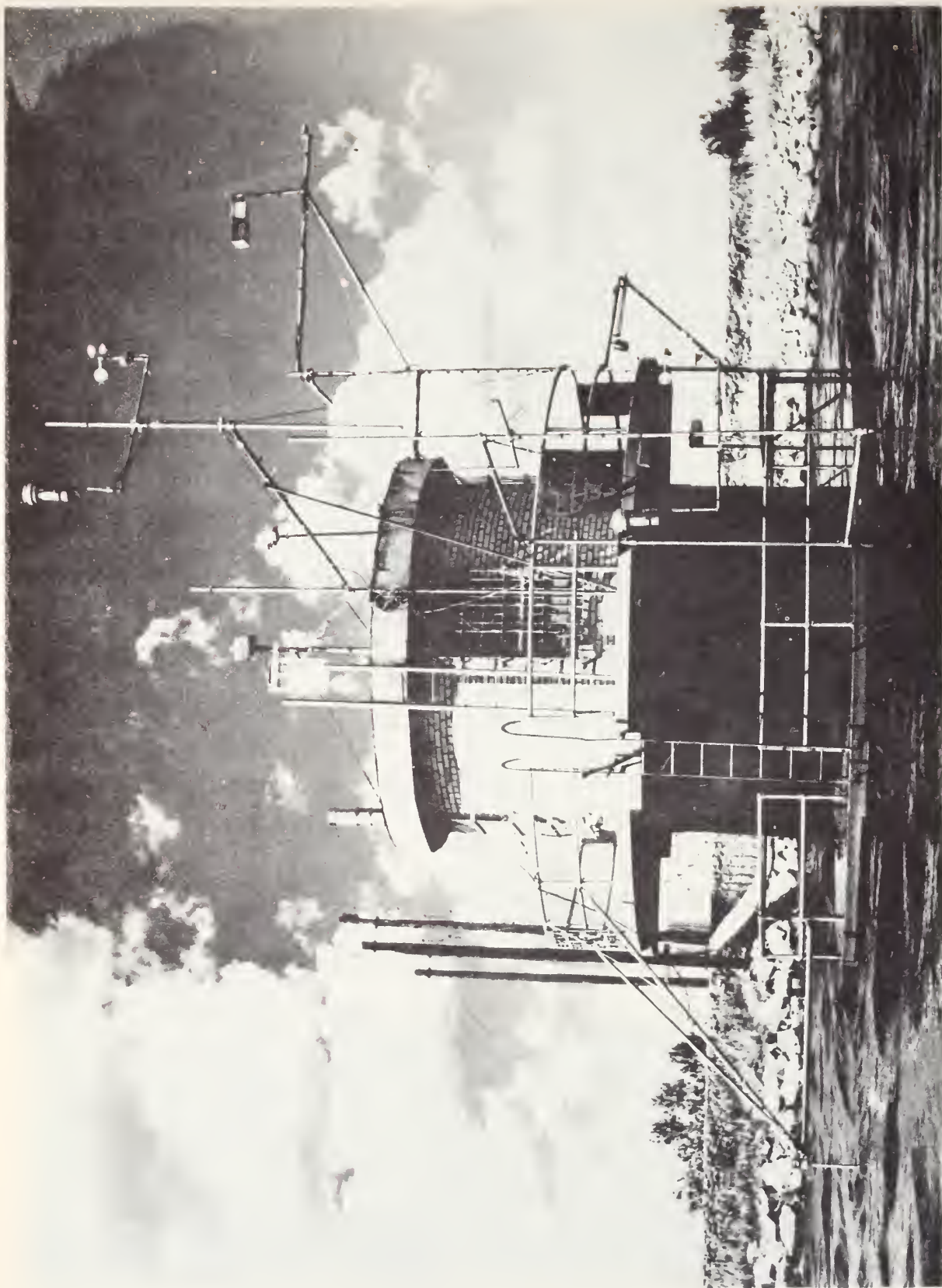
Figure 4. The north site, Lake Hefner experiment.

12

(3)   Eight-meter level measurements of the temperature, relative humidity, vector wind, refractivity, and vertical wind with a sonic anemometer.

(4)   Sixteen-meter level measurements of the temperature difference, ΔT, between the 16-m and 8-m levels, relative humidity, and vector wind.

At the north site (fig. 4), measurements were identical to those at the south site; the sensors and subsystems used are considered in detail in appendix E. On the east and west shores, terminals were established for the microwave phase system and an auxiliary laser beam system (for temperature correction) in such a way that the propagation path crossed the tower at the lake site. At 1 m from the surface, measurements of wind, temperature, and humidity were made at both the east and west terminals.

The experiment carried out during the summer of 1967 incorporated the same instrumentation except that only the south and lake sites were used. At the lake site, along with the other instrumentation, the evaporation at the 2-m level was measured directly with the microwave evapotron, having an absolute error from all sources of ≤ 0.03 cm/day. The recording levels at the lake site were changed to surface, 2 m, and 10 m. The surface of the lake at the time was approximately 2 m below the 1966 level.

The monomolecular film, a mixture of a 40 percent hexadecanol and 60 percent octadecanol, was spread on the lake surface via a sprinkler system located near the south end of the lake (see fig. 1). The prevailing southerly winds during the summer months were relied upon to spread the film across the lake. Evaporation was measured at the lake site (tower) before application of the film, during film cover under the sensors, and after passage of the film.

13

5. RESULTS

5.1. Point Measurements - 1966

Because of the restrictions that wind conditions imposed on the application of the film, much time was spent waiting for proper conditions. A southerly wind of less than 6 m/sec was required for proper application. Although the "predominant" wind in late summer is supposed to be southerly, it proved to be other than southerly for a major portion of the time, especially in 1967.

From the 1966 data, the period 25-30 August was selected for analysis. During this period, good film cover over the lake surface was maintained; consequently, the effect of the film as an evaporation suppressant could be calculated with minimal uncertainties. Figure 5 illustrates the effect of the film on the relative humidity at the 2-m level at the center tower. Note that the presence of the film under the tower sensor influences both the amplitude and the frequency of the humidity variations. The prevailing southerly winds, of the order of 1 to 6 m/sec, were ideal for spreading the film onto the lake surface, and recordings of the physical parameters described in the previous section were made continuously. From these records, thirty-seven 10-min samples were selected for detailed analysis. The recorded data were sampled and digitized at the rate of 25 samples/sec in 10-min blocks. The digitized samples were averaged in non-overlapping sets of 25 samples to obtain a sample rate of 1 sample/sec; this smoothing was deemed proper since previous spectral analyses indicated that very little spectral energy existed beyond 1 Hz. These data became the primary source for analysis. Ten-minute averages were obtained for $\overline{\rho'_w w'}$. Figure 6 illustrates the variation in evaporation as a function of time as measured by the eddy correlation method at the 2-, 8-, and 16-m levels at the lake site in 1966. The cross-hatched areas indicate
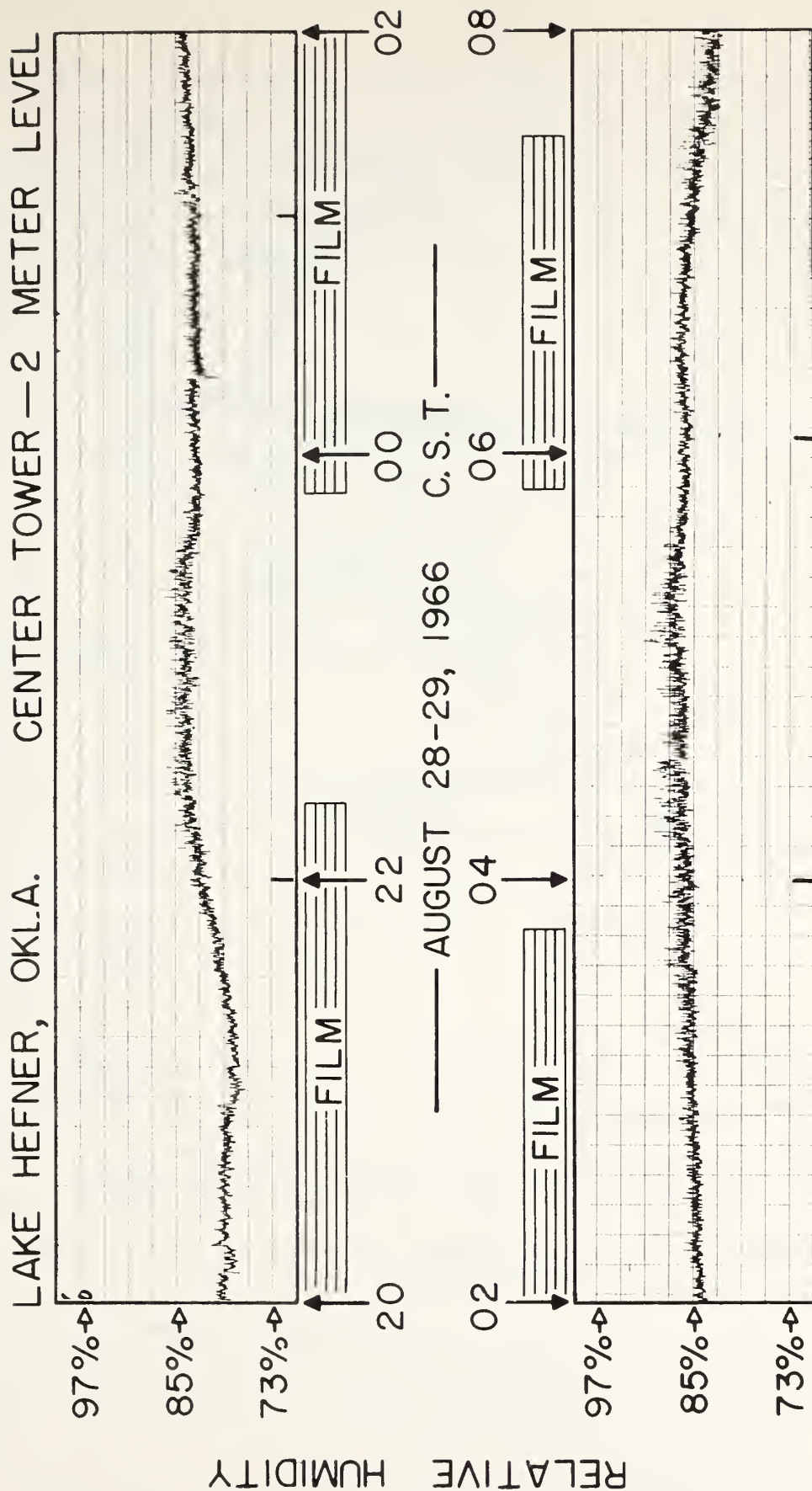
Figure 5. Fluctuations in relative humidity as the evaporation-reducing film passes under the observing tower. Note that the presence of the film tends to lower the relative humidity and to change the character of the short-term fluctuations.
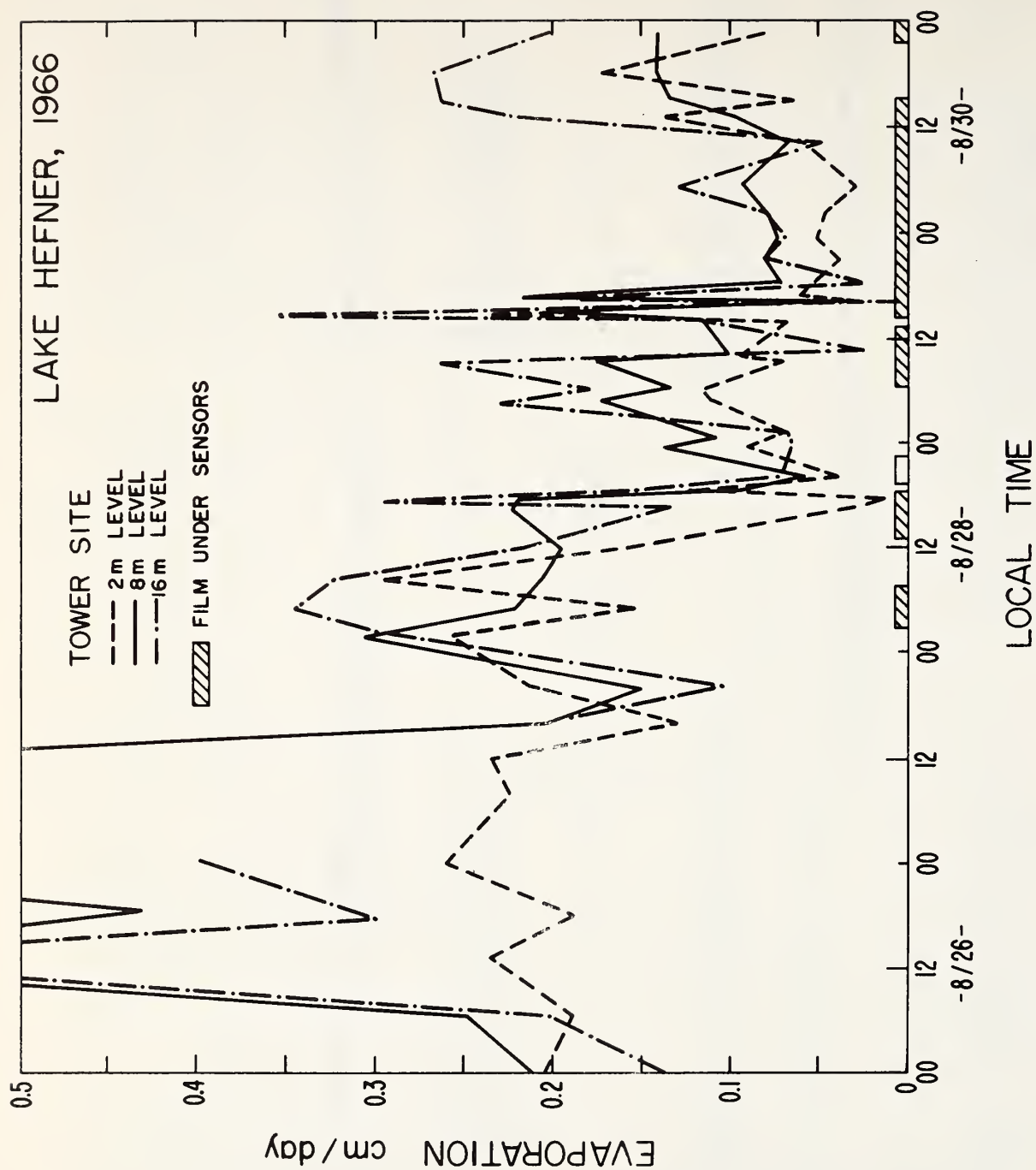
Figure 6. Evaporation determined by the eddy correlation method with and without the film under the observing tower.

times when the evaporation-suppressing film was under the sensors.

We see from figure 6 that the most pronounced effect of the film on the surface is to reduce evaporation considerably. Note, also, that the arrival and departure of the film is anticipated by the sensors because of the wind carrying air from above the water some distance upwind. This period was chosen for evaluation of evaporation through (1). The values of E so determined for the 2-m level were then simply connected by straight lines. The ratio γ of the areas under the curve, with and without film both normalized to a 1-hour period, indicated that the film reduces evaporation by as much as 58 percent, i.e.,

$$\gamma = \frac{E \text{ (area with film)}}{E \text{ (area without film)}} = 0.42; \qquad (5)$$

hence, the average reduction in evaporation is

$$100 \ (1 - \gamma) = 58\% \ .$$

The 58 percent reduction in evaporation affected by the monomolecular film during the 3-day test period is in excellent agreement with values of 54 percent and 56 percent obtained in screening tests of the film-forming material. The screening tests were made under field conditions in standard evaporation pans 4 ft in diameter during a 1-month period.

One would expect the film cover over the lake surface to have two basic effects upon the water vapor density observed at the tower site: (1) to reduce the water vapor density by reducing evaporation, and (2) to warm the ambient air by reducing evaporative cooling and thus lowering the relative humidity. The latter effect was not observed in this experiment, as the relative humidity behaves in the opposite fashion, owing to the nearly constant air temperature during the period of study. The variation of relative humidity thus reflects the former

17

effect in the water vapor density as it varied from 0.1 to 0.6 g/m^3 in the proper direction with changes from film cover under the sensors to no film cover under the sensors. Consequently, the main effect of the film is to suppress the amplitude of the short-term variations of humidity and thus to affect the magnitude of ρ_w' (Bean and Florey, 1968).

Figure 7 illustrates the eddy flux measured at the south site at the 2-m and 8-m levels in 1966. Evaporation is as expected over land where the diurnal trend is the most obvious characteristic. During the day when the temperature is high, the evaporation is at a maximum; during the night when cooling has occurred, it is at a minimum. At times the evaporation is negative, indicating that water vapor is being transported to the ground, probably forming dew.

The evaporation at the north site during the same period did not behave as expected. We tried to place the central tower in the lake somewhat near the peak of the evaporation curve. Because of the 2-mi fetch along the lake, we expected that near-saturation conditions would occur at the north site, with a resultant decrease in evaporation. Figure 8 indicates that this was not the case, perhaps because the fetch is insufficient to establish steady-state conditions, but more probably the presence of the dam behind the sensing location was influencing the air flow, causing a vertical wind which was a product of the geometry rather than the evaporation process (see fig. 4). It is questioned whether or not the measurements at the north site are valid.

If a comparison is made at the lake site among the eddy flux measures at 2-m, 8-m, and 16-m, we notice that the average evaporation especially in the presence of film seems to increase as a function of height. Again, it is more difficult to see the effect of the film at the greater heights. This apparent discrepancy can be explained in terms of the fetch. Dyer (1963) considered its effect on the accuracy of flux

18
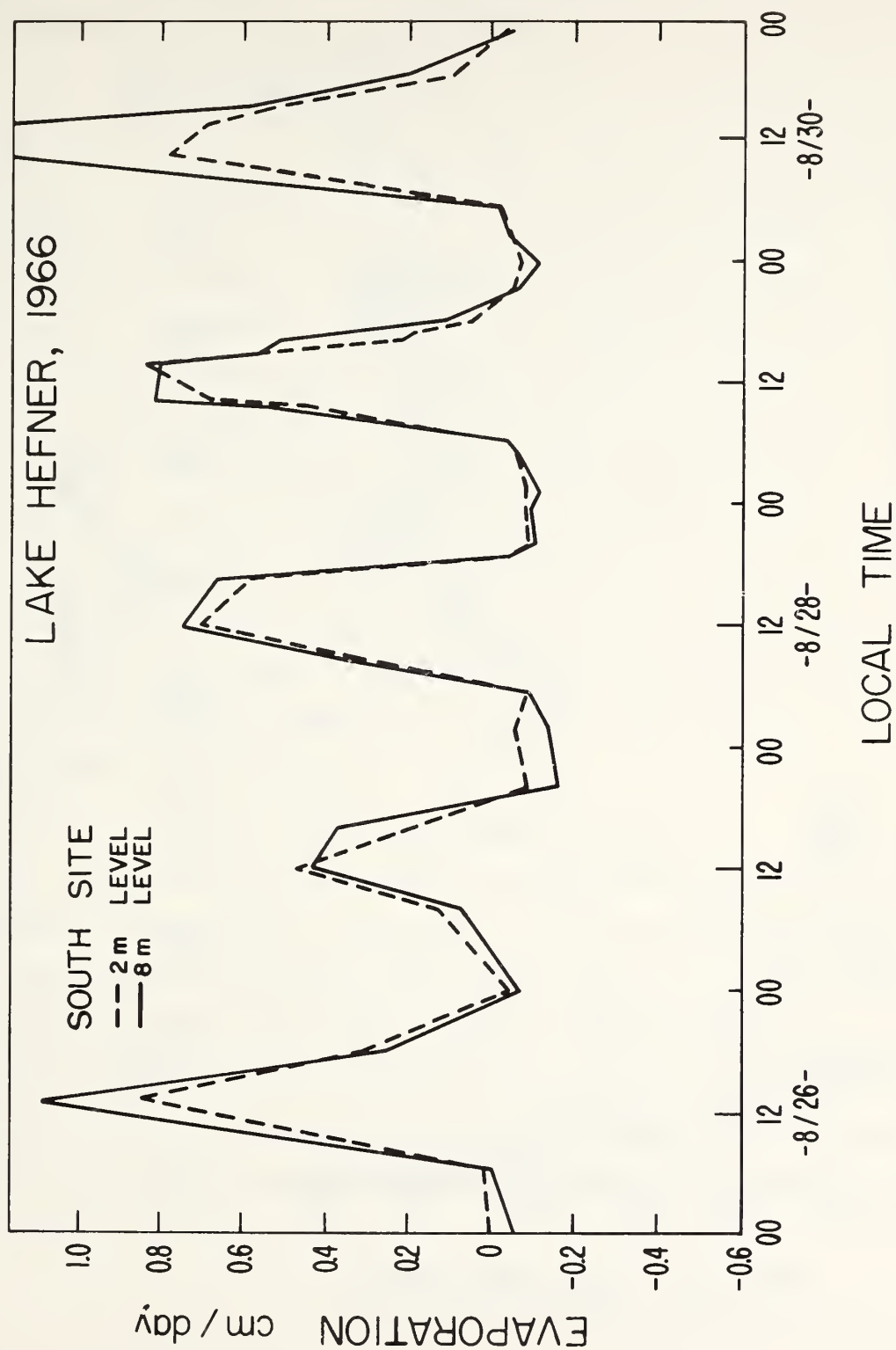
Figure 7. Evaporation as determined by the eddy correlation method at the south site.

19
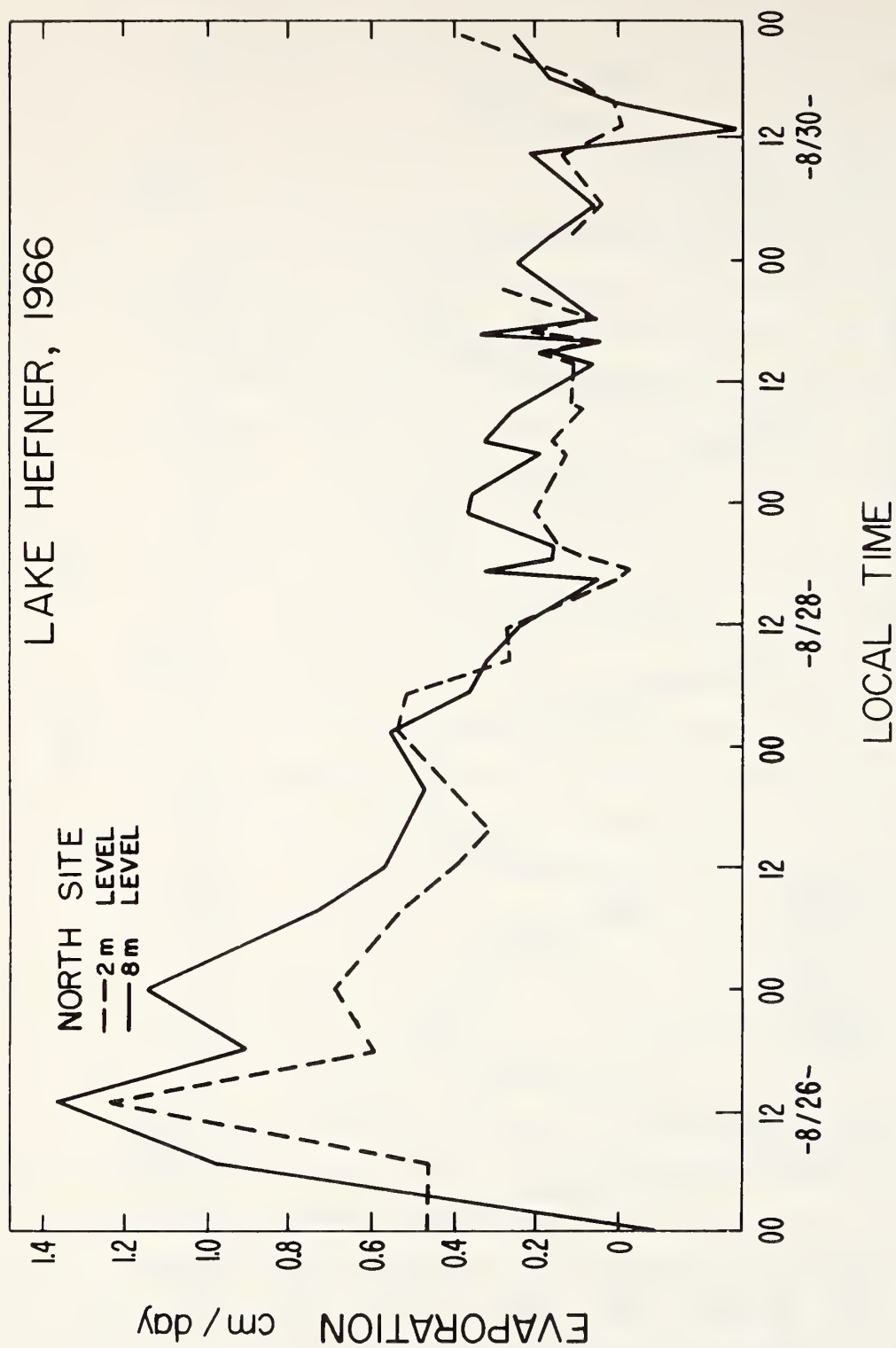
Figure 8. Evaporation as determined by the eddy correlation method at the north site.

measurements. He assumed a dry air mass passed from a nonevaporating to a uniformly evaporating surface and calculated what percentage adjustment the air mass made toward uniform conditions as a function of fetch. Figure 9 illustrates Dyer's conclusions applied to the Lake Hefner experiment. These curves apply over a wide range of wind velocities. The location of the south shore and the sprinkler system is shown in the figure. Note that the 2-m sensor has adjusted to 93 percent of the expected flux under uniform conditions for a fetch of 400 m (distance to sprinklers). The 8-m level exhibits only 55 percent and the 16-m level but 24 percent. This indicates that the 8-m and 16-m sensors are highly influenced by both overriding air and the evaporation from south of the sprinkling system. It appears that the fetch would have to be 2.5 km for the 8-m sensors to exhibit the same measuring characteristics as the 2-m sensors, while the 16-m sensors would require a fetch of 6.5 km. These figures are meant only as approximations, reflecting more of a qualitative description of the results. It is sufficient to say that under these conditions the 2-m measurements are considerably more accurate.

5.2. Point Measurements--1967

The period of 20 August to 16 September constituted the field program at Lake Hefner during 1967. The recording program, however, was harassed by cold frontal passages during August and September, these being more frequent than normally expected. In fact, analysis of weather records indicate that from 21 to 31 August 1967 favorable conditions prevailed only 27 percent of the time, while 1 to 16 September 1967 was marked by very unfavorable conditions; only 2 percent of the time was favorable.
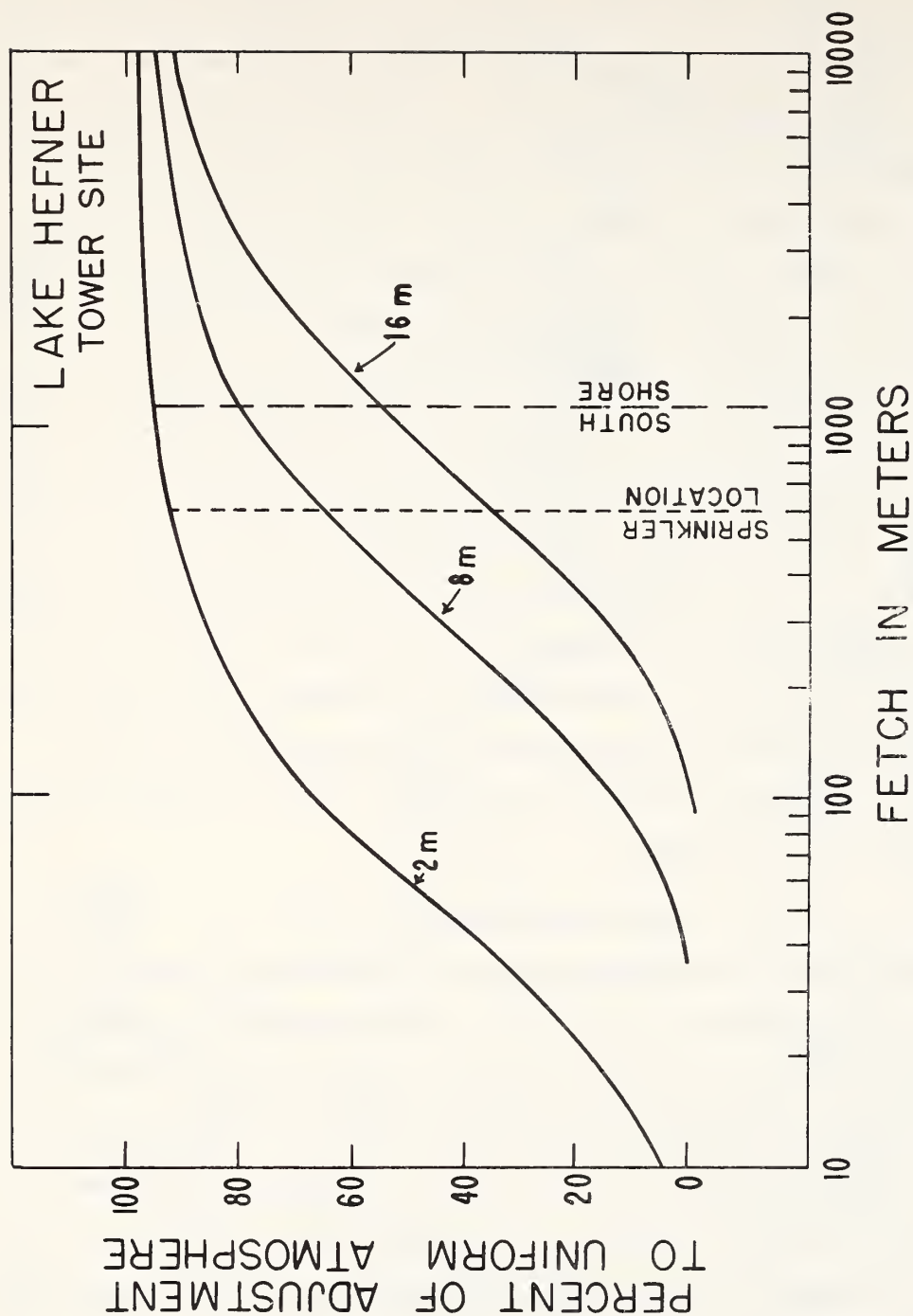
Figure 9. The effect of the fetch of the wind on the accuracy of the flux measurements.

22

The unfavorable weather conditions impeded film application on the lake surface. Measurements of the evaporation with the microwave evapotron at the 2-m level are presented only for 22 to 26 August (fig. 10). The microwave evapotron, discussed in appendix B, uses the eddy correlation method to measure the evaporation directly.

The 1967 results are essentially the same as those for 1966. The effectiveness of the film was 55 percent in 1967 as compared to 58 percent in 1966. Toward the end of this sample period, an additional film, ethoxylated alcohol, was applied to provide a comparison between the effectiveness of the two different films. The results were meager and did not show either to be more effective than the other.

5.3. Integrated Measurements--1966

The velocity of propagation of a radio wave may be used to determine the water vapor content of the atmosphere along the propagation path. The details of such an analysis are given in appendix E. At the Lake Hefner experiment a microwave phase system was used to measure, continuously, changes in radio path length, hence the amount of water vapor content of the atmosphere along the propagation path. Analysis of the available data, however, proved inconclusive, although the correlation between the average fluctuations in radio path length L_r and the average absolute humidity measured at the tower site was 0.90 (see fig. 11). The accuracy of these results from the microwave phase system was significantly improved when the integrated temperature was applied from the results of the optical path. The corrected correlation coefficient between the fluctuations in radio path length and absolute humidity was 0.95.

23
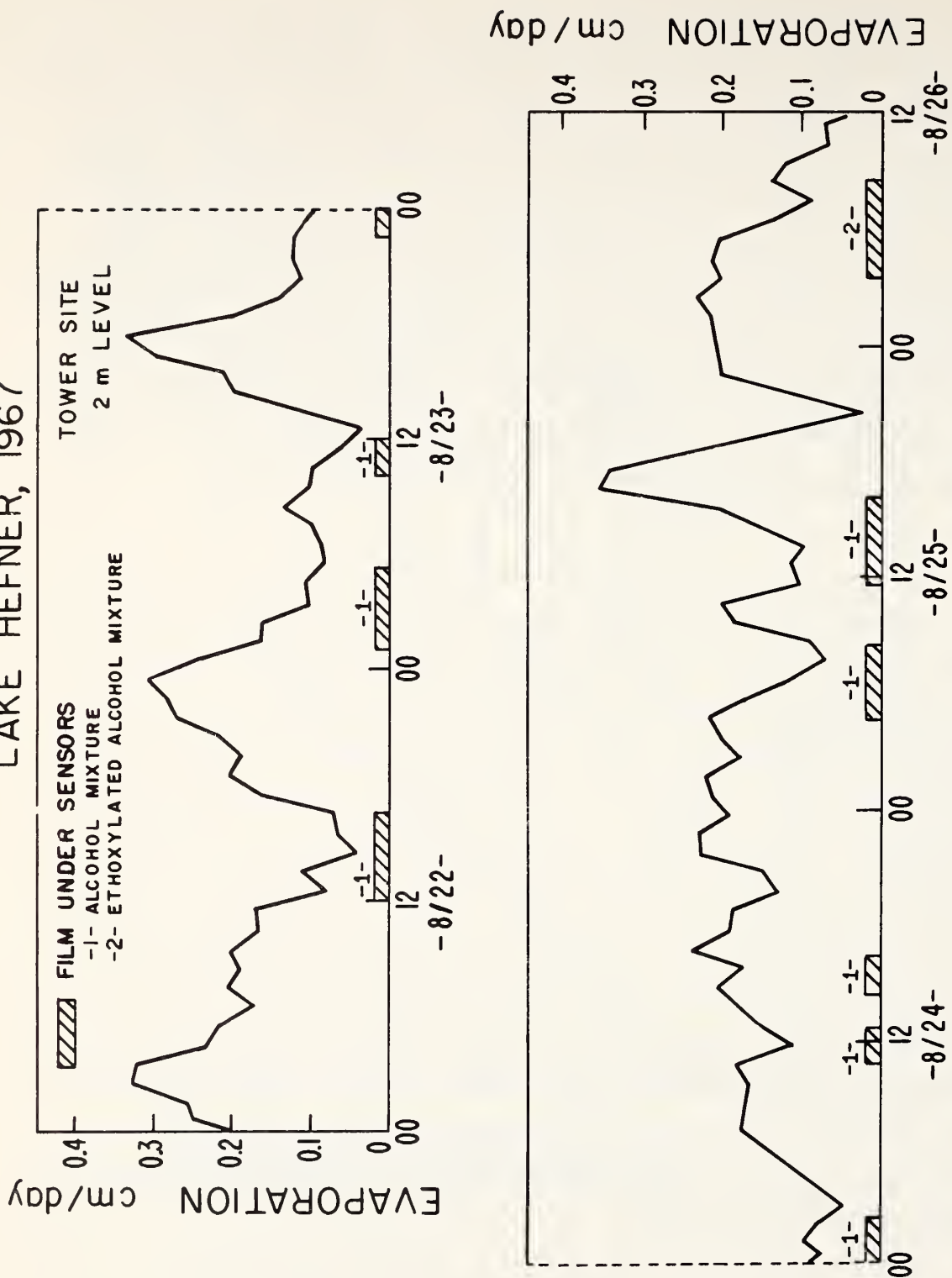
Figure 10. Evaporation as determined by the eddy correlation method at the tower site.

24
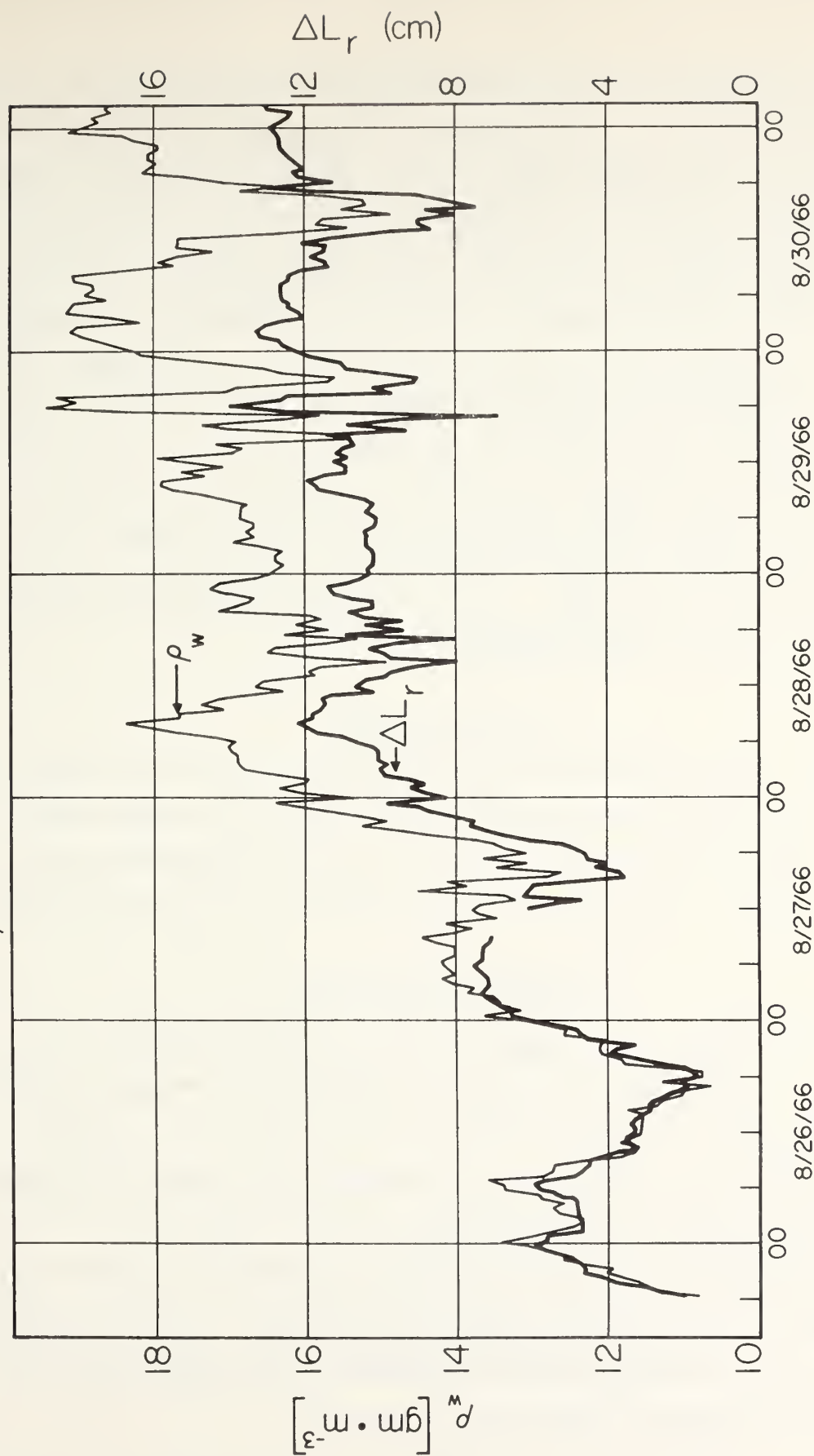
Figure 11. A comparison of the radio path length fluctuations ΔL_r with variations in the water vapor density ρ_w.

25

The inability to maintain complete film coverage under the propagation path accounts, in part, for the inconclusive results obtained from the microwave phase system. Areas of open water contaminated the integrated measurements; hence, the phase measurements could not yield reliable information for evaporation. Winds higher than about 4 m/sec tend to break up the film cover, since winds of this magnitude produce cresting of the waves. The latter seems to be of greater importance in field work because wind speeds cannot be satisfactorily predicted. What is actually observed is a "patchy" structure in the film cover over the lake surface at any time. Wind direction is also an erratic phenomenon, tending to produce long streaks of film cover along the direction of the wind. It is this "patchy" cover that the microwave phase system cannot distinguish.

6. CONCLUSIONS

The applicability of the eddy correlation method to the measurement of evaporation from large bodies of water, such as Lake Hefner, has been amply demonstrated. The inherent accuracy and the flexibility in the required averaging time of the eddy correlation method make it far more advantageous in evaporation studies than any of the competing methods. In fact, the eddy correlation method gives very reliable estimates of evaporation if 10-min samples are used. Since the method makes use of point measurements, it can be used successfully to determine evaporation over relatively small evaporating surfaces, and for large evaporating surfaces spatial variation in evaporation may be obtained with relative ease.

A relatively compact and accurate "microwave evapotron" was developed and used in the Lake Hefner field studies. It yields estimates of evaporation directly and, under conditions normally expected in the field, has an accuracy of better than 5 percent.

The evaporation-suppressing qualities of the hexadecanol film used in the 1966 studies proved to be better than 55 percent based on point measurements made at a height of 2-m at the tower site, with the underlying water surface being covered by a monolayer of hexadecanol. The 1967 experiments also indicate a reduction in evaporation of the same order of magnitude, but this is a collective result rather than a point by point.

Although the effectiveness of the film as a suppressant to evaporation was successfully demonstrated, maintaining the film cover on the water surface presents a problem in its use over extended water surfaces. Excessive wind speed and change in wind direction tend to tear the film, producing a patchy surface. This effect was most pronounced when the evaporation over a long path was to be measured by microwave phase techniques. Measurements of the integrated water vapor along the path correlated well with the average water vapor density measured at the center of the path; however, it was difficult for the microwave phase system to "see" the film because of the many open water areas along the path. The results on the evaporation measurements integrated over an extended path are, therefore, inconclusive.

7. ACKNOWLEDGEMENTS

8. REFERENCES

Bean, B. R., and E. J. Dutton (1966), Radio Meteorology, NBS Monograph 92 (U.S. Printing Office, Washington, D. C.).

Bean, B. R., and Q. L. Florey (1968), A field study of the effectiveness of fatty alcohol mixtures as evaporation reducing monomolecular films, Water Resources Res. 4, No. 1, 206-208.

Bean, B. R., and R. E. McGavin (1965), The use of the radio refractometer to measure water vapor turbulence, Proc. Intern. Symp. on Humidity and Moisture, II, 561-568 (Reinhold, New York, N. Y.).

Dyer, A. J. (1961), Measurement of evaporation and heat transfer in the lower atmosphere by an automatic eddy-correlation technique, Quart. J. Roy. Meteorol. Soc. 87, No. 373, 401-412.

Dyer, A. J. (1963), The adjustment of profiles and eddy fluxes, Quart. J. Roy. Meteorol. Soc. 89, No. 380, 276-280.

Frenkiel, J. (1963), On the accuracy of the combined energy-budget and mass-transfer method, J. Geophys. Res. 68, No. 17.

Maher, F. J. (1965), The Evapotron - an electronic instrument for measuring evaporation from natural surfaces. Proc. IREE Australia 21, No. 10, 332-337.

McGavin, R. E., and M. J. Vetter (1965), Radio refractometry and its potential for humidity studies, Proc. Intern. Conf. on Humidity and Moisture, II, 553-560 (Reinhold, New York, N. Y.).

Swinbank, W. C. (1951), The measurement of vertical transfer of heat and water vapor and momentum in the lower atmosphere with some results, J. Meteorol. 8, 135-145.

Webb, E. K. (1960), An investigation of the evaporation from Lake Eucumbene, Meteorol. Phys. Tech. Paper No. 10, Commonwealth Scientific and Industrial Research Organization.

APPENDIX A

MEASUREMENT OF EVAPORATION BY THE
EDDY FLUX METHOD

A.1. Eddy Flux of Water Vapor

The evaporation from a water surface is defined as the amount
of water vapor carried aloft from unit area per unit time; hence,

$$E = \rho_w \, w \, , \tag{A-1}$$

where ρ_w is the water vapor density in g/m^3, and w is the vertical com-
ponent of the wind in m/sec. Normally the determination of the evapo-
ration implies a time average of ρ_w and w; hence, if we express ρ_w and
w as being composed of a mean value denoted by an overbar and a de-
parture from the mean denoted by a prime, then

$$\rho_w = \overline{\rho_w} + \rho_w'$$
$$w = \overline{w} + w' , \tag{A-2}$$

and the evaporation then takes the form

$$E = \overline{(\overline{\rho_w} + \rho_w')(\overline{w} + w')} . \tag{A-3}$$

Expanding and invoking the Reynolds rules of averaging, we obtain

$$E = \overline{\rho_w' \, w'} + \overline{\rho_w} \, \overline{w} , \tag{A-4}$$

where the first term on the right is the eddy flux. When we use a
sufficiently long averaging time, $\overline{w} \equiv 0$; hence

$$E = \overline{\rho_w' \, w'} \quad (g/m^2 \text{ sec}) \, , \tag{A-5}$$

or the eddy flux of water vapor is equal to the evaporation. The aver-
aging time is important. Swinbank (1955) determined that the minimum
sample size to insure the presence of all the flux information of a
passive parameter was approximately 100 sec. If the sample is too
long, the diurnal cycle will affect the results and destroy stationarity.
Any sample in excess of 100 sec but less than 1 hour, except at sunrise
or sunset, should provide an adequate averaging interval.

A. 2. Error Analysis

The expression $\overline{\rho'_w \, w'}$ is actually the covariance between the
water vapor and the vertical wind, which implies that some correlation
exists between the two variables whenever evaporation occurs. This
should be noted when the effect of errors in the determination of evap-
oration is considered.

The covariance between two variables X and Y is defined as

$$\text{Cov } (X, \ Y) \equiv \overline{(X - \overline{X})(Y - \overline{Y})}. \tag{A-6}$$

For the first case assume a constant bias in each of the measurements
so that

$$X = X_T + \epsilon \ ,$$

$$Y = Y_T + \delta \ ,$$

where the subscripts indicate the true values, and ϵ and δ are the
biases of measurement. Then

$$\text{Cov } (X, \ Y) = \overline{[X_T + \epsilon - (\overline{X_T + \epsilon})][Y_T + \delta - (\overline{Y_T + \delta})]}. \tag{A-7}$$

Since ϵ and δ are constants,

$$\text{Cov } (X, \ Y) = \overline{(X_T - \overline{X}_T)(Y_T - \overline{Y}_T)},$$

indicating that a constant bias in either measurement has no effect on
the accuracy of the measurement.

Now assume that ϵ and δ are random errors. Also, assume that they are normally distributed. Then (A-7) when expanded and under the assumption of Reynolds averaging becomes

$$\text{Cov}(X, Y) = \text{Cov}(X_T, Y_T) + \text{Cov}(\epsilon, Y_T) + \text{Cov}(\delta, Y_T) + \text{Cov}(\epsilon, \delta) \tag{A-8}$$

The last three terms are the effects of the error in measurement. If the measurement of X is independent of the measurement of Y, and, therefore, the error in measuring X is not related to the error in measuring Y, then these terms are essentially zero, since they are the covariances between independent variables. This does not imply that X and Y are independent but merely that the error in the measurement of X is independent of the error in the measurement of Y.

If we assume the averaging time is chosen to represent a stationary sample of the total water vapor flux, the determination of the eddy flux is essentially free from the effects of error in measurement.

The sampling rate will have an influence on the accuracy of the determination of the eddy flux. Spectral analysis of both the water vapor density and the vertical wind indicated that the spectral energy beyond 1 Hz was negligible even under unstable conditions; therefore, any sampling rate in excess of 1 Hz will yield virtually the total flux.

Reference

Swinbank, W. C. (1955), An experimental study of eddy transports in the lower atmosphere, Meteorol. Phys. Tech. Paper No. 2, Commonwealth Scientific and Industrial Research Organization.

APPENDIX B

A PULSED TWO-TRANSDUCER SONIC ANEMOMETER

P. B. Uhlenhopp and L. G. Smeins

B.1. Introduction

One of the most formidable measurements in turbulence studies is that of the vertical wind, particularly if one is interested in rapid response and accurate mean values. Rotating anemometers and bivanes are limited in this regard. Sonic techniques seem well suited to this problem since they lack the inertia of moving parts. Schotland (1955) points out that, since sound propagates by virtue of the elastic properties of the atmosphere, a propagated sound wave is superimposed on the moving atmosphere, with consequent summation of their velocities. Many sonic instruments, which essentially fall in two categories, have been developed to measure components of the wind (Gurvich 1959; Suomi et al., 1959; Stewart et al., 1962; Kaimal et al., 1963; Oleson 1965). Continuous wave devices propagate sonic signals in opposite directions along parallel paths; the phase difference between the two waves is a measure of wind velocity along the path. Pulse systems transmit bursts of sonic energy in opposite directions along the same or parallel paths; the difference in transit time is the measure of wind velocity along the path.

A pulse system operating over a single path has several inherent advantages: two transducers are needed instead of four, reducing the bulk of the sensor and consequently wake effects; the single path reduces differential thermal expansion effects present in a two-path system, i.e., the frame on one path may expand more than the frame on the second; and since a common path is used for both signals, slight changes in the temperature of the medium are minimized (Suomi, 1956).

The single-path system requires a time share provision. One transducer transmits and the second transducer receives; the process then alternates with the above receiver acting as the transmitter, etc. The difference between the two transit times is a measure of the wind along the path.

Schotland (1955) showed that the time difference between two sonic waves propagated over a common path in opposite directions in the presence of a three-dimensional wind (fig. B.1) is

$$\Delta t_{12} = \frac{2 V_x X}{c^2 - V_T^2} \quad , \tag{B-1}$$

where

Δt_{12} = the time difference between the two signals,

X = the path length,

V_x = the wind velocity along the path,

V_T = the total wind velocity,

c = the velocity of sound.

Since $c \gg V_x$, V_T^2 can be neglected,

$$V_x = \frac{c^2}{2 X} \Delta t_{12} \quad . \tag{B-2}$$

The velocity of sound c is a function of T:

$$c = \sqrt{\gamma R T^*} \approx \sqrt{\gamma R T} \quad , \tag{B-3}$$

where γ is the ratio of specific heat, R is the gas constant, and T^* is the virtual sound temperature and is dependent not only on temperature but also the humidity. Except for extreme cases the error is small if the ambient temperature is used in place of the virtual temperature. (At $T = 20^{\circ}C$, $P = 1000$ mb, $RH = 50\%$ the difference between ambient and virtual temperature is $1.5^{\circ}C$, an error of less than 0.5%.)

33

Ishii (1935) presented an empirical formula for the velocity of sound,

$$c = 20.067 \sqrt{T},$$ (B-4)

where c, the velocity of sound, is expressed in m/sec and T, the ambient temperature, in °K.

B.2. Operating Characteristics

A time-shared system was developed in which only two transducers were used to avoid the bulk of a four-transducer array and its associated temperature problems. Time-sharing implies that the system be of the pulse type, where bursts of ultrasonic energy are alternately transmitted and received on a single transducer.

The operation of the device can be described as follows: Transducer No. 1 emits a short burst of 40-kHz ultrasonic energy. The signal is propagated across the path and received at transducer No. 2. The receiver circuitry at transducer No. 2 is designed so that the wind information is always taken from the same cycle of the received signal and converted into a d-c voltage. Transducer No. 2 then transmits short burst of ultrasonic energy that is received at transducer No. 1. Since the design of the receiver circuitry at transducer No. 1 is identical with that at transducer No. 2, the values of the two transit times are contained in two d-c voltages. These d-c voltages are compared differentially as dictated by (B-2) to obtain the one-dimensional wind velocity. The transmission, reception, and comparison process is repeated several times a second upon command from a clock system. This explanation is oversimplified but is presented to provide the reader with some insight into the operation of the device.

B.3. Experimental Design

A typical received burst in a pulsed system would appear as shown in figure B.2, where the shape of the signal envelope is primarily dependent on the "Q" of the transducer.

If we designate the arrival of a sound pulse as the instant when the received signal reaches a predetermined amplitude, fluctuations in the amplitude of the signal during turbulent conditions result in an uncertainty in the measurement of the transit times. A possible solution to this problem is to lower the "Q" of the transducer to produce a received signal with an envelope that resembles a square pulse. A two-transducer, single-path sonic has recently been developed by building low "Q" transducers, with sufficient sensitivity for transmission over an air path.* Here, we followed the lead of Stewart et al. (1964) and used the TR-7 transducer, a barium titanate device similar to those used in the remote control of television sets. The TR-7, for sonic purposes, can be considered a high "Q" device; consequently, it is essential that a scheme to eliminate uncertainties because of amplitude fluctuations be incorporated into the design of the instrument.

Figure B.2 gives an example of the received signal as it appears on the TR-7 transducer. The time from the transmitted pulse to the peak amplitude of the received signal can be measured with an oscilloscope with a delayed sweep. From this information, a proper delay pulse, generated from the master clock, can be selected to coincide with the peak amplitude of the received signal. A small portion of the received signal is also shown in figure B.2 on an expanded time scale.

---

*Air Force Cambridge Research Laboratories, New Bedford, Mass., has developed a low "Q" sonic transducer with sufficient sensitivity to transmit over a 15-inch path.
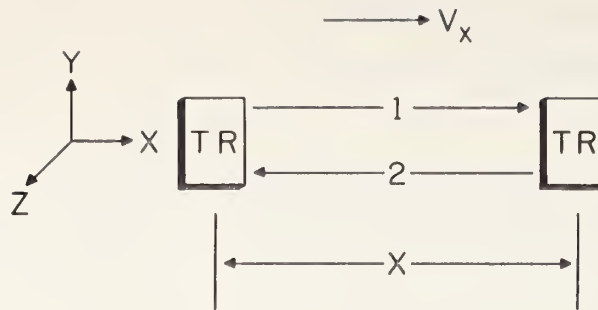
Figure B.1. Transducer configuration in the sonic array.
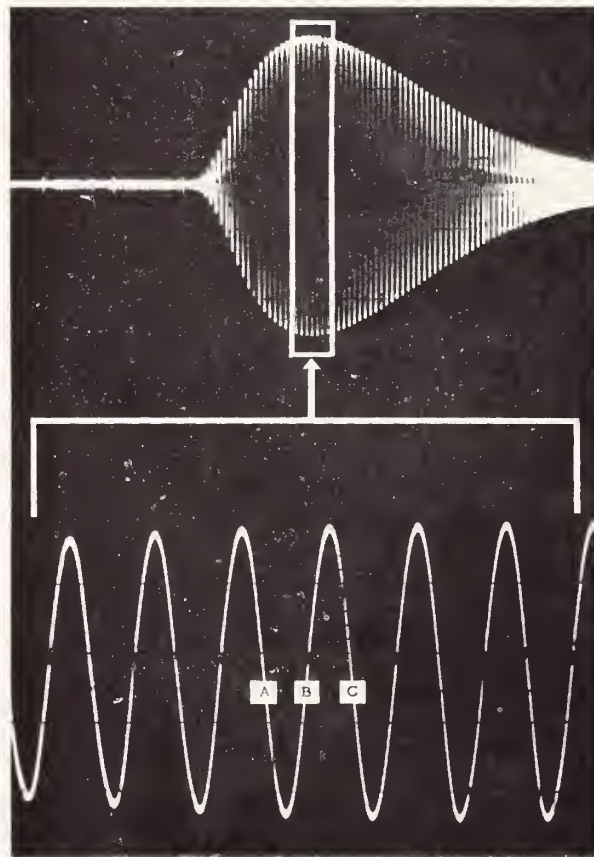
Figure B.2. Received sonic signal top with a portion expanded (bottom).

36

The wind information is obtained from the first positive zero crossing of the received signal (B in fig. B.2) occurring after the delay pulse from the master clock. The measurement is similar to that of a continuous-wave system with the associated limitation in range, without ambiguity, being one complete cycle of the received signal (A to C in fig. B.2). However, the desired zero crossing moves in time not only with the wind but also with temperature fluctuations. The clock signal used to select the desired cycle must, therefore, vary in time to compensate for the variations in the received signal due to temperature-induced changes in the speed of sound. This is accomplished by an independent temperature measurement with two silicon diodes whose junction voltages control the period of a delay circuit, which is, in turn, activated by a proper signal from the master clock. The tracking is such that a full cycle of the received signal is maintained as the range of the instrument. This is the method used to compensate for temperature induced variations in the speed of sound.

It should be emphasized that the tracking of the received signal to maintain the desired range is not to be confused with the actual differential measurement of the transit times of the two channels to obtain the wind speed in accordance with (B-2). The measurement of a zero crossing of the received signal is necessary because of the uncertainties encountered in the amplitude measurement. Use of a fixed point in time to select the desired zero crossing would severely limit the wind range of the sonic instrument because the received signal transit time varies not only with the wind but also with the temperature fluctuations. The additional temperature measurement preserves the one full cycle range of the instrument and has no other connection to the actual wind measurement. A functional diagram of the sonic anemometer is shown in figure B.3, with the associated timing diagram in figure B.4.

37
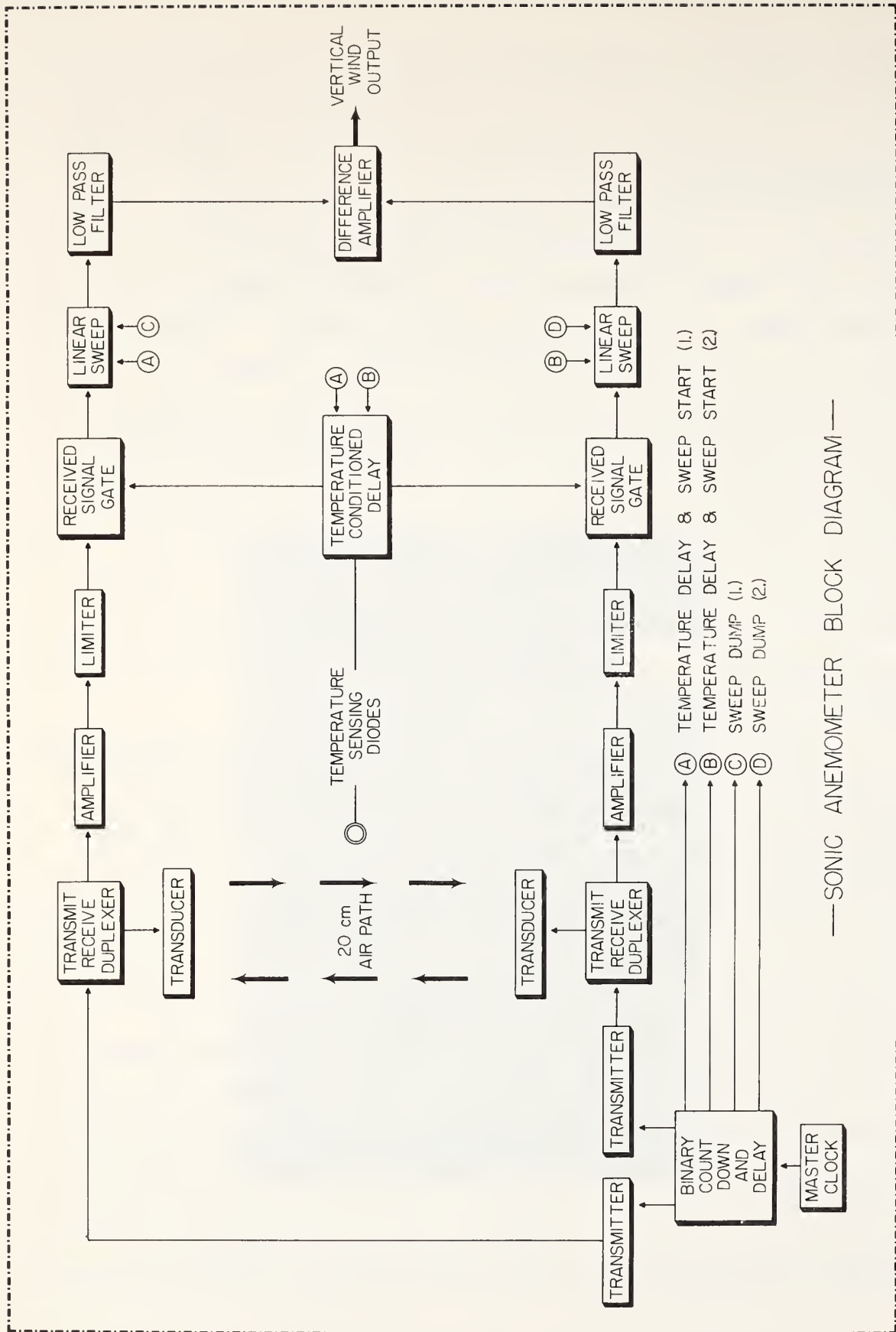
Figure B.3. Sonic anemometer block diagram.
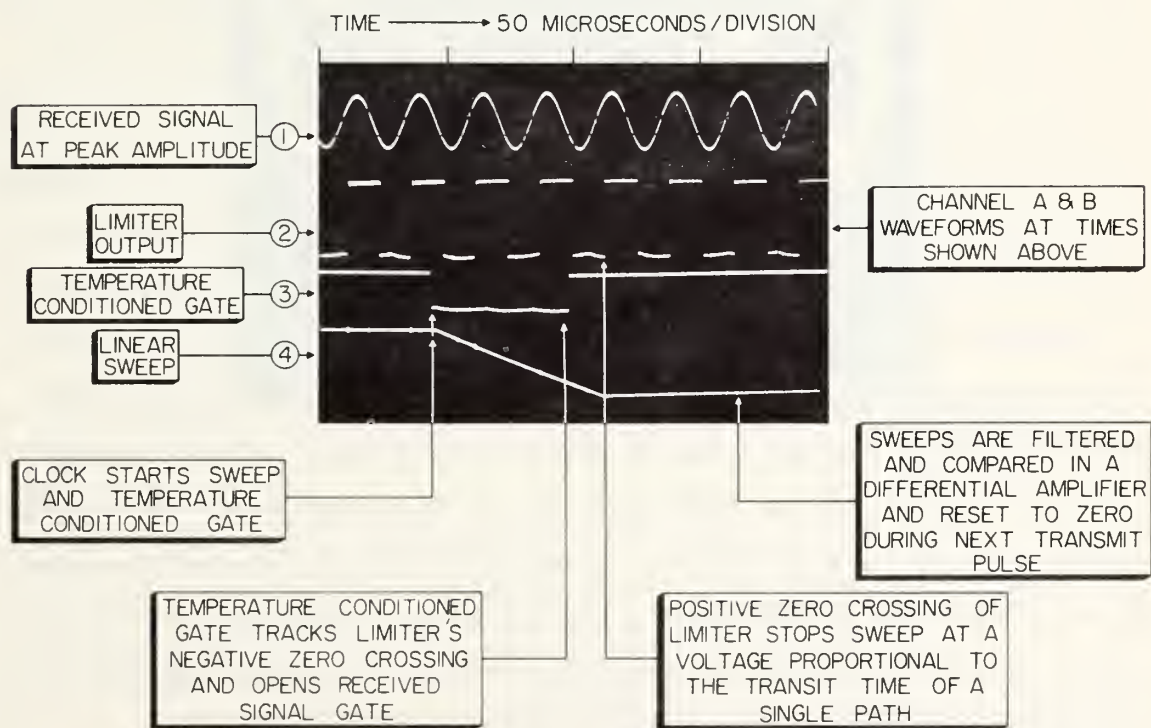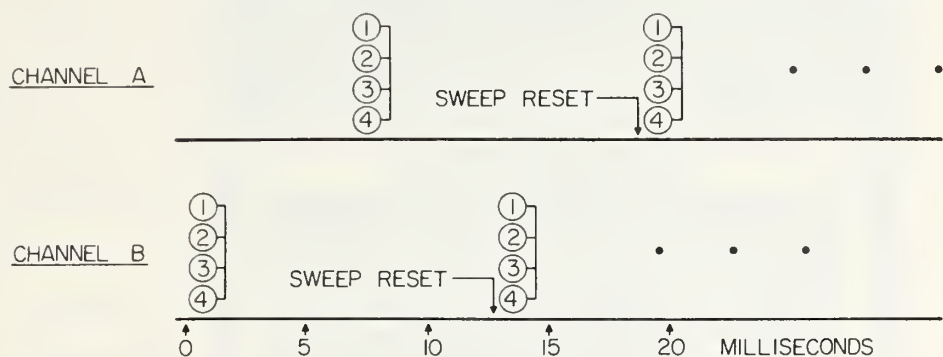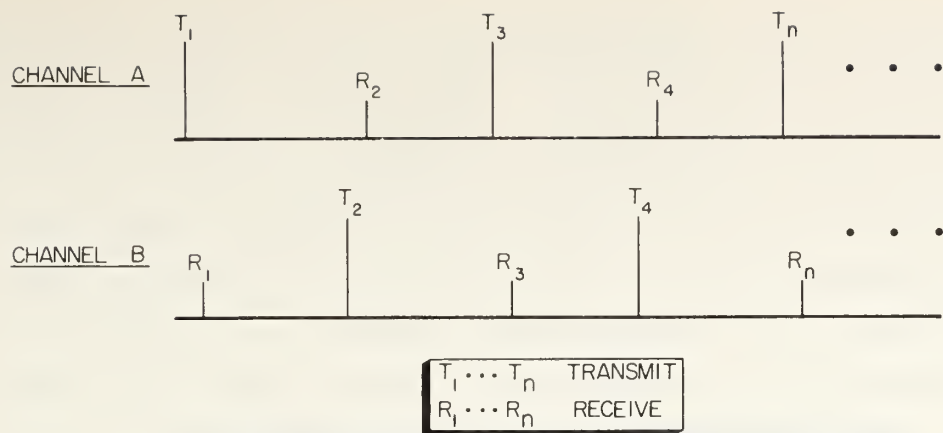
Figure B.4. Sonic anemometer timing diagram.

39

The two transducers are alternately pulsed with short bursts of 40 kHz of electrical energy at a 140-Hz rate. The received signals are taken from transmit-receive duplexers and amplified to a level sufficient to drive the limiter circuits. The square wave outputs from the limiter circuits are connected to the reset function of a received signal gate, which is normally in the reset position. As discussed in detail previously, a signal from the master clock, properly conditioned by the ambient air temperature, determines the cycle of the received signal, which is used to generate the transit time information. The master clock signal places the gate in the set position. The first zero crossing of the received signal triggers the gate to the reset position, thus generating a signal containing the transit time information. This signal is used to stop a linear sweep started earlier by a signal from the master clock. The final sweep voltage is contained in a high quality Mylar capacitor connected to a low pass filter with a high input impedance. The capacitor holds the peak voltage until a dump signal from the master clock resets its value to zero. Since the two channels are identical, the final result is contained in two d-c signals; the values are dependent on the ambient temperature and wind in the path. If these two voltages are compared in a differential amplifier, the output is consistent with (B-2) and is representative of the wind in the path. The full-scale or calibration factor for the sonic is still dependent on the ambient air temperature, since c appears in (B-2), but the dependence is a weak one so that only a rough measurement of the temperature is adequate for calibration purposes. The instrument described here uses an ultrasonic frequency of 40 kHz (i.e., a period of 25μ s) and a path length of 20 cm. The use of these numbers in (B-2) at a temperature of 300°K results in a full scale of approximately ± 7 m/ sec that is adequate for vertical wind studies. The array is illustrated in figure B. 5.
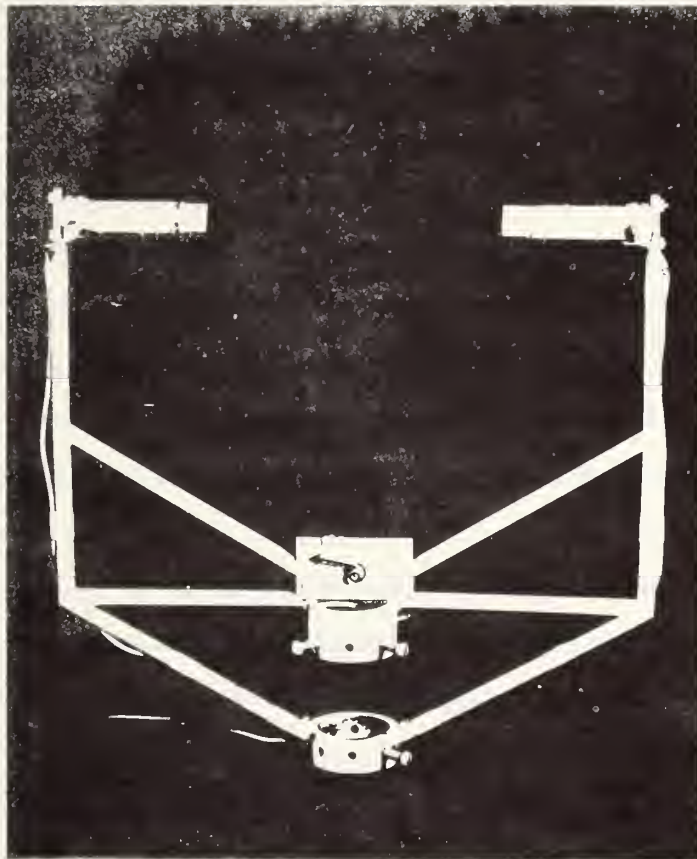
Figure B.5.   Transducer array used in the experiment.

B.4. System Accuracy

By its differential nature, the two-transducer system is virtually free from drift of the zero wind point, but this is not completely true in practice, possibly because the received signal level is normally 100 dB below the transmitted signal. Each transducer would, therefore, have to have static phase characteristics <u>versus</u> ambient temperature over the entire dynamic range to completely eliminate differences in the phase of the transmitted and received signals. Long-term laboratory tests (more than 24 hours) indicate that departure from the zero point is not greater than ± 3 cm/sec for temperature changes of the order of 20°C. Measurements of the short-term noise were also taken during the drift tests. The peak-to-peak noise levels, as observed on a high frequency paper chart recorder, were equivalent to 3 cm/sec in actual wind velocity. The primary source of noise in the system results from the received amplifiers rather than from the sonic transducers; further improvements in the receiver section could reduce the noise level to 1 cm/sec.

The total sampling rate of the instrument is 70 Hz, but the spatial resolution is actually limited by the length of the acoustical path. The effect produces an artifical cutoff in the frequency spectrum for eddy diameters smaller than the acoustical path length. If we can make a crude estimate of the cutoff frequency f_c by assuming that turbulent eddies are spherical in shape and are transported horizontally by the mean wind $\bar{u}$, then

$$f_c = \frac{\bar{u}}{x} .$$
(B-5)

A more realistic cutoff frequency, the point where the sonic senses 90 percent of the true wind, is discussed in detail by Mitsuta (1966). The resulting expression is

$$f_{90\%} = 0.26 \, \frac{\bar{u}}{x} . \qquad\qquad (B-6)$$

Problems and errors encountered when moving the instrument from the laboratory into actual field conditions are often overlooked. Improper placement of the anemometer could create errors, particularly in the vertical coordinate. Errors of this type are difficult to define, even when the data from the field measurements are available. Wake effects constitute another source of errors that are difficult to assess in terms of absolute numbers. They are assumed to be small for wind flow normal or near normal to the acoustical path;[*] however, it would be advantageous to keep the ratio of path length to transducer diameter as high as possible, while maintaining the desired sensitivity for the instrument.

Frame vibration or slight changes in the path length will cause an error in the full-scale reading. For a full-scale accuracy of ± 1 percent on a 20-cm path, the limit of movement would be ± 2 mm.

A simple calculation will show that misalignment of the frame will create an error in the mean value of the desired component. In the vertical wind case, for example, if the average horizontal wind is 4 m/sec, and the frame is misaligned by 1°, which contaminates the vertical wind data with the horizontal component, the error in the vertical zero can be as high as 8.5 cm/sec. With varying horizontal winds, relative wind errors would also appear in the vertical component. This error is serious enough to merit careful alignment of the frame.

[*]Bolt Beranek and Newman, Inc., of Cambridge, Mass., tested a similar frame assembly in a smoke tunnel. The results indicate little effect from the wake for air flow normal or near normal to the acoustical path.

B.5. Performance and Conclusions

The anemometer was successfully tested in the laboratory and subsequently used at Lake Hefner, Oklahoma, in conjunction with an evaporation experiment conducted there during August 1966. The instrument was used alongside a bivane to measure the vertical wind for a continuous 5-day period. Considering the limitation in the vertical measurement imposed by the bivane, the outputs from the two instruments compare favorably as shown in figure B.6. The vertical wind speed is obtained from the bivane by multipling the sine of the elevation angle ϕ by the total wind velocity, which is essentially the horizontal component of the wind speed. In particular, note the sharp change in the horizontal wind azimuth accompanied by extreme turbulence, as measured by both instruments. The 30-sec sample shown in figure B.6 was chosen to demonstrate the capabilities of the sonic instrument. A close examination of the sonic record indicates rapid time fluctuations to at least 10 Hz. Above this frequency the validity of the data would be questionable because of the 90 percent limitation of (B-6).

To simulate an accurate zero wind condition, a suitcase was modified to fit over the sonic sensor array, and the zero point was measured three times.

It was found to be within the previously established stabilities of ± 3 cm/sec obtained under laboratory conditions. The drift and noise of the system, along with wake effects and frame vibration, result in errors in the measurement of full-scale wind velocity. One of the advantages of the two-transducer system is that the frame assembly can be constructed from lightweight material. If the transducers are mounted some distance away from a rigid stainless steel assembly, as shown in figure B.5, errors resulting from wake effects and vibration are significantly reduced.

44

— 270° WEST

— 180° SOUTH

— 90° EAST   BIVANE AZIMUTH ANGLE IN DEGREES

— 0 M/S

— 13.5 M/S   HORIZONTAL WIND   VELOCITY M/S

— 20° UP

— 0°

— 20° DOWN   BIVANE ELEVATION ANGLE IN DEGREES
— 3 M/S UP

— 0

— 3 M/S DOWN   SONIC ANEMOMETER VERTICAL WIND M/S

TIME IN SECONDS
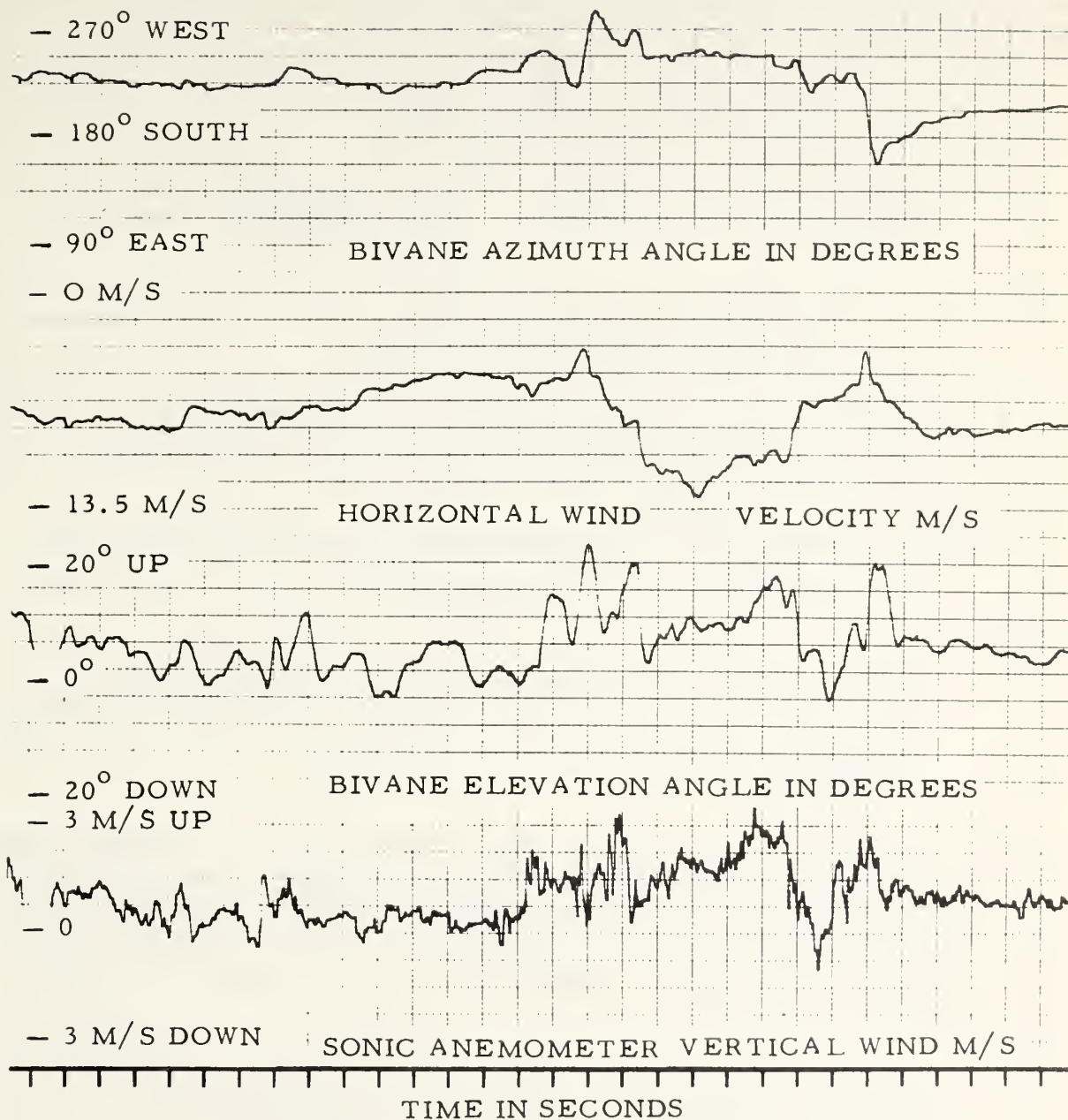
Figure B.6.   Simultaneous recordings from a bivane and sonic
anemometer taken from the 8-m level of a tower
in the center of Lake Hefner on August 26, 1966.

45

References

Gurvich, A. S. (1959), Acoustical micro-anemometer for investigating micro-structure of turbulence, J. Acoust. USSR (English transl. by Am. Inst. Phys.) 5, No. 3, 375-376.

Ishii, Ch. (1935), Supersonic velocities in gases, Sci. Papers Inst. Phys. Chem. Res. (Tokyo) 26, 201, 207.

Kaimal, J. C., and J. A. Businger (1963), A continuous wave sonic anemometer--thermometer, J. Appl. Meteorol. 2, No. 1, 156-164.

Mitsuta, Yasushi (1966), Some anemometer--thermometer for general use, J. Meteorol. Soc. Japan, 44, No. 1.

Oleson, S.(1965), An improved sonic anemometer--thermometer, SRI Final Rept. Proj. PHU-4806, Stanford Research Institute, Menlo Park, Calif.

Schotland, R. M. (1955), The measurement of wind velocity by sonic means, J. Meteorol. 12, 386-370.

Stewart, R. M., Jr., R. E. Post, and R. W. Johnson (1964), Fast response instrumentation for the measurement of turbulent fluxes in the lower atmosphere, AFCRL Final Rept. No. 64-147, Contract No. AF19(604)-5457, Air Force Cambridge Research Laboratories, New Bedford, Mass.

Stewart, R. M. Jr., R. E. Post, T. A. Smay, and J. E. Carson (1962), Sonic anemometer data acquisition and analysis system and calculation of Eulerian scale of turbulence from bivane data, AFCRL Res. Rept. No. 62-465, Air Force Cambridge Research Laboratories, New Bedford, Mass.

Suomi, V. E. (1956), Energy budget studies at the earth's surface and development of the sonic anemometer for power spectrum analysis, AFCRL Tech. Rept. 56-274, Contract No. AF 19(122)-461, Dept. of Meteorol., University of Wisconsin.

Suomi, V. E. and J. A. Businger (1959), Sonic anemometer--thermo meter, ASTIA Document No. AD-217076 (Clearinghouse for Federal Scientific and Technical Information, Springfield, Va.).

APPENDIX C

THE MICROWAVE EVAPOTRON

The eddy flux method of measuring evaporation led to the development of a direct-reading water vapor flux meter. The component parts of this device are:

    (a) a modified microwave refractometer (microwave hygrometer), and

    (b) a sonic anemometer.

C.1. The Microwave Hygrometer

The microwave refractometer was originally designed by Birnbaum (1950). Refinements have been made since that time to improve its operation and stability. The instrument is based on the relationship between the resonant frequency f of a microwave cavity, its dimensions K, and the refractive index n of the contents, i.e.,

$$f = -Kn; \tag{C-1}$$

then,

$$\frac{\Delta f}{f} = -\frac{\Delta n}{n} \approx -\Delta n \quad \text{since } n \approx 1.000300, \tag{C-2}$$

or the relative change in the refractive index of the air inside a microwave cavity is equal to the relative change in the resonsant frequency. If the operating frequency is 10 GHz and if the change in the refractive index is 1 ppm, the resonant frequency of the cavity will change by 10 KHz.

If a sealed cavity is used as a reference, the difference between the resonant frequencies of the sampling cavity and the reference cavity is a measure of the refractive index of the air passing through the sampling cavity.

A klystron is used as a variable frequency source in the Birnbaum refractometer. The repeller of the klystron is swept with a sawtooth voltage that varies the frequency. As the frequency passes through the resonant frequency of each cavity a pulse is detected at the output of the cavity. The time difference between the two pulses is a measure of the frequency difference between the two cavities, and, therefore, is a measure of the refractive index of the air in the sampling cavity. The accuracy of the refractometer is approximately 1 ppm in radio refractive index; the resolution is 0.01 ppm.

Since the refractive index n is a number, such as 1.000300, it has been common practice to scale the index up, i.e.,

$$N = (n-1) \, 10^6, \tag{C-3}$$

where N is called the refractivity and is related to meteorological parameters by

$$N = 77.6 \frac{P}{T} + 1.72 \times 10^3 \frac{\rho_w}{T}. \tag{C-4}$$

Here P is the total pressure in mb, T is the temperature in $^{\circ}K$, and ρ_w is the water vapor density in g/m^3 (Bean and Dutton, 1966). Then

$$\rho_w = 5.81 \times 10^{-4} \, NT - 4.51 \times 10^{-2} \, P. \tag{C-5}$$

This relationship can be accomplished in an analog fashion as shown in figure C.1. The output can then be calibrated in grams per cubic meter. The absolute accuracy is approximately 0.2 g/m^3, and the resolution is 0.02 g/m^3 under normal operating conditions (McGavin and Vetter, 1965).

C.2. The Sonic Anemometer

When a sound wave is propagated through the air, its velocity of propagation is the vector sum of the sound velocity in still air and the velocity of the medium (wind speed). If two sound waves are sent
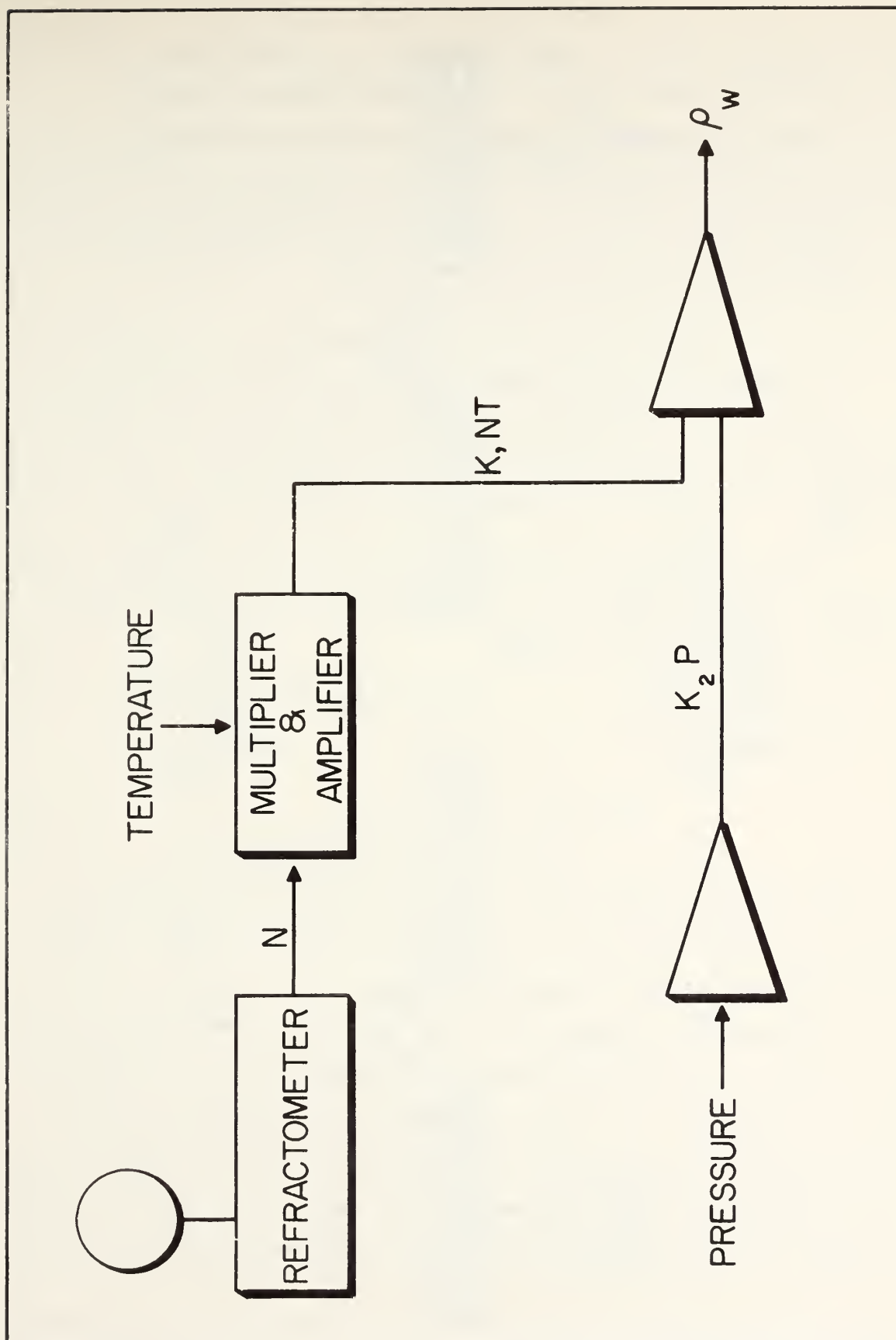
Figure C.1. The microwave hygrometer.

49

across the same path X in opposite directions, the difference in the transit times Δt is a measure of the wind velocity along the path.

The sonic anemometer used to measure the vertical wind is described in appendix B. It has a full scale of approximately 7 m/sec. The noise level is 3 cm/sec, and the accuracy is dependent mainly upon the manner in which the instrument is mounted.

C.3. The Microwave Evapotron

To obtain the vertical water vapor flux, the microwave hygrometer and the sonic anemometer are combined (see fig. C.2). The high-pass filters eliminate the mean values, producing the eddy flux at the output.

The output of the microwave evapotron was so conditioned as to provide an output in evaporation in centimeters per day. The instrument is designed in such a way that

$$1 \text{ g/m}^3 = 2.5 \text{V} \qquad \text{Time constant} = 5 \text{ sec}$$
$$1 \text{ m/sec} = 2.5 \text{ V} \qquad \text{Gain} \qquad = 0.1$$

$$\text{Integrating time} = 10 \text{ min}$$
$$1 \text{ cm/day} = 8.68 \text{ V/10 min} \; ,$$

i.e., the difference in the voltage from the integrator over a 10-min period is divided by 8.68 (or multiplied by 0.115) to yield the average evaporation over a 10-min period in cm/day.

The integrator operates over a v range, which is then dumped at the 10-v level. Actual field recordings from the microwave evapotron are shown in figure C.3. The evaporation at time (A-B)=.115 (B-A) cm/day, which is approximately 0.71 cm/day. At time (C-D) the evaporation is approximately 0.24 cm/day. The accuracy of the water vapor flux meter is approximately 0.03 cm/day, the resolution 0.002 cm/day.

50
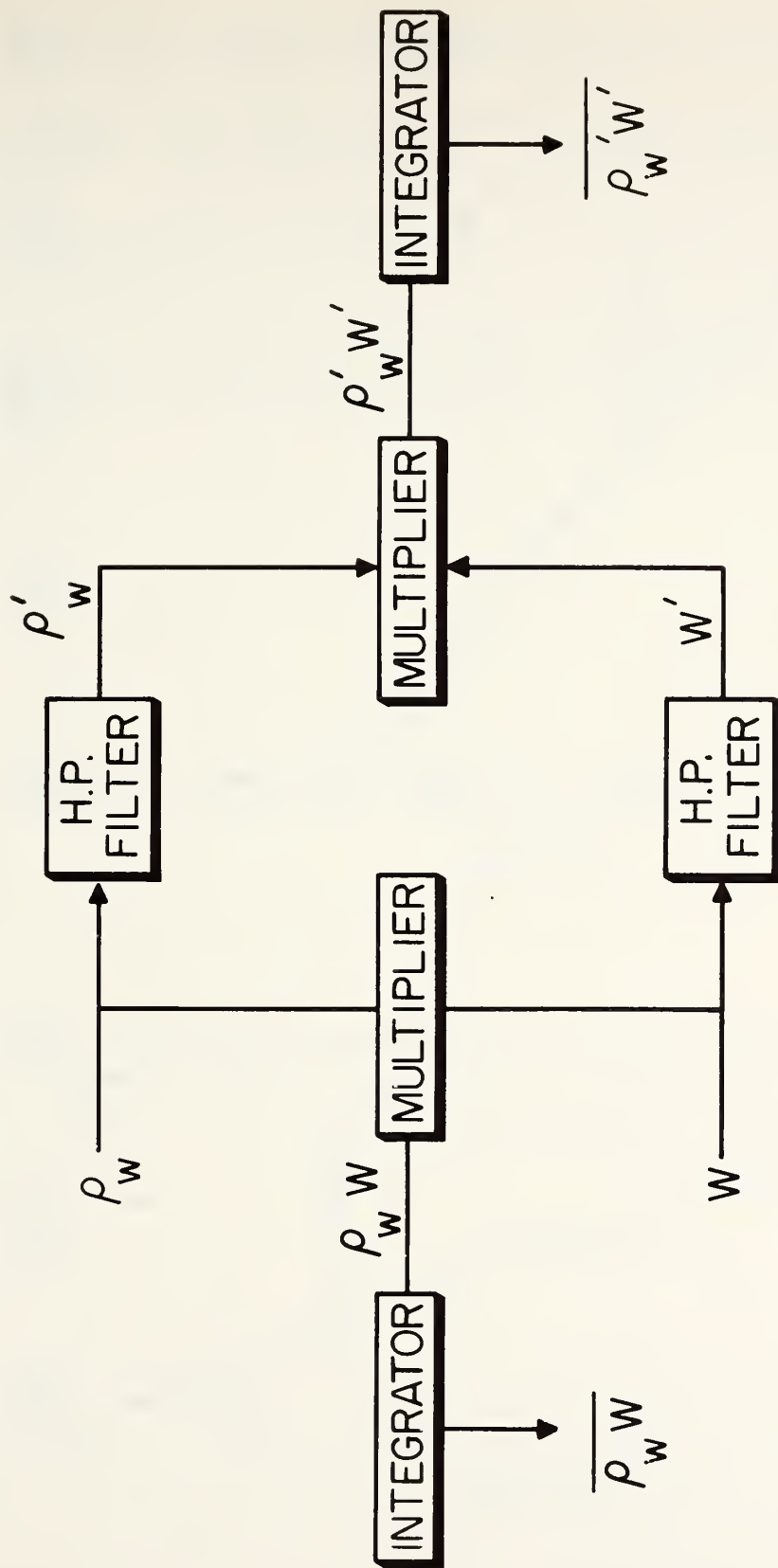
Figure C.2. The microwave evapotron.

51
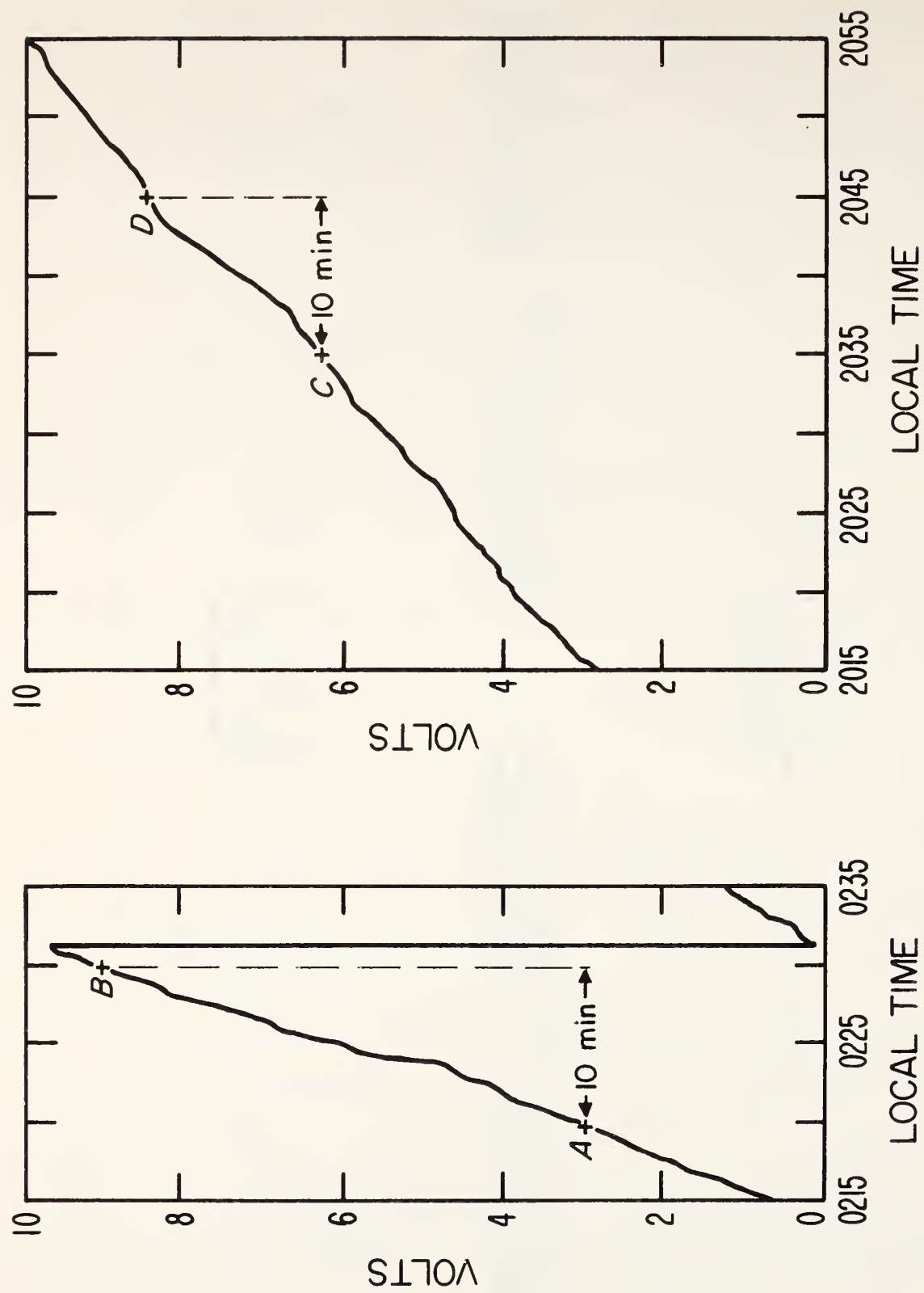
Figure C.3. Typical output of the microwave evapotron.

52

References

Bean, B. R., and E. J. Dutton (1966), Radio Meteorology, NBS Mono-
    graph 92 (U. S. Government Printing Office, Washington, D.C.).

Birnbaum, G. A. (1950), Recording microwave refractometer, Rev.
    Sci. Instr. 21, No. 2, 169-176.

McGavin, R. E., and M. T. Vetter (1963), Radio refractometry and its
    potential for humidity studies, Proc. Intern. Conf. on Humidity
    and Moisture, II, 553-560 (Reinhold, New York, N. Y.).

APPENDIX D

A SOLID-STATE SYSTEM FOR MEASUREMENT OF INTEGRATED REFRACTIVE INDEX

R. O. Gilmer and D. M. Waters

D.1. Introduction

While the gradient of the refractive index determines the refraction of radio waves, phase and amplitude scintillations of the radio signal are attributed to the rapid temporal or spatial variations of the refractive index; therefore, the turbulent conditions of water vapor and temperature that influence the refractive index affect the phase (apparent range) and, to a lesser extent, the amplitude of radio signals along line-of-sight propagation paths. It has been proven feasible to measure phase variations of a radio wave to indicate the integrated variations of the refractive index. Comparison of the measurements at radio and optical frequencies will give both variability in water vapor and in temperature over a common path.

Microwave phase systems have been used to study refractive index variations of the atmosphere and the error the variations induce in microwave baseline-tracking systems (Herbstreit and Thompson, 1955; Janes and Thompson, 1964); they have also been used as electronic distance-measuring devices. Bean and McGavin (1963) have found a high correlation between refractive index variations and water vapor variations over short periods (up to 20 min) for both stable and unstable conditions. If these results have general applications, then a microwave phase system should yield measurements of the variations of water vapor integrated over a considerable volume of the atmosphere. (Such a system has been used in an evaporation study at Lake Hefner, Oklahoma and has been referred to as a volume integral refractometer.)

The phase of a radio signal transmitted from one point to another is affected by the medium in which it propagates in the following manner:

$$\phi(t) = \frac{360\, S f \left[1 + N(t) \times 10^{-6} \right]}{c} \text{ degrees (Janes et al., 1965),} \qquad \text{(D-1)}$$

where

ϕ = phase length of path in degrees,

$\overline{N}(t)$* = refractivity averaged over the path,

S = path length (meters),

f = frequency (9.6 GHz), and

c = velocity of light (3×10^8 m/sec).

The change in refractivity is related to changes in path length by

$$\Delta \overline{N}(t) = \Delta \phi(t) \left[\frac{c}{360\, Sf} \times 10^6 \right]. \qquad \text{(D-2)}$$

Thus, the change in refractivity over a path can be determined from the change in path phase length when S is independently known, and the phase system may therefore be used as a volume-integral refractometer when S is determined. The measured refractivity changes are averaged over the path length between two antennas and over a volume dependent on antenna configuration.

A microwave integrating refractometer (described below) was used to study refractive index variations over a line-of-sight propagation path of 1.6 km. This system, constructed with all solid-state components, provides considerable improvement in reliability and microphonic characteristics as compared to the older klystron versions (Thompson and Vetter, 1958). The solid-state construction also makes for a lightweight system that requires a low power consumption.

---

*Because the atmospheric refractive index (n) differs from 1 by only a few hundred parts per million, it is convenient to use a quantity known as the refractivity, defined as $N = (n - 1) 10^6$.

D.2. System Operation

The following describes the operation and characteristics of a system capable of measuring the phase fluctuations expressed by (D-1).

The master oscillator (100 MHz multiplied to 9.6 GHz) delivers a minimum of 150 mW to the antenna (see fig. D.1). This signal propagates over the path. At the transponder, the incoming signal is mixed with the transponder signal, producing a 100-kHz IF signal that is connected to two IF amplifiers. The output of one, a limiter amplifier, is phase compared to a 100-kHz reference oscillator. Whenever the phase of the two 100-kHz signals differs from a fixed amount, the phase comparator supplies an error voltage that passes through an attenuator filter-network to the voltage-control-crystal-oscillator (VCXO) of the transponder. When the transponder frequency differs from the incoming master signal by more or less than the frequency of the reference oscillator, the phase detector will see the frequency error as an error in phase and will supply an error voltage to the VCXO to restore the difference frequency of 100 kHz. By this means the transponder is phase locked 100 kHz away from the master oscillator. Any changes in the phase (due to the atmosphere) of the incoming signal will produce an error signal at the phase detector. The error signal will advance or retard the frequency of the transponder until the transponder's phase tracks the phase of the incoming signal. Hence, the signal radiated from the transponder contains phase fluctuations of the one-way path, and the signal (9.6 GHz to 100 kHz) received at the master terminal carries the phase information of a two-way transit of the path (Peter and Strandberg, 1955).

The 100-kHz IF signal is also amplified by an AGC amplifier and used to frequency modulate a 99.6875-MHz VCXO, which is multiplied to 9.570 GHz. Any phase error contributed by the phase-lock system
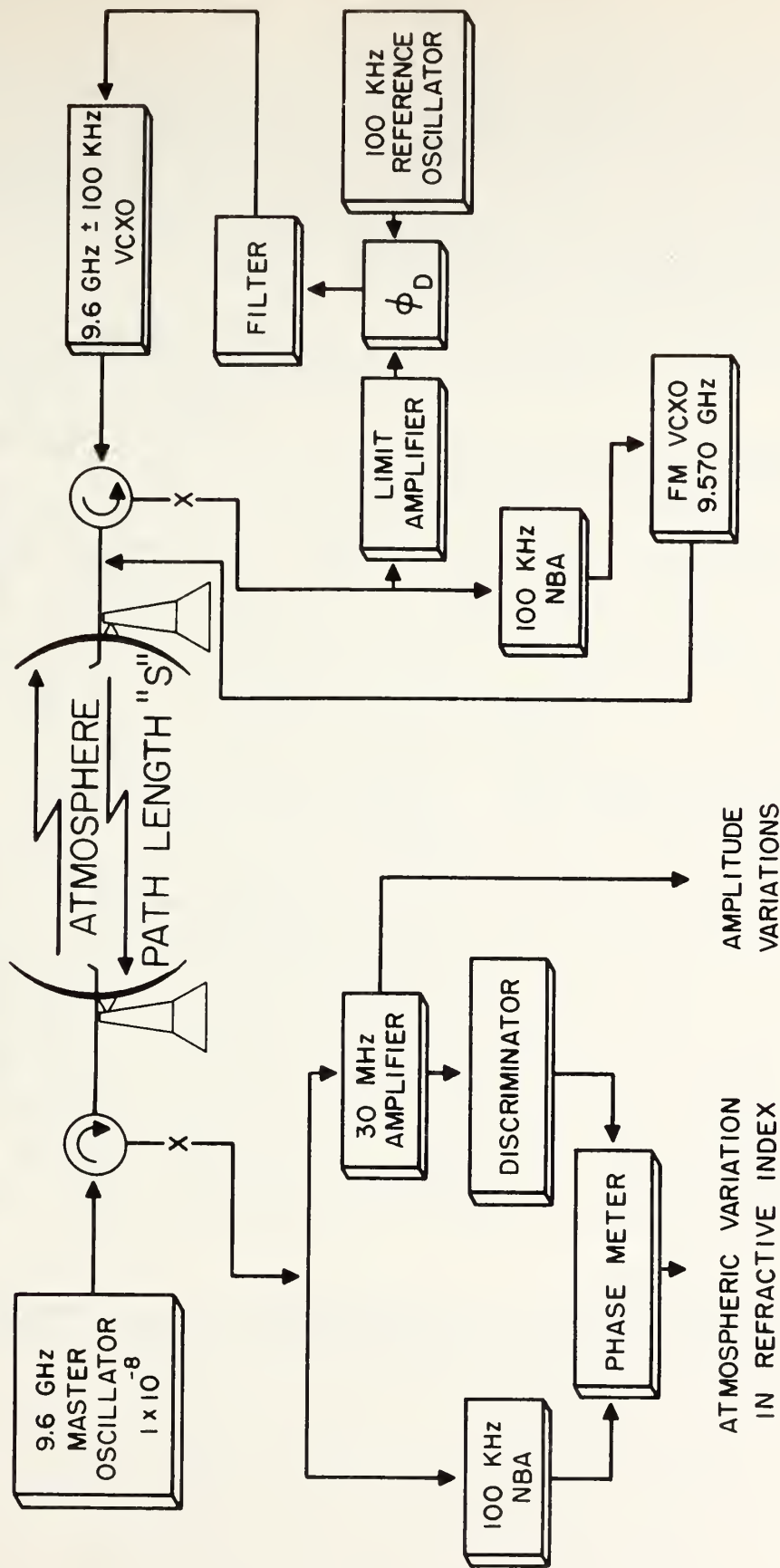
Figure D.1. Functional diagram of the microwave phase system.

$$\Delta L = -\left[\frac{360\ SF}{c} \times 10^{-6}\right] \Delta N$$

57

has the appearance of a phase change because of the atmosphere on the 9.6-GHz signal. This FM signal is fed to the transponder antenna and is propagated back to the primary antenna. The effect of the atmosphere on the phase of the 100-kHz signal is lower in magnitude than the 9.6-GHz signal by the ratio of 100 kHz to 9.6 GHz.

Two microwave signals arrive at the primary antenna; the transponder signal, 9.6 GHz minus 100 kHz, and an FM signal, 9.570 GHz. Both pass through the circulator and are mixed with the original frequency from the master oscillator 9.6 GHz. The resulting two frequencies, 100 kHz and 30 MHz, are separated. The 100-kHz signal contains twice the phase shift of the 9.6 GHz by the variations in refractivity of the atmospheric path, plus possible errors obtained in the transponder loop. The 100-kHz signal is amplified in an amplifier with identical characteristics to the one used on the 100 kHz that modulates the FM signal at the transponder. Common characteristic errors in the amplifiers should cancel out. The 100-kHz IF is applied to one side of a phase meter. The 30-MHz FM signal is amplified and fed to a discriminator, where the 100 kHz is extracted and applied to the other input of the phase meter.* Any transponder phase-lock errors will appear in both 100-kHz signals at the phase meter and, therefore, do not appear in the phase output. The phase meter output is recorded and represents the phase change along the path. Under conditions of no multipath, the phase changes are directly related to the refractivity changes.

---

*This signal contains common errors contributed by the transponder phase lock electronics with only negligible effects of path.

D.3. Characteristics of System

The overall accuracy of the system is dependent mainly upon the stability of the master transmitter. A 1-ppm change along a path is equal to 1 N-unit. The stability of the master transmitter is 1×10^{-8}/day or 1/100 of 1 N-unit/day. This accuracy is independent of path length. The short-term stability is 1×10^{-9}/sec. As the path length increases, the amount of N-change required to create a full-scale change of 360° decreases (see D-2).

The effect of a-c voltage changes on the four individual units and on the system as a whole does not exceed 0.1° or 0.085 mV for a-c supply voltages of 100 to 140 V. Alternating current voltage change from 80 to 140 V does not affect the performance of the FM, master transmitter, or transponder; however, should the input voltage drop below 100 V a-c, the phase meter is affected.

The maximum acceptable path loss, when we assume no antenna gain, was measured in the laboratory by simulating the path loss with two variable 50-dB attenuators placed in the closed path. At large path losses, the waveguide joint leakage at the transponder exceeded the signal received through the waveguide. This leakage was minimized by shielding each waveguide joint. The path attenuation was slowly increased until the FM transmitter signal affected the phase-lock loop. The maximum path loss termed acceptable was 80 dB, which produced a noise level on the phase meter output of 1.5° peak to peak. With the FM link disconnected from the system, the transponder would remain in "lock" with the master transmitter for a path loss up to 100 dB. In operation, however, additional path loss is compensated for by use of antennas of appropriate gain. The noise level from the phase meter as a function of path loss is shown in figure D.2. The noise level is constant until the path attenuation reaches 50 dB; from there it increases
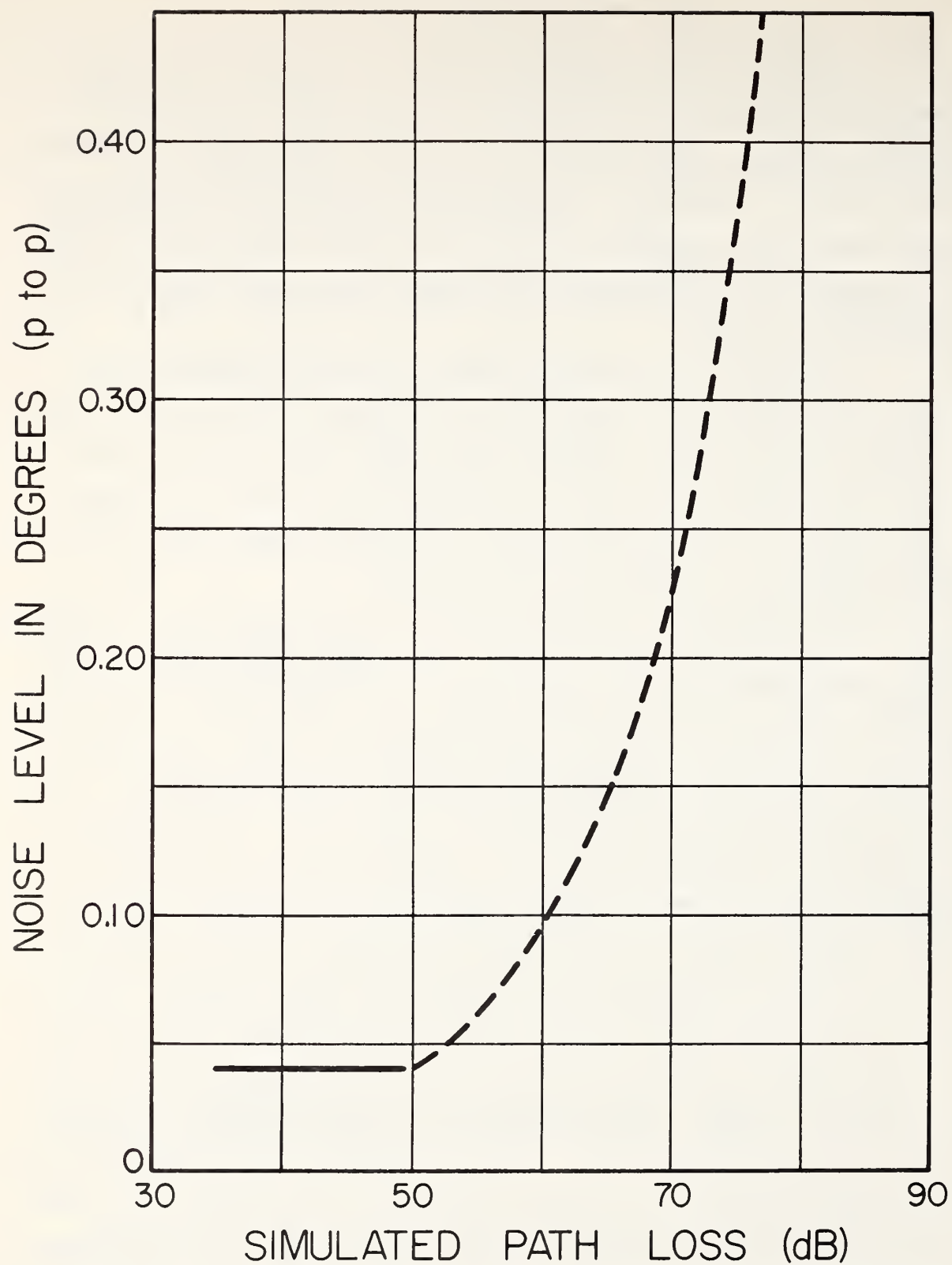
Figure D.2. Recorded noise level in degrees of phase of the phase system as a function of simulated path loss.

rapidly. The noise contributed by the phase meter was measured by placing a common signal into both inputs and was found to be less than 0.04° peak to peak.

To measure the phase meter response, a 100-kHz reference signal was compared with a variable frequency oscillator. The frequency of the variable oscillator was increased from 100 kHz to 101 kHz and the response recorded. The output response of the phase meter as noted on an oscilloscope was greater than 100 Hz.

D.4. Characteristics of Components

With few exceptions, the reported phase system uses commercial components having characteristics shown in table D.1. The exceptions are the limiter amplifier and the phase detector in the transponder, the AGC amplifiers, the 100-kHz filter and amplifier of the FM discriminator, and an offset amplifier for measuring the amplitude of the received FM signal. Some modifications are made to the commercial phase meter.

Limiter Amplifier. The limiter amplifier has four stages of emitter coupled transmitter pairs followed by two separate emitter followers (fig. D.3). The gain of the amplifier before limiting in 10^4, with the output limited to 2.8 V peak to peak.

Phase Detector. The phase detector is a two-transistor "chopper" that rectifies the 100 kHz from the reference oscillator; the chopper is driven by the limiter amplifier (i.e., the incoming signal, fig. D.4). The phase detector output is filtered and attenuated by a phase lead network before it is used as the VCXO control. An additional phase detector is driven from other windings on the input transformers, with an additional 90° of phase shift; the polarity of its output indicates to the transponder transmitter whether it is operating 100 kHz above or below

Table D.1. Component Characteristics

Component	Input	Output	Stability	Other	Size
Master Oscillator and oven	24-28 V dc regulated at 800 mA	10^8 Hz at 10 mW into 50-Ω load	$\pm 1 \times 10^8$/24 hr $\pm 1 \times 10^9$/sec over -20 to +60°C	Spurious output -40 dB	2" x 2" x 4"
Transponder oscillator	Same as above voltage control tuning of $\pm 2.3 \times 10^4$ Hz	Same as above	$\pm 1 \times 10^8$/24 hr over -20 to 60°C	Same, also mechanical tuning range $\pm 2 \times 10^3$ Hz	2" x 2" x 4"
FM oscillator	Same as master voltage control tuning range $\pm 5 \times 10^4$ Hz	9.9687×10^7 Hz	$\pm 1 \times 10^6$/24 hr oven -20 to +60°C	Same as master modulation rate 5×10^4 to 10^5 Hz	2" x 2" x 4"
Phase lock oscillator	+28 V dc at 11 mA	10^5 Hz 8.8 Vpp into 1 k load	0.0001% -20 to 60°C		4" long 3/4" radius
Multipliers	+28 V dc at 800 mA and approx. 10^8 Hz	150 mW min at 9.6×10^9 Hz		Bandwidth 0.1% min. spurious -40dB multiplication ratio 96	7" x 3" x $2\frac{1}{4}$"
Discriminator	Signal direct output from IF amplifier	10 V/10^6 Hz of deviation		Bandwidth 10^7 Hz peak to peak	$8\frac{1}{2}$" x $2\frac{1}{2}$" x $1\frac{1}{2}$"
FM IF Amplifier	3×10^7 Hz +12V d-cat 140mA -12V d-cat 150mA	Maximum 8 V		Bandwidth 1.15 x 10^7 Hz 93dB power gain noise.fig. 2dB 60dB gain control for 2 V dc	$6\frac{1}{2}$" x $3\frac{3}{4}$" x 3"
Power supplies	105 to 132 V ac at 45 to 440 Hz		0.03 %/°C	Regulation line -0.05%+4mW load -0.03%+3mW ripple 1mV to 3mVpp	$6\frac{1}{2}$" x $3\frac{3}{4}$" x 3"

LIMITER AMPLIFIER
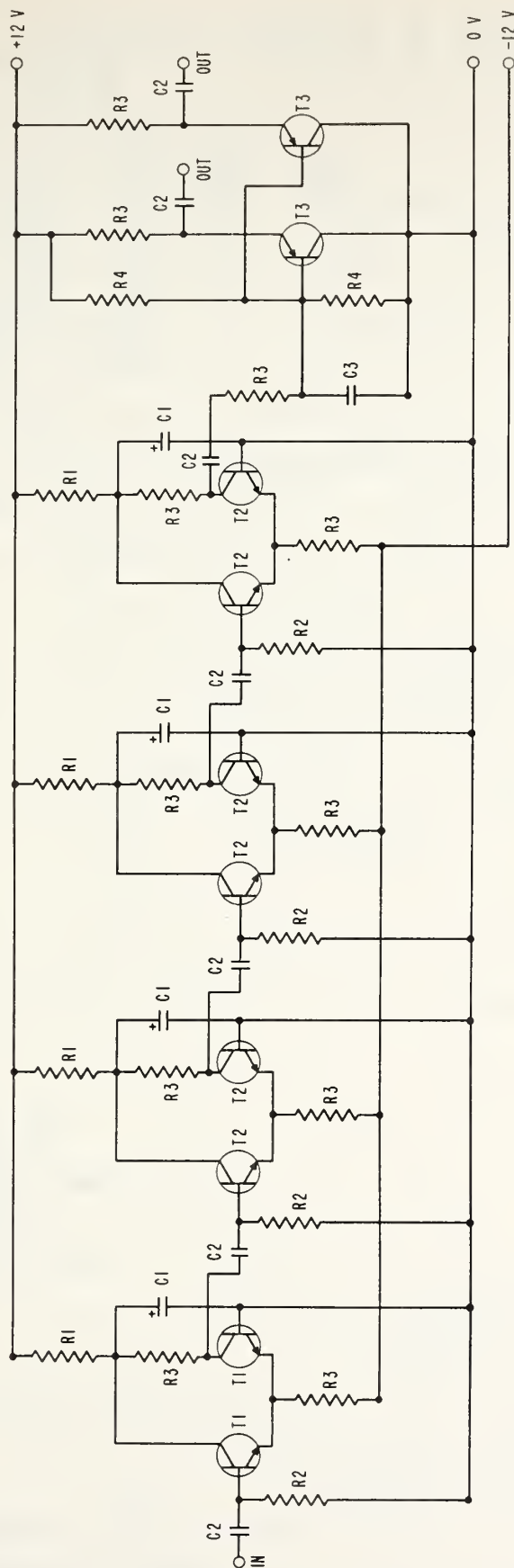
PARTS LIST

C1 —— 10 mf
C2 —— 0.1 mf
C3 —— 27 pf

R1 —— 1 K
R2 —— 510 Ω
R3 —— 5.1 K
R4 —— 100 K

T1 —— 2N 2219
T2 —— 2N 3904
T3 —— 2N 3154

Figure D.3.   Schematic of the four stage limiter amplifier used in phase-lock loop.

63

PHASE DETECTOR & SIDEBAND INDICATOR
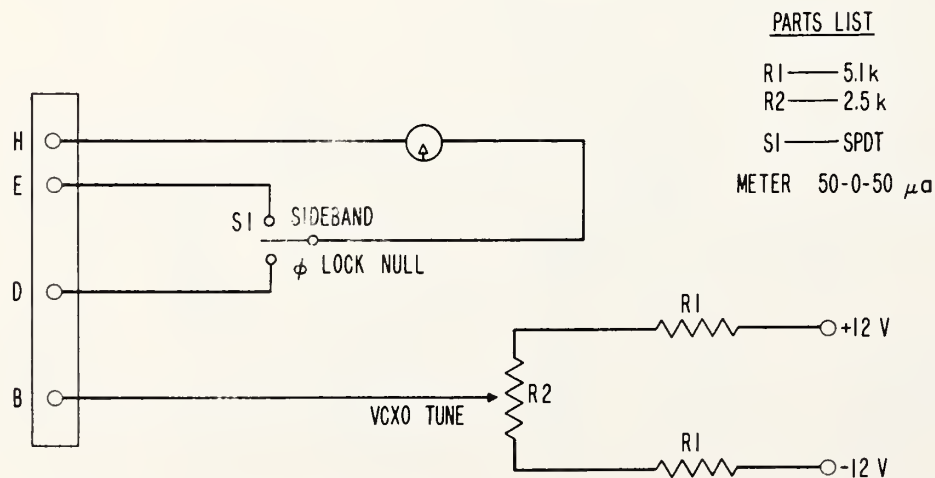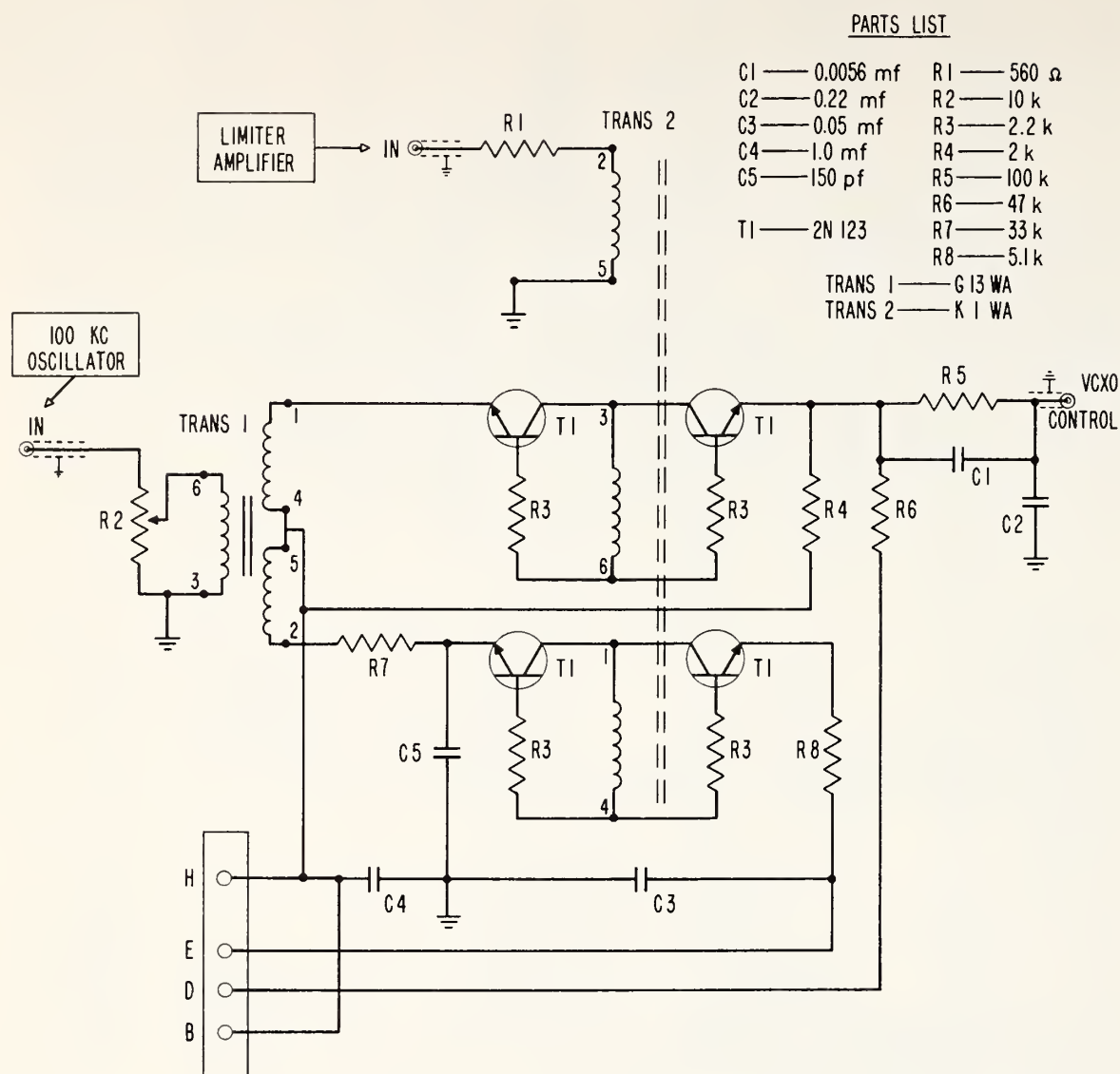
Figure D.4.   Schematic of the phase detector and sideband indicator used
to control the frequency of transponder VCXO.

64

the master transmitter frequency. The limiter amplifier phase detector combination will keep the VCXO locked to a signal 100 dB below the master transmitter signal.

The phase detector's transfer function is 2.5 V/π rad and the oscillator multiplier transfer function is $4.8\,\pi \times 10^6$ rad/V-sec. The gain between the two units is 0.13, giving a unity gain frequency for the loop of 1.6 MHz (curve 1, fig. D.5). As a result of bandwidth limitations introduced by the limiter amplifier, the phase-lock loop seems to be most stable when the bandwidth is reduced to about 10 kHz. The bandwidth is reduced by means of a phase lead network. The stability of the oscillator is 1 part in 10^6; the noise and microphonics are no greater than 1 part in 10^7, and the oscillator therefore remains locked even when shocked mechanically. The transponder oscillator with the above crystal characteristics can be tuned electrically to 100 kHz either above or below the master frequency. When the crystal in the oscillator was replaced with one of higher Q, the transfer function was reduced to $2.8\,\pi \times 10^6$ rad/V-sec. The unity gain frequency of the loop is reduced to 0.9×10^4 Hz (curve 2, fig. D.5). The phase lead network is modified to give the same unity gain frequency for the high Q crystal. Figure D.5 shows the gain frequency characteristics of the phase-lock loop with the two different crystals. The oscillator with the number 2 crystal will tune to only one sideband mechanically or electronically.

AGC Amplifiers. The AGC amplifiers provide a gain of 10^6, and a bandwidth of 3 kHz centered at 10^5 Hz. A 60-dB variation of signal voltage produces a change in the output voltage of only 0.2 dB. The amplifier uses FET's (field effect transistors) in the AGC stages. The FET-type used was selected to have the lowest gate to drain capacitance available to keep Miller capacitance variations with AGC to a minimum. Miller capacitance variations cause phase variations in the AGC amplifier. The tracking problem is less critical when two identical amplifiers are used.
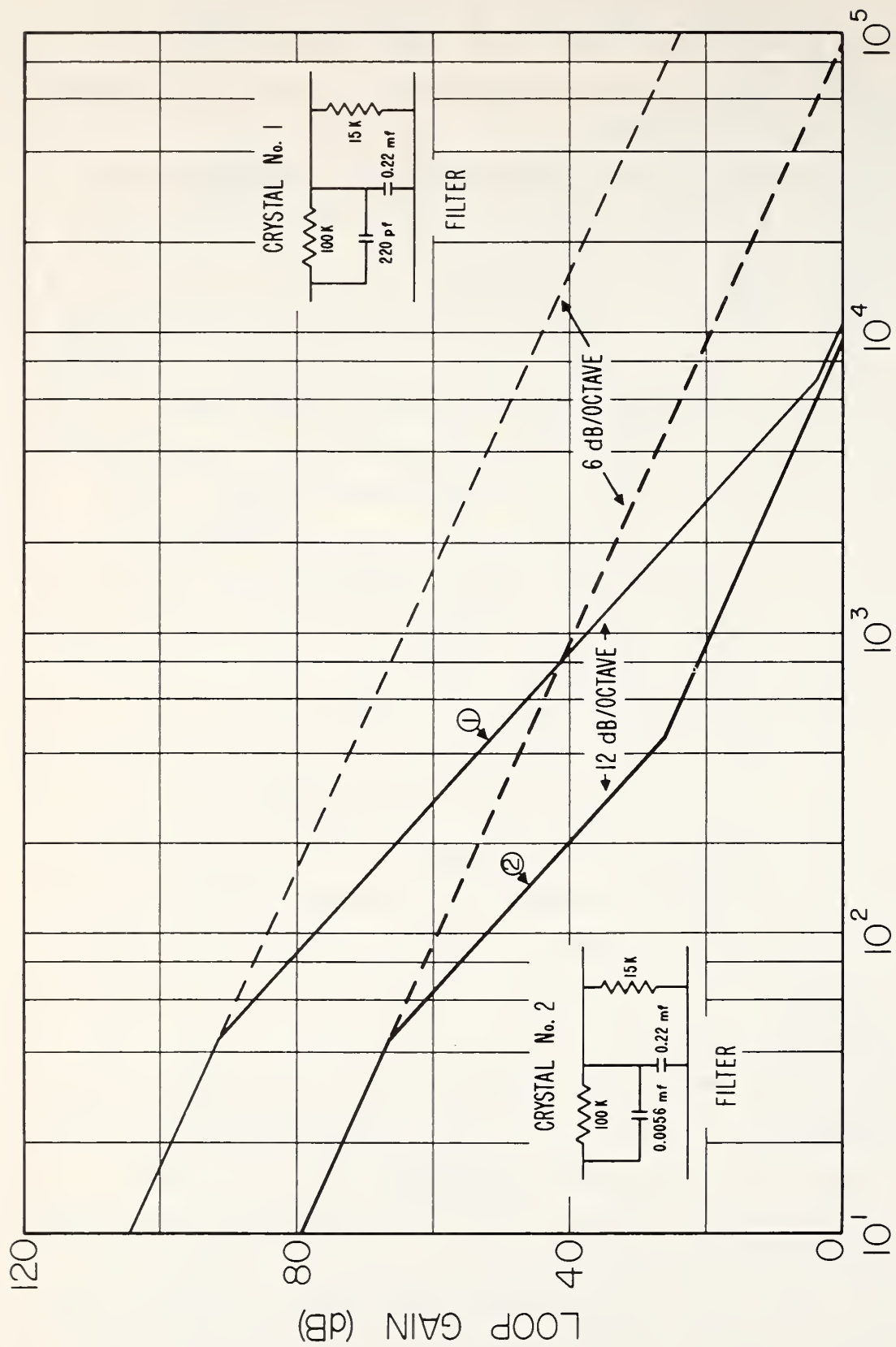
Figure D.5. Gain versus frequency characteristics of the phase-lock loop for two different crystals.

Phase Meter. A commercial phase meter was modified for use in this phase system. The phase variations on even a short path can exceed 360°; the phase meter will track these variations by shifting full scale. To avoid continued full-scale shifts, the phase meter was modified to shift by 180° when the indicated phase is 20° or 340°. The pulse from the multivibrator changes the state of a bistable flip-flop. The outputs of the flip-flop control 0° and 180° gates. The phase meter output is generally recorded on analog FM magnetic tape; in order to drive the tape machine, the output swing of the phase meter is reduced and a bias voltage applied so that the output swing will be -1.5V to +1.5V for a phase change of 0 to 360°.

The 30-MHz IF amplifier has a d-c output that is proportional to the input amplitude. This output is amplified and a bias offset voltage is applied to obtain a signal for recording on magnetic tape that is related to the amplitude of the received microwave signal.

References

Bean, B. R., and R. E. McGavin (1963), The use of the radio refractometer to measure water vapor turbulence, Proc. Intern. Symp. on Humidity and Moisture, II (Reinhold, New York, N. Y.).

Herbstreit, J. W., and M. C. Thompson (1955), Measurements of the phase of radio waves received over transmission paths with electrical lengths varying as a result of atmospheric turbulence, Proc. IRE 43, 1391-1401.

Janes, H. B., A. W. Kirkpatrick, D. M. Waters, and D. Smith (1965), Phase and amplitude diversity in overwater transmission at two microwave frequencies, NBS Tech. Note 307 (U. S. Government Printing Office, Washington, D. C.).

Janes, H.B., and M.C. Thompson, Jr. (1964), Errors induced by the atmosphere in microwave range measurements, Radio Sci. J. Res. NBS 68D, No. 11, 1229.

Peter, M., and M. W. P. Strandberg (1955), Phase stabilization of microwave oscillators, Proc. IRE 43, No. 7, 869.

Thompson, M. C., and M. J. Vetter (1958), Single path phase measuring system for three-centimeter radio waves, Rev. Sci. Instr. 29, No. 2, 148-150.

Additional References

Bender, P. L., and J. C. Owens (1965), Correction of optical distance measurements for the fluctuating atmospheric index of refraction, J. Geophys. Res. 70, No. 10, 2461.

Smith, E. K., and S. Weintraub (1953), The constants in the equation for atmospheric refractive index at radio frequencies, Proc. IRE 41, 1035-1037.

APPENDIX E

ELECTROMAGNETIC PHASE VARIABILITY AS A MEASURE
OF WATER VAPOR AND TEMPERATURE
VARIATIONS OVER LONG PATHS

E.1. Introduction

Until recently the atmospheric scientist was limited to point measurements of pertinent meteorological parameters. Probes that were used disturb the environment, and the point measurement was not necessarily characteristic of the region or even of another point not far removed from the observing point. For many applications, values of such parameters integrated over an area or along a path would be a more useful quantity. With the development of accurate electrical distance-measuring techniques, a promising method has become available for measuring water vapor and temperature over paths tens of kilometers long. The development of these techniques is the result of increased interest in accurate geodesy. Literature on this subject has been growing steadily during the past decade, and well-documented review papers are now available in which state-of-the-art techniques and expected accuracies are discussed (Bender, 1967; Thompson, 1967; Owens, 1967, private communication).

The electromagnetic path length can be shown to be a function of the refractive index, which in turn is a function of temperature, water vapor and pressure. We will analyze, first, the possibility of estimating water vapor density from radio path length measurements alone, and, second, the possibility of using a radio-optical system for estimating both water vapor density and temperature. The discussion here is confined to a dual frequency system (1 microwave and 1 optical), with

the realization that a three-frequency system would produce a significant increase in accuracy.

Attention will be concentrated on the uncertainties in the measurement of the water vapor density and temperature integrated over the path. These uncertainties arise because of limitations in instrumental capabilities, experimental evaluation of constants, and what are considered to be reasonable approximations. Uncertainty here is defined as the range of values that should contain the true value of the quantity desired. Where random errors (in absence of systematic errors) are encountered, the uncertainty is defined as one standard deviation. Bias errors caused by approximations are combined in a root sum square (rss) fashion with the standard deviations of random errors providing an estimate of the possible percent departure from the true value.

E.1. Atmospheric Effects on the Radio Path Length

E.2.1. Theory

The radio path length (L_r) is related to the geometric path length (S) by

$$L_r = \int_0^S n_r \, dS, \qquad (E-1)$$

where n_r is the refractive index at radio frequencies.[*] This can be written

$$L_r = <n_r> S, \qquad (E-2)$$

where $<n_r>$ is the space average of the refractive index over the path. In radio distance measuring, this relationship is used to determine the geometric distance from the radio path length. The measured radio path

---

[*]Usually n_r is expressed in terms of N_r where $N_r = (n_r - 1)10^6$

70

is corrected for the average value of the refractive index calculated from meteorological measurements at each terminal to provide an estimate of the geometric path length (S is not the exact straight-line distance, since the path is slightly curved by refraction). If the problem is inverted, i.e., if S is known from other sources, then the mean values and fluctuations of L_r will yield the mean value and fluctuations of the refractive index averaged over the path.

Now (Bean and Dutton, 1966),

$$n = 1 + K_1 \frac{P}{T} + K_2 \frac{\rho_w}{T},$$ (E-3)

where

$$K_1 \quad = 7.76 \times 10^{-5} \, {}^{o}K/mb,$$

$$K_2 \quad = 1.72 \times 10^{-3} \, {}^{o}K/g \, /m^3,$$

$$P \quad = \text{total pressure in mb},$$

$$T \quad = \text{temperature in } {}^{o}K,$$

$$\rho_w \quad = \text{water vapor density in } g/m^3,$$

and then, performing the space averaging and assuming $<\frac{x}{y}> \approx \frac{<x>}{<y>}$, we obtain

$$L_r \approx S \left[1 + K_1 \frac{<P>}{<T>} + K_2 \frac{<\rho_w>}{<T>} \right],$$ (E-4)

or

$$<\rho_w> = \left[\frac{L_r}{S} - 1 \right] \frac{<T>}{K_2} - \frac{K_1}{K_2} <P> .$$ (E-5)

If some estimates of $<T>$ and $<P>$ are available, then L_r will provide a measure of the integrated water vapor density over the path. Variations in the average water vapor density are given by

$$\Delta < \rho_w > = \frac{\partial < \rho_w >}{\partial < T >} \Delta(< T >) + \frac{\partial < \rho_w >}{\partial \left(\frac{L_r}{S} - 1\right)} \Delta \left(\frac{L_r}{S} - 1\right) + \frac{\partial < \rho_w >}{\partial < P >} \Delta P. \tag{E-6}$$

Assume that for average conditions

$$< \overline{T} > = 300 \ {}^\circ K,$$

and

$$\frac{\overline{L}}{S} - 1 = 3 \times 10^{-4} \text{ (equivalent to } <n> = 1.000300),$$

$$< \overline{P} > = 1000 \text{ mb},$$

where the overbar denotes a time average. Equation (E-6) then becomes

$$\Delta < \rho_w > = 0.174 \ \Delta(< T >) + 1.74 \times 10^5 \ \Delta \left(\frac{L_r}{S} - 1\right) - 0.045 \ \Delta(< P >), \tag{E-7}$$

which indicates the sensitivity of the measured integrated water vapor density to changes in integrated temperature and pressure, as well as to radio path length variations. The contribution from pressure variations is very small since P is not expected to change by more than a tenth of a millibar; however, the contribution of uncertainties in the assumed mean temperature is significant. If one uses a time average of temperature at a point as an estimate of integrated temperature, an error will be introduced. For example, from a recent experiment on a 1.65-km overwater path, the rms fluctuations in the temperature, as measured at the center of the path, were compared with those measured by optical path variations. The average over a number of 10-min samples indicated an rms variability of $0.2 \ {}^\circ K$ in the point measurements, where-as the rms variability in the optical path measurements was only a few hundredths of a degree (Owens, 1967); hence the use of a point measurement of temperature in (E-5) over this path could contribute an uncertainty of as much as 4 percent in $< \rho_w >$ because of temperature variability

72

alone. Contribution from the pressure was less than 0.1 percent. If the radio path length alone is to furnish an accurate estimate of the integrated water vapor over a path, it is evident that some better method must be used for an estimate of the integrated temperature.

E.2. Experimental Estimates

A direct test of how well the radio path length alone can yield estimates of water vapor density was made based on data from six paths taken from the literature (Thompson and Janes, 1959; 1964). These paths, ranging from 0.7 km to 17.1 km, represent two diverse climates and terrain settings: Boulder, Colorado (a dry climate and mountainous region), and Cape Kennedy, Florida (a moist climate and flat terrain). Estimates of the average temperature and pressure were obtained from measurements at both ends of the path. A comparison was made on samples of 10-sec averages taken every half hour. Figure E.1 illustrates one such comparison between $\widehat{\rho}_w$ determined by path length measurements and $\widetilde{\rho}_w$ determined by psychrometric measurements. There is surprisingly good agreement between $\widehat{\rho}_w$ and $\widetilde{\rho}_w$. The 17.1-km Cape Kennedy path yielded the highest correlation coefficient r (0.983), the 7.7-km path at the same location produced the lowest (0.622), and the remaining paths had correlation coefficients of 0.803, 0.871, 0.890, and 0.909. (It is interesting to note that even for point measurements most of the short-term variability in the refractive index is caused by variations in water vapor (Bean and McGavin, 1965).)

CAPE KENNEDY, FLORIDA
PATH LENGTH 17.1 km

$$\frac{\tilde{}}{\rho_w} = 1.060 \frac{\wedge}{\rho_w} - 3.793$$

$$r(\frac{\tilde{}}{\rho_w}, \frac{\wedge}{\rho_w}) = 0.983$$

Figure E.1. Comparison of radio integrated water vapor density with the averaged value calculated from psychrometric observations at both terminals.

74

E.3. Measurement of Water Vapor Density and Temperature
by Microwave-Optical Techniques

E.3.1. Theory

Microwave phase systems have been under continuous development since 1955 (Herbstreit and Thompson, 1955). Recently, comparable optical systems have been enjoying similar growth (Thompson, 1967; Earnshaw and Owens, 1967). The use of both microwave and optical techniques should provide estimates of both integrated water vapor density and integrated temperature. The microwave system is sensitive to both temperature and water vapor, but the optical system, while sensitive to temperature, is only weakly influenced by water vapor.

The optical path length can be expressed as

$$L_o \approx S \left[1 + K_3 \frac{<P>}{<T>} + K_4 <\rho_w> \right], \tag{E-8}$$

where, if the optical wavelength is 6328 Å,

$$K_3 = 8.09 \times 10^{-5} \; {}^oK/mb,$$

$$K_4 = -5.33 \times 10^{-2}/m^3/g \quad .$$

If this is combined with (E-4),

$$\frac{L_r - L_o}{S} = \left[K_1 - K_3 \right] \frac{<P>}{<T>} + K_2 \frac{<\rho_w>}{<T>} - K_4 <\rho_w>. \tag{E-9}$$

For convenience we define a new parameter K_5 by

$$\frac{K_2}{<T>} - K_4 = \frac{K_5}{<T>},$$

where for $<T> = 293 \; {}^oK$, which becomes

$$K_5 = 1.74 \times 10^{-3} \; {}^oK/g/m^3. \tag{E-10}$$

Using this constant value of K_5 will result in a maximum possible error of 0.1 percent compared with (E-9) for a temperature range of 233°K to 303 °K. Hence,

$$\frac{L_r - L_o}{S} = -3.3 \times 10^{-8} \frac{<P>}{<T>} + 1.74 \times 10^{-3} \frac{<\rho_w>}{<T>} \qquad \text{(E-11)}$$

and

$$<\rho_w> = 575 \left(\frac{L_r - L_o}{S} \right) <T> + 0.0019 <P>, \qquad \text{(E-12)}$$

where $<\rho_w>$ is now a linear function of $<T>$ and $<P>$.

The average temperature is found from (E-8) to be

$$<T> = \frac{8.09 \times 10^{-5} <P>}{\left(\frac{L_o}{S} - 1 \right) + 5.33 \times 10^{-8} <\rho_w>} \quad . \qquad \text{(E-13)}$$

A further approximation can be made in the expression (E-12) for the average value of $<\rho_w>$. If average conditions are again assumed to be $<\overline{P}> = 1000$ mb, $<\overline{T}> = 293$ °K, and $<\overline{RH}> = 70$ percent, then

$$<T> = \frac{8.09 \times 10^{-5} <P>}{\left(\frac{L_o}{S} - 1 \right) + 4.80 \times 10^{-7}}, \qquad \text{(E-14)}$$

where the increase in the maximum possible error will be less than 0.2 percent over a reasonably expected range of humidity and temperature. Based on (E-14), (E-12) becomes

$$<\rho_w> = 4.65 \times 10^{-2} \left[\frac{\frac{L_o - L_r}{S}}{\frac{L_o}{S} - 1 + 4.80 \times 10^{-7}} + 0.041 \right] <P>. \qquad \text{(E-15)}$$

If $<P>$ does not vary by more than a few tenths of a millibar and if there are no instrumental errors, the total uncertainty in $<\rho_w>$ should not exceed 0.6 percent and that in ΔT should not exceed 0.3 percent, except when there are extreme changes in temperature or humidity. These coefficients can be determined for the particular location and season, and hence an accuracy of approximately 0.3 percent in $<\rho_w>$ should be achievable.

In addition, these expressions can be simplified to

$$<T> = 8.09 \times 10^{-5} \left(\frac{S}{L_o - S} \right) <P>$$

and

$$<\rho_w> = 4.65 \times 10^{-2} \left(\frac{L_r - L_o}{L_o - S} + 0.041 \right) <P>$$

$$\left. \right\}, \quad (E-16)$$

where the uncertainty due to the approximations and the coefficients in the equation for refractive index is 0.3 percent root sum square (rss) in $<T>$ and 0.65 percent (rss) in $<\rho_w>$.

E.3.2. Instrumental Limitations

Up to this point it has been assumed that L_r, L_o, and S are known exactly. It remains to find the uncertainty in $<\rho_w>$ due to inaccuracy in L_r, L_o, and S. Consider the finite differential of (E-16) under the assumption of $<\overline{P}> = 1000$ mb, $S = 1$ km, $<\overline{T}> = 293\ ^{\circ}K$, $<\overline{\rho_w}> = 10$ g/m^3:

$$\Delta (<T>) = 0.29\ \Delta(<P>) - 10.6\ \Delta L_o + 10.6\ \Delta S$$

$$(E-17)$$

$$\Delta(<\rho_w>) = 0.009\ \Delta(<P>) - 1.97\ \Delta L_o + 1.69\ \Delta L_r - 0.287\ \Delta S.$$

If, L_o and L_r can be measured with an uncertainty of no more than 1 ppm (i.e., 0.1 cm in 1 km), then the uncertainties in $<T>$ and $<\rho_w>$ will be 0.33 percent and 2 percent, respectively. It is also evident that if S can be measured with an equivalent accuracy (i.e., 1 ppm) then it likewise will give rise to an uncertainty of 0.33 percent in $<T>$ and approximately 0.3 percent in $<\rho_w>$.

An indirect method of determining S was tested in the Lake Hefner overwater experiment. Forty-two determinations of L_r were made over the 1.65-km path during a 5 1/2-day period. The refractive index was measured at both ends of the path at the times of these measurements. Over the entire period L varied 8 cm, but when corrected for the refractive index as measured at the terminals, the range was reduced to 2 cm. The mean value of the 42 determinations of S was 164, 982.3 cm; the standard deviation was 0.52 cm; hence, the standard error of the mean was less than 0.1 cm, representing an uncertainty of about 1 ppm.

E.3.3. Summary

The accuracy in $<\rho_w>$ and $<T>$ expected under these measurement conditions yields an uncertainty in the absolute values of 2.6 percent (rss) in $<\rho_w>$ and less than 0.5 percent (rss) in $<T>$. When all the uncertainties are considered (i.e., accuracies of the constants in the equations for refractive index, approximations used, and the measurement accuracies) the overall uncertainty in $<\rho_w>$ is approximately 2.75 percent (rss), and that in $<T>$ is approximately 0.6 percent (rss). Most of this uncertainty in $<\rho_w>$ is from measurement capabilities, which probably can be improved. The remainder is divided between the accuracies in the coefficients in the refractive index equations and the approximations used.

If ΔL_r, ΔL_o and S exhibited uncertainties of 1 part in 10^7, then the uncertainty in $<T>$ would be .05 percent, and that in $<\rho_w>$ would be 0.3 percent due only to measurement. There are experimental systems which exhibit these capabilities today, but it may be some time before such devices are commercially available. Further improvement in the residual uncertainty of approximately 0.5 percent would require that the coefficients be more exact in the equations for the refractive index.

E.3.4. Measurement of Fluctuations

This process can be simplified if only small variations about an arbitrary mean are of interest. The total differentials in finite form of (E-4) and (E-7) yield expressions of the form

$$
\left.
\begin{aligned}
\Delta(<\rho_w>) &= \frac{A}{S} \left[\Delta L_r - B \Delta L_o \right] - C \Delta(<P>) \\
\Delta(<T>) &= \frac{D}{S} \left[\Delta L_r - E \Delta L_o \right] - F \Delta(<P>)
\end{aligned}
\right\}
\qquad , \qquad (E-18)
$$

where the coefficients in (E-18) involve the constants K_1 to K_4 and the average values of the temperature, pressure, and water vapor density. These coefficients are sensitive to the average conditions selected and can change appreciably. Graphs can be constructed so that appropriate coefficients can be chosen. For assumed values of

$$
<\bar{P}> = 1000 \text{ mb},
$$

$$
<\bar{T}> = 293 \, ^{\circ}K,
$$

$$
<\bar{\rho}_w> = 10 \text{ g/m}^3 \text{ (RH = 58\%)},
$$

79

$$\Delta <\rho_w> = \frac{1.69 \times 10^5}{S} [\Delta L_r - 1.17 \Delta L_o] + 0.009 \Delta <P>$$

$$\Delta <T> = \frac{1.05 \times 10^6}{S} [-0.0091 \Delta L_r - \Delta L_o] + 0.292 \Delta <P>$$, (E-19)

which is of course similar to (E-17). We see that $\Delta <\rho_w>$ is only weakly dependent upon pressure changes, whereas $\Delta <T>$ is significantly influenced. The sensitivity of the coefficients in these expressions can be appreciated when it is realized that a change in the mean value of $<\rho_w>$ of 2 g/m³ (a change of 12 percent in relative humidity at 293 °K) produced négligible change in either $\Delta <\rho_w>$ or $\Delta <T>$; a change of 10 mb in the pressure reflected a change of less than 1 percent in the amplitude of $\Delta <\rho_w>$ or $\Delta <T>$; a change of 5 °C in the mean value of the temperature will cause approximately a 3.5 percent change in the apparent amplitude of both $\Delta <\rho_w>$ and $\Delta <T>$. Hence, the degree of accuracy desired in the estimation of fluctuations of $<\rho_w>$ or $<T>$ about an arbitrary mean will determine the range over which these coefficients can be assumed constant. This is, more or less, under the control of the experimenter.

Consider how these perturbations are affected by the precision in ΔL_r and ΔL_o. A precision of approximately 1 part in 10^7 would be required for ΔL_r and ΔL_o. Then, from (E-19), the resolution in $\Delta <T>$ would be approximately 0.1 °C and that of $\Delta <\rho_w>$ would be 0.02 g/m³.

E.4. Experimental Use of a Microwave-Optical System to Measure Water Vapor Density Variability

For a 5 1/2-day period at Lake Hefner, Oklahoma, in August 1966, a microwave phase system (Gilmer and Waters, 1967, app. D), as well as an optical distance-measuring system (Earnshaw and Owens, 1967) were installed on a 1.65-km path over the lake.

Meteorological measurements were made at both terminals and on a tower at the path. Since evaporation-suppressing films were spread from time to time on the surface of the lake, a large range of humidities were provided (based on 107 samples of 10-sec averages taken every half hour). The initial results have been published by Bean and Emmanuel (1967). Figure E.2 illustrates the comparison between the fluctuations in the radio path length and the variations in the water vapor density measured at the center of the path. Figure E.3 shows the relationship between variations in the optical path length, L_o, and temperature variations at the center of the path. The correlation coefficients between these variables (where ρ in the air density) are as follows:

Variables	Correlation
L_o vs. T	-0.915
L_o vs. ρ	0.923
L_r vs. ρ_w	0.956
$T(L_r - L_o)$ vs. ρ_w	0.978

It can be seen that the correlation between the radio path length, an integrated measurement, and the water vapor density, a point measurement, is quite good; however, a definite improvement results when the radio path is corrected by the optical path. The correction applied here was a first approximation, since we assumed that the effect of the air density was the same at both radio and optical frequencies.

On the average, good agreement is found between water vapor fluctuations and radio and optical path length variations. One can also compare the variance of water vapor density as measured at a point with that of the radio path length. Twenty-three 10-min samples (sampling rate= 1 sample/sec) were selected of the variance of the radio path length and of the variances of both water vapor density and the radio
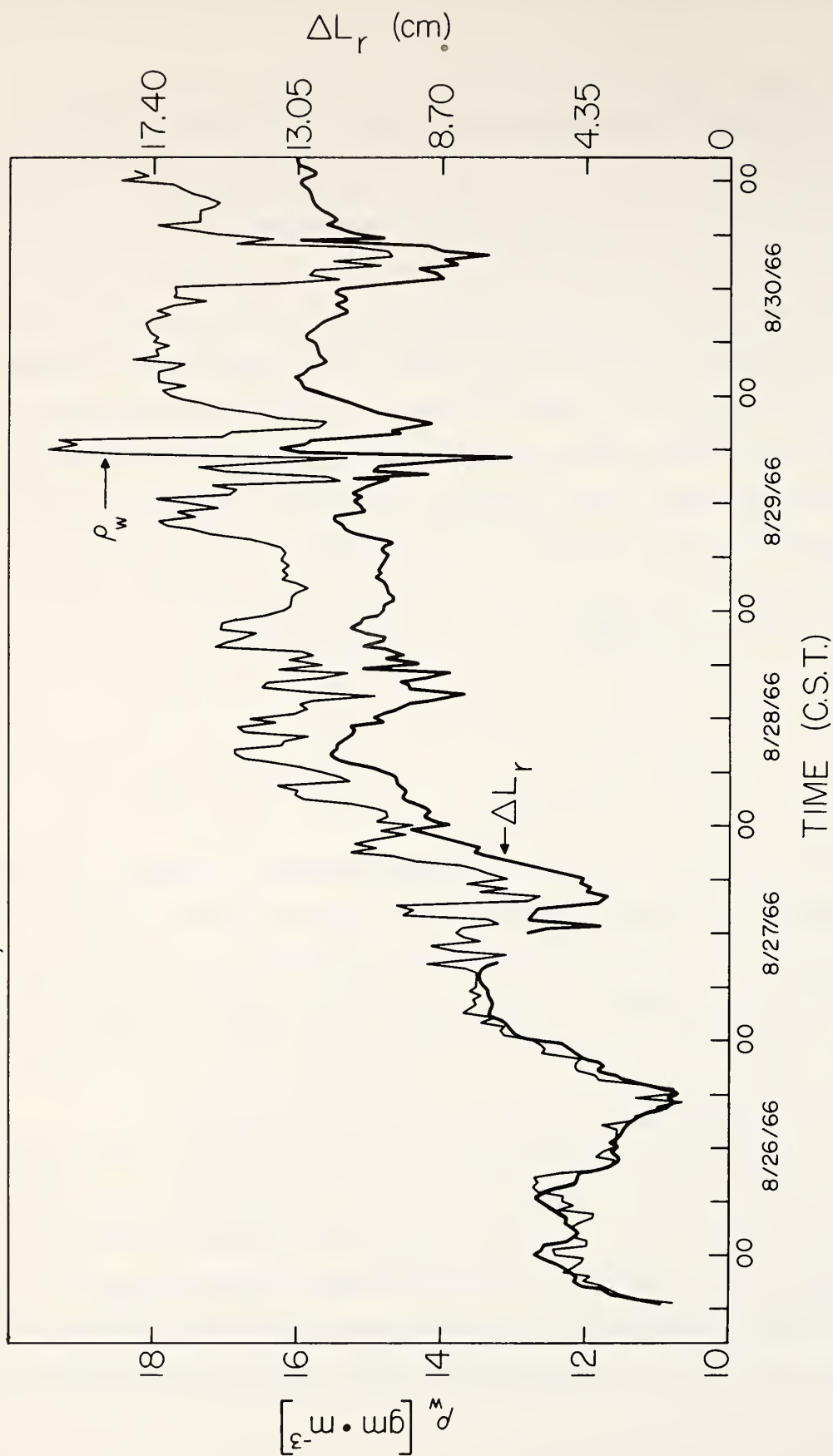
Figure E.2. A comparison of the radio path length fluctuations ΔL_r with variations in the water vapor density ρ_w.

82
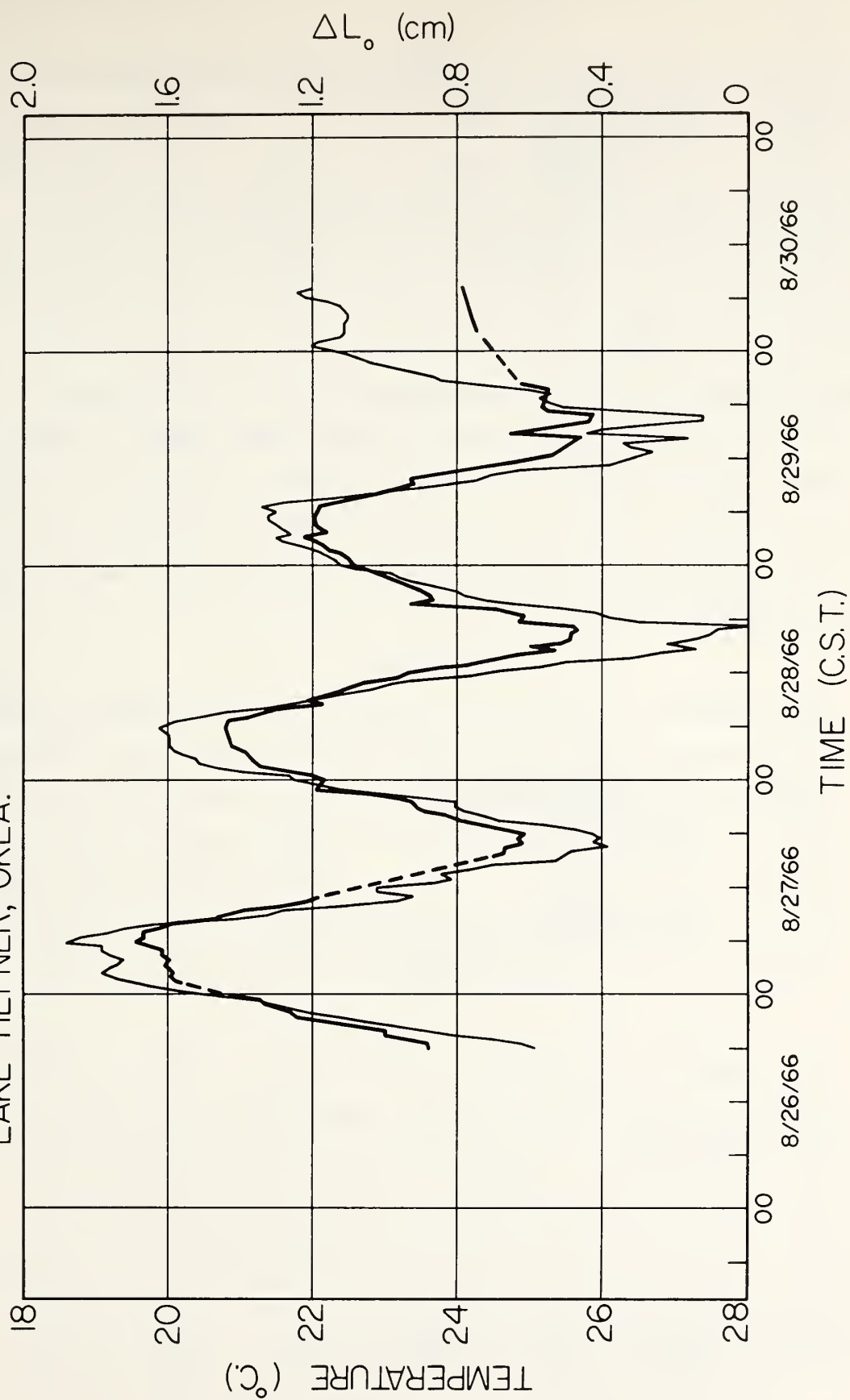
Figure E.3. A comparison of the optical path length fluctuations, ΔL_o (heavy line) with temperature.

83

refractive index at the center of the path. The correlation between the variance of the refractive index and the variance of water vapor density, both measured at the center of the lake is, as expected, quite high (0.920). The correlation between the variance of the point measurement of the refractive index and the variance of the radio path length is lower (0.732) and that between the variances of water vapor density and the radio path still lower (0.554). Again one may wish to know how these variances are distributed and compare the spectrum of the water vapor density at the center of the path to the spectrum of the radio path length. Figure E.4 shows the spectrum of the water vapor density at the path for daytime and nighttime conditions with and without the evaporation suppressing film on the water surface. Figure E.5 is the spectrum of the radio path during the same times.

E.5. Conclusions

Measurement of both the radio and optical path lengths to determine integrated water vapor density and temperature over a path appears to be a useful technique. The absolute value of $<\rho_w>$ can be measured with an uncertainty of approximately 2.75 percent, while that of $<T>$ reflects an uncertainty of approximately 0.6 percent. Under average temperate conditions, such techniques can resolve variations in $<\rho_w>$ of approximately 0.02 g/m^3 and can resolve variations in $<T>$ of approximately 0.01 $^\circ$C.

With expected improvements in these techniques, it is possible that the uncertainties due to measurement capabilities can be reduced to several tenths of a percent. When these system improvements become available, the applicability of the approximations used here would be questionable. Ultimately the precision of the coefficients in the equations for refractive index would be the limiting factor. This is particularly true for the coefficient for the water vapor term.

84
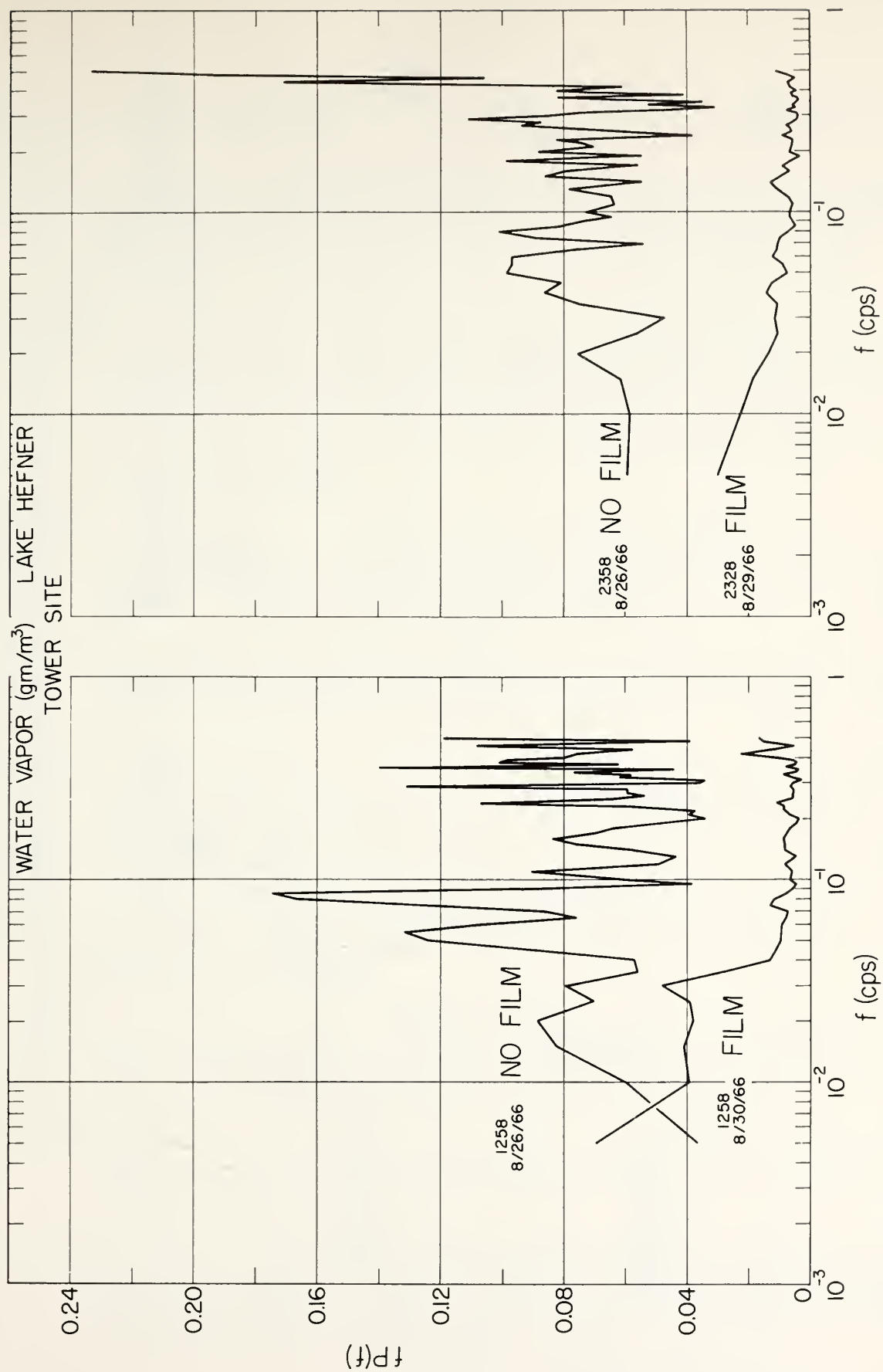
Figure E.4. Spectral variation of water vapor density as observed with tower-mounted barium fluoride elements at Lake Hefner, Oklahoma.

85
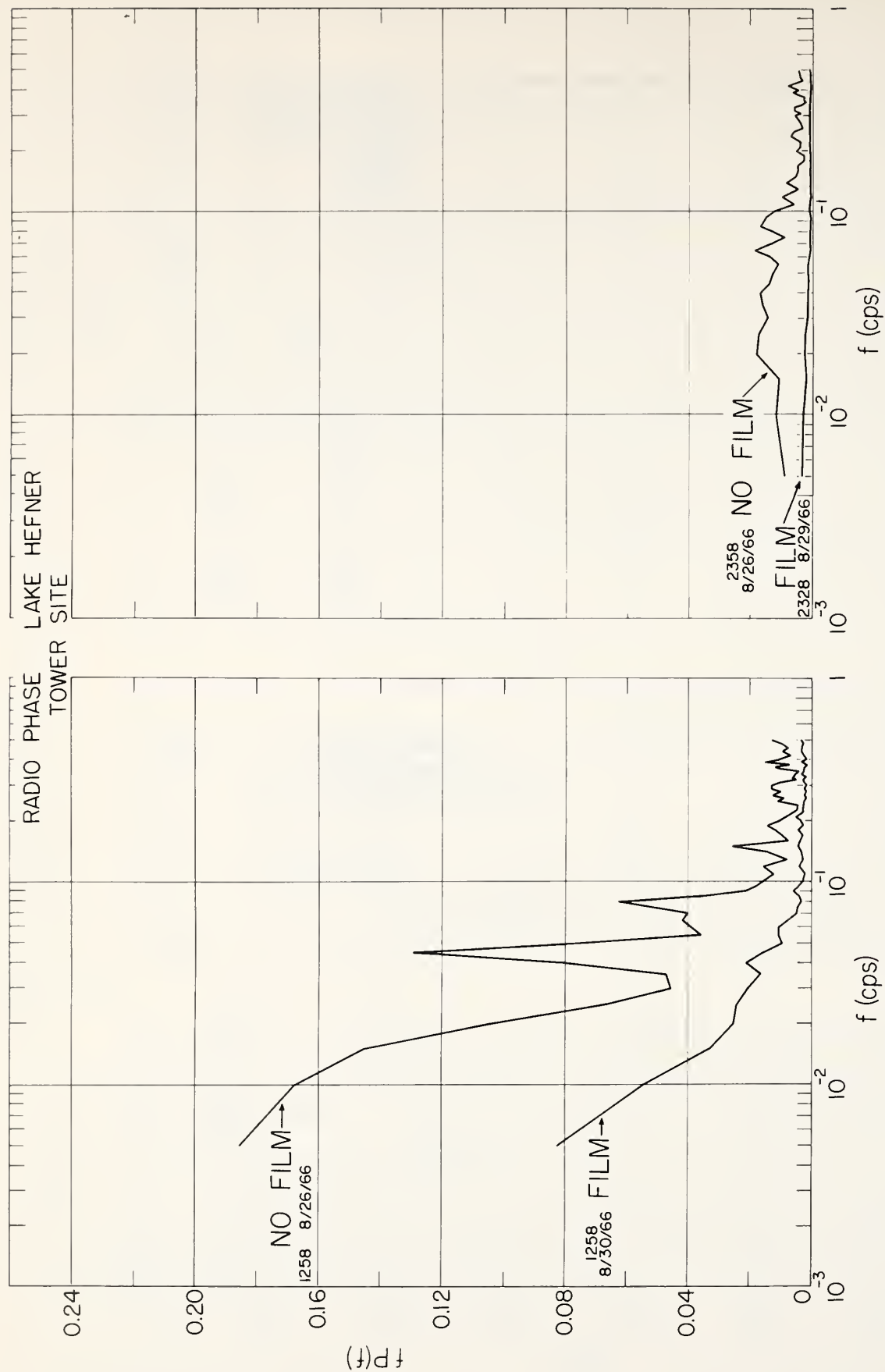
Figure E.5. Spectral variation of radio phase as observed with and without film under the sensors.

References

Bean, B. R., and E. J. Dutton (1966), Radio Meteorology, NBS Monograph 92 (U. S. Government Printing Office, Washington, D.C.).

Bean, B. R. and C. B. Emmanuel (1967), Application of radio and optical path length measurements to studies of low-level turbulence, Proc. Tech. Exchange Conference, Air Weather Service, U.S. Air Force, 294-296.

Bean, B. R. and R. E. McGavin (1965), The use of the radio refractometer to measure water vapor turbulence, Proc. Intern. Symp. On Humidity and Moisture, II (Reinhold, New York, N.Y.)

Bender, P. L. (1967), Laser measurements of long distances, Proc. IEEE 55, 1039-1045.

Earnshaw, K. B. and J. C. Owens (1967), A dual wavelength optical distance measuring instrument which corrects for air density, IEEE J. Quantum Electronics 3, 544-550.

Gilmer, R. O. and D. M. Waters (1967), A solid state system for measurement of integrated refractive index. Tech. Rept. IER 40-ITSA 40 (U.S. Government Printing Office, Washington, D.C.).

Herbstreit, J. W. and M. C. Thompson, Jr. (1955), Measurement of the phase of radio waves received over transmission paths with electrical lengths varying as a result of atmospheric turbulence, Proc. IRE 43, No. 10, 1391-1401.

Owens, J. C. (1967), The use of atmospheric dispersion in optical distance measurements, Rept. to XIV General Assembly IUGG, Lucerne, Switzerland.

Thompson, M. C., Jr. and H. B. Janes (1964), Radio path length stability of ground-to-ground microwave links. NBS Tech. Note No. 219. (U.S. Government Printing Office, Washington, D. C.).

Thompson, M.C., Jr. and H. B. Janes (1959), Measurement of phase stability over a low level tropospheric path, J. Res. NBS 63D (Radio Prop.) No. 1, 45-51.

Thompson, M. C., Jr. (1967), A summary of progress in problems related to terrestrial electronic distance measuring in the U. S. since 1963, AGU Rept. to IUGG General Assembly, Geodesy Section, Lucerne, Switzerland.

APPENDIX F

CHARACTERISTICS OF SENSORS AND RECORDING EQUIPMENT
LAKE HEFNER, OKLAHOMA, 1966 AND 1967

F.1. Temperature

Sensor: Thermocouple, welded, 2-mil, copper-constantan junction. Estimated 0.05 sec for 95 percent recovery of a step change.

Signal conditioning: D-C amplifier, high gain, differential, guarded, low noise, stable.

Accuracy: Absolute error from all sources (with periodic calibration checks) $\leq 0.1\ ^{\circ}C$. Relative response to change better than $0.05\ ^{\circ}C$.

Response time: Overall response is flat from d-c to 10 Hz (limited by filters in recorder).

F.2. Relative Humidity

Sensor: Variable resistance strip - barium fluoride (BaF_2) deposited on glass strip. Resistance varies logarithmically with relative humidity. Estimated 0.05 sec or 95 percent recovery of a step change.

Signal conditioning: Log-to-linear electronics designed by ESSA. Overlapping ranges of output linear with changing relative humidity.

Accuracy: Absolute error from all sources (with periodic calibration checks) ≤ 2 percent. Relative response to change better than 1 percent RH.

F.3. Vector Wind

Sensor: Anemometer bivane, low inertia, fast response, bidirectional vane. Propeller-driven wind speed with matched dynamic response.

Signal conditioning: Power supply for excitation of potentiometers for wind vane. Wind speed signal is obtained from miniature d-c tachometer and is amplified for recording.

Accuracy and response time: Threshold sensitivity of vane and propeller, 0.13 to 0.22 mps. Damped natural wavelength of vane, 5.8 m. Maximum overshoot for sinusoidal fluctuations 2 percent. Distance constant of propeller is .75m. At wind speeds above 2.7 mps, all wind direction fluctuations up to 0.5 Hz are recorded accurately. More rapid fluctuations are recorded with a reduced amplitude. The propeller rotates accurately for all wind speeds above 1.2 mps, with increasing slippage down to the threshold speed.

F.4. Radio Refractivity

Sensor: Microwave cavity of rapid response (see Gilmer et al., 1965).

Signal conditioning: NBS relative refractometer

Accuracy: For wind speeds less than 13 mps, the error is less than 0.1 N units.

Response: For uniform air flow in excess of 4.5 mps, the cavity is expected to resolve variations separated by 1 m. Variations separated by .4m are estimated to be in error by as much as 20 percent with rapid degradation of response as separation of variations decreases.

F.5. Vertical Wind

Sensor: Two-transducer pulsed type sonic anemometer.

Signal conditioning: Electronics to measure transit time of the sound pulse.

Accuracy: Zero drift less than ± 3 cm/sec for temperature changes of the order of 20 $^\circ$C. Peak-to-peak noise less than 3 cm/sec in actual wind velocities encountered.

Response: The total sampling rate of the instrument is 70 Hz, but the spatial resolution is actually limited by the length of the acoustical path (20 cm).

Reference

Gilmer, R. O., R. E. McGavin, and B. R. Bean (1965), Response of NBS microwave refractometer cavaties to atmospheric varia- tions, Radio Sci. 69D, No. 9, 1213-1217.

APPENDIX G

THE EFFECT OF EVAPORATION ON THE STABILITY OF THE ATMOSPHERE IN THE BOUNDARY LAYER

G.1. Introduction

The stability of the atmosphere in the boundary layer is usually described by the dimensionless parameter z/L, where L is the Monin-Obukhov length defined by

$$L \equiv - \frac{\rho c_p u_*^3 T}{kgH} .$$
(G-1)

In (G-), ρ is the air density; c_p is the specific heat at constant pressure; u_* is the friction velocity; T is the temperature; k is the von Karman constant; g is the acceleration due to gravity; and H is the vertical heat exchange per unit area. Substituting the defining equations for u_* and H in (G-1) results in

$$L \equiv - \frac{[<u'w'>]^{3/2} T}{kg <w'T'>} ,$$
(G-2)

where u and w refer to the horizontal and vertical wind components, respectively, and the primes denote the fluctuations about the mean value of the appropriate quantities. The $<>$ imply a time average. As defined by (G-2), however, L does not include an appropriate term to account for the effect of evaporation. This effect is not expected to be of importance on measurements made over dry land; nevertheless, conditions might occur, especially if open water exists upwind, when the effect of evaporation may not be negligible.

G. 2. Theoretical Development

A rather simple approach in the determination of the effect of evaporation on the stability parameter, as expressed by z/L, was suggested by Swinbank (1964), although the prevailing experimental conditions were such that they afforded the omission of evaporation from his discussion of the exponential wind profile.

The effect of evaporation may be considered by introducing in the conservation of energy expression for a parcel of air the appropriate buoyant term to accommodate such an effect. Thus, we may write

$$\frac{\partial F}{\partial z} + \varepsilon = \tau \frac{\partial u}{\partial z} + g \left[\frac{\rho <w' T'>}{T} + \frac{3}{5} <\rho_w' w'> \right] , \qquad (G-3)$$

where the left side refers to the kinetic energy of turbulence (the first term being the divergence of its vertical flux, ε the rate of dissipation by viscous forces), and the right side represents the rate of working of the shearing stress on the mean rate of strain and by buoyancy against gravity (τ being the shearing stress, ρ_w' the flucutations of the water vapor density about the mean value). The factor 3/5 comes about because the form of the buoyance term is

$$\left[\frac{R'}{R} - 1 \right] <\rho_w' w'>, \qquad (G-4)$$

where the ratio of the gas constants for water vapor to dry air, R'/R, is, approximately, 8/5.

Following the argument given by Swinbank (1964), let us now define a nonlinear height variable x so that

$$\frac{\partial u}{\partial x} = \frac{u_*}{k x} \qquad (G-5)$$

is satisfied. Similarly, let us assume that

92

$$\tau \frac{\partial u}{\partial x} + g \left[\frac{\rho <w'T'>}{T'} + \frac{3}{5} <\rho_w{'}w'> \right] = \tau \frac{\partial u}{\partial x} . \qquad (G-6)$$

Elimination of u between (G-5) and (G-6) yields

$$\frac{dx}{dz} = 1 - \frac{k_g <w'T'>}{u_*^3 T} x - \frac{3}{5} \frac{k_g <\rho_w{'}w>}{\rho u_*^3} x , \qquad (G-7)$$

where use has been made of the fact that

$$\tau = \rho u_*^2 .$$

Let

$$\beta \equiv \frac{3}{5} \frac{k_g <\rho_w{'}w>}{\rho u^3} , \qquad (G-8)$$

then (G-7) takes the form

$$\frac{dx}{dz} - \left[\frac{1}{L} - \beta \right] x = 1, \qquad (G-9)$$

which upon integration yields

$$x = \frac{L}{1 - L\beta} \left[\exp\left(\frac{z}{\dfrac{L}{1 - L\beta}} \right) - 1 \right] . \qquad (G-10)$$

Comparison of this expression with that given by Swinbank (1964) results in a definition of the Monin-Obukhov length with the effect of evaporation included as

$$L* \equiv \frac{L}{1 - L\beta} , \qquad (G-11)$$

or

$$L^* \equiv \frac{L}{1 + \dfrac{3}{5} \dfrac{T}{\rho} \left(\dfrac{<\rho_{w'}w'>}{<w'T'>} \right)} . \qquad (G-12)$$

93

We can readily see from this expression that the magnitude of the ratio of the water vapor flux to the temperature flux determines the departure of L^* from L. It is, therefore, quite conceivable that occasions might arise even over dry land when such a ratio is not insignificant, making a significant contribution to L.

G.3. Some Experimental Results

Recent experimental studies conducted at Lake Hefner, Oklahoma, on the evaporation suppressing qualities of monomolecular films (Bean and Florey, 1968) have also yielded information on the effect of evaporation on the Monin-Obukhov length L.

A tower was installed about one-third the distance across the lake on a north-south line. Measurements of temperature, relative humidity, and vector wind were obtained at 2 m above the lake surface. The signals from all sensors were preconditioned, and the information was recorded on magnetic tape by an analog FM method. The recorded data were then sampled and digitized at the rate of 25 samples/sec in 10-min blocks. From these data, 10-min average values were obtained for the momentum, temperature, and water vapor fluxes. In addition, 10-min average values were obtained for the absolute temperature, T.

Thirty-seven 10-min periods were chosen for analysis from data taken during a 5-day period commencing on 25 August and terminating on 30 August, 1966. Figure G.1 presents the results of the analysis. Note that 80 percent of the time $L^* > L$; hence

$$(z/L) > (z/L^*).$$

In those samples where $L^* < L$, $<w'T'>$ is negative, implying conditions of thermal stability.
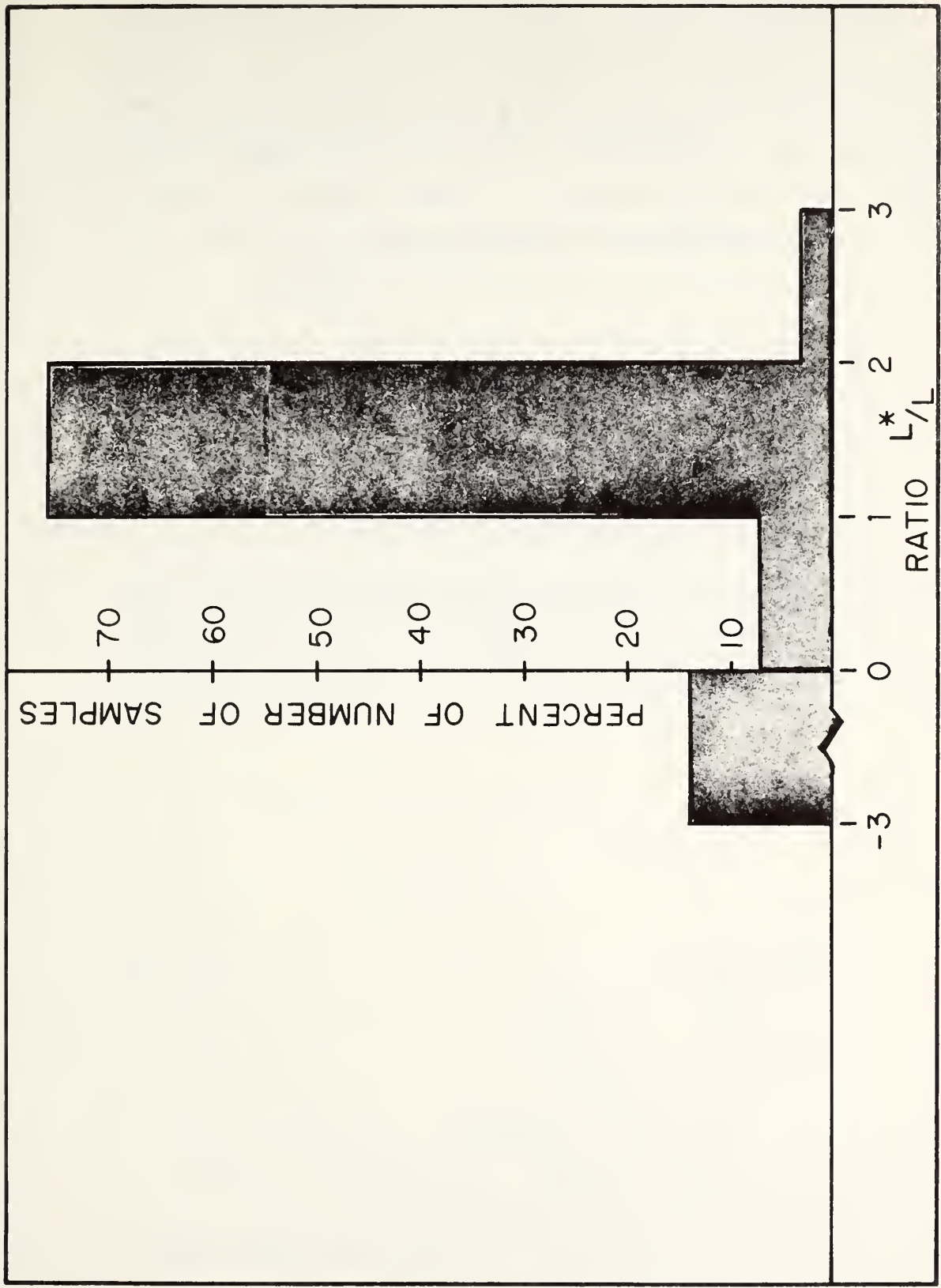
Figure G.1. The effect of evaporation on the stability parameter L.

G. 4. Conclusions

Although the behavior of temperature and momentum fluxes is both complex and erratic, due in part to the presence of the evaporation suppressing film, the foregoing results indicate that evaporation plays a significant role in the establishment of the stability level of the boundary layer. The results shown in fig. G.1 indicate that the presence of evaporation has the effect of decreasing the level of stability; hence its effect cannot be neglected from stability considerations.

References

Bean, B. R., and Florey, Q. L. (1968), A Field Study of the Effectiveness of Fatty Alcohol Mixtures as Evaporation Reducing Monomolecular Films, Water Resources Research, 4, No. 1, 206-208.

Swinbank, W. C. (1964), The Exponential Wind Profile, Quart. J.R. Met. Soc. 90, No. 384, 119-135.

SOME RADIO-PHYSICAL CONSIDERATIONS
IN STUDIES OF THE FINE SCALE STRUCTURE
OF THE ATMOSPHERE

B. R. BEAN and B. D. WARNER

*National Burreau of Standards, Boulder,
Colorado, U.S.A.*

1. INTRODUCTION

This conference is concerned with radio and meteorological studies of atmospheric structure with particular emphasis upon scales of motion less than about 20 metres. One is guided in these studies by an awareness that the basic physical processes involved are abundantly disguised by the stochastic nature of the atmosphere in which these studies must be conducted. It is the purpose of this paper to present some of the background to the author's present work.

2. RADAR PROBING OF THE CLEAR AIR

There is abundant evidence that radar returns are obtained from the clear atmosphere (Saxton, *et al* [6], Fehlhaber and Grosskopf [3], Eklund [2]). There remains however, a question as to the physical cause of the returns with some arguments favouring sharp atmospheric refractive index discontinuities while others favour scattering from insects or birds [See Proceedings of the 1964 World Conference on Radio-Meteorology]. It seems reasonable however, that whatever the eventual source of such returns might be — a «signature» of the source will be contained in the angular dependence of such returns.
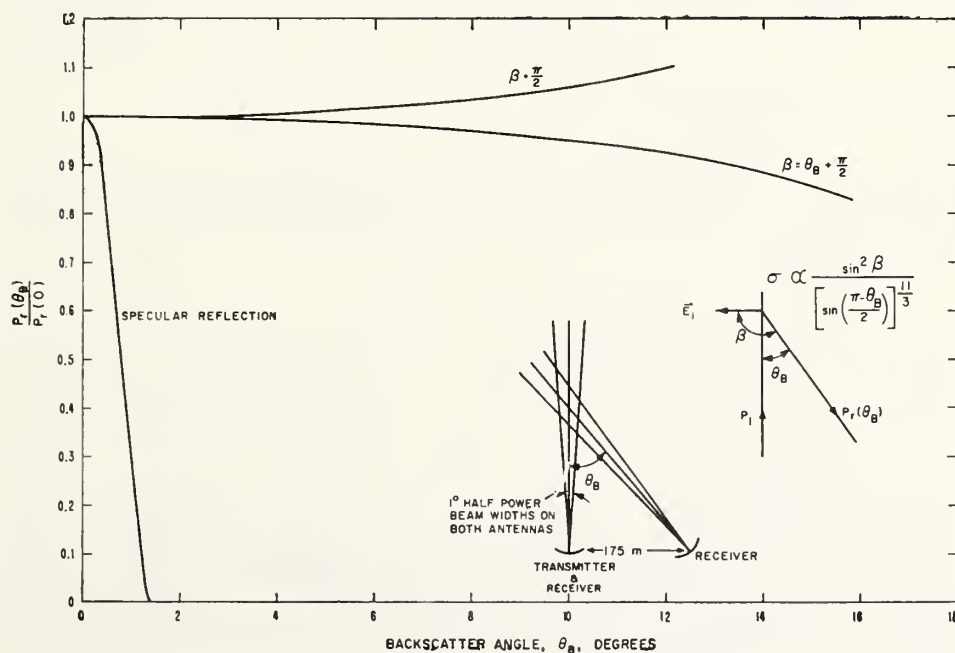
Fig. 1. Bi-static radar experiment

An experiment was devised to test this hypothesis. The essential geometry is shown in Fig. 1 where a radar pulse is received at both the transmitting antenna and a passive receiver separated by an angular distance θ_B from the source of the clear air returns. One now considers the ratio of the power received at angle θ_B to that received from vertical incidence,

$$P_r(\theta_B)/P_r(0). \tag{1}$$

The power ratio for volume scatter may be estimated from the scattering cross-section (Saxton, *et al* [6])

$$\sigma_V = \frac{\overline{(\Delta n)^2} \sin^2 \beta}{32 \sin^4\left[\dfrac{\pi - \theta_B}{2}\right]} K^2 F_n(K) \tag{2}$$

where $\overline{(\Delta n)^2}$ = total mean square fluctuation of refractive index

θ_B = backscatter angle

β = angle between the direction of scattering and the incident electric field vector

K = wave number of spatial-index fluctuations selected by transmitter wavelength with

$$K = \frac{4\pi}{\lambda} \sin\left[\frac{(\pi - \theta_B)}{2}\right]$$

$F_n(K)$ = value of normalized spectral density of $\overline{(\Delta n)^2}$ at wave number K. For the purpose of this discussion, the spectral density, $F_n(k)$, shall be taken as that derived by Oboukhov,

$$F_n(k) = \frac{2}{3} k_1^{2/3} k^{-5/3} \tag{3}$$

where k is now the general wave number and k_1 is a number describing the large — eddy end of the spectrum. The ratio of angular backscatter, $\sigma_V(\theta_B)$, to direct backscatter, $\sigma_V(0)$, is then given by

$$\frac{P_r(\theta_B)}{P_r(0)} \propto \frac{\sigma_V(\theta_B)}{\sigma_V(0)} = \frac{\sin^2 \beta}{\sin^{11/3}\left(\dfrac{\pi - \theta_B}{2}\right)} \tag{4}$$

Note that

$$P_r(\theta_B)/P_r(0) \geqslant 0.85 \tag{5}$$

throughout the range $\theta_B \leqslant 15°$. Compare this angular variation of power ratios, however, with that for specular reflection from a horizontal flat plate as obtained by

$$\frac{P_r(\theta_B)}{P_r(0)} \approx \frac{\Gamma(\theta) G(\theta) G(\theta_B - \theta)}{G^2(0)} \approx \frac{G(\theta) G(\theta_B - \theta)}{G^2(0)} \tag{6}$$

where θ is the angle of incidence, θ_B is the backscatter angle, $\Gamma(\theta)$ is the power reflection coefficient, and $G(\theta_B - \theta)$ is the antenna gain as a function of angle. The geometry for this condition results from image theory and is shown in Fig. 2.

It is evident that these simple models of the source of clear air returns give remarkably different distributions of $P_r(\theta_B)/P_r(0)$. Fig. 3 gives the first results of an experiment carried out with 3 — cm radars at Gunbarrel Hill, Colorado. The data made it evident that these initial angular returns during the turbulent daytime hours are best interpreted as a result of scattering. Therefore, the figure is presented in terms of the ratio $\sigma_V(\theta_B)/\sigma_V(0)$ rather than power ratios, where $\sigma_V(\theta_B)$ is the volume scattering coefficient with dimension L^{-1} at the angle θ_B.

216

The data were obtained for two conditions of relative antenna positions: polarized and cross-polarized. For the polarized condition, both antennas were aligned such that their E-planes were parallel with the plane of Fig. 1, corresponding to $\beta = \theta_B + \pi/2$. The cross-polarized condition was obtained by rotating the transmitting antenna so the E-plane becomes normal to the plane of Fig. 1 while keeping the E-plane of the receiving antenna in the plane of Fig. 1. The cross-polarized condition corresponds to $\beta = \pi/2$ with the receiving antenna orthogonal to the transmitting antenna.

The data points are the mean values of time coincident samples of $\sigma_V(\theta_B)/\sigma_V(0)$ with the number of samples used indicated by each data point. The cross-polarized data contained a considerable amount of time where a coincident return could not be found on the spaced receiver. These points were included as zeros in computations of the means.

Fig. 2. Specular reflection geometry

The four data points for polarized antennas are within 1 dB of the isotropic line $(\sigma_V(\theta_B)/\sigma_V(0) = 1.0)$ while the cross-polarized antennas give data points which are 10 dB or more below the isotropic line. Even if the samples which are zero are removed from the cross-polarized data, the points are still 8 dB or more below the isotropic line.
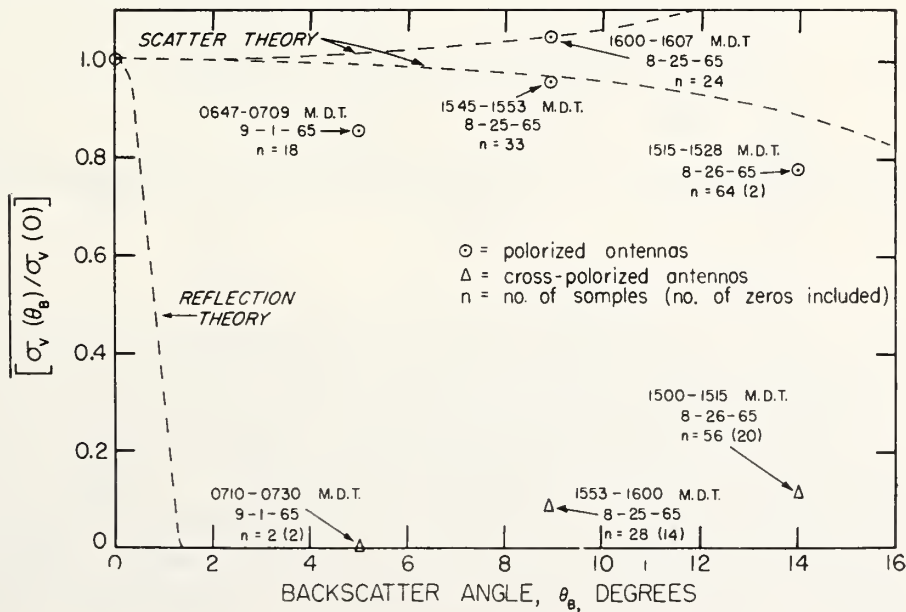
Fig. 3. Experimental results

These first tentative data indicate that dot angel returns appear to be of a scattered origin. It is evident from the raw data that the early morning returns were of a different class than those of the afternoon; the scattering cross-sections are of the order of 10 to 20 dB higher in the early morning. There was also observed a rapid decrease in the frequency of occurrence of returns during two consecutive twenty-minute periods during the early morning hours. The frequency of occurrence of afternoon returns is approximately 4 to 5 times that of the early morning scatterers, in general agreement with the experience of others (Ottersten [5]). These observations will probably lead to more than one classification of echoes as the data analysis continues. At this time, it is not inconceivable to presume that there may be both specular and scatter type dot angels, both of which appear to be of a coherent origin. It is also evident the cross-polarized echoes must be examined closely.

3. VARIATION OF RADIO PATH LENGTH

One must bear in mind that although the propagation of radio waves through the troposphere is controlled by the refractive index, the variations of the refractive index are often controlled by those of atmospheric water vapour. As an example, consider the variation of radio path length, L, as measured over a path of geometric distance S

$$L = \int_0^S n \, ds \tag{7}$$

where n is the radio refractive index. The refractive index may be written

$$n = 1 + K_1 \rho + \frac{K_2 \rho_w}{T} \tag{8}$$

where ρ = density of air (gm/m^{-3})
ρ_w = density of water vapour.
T = temperature in degrees Celsius.
If one now assumes an average, T, ρ and ρ_w over the radio path (7) becomes

$$L = S + K_1 \bar{\rho} S + K_2 \frac{\overline{\rho_w}}{T} S \tag{9}$$

where the overbar denotes the path average. Rewriting (9)

$$\frac{L - S}{S} = K_1 \bar{\rho} + \frac{K_2 \bar{\rho}_w}{\overline{T}}. \tag{10}$$

One may obtain an estimate of the space averaged — or integrated water vapour density from

$$\bar{\rho}_w = \frac{\overline{T}}{K_2} \left(\frac{L - S}{S} - K_1 \bar{\rho} \right). \tag{11}$$

Fig. 4 illustrates this procedure where, for convenience, all data are expressed in parts per million (ppm). These data, taken by Dr. M. C. Thompson of the CRPL during May 9—12, 1961 and kindly provided to the authors, were for a 15.5 km path near Boulder, Colorado. Available throughout the three days period were the single path phase, expressed in ppm and thus fully equivalent to $(L - S)/S$ in ppm, temperature, pressure and water vapour density as deduced from standard psychrometric observations at both terminals of the radio path. The upper curve in Fig. 4, radio path length, represents a 5-minute time average taken every half hour and varies from 221 to 262 ppm throughout the three days period of observation. The rapid rise of radio path length of over 30 ppm in the morning of May 12 coincides with the passage
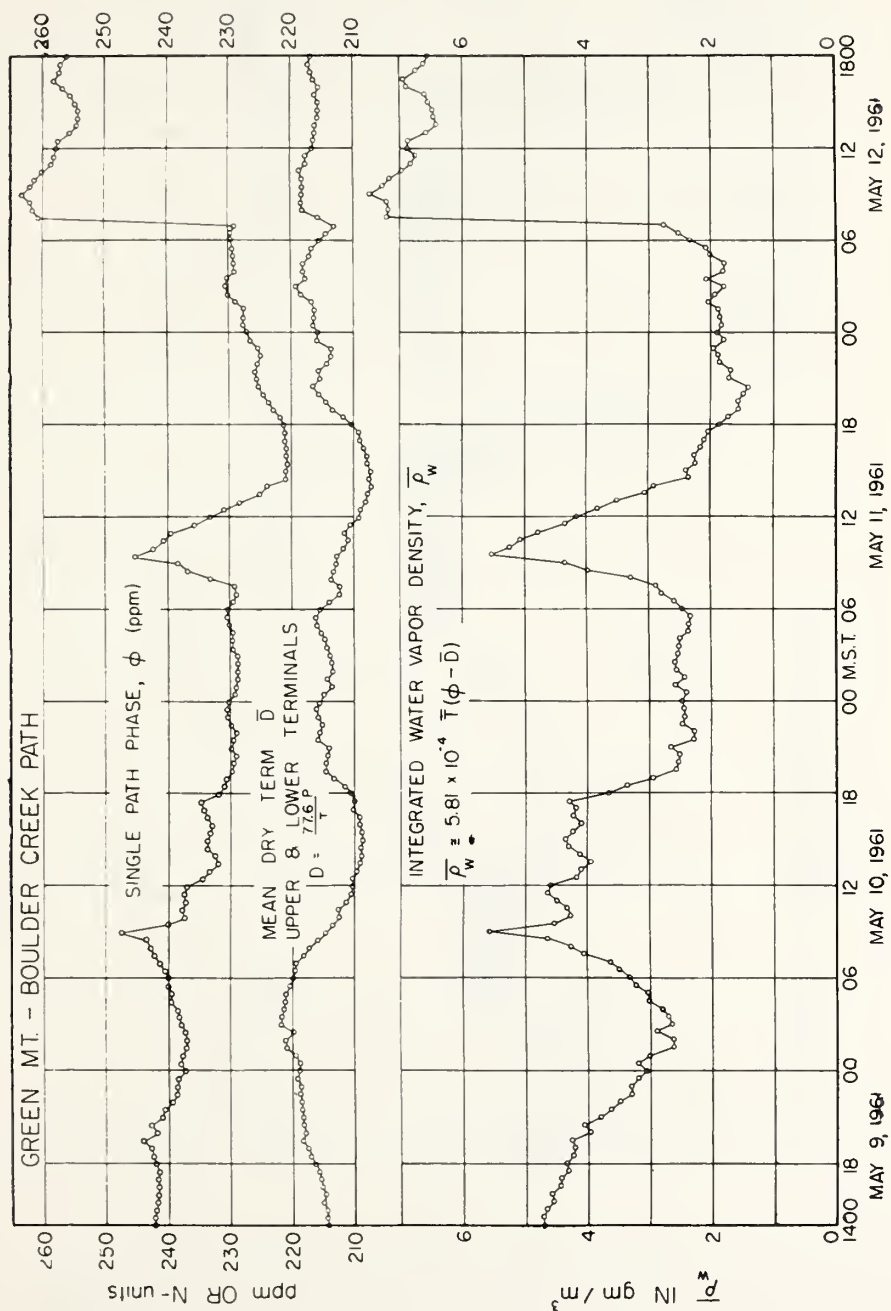
Fig. 4. Integrated water vapour density determined from variations of radio path length, temperature, and pressure
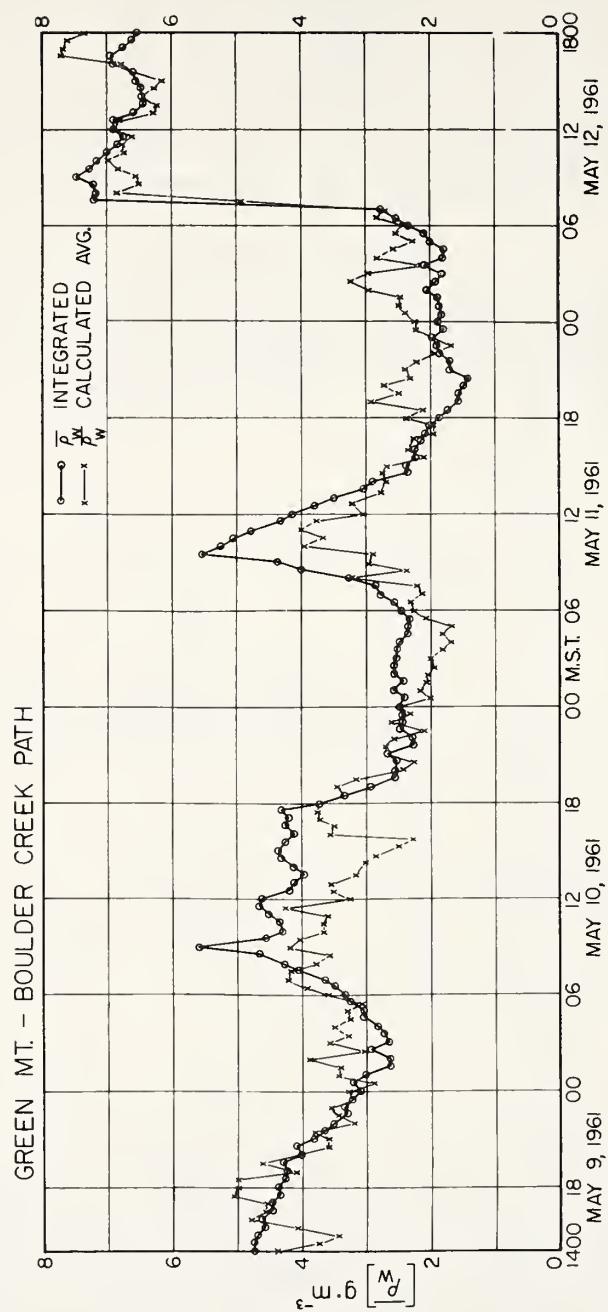
Fig. 5. Integrated water vapour density as compared to calculated average terminal point water vapour density
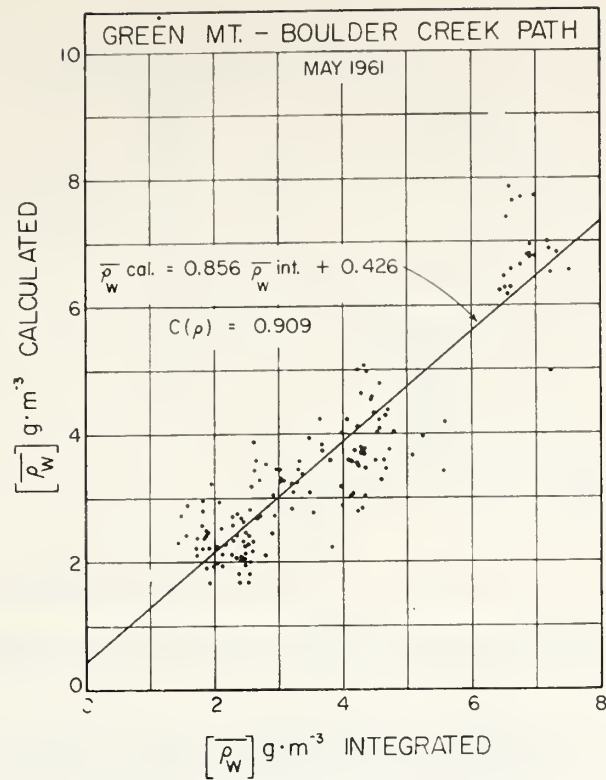
Fig. 6. Calculated versus integrated water vapour density
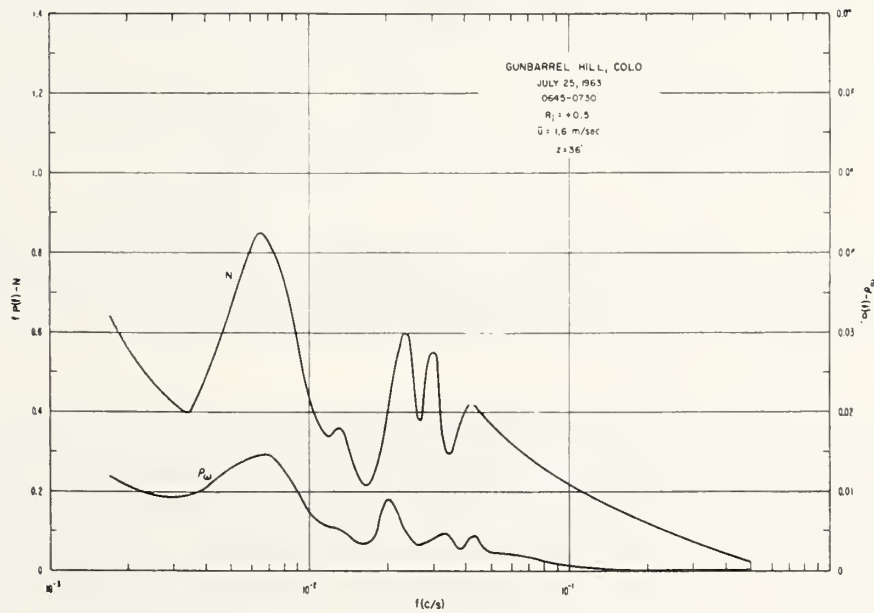
Fig. 7. Refractive index and water vapour density spectra for stable conditions
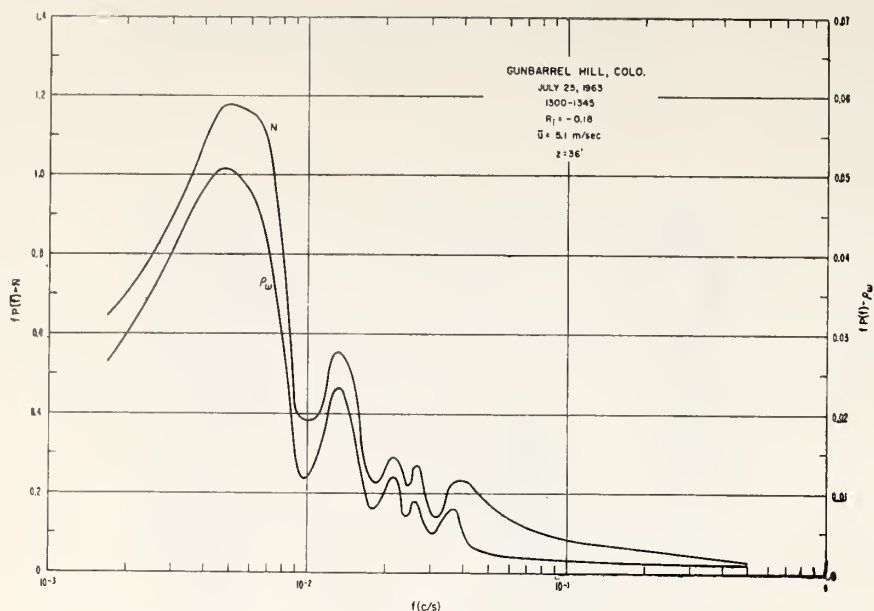
Fig. 8. Refractive index and water vapour density spectra for unstable conditions

of a cold front over the radio path. The smaller peaks at 0800 on May 10 and 11 appear to be associated with the diurnal heating pattern of the slopes of Green Mountain. The lower curve in Fig. 4 represents the average water vapour density as determined from (11). Note that these values of water vapour density are determined *solely from measurements of the radio path length and atmospheric pressure and temperature*. This integrated water vapour density is compared to the averaged water vapour density from the radio path terminals in Fig. 5 and 6. The two estimates of water vapour density are in reasonable agreement throughout the period of observations.

These data suggest that radio path length measurements may be used as a method of studying humidity. The authors are, in fact, presently applying this technique to studies of evaporation from reservoirs.

The controlling effect of water vapour upon refractive index fluctuations may also be examined as a function of the frequency of fluctuations. Examples for stable conditions (Richardson's number, $R_i = +0.5$) and unstable conditions ($R_i = -0.18$) were drawn from the general turbulence studies conducted at Gunbarrel Hill at a height of 36 feet (Figs. 7 and 8). The refractive index was measured with a microwave refractometer and is given as

$$N = (n-1) \cdot 10^6 \qquad (12)$$

while the water vapour density was determined from wet and dry thermocouples. More information on experimental techniques and accuracies are given by Bean and McGavin [1]. Although one notes a general coincidence in the spectral distributions of N and ρ_w for both cases the unstable case, with large eddies of convective origin present, shows the best agreement. One may express this agreement in terms of the square root of the spectral coherence, which is similar to a correlation coefficient but is a function of frequency (Lumley and Panofsky [4]). The square root of the coherence is plotted in Fig. 9 versus wavelength as determined from $\bar{\mu}/f$ where $\bar{\mu}$ is the mean wind and f the frequency. It is seen that for both examples the (coherence)$^{1/2}$ exceeds 0.6 for wavelengths greater than 100 metres for both examples and decreases more rapidly for smaller scales for the unstable than for the stable case. This perhaps indi-

222
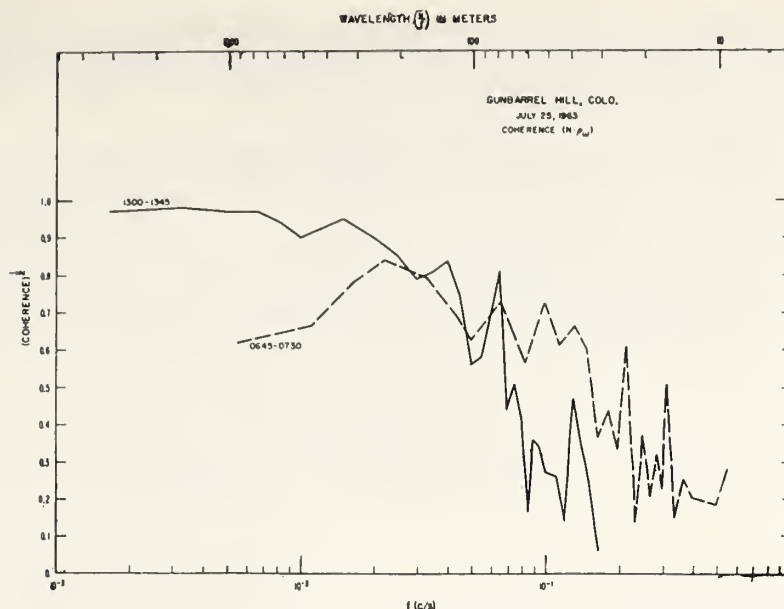
Fig. 9. Spectral coherence of refractive index and water vapour density

cates that throughout the range of eddies of wavelength greater than 100 metres, and thus containing a large percentage of the total power, refractive index fluctuations are controlled by those of water vapour.

4. CONCLUSIONS

This background paper has attempted to demonstrate that

(a) the angular pattern of radar returns from the clear air offers new information on the origin of such returns;

(b) variation in radio path length may closely coincide with those of water vapour density;

(c) the spectral density of the radio refractive index is frequently controlled by that of water vapour density.

REFERENCES

1. B. R. B e a n and R. E. M c G a v i n. The Use of the Radio Refractometer to Measure Water Vapour Turbulence. *Proceedings of the International Conference on Humidity and Moisture*, 1963. *Reinhold Publishing Corporation, New York*, 1963, 2.
2. F. E k l u n d. Models of the Troposphere Derived from Radiowave Propagation Experiments. *Progress in Radio Science*, 1960—1963, *Elsevier Publishing Co., Amsterdam, London, N. Y.*, 1965, 60—79.
3. Von L. F e h l h a b e r and J. G r o s s k o p f. Untersuchung der Struktur der Troposphäre mit einem Vertikalradar. *NTZ*, 1964, 17, 503—507.
4. L. L u m l e y and Hans A. P a n o f s k y. The Structure of Atmospheric Turbulence. *Interscience Publishers — John Wiley and Sons, N. Y.*, 1964.
5. H. O t t e r s t e n. Occurrence and Characteristics of Radar Angels Observed with a Vertically-pointing Pulse Radar. *Proc. of 1964 World Conference on Radio Meteorology*, 1964, 22—27.
6. J. A. S a x t o n, J. A. L a n e, R. W. M e a d o w s and P. A. M a t h e w s. Layer Structure of the Troposphere. *Proc. IEE*, 1964, 3, 275—283.

Discussion

J. A. Lane — Can Mr. Bean comment from his results on the effect of thermal stability on the spectral law and scale size of the refractive index irregularities?

B. R. Bean—Our preliminary results indicate that the refractive index spectra vary by a factor of 3 for conditions changing from stable to convectively unstable for periods of the order of 10 minutes. Our data do not as yet extend into the inertial subrange and thus do not give a measure of the slope in the inertial subrange.

H. A. Panofsky — Temperature and humidity spectra are available for the inertial subrange and indicate that the refractive index should follow the $-\,^5/_3$ law.

E. E. Gossard—Some measurements of refractive index fluctuations were carried out in 1964. Small deviations of spectra slope from $-\,^5/_3$ law were observed at low frequencies. The deviations were connected, perhaps, with the influence of gravity waves. At high frequencies spectra follow the $-\,^5/_3$ law.

"SUBSONIC" WAVES AND SEVERE WEATHER PHENOMENA

Howard S. Bowman

Environmental Science Services Administration

Geoacoustics Group

Rockville, Maryland 20852

A class of slow-traveling, low-frequency barometric-pressure associated waves was observed in the Washington, D. C. area. These waves are apparently associated with severe states of the local atmosphere. They were measured at the earth's surface and have characteristics similar to those of gravity waves. Experimental data are presented to verify a correlation.

At the infrasonic station in Washington, D. C., a class of slow-traveling, low-frequency waves was observed at the earth's surface. These waves have periods and velocities similar to certain internal gravity waves. In this report the waves are referred to as "subsonic" in the strict sense because their speed and frequency are below that of audible sound. Some of them have been associated with the jet stream near the tropopause, and some have been recently related to specific types of barometric pressure fluctuations. The literature (1,2,3, 4,5) gives account of measurements of the movement of pressure systems across the earth's surface, and it is already known that some moving pressure systems are related to weather extremes. The object of this report is to present experimental data which tend to show a possible relation between a particular class of "subsonic" waves and severe or unusual weather phenomena. The particular weather conditions considered are those given in U. S. Department of Commerce's "Storm Data" reports containing data for the Washington, D. C. area between 1963 and 1968. In this paper, emphasis is placed on such weather types as severe snowstorms and hail-producing thunderstorms. Accounts of the particular weather phenomena are shown in the appendix.

Local weather information and barometric pressure data were obtained from the National Weather Records Center in Asheville, North Carolina; radar data were obtained from the Washington, D. C. National Airport weather station. Barometric pressure data were also obtained from records made in our laboratory on a specially designed, highly sensitive milli-barograph that responds to short-period oscillations of atmospheric pressure in the order of minutes. Full-scale deflection on this instrument's recorder corresponds to ten millibars and the frequency response is within ± 1 dB between 0.1 and 0.001 Hz.

The "subsonic" waves were observed as ink tracings on transparent paper tapes. The tracings are the end product output of four infrasonic line microphones located about 5 to 10 km apart in the vicinity of Washington, D. C. The infrasonic measuring instrumentation has been described in the literature (6,7,8). Figure 1 is an example of four microphones' outputs. (In this figure and in Figure 3 a code is used to specify individual records, such as N9-8, D9-8, etc., where the letter refers to the microphone location, the first number refers to the pass band of interest, and the second number refers to the amplifier sensitivity setting.) The overlaid tracings in the lower portion of Figure 1 show the degree of coherence between the tracings when displaced along the time axis. The coherence of the overlay gives evidence of plane wave fronts passing the microphone array. Information on the time displacement of the overlaid traces and the known microphone locations was necessary to compute the horizontal trace velocity of the waves studied. The observed waves had periods between 4 and 15 min. and horizontal speeds between 10 and 100 m/s. The directions of the surface waves were associated with upper tropospheric jet winds and/or barometric pressure systems that were usually accompanied by severe local weather conditions.

The coherent waves noted on the overlaid tapes occurred during the same hour in which thunder was reported. These waves penetrated the high-frequency background pressure modulation of 7.6 m/s (17.0 mi/hr) local wind noise that existed throughout the entire interval. The "subsonic" waves and the thunder report were noted also during the time interval when the solid precipitation underwent a change of state (i.e., from light snow to light snow grains).

SNOW AND THUNDER-RELATED
SUBSONIC WAVES
WASH., D.C. AREA
(1/13/64)
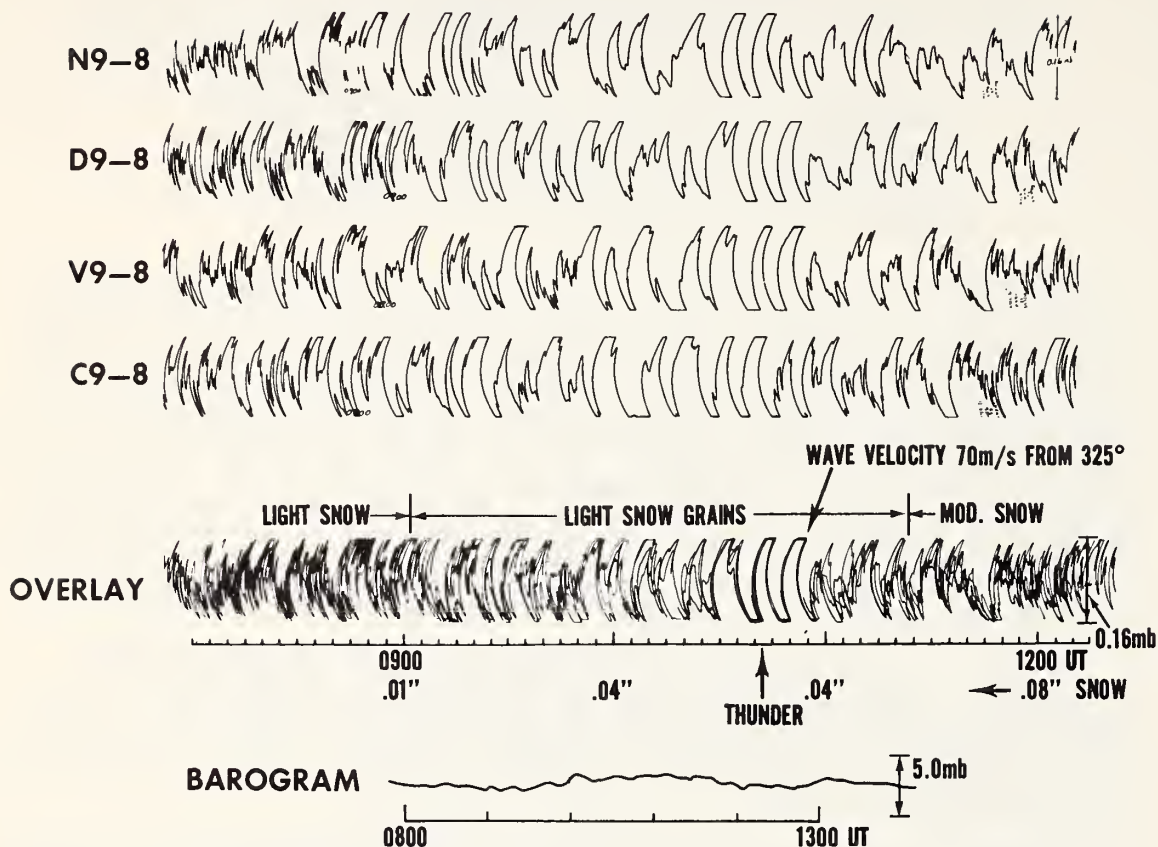
Figure 1. Tracings of four infrasonic microphones' outputs and corresponding barogram. The overlaid records and weather data show evidence of wave motion apparently associated with thunder and a change of state of solid precipitation in the area during a snowstorm.

The barogram given at the bottom of Figure 1 covers the same time interval as that of the curves above. The pressures considered in this report are peak-to-peak and not absolute values. The barometer used was a conventional aneroid type microbarograph which evidently does not respond to the short-period waves. In fact, the waves of approximately 7-min periods occurring at about 1045 UT are not shown on the barogram.

Concurrent records from the specially designed millibarograph and the infrasonic station showed a one-to-one correspondence between measurements of pressure changes. Figure 2 gives typical examples. The infrasonic wave phenomena displayed at the top left are characteristic of snow which started between 0840 and 0940 UT according to the radar report.

The snow-related waves were continuous during precipitation. The example for March 13, 1968, illustrates characteristic "subsonic" data related to a thunderstorm as compared with the atmospheric pressure data at the right. The first radar report of a thunderstorm coincides in time with the pulse on the infrasonic records and the pressure jump on the millibarograph record. Mr. A. J. Bedard, Jr., of our laboratory, associated "subsonic" waves with local thunderstorm
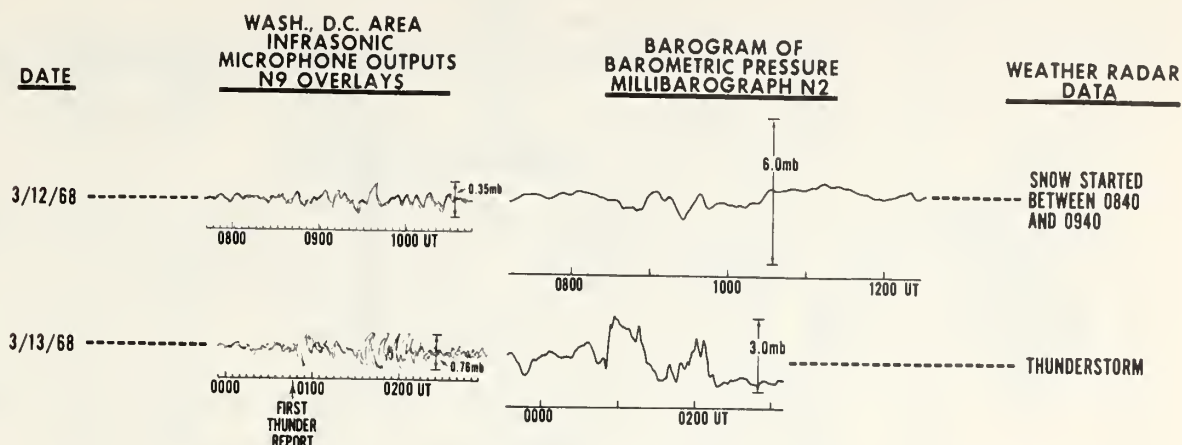
Figure 2. Records of infrasonic microphones' outputs with barometric pressure data from a highly sensitive millibarograph; also corresponding weather information.

activity, and the data presented here are in good agreement with his findings. The two events are not classed as severe. The data are shown in order to point out the fact that the infrasonic equipment responds to mild forms of certain weather phenomena.

An example of recorded "subsonic" pressure waves associated with a typical snowstorm yielding 3.4 in. of snow in 6-hr is given in Figure 3 for January 26, 1966. The computed horizontal trace velocity of the ground wave of 61 m/s from a direction of 230° is in good agreement with the winds near the tropopause. The vertical profiles of wind and temperature are shown at the right. The overlaid traces show good coherence throughout the interval.

Further examples of severe snowstorm-related "subsonic" waves are illustrated in Figure 4. The overlaid curves are presented, with corresponding weather data given below. The first set of curves for February 11, 1964, shows wave motion measured when 0.32 in. of snow and sleet fell during the 4-hr interval. Local wind speeds averaged 8.1 m/s (18.2 mi/hr) for the time shown. During this entire event local gusty winds reached gale proportions. The longest wave was noted when the radar echoes covered more than nine-tenths of the reported area. In that interval no jet stream existed aloft. However the speed of the "subsonic" waves at the earth's surface was approximately that of the wind speed near the tropopause. The set of curves for January 26, 1966, was discussed previously. Here the maximum pressure amplitudes measured approximately 240 dyn/cm². In all cases the speed and direction of the ground waves were found to agree fairly well with the wind velocities in the neighborhood of the tropopause. This suggests a generating mechanism in that region. Waves of similar character have been observed in noctilucent clouds at altitudes near the mesopause, and their origin has been related to the region of the tropopause (9, 10). Whether the ground waves and noctilucent cloud waves stem from the same or similar source mechanism is a good question. The direction of the wave motion is in general the same as that of the moving weather systems as shown in Table I. Again, the wave motion is essentially continuous during the solid precipitation. The curves at the bottom of Figure 4 for January 29 and 30, 1966, are continuous data for the early stages of a snowstorm that reached blizzard proportions. Continuous coherent waves existed with constant velocity throughout the 12-hr interval shown.

The nature of the "subsonic" waves associated with thunderstorms was sporadic, and the longest period waves were in most cases related to hail-producing storms. Figure 5 gives examples of infrasonic data taken during times of typical hail-producing thunderstorms. The first two sets of curves show preliminary records for storms that produced hail about 5-hr later. The records show sporadic wave phenomena that coincide in time with the thunder reports. The two sets of curves at the bottom show infrasonic records for time intervals in which the hail was reported. The hail reports shown occurred for times corresponding to the long-period wave motion. Unfortunately the maximum amplitudes of these waves could not be determined because

-217-
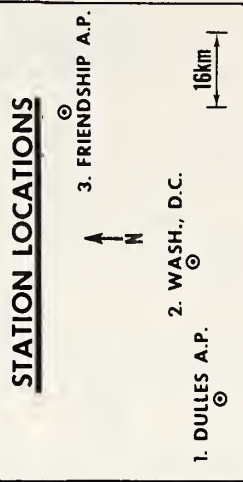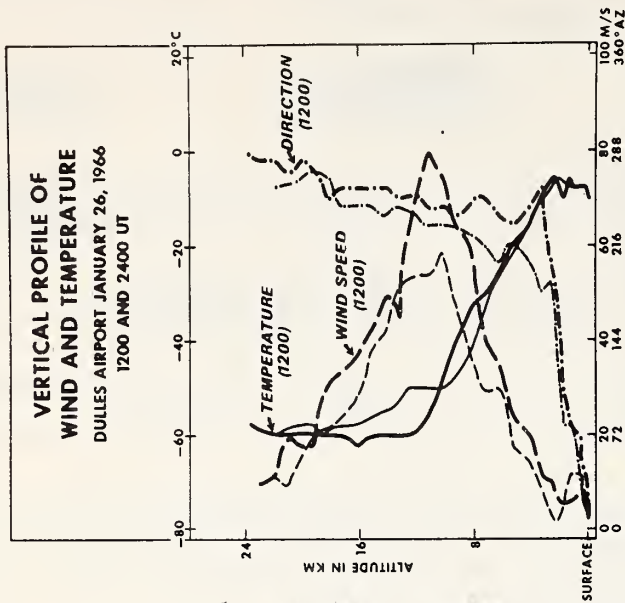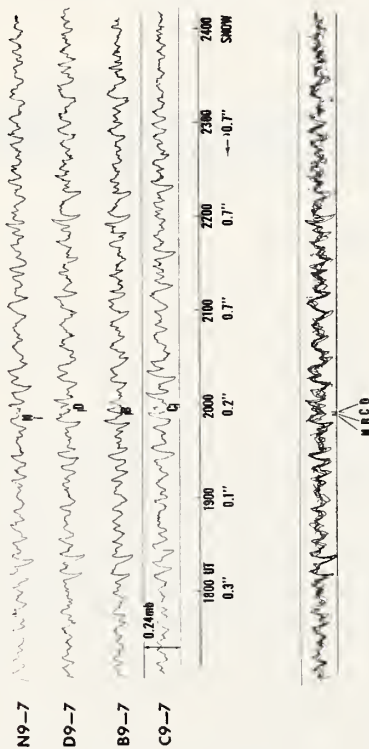
Figure 3. Low-frequency pressure waves, vertical wind and temperature profile, and station locations. The measured horizontal phase velocity of the "subsonic" ground waves shown above agrees well with the wind velocity near the tropopause. The overlaid traces show continuous wave motion from a fairly constant direction for approximately 7-hr. Snowfall totaled 3.4 in. for the interval. The winds near the tropopause were of jet proportions from about the same direction at each of the soundings reported. The relative location of the experimental stations are given at the right.

SNOWSTORM-RELATED
SUBSONIC WAVES
WASH., D.C. AREA
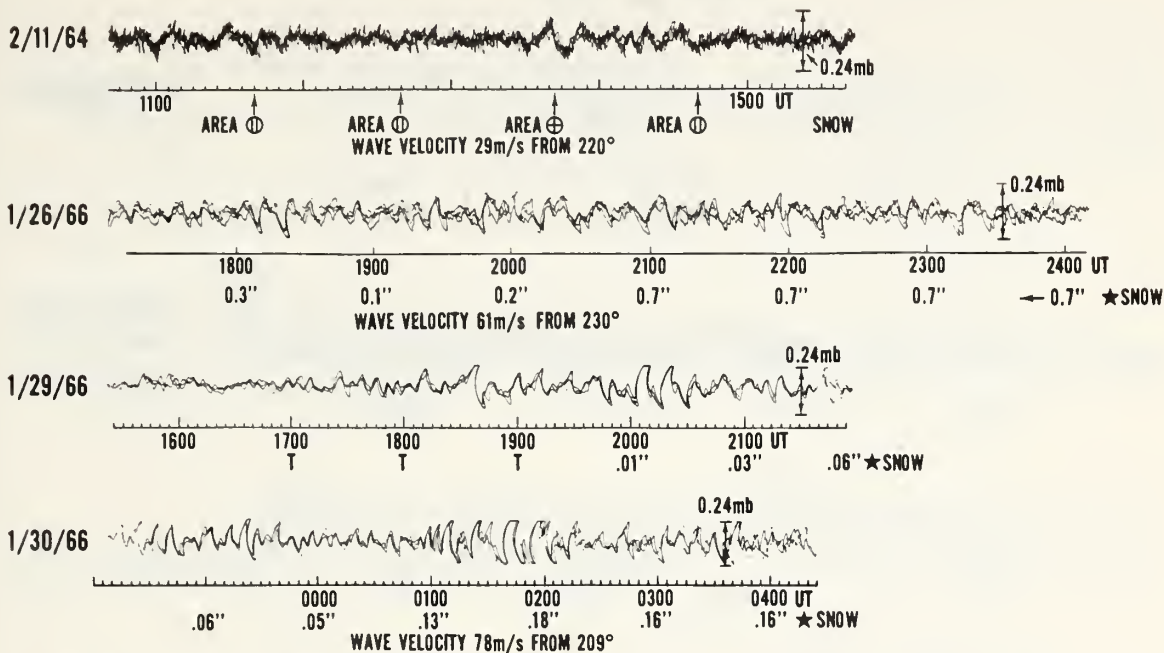
Figure 4. "Subsonic" wave data and corresponding weather radar information and hourly reports of solid precipitation in the area.

Table I. "Subsonic" Wave and Local Weather Data

Date	Wave Data			Weather Data			
	Universal time	Azimuth degrees	Speed m/s	Universal time	Azimuth degrees	Speed m/s	Type
5/20/63	1752	307	13	1744	315	15	Thunder
1/27/67	1643	259	60	1641	260	12 1/2	Thunder
				1641	250	15	Thunder
4/23/63	0745	262	28 1/2	0744	286	24	Thunder & Hail
12/25/65	2000	271	17	1945	270	12	Thunder & Hail
1/13/64	1045	325	70	1044	340	20	Snow & Thunder
2/11/64	1245	220	29	1241	225	8	Snow
1/29/66	1900	209	78	1840	240	22 1/2	Snow

-219-

HAILSTORM-RELATED
SUBSONIC WAVES
WASH., D.C. AREA
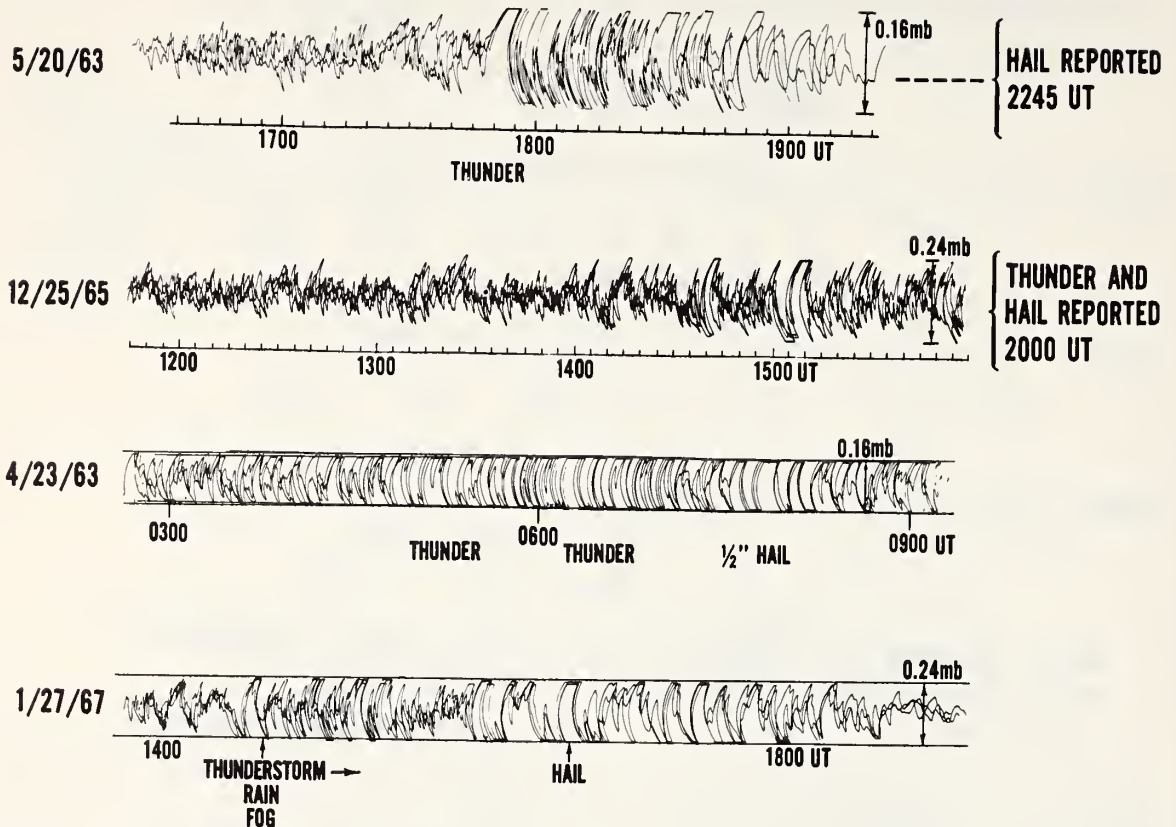
Figure 5. Hailstorm-related "subsonic" waves, with weather data noted as reported.

---

the recorders went over full scale at the time of the disturbances. These disturbances were not anticipated.

Observations were made during 18-hr before the occurrence of a tornado that was reported within a 60-mi radius of Washington, D. C., (See Appendix). Figure 6 shows the low-frequency information from the infrasonic station and the corresponding barometric pressure data from two ordinary aneroid barometers. All stations were inside the 60-mi radius. Being the only data available, these are shown merely to indicate their possible use in studying tornadic storms. A significant characteristic of the data is a series of sporadic events that occurred in about a 10-hr interval before 1805 UT when the tornado was observed about 60-mi away from the infrasonic microphones. The barogram trace for Dulles International Airport indicates a pressure jump of more than 5 mb at 1530 UT. The trace for Friendship International Airport about 65-mi away shows an even greater barometric pressure jump at 1630 UT. This information related favorably to an apparent moving pressure system and to the hail report in the Washington, D. C., area at about 1620 UT.

In conclusion, experimental evidence demonstrates that barometric-pressure-related "subsonic" waves are apparently associated with extreme weather phenomena. These particular waves were observed at the earth's surface on very sensitive infrasonic measuring equipment and were related to snowstorms and thunderstorms. The hail-producing thunderstorms were associated with waves of the longest periods. The directions of the moving waves were in general related to that of the weather systems and/or upper winds. The horizontal speed of the waves also appeared to be under the influence of winds aloft.

LOW FREQUENCY PRESSURE WAVES
WASH., D.C. AREA
(1/27/67)
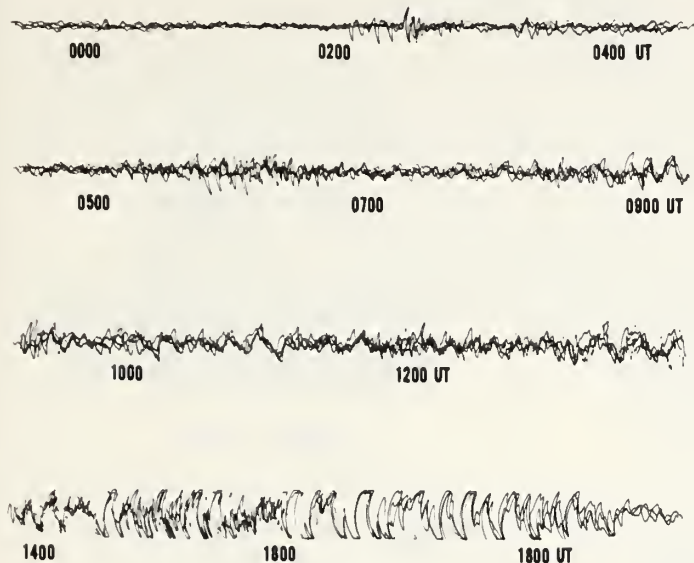
BAROMETRIC PRESSURE DATA
(1/27/67)
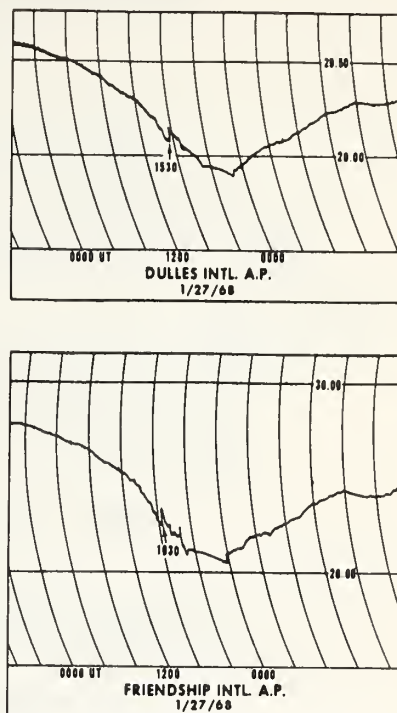
Figure 6. Low frequency pressure wave data and barometric pressure data for a time period associated with a tornado occurring at 1805 UT within a 60 mile radius of the Washington, D. C infrasonic station.

References

1. A.H.R. Goldie, "Waves at an Approximately Horizontal Surface of Discontinuity in the Atmosphere," Quart. J. Roy. Meteorol. Soc., Vol. 51, (1925)
2. R.D.M. Clark, "Atmosphere Micro-Oscillations," J. Meteorol. Vol. 7, (1949)
3. E.E. Gossard, "Gravity Waves in the Lower Troposphere over Southern California," U. S. Navy Electronics Lab. Report 709, San Diego, California, (1956)
4. C. East, "A Technique for Analysing Meso-Scale Pressure Patterns," McGill Univ. Scientific Report MW-35, (1961)
5. W.L. Donn & W.T. McGuinness, "Air Coupled Long Waves in the Ocean," J. Meteorol., Oct. (1960)
6. P. Chrzanowski, G. Greene, K. T. Lemmon, & J. M. Young, "Traveling Pressure Waves Associated with Geomagnetic Activity," J. Geophys. Res., Vol. 66, No. 11, Nov. 1961, pp. 3727-3733
7. R.K. Cook, "Subsonic Atmospheric Oscillations," presentation at the Symposium on Acoustic Gravity Waves, ESSA/ARPA, Boulder, Colorado, July 15-17, 1968
8. J. M. Young, "Experimental Observations of Tropospheric Jet Stream Waves," presentation at the Symposium on Acoustic Gravity Waves, ESSA/ARPA, Boulder, Colorado, July 15-17, 1968
9. B. Haurwitz, "Wave Motion in Noctilucent Clouds," presentation 49th Annual Meeting, American Geophysical Union, Washington, D. C. (1968)
10. A.D. Christie, "Synoptic Distributions of Noctilucent Clouds," presentation 49th Annual Meeting, American Geophysical Union, Washington, D. C. (1968)

APPENDIX

U. S. DEPARTMENT OF COMMERCE
C.R. SMITH Secretary
ENVIRONMENTAL SCIENCE SERVICES ADMINISTRATION
ENVIRONMENTAL DATA SERVICE

STORM DATA AND UNUSUAL WEATHER PHENOMENA

PLACE	DATE	TIME	LENGTH OF PATH (MILES)	WIDTH OF PATH (YARDS)	NO OF PERSONS KILLED	INJURED	ESTIMATED DAMAGE PROPERTY	CROPS	CHARACTER OF STORM

(JAN. 1964)

MARYLAND

| Statewide and District of Columbia | 12-13 | | | | 10 | 28+ | 4 | 0 | Snow, strong winds high tides. |

Snow, ranging from 4-6 inches in southern areas, to 16-18 inches in mountains, was heaviest in 5-6 years for some areas; over the coastal areas of southern Eastern Shore it was mostly rain. Drifting snow kept road crews busy. At least two traffic fatalities occurred during storm. Two deaths in Baltimore and at least one in the area (Goldsboro) were caused by snow shoveling. Five deaths in Washington, D. C. were attributed to storm. At least 28 persons were treated in Baltimore hospitals for injuries from falls. High tides, 2 to 4 feet above normal, flooded many streets in Ocean City but little damage was reported. During snowstorm a thunderstorm was reported in both Talbot and Kent counties between 5 and 6AM of 13th.

(FEB. 1964)

| Statewide, including District of Columbia | 10-11 | | | | 0 | 0 | 4 | 0 | Snow |

Storm yielded from 4 to over 11 inches of snow with heaviest amounts in the central and north-central sections. Heavy snow removal equipment brought out in force. Many minor traffic accidents reported. At least one death, that of a man in Washington, D. C. from overexertion in shoveling snow, was indirectly caused by storm.

(JAN. 1966)

| Statewide and District of Columbia | 26-27 | | | | | | | | Snow |

A second major storm followed closely the weekend storm of January 22nd-23rd. Heaviest snowfall was in the southern and central portion where totals ranged from 10 to 17 inches; elsewhere it ranged from 6 to 10 inches except in western portion where totals were generally the least, from 2 to 5 inches. Snowfall, 11 to 14-inch in Southern Eastern Shore and 12 to 17-inch in the St. Marys county area, was the heaviest since January 1940. Drifts up to 6 feet were reported in almost all areas; these greatly hampered transportation and travel. Traffic accidents, however, were generally the "fender-bender" variety. Newspapers listed at least four storm deaths, three in Maryland and one in District of Columbia. All were heart attack victims apparently from overexertion from shoveling snow or pushing stalled automobiles. Schools were closed one to two days.

(JAN. 1966)

| Statewide and District of Columbia | 29-30 | | | 12 | | | | | Blizzard |

This third and the most severe storm since January 22nd, met the weather Bureau definition of a blizzard. Snowfall was heavy, 16 inches or more in Northern Central, Lower Southern and Central Eastern Shore Divisions and also in some areas of the Appalachian Mountain Division. The least amount was found in Garrett County area where 6 to 13 inches were reported. Winds, reaching gale force, caused heavy drifting generally 3 to 6 feet but as much as 12 to 15 feet. Near zero or sub-zero temperatures were recorded on the 29th and temperature on both days did not generally reach 30°F above. This snowfall plus the previous snowfall gave some record or near record depths. Depths of 20 inches or greater were found in all areas of the state; the greatest was 34 inches reported at Catoctin Mountain Park near Thurmont. Practically every highway was closed at one time or other. Helicopters were used to airlift patients and drop supplies. State newspapers reported at least 35 storm-related deaths in Maryland and 3 in District of Columbia; of these, as many as 20 were victims of heart attacks apparently from shoveling snow or trudging through snow. Many schools were closed as many as 5 days. The Coast Guard reported extremely hazardous conditions on the Chesapeake Bay with gale force winds and up to 7 inches of solid ice in the upper portions of the Bay. The problem of getting and keeping roads and streets open was a most costly one for state, county and municipal governments. Fortunately, telephone and power service was little affected by this storm as well as the 2 earlier ones.

PLACE	DATE	TIME	LENGTH OF PATH (MILES)	WIDTH OF PATH (YARDS)	NO OF PERSONS KILLED	INJURED	ESTIMATED † DAMAGE PROPERTY	CROPS	CHARACTER OF STORM

(APR. 1963)

MARYLAND
Entire State

| | 23 | 3:00PM - 8:00PM | | | 1 | 16+ | 3 | 3 | Wind |

Again winds reached 60-70 mph in gusts, breaking windows, blowing down signs and trees. One man was killed near Piscataway when a tree fell on him. At least 6 others were injured by falling limbs and trees. Ten men were injured when winds caused the collapse of 2 apartment buildings at Riverdale. A brick bearing wall was blown out in Carroll County. Hail the size of marbles fell north of Hagerstown. Blossoms and spurs were blown from fruit trees. A Greenhouse at Bowmen was damaged. Utility lines were broken and roads blocked by fallen trees.

(MAY 1963)

| BelAir ★ | 20 | After-noon | | | 0 | 1 | 4 | 0 | Wind |

Windstorm of "Tornadic" force blew down trees and utility wires.

(DEC. 1965)

| Central and Eastern Counties and District of Columbia | 25 | Afternoon and Evening | | | 0 | 0 | 0 | 0 | Thunderstorms |

Numerous thunderstorms and unseasonably warm temperatures were reported on Christmas Day. Hail, ½-inch in size, was also observed in north central area. Rain totals were generally ½-inch or less. This was the first time thunderstorms were reported for this date by Baltimore Weather Bureau; records include period from 1891.

(JAN. 1967)

| Statewide | 27 | Late morning & afternoon | | | 0 | 0 | 5 | 0 | Lightning, wind & hail |

Widespread thunderstorm activity was reported. Several homes were struck by lightning and a Baltimore club was damaged to the extent of several hundred thousand dollars by a fire apparently started by a lightning strike. Strong gusty winds caused some local damage, including the snapping of several telephone poles in Cambridge area. Hail was also reported but no size was given.

| Hollywood, St. Mary's County ★ | 27 | 1:05 p. | 2½ | 30-50 | 0 | 0 | 3 | 0 | Tornado |

A black funnel cloud was observed, moving in a narrow line from SW to NE and touching ground in several places. Damage was limited to uprooting sixteen large trees in a line, ripping off a section of a school roof and demolishing several sheds.

† Storm damages are placed in categories varying from 1 to 9 as follows:
1 Less than $50
2 $50 to $500
3 $500 to $5,000
4 $5,000 to $50,000
5 $50,000 to $500,000
6 $500,000 to $5,000,000
7 $5,000,000 to $50,000,000
8 $50,000,000 to $500,000,000
9 $500,000,000 to $5,000,000,000,

★ WITHIN 60 MI. RADIUS OF WASH., D.C.

Radiative Equilibrium Temperature Distribution
of the Atmosphere of Mars

C. B. Emmanuel

Research Laboratories, ESSA, Boulder, Colorado 80302

Selected surface temperatures, consistent with the Mariner 4 observations, are used to calculate the radiative heat budget and radiative equilibrium temperature distributions of the atmosphere of Mars as a function of latitude for the summer season. The results indicate that below about 40° latitude there is a surplus of radiational energy and that above 40° latitude there is a deficit. For balance to prevail, there must exist a transport of energy across the 40° latitude of about 10^{16} cal min^{-1}. Radiative cooling due to the 15-μ band of CO_2 predominates at all levels and latitudes except at a height of about 7.5 km and is about an order of magnitude greater than the heating due to incoming solar radiation. The radiative equilibrium temperature distribution indicates an isothermal layer above about 60 km, but this region is not well defined.

Introduction

Infrared radiation and convection are expected to be the processes most likely to affect the vertical distribution of temperature. The atmosphere of Mars is largely transparent to solar radiation; consequently, most of the solar radiation is not absorbed directly in the atmosphere but instead is absorbed at the surface. This energy is then transmitted to the atmosphere by infrared radiative and convective transfer.

A considerable part of the observed radiation originates from the planetary surface; consequently, the vertical structure of the temperature cannot be determined from radiometric observations. If, however, the atmospheric composition and its vertical distribution are known along with the appropriate spectroscopic constants for the constituent radiating gas molecules, the radiative equilibrium temperature distribution can be determined. At present, a precise knowledge of the atmospheric composition, mean surface pressure, temperature, and albedo is not available. There does exist, however, sufficient information [*Anderson*, 1965; *Kliore et al.*, 1965; *Fjeldbo et al.*, 1966] to allow construction of atmospheric models that can be used for preliminary estimates of the radiative heat budget and radiative equilibrium temperature distribution of the atmosphere of Mars.

The physical model presented here differs from models previously published in that it is a latitudinal study and assumes a surface pressure of 5.5 mb. The radiative equilibrium temperature distribution is obtained by setting up a system of inhomogeneous equations (one for each atmospheric layer) that include the Planck function $B(\bar{T}_i)$. Solution for $B(\bar{T}_i)$ is obtained by invoking the matrix inversion technique.

Atmospheric Model

In the analysis that follows, the following data have been used:

Composition	100% CO_2
Acceleration due to gravity	372 cm sec^{-2}

Surface Conditions

	Pressure, mb	Temperature, °K	Albedo
Equator	5.5	275	0.200
30° NH	5.5	250	0.181
60° NH	5.5	225	0.155
90° NH	5.5	200	0.185

The vertical temperature and pressure distributions were obtained from the results of the Mariner 4 data [*Anderson*, 1965]. These distributions are shown in Figure 1.

Local thermodynamic equilibrium has been assumed to exist to an altitude of about 60 km. This implies that the population densities of the molecular states are given by a Boltzmann distribution; thus, the inequality

$$\epsilon \equiv C_{UL}/A_{UL} \gg 1 \tag{1}$$
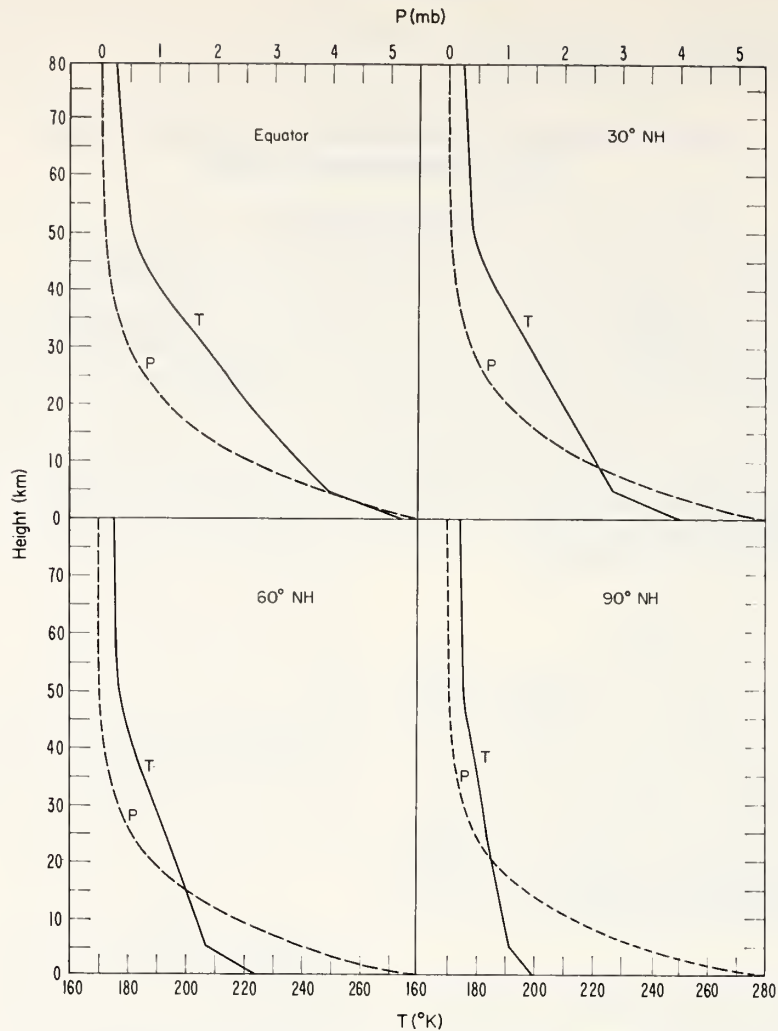
Fig. 1. Temperature and pressure distribution for the atmosphere of Mars.

must be valid for all molecular transitions considered [*Kuhn*, 1966]. In (1), C_{vL} is the probability of a collisional de-excitation per unit time per molecule, A_{vL} is the probability of a spontaneous de-excitation per unit time per molecule, and U and L refer to the upper and lower states, respectively. The radiative lifetime for the 15-μ band of CO_2 is [*Goody*, 1964]

$$A_{UL} \simeq 3.0 \text{ sec}^{-1}$$

The collisional rate is a very difficult parameter to determine theoretically or experimentally [e.g., *Herzfeld and Litovitz*, 1959]. A value of $3 \times 10^5 \text{ sec}^{-1}$ (NTP) has been assumed for the present study. Neglecting any temperature de-

pendence of the collisional rate, C_{vL} at an arbitrary pressure, p, is given by

$$C_{UL}(p) = C_{UL}(p_0)(p/p_0) \qquad (2)$$

With these rates, (1) is found to be satisfied to an altitude of about 60 km for the 15-μ band of CO_2. Local thermodynamic equilibrium may not prevail to this altitude for the 2.7- and 4.3-μ bands of CO_2, since the rates are expected to be different. They have not been considered here, because, as we shall see later, the contribution by the 15-μ band of CO_2 to planetary radiation is much larger than the contributions from the 2.7- and 4.3-μ bands of CO_2.

Radiative Heat Budget and Equilibrium Temperature Distributions

The atmosphere of Mars, to an altitude of 80 km, was divided into five arbitrary layers: 0–5, 5–10, 10–20, 20–40, and 40–80 km. Transmission values for the planetary radiation were calculated for the 2.7-, 4.3-, and 15-μ bands of CO_2. For the incoming solar radiation, transmission values were calculated for the 1.3-, 1.4-, 1.6-, 2.0-, 2.7-, 4.3-, and 15-μ bands of CO_2. We found that in the case of planetary radiation, the 15-μ band of CO_2 is the only contributor (the flux levels of the 2.7- and 4.3-μ bands of CO_2 were at least two orders of magnitude below that of the 15-μ band level), whereas in the case of solar heating there is no contribution at 15 μ. The primary contribution comes from the 1.3-, 1.4-, 1.6-, and 2.0-μ bands of CO_2.

For the calculation of absorption and emission of far infrared energy by CO_2 in the atmosphere of Mars, the 'strong' line approximation [*Plass*, 1960] was employed. The transmission τ may then be expressed as

$$\tau = \exp -\left(\frac{2}{\pi}\beta^2\gamma^2\right)^{1/2} \qquad (3)$$

where

$$\beta = (2\pi/d)\alpha \qquad (4)$$
$$\gamma = (S/2\pi\alpha)u$$

In (4), α is the half-width of the lines in the band, d is the mean spacing of the lines, u is the mass path length of the absorbing gas, and S is the total line intensity. The mean half-width of the CO_2 lines was obtained from *Prabhakara and Hogan* [1965]. The mean line intensity S and the mean spacing d of the CO_2 lines were obtained from *Stull et al.* [1963]. The path length u of the absorbing gas is given by

$$u = \int_{z_1}^{z_2} \rho_{CO_2}(z)\, dz$$

or

$$u = \frac{1}{g} \int_{P(z_1)}^{P(z_2)} w(p)\, dp$$

where $w(p)$ is the mixing ratio. For a constant mixing ratio this expression reduces to

$$u = (w/g)(P_L - P_U)$$

where P is in dynes per square centimeter and u is in grams per square centimeter.

The mean half-width of a collision broadened line may be expressed as

$$\alpha = \alpha_0(\bar{P}/P_0)(T_0/\bar{T})^{1/2} \qquad (5)$$

where α_0 is the half-width of the line at NTP. The Curtis-Godson approximation has been employed in the evaluation of the mean layer pressure $\bar{P}$. The average layer pressure is defined as

$$\bar{P} = \int_{P_U}^{P_L} w(p)p\, dp \bigg/ \int_{P_U}^{P_L} w(p)\, dp$$

where $w(p)$ refers to the mixing ratio. In the present case $w(p)$ remains constant with height, so that

$$\bar{P} = \tfrac{1}{2}(P_U + P_L)$$

Similarly, we define a mean layer temperature as

$$\bar{T} = \tfrac{1}{2}(T_U + T_L)$$

Expression 3 now takes the form

$$\tau = \exp -\left[4\frac{\alpha_0}{d^2}\left(\frac{\bar{P}}{P_0}\right)\left(\frac{T_0}{\bar{T}}\right)^{1/2} Su\right]^{1/2} \qquad (6)$$

where it has been tacitly assumed that the effect of Doppler broadening of the infrared lines of CO_2 is negligible. Expression 6 was used for the calculation of the transmission values for each layer.

The condition for a planetary atmosphere to be in radiative equilibrium is that

$$\Delta F/\Delta P = 0 \qquad (7)$$

for each layer. In (7), the flux F into or out of a layer may be given by

$$F_i = [\tau_s B_g(\bar{T}_g) + \tau_k B_s(\bar{T}_s) + \sum_j B_j(\bar{T}_j)\, \Delta\tau_{ji}]\pi\, \Delta\omega \qquad (8)$$

where $B_g(\bar{T}_g)$ is the known Planck function at the surface, $B_s(\bar{T}_s)$ is the mean Planck function representing the incoming solar radiation, $B_j(\bar{T}_j)$ is the mean Planck function for a particular layer, $\Delta\tau_{ji}$ is the transmission increment, and $\Delta\omega$ is the bandwidth. It is understood, of course, that $B_g(\bar{T}_g)$ contributes only to outgoing flux calculations and $B_s(\bar{T}_s)$ contributes only to incoming flux calculations.

TABLE 1.   Cooling and Heating Rates (°K/day) in the Atmosphere of Mars
(Values in parentheses represent heating due to incoming solar radiation.)

Layer	Equator	30° NH	60° NH	90° NH
0–5 km	10.56 (0.91)	10.53 (0.69)	4.00 (0.57)	8.06 (0.61)
5–10 km	−11.92 (1.04)	−12.01 (0.85)	−6.95 (0.66)	−2.92 (0.68)
10–20 km	16.74 (1.11)	18.05 (1.01)	14.57 (0.84)	14.22 (0.84)
20–40 km	11.54 (1.22)	10.14 (1.46)	16.27 (1.25)	9.82 (1.01)
40–80 km	8.56 (4.69)	5.63 (2.40)	14.45 (2.15)	16.39 (2.01)

The time rate of change of temperature is given by

$$\frac{\Delta T}{\Delta t} = g c_p^{-1} \frac{\Delta F}{\Delta P} \quad °\text{K min}^{-1} \quad (9)$$

where g is the acceleration due to gravity and c_p is the specific heat at constant pressure. In (9), positive values represent cooling and negative values represent heating. Table 1 gives the cooling and heating rates (°K/day) due to the 15-μ band of CO_2 and the heating rates (°K/day) due to the incoming solar radiation (values in parentheses).

Flux values for the incoming solar radiation and outgoing planetary radiation were calculated for each layer for the latitudes indicated. The results of this analysis are shown in Figure 2, where, for comparison, the results of *Ohring et al.* [1964] are also shown. The abscissa is a cosine scale, the length being proportional to the area of the latitude belt. *Ohring et al.* [1964] found that the energy transport across the 35° latitude required to maintain the annual balance is of the order of 0.5×10^{16} cal/min.

Application of (8) to the five-layer Martian atmosphere yields an inhomogeneous system of equations that may be solved easily by matrix inversion for the mean Planck function for each layer. It must be emphasized, however, that such a system of equations becomes highly unstable when an arbitrarily large number of layers is considered because $\Delta \tau_{ji}$ becomes infinitesimal as the mass path in the layer assumes smaller and smaller values. The temperature $\bar{T}_i$ may then be obtained from Planck's well-known expression

$$B_i(\bar{T}_i) = 2hc^2 \omega_0^3 \left[\exp\left(\frac{hc\omega_0}{k\bar{T}_i}\right) - 1 \right]^{-1} \quad (10)$$

where all the symbols have their usual meaning. In the lowest atmospheric layers, the infrared

radiative equilibrium temperature profile is marked by convective instability resulting in the adiabatic lapse rate of temperature, given by

$$\gamma \equiv g/c_p$$

where g is the acceleration due to gravity and c_p is the mean value of the specific heat capacity at constant pressure. For the lowest layers g can be taken to be constant; however, c_p for CO_2 is temperature dependent, so that γ varies with temperature [*Anderson*, 1965]. Figure 3 represents the results of this analysis, where the height of the computed tropopause is indicated by a short horizontal bar. Both the results of *Prabhakara and Hogan* [1965] and the more recent work of *Ohring and Mariano* [1966] agree reasonably well with the results presented here. The temperature profiles shown in Figure 3 confirm their conclusions that the tropopause height increases with increasing surface temperature and that at upper levels the temperature profiles converge to a constant temperature. In the present analysis this temperature is approximately 163°K.

CONCLUSIONS

The net radiative heating and cooling repre-
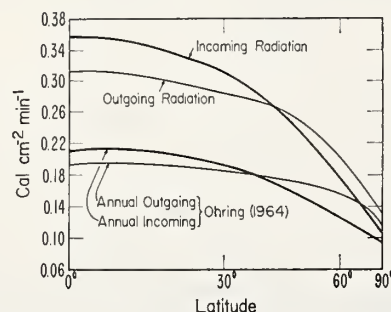
Fig. 2. Summer heat budget for the atmosphere of Mars.
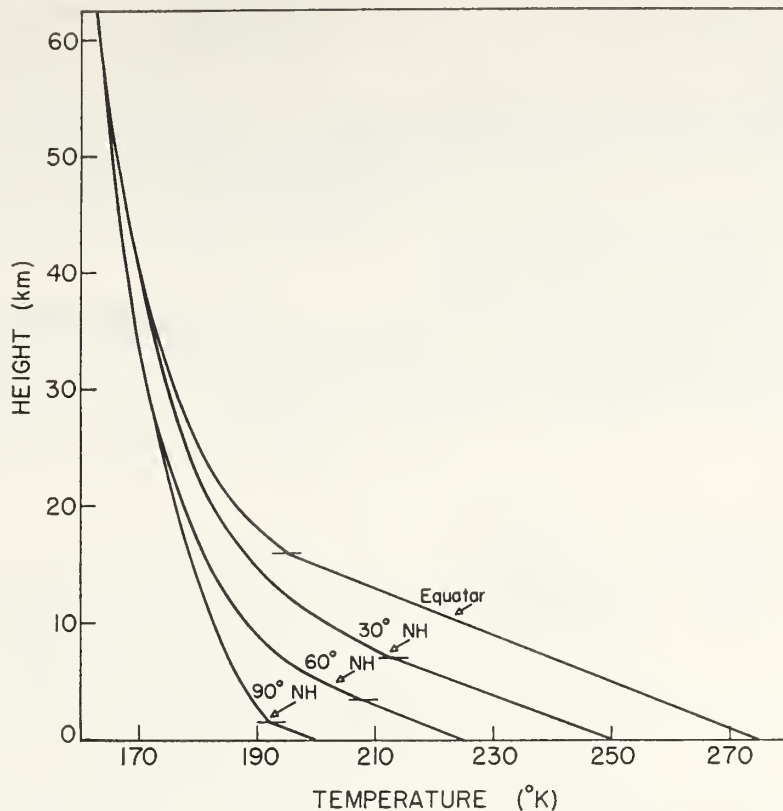
Fig. 3. The radiative equilibrium temperature distribution for the atmosphere of Mars with convective adjustment.

sent the contribution of radiation to the net heat budget of the planetary atmosphere. Radiative cooling and heating rates were computed for the 15-μ band of CO_2. Radiative cooling was found to predominate at all heights and latitudes, except at a height of about 7.5 km, where heating of approximately 8°K/day seems to prevail.

The transport of energy across the 40° latitude in the atmosphere of Mars amounts to about one-fifth that of the annual transport of energy across the 40° latitude on the earth [*London*, 1957].

The radiative equilibrium temperature distribution for the atmosphere of Mars has been obtained by setting up a matrix involving the mean Planck function for each layer as the unknown quantity. Solution of the matrix for the mean Planck function was accomplished by matrix inversion. An isothermal layer above about 60 km is indicated, but this region is not well defined. The breakdown of local thermody-

namic equilibrium and the effects of CO_2 photochemistry could very well account for this uncertainty. This has very clearly been brought out by the work of *Prabhakara and Hogan* [1965].

REFERENCES

Anderson, A. D., A model for the lower atmosphere of Mars based on the Mariner 4 occultation data, *Lockheed Palo Alto Res. Lab. 6-75-65-62*, 1965.

Fjeldbo, G., W. C. Fjeldbo, and V. R. Eshleman, Modes for the atmosphere of Mars based on the Mariner 4 occultation experiment, *J. Geophys. Res., 71*(9), 2307, 1966.

Goody, R. M., *Atmospheric Radiation,* vol 1, Clarendon Press, Oxford, 1964.

Herzfeld, K. F., and T. A. Litovitz, *Absorption and Dispersion of Ultrasonic Waves,* Academic Press, New York, 1959.

Kliore, A. J., D. L. Cain, G. S. Levy, V. R. Eshleman, G. Fjeldbo, and F. D. Drake, Occul-

tation experiment: Results of the first direct measurement of Mars' atmosphere and ionosphere, *Science, 149,* 1243, 1965.

Kuhn, W. R., Infrared radiative transfer in the upper stratosphere and mesosphere, Ph.D. dissertation, University of Colorado, Boulder, 1966.

London, J., A study of the atmospheric heat balance, *Final Rept. Contract AF 19 (122)-165, AD 117227,* 1957.

Ohring, G., E. M. Brooks, and J. Mariano, The meteorology of Mars and Venus, *NASA Rept. CR 75315,* Washington, D. C., 1964.

Ohring, J., and J. Mariano, The vertical temperature distribution in the Martian atmosphere, *J. Atmospheric Sci., 23*(2), 251, 1966.

Plass, G. N., Useful representations for measurements of spectral band absorption, *J. Opt. Soc. Am., 50*(9), 868, 1960.

Prabhakara, C., and J. S. Hogan, Jr., Ozone and carbon dioxide heating in the Martian atmosphere, *J. Atmospheric Sci., 22*(2), 97, 1965.

Stull, V. R., P. J. Wyatt, and G. N. Plass, The infrared absorption of carbon dioxide, infrared transmission studies, 3, *Rept. Contract SSD-TDR-62-127, Space Systems Div. Air Force Systems Command,* Los Angeles, Calif., 1963.

Airborne Infrared Radiometer Investigation of Water Surface Temperature with and without an Evaporation-Retarding Monomolecular Layer

R. L. Grossman,[1] B. R. Bean,[2] and W. E. Marlatt[1]

Airborne infrared radiometer measurements of water surface temperatures at Lake Hefner, Oklahoma, show an average diurnal variation of about 1°C for late summer conditions. The lake surface, cooled by evaporation, was 0.4° to 0.9°C cooler than the water about 1 cm below the surface. Applications of an evaporation-reducing monomolecular film reversed this gradient. The surface water temperature was 0.3°C warmer under the monomolecular layer than in the surrounding open water.

INTRODUCTION

This paper reports on the effect of an evaporation-retarding monomolecular layer of fatty alcohol on the surface temperature of Lake Hefner, Oklahoma. The temperature was determined by airborne and boatborne infrared radiometers and by a floating thermistor technique described by *Marlatt* [1967]. The radiometers yield the effective blackbody temperature of the first 20 μ below the water surface by measuring emitted radiation in the 8- to 12-μ band, whereas the floating thermistor obtains an average temperature between 0.5 and 2 cm below the surface. The fatty alcohol mixture (hexadecanol-octodecanol) has been found to reduce evaporation by 60% under field conditions [*Bean and Florey*, 1968].

EXPERIMENT

The aircraft, a Piper Twin Commanche, was flown in a preset pattern at a relative altitude of 300 meters (Figure 1). Federal Aviation Administration regulations prohibited flying at a lower altitude. Spatial accuracy of the measurements was maintained at ±50 meters by analysis of the infrared temperature strip charts between event markers denoting known positions on the ground. The root-sum-square errors of the various measurements were:

Instrument	Absolute Error	Relative Error
Aircraft radiometer	±0.5°C	±0.1°C
Boat radiometer	±1.0°C	±0.7°C
Floating thermistor	±0.3°C	±0.1°C

The relative error of the aircraft radiometer was found by testing its repeatability under flight conditions.

The effect of the intervening atmosphere caused the airborne measurements to be about 1°C cooler than measurements obtained by the radiometer in the boat. Application of a computer program for correcting the intervening atmosphere effect as well as accounting for the emissivity of water [*Shaw*, 1966] brought the two measurements into agreement, within measurement error, in five out of the six cases for which the input data could be unambiguously applied. Input to the program was air temperature, pressure, and specific humidity for the first 300 meters of the Tinker Air Force Base or Will Rodgers International Airport radiosonde flights. Both stations are within 10 miles of the lake and upwind of it.

RESULTS

When possible, airborne water surface temperature measurements were made every 4 hours in a given study period (24 hours). Studies were performed during the period August 17–30, 1966. The evaporation-retarding monolayer was systematically applied from August 28 to August 30, 1966. A few measurements were made with the monomolecular layer on the lake before August 25.

The water surface temperatures, obtained by

[1] Department of Atmospheric Science, Colorado State University, Fort Collins, Colorado 80521.
[2] Wave Propagation Laboratory, ESSA Research Laboratories, Boulder, Colorado 80302.
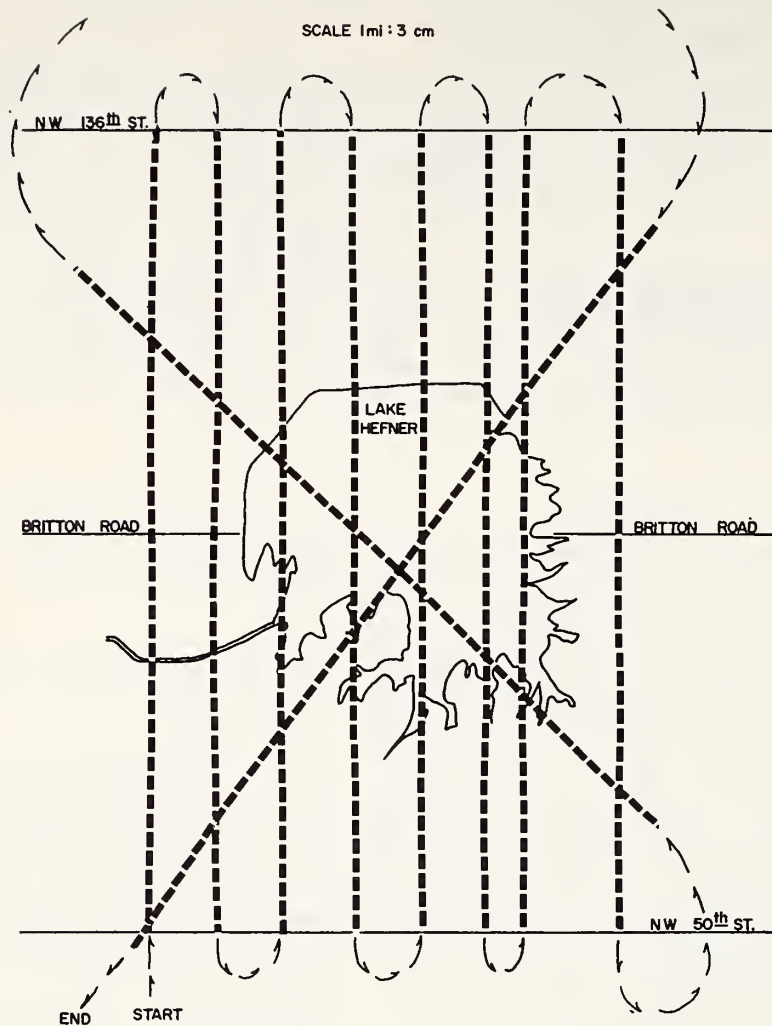
Fig. 1. Map of aircraft flight path.

the airborne equipment and corrected by the computer program, were averaged over the entire lake for each flight to yield a diurnal variation (Figure 2). The average temperature was also obtained for the four quadrants of the lake, as shown on Figure 3, and examined as a function of wind direction. The effects of wind waves and surface currents on surface temperature patterns were assumed to be small because of the low wind speeds that occurred during the experimental period (less than 10 knots) and the short lake fetch. The supply of water into the lake by its single inflow canal was negligible. In almost every case, when a south wind was blowing, water surface temperatures were cooler

(about 0.6°C) in the southern area than in the northern area. In the one case that appears anomalous (squares in the figure) the wind was shifting rapidly from west to south. This temperature structure, if it is indeed related to evaporative cooling, agrees with the model described by *Anderson et al.* [1950] for the variation of evaporation with fetch. In this model, the vapor pressure gradient decreases and the wind speed increases with fetch so that maximum evaporation results near the windward side of the lake.

Evidence of a thermal gradient in the upper few millimeters of the lake appears when one compares the mean or average water surface
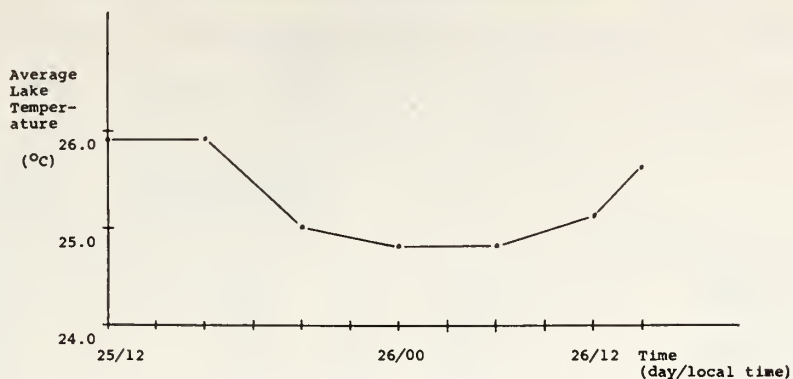
Fig. 2. Average lake surface temperature versus time, Lake Hefner, August 1966.

temperatures determined from the aircraft measurements with the subsurface temperature obtained from the floating thermistor. (The mean or average surface temperature was computed from the arithmetic mean of the aircraft data sample of lake temperatures.) The existence of the thermal gradient is confirmed by noting that a temperature difference is sig-

nificant at the 10% level of a Student's t test on the two mean temperatures (Table 1). More important, perhaps, is the reversal of the gradient concurrent with the regular application of the monomolecular film on August 28. This is an expected result since the immediate effect of the monomolecular layer would be to reduce the evaporative cooling of the water surface. It has
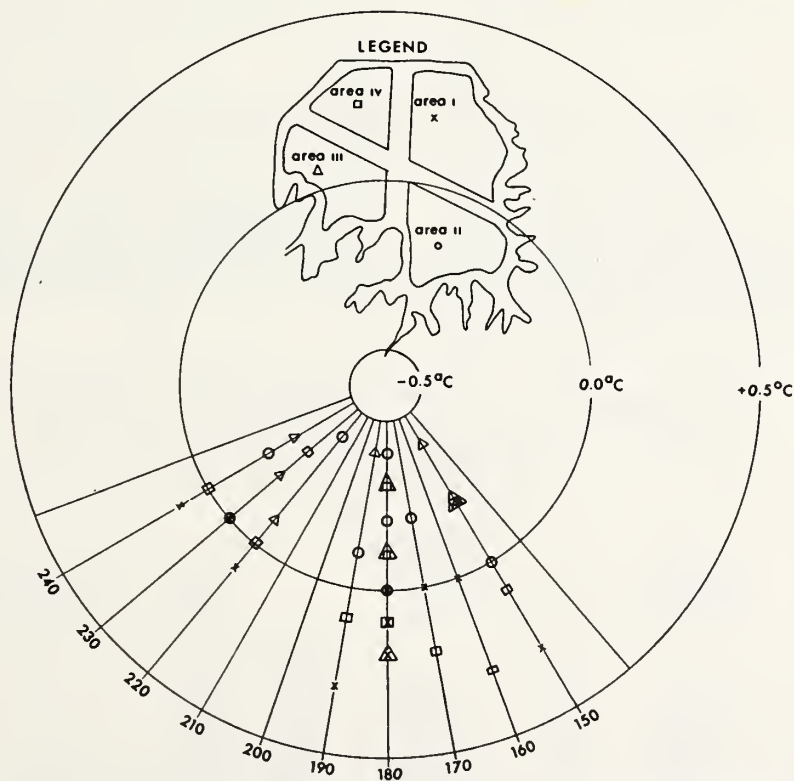
Fig. 3. Deviation from average surface temperature versus wind direction.

TABLE 1. Summary of Statistical Tests of Hypothesis: $\bar{T}_{\text{Boat Thermistor}} = \bar{T}_{a/c}$ (aircraft radiometer) for Lake Hefner, August 1966

Average Data Sample for $\bar{T}_{\text{Boat Therm}} = 10$; for $\bar{T}_{a/c}$ (aircraft radiometer) $= 200$; σ is standard deviation about the mean.

Date and Local Time	$\bar{T}_{\text{Boat Therm}} - \bar{T}_{a/c}$ (°C)	t Using σ = rms Error of Thermistor and $\sigma_{\text{Boat Therm}} \neq \sigma_{a/c}$	Reject Hypothesis $\bar{T}_{\text{Boat Therm}} = \bar{T}_{a/c}$ at 10% Level
Aug. 25, 1200	+0.6	6.3	Yes
Aug. 25, 1600	+0.4	4.2	Yes
Aug. 26, 0000	+0.9	9.5	Yes
Aug. 26, 0400	+0.9	9.5	Yes
Aug. 26, 0800	+0.4	4.2	Yes
Aug. 26, 1200	0.0	0.0	No
Aug. 28, 0100	−0.1	1.0	No
Aug. 28, 1400	−0.5	5.2	Yes
Aug. 28, 2000	−0.8	8.2	Yes
Aug. 29, 1300	−0.4	4.2	Yes
Aug. 30, 1400	−0.3	3.2	Yes

also been shown by *Saunders* [1967] that a surface film will thicken the viscous boundary layer within the water making conduction of heat to or from the surface less effective.

Six aerial observations of water surface temperature were made during the time a monolayer covered parts of the lake. A significant rise of surface temperature occurred within the film boundary in three of the cases and only when the monomolecular layer covered more than 40% of the total lake surface. A map of film cover nearest flight time was overlaid on the lake surface temperature field derived from the aerial observations. Temperatures inside and outside the film cover boundary were averaged

arithmetically. The effect of the film on water emissivity was neglected because of its thickness [*Ragotzkie and Menon*, 1967]. A Student's t test was performed on the hypothesis that the mean surface temperature inside the film boundary was equal to the mean surface temperature outside it. As Table 2 shows, for observations taken on August 28, at 1400 CST and 2000 CST, and on August 30 at 1400 CST, this hypothesis was rejected at the 10% significance level. It was concluded that in these cases the evaporation-retarding agent raised the water surface temperature by an average of 0.3°C only for film coverage of more than 40% of the lake.

TABLE 2. Mean Surface Temperature (°C) Obtained by Aircraft and First Standard Deviation (σ) inside and outside Film Cover and Results of Student t Test on the Means

Lake Hefner, August 1966
Data samples are in parentheses.

Date and Time	Average Temperature in Film ($\bar{T}_{\text{in}}$)	σ_{in}	Average Temperature out of Film ($\bar{T}_{\text{out}}$)	σ_{out}	Film Cover, %	Value of t	Accept Hypothesis $\bar{T}_{\text{in}} = \bar{T}_{\text{out}}$ at 10% Level
Aug. 17, 1200	28.1(50)	±.46	28.0(120)	±.32	19.0		Yes
Aug. 17, 1600	28.5(53)	±.30	28.5(75)	±.28	33.0		Yes
Aug. 28, 1400	26.0(89)	±.32	25.7(62)	±.28	43.0	5.77	No
Aug. 28, 2000	25.6(98)	±.21	25.3(116)	±.26	50.0	1.47	No
Aug. 29, 1300	24.9(87)	±.21	24.9(102)	±.24	39.0		Yes
Aug. 30, 1400	24.7(51)	±.29	24.4(72)	±.24	54.0	1.25	No
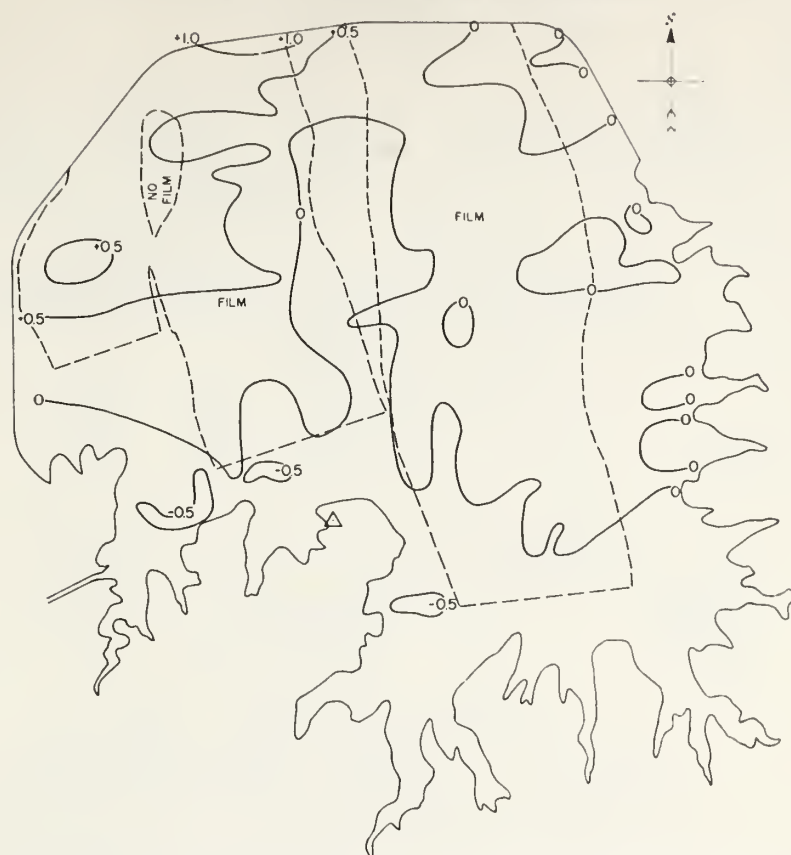
Fig. 4. Deviation from mean surface temperature for August 30, 1966, 1400 CST, with 1400 CST map of hexadecanol cover. Scale: 1 mile = 6.26 cm.

Of the three cases showing a temperature rise, two show a qualitative correspondence between the mean surface temperature, or zero deviation isoline (see Figure 4), and the film boundary. Figure 4 presents the results of the August 30, 1400 CST, run. The southern edge of the film seems well defined by the zero deviation isoline, but the eastern edge lacks such definition. A break in the monomolecular layer near the north-central part of the lake appears in the isotherm analysis. Figure 5 is a surface temperature analysis for a day on which the film was applied to the lake but covered less than 40% of the lake surface.

These observations carry practical implications for the use of monomolecular layers in evaporation reduction. One goal of past experiments has been to apply the layers to lakes in order to maintain complete coverage for the entire evaporation season. This technique has the disadvantage of producing warmer and warmer water under the layer with a resultant significant increase in evaporation when the layer is removed. Our data indicate, however, some probable advantages of intermittent layer application of 2 to 4 hours. For the conditions of the experiment, the saturation vapor pressure immediately above a water surface with a temperature of 25.5°C would be 32.6 mb in comparison with an ambient air vapor pressure of 15 mb. These values are typical for Lake Hefner. The 0.3°C increase in water temperature would increase the saturation vapor pressure to 33.2 mb, producing a percentage increase of evaporation of

$$\frac{33.2 - 32.6}{33.2 - 15} \times 100 = 3.3\%$$

which is small when compared with the 60% reduction in evaporation observed under these conditions.
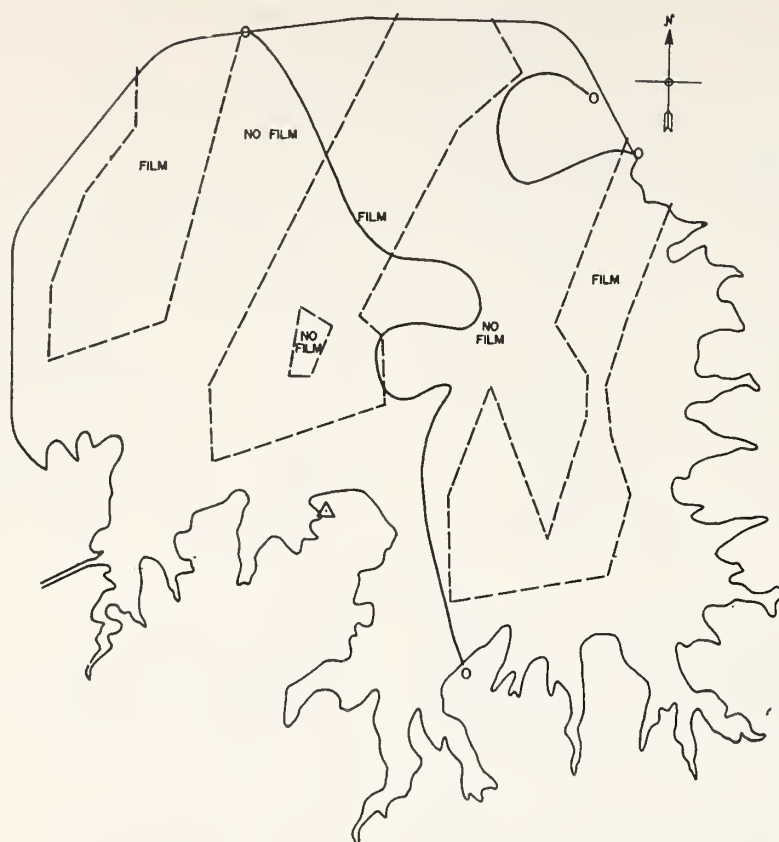
Fig. 5. Deviation from mean surface temperature for August 17, 1966, 1600 CST, film cover only over 33% of lake. Note poor correlation of film with zero deviation isoline in comparison to Figure 4. Scale: 1 mile = 6.26 cm.

REFERENCES

Anderson, E. R., et al., A review of evaporation theory and development of instrumentation, *U. S. Naval Electronics Lab. Rept.* 159, San Diego, Calif., 70 pp., 1950.

Bean, B. R., and Q. Florey, Field study of the effectiveness of fatty alcohol mixtures as evaporation reducing monomolecular films, *Water Resources Res., 4,* 206–208, 1968.

Marlatt, W. E., Remote and *in situ* temperature measurements of land and water surfaces, *J. Appl. Meteorol., 6,* 269–272, 1967.

Ragotzkie, R. A., and K. Menon, Remote sensing by infrared thermometer and microwave radiometry, *Dept. Meteorol., Univ. Wisconsin, Tech. Rept. 31,* 7–16, 1967.

Saunders, P., The temperature at the ocean-air interface, *J. Atmospheric Sci., 24,* 269–273, 1967.

Shaw, R. W., Environmental errors in the use of the airborne radiation thermometer, M.A. thesis, Department of Physics, University of Toronto, Toronto, Canada, 58 pp., 1966.

REMOTE PROBING OF WIND AND TURBULENCE
THROUGH CROSS-CORRELATION OF PASSIVE SIGNALS

F. R. Krause

NASA-George C. Marshall Space Flight Center
Huntsville, Alabama

and

V. E. Derr, N. L. Abshire, and R. G. Strauch

ESSA Wave Propagation Laboratory
Boulder, Colorado

ABSTRACT

Measurement of heat and humidity fluxes by cross cor-
relation passive techniques is discussed. The atmospheric
parameters, instrumental design, and sophisticated corre-
lation algorithms necessary for successful experiments are
described and the results of recent tests at the Haswell me-
teorological tower are presented.

---

1. INTRODUCTION

Humidity fluxes, heat fluxes and surface winds must be measured to study the energy release
in the earth's atmosphere by thermal radiation, and by evaporation. Evaporation accounts for al-
most 28% of the entire energy which the sun delivers toward the earth and the amount of moisture
present in the atmosphere is nearly 1.3×10^{13} tons. However, precipitation delivers to the
earth's surface 40 times this amount per year. The great intensity of the associated moisture and
heat exchange between the earth's surface and atmosphere determines the global weather, the gen-
eration of tropical storms and supply and reclamation of water. Humidity fluxes, heat fluxes, and
surface winds must therefore be monitored in remote, inaccessible or sparsely instrumented oceans
and land masses if a practical solution is to be found for the prediction and control of the weather
and the supply or reclamation of water.

Present meteorological sensors are impractical for the above tasks. They lack the essential
capability to measure fluxes over large volumes; the variability of fluxes over land and water is so
great that a very dense network of point sensors would be required to obtain statistically significant
average fluxes. Calorimetric determination of the heat flux from and to the soil is most diffi-
cult, since the heat capacity and the heat conductivity of the soil varies strongly in space and time
with the percentage of porous space occupied by water and air. The desired measurements are
thus very difficult even for specialized meteorological test teams, and the desired global measure-
ments can probably only be obtained from sensors on unattended buoys or stations, that can be in-
terrogated by communication satellites. We have therefore initiated a fundamental research pro-
gram for the development of passive sensors. Radiometers inside an unattended buoy would moni-
tor variations of the local heat radiation without exposure to salt water. The outputs from these
radiometers are then used to calculate the desired wind, humidity flux, and heat flux components.
In this way, one directly measures the heat input by thermal radiation, besides determining the
desired motions and fluxes. These calculations represent an engineering application of advanced
data processing and statistical correlation techniques, which were developed at the NASA Marshall

Space Flight Center for the analysis of radiation from rocket exhausts. The feasibility of applying this "Crossed Beam Technology" to wind and humidity flux measurements has been studied experimentally by the Wave Propagation Laboratory, ESSA Research Laboratories.

The success of a passive crossed beam correlation experiment is dependent on the proper evaluation of the emission characteristics of the atmosphere, the design of a radiometer system with sufficient sensitivity and low noise level, and a method of eliminating background noise. In addition the radiometer must be a. c. coupled to prevent large trends from masking small flucutations and exceeding the dynamic range of amplifiers and recorders. Further, it is necessary to have a powerful computing technique in the processing of the data, so as to remove the remaining trends and to detect and separate changing meteorological parameters. These topics will be considered in the following sections. Section 2 is concerned with the concept of remote sensing by passive means. The remainder of the article deals with the theoretical analysis and the experimental results which prove the feasibility of the method.

2. CONCEPT OF PASSIVE HUMIDITY AND HEAT FLUX MONITORING SYSTEM

The production of water vapor from land or water surfaces is usually quite uneven, as is the production of heated air from the ground or water. Typically the cells of heated or humid air found moving downwind over land are a few hundred meters in width, separated by similar distances. The scales of such eddies over the ocean will be better known after the analysis of the BOMEX data. These eddy scales are very height dependent, with better mixing near the ground. Even at the ground, however, the mixing is seldom complete. Except when the mixing is complete the inhomogeneities of water vapor density and temperature will produce inhomogeneous thermal emission at the wavelengths of the infrared absorption band of H_2O. Temperature variations of other constituents with infrared absorption bands will produce thermal emission fluctuations as eddies move across the radiometer beam. The thermal emission from CO_2 has been employed previously to obtain temperature profiles in the atmosphere.

Thus the fluctuations of thermal emission detected by a radiometer are associated with heat or mass flux transverse to the radiometer beam. The use of several wavelengths may allow the separation of temperature and mass fluctuations. The remainder of this section is devoted to the concept of such flux measurements.

2.1. TEST ARRANGEMENT

Consider the test arrangement shown in Fig. 1. Two periscopes protrude from a submerged buoy and look over the edge of the buoy. The first periscope monitors the heat radiation that is emitted from the evaporating water vapor and atmospheric CO_2 in the vicinity of the buoy. This thermal radiation is collected by a high resolution radiometer inside a narrow and horizontal field of view, which is denoted by "beam A". The second periscope employs a plurality of such radiometers, which collect thermal radiation from a fan beam arrangement. The lowest beam of the fan, B_o, intersects the beam of periscope A at a chosen point on the side of the buoy. This point is the spot where evaporation and heat fluxes are monitored. A vertical flux at this point would move the same eddy so that it traverses all other beams, B_1, B_2 ... along the fan normal. The emission fluctuations, which are caused by such an eddy, will produce similar signals in all radiometer outputs which are separated in time by the transit time τ_m, i. e. the time the eddy needs to travel from the chosen spot to one of the separated beams.

2.2. CONTINUOUS ON-BOARD COMPUTATIONS

Transit times or transit distances of thermal emission disturbances between spatially separated lines of sight may be retrieved by statistical cross-correlation computations. This computation should be performed by an on-board computer to avoid telemetry of unmanageable, large data volumes as well as problems of phase and impedance matching. The concept of such on-board correlation computations is illustrated in Fig. 2. The photometer record of the lowest

beam B_o has information from the chosen spot, since this spot is defined by the intersection with beam A. An optical filter is included in the photometer A in order to select either humidity or heat motions. The signal from beam B_o has thus some emission from fluctuations in common with beam A. These common signals are produced by the series of eddies which pass the intersection point. All other signals in beams A and B_o are produced by physically unrelated processes. They will therefore be cancelled during the statistical cross correlation computations, provided that enough information is processed. The correlation computer will thus accept the incoming signal time histories until all uncorrelated original components have cancelled each other in the averaging process.

Up to this point we have considered only the cross-correlation of the two intersecting beams A and B_o. Common signals between any of the other beams, B_1, B_2, etc. and beam A cannot be expected, since these beams are usually separated from beam A by more than one eddy diameter. However, an eddy, which has passed beam A at time t, may pass one or any of these beams at a later time $t + \tau_m$. Common signals may thus occur, if the signals from these beams are delayed by a time interval τ, that approximates the transit time, τ_m. Such time delays are introduced by the correlation computer. For each time delay a complete correlation loop is calculated for each of the beams B_1 through B_5. Conversely, a peak correlation between two beams, that are separated by the distance ξ, and the time delay τ indicates that there must be a streamline, which intersects the two separated beams in such a way that the velocity component along the fan normal is equal to ξ/τ.

The above considerations indicate that the transit times or transit distance of eddies between beams A or B_o and beam B_1 through B_5 may be obtained by analyzing the shape of the correlation curves, which the on-board computer calculated for the associated radiometer outputs I_A, and I_{B_o} through I_{B_5}. For remote installations the output may be broadcast from the on-board computer via a communication satellite to the remote user. The actual interpretations of the transmitted correlations in terms of fluxes would then be conducted by the user.

2.3. REMOTE DISPLAY OF CORRELATION BROADCASTS

The interpretation of correlation functions in terms of flux component variations has been studied analytically by Krause, Su, and Klugman [1969] and the theoretical results indicate a special graphical format for the broadcast of the correlation computations. This display would present graphically the most probable flux component and its turbulence level and allow verification of the accuracy of this graphical interpretation.

The graphical presentation of the transmitted correlation computations is illustrated in Fig. 3. The upper portion of this figure represents a screen, which displays the information that was broadcasted by the buoy and which has been interrogated via a communication satellite. The abscissa of this display has the dimension of a speed and is given by dividing the time delay, τ, which was set by the correlation computer, into the beam separation distance, ξ, which was set by remote controls. The ordinate displays the output of the buoy's special correlation computer. This output was calculated by adding the lagged products of the radiometer output time derivitives. The most probable flux speed is indicated by the peak of the displayed curve and the root mean square fluctuation around this most probable speed is given by the width of the curve. The displayed flux describes the exchange of water vapor or heat, depending on the absorption band which was selected by the remote controls of the optical filters. Theory indicates that the above interpretation is a valid approximation for a wide range of time and space separations of the optical signals. The remote user can therefore check the accuracy of the display (calibration) by comparing curves that have been calculated for different time delay parameters. The deviation between such curves gives the measurement accuracy. For good measurement the curves should become one line. The effect of a time delay change is then to move the data points along this line. This is the reason why an accurate display may be achieved with comparatively few, (≈ 6) beams in the fan.

The test arrangement in Fig. 1 was selected to measure vertical flux components. However, the system is not restricted to vertical components. This becomes clear by considering the motion of an eddy along a line of sight. This motion will not change the associated radiometer output. All motions along the beam A or the beams B_i will thus not effect the correlation compu-

329

tations. The measured speed refers always to the flux component along the fan beam normal. Horizontal flux components, i.e., ground winds, can thus also be measured by a second pair of periscopes on the unattended buoy. These periscopes must be set such that their fan normal is in a horizontal position.

3. OPERATIONAL CORRELATION ALGORITHMS

Cross correlation computations require special algorithms which are sufficiently general to process signals from a variety of electromagnetic sensors during all weather conditions of practical interest. Such algorithms do not exist, since the amplitude and the spectrum of heat radiation fluctuations are changing with atmospheric stability conditions, precipitation, daily temperature variation, fog etc. in a way which defies present statistical models of stationary time series and present analog recording devices. New "piecewise" correlation algorithms have been developed since 1966 [Krause and Havlutzel, 1968] which have already successfully recognized and corrected many of the environmental variations of heat radiation. The corrections could also be used for self-adaptive control of the data conditioning electronics. The special features of these algorithms will now be illustrated in terms of the modifications which they introduce in the recorded time series. Error criteria are also included in these programs which automatically indicate the validity of the modifications.

3.1. PIECEWISE DETRENDING AND NORMALIZATION OF RADIOMETER RECORDS

Standard correlation techniques will cancel unrelated signals from two radiometer outputs only if the data records are stationary, or, if the environment of the radiometer's field of view does not change during the run. In piecewise correlation techniques this condition is approximated by integrating only over a short piece of the record since the environment does not change significantly over relatively short time intervals, ΔT. More precisely, the changes that the ever – changing environment will produce in a record piece are approximated by piecewise variations of DC shifts, DC trends and RMS amplitudes. Detrending and normalization procedures are then applied to each piece prior to averaging over many pieces.

The calculations of DC shifts, DC trends and RMS amplitudes are illustrated in Fig. 6. The left part of the figure shows a slightly smoothed trace of a DC coupled radiometer output over a record piece which is 50 seconds long. The DC shift of this piece is given by the piecewise average

$$\overline{(x)}_i = \frac{1}{\Delta T} \int_{(i-1)\Delta T}^{i\Delta T} x(t)dt. \tag{1}$$

This value is graphically illustrated by a broken line. The position of this line is such that the shaded area above this line is equal to the shaded area below the line.

DC trends are introduced by assuming that the photometer outputs, x and y, may be split into piecewise linear components and the stationary components x_1 and x_2.

$$x(t) = x_1(t) + a_{1i}\left(t - (i - \tfrac{1}{2})\Delta T\right) + \overline{x}_i$$

$$y(t) = x_2(t) + a_{2i}\left(t - (i - \tfrac{1}{2})\Delta T\right) + \overline{y}_i \tag{2}$$

for $(i-1) \le t \le i\Delta T$.

The addition of a linear component to stationary data will shift the position of the autocovariance curve. This autocovariance curve is defined by

$$\overline{\left(C_{xx}(\tau)\right)}_i = \overline{\left(x(t) - \overline{x}_i\right)\left(x(t+\tau) - \overline{x}_i\right)}_i . \tag{3}$$

In the presence of linear components the area under this covariance curve will have the value [Krause, 1969]

$$\frac{1}{3}\left(\frac{a_1 \Delta T}{2}\right)^2 = \frac{1}{2\tau_m} \int_{-\tau_m}^{+\tau_m} \overline{\left(C_{xx}(\tau)\right)}_i \, d\tau = \overline{\tau\left(C'_{xx}\right)}_i \, . \tag{4}$$

This value is graphically illustrated in Fig. 4 by shading the areas above and below the associated ordinate, $\overline{\tau\left(R_{xx}\right)}_i$. The absolute value of the DC trends, $\left|\frac{a_1 \Delta T}{2}\right|$, may thus be found from calculating the area under the autocovariance curve. Furthermore, the effects of these trends may be eliminated by shifting the covariance curves until the area of the shifted curve is zero.

The RMS amplitude of the stationary component follows from the condition that the mean square value of a detrended auto-covariance curve should be equal to the mean square value of the stationary component.

$$\overline{\left(\sigma_x^2\right)} = \overline{\left(x_1^2\right)}_i = C_{xx}(\tau = 0) - \overline{\tau\left(C_{xx}\right)}_i . \tag{5}$$

The RMS amplitude may thus also be evaluated graphically by bisecting the covariance curve in area equal parts as illustrated. The values of σ_i which have been obtained provide a range for the stationary component. This range is shown by drawing equidistant lines to the linear component. The resulting "corridor" should contain most, but not all of the piecewise record as indicated by Fig. 4.

This marginal record piece was chosen for the above illustration where the DC trends are so strong that the test operator had to reset the DC bias voltage to keep the signal within the dynamic range of the amplifier. This change of bias voltage is indicated by the sudden signal drop at 586 seconds. As a result of this bias switch, the calculated trend is smaller than the actual trend.

3.2. INFORMATION RETRIEVAL BY ACCUMULATION OF RECORD PIECES

Environmental variations are approximated in the present algorithms by the piecewise variations of DC shift, $\overline{x}_i$, DC trends $\overline{(a\Delta T/2)}$, and RMS amplitudes, $\overline{\sigma}_i$. The effect of these variations on the correlation computation is then minimized by replacing the actual signal, x, with its piecewise normalized stationary components, x_1/σ_i. The same procedure is applied to the second photometer output. The information, which is common to the two photometer records x and y, is then retrieved by applying the correlation analysis of stationary time series to the piecewise normalized stationary components x_1/σ_{xi} and x_2/σ_{yi}. The correlation function, which is obtained from one piece, is given by the piecewise average

$$\overline{\left(c_{xy}(\tau)\right)}_i = \frac{\overline{x_1(t)x_2(t+\tau)}_i}{\overline{(\sigma_x)}_i \, \overline{(\sigma_y)}_i} = \frac{\overline{C_{xy}(\tau)}_i - \overline{\tau\left(C_{xy}\right)}_i}{\overline{(\sigma_x)}_i \, \overline{(\sigma_y)}_i} . \tag{6}$$

The correlation, which is obtained for an entire record of m pieces, follows by the accumulation of piecewise averages. This gives the accumulative average

$$\overline{\overline{\left(c_{xy}(\tau)\right)}}_m = \frac{1}{m} \sum_{i=1}^{m} \overline{\left(c_{xy}(\tau)\right)}_i . \tag{7}$$

Fig. 5 illustrates such accumulative covariance functions for the same marginal run on Fig. 4. The run consisted of 66 pieces. Strong DC trends occurred in both channels and the test operator had to reset the bias voltage many times. However, it appears that the large correlations at the maximum time delay, which a bias change introduces as indicated in Fig. 4, cancel each other in the accumulation process. The accumulative auto-correlations do not show extrema at the high time delays. The auto-correlations are also very similar for both channels, i.e., the normalized stationary components have the same power spectrum. The peak power spectrum should occur at a frequency, f_{peak}, which has a period that is four times the first zero crossing of the auto-correlation. This period is 68 seconds and exceeds the piecelength, $\Delta T = 50$ seconds.

331

Each piece of a stationary data record represents an independent experiment that has been repeated under the same environmental conditions. The 66 pieces of the above record may thus be treated as 66 repeated experiments, if the stationary components are really stationary. This gives the opportunity to estimate the accuracy of the accumulative correlation functions from the deviations between an individual experiment and the average over all experiments. The mean square error of an individual lag point is

$$\left(\overline{\overline{\Delta(c_{xy}(\tau))}}_m\right)^2 = \frac{1}{m(m-1)} \sum_{i=1}^{m} \left(\overline{(c_{xy}(\tau))}_i - \overline{(c_{xy}(\tau))}_m\right)^2. \tag{8}$$

This error is also plotted in Fig. 5 as a function of time delay. The errors of the auto-correlation functions are quite small and are virtually independent of the time delay. The drop to zero at zero time delay is artifically enforced by the piecewise normalization. At zero time delay all auto-correlations were set to one as per definition of the RMS amplitude, such that no variation can occur between pieces.

The cross correlation between the two photometer records is shown in the lower portion of Fig. 5. The peak correlation occurs approximately at zero time delay. This indicates zero transit times of common disturbances between the two beams. This result was expected since the photometric lines of sight intersected approximately 50 feet above the ground. The value of the correlation peak is 0.22. This indicates that only 22% of the entire signal power is common to both beams. The common signals were thus buried in noise and have been retrieved only by the accumulative of many pieces.

The root mean square error of the cross correlation is also plotted in Fig. 5. Its absolute value is approximately equal to the error of the auto-correlations, if one considers the lag interval around zero delay. This result is expected for stationary data, where the remaining errors represent the amount of noise that has not yet been cancelled, since our finite record length $T = m\Delta T$, provides only a finite number of noise oscillations. The average error of the cross-correlation may thus be used to estimate the uncancelled fraction of noise that is still left in the cross-correlation of the normalized stationary components. This uncancelled fraction of noise is

$$\delta \cdot \overline{\overline{(c_{xy})}}_m = \sqrt{\frac{1}{2\tau_m} \int_{-\tau_m}^{\tau_m} \left[\overline{\overline{\Delta(c_{xy}(\tau))}}_m\right]^2 d\tau}. \tag{9}$$

The error of the cross-correlation increases significantly near the maximum time delay. Its value approaches that of the cross-correlation itself and exceeds the errors of the autocorrelation by a factor of two. The second peak of the cross-correlation is thus statistically insignificant. Furthermore, its value reflects environmental variations, since the level of uncancelled noise is much smaller. The previous discussion of bias switches make us believe that the correlation peak at τ_m does probably reflect the change of bias voltage, which the test operator introduced during the run.

3.3. STATISTICAL AND ENVIRONMENTAL VARIATIONS DURING A TEST

The retrieval of common signals by accumulation of piecewise averages is successful only if the detrending and normalization of record pieces reduces the amplitude of the environmental variations below the limit of acceptable noise of the stationary components. This condition must be checked for each run since large variations of heat radiation often occur during changes of the atmospheric environment. Our present tests rely on the change of the statistical error of our accumulative average with increasing integration time, as illustrated in Fig. 6. Practical implications of the central limit theorem imply that the variations between piecewise averages should be normally distributed regardless of the physical phenomenon that was recorded, if and only if, the environment did not change during the run. In this case, the accumulative mean

$$\overline{\overline{(\ )}}_m = \frac{1}{m} \sum_{i=1}^{m} \overline{(\ )}_i \tag{10}$$

332

should asymptotically approach a limiting or true value, $E\left[\overline{(\ )}\right]$, with increasing record length $T = m\Delta T$. This true mean deviates from the sample mean $\overline{(\ )}_m$, by the amount $\overline{(\ )}_m - E\left[\overline{(\ )}\right]$. If the experiment could be repeated many times, each repeated run would give a different deviation of the accumulative mean, $\overline{(\ )}_m$, from the true mean, $E\left[\overline{(\ )}\right]$. These deviations should further more follow the χ distribution. Knowing this distribution, one can express the expected statistical error of the accumulative mean by

$$E\left[\left(\overline{(\ )}_m - E\left[\overline{(\ )}\right]\right)^2\right]^{\frac{1}{2}} = \sqrt{\frac{m-1}{m}}\ \frac{A}{\sqrt{T}}\ . \qquad (11)$$

The calculation of the noise factor A will be treated later. The actual error might deviate from this expected error within a confidence interval, which is also given by the χ^2 distribution. Only 10% of all repeated runs will show an error, which is smaller than the lower confidence level, subscript 0.1

$$\left|\overline{(\ )}_m - E\left[\overline{(\ )}\right]\right| \leq \frac{\chi_{0.1(m)}}{\sqrt{m}}\ \frac{A}{\sqrt{T}} \quad \text{for 10\% of all runs.} \qquad (12)$$

However, 90% of all repeated runs will show errors, which are exceeded by the upper confidence level, subscript 0.9

$$\left|\overline{(\ )}_m - E\left[\overline{(\ )}\right]\right| \leq \frac{\chi_{0.9(m)}}{\sqrt{m}}\ \frac{A}{\sqrt{T}} \quad \text{for 90\% of all runs.} \qquad (13)$$

The expected error curves might thus be summarized as follows:

$$\frac{\chi_{0.1(m)}}{\sqrt{m}}\ \frac{A}{\sqrt{T}} \qquad \text{lower confidence level,}$$

$$\sqrt{\frac{m-1}{m}}\ \frac{A}{T} \qquad \text{expected error of accumulative mean,}$$

$$\frac{\chi_{0.9(m)}}{\sqrt{m}}\ \frac{A}{\sqrt{T}} \qquad \text{upper confidence level.}$$

The functions $\chi_{0.1}(m)$ and $\chi_{0.9(m)}$ are available in statistical handbooks and are given in Table 1. The expected statistical error, Eq. 11, indicates, how the errors of accumulative means should decrease with increasing integration time $T = m\Delta T$ or piece number, m, in the absence of environmental variations. The amount of environmental variations may thus be judged by comparing the expected error with the samples of this error which have been calculated directly from the deviations between piecewise averages, $\overline{(\ )}$, and their accumulative averages, $\overline{(\ )}_m$,

$$\Delta\overline{\overline{(\ )}}_m = \frac{1}{m(m-1)} \sum_{i=1}^{m} \left(\overline{(\ )}_i - \overline{(\ )}_m\right)^2 . \qquad (14)$$

The discussion of statistical and environmental variation now proceeds in two steps. In the first step the noise factor, A, is calculated by fitting the actual error curve $\Delta\overline{(\ )}_m$ with the expected error curve, Eq. 11. The noise factor A is chosen such that the relative mean square deviations between these two curves is a minimum. Let M denote the number all available pieces. The best curve fit may then be expressed by the conditions:

$$\frac{\partial}{\partial A} \sum_{m=2}^{M} \left\{ \frac{\Delta\overline{(\ )}_m - \sqrt{\frac{m-1}{m}}\ \frac{A}{m\Delta T}}{\sqrt{\frac{m-1}{m}}\ \frac{A}{\sqrt{m\Delta T}}} \right\}^2 = 0. \qquad (15)$$

333

The partial differentiation of Eq. 15 gives an algebraic equation for A. The solution of this equation gives the desired computer estimate of the noise factor

$$A = \sqrt{\Delta T} \ \frac{\displaystyle\sum_{m=2}^{M} \frac{m^2 \Delta (\overline{\overline{}})^2_m}{m-1}}{\displaystyle\sum_{m=2}^{M} \frac{m \Delta (\overline{\overline{}})_m}{\sqrt{m-1}}} .$$ (16)

The second step is to plot the expected error curves, and their confidence levels together with the actual error samples as illustrated in Fig. 6. The solid circles represent the statistical error, that is given by the fraction of uncancelled noise, Eq. 9. This curve agrees closely with the associated expected error, $\sqrt{m-1} \ A_C/\sqrt{mT}$, within the associated confidence levels $\chi_{.9} \ A_C/\sqrt{mT}$ and $\chi_{.1} \ A_C/\sqrt{mT}$. This good agreement illustrates that the stationary components, which provided the correlation $(C_{xy})_m$, are indeed stationary. A deviation from stationarity seems to occur only at the last piece, which falls outside the confidence interval of statistical variations. One possible explanation would be an increase of bias switches as discussed in the last section.

The piecewise normalization will smooth all variations of the common signal power, which might be introduced by intermittency of atmospheric turbulence near the beam intersection, or other phenomena. The variations of the common power must therefore be estimated in a different way. The absolute value of the common signal power is given by $(\overline{\overline{\sigma}}_x^2)_{66} (\overline{\overline{\sigma}}_y)_{66} (\overline{\overline{c_{xy}}})_{66, \text{peak}}$. Its uncancelled variations may be estimated by assuming that the uncertainty of the absolute signal power $\Delta(\overline{\overline{\sigma}}_x^2)_m$ and $\Delta(\overline{\overline{\sigma}}_y^2)_m$ are ultimately caused by environmental variations which are common to both records. The amount of these common power variations might then be approximated by $\left(\Delta(\overline{\overline{\sigma}}_x^2)_m \ \Delta(\overline{\overline{\sigma}}_y^2)_m\right)^{\frac{1}{2}}$. The associated error curve is also plotted in Fig. 6. Most of these errors fall outside the confidence interval for the fraction of uncancelled noise. The variation of signal power between pieces is thus so large, that an environmental variation of signal power is more likely than a statistical variation of the uncancelled noise which remains in the stationary components. The environmental variations are so strong, that the error increased when processing pieces 12 to 22. Processing 10 new pieces therefore did not improve the statistical accuracy of the common power estimate but decreased it although more information was processed. Results of this nature underline the need to normalize prior to the accumulation of pieces.

3.4. CORRELATION OF TIME DERIVATIVES

The remote probing of humidity fluxes, heat fluxes and surface winds, that was outlined in Section 2.3, requires correlation of time derivatives of the radiometer output signals. Our present programs approximate such correlation of time derivatives by replacing the recorded time history with its moving central difference. The resulting new time series is then detrended and normalized prior to the accumulation of pieces. This eliminates the problems of D.C. shifts, trends and amplitude variations as discussed in the previous chapter.

The approximation of time derivatives with central differences introduces two additional problems which are absent in normal correlation computations. These problems are: (a) the weighting of high frequency noise components with the square of the frequency and (b) quantization errors, which may introduce large errors in the calculated difference between two closely spaced sample points. Both problems have been overcome by Su through application of moving or jumping means. Moving means are used as digital filters. They have successfully smoothed out high frequency noise components beyond a choosen frequency cut off. [Su, 1969a]. Jumping means are used to reduce quantization errors by sampling a record very fast and by replacing a group of up to 5 samples with new sample point. This point is equal to the sum of the 5 samples. It is more accurate than the individual samples, since the quantization error of the samples cancel each other partially during the summation [Su, 1969b].

334

Pilot experiments on the optical approximation of ground wind speeds and turbulence levels were conducted by Colorado State University. A simple photodiode monitored changes of scattered sunlight. The results thus refer to an aerosol flux, not to a heat or humidity flux. Two ground telescopes look at the top of a meteorological tower and their lines of sight are separated along the mean wind direction, that is indicated by an anemometer at the tower top. For known and steady wind direction all common eddies will then travel along this separation line and the crossed beam concept can thus be verified with two beams rather than a more complicated fan beam combination. The results of such a test are shown in the lower part of Fig. 4 together with the direct speed readings of the anemometer. The comparison of the anemometer and crossed beam outputs indicates that the most probable speeds agree very closely and that the turbulence levels agree reasonably well.

The above example illustrates that special correlation algorithms can be developed which retrieve local information out of large noise. The level of the remaining uncancelled noise may be reduced below the amplitude of usually large environmental variations through a modification of the recorded time series. The ability of such algorithms to retrieve common thermal emission fluctuation in all weather conditions of practical interest depends on the generality of the statistical model which is used for determining the signal modification. Our present algorithms use piecewise changes of DC trends, DC shifts and gain factors to describe unknown environmental variations. These algorithms have been very successful in the few experiments where a comparison between remote and direct flux measurement was possible. However a statistically significant large amount of data must still be collected and processed, to evaluate whether these algorithms are sufficiently general for flux retrieval in all weather conditions of practical interest.

4. SIGNAL AND NOISE LEVELS OF ATMOSPHERIC THERMAL EMISSION FLUCTUATIONS

As stated in the introduction, it is required, for successful design of passive cross beam systems, to determine the emission from the atmosphere expected at the receivers. It is desirable to calculate the mean levels and the fluctuations of the signals and noise.

The relationship between the signal received and the structure of the turbulence may be seen by considering the effect of the eddies on emission. This may be evaluated without a knowledge of structures, since in the case of thermal radiation emitted by a specific volume, the intensity is dependent on the temperature of the material in the cell and its mass. Because of its strong absorption in the infrared region between 2 and 10 μ, the principal constituent producing significant thermal emission is water vapor. Carbon dioxide in its bands near 2.7μ or 4.3μ may be important at low humidity, but is so well mixed that only its temperature is important. Thus, generally speaking, the variation of signal in the infrared receiver is due to the fluctuations of temperature and humidity in the correlation region and the noise is due to the fluctuations in the remainder of the beam.

In the visible, thermal effects are small, and the signal arises from either Rayleigh scattering (depending on the mass of the material present), or from scattering by fluctuations of index of refraction or by the scattering from aerosols. It is not known at present which effect is predominant. In this report we consider only on-frequency scattering, excluding Raman and fluorescent effects. Further, no consideration is given to aerosols, either in a thermal or scattering mode. The discussion will center on thermal effects in the region of $2-8\mu$.

4.1. PASSIVE SYSTEMS

For simplicity, we will consider only a pair of radiometer systems. Passive crossed beam correlation systems are valued for their simplicity, consisting of two steerable telescopes, detectors, electronic equipment and recording devices. The receivers should be identical in gain, phase, frequency response and noise. Their overall electronic bandwidth must be wide enough to allow observation of the full bandwidth of the turbulent structure, the spectrum of most interest lying between 0.01 and 3 Hz. Their optical bandwidth is chosen to maximize performance under background noise and detector noise conditions. Since opening the optical bandwidth adds approximately equal amounts of noise and signal, the bandwidth is chosen wide enough so that the signal is much greater than detector noise. It should be noted that the signal and noise arise from identical phenomena, have the same bandwidth and statistics, and differ in that they come from different portions of the atmosphere.

335

4.2. S/N IN PASSIVE SYSTEMS

A phenomenological way of estimating the signal-to-noise ratio in a single receiver is to consider the beam divided into cells similar to the cell of interest, and to determine the relative intensity from these regions. Such a phenomenological estimate is independent of the wavelength region used and the source of the radiation, thermal or scattered.

The radiation from the beam is dependent on the temperature and mass of material in the beam and on the attenuation due to the intervening atmosphere. The largest signal-to-noise ratios will occur only when the cell of interest is large and close to the receiver and the attenuation is sufficiently large to prevent more distant parts of the atmosphere lying within the beam from being effective. On occasion it may be desirable to accept less energy from the crossing cell in order to block the large noise from distant clouds.

In computing the signal to noise ratio the following assumptions are made:

1. The noise has essentially the same spectral statistical properties as the signal.
2. The noise comes from cells similar to the common cell and radiation from each cell is statistically independent of radiation from any other cell. Thus, we may assume that the intensities from each cell add.
3. The whole beam volume may be divided into non-overlapping cells each of which acts as a source of noise.

The choice of the cells depends upon the turbulent structure of the atmosphere, which is quite variable. However, the theory may be developed with sufficient generality so that any structure function may be used subject to the three assumptions above.

We will here make the assumption that the beam is divided into cells each of the same thickness, d. Let m be the ordinal number of the cell of interest. Then the radiation from each cell, depending on the area of the base of the cell, increases as $(md)^2$. But by the inverse square law, it likewise diminishes by $(1/md)^2$. Thus, the intensity from each cell, reaching the receiver, is the same except for attenuation, assumed due principally to water vapor. The signal reaching the receiver is then

$$x_S = I e^{-KR} , \tag{17}$$

where R = Md is the distance to the signal cell and I is the intensity at the receiver when K = 0. Here K is the intensity absorption coefficient suitably averaged over the bandwidth, twice the amplitude absorption coefficient. The noise arises then from all other cells (here we include the cell of interest)

$$x_N = I \sum_{m=0} e^{mKd} . \tag{18}$$

The upper limit on the sum is not specified. It only has to be sufficiently large that the remaining terms may be neglected or to include all the atmosphere when the absorption coefficient is small. The signal-to-noise ratio is then

$$\frac{x_S}{x_N} = \frac{e^{-KR}}{\sum_{m=0} e^{-mKd}} . \tag{19}$$

The denominator is a (possibly truncated) geometric series and is either equal to or can be approximated by $\frac{1}{1-e^{-Kd}}$. Then,

$$\frac{x_S}{x_N} = e^{-KR} \left(1 - e^{-Kd} \right) . \tag{20}$$

An obvious calculation shows that the optimum choice of absorption coefficient K is

$$K = \frac{1}{d} \log_e \left(1 + \frac{1}{M}\right) \approx \frac{1}{dM} = \frac{1}{R} \qquad (21)$$

where we have let $dM = R$. Thus a good approximation for a maximum x_s / x_N, when the correlation cell is sufficiently far from the receiver, is to choose the wavelength so that the absorption coefficient is the reciprocal of the distance of the cell from the receiver. When $k = \frac{1}{R}$, then the optimum x_s / x_N is $1/Me$ where e is the Napierian base of logarithms. Thus we are always dealing with signal to noise ratios less than one.

The assumption has been made that the degree of turbulence is the same in each cell. However, the small scale turbulence near the ground is much larger than that at 50 meters height under a majority of meteorological conditions. Thus, since the turbulence near the receiver is larger than that further out, the signal-to-noise ratio from the cell of interest is decreased if it is located far out under these conditions.

The infrared, as seen in Fig. 8, offers the possibility of eliminating noise due to clouds by chosing a strong attenuation region. For this region we wish to determine the expected signal levels.

The previous discussion gives no idea of the levels of the incident radiation. If these are significantly below the detector noise after rectification, their fluctuations will be difficult to observe. In order to calculate the radiation reaching the receiver from a given cell of interest it is necessary to solve the radiation transfer equation. The details of this calculation may be found in a forth-coming ESSA Technical Report, and will be only summarized here. Crucial to this calculation is a detailed knowledge of the water molecule lines in the $2-8\mu$ region. The results of the calculation, done by R. Calfee, are shown in Fig. 9.

It is seen that in part of the spectral region, the signals are well above the noise of good infrared detectors such as lead selenide or mercury-doped germanium. The parameters of the cell size and receiver have been kept conservative, so that good performance may be expected by infrared radiometer systems over the whole range of $2-8\mu$. The choice of wavelength would be made principally to eliminate cloud backgrounds.

We have, up to this point, discussed the S/N ratio, and the mean level of radiation falling on a receiver. Since the signals of interest are not so much the mean level, but the fluctuations, it is necessary to examine some data from meteorological observations in order to determine whether the fluctuations of temperature, for example, are sufficiently high under average conditions to be observed above detector noise.

4.3. ATMOSPHERIC TEMPERATURE FLUCTUATIONS

Data taken at the ESSA meteorological tower at Gunbarrel Hill near Boulder Colorado, have been examined to determine some average values of temperature and humidity fluctuations. Two types of days, stable and unstable, were evaluated. Means and variances were calculated from data taken in 76 one hour periods during five days by sensors responding in the frequency range 0-10 Hz.

The measurements are taken in a small volume, essentially a point, whereas volume averages are needed. A private communication from S. Clifford, ESSA Wave Propagation Laboratory, shows that the ratio of the average square of the volume averaged temperature to the average square of the point temperature $<\widetilde{T}^2>/<T^2> = R$ is

$$R = \frac{18^{\frac{11}{6}}}{x^2 \Gamma\left(\frac{1}{3}\right) \Gamma\left(\frac{3}{2}\right)} \int_o^\infty \frac{du}{(1+u^2)^{11/6}} \left[\frac{\sin ux - ux \cos ux}{(ux)^2}\right] , \qquad (22)$$

where $x = a/L_o$, a the radius of the volume, L_o the outer scale of turbulence, and Γ is the gamma function. For a choice of $L_o = 1$, $a = 10$ meters, the ratio of the standard deviation is 0.548. Thus for volumes of interest in the crossed beam experiment the standard deviations of tempera-

337

ture and humidity may be taken as one-half the point measurements.

The observations considered here were 76 one hour samples in 5 days, at 10, 20, 50, 100 and 150 feet above ground. The standard deviations of temperature average .61°C and range from 0.1 to 1.7°C. The standard deviations of humidity average 0.18 gm m^{-3} and range from 0.02 to 0.86 gm m^{-3}. The radiometers used in crossed beam experiments at Haswell, described in section 5 of this article detect a temperature difference of 0.005°C of a black body which fills the aperature. The atmospheric cells are not black bodies, but at strong absorption frequencies approach an absorptivity of 0.5. Thus we see that the fluctuations of temperature should be observable most of the time.

4.4. ERROR IN THE CORRELATION FUNCTION ESTIMATE

We must now investigate the effectiveness of the estimate of the correlation function as a tool for obtaining the common signal in the midst of noise. We will calculate an error for a specific spectrum with Gaussian statistics. In particular we will now determine the integration time required to bring the estimated correlation function sufficiently near the time correlation function of a stationary process. It is clear that the atmosphere is stationary for only short periods at most, and we must use detrending methods to allow sufficiently long integration times.

Each radiometer in a crossed beam experiment produces a voltage output which consists of the signal from the correlation cell and the emission from the remainder of the beam. The character of these received fluctuations depends strongly on the size of the eddies crossing the beam in comparison with beam dimensions and crossing height and radiometer separations.

If one considers a summer day, in midwest plains, with convection and humidity cells arising from the ground, typically a few hundred meters in size, moved by a moderate breeze, it is easy to see that many such cells may intersect large portions of both beams nearly simultaneously when crossed without delay, and perhaps when crossed with delay, when the vertical planes of the beams are not perpendicular to the wind. In this case the large eddies will produce relatively large fluctuations at low frequencies which are not associated with the geometrical common volume of the two beams or the projected common volume.

Usually, the correlation volume is much larger than the common volume. The choice of signal and noise powers in our result will determine the relative sizes of the correlation volume and the volume of the radiometer beam which produces noise. The calculation here does not have the generality of the error calculations of Sec. 3, but has the advantage that bandwidth and effects on the error may be determined. For another view of this same problem see Jayroe and Su [1968]. It is again important to note that the noise has the same bandwidth and statistics as the signal of interest and hence may not be separated by filtering. Correlation or some high order statistical process is the only way to distinguish the correlation volume from the remainder of the beams.

The signal (from the common cell of the two beams) and the noise (from the remainder of the beams) are each from a similar random ensemble, and thus we must consider the estimate of the correlation function (the integration time T finite) also to be a member of an ensemble of random functions. It is difficult to obtain the distribution function of this random ensemble so we will evaluate its variance as a function of T. This quantity will be a measure of the error arising in estimating the correlation of the common signals by the finite correlation of the signals plus noise, i.e. the outputs of the radiometers.

Let x, y be the a.c. coupled voltages (of zero mean) from the two radiometers. We assume that the detectors are perfect power law detectors, with no mixing of components. The random function $x = x_C + x_N$ and $y = y_C + y_N$, where x_C and y_C are the signals from the cell of interest and x_N and y_N are the noise functions. The estimate of the correlation function is

$$\overline{R_{xy}(\tau)} = \frac{1}{T} \int_0^T x(t)\, y(t+\tau)\, dt \ . \tag{23}$$

We wish to obtain the variance of this quantity, which is a function of T, as a function also of the delay between the two signals. The variance is

$$\text{Var}\left[\overline{R_{xy}(\tau)}\right] = E\left\{\left[\overline{R_{xy}(\tau)} - E\left(\overline{R_{xy}(\tau)}\right)\right]^2\right\}$$

$$= E\left[\left(\overline{R_{xy}(\tau)}\right)^2\right] - \left[E\left(\overline{R_{xy}(\tau)}\right)\right]^2 \tag{24}$$

We may calculate the second term of the right hand side of the equation by substituting for x_1 and y_2. Assuming stationarity, all terms are zero except

$$E\left[\overline{R_{xy}(\tau)}\right] = \frac{1}{T}\int_0^T E\left[y_C(t)\, y_C(t+\tau-\tau_m)\right] dt = Ry_C(\tau-\tau_m) \tag{25}$$

which is the autocorrelation function of the signal y_C. The elimination of the other terms occurs because noise-noise and noise-signal correlations are zero. Here we have assumed that $x_C(t) = y_C(t + \tau_m)$, where τ_m is the delay caused by the time of travel of an eddy between the two beams. This is equivalent to assuming that an eddy retains its character in the time of travel between the two beams. This has only the virtue of simplicity. To assume that $y_C(t + \tau_m)$ is a stochastic function of $x_C(t)$ would be more correct but would prevent any evaluation of the influence of integration time on accuracy. The effect of the assumption is to confine us to zero or small delays. We see from this result that the expected value of the finite correlation function over the ensemble of random radiometer outputs is just the correlation function of the signal, with proper delay; the noise does not enter into this quantity.

The calculation of the first term in Eq. 24 is made tedious by the many terms which arise. However, after substituting for S_1 and S_2 and replacing the product of integrals by a double integral and then performing the required multiplications, most terms are found to be zero just as above. The task is simplified by employing the theorem (applicable to Gaussian distributions, which are assumed here):

$$E\left[X_1 X_2 X_3 X_4\right] = E\left[X_1 X_2\right] E\left[X_3 X_4\right] + E\left[X_1 X_3\right] E\left[X_2 X_4\right] + E\left[X_1 X_4\right] E\left[X_2 X_3\right].$$

With the notation $\theta = \tau - \tau_m$ and an obvious extension of the notation above for auto-correlation functions, we obtain:

$$\text{Var}\left[\overline{R_{xy}(\tau)}\right] = \frac{1}{T^2}\int_0^T dt_1 \int_0^T dt_2 \left[\left(Ry_C(t_2 - t_1) + Ry_N(t_2 - t_1)\right)^2 \right.$$

$$\left. + Ry_C(t_2 - t_1 + \theta)\, Ry_C(t_2 - t_1 - \theta)\right]. \tag{26}$$

Changing variables, $t_2 - t_1 = \gamma$, and integrating once (using the eveness of the resulting integrand to change the integration range) we obtain:

$$\text{Var}\left[\overline{R_{xy}(\tau)}\right] = \frac{2}{T}\int_0^T \left(1 - \frac{\gamma}{T}\right)\left[Ry_C(\gamma) + Ry_N(\gamma)\right]^2 d\gamma + \frac{2}{T}\int_0^T \left(1 - \frac{\gamma}{T}\right)\left[Ry_C(\gamma + \theta)Ry_C(\gamma - \theta)\right] d\gamma. \tag{27}$$

All time varying functions in the discussion are assumed Gaussian, stationary, bandwidth-limited white noise. The correlation functions are of the form:

$$CB \frac{\sin \pi B\tau}{\pi B\tau} \cos 2\pi f_o \tau \tag{28}$$

and the power spectral density function is

$$C_O(f) = \begin{cases} C, & 0 \le f_o - B/2 \le f \le f_o + B/2 \\ 0, & \text{otherwise} \end{cases}$$

where B is the bandwidth, f_o the center frequency and C is the peak power density. We use $C = C_{ON}$ for the noise power and $C = C_{OS}$ for the signal power. Thus

$$\text{Var}\left[R_{xy}(\tau) \right] = \frac{2(C_{OS} + C_{ON})^2 B^2}{T} \int_o^T \left(1 - \frac{\gamma}{T} \right) \left[\frac{\sin \pi B\gamma}{\pi B \gamma} \cos 2\pi f_o \right]^2 d\gamma$$

$$+ \frac{2C_{OS}^2 B^2}{T} \int_o^T \left(1 - \frac{\gamma}{T} \right) \left[\frac{\sin \pi B(\gamma + \beta)}{\pi B (\gamma + \beta)} \cos 2\pi f_o(\gamma + \beta) \frac{\sin \pi B(\gamma - \beta)}{\pi B(\gamma - \beta)} \cos 2\pi f_o(\gamma - \beta) \right] d\gamma. \tag{29}$$

It is obvious that the variance tends to zero as $T \to \infty$ even when noise is present. The error may be estimated for any particular case by numerical computation of these integrals, and we may thus estimate the required integration in order to reduce the error to a specified level.

We may, for illustration, assume the especially simple case when $C_{ON} = f_o = \beta = 0$ and assume T sufficiently large so that $\frac{\gamma}{T} << 1$. Then the standard deviation is $C_{OS}\sqrt{\frac{2B}{T}}$. In this case the correlation function is, for zero delay, $C_{OS}B$. The ratio of these is $\sqrt{\frac{2}{BT}}$. A typical bandwidth is of the order of 1 Hz. Thus for the ratio to be 1/10, T = 200 sec without any noise present. It is clear that with noise present, much larger integration times will be required. Typically these have been found to be of the order of an hour when only small eddies are present in order to have a satisfactory confidence level. When larger eddies are present or the common volume is large, statistically significant correlation functions may be obtained in a few minutes.

5. REMOTE SENSING EXPERIMENTS AT HASWELL, COLORADO

Two sets of experiments have been performed on crossed beam correlation systems at the Haswell meteorological tower (500 feet high), Fig. 10. This tower is located in the plains area of Colorado. The first set of experiments was in the period of 14-19 September 1969. The second set occurred during 1-10 October 1969. Only the first set will be considered here since insufficient time was available to process the second set before submission of this manuscript.

The objectives of the Haswell crossed beam experiments were:

1) To determine the fluctuation of the temperature and humidity of the atmosphere, up to heights of 500 ft., under various meteorological conditions, by the use of the visible and infrared radiometers.

2) To investigate the correlation of atmospheric turbulence observed by two radiometers looking at a common cell as a function of height.

3) To determine the correlation between a single radiometer and temperature and humidity fluctuations in the output of the beam, as measured by meteorological instruments on the tower.

4) To investigate the effect of temperature quiescence [Coulman, 1969] and humidity variations in the processing of correlation data; consider especially the variation of temperature quiescence with height, and optimum statistical processing with various crossing heights.

5) To investigate the relative effect of aerosols compared with temperature and humidity variations in the detection of turbulence.

6) To investigate the effect of wavelength in elimination of background noise, especially clouds.

7) If the results of the preliminary experiments indicate that turbulence can be observed by correlation techniques, the second group of experiments will seek the distance and time over which eddies retain an identity recognizable by their scattering or emission.

In the set of experiments to be considered here, only the infrared radiometers were used.

It can be seen that the basic purpose of the experiments was to establish whether correlation of atmospheric fluctuations may be observed by the use of radiometers separated in space. It was believed that it was necessary to establish even the most obvious of points by experimental evidence since little or no experimentation had been done in the past at infrared wavelengths under meteorologically known conditions.

The infrared radiometers were specified by V. E. Derr and N. L. Abshire of ESSA and designed by A. Montgomery, H. Betz and A. Weigandt of IIT Research Institute. The design was a compromise between sensitivity and cost. The collecting telescope is Newtonian, with a collecting area of 300 cm^2 and an optical beam width of 6×10^3 radians. A circular variable filter produces 0.2μ bandwidth from 2 to 7μ. The detector is a Joule-Thomson expansion-cooled lead selenide type. The chopper frequency is 720 Hz, and the chopper blade is shielded from the heat of the chopper motor. The detector output is impedance matched to a preamplifier and detected by a lock-in amplifier. The signal from the lock-in is kept at a sufficiently low level that it is not necessary to switch ranges during an experiment unless an extreme temperature or humidity change occurs. In order to observe the fluctuations, the output of the lock-in is a.c. coupled to another amplifier, with a low frequency R C network cutoff at 0.01 Hz. This choice was made on the basis of an analysis of many trial observations with d.c. coupling. Almost all drifts in temperature or humidity expected in the Haswell experiments would be eliminated by this choice. The upper frequency cutoff was determined by the integration time constant of the lock-in amplifier. Here, after initial experimentation with time constants, it would be advisable to choose the shortest integration time feasible, since further smoothing, if desirable, would be possible during data processing, and more information would be recorded. The practical lower limit on integration in the system used was 0.3 sec. Shorter times generally produced fluctuations which exceed the dynamic range of the tape recorder and chart recorder. Lowering the gain of the tape recorder to keep the signal within the dynamic range is not advisable, because the signals sought, the cell correlation signals, which are much less than the apparent fluctuations, should not be lowered beyond the tape recorder noise.

It is imperative in a system of this kind to analyze the noise of each component, to make certain that the noise level of the detector is the limiting system noise. This is done by correct choice of amplifier gain, by impedance matching, and by using the maximum possible dynamic range of the tape recorder. Further, since we are looking for cross-correlations in delay, the systems must be phase-matched.

The first set of Haswell experiments included calibration with a black body and common volume experiments with the radiometers aimed at each other for preliminary instrument evaluation. A group of experiments with variation of the infrared center frequency and recording time constants were performed with the two radiometers separated by 7 feet, pointing straight up parallel to the tower, on the upwind side, with the beam approximately 5 feet from the sensors at 128', 311' and 495'. The beams did not significantly overlap below the 500-foot level. In this position, one could expect a large correlation of the signals from the beams. Cross correlation of the beam signals with the sensor signals at the various levels will reveal whether the vertical atmospheric structure may be determined by radiometric means. Other experiments had the radiometers separated by 35 feet and with crossed beams, crossing first at 128 feet, then at 50 feet. Meteorological data is available at the crossing point as well as at the other stations for most experiments. An elevator provided meteorological data between stations. A final set of experiments had the beams crossed in projection with a delay distance of approximately 40 feet

apart, their planes parallel, and perpendicular to the average wind direction.

These initial experiments were entirely successful in providing a basis for choosing optimum time constants, optimum wavelengths, and verifying that the structure of eddies at least over short distances is maintained sufficiently to observe by their thermal emission. They confirmed the original estimates of mean radiative power and fluctuation amplitude.

Initial processing of selected record portions by a simplified procedure, without the full power of the method previously described, has shown strong correlation in many cases even with very short records.

Insufficient time was available for the complete processing of data before the submission of this manuscript, so selected portions of the data were processed to obtain correlation functions for several experimental situations. Because the preliminary processing method could only sample at approximately one per second, higher frequency information is lost. The full power of the correlation algorithm previously described was not used. Instead the means were subtracted, the functions normalized and the correlation function computed as a function of delay. A future report from ESSA and NASA will analyze in detail all data obtained.

The results of the computations are presented in Figs. 11-14. Fig. 11 is from an experiment in which the radiometer beams were vertical, parallel to the tower, separated at the base by 7 feet. Although parallel, they did not overlap until near the 500 feet level. The purpose of the experiment was to observe correlations between the two beams under slightly separated conditions and the degree of correlation between the radiometer signal and the meteorological sensors on the tower. As can be seen, the correlation is a maximum at zero, with a correlation function of 0.87. During this experiment the wind was variable in direction and velocity (5-15 mph), with an average direction perpendicular to the plane of the two beams. Thus, it is clear that the eddies in general are correlated over both beams, hence are larger than the separation.

By increasing the distance between the two vertical beams the distribution of eddy sizes could be obtained.

In Fig. 12 the radiometers are separated by 35 feet and the beams cross at 50 feet, on the approximately upwind side of the tower. The winds during the experiment were partially across the beam. Thus the large convection cells arrive at a large portion of one beam before the other, giving the autocorrelation maximum off zero. The peak here is well-defined but broader than the previous case due to variability of conditions during the run.

In contrast, an experiment with the beams crossed at 128', shown in Fig. 13, had stable wind directions during the entire run and its correlation peak (.75) is at zero delay and very well defined. The wind direction here was almost always nearly perpendicular to the plane of the crossed beams.

Finally several separated beam experiments were performed. The projection of the crossing point was 50 feet above the ground, the beams were separated by 40 feet. The wind was quite variable in direction and speed but Fig. 14 shows the correlation function for a short portion of 14 minutes during which the winds remained relatively constant. The broad peak centers at the average wind speeds during this period.

It must be cautioned that the portions of the records processed and shown here are only a small part of the data. A definitive evaluation of all the data will be reported.

6. CONCLUSIONS

The preliminary tests analyzed in detail by the complete correlation algorithm described in Section 3 were, in terms of trends and shifts of operating conditions, more exacting than any expected field data. The method was successful in eliminating trends and obtaining statistically significant correlation functions. The piecewise accumulation of statistics is advantageous in revealing changing conditions and in determining optimum averaging times. Such accumulation is a necessity for a system which is broadcasting remotely gathered data in order to avoid excessively wide band data channels.

342

The demands on the sophisticated correlation algorithm are lessened by the use of a.c. coupling and the confidence factor of the results can be increased. Some of the experiments at Haswell where a.c. coupling was used were satisfactorily, but not definitively examined by simplified methods. This preliminary analysis has, as shown above, revealed that fluctuations of water vapor mass and temperature can be observed by radiometers, and further, that strong correlation exists in the signals of separated infrared radiometers observing the same fluctuations. This conclusion is not a trivial one, since experiments with visible passive radiometers show much less correlation and require much more extensive data and processing in order to produce a satisfactorily low error in the estimate of the correlation function. With the infrared radiometers the correlation may, in many experimental situations, be seen by examination of the recorder charts as the signal is received. This is true whenever the common volume observed is large or large eddies pass. Also it is clear that the use of the infrared radiometer has been justified by its ability to discriminate against cloud backgrounds which have previously distressed experimenters working at visible wavelengths. The simple choice of a relatively strong absorption band will eliminate all cloud background noise.

An important modification in the data processing becomes apparent after examination of large quantities of field data. The large eddies, which correlate well, are intermittent, particularly above 150 feet. This intermittency, probably the same as the quiescent periods measured by Coulman [1969], produces a large error in the estimate of the correlation function by diluting the data with quiet periods in which the signals are quite random, being due to many small eddies. The large signals, if processed separately from the intervening quiescent periods, would be useful in measuring fluxes. Thus, an on-line statistical processing system would benefit from an objective criterion for the selection of such intermittent signals. A future test program must thoroughly explore the time structure of the radiometer signals to establish parameters needed in the selection of statistical criteria.

Essentially it has been established that the correlation method is useful for observing turbulence and measuring some characteristics such as eddy scales. However there remains much testing to determine the extent to which it can be employed as a measuring tool rather than an observational one. Among the many things which remain to be done is the exploration of active systems which give promise particularly at visible wavelengths, utilizing lasers. Such systems, of course, suffer from the inverse square law disadvantage; the great advantage of a passive system is that it is independent of range if the object fills the aperture. In any event the many promising results encourage further exploration.

7. ACKNOWLEDGEMENTS

8. REFERENCES

Coulman, C. E. (1969), "A Quantitative Discussion of 'Solar Seeing', I," Solar Phys. 7, 122-143.

Jayroe, R. R. Jr. and M. Y. Su, (1968), "Optimum Averaging Time of Meteorological Data with Time Dependent Means," NASA TMX 53782, 103-114.

Krause, F. R. (1969), "Remote Probing of Wind Components Using Transit Distances of Optical Disturbances," NASA MSFC Internal Note L-AERO-69-2.

Krause, F. R. and B. C. Havlutzel (1968), "Noise Elimination by Piecewise Cross-Correlation of Photometer Outputs," Proceedings of the Scientific Meetings of the Panel on Remote Atmospheric Probing, National Academy of Sciences, May 16-17, 555-589.

Krause, F. R., M. Y. Su, and E. H. Klugman (1969), "Passive Optical Detection of Meteorological Parameters in Launch Vehicle Environments," Article Accepted by Journal of Applied Optics.

Sandborn, V. A. and D. J. Pickelmer (1969), "Measurement of Wind Speeds with an Optical Cross Beam System," International Aeroscience Electronics Symposium, Washington, D.C.

Su, M. Y. (1969a), "Digital Data Conditioning for Evaluation of the Cross-Correlation and its Second Derivatives," Northrup Corp. Office Memo M-794-9-574, Contract NAS 8-30518.

Su, M. Y. (1969b), "Quantization Errors and their Reduction for Digital Time Histories," NASA CR-61302.
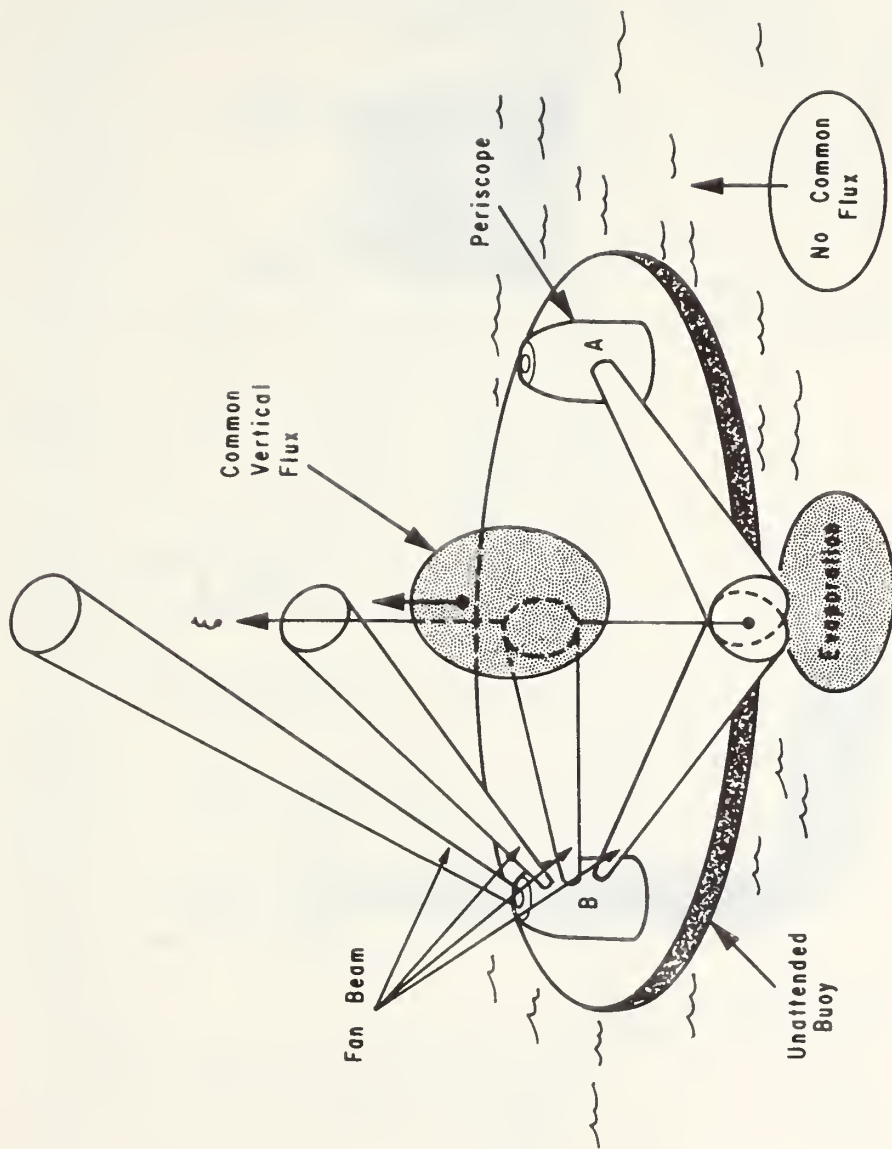
FIG. 1. PASSIVE OPTICAL HUMIDITY AND HEAT FLUX MONITORING SYSTEM
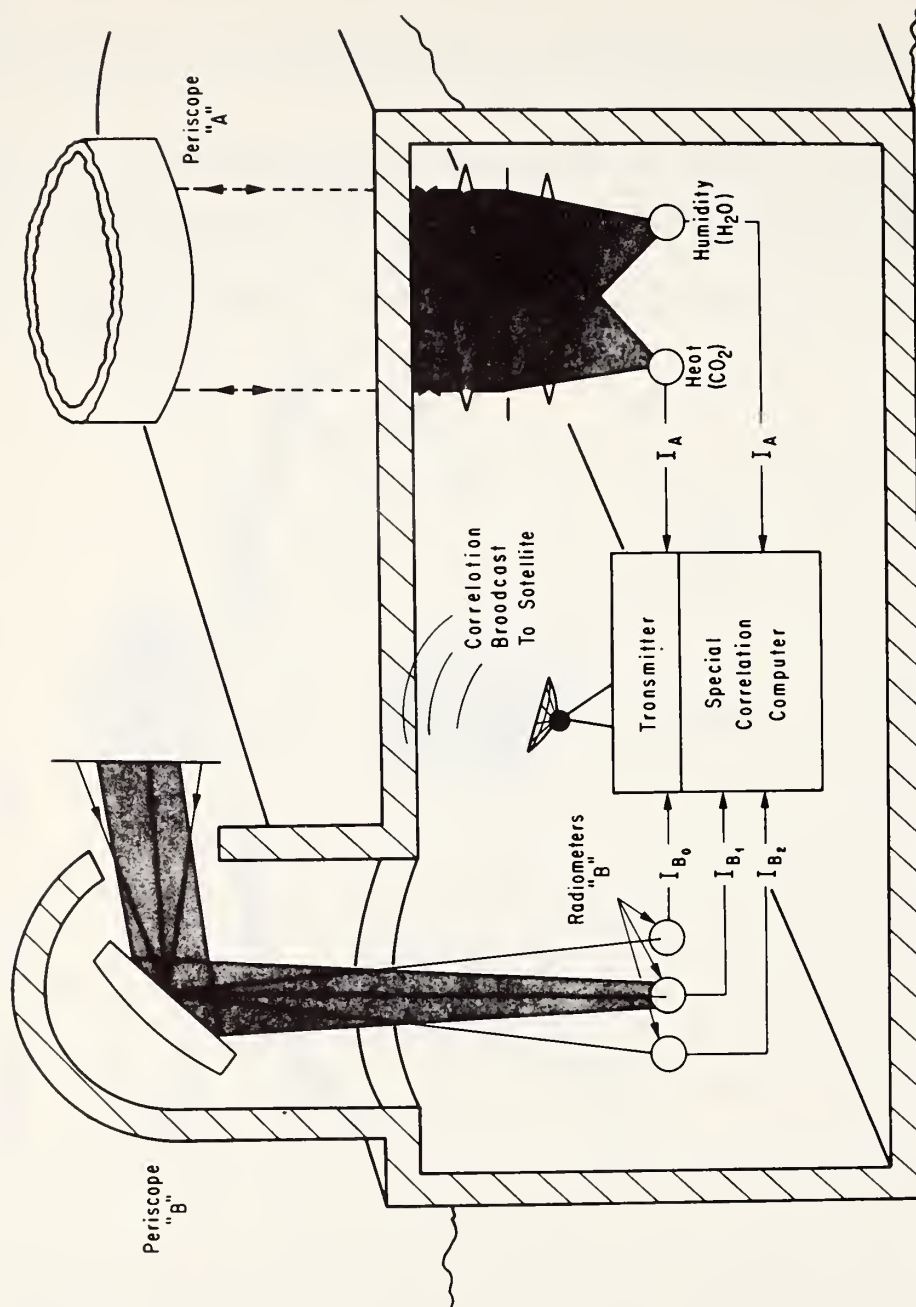
FIG. 2. CONTINUOUS ON-BOARD CORRELATION COMPUTATIONS
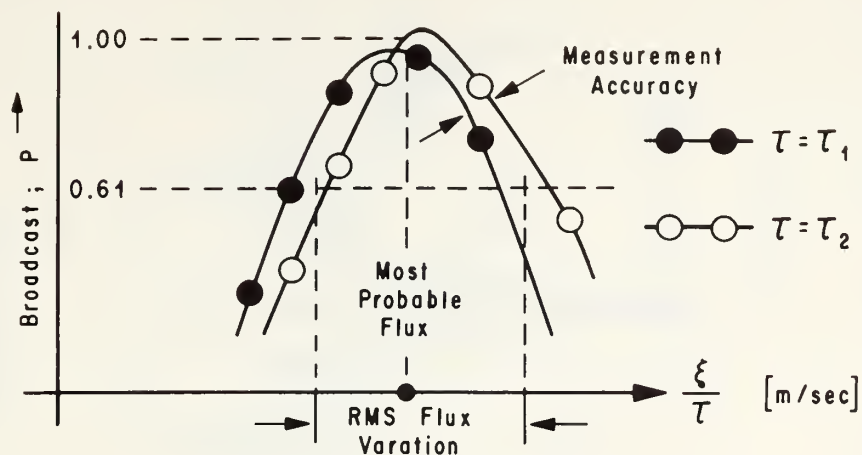
$$P = \frac{\tau}{\xi} \left\langle \frac{\partial I_A}{\partial t} (t - \tau; \lambda) \frac{\partial I_B}{\partial t} (t; \xi; \lambda_1) \right\rangle$$

Remote Controls:

ξ = Beam Seperation Along Fan Normal

τ = Time Delay Approximating Transit Time

λ = Optical Wave Length Selecting Heat or Mass Flux

FIG. 3.   REMOTE   DISPLAY   OF

CONTINUOUS   CORRELATIONS   BROADCAST

347

a. SLIGHTLY SMOOTHED SIGNAL

b. AUTOCOVARIANCE

$$\overline{\left(C_{xx}(\tau)\right)}_i = \overline{\left(x(t) - \bar{x}_i\right)\left(x(t+\tau) - \bar{x}_i\right)}_i$$
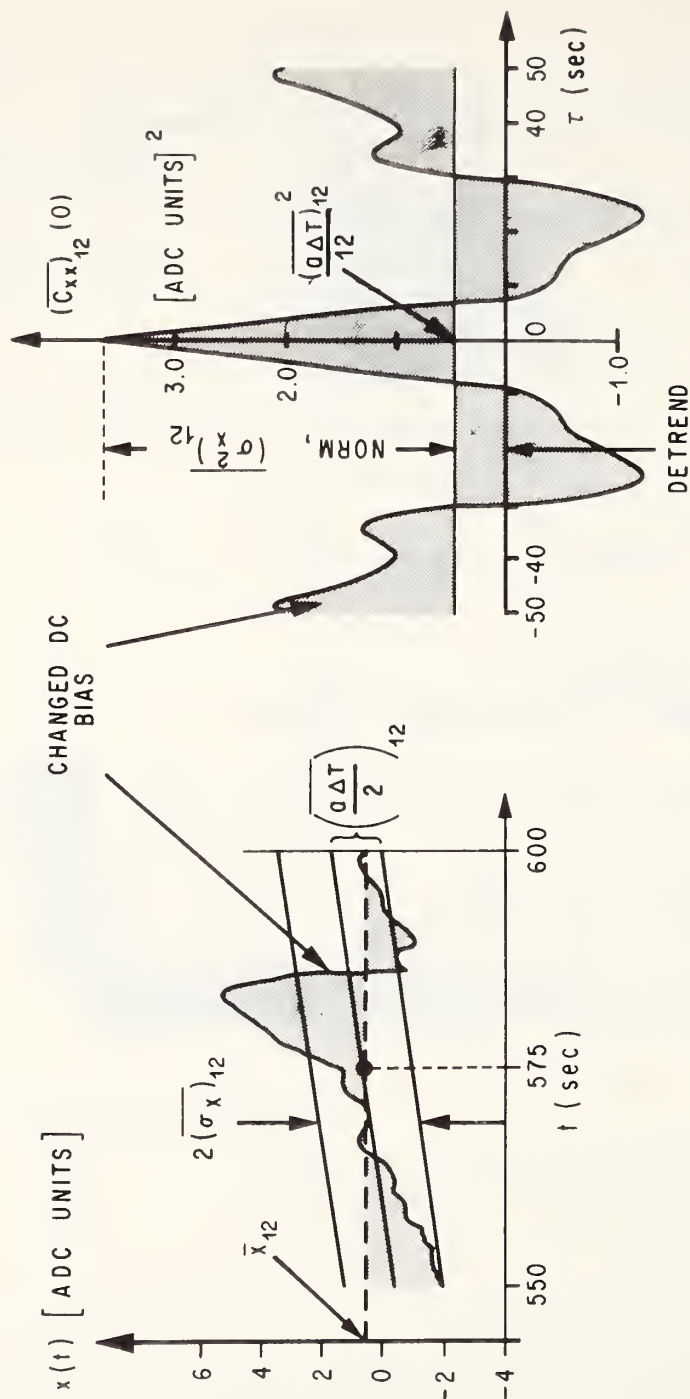
FIG. 4

DETRENDING AND NORMALIZATION PARAMETERS

FOR PIECE 12 OF IR RUN 7, TRACK 1

348

FIG. 5   INFORMATION   RETREVAL   BY   ACCUMULATION   OF   RECORD   PIECES
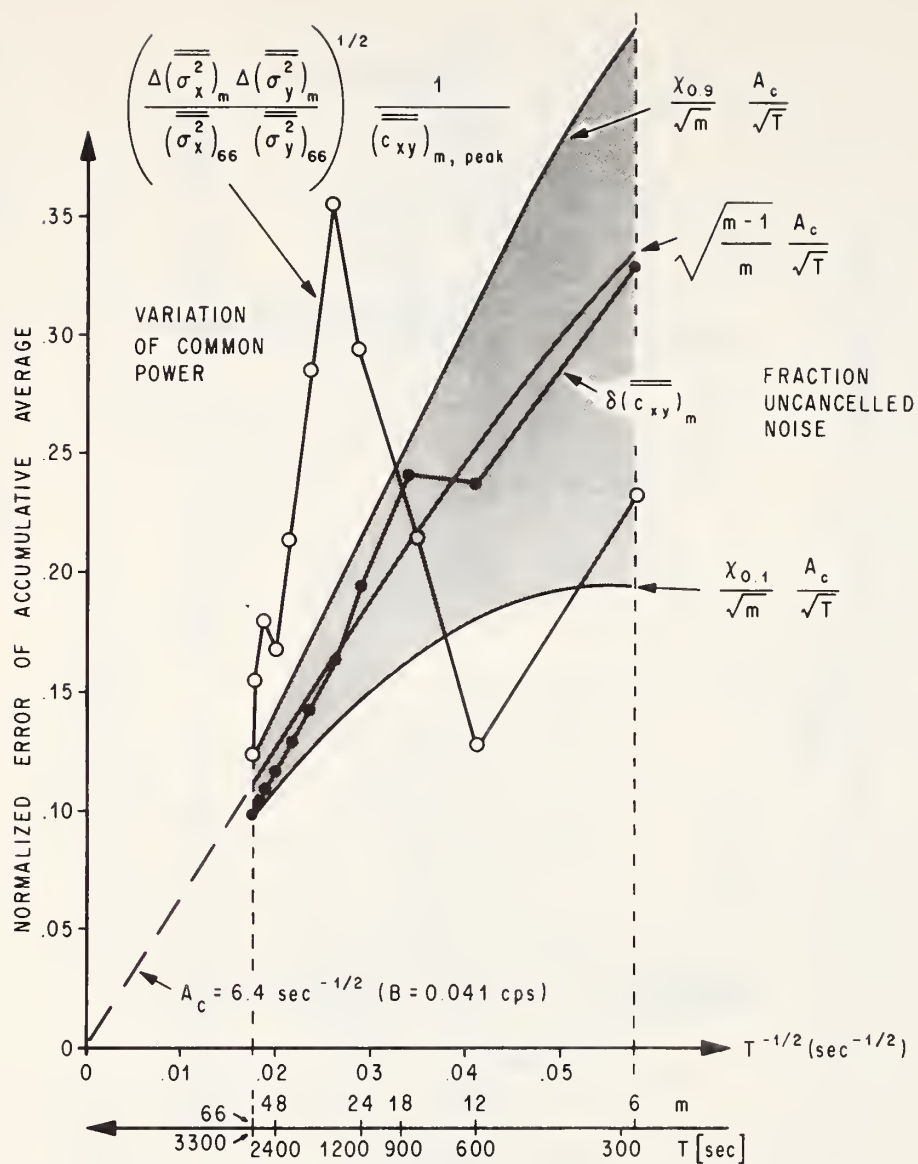
FIG. 6. STATISTICAL AND ENVIRONMENTAL VARATIONS OF
SIGNAL POWER DURING IR RUN 7

350
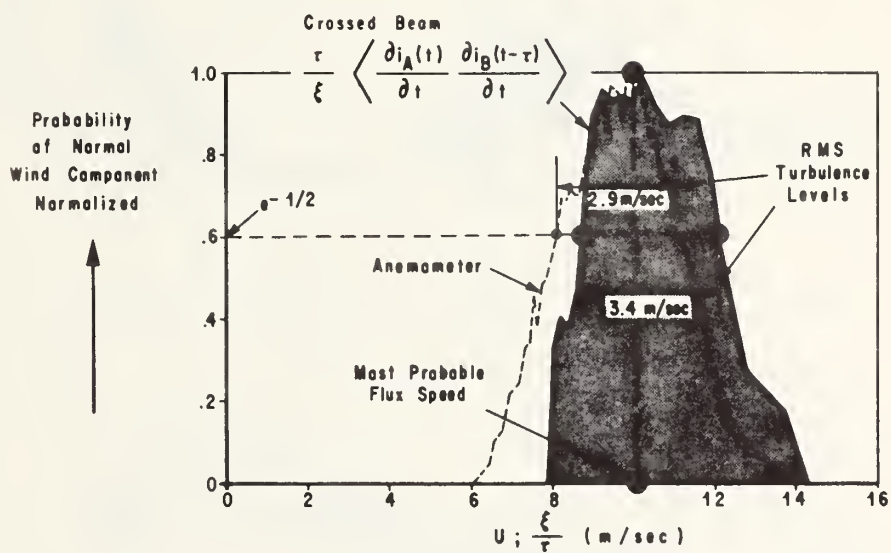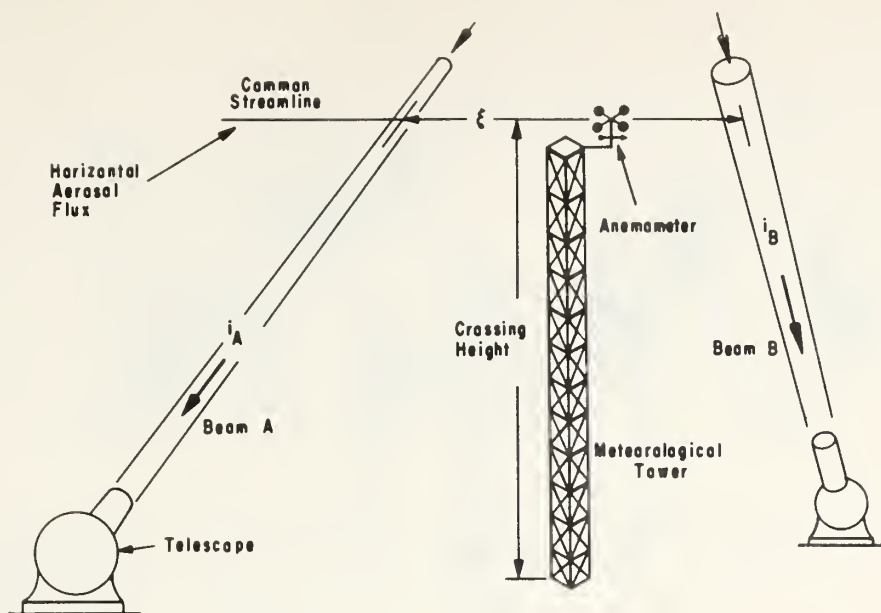
FIG. 7   TIME DERIVATIVE CORRELATION AND FLUX SPEED VARIATION

351
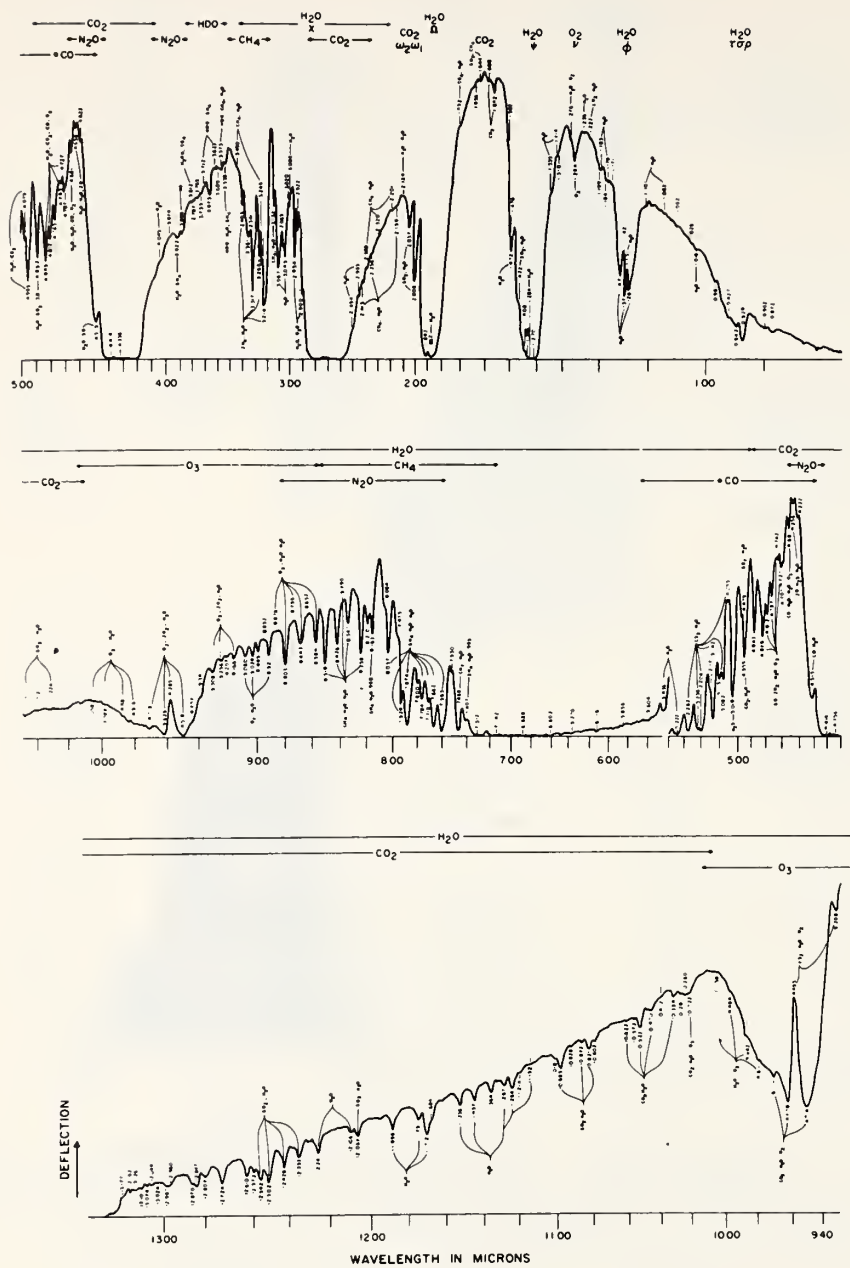
FIGURE 8. ATMOSPHERIC ABSORPTION, 1-13 μ
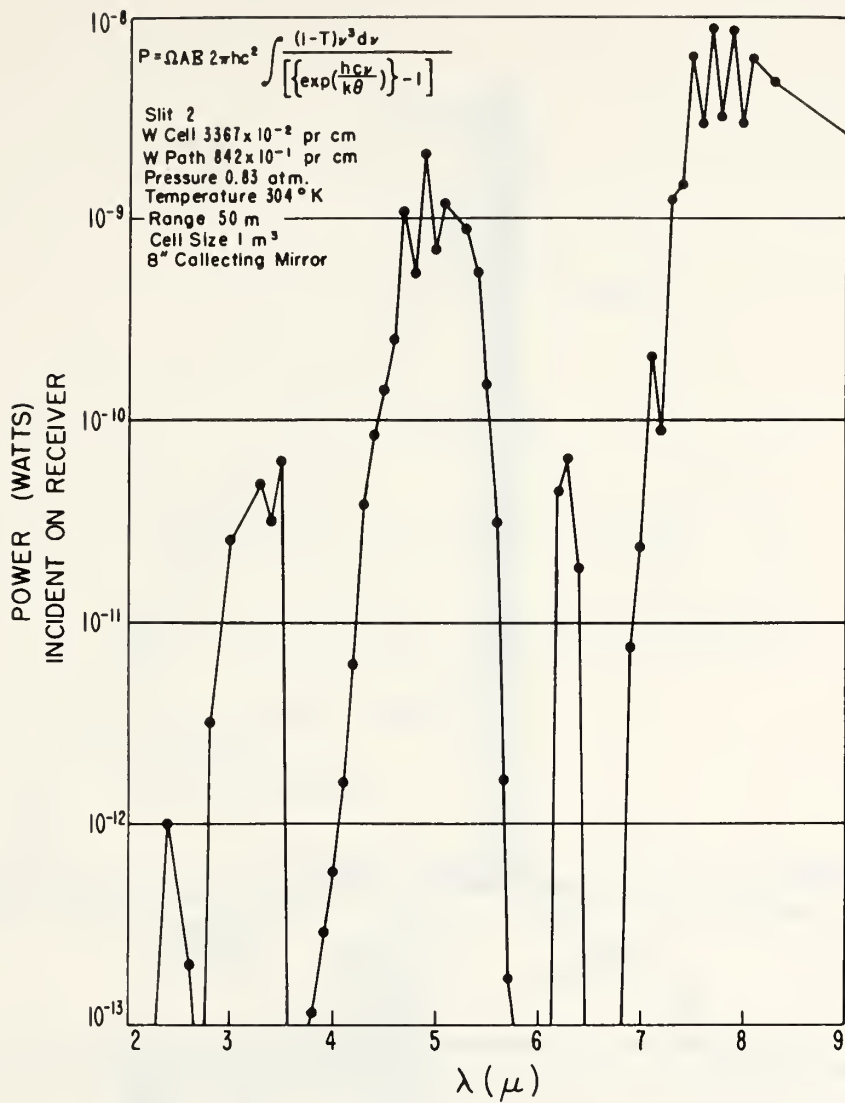
FIGURE 9. POWER INCIDENT ON RADIOMETER

495'

ELEVATOR

311'

128'

500' TOWER

WINCH
HOUSE

CABLE
HOUSE

INSTRUMENT
CABLES

DUGOUT
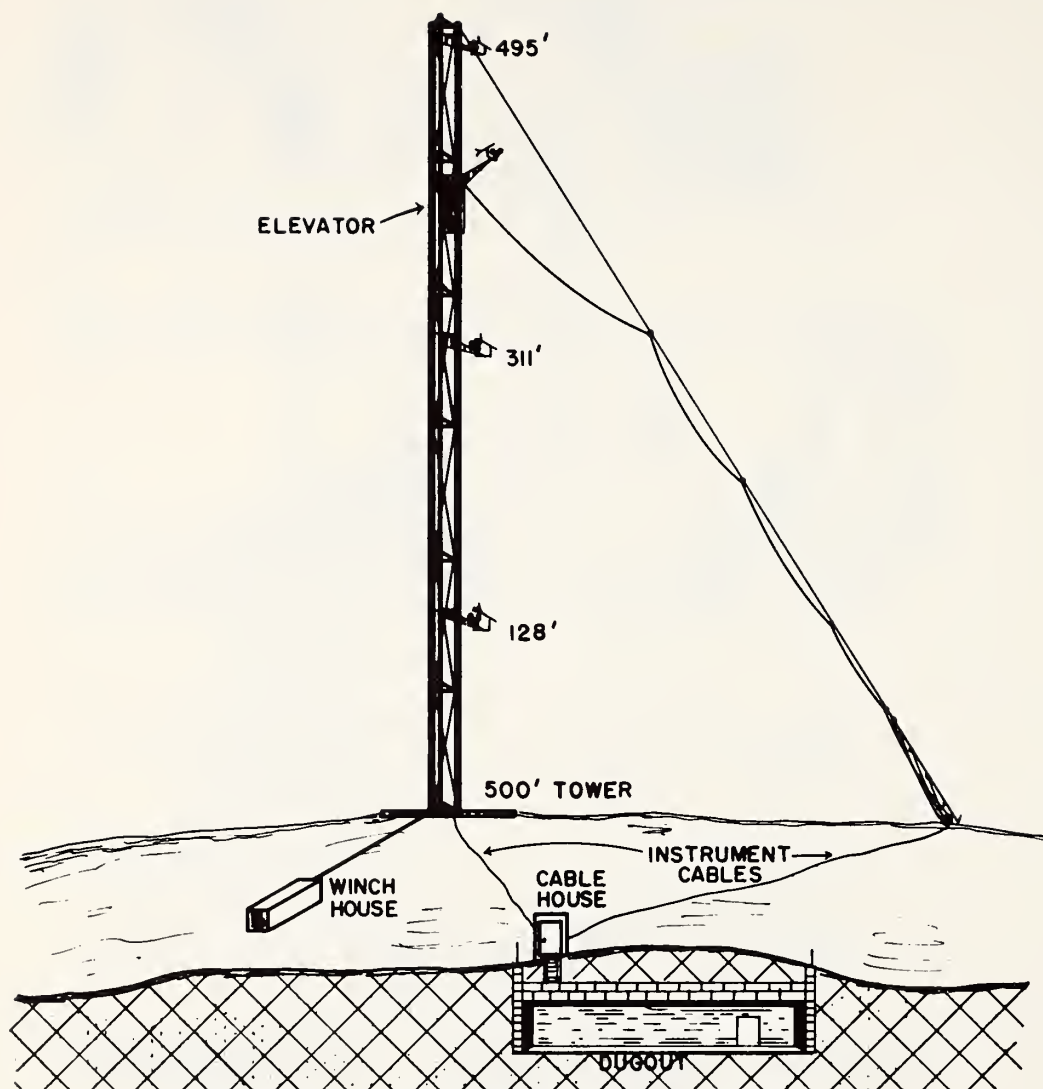
HASWELL METEOROLOGICAL TOWER
FIGURE 10

RUN 44 A

$|R_{xy}|$
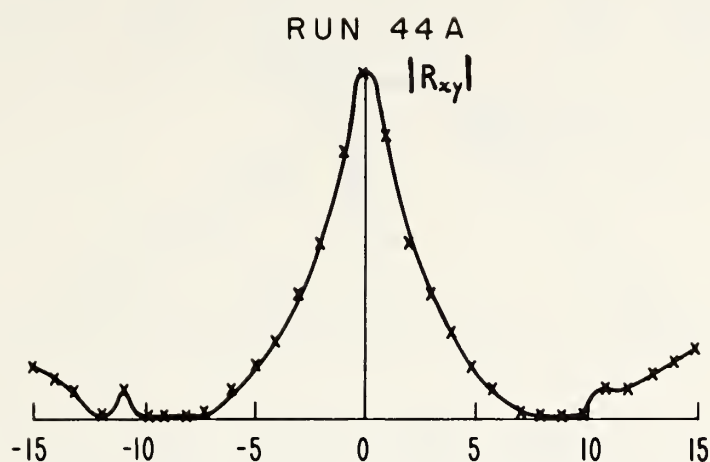
PEAK CORRELATION = 0.85 AT ZERO DELAY

BEAM SEPARATION 7 feet
INFRARED λ   5.9 μ
TIME CONSTANT   1 sec

CROSS-CORRELATION FUNCTION, PARALLEL BEAMS

FIGURE 11

RUN 26
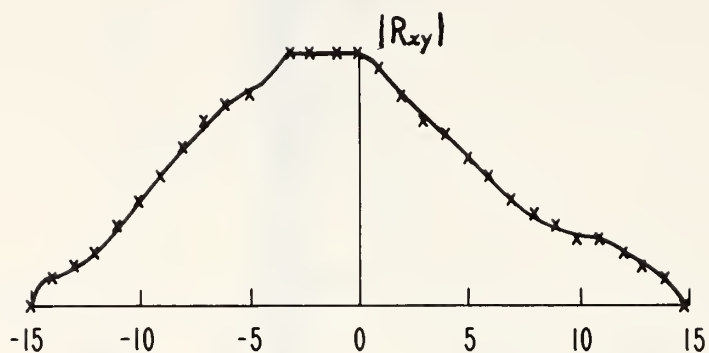
PEAK CORRELATION = .61 AT −1 sec. DELAY

INFRARED: $\lambda = 5.4\,\mu$
TIME CONSTANT: 1 sec.
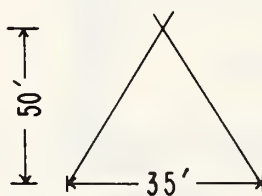
CROSS-CORRELATION FUNCTION, BEAMS CROSSING AT 50'
FIGURE 12

RUN 14

$|R_{xy}|$

PEAK CORRELATION = .75 AT ZERO DELAY

INFRARED: λ = 5.4 μ
TIME CONSTANT: 1.0 sec

128'

35'
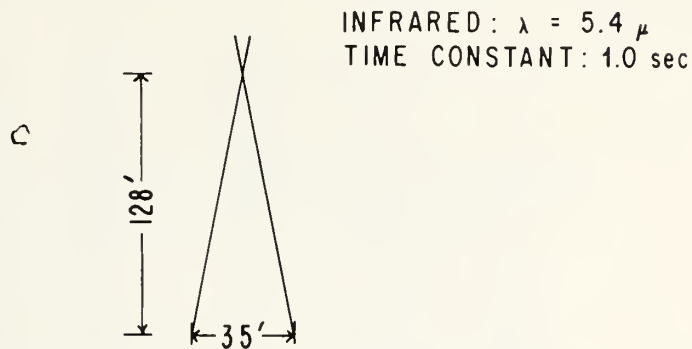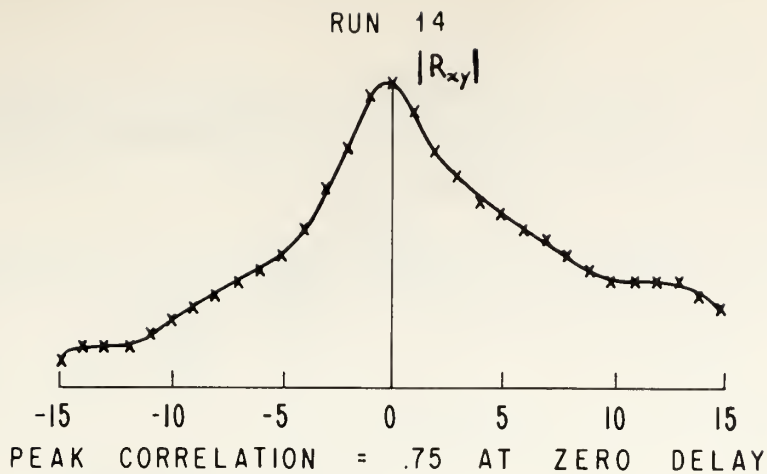
CROSS-CORRELATION FUNCTION, BEAMS CROSSING AT 128'

FIGURE 13

RUN 48

$|R_{xy}|$

PEAK CORRELATION = .27 AT 10 sec. DELAY
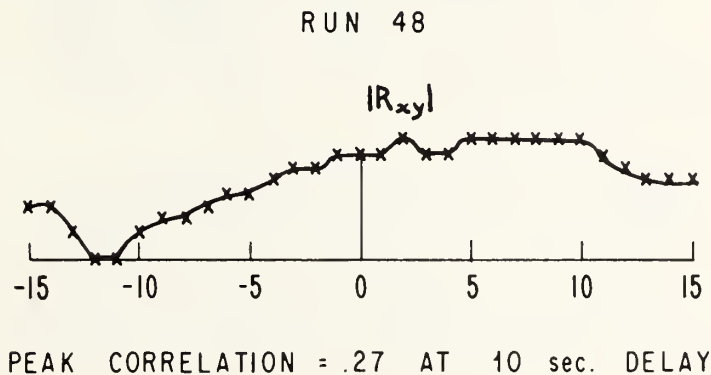
INFRARED, λ = 5.9 μ
TIME CONSTANT: 0.3 sec.
WINDS, LIGHT (3-15 mph), VARIABLE DIRECTION,
MOSTLY PERPENDICULAR TO BEAM PLANES

FIG. 14 CROSS-CORRELATION FUNCTION, BEAMS
CROSSING AT 50' WITH 40' SEPARATION

357

TABLE 1. EXPECTED ERROR AND CONFIDENCE LEVELS*

(a) Expected error of accumulative mean

$$E \left| \ (\overline{\overline{\ }})_m - E\left[(\overline{\ })\right] \right| = \sqrt{\frac{m-1}{m}} \ \frac{A}{\sqrt{T}}$$

(b) Associated confidence levels

$$\frac{\chi_{0.1}}{\sqrt{m}} \ \frac{A}{\sqrt{T}} \ \leq \ \left| \ (\overline{\overline{\ }})_m - E\left[(\overline{\ })\right] \right| \leq \ \frac{\chi_{0.9}}{\sqrt{m}} \ \frac{A}{\sqrt{T}}$$

(c) Confidence factors of χ^2 distribution

m	$\chi^2_{0.1}$	$\chi^2_{0.9}$	$\frac{m-1}{m}$	$\chi_{0.1}/m$	$\chi_{0.9}/m$
2	0.0158	2.71	0.707	0.09	1.16
3	0.211	4.61	0.817	0.27	1.24
4	0.584	6.25	0.866	0.382	1.25
5	1.06	7.78	0.894	0.46	1.25
6	1.61	9.24	0.913	0.52	1.24
7	2.20	10.6	0.926	0.56	1.23
8	2.83	12.0	0.935	0.59	1.22
9	3.49	13.4	0.942	0.62	1.22
10	4.17	14.7	0.949	0.65	1.21
11	4.87	16.0	0.953	0.67	1.21
12	5.58	17.3	0.958	0.682	1.20
14	7.04	19.8	0.964	0.709	1.19
16	8.55	22.3	0.968	0.730	1.18
18	10.1	24.8	0.972	0.750	1.17
20	11.7	27.2	0.976	0.765	1.17
25	15.7	33.2	0.980	0.792	1.15
30	19.8	39.1	0.983	0.812	1.14
61	46.5	74.4	0.992	0.873	1.10
∞	m	m	1.0	1.0	1.0

*Computer estimate of A

REMOTE ATMOSPHERIC PROBING BY GROUND-TO-GROUND LINE-OF-SIGHT OPTICAL METHODS

Robert S. Lawrence
ESSA Research Laboratories, Boulder, Colorado

ABSTRACT

We describe qualitatively the optical
effects arising from refractive-index vari-
ations in the clear air and discuss the
possibilities of using those effects for
remotely sensing the physical properties
of the atmosphere. The effects include
scintillations, path-length fluctuations,
spreading of a laser beam, deflection of the
beam, and depolarization. The physical
properties that may be measured include
the average temperature along the path, the
vertical temperature gradient, and the dis-
tribution along the path of the strength of
turbulence and the transverse wind velocity.

Line-of-sight laser-beam methods are
clearly effective in measuring the average
properties, but less effective in measuring
distributions along the path. Fundamental
limitations to the resolution are pointed out
and experiments are recommended to inves-
tigate the practicality of the methods.

1. INTRODUCTION

This paper deals with the optical effects arising from variations of the
refractive index of the clear atmosphere. It does not consider the effects of
absorption or scattering by either aerosols or molecules. Thus, there will
be no discussion of radiometry, spectroscopy, or spectrophotometry.

The atmospheric effects that remain include the modification of the opti-
cal path by the mean refractive index along the line of sight and the distortion
of an optical wave by the temporal and spatial variations in the refractive
index   Sections 2 through 4 summarize those atmospheric effects that may

be relevant to the problem of remote probing. The remaining sections describe briefly some methods for using the effects.

2. EFFECTS OF TURBULENCE

2.1 The Refractive-Index Variations

The twinkling of stars and the variable blurring of their images in a telescope are caused by the small-scale and rapidly varying density fluctuations associated with atmospheric turbulence. Density is the pertinent physical property because the optical refractivity, n-1, is proportional to density. In the open atmosphere the variation in density of a small parcel of air depends only on variation of its temperature because pressure differences are smoothed out with the velocity of sound. Thus, in what follows, we shall be safe in making no distinction between the refractive-index fluctuations and the temperature fluctuations. Notice, however, that these fluctuations are not necessarily identical to the velocity fluctuations measured by the hot-wire probes so commonly used in studies of turbulence. If the atmosphere is in neutral thermal stability, i.e. if the temperature lapse rate is adiabatic, strong mechanical turbulence may exist with little or no optical effect.

The direct relationship between temperature fluctuations and optical effects suggests the use of small, high-speed thermometers to measure directly the strength and the structure of turbulence as it affects light waves. Resistance thermometers having dimensions less than a millimeter and response times less than a millisecond are regularly used by ERL in Boulder to "calibrate" the atmosphere whenever optical measurements are in progress (see Ochs, 1967).

As we shall see later, the thermal irregularities that are most effective in producing optical effects range in size from a few millimeters to about ten centimeters. Over this range of sizes, and indeed to much larger scales, the turbulence follows closely the Kolmogorov-Obukov model which predicts that the power spectrum of temperature fluctuations will vary as the -5/3 power of the wave number. Measurements made at Boulder have shown the "inertial sub-range," in which the -5/3 spectrum holds, to extend to irregularities as small as 2 or 3 mm. At smaller sizes, the spectrum steepens as viscous damping destroys the turbulence.

2.2 Intensity Effects on a Light Wave

Let us consider the behavior of a light wave as it travels outward from a point source through the turbulent atmosphere (Figure 1). The wave front is initially spherical, as at A. Upon passing through irregularities to reach position B it becomes distorted. Since absorption and wide-angle scattering are negligible, the energy density of the wavefront B is still uniform and equal to its free-space value. Thus an ordinary square-law detector located at B would be unaffected by the irregularities and incapable of measuring

2

them. The irregularities in the wave front can, of course, be measured by a phase-sensitive detector such as an interferometer.
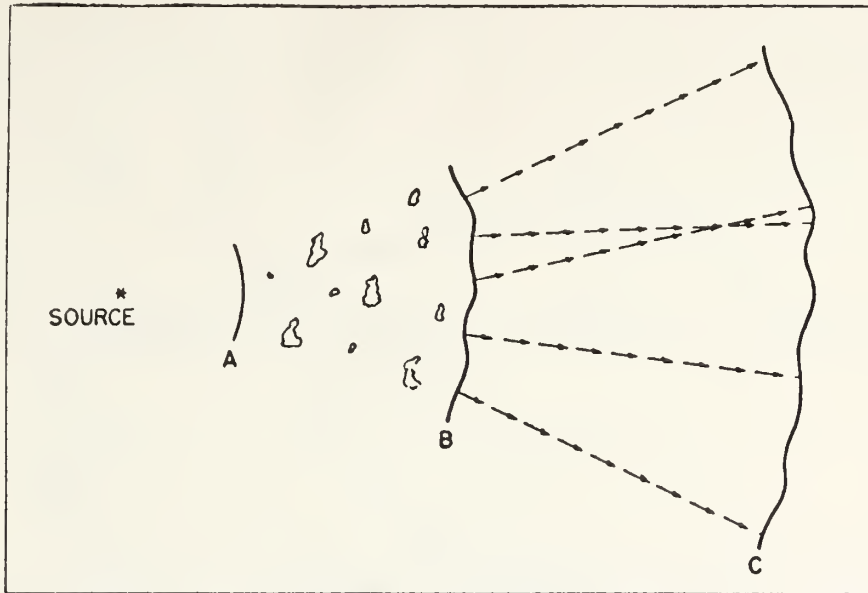
Figure 1. Schematic diagram of the propagation of a spherical light wave through a turbulent atmosphere. Phase fluctuations at B develop into phase and intensity fluctuations at C.

As the wave progresses from B toward C, the various portions of the distorted wave front travel in slightly different directions and eventually begin to interfere. The interference is equivalent to a redistribution of energy in the wave and causes intensity fluctuations (scintillations) which can be detected by a square-law detector. On the way from B to C the wave front passes through additional refractive-index irregularities and so suffers additional phase perturbations. These new irregularities are, however, relatively ineffective in producing intensity fluctuations.

Let us examine the criteria that determine which of the turbulent irregularities along a line of sight are most effective in producing intensity fluctuations. In Figure 2, consider an irregularity of radius r at an arbitrary point A on the line of sight between the source S and the receiver R. That irregularity can be fully effective in producing intensity variations only if the extreme ray paths, SAR and SBR, involving it differ in length by at least half a wavelength, i.e. the irregularity must be at least equal in size to the first zone of a Fresnel zone plate situated at A. This minimum effective size is, in fact, the optimum size for the irregularity. Larger irregularities at the same point are rendered ineffective by the smaller ones just as a lens is rendered ineffective by a ground-glass surface.
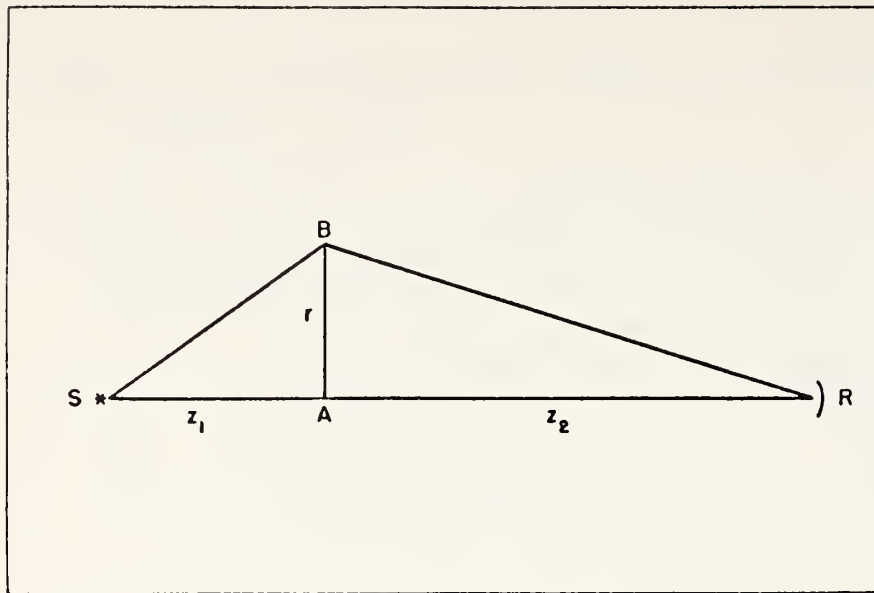
Figure 2. The geometry involved in determining the irregularity size most effective in producing scintillations.

Working out the geometry of Figure 2, we find that the radius of the most effective irregularity is $r \approx \sqrt{q\lambda}$, where λ is the wavelength and $q = \frac{z_1 z_2}{z_1 + z_2}$ depends upon the position of A. This radius is plotted in Figure 3 for a wavelength of 6328 Å and a path length of 10 km.

If we assume, for the moment, that the turbulence is uniformly distributed along the path and has a Komogorov spectrum, it is clear that the mean-square fluctuation of refractive index attributable to irregularities of optimum size varies systematically along the path. There is, therefore, a weighting function that expresses the relative effectiveness of turbulence in producing intensity fluctuations as a function of position along the path. From Figure 3 it is clear that this weighting function must reach a maximum at the midpoint of the path and must drop symmetrically to zero at the ends. An expression for this function has been derived (Fried, 1967a). It is

$$E = \int_0^{\infty} x^{-11/6} \sin^2 \left(\frac{q\lambda}{4\pi} x \right) dx \; .$$
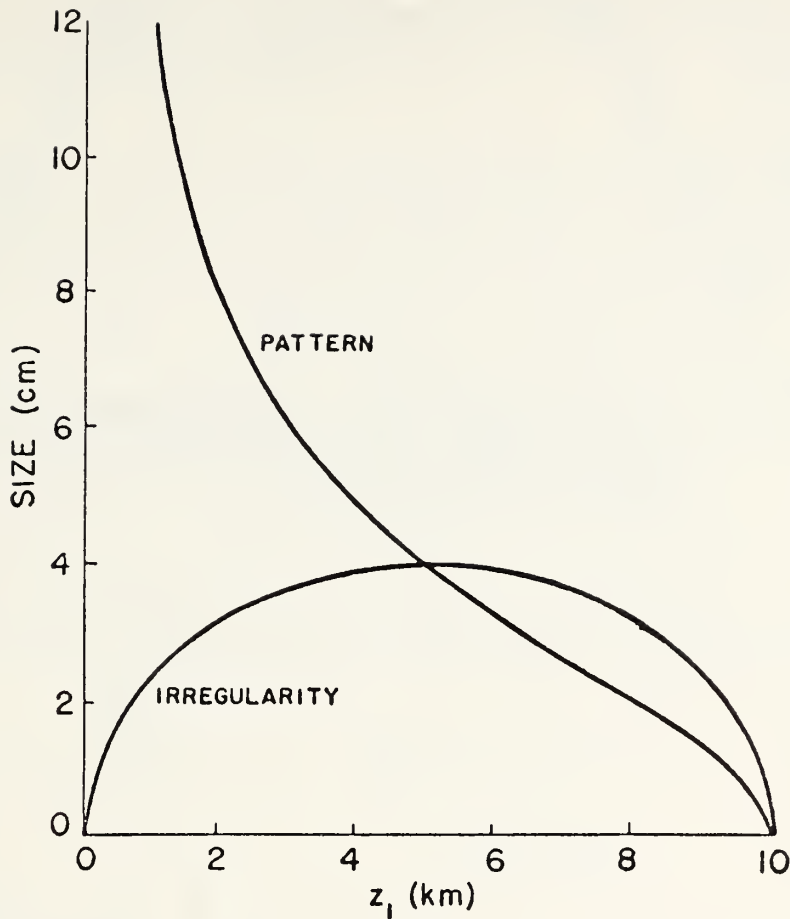
Figure 3. The radius of the most effective irregularity at various points along a 10 km path, and the resulting pattern size.

Figure 4 compares this integral, evaluated numerically as a function of position along the path, with the best-fitting parabola. In summary, the relative effectiveness of a uniformly turbulent atmosphere in producing intensity scintillations is approximately a parabolic function of position along the path, being a maximum at the midpoint and zero at the ends.
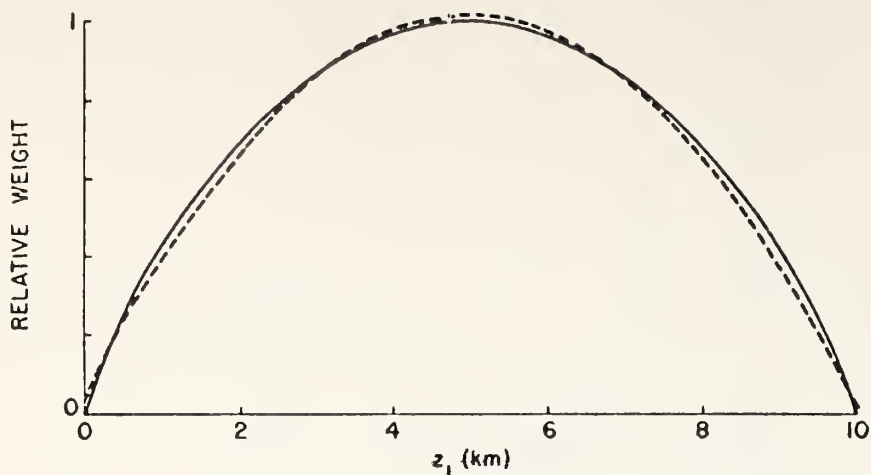
Figure 4. The relative effectiveness of Kolmogorov turbulence at various points along a 10 km path in producing intensity fluctuations. The dashed curve is the best-fit parabolic approximation.

Next, let us examine the scale sizes of the intensity patterns at the receiver due to the optimum-sized refractive-index irregularities located at various points along the path. Referring to Figure 5 and recalling that the
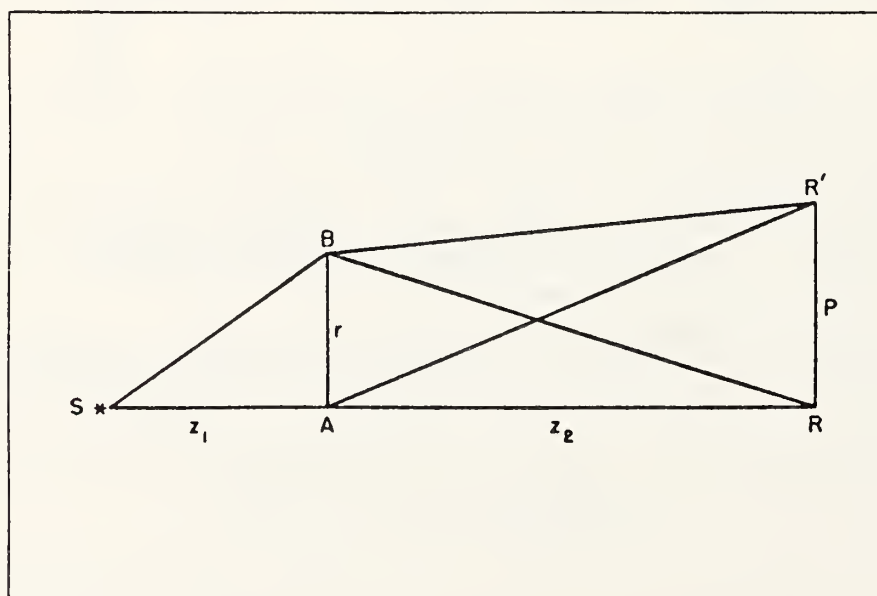
Figure 5. The geometry involved in determining the pattern size produced by the most effective irregularities.

6

radius r of the optimum-sized irregularity of A was such that SBR exceeded SAR by a half wavelength, we can see that the size p of the pattern at the receiver is determined by the requirement that SBR' must equal SAR'. Then, when destructive interference is present at R, constructive interference will occur at R'. Working out the geometry, we find that the pattern is larger than the turbulent irregularity by the factor $p/r = \frac{1}{2}(1 + z_2/z_1)$. The pattern size p is shown in Figure 3 for a 10 km path.

We have seen that the diffraction process that produces intensity fluctuations in the light wave selects only certain optimum sizes from the broad spectrum of irregularities available in Kolmogorov turbulence. The optimum size selected depends on the position along the path, and each position produces a predominant, and unique, pattern size at the receiver. When the weighting function shown in Figure 4 is combined with the pattern-size function of Figure 3, there results the composite spectrum of sizes observable in the intensity pattern. Notice that, for turbulence distributed uniformly along the path, this composite spectrum of sizes depends only on the wavelength and the path length; it is not indicative of any preferred size of turbulent eddies in the atmosphere. An expression for this spectrum, or rather, its Fourier transform, the covariance function, has been derived by Fried (1967b), and is compared with observational data in Figure 6. In the figure,
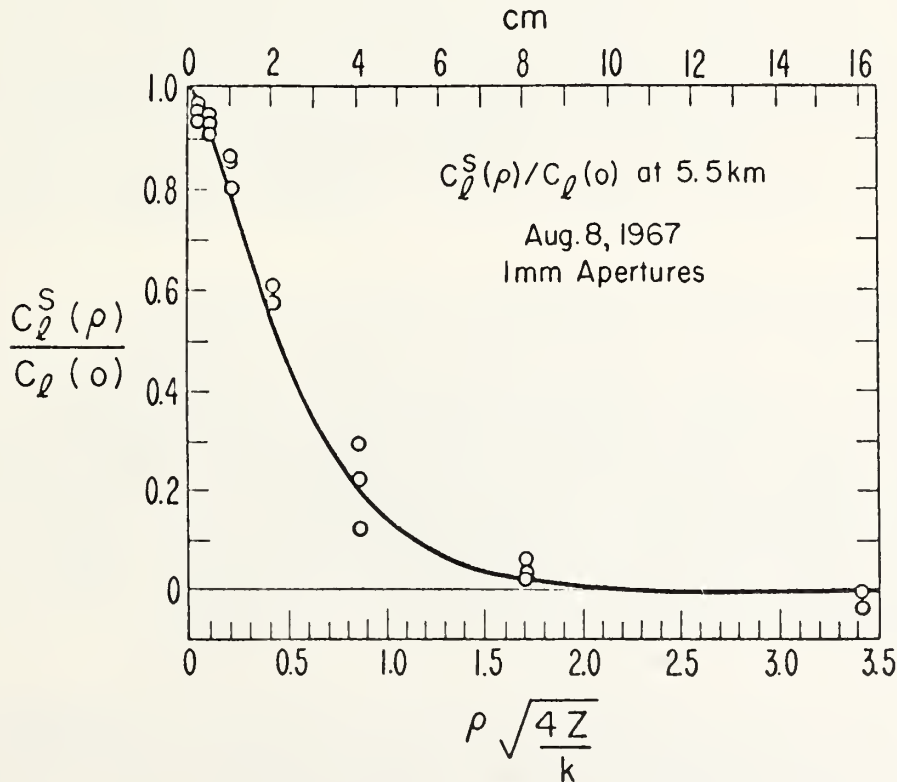
Figure 6. The covariance function of intensity fluctuations calculated (from Fried) and observed over a 5.5 km path.

the normalized covariance of log-amplitude measurements made on spaced detectors is plotted as a function of detector spacing p.

The temporal fluctuations of intensity observed at a point arise from two causes. First, the intensity pattern at the receiver plane is continuously changing in detail because of the random velocities of the various turbulent eddies in the atmosphere. Second, the entire pattern drifts past the detector as the result of the transverse component of the mean wind. The power spectrum of intensity fluctuations is closely related to the spatial spectrum of the intensity pattern, and derived from it by including the effect of the mean transverse wind. As in the case of the spatial spectrum, the power spectrum resulting from uniformly distributed turbulence depends only on the wavelength of the light and the path length, shifted in frequency in proportion to the transverse wind velocity.

Incidentally, though the topic is outside the scope of this paper, the power spectrum changes radically if raindrops enter the beam. This effect has not been investigated but might prove useful in remotely measuring the presence of rain, or maybe even the drop size distribution.

As we have seen, the spectrum of pattern sizes and the power spectrum of temporal fluctuations depend on the wavelength of the light, but they are not ordinarily indicative of any preferred size of turbulent eddies in the atmosphere. Thus, when dealing with a Kolmogorov spectrum of turbulence, we should not expect to obtain independent information by observing on two or more wavelengths simultaneously. However, such multiple-wavelength observations might prove useful in investigating departures from the Kolmogorov spectrum. A possible application is the use of short paths and multiple frequencies to observe the steepening of the turbulent spectrum for small eddies where viscous damping becomes effective.

2.3   Optical Path Length Fluctuations

The cumulative effect of the phase distortions of the wavefront combines with the random velocities of the turbulent eddies to produce temporal fluctuations in the phase of the received light wave or, what is equivalent, changes in the optical length of the path. Over short paths where the intensity effects are not fully developed, the path-length changes can be measured by interferometry. A typical 4-second sample of such measurements over a 25-meter path is shown in Figure 7. The second-to-second fluctuation of such a path is of the order of a few parts in 10^8 after long-term (10-second) trends have been removed.

As the path length is increased so that the intensity effects become well developed, interferometer measurements begin to suffer from ambiguities during the intensity minima. Then it is more convenient to measure path length by modulating the light beam, much as Fizeau did with his toothed wheel when measuring the velocity of light. With a modulated beam, the group path length rather than the phase path length is measured because of

the optical dispersion of air. A 110-second sample of such a measurement, using 10 cm modulation wavelength over a 5 km path, is shown in Figure 8. Here the second-to-second fluctuation is a few parts in 10^9 after the slow drift is removed.
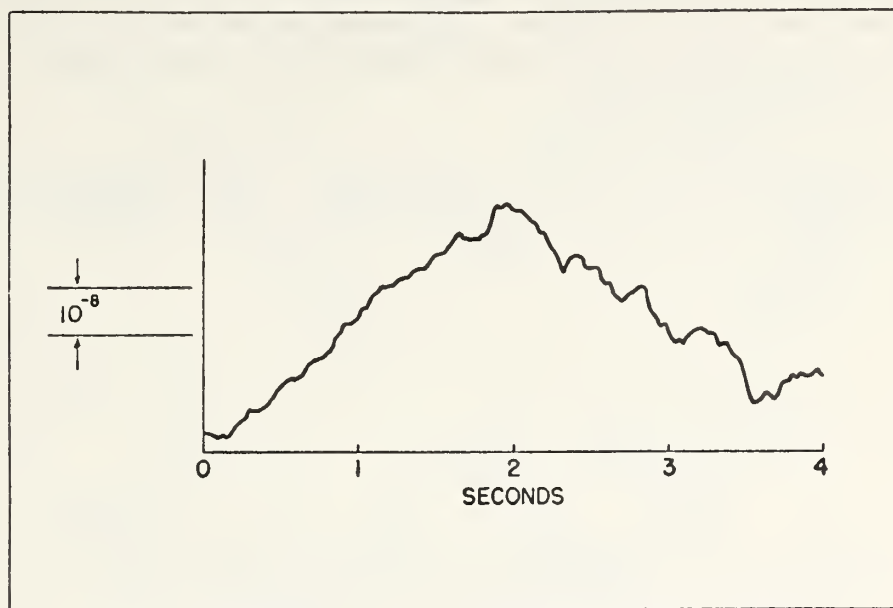
Figure 7. A typical four-second measurement of optical path-length changes over a 25 m path.
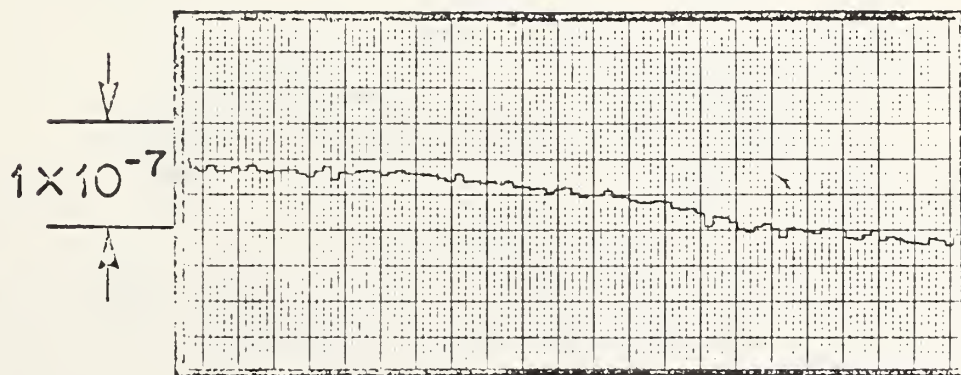
Figure 8. A typical 110-second recording of optical path-length changes over a 5 km path. The individual measurements are one-second averages.

9

2.4 Spreading of a Laser Beam

If the light is restricted to a narrow beam from a well collimated laser, the phase fluctuations in the wavefront which, at position B of Figure 1, cause portions of the wave to propagate in slightly different directions will produce a measurable spreading of the beam. Rigorous analysis of this effect is surprisingly difficult, though an approximate geometrical solution has been presented by Beckmann (1965).

The weighting function for beam spreading is very different from that for intensity fluctuations. We can see its approximate nature from the following simple argument. Referring to Figure 9, consider a laser source L which,
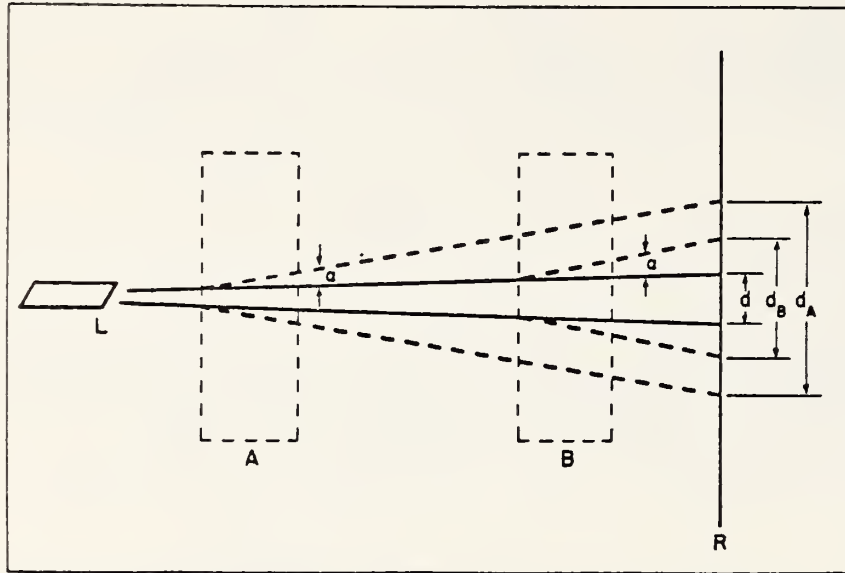
Figure 9. The geometry involved in determining the relative effectiveness of turbulence at various points along the path in producing beam spread.

in the absence of an atmosphere, would produce a spot of diameter d on the receiving screen R. If a parcel of turbulent atmosphere (not a single refractive-index irregularity but a complete, bounded region containing a Kolmogorov spectrum of irregularities) were inserted in the beam at point A, it would cause some additional beam spreading of angle α and would result in a spot at R of diameter d_A. If, instead, the same parcel of turbulent atmosphere is located at point B, the beam spreading caused by it will still have the same angle α, but now the spot on the receiving screen will be only d_B in diameter. Thus, if the inherent angular divergence of the laser beam is much smaller than the atmospheric effect α, the weighting function that describes the effectiveness for beam spreading of turbulence at various positions along the path is linear. It is a maximum at the laser and drops to zero at the receiver.

Figure 10 shows the typical diurnal variation of beamwidth as measured over 5.5 and 15 km paths near Boulder, Colorado. The laser beam was expanded and collimated so that its intrinsic divergence was only 5 μrad. The average height above ground of the paths is 50 and 80 m respectively.
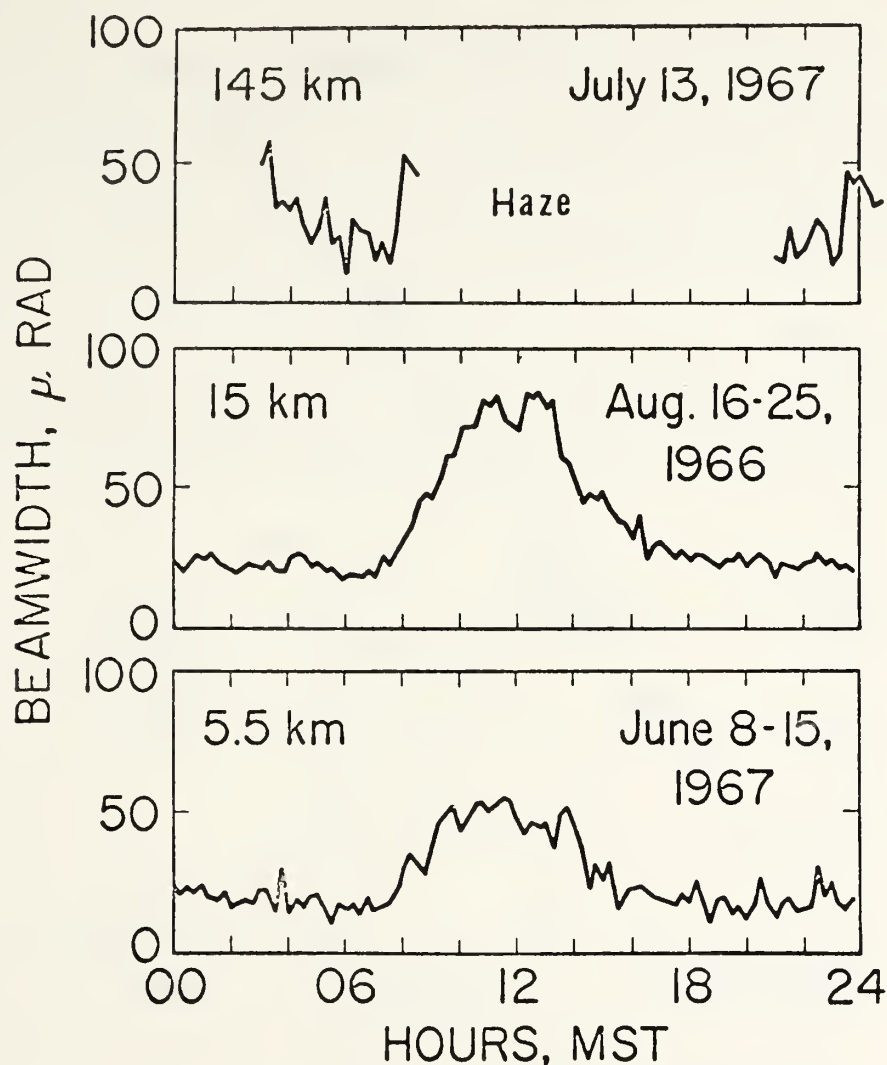
Figure 10. Typical diurnal variation of beam width observed over three paths near Boulder, Colorado.

Figure 11 presents some slight evidence in support of a linear weighting function for beamwidth. The line and the solid dots show the close relationship between beamwidth observed over an irregular 5 km path on a sunny summer afternoon and the mean square temperature fluctuation measured along the beam with a high-speed thermometer mounted on an airplane. Here,
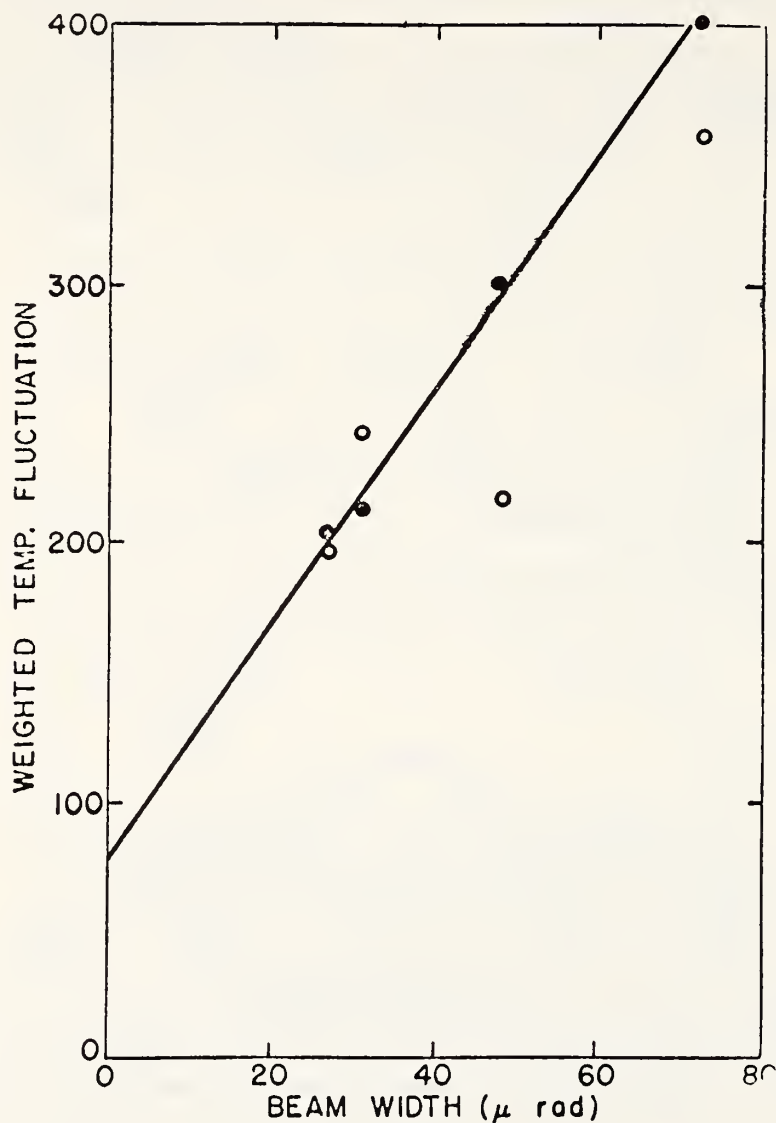
Figure 11. The dark circles show the close relationship between observed beamwidth and properly weighted airborne measurements of turbulence along a 5 km path. The open circles show how the relationship deteriorates when an improper weighting function is used.

linear weighting of the temperature measurements has been used, counting the fluctuations near the laser most heavily and those near the receiver not at all. The open circles show how this close relationship is lost if reverse linear weighting is used, as would be appropriate were the laser and receiver interchanged. Although the experiment is still to be done, we may infer that the beamwidth would be very different on this path if measured in the opposite direction.

3.   EFFECTS OF LARGE-SCALE REFRACTIVE-INDEX VARIATIONS

Large-scale variations in the refractive index of the atmosphere are primarily controlled by temperature and barometric pressure. The large-scale phenomena that are most important to ground-to-ground optical propagation are changes in the average temperature along the path, changes in the barometric pressure, and changes in the vertical gradient of temperature. Minor effects result from changes in the water-vapor content of the atmosphere and from horizontal temperature gradients.

A laser beam sufficiently narrow to be dominated by turbulent spreading typically wanders from its mean position by several times its own diameter. This wandering is primarily in the vertical direction because of the predominance of vertical temperature gradients. Figure 12 illustrates this effect with
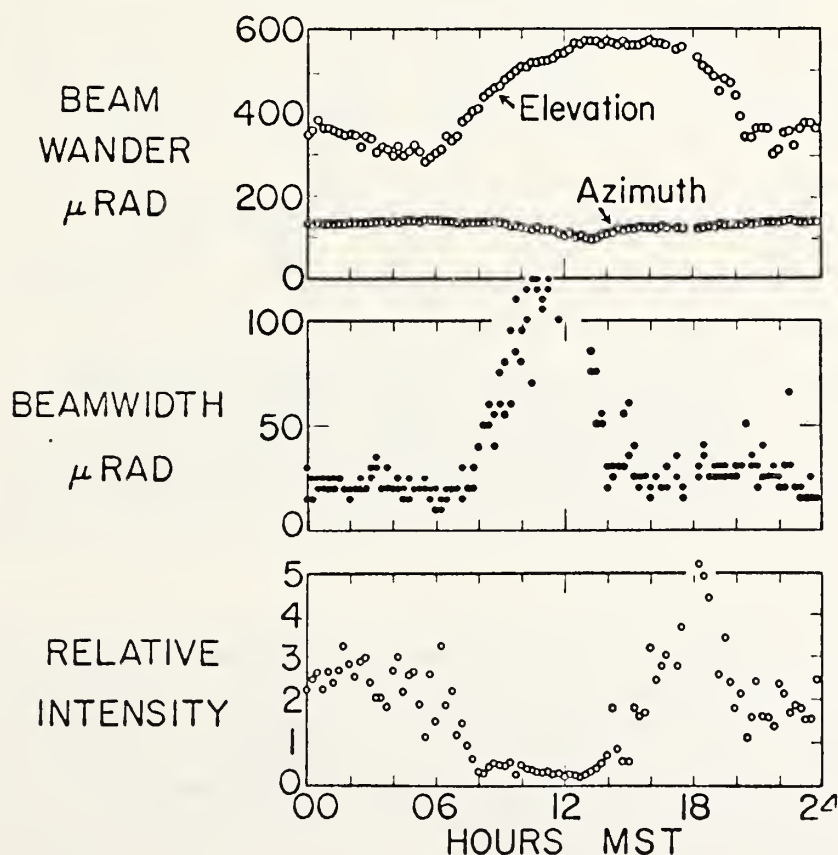
Figure 12. A typical day's measurements, made every 15 minutes, of beam width and beam wander over a 15 km path.

a series of beam positions measured every 15 minutes during a typical day. When, upon occasion, the beam passes through a temperature inversion, the vertical deflections are greatly enhanced as in the case of a mirage. In addition, it is common in these cases to observe nearly periodic vertical oscillations, presumably caused by gravity waves.

The average density of the air along the path determines the optical path length. A change of 1 K in temperature or of 3 mb in pressure is sufficient to affect the optical path length nL by one part in 10^6. Notice that this is several hundred times greater than the second-to-second fluctuation typically caused by turbulence. Figure 13 shows an example of this effect measured over a 3 km round-trip path. The reference temperature was measured with a thermometer at the center of the path. Δ (nL) is the difference in optical path length between red light and blue light.
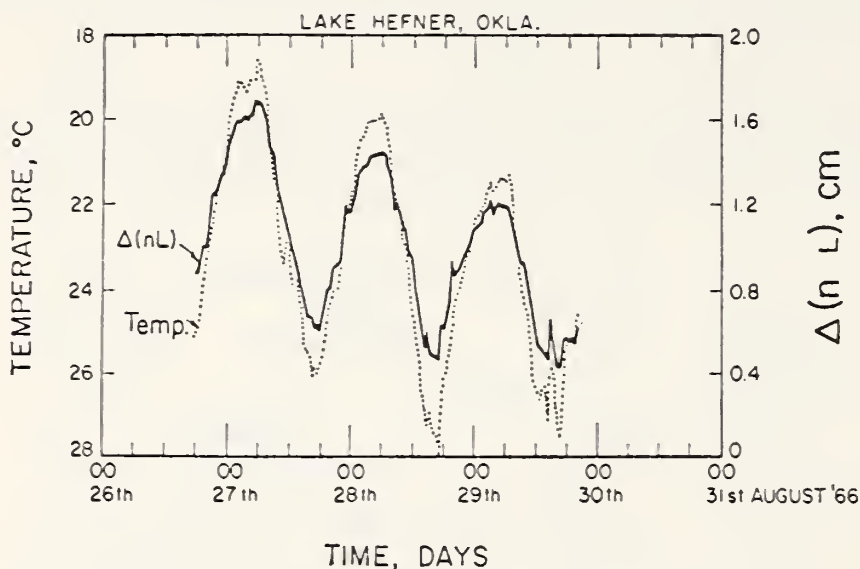
Figure 13. The relationship between optical path length over a 1.5 km path and the temperature measured at the midpoint. In this plot the relative scales have not been properly adjusted, so the variation of path length appears too small.

4.   POLARIZATION EFFECTS

In theory, the turbulent irregularities in the atmosphere should depolarize a linearly polarized light wave. The effect has been calculated by Saleh (1967) and estimated to be about 10^{-9} per km. He was unable to observe the depolarizing effect of the atmosphere on a 2.6 km path, even with an equipment sensitivity of -42 db. We conclude that at the present time polarization effects are of no practical interest for optical remote sensing of the clear atmosphere using line-of-sight paths.

14

5. THE DETERMINATION OF AVERAGE TEMPERATURE

If we assume that the barometric pressure is known, the average temper-
ature along a fixed open-air path can be determined by comparing the optical
path length with the known true geometrical length. The apparatus for doing
this could, in principle, be as simple as that shown in Figure 14. This is a
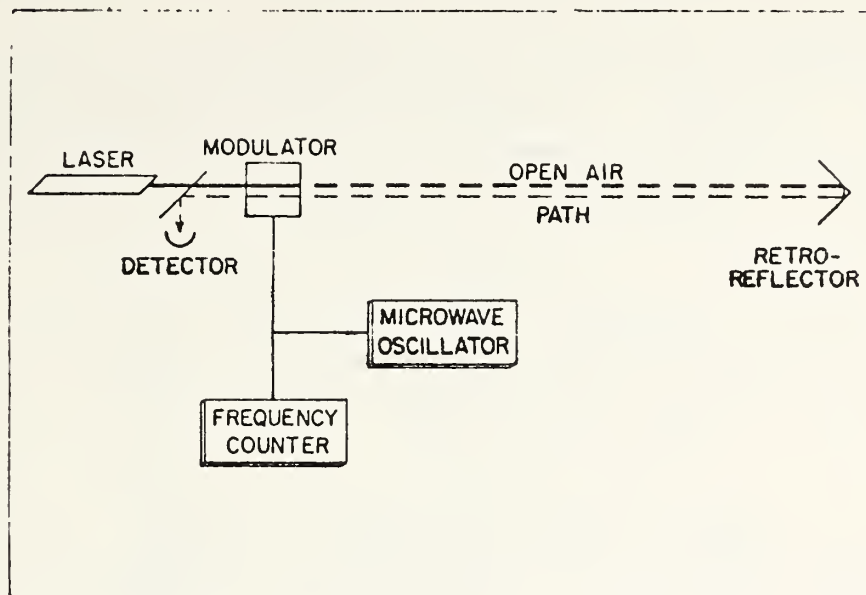
Figure 14. A block diagram of a simple device for measur-
ing average temperature over a fixed path.

modern version of Fizeau's classical experiment. A laser beam is passed
through an amplitude modulator and traverses the open-air path to a retro-
reflector. It returns through the modulator and is deflected by a beam
splitter to a detector. A small adjustment of the modulation frequency is
made to minimize the detector output, and the modulation frequency is then
measured by the counter. In practice, it would be desirable to provide a
means for servo-controlling the oscillator to maintain a null output. The
frequency read from the counter provides the optical path length. This can
be converted to temperature given only the barometric pressure.

We have already noted that the second-to-second fluctuation in path length
caused by turbulence corresponds to a temperature change of less than 0.01 K
along the whole path. Thus, turbulence will not be a limitation to measure-
ments of average temperature unless the required accuracy is better than
about 0.1 K. For 0.1 K temperature accuracy, the barometric pressure must
be measured to 0.3 mb. and both the modulation frequency and the fixed geo-
metrical length of the path to 1 part in 10^7. The effect of varying composition
of the air, particularly the effect of water vapor, has been discussed in detail
by Owens (1967a). For temperatures near 20° C., a relative humidity error
of 15 percent results in a temperature error of 0.1 K.

PROBING BY OPTICAL METHODS

Determination of the geometrical length to one part in 10^7 is at, or per-
haps just beyond, the limit of the state of the art, and requires the averaging
of a large number of optical measurements taken under various carefully meas-
ured weather conditions. In summary, absolute temperature measurements
with an accuracy of 1 K or, perhaps, 0.1 K are feasible, and temperature-
difference measurements to 0.01 K are possible if the humidity along the path
can be measured sufficiently well.

If the path is not fixed, or if the path length is unknown, a more compli-
cated variant of the optical path-length method can be used, utilizing the dis-
persion of the atmosphere. In round numbers, the atmosphere reduces the
velocity of blue light by 330 parts per million while it reduces the velocity of
red light by only 300 ppm. Both these numbers are proportional to atmos-
pheric density and therefore, for a given barometric pressure, inversely pro-
portional to temperature. Simultaneous measurement of optical path length
with both red and blue light provides the two equations needed to solve for the
path length and the temperature. A discussion of this method and its accuracy
has been given by Owens (1967b). Briefly, temperature measurements to 1 K
are feasible and, with a little elaboration to remove ambiguities, would pro-
duce as a byproduct distance measurements accurate to one part in 10^6.

A quite different application of the two-frequency principle suggests
itself and is now being investigated in Boulder. Simultaneous measurement
of apparent path length with optical and microwave frequencies over a fixed
path yields the average temperature and the average water-vapor content.
The method has been described by Bean and McGavin.

6.   THE DETERMINATION OF VERTICAL TEMPERATURE GRADIENT

The beam wandering discussed in section 3 and illustrated in Figure 12
provides a direct indication of temperature gradients along the path. The
predominant temperature gradients are in the vertical direction so it is these
that are most readily measurable. The sensitivity of the method increases in
proportion to path length and, for a 10 km path, a temperature gradient of
1 K/100 m. results in a beam deflection of about 75 μrad. This angle is
comparable to moderately strong turbulent broadening of the beam and is
easily measurable.

7.   THE DETERMINATION OF TURBULENCE ALONG THE PATH

We have seen in section 2 that the turbulence along the path must be
weighted linearly to account for its effect upon beamwidth, while it has a
symmetrical, nearly parabolic weight in its effect upon intensity fluctuations.
If the turbulence is uniformly distributed along the path there will be a fixed
relationship between beamwidth and log-amplitude variance, at least until the
turbulence becomes sufficiently strong to saturate the scintillations. If the
turbulence is not uniformly distributed, this relationship will not hold in general.
Thus, the simultaneous observation of beam spread and log-amplitude variance

can be used to check the uniformity of the turbulence along a path. There is not, however, enough information in such a pair of measurements to invert the integral and learn any appreciable details of how the turbulence is distributed along the path.

The covariance function of intensity scintillations was shown in Figure 6. The discussion in section 2 showed how this function (or its Fourier transform, the spatial spectrum of the fluctuations) results from the combined effects of the turbulence along the path. The turbulence at each point contributes to the spectrum a limited range of pattern sizes distributed closely around the sizes shown, for example, in Figure 3. Accordingly, if turbulence were absent over a portion of the path, the spectrum of the intensity fluctuations would be distorted in a characteristic way. Figure 15 illustrates this
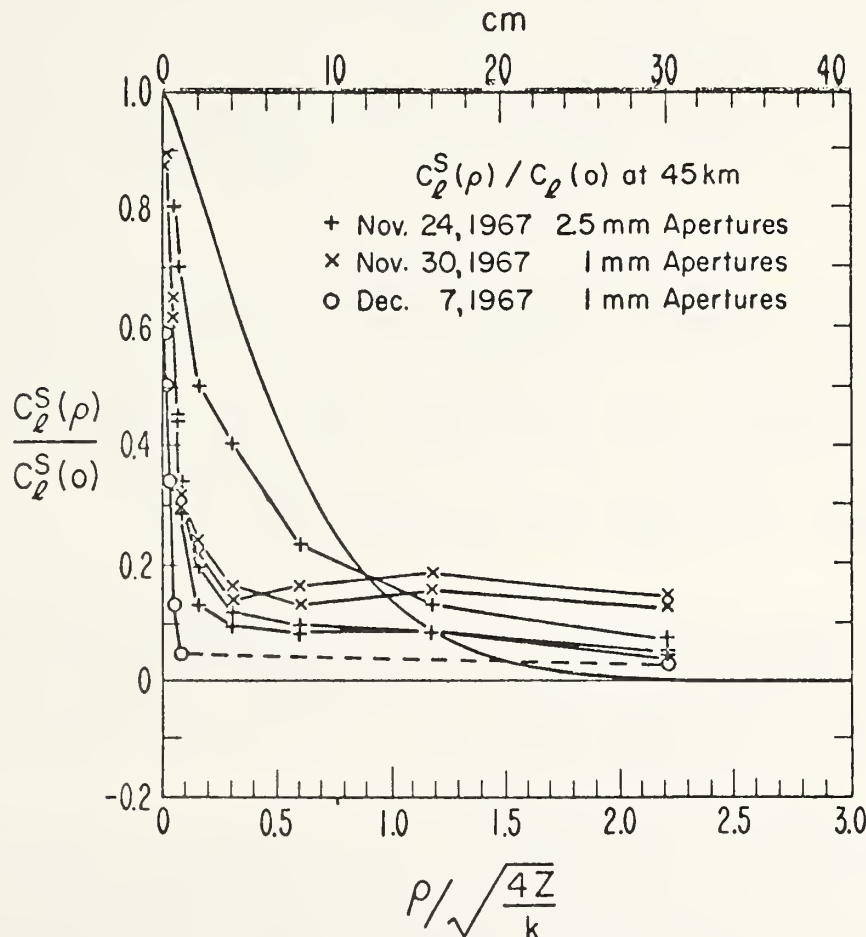
Figure 15. Measurements of the covariance function of scintillations over a 45 km path demonstrate poor agreement with the theoretical curve. This is explained by the concentration of turbulence near the end-points of the path.

effect with measurements taken over a 45 km path near Boulder, Colorado. The smooth, unmarked curve is the theoretical covariance function for uniformly distributed turbulence, taken from Fried (1967b) and plotted for the particular path length and wavelength. The six broken curves, connecting observations made on three different nights, differ systematically from the theoretical curve. The sharp spike with a width of less than 1 cm represents small-scale structure caused by turbulence near the receiver. The long tail, sometimes even peaking in the vicinity of 18 cm, represents large-scale structure caused by turbulence near the transmitter. The absence of scale sizes between these two extremes indicates an absence of turbulence at the middle of the path. This is exactly what might be expected because the path lies between two mountain tops and, except near the end points, is never less than 150 meters above the ground. It is well known that turbulence generally decreases rapidly with height above the ground; Hufnagel (1966) indicates that the turbulence may be expected to have 1600 times less optical effect per unit path length at 150 meters height than at ground level.

Thus, we have a possible method for determining the distribution of turbulence along the path. Like so many remote-sensing techniques, it involves the inversion of an integral to obtain the desired answer. The measurements, themselves, are statistical in nature and so contain a random element, i.e. they are inherently noisy. The noise cannot be reduced indefinitely by extending the observation period because the open atmosphere is notorious for yielding non-stationary time series. Although guesses can be made at the present time, it remains for experiment to disclose how accurate the method can be. Such experiments are in progress at Boulder. Our expectation is that the turbulence distribution can be represented in terms of a third or fourth order polynomial, but probably not in much more detail. Inclusion of beam-spread measurements might yield a slight improvement.

8. THE DETERMINATION OF TRANSVERSE WINDS

As a uniform wind blows across the path, it is obvious that the pattern drift velocity will be greater for a pattern caused by irregularities near the laser than for a pattern arising near the receiver. Also, as shown in Figure 3, the former pattern will have a larger scale. Thus, for a uniform wind, the large-scale intensity fluctuations will drift past the receiver more rapidly than will the fine-scale structure.

Now consider the correlation between the intensity fluctuations observed by two point detectors separated by a variable horizontal distance transverse to the optical path. For any given time lag there is a spacing of the detectors that will maximize the correlation. The ratio of this spacing to the time lag determines the drift velocity of those components of the intensity pattern having a size comparable to or larger than the detector spacing. (Notice that the drift velocity is not the same as the apparent velocity that would result from holding the spacing fixed and varying the time lag to maximize the correlation. The difference between these two velocities has been discussed

at length by Briggs, Phillips and Shinn (1950)). It has proved possible to check these ideas with a laboratory setup where two hair driers were arranged to blow hot, turbulent air across a 10-meter laser beam. It was quite easy to observe a bi-modal time-lagged correlogram, the two humps corresponding to the air streams from the two fans. Outdoor experiments, calibrated by a large number of anemometers, are in preparation.

The correlation between the two detectors is a surface parametric in time lag and detector spacing. From the theory of wave propagation through turbulent media it must be possible to express this correlation as an integral of the transverse wind velocity and the strength of turbulence along the path. The determination of wind velocity from scintillation observations then becomes the familiar remote-sensing problem of inverting the integral. Notice that the wind determination is intimately tied to the determination of the distribution of turbulence. As in the previous problem, we can only guess what will be the practical accuracy achievable by this method. Once again, we must deal with observations that are, by their very nature, severely contaminated by noise. Again I suspect that the best we can do may be to determine the coefficients of a third or fourth order polymonial describing the distribution of transverse wind velocities along the path.

9. SUMMARY

We have presented, in a mostly qualitative manner and with heuristic arguments, a description of the principal effects of the clear atmosphere upon optical propagation. Several of these phenomena offer possibilities for the remote sensing of atmospheric properties, and we have mentioned in particular the measurement of average temperature, average vertical temperature gradient, and the distribution of turbulence and transverse wind velocity along the path. The first of these has been tested in the field. The second and third have been demonstrated qualitatively with outdoor data, and the fourth has been demonstrated only in the laboratory.

Observation of integrated effects over a line-of-sight path is naturally more practical for the determination of average values over the path than it is for the determination of distributions along the path. While the former may confidently be pursued, the latter should be approached with cautious optimism. We have seen that the appropriate weighting functions and the spectrum of turbulence are smoothly varying. This means that the contribution to the integral from a parcel of atmosphere located at a particular point on the path is irrevocably mixed with the contribution from nearby parcels. Thus it is, in principle, impossible to determine distributions in great detail. We have guessed that four or five independent parameters will be the limiting resolution, but actual tests must be made in the open atmosphere.

REFERENCES

Bean, B. R. and McGavin, R. E., 1967: Electromagnetic phase variability as a measure of water vapor and temperature variations over extended paths, Proceedings of the AGARD-EPC Symposium of Phase and Frequency Instability in Electromagnetic Wave Propagation, Ankara, Turkey, 1967, to be published.

Beckmann, P., 1965: Signal degeneration in laser beams propagated through a turbulent atmosphere, Radio Science 69D, 4, 629-640.

Briggs, B. H., Phillips, G. J., and Shinn, D.H., 1950: The analysis of observations on spaced receivers of the fading of radio signals, Proc. Phys. Soc. B63, 106-121.

Fried, D. L., 1967a: private communication

Fried, D. L., 1967b: Propagation of a spherical wave in a turbulent medium, J. Opt. Soc. Am. 57, 2, 175-180.

Hufnagel, R. E., 1966: An improved model turbulent atmosphere, Appendix 3 of: Restoration of Atmospherically Degraded Images, Woods Hole Summer Study, July 1966, National Academy of Sciences, National Research Council.

Ochs, G. R., 1967: A resistance thermometer for measurement of rapid air temperature fluctuations, ESSA Tech. Rep't. IER 47-ITSA 46.

Owens, J. C., 1967a: Optical refractive index of air: dependence on pressure, temperature, and composition, Applied Optics 6, 51-59.

Owens, J. C., 1967b: Recent progress in optical distance measurement: lasers and atmospheric dispersion, Proc. International Symposium Figure of the Earth and Refraction, Osterreichischen Zeitschrift fur Vermessungswesen 25, 153-161.

Saleh, A. A. M., 1967: An investigation of laser wave depolarization due to atmospheric transmission, IEEE J. Quantum Electronics QE-3, 11, 540-543.

Roger M. Lhermitte

Environmental Science Services Administration

Research Laboratories

Wave Propagation Laboratory

ABSTRACT

This paper is a survey of the application
of Doppler techniques to the study of
atmospheric phenomena. Particular empha-
sis is placed on the requirement of ade-
quate digital processing means for the
Doppler signal and the Doppler data which
are acquired at a very high rate. The
paper also discusses the need of a two or
three Doppler method as an ultimate ap-
proach to the problem of observing the
three-dimensional field of particle motion
inside convective storms.

1. INTRODUCTION

Although conventional radar techniques have been extensively used for years in the study of atmospheric phenomena, Doppler radar techniques were introduced to this field only a decade or so ago. Experiments based on the use of continuous wave Doppler radar were conducted as early as 1958; however, this report will essentially deal with pulse Doppler radar techniques having the same ranging capabilities as conventional pulse radars. The radar wavelengths covered in this report range from X-band (3 cm) to S-band (10 m).

The first papers on the meteorological use of pulse Doppler radar techniques were presented in 1960 at the Eighth Weather Radar Conference and were concerned with the analysis of the vertical motion of precipitating particles using a vertically pointing beam.

Discussion of the earliest experiments, involving the use of a scanning Doppler radar beam for the purpose of analyzing wind field from observation of the motion of precipitation particles, was presented a year later at the Ninth Weather Radar Conference. Since the time of these early experiments, the number of pulse Doppler radars specifically designed for meteorological studies has been steadily increasing. There are now five meteorologically-oriented pulse Doppler radars in the United States, two in England and one in Japan. These radars were designed and built for the purpose of the study of atmospheric phenomena. The use of pulse Doppler radar for atmospheric physics studies has also been mentioned in the Russian literature on meteorological research. However, no information was provided as to the nature of the Doppler equipment involved in these experiments. More sophisticated equipment is now being built such as the Environmental Science Services Administration's planned system of three identical radar sets to be used for the study of the three-dimensional field of particle motion inside convective storms.

Considerable experience on the capabilities and usefulness of pulse Doppler radars has been acquired through their use. These experiments also have revealed the weaknesses and limitations of the single Doppler radar method which need to be overcome in order to increase the capabilities of the Doppler methodology toward its ultimate potential.

This report is a brief review of the meteorological Doppler technique, as well as a summary of the results which have already been acquired in several areas of atmospheric research. We will also propose improvements aimed towards the design of a more elaborate and appropriate Doppler radar methodology. The opinion of the writer is that the potential of the Doppler methods is far from being developed to its full capability and the use of more complex and sophisticated systems will provide us with a methodology capable of solving a large number of problems related to the study of micro-scale and mesoscale atmospheric phenomena. The design of multi-unit Doppler radar systems and the use of advanced data storing and processing techniques, compatible with large computers, will be an essential part of the proposed effort.

2. THE DOPPLER RADAR SPECTRUM

Numerous discussions of the Doppler radar method applied to the study of atmospheric phenomena have been given in various articles (Lhermitte 1963, Atlas 1964, Lhermitte 1966). It appears only necessary in this report to briefly mention the basic principles of the method. Only pulse Doppler radar techniques, having the same ranging capabilities as conventional radars, will be discussed.

In addition to the conventional radar capabilities of observing back-scattered signal amplitude, the pulse Doppler radar provides information on the rate of change of the phase, ϕ, of the backscattered signal returned by the radar-detected target. By use of appropriate design of the Doppler circuits, the phase difference between transmitted and received signals, which is observed by the coherent radar, is a function only of the distance between the target and the radar. The rate of phase change, $d\phi/dt$, will therefore provide knowledge of the radial velocity dR/dt of the target. We can then write $\frac{d\phi}{dt} = \frac{4\pi}{\lambda}\frac{dR}{dt}$ where λ is the wavelength of the transmitted signal. This expression shows that there is a complete cycle of phase change everytime the target moves by $\lambda/2$. The pulse Doppler radar is thus an accurate ranging device which provides knowledge of the rate of change of target range, i. e., the radial velocity. If the target is approaching the radar, the phase of the signal is increasing as a function of time and $d\phi/dt$ is a positive quantity which is equivalent to an increase of the transmitted frequency of the radar. On the other hand if the target is receding $d\phi/dt$ becomes a negative quantity which is equivalent to an effective decrease of the transmitter frequency. The sign of $d\phi/dt$ is opposite to the sign of motion derived from the convention that kinematic divergence is a positive quantity. It therefore appears that it is more appropriate in meteorological work to consider that the receding targets have positive velocity. If the target moves in a direction different from the radar beam axis, only the radial velocity, i. e., the component of the target's vectorial velocity along the axis of the radar beam, will be measured. This statement reveals the ambiguities of dealing with radial velocities, which can partially or completely be overcome in certain ways described in this report.

Since we are discussing the application of Doppler techniques for the study of atmospheric phenomena, we are dealing with volume scattering due to an extended or "distributed" target composed of large numbers of scatterers.

The classical analysis of the backscattered signal received by conventional pulse radars from distributed targets, shows that the signal amplitude at any selected point in the radar range is due to the contribution of the signals re-radiated by scatterers existing inside a scattering volume defined by the cross-section of the radar beam and the pulse length of the radar. The pulse Doppler radar will be concerned with the same type of analysis but also provides information on signal phase.

Assuming the signal backscattered from a scatterer, i, has constant amplitude, α_i and phase, ϕ_i, the total backscatter signal, $A(t)$, will be given by the following expression:

$$A(t) = \sum_{i=1}^{N} \alpha_i \, e^{-j(\omega_o t + \phi_i)} \qquad\qquad (1)$$

$\omega_o = 2\pi \, f_o$ with f_o being the transmitted signal frequency.

The signal phase, ϕ, can be split into a component, ϕ_o, corresponding to some conditions at the origin and a variable term $\omega_d t$ where $\omega_d = d\phi/dt$ (Doppler shift); therefore we can write:

$$A(t) = e^{-j \, \omega_o t} \sum_{i=1}^{N} \alpha_i \, e^{-j(\omega d_i t + \phi_{oi})} \qquad\qquad (2)$$

The above relationship implies statistical independence of motion between scatterers and also implies that there is no collision processes between scatterers. It also relies on the fact that scatterers are moving freely for several radar wavelengths therefore leading to a clear definition of the Doppler shift. If the scatterers are submitted to a random displacement limited to a small fraction of the radar wavelength a different and more complicated expression of A(t) will be needed.

In the case of pulse radars, the time function A(t) is sampled at the radar pulse repetition rate. Selection of the signal at any radar range can be done by use of conventional range-sampling units assisted by signal-holding circuits which restore the time continuity of the signal between radar pulses and therefore provide a time function of the form of equation (1). However, the sampling and transformation of the signal in the radar circuits slightly modifies the spectral characteristic of the signal represented in A(t) especially for frequencies approaching half of the radar pulse-repetition rate. This effect is well known and usually is corrected by appropriate means.

Equation (1) shows that the power density spectrum of A(t) is the probability density function for the backscattered power expressed as a function of the Doppler shift and is called the Doppler spectrum. If the radar cross section of the scatterers exhibits time variations, the spectrum of A(t) will include the Fourier components generated by amplitude modulation due to this effect, Brook and Latham (1968).

Figure 1 shows an example of a Doppler spectrum obtained with a vertically pointing radar beam in falling snow conditions. This example illustrates the excellent velocity resolution of the radar system.

3. COHERENT RADAR DESIGN AND SPECTRUM RECORDING MEANS

Radar equipment capable of observing the phase difference between back-scattered and transmitted signals is called phase-coherent or simply "coherent".

The simplest method for comparing phases is based on mixing the signal returned by the moving target with the signal reflected by a fixed target at the same range. This "external-coherence" method, which is often used in airborne navigational Doppler radars, has been applied to the study of the motion of precipitating particles, Lhermitte (1960b). However, the usefulness of this method is seriously limited by the need for a fixed target to be at exactly the same range as the moving target under study. The transmitter

pulse signal can also be stored in microwave cavities but this technique is limited to short ranges by fast time decay of the stored signal. The above solutions have not been used extensively in the design of meteorological Doppler radars because they can be replaced by more appropriate systems described below.
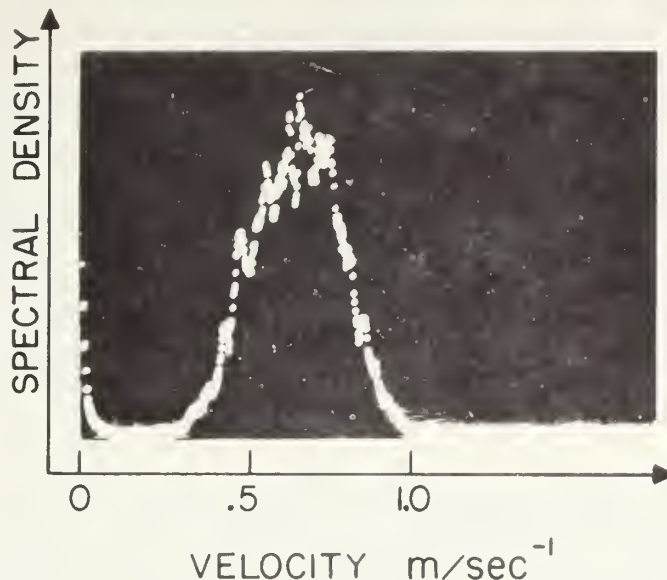
Figure 1. Doppler spectrum obtained in snow with a vertically pointing Doppler radar beam. Note the excellent velocity resolution of the system.

The most effective and accurate system is based on a primary stable microwave source called a STALO (Stable Local Oscillator). The microwave signal generated by the STALO is amplified, pulsed by a phase-coherent amplifier and radiated by the antenna. The scattered signal coming from the moving target is compared to the STALO signal and the signal phase analysis is performed by systems sensitive to the phase difference $\Delta\phi$ between successive pulses. The quality of this system depends upon the frequency stability of the microwave oscillator during the time interval between radiation of a pulse and the return of the scattered signal. Therefore it involves only the "short term" frequency instabilities of the STALO. Relative frequency stabilities of 10^{-10} can be easily achieved for longer than one millisecond and with Doppler phase jitter smaller than 5×10^{-3} radian.

System performance can be analyzed in terms of these estimated random phase instabilities occurring from pulse to pulse. If these phase instabilities are uncorrelated and limited to a small fraction of 2π, they cause the presence, in the radar signal, of a radar-sampled white spectrum superimposed on the signal Doppler spectrum. The Doppler signal to noise ratio is given by the ratio between the signal phase variance (Doppler) and the contribution of the variance due to random phase instabilities, Lhermitte and Kessler (1964). If this is due to STALO phase instabilities, this ratio will typically be better than 50 db. We must emphasize that small STALO frequency instabilities will not limit the ability of the radar to observe very slow target motion which is only limited by the signal dwell time and the stability of the mean index of refraction in the path during this time. The instabilities

will only generate a phase noise which limits the dynamic range of the Doppler spectrum, and thereby inhibits the clear definition of the spectrum boundaries. The STALO contribution to phase instability increases systematically with target distance. In a well designed, fully coherent system, the STALO contribution to phase instabilities largely exceeds other contributions.

The need for a coherent microwave amplifier can be overcome by use of a conventional (but stable) magnetron microwave oscillator assisted by a transmitter phase-locked system (COHO) which stores the phase of the transmitter signal. This is the classical MTI radar which has been known and utilized for years. Phase-locking is usually done at the intermediate radar frequency and the basic requirements on the STALO remain the same as they are for fully coherent systems. High quality, commercially available magnetron oscillators have acceptable frequency stability. However, there is more phase noise generated by the magnetron and by the instabilities in phase-locking the COHO than in a system utilizing a STALO and a microwave coherent amplifier. The ratio of signal-phase to phase-noise, better than 50 db for fully coherent systems, is reduced to 30 to 35 db in the case of the MTI system. This phase noise contribution is independent of the radar range.

The above discussion shows that frequency analysis of the Doppler signal must be obtained prior to any reduction of the data. As discussed in section 8 of this report, multirange signal sampling and digitizing followed by digital computations of fast Fourier transforms offer the most flexible and effective means for this requirement. These techniques are, however, in a developing stage and have been temporarily replaced, in the present experimental work discussed in this report, by the following methods:

a. Range-gating associated with either a signal crossing technique which provides the spectrum's second moment, Lhermitte (1963), or a velocity tracking system which essentially processes the spectrum median frequency, Tripp (1964). This technique has the advantage of simplicity but it doesn't provide information on the spectrum width and shape, and is only acceptable in the case of narrow or, at least, symmetric spectra for which only the knowledge of the average frequency is required.

b. Range-gating associated with the use of multifilter frequency analyzer. This method leads to acceptable knowledge of the spectrum shape especially if integration means are provided for the signal at the output of every filter. It is, however, a slow process which doesn't match the requirements imposed by the study of atmospheric phenomena.

c. Coherent memory filter or velocity-indicator coherent integrator (VICI). The application of this device to meteorological work, which was first proposed by Chimera (1960), allows quick display of the distribution of the Doppler velocity as a function of radar range (Range velocity indicator, RVI). The device is extremely fast but it suffers from restricted range and velocity resolutions due to practical limitations of the system. The device is also unable to provide or display the signal power spectral density in a quantitative manner and therefore fails to indicate the Doppler spectrum shape. In its present form, the coherent memory filter also fails to produce data in a digital format which seems to be the only way to cope with the type of information provided by this system. An extension of its use for PPI display has been recently proposed by Armstrong and Donaldson (1968).

d. Time compression scheme. Several range gates can be Doppler analyzed in a short time by use of signal multiplexing techniques and time compression schemes. The digital time compression essentially allows that quick analysis of the spectra be done by use of fast scanning filters. The system is capable of analyzing the Doppler information at ten range gates in a time of the order of a few seconds. The complexity of this system, which involves digital techniques, approaches that of a purely digital system such as the one described in section 8 of this report. However, it doesn't have the flexibility of the digital computations and doesn't provide the digital output which is required for easy handling and processing of the data.

e. If real-time operation is not necessary, the recording of the Doppler signal by aid of a multi-track magnetic tape recorder offers a high rate of data acquisition which matches most of the requirements. Complementary informations can also be recorded on a separate track. The processing of the recorded signals can be done with the aid of specialized digital devices which provide a digital output. This seems to be the closest approach to the sophisticated digital system proposed in section 8 of this report.

4. VERTICAL BEAM METHOD

The method, which was first proposed by Boyenval (1960), Probert-Jones (1960), Lhermitte (1960), relies on the operation of a fixed, vertically pointing, radar beam. The method is attractive from the point of view of data processing in that antenna orientation need not be recorded. The radar observes only the target's vertical motion by aid of a very narrow, perfectly vertical, radar beam. Smearing of the Doppler spectrum by the horizontal wind will occur in the case of a finite size beam. However, this effect is practically negligible for beam widths of the order of 1° if the tangential speed is limited to less than 30 m sec^{-1}.

Let us accept the fact that we are essentially dealing with the vertical velocity of the precipitating particles. The analysis of the data will still be ambiguous since the particles' vertical velocity is due to the contribution of both particle terminal speed and vertical air motion. In the case of stratiform precipitation, vertical air motion may be assumed to be negligible. Furthermore if we are observing raindrops, a relationship between particles' radar cross section and particles' vertical speed can be established thereby allowing the Doppler spectrum to be predicted on the basis of the knowledge of the particles' size distribution. The inverse proposition is true and the size distribution of raindrops have been derived from the vertical velocity Doppler data, Probert-Jones (1960), Rogers and Pilié (1962), Caton (1963), Rogers (1966).

For study of raindrop growth or evaporation in stratiform conditions this method of observing drop-size distribution is excellent. However, the results are very sensitive to the presence of air motion, especially where the speeds correspond to large drops whose terminal velocity is weakly related to drop diameters. In practice, this limits the method to nonconvective precipitation. Also, large particle scattering in case of limited signal dynamic range might overwhelm the weak contribution due to the smaller particles scattering and prevent accurate knowledge of the relative concentration of smaller size raindrops.

Provided that the antenna radiation pattern is excellent, fully coherent radar provides adequate spectrum dynamic range allowing good estimates of the presence of small raindrops. We may also mention that combined study of vertical velocity spectra and signal intensity in stratiform precipitation, Lhermitte and Atlas (1963), may lead to a better understanding of precipitation growth mechanisms.

Although the above comments indicate that the vertical beam method is useful, its systematic application to the study of convective storm processes is still very limited. In these cases it is unreasonable to expect that the altitude-time display of the particles' vertical velocity is significantly representative of the actual, time evolving, three-dimensional structure of the storm. Furthermore the vertical velocity observed by the radar will be difficult to resolve in its two components, the particle terminal speed and the vertical air motion.

To obtain estimates of the vertical air motion Rogers (1963) assumed an exponential (Marshall Palmer) model of raindrops size distribution of the form:

$$n(D).dD = N_o e^{-\Lambda D} .dD \tag{3}$$

where $n(D)dD$ is the number of drops per unit volume in the diameter interval dD, N_o is a constant, and Λ is a parameter that depends upon rainfall rate. By further assuming a relation between terminal fall velocity and size, Spilhaus (1948), and also Rayleigh scattering, Rogers arrived at an expression of the relationship between the average vertical velocity, $\overline{V}_f$, and radar reflectivity, Z, which is the following: $\overline{V}_f = 3.8 Z^{1/14}$. He concluded that any departure from the above equation will be due to vertical air speed. The application of the above treatment seems to be only practical in stratiform rain, for average quantities obtained over long periods of time.

Similar assumptions have been made by Donaldson et al (1966) and Donaldson (1967a). In this work the analysis was restricted to regions where Z>10, and the following expression between $\overline{V}_f$ and Z was derived:

$$\overline{V}_f = 2 \log Z - 2 \tag{4}$$

The estimated vertical air speed, $\hat{W}$, was also derived from the following equation:

$$\hat{W} = \overline{V}_f + 2 \log Z - 2 \tag{5}$$

A different method to estimate updrafts has been used by Probert-Jones and Harper (1961) for the study of small convective storms. They suggested that above the 0° C level in the convective storm, precipitation was present in the form of large ice crystals or snow flakes. The assumption of a terminal fall velocity of 1 m sec^{-1} $\pm$ 0.5 m sec^{-1} provided Probert-Jones and Harper with means to estimate vertical air motion. They extended the analysis below the melting level by assuming continuity of air motion through the melting level and by further assuming that there was very little change of the terminal velocity of the drops between the melting level and the ground.

Although numerous assumptions were present in the analysis, the method showed a surprisingly well organized pattern of motion in the convective storm which could be used for a model of the structure of the air circulation within the storm. The model seems to have questionable application to larger convective systems where the melting level is not as clearly defined as in the convective storm analyzed by Probert-Jones and Harper.

A different approach to estimating updraft velocities has been used by Battan (1963a) and Battan and Theiss (1966, 1967). They suggested that the lowest part of the velocity spectrum is related to the small size precipitation particles which can be estimated by assuming a threshold of detection. Since the terminal speed for such precipitation particles was known, updraft could then be determined from this lower boundary of the vertical velocity spectrum. There is, however, some difficulty in estimating the lowest velocity boundary of the spectrum since its dynamic range is limited by the noise generated by or accepted in the radar circuit. This noise is mainly due to the radar phase noise generated by the radar equipment, but also includes contributions due to backscattering received outside the antenna main beam as allowed by the complex nature of the radiation pattern of the radar antenna. The spectrum dynamic range can also be degraded by signal processing such as the single sideband detection scheme used by Battan and Theiss (1966).

In spite of the restrictive assumptions, there is acceptable consistency in the published radar observations of vertical Doppler speed. These have covered a wide range of updraft speeds from 4 m sec^{-1} deduced by Probert-Jones and Harper (1961) in a weak convective storm, to 20 m sec^{-1} deduced by Battan and Theiss (1966). Updraft speeds larger than 16 m sec^{-1} have also been observed by Donaldson et al (1966). These observations reveal that updrafts are found mostly above the $0°$ C level and downdrafts below this level.

The application of the previous methods to the estimate of updrafts and other processes inside storms is, however, questionable. Noticeable departure of the drop size distribution from the exponential Marshall Palmer mode, which will reduce the applicability of the updraft estimates, will occur in a variety of cases. Sorting of the precipitation particles is a frequent cause of drastic modification of spectrum size. The presence of hail will completely upset the estimated relationship between radar reflectivity and $\overline{V}_f$, presented above.

The validity of the assumptions involved in estimating updraft speeds might be further questioned on the basis of some of the published results indicating very high air vertical velocity gradients dw/dz, Donaldson (1967). One sees that the Donaldson results shown in Figure 2 indicate that, between 1641 and 1642 EST, dw/dz was larger than $10^{-2} sec^{-1}$ at an altitude of 8 kms, therefore requiring that horizontal divergence of the same order of magnitude be present at this altitude. Results recently obtained by Donaldson (1968) indicate that dw/dz can reach a maximum value of $3.10^{-2} sec^{-1}$.

The vertical beam method requires that some stratification or steady state process be realized for a reasonable length of time. These conditions will seldom be met in the case of convective storms.
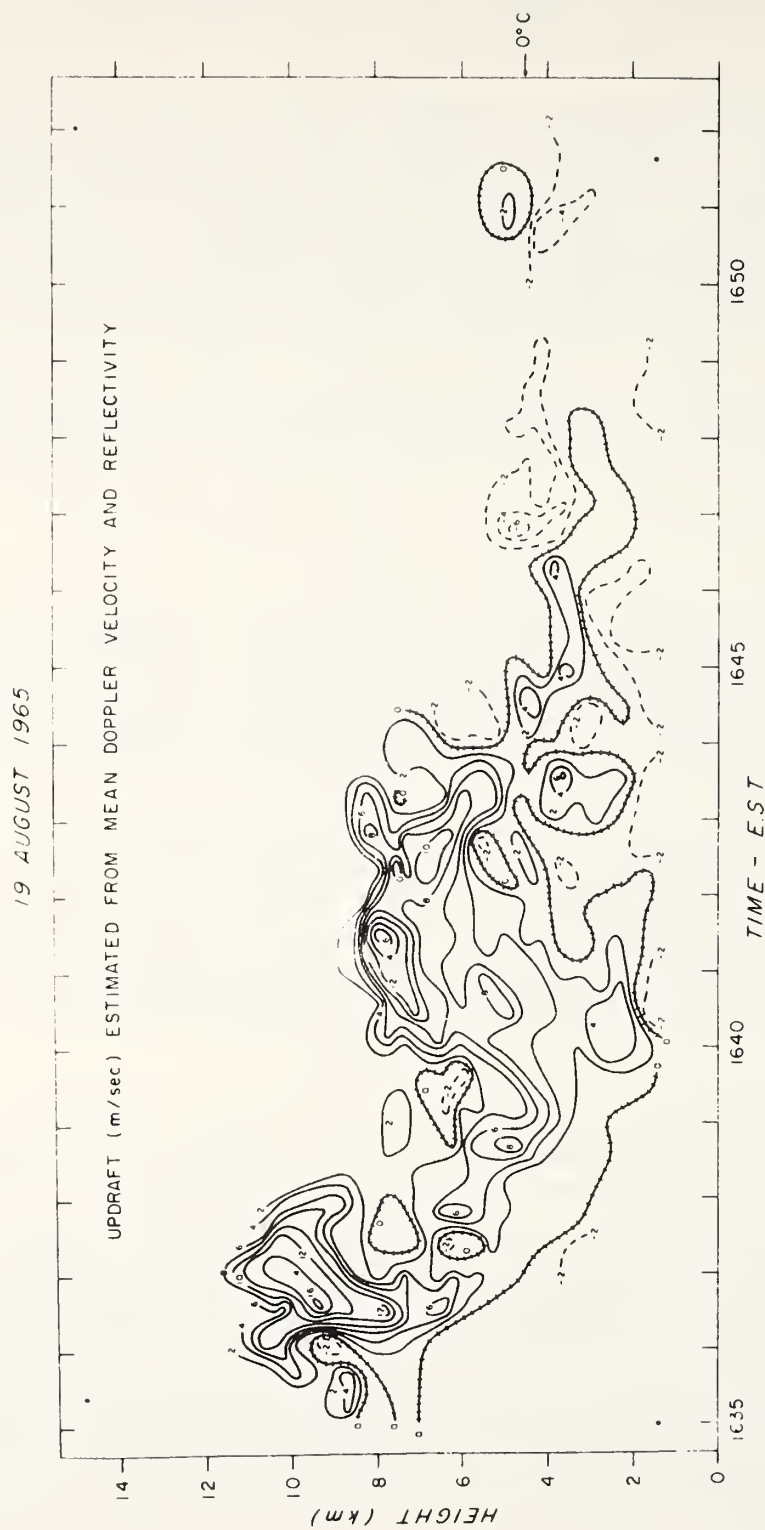
Figure 2. Vertical air motion field estimated from mean Doppler velocity and an assumed relationship between reflectivity and mean particle fall speed. Updrafts are solid contours, and downdrafts are dashed contours, with railroad tracks showing locations of zero vertical air motion. (After Donaldson, 1968).

In order to give meteorological significance to the Doppler data, the experimenter must rely on arbitrary assumptions which are not derived from sound physical reasoning. This attitude is reflected on the controversy surrounding the existence of a "balance level" proposed by Atlas (1966) and its significance as an important part of the storm processes. The balance level is characterized by the altitude at which the mean vertical Doppler velocity is zero. It is adventurous to specify such quantity without some knowledge of the spectrum shape. Furthermore, as indicated by Donaldson and Wexler (1968) the restricted significance of altitude-time cross sections does not allow any firm conclusion as to the presence of an accumulation zone or region of particle growth in the three-dimensional storm structure.

Since critical phases of the analysis of data derived from vertically pointing radar rely on arbitrary assumptions used as a substitute for the lack of knowledge of the storm processes outside of the region observed, the reader is referred to the above mentioned papers for a more detailed discussion on the significance of the balance level.

To summarize, it is the author's opinion that a single, vertically-pointing radar has and will continue to have severely limited application for the study of convective processes inside storms and should be replaced by the multiple Doppler radar method discussed at the end of this report.

5. VAD METHODOLOGY

If we assume statistical homogeneity of the speed of the particles in the area covered by the radar equipment and if we are interested in deriving average properties of the wind field, it is appropriate to observe several radial components of the particle motion obtained in different directions, by means of azimuth scanning of the radar beam and display of the velocity azimuth function (Velocity-Azimuth-Display). With appropriate programming of the radar beam elevation angles and also selected ranges, the data can be representative of a range of altitude levels in the storm, thereby leading to a definition of the vertical distribution of the properties of the motion field.

The method was first proposed, Lhermitte and Atlas (1961), for the purpose of measuring the wind vertical profiles within a snow storm. An example of the method capability is shown in Figure 3. The particle radial velocity, V_R, at a certain altitude level in a snow storm is continuously recorded as a function of the azimuth of the radar beam, β. V_R is expressed as a function of the horizontal motion speed, V_h, and direction, β_o, the radar beam elevation angle, Θ, and the particle vertical velocity, V_f, by the following equation:

$$V_R = V_h \cos \Theta \cos (\beta - \beta_o) + V_f \sin \Theta \qquad (6)$$

V_R is in fact a spectrum whose variance is due to the contribution of V_h variance, σ_h^2, V_f variance, σ_f^2 (due mainly to the distribution of particle terminal speed), and the covariance between V_f and V_h. The estimate of the mean velocity V_R (spectrum first moment) collected as a function of radar beam azimuth, offers means to determine a least square fit of equation (6) which permits a prediction of the average quantities: $\overline{V}_h$, $\overline{V}_f$ and $\overline{\beta}_o$.

$$V_R = V_h \cos \theta \cos (\beta - \beta_0) + V_f \sin \theta$$
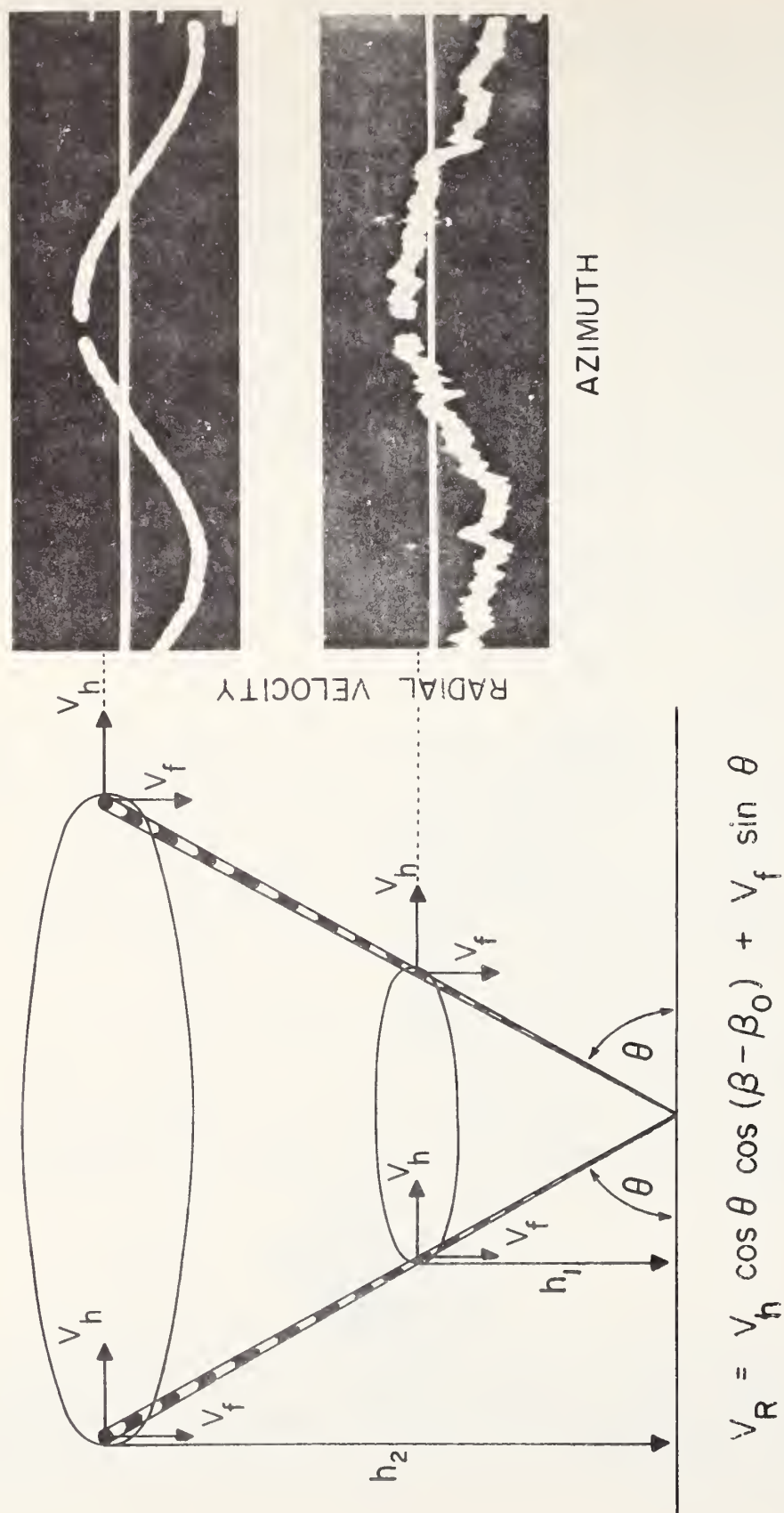
Figure 3. Velocity azimuth display with examples of actual results.

There is, however, an ambiguity in the prediction of $\overline{V}_f$ which is due to the possible presence of wind convergence in the wind field. This is easily shown by integrating V_R as a function of β. We have:

$$\int_0^{2\pi} V_R(\beta) d\beta = \cos\Theta \int_0^{2\pi} V_h \cos(\beta-\beta_0) d\beta + \sin\Theta \int_0^{2\pi} V_f d\beta \qquad (7)$$

The term $\int_0^{2\pi} V_h \cos(\beta-\beta_0)d\beta$ will be null only if there is no wind convergence.

We then can write: $$\int_0^{2\pi} V_R(\beta) d\beta = \sin\Theta \int_0^{2\pi} V_f d\beta \qquad (8)$$

and therefore estimate $\overline{V}_f$. However, if there is wind convergence the term,

$$\int_0^{2\pi} V_h \cos(\beta-\beta_0) d\beta$$

will not be zero and will contribute to the term on the right hand of equation (7). By further manipulating the equations we can estimate the wind divergence, $\mathrm{div}_2 \vec{V}$ by the following expression:

$$\mathrm{div}_2 \vec{V} = \frac{1}{\pi r} \int_0^{2\pi} \frac{V_R(\beta) d\beta}{\cos\Theta} - \left(\frac{2 \overline{V}_f \tan\Theta}{r}\right) \qquad (9)$$

In this equation, r is the radius of the circle scanned by the radar beam at the selected range or altitude. The method is capable of an accurate estimate of the wind convergence if Θ is small and if the particle fall speed can be estimated accurately, i.e., (snowflakes falling in still air). For instance, if $\Theta = 10^{\circ}$ a change of the estimate of V_f by 0.5 m sec^{-1} will modify the convergence estimate by 2×10^{-5} sec^{-1} at r = 15 kms.

This method of measuring wind convergence has been first proposed and applied by Caton (1963). It reliably applies only to snow storms or the region of the atmosphere where the fall velocity of targets is either small or accurately estimated. Browning and Wexler (1966) have extended these computations to the study of other properties of the wind field such as deformation. Vorticity can not be observed with a single Doppler radar since it requires that the tangential component of the motion be known.

Wind fluctuations of smaller scale can also be estimated by classical Fourier analysis of the $V_R(\beta)$ function and the Fourier components expressed in the following equation:

$$C_n = \int_0^{2\pi} V_R(\beta) e^{-jn\beta} d\beta \qquad (10)$$

C_n is indeed a complex quantity containing information of the phase and amplitude of the Fourier components.

$$c_o = \int_o^{2\pi} V_R (\beta) \, d\beta$$ is the "DC" term controlled by both the vertical velocity

and the wind convergence which was discussed above. The method can bring information on the small scale variability of the wind, Lhermitte (1968b).

The design of the experiments with a program of elevation angles, Θ, provides more flexibility in analyzing the data since the relative contribution of the vertical and horizontal motion to the radial velocity will be modified by varying Θ.

The method is now largely being used for the study of mesoscale phenomena in widespread storms. Its capabilities of analyzing the wind field properties inside snowstorms are excellent. Mesoscale wind properties as well as turbulent eddy sizes and eddy dissipation rate can be observed and analyzed if the data are acquired at a high rate, simultaneously at different altitudes. However, in order to utilize the method to its full capabilities, the data have to be produced in digital form for efficient reduction by digital computers.

o. COMMENTS ON THE USE OF A SINGLE DOPPLER RADAR FOR THE STUDY OF CONVECTIVE
     STORMS

Attempts have been made to analyze the horizontal wind field in a convective storm system from a slightly tilted Doppler radar beam. Donaldson (1967b) presented such experiments which were made by azimuth scanning of the convective cells, with elevation angle limited to 1^O, 3°, and 5°, for which the contribution due to particle vertical velocity was negligible. However, even if restricted to the storm's lowest levels the results are not representative of the storm circulation since only the radial particle velocity is observed. Even with assumptions about mean wind, whose significance is questionable in the strongly perturbed storm environment, the results do not show any convincing pattern leading to estimates of the storm wind field properties such as convergence and vorticity. The results obtained with such a technique will always be inconclusive except in the case where the azimuth scanning is limited to a small range of azimuth. One objective of such experiments might be to specify the scales of variance of the storm particle motion which can be used to assess the optimum sampling interval in future experiments involving the simultaneous use of several radars.

It is the writer's opinion that neither the vertical beam method nor the single radar horizontal scanning beam will provide significant improvements of the storm circulation knowledge. The prospects are much better if the measurements are based on a two radar system from which two radial components of the motion can be observed. By restricting the observations to low elevation angles, i.e., the storm's lowest levels, the analysis will bring a fairly good knowledge of the wind field leading to estimates of kinematic properties such as convergence. Vertical drafts can be estimated in the low levels of the storm by applying the equation of continuity to the wind fields observed at several altitude levels in the storm.

The Environmental Science Services Administration is developing a system of two compatible Doppler radars which will be tested during summer 1968 and should allow an assessment of the logistic problems involved. The two-Doppler radar method is a necessary step towards the design of a three-Doppler method described in section 9 of this report. Since the three-Doppler method retains the continuity of radar scanning it is more appropriate for the probing of the three-dimensional structure of a storm than the use of a network of vertically pointing Doppler radars, which was proposed by Browning (1966)*.

7. DOPPLER STUDY OF CLEAR AIR MOTION

Doppler methods have also been used for the study of clear air targets (CAR) commonly called "Angels". The experiments were concerned with the observation of the speed of these targets for the purpose of identifying their nature and also the motion of the surrounding air. A much better identification of the target is possible with the phase information provided by the Doppler radar. For instance, birds species can be identified on the basis of the characteristics of the Doppler spectrum as related to the motion of their wings. On the other hand, insects which are smaller than the radar wavelength will only provide a small phase modulation of the signal, which can be used as information to recognize their nature. Although this sort of information would be helpful to entomologists and ornithologists interested in the migration of insects or birds species there has not been any real attempt to direct the analysis of the Doppler data to this use. Expected differences between the Doppler spectra might sometime resolve the controversy between the attribution of clear air radar returns to either sharp index of refraction discontinuity or the presence of small physical targets. It is, however, surprising to notice that there has been no published paper devoted to detailed analysis of the Doppler spectrum as means of identifying the targets detected in clear air. Only the mean Doppler frequency is usually observed and analyzed. The first data of this kind have been acquired with a vertically pointing beam, Battan (1960; 1963). The targets' vertical motion was observed as limited to ± 1 m sec^{-1}. The analysis of the data was based on the assumption that the radar signals were due to air bubbles generated by thermal convection.

By use of the VAD technique described above Lhermitte (1966), Browning and Atlas (1966) were able to analyze the horizontal motion of the clear air targets. The Lhermitte observations, which are illustrated in Figure 5, were obtained in central Oklahoma and showed unambiguously that the targets were moving with the horizontal wind. Furthermore, the analysis showed that the method was capable of providing useful data on the vertical structure of the horizontal wind, almost continuously and over long periods of time. The low level jet frequent in central Oklahoma and northeastern Texas, when analyzed by use of this method, revealed a structure of the jet consistent with the classical studies of these boundary layer phenomena. Correlation between the clear air target horizontal motion and the presence of synoptic features such as cold fronts have been also analyzed by Lhermitte and Dooley (1966) for the spring and summer months in Oklahoma when the concentration of targets is very great. A summary of the observations of clear air target motion showed that vertical profiles of the wind can be often estimated by the method up to 1 or 2 km of altitude. The conclusions as to the nature of

---

*Private communication.
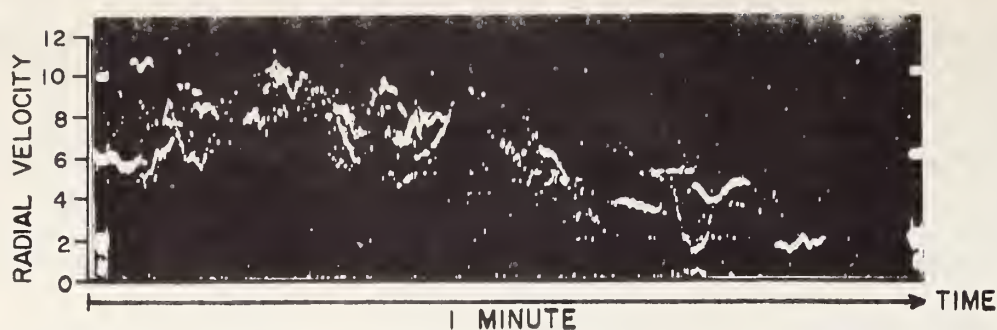
Figure 4. Time velocity variations of clear air target at a fixed point in space. Note the average trend which can be attributed to change of air motion speed.
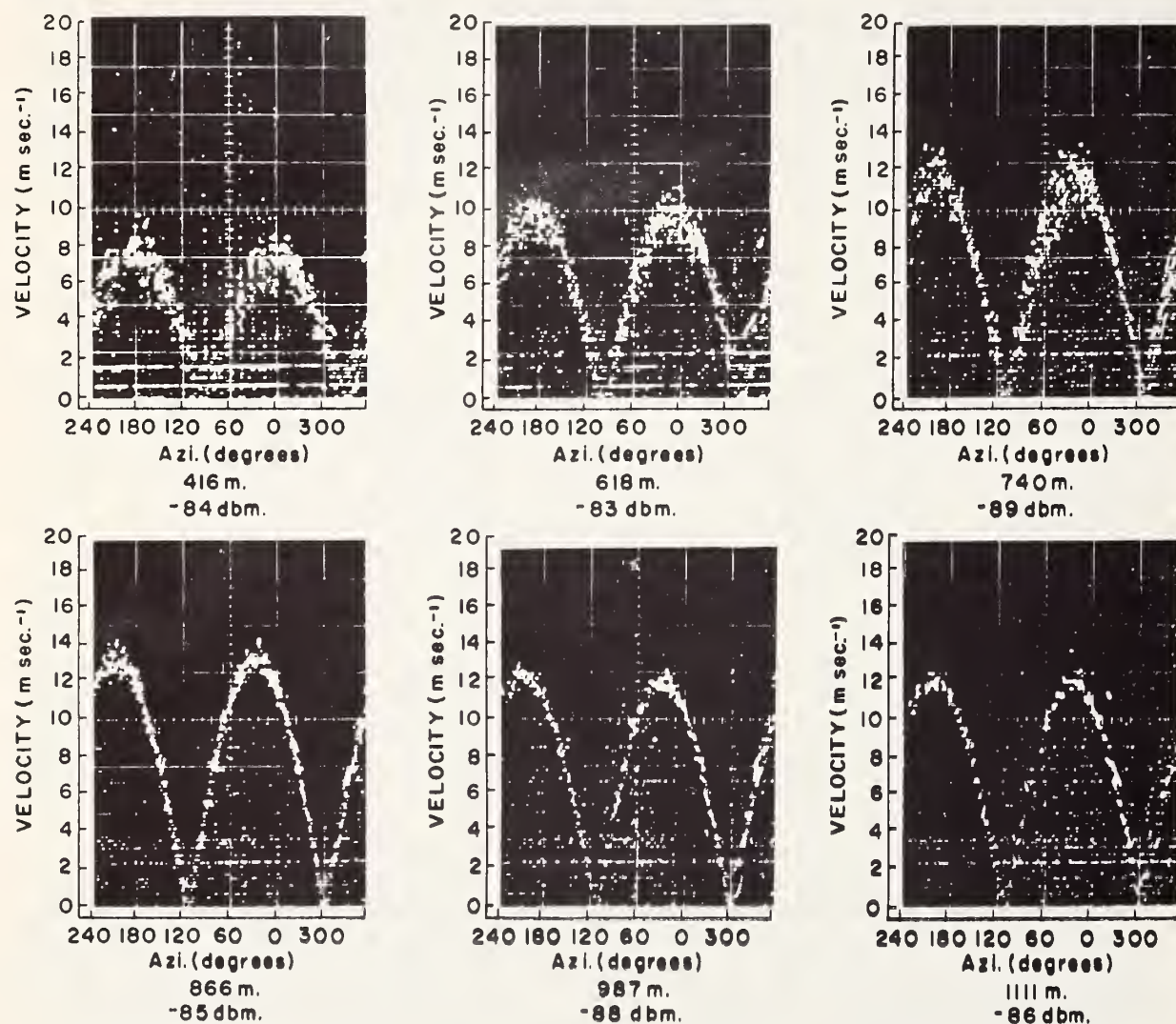
Figure 5. Velocity-Azimuth displays showing the CAR radial velocity at several altitudes. Radar beam elevation angle 20°. Radar site, Norman, Okla. Time 2023 to 2031 CST, 26 June. Signal mean intensity is indicated in -dbm.

the targets was uncertain although there was a high probability that they were
insects drifting at air speed. In certain cases the space variance of the
motion, with respect to the average wind, was so small that it would indicate
very poor ability for these insects to react to the environment. More of
these studies should be made to further specify the nature of the target and
the capability of using the method for wind sounding techniques.

Tracers, such as "chaff" dipoles, offer an extremely interesting possi-
bility for the probing of steady and turbulent air motion. The Doppler spec-
trum will be controlled by the turbulent processes and will contain informa-
tion on turbulent parameters such as the eddy dissipation rate. Furthermore,
by extending the observations to different regions of space by means of beam
scanning, the study of turbulence homogeneity and large scale wind fluctuation
can be performed. The material can be dispersed, either in bundles which will
drift with the wind and expand through turbulent diffusion process, or intro-
duced over large areas. The method will provide means to analyze the field
of turbulent and steady clear air motion. The variance of the Doppler spec-
trum obtained under these conditions will be controlled by the variance of the
horizontal motion, σ_h^2, the variance of vertical motion, σ_f^2, and the covariance
between these two quantities. The covariance can be separated from the other
variances by acquiring the Doppler information in such a way that positive and
negative signs for the covariance will be available in the data analysis. The
observation of the covariance between the horizontal and vertical component of
the motion will provide means to probe the vertical transport of momentum in
the friction layer, which is due to the interaction between the turbulent
atmosphere and the earth's surface acting as a boundary, Lhermitte (1968b).
The vertical distribution of the vertical motion variance, σ_f^2, can be easily
obtained from a vertically pointing beam. Also the differences between
Lagrangian (space variability) and Eulerian (time variability) scales of
motion variance can be easily studied by comparing the cross correlation of co-
variance spectrum of the motion observed simultaneously at two points in space
with the time autocorrelation or autocovariance of the individual motion sample.
A scheme similar to this was presented by Gorelik (1965) and more recently by
Boucher (1968). These methods present an extremely good prospect for the
study of turbulent diffusion processes in critical areas where this is becom-
ing an important factor (pollution zone). Surprisingly little work has been
done in this research area and we recommend that such activity be included in
research projects in the next few years. An X-band Doppler radar (or shorter
wavelength) is appropriate for this kind of experiment. If the chaff is re-
leased by airplane the method also offers the possibility of probing the high
altitude clear air turbulence.

8. ADVANCED DOPPLER SIGNAL PROCESSING AND DOPPLER DATA STORING

Most of the results which have been discussed in the previous section
have been obtained through the use of relatively simple signal processing and
data storing techniques which have severely limited the analysis of the data
and have prevented the use of the method to its full capability. Since most
of the data have been hand reduced, an extremely time consuming analysis was
needed, which has prevented the statistical treatment of the very large
amounts of data provided by the method.

Recently, signal and data processing methods have drastically improved
through the use of modern general purpose digital computers and also by the

269

aid of special purpose processing systems based on the use of modern digital hardware such as integrated circuits. The meteorological Doppler radar system, with its high rate of information flow, can benefit dramatically from the introduction of modern digital circuitry and methods for the processing and storing of the Doppler information. This section is devoted to analyzing the problems and predicting solutions which are expected to take place in the next few years for the treatment of the Doppler radar information to such an extent that the potential of the method will be fully realized.

As mentioned in the first part of this report, the Doppler signal which contains backscattering phase and amplitude information, must be processed to provide useful information on the spectrum of radial velocity of the scatterers. The transformation required is a conventional Fourier transform or its equivalent such as the processing of the signal by use of an analog type frequency analyzer.

Although digital computations of the Doppler signal power density spectrum have been involved in some of the experiments mentioned previously in this report, Battan (1964), they have not been widely used because of the time consuming nature of the operation. However, substantial progress has been made in the field of power density spectrum computation by digital computers, and efficient algorithms are now available which match the digital computer methods with the mathematics of the Fourier transform, Cooley, Tukey (1965). This fast Fourier method allows a substantial reduction of the time requirement for the digital computations of Fourier transforms.

The digital Fourier transform is based on the availability of digitized time samples, a_k, of the signal to be analyzed. The spectral power density estimates, S_j, are computed according to the following equations:

$$A_j = \sum_{k=1}^{N} a_k \cos 2\pi K_j/N$$

$$B_j = \sum_{1}^{N} a_k \sin 2\pi K_j/N$$

$$S_j = A^2_j + B^2_j \tag{11}$$

The method provides N non-redundant frequency samples from N time samples thus requiring that N^2 multiplications be done per complete spectrum. It is usually admitted that 500 time samples are fairly representative of the spectral information in a time signal, requiring that 250,000 multiplications be done for each conventional Fourier transform. With modern fast digital computers the computing time will be on the order of, or less than, one second which is comparable to the signal dwell time required to build an acceptable knowledge of the spectrum. Therefore real-time digital computations by conventional Fourier algorithms are, at least, as effective as the filter bank method. In addition, the digital computer offers complete flexibility in the choice of appropriate frequency filter characteristics and the frequency coverage which is controlled by the signal sampling rate. See Blackman and Tukey (1958). Since it is based on the unambiguous Fourier transform mathematical expression, the digital frequency analyzer provides a well-defined answer

for the spectral density estimate which is easier to use in the analysis of the data.

The use of fast Fourier transform algorithms decreases the required number of multiplications to $2 N \log_2 N$ instead of N^2. This will considerably reduce the computation time to much less than signal dwell time and thereby making it feasible to process several radar ranges in a time less than a few seconds. This involves the use of a high speed, elaborate system for multiplexing, and analog-to-digital conversion, of the Doppler signal. It also requires core memories which are organized in such a way that the sequence of the Fourier transforms can be easily computed, range after range, from the stored digital data. Such systems can be built at an acceptable cost by use of modern integrated circuit digital hardware. The expected maximum rate of data which can be processed by the system is on the order of 2,000 (20 ranges, 50 velocities) samples every two seconds. By use of a logarithmic scale only one BCD coded character will be necessary to represent the spectral density at a given range-velocity address. The storing of the Doppler data with range-velocity addresses will be done on magnetic tape with a format compatible with the requirement of general purpose digital computer (BCD format suitable for Fortran IV programming). Figure 6 illustrates the capabilities of the digital method for reducing and even presenting a three-dimensional display of the Doppler radar information. Such displays can be obtained in very short times by use of output devices usually associated with large computers.

The system is capable of processing signals recorded at an average speed of 10 to 20 spectra per second, which is compatible with the scanning capabilities of the radar beam and signal dwell time requirements (one or two beam width per second).

Let us inquire if the method has an acceptable observational speed to define convective storm processes known and anticipated. The evaluation of the number of points, which are needed to adequately sample the field of particle motion inside a convective storm, depends on the scale of the motion variance and the size of the storm. Although this information has to be acquired through actual experiments yet to be performed, it is reasonable to accept a few hundred meters as an appropriate space sampling interval.

This estimate is consistent with the radar angular resolution for nearby storms. If we analyze the problem in terms of the radar polar coordinates we will deduce that, (with a one degree beam width) an adequate description of the storm will be obtained with approximately 50 beam-widths in azimuth and 10 to 20 elevation angles. Assuming as mentioned before that the beam will stay in a fixed position for a time on the order of 0.5 second i.e., 20 to 30 spectra will be processed in one second, the total time required for exploring the storm will be on the order of 250 to 500 seconds or 4 to 8 minutes. This is marginal since the storm will be translating and evolving during this time. This effect can, however, be accounted for in the computation of radial velocity field estimates.

It is important to note that the rate at which the Doppler data are acquired and stored can be increased well beyond the limits expressed above. The expected availability of large scale integration (LSI) digital hardware along with the increasing speed capability of integrated circuits can increase

the data acquisition rate expressed above, by one order of magnitude. The capability of the system will still be limited to the scanning speed capabilities of radar antennas, although this, too, might ultimately be overcome by the development of electronic beam scanning techniques; but, isn't it dreaming??
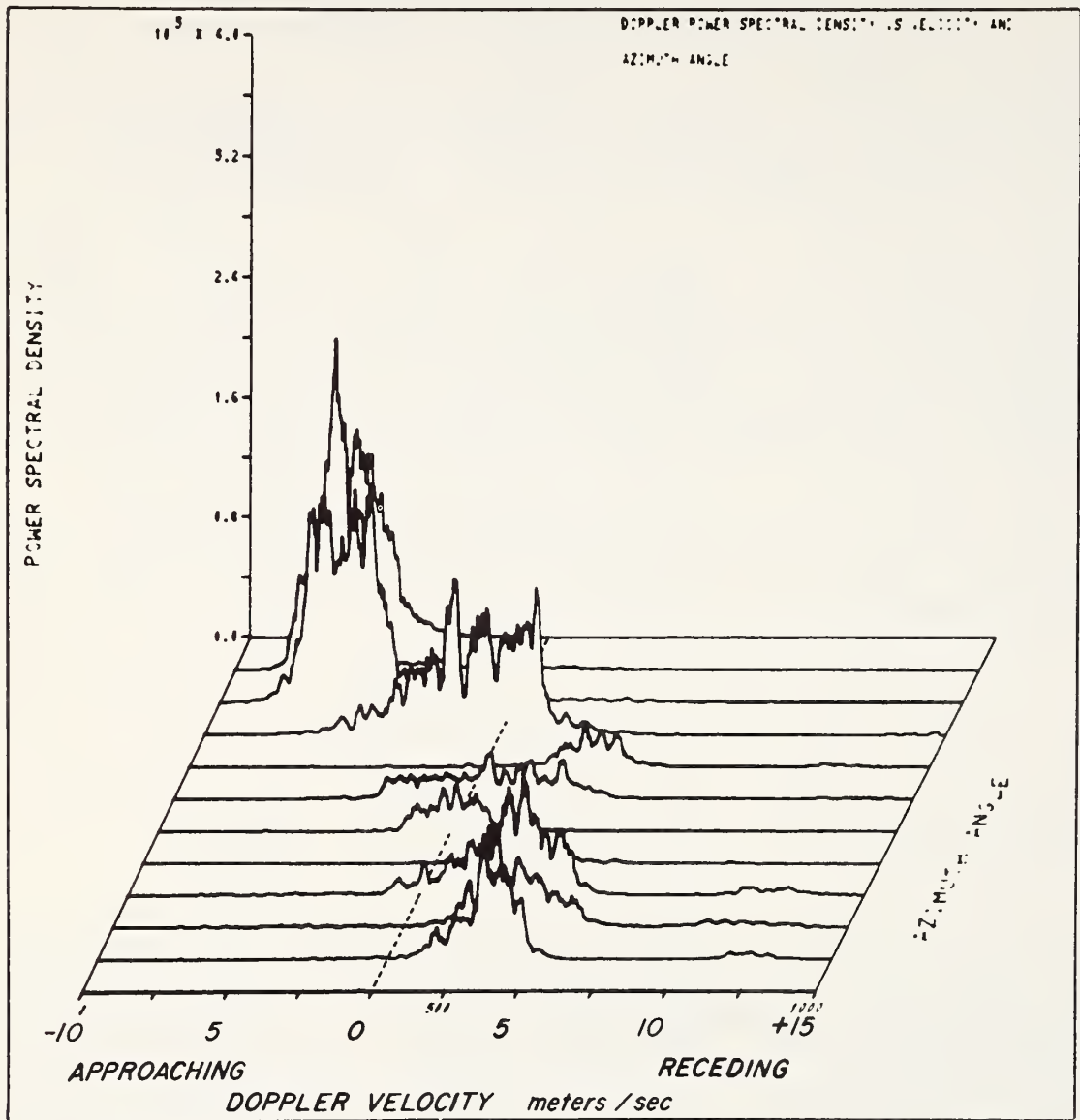
Figure 6. Three dimensional display of Doppler-azimuth patterns obtained with the cathode ray tube plotter of a CDC 3800 digital computer.

9. THE THREE DOPPLER RADAR METHOD

As mentioned in the previous section of the report the real weakness of the Doppler radar method is that it only provides the scatterers radial velocity. Since the vertical beam method is sensitive only to particle vertical velocity, it is less ambiguous and in the case of marked stratification, very useful. But, the method fails to exploit the outstanding capability of the radar, i.e., its ability to acquire data distributed in three coordinates of space. The observation of particle vertical velocity along a vertical co-ordinate is hardly respresentative of the storm processes except in the case of stratiform storms.

The use of a single radar scanning beam is useful and effective if assumptions about statistical homogeneities of particle motion in the region covered by the radar can be accepted. The most commonly employed scanning scheme is based on continuous azimuth scanning of the radar beam with a pro-grammed elevation angle (VAD). The method, which was discussed in section 5 of the report, has an extremely good potential for the study of the dynamics of widespread storms by providing separate estimates of the mean properties of the horizontal wind field (magnitude, direction, convergence) and the ver-tical motion of the targets.

However, because of the absence of stratification and the non-uniformi-ties of wind field, neither the vertical beam nor the VAD methods are appli-cable to observing the particle motion field inside convective storm systems. The understanding of the physical and dynamical processes involved in these storms fall in the most stimulating and unknown areas of meteorological re-search and have received a large attention from the meteorologist. However, progress on the study of storm dynamics has been slow mainly because of the lack of experimental data at the required scales. Theoretical work has al-ways been limited to crude modeling far from the actual complexity of the storm's circulation patterns.

The main reason for this slow progress is the lack of appropriate means for observing the storm inner processes. The use of airplane as a means to acquire such data has been limited to a poor sampling of the storm environ-ment since penetration of the storm was always questionable. Radiosonde net-works have been useful to specify the condition of the storm environment and its link to the mesoscale or synoptic scale but, because of the techniques in-volved, they again provide only a poor time and space sampling far from the resolution required to adequately define the inner processes and evolution of a convective storm. Conventional radars have brought a much better under-standing of the structure of the storm systems, which is still being devel-oped, through the use of more elaborate quantitative processing of the radar signal.

As mentioned in section 6, the use of two Doppler radars, installed at different locations and simultaneously observing the same storm, drastically improves the capability of the single Doppler radar method. Figure 7 illus-trates the concept. The same region of a storm is observed by two radars, R_1 and R_2, installed at different locations thereby providing two radial compo-nents of the particles' motion, V_1 and V_2. The two components, V_1 and V_2, can be expressed by the following equations:

$$V_1 = V_h \cos\alpha \cos\Theta_1 + (V_t + w)\sin\Theta_1 \tag{12}$$

$$V_2 = \cos(\beta_1 + \beta_2 - \alpha)\cos\Theta_2 + (V_t + w)\sin\Theta_2 \tag{13}$$

In these equations β_1 and Θ_2 respectively are the azimuth and elevation angles for R_1; β_2 and Θ_2 respectively are the azimuth and elevation angles for R_2; V_h is the horizontal motion speed; α is the azimuth angle between the direction of the motion and β_1; $V_t + w$, the particles' vertical velocity (V_t is the terminal speed and w the air vertical motion). If the contribution to the Doppler due to vertical motion can be neglected, i.e., $(V_t + w)\sin\Theta \simeq 0$, equations (12) and (13) can be solved for V_h and α according to the following expressions:

$$V_h^2 = \frac{1}{\sin^2(\beta_1 + \beta_2)}\left[\frac{V_1^2}{\cos^2\Theta_1} + \frac{V_2^2}{\cos^2\Theta_2} + \frac{2V_1 V_2 \cos(\beta_1 + \beta_2)}{\cos\Theta_1 \cos\Theta_2}\right] \tag{14}$$

$$\tan\alpha = -\frac{1}{\sin(\beta_1 + \beta_2)}\left[\frac{V_2}{V_1}\frac{\cos\Theta_1}{\cos\Theta_2} + \cos(\beta_1 + \beta_2)\right] \tag{15}$$
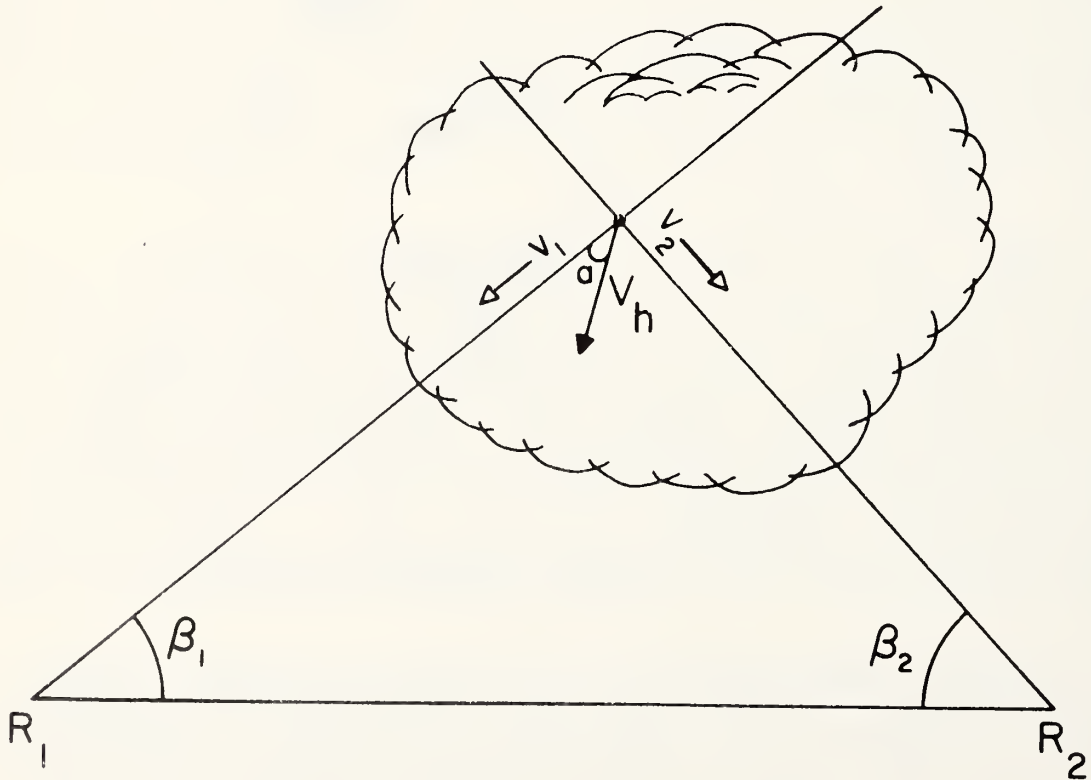
Figure 7. Measuring two-dimensional horizontal particle velocities by use of two Doppler radars observing the same storm from different directions.

   The optimum spacing between the two radars depends on their character-
istics but it is on the order of 20 to 60 kms.

   The method offers excellent potential for mapping the particles' horizon-
tal motion field inside convective cells for nearly horizontal radar beams.
However, radar beam elevation angle smaller than 5° to 10° can be accepted in
the scheme allowing the observation of the horizontal motion field up to alti-
tudes on the order of 10,000 to 15,000 feet. The only assumption which is
needed is to neglect the contribution due to particles' vertical motion. For
targets which are outside of the line of sight between the two radars, the
method offers accurate and non-ambiguous results which should clearly reveal
convergence and vorticity patterns in the low levels of a convective storm.

   If assumptions about the terminal velocity of the particles are adopted,
the method can be extended to observations from larger elevation angles for
which a significant contribution to the Doppler, due to the particles' vertical
velocities, is likely. The method is also capable of providing estimates of
the vertical air motion from convergence estimates made at several altitudes.

$$V_1 = V_h \cos(\beta_1 - \beta_o)\cos\Theta_1 + V_f \sin\Theta_1$$
$$V_2 = V_h \cos(\beta_2 - \beta_o)\cos\Theta_2 + V_f \sin\Theta_2$$
$$V_3 = V_h \cos(\beta_3 - \beta_o)\cos\Theta_3 + V_f \sin\Theta_3$$

$$V_f = V_t + w$$

$\underline{w \text{ estimated from}} \quad \dfrac{\partial w}{\partial z} = -\left[\dfrac{\partial u}{\partial x} + \dfrac{\partial v}{\partial y}\right]$

Figure 8. The three-Doppler radar method

   Although it is a reasonable step towards the design of more elaborate
systems, the dual Doppler radar method described above fails to provide use-
ful horizontal wind information for targets situated on the line of sight be-
tween the two radars. It does not provide a complete knowledge of the three-
dimensional field of the V_x, V_y, V_z components of the storm's particles' mo-
tion. This objective may be achieved from data collected by a well designed
system of three Doppler radars, installed at three different locations which
simultaneously observe the same convective storm. Figure 8 illustrates this
concept and shows that the radial velocity at a given point in space can be
observed from three different directions. The system of three equations in-
dicated in Figure 6 provides the basis for computing the value of the three
components of the motion. Therefore, by combining the radial velocity

information provided by the three Doppler radars, it is indeed possible to isolate and evaluate the three dimensional distribution, in Cartesian coordinates x, y, z, of V_x, V_y, V_z. This information can be sampled periodically provided that the storm is within the maximum range of the equipment. The time and space sampling capabilities are discussed below.

As an example of the unique capability of the method, the three dimensional field of particles' motion can be analyzed in the following manner:

First, it is assumed that precipitation particles are moving in the same direction and at the same speed as the horizontal wind. This assumption is valid except when particles are falling in regions of strong wind shear which might introduce a lag of the particles' velocity with respect to the environment. This effect is negligible for most of the precipitation particles; large hailstones are a marginal case. If we accept the above assumption, the particles horizontal motion field may be taken as that of the horizontal wind. The mean speed (first moment of the velocity spectrum) must be computed to provide basis for interpreting the two dimensional field. Theoretically, the estimated horizontal motion components do not include the variance due to particles' vertical speed distribution. The data are sorted according to their x, y and z coordinates evaluated from radar polar coordinates R, β and Θ. The two dimensional estimates of the two quadratic components u and v of the estimated "wind" can then be defined at selected altitudes in the storm. The application of the equation of continuity, within the assumption of incompressibility, to the horizontal wind field, identified convergence with the estimates of air vertical velocity gradients, $\partial w/\partial z$. By integrating $\partial w/\partial z$ with suitable boundary conditions, it is possible to estimate, not only one vertical updraft profile, but the complete structure of updrafts inside the whole storm. Details on the structure of updrafts will be controlled by the sharpness of the velocity gradients and the inherent velocity resolution of the radar equipment.

Comparison of the updrafts structure with the three dimensional distribution of the particles' vertical velocity (and its spectrum) which is derived simultaneously from the Doppler data, provides knowledge of the distribution of particles' terminal speed within the storm. This, in turn, provides means for defining, in any region of the observed storm the precipitation particles' terminal velocities and therefore their size distribution. The method has obvious application for the monitoring and study of such important processes as hail formation; its use should provide significant improvement of our knowledge of convective storm processes and provide a firm basis for a more efficient control of their behavior.

The three Doppler radar concept is far more complicated than the usual weather radar systems presently used in meteorological research. It can operate effectively only if efficient digital computer means are used to process the data. The Doppler information must by necessity be stored in a digital format compatible with computer use.

It is impractical and time consuming for the systematic scanning of a storm to restrict the Doppler observations obtained at a given time, to the intersection of the three radar beams in space. Indeed, when the radar beam is aimed in a fixed direction, a large number of ranges can be simultaneously

processed therefore adding to the Doppler information with respect to that provided by only one selected region. It is more appropriate that the radial velocity data provided by the three radars be acquired and processed separately, thereby leading to separate estimates of the three radial velocity fields. Since the process of scanning the storm will take an appreciable time, time-space interpolation techniques will be necessary to express the radial motion fields at the same time.

Radar beam scanning systems capable of systematically and automatically acquiring the Doppler data in limited angular regions controlled by the storm position with respect to the radar, are required for efficient use of the method. Digital control of a stepping radar beam must be preferred, as means for providing data easier to manipulate with digital computers.

The proposed method might seem to be difficult to implement because of the three-Doppler radar logistic problems involved. Let me make a few comments.

The velocity resolution of a well designed Doppler radar is sufficient to provide acceptable accuracy for estimating convergence or vorticity. If the radar beams are less than 1^O, their cross section at distances of less than 50 kms ($\leq$ 800 m), will not seriously limit the value of the data and the experiments. Velocity ambiguities can be removed through assumption of continuity of the velocity field therefore providing large nonambiguous maximum ranges. Real-time processing of the data by digital computer in the field will bring serious logistic problems and might be beyond our present capabilities. They can be replaced by the processing, by a large computer, of the data stored on magnetic tape. The use of digital computer is recommended as providing objective methods for filtering, interpolating, and redigitizing the estimated least square field. In order to minimize the problems involved in directing three radar beams at the same time, to the same point in space, it is suggested that the X, Y, Z distribution of three radial velocity fields be separately estimated.

After the three radial velocity fields estimates are digitized in a three dimensional coordinates system common to the three radars, their combination in a set of equations aimed to restore the three components of the motion (and their spectra) will generate the X, Y, Z fields of the three components of particle speed discussed above.

It might be objected that the proposed scheme of three radars is much more sophisticated than the degree of complexity presently used in meteorological radar research. It really is, but it is still far from being as sophisticated as some military radars and certainly can be built at an acceptable cost. The approach to this objective is to design two mobile, low cost, radar prototypes using a wavelength leading to acceptable antenna size (X-band). The testing of these equipments in the field with appropriate Doppler signal recording systems will provide knowledge of the capabilities of the method and open the way for the three radar scheme.

Because of the unusual opportunities of the method and its unique potential for the study of three dimensionally distributed atmospheric phenomenon (such as convective storms), it is hoped that its implementation will represent the most significant contribution of Doppler radar techniques to the field of meteorology.

10. AIRBORNE PULSE DOPPLER RADAR

Ground-based equipment often suffers from lack of mobility e.g., when the observations require that the radar equipment be in close proximity of storms sparsely distributed over large areas. The airborne platform has the required mobility and can be used to analyze convective storm processes by pulse Doppler radar methods.

A vertical pulse Doppler radar beam can be carried by an airplane for the purpose of analyzing the observed vertical motion in a convective storm. The capability of the method is different from that of a ground-based vertically pointing Doppler radar, because the airplane can fly at a speed that is much higher than the storm motion. This capability would permit the vertical velocities of the storm particles to be observed and displayed in vertical cross section as the plane traverses the storm. Furthermore, this scheme could be repeated several times during the life of the storm therefore leading to an estimate of the three dimensional structure of particle vertical velocity. If medium ceiling airplanes are used, the scheme requires that the airplane fly through the storm, which is not applicable to the study of severe storms. However high-ceiling airplanes will have the capability of flying above the storm in regions where flight is not dangerous. The scheme was first proposed by Atlas (1962)*. Logistic and technical problems were involved in the approach, which prevented actual experiments from being conducted. Since then, Doppler radar techniques have improved to the point that it is now feasible to consider that an airborne pulse Doppler radar can be developed at reasonable cost with acceptable chances of success. The magnetic tape recording of the signal aboard the airplane simplifies the scheme, and permits data acquisition techniques which are identical to the ones used by ground-based equipment.

The method can be extended to analyzing the wind field structure inside the storm by means of a side looking radar. Lhermitte and Weickmann (private communication) recommended that two airplanes, flying horizontally along perpendicular paths could look at the same storm, thereby providing the two components of the horizontal particle motion at flight level. This information will allow the estimate of the horizontal motion field, from which estimates of wind convergence can be derived. Slight tilt in the vertical plane of the side-looking radar beams, could provide some altitude scanning. This would allow the observation of the wind at different altitude levels without impairing the data by introducing significant vertical contribution due to the particle's velocities.

The airborne pulse Doppler radar scheme is particularly suited to the study of convective storms. The cost involved in conducting a feasibility study of the method can be held at a reasonable level by utilizing the techniques identical to these proposed for ground-based Doppler radars. Some of the problems related to the stability of the airborne platform can be solved by classical means or even by proper recording of the directional information for the radar antenna. The airplane is flying at a high speed (50 to 200 m per sec) therefore requiring that the beam be accurately perpendicular to the airplane motion. Smearing of the Doppler by the combination of the airplane's motion and the finite size of the beam will always occur. This effect can however be held to acceptable limits if the antenna width in

*Private communication

the direction of the flight of the airplane is less than 1°. In view of the indicated potential it is therefore recommended that such studies be undertaken in the next few years.

11. CONCLUSION

It is hoped that this review of the applications of pulse Doppler radar techniques to the observation and study of atmospheric phenomena, has adequately demonstrated their excellent potential for solving urgent meteorological problems such as the monitoring and study of processes inside convective storms.

The present method of a ground-based single Doppler radar, with limited signal processing capabilities, suffers from two main weaknesses: (1) only the targets' radial velocity is observed; (2) the signal processing and attainable data reduction techniques fall far short of taking full advantage of the information pertaining to three dimensional fields of motion.

The opinion of the writer is that the subject of meteorological Doppler radars should be enlarged by extending the method to more sophisticated concepts, such as the design and application of a three Doppler radar technique assisted by adequate means for digital recording and processing of the Doppler spectrum. If we do so, the method will provide outstanding results in the study of currently undetectable and poorly understood meteorological phenomena such as convective storms and atmospheric turbulence.

Of course we should not forget that single Doppler radar techniques can also be used to improve the capabilities of conventional radar for the detection, monitoring, and tracking of storms.

The monitoring of hurricane evolution for instance, should be strengthened by continuous observations of the particle radial speed with a horizontal radar beam. Tornadoes might be more easily detected if information on particle radial speeds is added to the information on radar reflectivity. In order to retain the scanning capability of the radars, these techniques should preserve the two-dimensional display (PPI, RHI) of the information which is usual in conventional radar design. We therefore would recommend that radial velocity gating systems be used and that velocity contours be presented on PPI and RHI by use of appropriate methods.

ACKNOWLEDGMENT

REFERENCES

Aoyagi, J., Fugiwara, M., Yangisawa, Z., and Kodaira, N., 1966: Doppler radar observations of snow showers; Proc. Twelfth Wea. Rad. Conf., Boston, American Met. Soc., 112-116.

*Aoyagi, Jiro, 1968: Mean Doppler Velocities of Precipitation near the Ground, 13th Radar Meteor. Conf., 22-25.

*Aoyagi, Jiro, 1968: A multi-channel Doppler frequency analyzer, 13th Radar Meteor. Conf., 324-327.

*Armstrong, Graham M., & Donaldson, R. J., Jr., 1968: A convenient indicator of tangential shear in radial velocity, 13th Radar Meteor. Conf., 50-52.

Atlas, D., 1963: Radar analysis of severe storms, Meteor. Monograph, Vol. 5, No. 27, 177-220.

Atlas, D., 1964: Advances in radar meteorology. Adv. Geo-phys., 10, New York Academic Press, 317-478.

Atlas, D., Aoyagi, J., and Donaldson, R. J., Jr., 1965: Doppler analysis of the physical dynamics of a convective storm. Proc. Conf. Cloud Physics, Tokyo, 314-318.

Atlas, D., 1966: The balance level in convective storms. J. Atmos. Sci., 23, 635-651.

*Atlas, D., and Tatehira, R., 1968: Precipitation-induced mesoscale wind perturbations, 13th Radar Meteor. Conf., 166-175.

Battan, Louis J., 1963a: Some observations of vertical velocities and precipitation sizes in a thunderstorm. Proc. Tenth Weather Radar Conf., Boston, Amer. Meteor. Soc., 303-308.

Battan, Louis J., 1963b: The vertical velocities of angel echoes. Proc. Tenth Weather Radar Conf., Boston, Amer. Meteor. Soc., 309-315.

Battan, Louis J., 1964: Some observations of vertical velocities and precipitation sizes in a thunderstorm. J. Appl. Meteor., 3, 415-520.

Battan, Louis J., and Theiss, J. B., 1967: Measurement of draft speeds in convective clouds by means of pulsed-Doppler radar, Univ. of Arizona, Inst. Atmos. Phys., Sci. Rept. No. 22, 23 pp.

*Battan, Louis J., and Theiss, John B., 1968: Measurement of draft speeds in convective clouds by means of pulsed-Doppler radar, 13th Radar Meteor. Conf., 26-29.

Blackman, R. B., and Tukey, J. W., 1958: The measurement of power spectra. New York, Dover Publications, 190 pp.

Boucher, R., Wexler, R. and Atlas, D. and Lhermitte, R., 1965: Meso-scale wind structure revealed by Doppler radar. J. Appl. Meteor., 4, 590-597.

*Boucher, Roland J., 1968: Characteristics of turbulent structures observed by Doppler radar in snow., 13th Radar Meteor. Conf., 480-485.

Boyenval, E. H., 1960: Echoes from precipitation using pulse Doppler radar, Proc. Eighth Wea. Radar Conf., Boston, Amer. Meteor. Soc., 57-64.

Brantley, James Q., Jr., 1957: Some weather observations with a continuous wave Doppler radar. Proc. Sixth Wea. Radar Conf., Boston, Amer. Meteor. Soc., 297-306.

*Brook, Marx and Latham, D., 1968: The fluctuating radar echo. I. Modulation by vibrating Drops, 13th Radar Meteor. Conf., 2-7.

*Brown, Rodger A., and Peace, Robert L., Jr., 1968: Mesoanalysis of convective storms utilizing observations from two Doppler radars, 13th radar Meteor. Conf., 188-191.

Browning, Keith A., and Atlas, D., 1966: Velocity characteristics of some clear air dot angels. J. Atmos. Sci., 23, 592-604.

Browning, K. A., and Wexler, R., 1966: The determination of kinematic properties of a wind field using a singel Doppler radar. Proc. Twelfth Wea. Radar Conf., Boston Amer. Meteor. Soc., 125-127.

Browning, K. A., and Wexler, R., 1968: A determination of kinematic properties of a wind field using Doppler radar. J. Appl. Meteor. 7, 105-113.

*Browning, K. A., Harrold, T. W., Whyman, A. M., and Beimers, J. G. D., 1968: Horizontal and vertical air motion, and precipitation growth, within a shower, 13th Radar Meteor. Conf., 122-127.

Caton, P. G. G., 1963: The measurement of wind and convergence by Doppler radar. Proc. Tenth Wea. Radar Conf., Boston, Amer. Meteor. Soc., 290-296.

Cooley, J. W. and Tukey, J., 1965: An algorithm for the machine calcuation of complex Fourier series. Mathematics of Computation, 19, 297-301.

Cox, E. G. and Groginsky, H. L., 1966: An analysis of the estimates of wind parameters using the VAD technique. Proc. Twelfth Wea. Rad. Conf., Boston Amer. Meteo. Soc. 44-51.

Donaldson, R. J., Jr., Armstrong, G. M., and Atlas, D., 1966: Doppler measurements of horizontal and vertical motions in a paired instability line. Proc. Twelfth Conf. Radar Meteor., Boston Amer. Meteor. Soc., 392-397.

Donaldson, R. J., 1967a: A preliminary report on Doppler radar observation of turbulence in a thunderstorm. Air Force Cambridge Research Laboratories Environmental Research Paper No. 255.

Donaldson, R. J., 1967b: Horizontal wind measurement by Doppler radar in a severe squall line, Air Force Cambridge Research Laboratories, Proc. Conf. on Severe Local Storms, St. Louis, 89-98.

Donaldson, R. J., Jr., 1968: Measurement of air motion in a thunderstorm anvil by Doppler radar. Paper presented at the 48th meeting Amer. Meteor. Soc., San Francisco.

Donaldson, R. J., Jr., and Wexler, R. 1968: Notes on thunderstorm observation by fixed-beam Doppler radar. Journal of Atmos. Sci., Jan 1968, Vol 25, No. 1, 139-144.

*Donaldson, Ralph J., Jr., and Chmela, Albert C., 1968: Distribution of vertical velocity mean and variance in a thunderstorm, 13th Radar Meteor. Conf., 492-497.

*Dyer, Rosemary, 1968: Doppler measurements in stratiform rain, 13th Radar Meteor. Conf., 144-147.

Easterbrook, C. C., 1967: Some Doppler radar measurement of circulation patterns in convective storms. J. Appl. Meteor., 6, 882-888.

Glover, K., 1966: The feasibility of detecting shock waves by pulse Doppler radar, AFCRL-66-378, Environmental Research Paper #200.

*Glover, Kenneth M., Bishop, A. W., and Lob, W., 1968: Wind measurement by dual beam radar, 13th Radar Meteor. Conf., 456-463.

Gorelik, A. G., 1965: Simultaneous measurements of Langrangian and Eulerian turbulence in snow precipitation. Atmospheric Oceanic Physics Series, Vol. 1, No. 9, 1965, 989-991, translated by Kenneth Syers.

Gorelik, A. G., Kostarev, V. V., Chernikov, A. A., 1962: New possibilities of radar measurement of the wind. Meteorologiya i Gidrologiya, No. 7., Moscow, 1962, 34-39.

Gorelik, A. G., Mel'Nichuk, V., Chernikow, A. A., 1965: The statistical characteristics of the radar echo as a function of the dynamic processes and microstructure of the meteorological entity, AFCRL August 1965, T-R-479.

Gorelik, A. G., et al, 1965: The coordinate-Doppler method of wind observation, American Meteo. Soc., Boston, Dec. 1965.

Gorelik, A. G. and Mel'Nichuk, V., 1966: Radar measurements of turbulent parameters in clouds and precipitations (Abstract only) Proc. Twelfth Wea. Radar Conf., Boston Amer. Meteo. Soc. 104.

*Gorelik, A. G., 1968: Wind structure investigations of boundary layer by radar "clear air" returns, 13th Radar Meteor. Conf., 248-251.

*Gorelik, A. G., and Logunov, V. F., 1968: Determination of vertical air motion velocity in rainfall by Doppler radar, 13th Radar Meteor. Conf. 18-21.

Groginsky, H. L., 1966: Digital processing of the spectra of pulse Doppler radar precipitation echoes, Proc. Twelfth Wea. Rad. Conf., Boston Amer. Meteo. Soc., 34-43.

*Groginsky, Herbert L., 1968: Unambiguous measurement of updraft velocity and drop size distribution. 13th Radar Meteor. Conf., 30-34.

*Groginsky, Hervert L., 1968: Scanning requirements of the (VAD) operation of a pulse Doppler weather radar. 13th Radar Meteor. Conf., (abstract of late paper). p 35.

Harrold, T. W., 1966: Measurement of horizontal convergence in precipitation using a Doppler radar - a case study. Quart. J. R. Meteor. Soc., 92, 31-40.

Harrold, T. W., and Browning, K. A., 1967: Mesoscale wind fluctuations below 1500 meters, Meteorological Magazine, Vol. 96, 367-376.

*Harrold, T. W. and Browning, K. A., 1968: Low-level airflow at a cold front, 13th Radar Meteor. Conf., 222-225.

Holmes, D. W., and R. L. Smith, 1958: Doppler radar for weather investigations. Proc. Seventh Wea. Radar Conf., Boston, Amer. Meteor. Soc. F-29 to F-33.

Kodaira, Nobuhiko, 1964: A pulsed-Doppler radar for weather observations. Proc. Wea. Conf. on Rad. Meteor., Boston, Amer. Meteor. Soc., 300-303.

Kodaira, N., and Zenji Yanagisawa, 1965: The MRI pulse Doppler radar. Proc. Internat. Conf. on Cloud Physics, Tokyo, 309-313.

Lhermitte, Roger M., 1960a: Variations de la vitesse de chute des particules d'une précipitation etendue, a différents niveaux. Comptes Rendus des Seances de l'Académie des Sciences, 250, 899-901.

Lhermitte, Roger M., 1960b: The use of a special pulse Doppler radar in measurement of particles fall velocities. Proc. Eighth Wea. Radar Conf., Boston, Amer. Meteor. Soc., 269-275.

Lhermitte, Roger M., 1962: Note on wind variability with Doppler radar. J. Atmos. Sci., 19, 343-346.

Lhermitte, Roger M., 1963: Weather echoes in Doppler and conventional radars. Proc. Tenth Wea. Radar Conf., Boston, Amer. Meteor. Soc., 323-329.

Lhermitte, Roger M., 1964: Doppler radars as severe storm sensors. Bul. Amer. Meteor. Soc., 45, 587-596.

Lhermitte, Roger M., 1966: Probing air motion by Doppler analysis of radar clear air returns. J. Atmos. Sci., 23, 575-591.

Lhermitte, Roger M., 1966: Application of pulse Doppler radar technique to meteorology. Bul. Amer. Meteor. Soc., Vol. 47, No. 9, Sep 1966, 703-711.

Lhermitte, Roger M., 1966: Doppler observation of particle velocities in a snowstorm. Proc. Twelfth Wea. Rad. Conf., Boston, Amer. Meteor. Soc. 117-124.

Lhermitte, Roger M., and Atlas, D., 1961: Precipitation motion by pulse Doppler radar, Proc. Ninth Wea. Radar Conf., Boston, Amer. Metoer. Soc., 218-223.

Lhermitte, Roger M., and Atlas, D., 1963: Doppler fall speed and particle growth in stratiform precipitation. Proc. Tenth Wea. Radar Conf., Boston, Amer. Meteor. Soc., 297-302.

Lhermitte, R. M., and Kessler, Edwin, 1964: An experimental pulse Doppler radar for severe storm investigations. World Conf. on Radio Meteor., Boston, Amer. Meteor. Soc., 304-309.

Lhermitte, R. M., and Dooley, J., 1966: Study of the motion of clear air targets. Proc. Twelfth Wea. Radar Conf., Boston, Amer. Meteor. Soc., 293-299.

*Lhermitte, Roger M., 1968a: New developments in Doppler radar methods. 13th Radar Meteor. Conf., 14-17.

*Lhermitte, Roger M., 1968b: Turbulent air motion as observed by Doppler radar, 13th Radar Meteor. Conf., 498-503.

*Peace, Robert L., Jr., and Brown, Rodger A., 1968: Single and double radar velocity measurements in convective storms, 13th Radar Meteor. Conf., 464-470.

Peace, Robert L., Jr., et al, 1968: Horizontal motion field observations with a single pulse Doppler radar, Cornell Aero. Lab Report.

Pilie, R. J., Jiusto, J. E., Rogers, R. R., 1963: Wind velocity measurement with Doppler radar. Proc. Tenth Wea. Radar Conf., Boston, Amer. Meteor. Soc., 329a-329L.

Probert-Jones, J. R., 1960: The analysis of Doppler radar echoes from precipitation. Proc. Eighth Wea. Radar Conf., Boston, Amer. Meteor. Soc., 377-385.

Probert-Jones, J. R., and Harper, W. G., 1961: Vertical air motion in showers as revealed by Doppler radar. Proc. Ninth Wea. Radar Conf., Boston, Amer. Meteor. Soc., 225-232.

Rogers, R. R., 1963: Investigation of precipitation processes. Technical Report, Cornell Aero Lab., Inc., 1-17.

Rogers, R. R., 1964: An extension of the Z-R relationship for Doppler radar. World Conf. Rad. Meteor. and Eleventh Wea. Rad. Conf., 158-160.

Rogers, R. R., 1966: Doppler radar investigation of Hawaiian rain. Proc. Twelfth Wea. Rad. Conf., Boston, Amer. Meteor. Soc., 128-134.

Rogers, R. R., 1966: Project Hawaii - an investigation of rain on the island of Hawaii, Technical Report, CAL No. VC-2049-P-1, Cornell

Rogers, R. R., and Chimera, A. J., 1960: Doppler spectra from meteorological radar targets. Proc. Eighth Wea. Radar Conf., Boston, Amer. Meteor. Soc., 377-385.

Rogers, R. R., and Pilie, R. J., 1962: Radar measurements of drop size distribution. J. Atmos. Sci., 19, 503-506.

*Sloss, Peter W., and Atlas, David, 1968: Wind shear and reflectivity gradient effects on Doppler radar spectra, 13th Radar Meteor. Conf., 44-49.

Spilhaus, A. F., 1948: The distribution of raindrops with size. J. Meteor., 5, 161-164.

*Tatehira, R., and Srivastava, R. C., 1968: Note on updraft estimation with Doppler radar, 13th Radar Meteor. Conf., 36-43.

Theiss, J. B., 1963: More target data with sideband coherent data. Electronics, 36, 40-43.

Tripp, Riley, 1964: The CAL pulse Doppler radar. World Conf. Radio Meteor., Boston, Amer. Meteor. Soc., 330-337.

Wexler, R., Chemla, A. C., and Armstrong, G. M., 1967: Wind field observations by Doppler radar in a New England snowstorm, Published in December issue of Monthly Weather Review.

*Wexler, R., 1968: Doppler radar measurements in a rainstorm with a spiral band structure, 13th Radar Meteor. Conf., 192-193.

Wilson, D., 1963: Drop size distribution as recorded by pulsed Doppler radar. U. of Arizona Masters' thesis.

---

* presented at McGill University, Montreal, Canada, 13th Radar Meteorology Conference

DOPPLER RADAR OBSERVATION OF A CONVECTIVE STORM

by Roger M. Lhermitte

Environmental Science Services Administration

Wave Propagation Laboratory

Boulder, Colorado

ABSTRACT

Observation of the horizontal motion of precipitation particles in the low levels of a slow moving thunderstorm were conducted by use of an X-band Doppler radar. The distribution of Doppler velocities in the storm shows a consistent and slowly evolving pattern. However, the Doppler spectra exhibit significant width which must be attributed to the intense small-scale variability of the wind field. This paper discusses the results.

1. INTRODUCTION

Most experiments designed for the study of convective storms processes based on observing the velocity of precipitation particles by means of a Doppler radar have been restricted to the use of a vertically pointing radar beam which is sensitive only to the vertical component of the particles' motion. Observational data obtained by the use of a quasi-horizontal radar beam scanning a convective storm area in azimuth have been presented, Donaldson (1967); Easterbrook (1967), but have not revealed the detailed structure of the radial velocity field and its relation to the pattern of radar reflectivity.

Recently, the extension of the Doppler method to the simultaneous use of two or three Doppler radars, installed at different locations and observing the same storm, has been proposed, Lhermitte (1968). Although experiments have been conducted with a dual Doppler radar system, Brown and Peace (1968), these attempts have also failed to show detailed observations of the horizontal wind field inside the storm.

The full potential of the dual radar method for the study of convective storm dynamics relies on detailed, simultaneous PPI scanning of the same storm with the two Doppler radars operated at small elevation angles for which the contribution to the Doppler shift due to the vertical velocity of the particles will be minimized. This method should provide suitable material for small scale, detailed analysis of the horizontal wind field in the low levels of a convective storm up to altitudes on the order of 10,000 feet. Convergence and vorticity can be evaluated from the two dimensional wind fields and, if the observations are made in several layers at different altitudes, estimate of vertical air velocity can

be derived from the equation of continuity.

However, separate radial velocity fields must be observed by each radar in order to minimize logistical problems in the data acquisition scheme and, even more important, to increase the data acquisition rate well beyond that attainable by restricting the observations to the intersection between the two radar beams only. Since the method requires separate scanning of the same storm by the two radar beams, assumptions about either time stationarity of the velocity at one point in space, or systematic advection of the whole pattern allowing time-space interpolation, become important and need to be assessed in the case of actual convective storms at all stages of their development. This requirement is derived from the fact that, because of the independent scanning of the two beams, it is inevitable that a time lag exists between the velocity sampling at the same point in space by the two radars observing the storm from two different directions. If the storm circulation pattern is only advecting without significant evolution, the advection term can be identified from evaluating the space lagged correlation coefficient between two velocity fields observed at two different times. The estimated group motion can then be used as a correcting term in the estimate of the "frozen" field existing at a given time. However, if rapid, random evolution takes place, the treatment of the data will inevitably involve time and space smoothing of the two fields with the consequence that significant smaller scale features of the storm circulation might disappear in the analysis.

We already know that conventional radars are capable of showing persistent, well organized patterns of radar reflectivity which are indicative of steady state processes and indeed that such studies have contributed to a better understanding

of severe storm dynamics. However, it is not clear to what extent the three dimensional field of particle velocity, influenced by the storm circulation, has the same persistent and well organized characteristics typically observed in the reflectivity field which is controlled by the distribution of water substance and particle size. For instance, it will be shown in this paper that the width of the velocity distribution in the relatively small radar scattering volume, substantially exceeds the width predicted by the presence and magnitude of the average velocity gradients across the azimuth extent of the radar beam. We should therefore look for persistent features in the velocity fields as well as their temporal evolution and also correlate them with stationary features in the reflectivity patterns. The presence of these features and their time stability can be probed easily by use of a single Doppler radar operated at a low elevation angle for which no significant contribution from the vertical component of the particle velocities is expected. The steadiness of the radial velocity field should then be indicative of the stability of the two dimensional velocity field.

Doppler data acquired by a single radar are very limited in their ability to reveal important features of the storm dynamics since only the gradient terms corresponding to the radial component of the velocity are observed. In a Cartesian coordinate system where the coordinate, y, and the velocity component, v, are taken along the radar beam axis; the coordinate, x, and the velocity component, u, perpendicular to it, only two Doppler terms are generated: a convergence term, $\partial v/\partial y$ and a vorticity term, $\partial v/\partial x$. The fact that the terms $\partial u/\partial x$ and $\partial u/\partial y$ are not available seriously limits the objective treatment of the fields, and prevents reaching a definite conclusion as to the existence and magnitude of convergence and vorticity. However, as pointed out previously, Lhermitte (1966); Donaldson (1969), certain features of the storm circulation such as localized circular motion, have a specific Doppler signature and can be identified in the two dimensional radial velocity field. Also, the comparison between radar reflectivity and Doppler velocity patterns combined with some knowledge of the environmental flow, might offer a possibility of recognizing some of the conventional features of the storm circulation.

This paper is an attempt to investigate the ability of the Doppler radar techniques to reveal organized features of the storm circulation by presenting and discussing single station Doppler radar observations made on a stationary convective storm, occurring in the region of Denver, Colorado in the afternoon of July 19, 1968. The storm persisted for approximately 4 hours and was moving very slowly during this time. The radiosonde observations at Denver, Colorado, approximately 10 miles from the storm, were made at 1800 MST (approximately 3 hours after the Doppler data discussed in this paper were acquired) and indicate that the low level flow was essentially from the south southwest at 10 knots, decreasing to less than 5 knots northwest at an altitude of 14,000 feet, and reaching a steady 35 knots northwest above 20,000 feet.

2. METHOD OF OBSERVATION

The Doppler radar used in this experiment is an X-band system designed for automated azimuth-stepping operation and equipped with a system capable of recording the Doppler signal simultaneously at 13 selected ranges. The main characteristics of the radar are: wavelength 3.2 cm; peak power 20 kw; pulse duration 0.2 μs; 3 db antenna beamwidth 0.9°; radar repetition rate adjusted for a Doppler velocity coverage extending from -10 m sec^{-1} (approaching targets) to +15 m sec^{-1} (receding targets). This velocity range was determined after the average Doppler velocity in selected regions in the storm was quickly observed by use of a device available in the radar unit.

The receiver gain was adjusted to allow recording, without distortion, of the maximum signal intensity returned by the storm (reflectivity $Z=8.10^4$ at the maximum range). The available dynamic range of the recording system was 45 db although a better range could be obtained from the processing of the recorded signals in the play back operation. The radar antenna was operated in an azimuth-stepping manner at a fixed 3° elevation angle. With such an elevation angle a vertical velocity of 10 m sec^{-1} will only contribute 0.5 m sec^{-1} to the Doppler. The antenna beam was stepped every two seconds and remained in a fixed position for 1.7 seconds. A total number of eleven azimuth steps was used; the corresponding antenna positions were equally spaced between two azimuth boundaries, 118° to 139°. The sequence was continuously repeated in a sector scan mode with no interruption and with the same elevation angle for the 20 minutes of data discussed here. This procedure allows systematic computer treatment of the data and easy comparison between radar information obtained at the same point in space at different times, and therefore positive identification of the persistent features of the storm. The azimuth and range boundaries were chosen for a complete coverage of the radar echoes although the storm was moving out of range in the later part of the recorded data.

The signal recorded on magnetic tape was systematically processed track after track by use of a special purpose computer, programmed for calculating the Fourier transforms of the recorded time functions from which the Doppler spectrum of radial velocities is derived. The computer operation was controlled by timing signals recorded on an auxiliary tape recorder track, in such a manner that sampling and processing would occur only for signals recorded when the antenna had completed a step in azimuth and remained in a fixed position. Three successive spectra each consisting of 1,001 spectral density estimates were computed for each position of the antenna and each range gate. Spectral density estimates were added for these spectra pertaining to the same antenna position and the resulting spectrum was then recorded on digital magnetic tape for further processing of the data by a large computer (CDC 3800).

2

5θ1	2555252			29.97	0.22	0.48
5θ2	2255232			29.80	-1.75	0.46
5θ5	22445565676666542			40.14	-1.74	0.80
5θ4	24354666756666554445554552			41.41	-1.94	1.45
5θ5	444555566666656665555455533			42.12	-2.91	1.57
5θ6	555525 522 2 25552255545 55555555			55.52	-5.58	2.58
5θ7	2355 2 5354345254454535535435344452 225 2			57.20	-5.08	2.41
5θ8				15.91	0.00	0.00
5θ9	22 255554535555455535455545555555552 52			56.54	-2.84	2.45
59θ	2525442555525522252555525555552555			55.50	-4.60	2.21
591	.544444555666766666544522			41.57	-4.69	1.21
592	52445545666666666655564456454			41.20	-1.70	1.28
595	252446666766545			59.64	-1.71	0.67
594	552			27.77	-2.04	0.20

Appr. m sec⁻¹   Rec. m sec⁻¹   db $\overline{V}$ σ_v

Figure 1. Example of computer print out of the Doppler data. Average radial velocity, $\overline{V}$, and spectrum standard deviation, σ_v, are in m sec^{-1}. Spectra are quantized in 3 db levels. Signal power is in db above the receiver noise.

Figure 2. Three dimensional spectral density-azimuth-Doppler velocity graphs at 6 selected ranges for signals recorded at 15 h 11' MST. Doppler velocity range is from -10 m sec^{-1} to +15 m sec^{-1}. Azimuth scanning range is from 118° (front) to 139° (back). Radar reflectivity is proportional to the area under the spectra.

3

Figure 3. Evolution of the Doppler spectra recorded at range gate #12 for three successive azimuth scanning sequences separated by 22 seconds. Doppler range is between -10 to +15 m sec^{-1}. Azimuth range is from 118° (front) to 139° (back).
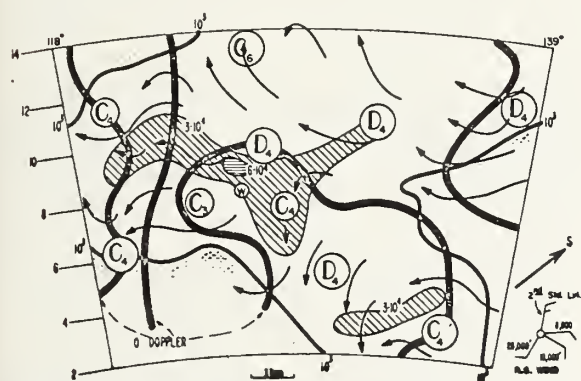
a. Radar reflectivity, Z; zero Doppler velocity contours and estimate of stream lines.
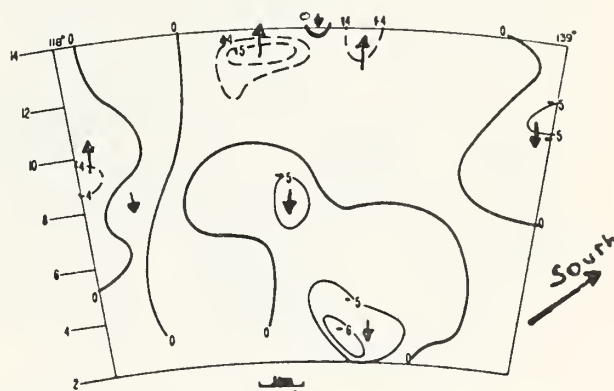
b. Radial velocity contours (m sec^{-1}) - - - rec.
————— appr

Figure 4. Azimuth-Range radar reflectivity and radial velocity patterns at 15:04 MST
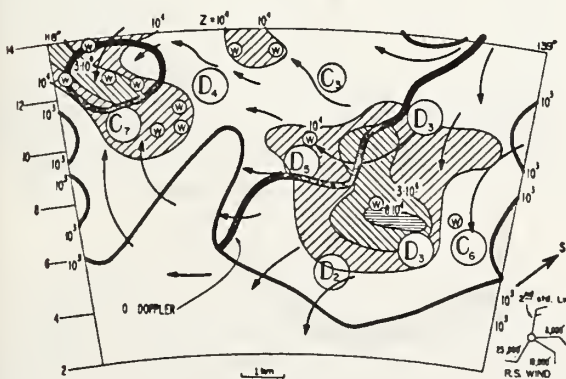
a. Radar reflectivity, Z; zero Doppler velocity contours and estimate of stream lines. C is a radial velocity convergence term; D is a divergence term. See Text.
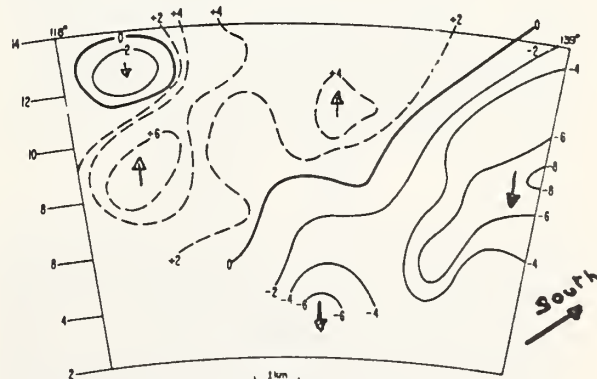
b. Radial velocity contours (m sec^{-1}) - - - rec.
————— appr.

Figure 5. Azimuth-Range radar reflectivity and radial velocity patterns at 15:11 MST

4

The processing of the digital magnetic tape by the CDC 3800 included the following: 1. frequency smoothing of the spectra to increase stability of the spectral density estimates; 2. calculation of the spectrum first moment $\overline{v} = \int S_{(v)} v \, dv$, where $S_{(v)}$ is the Doppler spectrum normalized to signal power; 3. calculation of the standard deviation of the spectrum $\sigma_v = \left[\int S_{(v)} (V-\overline{V})^2 \, dv \right]^{\frac{1}{2}}$ which is a measure of the spectrum width; 4. calculation of the signal average power to be used in the evaluation of the radar reflectivity of the storm, and; 5. printout of the Doppler spectra quantized in 3 db levels. An example of the computer printout is shown in Figure 1. Figure 2 and Figure 3 show examples of the three dimensional Doppler-azimuth-spectral density analog presentations of the spectra, obtained by use of the computer plotting facilities. It must be noted that the three dimensional presentation is useful as providing a quick insight of the space variation of the Doppler spectra.

The average Doppler velocity, $\overline{V}$, and the estimated radar reflectivity data were then plotted in range azimuth coordinates for every sequence lasting 22 seconds, for further analysis. Some of the plotted fields which have been selected for discussion in the following section are shown in Figure 4 and Figure 5. The fields are evaluated from an array of 13 ranges by 11 azimuths covering an area of approximately 10 x 8 km. The range gates separation was 600 meters and the distance between successive beamwidths was approximately 800 meters at the mean range at which the storm was observed (25 km). It should be noted that the size of the scattering volume for these samples was defined by a beam cross section of 300 meters and a half pulse length of 50 meters.

3. STABILITY OF THE RADIAL VELOCITY AND REFLECTIVITY FIELDS AND PERSISTENCE OF THE STORM CIRCULATION FEATURES.

The following discussion must be considered as a preliminary analysis of the Doppler data, mostly oriented to deriving general comments on the behavior of the Doppler and reflectivity fields and their interaction.

In order to estimate quantitatively the temporal evolution of either the reflectivity or the velocity field, the time correlation coefficient, $\rho(\Delta t)$, between two azimuth-range arrays of data, A_t, $A_{t+\Delta t}$ (representing either reflectivity or velocity fields) observed at time, t, and t+Δt, was computed according to the following expression:

$$\rho(\Delta t) = \frac{\overline{A_t A_{t+\Delta t}} - \overline{A_t}\, \overline{A_{t+\Delta t}}}{\left[\sigma_t^2 \quad \sigma_{t+\Delta t}^2 \right]^{\frac{1}{2}}}$$

$\overline{A}$ and σ^2 respectively are the mean and the variance of array A. No space lag was introduced in these preliminary estimates although this procedure could lead to an objective measurement of the advection of the patterns.

The correlation coefficients, $\rho(\Delta t)$, calculated from the expression above, were found to vary in the same manner for the reflectivity and the radial velocity fields. In the first part of

the recorded data (1500 MST) $\rho(\Delta t) = 0.94$ for $\Delta t = 22$ seconds, decreasing to $\rho(\Delta t) = 0.5$ for $\Delta t = 3$ minutes. At this time the storm was in a developing stage as indicated by the fairly complex patterns of radar reflectivity and Doppler velocity which are shown in Figure 4a and 4b.

Approximately 10 minutes after the first data were recorded, the radar reflectivity pattern had evolved and stabilized into a well-defined configuration of two cells of different size and intensity as shown in Figure 5a. Note that the larger cell exhibits a maximum reflectivity of $Z=8.10^4$. At this time, the correlation coefficient, $\rho(\Delta t)$, varies between 0.96 and 0.98 for both radial velocity and reflectivity fields and a time separation, Δt, of 22 seconds. Visual observation of the storm at this time indicated the presence of two distinct towers of different heights, the tallest one reaching approximately 30,000 feet above terrain. The Doppler velocity field observed at the same time is shown in Figure 5b. It must be noted again that the average Doppler velocity derived from the spectrum first moment is considered here. The shape and width of the Doppler spectra is presented for selected range gates in the three dimensional graphs shown in Figure 2. One notices in Figure 5b the well defined structure of the average radial velocity field showing the azimuth-range map clearly divided into two distinctive regions of different Doppler sign separated by the zero Doppler line. In the western part of the figure which includes the larger fraction of the most intense cell, the motion is consistently toward the radar with a maximum velocity of 8 m sec^{-1} found in the southwestern edge of this large cell. In the eastern part of the region covered by the radar, which includes the cell of smaller intensity, the motion is mostly away from the radar except for a small region on the eastern side of the small cell. The very rapid change of the Doppler sign in this region might suggest cyclonic vorticity, and the presence of a meso low. It will be shown below that double-peak spectra, characteristic of circular motion, are observed in this region.

Subsequent observations of the radial velocity field made at time intervals of 22 seconds show that the Doppler field at this time has a well organized structure which persists with essentially the same shape for a time on the order of 8 minutes or more. The slow evolution of the reflectivity and Doppler velocity fields is illustrated in Figure 6a, b, c, which show a sequence of reflectivity patterns obtained at 22 seconds time intervals, along with the position of the zero Doppler line and indication of the Doppler velocity where this velocity is locally maximum. Figure 3 shows the complete Doppler spectra recorded at range #12 at time intervals of 22 seconds.

Figure 4a also includes a tentative tracing of the stream lines starting with the estimated incoming flow relative to the quasi-stationary storm at this level, as derived from the Denver upper air observations mentioned above. The stream lines are estimated by assuming that they originate with the incoming flow and that their curvature is controlled by the magnitude and sign of the Doppler velocity. This method of stream line tracing relies on the assumption that the magnitude of the

observed horizontal velocity does not vary appreciably, thus providing a relationship between the Doppler and the direction of motion. The fact that stream lines may originate from the expected downdraft divergence in the vicinity of the large cell provides a different solution for the stream line tracing. The observational conditions reported in the paper with the incoming flow almost at right angle with the Doppler radar beam were favorable for this treatment. This estimate of the stream lines should be considered only as a tentative effort to analyze the two dimensional field of radial velocity, but should not be interpreted as a substitute for the dual Doppler radar method. The radial shear of the radial velocity is also shown in the azimuth-range map and indicated by circled letters with number subscripts, the letters indicating convergent or divergent flow and the subscripts the magnitude of the gradient in 10^{-3} sec^{-1}. The interpretation of radial gradients of the radial velocity as indicative of convergence of the wind field should be accepted with reservation since the component of the speed perpendicular to the radar beam is not available. However, the presence of the divergence zones in the outer edges of the large cell are consistent with the presence, at this low altitude, of a downdraft associated with the more intense precipitation in this region.

.   The patterns shown in Figures 4, 5 and 6 as well as the estimated stream lines indicated in Figures 4a and 5a suggest a strong relationship or interaction between the radial velocity and radar reflectivity fields. It must be noted that the flow is always deflected by cells of significant intensity but mostly toward the western part of the cell. This remark not only applies to the data shown in Figures 4, 5 and 6, but to any cell which was observed during the whole 20 minutes of recorded storm history. It must be noted that the maximum approaching velocities are not inside the cell, but a few kilometers on its western side. It is therefore attractive to relate these observations to divergence or outflow caused by the downdraft associated with the presence of intense cells at this low altitude (1200 meters above terrain). The contribution to the Doppler velocity which is expected from the downdraft vertical motion itself (0.5 m sec^{-1} for 10 m sec^{-1} of vertical speed) is considerably smaller than the observed variation of the Doppler speed (+6 to -8 m sec^{-1}).

There is also more variability of the Doppler velocity in the back side region of the stronger cell, in the vicinity of the smaller cell; this may be indicative of the disturbance of the incoming flow by the downdraft associated with the stronger cell.

4.   THE DOPPLER SPECTRUM WIDTH

The above treatment of the Doppler velocity fields relies on the estimate of the average Doppler velocity calculated from the first moment of the Doppler spectrum. However, as can be seen in the three dimensional plots such as shown in Figures 2 and 3, the spectrum width often exceeds the predicted width based on evaluating the systematic variation of the average Doppler velocity with azimuth angle, across the radar beamwidth.

This suggests that spectrum width might be due to local small scale turbulence or vorticity. As mentioned above, computation of the standard deviation, σ_v, of the spectrum (which is approximately 5 or 6 times less than the total spectrum width) is included in the computer treatment of the data. Inspection of these data shows that σ_v practically ranges from 0.3 m sec^{-1} to 3 m sec^{-1}.
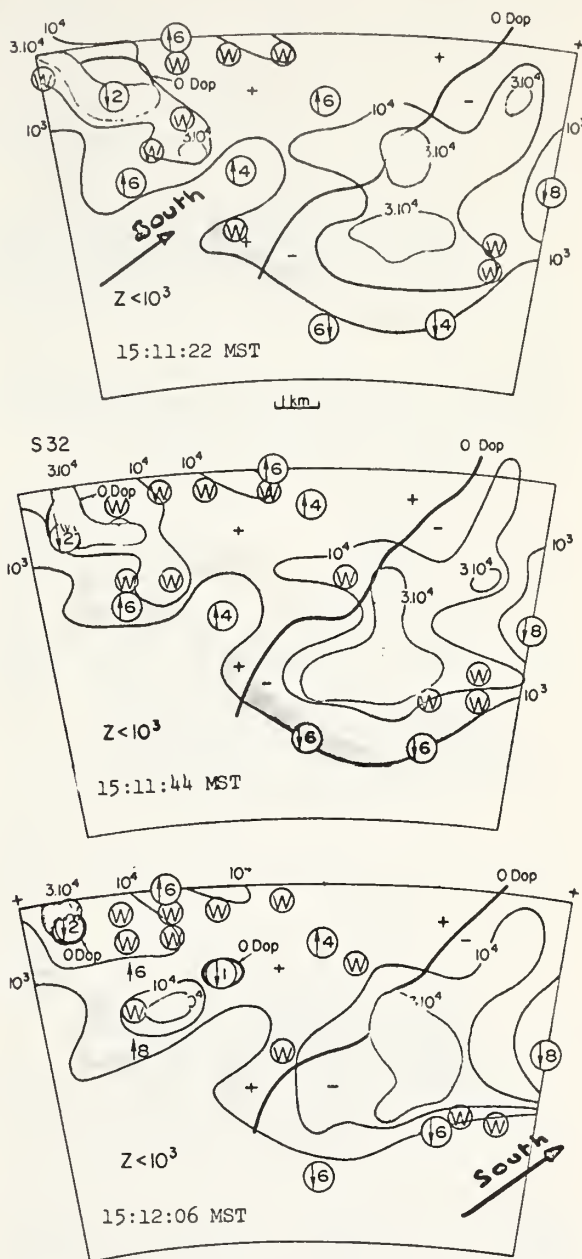
Figure 6.   Stability of the reflectivity and Doppler velocity fields illustrated by successive azimuth scanning sequences obtained every 22 seconds. Ⓦ indicates the presence of wide Doppler spectra. + refers to positive velocity (motion away); - refers to negative velocity. Reflectivity contours are in Z values.

Ⓥ indicates magnitude of the Doppler in m sec^{-1}.

In order to evaluate a possible relationship be-
tween either the reflectivity or radial velocity
fields and the occurrence of large spectrum width,
the regions where σ_v exceeds 2 m sec^{-1} have been
shown in the reflectivity and Doppler velocity
maps discussed above (Figure 5a and 6a, b, c).
One sees in Figure 6a, b, c, that there is a re-
peatable pattern of spectrum width. A large
spectrum width is found in the western boundaries
of the large cell in a region of appreciable re-
flectivity gradients but most of the wide spectra
are concentrated around the small cell in the
down stream side of the large cell in regions
where more instability of the reflectivity pattern
is also observed. Indeed about two minutes after
the data presented in Figure 6 were observed, a
double mode spectrum developed with a standard
deviation on 4 m sec^{-1} (18 m sec^{-1} total width).
The occurrence of such spectrum was attributed
to the presence of a circular eddy smaller than
the cross section of the radar beam estimated as
being 300 m at this range. The time evolution
of the Doppler spectra, similar to those shown in
Figure 7, suggests that the eddies were traveling
from left to right in a region where maximum re-
flectivity of the small cell was observed before.
It might be noted that funnel cloud sightings were
reported during the life of the storm.
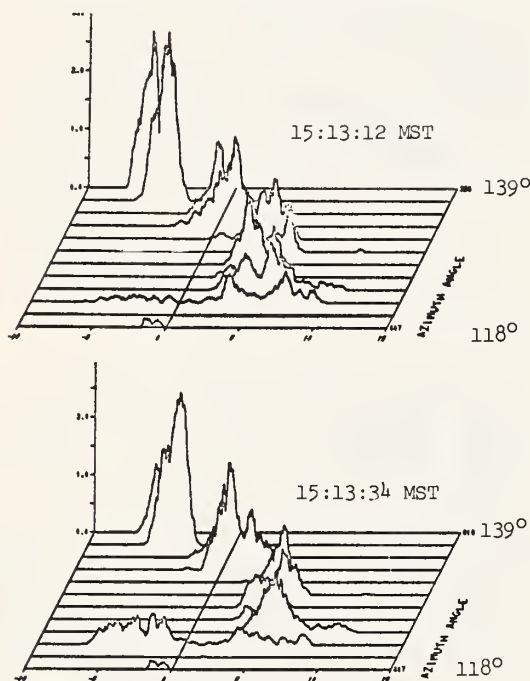
Figure 7. Azimuth-Doppler presentation of the
evolution of wide spectra indicative of advec-
ting vorticity. Note the rapid evolution of the
double peak spectra at 122°.

5. CONCLUSION

This paper has shown that persistent features
of the wind field – and their time evolution –
can be identified in the azimuth-range patterns of
radial velocity of particles provided by a Doppler
radar observing the storm. This preliminary anal-
ysis of the radar data also suggests a relation-
ship between the radial velocity and the radar

reflectivity fields. Persistent patterns of av-
erage radial velocity can be identified despite
the fact that wide Doppler spectra are commonly
observed, some of them having a width which may
be indicative of the presence of local intense
turbulence or vorticity. It must be noted how-
ever, that the interpretation of the average Dopp-
ler spectrum velocity as representative of the
mean flow might be questionable in the case of
strong gradients of radar reflectivity which can
bias the Doppler mean estimate.

It is hoped that the stability of the radial
velocity patterns observed for these data may be
a common feature of the circulation of convective
storms. This expectation would certainly allow
easy treatment of the information provided by a
dual radar method where each radar may be sampling
the radial velocity in the same region in space,
at slightly different times. It is expected,
however, that even if the structure of the wind
field inside convective storms might be more com-
plex than that of the radar reflectivity field,
the wind field will be at least as time persistent.
This preliminary study also shows, as noted previ-
ously, that processing of the Doppler information
requires methods far more sophisticated and ac-
curate than those now being used for the process-
ing of conventional radar information. This re-
quirement substantiates the fact that Doppler data
must be recorded in a format suitable for their
handling and processing by digital computers. A
system is now being developed to deal with the
problem which will produce, in real time, Doppler
data recorded on a digital magnetic tape with a
format compatible with large computer data pro-
cessing. It is anticipated that the computer pro-
cessing will provide three dimensional fields of
velocity in a form suitable for meteorological
analysis.

REFERENCES

Brown, Rodger A., and Peace, Robert L., Jr., 1968:
Mesoanalysis of convective storms utilizing obser-
vations from two Doppler radars, 13th Radar Meteor.
Conf., 188-191.

Donaldson, R. J., 1967b: Horizontal wind measure-
ment by Doppler radar in a severe squall line,
Proc. Conf. on Severe Local Storms, St. Louis, 89-98.

Donaldson, R. J., Armstrong, G. M., 1969, Plan
shear indicator for real-time Doppler radar ident.
of hazardous storm winds. Sub. to J. Appl. Meteor.

Easterbrook, C. C., 1967: Some Doppler radar
measurement of circulation patterns in convective
storms. J. Appl. Meteor., 6, 882-888.

Lhermitte, Roger M., 1966: Application of pulse
Doppler radar tech. to meteorology. Bul. Amer.
Meteor. Soc., Vol. 47, No. 9, Sep 1966, 703-711.

Lhermitte, Roger M., 1968: Atmospheric probing by
Doppler radar; Proc. of NAS/CAS Panel on Remote
Atmospheric Probing.

Note on the observation of small-scale atmospheric turbulence by Doppler radar techniques

Roger M. Lhermitte

Environmental Science Services Administration
Wave Propagation Laboratory, Boulder, Colorado 80302

The paper discusses the applicability of microwave pulse Doppler radar techniques to the observation of small-scale turbulent air motion. Emphasis is placed on a quantitative analysis method that utilizes the variance of the Doppler radar observed spectrum of velocity of man-made radar targets used as tracers for the turbulent air motion.

1. INTRODUCTION

Microwave Doppler radar techniques that use precipitation particles as tracers for air motion have been widely applied to the study of wind fields in precipitation conditions. The same methods can be applied to the observation of cloud-free air motion if suitable targets acting as tracers are present in the region of the atmosphere probed by the radar. Radar targets might exist in a dense smoke plume or in the clear atmosphere ('angels'). Man-made targets released in the atmosphere to provide the air motion tracers may be preferable since such targets having known characteristics will yield the true motion field.

The Doppler method is capable of probing air motion spectra down to scales limited only by the spacing of the targets. In addition, organized larger-scale features of the wind field (such as divergence and vorticity patterns in the scale of 50 meters to 5 km) can be observed by scanning the radar beam, by such methods as the VAD mode originally described by *Lhermitte and Atlas* [1961] or the evaluation of the correlation of the Doppler velocity observed at different ranges with a fixed beam direction [*Boucher*, 1968].

This note, however, will be concerned only with a discussion of the characteristics of the tracers' radial velocity spectrum at a given point in space and its relation to the turbulent air motion at scales smaller than the scattering volume size (i.e. 10 to 50 meters).

2. THE RADIAL VELOCITY SPECTRUM AND ITS METEOROLOGICAL SIGNIFICANCE

The nature of the Doppler information obtained from the backscattering of pulse radar signals has been widely discussed in various articles [i.e., see *Atlas*, 1964; *Lhermitte*, 1964, 1966a]. The information on the radial velocity of the targets that is contained in the phase of the backscattering signal is observed not at a point in space but, more precisely, inside a range-selectable scattering region defined by the radar beam cross section and half of the radar pulse length in space. Frequency analysis of the backscatter signal provides a spectrum of velocity representing the radial velocities of the detected targets weighted by a possible relationship between their radar cross section and velocity. This 'Doppler spectrum' can be reduced to an expression of the average velocity (first moment of the spectrum) and a spectrum variance (second central moment).

If the targets have a large range of sizes and shapes and if their motion relative to the air is influenced by their size and shape, the interpretation of the Doppler spectrum requires an assumption of the relationship between the target radar cross section and velocity. However, if the targets have a uniform size or if they respond to air motion in the same manner regardless of their size, the Doppler spectrum can be interpreted in terms of the statistics of the air radial velocity inside the scattering region. In the case of targets moving under the influence of air speed only, the average Doppler velocity is the mean air velocity and the Doppler spectrum variance is caused by the three-dimensional spectrum of turbulent air motion integrated from wave numbers
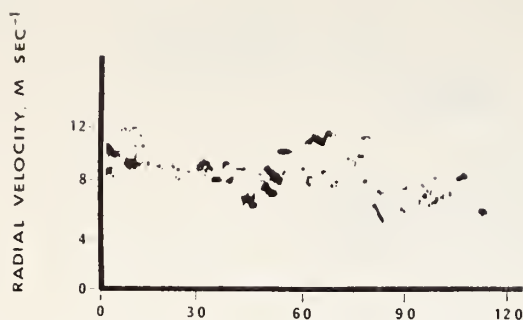
Fig. 1. Doppler velocity versus time for clear air targets. The Doppler signals were observed at a fixed region in space. A signal occurs each time that a target enters the scattering region. Note the small number of large intensity signals of point target nature that can be attributed to insects of large size. The large number of smaller targets can be due to a swarm of small insects such as mosquitoes. The mean air velocity can be estimated, but the deviation with respect to the mean speed seems to be due mainly to the ability of the insects to fly. Radar wavelength, 3.2 cm; radar range, 1.2 km; time is in seconds.

corresponding to the size of the scattering region to the smallest scale that can be reproduced by the spacing of the targets.

The Doppler radar measures only the targets' radial velocity V_R, which can be expressed as follows:

$$V_R = v \cos \beta \cos \theta + u \sin \beta \cos \theta + w \sin \theta \quad (1)$$

where β and θ, respectively, are the azimuth angle (relative to north) and the elevation angle of the radar beam; v, u, respectively, are the N–S and E–W components of the target horizontal motion, and w is the target's vertical velocity; V_R is positive for motion away from the radar, v is positive for south to north, u is positive for west to east, and w is positive upward. The expression of the Doppler spectrum variance σ_R^2, indicated by the spectrum width, is given from equation 1 by

$$\sigma_R^2 = \sigma_v^2 \cos^2 \beta \cos^2 \theta + \sigma_u^2 \sin^2 \beta \cos^2 \theta$$

$$+ \sigma_w^2 \sin^2 \theta + \cos^2 \theta \sin 2\beta \; \text{cov} \; (uv)$$

$$+ \cos \beta \sin 2\theta \; \text{cov} \; (vw) + \sin \beta \sin 2\theta \; \text{cov} \; (uw) \quad (2)$$

where σ_v^2, σ_u^2, σ_w^2 are, respectively, the variances for v, u, and w; cov $(uv) \cdots$ the covariance between v and u, etc.

It must be noted that the relative contribution of the v, u, w variances (and their covariances) to the radial velocity variance as expressed in (2) is modified significantly by varying the azimuth and elevation angles of the radar beam.

If the Doppler data are acquired by directing the radar beam along the mean wind at the selected
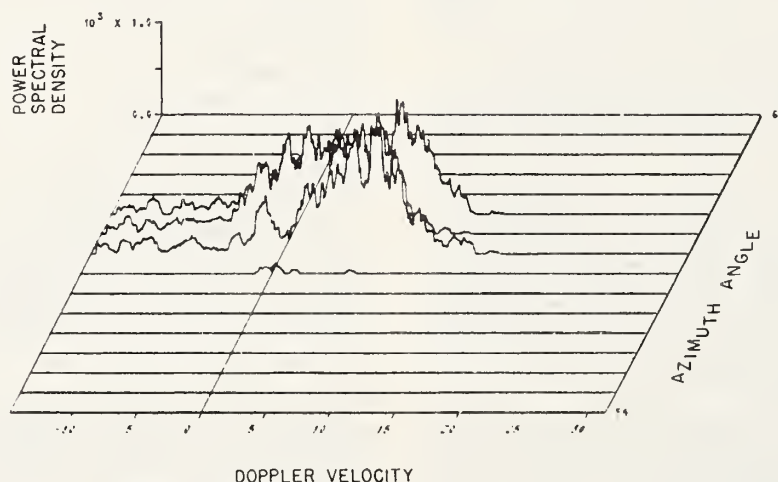
Fig. 2. Doppler spectra due to particle turbulent motion in a huge experimental fire. The data acquired at a fixed radar range are shown for different azimuths of the radar beam in a computer produced 3-D display. Note the systematic large width of the spectrum in the center of the graph, which corresponds to a radar scattering region directly above the fire. These data represent an extreme case of intensity of small-scale atmospheric turbulence. Doppler velocity range, —15 m sec⁻¹ (approaching) to +30 m sec⁻¹ (receding). Azimuth steps are separated by 2.5 degrees. Radar range, 1.5 km; elevation angle, 28°.

POWER SPECTRAL DENSITY

AZIMUTH ANGLE
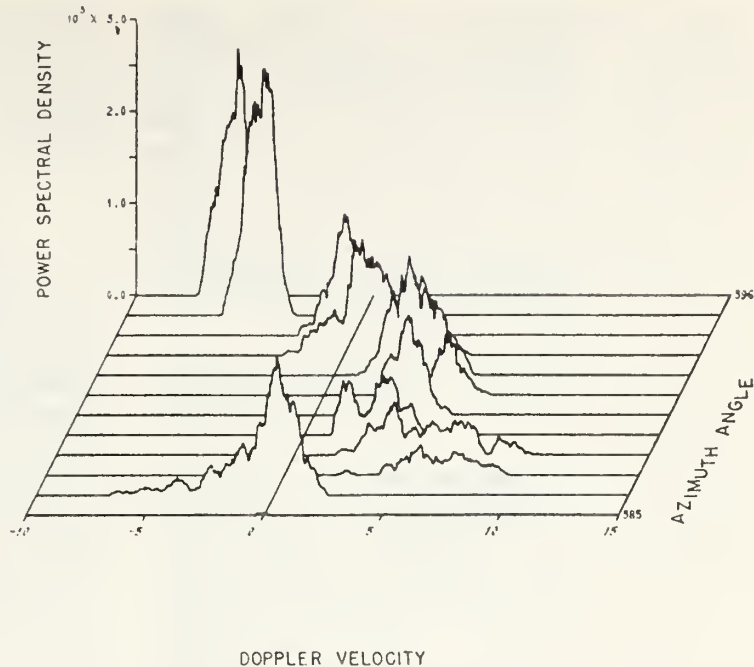
DOPPLER VELOCITY

Fig. 3. Doppler spectra obtained on particle horizontal motion inside a convective storm. Doppler velocity range is from —10 m sec⁻¹ (approaching) to 15 m sec⁻¹ (receding). Spectrum width ranges from 2 to 12 m sec⁻¹. Azimuth steps are separated by 2 degrees. Range gating is at 25 km.

altitude (upwind and downwind regions), the method will be sensitive only to V_l, the longitudinal component of the wind, and the vertical motion w. We then express the upwind (V_U), and the downwind (V_D), Doppler velocities by the following equations:

Upwind $\qquad V_U = V_l \cos \theta + w \sin \theta \qquad$ (3)

Downwind $\qquad V_D = -V_l \cos \theta + w \sin \theta \qquad$ (4)

where V_U and V_D are positive for motion away from the radar and w is positive upward, with the variances

Upwind $\qquad \sigma_U{}^2 = \sigma_l{}^2 \cos^2 \theta + \sigma_w{}^2 \sin^2 \theta$

$$+ \text{cov} (V_l w) \sin 2\theta \qquad (5)$$

Downwind $\qquad \sigma_D{}^2 = \sigma_l{}^2 \cos^2 \theta + \sigma_w{}^2 \sin^2 \theta$

$$- \text{cov} (V_l w) \sin 2\theta \qquad (6)$$

Since only the sign of the covariance changes from downwind to upwind, the difference between the Doppler spectrum upwind and downwind variances is a measure of the covariance between V_l and w. The covariance has a great importance in the boundary layer, since it is related to the shearing stresses due to the friction processes. To remove the contributions due to time or space variability of the above quantities, equations 5 and 6 should involve time averages of $\sigma_U{}^2$ and $\sigma_D{}^2$. The upwind-downwind method has been discussed earlier for Doppler data

obtained during a snowstorm [Lhermitte, 1968], where it was shown that the calculated cov ($V_l w$) is of the same order of magnitude as the Doppler spectrum variance.

3. EXAMPLES OF DOPPLER RADAR OBSERVATIONS

Since the Doppler radar offers excellent possibility for the study of small-scale turbulence by means of observing the Doppler spectrum variance, the availability of suitable targets occurring in clear air must be investigated. Besides precipitation particles, which are appropriate wind tracers in precipitation conditions, the natural radar targets that can be found in the atmosphere are particulate matter of radar detectable size, insects (flying or not), and finally the turbulent atmosphere itself.

Particulate matter or insects (atmospheric plankton) have often been detected by Doppler radars, especially in regions of dense animal life. These opportunities have indeed led to occasional probing of mesoscale wind features, such as the low-level jet occurring in central Oklahoma [Lhermitte, 1966b].

Although the technique is adequate for the observation of the mean wind in certain conditions, it is hardly applicable to the study of turbulent air motion as derived from observing the spread of velocity of the targets. Figure 1 shows an example

of radar signals presented in Doppler frequency-time coordinates, which are observed in clear air at a given range by an X-band (wavelength 3 cm) Doppler radar and which obviously reveal the active flying nature of the targets. The targets show a limited ability to react to the wind, however, and the mean motion can be identified easily. However, the target spread cannot be attributed safely to the variance of the air velocity itself because of the ability of the target to fly with respect to the air.

Doppler observations have recently been made in the dense smoke plume of a huge experimental fire. An example of the results is presented in Figure 2, which shows the Doppler spectra, presented in a three-dimensional computer display, recorded at the same range for different azimuths of the radar beam. One notices the wide range of the Doppler spectrum width, which reaches 40 m sec⁻¹. It is believed that the radar return was due to smoke and ash particles in the dense smoke cloud. Since each spectrum was observed in a scattering volume having a size of approximately $20 \times 20 \times 50$ meters, these data clearly reveal the ability to probe atmospheric motions of high variability in small regions in space.

Figure 3 shows the same presentation for data obtained on precipitation particles inside a convective storm. One notices that some of the spectra still have a radial velocity variability of more than 10 m sec⁻¹.

4.   DOPPLER RADAR INVESTIGATIONS USING CHAFF

Although the above examples clearly demonstrate the capability of the Doppler system for probing air movements, the application of the method in various meteorological conditions must rely on the presence of man-made passive targets, which can act as reliable tracers for the air motion. Targets designed for this purpose are commercially available under the name of 'chaff.' They are thin glass fibers coated with aluminum and cut in half the radar wavelength for maximum radar cross section.

The 'chaff' dipoles have low inertia, have small terminal speed ($\leq$30 cm sec⁻¹), and can be dispersed in large quantities. The radar cross section of each dipole is of the order of several square centimeters. Since a small package of dipoles of a few inches in size can contain several million dipoles,
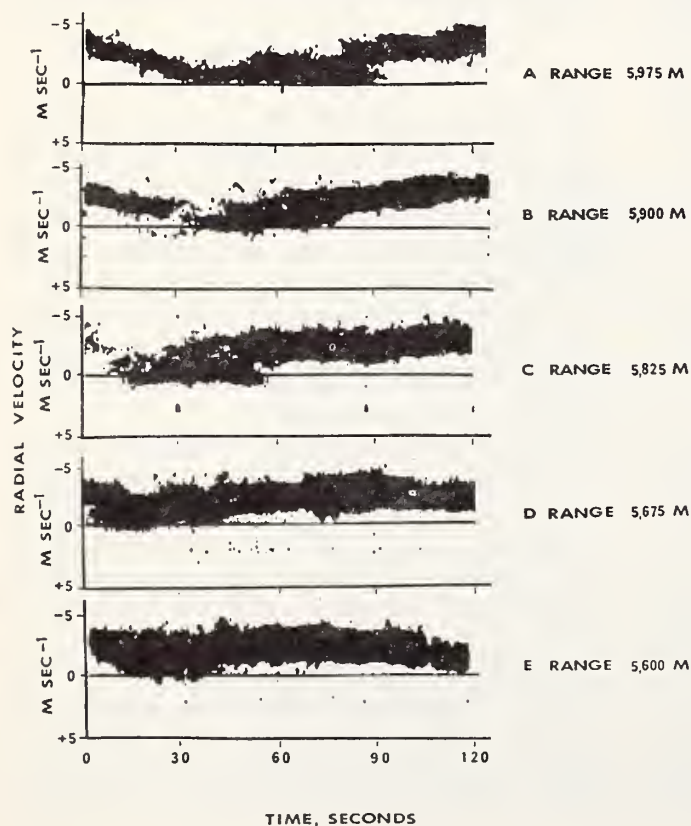
Fig. 4. Doppler spectrum-time function obtained on chaff. Time, 1210 PST; azimuth, 291°; elevation, 9°; negative velocity for approaching targets. Note the pattern discontinuity near 55 sec (4C), which appears at a different range (4A) at 90 sec. This discontinuity can be attributed to a microwind shear region advecting through the radar beam.
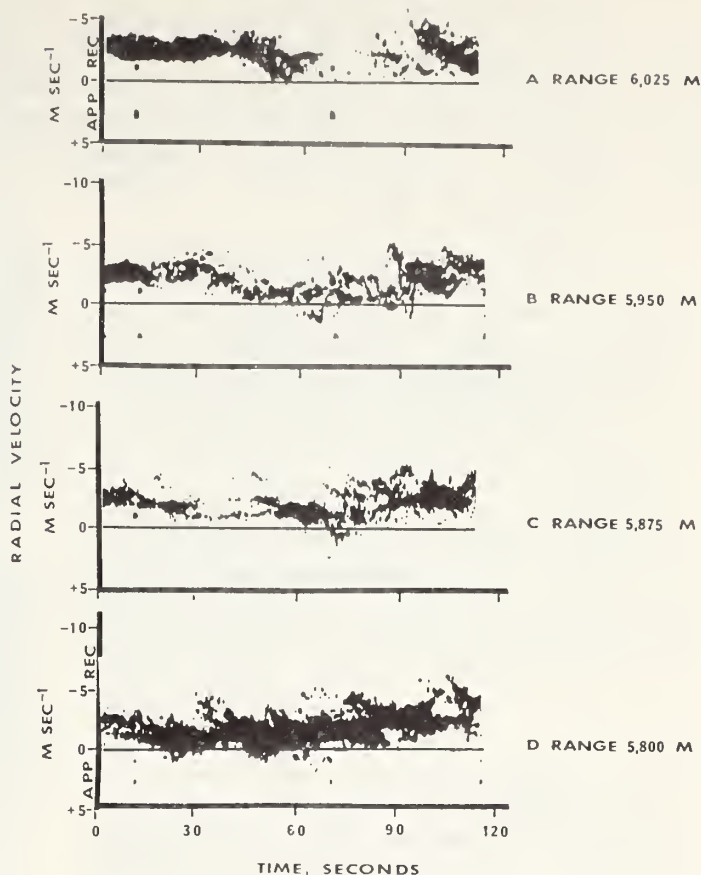
Fig. 5. Doppler spectrum-time patterns obtained in the case of low chaff density. Time, 1208 PST; azimuth, 291°; elevation, 13°; negative velocity for approaching targets. The patterns indicate that individual dipoles moving with the air are effectively observed, thereby leading to the observation of Lagrangian air motion variability.

a radar reflectivity equivalent to light snow (reflectivity factor $Z = 10^{-2}$) can be easily achieved over an area of 5×5 km and an average layer thickness of 0.5 km. At a distance of 5 km from the radar, more than 100 dipoles will be present in each radar scattering volume if the material is uniformly dispersed. It must be noted, however, that, for this low concentration, the average spacing between dipoles increases to more than 10 meters, thereby restricting the probing of the velocity spectrum to wave numbers less than the reciprocal of this scale.

Experiments aimed to assess the usefulness of the method for probing small-scale turbulence by using chaff dipoles as air motion tracers were conducted at Montgomery Pass, Nevada, during June 1968 in a high-altitude region (8000 feet) surrounded by higher mountains. The chaff material was dispersed at low altitudes by a small rocket system and was always found to spread rapidly and also to be carried aloft to altitudes of several thousand feet by high convection conditions. The wind speed at the ground was less than one or two meters per second.

The examples shown in Figure 4, which present

Doppler velocity-time patterns, are concerned with experiments made between the late morning and early afternoon of June 7, 1968. The radar characteristics are: wavelength, 3 cm; peak power, 25 kw; beamwidth, 0.9°; pulse width, 0.25 μsec; pulse repetition rate, 6 GHz. The Doppler radar was pointed in the direction of a 'chaff' cloud, which had expanded to a size of the order of 2 km from a single rocket release. The Doppler signals were gated at selected ranges spaced by 75 meters at a mean range of 5 km. The radar beam elevation angle was 9°, corresponding to an altitude of 900 meters above the terrain. Since the chaff material was released 30 minutes earlier at an altitude of approximately 100 meters, it is assumed that the material was carried aloft by the high convective activity occurring in the region of the experiment. Previous observations made at the same time of the day showed that the scattering material systematically reached an altitude of the order of 1 to 2 km above the terrain 10 to 20 minutes after its release.

By inspection of Figure 4 one sees that the spectral width varies from 3 to 5 m sec^{-1}. This is

smaller than the width observed for extreme conditions of convection existing inside the smoke plume previously mentioned but is much larger than the spectrum width observed in other experiments with higher wind [*Lhermitte,* 1966c]. This result must be attributed to a very high natural convective activity at that time of day.

One also notices that at certain times the velocity-time patterns show discontinuities that indicate the presence of microwind shear zones that are drifting through the scattering region. This feature of the turbulent wind structure has often been noticed in other chaff experiments and seems to indicate the presence of narrow radial velocity shear zones which are advecting.

This feature is clearly shown in Figure 4, where the same shear region appears first at a distance of 5825 meters and, 25 to 30 seconds later, at a distance of 5975 meters. This corresponds to an advection speed along the radar beam of the order of 4 m sec⁻¹. It must be noted that, on Figure 4a at 90 seconds for instance, two Doppler spectra appear clearly separated, which indicates a sharp velocity discontinuity, in contrast to the continuous spread of Doppler velocities usually observed in shear regions. It has been noted from other chaff experiments that these regions of microshear appear more often for low elevation angles (less than 5°), therefore rejecting the possibility of a significant contribution due to the targets' vertical velocity. Local clustering of the dipoles may result in a dispersion of the vertical velocity of the clusters. It is unlikely that vertical velocity differences larger than 0.5 to perhaps 1 m sec⁻¹ will result from this effect.

In these experiments the chaff cloud always appears to be well expanded 5 to 10 minutes after release, and at certain times scarcity of the chaff dipoles can be noticed in some of the patterns. An example of this condition is shown in Figure 5, where the spectrum loses its continuity and evolves toward statistics of individual Doppler signals with independent velocity patterns. If the chaff concentration becomes very small, it is anticipated that the motion of individual dipoles will be probed, thereby leading to the observation of Lagrangian air motion variability.

5. CONCLUSION

This paper has been written for the purpose of discussing some of the unique capabilities of the Doppler radar to probe turbulent air motion in the atmosphere and the feasibility of chaff dipoles for tracing air motion. It is hoped that more systematic experiments will be conducted in the near future for better understanding of the micro- and mesostructure of wind variability and the processes of atmospheric turbulent diffusion.

REFERENCES

Atlas, D. (1964), Advances in radar meteorology, *Advan. Geophys., 10,* 317–478.

Boucher, R. J. (1968), Characteristics of turbulent structures observed by Doppler radar in snow, in *Proc. 13th Radar Meteorol. Conf.* (McGill University, Montreal, Canada, August 20–23, 1968), pp. 480–485, American Meteorological Society, Boston, Massachusetts.

Lhermitte, Roger M. (1964), Doppler radars as severe storm sensors, *Bull Amer. Meteorol. Soc., 45*(9), 586.

Lhermitte, Roger M. (1966a), Application of pulse Doppler radar technique to meteorology, *Bull. Amer. Meteorol. Soc., 47*(9), 703–711.

Lhermitte, Roger M. (1966b), Probing air motion by Doppler analysis of radar clear air returns, *J. Atmos. Sci., 23,* 575–591.

Lhermitte, Roger M. (1966c), Doppler observation of particle velocities in a snowstorm, *Proc. 12th Radar Meteorol. Conf.* (Norman, Oklahoma, October 17–20, 1966), pp. 117–124, American Meteorological Society, Boston, Massachusetts.

Lhermitte, Roger M. (1968), Turbulent air motion as observed by Doppler radar, *Proc. 13th Radar Meteorol. Conf.* (McGill University, Montreal, Canada, August 20–23, 1968), pp. 498–503, American Meteorological Society, Boston, Massachusetts.

Lhermitte, Roger M., and D. Atlas (1961), Precipitation motion by pulse Doppler radar, *Proc. 9th Weather Radar Conf.* (Kansas City, Missouri, October 23–26, 1961), pp. 218–223, American Meteorological Society, Boston, Massachusetts.

Turbulent Air Motion as Observed by Doppler Radar **

Roger M. Lhermitte

Environmental Science Services Administration
Research Laboratories
Boulder, Colorado

I. INTRODUCTION

Ice and snow crystals have small inertia
and respond quickly to variations in air speed.
They are, therefore, excellent tracers of tur-
bulent air motion. Their terminal fall veloc-
ity is not negligible but its spread is
limited. Dry ice crystals have fall speeds on
the order of 0.3 m sec^{-1} to 0.5 m sec^{-1} which
depend primarily on their shape and which are
weakly related to their size (up to 5 or 6 mm)
(Nakaya and Terada, 1935).

Snow crystals have a fall velocity reach-
ing 1 m sec^{-1} for sizes approaching 1 to 2 cm.
Ice and snow crystals can be easily detected by
radar techniques and their motion accurately
observed by means of Doppler radar methods.
This paper describes Doppler radar observa-
tions of the variability of the motion of small
snow crystals and discusses the analysis of
turbulent processes in the boundary layer as
derived from the data.

Fig. 1 shows a typical vertical velocity
spectrum obtained by observing the fall speed
of dendritic snow crystals with a vertical
Doppler radar beam. One sees that the spec-
trum of vertical velocities ranges from 0.3
to 0.9 m sec^{-1} with an average velocity of
0.6 m sec^{-1}. Vertical air motion variance,
whose importance will be discussed in this
paper, is probably included in the velocity
spread shown in Fig. 1. It will be accepted
in this paper that, for a small radar beam
elevation angle, the contribution due to par-
ticles' terminal velocity variance can be neg-
lected. Therefore, it will be assumed that
the air motion variance is the main source of
the spectrum width.

II. METHOD

By use of appropriate systems, pulse
Doppler radars are capable of observing the
spectrum of target radial velocity at any par-
ticular range within the area covered by the
equipment.

If the radar beam is aimed in a fixed
direction inside a snowstorm, with Θ and β
respectively being the beam elevation and azi-
muth angles, the radial velocity of the pre-
cipitation particles selected at a given
distance, is expressed by the following
equation: (Lhermitte and Atlas, 1961).

$$V_r = V_h \cos\Theta \cos(\beta - \beta_0) + w \sin\Theta \qquad (1)$$

V_h and β_0 respectively are the speed and di-
rection of the horizontal motion and w the
vertical motion. By means of scanning the
azimuth angle β, the expression of V_r as a
function of β, can be obtained. By varying β
from 0 to 2π, and by assuming statistical
homogenity of air motion, the average quanti-
ties $\bar{V}_h$, $\bar{\beta}_0$ and $\bar{w}$ can be predicted from the
following equations:

$$\bar{w} = \frac{1}{\sin\Theta} \; \frac{1}{2\pi} \int_0^{2\pi} V_r \, d\beta \qquad (2)$$

Fig. 1. Doppler spectrum originated by snow
crystals fall velocities. The spectrum is
calculated and displayed by means of a spe-
cial purpose digital computer.

$$\overline{V}_h = (A^2 + B^2)^{1/2} \qquad (3)$$

$$\beta_o = \tan^{-1}(B/A) \qquad (4)$$

with
$$A = \frac{1}{\pi\cos\Theta} \int_0^{2\pi} V_r \cos\beta \, d\beta \qquad (5)$$

and
$$B = \frac{1}{\pi\cos\Theta} \int_0^{2\pi} V_r \sin\beta \, d\beta \qquad (6)$$

It must be noted that the estimate of $\overline{w}$ from equation (2) is accurate only if there is negligible distortion of the wind field such as convergence (Caton, 1963). V_h, β_o, w are fluctuating quantities which exhibit time and space variations; the above equations will provide least square predictions of their means, $\overline{V}_h$, $\overline{\beta}_o$, $\overline{w}$, over the area scanned by the radar beam at the selected range. In the case of fast beam azimuth scanning, temporal variations of these quantities can be neglected.

The deviations of V_h, and β_o with respect to their mean can be represented by a longitudinal deviation component, along the mean wind direction, u', and a lateral deviation component perpendicular to the wind direction, v'. In the case of a fixed radar beam with elevation angle, Θ, and azimuth angle, $\beta-\beta_o$, the variance of V_r inside the scattering volume, σ^2_r, can be represented by the following expression as derived from equation (1).

$$\sigma^2_r = \sigma^2_u \cos^2\Theta \cos^2(\beta-\beta_o) + \sigma^2_v \cos^2\Theta \sin^2(\beta-\beta_o)$$

$$+ \sigma^2_w \sin^2\Theta + 2\cos^2\Theta (\sin\beta-\beta_o) \cos(\beta-\beta_o)\text{cov}(uv)$$

$$+ 2 \sin\Theta \cos\Theta \cos(\beta-\beta_o) \, \text{cov}(uw)$$

$$+ 2 \sin\Theta \cos\Theta \sin(\beta-\beta_o) \, \text{cov}(vw) \qquad (7)$$

Where cov(uv) represents the covariance between u and v, etc.

The assumption involved in the inertial subrange[1] implies that the three u, v and w processes are isotropic and independent. This assumption is accepted for wave numbers about twice the distance of the observed layer to the ground (MacCready, 1962). In such a a case the covariance terms must be zero. Outside the inertial subrange, correlation between u, v and w may exist.

[1]See Lumley and Panofsky, 1964.

By azimuth scanning of the radar beam the variance of the mean Doppler (spectrum first moment) can also be observed and expressed as a function of a space coordinate.

The variance of the radial motion within the radar scattering volume, as indicated by the spectrum width, can be evaluated by integrating the high wave number region of the variance density spectrum up to scales corresponding to the scattering volume size. The variance of the mean Doppler, observed during beam scanning, can be estimated by integrating the variance density spectrum between a wavelength equal to the scattering volume size to a wavelength equal to the distance traveled by the range selected region during the azimuth scanning. If the data are concerned with a scanning region in the vicinity of, and centered on, either $\beta-\beta_o = 0$ (upwind) or $\beta-\beta_o = \pi$(downwind), the $\sin(\beta-\beta_o)$ terms will disappear from equation (7) applied to the expression of the variance of the mean Doppler in these regions. Therefore, the covariance terms involving the lateral variance process can be neglected in equation (7) and the following equation can be accepted as an expression of the variance of the mean Doppler during azimuth scanning.

$$\sigma^2_r = \sigma^2_{u,v} \cos^2\Theta + \sigma^2_w \sin^2\Theta$$

$$+ 2 \sin\Theta \cos\Theta \cos(\beta-\beta_o) \, \text{cov}(uw) \qquad (8)$$

The equation (8) will also apply to the relationship between the corresponding variance (and covariance) density spectra involved in the Doppler variance process. It must be noted that the term $\cos(\beta-\beta_o)$ will be +1 in the upwind region, and -1 in the downwind region. Therefore, the variance of the radial motion for upwind region, σ^2_{up}, and downwind region, σ^2_{do}, will be expressed by the following pair of equations:

$$\sigma^2_{up} = \sigma^2_u \cos^2\Theta + \sigma^2_w \sin^2\Theta$$

$$+ \text{cov}(uw) \, 2 \sin\Theta \cos\Theta \qquad (9)$$

$$\sigma^2_{do} = \sigma^2_u \cos^2\Theta + \sigma^2_w \sin^2\Theta$$

$$- \text{cov}(uw) \, 2 \sin\Theta \cos\Theta \qquad (10)$$

These equations can be solved to derive:

$$\sigma^2_u \cos^2\Theta + \sigma^2_w \sin^2\Theta = \frac{\sigma^2_{up} + \sigma^2_{do}}{2} \qquad (11)$$

and $$\text{cov}(uw) = \frac{\sigma^2_{up} - \sigma^2_{do}}{4 \sin\Theta \cos\Theta} \qquad (12)$$

The variance density spectrum $d\sigma^2/dk$ can be represented, for wavelengths between scattering volume dimension and distance traveled by

the range gated region, by the Fourier transform of the deviation of V_r with respect to its mean, obtained by scanning the radar beam in the vicinity of upwind or downwind regions. The method therefore allows the analysis of this part of the longitudinal variance spectrum as well as the spectrum of the covariance with vertical motion, as a function of a space coordinate essentially perpendicular to the wind direction.

III. RESULTS

The previous analytical method was applied to the study of turbulent air motion from Doppler data obtained during a snowstorm in central Oklahoma on Jan. 21, 1967. Some of the meteorological conditions and wind structure were discussed in a previous paper (Lhermitte, 1966). The results presented here are concerned with the Doppler observations made at an altitude of 140 meters, with a beam elevation angle of 10°. The beam cross section, at the distance where data are obtained, is approximately 20 meters. The radial extent of the scattering volume is 100 meters. The observed layer was in a region of strong vertical shear oriented in the direction of the mean wind ($1.5 \ 10^{-2} \text{sec}^{-1}$). The mean wind was 9 m sec^{-1}. Radiosonde data indicated that the temperature at this altitude was -7.5°C at 17:15 CST with slightly superadiabatic lapse rate of 1.0°C/100 meters. The data were selected during the afternoon and evening between 14:32 and 20:11 CST.

A typical aspect of the Doppler data is shown in Fig. 2. One sees a noticeable spread of the Doppler spectrum on the order of 3 m sec^{-1} and also apparent fluctuation of the mean Doppler occurring during the antenna beam azimuth scanning.

It is assumed, in this paper, that the variance of the Doppler information, either spectral width or fluctuation of the mean, is caused only by the air motion variance as expressed in equation (9). This assumption is fully justified when it is applied to the variation of the Doppler mean velocity during beam scanning, except in the improbable case of very heterogeneous precipitation intensity. Accordingly, the variance of the Doppler velocities discussed in this paper is attributed only to air motion variance as expressed in equation (9). The negligible contribution of wind shear and of the spread of precipitation particles' fall speed is discussed below.

RADAR BEAM AZIMUTH
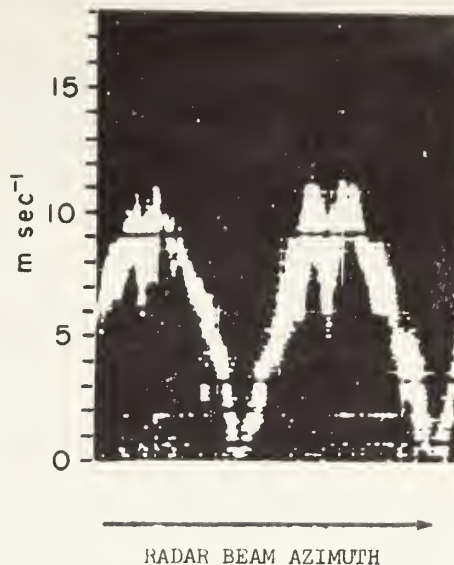
Fig. 2. Doppler velocity – Azimuth pattern recorded at an altitude of 140 m. Display represents Doppler shift without regard to sign. The first maximum is in the upwind region; the second maximum in the downwind region.

The variations of the mean Doppler velocity, which are clearly noticeable in the example shown in Fig. 2, can therefore be attributed to air motion variability along a path generated by the displacement of the range-selected region during the beam azimuth scanning. At the beam scanning rate used in these experiments, the virtual speed of the selected point in range was on the order of 100 m sec^{-1}. Temporal variations of the air motion could thus be neglected and the variance attributed only to space variability, which offers the possibility of analyzing the wave number variance density spectrum. The maximum wave number is limited by the azimuth angle resolution allowed on the records (3° between samples or a space interval of 50 meters). The lowest wave number is limited by the maximum azimuth scanning range as discussed in section 2. This range is ± 30° corresponding to a scanning distance of approximately 1 km. The estimate of the mean Doppler, (first moment of the Doppler spectrum), effectively removes the higher wave number part of the spectrum and prevents aliasing problems resulting from wave numbers larger than half the reciprocal of the sampling interval. The mean values, $\bar{V}_h$, $\bar{\beta}_0$, and $\bar{w}$ were accurately evaluated by applying equations (3, 4 and 5) to the V_r data obtained during the full 2π azimuth range scanning.

The estimated deviation of the wind, with respect to the predicted mean, was thus computed and expressed as a function of successive points in space corresponding to the 3^0 azimuth range of $\pm 30^0$ defined above. The spectrum of the variance density as a function of the wave number k was computed, from the V_i velocity deviation samples, according to the following equations:

$$A(k) = \frac{1}{N} \sum_{i=1}^{N} V_i \cos \frac{2\pi i k}{N} \quad (13)$$

$$B(k) = \frac{1}{N} \sum_{i=1}^{N} V_i \sin \frac{2\pi i k}{N} \quad (14)$$

$$S(k) = A^2(k) + B^2(k) \quad (15)$$

The evaluation of the power density spectrum S(k) was done separately for the upwind and downwind regions, from the 20 selected velocity samples obtained, in each 3^0 region of azimuth. The process was repeated every 10 minutes and, by assuming stationarity of the turbulent process, average spectra were computed over a period of several hours (18 to 20 spectra). Frequency smoothing was used to increase to more than 100, the number of degrees of freedom per spectral density estimate, thus leading to acceptable variance of the estimates. The results are presented in Fig. 3 for upwind and downwind region, and show that the average spectrum did not vary appreciably for the two time periods involved. This gives us confidence in the assumption of stationarity involved in the computation of average spectra. Although most of the data deal with wave numbers outside of the inertial subrange the computed spectrum exhibits a reasonable fit with the -5/3 law with, however, noticeable departure for wave numbers smaller than 1 cycle per km. These wave numbers are outside of the -5/3 region conventionally limited to wave numbers larger than about twice the reciprocal of the distance to the ground acting as a fixed boundary (MacCready, 1962).

If we extrapolate the predicted spectrum shown in Fig. 1 to much smaller scales it is possible to evaluate the variance of the Doppler spectrum, σ^2_s, indicated by the Doppler spectrum width, from the following equation,

$$\sigma^2_s = \int_{k_1}^{\infty} C_1 \, k^{-5/3} \, dk = \frac{3}{2} \, C_1 \, k_1^{-2/3} \quad (16)$$

where k_1 corresponds to the maximum dimension of the scattering volume (100 m). Such evaluation can thus be compared to the estimate of σ^2_s derived from assessing the total width of the Doppler spectrum assumed to be representative of 5 σ_s (90% confidence limits).

The results, which are shown in Table I, are very consistent and indicate that Doppler spectrum width can be accurately estimated by extrapolating the predicted Kolmogorov spectrum into the high wave numbers region of the inertial subrange. In our method, the probing of this part of the spectrum is limited by the average spacing of snow crystals and their inertia. This excellent agreement shows that other contributions to spectral width such as wind shear and spread of terminal velocities are effectively negligible.

On the basis of the experimental data shown in Fig. 3 the upwind and downwind spectra, respectively $S_{up}(k)$ and $S_{do}(k)$ can be approximated by the following equations:

$$S_{up}(k) = 0.9 \ k^{-5/3} \ m^2 \ sec^{-2} \ per \ cy \ km^{-1} \quad (17)$$

$$S_{do}(k) = 0.45 \ k^{-5/3} \ m^2 \ sec^{-2} \ per \ cy \ km^{-1} \quad (18)$$

These results indicate that the spectral density for the downwind region is half of the spectral density for the upwind region. According to the equations (9) and (10), the marked difference between $S_{up}(k)$ and $S_{do}(k)$ can be attributed to the covariance, cov(uw), between u and w (vertical transport of momentum). Within this assumption, cov(uw), and its spectrum, can be evaluated from the upwind and downwind spectra, by use of equation (13). The results on the estimate of covariance are shown in Table I. The sign of the covariance indicates a positive correlation between incoming wind and vertical motion. Since the upwind and downwind spectra have the same -5/3 slope and differ only by a constant, the spectrum of the covariance will also have a $k^{-5/3}$ form and will be given by:

$$\frac{\left[d \ cov(uw) \right]}{dk} = 0.11 \ k^{-5/3} \ m^2 \ sec^{-2} \Big/ cy \ km^{-1} \quad (19)$$

As seen in Fig. 3 there is however a noticeable decrease in the covariance in the vicinity of wave numbers on the order of 3 cy km^{-1}. At the altitude of the analyzed data (140 m) this wave number is the lowest accepted limit of the inertial subrange (MacCready, 1962).

Since $\Theta = 10^0$, the contribution due to σ^2_w in the equation (13) is very small ($\sin^2\Theta = 0.03$). Therefore, we can write

$$\sigma^2_u \cos^2\Theta \simeq \left(\sigma^2_{up} + \sigma^2_{do} \right) \Big/ 2 \quad (20)$$

This leads to the following expression for the spectral density of the wind longitudinal variance:

$$S_u(k) = 0.67 \ k^{-5/3} \ m^2 \ sec^{-2} \ cy \Big/ km^{-1} \quad (21)$$
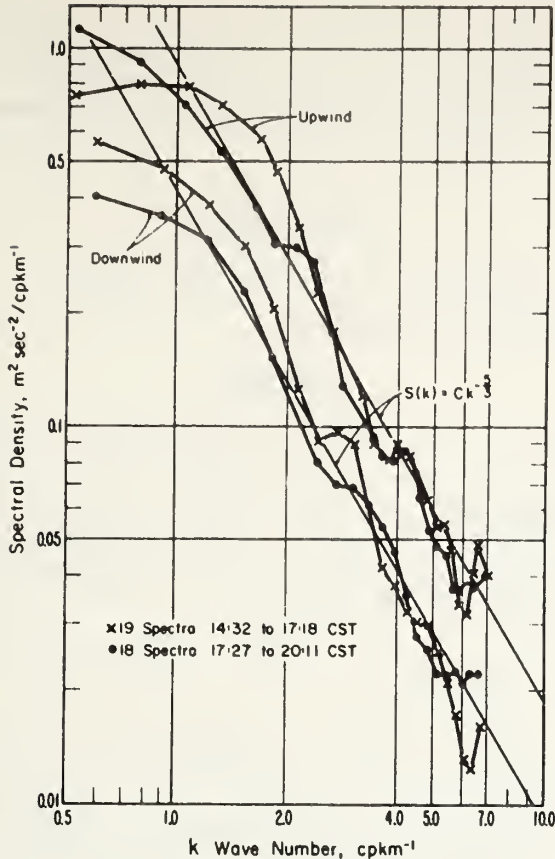
Fig. 3. Wave number spectrum of the variance density of the mean Doppler in the vicinity of upwind and downwind region.

Variance or Covariance $m^2\ sec^{-2}$	Estimated from $S(k) = Ck^{-5/3}$		Variance of Mean		Variance from Doppler Width	
	$\int_{K>10} S(\omega)dk$	$\int^{K>10} S(\omega)dk$	14:32 17:18	17:18 20:11	14:32 17:18	17:18 20:11
σ^2_{up}	0.30	1.05	1.0	0.99	0.25	0.2
σ^2_{do}	0.16	0.54	0.6	0.65	0.16	0.15
$\dfrac{\sigma^2_{up}+\sigma^2_{do}}{2}$	0.23	0.79	0.80	0.80	0.20	0.17
$cov(uw)=\dfrac{\sigma^2_{up}-\sigma^2_{do}}{4\cos\Theta\sin\Theta}$	0.21	0.79	0.6	0.44		
σ^2_w min	0.2	0.74	0.45	0.23		

TABLE I

The minimum vertical motion variance, σ^2_w, can be estimated by remembering that the cross correlation coefficient between u and w, ρ_{uw}, is given by:

$$\rho_{uw}= \frac{cov(uv)}{\sigma_u\ \sigma_w} \qquad (22)$$

and is limited to ± 1 range. Therefore we can write:

$$\sigma_w \geq \frac{|cov(uw)|}{\sigma_u} \qquad (23)$$

The results are shown in Table I. The estimated minimum variance, σ^2_w, is smaller than the values estimated for the longitudinal variance, σ^2_u. One also notices that σ^2_w and cov(uw) are smaller for the later time period (17:18 to 20:11) although σ^2_u remains essentially the same. This must be due to the change in the stress in the boundary layer due to the evolution of the temperature gradient from superdiabatic to neutral state.

IV. CONCLUSION

Doppler radar techniques are extremely useful means for the probing of turbulent atmospheric motion. This paper is written only as an example of these capabilities and shows that unique knowledge of the characteristics of wind motion variability over space can be obtained by use of these methods. Such probing of turbulent air motion by means of Doppler radars can be extended to the studies of the three dimensional distribution of kinematical and statistical processes in the boundary layer. The azimuth scanning technique which is described in this paper is appropriate but in its present form requires tedious data reduction process with limited possibilities for the statistical analysis of the data. Signal processing and data storing means must be improved to fully take advantage of the method. This requirement is imperative if the Doppler data are to be simultaneously acquired at several points in space. Present capabilities of a Doppler radar equipment built and operated at Boulder, Colorado, allows for the simultaneous recording of the Doppler signals at 14 different ranges, by means of a magnetic tape recorder.

An example of the volume of information provided by the method is shown in Fig. 4, where velocity azimuth patterns obtained in approximately one minute are shown at 10 different altitudes. In this presentation, the radial Doppler velocity is displayed as a function of the radar beam azimuth angle and therefore expressed by equation (1) in this paper. One sees that the motion variance is large in the low layers where a strong wind shear is also present. At an altitude of 895 meters,

however, the variability of the motion disappears. This is also an altitude where there is no wind shear. Above this altitude the motion becomes variable again. This example reveals a complex atmospheric structure organized in layers of different turbulence characteristics. Since the patterns have been obtained at the same time, the analysis of the correlation between the motion at different altitudes is possible. This correlation is small, and is due to significant spacing between range gates (800 meters).

during the presence of a snow storm. However, we must emphasize again that, to take full advantage of the method, the data must be recorded and reduced by means of methods compatible with the processing of the data by digital computers.

* * *

Acknowledgment

The author is indebted to Dr. Donald Lenschow for helpful discussions on the boundary layer processes.

References

Caton, P. G. G., 1963: The measurement of wind and convergence by Doppler radar. Proc. Tenth Wea. Radar Conf., Boston, Amer. Meteor. Soc., 290-296.

Lhermitte, R. M., 1966: Doppler observation of particle velocities in a snowstorm. Proc. Twelfth Wea. Radar Conf., Boston, Amer. Meteor. Soc., 117-124.

Lhermitte, R. M., & D. Atlas, 1961: Precipitation motion by pulse Doppler radar, Proc. Ninth Wea. Radar Conf., Boston, Amer. Meteor. Soc., 218-223.

Lumley, J. L., and H. A. Panofsky, 1964: The structure of atmospheric turbulence. John Wiley and Sons.

MacCready, P. B., Jr. (1962a). Turbulence measurements by sailplane. J. Geophys. Research, 67, p. 1041.

MacCready, P. B., Jr. (1962b). The inertial subrange of atmospheric turbulence. J. Geophys. Research, 67, p. 1051.

Nakaya, U., and Terada, T., Jr. (1935). Simultaneous observations of the mass, falling velocity and form of individual snow crystals, ibid. 1, p. 191. (169-71, 250, 261).
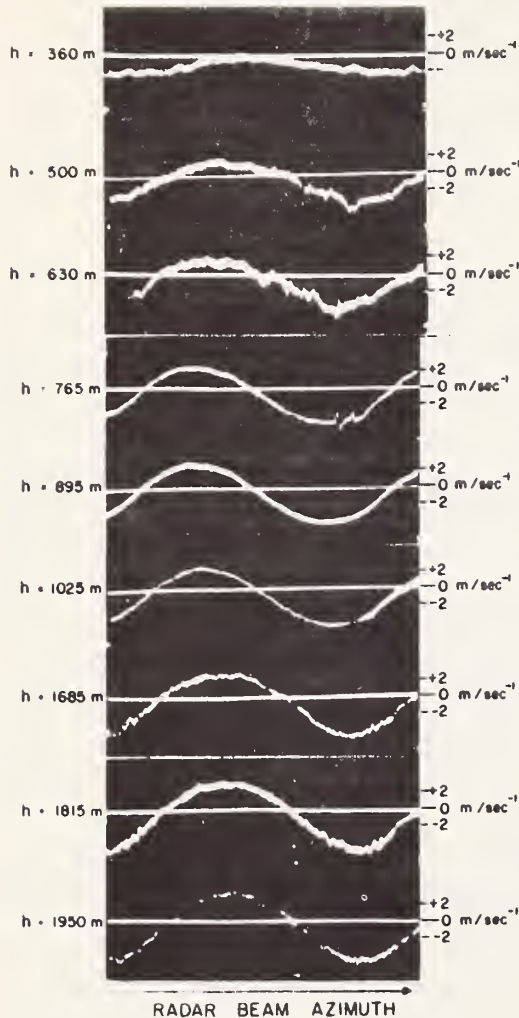
Fig. 4. Velocity-azimuth patterns simultaneously obtained at different altitudes. Note the smooth layer on 895m.

There is obviously a very large amount of information in the patterns shown in Fig. 4 since such data can be continuously obtained

Acoustic Methods for the Remote Probing of the Lower Atmosphere

C. GORDON LITTLE, FELLOW, IEEE

Abstract—The potential usefulness of acoustic methods for the remote probing of the lower atmosphere is reviewed. Starting with a comparison of the effects of temperature, wind, and humidity fluctuations upon the refractive index of air to electromagnetic and acoustic waves, it is shown that the fluctuations in acoustic refractive index may be expected to be about 1000 times stronger than in the radio case. The opportunities for passive and for line-of-sight remote acoustical sensing of the troposphere offered by this relatively strong interaction are briefly identified.

Since the scattered power is proportional to the square of the refractive index fluctuations, the scatter of acoustic waves may be expected to be roughly one million times stronger than for radio waves. Based on the theoretical work of Kallistratova (but including the effects of atmospheric absorption), the system parameters required for effective acoustic echo-sounding of the lower atmosphere are deduced. It is concluded that the acoustic sounding technique could be developed to monitor, to heights of at least 1500 meters, 1) the vertical profile of wind speed and direction, 2) the vertical profile of humidity, 3) the location and intensity of temperature inversions, 4) the three-dimensional spectrum of mechanical turbulence, and 5) the three-dimensional spectrum of temperature inhomogeneity (i.e., of optical refractive index fluctuation).

Typical time and height resolutions for the proposed acoustic echo-sounders could be of the order 10 seconds and 10 meters; the spatial wave number explored could range from about 10^{-2} m^{-1} to about 400 m^{-1}.

I. Introduction

REMOTE probing of the lower atmosphere by acoustic or electromagnetic waves involves the interaction of the waves with the atmosphere. Because the interaction of electromagnetic waves with the gases of the lower atmosphere is in general rather weak (except in the infrared

and millimeter wavelength regions where absorption is strong), sensitive and sophisticated equipment is often required to measure these interactions. It is important to recognize that the interaction of sound waves with the lower atmosphere is very much stronger than that for most parts of the electromagnetic spectrum, and that relatively simple equipment can be used.

The sensitivity of the interaction may be expressed in terms of the magnitude of the fluctuations in refractive index of the medium, i.e., of the phase velocity of the wave in the medium relative to the phase velocity for standard conditions (vacuum for electromagnetic waves, 1 atmosphere pressure of dry air at 0°C for acoustic waves). Thus, a 1°C fluctuation in temperature is equivalent to about 1700 N units change in sonic refractive index (1 N unit equals 1 part in 10^6), whereas for radio wavelengths the resultant change is of the order 1 N unit. For wind, the situation is even more striking; acoustic waves experience a 3000-N-unit change for a 1-meter-per-second variation in wind speed, whereas electromagnetic waves are essentially unaffected, the change due to the change in Fizeau drag being only 2×10^{-6} N unit. For humidity, the difference again is large; for sound waves a 1-mbar change in water vapor pressure corresponds to about 140 N units change in refractive index; for radio wavelengths the corresponding change is about 4 N units and for optical wavelengths about 0.04 N unit. From these figures, we see that the fluctuations in refractive index of air to sound waves tend to be dominated by the wind and temperature fluctuations, humidity fluctuations being relatively unimportant; for electromag-

netic waves the wind fluctuations have negligible effect; at optical frequencies the temperature fluctuations are dominant, but at radio frequencies both temperature and humidity fluctuations may be important.

The above figures show that the diurnal variation of sonic velocity is likely to be of the order 1 part in 100, as opposed to roughly 1 part in 10^5 for optical and radio waves. Refraction effects are also likely to be extremely severe for acoustic waves; the 157 N units/km decrease in refractivity with height required to give a horizontal ray a curvature equal to the curvature of the earth's surface would be produced by a temperature gradient of only $+0.1°C$ per kilometer, or by an increase of wind speed of only 5 cm/s per kilometer of height! Thus sound waves often cannot be considered as traveling in straight lines.

The scatter of acoustic or electromagnetic waves by atmospheric irregularities is proportional to $(\Delta n/n)^2$. For acoustic waves, the scattering cross section is therefore of the order one million times greater than for electromagnetic waves.

The above discussion is concerned with the relative sensitivity of the phase velocity of electromagnetic and acoustic waves to changes in atmospheric conditions; i.e., it deals with the real part of the complex refractive index. The acoustic refractive index also incorporates an imaginary component to describe the absorption of the wave as it propagates through the atmosphere. This absorption component is typically much larger than for electromagnetic waves. Thus the attenuation of a 3-cm-wavelength acoustic wave will be of the order 100 dB/km in the lower atmosphere; for radio waves of the same wavelength, the corresponding figure is only about 0.01 dB/km. In both cases, the absorption tends to increase rapidly with increasing frequency.

These relatively strong interactions of acoustic waves with the lower atmosphere therefore suggest that it is appropriate, and perhaps indeed important, to consider the different possible methods of using acoustic waves for the remote sensing of the lower atmosphere. In succeeding sections of the paper we 1) outline the passive approach to remote acoustic probing of the atmosphere, using acoustic waves of natural origin; 2) discuss briefly the line-of-sight approach, in which man-made acoustic signals are propagated directly from an acoustic transmitter to a receiver; and 3) treat in some detail the monostatic and bistatic radar approach, in which acoustic signals are detected after scatter or reflection by atmospheric irregularities.

II. Passive Probing of the Atmosphere, Using Acoustic Waves of Natural Origin

Acoustic pressure waves of natural origin have been studied for many years, particularly in the infrasonic range of frequencies [1]. Such waves propagate with very low attenuation, and may be observed at distances of many thousands of kilometers. In general, however, these pressure fluctuations have been interpreted primarily in terms of their origin (e.g., natural or man-made explosions, earth-

quakes, aurora, the jet stream, etc.) rather than in terms of the propagation, and hence relatively little atmospheric information has been derived by this method.

At higher frequencies, a microphone exposed to the atmosphere will register, in the absence of man-made noise or noise caused by other forms of life, pressure fluctuations of natural atmospheric origin. Some of these originate as wind noise associated with wind blowing on the microphone or on objects in the vicinity; others originate from the turbulent motions of the atmosphere. In calm stationary air a residual pressure fluctuation would still be observed, due to the random statistical kinetic motions of the air molecules. The acoustic noise power available from these ultimate residual pressure fluctuations is proportional to the ambient temperature—and (in concept at least) could be used to measure temperature.

The generation of acoustic waves by turbulence has been considered by Lighthill [2] and by Meecham and Ford [3]. The power radiated is a very strong function of the Mach number of the turbulence (total power proportional to M^8 for isotropic turbulence) and is therefore likely to be very low under normal atmospheric conditions. Nevertheless, passive remote sensing of turbulence-produced acoustic energy might well prove practicable, and indeed has been successful in the case of severe storms and tornadoes [4]. Here it is important to recognize that the "optical depth" of the atmosphere to acoustic waves is a strong function of frequency, and that it might be possible to estimate the range of the source from multifrequency observations.

III. Remote Probing of the Atmosphere Using Line-of-Sight Propagation Experiments

The velocity V of sound deduced by a stationary observer will be the sum of the velocity of sound C relative to the air, plus the velocity of the air W relative to the observer. Thus,

$$V = C + W.$$

The velocity of sound in dry air is given by

$$C = 20.05\sqrt{T} \text{ m/s},$$

where T is the absolute temperature of the air.

In moist air the velocity of sound is slightly higher, being increased by an amount proportional to the partial pressure of the water vapor:

$$C_{\text{moist}} = C_{\text{dry}}\left(1 + 0.14\frac{e}{p}\right),$$

where e/p is the ratio of water vapor pressure e to total pressure p. The total contribution of the atmospheric water vapor to the phase velocity of sound is typically less than about 1 m/s.

The sensitivity of sound velocity to changes in wind, temperature, and humidity is such that the humidity fluctuations can almost always be ignored. For remote probing purposes one is therefore left with the problem of being able

to identify separately the effects of wind and temperature fluctuations. This can readily be done, since the wind is a vector quantity, while the temperature is scalar; thus measurements of the time of arrival of a pulse, or of the phase of a received CW acoustic signal, taken on a ring of microphones surrounding a central loudspeaker could be used to measure both the mean temperature (from the average time delay around the ring) and the mean wind and wind direction (from the variation of time delay around the ring). These values are averaged over the diameter of the ring and hence are more representative of the ambient atmosphere than the rapidly fluctuating measurements taken at a single point. The data from the various microphones could also be used to derive information on the spatial scales of the turbulence and on the power spectra of the fluctuations in time. With a CW system, considerable sensitivity in mean wind speed and temperature could be achieved. A circle of 100-meter radius around which the relative phase of a 100-Hz acoustic signal could be measured to an accuracy of $(1/100)\lambda \equiv 3.6°$ would give mean wind speeds to about 10 cm/s. Temperature measurements to an accuracy of 0.2°C could be made, provided the partial pressure of water vapor was known to an accuracy of about 1 mbar.

Measurements of the mean humidity of the air could be made from studies of the variation of received power around the ring of microphones as the transmitted frequency is varied. As described later, the variation of absorption with acoustic frequency, relative humidity, and temperature is well known; a circular ring of microphones operated in a multifrequency mode should provide sufficient information to permit unambiguous derivation of the mean humidity, even in the presence of unknown refraction effects in the vertical plane due to vertical gradients in wind and/or temperature.

The above discussion relates to the measurement of atmospheric parameters at the surface of the earth. For many years, the rocket grenade technique [5] has proved of great value in deriving wind and temperature profiles to heights of the order of 90 km. It is possible that the broad-band noise radiated by aircraft engines or CW sources specially installed in aircraft could be used as elevated sources of sound. In either case, advantage could be taken of the very strong Doppler frequency shifts which occur with modern aircraft. The author has not conducted any acoustic ray-tracing analyses, but it would appear likely that useful profiles of wind, temperature, and relative humidity could be derived from such observations.

IV. The Use of Scatter for Remote Acoustical Probing

The scatter of sound by irregularities in the atmospheric wind or temperature fields has been investigated experimentally by several workers. One of the earliest of these was Tyndall [6], who in 1874 concluded that the long persisting echo which he obtained on occasion when using a fog siren on the south coast of England should be attributed to the "flocculent" nature of the atmosphere. In 1964, Gilman, Coxhead, and Willis of the Bell Telephone Laboratories reported [7] the detection of acoustic echoes of unexpectedly high intensity from the lowest few hundred feet of the atmosphere. Kallistratova [8]–[10] experimentally tested the theory of the scatter of sound by atmospheric irregularities in 1958 and 1959. Kelton and Bricout [11] in 1964 showed that the scattered acoustic signals were of sufficient intensity to permit Doppler measurements of wind velocity. Studies by Bellamy et al. [12] of scattering from considerably greater heights were inconclusive, and it remained for McAllister [13][1] to show that these echoes could readily be obtained and studied.

The theory of the scatter of sound by turbulent atmospheric velocity fluctuations, or by fluctuations in scalar atmospheric properties such as temperature, has been investigated by several authors. Thus Lighthill [14] and Kraichnan [15] treated the case of scatter by the turbulent velocity fluctuations, and Batchelor [16] the scatter of sound by temperature inhomogeneities. The broadening of the spectrum of the scattered energy due to the Doppler shifts associated with the turbulent velocity fields is discussed by Kraichnan [15] and by Ford and Meecham [17]. The scatter of sound by both temperature and velocity fluctuations has also been treated by Soviet workers (Tatarski [18], Kallistratova [19], and Monin [20]). Experimental checks of the theory have been made in the field by Kallistratova [8]–[10], [19] and in the laboratory by Baerg and Schwarz.

Following Monin [20], we can write for the scatter of sound inhomogeneities in dry air[2]

$$d\sigma = 2\pi k^4 V \cos^2 \theta \left[\frac{1}{C^2} E(K) \cos^2 \frac{\theta}{2} + \frac{1}{4T^2} \phi(K) \right] d\Omega, \quad (1)$$

where $d\sigma$ is the fraction of the incident acoustic power which is scattered by irregularities in volume V through an angle θ into a cone of solid angle $d\Omega$; $k = 2\pi/\lambda$ is the wave number of the acoustic wave; $K = 2k(\sin \theta/2)$ is the effective wave number at which an acoustic radar scattering through angle θ interrogates the medium; C and T are the mean velocity of sound and mean temperature of the scattering volume; and $E(K)$ and $\phi(K)$ are, respectively, the spectral intensity of the wind fluctuations and the temperature fluctuations at wave number K.

---

[1] See also L. G. McAllister, et al., this issue, pp. 579–587.

[2] This equation is not complete, since it does not include the Doppler effects due to the transportation of the small scattering eddies by larger scale eddies, discussed by Ford and Meecham [17]. The omission is equivalent to assuming that the echo power is measured with a receiver bandwidth several times broader than the Doppler broadening (assumed small) due to the larger-scale turbulence. Other limitations of this equation include the omission of any term to cover scatter by humidity fluctuations (this term would typically be two or three orders of magnitude lower than the wind of temperature terms and therefore can safely be ignored) and the inherent assumption that the wind and temperature fluctuations are uncorrelated. The latter assumption appears to have been made in all the acoustic scattering theories to date and probably warrants critical evaluation, especially under conditions of strong convection. Despite these limitations, the equation is adequate for a first-order discussion and calculation of the scatter of sound by atmospheric irregularities.

For a Kolmogorov spectrum of turbulence this reduces to

$$\sigma(\theta) = 0.03k^{1/3}\cos^2\theta\left[\frac{C_v^2}{C^2}\cos^2\frac{\theta}{2} + 0.13\frac{C_T^2}{T^2}\right]\left(\sin\frac{\theta}{2}\right)^{-11/3},$$

where $\sigma(\theta)$ is now the scattered power, per unit volume, per unit incident flux, per unit solid angle at an angle θ from the initial direction of propagation. The values of C_v and C_T may be obtained from measurements of the corresponding structure functions:

$$D_W = \overline{[W(x) - W(x + r)]^2} = C_v^2 r^{2/3},$$

$$D_T = \overline{[T(x) - T(x + r)]^2} = C_T^2 r^{2/3},$$

where $W(x)$ is the instantaneous wind speed at point x in the direction x to $x+r$, $T(x)$ is the instantaneous temperature at point x, and $W(x+r)$ and $T(x+r)$ are the corresponding instantaneous values at point $(x+r)$. Thus C_v and C_T are, respectively, the root mean square differences in longitudinal velocity or in temperature for two points separated by unit distance.

The above equation shows that

1) the scattered acoustic power resulting from illumination of a Kolmogorov spectrum of turbulence varies relatively weakly with wavelength ($\sigma \propto \lambda^{-1/3}$);
2) this scattered acoustic power is the sum of two terms, one due to the wind fluctuations (normalized by the mean velocity of sound in the medium) and one due to the temperature fluctuations (normalized by the mean temperature of the medium);
3) both wind- and temperature-scattering terms are multiplied by $\cos^2\theta$, which means that *no* power will be scattered at an angle of 90°;
4) the wind term includes a $\cos^2(\theta/2)$ multiplying term, which means that the wind fluctuations produce *no* scatter in the backward direction ($\theta = 180°$); and
5) both the wind and temperature components of the scatter are multiplied by a $(\sin\theta/2)^{-11/3}$ factor; i.e., most of the scatter is in the forward hemisphere.

This equation therefore indicates that a full measurement of the scattered power as a function of wave number and scatter angle would permit the following measurements:

1) $\phi(K)$, the intensity of temperature fluctuations at the three dimensional wave number K, could be measured as a function of direction, wave number, and height, and time. Note that this parameter is of considerable communication and atmospheric importance, being directly proportional to the refractive index fluctuations which are responsible for the scintillation of optical sources.

2) $E(K)$, the intensity of velocity fluctuations at wave number K, could be measured as a function of wave number, direction, height, and time. Note that this three-dimensional spectrum is of immediate concern to the meteorologist and those interested in atmospheric turbulence, diffusion, and pollution.

3) The mean wind speed and direction could be measured as a function of height, using Doppler techniques. A monostatic radar operated in the velocity-azimuth display mode, or a bistatic system, could be used for these measurements, which would be free of uncertainties caused by the unknown fall rates of hydrometeors or chaff. The measurements of Doppler frequency would provide information on the velocity field of the atmosphere surrounding the radar with spatial resolution determined by the pulse length and beamwidth, and could therefore be used for studies of large-scale atmospheric turbulence. In addition, the width of the Doppler spectrum of the echo from a given range element would be a measure of the velocity variation within the pulse volume (a 1° beam with 100-ms pulses would give scatter volumes at 1-km range of the order 15 to 20 m on a side).

4) Mirror-like reflections from horizontal stratifications of the atmosphere would be identified and evidenced by marked aspect sensitivity and narrowing of the frequency spectrum on a vertically directed monostatic radar, and would be readily distinguishable from regions of increased turbulence. In addition, a marked difference in wavelength dependence would be expected, with the echo strength tending to increase with increasing wavelength, as opposed to a $\lambda^{-1/3}$ law for a Kolmogorov spectrum of turbulence.

The continuous remote measurement of temperature inversions by this method would appear to be of great significance to meteorologists generally and especially to those concerned with atmospheric turbulence, diffusion, and pollution.

V. ON THE FEASIBILITY OF ACOUSTIC RADAR

The above discussion indicates that acoustic sounding offers considerable potential for remote measurement of atmospheric parameters. We therefore proceed to estimate the system requirements for an effective acoustic sounder.

The radar equation, applied to the monostatic case (i.e., colocated transmitter and receiver), gives the received power P_r as

$$P_r = P \cdot \sigma \cdot C\tau/2 \cdot A_r \cdot 1/R^2 \cdot L,$$

where P is the radiated acoustic power, σ is the scattering cross section of (1) with $\theta = 180°$, C is the velocity of sound in the scattering region, τ is the pulse length, A_r is the collecting area of the receiving antenna, R is the range to the scattering region, and L is an attenuation factor which takes into account antenna and transducer inefficiencies and any atmospheric attenuation along the double path to and from the scattering region.

Assuming for the moment

$$P = 10 \text{ watts}$$
$$\tau = 10^{-2} \text{ seconds (3.3-meter-long pulse)}$$
$$R = 150 \text{ meters}$$
$$A_r = 1 \text{ square meter},$$

then

$$P_r = 7.3 \times 10^{-4}\sigma L \text{ (MKS).}$$

For the backscatter case, (2) reduces to

$$\sigma = 0.0039\,(2\pi/\lambda)^{1/3}(C_T/T)^2.$$

Taking $\lambda = 2\pi \times 10^{-2}$ meter ($f \approx 5$ kHz), $C_T = 4.6 \times 10^{-2}$ deg$\cdot$m$^{-1/3}$ and $T = 300^\circ$ K, then

$$\sigma = 4.4 \times 10^{-10}\ \mathrm{m^2/m^3}.$$

Using this value of σ, we have

$$P_r = 3.2 \times 10^{-13}\,L\ \text{watt}.$$

In considering the detectability of this received power, we must first estimate L and then estimate the interfering noise power against which the signal must be detected.

The attenuation factor L is made up of the efficiency factor of the receiving antenna (i.e., the ratio of output electrical power from the microphone transducer to the acoustical power incident upon the geometrical area of the receiving antenna) and the absorption of acoustic energy occurring on the propagation path.

The efficiency factor of a loudspeaker at the focus of a paraboloid is likely to be of the order 0.05, based on an effective collecting area of about 0.5 of the geometrical area and a transducer efficiency of about 0.1.

The absorption of sound by the atmosphere is a strong function of frequency. It is conventional to divide this into two components: a classical absorption due to the sum of viscosity, conduction, diffusion, and radiation terms, and a nonclassical component due to the presence of water vapor. In the frequency range 1 to 10 kHz, the classical absorption is usually the smaller, and can be well predicted; at 5 kHz it is about 1.0 dB for the round-trip path to a height of 150 meters.

Detailed results for the classical and anomalous absorption of sound in air as a function of humidity and temperature have been presented by Harris [22]. Fig. 1 is representative of one of the many diagrams in his paper and shows that at 20° C and 50-percent humidity, the total attenuation at a frequency of 5 kHz would be about 10 dB for the round trip to 150 meters height. This figure decreases with increasing temperature and with increasing relative humidity.

Using the above values of receiving antenna efficiency and of atmospheric attenuation,

$$L = 5 \times 10^{-3},$$

whence

$$P_r = 1.6 \times 10^{-15}\ \text{watt}.$$

This electrical signal is now to be compared with the interfering noise level existing at the input to the preamplifier.

Five potential sources of noise must be considered in identifying the signal-to-noise ratio to be expected on an acoustic radar. The ultimate, ineluctable limit, to be achieved only under ideal conditions, will be set by the random pressure fluctuations experienced by the microphone due to the random thermal motion of the atmospheric molecules. The available acoustic noise power is given by
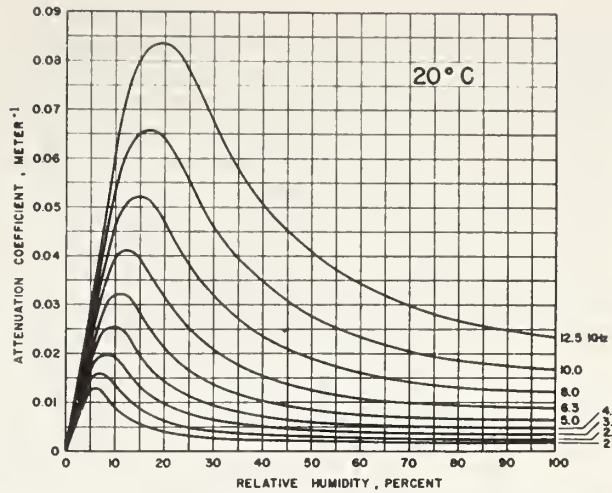
Fig. 1. Total attenuation coefficient m versus percent relative humidity for air at 20°C and normal atmospheric pressure for frequencies between 2.0 and 12.5 kHz at $\frac{1}{3}$ octave intervals. To obtain the attenuation in dB/m, multiply the ordinate by 4.34 (from Harris [22]).

$$P_a = kTB,$$

where $k =$ Boltzmann's constant, $T =$ absolute temperature of air, and $B =$ observing bandwidth. For a bandwidth of 100 Hz and normal atmospheric temperatures, this thermal acoustic noise power would be about 4.2×10^{-19} watt.

Electron shot noise in the receiving preamplifier must also be considered. At audiofrequencies there should, however, be no difficulty in building a preamplifier which generates no more noise than that of a resistor at room temperature. For a 100-Hz bandwidth, this noise power also is about 4.2×10^{-19} watt.

Wind noise on the receiving microphone is likely to prove a more serious limit to the sensitivity of the radar. The effect of this noise can, however, be greatly reduced by placing the microphone as close to the surface of the earth as practicable, by using an array of microphones (since the wind noise will not be correlated on microphones more than a wavelength apart), and by screening the microphone from the wind. A combination of these techniques may be expected to reduce this problem until it is no longer limiting, at least under low wind conditions.

In addition to wind-induced noise created at the microphone itself, atmospheric turbulence may create pressure fluctuations which propagate as sound waves of natural atmospheric origin. Pressure fluctuations of subaudible frequencies attributable to the jet stream, severe storms, etc., have been detected at considerable ranges; the intensity of these pressure fluctuations is believed to drop off rapidly with frequency. We do not know to what extent acoustic noise generated by atmospheric turbulence may at times limit the sensitivity of an acoustic radar, but if this should occur, the technique may provide a new *passive* method of sensing atmospheric turbulence.

The final noise limitation to be considered is that of acoustical energy from nonatmospheric sources, such as

vehicles, insects, etc. This energy may be estimated from data summarized by Stevens and Baruch [23], who show that the ambient acoustic noise power at a quiet site is of the order 20 dB above 10^{-16} W·cm^{-2} for an octave band centered at 1 kHz and decreases by about 5 dB per octave increase in frequency. From these figures, an acoustic noise power of about $+8$ dB per octave at 5 kHz would be expected; for a 100-Hz bandwidth at 5 kHz the noise power flux would be of the order -9 dB relative to 10^{-16} W·cm^{-2} or 1.25×10^{-17} W·cm^{-2}. If we assume that the noise is isotropic in origin, the effective collecting area for this noise will be $\lambda^2/4\pi = 3$ cm^2, leading to an acoustic noise power of 3.75×10^{-17} watt. This acoustic noise power is, however, reduced to 3.75×10^{-18} watt because of the transducer inefficiency. This result suggests that even at a quiet site the 5-kHz acoustical interference is likely to be some 10 dB above the equivalent electrical noise input power due to the preamplifier noise.

The expected received signal power of 1.6×10^{-15} watt exceeds the predicted interference noise power of about 4×10^{-18} watt by a factor of 400, or $+26$ dB; that is, the expected signal-to-noise ratio is $+26$ dB.

VI. Choice of the Optimum Frequency Range for an Acoustic Radar

The optimum frequency range for an acoustic radar will be a compromise between the increase in directivity, the improved Doppler resolution and the reduced interference potentially available at the higher frequencies, and the undesired increase in attenuation experienced as one goes to higher frequencies. The optimum frequency will be a strong function of the range over which the radar is to work, being lower for the larger ranges. Thus the calculations above give a predicted 26-dB signal-to-noise ratio for a range of 150 meters and a frequency of 5 kHz. At ten times the range, the atmospheric absorption would be 100 dB instead of 10 dB, making a lower frequency imperative. Computations similar to the above indicate that a backscattered signal-to-noise ratio of 20 dB could still be obtained at a range of 1.5 km, but would require 100-watt, 100-ms, 1-kHz acoustic pulses radiated and received on a 10-m^2 acoustic antenna.

Note that the above signal-to-noise estimates are based on backscatter, i.e., on the least favorable case. For $\theta \neq 180°$ the echo strength is likely to be stronger (except near $\theta = 90°$), due to the appearance of scatter due to wind turbulence, and to the $(\sin \theta/2)^{-11/3}$ angle dependence of both wind and temperature scattering terms. This suggests that the acoustic analog of the electromagnetic forward scatter systems could be used to measure atmospheric parameters to heights and distances considerably greater than the 1.5 km mentioned above.

VII. A Possible Technique for the Measurement of Humidity Profiles

As already indicated, the scattering cross section for acoustic waves in the inertial subrange of the Kolmogorov
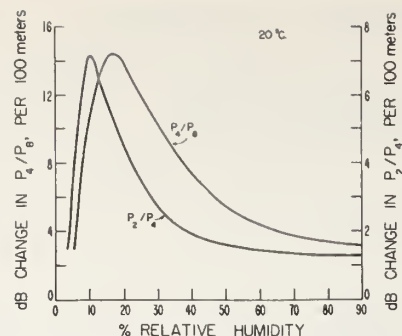
Fig. 2. Variation with relative humidity of the increase, per 100 meters increase in height, of the ratio of echo powers P_2/P_4 and P_4/P_8 for acoustic radars operating at 2, 4, and 8 kHz. Atmospheric temperature assumed to be 20°C.

spectrum of turbulence varies relatively weakly with wavelength ($\sigma \propto \lambda^{-1/3}$). The molecular absorption of the sound, however, varies quite strongly with frequency and humidity. This fact suggests that measurements of the received echo strength as a function of frequency and height could be used to derive information on the variation of humidity with height. A possible method is outlined below.

Consider the case in which two acoustic radars are used in the backscatter mode to obtain echoes successively from the same volume of space on two frequencies of 4 kHz and 8 kHz. Let us suppose that the same peak power, antennas, transducer efficiencies, etc., apply to each radar. In the absence of any atmospheric attenuation, the 8-kHz radar echoes should be 1 dB stronger than the 4-kHz echoes at all heights, because of the $\lambda^{-1/3}$ increase in effective scattering cross section. The classical absorption of acoustic energy would result in a weakening of the 8-kHz echoes relative to the 4-kHz by a known amount (approximately 1 dB per 100 meters increase in height). Any additional decrease in the ratio of 8-kHz to 4-kHz echo power with height could be attributed to molecular absorption due to water vapor; the known dependence of this absorption upon humidity could be used to derive the humidity profile. Thus Fig. 2 indicates that a 5.75-dB decrease in the ratio of 8-kHz echo power to 4-kHz echo power, per 100 meters increase in height, implies a 50 percent relative humidity if the temperature is 20°C. Ambiguity might occur for values near 12-dB change in echo ratio per 100 meters, which could be interpreted as about 12 percent or about 30 percent relative humidity; this ambiguity could be fully resolved if the radar could also operate at 2 kHz. In this case the right-hand scale shows that the 4-kHz/2-kHz change in ratio would either be 7 dB per 100 meters for 12-percent relative humidity or 2.8 dB per 100 meters for 30-percent relative humidity, a difference which could presumably be easily resolved.

One obvious weakness of this method is the assumption of an isotropic, homogeneous Kolmogorov spectrum of turbulence. However, the effect of temperature inversions could be identified and avoided by using different elevation angles, and checks of the spectrum of turbulence could also be made using bistatic systems.

VIII. Some Other Acoustic Techniques

Two other acoustic techniques relevant to remote sensing of the lower atmosphere should be mentioned.

The first of these is the scatter of sound by high-intensity sound waves. The high-intensity sound waves modulate the temperature of the air and hence the velocity of sound; sound waves incident at right angles upon the high-power beam will be scattered, and sum and difference frequencies will be created. However, both theory and experiment [24] show that this nonlinear interaction of the two beams is extremely weak and is not likely to be of practical value for remote sensing purposes.

The scatter of electromagnetic waves by high-intensity sound waves has also been considered, notably by M.I.T. [25] in 1957, and by the Midwest Research Center [26] since 1960. In this concept a high-power acoustic source is used to send a beam of acoustic energy into the atmosphere. The density fluctuations associated with the high-intensity sound beam result in a spatial modulation of the electromagnetic refractive index of the atmosphere. This spatial modulation of refractive index is capable of scattering electromagnetic waves, with coherent addition of the scattered energy when the Bragg scattering condition is fulfilled. The electromagnetic refractive index structure is of course moving with the speed of the sound wave, and, in principle at least, measurements of the Doppler shifts of the scattered electromagnetic waves could be used to measure both the temperature and the wind speed.

Experimental investigations of the feasibility of the EMAC (electromagnetic-acoustic) probe for the measurement of wind speed were made by Smith and Fetter [26]. The technique was found to be limited, with the equipment used, to distances of several tens of feet. The density modulations produced by even an intense source of sound are weak and it does not appear that this concept will be of much use for remote probing of the lower atmosphere.

IX. Some Limitations of the Echo-Sounding Technique

The above discussion of the acoustic echo-sounding technique indicates that it offers the greatest promise for remote acoustic probing of the atmospheric boundary layer. It is therefore important to identify some of the probable limitations of the technique.

The primary limitation of the acoustic sounding technique is likely to be one of range. If round-trip attenuations due to anomalous absorption are to be less than 10 dB, ranges will have to be limited to roughly 150 meters at 5 kHz and 1.5 km at 1 kHz, depending upon humidity. While greater heights could be obtained with frequencies below 1 kHz, large acoustic antennas would be required to achieve adequate directivity and to overcome the increased noise level at the lower frequencies. Alternatively, longer pulses and reduced receiver bandwidth could be used at the expense of reduced resolution in range. A second limitation may arise due to strength of the interaction of the acoustic waves with the atmospheric irregularities. The theory presented earlier is a single-scatter theory, and assumes that the

acoustic beam remains virtually unaffected by the atmosphere, except for the very small fraction of the energy which is scattered. In other words, the attenuation or broadening of the beam by the scatter process is assumed to be negligible. This assumption warrants further investigation, since multiple scatter is likely to degrade the performance of the echo-sounder at long ranges, or under conditions of strong turbulence.

Tatarski [18] has discussed the propagation of sound in an inhomogenous medium. For the case of a spherical wave propagating through a region in which the inhomogeneities are characterized by the Kolmogorov spectrum of turbulence, he derives

$$\overline{\chi^2} = 0.13 C_n^2 k^{7/6} L^{11/6},$$

where

$\overline{\chi^2} = \overline{(\log_e A/A_0)^2} =$ mean square fluctuation of the logarithm of the ratio of the instantaneous amplitude of the wave to the mean amplitude

$C_n =$ structure constant of the (acoustic) refractive index

$k = 2\pi/\lambda$, $\lambda =$ acoustic wavelength

$L =$ length of acoustic path

$C_n = C_T/2T$.

For the case already considered ($\lambda = 6 \times 10^{-2}$ meter, $C_T = 4.6 \times 10^{-2}$ m$^{-1/3}$, $L = 150$ meters)

$$\chi \approx 0.04,$$

from which we see that the acoustic beam will propagate to 150-meter height with only minor amplitude scintillation. For $\lambda = 0.3$ meter, $C_T = 4.6 \times 10^{-2}$ m$^{-1/3}$, and $L = 1500$ meters,

$$\chi \approx 0.13,$$

and the amplitude scintillations are still not fully developed.

We may conclude that, for the experimental conditions used as examples in this paper, multiple scatter will not be a serious factor. However, for more turbulent conditions, or for longer paths or shorter wavelengths, a multiple-scatter theory may be required.

A third limitation arises from the susceptibility of the receiving system to adverse weather conditions, such as strong wind or rain or hail, which would tend to enhance the ambient noise level. Other difficulties include the relatively low information rate (one pulse per second to 150 meters height, less frequently for greater heights) and the effects of beam refraction due to wind or temperature gradients. In addition, the problems of the susceptibility of the radar to man-made noise, and of man to the acoustic signals from the sounder, have not been adequately investigated; some preliminary tests by the author of a low-side-lobe acoustic antenna suggest that these need not be a serious problem.

X. Conclusion

Despite the somewhat unknown magnitude of these limitations, we conclude that the acoustic echo-sounding

technique could be developed to measure, to heights of at least 1500 meters:

1) the vertical profile of wind speed and direction (by utilizing the Doppler technique),

2) the vertical profile of humidity (by means of a multi-wavelength system),

3) the location and intensity of temperature inversions (by using a monostatic system to study the echo power and frequency spectrum, as a function of elevation angle, range, and wavelength),

4) the three-dimensional spectrum of temperature inhomogeneity (by using a monostatic system to study the echo power as a function of wavelength, azimuth, and elevation),

5) the three-dimensional spectrum of mechanical turbulence (by using both monostatic and bistatic systems to study the echo power as a function of scatter angle, wavelength, and direction).

Typical height resolutions attainable would be of the order one half of the pulse length, i.e. about 10 meters if a 60-ms pulse is used. Spatial wave numbers could be explored over the range from $4\pi/\lambda_{min}$ (about 400 m^{-1}) to about 10^{-2} m^{-1} in the case of mechanical turbulence, and 400 m^{-1} to 40 m^{-1} for the temperature inhomogeneities, the difference being due to the ability of the Doppler radar to measure the radial velocities at different points along the beam simultaneously. Time resolutions for successive independent measurements to heights of 1500 meters would be about 10 seconds.

The above potentialities suggest that the acoustic sounding technique will prove a uniquely valuable remote sensing concept for atmospheric boundary-layer studies. In particular, the author suggests that active consideration be given to its application to the meteorological aspects of air pollution, and to such airport problems as the measurement of low-level wind shear and the detection of wake turbulence. In lower atmosphere research, its strongest contribution is likely to be in the field of atmospheric turbulence and the measurement of vertical fluxes of heat, momentum, and water vapor. If necessary, the atmospheric structure responsible for the scattering of the sound waves could presumably be made "visible" by acoustic holography [27]. Strong contributions to electromagnetic propagation research may also be anticipated, as the acoustic sounder reveals the atmospheric structure largely responsible for the fluctuations in microwave and optical propagation. The scatter of sound by cloud droplets and precipitating particles also warrants investigation.

Acknowledgment

References

[1] R. K. Cook, "Strange sounds in the atmosphere," *Sound*, vol. 1, no. 2, pp. 12–16, 1962; R. K. Cook and J. M. Young, *ibid.*, no. 3, pp. 25–33, 1962.

[2] M. J. Lighthill, "On sound generated aerodynamically: I. General theory," *Proc. Roy. Soc.* (London), ser. A, vol. 211, pp. 564–587, 1952.

[3] W. C. Meecham and G. W. Ford, "Acoustic radiation from isotropic turbulence," *J. Acoust. Soc. Am.*, vol. 30, pp. 318–322, April 1958.

[4] V. H. Goerke and M. W. Woodward, "Infrasonic observation of a severe weather system," *Monthly Weather Rev.*, vol. 94, pp. 395–398, June 1966.

[5] W. G. Strand, W. Nordberg, and J. R. Walsh, "Atmospheric temperatures and winds between 30 and 80 km," *J. Geophys. Res.*, vol. 61, pp. 45–56, January 1956.

[6] J. Tyndall, "On the atmosphere as a vehicle of sound," *Phil. Trans. Roy. Soc.*, vol. 164, pp. 183–244, 1874. See also J. Tyndall, *Sound*, 3rd ed., 1875.

[7] G. W. Gilman, H. B. Coxhead, and F. H. Willis, "Reflection of sound signals in the troposphere," *J. Acoust. Soc. Am.*, vol. 18, pp. 274–283, October 1946.

[8] M. A. Kallistratova, "An experimental investigation into the scattering of sound in a turbulent atmosphere," *Dokl. Akad. Nauk SSSR*, vol. 125, no. 1, pp. 69–72, 1959.

[9] ——, "Procedure for investigating sound scattering in the atmosphere," *Akust. Zh.*, vol. 5, pp. 496–498, October–December 1959 (*Soviet Phys.–Acoustics*, vol. 5, pp. 512–514, 1959).

[10] M. A. Kallistratova and V. I. Tatarski, "Accounting for wind turbulence in the calculation of sound scattering in the atmosphere," *Akust. Zh.*, vol. 6, pp. 503–505, October–December 1960 (*Soviet Phys.–Acoustics*, vol. 6, pp. 503–505, 1960).

[11] G. Kelton and P. Bricout, "Wind velocity measurements using sonic techniques," *Bull. Am. Met. Soc.*, vol. 45, pp. 571–580, September 1964.

[12] J. C. Bellamy, R. F. Bosshart, *et al.*, "Investigation of the feasibility of acoustic soundings of the atmosphere," Cook Res. Labs., Skokie, Ill., Final Rept., 1958.

[13] L. G. McAllister, "Acoustic sounding of the lower troposphere," *J. Atmos. Terr. Phys.*, vol. 30, pp. 1439–1440, 1968.

[14] M. J. Lighthill, "On the energy scattered from the interaction of turbulence with sound or shock waves," *Proc. Cambridge Phil. Soc.*, vol. 49, pp. 531–555, 1953.

[15] R. H. Kraichnan, "The scattering of sound in a turbulent medium," *J. Acoust. Soc. Am.*, vol. 25, pp. 1096–1104, November 1953.

[16] G. K. Batchelor, "Wave scattering due to turbulence," *Symp. on Naval Hydrodynamics*, F. S. Sherman, Ed., NAS-NRC Publ. 515, pp. 409–430, 1957.

[17] G. W. Ford and W. C. Meecham, "Scattering of sound by isotropic turbulence of large Reynolds number," *J. Acoust. Soc. Am.*, vol. 32, pp. 1668–1672, December 1960.

[18] V. I. Tatarski, *Wave Propagation in a Turbulent Medium* (R. A. Silverman, transl.) New York: McGraw-Hill, 1961.

[19] M. A. Kallistratova, "Experimental investigation of sound wave scattering in the atmosphere," *Trudy Inst. Fiz. Atmos., Atmos. Turbulentnost*, no. 4, pp. 203–256, 1961.

[20] A. S. Monin, "Characteristics of the scattering of sound in a turbulent atmosphere," *Akust. Zh.*, vol. 7, pp. 457–461, October–December 1961 (*Sov. Phys.–Acoustics*, vol. 7, pp. 370–373, 1962).

[21] W. Baerg and W. H. Schwarz, "Measurements of the scattering of sound from turbulence," *J. Acoust. Soc. Am.*, vol. 39, pp. 1125–1132, June 1966.

[22] C. M. Harris, "Absorption of sound in air versus humidity and temperature," *J. Acoust. Soc. Am.*, vol. 40, pp. 148–159, July 1966.

[23] K. N. Stevens and J. J. Baruch, *Handbook of Noise Control*, C. M. Harris, Ed. New York: McGraw-Hill, 1957, pp. 35-1–35-17.

[24] V. Lauvstad and S. Tjtta, "Problem of sound scattered by sound," *J. Acoust. Soc. Am.*, vol. 34, pp. 1045–1050, 1962.

[25] L. J. Eyges, "Proposal for improving tropospheric propagation," M.I.T. Lincoln Lab., Lexington, Mass., Lincoln Lab. Rept., 1957.

[26] P. J. Smith, Jr., and R. W. Fetter, "Remote measurement of wind velocity by the electromagnetic-acoustic probe," *Conf. Proc. 5th Nat'l Conv. on Military Electronics* (Washington, D. C., June 1961), pp. 48–59.

[27] A. F. Metherell, "Holography with sound," *Sci. J.*, vol. 4, pp. 57–62, 1968.

MONITORING THE EARTH ENVIRONMENT

AIAA Lecture, July 20, 1968
Colorado State University

C. G. Little

1. Introduction

I propose to divide my talk into two main parts. First, I plan to describe the mission of the Environmental Science Services Administration, and to discuss the importance of remote sensing to that mission. I plan to illustrate this part of the talk with three current examples of the way ESSA is using remote sensors to study the earth's atmospheric environment: a) the meteorological satellites, which study the lower atmosphere; b) the top-side sounding satellites, which study the outer ionosphere; and c) the ground-based incoherent scatter (Thomson scatter) radar system which probes the ionosphere and the magnetosphere out to one earth radius.

In the second part of my talk I hope to build the case that sound waves can, and should, be used for remote sensing of the lower atmosphere. Proposing the question, "How can sound waves be used to sense atmospheric parameters?" I hope to answer by showing that they could be used to measure atmospheric temperature, wind speed, and wind direction at the surface of the earth; the vertical gradient of temperature and wind speed at the surface; the wind speed and direction as a function of height; the intensity of mechanical turbulence versus height; the intensity of the temperature fluctuations as a function of height; the location and intensity of strong horizontal stratifications of temperature, and possibly the temperature versus height.

2. ESSA's Mission and the Importance of Remote Sensing to ESSA

2.1 ESSA's Mission

In 1965, President Johnson conducted a reorganization of the Department of Commerce which resulted in the formation of a new Federal agency, ESSA, the Environmental Science Services Administration. This agency was formed by combining the Weather Bureau, the Coast and Geodetic Survey, and that part of the National Bureau of Standards known as the Central Radio Propagation Laboratory. It was created, to quote President Johnson, "to provide

a single national focus to describe, understand, and predict the state of the oceans, the state of the upper and lower atmosphere, and the size and shape of the earth". With the notable exception of the Geological Survey of the Department of Interior, this was therefore the amalgamation of the country's main non-military Federal activities in geophysical science, to form a single centralized geophysical entity competent to perform a broad range of research and services relating to man's total geophysical environment. Specifically, for the first time, a single Federal agency was assigned the broad responsibility of dealing simultaneously with the solid earth, its oceans and waters, and its atmosphere, including the upper atmosphere and its environment in space. Based on the concept that geophysical science is one science, best studied as one science rather than a series of unrelated and disconnected sciences, ESSA is already benefiting from this approach and is likely to reap considerably greater benefits in the future.

2.2 The Importance of Remote Sensing to ESSA's Mission

A consideration of ESSA's mission makes it apparent that its task of observing, understanding, and predicting man's geophysical environment is impossible to fulfill in any complete sense. Not only is the number of significant physical and chemical parameters which must be studied very large, but a full understanding requires global coverage involving space scale from the atomic and molecular dimensions to the intercontinental and indeed solar system dimensions, as well as time scales from fractions of a second (such as lightning flashes) to geological processes taking hundreds of million of years. So ESSA must do the best it can with its limited resources, and in particular (from the point of view of this lecture), must use its expenditures on geophysical observation as efficiently as it can.

Here is where "remote sensing" potentially offers extraordinarily important opportunities. In situ measurements, which measure some particular physical property of the medium at a point, or over some very small area or volume immediately surrounding and in contact with the sensor, are perhaps practicable in cases where one is dealing with small numbers of sensors located near the surface of the earth in accessible geophysical regions. But our modern commercial and military activities are increasingly dependent upon environmental information, often from remote parts of the world, or

relating to considerable altitudes in the atmosphere. Under such circumstances, we rapidly find that we are information-limited, and that the costs of procuring an adequate grid of such information by point measurements would be prohibitively expensive. The geophysicist therefore has a very strong motivation to explore the usefulness of remote-sensing techniques for providing environmental information. One important example of such remote sensing, already in wide use, is the weather radar; such devices illustrate very well the striking advantages of remote sensing - the ability to get excellent time and space coverage from a single location, with a minimum of manpower and no need for a great network of instrumentation and communications. Many of the regions the geophysicist wishes to explore are not readily accessible to instrumentation - e.g. deep in the interior of the earth or the oceans, or high in the ionosphere; especially in these regions, remote sensing may offer unique and perhaps the only opportunity for geophysical measurement.

Let me turn therefore to three important examples for ESSA's use of remote sensing.

2.3 Weather Satellites

Weather satellites form a very important class of remote sensing satellites. Since their inception in April 1960, some twenty weather satellites have been launched; in May of this year the millionth ESSA weather satellite picture was radioed to the ground.

The ten ESSA TIROS and six ESSA TOS satellites are similar in appearance and identical in size. Each weighs about 300 pounds, is 19 inches high and 42 inches in diameter. The top and sides of this roughly cylindrical spacecraft are covered with more than 9,000 solar cells which provide the power to operate all systems on board. The primary sensors are television cameras and infrared radiometers. TIROS cameras, with the exception of the Automatic Picture Transmission (APT) type of camera, made use of half inch vidicons. The vidicon is similar in principle to those used in TV vameras, with a photo sensitive face, and an internal scanning device which converts the image on the tube face to an analog signal. Five hundred scan lines are used in the 1/2 inch vidicon. The infrared radiometers and the APT system are described later.

Currently, ESSA is using the TOS (Tiros Operational Satellite) system. In configuration, these satellites look like a wheel rolling round their 750 nautical mile high orbit. Each satellite carries two cameras pointing radially outward from opposite ends of a diameter; one camera serves as a spare. Each picture covers about 1800 nautical miles on a side; the resolution is from 2 to 4.5 miles. The near retrograde orbit is chose to ensure that the satellite crosses the equator at the same local sun time each day, and that all parts of the earth, except those in polar night, will be photographed at least once every twenty four hours. About 150 photographs each day are required to give this coverage.

The current TOS system consists of two satellites in orbit simultaneously. One is equipped with two Advanced Vidicon Camera System (AVCS) cameras with associated tape recorders to store pictures for later high speed transmission to the Command and Data Acquisition stations in Alaska and Virginia. ESSA 3, launched October 2, 1966, was the first standard AVCS satellite of the TOS system. The other has two APT cameras to provide direct transmission to all ground stations having suitable APT receivers. The AVCS satellite also carriers Low Resolution Infrared Sensors to obtain information on the heat balance of the earth-atmosphere system.

Up to 32 pictures can be stored on the AVCS satellites, and later played back, upon command, to one of the two Command and Data Acquisition (CDA) stations. The APT (Automatic Picture Transmission) satellites take cloud photograph and broadcast them immediately to simple receiving stations on the ground. Overlapping pictures are taken at the rate of roughly one every six minutes; 200 seconds is taken to transmit each picture, line by line, to any ground station that is within line-of-sight. More than 300 APT receiving stations were in operation worldwide by early 1968.

Satellite pictures are observations that contain information on the current state of weather in the pictured areas. A skillful interpreter can locate the position and areal extent of fronts, cyclonic storms, high and low pressure areas, the jet stream, severe weather patterns, tropical storms, sea-ice conditions, and snow cover. Meteorologists can estimate the stage of development of normal middle latitude cyclones and tropical storms, such as hurricanes and typhoons. In some cases it is possible to infer the

presence of turbulence, the existence or lack of stability, the orientation of surface winds, the conditions of the sea, and, in a few instances, it is even possible to determine whether the ground is wet or dry.

To a person familiar with satellite photographs much information on the current state of the atmosphere is obvious just by looking. The broadscale patterns stand out clearly; some of the smaller cloud patterns indicate specific atmospheric conditions. Not so apparent is the information implicit in the cloud patterns: quantities such as vertical velocities, vorticity, divergence, and so forth. Some success has been attained in research directed toward extracting such information for use in computer forecasting.

By visual examination, much information can be obtained from the pictures to supplement normal observations from the ground and to obtain weather information over data-sparse areas.

A High Resolution Infrared (HRIR) system was tested on Numbus I and II. This system, which obtained measurements in the 3.4 to 4.2 micron water vapor "window" of the infrared spectrum, scanned across the orbital path from horizon to horizon, with a best resolution of about 4 miles directly below the satellite.

The next development in ESSA's National Operational Meteorological Satellite System (NOMSS) is TIROS M, to be launched next year, which in a single satellite combines both the AVCS storage function and the APT broadcast function. The 625 lb satellite will also carry a Solar Proton Monitor, to be used for warnings of disturbances in the solar cosmic ray flux, of importance to astronauts, SST and radio communications.

The TIROS M/I-TOS spacecraft is considerably different in appearance from the earlier TIROS and ESSA satellites. The spacecraft is 40" x 40" x 48", weighs 625 lbs., and carries three 36" x 63" solar paddles to generate between 200 and 400 watts of electrical power. The satellite will be earth-oriented with stabilization provided by a flywheel rotating at 150 rpm. It will carry 2 AVCS, 2 APT, 2 two-channel Scanning Radiometers, a Solar Proton Monitor, and a flat plate radiometer (FPR). The two channel scanning radiometer will sense in the 0.5 to 0.7 μ (visible) region and the 10.5 to 12.5 μ (water vapor window) region to provide both day and night viewing capability. The

FPR will furnish atmospheric heat balance measurements. The orbit planned for I/TOS is identical with those of the TOS system ESSA satellites: sun-synchronous, near-polar, at 750 n. mi. altitude.

As experience is gained with I/TOS other instruments will be added, and existing systems will be replaced with improved or substitute systems to provide equivalent, improved, or additional sensor capability.

Further into the future, ESSA is planning for a Geostationary Operational Environmental Satellite (GOES) system. Two satellites would be involved, one over the Atlantic, one over the Pacific, transmitting to a single CDA station. These spacecraft would have on board the spin-scan cloud camera used in ATS-1 ATS-3, a data collection/data relay system and a solar proton monitoring capability.

2.4 Top-side Sounding Satellites

The meteorological satellites make use of optical and infra-red picture-taking and scanning capabilities to sense the lower atmosphere remotely using passive reception techniques to measure thermal radiation or scattered sun-light. ESSA is also active in remote sensing of the upper atmosphere (iono-sphere) using a satellite radar technique - or active remote probing technique.

Interestingly enough, the first use of radar was to detect and measure the ionosphere, and it is perhaps particularly appropriate that the first use of satellite-borne-radar was to study the top side of the ionosphere (hence the name "topside-sounders".

The refractive index of the ionosphere is reduced by the presence of the free electrons. Ignoring the effect of the magnetic field, the refractive index is given by

$$n^2 = 1 - \frac{Ne^2}{m\omega^2}$$

where N is the number density of free electrons, e and m are the electronic charge and mass respectively, and ω the angular frequency of the radio waves. At vertical incidence, radio frequencies penetrate to a height where the refractive index is zero or

$$N = \frac{m\omega^2}{e^2}.$$

Different frequencies therefore penetrate to different heights in the iono-
sphere. Since the mid 30's the sweep-frequency ionosonde (a sweep-frequency
hf radar usually scanning the 1 to 25 MHz range) has been a standard research
tool of the ionospheric radiophysicist.

With the arrival of the space age, several groups suggested the use of
ionosondes in satellites. The ISIS program (International Satellites for
Ionospheric Measurements) was started, and has resulted in an extremely
valuable and successful program of four satellites. Obviously, satellites
have the unique advantage that they can readily give full global coverage.
Often, however, the satellite is used to give information only about the
medium immediately surrounding the satellite, or to view some distant surface,
such as the surface of the earth; in the case of the top-side sounder satel-
lites, a sweep-frequency radar or a series of fixed-frequency radars is used
to derive information at many heights at and below the satellite. As a result
of this remote probing at many depths, this ISIS program has been an unusually
valuable and successful scientific program. Many unexpected features have
been discovered, several of which could not have been identified by any other
technique. A few of the highlights of this program are summarized below:

1. Over a million top-side soundings have been made around the globe.
   These have revealed, for the first time, the existence of a deep
   "trough" in the night-time ionosphere near the auroral zones, the
   nature of the topside of the important equatorial anomaly, and
   many other details of the topside of the ionosphere.

2. The presence of several forms of ionospheric irregularities.
   Among the most intriguing of these are "ducts" - ionospheric
   irregularities only a few kilometers in cross section which are
   aligned along the earth's magnetic field lines in such a way as
   to guide hf radio energy from one hemisphere to another and back
   again for repeated bounces.

3. The occurrence of "plasma resonances" associated with the excitation
   of the ionospheric plasma surrounding the satellite by the rf field
   of the satellite transmitter. These plasma resonances occur at the
   gyro-frequency of the electrons and its harmonics, at the plasma
   frequency, at the upper hybrid frequency $\omega_T = (\omega_N^2 + \omega_H^2)^{1/2}$ and
   at $2\omega_T$.

4. The reduction of temperate latitude electron density throughout the
    F region of the ionosphere associated with strong magnetic storms.

2.5 Incoherent (Thomson) Scatter Sounding of the Ionosphere

The most sophisticated and successful remote sensing technique ever used
in geophysics is that of incoherent (or Thomson) scatter. It was shown by
Thomson that free electrons would scatter electromagnetic energy weakly;
since 1958, radiophysicists have been exploiting this weak scattering effect
to study the ionosphere at heights up to one earth radius. Very powerful
radar transmitters, coupled to large antennas, and complex data processing
techniques are required to achieve adequate signal/noise ratio. With such
a facility (which typically costs up to several million dollars) the staff
of the ESSA Jicamarca (Peru) Radar Observatory have shown that it is possible
to measure, or deduce, the variation with height and time of an astounding
number of ionospheric parameters. Remembering that one is studying what to
the laboratory physicist would be essentially a perfect vacuum at a range of
hundreds or even a few thousand kilometers, their successes indeed form a
striking demonstration of the potentialities of remote sensing.

The primary parameter measured is that of echo power as a function of
time delay, or height. By adding to this parameter detailed analyses of
the frequency spectrum, polarization and angle of arrival of the echoes, the
following parameters of the ionosphere can be measured as a function of height
and times:

Electron density (from amplitude and polarization data)

Electron temperature (from frequency spectrum of echo)

Ion drift velocity (from Doppler shift of spectrum)

Ion densities of the different ionic constituents (from spectrum
   of echo)

Ion temperature (from spectrum of echo)

Magnetic field strength (from polarization data)

Magnetic field direction (from polarization data)

These measurements then permit the deduction of many other parameters of the
ionosphere, such as:

Electric field strength

Electric current flow

Rate of production of electrons by solar energy

Rate of loss of electrons

Rate of solar energy absorption

Neutral gas temperature

Neutral gas densities

3. Possibilities for Ground-Based Remote Sensing of the Lower Atmosphere Using Sound Waves

With the exception of scent (a remote sensing method not yet on a quantitative basis) remote sensing techniques rely on the propagation of waves. These may be electromagnetic waves, of any appropriate frequency, or compression waves, such as acoustic and seismic waves.

Remote sensing of atmospheric parameters requires therefore that the atmosphere impose some characteristic signature on the wave. The interaction is described in terms of the complex (and perhaps anisotropic) refractive index of the medium, n', which describes the effect of the medium upon the velocity and the amplitude of the wave. n' is given by

$$n' = n - ik,$$

where the real component of the refractive index, n gives the phase velocity v, of the wave from the relationship

$$n = c/v,$$

and $2\pi k$ is the exponential decay factor of the amplitude due to the absorption of the wave per wavelength in the medium.

For air, the refractive index over much of the electromagnetic spectrum is very close to unity ($n \approx 1.0003$, $k \leq 10^{-8}$ at NTP for the normal radio frequencies).

Under such circumstances the interaction of the waves with the medium is very slight, and there is little opportunity to use electromagnetic waves for remote probing of the atmospheric gases. On the other hand, the refractive index of hydrometeors and aerosol particles differs markedly from unity,

(e.g. n = 1.33 for water at visible wavelengths) and hence the interaction of electromagnetic waves with such particles is relatively strong and can readily be used for remote sensing purposes - as, for example, in the case of weather radar.

In the case of sound, however, the velocity of the wave is strongly affected by both the wind and the temperature. The velocity of sound propagating in a moving medium is the vector sum of the velocity of sound relative to the medium, $\vec{C}$, and the velocity of the medium, $\vec{W}$.

$$\vec{V} = \vec{C} + \vec{W}$$

where C is given, in air, by $C = 20.05\ T^{1/2}$ meters/sec, where T is the temperature of the air in degrees Kelvin.

Consideration of the relative magnitudes of C and W, and of the changes of T occur in the atmosphere, show that the "refractive index" of the air to sound waves fluctuates much more strongly in the case of sound waves than for electromagnetic waves. Thus, while the diurnal variation of electromagnetic refractive index is of the order 10^{-5}, for acoustic waves it is of the order 10^{-2}, i.e. roughly 1000 times stronger. Similarly, turbulent irregularities in the lower atmosphere cause refractive index fluctuations of the order 10^{-6} for electromagnetic waves and roughly 10^{-3} for sound waves. It is important to recognize that the scatter or reflection of waves by fluctuations in refractive index goes as $(\Delta n)^2$; the scatter or partial reflection of sound by atmospheric temperature gradients is therefore roughly 10^6 times greater than for electromagnetic waves. This relatively strong interaction of sound waves with the medium therefore suggests that sound waves could readily be used to monitor atmospheric parameters.

However, there is an immediate complication. As indicated above, the velocity of sound is affected both by temperature and wind, i.e. $\vec{V} = F(T) + B(\vec{W})$. The naturally occurring fluctuations in these parameters usually are of comparable magnitude, and in general one cannot ignore one term relative to the other, but must find ways of measuring them seperately.

Fortunately, one simple fact exists which readily permits this seperation, namely the fact that the temperature is a scalar quantity, while the wind is a

vector quantity. This means that the temperature term affects all directions equally; the effect of the wind is vectorial, and will increase the apparent speed of sound in some directions while decreasing it in others. Therefore, by taking measurements of the relative phase, or the relative time-of-flight of a sound pulse, in three or more directions one can derive the temperature of the air and the velocity and direction of the wind.

To illustrate this point, consider the case of a sound source at the surface of the earth, surrounded at a distance R by a ring of microphones. Let us consider, for a series of atmospheric models of increasing complexity, the distribution of received amplitude and of time delay around the ring.

Assume first the simplest model - no wind, and temperature constant with height. In this case the received amplitude will be constant with azimuth; the phase (or time delay) of the received signal relative to the transmitted signal will also be constant around the ring. Note that the temperature of the air is given by the relationship

$$T = \frac{1}{(20.05)^2} \cdot \frac{R^2}{(\Delta t)^2} \quad (R \text{ in meters, } \Delta t \text{ in seconds})$$

Taking next the case of uniform temperature and a wind of velocity W blowing toward azimuth angle θ_1, and constant with height. In this case, the speed of the sound is increased in the direction θ_1 and reduced in the opposite direction, resulting in a quasi-sinusoidal variation of time delay around the mean value. The received amplitude will also show a quasi-sinusoidal variation, with maximum in the direction θ_1, associated with the transportation of the expanding sound wave in that direction. Note, (1) that the direction of the wind is given by the direction of minimum time delay; (2) that the wind speed is given by $W = R/2 (1/T_{min} - 1/T_{max})$, and (3) that the temperature may be derived from the mean value of time delay in the directions θ_1 and $\theta_1 + 180^\circ$.

Consider now the effect of a uniform wind, plus a temperature which is not constant with height. If the temperature gradient near the surface is positive, the speed of sound increases with height and upward-going sound tends to be refracted back toward the ground, resulting in an increase in

received amplitude. The opposite will be true in the case of a decrease of temperature with height. From this it will be seen that the mean level of received amplitude around the circle is an indicator of the temperature gradient in the immediate vicinity of the ground. The presence of a wind will not affect this dependence of mean amplitude upon temperature gradient, provided that its velocity is constant with height.

Take now the case where the temperature is constant, but the wind increases with height. In this common situation the sound is refracted downwards in the direction toward which the wind is blowing, and is refracted upwards (away from the microphones) in the opposite direction. The result of a gradient in the wind is therefore a non-uniform change in received amplitude around the ring; one should therefore be able to differentiate between temperature gradients and wind gradients by checking for a uniform or non-uniform change of amplitude around the ring. In estimating the vertical wind gradient, it will of course be necessary to put in the appropriate correction for the amplitude increase in the direction θ_1 due to the reduced expansion time of the sound wave as it reaches the microphones in that direction.

Consider now the effects of turbulence upon the received signal. In this case, measurements of Δt and A at each location will fluctuate; measurements of the time-averaged values around the ring will give information on the time average values of temperature, wind velocity and wind direction, and mean surface gradients of temperature and wind, while detailed analysis of the time-delay and amplitude information should permit derivation of information on the time scales and spatial scales and intensities of the turbulent fluctuations in velocity and temperature.

Suppose now that the acoustic system is transformed into a directional radar system to study the scatter of sound by turbulent atmospheric irregularities, rather than the direct transmitter-microphone wave.

The theory of such an acoustic radar system was worked out by Russian workers in the late fifties. They have shown that, for a Kolmogorov spectrum of turbulence, the energy scattered through an angle θ is given by

$$\sigma(\theta) = 0.03 \ (2\pi/\lambda)^{1/3} \cos^2 \theta \left[c_V^2/c^2 \cos^2 \theta/2 + 0.13 \ c_T^2/T^2 \right] \sin^{-11/3} (\theta/2)$$

where $\sigma(\theta)$ is the scattered power per unit volume in direction θ away from the incident direction, per unit incident flux, per unit solid angle. The two terms within the bracket are respectively due to eddies in the wind velocity, normalized by the velocity of sound, C, and the fluctuations in temperature, normalized by the mean temperature, T. C_V and C_T are derived from measurements of the structure functions

$$D_{rr} = \overline{\left(U(x) - U(x+r) \right)^2} = c_V^2 \ r^{2/3}$$

and

$$D_T = \overline{\left(T(x) - T(x+r) \right)^2} = c_T^2 \ r^{2/3}$$

From this expression we see:

1. that the scattered power is weakly dependent upon wavelength

$$(p \propto \lambda^{-1/3}) \ ;$$

2. that the $\cos^2 \theta$ term, which multiplies both the wind scatter term and the temperature scatter term, means that there is a null in the energy scattered through an angle of 90°, and a subsidiary maximum in the backscattered direction;

3. that the wind scatter term, which is multiplied by $\cos^2 \theta/2$, is largest in the forward direction and falls to zero in the back direction;

4. that the scatter term due to temperature fluctuations shows no such null in the back direction ($\theta = 180^{\circ}$);

5. that there is a strong angle dependence, proportional to $(\sin \theta/2)^{-11/3}$ or almost $1/(\sin \theta/2)^4$ affecting both the wind scatter and the temperature scatter terms, which make the backscattered signal much weaker than the forward scattered signal.

-13-

Since c_V^2/c^2 is often of the order c_T^2/T^2, the temperature term (including the 0.13) is often roughly one order of magnitude less than the wind term. However, this is <u>not</u> true in the back direction, where the wind term is zero.

This Russian work, for which they have some experimental verification, suggests that an acoustic radar system, capable of measuring the angle dependence of the scatter could be used to measure several important atmospheric parameters. Thus the use of a narrow-beam vertically-directed radar would give direct information on the variation of c_T^2 (proportional to the intensity of the temperature fluctuations) with height. The variation of c_V^2 with height could then be deduced by measuring $\sigma(\theta)$ at values of θ other than 180°, using a distatic system. This experiment could be performed using a single vertical transmitting beam and a receiving beam steerable in elevation; alternatively two steerable beams could be used, thereby obtaining redundant data.

The intensity of the turbulence of various scale sizes, and its isotropic or anisotropic nature could also be tested, by changing acoustic frequency and illuminating the scattered from different directions.

Two additional important features could be explored by studying the <u>frequency</u> spectrum of the received acoustic echo. Scattering from irregularities moving with the mean wind speed would in general result in Doppler shifts, which could be used to derive the wind speed (and direction) versus height. The analysis of the spectrum of the received echo would also be valuable in identifying the presence of specular reflection from a smooth, mirror-like temperature inversion layer. Such an echo would not show spectral broadening and the specular component could therefore be readily identified. Alternatively, radial measurements of the distribution of amplitude of the echo could be used to identify specular reflection, as opposed to turbulent scatter conditions.

Finally, it would appear possible that a combination of vertical angle of arrival and time-of-flight measurements, conducted at various radial distances and in different directions might permit the derivation of temperature versus height profiles.

The above discussion is obviously idealized and in practice it may be difficult to make the desired frequency or amplitude measurements with adequate accuracy. However, since <u>no</u> simple technique currently exists for the remote measurement of atmospheric wind, temperature and turbulence profiles, the ideas would certainly appear to warrant further theoretical and experimental investigation. Notice that the technique works in the boundary layer - the layer of primary concern to the meteorologist, the aviation community, and the pollution experts; and that the data will have major relevance to such problems as the propagation of sound, and sound pollution.

Slides and Illustrations

This lecture will be illustrated by approximately 30 slides and diagrams as follows:

2.3 Remote sounding using weather satellites

  - ESSA TIROS Operational satellite TOS-3A
  - ESSA TOS orbit
  - Montage of 156 TOS AVCS pictures
  - Cyclone over mid Atlantic
  - Stages in cyclone development
  - Development of a cyclone
  - Pacific vortex and frontal system
  - ATS-III color photo over Atlantic

2.4 Remote sounding using ionospheric top-side sounders

  - Alouette 1 sweep-frequency top-side sounder
  - Contours of electron density
  - Example of top-side ionogram
  - Identification of plasma resonances
  - Example of conjugate point ducting
  - Effect of magnetic storm

2.5 Remote sounding using the Thomson scatter technique

  - Thomson scatter field site
  - Thomson scatter antenna (close up)
  - Thomson scatter antenna (close up)
  - Series of four graphs giving T_e, T_i, ionic constitutents
      and electron density profiles for four times of day
  - Correlation between F region vertical drift velocity and E region
      East-West drift velocity

3. Acoustic sounding of the lower atmosphere

  - Transmitter with circular array of microphones
  - Amplitude (A) and time delay (Δt) vs. azimuth (θ) - no wind;
      constant temperature
  - A (θ) and $\Delta t(\theta)$ curves - constant wind; constant temperature

- A (θ) and $\Delta t(\theta)$ curves - constant wind; + ve, zero and - ve temperature gradients
- (θ) and $\Delta t(\theta)$ curves - wind gradient; temperature gradient
- Acoustic radar - $(C_T/T)^2$ vs. height mode
- Acoustic radar - $(C_V/C)^2$ vs. height mode
- Acoustic radar - W,θ vs. height mode
- Australian acoustic radar (McAllister)
- Feed horn for acoustic radar (McAllister)
- Acoustic echoes from elevated layers (McAllister)

33

Optical Doppler Measurement of Microscale Wind Velocity

JAMES C. OWENS, MEMBER, IEEE

Abstract—A system analysis of the feasibility of optical heterodyne measurement of Doppler shifts as a method for the remote determination of vector wind velocity is carried out. It is found that with a 50-mW laser at 6328 Å, naturally occurring aerosols in clear air will permit measurements at distances of only a few tens of centimeters, but haze and dust will extend this range to a few tens of meters and fog to 75 meters. By generating smoke to enhance the scatter, a range of about 40 meters will be achievable. The use of a 1-watt argon laser will extend the clear-air and smoke-plume ranges by a factor of 48 and the ranges in uniform dust or fog by smaller amounts. Hence useful measurements in the boundary layer of the atmosphere are possible although they will require some artificial contamination of the air to give consistently good results. Remote temperature measurement is not possible using this technique.

I. INTRODUCTION

MONOSTATIC microwave Doppler radar techniques are commonly used for tropospheric measurements of wind velocity in storms and for ionospheric studies of electron and ion densities and temper-

atures. The mean velocity component of the scattering elements along the beam direction is given by the mean Doppler shift of the received signal, while the spectral width of the signal provides a measure of the range of scattering element velocities within the scattering volume. In the case of ionospheric Thomson scatter, this spectral width can be used to calculate the kinetic temperatures of the scattering elements. Because the fractional Doppler shifts are very small, coherent detection is required. The development of lasers has made possible the extension of these techniques to the optical spectral region. The principal advantage of this extension is that with the very short wavelength of visible light much greater spatial resolution is possible than with radio or microwave systems; when the beam is focused, volumes as small as 1×10^{-6} cm^3 can be examined at a distance of a meter or more. In addition, although the fractional Doppler shift is independent of carrier frequency, the absolute shift is much larger at optical than at radio frequencies, thus offering the possibility of improved precision in the velocity measurement. For these reasons, optical Doppler measurements of fluid velocity [1] and of the ve-

locity and displacement of vibrating surfaces [2] have been undertaken by several groups.

In this paper we examine the sensitivity and operating range of such measurements in air, considering both molecular and aerosol scattering, in order to ascertain the utility of the method for meteorological remote sensing. It is found that, in contrast to the ranges of tens of kilometers over which aerosols can be detected with simple LIDAR systems, the coherence requirements of Doppler measurements limit operating range with a 50-mW helium-neon laser to a few tens of meters with natural aerosols or smoke and to about 75 meters in fog. Remote temperature measurements are not possible using this technique. Nevertheless, it is clear that high-speed measurements of one or all three vector components of wind velocity can be made using very small sampling volumes in the boundary layer of the atmosphere as well as in the laboratory, thus providing a useful tool for micrometeorological studies and, through the use of more powerful lasers, for such applications as the determination of low-level wind profiles over airports.

II. Scattering Cross Section of a Single Particle

The theory of scattering by a spherical homogeneous particle of arbitrary size has been well summarized by Goody [3]. We consider a particular direction of scattering from the particle specified by the angles (θ, ϕ) as indicated in Fig. 1. The scattered irradiance I at distance R is related to the irradiance I_0 of the incident beam by

$$\frac{I}{I_0} = \frac{\sigma(\theta, \phi)}{R^2}. \tag{1}$$

In the scattering of linearly polarized light by optically small particles, for which the condition $2\pi a m' \ll \lambda_0$ is satisfied, where a is the particle radius, m' is the refractive index of the particle, and λ_0 is the vacuum wavelength of the radiation, the angular scattering cross section may be written

$$\sigma(\theta, \phi) = \frac{(2\pi)^2 (m-1)^2}{n^2 \lambda_0^4} \sin^2 \phi \tag{2}$$

where m is the refractive index of the gas rather than of the individual particles and n is the number density of particles. The total cross section σ is found by integrating over all angles. For air under standard conditions and light of wavelength 6328 Å, $\sigma(\theta, \pi/2)$ is only 2.6×10^{-28} cm². We note that the scattering efficiency $Q_s = \sigma/\pi a^2$ is very small for the molecules found in normal air, only about 3×10^{-12}.

In scattering by spheres which are not small compared with λ_0, the scattering is strongly forward directed, may have several lobes, and varies less strongly with wavelength than in the Rayleigh case. The most striking change, however, is the greatly enhanced efficiency of scattering. It can be shown from general arguments based on Babinet's principle that Q_s must approach the value 2 as the quantity $2\pi a m'$ increases beyond λ_0. For a water droplet of radius 1 μm, the scattering efficiency happens to reach its maximum value, 4, at a wavelength of 6328 Å, giving a total cross section of
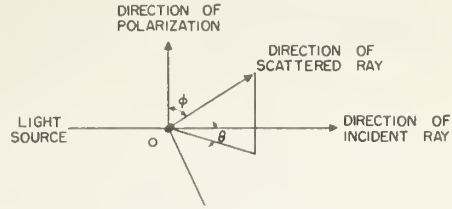
Fig. 1. Geometry of light scattering from particle at O.
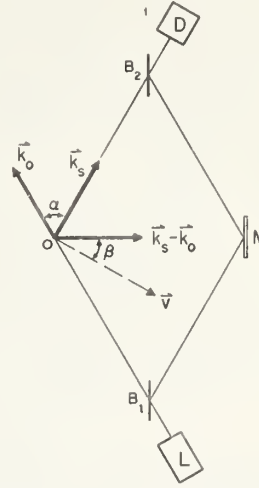
Fig. 2. Geometry of optical system for Doppler shift measurement, showing laser L, scatterer O, detector D, beam splitters B_1 and B_2, mirror M, wave vectors k_0 and k_s, and velocity v.

1.3×10^{-7} cm². The total scattering from a single fog droplet is thus 6×10^{19} times as large as that from a single oxygen or nitrogen molecule and equal to that from molecular scattering in a volume of 2.2 cm³.

The aerosol particles of principal importance in atmospheric optics are those with radii between 0.1 and 1.0 μm, for these particles make the greatest contribution to the effective cross section, the integral of particle number density times cross section per particle. For our purposes it is adequate to describe the variation of Q_s in this range, given in Goody's graphs, by the two-part linear function

$$Q_s = \begin{cases} (11.7 \times 10^4)a - 0.67 & \text{for } a = 0.1 \text{ to } 0.4 \times 10^{-4} \text{ cm} \\ -(3.3 \times 10^4)a + 5.3 & \text{for } a = 0.4 \text{ to } 1.0 \times 10^{-4} \text{ cm.} \end{cases} \tag{3}$$

III. Doppler Shift for a Single Scatterer

Consider the scattering geometry shown in Fig. 2. Light from the laser L, with frequency ν_0 and wave vector k_0, is incident on the scattering element at O, which is moving at velocity v in a medium of refractive index m. The scattered light, with frequency ν_s and wave vector k_s is received at square-law detector D. Part of the original laser beam is split off by beam splitter B_1, reflected by mirror M, and recombined with the scattered light by beam splitter B_2 after traversing an approximately equal optical path length. If the wavefronts are suitably matched at D, the detector output current will have a component at the difference

frequency $\Delta v = v_s - v_0$. It can be shown [4] that this Doppler shift Δv is given to first order by

$$\Delta v = \frac{1}{2\pi}(k_s - k_0) \cdot v$$

$$= \frac{2mv}{\lambda_0} \sin\left(\frac{\alpha}{2}\right) \cos \beta \tag{4}$$

where α is the scattering angle as normally defined and β is the angle between v and $(k_s - k_0)$.

We note, first, that only the magnitude of the component of v in the direction $(k_s - k_0)$ is measured. To determine the sign of this component we must offset the frequency of the reference beam so that the beat frequency will not pass through zero for the largest Doppler shift expected. This can be conveniently done with a traveling-wave acoustic diffraction modulator [5].

Second, we see that if the scattering particles are large there is a tradeoff between Doppler shift, which increases with scattering angle, and scattering cross section, which decreases sharply. (For a 1-μm water droplet at 6328 Å, the cross section given by Goody varies approximately as $\exp(-\alpha/16°)$.) In a practical system it will usually be desirable to use small scattering angles, in the range 5° to 20°.

Third, we can measure all three orthogonal components of velocity using one laser and three detectors located at the four vertices of a tetrahedron with the scattering volume in the center, as indicated in Fig. 3. If two, rather than three, of the vertices rest on the ground, the components measured directly have the normal horizontal-vertical orientation. For this tetrahedral case the scattering angle is 70.5° and the Doppler shift is 18.2 kHz/(cm/s) or about 8.2 MHz for a 10-mi/h wind. No significant signal loss will result from polarization mismatch if aerosol scattering is used.

IV. Coherent Detection for a Single Scatterer

Optical heterodyne detection has been analyzed extensively [6], and we summarize here only those results needed for the problem at hand. We consider the system of Fig. 2, assuming that the scattering element is a single small particle so that the scattered wave is spatially coherent, and that the signal and reference (LO) wavefronts are accurately aligned. We shall also assume for simplicity that the amplitudes of the two waves are uniform over the detector, for it has been shown [2] that replacing the actual diffraction pattern in the image of an elementary point source by a disk of constant amplitude and phase results is an overestimation of the signal current by a factor of only about 2. The rms signal current at the frequency Δv is given by $i_S = (2I_S I_{LO})^{\frac{1}{2}}$, where I_S and I_{LO} are the direct currents that would be produced by the signal and LO waves alone. The rms noise current, if we assume as usual that shot noise due to I_{LO} is the dominant source of noise, is given by $i_N = (2eI_{LO}B)^{\frac{1}{2}}$, where e is the electronic charge and B is the system bandwidth. The additional noise due to background light, such as scattered sunlight, is negligible in the visible spectral region [6]. We can write the signal-to-noise
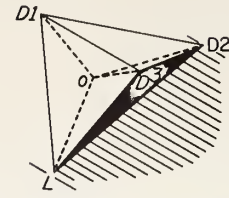
Fig. 3.   Tetrahedral array of laser L and three detectors D around scattering volume O for measurement of all three vector components of wind velocity.

ratio, $\psi = (i_S/i_N)^2$, in terms of the intercepted optical signal power P_S by noting that for a detector of quantum efficiency η the current is given by $I_S = \eta \, eP_S/hv$, where hv is the energy of a single photon:

$$\psi = \frac{\eta P_S}{hvB}. \tag{5}$$

If the laser power is P_0, we may write the LO and signal powers as

$$\begin{align} P_{LO} &= C_r^2 P_0 \\ P_S &= Q C_t^2 P_0 \end{align} \tag{6}$$

where C_r and C_t are the beam-splitter power reflectance and transmittance, respectively; these are squared because two beam splitters are used. The factor Q is the power scattering efficiency of the entire system including the elementary scatterer, and may be shown from (1) to be

$$A = \left(\frac{D}{dR}\right)^2 \sigma(\theta, \phi) \tag{7}$$

where d is the diameter of the (assumed uniform) laser beam at the scatterer, D is the diameter of the receiving optical system aperture, and R is the distance from the scattering volume to the receiver. Hence we may write (5) as

$$\psi = \frac{\eta C_t^2 P_0}{hvB}\left(\frac{D}{dR}\right)^2 \sigma(\theta, \phi). \tag{8}$$

Although i_s is maximized for $C_r = C_t$, the signal-to-noise ratio (8) is maximized by making C_t as large as possible subject to the constraints $C_r + C_t \leq 1$ and $P_{LO} \gg P_S$. It is clear that Q will be small for practical systems, even if focused so that the size of the scattering volume is diffraction limited, and hence the maximum signal-to-noise ratio will be achieved with $C_t \simeq 1$, when almost all the laser power is transmitted to the scattering volume and the LO beam is only strong enough to dominate the noise. Thus, we have finally

$$\psi = \frac{\eta P_0}{hvB}\left(\frac{D}{dR}\right)^2 \sigma(\theta, \phi). \tag{9}$$

V. Typical Molecular and Aerosol Densities

A 22.4-liter volume of gas under standard conditions contains Avogadro's number of molecules, and hence the number density is 2.69×10^{19} cm^{-3} and the average distance between molecules is $n^{-\frac{1}{3}} = 33.4$ Å. Aerosols are, of course, highly variable. In nature, aerosol particles are found with

radii from 10^{-3} to 10^2 μm. Smoke is the most common source of particles having radii less than 0.1 μm, while those having radii greater than 0.1 μm are largely dust over land and sea spray over the ocean. The "typical" aerosol number densities we shall use are [7]:

clean country air: $5 \times 10^2 \text{cm}^{-3}$ in the range 0.1 to 1.0 μm

dusty air, especially over the desert: 10^4 cm^{-3} with radii greater than 0.1 μm

moderate haze: 10^5 cm^{-3} in the range 0.03 to 0.2 μm

dense haze and smoke: 10^6 to 10^7 cm^{-3} in the range 0.03 to 1.0 μm

clouds and fog: 10^2 to 10^3 cm^{-3}, with peak of distribution at 3 μm.

For natural aerosols near the surface in clear continental air, we will need the distribution of particle sizes. It is known empirically [7] that

$$\frac{dM}{d(\log a)} \propto a^{-3} \tag{10}$$

where M is the total number of particles from the smallest up to those of radius a. The derivative of this expression is the number of particles per cm^3 per unit increment of a. Evaluating the constant using the number given above, we have

$$n(a) = (1.7 \times 10^{-12})a^{-4}. \tag{11}$$

VI. Coherent Detection with a Volume Distribution of Scatterers

If the scattering volume contains a number of particles moving in different directions at different velocities, the resultant signal will on the average be larger than for one particle, but interference effects will cause the heterodyne current to vary rapidly around the most probable value. The mean Doppler shift will give the mean velocity of the particles, while the spectral width of the signal will be related to, but not necessarily the same as, the superposition of the Doppler shifts for each particle. We must consider not only the particle radius a and the wavelength λ, but also the mean particle separation $l = n^{-\frac{1}{3}}$, the mean free path δ, and the diameter d of the scattering volume.

A. Heterodyne Current

For neutral particles having a mean separation of many particle diameters, and hence an adequately random spatial distribution, the signals from the individual scatterers add up as vectors in a two-dimensional random walk. The signal amplitude at the detector due to one particle is $(QP_0)^{\frac{1}{2}}$, and if there are on the average N particles in the scattering volume the resultant signal amplitude is Rayleigh distributed [8] with mean square value NQP_0. The heterodyne current is also Rayleigh distributed, its probability density given by

$$p(i_S) = \frac{2i_S}{I^2} \exp\left(-\frac{i_S}{I}\right)^2, \qquad i_S \geq 0 \tag{12}$$

where $I^2 = \langle i_S^2 \rangle$ is the mean square value of the current, given by

$$I = \sqrt{2I_{\text{LO}}I_S} \tag{13}$$

where

$$I_S = \frac{\eta e}{h\nu} NQP_0. \tag{14}$$

The mean value of i_S is $\langle i_S \rangle = (\sqrt{\pi}/2)\, I$, and the variance is $\sigma^2 = \langle i_S^2 \rangle - \langle i_S \rangle^2 = (1 - \pi/4)I^2$, about 25 percent of the mean square. This broad peaking of the Rayleigh probability density indicates that there is a considerable probability that the heterodyne current will differ substantially from the mean value. The corresponding variations in power or signal-to-noise ratio will be even greater. Because the ratio of variance to mean square is a constant independent of the number of particles in the scattering volume (for large N), then although the average heterodyne current and thus the average signal-to-noise ratio increase with N, the relative fluctuations in signal do not change. Hence we note that there can be a significant problem with signal dropouts, periods when the signal is too small to measure, even when N is large. Even worse, we shall find later that it is advantageous to focus the light and use a small scattering volume, making N small, and therefore this problem can be an important one in applications requiring high-speed sampling. If, however, the scattering particles are in rapid motion, so that the particle arrangement changes significantly during a measurement interval, the resulting signal is unlikely to be far from the mean value.

When there are many particles in a volume λ^3, as in Rayleigh scatter at altitudes below about 150 km, the particles cannot be resolved and hence the scatter from neighboring particles is effectively coherent. In this case we need not consider the individual particles but can take the elementary scatterers to be volumes of characteristic dimension $\lambda/4$. If the particle positions are actually uncorrelated the final result must, of course, be the same as before. If, in addition, the scattering volume is much larger than λ^3, it is possible and much simpler to consider the fluctuations in density, and hence in refractive index, of the elementary volumes rather than the positions and velocities of the actual particles. It is well known that the spatial Fourier component of refractive index at the appropriate wave vector, found from the integral over the scattering volume of the spatial auto-correlation function of refractive index, gives the complete solution to the scattering problem: the amplitude of this component gives the scattered amplitude, and the temporal behavior of the component gives the Doppler broadening.

B. Doppler Shift and Spectrum

For the aerosol case, where $l \gg \lambda$, the phase of the resultant signal is uniformly distributed in the interval 0 to 2π rad, and the scatter from each particle appears at the Doppler-shifted frequency corresponding to its velocity component in the direction $(k_s - k_0)$. This velocity is due to both the Brownian motion of the particle and the gross motion of the medium. If the diameter of the scattering volume is small compared with the scale of turbulence of the medium and the sample averaging time is short com-

pared with the characteristic time of the turbulence, the contribution of gross motion is the same for all the particles and the Brownian motion will be the principal source of spectral width. The spectrum of the scattered energy then has the same form as the probability density function describing the number of scatterers at each velocity, which is Gaussian (one-dimensional Maxwellian) [9] around the frequency corresponding to the mean wind velocity:

$$S(v) = S(v_m) \exp\left[-\frac{v - v_m}{\dfrac{2 \sin{(\alpha/2)}}{\lambda} \left(\dfrac{2kT}{m}\right)^{\frac{1}{2}}} \right]. \quad (15)$$

Here $S(v)$ is the power spectral density at frequency v, v_m is the Doppler-shifted frequency due to the mean wind, k is Boltzmann's constant, T is the absolute temperature of the surrounding gas, and m is the mass of the scattering particle. For aerosols, this spreading is quite small. For a water droplet with a radius of 1 μm and a temperature of 300°K, the rms value of one component of its velocity, $(kT/m)^{\frac{1}{2}}$, is only 0.1 cm/s, and the full width at half-power of the Doppler-broadened spectrum (15) for the 70.5° scattering angle shown in Fig. 3 is only 4.3 kHz. This will normally be masked and hence unobservable using large scattering volumes or long sample averaging times, when variations in the gross wind velocity dominate the measured width.

In considering the use of molecular rather than aerosol scattering, we must introduce the mean free path δ of the particles. Dougherty and Farley [10] have pointed out that the density fluctuations and resultant scattering in a neutral gas are rather different in the two cases $\lambda \gg \delta$ and $\lambda \ll \delta$. For $\lambda \ll \delta$, the density fluctuations that scatter the wave are stochastic, and Dougherty and Farley have shown that the amplitude and spectrum of the scattered waves are exactly the same as those calculated by considering each particle to scatter independently and incoherently. Hence (15) is valid here also. For $\lambda \gg \delta$, however, both the intensity and the spectrum differ. The scattered intensity is reduced by a factor γ, the usual specific heat ratio (equal to 5/3 for an ideal gas), while the change in the spectrum is even more significant. We now have scattering from harmonic waves rather than random fluctuations, and hence the scattered light occurs at two discrete Doppler shifts corresponding to the velocities of the appropriate sound waves approaching and receding (just as for Brillouin scattering in solids) rather than having the earlier Gaussian spectrum. Although the shape of the spectrum changes with the ratio of λ to δ, the spectral width, appropriately defined, is similar and is a measure of temperature in either case. This width is much larger for molecular than for aerosol scattering, of course; using the average molecular weight of air, 28.97, a temperature of 300°K, and the other parameters as before, we find the Gaussian full width to be 1.26 GHz.

The mean free path of oxygen and nitrogen molecules at sea level is slightly less than 0.1 μm. Hence, for light at 6328 Å, we have $\lambda > \delta$, the second case. The mean free path varies inversely with air density, and at elevations of 20 to 25 km the two numbers are nearly equal. In most of the troposphere, therefore, the Doppler spectrum is intermediate between the forms considered.

C. The Effect of Focusing

We now take the number density of scatterers n to be fixed and consider changing the scattering volume. We assume that the instrument is bistatic and symmetrical, with transmitting and receiving optics of equal diameter, similarly focused, and equidistant from the scattering volume. Since we found the rms scattered signal amplitude to be $(NQP_0)^{\frac{1}{2}}$, the signal-to-noise ratio (9) becomes

$$\psi = \frac{\eta P_0}{h\nu B}\left(\frac{D}{dR}\right)^2 N\sigma(\theta, \phi). \quad (16)$$

The scattering volume is a sphere of diameter d, and hence $N = \pi d^3 n/6$. The solid angle of the receiver field of view is $\Omega_r = \pi d^2/4R^2$ and the area of the receiver is $A_r = \pi D^2/4$. Substituting these quantities into (16) and using the well-known antenna theorem [11]

$$A_r\Omega_r = \lambda^2 \quad (17)$$

we have

$$\psi = \frac{\eta P_0}{h\nu B}\frac{8}{3\pi}\frac{n\lambda^2\sigma(\theta, \phi)}{d}. \quad (18)$$

This expression, incidentally, agrees with Siegman's maximum-signal theorem [11]. Chu has recently shown [12] that the received power (and hence ψ) may in fact be a factor π larger for Gaussian beams than for the uniform ones assumed here.

The result of principal interest is that the signal-to-noise ratio is maximized at a minimum value of d. Since $d \approx 2\lambda(R/D)$, this means that for a given working distance the largest practical optics should be used and both transmitter and receiver should be focused to the minimum possible spot size. (In general, of course, it will be necessary to make R/D of the order of 10 to 100 to achieve a reasonable working distance.) This result may be surprising, since we found earlier that the scattered signal amplitude is proportional to $\sqrt{N}$, but the reason for this result is fairly obvious. The scattered signal power is proportional to the product of power density at the scattering volume (which is proportional to $1/d^2$), the number of scatterers in the volume (d^3), and the effective area of the receiver ($1/d^2$, by the antenna theorem above); hence the received power and the signal-to-noise ratio are proportional to $1/d$. We recall, of course, that to prevent dropouts several particles should pass through the scattering volume during each measurement period.

Massey analyzed the similar problem of scattering from a rough surface [2] and found that the receiving aperture should be just large enough to resolve the focused spot and that a larger aperture gives neither improvement nor degradation. If the receiver is too small, its field of view is larger than necessary and its effective aperture is smaller than optimum. Increasing the receiver aperture up to the point where the spot is just resolved therefore increases the signal, although increasing it further has no effect because one

merely collects light from a decreasing fraction of the spot into an increasing solid angle, and these two effects just cancel each other. Massey also noted that if the transmitter and receiver have the same diameter and are at the same distance from the focused spot, the spot is automatically at the receiver's resolution limit and the scattered wave entering the receiver is spatially coherent. If the particles are small enough to scatter isotropically, one need only calculate the fraction of the incident light reaching the receiver to find the coherent signal. This is done by merely multiplying the total scattered power by the ratio of the solid angle subtended by the receiver at the spot to 4π.

VII. THE EFFECT OF ATMOSPHERIC TURBULENCE

In order to achieve the calculated sensitivity and signal-to-noise ratio, the signal and reference wavefronts must be matched at the detector. We have found that for a given density of scattering particles and a given working distance, the signal-to-noise ratio increases with increasing diameter of the optics. However, it is well known that this improvement continues only until the aperture is approximately as large as the transverse phase coherence area, which is limited by atmospheric turbulence [6]. Larger apertures do not further reduce the size of the focused spot, and in fact they cause the variance of signal power to increase [13]. Although there have been very few direct measurements of the phase structure function [14], propagation theory [15] combined with direct measurements of the temperature structure function [16] show that this coherence degradation will not be a problem with optics of practical size at distances of a few meters. For horizontal paths 100 meters long and 2 meters above the ground, however, the maximum useful aperture may be limited to 1 cm in daytime and to 10 cm at night. The second atmospheric effect, fluctuation in the mean temperature and hence in the optical path length between source and receiver, gives rise to an apparent but spurious Doppler shift. It is expected theoretically [13], however, that this effect will be negligible. This expectation has been supported by direct interferometric measurements [17], which have shown the spectral width to be only a few hertz for a path length of 100 meters at night, and by modulated-light measurements over a path of 5.3 km [18].

VIII. NUMERICAL EXAMPLES

We now calculate the maximum range that could be attained in wind or temperature measurement using aerosol or molecular scattering, assuming reasonable values for the system parameters and setting the signal-to-noise ratio equal to 1. Substituting $2\lambda(R/D)$ for d, setting $\psi = 1$, and solving (18) for R, we find

$$R = \frac{\eta P_0}{hvB} \frac{8}{6\pi} n\lambda\sigma(\theta, \phi)D. \qquad (19)$$

We assume these values:

$$\eta = 0.05$$
$$P_0 = 50 \text{ mW}$$
$$\lambda = 6328 \text{ Å}$$
$$D = 15 \text{ cm}.$$

Then (19) becomes

$$R = (3.2 \times 10^{12}) \frac{n\sigma(\theta, \phi)}{B} \qquad (20)$$

where R is in centimeters. We can go one step further and give a simpler approximate formula by replacing $\sigma(\theta, \phi)$ by an average differential cross section defined by $\langle\sigma(\theta, \phi)\rangle = \sigma/4\pi$, where σ is given by $\sigma = Q_s\pi a^2$, and setting B equal to the full width at half-maximum of the Doppler spectrum at the 70.5° scattering angle of the tetrahedral array. We then find

$$R = (1.86 \times 10^{14})nQ_sa^{7/2}. \qquad (21)$$

A. Wind Measurement Using Natural Aerosols

The mean Doppler shift can sweep over a wide frequency range, 0 to 25 MHz corresponding to winds of 0 to 30 mi/h, although the frequency of variation of the mean will be low, a few hertz at most. The width of the Doppler spectrum for 0.2-μm particles will be about 48 kHz. The simplest type of receiver would have an instantaneous bandwidth of the full range, 25 MHz, and use a spectrum analyzer or a limiter and discriminator for display. Estimating the position of the center of the spectrum would give the mean wind, and the width would give the variations. Such a receiver gives a poor signal-to-noise ratio, however, because of its broad bandwidth, and it is better to use a tracking receiver (a phase-locked loop) that has a narrow instantaneous bandwidth but is capable of tracking the mean frequency over wide excursions. Although the final output bandwidth of the system need be only a few hertz, the bandwidth of the phase-locked loop (which determines the sensitivity of the system) must be greater than the width of the Doppler spectrum so that the receiver will remain phase locked even if there is on the average only one particle in the scattering volume. If $N \gg 1$, B can be made somewhat smaller, but not less than 50 kHz for natural minimum-aerosol conditions.

For clear air, then, we use $B = 50$ kHz and the expressions (3) and (11), finding by integration over a from 0.1 to 1.0 μm that the mean value of $n\langle\sigma(\theta, \phi)\rangle$ is 8.6×10^{-7} cm^{-1}. The maximum range found from (20) is then 55 cm.

A moderate haze giving a visibility of a mile or so, as is often found in cities, would give a marked improvement. Dust is even better because of the presence of large particles. For the latter case, assuming a particle concentration 100 times that for clear air, we find that ranges of several tens of meters are possible. Fog and clouds would be better yet, for the large droplets have both larger cross sections and smaller Doppler widths than dust or haze particles. For $n = 10^2$cm^{-3}, $a = 3$ μm, we find that $B = 825$ Hz is adequate and that the maximum range is 175 meters. This distance could not actually be achieved under conditions of uniform aerosol density, however, because increases in particle concentration increase not only the scattering in the sample volume but also the scattering loss along the transmission paths. It can be shown from Bouguer's law [19] that the attenuation L in dB/km is given by

$$L = (1.36 \times 10^6) \bar{n} Q_s a^2 \qquad (22)$$

which for the fog just considered is 24.6 dB/km, reducing the maximum range to 75 meters. To achieve even this requires that the scattering angle be much smaller than the 70.5° of the tetrahedral system because of the strong forward scatter of these large particles.

B. Wind Measurement Using Smoke

We next assume that by using smoke candles we can generate a distant smoke plume of density 10^7 cm^{-3} particles of radius 0.1 μm. For such particles Q_s is about 0.5, and hence $\langle \sigma(\theta, \phi) \rangle$ is approximately 1.25×10^{-11} cm^2. A bandwidth of 100 kHz is required, and the maximum range is 40 meters.

C. Wind Measurement Using Rayleigh Scatter

At sea level, we have $n = 2.7 \times 10^{19}$ cm^{-3} and $\langle \sigma(\theta, \phi) \rangle = 2.6 \times 10^{-28}$ cm^2. However, the Doppler width due to thermal motion of the molecules is so great (1.26 GHz) that the calculated range is only 1.8×10^{-5} cm, which is, of course, to say that the measurement is impossible. This is of no great importance, however, since the Rayleigh signal is negligible if even one aerosol particle is in the scattering volume.

D. Temperature Measurement Using Rayleigh or Aerosol Scatter

In principle we might measure temperature by observing the full width of the Doppler spectrum for molecular scattering. A simple receiver with a spectrum analyzer display would be used, for the required bandwidth is approximately 1 GHz if only half the spectrum is displayed. The numbers are the same as in the preceding example, and hence this is impossible. Failing in this, we might consider measuring the spectral width for aerosol scattering, which is only about 4 kHz. Here, unfortunately, although the bandwidth is not prohibitive, the desired width will in general be masked by the variations in mean frequency due to turbulence.

IX. Conclusions

We have shown that optical heterodyne measurement of Doppler shifts is a feasible method for remotely determining vector wind velocity. With a 50-mW helium-neon laser, naturally occurring aerosols in clear air will permit measurement at distances of only a few tens of centimeters, but haze and dust will extend this range to a few tens of meters and fog to 75 meters. By generating smoke to enhance the scatter, a range of about 40 meters will be achievable. Hence measurements in the boundary layer of the atmosphere should be successful, although they will probably require some artificial contamination of the air to give consistently good results. Remote temperature measurement, unfortunately, is impossible.

These conclusions have been qualitatively confirmed by Foreman et al [1], who found that measurements could be made on rocket plumes at a distance of at least 8 feet and that, at least for shorter distances, one aerosol particle in the

scattering volume was adequate. Their results in ordinary room air, rather than smoke or liquids, were only marginal however, which also agrees with our predictions.

The use of improved lasers will give dramatic increases in range for those cases not limited by scattering loss along the transmission paths. An argon laser giving 1 watt at 4880 Å, for example, used with a photomultiplier of 20-percent quantum efficiency, would permit the use of operating distances 48 times as large as those listed above for measurements in clear air or on smoke plumes, while the improvement in dust would be 10 and that in fog, 4. The distances achievable with such a system are clearly of practical significance.

References

[1] J. W. Foreman, Jr., E. W. George, J. L. Jetton, R. D. Lewis, J. R. Thornton, and H. J. Watson, "Fluid flow measurements with a laser Doppler velocimeter," *IEEE J. Quantum Electronics*, vol. QE-2, pp. 260–266, August 1966. See also R. C. Watson, Jr., R. D. Lewis, and H. J. Watson, "Instruments for motion measurement using laser Doppler heterodyning techniques," in *Advances in Test Measurement, Proc. ISA Ann. Conf.* (New York, October 28–31, 1968), vol. 5, 1968; and D. T. Davis, "Analysis of a laser Doppler velocimeter," *ISA Trans.*, vol. 7, pp. 43–51, 1968.

[2] G. A. Massey, "Photomixing with diffusely reflected light," *Appl. Opt.*, vol. 4, pp. 781–784, July 1965. Further details are given in an unpublished technical report by Massey, "Study of vibration measurement by laser methods," Sylvania Electronic Systems, Mountain View, Calif., December 1966, and in G. A. Massey and R. R. Carter, "Portable laser instrument for vibration analysis and transducer calibration," *Shock and Vibration Bull.* (U. S. Naval Research Lab., Washington, D.C.), pp. 1–6, January 1968.

[3] R. M. Goody, *Atmospheric Radiation.* Clarendon Press, 1964, ch. 7.

[4] R. W. Ditchburn, *Light.* New York: Interscience, 1953, ch. 11.

[5] E. I. Gordon, "A review of acoustooptical deflection and modulation devices," *Proc. IEEE*, vol. 54, pp. 1391–1401, October 1966.

[6] J. R. Kerr, "Microwave-bandwidth optical receiver systems," *Proc. IEEE*, vol. 55, pp. 1686–1700, October 1967.

[7] *Handbook of Geophysics and Space Environments*, S. L. Valley, Ed. Bedford, Mass.: USAF Cambridge Research Labs., 1965, ch. 5.

[8] J. A. Ratcliffe, "Some aspects of diffraction theory and their application to the ionosphere," *Rept. Progr. Phys.*, vol. 19, pp. 188–267, 1956.

[9] W. J. Moore, *Physical Chemistry.* Englewood Cliffs, N. J.: Prentice-Hall, 1955, ch. 7.

[10] J. P. Dougherty and D. T. Farley, "A theory of incoherent scattering of radio waves by a plasma," *Proc. Roy. Soc.* (London), vol. 259A, pp. 79–99, November 1960.

[11] A. E. Siegman, "The antenna properties of optical heterodyne receivers," *Proc. IEEE*, vol. 54, pp. 1350–1356, October 1966.

[12] T. S. Chu, "On coherent detection of scattered light," *IEEE Trans. Antennas and Propagation* (Communications), vol. AP-15, pp. 703–704, September 1967.

[13] D. L. Fried, "Atmospheric modulation noise in an optical heterodyne receiver," *IEEE J. Quantum Electronics*, vol. QE-3, pp. 213–221, June 1967.

[14] M. Bertolotti, M. Carnevale, L. Muzii, and D. Sette, "Interferometric study of phase fluctuations of a laser beam through the turbulent atmosphere," *Appl. Opt.*, vol. 7, pp. 2246–2251, November 1968.

[15] D. L. Fried, "Optical heterodyne detection of an atmospherically distorted signal wave front," *Proc. IEEE*, vol. 55, pp. 57–67, January 1967.

[16] G. R. Ochs, "Laser beam scintillation over horizontal paths from 5.5 to 145 kilometers," to be published.

[17] G. M. B. Bouricius, private communication on work in progress.

[18] J. C. Owens and K. B. Earnshaw, "Optical ranging utilizing atmospheric dispersion to correct for air density variations," *Proc. Soc. Photo-Optical Instr. Engrs. Seminar on Laser Range Instr.*, (El Paso, Tex., October 16–17, 1967), pp. 25–34.

[19] W. D. Conner and J. R. Hodkinson, "Optical properties and visual effects of smoke-stack plumes," U. S. Dept. of Health, Education, and Welfare, Public Health Service Pub. 999-AP-30, 1967.

Statistical Information Content of Radiation Measurements used in Indirect Sensing[1]

Ed R. Westwater and Otto Neall Strand

Institute for Telecommunication Sciences and Aeronomy, ESSA, Boulder, Colo.

(Manuscript received 17 October 1967)

ABSTRACT

The information content of radiation measurements used in inferring profiles is defined as a reduction in uncertainty in the estimation of a profile after the measurements are introduced. The information is shown to depend directly on the kernel of the equation of radiative transfer, the covariance matrix of experimental error, and the covariance matrix of the *a priori* statistical information. Calculations based on the minimum rms inversion method are applied to the indirect probing of the vertical temperature distribution by microwave measurements of oxygen thermal emission. Choice of optimum location of measurements is discussed and comparison of the proposed method with that of Twomey is given.

1. Introduction

The information content of radiation measurements has been studied previously by Twomey (1965, 1966) and Mateer (1965). These studies have shown that the information obtainable from indirect soundings is severely limited by the interdependence of the measurements themselves. In a loose sense, the "number of independent pieces of information" was taken to be the number of eigenvalues of a kernel-determined matrix which were greater than some assigned noise level. However, the information content of a signal should be judged by the *new* information that it adds to information already known. In many problems of indirect sensing, statistical information about the profile is known before any radiation measurements are made. This *a priori* knowledge is embodied in the mean and the covariance matrix, both of which can be estimated from past data (usually taken by direct measurements). Such data are currently being used in remote sensing problems in the construction of empirical orthogonal functions (Wark and Fleming, 1966; Alishouse *et al.*, 1967). The use of such data to assess the usefulness of radiation measurements in reducing the statistical variance of the unknown function is not well known.

In Section 2, we summarize recently developed inversion techniques (Strand and Westwater, 1968a, b), which lead quite naturally to a definition of information content. Applications of this quantity to remote probing of tropospheric temperature structure by the microwave emission lines of oxygen are given in Section 3. The choice of optimum frequencies is discussed, and our method of choice is compared with that of Twomey (1966).

2. The minimum rms inversion method and its relation to information content

Let $f(y)$ be a continuous random function on the interval $[a,b]$. If $K(x,y)$ is a continuous function of x and y and if

$$\int_a^b K(x,y)f(y)dy = g(x), \qquad (1)$$

then $g(x)$ is also a continuous random function. In indirect-sensing problems, it is wished to infer $f(y)$ by measuring $g(x)$ at a set of values of x, say x_i, $i=1$, 2, $\cdots$, n. Introducing a suitable quadrature approximation to (1) gives the matrix equation

$$\mathbf{Af} = \mathbf{g}, \qquad (2)$$

where

$\mathbf{A} = (A_{ij})$, $i = 1$, 2, $\cdots$, n; $j = 1$, 2, $\cdots$, m,
m is the number of quadrature abscissas,
n is the number of observations of $g(x)$,
$A_{ij} = w_j K(x_i, y_j)$,
$y_j =$ quadrature abscissas,
$x_i =$ values of x for which $g(x)$ is observed,
$w_j =$ quadrature weight associated with y_j,
$f_j = f(y_j)$,
$g_i = g(x_i)$,
$\mathbf{f} = [f_1 f_2 \cdots f_m]^T$ is the column vector of unknown functional values (the superscript T denotes matrix transposition), and
$\mathbf{g} = [g_1 g_2 \cdots g_n]^T$ is the column vector of values of $g(x)$.

Assume that the mean vector $\mathbf{E}(\mathbf{f}) = \mathbf{f}_0$ and the covariance matrix, $\mathbf{S}_f \equiv \mathbf{E}[(\mathbf{f}-\mathbf{f}_0)(\mathbf{f}-\mathbf{f}_0)^T]$ are known. [$\mathbf{E}(\ )$ denotes the expected value operator and $\mathbf{S}_v$ denotes the covariance matrix of any vector $\mathbf{v}$]. In prac-

tice, $\mathbf{f}_0$ and $\mathbf{S}_f$ may be estimated from the past history of the function f. By the linearity $\mathbf{E}$ and the propagation rule for covariance matrices (Deutsch, 1965), we have $\mathbf{E}(\mathbf{g}) = \mathbf{g}_0$ and $\mathbf{S}_g = \mathbf{A}\mathbf{S}_f\mathbf{A}^T$. In the problem of interest here, $\mathbf{g}$ is a vector of measurements subject to error. Thus, one observes

$$\mathbf{g}_e = \mathbf{g} + \varepsilon \qquad (3)$$

instead of $\mathbf{g}$. In addition to the above assumptions, we assume 1) the errors ϵ_i are independent of $\mathbf{f}$, and hence are independent of $\mathbf{g}$; 2) the errors ϵ_i have a multivariate distribution with mean zero and known covariance $\mathbf{S}_\epsilon$; 3) the errors introduced by the quadrature approximation of Eqs. (1) and (2) are negligible with respect to ε; and, 4) $\mathbf{S}_\epsilon$ and $\mathbf{S}_f$ are both nonsingular with dimensions $n \times n$ and $m \times m$, respectively.

Much of the previous work in the field has emphasized the importance of representing the solution by means of a suitable basis (Wark and Fleming, 1966; Alishouse et al., 1967). This representation was necessary because previous inversion methods solved for a fixed number of parameters (usually small), the number being determined by the degree of independence of the measurements and the measurement noise level. The usual bases chosen in these methods were the eigenvectors of $\mathbf{S}_f$, arranged in decreasing order of eigenvalues. However, it was shown by Strand and Westwater (1968b) that with the minimum rms inversion method the introduction of a basis matrix to represent the solution (other than the identity in m dimensions) is neither necessary nor desirable. The computational difficulties which occur in determining the eigenvectors and eigenvalues of a large matrix may be circumvented by this method. Hence, in the following, the only desired representation of the unknown function will be its values at the m quadrature points. The following will summarize the results of Strand and Westwater (1968b).

Let $\eta = \mathbf{f} - \mathbf{f}_0$, $\mathbf{h} = \mathbf{g} - \mathbf{g}_0 = \mathbf{A}(\mathbf{f} - \mathbf{f}_0) = \mathbf{A}\eta$ and let the reduced observed data (with respect to the mean) be $\mathbf{h}_e$, where

$$\mathbf{h}_e = \mathbf{A}\eta + \varepsilon. \qquad (4)$$

The estimate of η, $\hat{\eta}$, is determined as a linear combination of the data

$$\hat{\eta} = \mathbf{B}\mathbf{h}_e, \qquad (5)$$

where $\mathbf{B}$ is an $m \times n$ matrix to be determined. The matrix $\mathbf{B}$ is uniquely determined by requiring that the fit to η be the best on the average in the mean-square sense, i.e., that $\mathbf{E}\{(\hat{\eta} - \eta)^T(\hat{\eta} - \eta)\}$ is minimized with respect to $\mathbf{B}$. Here, the expected value is taken over the joint probability distribution of $\mathbf{f}$ and ε. This requirement leads to the optimum linear unbiased estimate of η as

$$\hat{\eta} = \mathbf{S}_f\mathbf{A}^T\mathbf{H}^{-1}\mathbf{h}_e, \qquad (6a)$$

where

$$\mathbf{H} = \mathbf{S}_\epsilon + \mathbf{A}\mathbf{S}_f\mathbf{A}^T,$$

or alternatively

$$\hat{\eta} = \mathbf{X}^{-1}\mathbf{A}^T\mathbf{S}_\epsilon^{-1}\mathbf{h}_e, \qquad (6b)$$

where

$$\mathbf{X} = \mathbf{S}_f^{-1} + \mathbf{A}^T\mathbf{S}_\epsilon^{-1}\mathbf{A}.$$

The equivalence of (6a) and (6b) follows from the identity

$$\mathbf{A}^T\mathbf{S}_\epsilon^{-1}\mathbf{H} = \mathbf{X}\mathbf{S}_f\mathbf{A}^T, \qquad (7)$$

which relates the $n \times n$ matrix $\mathbf{H}$ to the $m \times m$ matrix $\mathbf{X}$. Similar results have been obtained by C. D. Rodgers[2] of Oxford University. The covariance matrix of the solution, $\mathbf{S}_{\hat{\eta}-\eta}$, is given by

$$\mathbf{S}_{\hat{\eta}-\eta} = \mathbf{X}^{-1}. \qquad (8)$$

A convenient overall quality criterion is the sum of the diagonal elements of $\mathbf{S}_{\hat{\eta}-\eta}$, i.e., $\mathrm{Tr}(\mathbf{S}_{\hat{\eta}-\eta})$ where $\mathrm{Tr}(\ )$ denotes the trace. Thus,

$$\mathrm{Tr}\{\mathbf{S}_{\hat{\eta}-\eta}\} = \mathrm{Tr}\mathbf{X}^{-1}. \qquad (9)$$

It can be shown that the trace of $\mathbf{S}_{\hat{\eta}-\eta}$ is m times the expected mean-square error.

The statistical information added by the radiation measurements may be determined by comparison of (9) with the trace of $\mathbf{S}_f$. In the absence of any measurements the best estimate of $\mathbf{f}$ is $\mathbf{f} = \mathbf{f}_0 (\eta = 0)$ with an overall variance $\mathrm{Tr}\mathbf{S}_f$. Adding measurements modifies the estimate to (6), reduces the overall variance to $\mathrm{Tr}\mathbf{X}^{-1}$, and reduces the variance by $\mathrm{Tr}(\mathbf{S}_f - \mathbf{X}^{-1})$. Useful quantities for judging the information are

$$R = \mathrm{Tr}(\mathbf{S}_f - \mathbf{X}^{-1}), \qquad (10)$$

$$F = \frac{\mathrm{Tr}(\mathbf{S}_f - \mathbf{X}^{-1})}{\mathrm{Tr}\mathbf{S}_f}, \qquad (11)$$

$$U = \left(\frac{\mathrm{Tr}\mathbf{X}^{-1}}{m}\right)^{\frac{1}{2}}, \qquad (12)$$

where R is the total reduction in variance, F is the fractional reduction, and U is the standard deviation per point. From this point of view, the maximum reduction in variance yielded by m independent errorless measurements would be $\mathrm{Tr}\mathbf{S}_f$. The information contained in $n (< m)$ independent errorless measurements is easily obtained by letting $\mathbf{S}_\epsilon \to 0$ in (6), (7), and (8) as

$$R = \mathrm{Tr}\{\mathbf{S}_f - \mathbf{S}_f\mathbf{A}^T(\mathbf{A}\mathbf{S}_f\mathbf{A}^T)^{-1}\mathbf{A}\mathbf{S}_f\}. \qquad (13)$$

In any practical remote-sensing experiment, information is limited in two ways: 1) the number of independent measurements that can be taken is small, and 2) measurement errors are always present. The usefulness of the experiment can be judged by determining

[2] Dr. Rodgers has graciously shown us his results for comparison of inversion methods.

R, F and U as functions of $\mathbf{S}_f$, $\mathbf{S}_\epsilon$ and $\mathbf{A}$. If F is used, the theoretical maximum achievable information is $F = 1$ and occurs when $n = m$ and $\mathbf{S}_\epsilon = 0$.

The quantity R (or F) may also be used to study the optimum placement of measurements. The optimum placement is achieved, given that the number n is fixed, when the function R (or F) achieves its maximum over the range of x. The optimum set derived in this way can differ considerably from the set as chosen by the method of Twomey (1966). This is shown in the following section by a physically-reasonable numerical example. Since R depends on $\mathbf{S}_f$, the optimum set also depends on $\mathbf{S}_f$. This implies that large seasonal or geographic variations could influence the optimum choice.

3. Application to indirect temperature sensing

The possibilities of inferring the vertical temperature profile from measurements of microwave thermal emission by oxygen are well known. Meeks and Lilley (1963) discussed the determination of the gross temperature profile from 40 km to sea level by satellite observations; Westwater (1965) discussed determining the tropospheric temperature profile by ground-based techniques. The calculations reported here are intended to illustrate the usefulness of the quality criteria given in Section 2 in planning indirect-sensing experiments and to indicate the accuracy that oxygen thermal emission measurements can yield.

Microwave radiometric measurements are usually expressed as an equivalent emission temperature or effective antenna temperature (Shklovsky, 1960). This effective temperature is both the frequency average over the bandwidth of the receiver and the weighted directional average over the radiometer's antenna pattern of radiation received from all frequencies and directions. The uni-directional, monochromatic radiation from any infinitesimal solid angle is expressed as the brightness temperature $T_b(\nu)$ at frequency ν. Thus,

the brightness temperature may be regarded as the antenna temperature of an idealized radiometer which only accepts radiation from a single direction and frequency. The brightness temperature observed looking vertically through an atmosphere of thickness H is given by

$$T_b(\nu) = T_b{}^0(\nu) \exp[-\tau_\nu(0,H)]$$
$$+ \int_0^H T(h)\alpha_\nu(h) \exp[-\tau_\nu(0,h)]dh, \quad (14)$$

where

$$\tau_\nu(0,h) = \int_0^h \alpha_\nu(h)dh,$$

$\alpha_\nu(h)$ is the absorption per unit length, $T(h)$ temperature, h the distance from radiometer, and $T_b{}^0(\nu)$ the unattenuated brightness temperature from external sources.

The microwave absorption coefficient α_ν is due to water vapor and oxygen. At frequencies near 60 GHz, the fractional contribution due to water vapor is small and will be neglected here. For humid locations the introduction of a model atmosphere to account for the wet component might be justified (Dutton and Bean, 1965). The absorption due to oxygen can be calculated as a function of temperature and pressure from the Van Vleck equation (Van Vleck, 1947). The major uncertainty in these calculations is the pressure dependence of the oxygen line widths (Meeks and Lilley, 1963). The calculations here are based on a quadratic expansion of line width as a function of pressure, with constants derived from a least-squares fit to the data of Artman (1953); the line widths are assumed to have a temperature dependence of $T^{-0.85}$. The details of the line width analysis are given by Westwater and Strand (1967). In the height region of interest here (0 − 10 km) Doppler and Zeeman broadening are negligible.

The temperature mean and covariance matrices were obtained by averaging 5 years of February radiosonde data (163 soundings) taken at Denver, Colo. If we denote the mean temperature at the quadrature point h_i by $\bar{T}(h_i)$ and the i, j element of the covariance matrix by $(\mathbf{S}_T)_{ij} \equiv \mathbf{S}_T(h_i,h_j)$, then

$$\bar{T}(h_i) = \frac{1}{N}\sum_{\rho=1}^{N} T_\rho(h_i), \quad (15)$$

and

$$\mathbf{S}_T(h_i,h_j) = \frac{1}{N-1}\sum_{\rho=1}^{N}[T_\rho(h_i) - \bar{T}(h_i)]$$
$$\times[T_\rho(h_j) - \bar{T}(h_j)], \quad (16)$$

where N is the number of pieces of data and ρ is an index for each member of the sample. Table 1 gives the mean T and P at the Gauss-Legendre quadrature heights

TABLE 1. Mean temperature and pressure for Denver, February (h is height above surface in km).

Downward			Upward		
$s = 10-h$ (km)	$\bar{T}(s)$ (°K)	$\bar{P}(s)$ (mb)	h (km)	$\bar{T}(h)$ (°K)	$\bar{P}(h)$ (mb)
0.060	217.315	201.659	0.000	267.956	831.423
0.314	217.666	209.799	0.140	269.781	816.770
0.759	218.282	224.897	0.416	269.474	788.533
1.378	219.138	247.703	0.723	268.102	758.244
2.145	222.138	278.691	0.943	266.806	737.167
3.029	226.598	318.933	1.094	265.866	722.982
3.994	232.577	368.134	1.462	263.574	689.408
5.000	239.914	425.960	2.000	260.161	642.664
6.006	247.069	490.838	2.538	256.857	598.547
6.971	253.704	560.410	2.906	254.517	569.811
7.855	259.270	630.462	3.328	251.729	538.201
8.622	264.095	696.903	4.615	242.720	450.398
9.241	267.891	754.769	6.500	228.973	342.680
9.686	269.588	798.907	8.385	219.466	257.053
9.940	268.740	825.097	9.672	217.686	210.282

TABLE 2. Temperature covariance matrix for downward inversion for Denver, February. $(S_T)_{ij} = S_T(s_i,s_j)$ [°K²] and s_i are the quadrature distances (km) given in Table 1.

35.50	33.10	26.59	15.06	0.00	−13.24	−18.91	−21.80	−22.54	−22.76	−24.80	−26.39	−27.44	−25.87	−15.46
	32.49	27.03	16.14	1.44	−11.60	−17.49	−20.67	−21.20	−21.25	−23.12	−24.63	−25.33	−23.74	−14.07
		25.70	17.42	4.59	−7.13	−12.89	−16.34	−16.64	−16.72	−18.27	−19.78	−20.24	−18.65	−11.42
			16.18	8.58	.28	−4.63	−7.74	−8.23	−8.44	−9.41	−10.55	−10.82	−9.21	−5.79
				12.19	11.30	8.98	6.65	5.83	5.29	4.89	4.61	4.55	4.96	2.25
					21.24	22.25	20.76	19.82	19.16	20.08	20.47	20.34	19.35	12.21
						27.55	28.25	27.75	27.09	27.77	28.36	28.34	27.02	18.41
							32.12	31.93	31.00	31.28	32.10	32.42	30.78	21.07
$(S_T)_{ij}=(S_T)_{ji}$								33.85	33.54	33.54	34.04	34.38	32.48	22.81
									35.22	35.47	35.75	36.19	34.27	24.80
										39.46	40.49	40.93	38.76	28.29
											45.62	47.43	44.77	31.98
												51.39	49.17	35.14
													50.98	36.61
														36.07

used in the downward inversion and at the three-interval Gauss-Radau quadrature heights for the upward inversion. The covariance matrix for downward inversion is given in Table 2. These matrix elements are associated with height as

$$(S_T)_{ij} \equiv S_T(s_i,s_j) \equiv S_T(10-h_i,\, 10-h_j),$$

where s_k is the distance from the radiometer.

For many ground-based probing schemes, the value of the unknown $\mathbf{f}$ at the surface can usually be measured directly. This constrained point can be used to modify the statistical estimation and its uncertainty as follows. First, the constraint can be incorporated directly into the integral equation by using a quadrature formula (such as Gauss-Radau), which uses the value f_1 of the function at 0, directly, i.e.,

$$\int_0^H K(x,y)f(y)dy = \sum_{j=1}^m w_j K(x,y_j)f(y_j)$$

$$= w_1 K(x,0)f_1 + \sum_{j=2}^m w_j K(z,y_j)f(y_j). \quad (17)$$

By subtracting $w_1 K(x,0)f_1$ from the reduced measured quantity h_e, a matrix equation to be solved for the $(m-1)$ components of the function $\mathbf{f}$ is obtained.

Second, knowing f_1 reduces the uncertainty in all the other functional values. The new covariance matrix $S_f^{(c)}$, of dimension $(m-1) \times (m-1)$, has elements

$$S_{ij}^{(c)} = S_{ij} - \frac{S_{1i}S_{1j}}{S_{11}}, \quad i,\, j = 2, 3, \cdots, m,$$

where

$$S_f \equiv (S_{ij}) \quad \text{and} \quad S_f^{(c)} = (S_{ij}^{(c)}). \quad (18)$$

For convenience, the matrix $S_f^{(c)}$ will be referred to in the following as the constrained covariance matrix. Furthermore, instead of the mean f_0 as the best *a priori* estimate of $\mathbf{f}$, the effect of knowing the first value f_1 modifies this optimum *a priori* estimate to $\hat{\mathbf{f}}$, where

$$\hat{f}_i = f_{0i} + \frac{S_{i1}}{S_{11}}(f_1 - f_{01}), \quad i = 2, 3, \cdots, m. \quad (19)$$

Eqs. (18) and (19) may be derived from linear regressions of the $(m-1)$ functional values $f_2, f_3, \cdots f_m$ as functions of the surface value f_1 (Westwater and Strand, 1967).

The unconstrained and constrained "upward" covariance matrices for the Denver February temperature structure are shown in Tables 3 and 4, respectively.

TABLE 3. Temperature covariance matrix for upward unconstrained inversion for Denver, February. $(S_T)_{ij} = S_T(h_i,h_j)$ [°K²] and h_i are the quadrature heights (km) given in Table 1.

35.49	36.36	35.51	34.39	33.56	32.89	30.85	28.41	25.15	23.89	23.43	20.25	15.14	−2.74	−12.39
	46.54	46.24	44.50	43.30	42.38	39.66	36.11	31.85	30.47	30.22	27.30	20.90	−3.94	−19.63
		50.74	49.92	48.80	47.83	44.82	40.65	35.67	34.13	33.91	30.91	23.71	−4.95	−23.01
			51.19	50.33	49.46	46.49	42.17	37.05	35.54	35.39	32.10	24.57	−6.00	−24.12
				49.94	49.19	46.55	42.34	37.28	35.78	35.59	32.29	24.93	−5.94	−24.04
					48.59	46.18	42.13	37.14	35.61	35.42	32.15	24.97	−5.97	−23.99
$(S_T)_{ij}=(S_T)_{ji}$						44.77	41.53	36.93	35.36	35.17	31.97	24.88	−5.92	−23.64
							40.34	36.70	35.16	34.93	31.56	24.65	−5.32	−22.79
								35.41	34.39	34.16	30.37	23.39	−4.52	−20.87
									34.11	34.20	30.49	23.29	−4.15	−20.34
										34.82	31.28	23.68	−4.01	−20.34
											31.59	24.37	−3.12	−20.09
												24.47	1.38	−14.57
													12.96	11.21
														31.85

TABLE 4. Temperature covariance matrix for upward constrained inversion for Denver, February. $(S_{T^{(c)}})_{ij} = S_{T^{(c)}}(h_{i+1}, h_{j+1})$ [°K²] and h_i are the quadrature heights (km) given in Table 1.

9.29	9.86	9.27	8.92	8.68	8.05	7.00	6.08	5.99	6.22	6.55	5.39	−1.13	−6.94
	15.21	15.51	15.22	14.92	13.95	12.22	10.51	10.23	10.47	10.65	8.56	−2.21	−10.61
		17.87	17.81	17.59	16.60	14.64	12.68	12.39	12.69	12.48	9.90	−3.34	−12.11
			18.21	18.09	17.38	15.47	13.50	13.19	13.43	13.14	10.61	−3.35	−12.32
				18.11	17.59	15.80	13.83	13.47	13.71	13.38	10.94	−3.43	−12.51
					17.95	16.83	15.07	14.59	14.80	14.37	11.72	−3.54	−12.87
						17.60	16.57	16.04	16.17	15.35	12.53	−3.13	−12.87
							17.59	17.46	17.56	16.02	12.66	−2.58	−12.09
								18.03	18.43	16.86	13.10	−2.31	−12.00
									19.35	17.91	13.68	−2.20	−12.05
										20.04	15.73	−1.56	−13.02
											18.01	2.55	−9.28
												12.75	10.25
													27.52

$(S_{T^{(c)}})_{ij} = (S_{T^{(c)}})_{ji}$

Here $(S_T)_{ij} = S_T(h_i, h_j)$ and $(S_{T^{(c)}})_{ij} = S_{T^{(c)}}(h_{i+1}, h_{j+1})$, where the h_k are the quadrature heights given in Table 1. The surface constraint reduces the matrix elements describing the lower atmosphere but has little effect on the upper levels. The trace is reduced from 572.81 (°K)² to 247.52 (°K)².

To study the information added by oxygen emission measurements, calculations were made for five frequencies and several choices of measurement error for both upward and downward inversion over the 10-km height interval. The kernel was determined from the mean temperature and pressure data given in Table 1. Since the kernel is temperature-dependent, an inversion scheme based on the linear methods given here would necessarily be iterative (Westwater, 1965). The brightness temperatures and optical depths for the mean profile are given in Table 5. In the upward

calculations, the emission above 10 km is neglected; in the downward case, the ground is assumed to be a blackbody radiating at the surface temperature T_0. An example of a solution covariance matrix is given in Table 6 for the downward inversion with each of the five measurements having an assumed rms error of 0.1K in the brightness temperature. This matrix is to be compared with Table 2 to show the reduction in uncertainty of the profile estimation by the introduction of the five measurements.

The meaning of a 15×15 covariance matrix is difficult to present in simple form. A rough estimate of the standard deviation to be expected at each quadrature height is given by the square root of the corresponding diagonal element of the covariance matrix. These quantities are plotted as functions of height in Figs. 1–3. In all cases shown, the measurement error covariance matrix is scalar, $S_\epsilon = \sigma_\epsilon^2 I$, where σ_ϵ is the standard deviation in °K and I is the $n \times n$ identity matrix. The reduction of the total error in the temperature profile by various choices of σ_ϵ is given in Table 7. For example, in the case of upward constrained inversion with brightness temperature errors of 1K in each of the five measurements, the variance is reduced by $R = 178.13$ (°K)², the fractional reduction $F = 0.72$, and the remaining uncertainty per point U is 2.1K. It is apparent that many experimental possibilities can be investigated with the preceding methods.

TABLE 5. Calculated brightness temperature, T_b and optical depths τ, for Denver, February, mean profile; $T_0 = 267.956$K.

	Upward		Downward	
ν (GHz)	T_b (°K)	τ	T_b (°K)	$T_b + T_0 e^{-\tau}$ (°K)
51.2	100.699	0.514	98.665	259.461
53.3	195.022	1.448	184.798	248.055
55.0	260.669	4.668	226.924	229.459
57.3	268.089	14.674	219.516	219.516
61.193059	268.633	20.677	218.731	218.731

TABLE 6. Solution covariance matrix for downward inversion for Denver, February. $\sigma_\epsilon = 0.1$K; $X_{ij}^{-1} = X^{-1}(s_i, s_j)$ [°K²]; and s_i are the quadrature distances (km) given in Table 1.

1.70	0.41	−0.76	−0.81	−0.11	0.32	0.42	0.43	0.07	−0.11	−0.17	−0.10	−0.36	−0.43	−0.23
	0.57	−0.32	−0.61	−0.16	0.26	0.28	0.21	0.04	−0.03	−0.10	−0.09	−0.13	−0.24	−0.10
		0.81	0.13	−0.33	−0.21	−0.03	−0.01	0.19	0.17	0.09	−0.09	−0.06	−0.14	−0.24
			1.38	0.19	−0.60	−0.57	−0.26	0.01	0.14	0.17	0.06	0.14	0.45	0.54
				1.26	−0.05	−0.52	−0.56	−0.44	−0.20	−0.04	0.40	0.68	0.77	0.19
					1.47	0.38	−0.72	−0.99	−0.79	0.12	0.64	0.71	0.50	0.32
						1.87	0.28	−0.18	−0.34	−0.23	−0.13	−0.23	−0.16	0.22
							1.65	0.93	0.10	−0.66	−0.84	−0.87	−0.78	−0.67
								1.84	1.21	−0.27	−1.24	−1.56	−1.69	−1.28
									2.15	0.47	−1.19	−1.76	−1.94	−1.19
										1.87	0.28	−1.19	−0.75	−0.67
											2.08	1.95	1.01	−0.08
												3.64	3.08	1.14
													6.37	3.59
														10.74

$(X^{-1})_{ij} = (X^{-1})_{ji}$

Table 7. Solution error vs error in brightness temperature for five frequencies of Table 5.
$S_\epsilon = \sigma_\epsilon^2 I \, [°K]^2$. All values in $(°K)^2$.

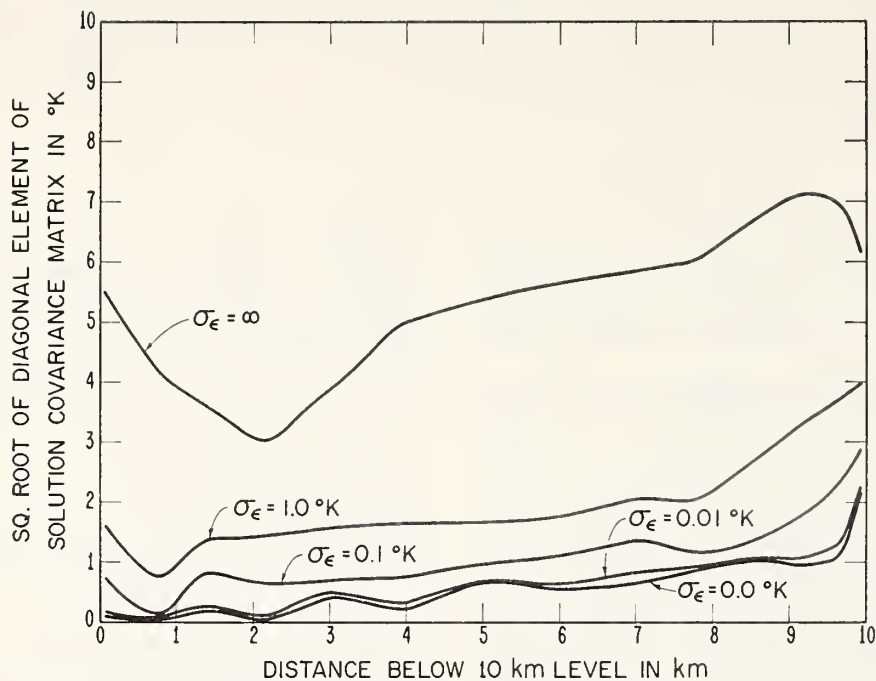|	TrS_T	$\sigma_\epsilon = 0$	$\sigma_\epsilon = 0.01$	$\sigma_\epsilon = 0.1$	TrX^{-1} $\sigma_\epsilon = 0.5$	$\sigma_\epsilon = 1.0$	$\sigma_\epsilon = 1.5$	$\sigma_\epsilon = 2.0$
Downward	495.56	19.68	21.63	38.39	66.61	91.45	114.10	138.23
Upward	572.81	21.83	27.54	44.17	63.68	78.63	91.98	104.07
Upward constrained	247.52	18.27	23.19	37.85	55.54	69.29	81.53	92.79

Fig. 1. Square root of diagonal element of solution covariance matrix (°K) vs distance below 10-km level for various values of σ_ϵ. Downward inversion, five frequencies, Denver, February.
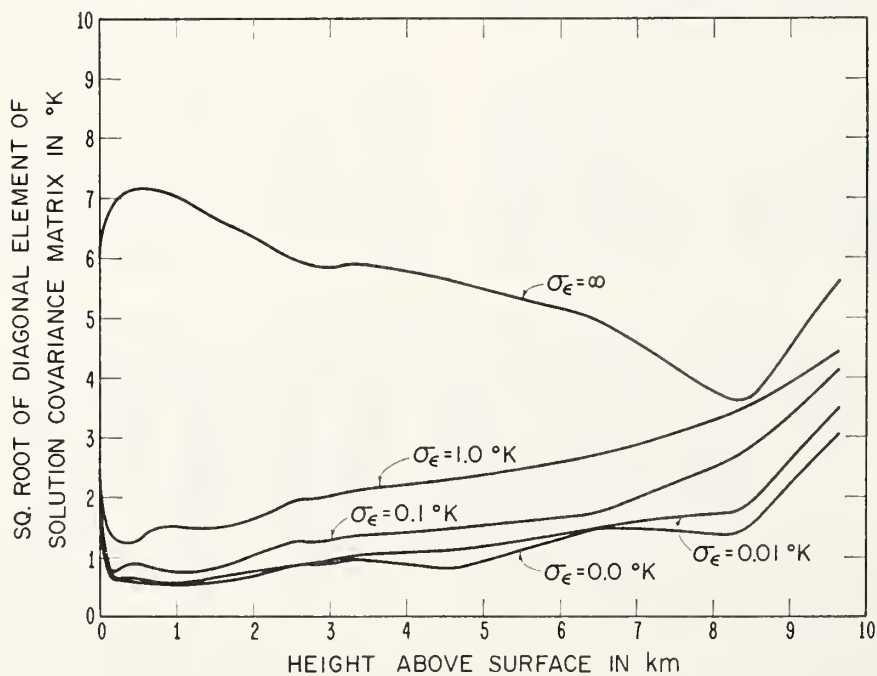
Fig. 2. Same as Fig. 1 except for height above surface and unconstrained upward inversion.
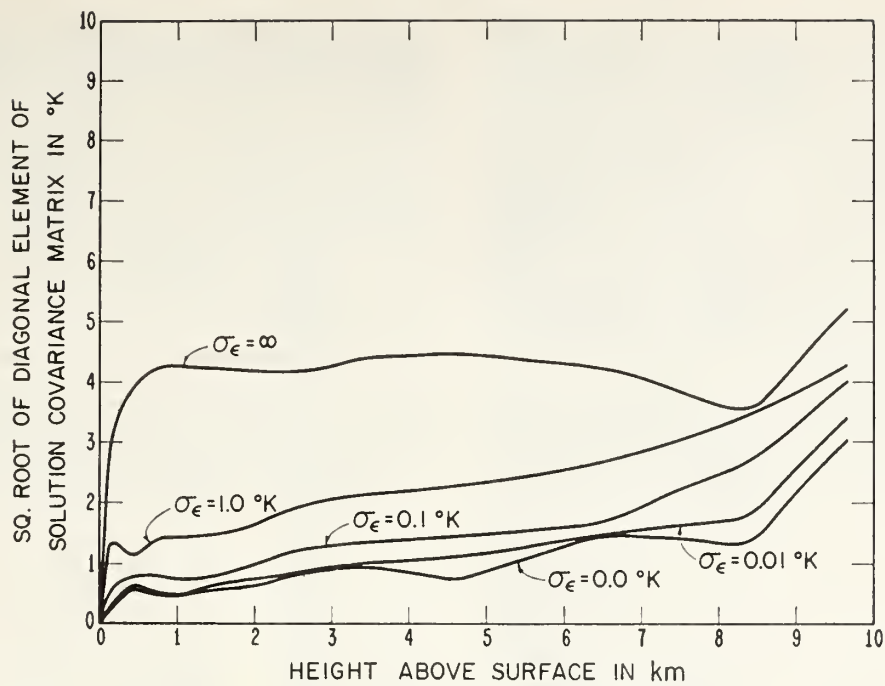
FIG. 3. Same as Fig. 2 except for constrained upward inversion.

4. Interdependence and optimum location of measurements

Twomey (1966) has given an explicit procedure for determining the optimum location of measurements. This method orders a set of measurements by systematically eliminating the most redundant of the set and is based entirely on the properties of the kernel. However, when the information contained in the *a priori* statistics, S_f, is introduced, an additional correlation between radiation measurements and S_f occurs. Thus, if we define the optimum subset of a large set of measurements as the subset which yields a minimum TrX^{-1} (i.e., minimum expected mean-square error), the order-

TABLE 8. Solution variance TrX^{-1} [°K²] resulting from successive introduction of measurements for Denver, February. $TrS_f^{(D)}$ = 495.56 (°K)², $TrS_f^{(UU)}$ = 572.81 (°K)², $TrS_f^{(UC)}$ = 247.52 (°K)² where D is downward, UU upward unconstrained, UC upward constrained; frequency is in GHz and σ_ϵ is the rms measurement error.

		σ_ϵ (°K)				
		0.0	0.1	0.5	1.0	Twomey's downward frequency ranking (GHz)
1 Freq (1)	D	292.01	292.11	294.51	301.66	(1) 61.193059
	UU	136.26	136.36	138.74	146.01	(2) 55.0
	UC	119.31	119.47	123.09	133.20	(3) 53.3
						(4) 57.3
						(5) 51.2
2 Freq (1, 2)	D	109.63	110.03	119.39	145.33	Twomey's upward unconstrained frequency ranking (GHz)
	UU	65.50	65.89	74.18	92.93	(1) 61.193059
	UC	58.78	59.31	69.10	85.28	(2) 53.3
						(3) 57.3
3 Freq (1, 2, 3)	D	47.15	48.94	73.13	100.77	(4) 55.0
	UU	50.10	53.57	71.11	88.90	(5) 51.2
	UC	40.51	42.82	58.76	73.28	Twomey's upward constrained frequency ranking (GHz)
4 Freq (1, 2, 3, 4)	D	32.40	41.68	71.89	97.93	(1) 61.193059
	UU	36.18	46.28	65.62	80.89	(2) 55.0
	UC	29.07	39.98	57.45	71.54	(3) 53.3
						(4) 57.3
						(5) 51.2
5 Freq (1, 2, 3, 4, 5)	D	19.68	38.39	66.61	91.45	
	UU	21.83	44.17	63.68	78.63	
	UC	18.27	37.85	55.54	69.29	

ing of sets will differ, in general from that obtained by Twomey's method. In addition, the dependence of observations is described differently here. Instead of an effective "number of independent pieces of information," all measurements will reduce the variance of the solution and are considered as information. The dependence of measurements is seen as a law of diminishing returns and adding additional dependent measurements reduces the variance very little. However, if one is willing to pay the cost, the variance can be reduced to any arbitrarily small level by proper selection of a large number of observations.

The effect of dependence of measurements was studied for the microwave inversion problem as follows. Kernels corresponding to the five frequencies of Table 5 were ranked in the order of decreasing strength by the method of Twomey. The solution variance was calculated for a number of assumed experimental errors as each of these observations was successively added. These results are shown in Table 8. In the errorless cases, each successive measurement reduces the variance by substantial amounts; when errors are introduced, the reduction of variance after the first two or three measurements are added is small. The non-optimality of Twomey's method of measurement ranking is evident since cases occur when the addition of a channel reduces the variance more than its predecessor.

The optimum subset of a large number of possible measurements will depend on the kernel and the covariance matrices of the statistics and experimental error. In general, the optimum will also depend on the number of elements in the subset. The rankings of the five frequencies for one-frequency and two-frequency optimums are shown in Tables 9 and 10, respectively, for the upward constrained case. Note that the ranking changes for different choices of experimental error, and that all rankings differ from those based from Twomey's scheme which is based only on the kernel.

The determination of an optimum set of frequencies from an ensemble large enough to adequately cover the entire oxygen band would be a large computational chore. If N frequencies suffice to cover the band and one wishes to determine an optimum M of them, then $N!/(N-M)!M!$ trace computations must be compared

TABLE 9. One-frequency expected mean-square errors TrX^{-1} [°K²] for Denver, February; upward constrained inversion. Ranking according to minimum trace criterion is enclosed in parentheses. $TrS_f = 274.52$ (°K)² and σ_ϵ is the rms measurement error.

| Twomey's ranking | Frequency (GHz) | σ_ϵ(°K) | | |
		0.0	0.5	1.0
1	61.193059	119.31 (5)	123.09 (5)	133.20 (4)
2	55.0	78.09 (2)	81.70 (2)	91.68 (1)
3	53.3	74.30 (1)	80.73 (1)	97.43 (2)
4	57.3	105.45 (4)	109.03 (4)	118.78 (3)
5	51.2	79.44 (3)	101.46 (3)	142.66 (5)

TABLE 10. Two-frequency expected mean-square errors TrX^{-1} [°K²] for Denver, February; upward constrained inversion. Ranking according to minimum; trace criterion is enclosed in parentheses. $TrS_f = 247.52$ (°K)² and σ_ϵ is the rms measurement error.

| Twomey's ranking | Frequency (GHz) | σ_ϵ(°K) | | |
		0.0	0.5	1.0
1 2	61.193059 55.0	58.78 (9)	69.10 (4)	85.28 (4)
1 3	61.193059 53.3	56.40 (7)	65.14 (2)	82.61 (3)
1 4	61.193059 57.3	75.89 (10)	106.30 (10)	116.63 (10)
1 5	61.193059 51.2	58.58 (8)	77.66 (8)	103.86 (9)
2 3	55.0 53.3	50.54 (2)	66.23 (3)	79.95 (1)
2 4	55.0 57.3	55.48 (5)	69.53 (5)	85.77 (6)
2 5	55.0 51.2	51.12 (3)	69.99 (6)	85.34 (5)
3 4	53.3 57.3	54.01 (4)	63.54 (1)	80.69 (2)
3 5	53.3 51.2	49.38 (1)	78.62 (9)	93.53 (7)
4 5	57.3 51.2	55.79 (6)	74.30 (7)	97.39 (8)

to determine a minimum. In view of the high cost of microwave radiometers, however, such calculations might be in order.

5. Conclusion

It was shown that the information content of radiation measurements used for remote probing can be defined with reference to *a priori* information. Comparison of the solution quality criterion, TrX^{-1} (m times the mean-square error), with the trace of the *a priori* covariance matrix, TrS_f, can be used to judge the information content. An optimum set of measurements can be defined as the set which minimizes TrX^{-1}, and is shown to depend on the *a priori* knowledge, the measurement covariance matrix, the kernel of the equation, and the order (number of elements) of the set.

Calculations of information obtainable from microwave measurements of oxygen thermal emission were carried out for a radiometer measuring upwelling and downwelling radiation from a 10-km height interval in the troposphere. Out of an initial choice of five frequencies a one-frequency and two-frequency optimum set was obtained, and comparisons were made with the optimum set obtained by the method of Twomey. The two methods differ considerably in optimum ranking.

REFERENCES

Alishouse, J. C., L. J. Crone, H. E. Fleming, F. L. Van Cleef and D. Q. Wark, 1967: A discussion of empirical orthogonal functions and their application to vertical temperature profiles. *Tellus*, 19, 477–482.

Artman, J. O., 1953: Absorption of microwaves by oxygen in the millimeter wavelength region. Columbia Radiation Laboratory Rept., 84 pp.

Deutsch, R., 1965: *Estimation Theory*. Englewood Cliffs, N. J., Prentice-Hall, Inc., 267 pp.

Dutton, E. J., and B. R. Bean, 1965: The biexponential nature of tropospheric gaseous absorption of radio waves. *Radio Sci., J. Res. Natl. Bur. Std.*, **69**D, 885–891.

Mateer, C. L., 1965: On the information content of Umkehr observations. *J. Atmos. Sci.*, **22**, 370–381.

Meeks, M. L., and A. E. Lilley, 1963: The microwave spectrum of oxygen in the earth's atmosphere. *J. Geophys. Res.*, **68**, 1683–1703.

Shklovsky, I. S., 1960: *Cosmic Radio Waves*. Harvard University Press, 444 pp.

Strand, O. N., and E. R. Westwater, 1968a: The statistical estimation of the numerical solution of a Fredholm integral equation of the first kind. *J. Assoc. Comp. Mach.*, **15**, 100–115.

——, and ——, 1968b: Minimum-rms estimation of the numeri-

cal solution of a Fredholm integral equation of the first kind. *Siam J. Numerical Anal.* (in press).

Twomey, S., 1965: The application of numerical filtering to the solution of integral equations encountered in indirect sensing measurements. *J. Franklin Inst.*, **279**, 95–109.

——, 1966: Indirect measurements of atmospheric temperature profiles from satellites: II. Mathematical aspects of the inversion problem. *Mon. Wea. Rev.*, **94**, 363–366.

Van Vleck, J. H., 1947: The absorption of microwaves by oxygen. *Phys. Rev.*, **71**, 413–424.

Wark, D. Q., and H. E. Fleming, 1966: Indirect measurements of atmospheric temperature profiles from satellites: I. Introduction. *Mon. Wea. Rev.*, **94**, 351–362.

Westwater, E. R., 1965: Ground-based passive probing using the microwave spectrum of oxygen. *Radio Sci., J. Res. Natl. Bur. Std.*, **69**D, 1201–1211.

——, and O. N. Strand, 1967: Application of statistical estimation techniques to ground-based passive probing of the tropospheric temperature structure. ESSA Tech. Rept. IER 37-ITSA 37, 87 pp.

Comparison of barium fluoride humidity element with the microwave refractometer for studies of rapid fluctuations of atmospheric humidity

B. R. Bean and R. O. Gilmer

Wave Propagation Laboratory
ESSA Research Laboratories, Boulder, Colorado 80302

Fluctuations of atmospheric humidity measured with a barium fluoride element and radio refractive index measured by a microwave refractometer are compared for a separation of 6 inches. Spectral coherence indicates good agreement up to frequencies of 2 to 4 Hz, which is also the frequency limit for good agreement between 2 refractometer cavities 12 inches apart.

The rapid variations of radio refractivity N were compared with those of relative humidity as measured with a barium fluoride (BaF_2) sensor. This device [*Jones and Wexler*, 1960], although still in the experimental stage as a field instrument, may be used to resolve variations of less than 1% relative humid-

ity up to frequencies of about 10 Hz. This instrument and two microwave refractometers were mounted at the 15-meter-level of the Gunbarrel Hill, Colorado tower and simultaneous observations were made during the breakup of a radiation inversion on the morning of October 31, 1965. Details of the site and experimental procedures have been reported by *Bean*
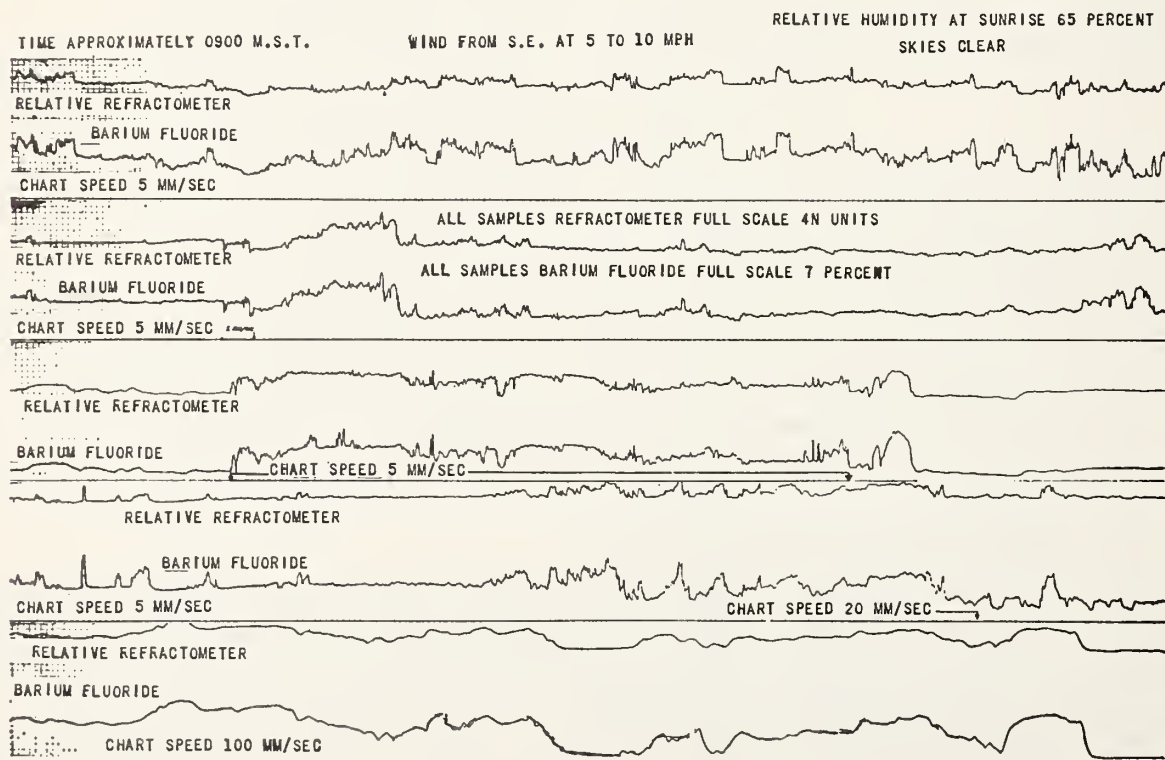
Fig. 1. Comparison between barium fluoride relative humidity sensing element and microwave relative refractometer transducers spaced 6 inches apart, 50 feet from surface of the earth, and orientated into mean wind, at Gunbarrel Hill, Colorado, October 31, 1965. Chart speeds are as marked over the indicated sample length. Each major division is 5 mm. Time elapsed for full chart length is: 5 mm/sec = 205 sec; 20 mm/sec = 51.25 sec; 100 mm/sec = 2.05 sec.

SAMPLE 1
2 Min
Δt = 1/25 sec
SPACING 6"
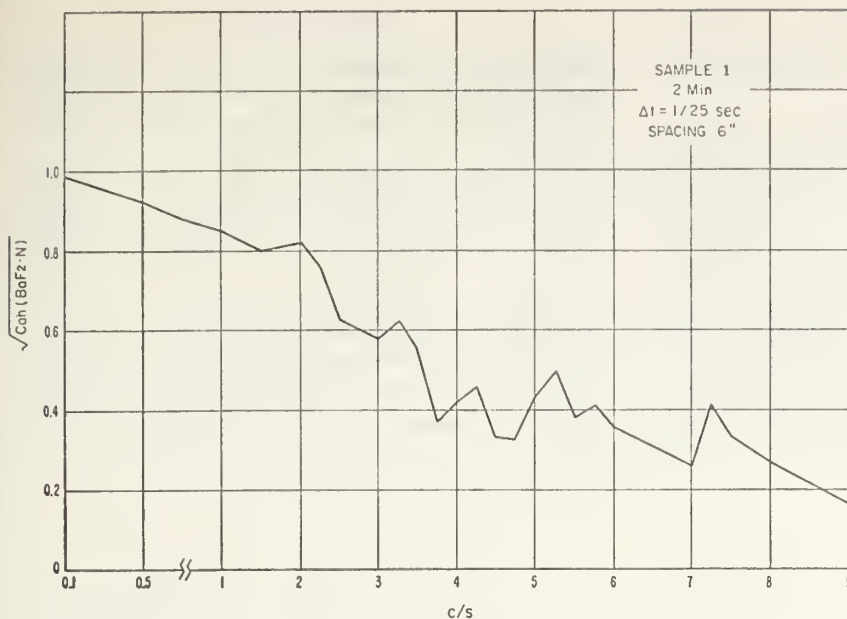
Fig. 2. Coherence of barium fluoride versus N, Gunbarrel Hill, Colorado, October 31, 1965.

. et al. [1967]. Selected samples of the data are shown in Figure 1. The two types of sensors were mounted away from the tower into the prevailing wind and showed good agreement when compared visually (Figure 1). Several samples of the data recorded on magnetic tape were digitized, and the relative humidity was converted to water vapor density and spectrally analyzed for the spectral coherence, as shown in Figures 2 and 3. The coherence plays the same role in the spectral domain as the correlation coefficient in bivariate time series analysis. It thus assumes values between zero and one. Although what one chooses as a 'significant' level of (coherence)$^{1/2}$ is quite arbitrary, the value of 0.7 (or about 50% of the spectral density) was selected. The coherence decreases to this value on all three samples between 2 and 4 Hz. One then notes (Figure 3) that the same value of coherence is reached at about 2 Hz for two refractometer cavities spaced 12 inches apart. For the average wind speeds of 5–10 mph during the experiment, one would expect 2.2 to 4.4 meters of air to pass the sampling elements per second. The observed 2 to 4 Hz would then correspond to a range of eddy sizes of 0.55 to 2.2 meters, which is in good
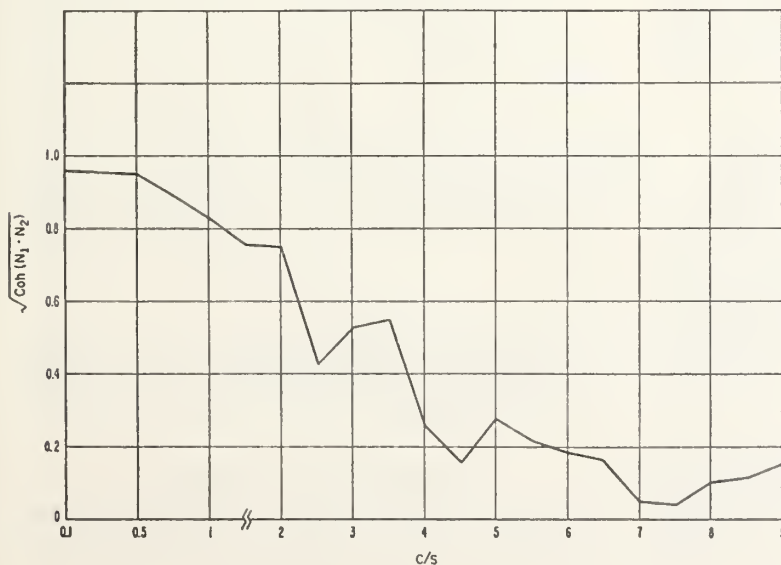
Fig. 3. Coherence of refractometer 1 versus refractometer 2, spacing 12 inches, Gunbarrel Hill, Colorado, October 31, 1965.

agreement with the 1.75 meters found as the spatial resolution of refractometer cavities determined in the wind tunnel [*Gilmer et al.* 1965].

Visual inspection of Figure 1 leads one to conclude that N and RH are nearly perfectly correlated to perhaps 10 Hz, since both track 'square-sided' changes that appear at random times on the record.

This comparison of the relative spectral response of the BaF_2 sensor and the radio refractometer was sufficiently favorable to encourage adoption of the BaF_2 elements as a sensor for measuring fine-scale humidity fluctuations, such as for the evaporation studies reported elsewhere [*Bean and Florey,* 1968].

REFERENCES

Bean, B. R., C. B. Emmanuel, and R. W. Krinks (1967), Some spectral characteristics of the radio refractivity in the surface layer of the atmosphere, *Radio Sci.,* 2(5), 503–510.

Bean, B. R., and Q. L. Florey (1968), A field study of the effectiveness of fatty alcohol mixtures as evaporation reducing monomolecular films, *Water Resour. Res.,* 4, 206–208.

Gilmer, R. O., R. E. McGavin, and B. R. Bean (1965), Response of NBS microwave refractometer cavities to atmospheric variations, *Radio Sci.,* 69D, 1213–1217.

Jones, F. E., and A. Wexler (1960), A barium fluoride film hygrometer element, *J. Geophys. Res.,* 65, 2087–2095.

36

An expansion of the Helmholtz integral and its evaluation

H. T. Dougherty

Radio Meteorology, Wave Propagation Laboratory, ESSA, Boulder, Colorado 80302

The Helmholtz integral theorem for the scattering or radiation of radio waves from surfaces is examined to obtain a more general approximation of the observed field distribution. The resulting new integral expansion is particularly responsive to evaluation by the method of stationary phases, yielding a quantitative solution applicable to a more general class of surfaces and aperture boundaries than was previously feasible. The problem of reflection from finite irregular surfaces, such as terrain or atmospheric layers, is evaluated formally. The result indicates a source of significant reflections not generally treated by ray theory.

INTRODUCTION

In our efforts to provide a quantitative description of tropospheric microwave propagation, major difficulties occur that are associated with reflections from terrain or atmospheric layers, or both. Some of these difficulties are traceable to the problems of quantitatively evaluating the Helmholtz integral that occurs in a formulation of the scattering or radiation problem for irregular surfaces [*Silver*, 1949; *Mentzer*, 1955; *Harrington*, 1961; *Born and Wolf*, 1964]. This paper presents a new expansion of the basic integral involved and an evaluation technique appropriate for arbitrary surfaces and field distributions.

Consider the general radiation problem for which the observed field for a homogeneous region is given by the Helmholtz integral theorem. For each of the orthogonal vector field components, the amplitude and phase is given by the scalar expression

$$V(R) = -\frac{1}{4\pi} \int_s [\Phi_2(\mathbf{n} \cdot \nabla)V - V(\mathbf{n} \cdot \nabla)\Phi_2] \, d\xi \, d\eta \quad (1)$$

where the surface normal $\mathbf{n}$ is directed out of the region containing the field source at T and into the region containing the point of observation R. We choose the free-space function

$$\Phi_2 = r_2^{-1} \exp(-ikr_2) \quad (2)$$

where k is the wave number and r_2 is the distance from R to the arbitrary point P on S. The field at P, a distance r_1 from T, may be expressed as

$$V = a\Phi_1 = (a/r_1) \exp(-ikr_1) \quad (3)$$

where a is an unspecified function of r_1, r_2, and the surface constants. For (3), the expression (1) becomes

$$4\pi V(R) = \int_s \{a\mathbf{n} \cdot [\Phi_1 \nabla \Phi_2 - \Phi_2 \nabla \Phi_1]$$
$$- \Phi_1 \Phi_2(\mathbf{n} \cdot \nabla)a\} \, d\xi \, d\eta \quad (4)$$

Ordinarily, the surface of interest is a closed one containing a closed contour C separating the aperture surface A and the screen surface B. For example, the surface S may be closed at infinity as in Figure 1a. There the contour C, separating A and B, is also closed at infinity. The usual procedure is to apply the Kirchhoff approximation, specifying the $a(A)$ as unity and $a(B)$ as zero. Here, however, this method is much too restrictive and an alternative is desirable for applications where reasonable approximations of the field distributions over A or B, or both, are available [*Wait*, 1956; *Hasserjian and Ishimaru*, 1962].

THE INTEGRAL EXPANSION

Except for the simplest contours (circles and rectangles) of dimensions that are small relative to r_2, the direct integration of (4) is generally not feasible. The problem is eased, however, even for arbitrary contours, with an appropriate expansion of the integral of (4). We introduce Maggi's auxiliary vector B, for which

$$\nabla \times \mathbf{B} = \Phi_2 \nabla \Phi_1 - \Phi_1 \nabla \Phi_2 \quad (5)$$

From Baker's and Copson's exposition of the Maggi transformation [*Maggi*, 1888; *Baker and Copson*, 1953],
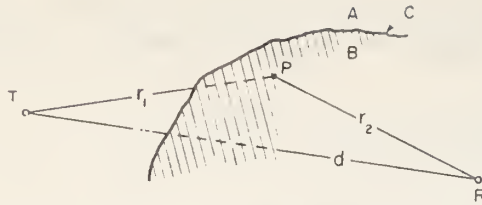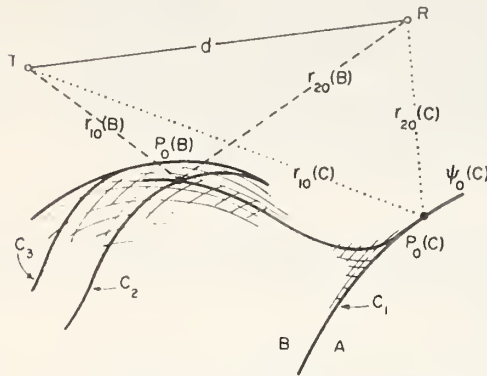
Fig. 1a.   Geometry for an irregular aperture.

Fig. 1b.   Geometry for an irregular surface.

$$\mathbf{B} = \mathbf{u}\Phi_1\Phi_2 \sin \psi/(1 - \cos \psi) \qquad (6)$$

Where ψ is the angle in the direction PR relative to the direction TP and $\mathbf{u}$ is a unit vector normal to the plane containing r_1 and r_2 or T, P, and R. Combining (4) and (5), we use Stoke's theorem and the vector analysis expansion of $\nabla \times (a\mathbf{B})$ to obtain a new expansion of (1).

$$V(R) = a_0(A \text{ or } B)\Phi_d$$

$$\pm \int_c \frac{\Phi_1\Phi_2}{4\pi} [a(B) - a(A)] \frac{\sin \psi \mathbf{u}\cdot\mathbf{t}}{1 - \cos \psi} \, d\xi$$

$$- \int_s \frac{\Phi_1\Phi_2}{4\pi} \left(\mathbf{n} + \frac{\mathbf{n} \times \mathbf{u} \sin \psi}{1 - \cos \psi}\right)$$

$$\cdot \nabla a(S) \, d\xi d\eta + \cdots \qquad (7a)$$

for

$$\Phi_d = d^{-1} \exp (-ikd) \qquad (7b)$$

where $\mathbf{t}$ is the unit tangent vector of the curve C, ξ is the coordinate along C, and ξ, η are orthogonal curvilinear coordinates on A and B. The a_0 (A or B) is the contribution of the surface integral part of Stoke's theorem due to the singularity of (6) at P_0, i.e. where T, P_0, and R lie on a straight line (more precisely, $\mathbf{P}_1 \cdot \mathbf{P}_2 = -1$ at P_0) and ψ is zero [Fabianski, 1963]. This contribution to (7a) has been evaluated for $a_0 = 1$ by Marchand and Wolf [1962]. The contri-

bution when the singularity occurs on C is contained in the line integral term of (7a) and was given for $a(B) - a(A) = 1$ by Rubinowicz [1938]. The positive sign is chosen for the line integral when P_0 is on A or C; the negative sign is chosen when P_0 is on B. The indication of additional terms on (7a) refers to two line integrals [Kottler, 1923; Stratton and Chu, 1939] that contain the integrand factor $a(B) - a(A)$ and that are of the order of $\tan \psi$ or less, relative to the line integral specified in (7a).

The novel features of (7a) are the presence of factor $a(B) - a(A)$ in the line integral and the presence of the surface integral. This assumes that a is well behaved over S with, at worst, only finite step discontinuities. Miyamoto [1962] arrived at (7a) with $a = 1$ in the first term, $a(B) = 0$ in the second (line integral) term, and omission of the surface and indicated additional integrals. This solution was quite proper for his application; he assumed that the field was zero on the shadowed side of a screen. He omitted the surface integral because its series expansion [Miyamoto and Wolf, 1962] was of the order of $1/k$ and negligible for the extremely small wavelengths of interest there. For many tropospheric radio propagation applications, however, the surface integral of (7a) must be retained as the dominant term. For its asymptotic expansion, we therefore subsequently choose a parameter s that is proportional to k but large-valued for the applications of interest.

Note that for the condition a constant on A and on B, the surface integral drops out and (7a) reduces to the Maggi transformation [Kottler, 1923; Baker and Copson, 1953]. At first glance (7a) may not appear to be an improvement over (1); however, these line and surface integrals are readily evaluated by Laplace's method of stationary phase [Wintner, 1945; Erdelyi, 1956] and require estimates of the value of a only at specific points (of stationary phase).

EVALUATION OF THE EXPANSION

This new expanded form (7a) of $V(R)$ may be normalized to the free-space field at R. Also, for the large-valued parameter

$$S = k(r_{10}r_{20})^{1/2} \qquad (8)$$

the integrand phase function is given by

$$f = (r_1 + r_2 - d)/(r_{10}r_{20})^{1/2} \qquad (9)$$

This assumes that the phase of a varies much more slowly than (9) in the vicinity of points of stationary

phase; otherwise a correction term is required in (9). The subscript zero (appended to any quantity's symbol) indicates the quantity evaluated at ξ_0 (or ξ_0, η_0), the point of stationary phase. Because of the quantity $(1 - \cos \psi)$, the integrands of (7a) could vary rapidly in the vicinity of the point of stationary phase. To offset such an effect, we resort to the method of *Rubinowicz* [1957] and *Karczewski* [1963]. That is, for an integral

$$I = \int_{-\infty}^{\infty} [g(l)/h(l)] \exp \{-isf\} \, dl \qquad (10)$$

with a point of stationary phase, $f'(l_0) = 0$, Rubinowicz defined an auxiliary integral $U = \partial I/\partial S$. The inverse of this then determined I in terms of the U that was evaluated by Laplace's method of stationary phase. That is,

$$I = g_0 f_0 / h_0 \left[\frac{i2\pi}{f''(l_0)}\right]^{1/2}$$
$$\cdot \int_S^{-\imath\infty} \frac{e^{-itf_0}}{(t)^{1/2}} \, dt [1 + O(S^{-1/2})] \qquad (11)$$

If $h(x) = 1$ in (10), then multiply (11) by i/f_0 and differentiate it with respect to s. For the line integral of (7a), the definition

$$sf_0 = \pi v^2/2 \qquad (12)$$

combined with (8), (9), and (11) for $h(\xi) = 1 - \cos \psi$, will lead after some manipulation to

$$I_c(\xi_0) = a_0 T(\xi_0) a(v, \theta_0)$$
$$\cdot \left(\frac{2d^2/(r_{10} + r_{20})}{d + r_{10} + r_{20}}\right)^{1/2} [1 + O(s^{-1/2})] \qquad (13)$$

where

$$T_c^2(\xi_0) = \left[\frac{\partial^2 f}{\partial \xi^2}\right]_0 \Big/ \left[\frac{\partial^2 f}{\partial l^2}\right]_0 \qquad (14)$$

is the effect of the departure of C from linearity in the vicinity of the point of stationary phase. The angle θ_0 is the projection of the scattering angle ψ_0 on the contour normal plane at ξ_0. The $a(v, \theta_0)$ is given by $\cos(\theta_0/2)$ times the Fresnel integral

$$a(v, 0) = \left(\frac{if_0}{4\pi}\right)^{1/2} \int_s^{\infty} \frac{e^{-itf_0}}{(t)^{1/2}} \, dt \qquad (15)$$

which is plotted in Figure 2 for v defined by (12), or

$$v = \left| 2 \sin \frac{\psi_0}{2} \left[\frac{2kr_{10}r_{20}}{\pi(d + r_{10} + r_{20})}\right]^{1/2} \right| \qquad (16)$$

The contour C will have at least one point of sta-

tionary phase and will generally have several for arbitrary shapes. Each ξ_0 will provide its own contribution (13) to the line integral of (7a), assuming the adjacent points of stationary phase are not too closely spaced. This is discussed further in a subsequent paper [*Dougherty*, 1970]. Similarly, the surface integral of (7) can be evaluated by combining Rubinowicz's method with that of *Van Kampen* [1949] for surface integrals.

Van Kampen [1949] indentifies points of stationary phase as belonging to the first kind when TP_0R is a straight line ($\psi_0 = 0$) and to the second when TP_0R is not a straight line ($\psi_0 \neq 0$). This has much significance for the contribution of the first term a_0 (A or B) of (7a). Thus, only (actual or equivalent) sources on an extension from T of the line TR can contribute to a singularity at $P_0(S)$ and the value $a_0(A) = 1$ is true and not merely an assumption. Further, $a_0(B)$ is a function of the screen surface constants and represents, on the shadowed side of the screen, *only the attenuated field* (due to the source at T) that has *penetrated* the screen. The total field at $P_0(A$ or $B)$ may be separated into three portions, each of which is due to actual or equivalent field sources for which $P_0(A$ or $B)$ is either (a) not a point of stationary phase, (b) a point of stationary phase of the first kind, or (c) a point of stationary phase of the second kind. For that portion of the field at $P_0(A$ and $B)$ corresponding to (a), there is no local contribution to the received field. For the portion corresponding to (b), the contribution is given by the first term of (7a) as described above, whereas for the portion corresponding to (c), the contribution is given by the integrals of (7a).

APPLICATION

A limited application of the foregoing is considered here for the situation in Figure 1b, where the aperture surface A joins B along C and extends so as to separate the regions containing T and R. If the only points of stationary phase are the $P_0(B)$ and $P_0(C)$ indicated in Figure 1b and the $P_0(A)$ wherever TR pierces A, the field is given by (7a) with $a_0(A) = 1.0$ and the contribution of the line integral of (7a) for $P_0(c)$. If $P_0(C)$ is sufficiently separated from $P_0(B)$, the contribution of the surface integral for $P_0(B)$ is essentially $\rho(B)\Phi_1$, where $\rho(B)$ is the reflection for the surface B. The total effective reflection function $\rho(R)$ is given by the ratio of the integral terms of (7a) to the first term. That is, from (7a), (13), and (14),
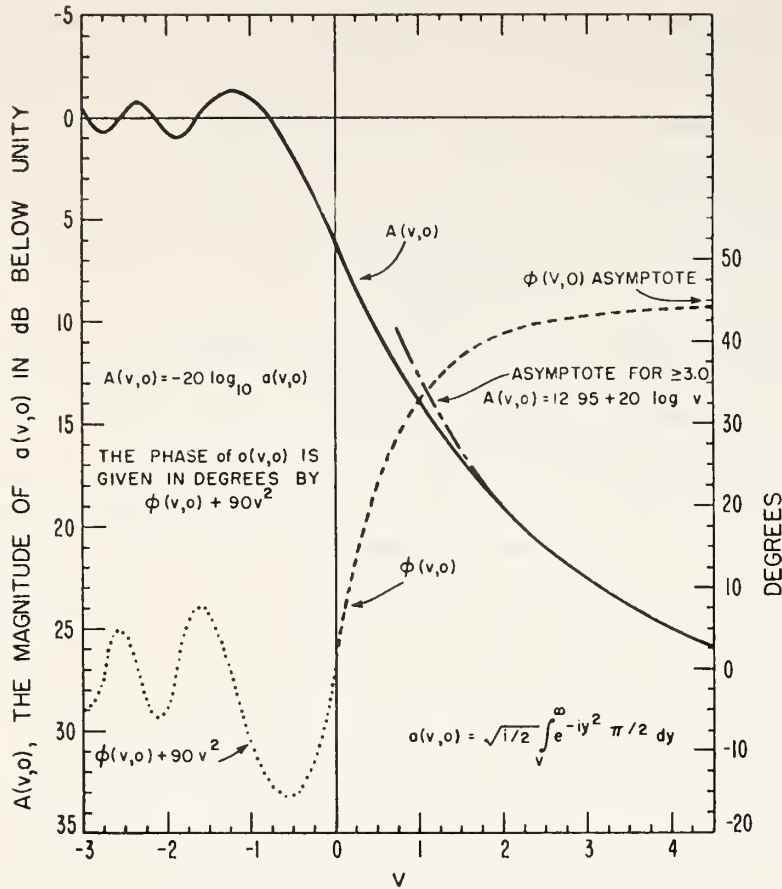
Fig. 2.   The Fresnel-Kirchhoff function $a(v, 0)$.

$$-\rho(R) \approx \rho(B) - a(\xi_0)a(v, \Phi_0)T_c(\xi_0)$$
$$\cdot \left\{ \frac{2d^2/[r_{10}(c) + r_{20}(c)]}{d + r_{10}(c) + r_{20}(c)} \right\}^{1/2} \quad (17)$$

Additional points of stationary phase on B and C would, of course, generate additional terms, such as those of (17). The point of significance here is that (17) has the form of an equivalent aperture problem, where C is the aperture edge and $a_0(B) = \rho(B)$ is an aperture transmission factor. The effect of shifting C is to modify the value of $\rho(R)$. For example, if B were plane and T and R were more remote from $P_0(B)$, from $P_0(C)$, and from each other than from the surface B, the $\rho(B)$ would approach unity and

$$-\rho(R) \approx 1 - a(v, 0) \quad (18)$$

That is, the $-\rho(R)$ would be approximated by the $a(v, 0)$ of Figure 2 with $v < 0$ for C_1 to the right of C_2 and $v > 0$ for C_1 to the left of C_2. It can be shown that for C_1 coincident with C_2, the net effect is a value $\rho(B)$ approximately half that for C_1 displaced far to the right.

In the case of (17), the value would be given by $\rho(B)$ times a bracketed quantity that is similar to

(18). If B were bounded by C_1 coincident with C_2, then $|\rho(R)| \approx 0.5$. Further, $0 < |\rho(B)| < 0.5$ would result when C_1 is displaced to C_3 and $P_0(B)$ is on an imaginary extension of B. Simple ray theory would probably tolerate the former but would eliminate the latter, and possibly significant, reflections.

The idea of treating a plane reflecting region as an aperture is an old one [*National Defense Research Committee*, 1946; *Booker and Clemmow*, 1950] that has been verified experimentally only for the simplest contours [*Bussey*, 1950]. Expression 17 is possible in closed form because of the expansion (7a) which avoids the difficulties experienced for the direct integration of (1) even with the simplest nonplanar smooth surfaces and contours [*Meecham*, 1956; *Micheletta*, 1963]. The effect of surface roughness is included by incorporating the roughness factors generated by the techniques of *Beckmann and Spizzichino* [1963].

CONCLUSION

By virtue of the integral expansion of (1) into (7a), solution of the Helmholtz integral becomes

feasible for a much wider class of surfaces, apertures, and field distributions because the new line and surface integral formulations are readily evaluated by the methods of stationary phases, yielding asymptotic, closed-form solutions. Of course, in formulating this solution, we assume that the field distributions, surfaces, and contours are 'well behaved' and involve, at worst, only finite step discontinuities.

Although the restriction may be partially relaxed, the formulation given here requires that both source and point of observation be more than a few wavelengths from the surface and contour of integration. The technique is applied to the problem of reflections from an irregular finite surface area, and the result indicates a possible omission of significant reflections for ray-theory approaches.

REFERENCES

Baker, B. B., and E. T. Copson (1953), *The Mathematical Theory of Huygen's Principle*, Oxford University Press, London.

Beckmann, P., and A. Spizzichino (1963), *The Scattering of Electromagnetic Waves from Rough Surfaces*, MacMillan, N. Y.

Booker, H. G., and P. C. Clemmow (1950), A relation between the Sommerfeld theory of radio propagation over a flat earth and the theory of diffraction at a straight edge, *Proc. IRE, 97*, part 3, no. 45, 18–27.

Born, M., and E. Wolf (1964), *Principles of Optics*, Pergamon Press, N. Y.

Bussey, H. E. (1950), Reflected ray suppression, *Proc. IRE, 38*(12), 1453.

Dougherty, H. T. (1970), The application of stationary phase to radio propagation for finite limits of integration, *Radio Sci., 5*(1).

Erdelyi, A. (1956), *Asymptotic Expansions*, Dover Publ., N. Y.

Fabianski, B. Z. (1963), The phase jump at the focal point in the case of electromagnetic waves, *Acta Phys. Pol., 24*(3), 317–321.

Harrington, R. F. (1961), *Time Harmonic Electromagnetic Fields*, McGraw-Hill, N. Y.

Hasserjian, G., and H. Ishimaru (1962), Excitation of a conducting cylindrical surface of large radius of curvature, *IRE Trans. Antennas Propagat., 10*, May, 264–273.

Karczewski, B. (1963), The Fresnel field in Kottler's diffraction theory, *Can. J. Phys., 41*(10), 1623–1628.

Kottler, F. (1923), On the theory of diffraction by a black screen (in German), *Ann. Phys., 70*(6), 406–456.

Maggi, G. A. (1888), Sulla propagazione libere e perturbata delle onde luminose in un mezzo isotropo, *Anno. Mat. Pura Appl. 16*, 21–48.

Marchand, E. W., and E. Wolf (1962), Boundary diffraction wave in the domain of the Rayleigh-Kirchhoff diffraction theory, *J. Opt. Soc. Amer., 52*(7), 761–767.

Meecham, W. C. (1956), Fourier transform method for the treatment of the problem of the reflection of radiation from irregular surfaces, *J. Acoust. Soc. Amer., 28*(3), 370–377.

Mentzer, J. R. (1955), *Scattering and Diffraction of Radio Waves*, Pergamon Press, N. Y.

Micheletta, C. (1963), Radio wave diffraction on limited areas of ground, *Alta Freq.* (Italy), *32*(2), 127–132.

Miyamoto, K. (1962), New representation of wave field, *Proc. Phys. Soc. London, 79*, 617–629.

Miyamoto, K., and E. Wolf (1962), Generalization of Maggi-Rubinowicz theory of the boundary diffraction wave, 2, *J. Opt. Soc. Amer., 52*(6), 626–637.

National Defense Research Committee (1946), *The Propagation of Radio Waves Through the Standard Atmosphere*, Summary Tech. Rep., vol. 3, Office of Naval Research, Washington, D. C.

Rubinowicz, A. (1938), On the anomalous propagation of phase in the focus, *Phys. Rev., 54*(12), 931–936.

Rubinowicz, A. (1957), *Die Beugungswelle in der Kirchhoffschen Theorie der Beugung*, Polska Akademia Nauk., Warsaw, Poland.

Silver, S. (1949), Microwave Antenna Theory and Design, Mass. Inst. Tech. Radiation Lab. Series, No. 12, McGraw-Hill, N. Y.

Stratton, J. A., and L. J. Chu (1939), Diffraction theory of electromagnetic waves, *Phys. Rev., 56*(7), 99–107.

Van Kampen, N. G. (1949), An asymptotic treatment of diffraction problems, *Physica, 14*(9), 575–587.

Wait, J. R. (1956), Currents excited on a conducting cylindrical surface of large radius of curvature, *IRE Trans. Antennas Propagat., 10*, May, 264–273.

Wintner, A. (1954), Remarks on the method of stationary phases, *J. Math. Phys., 24*, 127–130.

Radio wave propagation for irregular boundaries

H. T. Dougherty

Radio Meteorology Program Area, Wave Propagation Laboratory

ESSA, Boulder, Colorado 80302

A new, vectorial, approximate solution is presented for a particular class of problems: that of a vector wave propagated through a linear, isotropic, piecewise-homogeneous medium with irregular interfaces and boundaries. This class of problems lacks not only an exact method of solution but also a reliable method of approximation for tropospheric radio propagation at VHF and higher frequencies. A method is proposed that incorporates a recent expansion of the Helmholtz integral to evaluate the Stratton-Chu integral by the methods of stationary phase. To demonstrate its potential, the method is applied to two of the simplest thin-screen problems.

1. INTRODUCTION

Both remote sensing of atmospheric structure by microwave transmissions and its inverse, telecommunication performance prediction, *presuppose* a reliable solution of the propagation problem. For example, it is recognized that the tropospheric propagation of microwave frequencies in both instances is particularly sensitive to stratification of the atmosphere and proximity of terrain. Of the two, remote sensing requires the more detailed and discriminating description of the field in terms of the medium characteristics and the geometry of its boundaries, and it requires the more accurate solution of the wave propagation problem. At best, the problem is that of wave propagation through a medium that is linear, isotropic, and piecewise homogeneous and has irregular interfaces or boundaries. There is no exact solution to this problem, nor even an approximate one that is sufficiently reliable for telecommunication predictions at microwave frequencies.

Historically, the tropospheric propagation problem has been reduced to a two-dimensional or scalar problem for which exact solutions, or their closed-form approximations, are available [*Norton*, 1941; *Rice*, 1954; *Wait and Conda*, 1959]. This reduction is accomplished by approximating the boundary surfaces (of the atmospheric duct or layer and the terrain) by smooth *regular* (plane or cylindrical) surfaces [*Schelling et al.*, 1933; *Selvidge*, 1941; *Kerr*, 1951; *Norton et al.*, 1955; *Dougherty and Maloney*,

1964]. This approach, however, has become increasingly unreliable as the applications have progressed from VHF to higher frequencies [*Nishikori et al.*, 1957; *Barsis and Hause*, 1966]. This unreliability is primarily due to irregularities in the boundaries, which rarely resemble plane or cylindrical surfaces, and the consequent disregard for the effects of the boundary's transverse contours. An alternative approach is to approximate these boundaries more closely by choosing *irregular* surfaces that also approximate the transverse contours.

But, because of the variety of terrain and the vagaries of the troposphere encountered (particularly at UHF and microwave frequencies), the irregularities of the surface preclude exact methods of solution. Approximate solutions may be obtained, however, from an integral formulation of the problem. The approximation *results, of course, from the form assumed* for the unknown integrand factor [*Harrington*, 1961], but further approximation also may be required to obtain the solution in closed or graphical form. The method presented here incorporates an expansion of the Helmholtz integral [*Dougherty*, 1969] to evaluate the Stratton and Chu vector integral by the method of stationary phase. To demonstrate its potential, the method is then applied to two of the simplest thin-screen problems.

2. THE INTEGRAL FORM OF THE PROBLEM

Let S be a surface chosen to enclose the source T of a field V that satisfied the vector the wave equation. Let C be a closed contour that divides S into two

subsurfaces A and B, delineating discontinuities in the field or surface parameters. For example, V is well behaved everywhere except, perhaps, across C where it may have a jump discontinuity. At a point R, outside of S and at a distance d from T, the observed field is given [Stratton and Chu, 1939; Stratton, 1941] by

$$V(R) = \frac{1}{4\pi} \int_S [V(P)(\mathbf{n} \cdot \nabla)\Phi_2 - \Phi_2(\mathbf{n} \cdot \nabla)V(P)]\, dS$$

$$- \frac{1}{4\pi} \oint_C \Phi_2[V_A(P) - V_B(P)] \times \mathbf{t}\, dl$$

$$+ \frac{1}{4\pi} \oint_C \frac{\nabla\Phi_2}{k^2} \{\mathbf{t} \cdot [\nabla \times V_A(P) - \nabla \times V_B(P)]\}\, dl$$

$$(1)$$

The notation $V_A(P)$, for example, indicates the field at an arbitrary point P on the surface A. Also,

$$\Phi_J = r_J^{-1} \exp(-ikr_J), \qquad J = 1 \text{ or } 2 \qquad (2)$$

where r_1 and r_2 are the distances from, respectively, T and R to the point P on S. Further,

$$k = [2\pi(\mu\epsilon_c)^{1/2}]/\lambda \qquad (3)$$

where λ is the free-space wavelength, μ is the relative permeability, and ϵ_c is the complex dielectric constant. The $\mathbf{n}$ denotes the outward-directed unit surface normal of S, the $\mathbf{t}$ is the unit vector tangent to C and oriented so that $\mathbf{n} \times \mathbf{t}$ points toward the surface A. The time dependency is $\exp(i\omega t)$, and the International System of Units (S.I.) is assumed.

Although Stratton and Chu arrived at the form of (1) from their vector analogs to Green's theorems, it is applicable (by virtue of Fubini's theorem [Page, 1955; Korn and Korn, 1961]) to continuous or piece-wise-continuous fields, surfaces, and contours. Although Stratton and Chu originally appended the line integrals in (1) by dint of physical argument [Kottler, 1923], the additions have since been given mathematical support by Sancer [1968]. Additional contours would produce further subdivisions of S and generate additional line integral terms on (1).

3. THE FORMAL SOLUTION

The first source of difficulty in solving (1) is the unknown V in the integrands. We may formally designate the value of V on the surface as the primary field plus the effect of some operation (on the primary field) that produces the secondary field [Harrington, 1959]. That is

$$V_S(P) = \mathbf{u}_1 V_1 \Phi_1 + \Gamma(\mathbf{u}_1 V_1 \Phi_1) \qquad (4)$$

where $\mathbf{u}_1$ is the primary field *unit* directional vector, V_1 is an amplitude factor, and Γ is the unknown operator. We assume that Γ is a linear operator of integral, differential, and/or algebraic form such that (4) reduces to

Assumption I

$$V_s(P) = V_1(\mathbf{u}_1 b + \mathbf{u}_2 a)\Phi_1 \qquad (5)$$

where $\mathbf{u}_2$ is the secondary field *unit* directional vector. This assumes linearly polarized fields, but (5) could be extended to include elliptical polarization that may be encountered in, for example, the case of reflection. The a and b may be considered as attenuation factors that are, in general, functions of position and of the electromagnetic constants of the surface. The $\mathbf{u}_2$, a and b are described further in subsequent sections.

An approximate expression for $V(R)$ is obtained by substituting (5) into (1). The form of the surface integral is then suitable for applying an integral expansion. Let V represent the electric field component due to the source at T; then, $\mathbf{u}_1$ and $\mathbf{u}_2$ are unit vectors for the direction of the field polarizations. If we designate $E(R)$ as the *approximation of* $V(R)$, then (1), (5), and an expansion of the Helmholtz integral [Dougherty, 1969] lead to

$$E(R) = \mathbf{a}(R)(V_1/d) \exp(-ikd) \qquad (6)$$

where

$$\mathbf{a}(R) = b(P_0)\mathbf{u}_{10} \pm \frac{d}{4\pi} \oint_C \alpha(P)\Phi\mathbf{u}_2 \times t\, dl$$

$$\pm \frac{d}{4\pi} \oint_C \mathbf{u}_2 \frac{\Phi \sin\psi}{1 - \cos\psi} \alpha(P)\mathbf{u}_v \cdot \mathbf{t}\, dl$$

$$- \frac{d}{4\pi} \int_S \sum_i e_i \Phi \left\{\mathbf{n} + \mathbf{n} \times \mathbf{u}_v \frac{\sin\psi}{1 - \cos\psi}\right\}$$

$$\cdot \nabla \beta_i(P)\, dS \qquad (7)$$

The term containing $b(P_0)$, the second line integral, and the surface integral all result from the expansion of the surface integral of (1). The $b(P_0)$ is the contribution of the surface integral of (1) associated with the point P_0 where the TR line pierces the surface S; $b(P_0)$ is the attenuation of the direct field that penetrates to the surface at P_0. Additional P_0 points would provide additional $b(P_0)$ terms to (7). The contribution of the third line integral of (1) has been omitted from (7) because it does not provide a propagated contribution at R; the $\nabla\Phi_2$ is a vector parallel to $-P_2$, the unit directional vector for propagation

from P to R. The $\alpha(P)$, $\beta_i(P)$, Φ, ψ, and u_ν are defined by

$$\alpha(P) = [V_B(P) - V_A(P)]/V_1 \tag{8a}$$

$$\beta_i(P) = \mathbf{e}_i \cdot \mathbf{u}_2 V(P)/V_1 \tag{8b}$$

$$\Phi = (r_1 r_2)^{-1} \exp[-ik(r_1 + r_2 - d)] \tag{9}$$

$$\cos \psi = -\mathbf{p}_1 \cdot \mathbf{p}_2, \tag{10a}$$

and

$$\sin \psi \, \mathbf{u}_\nu = \mathbf{p}_1 \cdot \mathbf{p}_2 \tag{10b}$$

where

$$\mathbf{TP} = \mathbf{r}_1 = r_1 \mathbf{p}_1 \tag{11a}$$

$$\mathbf{RP} = \mathbf{r}_2 = r_2 \mathbf{p}_2 \tag{11b}$$

and the $\mathbf{e}_i$ represents a convenient set of Cartesian unit vectors. The choice of plus or minus signs for the line integrals of (7) is determined by the location of P_0. If P_0 is on A or C, the plus signs apply; if P_0 is on B, the minus signs apply.

4. THE CLOSED-FORM SOLUTION

Here we exploit one of the implicit advantages of the form of (7). That is, we obtain an easily calculated expression for (7) with only those simple restrictions that are already implicit in the applications of interest. We assume that both T and R are more than a few wavelengths from the surface and contour of interest; this condition can be relaxed, permitting R on S [Hufford, 1952]. We now define a large-valued parameter

$$s = k_1 (r_{10} r_{20})^{1/2} \tag{12}$$

where k_1 is the real part of (3), and the subscript zero appended to a quantity's symbol indicates the value of that quantity at the point of stationary phase. The major phase function of the integrands of (7) is then sf, where

$$f = (r_1 + r_2 - d)/(r_{10} r_{20})^{1/2} \tag{13}$$

At the first-order point of stationary phase, we relate (12) to the Fresnel parameter v

$$sf_0 = \pi v^2/2 \tag{14a}$$

or

$$v = \left| 2 \sin \frac{\psi_0}{2} \left[\frac{2k_1 r_{10} r_{20}}{\pi(d + r_{10} + r_{20})} \right]^{1/2} \right| \tag{14b}$$

and evaluate (7) by the methods of stationary phase, as outlined by *Karczewski* [1963] and *Dougherty*

[1969]. For N points of stationary phase (in addition to that at P_0), we obtain

$$a(R) = \mathbf{u}_{10} b(P_0)$$
$$+ \sum_n^N \mathbf{I}_n \left\{ T_c(l_0) \cos \frac{\phi_0}{2} \left[\frac{2d^2/(r_{10} + r_{20})}{d + r_{10} + r_{20}} \right]^{1/2} \right\}_n \tag{15}$$

where the angle ϕ_0 is the projection of ψ_0 on the normal plane of C at the point of stationary phase. If we designate l as a measure of length along C and ξ as the measure along the tangent to C at the point of stationary phase, then the transverse effect of the departure of C from a straight line is

$$T_c{}^2(l_0) = [\partial^2 f/\partial \xi^2]_{l_0}/[\partial^2 f/\partial l^2]_{l_0} \tag{16}$$

The vector $\mathbf{I}_n$ in (15) involves the $\alpha(P)$ and $\beta_i(P)$, evaluated as α_0 and β_{i0}, at each point of stationary phase. For each stationary point that occurs on A or B (other than the previously mentioned P_0), the contribution of the surface integral of (7) may be expressed as an asymptotic series in powers of the inverse of the large-valued parameter s. We defer that expression to a subsequent paper and direct our attention to the situation where $N = 1$ and where that point lies on C. The $\mathbf{I}$ is then given by

$$\pm \alpha_0 \left[\mathbf{u}_{20} a(v, 0) + \mathbf{u}_{20} \times \mathbf{t} \frac{2 \tan \phi_0/2}{\pi v} \frac{\partial a(v, 0)}{\partial v} \right]$$
$$\cdot [1 + 0(s^{-1/2})] \tag{17}$$

where $a(v, 0)$ is the Fresnel-Kirchhoff knife-edge attenuation function [*Dougherty*, 1969].

5. EVALUATION

The problem thus far has been stated in only the broadest terms, in the introductory paragraphs of sections 3 and 4; nevertheless, the Fresnel-Kirchhoff function is clearly a characteristic part of the closed-form solution (15) and (17). The point of stationary phase and the value of the Fresnel-Kirchhoff parameter v describe the specific geometry and wavelength of any particular application. There are, however, still some undetermined aspects of the solution.

The unit vector $\mathbf{u}_{20}$ defining the linear polarization of the secondary field in (17) should be determined in part by the $\mathbf{u}_{10}$. For example, if the point of stationary phase were a reflection point $\psi_0 < 0$, available procedures would determine $\mathbf{u}_{20}$ from $\mathbf{u}_{10}$ and the surface electromagnetic constants. We assume that a similar procedure will determine $\mathbf{u}_{20}$ when the stationary point is a diffraction point $\psi_0 \geq 0$. It can be shown that $f = $ constant (see equation 13) implies a system

of confocal ellipsoids for $\psi_0 > 0$ and defines a 'plane of symmetry' at the stationary point that may be used to relate u_{10} and u_{20}. This plane will be tangent to C, A, or B at the stationary point, will have a normal n_0 that lies in the plane of T, P, and R, and will bisect the angle ψ_0 there. Therefore, we choose

Assumption II

$$t_0 \cdot (u_{10} + u_{20}) = 0$$

$$t_0 \times n_0 \cdot (u_{10} + u_{20}) = 0 \qquad (18)$$

$$n_0 \cdot (u_{10} - u_{20}) = 0$$

If the field $V(R)$ were the magnetic field, u_{10} and u_{20} would simply be the unit directional vectors of the field and (18) would apply if the plus signs were changed to minus, and vice versa.

One unsettled point remains. Although α_0 has been specified in only a general manner, the closed-form solution (15) requires the specific point values α_0 and $\nabla\beta_{10}$. Because these are still generally unknown, some further specification is required. We consider the alternatives

Alternative A

$$\alpha_0 = 0 \qquad (19)$$

or

Alternative B

$$\nabla\beta_{10} = 0(d^{-1}) \qquad (20)$$

Alternative A says that the fields and surface characteristics are continuous across the contour C; this has the effect of eliminating (17), the contributions of the line integrals of (7). This is most realistic and convenient at points where the surface radius of curvature is large relative to the wavelength of transmission. Alternative B has the effect of submerging the contribution of the surface integral of (7). This is most convenient at points where the radius of curvature is of the order of, or less than, the wavelength. Assumptions I and II and alternatives A or B are presented sequentially here, interspersed with their effects upon the solution, only for convenience of presentation, but they should be thought of as a set of conditions that transforms the exact expression (1) for $V(R)$ into its approximate evaluation $E(R)$ obtained from (15).

6. APPLICATION

We will now subject the foregoing expressions to two simple tests to demonstrate their validity and

potential. We apply them first to the simplest problem for which an exact solution exists and for which its verified, closed-form approximation is available for comparison. We then apply them to a problem that lacks both an exact solution and an approximate closed-form solution but for which experimental data *is* available for comparison. Both problems involve diffraction by a thin-edged metallic screen with one point of stationary phase on the contour C defining the screen edge and one point of stationary phase on S where the line TR pierces the surface ($\sin\psi_0 = 0$). Accordingly, we choose alternative B so that the closed-form approximate solution (15) and (17) will take the form

$$a(R) = \alpha_0 T_c(l_0) \cos\frac{\phi_0}{2}$$

$$\cdot \left[\frac{2d^2/(r_{10} + r_{20})}{d + r_{10} + r_{20}}\right]^{1/2} [1 + 0(s^{-1/2})]$$

$$\cdot a(v, 0)\left[u_{20} + \frac{2\tan(\phi_0/2)}{\pi v a(v, 0)}\frac{\partial a(v, 0)}{\partial v}u_{20} \times t\right] \qquad (21)$$

for $\psi_0 > 0$, since $b(P_0) = 0$. For $\psi_0 \leq 0$, $b(P_0) = 1$ and we obtain $a(R)$ by subtracting (21) from u_{10}.

The simple knife edge. Let S be an infinite plane surface whose lower half coincides with a semi-infinite plane metallic screen. We choose the screen edge as the ξ axis of an $\xi\eta\zeta$ Cartesian coordinate system such that the source at T lies in the $\xi\zeta$ plane and the origin coincides with the point of stationary phase where [*Van Kampen, 1949*]

$$p_{10} \cdot u_\xi = -p_{20} \cdot u_\xi = \cos\gamma_0 \qquad (22)$$

The geometry is illustrated in Figure 1. Note that the projection of TR on the $\xi\zeta$ plane intersects the ξ axis at O' and, since C is a straight line, the T_e given by (16) is unity. Further, $t_0 = u_\xi$ and $n_0 = u_\eta \cos(\phi_0/2) + u_\zeta \sin\phi_0/2$.

Consider the Sommerfeld problem of a plane wave incident normally upon the half-plane. For such a condition, T is remote, the quantity under the radicand of (21) is unity, and $\phi_0 = \psi_0$. Therefore,

$$[a(R)]_{KE} = \alpha_0 \cos(\psi_0/2)a(v, 0)[1 + O(s^{-1})]U \qquad (23)$$

which, except for the first and second factor, is Sommerfeld's exact solution [*Sommerfeld*, 1964; *Born and Wolf*, 1964]. The α_0 is not a problem, since Sommerfeld's solution contained an unspecified constant of proportionality; others have also obtained the trigonometric factor [*Born and Wolf*, 1964; *Van Bladel*, 1964]. By further integration, *Senior* [1953
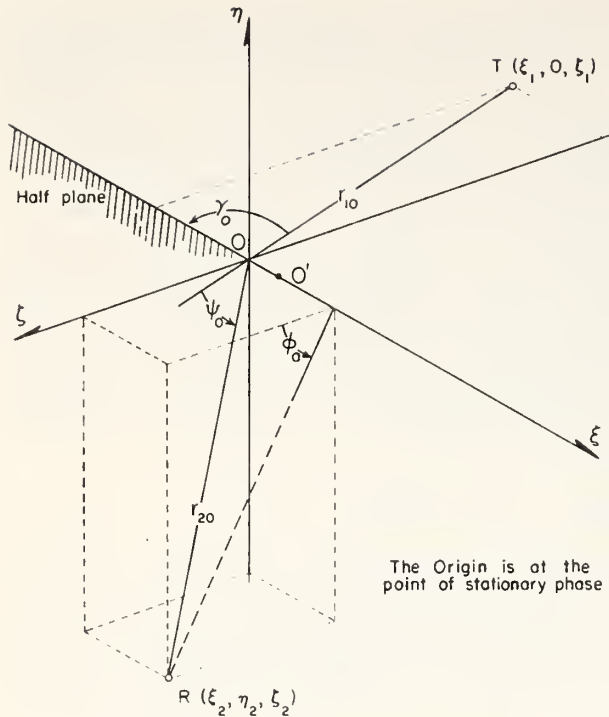
Fig. 1.   Geometry for the simple knife edge.

These exhibit the features of knife-edge diffraction observed experimentally for large diffracting angles: (1) a greater loss for horizontally than for vertically polarized waves and (2) a cross-polarization effect for horizontally polarized wave at an oblique incidence [*Baker and Copson*, 1953; *Born and Wolf*, 1964].

An irregular knife edge. Consider a knife edge consisting of a semicircular disk of radius ρ superimposed on the straight edge of the screen just evaluated. If the TR line pierces the disk at P, a distance $h < \rho$ from the disk edge, then the single point of stationary phase will lie on the disk edge and at the endpoint of the radius through P. Again we choose a $\xi\eta\zeta$ Cartesian coordinate system with the origin at the point of stationary phase and the ξ axis tangent to the disk edge. The $\xi\zeta$ plane is chosen to contain the source at T, and σ will be the angle between the normal to the plane of the disk and the $\xi\zeta$ plane.

was able to extend Sommerfeld's solution to cover spherical wave incidence. This has the effect of reintroducing the square-root factor of (21). Comparison with experimental data shows that α_0 must be close to unity.

The **U**, indentified from (21) and (23) is expressed as

$$\mathbf{U} \approx \mathbf{u}_{20} + \tan \phi_0/2(\mathbf{u}_{20} \times \mathbf{t}) \qquad (24)$$

Some factors have been omitted from the second term of (24) because their product is approximately unity when $\tan \phi_0/2$ is sufficiently large to require retention of the second term. For vertical (+) polarization, $\mathbf{u}_{10}^+ = \mathbf{u}_\eta$, and the application of (18) and (24) leads to

$$\mathbf{u}_{20}^+ = \mathbf{u}_\eta \cos \phi_0 + \mathbf{u}_\zeta \sin \phi_0 \qquad (25a)$$

$$\mathbf{U}^+ = \mathbf{u}_{10}^+ + \mathbf{u}_\zeta \tan (\phi_0/2) \qquad (25b)$$

Similarly, in the general case where $\gamma_0 \leq \pi/2$ and for horizontal (−) polarization,

$$\mathbf{u}_{10}^- = \mathbf{u}_\xi \sin \gamma_0 - \mathbf{u}_\zeta \cos \gamma_0 \qquad (26a)$$

leads to

$$- \mathbf{u}_{20}^- = \mathbf{u}_\xi \sin \gamma_0 + \mathbf{u}_\eta \cos \gamma_0 \sin \phi_0$$
$$- \mathbf{u}_\zeta \cos \gamma_0 \cos \phi_0 \qquad (26b)$$

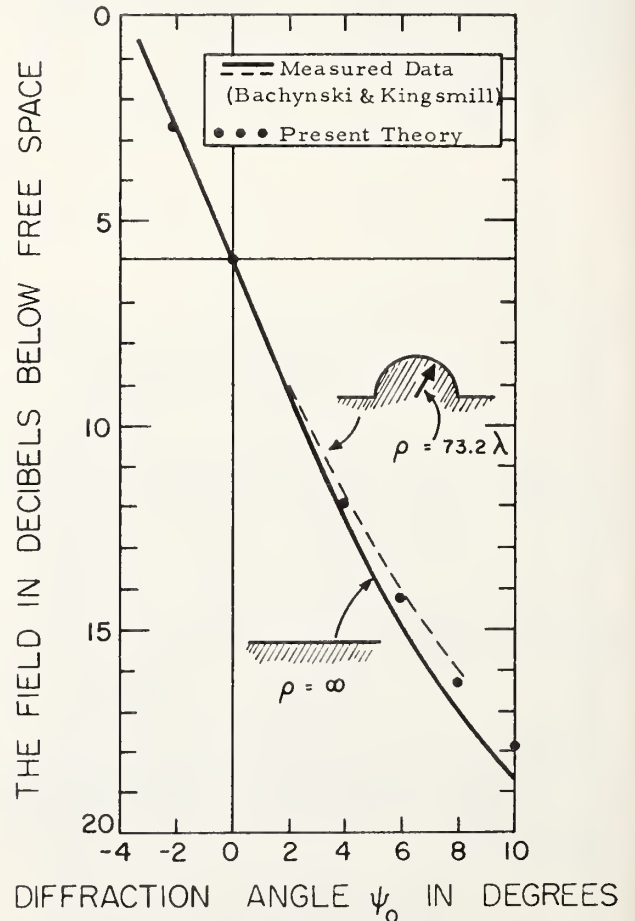$$- \mathbf{U}^- = \mathbf{u}_{10}^- + \mathbf{u}_\eta \cos \gamma_0 \tan \phi_0/2 \qquad (26c)$$

Fig. 2. A comparison of theory and measurement for a disk-edged screen.

From (11), (14), and the equation of the disk, we obtain

$$T_e(l_0) = \left[1 - \frac{r_{10}r_{20}\cos\sigma}{\rho(r_{10} + r_{20})}\right.$$
$$\left. \cdot \sin\phi_0\left(1 - \frac{\tan\sigma}{\tan\phi_0/2}\right)\right]^{-1/2} \quad (27)$$

The solution is given by the product of (23) and (27), since the circular edge represents a correction on the simple straight edge.

Bachynski and Kingsmill [1962] have reported extensive measurements for a screen with the geometry described above, for $\sigma = 0$ and $h < \rho$. The r_{10} was 150 λ and the r_{20} was 113 $\lambda/\cos\phi_0$ and various radii ($\rho = 42.3\ \lambda$, 73.2 λ, and 186.6 λ) were used. The measurements showed a trend of field enhancement due to the disk-shaped edge that increased with

increasing angle and curvature. Figure 2 shows a comparison of theory and experiment. The measurements are represented by the solid- and dashed-line curves, adapted from Bachynski and Kingsmill [1962, Figure 3]. The new theory is represented by the plotted points computed from (23) and (25b) and their product with (27). Table 1 presents a further comparison of theoretical values with experimental data for the disk-edged screen [Bachynski and Kingsmill, 1962; Bachynski, 1963]. The simple knife edge is tabulated for $\rho = \infty$.

Ufimtsev [1958a, b] considered the problem of a plane wave obliquely incident on a metallic disk (for $h = \rho$) and obtained a similar solution by Laplace's method. However, he had assumed that the diffraction effect of a disk would be the same as that for an infinite metallic strip, thus eliminating T_e of (27).

TABLE 1. Comparison of measurement and theory for the $a(R)$ of a disk-edged screen in decibels

ρ/λ	ψ_0, deg	Fig. 2*	Fig. 3*	Fig. 4c*	Fig. 5e*	Fig. 9†	Present Theory‡
42.3	−1			4.0			4.3
	0			5.9			6.0
	2			8.7			9.0
	4			11.7			11.9
	6			15.9			14.0
	8			17.9			15.9
	10						17.3
72.3	−1		4.4	4.3			4.3
	0		6.0	6.0	6.0		6.0
	2		9.0	9.2			9.1
	4		11.8	12.9	12.0		12.1
	6		14.0	15.8			14.3
	8		16.0	18.7	18.3		16.4
	10						18.0
186.6	−1			3.6			4.4
	0			6.0			6.0
	2			9.8			9.2
	4			13.0			12.3
	6			15.9			14.6
	8			19.1			16.7
	10						18.4
∞	−1		4.4				4.2
	0	6.0	6.0			6.0	6.0
	2	9.0	9.2			9.8	9.6
	4	12.8	12.4			13.6	12.6
	6		14.75			17.0	15.1
	8		17.0			19.8	17.4
	10		18.7			22.5	19.2

* [Bachynski and Kingsmill, 1962].
† [Bachynski, 1963].
‡ $a_e(R) = 1 - a_{KE}(R)T_e(l_0)$, $\psi_0 \leq 0$, $a_{KE}(R)T_e(l_0)$, $\psi_0 > 0$, where $a_{KE}(R)$ indicates the diffraction loss for a simple knife edge. For ρ finite, the theoretical correction is applied to the measured values for the simple knife edge (Figure 3), rather than to the theoretical values.

The lack of T_c, however, was not serious for his particular application. If $h > \rho$, there will be two additional points of stationary phase where the disk edge joins the straight-edge portions of the screen. Their contribution would require an extension of the present method of evaluation and will be the subject of a subsequent paper. The solution for $h = \rho$ and TR normal to the disk is simply related to the classical disk problem where the entire disk perimeter constitutes a curve of stationary phase.

7. CONCLUSION

A method of close approximation, previously lacking for the general problem of propagation above 30 MHz in the presence of irregular boundaries, has been presented. A simple approximation for the surface field distribution, assumption I in (5), leads to an expansion of the scalar Helmholtz integral. A second simple assumption II in (18), permits inclusion of this expansion of the Helmholtz integral in the Stratton-Chu vector equation. Examination of the result, (7), shows that assumptions I and II correspond to a choice of equivalent vector field source distributions quite different from those of either physical optics or the equivalence theorem [*Harrington*, 1959].

For an integrand phase function defined by (13), every physically real surface will provide at least one point of stationary phase, and the new vector field expression (7) is, therefore, readily evaluated by the methods of stationary phase. For most applications of interest, this leads to a closed-form solution (15) that characteristically includes the Fresnel-Kirchhoff knife-edge function. The effect of departures of the transverse profile from the simple knife edge is reflected primarily in the normalized curvature (16) at the point of stationary phase.

Alternate choices, alternatives A and B in (19) and (20), are proposed to reduce the number of unknowns. Alternative A, the more reasonable for most applications, is the subject of a subsequent paper. Alternative B, perhaps less reasonable, is still preferable to (and less restrictive than) the classical Fresnel-Kirchhoff approximation and (more to the point) appears to lead to reliable closed-form solutions for the thin-edged screen diffraction problem. The application of (15) and alternative B yields not only the classical half-plane solution readily but also demonstrates an advantage of the method presented: the problem for a spherical wave source is as easily treated as that for plane wave incidence. Finally, the

closed-form solution for the disk-topped knife edge was found to agree well with experimental data, demonstrating the potential of the new method of approximation by providing a new closed-form solution where none existed previously.

From the foregoing, we may conclude that the application of (21) to an irregular screen (a three-dimensional vector problem) involves the superposition of the modified two-dimensional scalar solutions corresponding to the various points of stationary phase. At each point, the scalar two-dimensional solution requires modification by two factors: The first, $T_c(l_0)$, reflects the effect of the screen's transverse profile at that point. The second is a weighting factor that may be required if this point is too close to the adjacent points of stationary phase.

REFERENCES

Bachynski, M. P. (1963), Scale model investigations of electromagnetic wave propagation over natural obstacles, *RCA Rev. 25*(1), 105–144.

Bachynski, M. P., and M. G. Kingsmill (1962), Effect of obstacle profile on knife-edge diffraction, *IRE Trans. Antennas Propagat., 10*, 201–205.

Baker, R. B., and E. T. Copson (1953), *The Mathematical Theory of Huygen's Principle,* 192 pp., University Press, Oxford.

Barsis, A. P., and L. G. Hause (1966), Mountain obstacle diffraction measurements at 751 Mc/s and 9.2 Gc/s, *Radio Sci., 1*(1), 67–78.

Born, M., and E. Wolf (1964), *Principles of Optics*, 808 pp., Pergamon Press, New York.

Dougherty, H. T. (1969), An expansion of the Helmholtz integral and its evaluation, *Radio Sci., 4*(11), this issue.

Dougherty, H. T., and L. J. Maloney (1964), Application of diffraction by convex surfaces to irregular terrain situations, *Radio Sci., 68D*(2), 284–305.

Harrington, R. F. (1959), On scattering by large conducting bodies, *Trans. IRE, Antennas Propagat., 7,* 150–153.

Harrington, R. F. (1961), *Time Harmonic Electromagnetic Fields,* 480 pp., McGraw-Hill, New York.

Hufford, G. A. (1952), An integral equation approach to the problem of wave propagation over an irregular surface, *Quart. Appl. Math., 9*(4), 391–404.

Karczewski, B. (1963), The Fresnel field in Kottler's diffraction theory, *Can. J. Phys., 41*(10), 1623–1628.

Kerr, D. E. (1951), *Propagation of Short Radio Waves,* 728 pp., McGraw-Hill, New York.

Korn, G. A., and T. M. Korn (1961), *Mathematical Handbook For Scientists and Engineers,* 943 pp., McGraw-Hill, New York.

Kottler, F. (1923), On the theory of diffraction by a black screen (in German), *Ann. Phys., 70*(6), 406–456.

Nishikori, K., Y. Kurihara, M. Fudushima, and M. Ikeda (1957), Broad and narrow beam investigations of SHF

diffraction by mountain ridges, *J. Japan Radio Res. Labs.*, *4*(18), 407–422.

Norton, K. A. (1941), The calculation of ground-wave field intensity over a finitely conducting spherical earth, *Proc. IRE, 29*, 623–639.

Norton, K. A., P. L. Rice, and L. E. Vogler (1955), Use of angular distance in estimating transmission loss and fading range for propagation through a turbulent atmosphere over irregular terrain, *Proc. IRE, 43*, 1488–1526.

Page, C. H. (1955), *Physical Mathematics,* Van Nostrand, New York.

Rice, S. O. (1954), Diffraction of plane radio waves by parabolic cylinder, *Bell Syst. Tech. J., 33*(2), 417–504.

Sancer, M. I. (1968), An analysis of the vector Kirchhoff equations and the associated boundary-line charge, *Radio Sci., 3*(2), 141–144.

Schelleng, J. C., C. R. Burrows, and E. B. Ferrell (1933), Ultra shortwave propagation, *Proc. IRE, 21*(3), 427–463.

Selvidge, H. (1941), Diffraction measurements at ultra-high frequencies, *Proc. IRE 29*(1), 10–16.

Senior, T. B. A. (1953), The diffraction of a dipole field by a perfectly conducting half-plane, *Quart. J. Mech. Appl. Math. 6*(3), 101–114.

Sommerfield, A. (1964), *Optics,* Academic Press, New York.

Stratton, J. A. (1941), *Electromagnetic Theory,* McGraw-Hill, New York.

Ufimstev, P. I. (1958*a*), Secondary diffraction of electromagnetic waves by a disk, *Soviet Phys.-Tech. Phys. 3,* 549–556.

Ufimstev, P. I. (1958*b*), Approximate calculation of the diffraction of plane electromagnetic waves by a disk and by a finite cylinder, *Soviet Phys. Tech. Phys. 3,* 2386–2396.

Van Bladel, J. (1964), *Electromagnetic Felds,* McGraw-Hill, New York.

Van Kampen, N. G. (1949), An asymptotic treatment of diffraction problems, *Physica, 14*(9), 575–587.

Wait, J. R., and A. M. Conda (1959), Diffraction of electromagnetic waves by smooth obstacles for grazing angles, *J. Res. NBS, 63D*(2), 181–197.

New Developments in Doppler Radar Methods[**]

Roger M. Lhermitte

Environmental Science Services Administration

Research Laboratories

Boulder, Colorado

I. INTRODUCTION

In the past few years, Doppler radar techniques have been extensively used for the observation and study of the motion of precipitation particles inside storms for the purpose of improving the understanding of storm physics and dynamics. However, the capability of the method for observing the particle motion field in a highly disturbed environment, such as a convective storm, has been limited by the fact that only the radial velocity of the particle motion is observed by a Doppler radar. Furthermore, the treatment of the Doppler information for isolating the three dimensional field of motion requires that appropriate means, such as digital computers, be used for data reduction and analysis. These means are by necessity far more sophisticated than the techniques presently used in the analysis of conventional and Doppler weather radar data.

This paper outlines the design of a Doppler radar probing and data processing system, motivated by the recognized potential of the equipment and the recent availability of the necessary computational techniques, which is capable of providing significant advances in our understanding of convective storm processes.

II. LIMITATIONS OF A SINGLE DOPPLER RADAR

Doppler radar methods are capable of sensing only the radial velocity of the particles, i.e., the velocity component projected onto the radar beam axis. Therefore, the analysis of the data provided by a single Doppler radar relies heavily on assumptions used as a substitute for the lack of knowledge of the complete vectorial velocity information. Since it is sensitive only to the vertical velocity, the vertical beam method is less ambiguous and in the case of marked stratification, very useful. However, the method fails to exploit the outstanding capability of the radar technique, i.e., its ability to acquire data distributed in three coordinates of space. Time-altitude histories of particle motion have proven useful in the study of stratiform precipitation clouds, but have been of little value in interpreting convective storm processes since restrictive assumptions involved
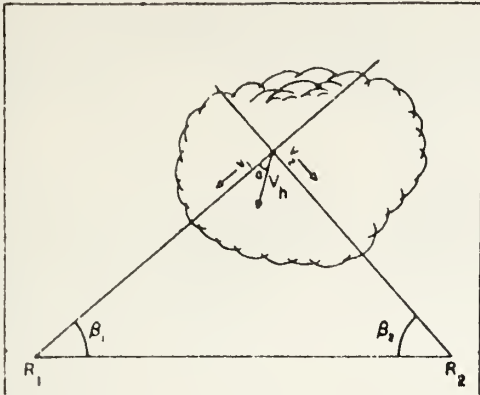
in the technique become invalid.

The use of a single radar scanning beam is useful and effective if assumptions about statistical homogeneities of the precipitation particle motion is accepted in the analysis of the data. The most commonly used scanning scheme relies on continuous azimuth scanning of the radar beam with a programmed elevation angle stepping operation. The Doppler radial velocity is usually displayed as a function of the radar beam azimuth angle by use of appropriate indicators (velocity-azimuth-display, VAD), Lhermitte and Atlas (1961). The method is applicable to the study of the mesoscale wind field in large systems, such as widespread winter storms, and provides vertical profiles of the mean properties of the horizontal wind field (speed, direction, convergence) and the average vertical motion of the precipitation particles. However, because of the complexity and non-uniformity of their wind fields, neither the vertical beam nor the VAD method are satisfactory for observing the motion field of the particles inside convective storm systems.

Donaldson (1967) has endeavored to analyze the horizontal wind field in a convective storm system from data obtained at low beam angles. Azimuth scanning at elevation angles limited to 1°, 3°, and 5° failed to reveal the storm horizontal circulation since the data were still derived from the interpretation of radial velocity alone.

The assumption that a non-evolutive, three dimensional pattern of circulation is translating with the storm, Peace, et al (1968), offers means to analyze the motion field, provided that the storm can be observed from different directions by the radar during its motion. However, such assumptions are restrictive and may be questionable in the case of complex storm systems which are continuously evolving and for which translation speed and direction can not be easily observed.

[**]Presented in the Techniques and Interpretation Session, 13th Radar Meteorology Conference, McGill University, Montreal, Canada, August 1968.

III. THE TWO DOPPLER RADAR METHOD

Fig. 1. R_1 and R_2 are two Doppler Radars

The use of two Doppler radars, installed at different locations and simultaneously observing the same storm, drastically improves the capability of the Doppler method. Fig. 1 illustrates the concept. The same region of a storm is observed by two radars, R_1 and R_2, installed at different locations thereby providing two radial components of the particles' motion, V_1 and V_2. The two components, V_1 and V_2, can be expressed by the following equations:

$$V_1 = V_h \cos\alpha \cos\Theta_1 + (V_t + w)\sin\Theta_1 \qquad (1)$$

$$V_2 = V_h \cos(\beta_1 + \beta_2 - \alpha)\cos\Theta_2 + (V_t + w)\sin\Theta_2 \qquad (2)$$

In these equations β_1 and Θ_2 respectively are the azimuth and elevation angles for R_1; β_2 and Θ_2 respectively are the azimuth and elevation angles for R_2; V_h is the horizontal motion speed; α is the azimuth angle between the direction of the motion and β_1; $V_t + w$, the particles' vertical velocity (V_t is the terminal speed and w the air vertical motion). If the contribution to the Doppler due to vertical motion can be neglected, i.e., $(V_t + w)\sin\Theta \approx 0$, equations (1) and (2) can be solved for V_h and α according to the following expressions:

$$V_h^2 = \frac{1}{\sin^2(\beta_1+\beta_2)}\left[\frac{V_1^2}{\cos^2\Theta_1} + \frac{V_2^2}{\cos^2\Theta_2} + \frac{2V_1V_2\cos(\beta_1+\beta_2)}{\cos\Theta_1 \cos\Theta_2}\right] \qquad (3)$$
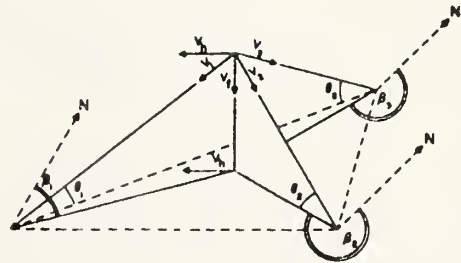
$$\tan\alpha = -\frac{1}{\sin(\beta_1+\beta_2)}\left[\frac{V_2}{V_1}\frac{\cos\Theta_1}{\cos\Theta_2} + \cos(\beta_1+\beta_2)\right] \qquad (4)$$

The optimum spacing between the two radars depends on their characteristics but it is on the order of 20 to 60 kms.

The method offers excellent potential for mapping the particles' horizontal motion field inside convective cells for nearly horizontal radar beams. However, radar beam elevation angle smaller than $5°$ to $10°$ can be accepted in the scheme allowing the observation of the horizontal motion field up to altitudes on the order of 10,000 to 15,000 feet. The only assumption which is needed is to neglect the contribution due to particles' vertical motion. For targets which are outside of the line of sight between the two radars, the method offers accurate and unambiguous results which should clearly reveal convergence and vorticity patterns in the low levels of a convective storm.

If assumptions about the terminal velocity of the particles are adopted, the method can be extended to observations from larger elevation angles for which a significant contribution to the Doppler, due to the particles' vertical velocities, is likely. The method is also capable of providing estimates of the vertical air motion from convergence estimates made at several altitudes.

IV. THE THREE DOPPLER RADAR METHOD

$$\left\{\begin{array}{l} V_1 = V_h \cos(\beta_1-\beta_0)\cos\Theta_1 + V_1 \sin\Theta_1 \\ V_2 = V_h \cos(\beta_2-\beta_0)\cos\Theta_2 + V_1 \sin\Theta_2 \\ V_3 = V_h \cos(\beta_3-\beta_0)\cos\Theta_3 + V_1 \sin\Theta_3 \end{array}\right\} \quad V_1 = V_T + w$$

w estimated from

$$\frac{\partial w}{\partial t} = -\left[\frac{\partial u}{\partial x} + \frac{\partial v}{\partial y}\right]$$

The Three Doppler Radar Method - Cont.

Although it is a reasonable step towards the design of more elaborate systems, the dual Doppler radar method described above fails to provide useful horizontal wind information for targets situated on the line of sight between the two radars. It does not provide a complete knowledge of the three dimensional field of the V_x, V_y, V_z components of the storm's particles' motion. This objective may be achieved from data collected by a well designed system of three Doppler radars, installed at three different locations which simultaneously observe the same convective storm. Fig. 2 illustrates this concept and shows that the radial velocity at a given point in space can be observed from three different directions. The system of three equations indicated in Fig. 1 provides the basis for computing the value of the three components of the motion. Therefore, by combining the radial velocity information provided by the three Doppler radars, it is indeed possible to isolate and evaluate the three dimensional distribution, in Cartesian coordinates x, y, z, of V_x, V_y, V_z. This information can be sampled periodically provided that the storm is within the maximum range of the equipment. The time and space sampling capabilities are discussed below.

As an example of the unique capability of the method, the three dimensional field of particles' motion can be analyzed in the following manner:

First, it is assumed that precipitation particles are moving in the same direction and at the same speed as the horizontal wind. This assumption is valid except when particles are falling in regions of strong wind shear which might introduce a lag of the particles' velocity with respect to the environment. This effect is negligible for most of the precipitation particles; large hailstones are a marginal case. If we accept the above assumption, the particles' horizontal motion field may be taken as that of the horizontal wind. The mean speed (first moment of the velocity spectrum) must be computed to provide basis for interpreting the two dimensional field. Theoretically, the estimated horizontal motion components do not include the variance due to particles' vertical speed distribution. The data are sorted according to their x, y and z coordinates evaluated from radar polar coordinates R, β and θ. The two dimensional estimates of the two quadratic components u and v of the estimated "wind" can then be defined at selected altitudes in the storm. The application of the equation of continuity, within the assumption of incompressibility, to the hori-

zontal wind field, identifies convergence with the estimates of air vertical velocity gradients, $\partial w / \partial z$. By integrating $\partial w / \partial z$ with suitable boundary conditions, it is possible to estimate, not only one vertical updraft profile, but the complete structure of updrafts inside the whole storm. Details on the structure of updrafts will be controlled by the sharpness of the velocity gradients and the inherent velocity resolution of the radar equipment.

Comparison of the updrafts structure with the three dimensional distribution of the particles' vertical velocity (and its spectrum) which is derived simultaneously from the Doppler data, provides knowledge of the distribution of particles' terminal speed within the storm. This, in turn, provides means for defining, in any region of the observed storm, the precipitation particles' terminal velocities and therefore their size distribution. The method has obvious application for the monitoring and study of such important processes as hail formation; its use should provide significant improvement of our knowledge of convective storm processes and provide a firm basis for a more efficient control of their behavior.

The three Doppler radar concept is far more complicated than the usual weather radar systems presently used in meteorological research. It can operate effectively only if efficient digital computer means are used to process the data. The Doppler information must by necessity be stored in a digital format compatible with computer use.

It is impractical and time consuming for the systematic scanning of a storm to restrict the Doppler observations obtained at a given time, to the intersection of the three radar beams in space. Indeed, when the radar beam is aimed in a fixed direction, a large number of ranges can be simultaneously processed therefore adding to the Doppler information with respect to that provided by only one selected region. It is more appropriate that the radial velocity data provided by the three radars be acquired and processed separately, thereby leading to separate estimates of the three radial velocity fields. Since the process of scanning the storm will take an appreciable time, time-space interpolation techniques will be necessary to express the radial motion fields at the same time.

Radar beam scanning systems capable of systematically and automatically acquiring the Doppler data in limited angular regions controlled by the storm position with respect to the radar are required for efficient use of the

3

method. Digital control of a stepping radar beam must be preferred, as means for providing data easier to manipulate with digital computers.

V. DOPPLER SIGNAL PROCESSING REQUIREMENTS

Most of the Doppler studies of atmospheric phenomena have been done by aid of unsophisticated, time consuming, procedures of signal and data processing which have severely limited the analysis of the data and the use of the method to its fullest capability.

Recently, signal and data processing methods have been drastically improved through the increased availability of modern general purpose digital computers and also by the introduction of special purpose processing systems based on the use of modern digital hardware such as integrated circuits. The practicality of the three-Doppler-radar method, with its high rate of information flow, draws benefit from the availability of modern digital methods for the processing and storing of the Doppler radar information.

The most time consuming requirement for Doppler radar information processing, is that of the power density spectrum analysis of a radar signal, simultaneously at a large number of different ranges. The transformation required is a conventional Fourier transform or an equivalent method such as the processing of the signal by use of analog type frequency analyzers. Through applications of digital techniques, computations of the signal power density spectrum are more efficient and also more flexible. The digital approach provides N nonredundant frequency samples from N time samples, thus requiring that N^2 multiplications be done per complete spectrum. If we recognize that 256 time samples are fairly representative of the spectral information in a time signal, then 70,000 multiplications must be done for each conventional Fourier transform. With modern fast digital computers the computing time will be of the order of, or less than, one second; this is comparable to the signal dwell time required to build an acceptable knowledge of the spectrum. Therefore, real-time digital computations by conventional Fourier algorithms are, at least, as effective as the classical method using a bank of filters. In addition, the digital computer offers complete flexibility in the choice of appropriate frequency filter characteristics and frequency coverage which is controlled by the signal sampling rate. Since it is based on the unequivocal Fourier transform mathematical expression, the digital frequency analyzer provides a well defined answer for the spectral density estimates, which is easier to manipulate in the analysis of the data.

The use of fast Fourier transform algorithms (Cooley and Tukey, 1965) decreases the required number of multiplications to $2N \log_2 N$ instead of N^2. This considerably reduces computation time to much less than signal dwell time, thereby making it feasible to process several radar ranges in a time less than a few seconds. This involves the use of high speed, elaborate signal processing systems for the multiplexing, and the analog to digital conversion, of the Doppler signal. It also requires core memories which are organized in such a way that the sequence of the Fourier transforms can be easily computed, range after range, from the stored digital data. Such systems can be built at an acceptable cost by use of modern integrated circuit digital hardware.

These systems are capable of a data acquisition speed which matches the requirements indicated by the estimated time evolution of a convective storm. We must remember, however, that the scanning rate of the radar antenna will still be a limiting factor for high speed data acquisition systems.

CONCLUSION

This paper has been written to discuss the importance of a three-Doppler radar methodology for the study of convective storm processes. It is the author's opinion that such an endeavor will contribute to the study and understanding of the storm's processes in a manner which could not be attained by any other observational means.

Acknowledgment

References

Cooley and Tukey, 1965: An algorithm for the machine calculations of complex Fourier series, Math. of Computation, 19, 297-301.

Donaldson, R., 1967: Horizontal wind measurement by Doppler radar in a severe squall line, Proc. Conf. on Severe Local Storms, St. Louis, pp. 89-98.

Lhermitte and Atlas, 1961: Precipitation motion by pulse Doppler radar, Proc. 9th Wea. Radar Conf., pp. 218-223.

Peace, R., et al, 1968: Horizontal Motion Field Observations with a Single Pulse Doppler Radar, Cornell Aero. Lab. Report.

Analysis of the Cylindrical Confocal Laser Resonator Having a Single Circular Coupling Aperture

GARNER T. McNICE, MEMBER, IEEE, AND VERNON E. DERR, SENIOR MEMBER, IEEE

Abstract—The diffraction losses of the cylindrical confocal resonator having a circular coupling aperture in the center of one of the resonator mirrors have been calculated over the range of resonator Fresnel numbers $0 \leq N_b \leq 1.6$ by the numerical iteration technique of Fox and Li. The specific paths by which energy is diffracted from the resonator have also been investigated and a class of equivalent resonators found that maximizes the energy diffracted through the aperture for a given value of total diffraction loss.

INTRODUCTION

THE cylindrical confocal resonator has become well established as an aid[1] in the design of lasers operating in the visible or near infrared, where the output power can be coupled from the resonator through low-loss, partially transmitting dielectric coatings deposited on the resonator mirrors [2]–[4]. In the far infrared, however, such coatings are not yet available and other coupling techniques are required. One of these is the use of a coupling aperture in the center of the output mirror [5].

For relatively low-gain laser transitions, only a small aperture is required to achieve maximum output power, and the mode structure of the resonator remains virtually unchanged by the introduction of the coupling aperture. The optimum size for the coupling aperture can then be calculated on the basis of conventional confocal resonator theory and a knowledge of the optimum coupling coefficient [6] for the laser. Some of the far-infrared lasers have high-gain transitions (HCN at 337 and 311 μ, for instance) [7], [8] and can utilize coupling apertures of sufficient size to produce large changes in the resonator mode structure. In this case the theory of conventional confocal resonators is clearly not applicable.

Analyses of the cylindrical resonator having coupling apertures in both mirrors have been performed for the confocal resonator by McCumber [9] and for the plane-parallel Fabry–Perot resonator by Li and Zucker [10]. While these calculations are more pertinent to this problem, they do not provide quantitative information about the resonator with a single aperture.

[1] The strictly confocal system rarely appears in practice due to its unique position on the resonator stability diagram [1], but the results of its analysis are widely used to estimate the parameters of the more complex nonconfocal systems.

MODES AND DIFFRACTION LOSSES

The resonator under consideration is shown in Fig. 1. Assuming the surfaces to be perfectly reflecting, the resonator dimensions to be much larger than a wavelength, and the resonator length to be much larger than the mirror diameter, the normalized electric field at the mirror surfaces has been shown to be described by the following set of equations [1], [2], [11]:

$$E_{lp}^{(1)}(r_1, \theta_1) = F_{lp}^{(1)}(r_1)e^{-il\theta_1}$$
$$E_{lp}^{(2)}(r_2, \theta_2) = F_{lp}^{(2)}(r_2)e^{-il\theta_2} \tag{1}$$

$$\gamma_{lp}^{(2)}F_{lp}^{(2)}(r_2) = (2\pi/\lambda d)\int_a^b J_l\left(\frac{2\pi r_1 r_2}{\lambda d}\right)F_{lp}^{(1)}(r_1)r_1\,dr_1$$
$$\gamma_{lp}^{(1)}F_{lp}(r_1) = (2\pi/\lambda d)\int_0^b J_l\left(\frac{2\pi r_1 r_2}{\lambda d}\right)F_{lp}^{(2)}(r_2)r_2\,dr_2, \tag{2}$$

where $E_{lp}^{(1)}(r_1, \theta_1)$ and $E_{lp}^{(2)}(r_2, \theta_2)$ are the normalized electric fields of the TEM$_{lp}$ mode at Mirrors 1 and 2, respectively; λ is the wavelength; d is the distance between the two mirrors (which is also equal to the radius of curvature of the two spherical mirror surfaces); $2b$ is the outer diameter of the mirror; $2a$ is the diameter of the coupling hole; r_1, θ_1 and r_2, θ_2 are polar coordinates at Mirrors 1 and 2, respectively, in a plane perpendicular to the resonator longitudinal axis; $J_l(x)$ is the lth-order Bessel function of the first kind [12]; and $|\gamma_{lp}^{(1)}|^2$ and $|\gamma_{lp}^{(2)}|^2$ can be interpreted as power reflection coefficients [9] associated with Mirrors 1 and 2, respectively, if the field distributions are normalized so that

$$\int_a^b |F_{lp}^{(1)}(r_1)|^2\,r_1\,dr_1 = \int_0^b |F_{lp}^{(2)}(r_2)|^2\,r_2\,dr_2.$$

The fractional power loss at Mirrors 1 and 2 is $1 - |\gamma_{lp}^{(1)}|^2$ and $1 - |\gamma_{lp}^{(2)}|^2$, respectively, and the fractional power loss for a two-way transit is $1 - |\gamma_{lp}^{(1)}\gamma_{lp}^{(2)}|^2$. These equations are valid on the condition that the electric field at each of the mirrors be self-reproducing and that the resonance condition

$$4d/\lambda = 2q + l + 2p + 1, \qquad q = 1, 2, 3, \cdots ,$$
$$l, p = 0, 1, 2, \cdots , \tag{3}$$

be met [3], [4].

It is convenient to express the variables r_1 and r_2 in terms of their associated Fresnel numbers, reducing (2) to
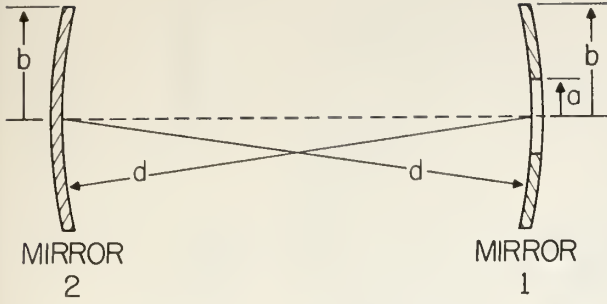
Fig. 1. Cross-sectional view of the cylindrical confocal resonator with a single coupling aperture. The resonator consists of circular mirrors of radius b having spherical surfaces with radius of curvature d equal to their separation. A circular aperture of radius a exists in the center of Mirror 1.

$$\gamma_{l\rho}^{(2)}R_{l\rho}^{(2)}(N_2) = \pi \int_{N_a}^{N_b} J_l[2\pi(N_1 N_2)^{1/2}]R_{l\rho}^{(1)}(N_1) \, dN_1 \qquad (4a)$$

$$\gamma_{l\rho}^{(1)}R_{l\rho}^{(1)}(N_1) = \pi \int_0^{N_b} J_l[2\pi(N_1 N_2)^{1/2}]R_{l\rho}^{(2)}(N_2) \, dN_2, \qquad (4b)$$

where

$$N_1 \equiv \frac{r_1^2}{(\lambda d)}, \qquad N_2 \equiv \frac{r_2^2}{(\lambda d)}, \qquad N_a \equiv \frac{a^2}{(\lambda d)}, \qquad N_b \equiv \frac{b^2}{(\lambda d)}$$

$$R_{l\rho}^{(1)}(N_1) \equiv F_{l\rho}^{(1)}(r_1), \qquad R_{l\rho}^{(2)}(N_2) \equiv F_{l\rho}^{(2)}(r_2).$$

Equation (4) can be further reduced to a single integral equation by substituting (4a) into (4b) and integrating over Mirror 2, producing

$$\gamma_{l\rho}^{(1)}\gamma_{l\rho}^{(2)}R_{l\rho}^{(1)}(N_1) = \pi^2 \int_{N_a}^{N_b} K_l(N_1, \tau)R_{l\rho}^{(1)}(\tau) \, d\tau, \qquad (5)$$

where

$$K_l(N_1, \tau) \equiv \int_0^{N_b} J_l[2\pi(N_1 N_2)^{1/2}]J_l[2\pi(N_2\tau)^{1/2}] \, dN_2$$

$$= \begin{cases} \dfrac{(N_1 N_2)^{1/2}J_{l+1}[2\pi(N_1 N_b)^{1/2}]J_l[2\pi(\tau N_b)^{1/2}] - (\tau N_b)^{1/2}J_l[2\pi(\tau N_b)^{1/2}]J_{l+1}[2\pi(\tau N_b)^{1/2}]}{N_1 - \tau} & \tau \neq N_1 \\[2ex] N_b\{J_l^2[2\pi(N_1 N_b)^{1/2}] + J_{l-1}^2[2\pi(N_1 N_b)^{1/2}]\} - (l/\pi)(N_b/N_1)^{1/2}J_l[2\pi(N_1 N_b)^{1/2}]J_{l+1}[2\pi(N_1 N_b)^{1/2}] & \tau = N_1 \end{cases}$$

and τ is a dummy variable.

We have solved (4) by using the numerical iteration technique of Fox and Li [2], performing the iteration alternately with (4a) and (4b). That is, initial values were assigned to $R_{l\rho}^{(1)}(N_1)$, and the integral of (4a) was evaluated. The value of this integral was then assigned to $\gamma_{l\rho}^{(2)}R_{l\rho}^{(2)}(N_2)$ and the integral of (4b) evaluated, its value being the new starting value for the next iteration.

This procedure yields only the TEM_{l0} modes, the TEM_{l1} modes being generated by subtraction of the contribution of the TEM_{l0} mode from the initial field distribution and repeating the calculation. Extension of this technique to higher orders in ρ is possible in prin-

ciple but frequently fails in practice because of accumulation of computational error. For these higher order modes the matrix eigenvalue technique of McCumber [9] and the recent resonance excitation technique of Fox and Li [13] are more effective.

Computations were performed on an SDS 940 time-sharing computer system. The numerical integrations were performed by Gauss' method with 10 points over each range of integration. Checks for sufficient resolution were made at some of the larger values of N_b by recalculating the solutions with a 20-point Gauss approximation. The results were found to agree in the limit of no aperture with the results obtained by Fox and Li [2] and under the condition of apertures in both mirrors with McCumber's [9] results. The single-aperture results were checked for self-consistency by means of (5).

Diffraction losses were calculated for six modes over the range $0.4 \leq N_b \leq 1.6$ and $0 \leq N_a \leq 1$. The results are presented in Figs. 2–5. The percent loss per transit shown in these curves is the average one-way loss, equal to

$$[1 - |\gamma_{l\rho}^{(1)}\gamma_{l\rho}^{(2)}|] \times 100.$$

This quantity was used rather than the two-way loss in order to conform to the conventions of the literature. The two are related by the expression

$$L_{\text{two-way}} = 2L_{\text{one-way}} - (L_{\text{one-way}})^2/100. \qquad (6)$$

The effect of the coupling aperture on the intensity distribution at the two mirrors was also calculated. It was found that the diffraction losses at both mirrors increase monotonically with increasing aperture size. The field distribution at the output mirror was found to behave similarly to that observed in a resonator having coupling apertures in both mirrors [9]: modes that would have intensity maxima at the center of the mirror in a conventional confocal resonator (the $\text{TEM}_{0\rho}$ modes) are especially sensitive to the introduction of the coupling aperture, while the modes that would have nulls at this point (the $l \neq 0$ modes) are relatively stable, retaining their essential features for all but very large aperture sizes. Across the back mirror, there is little change in the general shape of the distribution for any mode. The effect of the aperture on both classes of modes is illustrated by the TEM_{00} mode in Fig. 6 and by the TEM_{10} mode in Fig. 7. The solid and dashed curves are the intensity distributions across the output mirror and back mirror, respectively. These curves are all normalized to represent
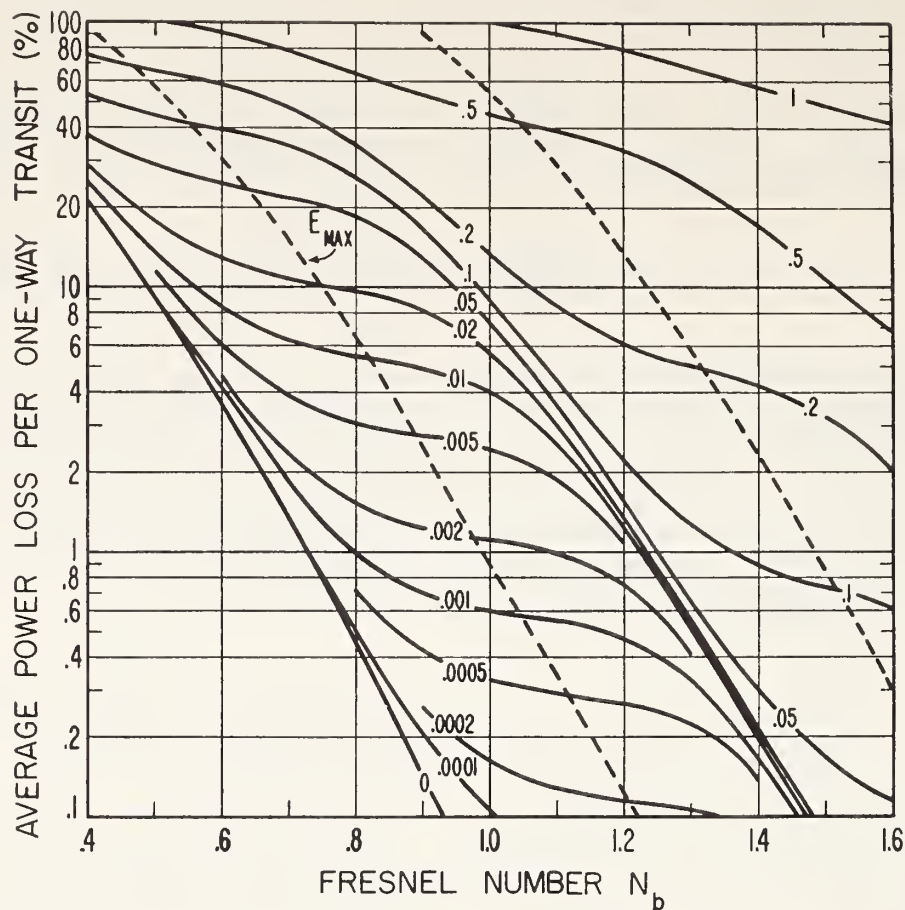
Fig. 2. Average power loss per one-way transit of the TEM_{00} mode versus mirror Fresnel number N_b for several values of aperture Fresnel number N_a. The dashed lines indicate the first two aperture efficiency maxima.
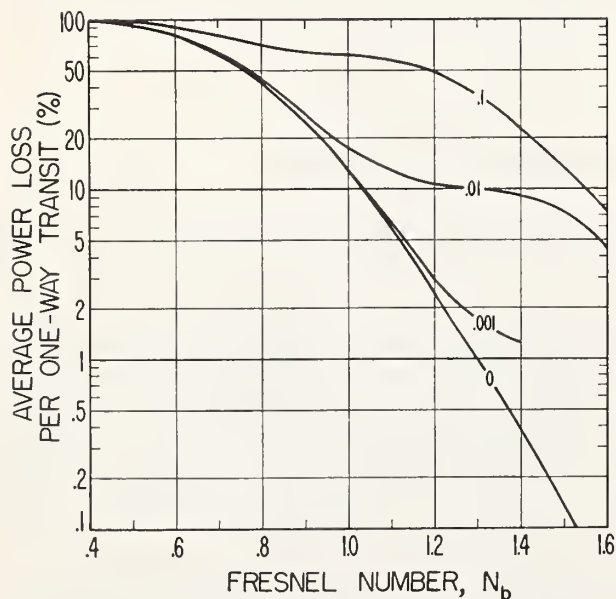

Fig. 3. Average power loss per one-way transit of the TEM_{01} mode versus mirror Fresnel number N_b for several values of aperture Fresnel number N_a.
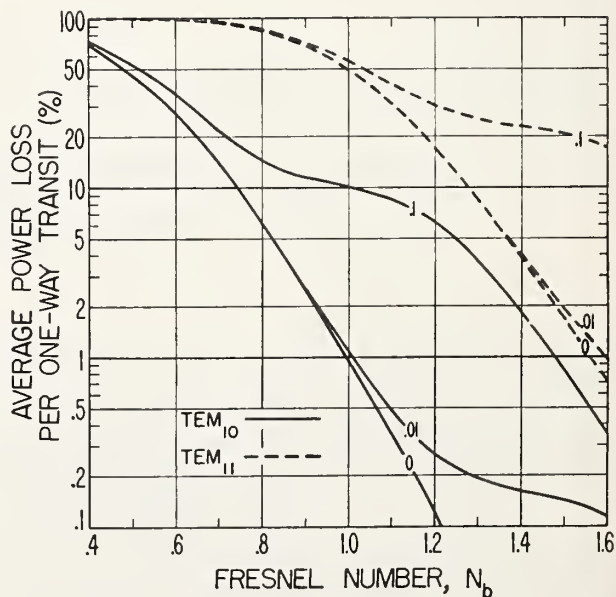
Fig. 4. Average power loss per one-way transit of the TEM_{10} and TEM_{11} modes versus mirror Fresnel number N_b for several values of aperture Fresnel number N_a.
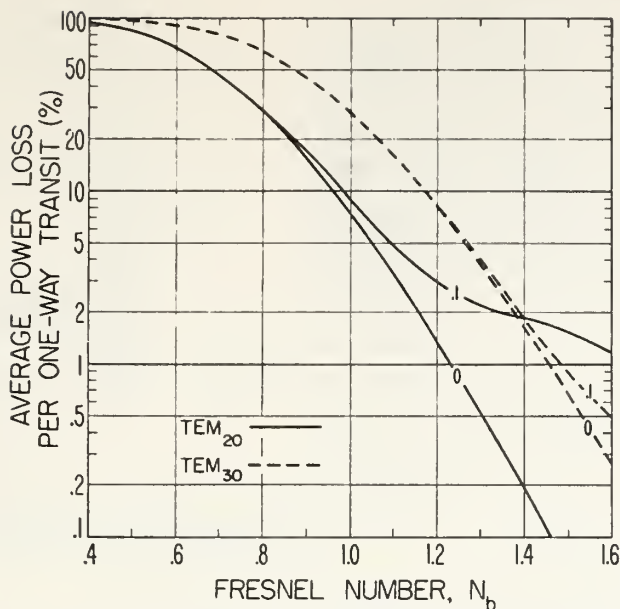
Fig. 5.   Average power loss per one-way transit of the TEM_{20} and TEM_{30} modes versus mirror Fresnel number N_b for several values of aperture Fresnel number N_a.
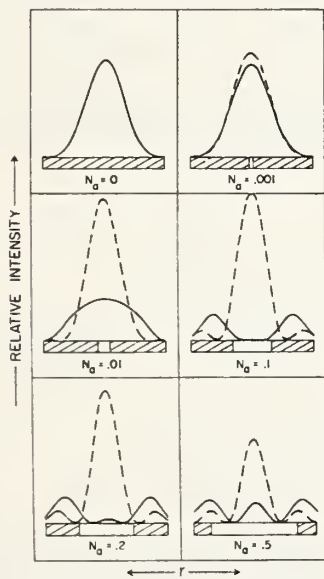

Fig. 6.   Relative intensity distributions of the TEM_{00} mode versus radial position r on the surface of the mirrors for a fixed Fresnel number ($N_b = 1$) and for several values of the aperture Fresnel number N_a. The solid curve is the output mirror distribution and the dashed curve is the back mirror distribution. The crosshatched rectangular section at the base of each figure represents a cross section of the output mirror associated with each value of N_a.
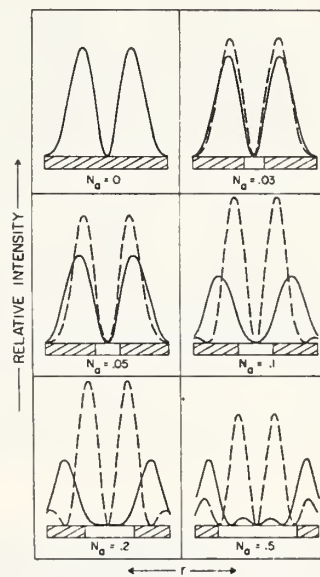
Fig. 7.   Relative intensity distributions of the TEM_{10} mode versus radial position r on the surface of the mirror for a fixed Fresnel number ($N_b = 1.2$) and for several values of the aperture Fresnel number N_a. The solid curve is the output mirror distribution and the dashed curve is the back mirror distribution. The crosshatched rectangular section at the base of each figure represents a cross section of the output mirror associated with each value of N_a.

the intensity distributions that remain after a two-way transit through the resonator, under the assumption of an initial excitation of one power unit in the given mode.

It is instructive to compare the diffraction loss curves for the TEM_{00} mode (Fig. 2) with the intensity distri-

bution curve across the output mirror for the same mode (Fig. 6). It is seen that the resonator loss for very small aperture sizes is almost constant and the intensity distribution is near Gaussian. Most of the energy lost from the resonator is diffracted around the outer edges of the mirrors. As the aperture size is increased, however,

the energy propagated through it becomes a significant portion of the total resonator loss, causing a sharp increase in the total loss of the resonator and a flattening of the intensity distribution curve. A further increase in aperture size causes a depression to appear in the center of the mode and the resonator again becomes relatively insensitive to further variation of the aperture size. In this region the diffraction loss curves are bunched closely together. With additional increase in the aperture size, an intensity maximum returns at the center of the mirror and the resonator losses again increase rapidly.

Similar calculations have also been performed on several nonconfocal systems using combinations of curved and flat mirrors and containing coupling apertures in one or both mirrors. Results pertaining to specific resonators of particular interest will be presented in a later paper.

APERTURE EFFICIENCY

Figs. 2–5 provide the magnitude of the resonator's total diffraction loss but shed no light on the specific manner in which the losses are incurred. In particular, they make no distinction between the energy lost around the edges of the mirrors and the energy propagated through the aperture. Such a distinction is desirable since, for most applications, energy lost around the edges of the mirrors does not constitute a useful output.

With this in mind, we consider the progress of a wave as it travels back and forth through the resonator. If observation of the wave is started at Mirror 1 (the mirror containing the aperture), it is seen that it propagates to Mirror 2, where it suffers diffraction loss around the outer edge of the mirror, is reflected, and returned to Mirror 1, where it suffers diffraction losses through the aperture as well as around the edge of the mirror. The energy lost through the aperture on the return trip can be characterized by the aperture efficiency defined as

$$E = 100 \times \frac{\text{power radiated through the aperture per two-way transit}}{\text{total diffraction loss per two-way transit}}$$

under the condition that the two-way transit start and end at Mirror 1. The aperture efficiency is essentially a figure of merit, useful in comparing two resonators having the same total diffraction loss; it is not, however, an unambiguous representation of resonator power efficiency.[2] In fact, it is doubtful if a meaningful measure of power efficiency can be defined without including the active medium in the calculation to produce a nontrivial equilibrium field distribution.

The aperture efficiency can be evaluated by assuming the wave leaves Mirror 1 in a mode of the resonator with intensity $|R_{lp}^{(1)}(N_1)|^2$. On its return, the intensity

[2] Taking the two-way transit from Mirror 2 and back, for instance, increases the aperture efficiency by a factor of $1/|\gamma_{lp}^{(1)}|^2$.
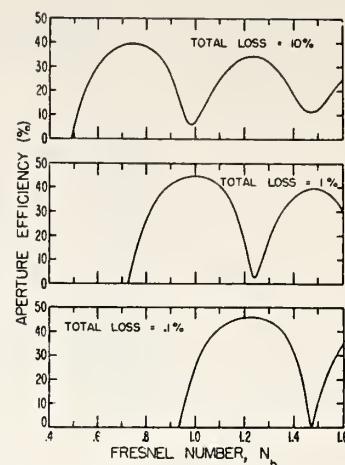
Fig. 8. Aperture efficiency of the TEM$_{00}$ mode versus mirror Fresnel number N_b, for average resonator losses of 0.1, 1, and 10 percent per one-way transit.

is reduced to

$$|\gamma_{lp}^{(1)}\gamma_{lp}^{(2)}R_{lp}^{(1)}(N_1)|^2.$$

The power radiated through the aperture is

$$|\gamma_{lp}^{(1)}\gamma_{lp}^{(2)}|^2 \int_0^{N_a} |R_{lp}^{(1)}(N_1)|^2 \, dN_1,$$

and the total diffraction loss (including the aperture loss) over the two-way transit is

$$[1 - |\gamma_{lp}^{(1)}\gamma_{lp}^{(2)}|^2] \int_{N_a}^{N_b} |R_{lp}^{(1)}(N_1)|^2 \, dN_1.$$

The aperture efficiency, then, is

$$E = 100 \times \frac{|\gamma_{lp}^{(1)}\gamma_{lp}^{(2)}|^2}{1 - |\gamma_{lp}^{(1)}\gamma_{lp}^{(2)}|^2} \times \frac{\int_0^{N_a} |R_{lp}^{(1)}(N_1)|^2 \, dN_1}{\int_{N_a}^{N_b} |R_{lp}^{(1)}(N_1)|^2 \, dN_1}. \tag{7}$$

The usefulness of the aperture efficiency lies in its application to the problem of optimum coupling. For optimum coupling, the total loss of the resonator is chosen so as to extract maximum power from the active medium. The aperture-coupled resonator, however, also requires that as much of this energy as possible exit through the aperture rather than around the mirror edges. This is equivalent to choosing a resonator so that the aperture efficiency is maximized while the total diffraction loss is maintained at a fixed value determined by the parameters of the active medium.

The aperture efficiency has been calculated for the TEM$_{00}$ mode over the range of parameters used in the previous curves. Some of the results are presented in Fig. 8 where E is plotted against N_b, with N_a being
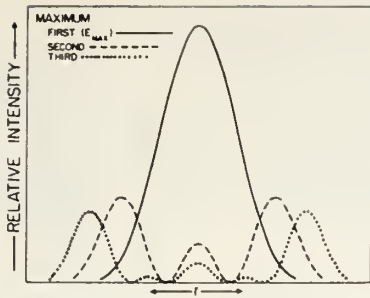
Fig. 9. Relative intensity distributions of the TEM_{00} mode versus radial position r at the output mirror for each of the first three aperture efficiency maxima. Average resonator loss is 10 percent per one-way transit.
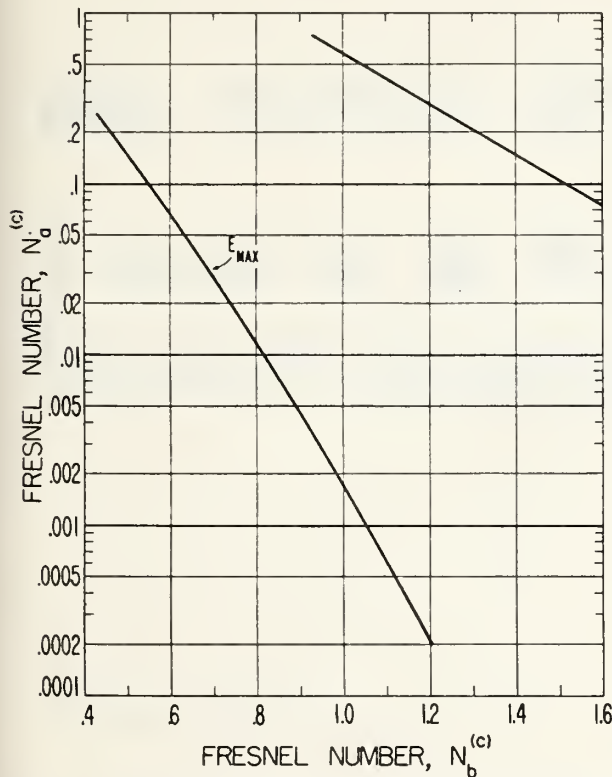

Fig. 10. Aperture Fresnel number $N_a^{(c)}$ versus mirror Fresnel number $N_b^{(c)}$ at the first two aperture efficiency maxima. A resonator chosen from these curves will lie on one of the dashed lines of Fig. 2.

adjusted to maintain the total diffraction loss at a fixed value. It is seen that the aperture efficiency does possess a maximum even though the total diffraction loss of the resonator is held constant. In fact, a series of maxima exists. The occurrence of these maxima has been investigated and found to be associated with the cyclic appearance of a central maximum in the intensity distribution function at the output mirror as N_b is increased. Typical distribution functions associated with the first three maxima are shown in Fig. 9.

The values of N_b associated with the first two aperture efficiency maxima are represented by the dashed lines in Fig. 2, the first (largest) maximum being designated as E_{max}. The corresponding values of N_a were extracted from the same figure and are presented in Fig. 10. Using these two figures, a class of equivalent resonators with maximum aperture efficiency can be associated with each value of total diffraction loss. Specifically, these are the resonators satisfying the relations

$$\frac{a^2}{(\lambda d)} = N_a^{(c)}$$
$$\frac{b^2}{(\lambda d)} = N_b^{(c)}, \tag{S}$$

where $N_a^{(c)}$ and $N_b^{(c)}$ are the values of N_a and N_b that generate the aperture efficiency maximum at the specified value of total diffraction loss.

Summary

The use of the aperture-coupled confocal resonator for far-infrared lasers can be expected to continue until efficient dielectric coatings become available at the longer wavelengths. Accordingly, we calculated diffraction losses and some intensity distributions for six low-loss modes over the range $0.4 \leq N_b \leq 1.6$.

We also investigated the manner in which the diffraction losses are distributed between the aperture loss and the loss around the outer edge of the mirrors. A class of equivalent resonators was found that maximizes the loss through the aperture for a specified value of total diffraction loss. This result is useful for optimum coupling in those applications where energy diffracted around the edge of the mirrors does not constitute a useful output.

Note added in proof: McCumber has recently considered this problem [14] and obtained results in agreement with those presented here. He generalizes the discussion by removing the restriction of equal mirror diameters, but does not consider the problem of optimum coupling.

References

[1] A. G. Fox and T. Li, "Modes in a maser interferometer with curved and tilted mirrors," *Proc. IEEE*, vol. 51, pp. 80–89, January 1963.
[2] ——, "Resonant modes in a maser interferometer," *Bell Sys. Tech. J.*, vol. 40, pp. 453–488, March 1961.
[3] G. D. Boyd and J. P. Gordon, "Confocal multimode resonator for millimeter through optical wavelength masers," *Bell Sys. Tech. J.*, vol. 40, pp. 489–508, March 1961.
[4] G. D. Boyd and H. Kogelnik, "Generalized confocal resonator theory," *Bell Sys. Tech. J.*, vol. 41, pp. 1347–1369, July 1962.
[5] C. K. N. Patel, W. L. Faust, and C. G. B. Garrett, "Laser action up to 57.355 μ in gaseous discharges (Ne, He–Ne)," *Appl. Phys. Letters*, vol. 4, pp. 18–19, January 1, 1964.
[6] A. Yariv, "Energy and power considerations in injection and optically pumped lasers," *Proc. IEEE*, vol. 51, pp. 1723–1731, December 1963.
[7] H. A. Gebbie, N. W. B. Stone, W. Slough, and J. E. Chamberlain, "Sub-millimetre maser amplification and continuous wave emission," *Nature*, vol. 211, p. 62, July 2, 1966.
[8] V. J. Corcoran, W. T. Smith, and J. J. Gallagher, "CW gain characteristics of the 890-GHz HCN laser line," *IEEE J.*

Quantum Electronics (Correspondence), vol. QE-5, pp. 292–293, June 1969.

[9] D. E. McCumber, "Eigenmodes of a symmetric cylindrical confocal laser resonator and their perturbation by output-coupling apertures," *Bell Sys. Tech. J.*, vol. 44, pp. 333–363, February 1965.

[10] T. Li and H. Zucker, "Modes of a Fabry–Perot resonator with output-coupling apertures," *J. Opt. Soc. Am.*, vol. 57, pp. 984–986, August 1967.

[11] J. P. Gordon and H. Kogelnik, "Equivalence relations among spherical mirror optical resonators," *Bell Sys. Tech. J.*, vol. 43, pp. 2873–2886, November 1964.

[12] G. N. Watson, *A Treatise on the Theory of Bessel Functions.* New York: Macmillan, 1948.

[13] A. G. Fox and T. Li, "Computation of optical resonator modes by the method of resonance excitation," *IEEE J. Quantum Electronics*, vol. QE-4, pp. 460–465, July 1968.

[14] D. E. McCumber, "Eigenmodes of an asymmetric confocal laser resonator with a single output-coupling aperture," *Bell Sys. Tech. J.*, vol. 48, pp. 1919–1937, July–August 1969.

U. S. DEPARTMENT OF COMMERCE
C. R. Smith, Secretary

ENVIRONMENTAL SCIENCE SERVICES ADMINISTRATION
Robert M. White, Administrator

ESSA RESEARCH LABORATORIES
George S. Benton, Director

ESSA TECHNICAL REPORT ERL 63-WPL 2

A Circuit For the Measurement of Normalized Crosscorrelations

GERARD R. OCHS

WAVE PROPAGATION LABORATORY
BOULDER, COLORADO
March 1968

A CIRCUIT FOR THE MEASUREMENT OF
NORMALIZED CROSSCORRELATIONS

Gerard R. Ochs

A circuit that measures the normalized cross-correlation of a pair of input voltages over a dynamic range of 10^3 in a 10-kHz bandwidth is described. The input signals should have a normal amplitude distribution, but useful approximations to the crosscorrelation can be obtained for noise-like signals differing considerably from normal.

At the expense of some computational efficiency, we know we may obtain the normalized crosscorrelation of two signals having a jointly normal distribution by merely observing the signs of the signals relative to their means (Van Vleck and Middleton, 1966; Weinreb, 1963; Ray et al.) The latter two references also discuss instruments using this principle which compute autocorrelation and cross spectral density, respectively. A simple circuit utilizing the method of signs to measure normalized crosscorrelations has found wide application in the Optical Propagation Program area. The circuit described here accepts a pair of input voltages with a dynamic range greater than 10^3 in a 10-kHz bandwidth and provides a measurement of the normalized correlation coefficient of the input voltages. The circuit is strictly accurate only for signals having a normal amplitude distribution, but will give a useful approximation for noise-like signals differing considerably from normal.

Van Vleck and Middleton (1966) and Weinreb (1963) explain the theory of operation, and it will not be discussed here; however, several of the results will be quoted. One is that the output voltage of the circuit is not linear with correlation, but follows the law,

$$\rho = \sin\left(\frac{\pi}{2} \frac{V}{V_{max}}\right) \quad , \tag{1}$$

where

ρ = normalized correlation coefficient

V = output voltage

V_{max} = output voltage for $\rho = 1$.

This relationship is plotted in fig. 1.

The second point concerns computational efficiency. The accuracy of the estimate obtained is of course less than if it were computed by the defining relation,

$$\rho = \frac{\overline{xy}}{\left(\overline{x^2}\,\overline{y^2}\right)^{1/2}} \qquad , \qquad (2)$$

where x and y are the signal deviations from their means, having crosscorrelation ρ. Near $\rho = 0$, the correlator requires about 2.5 times as much sample length as would be required by computing ρ directly (Barber, 1961). As the correlation increases, more time is required, approximately 3 times at $\rho = 0.5$, and 6.5 times at $\rho = 0.9$. The standard deviation of the estimate of ρ does, however, decrease with increasing ρ, but not as rapidly as when ρ is computed directly from the defining equation.

In the circuit (fig. 2), the combination of selectable coupling capacitors and 10-k resistors in series with the inputs determines the means of the two signals to be correlated. The time constant, τ, of these circuits (adjustable from 0.001 to 10 s) forms an exponential window in which present information is most heavily weighted and past information is gradually discounted. It is approximately the length of the time average represented by the bars in (2). Considering the circuit as a high pass filter, we find that the half-power frequency response, f_c, occurs at

2

$$f_c = \frac{1}{2\pi\tau} \tag{3}$$

and frequencies below this value get less and less consideration in the correlation, according to the 6-dB/octave rolloff law.

The signs of the signals relative to their means are determined by the operational amplifiers following the RC circuits. Within the voltage range needed to drive the micrologic circuits, the gain of the circuits is essentially the open loop gain of the amplifiers. The output voltage of the operational amplifiers must be constrained to that required for operation of the micrologic, to prevent overload of both the amplifier and the micrologic. The diodes form a nonlinear feedback circuit that sharply lowers the gain of the amplifiers as signal levels increase so that the maximum voltage excursion at the output is about 4 V. The current capability of the D-8 is such that $\pm$ 10 V referred to the mean may be applied before the amplifier loses its ability to hold the summing point at ground potential.

The dynamic range-bandwidth product of the correlator is largely determined by the gain-bandwidth product of the operational amplifiers, within the 2-MHz capability of the micrologic. For example, the D-8 units have a gain-bandwidth product of 1.5 MHz. If a 10-kHz bandwidth is required, the gain at 10 kHz will be $1.5 \times 10^6 / 10^4$ or 150. To have a sufficient voltage swing (2.5 V) to operate the micrologic, the input voltage must be 2.5/150 = 16.7 mV. The dynamic range is then the maximum input voltage swing divided by 16.7 mV or 20/.0167 = 1200. If a bandwidth of 100 kHz is desired, the dynamic range is then reduced to 120.

The micrologic units following the sign-determining circuits form an exclusive or circuit with an inverted output; i.e., the output is according to the following truth table:

3

Micrologic Input 1	Micrologic Input 2	Micrologic Output
1	1	1
1	0	0
0	1	0
0	0	1

Thus if the signals are alike, the output is one; and if unlike, the output is zero. Now the voltage (3.7 V) representing "one" corresponds to a correlation of one and the zero output (0.1 V), a correlation of minus one. For correlations between these two extremes, the output divides its time between the two levels.

The output circuitry provides the following functions: 1) it averages the fluctuating signal with an adjustable time constant (0.01 to 100 s) to read the fraction of time the signal is at one of the levels, 2) it biases the signal so that zero voltage corresponds to zero correlation (equal probability of being at either one or zero), 3) it provides a voltage output up to $\pm$ 10 V at 1 mA, and 4) it provides a current output for driving 1 mA chart recorders.

The correlator may be conveniently calibrated for zero correlation by using two audio signal generators set at different frequencies, which are not odd harmonics of each other. Obviously the same signal into both inputs produces a correlation of one, and a signal and its inversion, a correlation of minus one. For the minus one calibration, however, care must be taken to make sure that any time delay between the signal and its inversion is not significant.

The performance of the correlator may be checked experimentally on amplitude distributions other than Gaussian with the aid of a signal adder and a true rms voltmeter. Two samples of the signal, s_1 and s_2, known to have zero correlation but equal rms value are used. A portion of one of the signals, as_2, is added to the other and the crosscorrelation of $(s_1 + as_2)$ and s_2 is measured. It can be shown by insertion of these

4

values into the defining equation for ρ that the crosscorrelation of these two signals is

$$\rho = \left(\frac{a^2}{1+a^2} \right)^{1/2} \qquad , \qquad (4)$$

and this value may be compared to the correlator reading to assess the performance of the correlator with a given non-Gaussian amplitude distribution.

REFERENCES

Barber, N. F. (1961), "Experimental Correlograms and Fourier Transforms" (Pergamon Press, New York).

Ray, C. D., T. Tsukishima, R. N. Hyland, and C. K. McLane, "Analysis of a frequency-swept one-bit digital correlator" (submitted to J. Appl. Phys.).

Van Vleck, J. H., and David Middleton (1966), "The spectrum of clipped noise," Proc. IEEE, 54, No. 1, 2-19.

Weinreb, S. (1963), "A digital spectral analysis technique and its application to radio astronomy," Tech. Rept. 412, Res. Lab. of Electronics, MIT Cambridge, Mass.
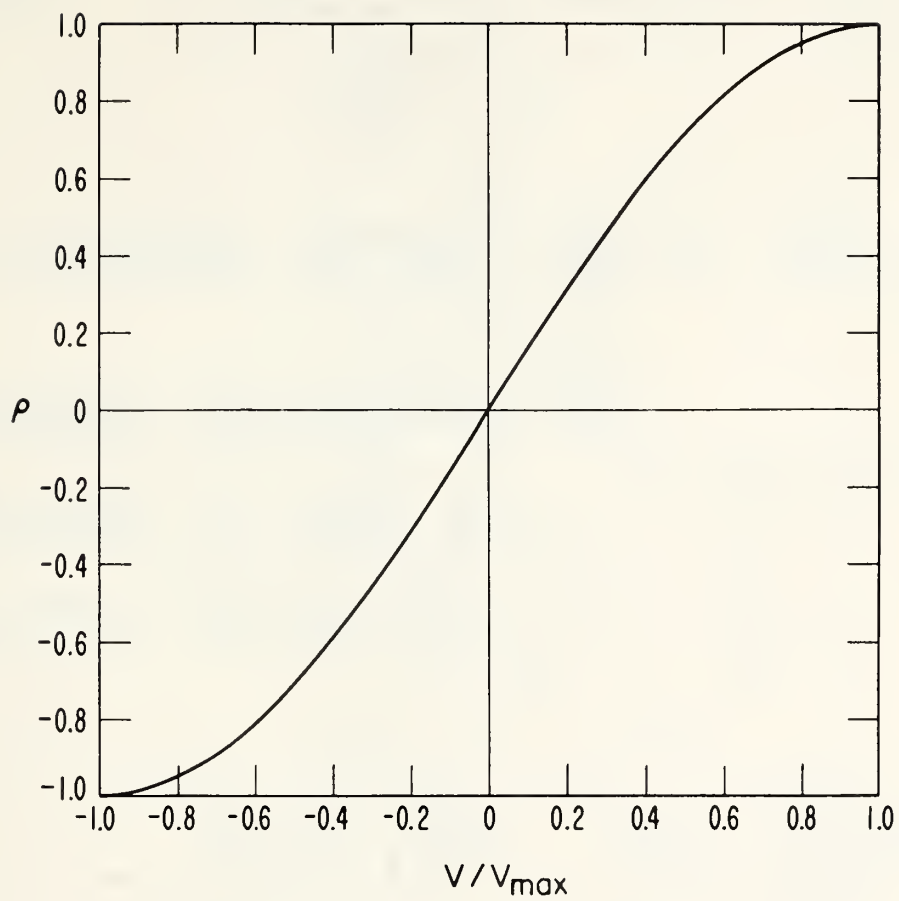
Figure 1.   Correlation versus output

Figure 2. Circuit diagram of correlator

7

U. S. DEPARTMENT OF COMMERCE
Alexander B. Trowbridge, Secretary
ENVIRONMENTAL SCIENCE SERVICES ADMINISTRATION
Robert M. White, Administrator
INSTITUTES FOR ENVIRONMENTAL RESEARCH
George S. Benton, Director

ESSA TECHNICAL REPORT IER 47-ITSA 46

A Resistance Thermometer for Measurement of Rapid Air Temperature Fluctuations

G. R. OCHS

INSTITUTE FOR TELECOMMUNICATION SCIENCES AND AERONOMY
BOULDER, COLORADO
October 1967

TABLE OF CONTENTS

A RESISTANCE THERMOMETER FOR MEASUREMENT OF
RAPID AIR TEMPERATURE FLUCTUATIONS

Gerard R. Ochs

A resistance thermometer capable of measuring air
temperature fluctuations in the frequency range 0.05 to
2000 Hz with a sensitivity of 0.1°C is described. Experi-
mental tests to verify the accuracy of a measurement of
this type are described.

1.   INTRODUCTION

The study of atmospheric turbulence is receiving increased atten-
tion from two relatively new fields; micrometeorology and optical
propagation. In these studies, the measurement of small-scale atmos-
pheric temperature variations, both spatial and temporal, is necessary
for a more complete understanding of the physical processes of turbulent
air movement in the atmosphere. Such measurement may be expected to
lead to a better understanding of the limitations to optical propagation
through the atmosphere; this was the incentive for the development of the
instrument to be described.

Atmospheric turbulence has concerned optical astronomers for
many years, since it places a severe limitation on the definition of tele-
scopes, especially those of large aperture. More recently, with the
advent of lasers and the possibility of wide-band communication at optical
carrier frequencies, there has been renewed interest in the effects of
atmospheric turbulence upon light transmission. The fluctuations in air
density, because of turbulence, result in changes in the index of refraction
and therefore affect the angular spectrum of the optical wave front propa-
gating through the atmosphere. Since variations in air pressure propagate
with the speed of sound, they do not contribute significantly to the small-
scale density inhomogeneities in the atmosphere. Rather, temperature
variations are responsible for the density inhomogeneities and hence the

deleterious effects upon optical images (Briggs, 1963). Ideally, an instrument for measuring these variations should be capable of measuring temperature at a point in the atmosphere without itself altering the temperature. Directly measuring the index of refraction by optical interferometry seemed attractive at first, because no heat exchange is required to make the measurement. Unfortunately, measuring small volumes of air involves the proximity of large pieces of glass, which disturb the air flow. An alternative approach involves the temperature measurement of a solid in near equilibrium with the surrounding air. A study of the performance of a resistance thermometer indicates that this means of air temperature measurement is sufficiently close to the ideal to be useful.*

2. DESCRIPTION OF THE INSTRUMENT

Basically, the instrument is a resistance thermometer connected to an amplifier having a maximum gain of 10^5 and a 16-kHz bandpass. A circuit diagram is shown in figure 1. A calibration circuit and a switch to remove the low-frequency cutoff have been included.

The resistance-sensing element is a length of Wollaston process platinum wire 0.63μ in diameter and 1 mm or less in length. A 120V pilot light bulb with its envelope and filament removed has been used as a convenient base for mounting the wire. These elements are fragile but, when new, clean, and dust free, they will not break in winds up to 11 m/sec (25 mph).

---

* Since the completion of this study, we found that a similar study has been made using a platinum-rhodium wire 0.6μ in diameter. This work is described in an unpublished report by J. L. Chao and V. A. Sandborn, Colorado State University, 1964.

2

In the Wollaston process, platinum wire is encased in a silver tube and the combination is drawn through a die. In this way, extremely small diameter wire can be made. The wire is furnished encased in the silver, and it is handled and mounted in this form on the lead-in wires originally connected to the lamp filament. When the mounting is completed, the silver is etched off with nitric acid, leaving the fine platinum filament.

The calibration arrangement is incorporated into the measurement current supply. Referring to figure 1, by changing the measuring current slightly by removal or insertion of known ΔR, it is possible to change V_f by the amount, ΔV_f, that would occur through a temperature change, ΔT, in the filament. Hence, this may be used as a calibration technique as long as the filament current, I, is small enough so that R_f does not change due to self-heating. Thus holding I constant,

$$\Delta T = \frac{\Delta V_f}{\alpha I R_f} \quad \text{for} \quad \begin{array}{c} R \gg \Delta R \\ R \gg R_f \end{array} \quad \alpha = \text{temperature coefficient of resistance of filament.}$$

and

$$\Delta V_f = \Delta T \alpha I R_f \tag{1}$$

But V_f may also be changed by changing I so

$$V_f = I R_f$$

and

$$\Delta V_f = -I R_f \frac{\Delta R}{R} \tag{2}$$

3

Equating (1) and (2), we find

$$\Delta T \alpha IR_f = -IR_f \frac{\Delta R}{R}$$

or

$$\Delta T = - \frac{\Delta R}{\alpha R} \tag{3}$$

Note that R_f does not appear in (3). Thus as long as $R \gg R_f$, filament length differences have no significant effect on the calibration.

The input impedance of the amplifier is 1000 ohms, nearly equal to R_f. The amplifier impedance has not been brought into the calculation, since it presents the same load to both the calibrating signal and the temperature induced signal and thus does not affect the calibration. The resistors in the circuit of figure 1 have been chosen so actuation of the switches shown produce step changes in the amplifier output corresponding to $-2°$, $-1°$, $+1°$, $+2°$ C temperature difference in a platinum filament. These calibrations are based upon $\alpha = 0.003$ for platinum. The overall calibration has been verified by measurements made with the filament immersed in an oil bath of controlled temperature. Since α is also a function of temperature, this calibration strictly applies to $20°C$ only, and corrections are necessary at other temperatures. The absolute calibration is not critical for most atmospheric measurements, however, and one calibration is probably sufficient for this purpose.

3. VERIFICATION OF TEMPERATURE MEASUREMENT

As with all instrumentation, it is important to examine critically just what is being measured and how close this quantity approaches the measurement actually desired. For a resistance thermometer to measure accurately microtemperature fluctuations in the atmosphere,

4

(1) the heat conduction between the air and the resistance element should be high enough to follow any air temperature change expected, (2) the thermal capacity of the resistance element should be small compared to the thermal capacity of the smallest volume of air of interest, (3) the radiation should not be an important factor, (4) the conduction between the filament and the filament supports should be negligible, (5) the supporting structure should not alter the natural flow of air, and (6) the increase in filament temperature due to the measuring current should be small compared to the temperature variations of interest.

These points were investigated using a straight platinum filament 3.3×10^{-2} cm long and 6.35×10^{-5} cm in diameter. This filament has a mass of 9.46×10^{-9} gm and a thermal capacity of 3.07×10^{-10} cal$^{\circ}$C^{-1}. The volume of air at room temperature and atmospheric pressure that has equal thermal capacity is 1.07×10^{-6}cm^3. The dimensions of this volume of air are small compared to the normally accepted values for the inner scale of turbulence in the atmosphere. In fact, a cube of this volume has an edge dimension smaller than the length of the filament, so the filament length determines the spatial resolution of the temperature measurement.

To measure thermal response time, it was necessary to resort to indirect methods. To heat the filament and then observe the time decay of the filament temperature is more informative than to blow heated air over the filament, since there is no independent way to measure the actual temperature gradient. The process of heating the filament and observing its temperature rise to equilibrium relative to the surrounding air is a reversal of the normal situation and its validity can be questioned. If the filament is heated with radiant energy, the heat is applied on the surface, just as it would be if heated by the air. In the case of electrical heating, the heat is produced throughout the volume of the filament,

5

but during its conduction to the surface the temperature gradient in the filament must be very similar to that during external cooling of the surface. In any event, the thermal conductivity of the metal is more than 10^3 times that of air, therefore the temperature gradient inside the wire is small compared to that in the surrounding air.

Two techniques were used to measure the thermal response time. In the first, an electrical current considerably larger than that used to measure resistance was suddenly applied to the filament in a bridge circuit. The rise time of the filament temperature to that required for constant heat transfer to the surroundings was measured. The time constant (time required for the filament temperature to rise to $1-1/e$ of its final value) of the filament thus measured was $250\,\mu\mathrm{sec}$. The filament was enclosed in a 250-ml flask to help stabilize air temperature fluctuations.

The time response of the filament largely depends upon the effective thermal conductivity of the air. The thermal conductivity of the filament itself is much greater than that of air, so that during a sharp temperature change almost all of the resulting temperature gradient is in the air. Thus, movement of air steepens this gradient resulting in more rapid filament response. The variation in time constant due to wind velocity is shown in figure 2. Since the filament response to a step function input is exponential, the curve in figure 2 is readily transformed into a set of frequency response curves for various wind velocities. This has been done in figure 3 for wind velocities of 0, 0.5, 1, 2, 4 m/sec.

In the second technique, the filament was heated by radiant energy. A helium-neon laser, square-wave intensity modulated at 200 Hz was focussed on the filament inside a 250-ml flask. The exponential rise and decay of the filament temperature, in response to this pulsed radiant energy, had a measured time constant of $220\,\mu\mathrm{sec}$, slightly shorter than the average determined by the electrical heating technique for the same filament.

6

The temperature calibration system is relatively unaffected by different filaments or by aging of a particular filament. The time response does vary, however, probably due to varying amounts of foreign matter on the surface of the filament. The values shown in figure 2 and 3 represent the slowest responses encountered and appear to be typical for filaments that have been used outdoors for several hours. Time constants as fast as $80\,\mu sec$ in still air have been measured for freshly etched filaments.

Figure 4 shows the temperature rise of the filament versus the energy input to it. The self-heating error introduced by the measuring current causes an offset, which in itself would not be objectionable. In the fashion of a hot-wire anemometer, however, the offset temperature is a function of wind velocity and therefore limits the accuracy of the turbulence measurement. In the instrument described here, the offset temperature is about $0.08^{\circ}C$. The rms noise level of the system, due to the resistance of the filament and the input noise level of the amplifier, corresponds to an rms temperature fluctuation of about $0.03^{\circ}C$.

Heat is exchanged between the filament and its surroundings by conduction and convection into the surrounding air, the desired route, and also by undesired paths, viz., by conduction through the filament supports and by radiation. To assess the importance of these latter paths, we again put the filament into a 250-ml flask with the air evacuated to a pressure of 0.2 mm Hg. The pressure was then slowly increased, and the time constant was measured periodically. Figure 5 is a plot of the reciprocal of the temperature time constant versus air pressure in the millimeter range. By extrapolating to zero pressure, a time constant may be estimated for heat exchange by mechanisms other than conduction and convection to air. This value, 30 msec, is more than 100 times the time constant of the sensor at atmospheric pressure.

The change in air flow caused by the filament support wires has not been evaluated. Certainly the much higher thermal capacity of the supports influences the flow of air over the filament, but the amount of change is difficult to evaluate experimentally.

Energy exchange through radiation is inconsequential compared to other mechanisms. This is indicated by the tests at reduced air pressure. The temperature rise due to direct sunlight may be calculated by multiplying the energy density of sunlight times the projected area of the filament. Assuming perfect absorption, we find the maximum energy input to the filament is $0.26\,\mu W$. From figure 4, this corresponds to a temperature rise of $0.007^{\circ}C$. When the filament is exposed to direct sunlight, the small temperature rise is not detectable, which would be expected.

The problem of determining the temperature field surrounding a cylinder immersed in an infinite heat sink of different temperature is not a trivial one. To make another estimate of the volume of air involved in the temperature measurement, an approximation to the actual problem was calculated as follows: If the air surrounding the filament is assumed to be in the form of a cylinder concentric with the filament, with the outer wall of the cylinder of radius r_2 at temperature θ_2 and the surface of the filament of radius r_1 at θ_1, then the radius of this cylinder of air may be calculated from the relationship (Zemansky, 1951)

$$\theta_1 - \theta_2 = \frac{\frac{dQ}{d\tau}}{2\pi Lk} \ln \frac{r_2}{r_1} \quad ,$$

where

$$\frac{dQ}{d\tau} = \text{rate of heat flow}$$

8

L = length of cylinder

k = thermal conductivity of air   .

Evaluating this expression with the aid of figure 4 and solving for r_2, we find the radius of the cylinder of air is 1.9×10^{-3} cm . The volume of this cylinder is 1.6×10^{-6} cm^3. This result agrees reasonably well with the earlier calculation showing that the volume of air having thermal capacity equal to that of the filament was 1.07×10^{-6} cm^3.

4.   RESULTS

Some measurements using the instrument are shown in figures 6 and 7. Figure 6 shows two samples of temperature variations occurring in a turbulent wind flowing at 3.5 m/sec in the laboratory. Figure 7 shows the vertical space correlation of two temperature sensors spaced at 1, 4, and 16 cm outdoors. The wind was 0.5 to 2.5 m/sec in bright sunlight with the average temperature 25°C and the humidity 24%. The sensors were approximately 70 cm above dry grass ground cover. One sensor output has been applied to the vertical deflection of an oscilloscope and the other to the horizontal deflection. The cross-correlation of the two signals may be estimated from a presentation of this type (Sugar, 1954).

ACKNOWLEDGEMENTS

Robert S. Lawrence suggested the need for a device of this type and the general approach to the problem. I acknowledge the helpful discussions and suggestions of Mr. Lawrence and Dr. C. Gordon Little.

REFERENCES

Briggs, J. (1963), "Stellar scintillation," The Meteorol. Mag., 92, No. 1088, 69-75.

Sugar, G. R. (1954), "Estimation of correlation coefficients from scatter diagrams," J. Appl. Phys., 25, No. 3, 354-357.

Zemansky, M. W. (1951), "Heat and Thermodynamics," 3rd ed. (McGraw-Hill Book Co.), New York, New York.
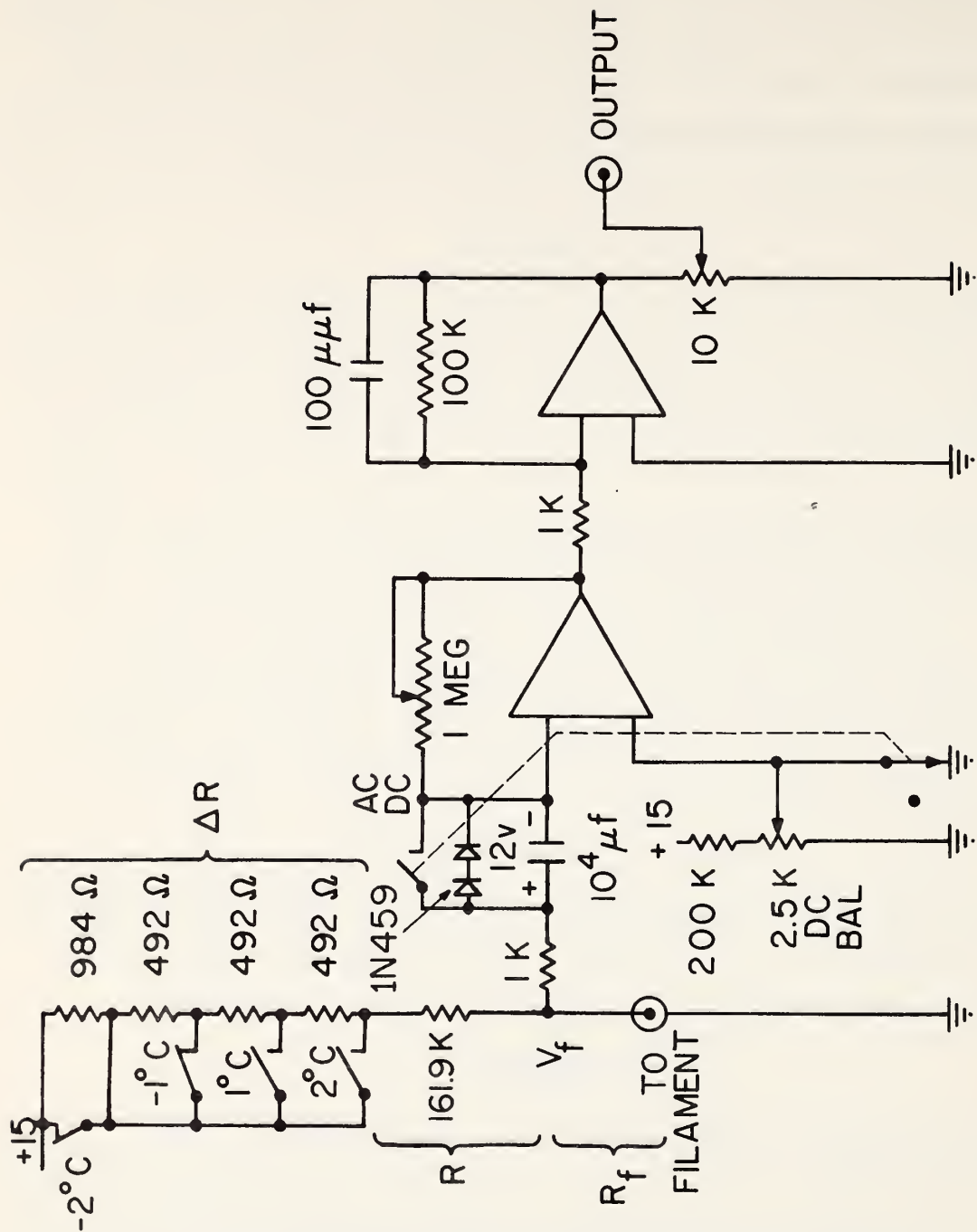
Figure 1. Resistance thermometer amplifier

10
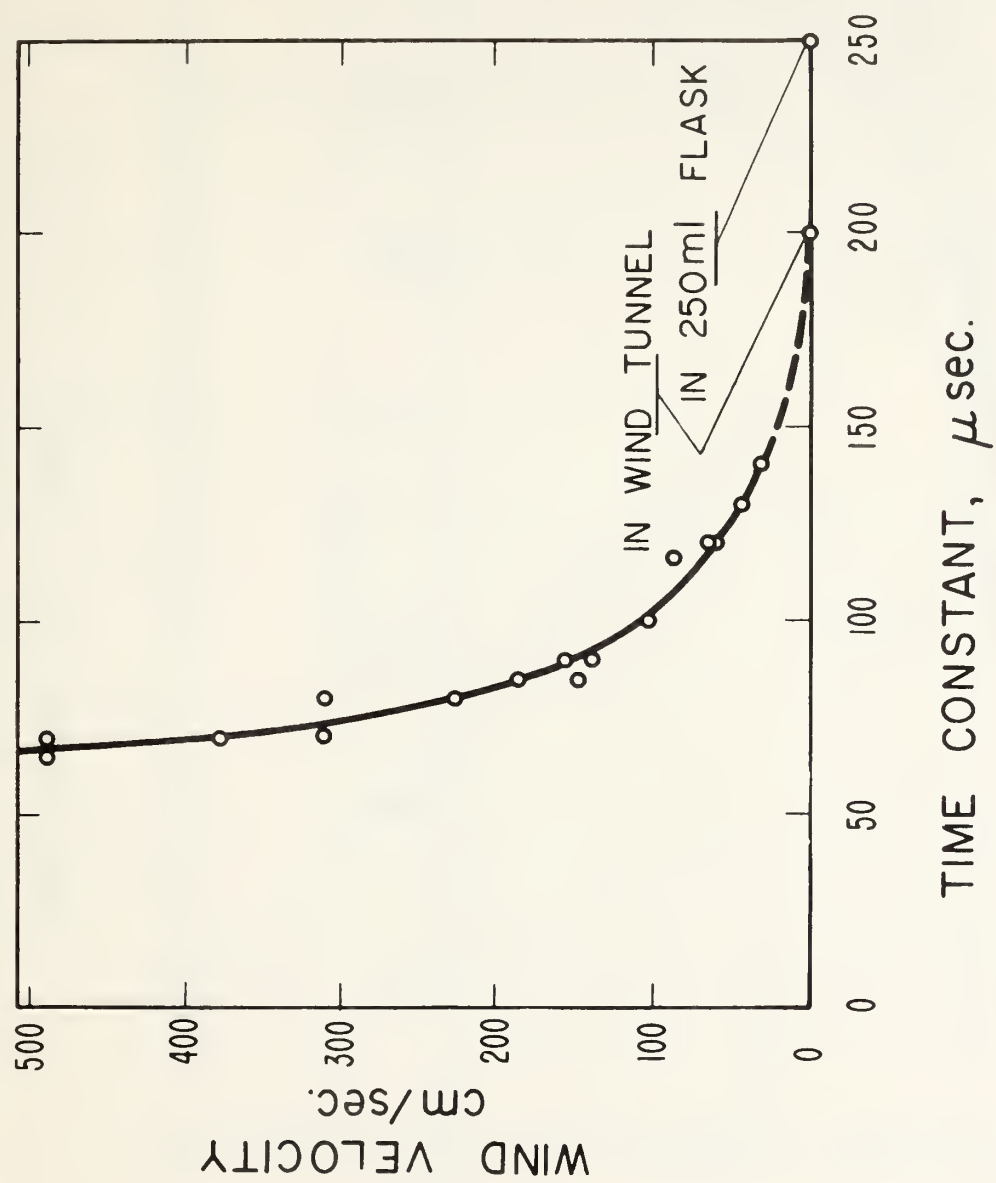
Figure 2. Temperature time constant as a function of wind velocity.
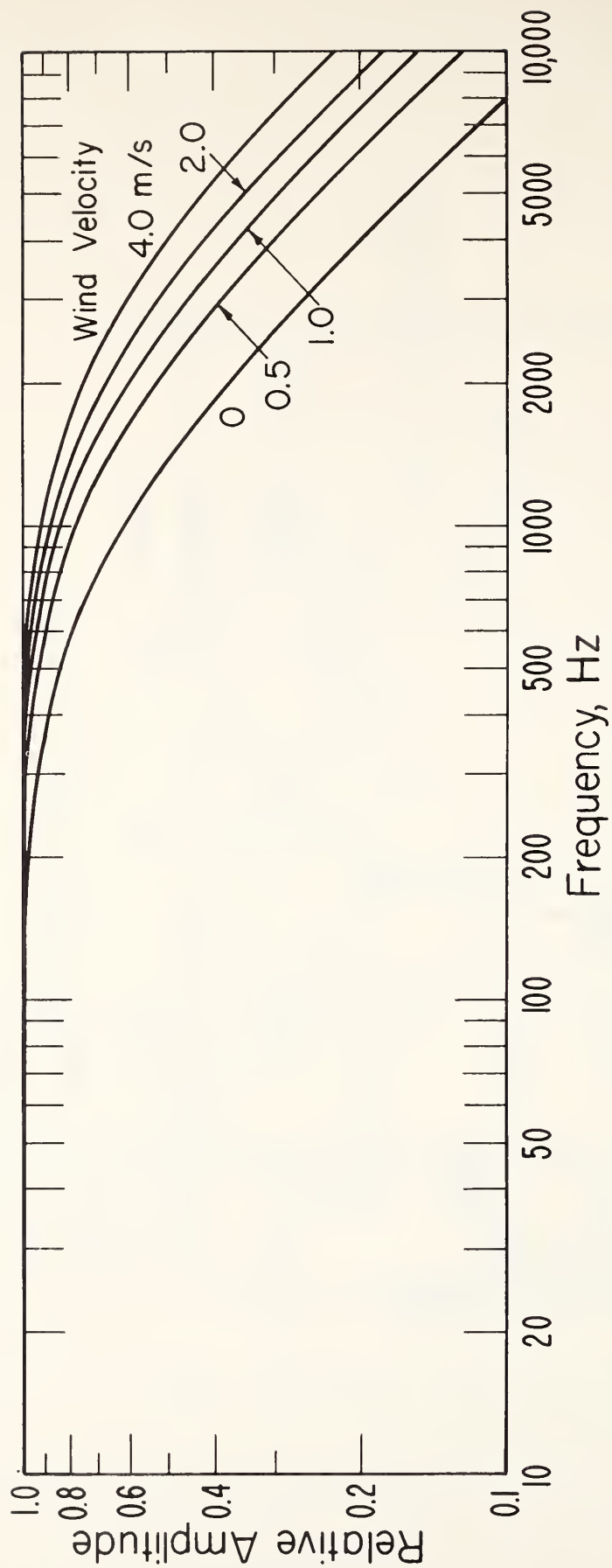
Figure 3. Frequency response of resistance thermometer to air temperature changes.

12
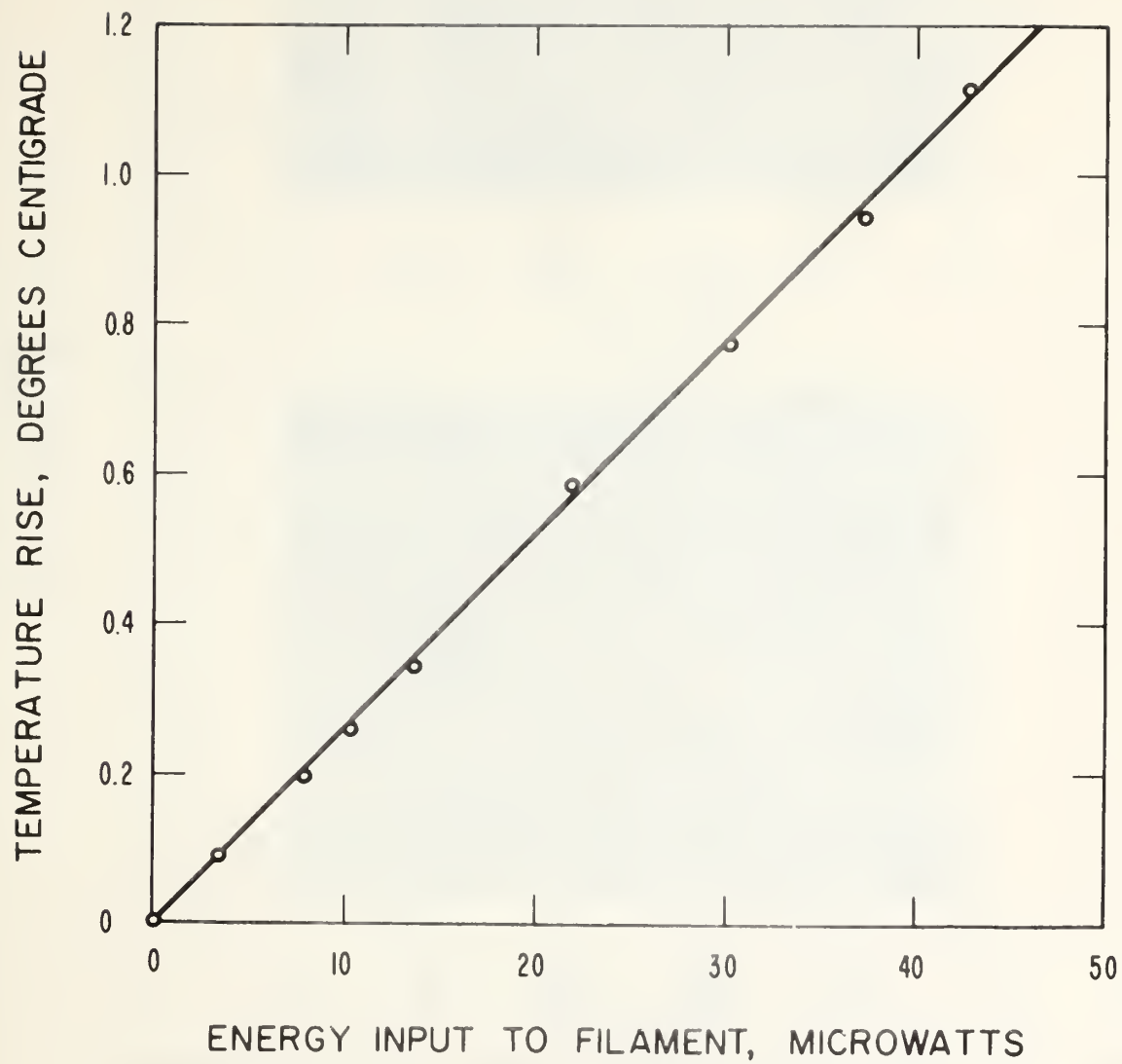
Figure 4. Temperature rise versus energy input to the filament.
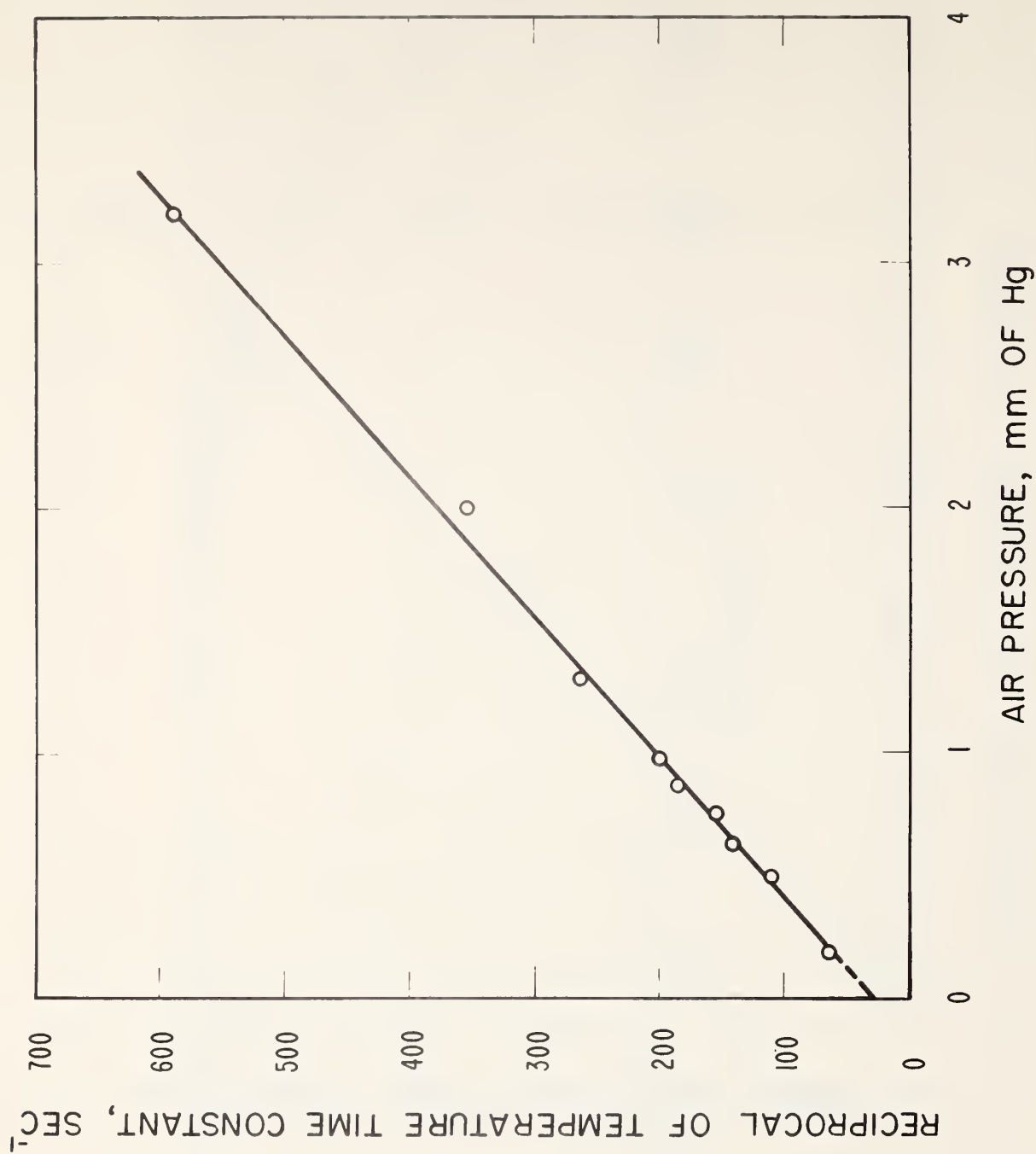
Figure 5. The reciprocal of the temperature time constant versus air pressure. The dotted portion of the line is an extrapolation.

14
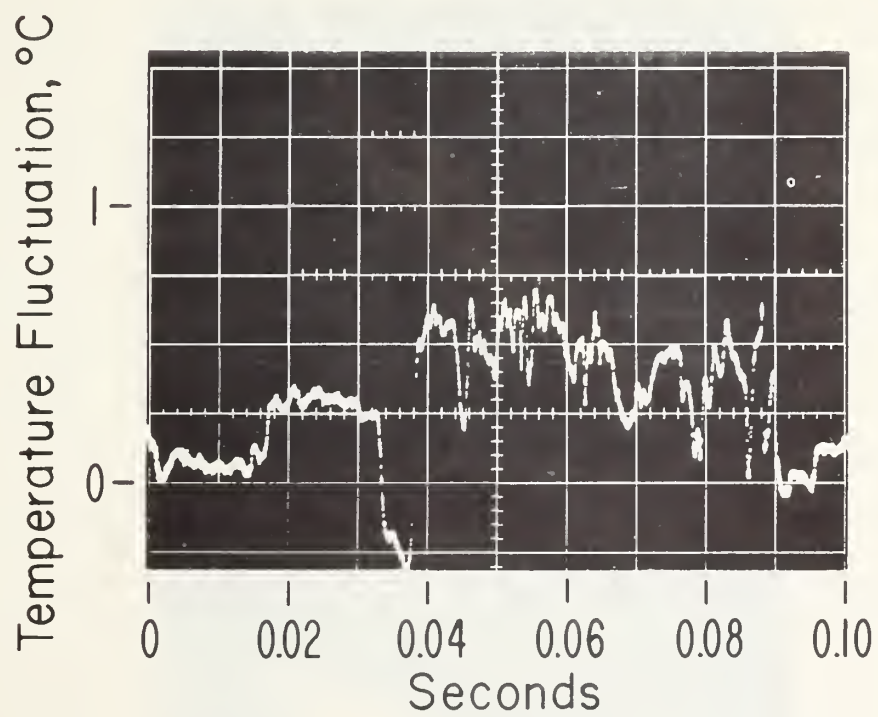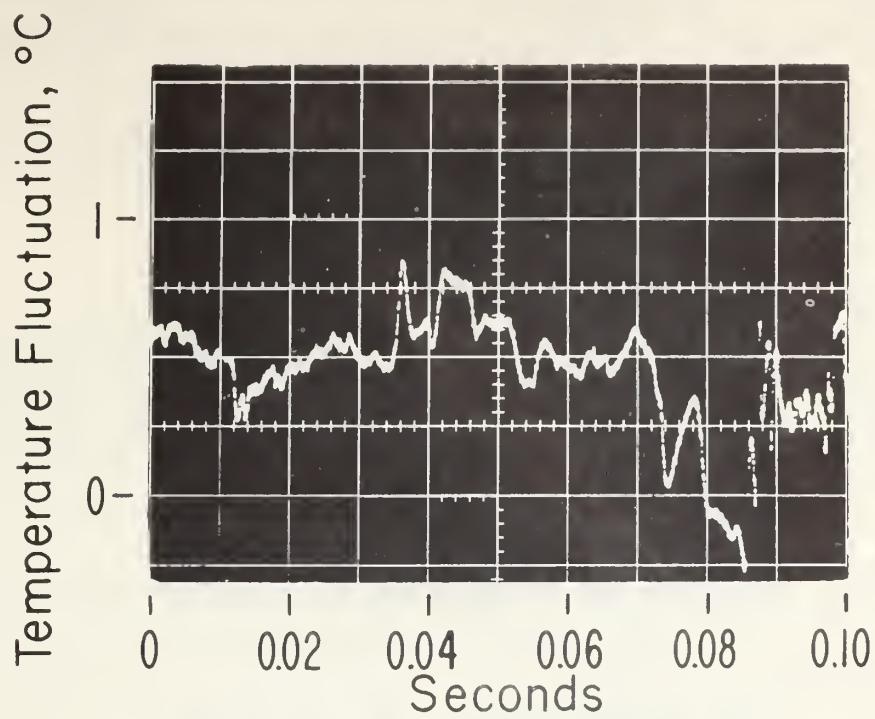
Figure 6.   Temperature fluctuations in a 3.5 m/sec air flow in the laboratory.

Figure 7. Vertical space correlation of temperature outdoors. The temperature scale is 1°C per division.
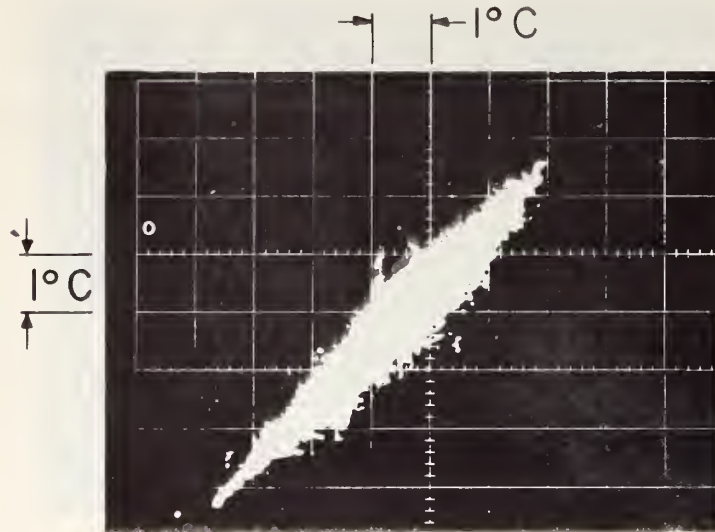
Vertical Spacing 1 cm
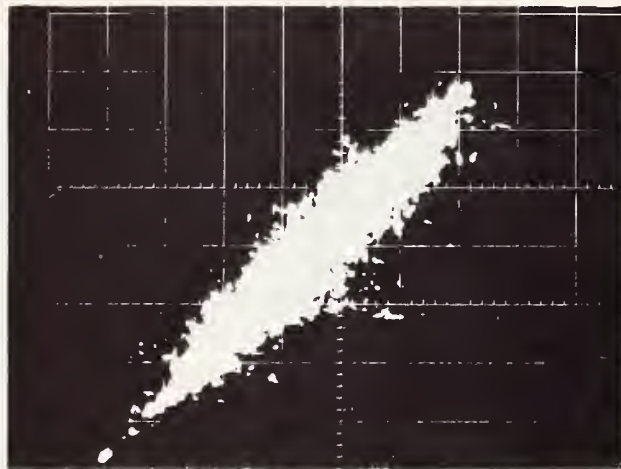
Vertical Spacing 4 cm
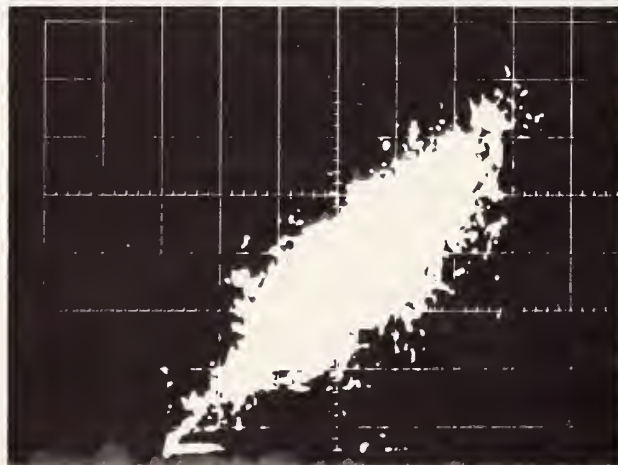
Vertical Spacing 16 cm

16

Optimum Illumination Geometry for Laser Raman Spectroscopy

R. L. Schwiesow*

ESSA Research Laboratories, Boulder, Colorado 80302
(Received 3 May 1969)

A focal-length-to-aperture ratio (F/D) for the illuminating laser beam in a scattering experiment where the scattered light is collected at right angles to the laser beam has been determined. This ratio allows a maximum amount of scattered light to be collected and depends on illuminating wave number $\nu = 1/\lambda$, spectrograph slit height h and width w, and collecting-optics magnification M. M should be as large as practical. If $(\nu h/14M)^{\frac{1}{2}}$ is less than $(1/7)(h/w)$, the value of F/D for maximum collected scattered flux is $(\nu h/14M)^{\frac{1}{2}}$. If $(\nu h/14M)^{\frac{1}{2}}$ is greater than $(1/7)(h/w)$, the collected scattered flux is maximum and constant for F/D over the range $(\nu h/14M)^{\frac{1}{2}}$ to $\nu w/2M$.

INDEX HEADINGS: Raman spectroscopy; Optical system.

Because Raman scattering is very weak, especially in gases, use of the most efficient illumination and collection optics is important in Raman spectroscopy. This paper evaluates the optimum value of variables in the illumination and collection optics for a Raman system with the following general characteristics: (1) a dispersive spectrograph with an entrance slit, (2) laser illumination, (3) unlimited sample volume, and (4) orthogonal illumination and observation axes, so that the image of the elongated cylindrical scattering volume is parallel to the spectrograph slit. No restrictions on polarization of incident and scattered beams are imposed, because the analysis is independent of polarization.

Criteria for illumination geometry have been discussed by Barrett and Adams[1] and Benedek and Fritsch.[2] The former consider only the narrow-slit case, while the latter tacitly consider only the wide-slit case. Our analysis, which is more general and includes both these conditions as special cases, is similar in principle to that of Barrett and Adams, but differs in both method and result. In view of the differing analytical results and the wide range of current practice for focused-laser illumination, a correct evaluation that includes both narrow- and wide-slit cases is in order. Optical systems with coaxial illumination and observation axes, which have been discussed earlier[3] and which make it difficult to measure polarization ratios and to match slit dimensions, are not dealt with here. Similarly, we do not include the usual multipass-cell system, which gives a spatially distributed source of scattered light, but the resonator-multipass system in which the sample cell inside the laser cavity is included.

Consider a plane-parallel illuminating beam of wave number $\nu = 1/\lambda$ and diameter D, filling the system aperture. A diffraction-limited lens of focal length F will provide an axially symmetric irradiance distribution at the focus. Over 95% of the first (three-dimensional)

maximum of the focal diffraction pattern is contained within a cylinder of diameter $d' = (2/\nu)(F/D)$ and length $l' = (14/\nu)(F/D)^2$ when $F > D$. These dimensions are found by choosing the dimensionless variables given by Born and Wolf[4] to be $v = 3.14$, $u = 11$, which are the approximate intersections of the 3% irradiance contour with the v, u axes. This cylinder contains about 80% of the total flux in the incident beam.[4] If the irradiance is a truncated gaussian across the system aperture, rather than uniform as we have assumed above, D is set equal to the $1/e^2$ truncation points on the irradiance distribution. In this case, the approximate 3% irradiance contour[5] of the focal cylinder is at $d' = (2.4/\nu)(F/D)$, $l' = (16/\nu)(F/D)^2$ which, incidentally, is the first zero of the uniformly-illuminated-aperture focal cylinder. Note that these focal dimensions differ by as much as a factor of 4 from earlier estimates based on diffraction theory[2] and confocal-resonator theory.[1]

We find the photon flux density at the focus, p', by multiplying the incident photon flux density p[photons/(area·time)] by the ratio of areas of the incident beam and focal cylinder, giving $p' = \frac{1}{4}p\nu^2 D^2(D/F)^2$. If the differential scattering probability $d\sigma/d\Omega'$ is small and approximately constant over the range of angles subtended by the collecting optics, the total number of scattered photons collected per unit time is given by $q = (d\sigma/d\Omega')p'nV\Omega'$, where n is the density of scatterers, Ω' is the solid angle subtended by the collecting optics, and V is the scattering volume. Nonisotropic scattering would result only in a factor multiplying Ω' and would not affect the geometrical optimization discussed here. When the expression for p' is substituted into the one for q, we find

$$q = (d\sigma/d\Omega')\tfrac{1}{4}p\nu^2 D^2(D/F)^2 nV\Omega' \propto (D/F)^2 V\Omega', \quad (1)$$

where the proportionality shows the variation of number of collected photons with the geometrical variables. Determination of the appropriate effective volume is crucial to our discussion.

[1] J. J. Barrett and N. I. Adams, III, J. Opt. Soc. Am. 58, 311 (1968).
[2] G. B. Benedek and K. Fritsch, Phys. Rev. 149, 647 (1966).
[3] See for example, J. Rud Nielsen, J. Opt. Soc. Am. 37, 494 (1947).
[4] M. Born and E. Wolf, *Principles of Optics* (Pergamon Press, Inc., London, 1965), 3rd ed., pp. 436–444.
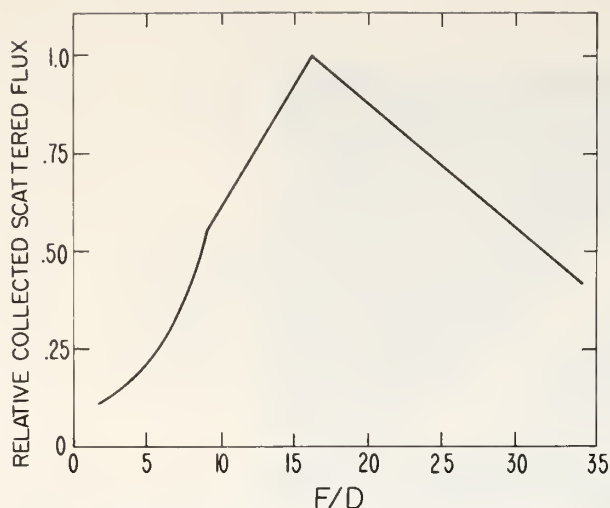[5] A. L. Buck, Proc. IEEE 55, 448 (1967).

Fig. 1. Scattered photons collected (relative scale) vs focal-length-to-aperture ratio (F/D) of illuminating beam, narrow-slit case; $w = 50\,\mu$, $h = 1$ cm, $M = 6$, and $\nu = 20\,490$ cm^{-1}.

The total sample volume is identical to the focal cylinder of diameter d' by length l'. It is imaged onto the spectrograph slit by the collecting optics. If these optics have linear magnification M, the image of the sample volume at the slits will have dimensions $d = Md'$ and $l = Ml'$, while the inherent acceptance angle of the spectrograph is enlarged from Ω to $\Omega' = M^2\Omega$ at the scattering volume. If the slit has width w and height h, the effective scattering volume will, in general, be a truncated circular cylinder having cylindrical segments removed from its sides by the slit jaws whenever $w < d$. The volume of the imaged cylinder is nearly the same as that of a rectangular prism d deep, the lesser of d and w wide, and the lesser of l and h high. The rectangular volume will be used in the calculation. Because the solid angle Ω is fixed by spectrometer design and Ω' is limited in practice to about 1 sr, M is limited by solid-angle considerations. Therefore, if the illuminating optics have sufficiently short focal length, it is possible to set $d < w$ and $l < h$.

For work where the slits are relatively narrow [a large (h/w) ratio], defined by $(h/w) > (l/d)$ over the range of (F/D) of interest, we consider the function $q(F/D, M)$ over three regions:

$$(1)\quad d < w, \quad l < h,$$
$$(2)\quad w < d, \quad l < h,$$
$$(3)\quad w < d, \quad h < l.$$

We note that increasing d' and l' corresponds to increasing (F/D).

Observe that the function $q(F/D, M)$ is continuous throughout these regions but not differentiable on the region boundaries. The number of scattered photons collected by the system in region (1) is given by $q(F/D, M) \propto (F/D)^2 M^3\Omega/\nu^3$. This function increases

monotonically with (F/D), or, equivalently, d', over the region and obviously reaches a maximum value at the region boundary of maximum $d = w = Md'$. The corresponding value of (F/D) for maximum collected scattering is

$$(F/D) = \nu w/2M. \tag{2}$$

In region (2), we find $q(F/D, M) \propto (F/D)wM^2\Omega/\nu^2$ is still increasing monotonically with (F/D), but more slowly than in region (1), and reaches a maximum at the boundary $l = h = Ml'$. At this point the optimum (F/D) is given by

$$(F/D) = (\nu h/14M)^{\frac{1}{2}} = (F/D)_{\text{opt}}. \tag{3}$$

In region (3),

$$q(F/D, M) \propto (D/F)Mwh\Omega/\nu \tag{4}$$

is a monotonically decreasing function of (F/D). Clearly q is maximum at the boundary $l = h = Ml'$ where Eq. (3) holds for (F/D). It is qualitatively evident from Eq. (4) why some focusing of the incident laser illumination is desirable. This justifies the initially unsupported assumption of some $F < \infty$. The behavior of $q(F/D, M)$ is shown in Fig. 1.

We therefore conclude that for the general Raman system under the condition of narrow slit width, $(h/w) > (l/d)$, (a) the magnification M of the collecting optics should be as large as possible, consistent with solid-angle considerations, and (b) the illuminating laser beam should be focused to the value

$$(F/D)_{\text{opt}} = (\nu h/14M)^{\frac{1}{2}}.$$

This theory may be compared with the experimental results obtained by Barrett and Adams,[1] who used $M = 6.3$, $h = 0.4$ cm, $w = 2.0 \times 10^{-3}$ cm, and $\nu = 20\,490$
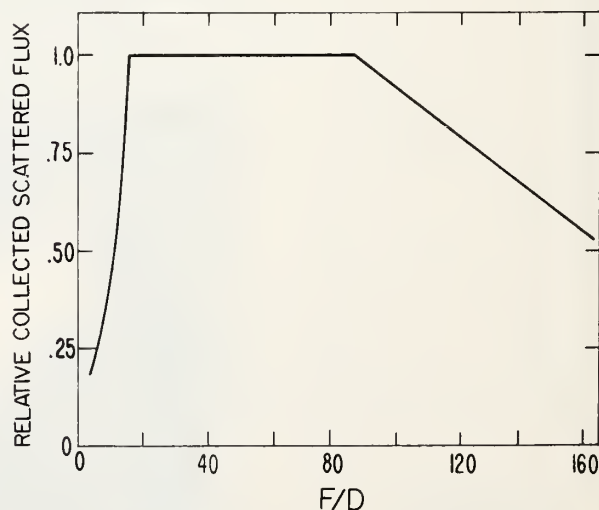

Fig. 2. Scattered photons collected (relative scale) vs focal-length-to-aperture ratio (F/D) of illuminating beam, wide-slit case; $w = 500\,\mu$, $h = 1$ cm, $M = 6$, and $\nu = 20\,490$ cm^{-1}.

cm^{-1}. With these values, $(F/D)_{opt}$ is found to be 9.65. In terms of focusing angle $\alpha = D/F$, we find $\alpha_{opt} = 0.104$, which is consistent with the experimental finding that $\alpha_{opt} \approx 0.10$. In contrast, the theory given by Barrett and Adams predicts only $0.0626 \leq \alpha_{opt} \approx 0.196$ for this case.

If, on the other hand, the slit is wide so that the (h/w) ratio is limited to $(l/d) > (h/w)$, in contrast to the narrow-slit case discussed previously, the regions become

(1) $d < w, \quad l < h,$

(2) $d < w, \quad h < l,$

(3) $w < d, \quad h < l,$

which have the same character as the regions discussed previously, except for (2). In the wide-slit region (2), the proportionality $q(F/D,M) \propto hM^2\Omega/\nu^2$ holds, independent of (F/D). Therefore, (F/D) may take values anywhere over the range defined by the boundaries of region (2), where $h = Ml' = l$ or where $w = Md' = d$, i.e., over the range given by

$$(\nu h/14M)^{\frac{1}{2}} \leq (F/D)_{opt} \leq \nu w/2M. \qquad (5)$$

For any reasonable values of parameters, the inequalities will hold in the direction shown whenever $w \geq 400 \mu$. For narrower slit widths and certain parameter ratios, the direction of the inequalities may be reversed, as they are for the narrow slit case discussed previously. The behavior of $q(F/D,M)$ is shown in Fig. 2.

We therefore conclude that for the general Raman system under the condition of wide slit width, $(l/d) > (h/w)$, (a) the magnification M of the collecting optics should be as large as possible, consistent with solid-angle considerations, and (b) the illuminating laser beam

should be focused in the range

$$(\nu h/14M)^{\frac{1}{2}} \leq (F/D) \leq \nu w/2M.$$

These results are comparable to the criteria presented by Benedek and Fritsch[2] but differ from them by a factor of at least two. For the case examined by the above authors, $M = 15$, $w = 2.5 \times 10^{-2}$ cm, and $\nu = 15\ 803$ cm^{-1} (we estimate h to be roughly 2 cm). The prediction of our theory is that (F/D) must be in the range $3.9 \leq (F/D)_{opt} \leq 13.2$, whereas Benedek and Fritsch suggest $(F/D) = \nu w/M \approx 26$. In this case, there is no experimental optimization of (F/D) with which to choose between the different predictions of the two theories. Similar wide-slit comparison is possible with the experimental setup described by Claassen et al.,[6] with which $M = 2.7$, $h = 2.0$ cm, $w = 5.0 \times 10^{-2}$ cm, and $\nu = 15\ 803$ cm^{-1}. Our criteria suggest that $(F/D)_{opt}$ can take any value between 29 and 146. Claassen et al. selected $(F/D) \approx 145$, which is within the optimum range of values given by our calculations. They report no experimental optimization or analytical results that may be used to check the present theory.

Operationally, the $(F/D)_{opt}$ value of Eq. (3) should be evaluated for the system parameters (w,h,ν,M) of interest. Using this (F/D), the ratio $(l/d) = 7(F/D)$ can be compared with (h/w). This equation follows directly from the definitions for d' and l' introduced earlier. If $(l/d) < (h/w)$, the narrow-slit case is applicable, and (F/D) may be set at the $(F/D)_{opt}$ value calculated above, or slightly smaller. If $(l/d) > (h/w)$, the wide-slit case is applicable, and (F/D) may be set at the originally calculated value or allowed to increase, up to the maximum set by Eq. (5). If $(l/d) = (h/w)$, region (2) collapses to zero width and the values of (F/D) given by Eqs. (2) and (3) become identical.

[6] H. H. Claassen, H. Selig, and J. Shamir, Appl. Spec. 23, 8 (1969).

RESEARCH NOTE

Refractive index of D_2O at the HCN laser frequency

THE D_2O transition that occurs at about 29·7 cm^{-1} (most likely assignment is $J\gamma + 6_{-4} \rightarrow 6_{-2}$) was studied by Bradley *et al.*[1] by measuring the pressure broadened absorption with an HCN laser. They inferred that the transition frequency of the line differed from the laser frequency by $(7·8 \pm 0·8) \times 10^{-3}$ cm^{-1}. Since the attenuation enters the absorption coefficient as the square of the difference between the transition frequency (v_1) and the laser frequency (v_0), they could not determine the sign of $v_1 - v_0$. We have been able to do so by observing the refractive index.

In our experiment we used a cell inside the laser cavity. A 0·1 mm polyethylene window, normal to the laser axis, was used to isolate approximately 0·29 m of one end of the laser cavity. The 0·29 m path length is not exact because the laser mirror is curved and the window is flexible. The pressure differential between the cell and the remainder of the laser cavity was kept below 10 mm to limit the force on the window. We observed the change in the refractive index by measuring the direction and distance the laser end mirror was moved to keep the laser tuned to its maximum output when gas was admitted to the cell. The cell was tested with Ar to insure that the flexing of the cell window did not cause tuning changes in the laser. No effect was observed. Figure 1 shows the refractive index change for D_2O and H_2O at 337 and 311 μ. The 337 μ laser oscillation stopped when the pressure of D_2O approached 2 mm Hg because of the increased absorption loss. The maximum measured change of refractive index for D_2O was approximately 88 ppm.
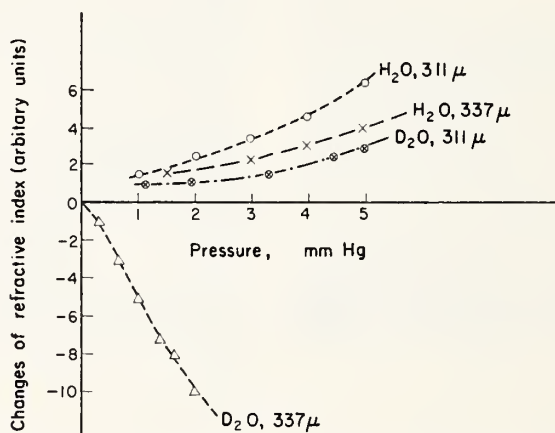
FIG. 1. Change of refractive index of D_2O and H_2O at 337 and 311 μ.

The result of this experiment shows that the frequency of the $6_{-4} \rightarrow 6_{-2}$ transition of D_2O occurs below the laser frequency. The laser frequency[2] is 29·71253 cm^{-1}, and using the value of Bradley *et al.*[1] for the difference frequency, the transition frequency is $(29·7047 \pm 0·008)$ cm^{-1}. The transition frequency assigned by W. S. Benedict (private communication) is 29·705 cm^{-1} based on the results of Bradley *et al.*,[1] and is confirmed by our conclusion that the frequency is less than the laser frequency.

No other signficant lines of D_2O lie near enough to the laser frequency to affect the result.

Wave Propagation Laboratory   R. G. STRAUCH
Environmental Science Services Administration   D. A. STEPHENSON*
Boulder, Colorado, 80302   V. E. DERR

REFERENCES

1. BRADLEY, C. C., W. J. BURROUGHS, H. A. GEBBIE and W. SLOUGH, *Infrared Phys.* **7**, 129–134 (1967).
2. HOCKER, L. O., A. JAVAN, D. RAMACHANDRA RAO, L. FRENKEL and T. SULLIVAN, *Appl. Phys. Lett.* **10**, 147 (1967).

*NRC-ESSA Postdoctoral Research Associate

TECHNIQUE FOR MEASUREMENT OF HCN-LASER LINEWIDTH

The spectrum of the 311 and 337μm lines of an HCN laser is examined with a high-resolution spectrum analyser. Although the outputs have spectral widths of the order of 100kHz, the spectral width of the difference frequency is less than 5kHz. The observed spectra widths are caused by mechanical instability.

HCN lasers provide c.w. outputs at wavelengths of 337μm (890GHz) and 311μm (964GHz). Measurement of the laser-signal spectral purity with a heterodyne analyser is limited by the stability characteristics of the local oscillator used in the heterodyne mixing process. The excellent short-term stability of a 74GHz klystron which is phase-locked onto a harmonic of a crystal oscillator provides a suitable reference signal. The laser output can be mixed with the 12th or 13th harmonic of the klystron output.[1,2] Frequency analysis of the mixer output provides a measurement of the laser spectrum within the stability tolerances imposed by the local oscillator.

The output of an HCN laser has been observed in this manner. The laser used in this experiment was operated at a pressure of 0·2torr natural gas and 0·2torr nitrogen. The laser mirrors have a 325cm radius of curvature and are separated by 370cm with a Fresnel number of approximately one. Discharge current was 0·4A, and the voltage across the tube was 2600V.

The measurement indicated that the laser outputs exhibit spectral width of the order of 100kHz, which significantly exceeds the contribution due to local-oscillator-frequency instability, and is therefore related only to the spectrum of the laser output. To determine the origin of the spectral width of the laser, the 73·5GHz difference frequency between the 890 and 964GHz lines was observed in the time domain and also frequency-analysed. The reference for comparison is a klystron phase-locked to a harmonic of a crystal frequency standard. Frequency analysis of the 73·5GHz signal shows a frequency spread of less than 5kHz, as shown in Fig. 1. When the signal was observed in the time domain (Fig. 2), the frequency modulation was found to be synchronised with mechanical vibrations. Modulation due to laser-current instability was not observed when the laser discharge current was modulated with current deviations greater than the discharge-current noise. The spectral width of the two laser lines is caused by a common influence which modulates their frequency difference with a deviation ratio which is equal to the difference of the deviation ratios of the laser outputs.

The spectral widths and modulation bandwidths measured in this experiment demonstrate that the HCN-laser output can be locked to a harmonic of a crystal oscillator with a phase-locked loop similar to that used for locking microwave oscillators. The application of a stabilised laser to a velocity-of-light measurement has been pointed out.[2] It has also been demonstrated that a free-running HCN laser with good mechanical stability will be suitable for a local oscillator in a superheterodyne receiver with single-ended mixing.

Fig. 1 *Spectrum-analyser response of 337 and 311 μm laser mixing with 714GHz phase-locked klystron (5kHz/cm)*

Fig. 2 *Zero beat of 337 and 311μm laser mixing with 74GHz swept klystron*

R. G. STRAUCH   *12th May 1969*

*Environmental Science Services Administration
Research Laboratories
Boulder, Colo. 80302, USA*

References

1 FRANKEL, L., SULLIVAN, T., POLLACK, M. A., and BRIDGES, T. J.: 'Absolute frequency measurement of 118·6πm water vapour laser transition', *Appl. Phys. Lett.*, 1967, **11**, pp. 344–345
2 HOCKER, L. O., JAVAN, A., RAO, D. R., FRANKEL, L., and SULLIVAN, T.: 'Absolute frequency measurement and spectroscopy of gas laser transitions in the far infrared', *ibid.*, 1967, **10**, pp. 147–149
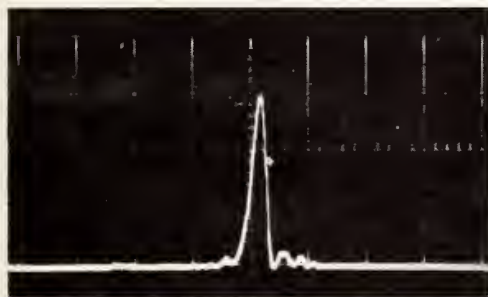
MINIMUM-RMS ESTIMATION OF THE NUMERICAL SOLUTION OF A FREDHOLM INTEGRAL EQUATION OF THE FIRST KIND*

OTTO NEALL STRAND AND ED R. WESTWATER†

Abstract. An estimate of the quadrature approximation to the solution of an integral equation of the first kind is derived. This estimate has a minimum expected mean-square error among all linear unbiased estimates. Expressions for the resulting expected mean-square error are derived, and numerical comparisons are made with an earlier solution. A consistent theory of optimum representation of the solution in terms of basis vectors is derived; this theory is only approximated by the classical theory. The minimum possible mean-square error may be used as a quality criterion for the solution and is identical to the quality criterion of the earlier solution.

1. Introduction. The solution of the quadrature approximation to a Fredholm equation of the first kind has received considerable attention in the past few years. In 1962 Phillips [1] applied a smoothing technique which employed the condition that the difference analogue to the second derivative of the solution should be small. This smoothing largely eliminated the wild oscillations that generally occur as the number of quadrature points is increased. In 1963 Twomey [2] streamlined the technique of Phillips and provided for smoothing using an a priori solution imposed with a weight, γ, which could be varied as desired. However, no method of determining γ was given. In 1968 Strand and Westwater [3] treated the problem as one of statistical estimation. Along with the statistical estimate, one also obtains its expected mean-square error, which makes it possible to assess the quality (on the average) of the solution. When any complete set of basis vectors is used, the expected mean-square error reduces to $\text{Tr } X^{-1}$ (notation of §2 below). The quantity $\text{Tr } X^{-1}$ may be computed without actually solving the equation and is used as a quality criterion to evaluate proposed experiments. Some results of such calculations are presented by Westwater and Strand [4].

The present paper accomplishes the following:

(a) A solution is derived (for a general basis) which has the minimum achievable expected mean-square error for a linear unbiased estimate. Gaussian statistics are not assumed.

(b) It is shown that the solution reduces to that of [3] when a full basis is used.

(c) The expected mean-square error of the estimate of the present paper is shown to be a monotone nonincreasing function of the number of basis vectors.

(d) Optimum basis theory is derived for the estimate of this paper; by the nature of its derivation it follows that the optimum basis gives the *best possible* linear unbiased estimate in terms of a fixed number of parameters.

(e) It follows from (c) and (d) above that Tr X^{-1} represents the *minimum achievable* expected mean-square error for a linear unbiased estimate.

(f) It is shown that no computational advantage is achieved by using a basis of dimensionality less than the number of quadrature points.

The notation of the present paper is the same as that of [3]. The results are derived in §2; §3 discusses the use of basis vectors, and §4 compares the results with those of [3].

2. Derivations. Let $\{f(y), a \leq y \leq b\}$ be a random process having continuous sample functions and for which the second moments exist. If $K(x, y)$ is a continuous function of x and y, and if

$$(1) \qquad \int_a^b K(x, y)f(y)\, dy = g(x),$$

then $g(x)$ is also a random process. The main idea is to estimate $f(y)$ by measuring $g(x)$ at various values of x, say $x = x_i$, $i = 1, \cdots, n$. Introducing a quadrature formula of the type $\int_a^b h(y)\, dy = \sum_{j=1}^m w_j h(y_j)$ gives a matrix equation

$$(2) \qquad\qquad\qquad Af = g,$$

where
  (i) $A = (A_{ij})$, $i = 1, 2, \cdots, n$, $j = 1, 2, \cdots, m$,
  (ii) m is the number of quadrature abscissas,
  (iii) n is the number of observations of $g(x)$,
  (iv) y_j are the quadrature abscissas,
  (v) x_i are the specific values of x for which $g(x)$ is observed,
  (vi) w_j are the weights associated with y_j,
  (vii) $f_j = f(y_j)$,
  (viii) $g_i = g(x_i)$,
  (ix) $A_{ij} = w_j K(x_i, y_j)$,
  (x) $f = [f_1 f_2 \cdots f_m]^T$ is the column vector of unknown functional values (the superscript T denotes matrix transposition) and
  (xi) $g = [g_1 g_2 \cdots g_n]^T$ is the column vector of values of $g(x)$.

We assume that the mean vector, $E(f) = f_0$, and the covariance matrix, S_f, of f are known. ($E(\cdot)$ and $\bar{E}(\cdot)$ denote, respectively, the expected-value operator over the distribution of f and over the joint distribution of f and the error vector ϵ (defined below); S_v denotes the covariance matrix

of any vector v.) By the linearity of E and the propagation rule for covariance matrices, respectively, we have $E(g) = g_0 = Af_0$ and $S_g = AS_fA^T$. In the cases of interest here g is a vector of measurements subject to error. Thus one observes

$$g_e = g + \epsilon$$

instead of g. In addition to the assumptions already made, we assume:
(a) the errors ϵ_i are independent of f, hence independent of g;
(b) the errors ϵ_i have a multivariate distribution with mean zero and known covariance matrix S_ϵ;
(c) the quadrature errors are negligible with respect to ϵ;
(d) S_ϵ and S_f are both nonsingular with dimensions $n \times n$ and $m \times m$, respectively.

Although it will be noted later that such a representation is usually unnecessary, we shall represent the solution in terms of a basis. We let $U = [U_1 \mid U_2 \mid \cdots \mid U_k]$ (lines denote matrix partitions throughout this paper) be a matrix of k linearly independent m-component basis column vectors and $C = [C_1 \, C_2 \, \cdots \, C_k]^T$ be a vector of coefficients to be determined, where $k \leqq m$. Let

$$\eta = f - f_0, \qquad h = g - g_0 = A(f - f_0) = A\eta,$$

and let our reduced observed data be h_e, where

$$h_e = h + \epsilon = A\eta + \epsilon.$$

We seek an estimate, $\hat{\eta}$, in the form $\hat{\eta} = UC$. Assume a linear unbiased estimate (i. e., such that $\bar{E}(\eta - \hat{\eta}) = 0$) in the form

$$(3) \qquad\qquad \hat{\eta} = UC \quad \text{with} \quad C = Bh_e,$$

where B is a $k \times n$ matrix to be determined. It will be shown that B is uniquely determined by the condition

$$(4) \quad F(B) \equiv \bar{E}\{(\hat{\eta} - \eta)^T(\hat{\eta} - \eta)\} = \text{minimum with respect to } B.$$

Inserting $\hat{\eta} = UBh_e$ from (3) into (4) gives the equivalent condition

$$F(B) = \text{Tr } S_{\hat{\eta}-\eta} = \text{Tr } \{UBHB^TU^T - S_fA^TB^TU^T - UBAS_f + S_f\}$$

$$(5) \qquad\qquad = \text{minimum},$$

where $H = AS_fA^T + S_\epsilon$ and $\text{Tr}\{\cdot\}$ denotes the trace. Differentiating with respect to the elements of B gives the equation

$$(6) \qquad\qquad U^TUBH = U^TS_fA^T,$$

from which the solution is

(7) $B = (U^T U)^{-1} U^T S_f A^T H^{-1} \equiv B_0 .$

This solution is unique; for suppose B_1 is any other solution of (6). Then by subtraction $U^T U (B_1 - B_0) H = 0$, and since both $U^T U$ and H are nonsingular, it follows that $B_1 = B_0 .$

To prove that B_0 actually provides a minimum, let B_1 and B_2 be any two real $k \times n$ matrices. It is easily verified by (5) that

$$F(B_1) - F(B_2) = \mathrm{Tr}\,\{(UB_1 - UB_2)H(UB_1 - UB_2)^T$$

(8) $-2(B_2{}^T - B_1{}^T)(U^T U B_2 H - U^T S_f A^T)\}.$

If we replace B_2 by B_0 as given by (7), the second term of (8) vanishes and we obtain

(9) $F(B_1) - F(B_0) = \mathrm{Tr}\,\{(UB_1 - UB_0)H(UB_1 - UB_0)^T\} \geqq 0.$

Therefore, B_0 actually minimizes the mean-square error $\mathrm{Tr}\,S_{\hat{\eta}-\eta}$. Note that (8) could have been used to derive B_0. Suppose $F(B_1) = F(B_0)$. Then

(10) $U(B_1 - B_0) = 0,$

as can be deduced by writing the trace in (9) as a sum of quadratic forms. Multiplying (10) on the left by U^T and noting that $U^T U$ is nonsingular shows that $F(B_1) = F(B_0)$ if and only if $B_1 = B_0 .$

Substituting (7) into (5) gives the solution covariance matrix

$$S_{vc-\eta} = S_f + U(U^T U)^{-1} U^T M U (U^T U)^{-1} U^T$$

(11) $-MU(U^T U)^{-1} U^T - U(U^T U)^{-1} U^T M,$

where $M = S_f A^T H^{-1} A S_f$. The corresponding expression for the resulting minimum expected mean-square error is

(12) $F(B_0) = \mathrm{Tr}\,\{S_f - U^T M U (U^T U)^{-1}\}.$

We show next that $F(B_0)$ is a monotone nonincreasing function of k. First, without loss of generality, we may assume orthogonality, i.e., $U^T U = I$. Under this assumption $F(B_0) = \mathrm{Tr}\,\{S_f - U^T M U\}$, where M is positive semidefinite. Breaking $\mathrm{Tr}\,\{U^T M U\}$ down into a sum of quadratic forms shows that adding another column to U cannot decrease $\mathrm{Tr}\,\{U^T M U\}$. Hence, $F(B_0)$ is a monotone nonincreasing function of k, a property that did not always hold for the previous estimate [3]. An optimum basis may be determined, if desired, by letting the columns of U consist of the k eigenvectors of M corresponding to maximal eigenvalues $\lambda_1 \geqq \lambda_2 \geqq \cdots \geqq \lambda_k \geqq 0$. The ratio

(13) $\alpha = \sum_{j=1}^{k} \dfrac{\lambda_j}{\mathrm{Tr}\,S_f}$

can be interpreted as the fraction of the variance of f "explained" by the fit. The arguments leading to these conclusions are given in [3] and also in papers by Obukhov [5] and Mateer [6].

If we require that the mean-square error in the residuals be minimized instead of the mean-square error in η, we obtain another estimate. Let

$$\hat{\epsilon} = h_e - A\hat{\eta}$$

or

$$(14) \qquad \hat{\epsilon} = h_e - AUBh_e,$$

and let

$$(15) \qquad G(B) = \operatorname{Tr} S_{\hat{\epsilon}-\epsilon} = \operatorname{Tr}\{A S_{\hat{\eta}-\eta} A^T\}$$

with the same assumptions as (3). By writing

$$G(B_2) - G(B_1) = \operatorname{Tr}\{(AUB_1 - AUB_2)H(AUB_1 - AUB_2)^T$$
$$(16) \qquad\qquad -2(B_2^T - B_1^T)(U^T A^T AUB_2 H - U^T A^T A S_f A^T)\}$$

we display the equation for B as

$$(17) \qquad U^T A^T AUBH - U^T A^T A S_f A^T = 0.$$

If rank $AU < k$, interchanging the roles of B_1 and B_2 in (16) shows that any two solutions of (17) produce the same minimum value of $G(B)$. The set of solutions of (17) does not, in general, include the solution of (6), because if a solution of (6) also satisfies (17) then it is necessarily true that $U^T A^T A(U^T U - I) S_f A^T = 0$. Calculating the left side in the case

$$A = \begin{pmatrix} 1 & 0 & 1 \\ 0 & 1 & 1 \end{pmatrix}, \quad U = (1 \quad 0 \quad 0)^T \quad \text{and} \quad S_f = I$$

gives a nonzero result. Since it has been established that $F(B_1) = F(B_0)$ if and only if $B_1 = B_0$, the solution of (17) does not, in general, minimize the mean-square error in η. As shown in the earlier paper [3], still another estimate is obtained by applying the Gauss-Markov principle of least squares in $(m + n)$-dimensional space, namely,

$$(18) \quad \hat{\eta} = UC = U(U^T S_f^{-1} U)^{-1} U^T A^T [S_\epsilon + AU(U^T S_f^{-1} U)^{-1} U^T A^T]^{-1} h_e.$$

The identity

$$(19) \qquad A^T S_\epsilon^{-1} H = X S_f A^T,$$

where

$$(20) \qquad X = S_f^{-1} + A^T S_\epsilon^{-1} A$$

is readily established. Using these results in (7) yields two alternative

forms for the minimum-rms solution:

(21a) $$\hat{\eta} = UC = U(U^T U)^{-1} U^T S_f A^T H^{-1} h_e$$

or

(21b) $$\hat{\eta} = UC = U(U^T U)^{-1} U^T X^{-1} A^T S_\epsilon^{-1} h_e .$$

Furthermore, $S_{\hat{\eta}-\eta}$ is given by (11) with either the form

$$M = S_f A^T H^{-1} A S_f$$

or

$$M = S_f - X^{-1}.$$

We now consider the important special case $k = m$. Our solutions (21) then reduce to

(22a) $$\hat{\eta} = S_f A^T H^{-1} h_e$$

or

(22b) $$\hat{\eta} = X^{-1} A^T S_\epsilon^{-1} h_e$$

by (21a) and (21b), respectively. Equations (11) and (12) may be written, respectively, in the form

(23) $$S_{\hat{\eta}-\eta} = S_f - M = X^{-1}$$

and

(24) $$\text{Tr}\{S_{\hat{\eta}-\eta}\} = \text{Tr } X^{-1}.$$

Putting $k = m$ in (17) gives a set of solutions which always includes (22). Also, note that when $k = m$, the solution of [3], given by (18), reduces to (22). Thus, the use of (22) (or (18), as in [3]) with a full complement of basis vectors insures both a minimum expected mean-square error and a minimum expected mean-square residual.

3. Basis vectors. Much of the previous literature on integral equations of the first kind [6], [7], [8], [9] has emphasized the importance of representing the solution in terms of k basis vectors, where $k \ll m$. Such a representation may have been convenient with the earlier methods, but in many cases the use of a basis other than $U = I$ (or $k = m$) with the present method is neither necessary nor desirable. In the event an optimum basis is desired, it may be constructed from M. By passing to the limit we see that $M \to S_f$ as $X^{-1} \to 0$. Thus, the set of "optimum" basis vectors usually constructed in the literature represents a limiting case of the optimum basis vectors for a minimum-rms estimate.

The matrix H is $n \times n$ and X is $m \times m$, and by (22) we may invert either to obtain the solution. If we choose (22b), we shall also have to invert
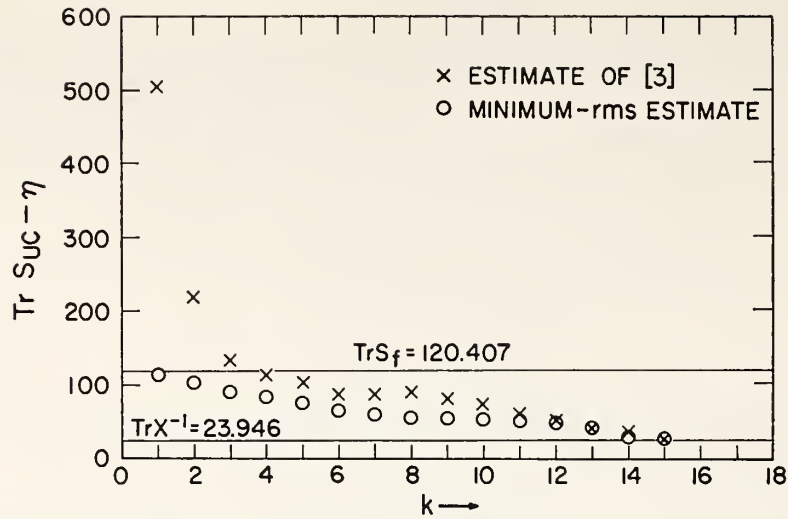
FIG. 1. Tr $S_{UC-\eta}$ vs. k; $n = 7$, $m = 15$, $S_\epsilon = 0.01\ I$, "unit" basis $U_{ij} = \delta_{ij}$

TABLE 1

Tr $S_{UC-\eta}$ for M-optimum and Obukhov bases with minimum-rms estimation and
Tr $S_{UC-\eta}$ for estimate of [3] using the Obukhov basis, conditions of [3, Fig. 1]
Tr $X^{-1} = 23.946$

k	Tr $S_{UC-\eta}$ (M-optimum, minimum rms)	Tr $S_{UC-\eta}$ (Obukhov, minimum rms)	Tr $S_{UC-\eta}$ (Obukhov, estimate of [3])
1	50.043	50.130	50.717
2	25.802	27.335	33.810
3	23.967	25.189	25.413
4	23.946	23.959	23.960
5		23.951	23.951
6		23.950	23.950
7		23.946	n.c.[1]
8			n.c.
9			23.946
10			n.c.
11			n.c.
12			23.946
13			n.c.
14			n.c.
15			23.946

[1] n.c. denotes "not computed".

S_f to form X. On the other hand, if (22a) is used, H may be formed without an inversion and then inverted. In many cases the number, n, of measurements of $g(x)$ is small so that the latter process will be much the easier. For example, many quadrature points could be used (if S_f can be properly

estimated) and the solution could be had, via (22a), with only the inversion of a matrix of smaller size. In contrast, the case of few quadrature points and many measurements would be more easily handled through (22b) if S_ϵ is diagonal, as in many applications. Examination of (21) shows that either an $m \times m$ or an $n \times n$ matrix must be inverted for any value of k. Thus no computational advantage is achieved by using a basis other than $U = I$. Hence if the only objective is to obtain the solution, an incomplete basis has no value. Use of such a basis can only be justified by convenience of representation.

4. Numerical example. The trace of the covariance matrix $S_{UC-\eta}$ was computed using (12) with exactly the same conditions and equation as [3, Fig. 2]. The results are plotted along with those of [3, Fig. 2], in Fig. 1 of this paper. Note that the trace of $S_{UC-\eta}$ is lowered substantially by using the estimate of this paper with the basis $U_{ij} = \delta_{ij}$. Of course, this basis would not ordinarily be used in practice, as it is not efficient.

Table 1 compares Tr $S_{UC-\eta}$ under the conditions of [3, Fig. 1] using the estimate of [3] and the estimate of this report for both the Obukhov basis derived from S_f and the optimum minimum-variance basis as derived from $M = S_f - X^{-1}$. The improvement in using the new estimate (21) over the results of [3] (equation (18)) is not dramatic; neither is the improvement due to using the M-optimum basis. However, from the nature of the derivation it is evident that estimate (21) together with the M-optimum basis gives the minimum mean-square error for any unbiased linear estimate in terms of k parameters. The earlier estimates of [3] would give as good results in practice, because Tr $S_{UC-\eta}$ is usually computed, and the solution would not be used unless Tr $S_{UC-\eta}$ − Tr X^{-1} is small. The estimate (21) is simpler, is theoretically optimum and is, of course, recommended.

5. Conclusions. The minimum-rms unbiased linear estimate of the solution of the quadrature approximation to a Fredholm integral equation of the first kind has been derived. We have shown that for a full complement of basis vectors the present solution is identical to the earlier estimate [3]. The quality-criterion theory is thus identical for the present estimate as in [3], and can further be interpreted as the minimum overall expected mean-square error achievable by means of an unbiased linear estimate. The numerical example suggests that in practice the present estimate does not have a much smaller mean-square error than that of [3]. The present method is simpler in theory and is recommended. For most applications the use of an "optimum" basis would not be necessary, although the construction of such a basis has been derived and the calculations are straightforward. Furthermore, no computational advantage is achieved by using an incomplete basis (i.e., such that $k < m$) to obtain the solution.

Acknowledgment. After the work in this paper was completed, it was brought to our attention that some results similar to ours were derived in a different context by Foster [10]. We thank H. E. Fleming of ESSA/ NESC for pointing this out.

REFERENCES

[1] D. L. Phillips, *A technique for the numerical solution of certain integral equations of the first kind*, J. Assoc. Comput. Mach., 9 (1962), pp. 84–97.

[2] S. Twomey, *On the numerical solution of Fredholm integral equations of the first kind by the inversion of the linear system produced by quadrature*, Ibid., 10 (1963), pp. 79–101.

[3] Otto Neall Strand and Ed R. Westwater, *The statistical estimation of the numerical solution of a Fredholm integral equation of the first kind*, Ibid., 15 (1968), pp. 100–114.

[4] Ed R. Westwater and Otto Neall Strand, *Application of statistical estimation techniques to ground-based passive probing of the trophospheric temperature structure*, ESSA Tech. Rep. IER 37/ITSA 37, Boulder, Colorado, 1967.

[5] A. M. Obukhov, *The statistically orthogonal expansion of empirical functions*, Bull. (Izv.) Acad. Sci. USSR Geophys. Ser., 1960, pp. 288–291.

[6] Carlton L. Mateer, *On the information content of Umkehr observations*, J. Atmospheric Sci., 22 (1965), pp. 370–381.

[7] S. Twomey, *The application of numerical filtering to the solution of integral equations encountered in indirect sensing measurements*, J. Franklin Inst., 279 (1965), pp. 95–109.

[8] ———, *Indirect measurements of atmospheric temperature profiles from satellites: II. Mathematical aspects of the inversion problem*, Monthly Weather Rev., 94 (1966), pp. 363–366.

[9] J. C. Alishous, L. J. Crone, H. E. Fleming, F. L. Van Cleef and D. Q. Wark, *A discussion of empirical orthogonal functions and their application to vertical temperature profiles*, TELLUS, 19 (1967), pp. 477–482.

[10] Manus Foster, *An application of the Wiener-Kolmogorov smoothing theory to matrix inversion*, J. Soc. Indust. Appl. Math., 9 (1961), pp. 387–392.

Statistical Estimation of the Numerical Solution of a
Fredholm Integral Equation of the First Kind

OTTO NEALL STRAND AND ED R. WESTWATER

Institute for Telecommunication Sciences and Aeronomy, * *Boulder, Colorado*

ABSTRACT. A method for the numerical solution of a Fredholm integral equation of the first kind is derived and illustrated. The method employs an a priori constraint vector together with covariances of both the constraint vector and the measurement errors. The method automatically incorporates an optimum amount of smoothing in the sense of maximum-likelihood estimation. The problem of obtaining optimum basis vectors is discussed. The trace of the covariance matrix of the error in the solution is used to estimate the accuracy of the results. This trace is used to derive a quality criterion for a set of measurements and a given set of constraint statistics. Examples are given in which the behavior of the solution as obtained from a specific integral equation is studied by the use of random input errors to simulate measurement errors and statistical sampling. The quality criterion and behavior of the trace of the error covariance matrix for various bases is also illustrated for the equation being considered.

KEY WORDS AND PHRASES: Fredholm integral equation of first kind, numerical solution, maximum likelihood, least-squares, accuracy criterion, optimum basis vectors

CR CATEGORIES: 5.5

1. *Introduction*

In recent publications Twomey [1, 2] and Twomey and Howell [3] have extended a method of Phillips [4] for the solution of integral equations of the first kind. Twomey's method uses a controlled amount of smoothing in solving the matrix system derived from a quadrature approximation, but gives no systematic method of determining the required amount of smoothing. In this paper a general least-squares process for estimating the solution is derived and illustrated, and it is shown that it contains Twomey's method of weighting an a priori constraint vector as a special case. The optimum amount of smoothing (in the sense of maximum-likelihood estimation) depends on certain covariance matrices describing the measurement process. In a manner similar to that of the more recent work [5–8], we derive and use statistically orthogonal basis vectors. Certain other bases are also used and numerical comparisons are made for a particular equation occurring in the theory of radiative transfer. In our method the covariance matrix of the error in the resulting solution is calculated and its trace is used as a measure of the error in the final results. It is shown in this paper that the trace of the error covariance matrix is minimized when the number of basis vectors equals the number of quadrature points. We use the resulting minimum trace as a quality criterion describing the effectiveness of a given matrix equation (with specified accuracy of observation and a specified distribution of the constraint vector) in reducing the variance of the a priori constraint

vector. We also derive and discuss the condition for an optimum basis and present numerical examples using random input errors to simulate the measurement process.

2. *Method*

Let $\{f(y), \quad a \leq y \leq b\}$ be a Gaussian random process having continuous sample functions. If $K(x, y)$ is a continuous function of x and y and if

$$\int_a^b K(x, y)f(y) \; dy = g(x), \tag{1}$$

then $g(x)$ is also a Gaussian process with continuous sample functions. The main idea is to estimate $f(y)$ by measuring $g(x)$ at various values of x, say $x = x_i, \quad i = 1, \cdots, n$. Introducing a quadrature formula of the type $\int_a^b h(y) \; dy = \sum_{j=1}^m w_j h(y_j)$ gives a matrix equation

$$Af = g, \tag{2}$$

where

$A \quad = (A_{ij}) \; i = 1, 2, \cdots, n; \quad j = 1, 2, \cdots, m,$
$m \quad =$ number of quadrature abscissas,
$n \quad =$ number of observations of $g(x)$,
$y_j \quad =$ the quadrature abscissas,
$x_i \quad =$ the specific values of x for which $g(x)$ is observed,
$w_j \quad =$ the weights associated with y_j,
$f_j \quad = f(y_j)$,
$g_i \quad = g(x_i)$,
$A_{ij} = w_j K(x_i, y_j)$,

$f = [f_1 f_2 \cdots f_m]^T$ is the column vector of unknown functional values (the superscript T denotes matrix transposition throughout this paper), and $g = [g_1 g_2 \cdots g_n]^T$ is the column vector of values of $g(x)$.

We assume that the mean vector $E(f) = f_0$ and the covariance matrix, S_f, of f are known. ($E(\quad)$ denotes the expected-value operator and S_v denotes the covariance matrix of any vector v throughout this paper.) By the linearity of E and the propagation rule for covariance matrices, respectively, we have $E(g) = g_0 = Af_0$ and $S_g = AS_fA^T$. In the cases of interest here, g is a vector of measurements subject to error. Thus one observes

$$g_e = g + \epsilon \tag{3}$$

instead of g. In addition to the assumptions already made, we assume:
1. The errors ϵ_i are independent of f, hence independent of g.
2. The errors ϵ_i are normally distributed with zero mean and known covariance matrix S_ϵ.
3. The quadrature errors are negligible with respect to ϵ.
4. S_ϵ and S_f are both nonsingular with dimensions $n \times n$ and $m \times m$, respectively.

It is convenient in practice to represent the solution in terms of a small number of basis vectors. We let $U = [U_1 \mid U_2 \mid \cdots \mid U_k]$ (lines denote matrix partitions throughout this paper) be a matrix of k linearly independent m-component basis

column vectors and $C = [C_1 C_2 \cdots C_k]^T$ be a vector of coefficients to be determined, where $k \le m$.

The inference problem to be solved is the following: Given the observed vector g_e and the covariance matrices S_f and S_ϵ, estimate f and ϵ under the constraint $g_e - Af = \epsilon$. Putting $\eta = f - f_0$, $h = g - g_0 = A(f - f_0) = A\eta$, and

$$h_e = h + \epsilon = A\eta + \epsilon, \tag{4}$$

where η is to be approximated by UC, gives an equivalent problem: Given h_e, estimate η and ϵ in the form $[UC/\hat{\epsilon}]$ subject to the constraint $h_e - AUC = \hat{\epsilon}$. First, note that the maximum likelihood estimate of η in the absence of measurements g_e is $\eta = 0$. The estimate $\eta = 0$ may be coupled with the set of measurements, g_e, to form an "effective" measurement vector $[0/h_e]$. From this vector and the Gauss-Markov least-squares principle for correlated variables [9], a maximum-likelihood estimate of $[\eta/\epsilon]$ can be obtained. Since the covariance matrix of $[\eta/\epsilon]$ is $\begin{bmatrix} S_f & | & 0 \\ 0 & | & S_\epsilon \end{bmatrix}$, the desired estimate $[UC/\hat{\epsilon}]$ must be such that $R(C, \epsilon)$ is rendered stationary, where

$$R(C, \epsilon) \equiv (UC)^T S_f^{-1} (UC) + \epsilon^T S_\epsilon^{-1} \epsilon + \mu^T(AUC - h_e + \epsilon), \tag{5}$$

and μ^T is a row matrix of Lagrange multipliers. Differentiating with respect to C, ϵ and μ, and equating to zero give the solution

$$UC = UD^{-1}U^T A^T S_\epsilon^{-1} h_e \tag{6}$$

and

$$\hat{\epsilon} = h_e - AUD^{-1}U^T A^T S_\epsilon^{-1} h_e, \tag{7}$$

where

$$D = U^T X U \quad \text{and} \quad X = S_f^{-1} + A^T S_\epsilon^{-1} A. \tag{8}$$

We may also rewrite (6) in the equivalent form

$$UC = U(U^T S_f^{-1} U)^{-1} U^T A^T [S_\epsilon + AU(U^T S_f^{-1} U)^{-1} U^T A^T]^{-1} h_e. \tag{9}$$

We apply the propagation rule for covariance matrices to $UC - \eta$, where UC is given by (6):

$$UC - \eta = UD^{-1}U^T A^T S_\epsilon^{-1}(A\eta + \epsilon) - \eta$$

and

$$S_{UC-\eta} = [UD^{-1}U^T A^T S_\epsilon^{-1} A - I]S_f[UD^{-1}U^T A^T S_\epsilon^{-1} A - I]^T$$
$$+ [UD^{-1}U^T A^T S_\epsilon^{-1}]S_\epsilon[UD^{-1}U^T A^T S_\epsilon^{-1}]^T,$$

so that

$$S_{UC-\eta} = TYS_f YT - (TYS_f + S_f YT) + S_f + TYT, \tag{10}$$

where

$$Y = A^T S_\epsilon^{-1} A \quad \text{and} \quad T = UD^{-1}U^T. \tag{11}$$

Substituting $Y = X - S_f^{-1}$ into (10) and noting that $TXT = T$ gives

$$S_{UC-\eta} = S_f + T + T(XS_f X)T - TXS_f - S_f XT, \tag{12}$$

and

$$S_{\hat{\epsilon}-\epsilon} = A S_{UC-\eta} A^T. \tag{13}$$

Expressions (6) (or (9)) and (7) give the desired statistical estimates of the solution for any given basis U. Equations (12) and (13) give the error covariance matrices by which the quality of the results may be estimated, as is shown in Section 3. In the work reported in this paper no use has been made of the estimate (7) of $\hat{\epsilon}$ or the expression (13) giving $S_{\hat{\epsilon}-\epsilon}$.

Various special cases may be noted. If $k = m$, that is, if U is a nonsingular $m \times m$ matrix, (6), (9), (12), and (13) become, respectively,

$$UC \equiv \hat{\eta} = X^{-1} A^T S_\epsilon^{-1} h_e, \tag{14}$$

$$\hat{\eta} = S_f A^T H^{-1} h_\iota, \tag{15}$$

$$S_{\hat{\eta}-\eta} = X^{-1}, \tag{16}$$

$$S_{\hat{\epsilon}-\epsilon} = A X^{-1} A^T, \tag{17}$$

where

$$H = S_\epsilon + A S_f A^T.$$

From (15), a result equivalent to (16) is

$$X^{-1} = S_{\hat{\eta}-\eta} = S_f P S_f P S_f - 2 S_f P S_f + S_f + S_f A^T H^{-1} S_\epsilon H^{-1} A S_f, \tag{18}$$

where

$$P = A^T H^{-1} A.$$

The study of special cases is confined to the case $k = m$ here. If $S_\epsilon^{-1} \to 0$, i.e., if the measurements have large errors, we obtain $\hat{\eta} = 0$ or $f = f_0$ and $S_{\hat{\eta}-\eta} = S_f$. If $S_f^{-1} \to 0$, then X will be nonsingular if and only if rank $A = m$. Then $\hat{\eta} = (A^T S_\epsilon^{-1} A)^{-1} A^T S_\epsilon^{-1} h_e$ and $S_{\hat{\eta}-\eta} = (A^T S_\epsilon^{-1} A)^{-1}$. If $S_\epsilon \to 0$, i.e., if the measurements of g are perfect, and if rank $A = n$, then $n \leq m$ and (15) and (16) become, respectively, $\hat{\eta} = S_f A^T [A S_f A^T]^{-1} h$ and $S_{\hat{\eta}-\eta} = S_f - S_f A^T (A S_f A^T)^{-1} A S_f$. In computational practice the latter situation will not occur, as the quadrature errors will invalidate the assumptions as $S_\epsilon \to 0$. Finally, if $S_f \to 0$, then (15) and (18) give, respectively, $\hat{\eta} = 0$ or $f = f_0$ and $S_{\hat{\eta}-\eta} = 0$.

We may show the correspondence of the present method with that of Twomey [2] as follows: For $k = m$, let $S_\epsilon = \sigma_\epsilon^2 I$, $S_f = \sigma_f^2 I$, $\gamma = \sigma_\epsilon^2 / \sigma_f^2$, $f_0 = \bar{p}$, $f_0 + \hat{\eta} = \bar{f}$, and $g_e = \bar{g}$ in (14) to correspond with Twomey's notation [2, p. 105]. Then

$$\bar{f} = [A^T A + \gamma I]^{-1} [A^T \bar{g} + \gamma \bar{p}], \tag{19}$$

which is identical to Twomey's (6) [2, p. 105]. Thus, if the covariance matrices S_f and S_ϵ are both scalar, the optimum choice of γ (in the sense of maximum-likelihood estimation) is given by the ratio of variances. However, in commonly occurring physical situations, S_f has substantial off-diagonal elements.

The basis $U = I$ with $m = k$ gives an adequate solution via (14), (16), and (17). However, it is often convenient to represent the solution in terms of k parameters, where $k < m$, using (6), (12), and (13). The quality of such a representation depends on the choice of basis. The problem of basis optimization is discussed in Section 3.

3. *Determination of Optimum Basis Vectors*

Previous solutions [7, 8] have employed basis vectors (i.e., columns of U) which were obtained to fit the data in an optimum manner without reference to the integral equation to be solved. It is shown below that the integral equation (as represented by the matrix A which is an ingredient of $S_{UC-\eta}$) plays a part in obtaining the optimum matrix U, but (see Section 4) the use of an exactly optimum basis U is often not critical, so that U as employed in earlier solutions [7, 8] should suffice. This classical determination of U (as exemplified by Obukhov [10], for example) is presented here and interpreted in terms of the covariance matrix of the residuals. The criterion which must be satisfied for an optimum basis for the integral equation is then easily seen.

Consider the quadratic form

$$(d - UC)^T(d - UC) \equiv q(U, C). \tag{20}$$

Here U and C have the same meaning as in Section 2 and d is a sample vector from a population having a multivariate m-dimensional normal distribution, say, with zero mean and covariance matrix S_d. For any specified basis U, $q(U, C)$ is minimized when

$$UC = U(U^TU)^{-1}U^Td, \tag{21}$$

as can be seen by differentiation. Thus the minimum value of $q(U, C)$ for any given basis U is given by

$$q_{\min}(U) = d^T[U(U^TU)^{-1}U^T - I]^T[U(U^TU)^{-1}U^T - I]d. \tag{22}$$

Various criteria may be used to determine what is meant by "smallness" of q. In the classical case the optimum U is that which minimizes the expected value of $q_{\min}(U)$. Let $\operatorname{Tr} B \equiv$ trace B denote the sum of the diagonal elements of any matrix B. By expanding and employing the linearity of the operator E we may show that

$$E[d^TQd] = \operatorname{Tr} S_d Q \tag{23}$$

for any real symmetric matrix Q. Applying (23) to (22) gives U as that basis which minimizes

$$\operatorname{Tr}\{S_d[I - U(U^TU)^{-1}U^T]\} = \operatorname{Tr} S_d - \operatorname{Tr} U^T S_d U(U^TU)^{-1}. \tag{24}$$

In the last expression we use the relation $\operatorname{Tr} AB = \operatorname{Tr} BA$, which holds whenever AB is square. Expression (24) is invariant with respect to replacement of U by UB, where B is any nonsingular $k \times k$ matrix. In fact, the matrix $S_d U(U^TU)^{-1}U^T$ is unaffected by such a transformation. Furthermore, let J be an $m \times m$ symmetric positive definite matrix and let V be any $m \times k$ basis matrix. Since V^TJV is positive definite, there exists [11] a real nonsingular upper triangular $k \times k$ matrix B^{-1} such that $V^TJV = (B^{-1})^T(B^{-1})$. Let $U = VB$. Then $U^TJU = B^T(V^TJV)B = I$. Thus any normalization of the form $U^TAU = I$ may be assumed without loss of generality. We suppose

$$U^TU = I. \tag{25}$$

Hence U must be found which maximizes $\operatorname{Tr}\{U^T S_d U\}$ subject to the constraint (25). By partitioning U into individual columns of basis vectors and considering the maximization process involved, it can be shown [12] that the columns of U

must be chosen as those eigenvectors corresponding to maximal eigenvalues $\lambda_1 \geq \cdots \geq \lambda_k > 0$ of S_d. Thus U must satisfy

$$S_d U = U\Lambda, \tag{26}$$

where

$$\Lambda = \text{diag}\,[\lambda_1 \lambda_2 \cdots \lambda_k].$$

Substituting (25) and (26) into (24) gives

$$E\{q_{\min}(U)\} = \text{Tr}\,S_d - \text{Tr}\,\Lambda = \sum_{i=k+1}^{m} \lambda_i$$

for optimum U. The ratio

$$\alpha = \frac{\sum_{i=1}^{k} \lambda_i}{\text{Tr}\,S_d} \tag{27}$$

is sometimes called [5] the fraction of the total variance "explained" by the basis U.

It follows from (21) and (24) by using the propagation rule for covariances, with $\text{Tr}\,AB = \text{Tr}\,BA$, that

$$E\{q_{\min}(U)\} = \text{Tr}\,S_{UC-d}.$$

Thus $E\{q_{\min}(U)\}$ may also be given another interpretation. As a criterion of the size of the errors resulting from a distribution having zero mean and second moments defined by a given covariance matrix S, we may choose $\text{Tr}\,S$. Since the trace is equal to the sum of the eigenvalues of a matrix, this interpretation is geometrically equivalent to defining the "size" of an m-dimensional ellipsoid as the sum of the squares of its semi-axes. The interpretation of $E\{q_{\min}(U)\}$ as the trace of the covariance matrix is freely used throughout the remainder of the report. It may be noted that $E\{q_{\min}(U)\}$ is also equal to m times the expected overall mean-square error of the approximation $d \sim UC$. Although no use is made of the result in what follows, it is interesting that the minimum of the quadratic form

$$q_d(U, C) \equiv (d - UC)^T S_d^{-1}(d - UC)$$

has the expected value $m - k$ for *any* choice of U, and therefore *cannot* be used to determine an optimum basis.

From the preceding discussion it follows that an optimum basis U for use with the integral equation would be that which minimizes

$$\text{Tr}\,S_{UC-\eta} \equiv \text{Tr}\,\{S_f + T + T(XS_fX)T - TXS_f - S_fXT\}. \tag{28}$$

From the definition of T we see that, even with the normalization $U^T X U = I$, expression (28) is of fourth degree in the elements of U. Since minimization of (28) is difficult, and since classical basis vectors seem to suffice in practice, the determination of U from (28) is not pursued further in this paper.

4. Quality Criterion

The quantity $\text{Tr}\,X^{-1}$ can be used as a measure of the accuracy to be expected from a given integral equation with given covariance matrices S_f and S_ϵ and a given set

$\{x_i\}$ of values of x. For $k = m$, i.e., for a nonsingular $m \times m$ matrix U, $S_{UC-\eta}$ reduces to X^{-1} by (16). Furthermore, it is shown below that $\mathrm{Tr}\, S_{UC-\eta} \geq \mathrm{Tr}\, X^{-1}$ for any basis U. Thus $\mathrm{Tr}\, X^{-1}$ is a measure of the best that can be done for a given problem. Calculating $\mathrm{Tr}\, X^{-1}$ and comparing with $\mathrm{Tr}\, S_f$ indicates the amount of improvement over the a priori statistical knowledge that can be expected in a given case.

THEOREM. $Tr\, S_{UC-\eta} - Tr\, X^{-1} \geq 0$, where, as previously defined,

$$X = S_f^{-1} + A^T S_\epsilon^{-1} A, \qquad D = U^T X U, \qquad T = U D^{-1} U^T.$$

$$Tr\, S_{UC-\eta} - Tr\, X^{-1} = Tr\{S_f + T + TXS_fXT - TXS_f - S_fXT - X^{-1}\},$$

$$U = \{\underbrace{[U_1 \mid U_2 \mid \cdots \mid U_k]}_{k}\} m,$$

where the U_i are linearly independent and $m \geq k$.

LEMMA. $Tr\, B^T S_f B \geq Tr\, B^T X^{-1} B$ where B is any real $m \times m$ matrix.

PROOF.   Let $S_f = (S_{ij})$, $X^{-1} = (X_{ij}^{-1})$, and $B = (B_{ij})$. By direct calculation,

$$\mathrm{Tr}\, B^T S_f B = \sum_{i,p,q} B_{pi} S_{pq} B_{qi} = \sum_{i=1}^{m} \left(\sum_{p=1}^{m} \sum_{q=1}^{m} S_{pq} B_{qi} B_{pi} \right) = \sum_{i=1}^{m} B_i^T S_f B_i,$$

where B_i is the ith column vector of B. By an extension [13] of Bergstrom's inequality we have, for any real column vectors y and z,
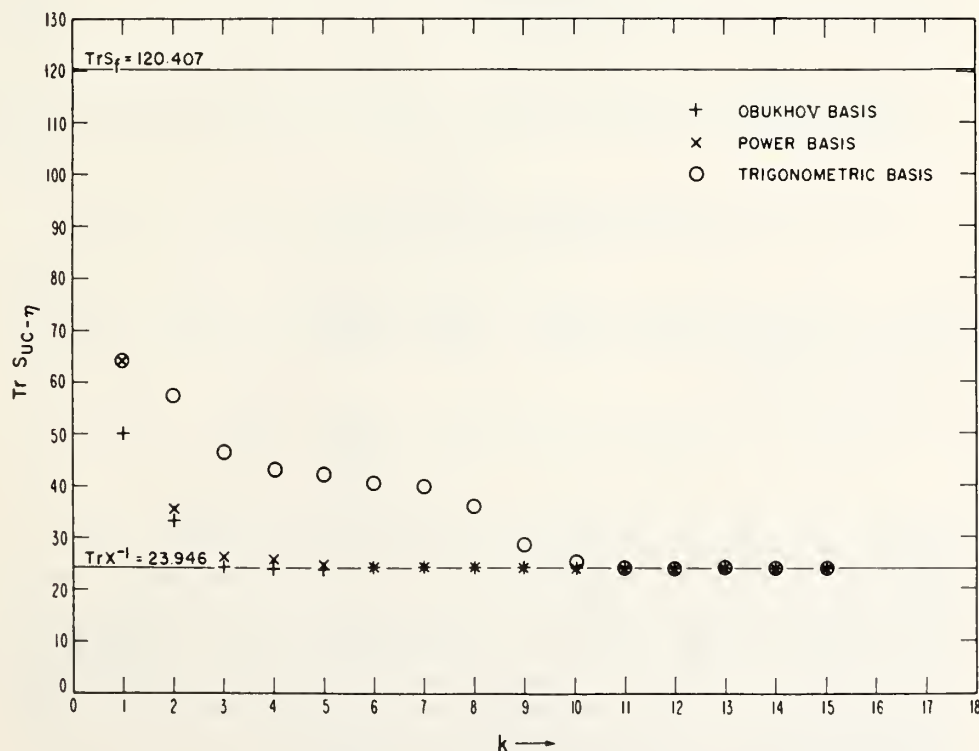
$$(y^T S_f y)(z^T S_f^{-1} z) \geq (y^T z)^2.$$

FIG. 1. $Tr\, S_{UC-\eta}$ versus k for three different bases. $n = 7$, $m = 15$,
$S_\epsilon = .01\, I$, S_f as in Table 1.

Since $X = S_f^{-1} + A^T S_\epsilon^{-1} A$ so that $z^T X z \geq z^T S_f^{-1} z$, we have $(y^T S_f y)(z^T X z) \geq (y^T z)^2$. Putting $y = B_i$, $z = X^{-1} B_i$ gives $(B_i^T S_f B_i)(B_i^T X^{-1} B_i) \geq (B_i^T X^{-1} B_i)^2$. If $B_i \neq 0$, dividing out the positive quantity $B_i^T X_i^{-1} B_i$ gives $B_i^T S_f B_i \geq B_i^T X^{-1} B_i$. (If $B_i = 0$, the inequality is trivially true.) Therefore,

$$\text{Tr } B^T S_f B = \sum_{i=1}^{m} B_i^T S_f B_i \geq \sum_{i=1}^{m} B_i^T X^{-1} B_i = \text{Tr } B^T X^{-1} B.$$
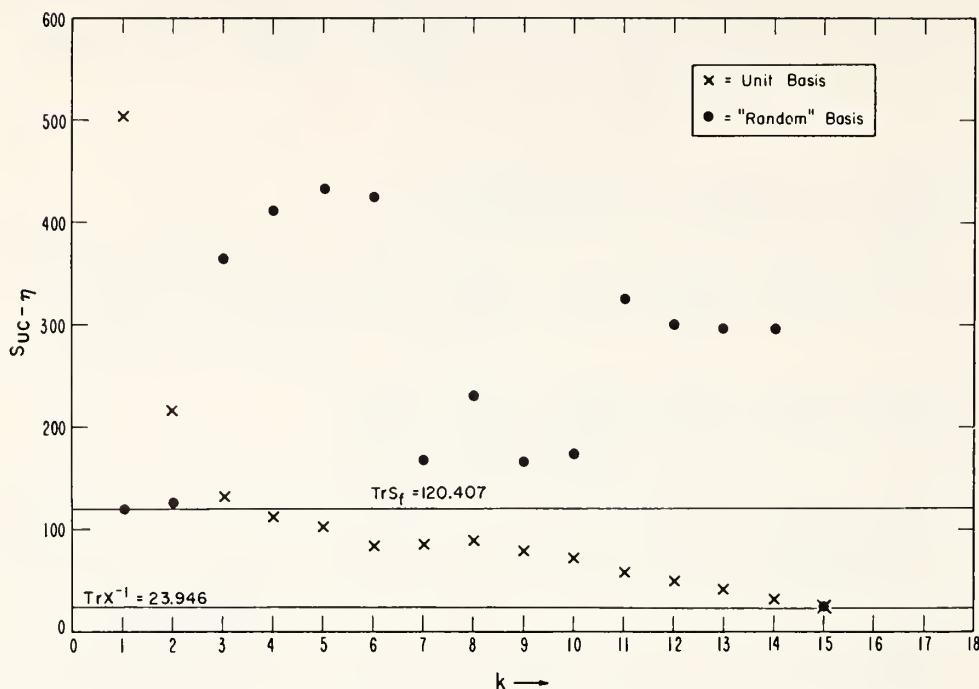

Fig. 2.   Tr $S_{UC-\eta}$ versus k for the "unit" basis $U_{ij} = \delta_{ij}$ and a "random" basis.
$n = 7$, $m = 15$, $S_\epsilon = .01\ I$, S_f as in Table 1.

This proves the lemma. It can now be applied to prove the theorem. Note that $S_{UC-\eta} - X^{-1}$ may be written as $S_{UC-\eta} - X^{-1} = (XT - I)^T S_f(XT - I) + T - X^{-1}$. By the lemma

$$\text{Tr } \{S_{UC-\eta} - X^{-1}\} \geq \text{Tr } \{(XT - I)^T X^{-1}(XT - I)\} + \text{Tr } T - \text{Tr } X^{-1}$$

$$= \text{Tr } \{TXT - 2T + X^{-1} + T - X^{-1}\}.$$

Since $TXT = T$ we have Tr $\{S_{UC-\eta} - X^{-1}\} \geq \text{Tr } 0 = 0$.   Q.E.D.

There are conditions for which a basis may be chosen such that Tr $S_{UC-\eta}$ decreases as k increases, and approaches Tr X^{-1} for k considerably less than m. Such behavior is illustrated in Figure 1, in which we present values of Tr $S_{UC-\eta}$ versus k for the integral equation (29), given and discussed in Section 5. The conditions are $S_\epsilon = .01\ I$, $n = 7$, $m = 15$ with $\{x_i\}$ and $\{y_j\}$ as given in Section 5. Results from three bases are shown: the Obukhov basis resulting from the S_f of Table 1, the power basis $U_{ij} = y_i^{j-1}$, and the trigonometric basis

$$U_{i,2j} = \sin\left(\frac{2\pi j y_i}{b - a}\right), \qquad i = 1, 2, \cdots, 15, \qquad j = 1, 2, \cdots, 7,$$

TABLE 1. COVARIANCE MATRIX OF f

$$(S_f)_{ij} = (S_f)_{ji}$$

8.9755535														
8.6021156	11.1039390													
8.1338120	10.5356010	11.0664880												
7.3367519	9.3309135	10.2237400	10.0039310											
6.8615990	8.6186485	9.5238762	9.4706230	9.1069946										
6.4772987	8.0642490	8.9444752	8.9470463	8.6704178	8.3230915									
5.5771370	6.7803764	7.5836792	7.6733322	7.5201874	7.3236942	6.7663212								
4.3791828	5.1479855	5.7305050	5.7692413	5.6861858	5.5819817	5.2912636	4.5418777							
3.6053905	4.0942955	4.5088978	4.4873428	4.4462719	4.4021187	4.2424870	3.8449001	3.5745201						
2.9826775	3.3040600	3.6088314	3.5468775	3.5193272	3.3929386	3.3929386	3.1595421	3.1170101	2.9533272					
2.5336666	2.6715965	2.8530483	2.7630234	2.7683067	2.7715549	2.7028866	2.6114368	2.7527428	2.7758484	2.9152298				
1.8136692	1.9302063	1.8008804	1.6039810	1.6487617	1.6857548	1.6659851	1.6611443	1.9668293	2.0802288	2.4205799	4.1648235			
2.0676384	1.9816360	1.9966049	1.8003082	1.9007072	1.9945393	2.0116425	2.0648975	2.4644127	2.6290016	3.0182819	4.1224384	6.9463997		
1.9209652	1.7310944	1.9574471	1.7649021	1.8582497	1.9951744	2.1009197	2.2155495	2.5499401	2.6650038	2.9421721	3.8302021	7.8068533	12.4839290	
0.9054108	0.8266125	1.1886635	1.0360413	1.0839691	1.2257671	1.4124765	1.5596924	1.8300867	1.9494619	2.1197109	2.7469778	7.0604353	13.6118110	17.4805740

$$U_{i,2j+1} = \cos\left(\frac{2\pi j y_i}{b-a}\right), \qquad i = 1, 2, \cdots, 15, \qquad j = 0, 1, 2, \cdots, 7.$$

Evidently $k = 3$ will suffice for the Obukhov basis, and $k = 6$ and $k = 11$ will suffice for the power and trigonometric bases, respectively.

The results of Figure 1 arise from reasonably well-chosen bases. The type of behavior to be expected for ill-chosen bases is indicated in Figure 2, where $\text{Tr } S_{UC-\eta}$ is presented for a basis consisting of a sample of random numbers uniformly distributed between -1 and $+1$ and also for the basis $U_{ij} = \delta_{ij}$. Clearly in these cases nothing less than a full complement of basis vectors (i.e., $k = m = 15$) will achieve the desired accuracy. By noting that $\text{Tr } S_{UC-\eta}$ is m times the theoretical overall mean-square error of the fit, we see that $\text{Tr } S_f = 120.407$ corresponds to an overall rms error of 2.88 and that $\text{Tr } X^{-1} = 23.946$ corresponds to an overall rms error of 1.26. This shows the extent to which the original statistics of f may be improved by using the integral equation in this particular case. The analysis presented here serves a similar purpose to the analysis of the "degree of independence" of the measurements of $g(x)$ as discussed by Twomey [2, 8]. However, in the present case the actual rms error to be expected is found and the results are necessarily dependent on the statistics S_ϵ and S_f as well as on the kernel of the integral equation.

5. *Numerical Inversion Results*

For purposes of numerical experimentation the following equation was used:

$$e^{-\alpha(x)H_0}\alpha(x)\int_0^H e^{-y/H_0}f(y)e^{\alpha(x)H_0e^{-y/H_0}}\,dy = g(x). \tag{29}$$

This equation occurs in remote atmospheric probing work if an exponential atmosphere is assumed. Here H_0 is a constant and $\alpha(x)$ is given by

$$\alpha(x) = 1.1\,x - 1 \tag{30}$$

TABLE 2. SOLUTION NO. 1 OF INTEGRAL EEQUATION, $f_c = 293.997$; SAMPLE RMS ERROR: 0.71

y	UC	$f = f_0 + UC$	f_0
.046910077	-1.220	294.02	295.24
.23076534	-1.894	293.25	295.15
.50000000	-2.687	293.86	296.55
.76923466	-3.018	295.07	298.09
.95308992	-3.075	295.03	298.10
1.0938202	-3.066	294.89	297.95
1.4615307	-2.944	294.05	297.00
2.0000000	-2.475	293.85	296.33
2.5384693	-2.155	293.60	295.75
2.9061798	-1.844	293.44	295.28
3.3283705	-1.598	293.98	295.58
4.6153574	-1.157	292.94	294.10
6.5000000	-1.779	295.16	296.94
8.3846426	-2.332	293.55	295.89
9.6716295	-2.268	294.52	296.79

for the purposes of this section. If $f = f_c = $ const. is inserted in the left-hand side of (29) and the integrations performed, the resulting right-hand side is:

$$g(x) = f_c[1 - \exp(-\alpha(x)H_0(1 - e^{-H/H_0}))]. \qquad (31)$$

Substituting (31) into (29) will, of course, give an integral equation whose correct solution is $f = f_c$. In the work reported here, the values $H = 10$, $H_0 = 5$, and $f_c = 293.997$ were assumed. To study the behavior of (29) in the presence of measurement error, random errors distributed in accordance with S_ϵ were added to $g(x)$ as given by (31) and the mean value f_0 was varied randomly from f_c in a manner determined by S_f, which is given in Table 1.

Numbers having an approximately Gaussian distribution with zero mean and covariance matrix S_f were generated internally in the computer in two stages. First, approximate random normal deviates were obtained from an existing uniform-distribution random number generator by using the central limit theorem. Then linear combinations of these random normal deviates were formed for which the covariance matrix was S_f. A check of the histogram frequencies for a sample of 9000 of the calculated random normal deviates indicated that they were essentially Gaussian.

Since the solution f simulates an atmospheric temperature profile, S_f was obtained from radiosonde data from 240 soundings during the month of August at Denver, Colorado. The matrix S_ϵ was assumed to be scalar and the values assumed will be indicated.
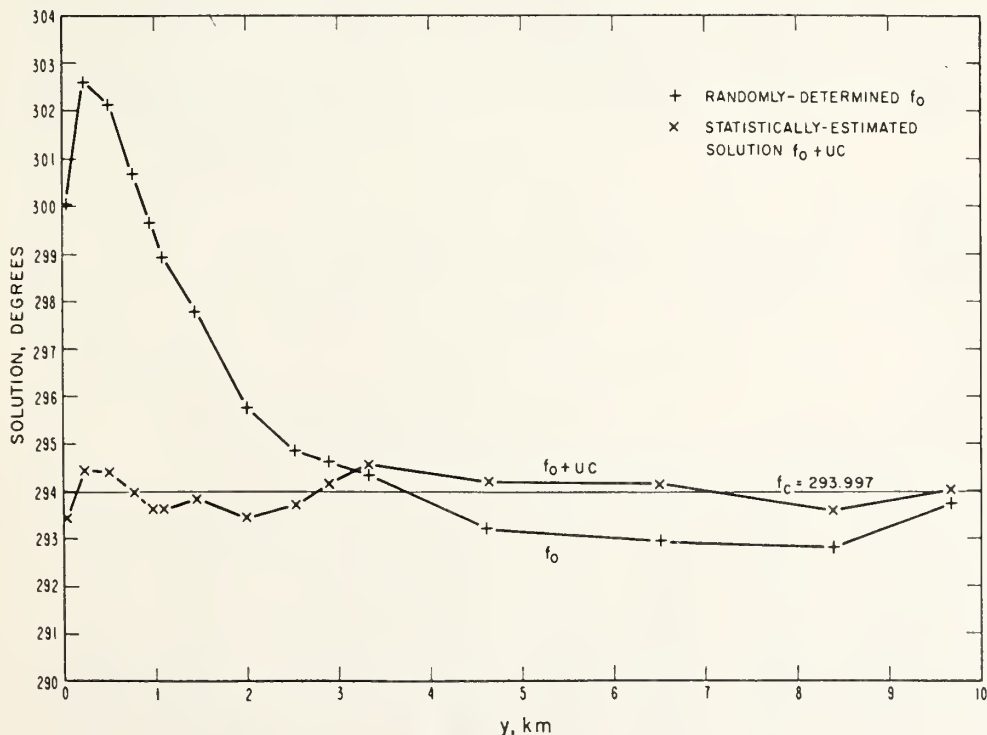

FIG. 3. Typical solution of integral equation with $S_\epsilon = 10^{-4} \cdot I$. Sample rms solution error $= 0.7$, S_f as in Table 1. $k = 5$, $n = 19$, $1 \leq x_i \leq 1.98$, Tr $X^{-1} = 12.8$.

In the simulation of errors the mean vector f_0 was varied rather than the sample vector f because the integration to give the right-hand side of (29) could then be obtained in closed form as (31), and a check on the accuracy of quadrature could also be obtained. A total of 15 quadrature abscissas were chosen; these consisted of 5 Gauss-Legendre values for each of 3 intervals: 0 to 1, 1 to 3, and 3 to 10, respectively. Intervals of different length were needed because of the general decaying-exponential character of the kernel. The interval enclosing the x_i was taken as $1 \leq x_i \leq 1.98$, $i = 1, \cdots, n$. The x_i were evenly spaced, and the values used are indicated later. Under these conditions a numerical integration with Gaussian quadrature was compared (for $f = f_c$) with (31) and the maximum quadrature error was found to be .0011 in the right-hand side, for which the actual value varied from about 103 to 292. All solutions used the classical Obukhov basis. In Table 2 results are shown for $x_i = 1(.0544 \cdots)1.98$, where the x_i are rounded to four decimal places. Here $n = 19$, $\alpha(x_i)$ is given by (30), S_f is as given in Table 1, $S_\epsilon =$

TABLE 3. TR X^{-1} FOR VARIOUS x-CONFIGURATIONS ON (1, 1.98)

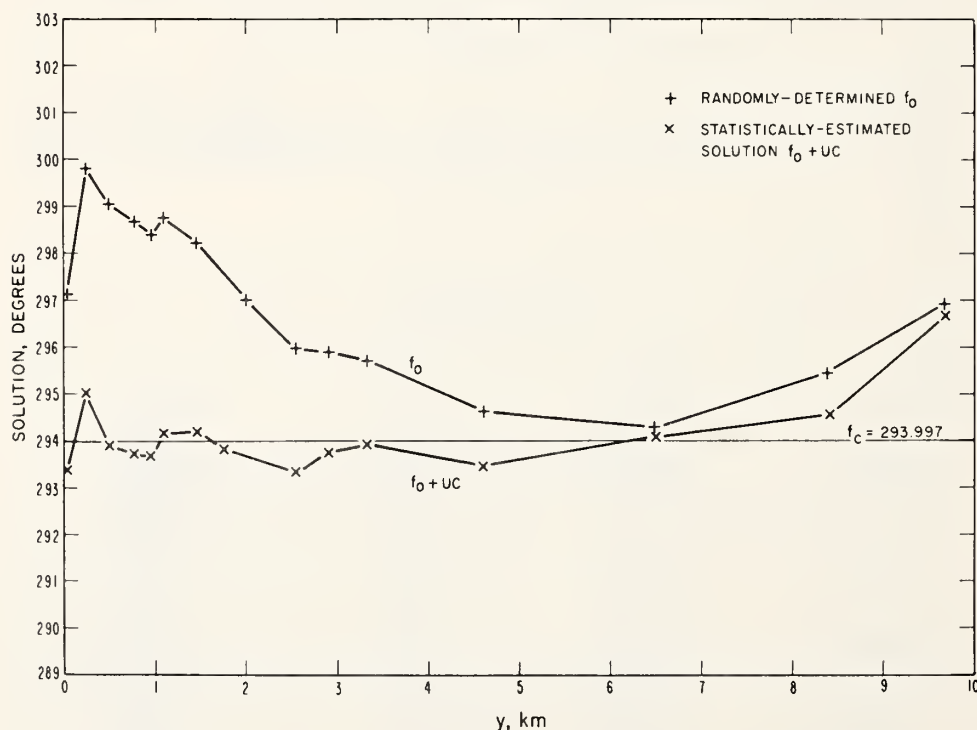| n	x_i	$Tr\ X^{-1}$	*Theoretical overall rms errors*
19	1(.0544)1.98	21.44	1.20
7	1(.1633)1.98	23.95	1.26
2	1(.98)1.98	27.45	1.35

FIG. 4. Typical solution of integral equation with $S_\epsilon = .01\ I$. Sample rms solution error = 0.8, S_f as in Table 1, $k = 4$, $n = 7$, $1 \leq x_i \leq 1.98$, Tr $X^{-1} = 23.95$.

$\sigma_\epsilon^2 I = 10^{-4} I$ and $f_c = 293.997$ as indicated. The solutions were run with $k = 5$. Under these conditions $\mathrm{Tr}\, S_{UC-\eta} = \mathrm{Tr}\, X^{-1} = 12.8$. There was some loss of accuracy in the computation, so that trace values are only good to one decimal place. These were the only trace computations for which the computation errors were noticeable; most other trace values were computed using double precision. The overall rms error corresponding to $\mathrm{Tr}\, X^{-1} = 12.8$ is .92. A solution with conditions the same as for Table 2 is shown graphically in Figure 3. The two solutions presented were selected as typical from a "run" of 40 solutions.

The index $\mathrm{Tr}\, X^{-1}$ was computed for exactly the same conditions as for the solutions of Figure 3 except that $S_\epsilon = \sigma_\epsilon^2 \cdot I = (.01) \cdot I$. Under these conditions it was found that $\mathrm{Tr}\, X^{-1} = 21.44$. Next, every second and third value of x_i was removed to give the set $x_i = 1(.1633\cdots)1.98$ where the resulting x_i were rounded to four decimals. In this case $n = 7$ and $\mathrm{Tr}\, X^{-1} = 23.95$. This is the case shown in Figure 1. It can be noted that decreasing n from 19 to 7 had very little effect on the expected error. The effect of changing n is summarized in Table 3. The theoretical rms error is not strongly influenced by n, as long as the interval $(1, 1.98)$ remains fixed. In Figure 4 we present a typical solution for the conditions of Table 3 with $n = 7$ and $k = 4$. This solution was also selected from a "run" of 40 solutions. It can be noted that the improvement of the solution over the statistical values is not as pronounced as in Figure 2, because of the increase of σ_ϵ from .01 to .1.

In order to get an indication of the behavior of the solution for an Obukhov basis when only the number of basis vectors is changed, the 40 solutions of which Figure 4 is a sample were each also rerun with $k = 1, 2, 3, 5, 6, 9, 12$, and 15 using, for this purpose, the same set of errors for each value of k. The results of Table 4, which are typical, show how the solution approaches the full-basis solution as k is increased. In the case shown here, as well as for the other 39 cases calculated, any value of k from 3 through 15 would have given essentially the same solution.

6. Summary

A method for the numerical solution of a Fredholm integral equation of the first kind is herein derived and illustrated. The calculation of the solution requires a

TABLE 4. TYPICAL SOLUTION OF INTEGRAL EQUATION FOR VARIOUS VALUES OF k WITH $n = 7$ AND $\sigma_\epsilon = 0.1$

y	$f_0 + UC$								
	$k = 1$	$k = 2$	$k = 3$	$k = 4$	$k = 5$	$k = 6$	$k = 9$	$k = 12$	$k = 15$
.047	294.218	294.016	294.012	294.126	294.072	294.070	294.072	294.072	294.072
.231	295.710	295.338	295.279	295.353	295.365	295.367	295.369	295.368	295.368
.500	294.900	294.550	294.478	294.470	294.493	294.494	294.490	294.491	294.491
.769	293.544	293.192	293.153	293.091	293.113	293.112	293.109	293.108	293.108
.953	293.395	293.104	293.095	293.020	293.038	293.037	293.035	293.034	293.034
1.094	293.115	292.895	292.902	292.822	292.834	292.833	292.833	292.832	292.832
1.462	293.033	292.937	292.979	292.892	292.887	292.886	292.891	292.891	292.891
2.000	293.146	293.219	293.305	293.241	293.217	293.217	293.220	293.221	293.221
2.538	292.684	292.936	293.068	293.033	293.004	293.004	293.004	293.003	293.003
2.906	292.432	292.786	292.933	292.922	292.894	292.895	292.890	292.889	292.888
3.328	292.639	293.118	293.293	293.310	293.287	293.288	293.280	293.281	293.281
4.615	295.179	295.953	296.155	296.246	296.275	296.275	296.287	296.287	296.287
6.500	293.284	294.923	294.845	294.931	294.952	294.951	294.942	294.942	294.942
8.385	293.519	296.201	295.528	295.559	295.553	295.552	295.545	295.545	295.545
9.672	293.805	296.935	295.811	295.780	295.757	295.758	295.761	295.761	295.761

priori knowledge of the mean, f_0, and covariance matrix, S_f, of the unknown function, f, and the covariance matrix of unbiased measurement errors, S_ϵ. In practice, f_0 and S_f may be determined from past history of f, usually in the form of direct measurements of $f(y)$ at various values of y. For example, if the solution represents the spacial distribution of some atmospheric quantity at some geographical location and time, then an analysis of available direct measurements (radiosonde data, rocket measurements, etc.) taken under similar conditions would give estimates of f and S_f. Known characteristics of the instrument which measures g in (2) can be used to estimate S_ϵ. The a priori information is combined with observed values of g to estimate f.

The algorithm for this method is described as follows. If the vector of observed values of g is g_e, we first compute $h_e = g_e - Af_0$ by (4). Then D and X are computed by (8), and the estimate UC is computed by (6). The solution for f is then given by $f = f_0 + UC$. The error covariance matrix of the solution is then obtained from (10), and the resulting mean-square error is calculated by taking the trace.

If both covariance matrices S_f and S_ϵ are scalar, our equations reduce to those of Twomey [2], where the optimum smoothing parameter γ is given by the ratio of variances between the diagonal elements of S_ϵ and S_f, respectively. The present method automatically incorporates the optimum amount of smoothing in the sense of maximum-likelihood estimation.

The trace of the error covariance matrix, $\mathrm{Tr}\, S_{UC-\eta}$, is used to estimate the precision of the solution. When $k = m$ (i.e., when the basis forms a nonsingular $m \times m$ matrix), $S_{UC-\eta}$ reduces to $X^{-1} \equiv (S_f^{-1} + A^T S_\epsilon^{-1} A)^{-1}$. The positive number $\mathrm{Tr}\, X^{-1}$ is related to the error to be expected in the solution and is used as a quality criterion. A comparison of $\mathrm{Tr}\, X^{-1}$ with $\mathrm{Tr}\, S_f$ indicates the amount of information contained in the integral equation with observation errors determined by S_ϵ. It is evident that $\mathrm{Tr}\, X^{-1}$ can be used to study optimization of the spacing of observations. Such a study could be quite valuable in planning measurement systems. To study a proposed measurement system, we require S_f, S_ϵ, and the matrix A, which represents the integral equation. Then X may be computed from (8) and X^{-1} and $\mathrm{Tr}\, X^{-1}$ can be obtained.

The method of estimation and the use of the quality criterion $\mathrm{Tr}\, X^{-1}$ were illustrated by studying the effect of various sequences of random errors on the solution of a specific integral equation. The results apparently have errors which agree with theoretical predictions, although confidence tests were not run. The effect of varying the number and type of basis vectors was also studied for this example.

REFERENCES

1. Twomey, S. On the numerical solution of Fredholm integral equations of the first kind by the inversion of the linear system produced by quadrature. *J. ACM 10* (1963), 79–101.
2. ——. The application of numerical filtering to the solution of integral equations encountered in indirect sensing measurements. *J. Franklin Inst. 279* (1965), 95–109.

3. ——— AND HOWELL, H. B.   A discussion of indirect sounding methods with special reference to the deduction of vertical ozone distribution from light scattering measurements. *Mon. Weather Rev. 91* (1963), 659–664.

4. PHILLIPS, D. L.   A technique for the numerical solution of certain integral equations of the first kind. *J. ACM 9* (1962), 84–97.

5. MATEER, CARLTON L.   On the information content of Umkehr observations. *J. Atmos. Sciences 22* (1965), 370–381.

6. ALISHOUS, J. C., CRONE, L. J., FLEMING, H. E., VAN CLEEF, F. L., AND WARK, D. Q.   A discussion of empirical orthogonal functions and their application to vertical temperature profiles. *Tellus 19*, 3 (1967), 477–482.

7. WARK, D. Q., AND FLEMING, H. E.   Indirect measurements of atmospheric temperature profiles from satellites: I. Introduction. *Mon. Weather Rev. 94*, 6 (1966), 351–362.

8. TWOMEY, S.   Indirect measurements of atmospheric temperature profiles from satellites: II. Mathematical aspects of the inversion problem. *Mon. Weather Rev. 94*, 6 (1966), 363–366.

9. DEUTSCH, RALPH.   *Estimation Theory.* Prentice-Hall, Englewood Cliffs, N. J., 1965.

10. OBUKHOV, A. M.   The statistically orthogonal expansion of empirical functions. *Akad. Nauk, SSR Izv. Seriya Geofiz.*, No. 3 (March 1960), 432–439. (English transl. by Amer. Geophys. Union, Nov. 1960, pp. 288–291.)

11. FADDEEVA, V. N.   Computational methods of linear algebra. Dover, New York, 1959, pp. 81–85.

12. COURANT, R., AND HILBERT, D.   *Methods of Mathematical Physics, Vol. 1.* Interscience, New York, 1953, pp. 23–27.

13. BECKENBACH, E. F., AND BELLMAN, R.   *Inequalities.* Springer-Verlag, Berlin, 1961, p. 69, Th. 12.

SESSION I: TECHNIQUES AND INTERPRETATION

New Developments in Doppler Radar Methods

Roger M. Lhermitte

Environmental Science Services Administration

Research Laboratories

Boulder, Colorado

I. INTRODUCTION

In the past few years, Doppler radar techniques have been extensively used for the observation and study of the motion of precipitation particles inside storms for the purpose of improving the understanding of storm physics and dynamics. However, the capability of the method for observing particles' motion field in a highly disturbed environment, such as a convective storm, has been limited by the fact that only the particles' radial velocity component is observed by a Doppler radar. Furthermore, the treatment of the Doppler information for isolating the three dimensional field of motion, requires that appropriate means, such as digital computers, be used for data reduction and analysis. These means are by necessity far more sophisticated than the techniques presently used in the analysis of conventional and Doppler weather radar data.

This paper outlines the design of a Doppler radar probing and data processing system, motivated by the recognized potential of the equipment and the recent availability of the necessary computational techniques, which is capable of providing significant advances in our understanding of convective storm processes.

II. LIMITATIONS OF A SINGLE DOPPLER RADAR

Doppler radar methods are capable of sensing only the particles' radial velocity, i.e., the velocity component projected onto the radar beam axis. Therefore, the analysis of the data provided by a single Doppler radar relies heavily on assumptions used as a substitute for the lack of knowledge of the complete vectorial velocity information. Since it is sensitive to particles' vertical velocity alone, the vertical beam method is less ambiguous and in the case of marked stratification, very useful. However, the method fails to exploit the outstanding capability of the radar technique, i.e., its ability to acquire data distributed in three coordinates of space. Time-altitude histories of particle motion have proven useful in the study of stratiform precipitation clouds, but have been of little value in interpreting convective

storm processes since restrictive assumptions involved in the technique become invalid.

The use of a single radar scanning beam is useful and effective if assumptions about statistical homogeneities of the precipitation particle motion is accepted in the analysis of the data. The most commonly used scanning scheme relies on continuous azimuth scanning of the radar beam with a programmed elevation angle stepping operation. The Doppler radial velocity is usually displayed as a function of the radar beam azimuth angle by use of appropriate indicators (velocity-azimuth-display, VAD), Lhermitte and Atlas (1961). The method is applicable to the study of the mesoscale wind field in large systems, such as widespread winter storms, and provides vertical profiles of the mean properties of the horizontal wind field (speed, direction, convergence) and the average vertical motion of the precipitation particles. However, because of the complexity and non-uniformity of their wind fields, neither the vertical beam nor the VAD method are satisfactory for observing the particles' motion field inside convective storm systems.

Donaldson (1967) has endeavored to analyze the horizontal wind field in a convective storm system from data obtained at low beam angles. Azimuth scanning at elevation angles limited to 1°, 3°, and 5° failed to reveal the storm horizontal circulation since the data were still derived from the interpretation of radial velocity alone.

The assumption that a non evolutive, three dimensional pattern of circulation is translating with the storm, Peace, et al (1968), offers means to analyze the motion field, provided that the storm can be observed from different directions by the radar during its motion. However, such assumptions are restrictive and may be questionable in the case of complex storm systems which are continuously evolving and for which translation speed and direction can not be easily observed.
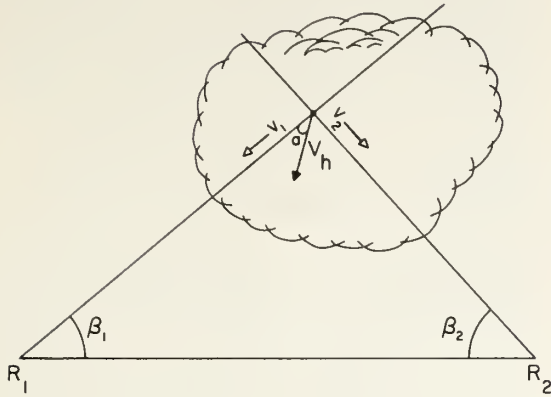
14

III. THE TWO DOPPLER RADAR METHOD

Fig.1. R_1 and R_2 are two Doppler radars.

The use of two Doppler radars, installed at different locations and simultaneously observing the same storm, drastically improves the capability of the Doppler method. Fig. 1 illustrates the concept. The same region of a storm is observed by two radars, R_1 and R_2, installed at different locations thereby providing two radial components of the particles' motion, V_1 and V_2. The two components, V_1 and V_2, can be expressed by the following equations:

$$V_1 = V_h \cos\alpha \, \cos\theta_1 + (V_t+w)\sin\theta_1 \qquad (1)$$

$$V_2 = V_h \cos(\beta_1+\beta_2-\alpha)\cos\theta_2+(V_t+w)\sin\theta_2 \qquad (2)$$

In these equations β_1 and θ_2 respectively are the azimuth and elevation angles for R_1; β_2 and θ_2 respectively are the azimuth and elevation angles for R_2; V_h is the horizontal motion speed; α is the azimuth angle between the direction of the motion and β_1; $V_t + w$, the particles' vertical velocity (V_t is the terminal speed and w the air vertical motion). If the contribution to the Doppler due to vertical motion can be neglected, i.e., $(V_t + w) \sin\theta \approx 0$, equations (1) and (2) can be solved for V_h and α according to the following expressions:

$$V_h^2 = \frac{1}{\sin^2(\beta_1+\beta_2)} \left[\frac{V_1^2}{\cos^2\theta_1} + \frac{V_2^2}{\cos^2\theta_2} + \frac{2V_1 V_2 \cos(\beta_1+\beta_2)}{\cos\theta_1 \, \cos\theta_2} \right] \quad (3)$$
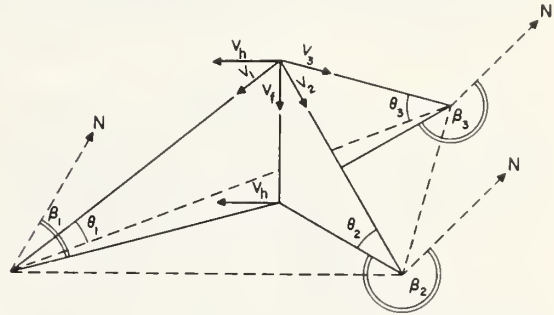
$$\tan\alpha = -\frac{1}{\sin(\beta_1+\beta_2)} \left[\frac{V_2}{V_1} \frac{\cos\theta_1}{\cos\theta_2} + \cos(\beta_1+\beta_2) \right] \quad (4)$$

The optimum spacing between the two radars depends on their characteristics but it is on the order of 20 to 60 kms.

The method offers excellent potential for mapping the particles' horizontal motion field inside convective cells for nearly horizontal radar beams. However, radar beam elevation angle smaller than 5° to 10° can be accepted in the scheme allowing the observation of the horizontal motion field up to altitudes on the order of 10,000 to 15,000 feet. The only assumption which is needed is to neglect the contribution due to particles' vertical motion. For targets which are outside of the line of sight between the two radars, the method offers accurate and non-ambiguous results which should clearly reveal convergence and vorticity patterns in the low levels of a convective storm.

If assumptions about the terminal velocity of the particles are adopted, the method can be extended to observations from larger elevation angles for which a significant contribution to the Doppler, due to the particles' vertical velocities, is likely. The method is also capable of providing estimates of the vertical air motion from convergence estimates made at several altitudes.

IV. THE THREE DOPPLER RADAR METHOD

$$\left\{ \begin{array}{l} V_1 = V_h \cos(\beta_1-\beta_0)\cos\theta_1 + V_f \sin\theta_1 \\ V_2 = V_h \cos(\beta_2-\beta_0)\cos\theta_2 + V_f \sin\theta_2 \\ V_3 = V_h \cos(\beta_3-\beta_0)\cos\theta_3 + V_f \sin\theta_3 \end{array} \right\} \quad V_f = V_T + w$$

w estimated from

$$\frac{\partial w}{\partial z} = -\left[\frac{\partial u}{\partial x} + \frac{\partial v}{\partial y} \right]$$

15

The Three Doppler Radar Method - Cont.

Although it is a reasonable step towards the design of more elaborate systems, the dual Doppler radar method described above fails to provide useful horizontal wind information for targets situated on the line of sight between the two radars. It does not provide a complete knowledge of the three dimensional field of the V_x, V_y, V_z components of the storm's particles' motion. This objective may be achieved from data collected by a well designed system of three Doppler radars, installed at three different locations which simultaneously observe the same convective storm. Fig. 2 illustrates this concept and shows that the radial velocity at a given point in space can be observed from three different directions. The system of three equations indicated in Fig. 1 provides the basis for computing the value of the three components of the motion. Therefore, by combining the radial velocity information provided by the three Doppler radars, it is indeed possible to isolate and evaluate the three dimensional distribution, in Cartesian coordinates x, y, z, of V_x, V_y, V_z. This information can be sampled periodically provided that the storm is within the maximum range of the equipment. The time and space sampling capabilities are discussed below.

As an example of the unique capability of the method, the three dimensional field of particles' motion can be analyzed in the following manner:

First, it is assumed that precipitation particles are moving in the same direction and at the same speed as the horizontal wind. This assumption is valid except when particles are falling in regions of strong wind shear which might introduce a lag of the particles' velocity with respect to the environment. This effect is negligible for most of the precipitation particles; large hailstones are a marginal case. If we accept the above assumption, the particles horizontal motion field may be taken as that of the horizontal wind. The mean speed (first moment of the velocity spectrum) must be computed to provide basis for interpreting the two dimensional field. Theoretically, the estimated horizontal motion components do not include the variance due to particles' vertical speed distribution. The data are sorted according to their x, y and z coordinates evaluated from radar polar coordinates R, β and Θ. The two dimensional estimates of the two quadratic components u and v of the estimated "wind" can then be defined at selected altitudes in the storm.

The application of the equation of continuity, within the assumption of incompressibility, to the horizontal wind field, identified convergence with the estimates of air vertical velocity gradients, ∂w/∂z. By integrating ∂w/∂z with suitable boundary conditions, it is possible to estimate, not only one vertical updraft profile, but the complete structure of updrafts inside the whole storm. Details on the structure of updrafts will be controlled by the sharpness of the velocity gradients and the inherent velocity resolution of the radar equipment.

Comparison of the updrafts structure with the three dimensional distribution of the particles' vertical velocity (and its spectrum) which is derived simultaneously from the Doppler data, provides knowledge of the distribution of particles' terminal speed within the storm. This, in turn, provides means for defining, in any region of the observed storm the precipitation particles' terminal velocities and therefore their size distribution. The method has obvious application for the monitoring and study of such important processes as hail formation; its use should provide significant improvement of our knowledge of convective storm processes and provide a firm basis for a more efficient control of their behavior.

The three Doppler radar concept is far more complicated than the usual weather radar systems presently used in meteorological research. It can operate effectively only if efficient digital computer means are used to process the data. The Doppler information must by necessity be stored in a digital format compatible with computer use.

It is impractical and time consuming for the systematic scanning of a storm to restrict the Doppler observations obtained at a given time, to the intersection of the three radar beams in space. Indeed, when the radar beam is aimed in a fixed direction, a large number of ranges can be simultaneously processed therefore adding to the Doppler information with respect to that provided by only one selected region. It is more appropriate that the radial velocity data provided by the three radars be acquired and processed separately, thereby leading to separate estimates of the three radial velocity fields. Since the process of scanning the storm will take an appreciable time, time-space interpolation techniques will be necessary to express the radial motion fields at the same time.

16

Radar beam scanning systems capable of systematically and automatically acquiring the Doppler data in limited angular regions controlled by the storm position with respect to the radar, are required for efficient use of the method. Digital control of a stepping radar beam must be preferred, as means for providing data easier to manipulate with digital computers.

V. DOPPLER SIGNAL PROCESSING REQUIREMENTS

Most of the Doppler studies of atmospheric phenomena have been done by aid of unsophisticated, time consuming, procedures of signal and data processing which have severely limited the analysis of the data and the use of the method to its fullest capability.

Recently, signal and data processing methods have been drastically improved through the increased availability of modern general purpose digital computers and also by the introduction of special purpose processing systems based on the use of modern digital hardware such as integrated circuits. The practicality of the three-Doppler-radar method, with its high rate of information flow, draws benefit from the availability of modern digital methods for the processing and storing of the Doppler radar information.

The most time consuming requirement, for Doppler radar information processing, is that of the power density spectrum analysis of a radar signal, simultaneously at a large number of different ranges. The transformation required is a conventional Fourier transform or an equivalent method such as the processing of the signal by use of analog type frequency analyzers. Through applications of digital techniques, computations of the signal power density spectrum are more efficient and also more flexible. The digital approach provides N non redundant frequency samples from N time samples, thus requiring that N^2 multiplications be done per complete spectrum. If we recognize that 256 time samples are fairly representative of the spectral information in a time signal, then 70,000 multiplications must be done for each conventional Fourier transform. With modern fast digital computers the computing time will be of the order of, or less than, one second; this is comparable to the signal dwell time required to build an acceptable knowledge of the spectrum. Therefore, real-time digital computations by conventional Fourier algorithms are, at least, as effective as the classical method using a bank of filters. In addition, the digital computer offers complete flexibility in the choice of appropriate frequency filter characteristics and frequency coverage which is controlled by the signal sampling rate. Since it is based on the nonequivocal Fourier transform mathematical expression, the digital frequency analyzer provides a well defined answer for the spectral density estimates, which is easier to manipulate in the analysis of the data.

The use of fast Fourier transform algorithms (Cooley and Tukey, 1965) decreases the required number of multiplications to $2 N \log_2 N$ instead of N^2. This considerably reduces computation time to much less than signal dwell time, thereby making it feasible to process several radar ranges in a time less than a few seconds. This involves the use of high speed, elaborate signal processing systems for the multiplexing, and the analog to digital conversion, of the Doppler signal. It also requires core memories which are organized in such a way that the sequence of the Fourier transforms can be easily computed, range after range, from the stored digital data. Such systems can be built at an acceptable cost by use of modern integrated circuit digital hardware.

These systems are capable of a data acquisition speed which matches the requirements indicated by the estimated time evolution of a convective storm. We must remember, however, that the scanning rate of the radar antenna will still be a limiting factor for high speed data acquisition systems.

CONCLUSION

This paper has been written to discuss the importance of a three-Doppler radar methodology for the study of convective storm processes. It is the author's opinion that such an endeavor will contribute to the study and understanding of the storm's processes in a manner which could not be attained by any other observational means.

References

Cooley & Tukey, 1965: An algorithm for the machine calculations of complex Fourier series. Math. of Computation, 19, 297-301.

Donaldson, R., 1967: Horizontal wind Measurement by Doppler radar in a severe squall line, Proc. Conf. on Severe Local Storms, St. Louis, pp. 89-98.

Lhermitte & Atlas, 1961: Precipitation motion by pulse Doppler radar, Proc. 9th Wea. Radar Conf., pp. 218-223.

Peace, R., et al, 1968: Horizontal Motion Field Observations with a single Pulse Doppler Radar, Cornell Aero. Lab. Report.